BEILSTEIN JOURNAL OF NANOTECHNOLOGY

Energy conversion, storage and environmental remediation using nanomaterials

Edited by Wee-Jun Ong, Xiaobo Chen and Rengui Li

Generated on 02 October 2026, 00:41

Imprint

Beilstein Journal of Nanotechnology
www.bjnano.org
ISSN 2190-4286
Email: journals-support@beilstein-institut.de

The *Beilstein Journal of Nanotechnology* is published by the Beilstein-Institut zur Förderung der Chemischen Wissenschaften.

Beilstein-Institut zur Förderung der Chemischen Wissenschaften
Trakehner Straße 7–9
60487 Frankfurt am Main
Germany
www.beilstein-institut.de

The copyright to this document as a whole, which is published in the *Beilstein Journal of Nanotechnology*, is held by the Beilstein-Institut zur Förderung der Chemischen Wissenschaften. The copyright to the individual articles in this document is held by the respective authors, subject to a Creative Commons Attribution license.

BEILSTEIN JOURNAL OF NANOTECHNOLOGY

Enhanced photoelectrochemical water splitting performance using morphology-controlled $BiVO_4$ with W doping

Xin Zhao and Zhong Chen*

Full Research Paper

Open Access

Address:
School of Materials Science and Engineering, Nanyang Technological University, 50 Nanyang Avenue, 639798, Singapore, Singapore

Email:
Zhong Chen* - ASZChen@ntu.edu.sg

* Corresponding author

Keywords:
bismuth vanadate; charge separation; nanostructure; photoelectrochemical water splitting

Beilstein J. Nanotechnol. **2017,** *8,* 2640–2647.
doi:10.3762/bjnano.8.264

Received: 06 September 2017
Accepted: 14 November 2017
Published: 07 December 2017

This article is part of the Thematic Series "Energy conversion, storage and environmental remediation using nanomaterials".

Guest Editor: W.-J. Ong

© 2017 Zhao and Chen; licensee Beilstein-Institut.
License and terms: see end of document.

Abstract

Nanostructures exhibit numerous merits to improve the efficiency in solar-to-energy conversion. These include shortened carrier collection pathways, an increased volume ratio between depletion layer and bulk, enhanced light capture due to multiple light scattering in nanostructures, and a high surface area for photochemical conversion reactions. In this study, we describe the synthesis of morphology-controlled W-doped $BiVO_4$ by simply tuning the solvent ratio in precursor solutions. Planar and porous W-doped $BiVO_4$ thin films were prepared and compared. The porous film, which exhibits increased surface area and enhanced light absorption, has displayed enhanced charge separation and interfacial charge injection. Our quantitative analysis showed an enhancement of about 50% of the photoelectrochemical performance for the porous structure compared to the planar structure. This enhancement is attributed to improved light absorption (13% increase), charge separation (14% increase), and interfacial charge injection (20% increase).

Introduction

Solar hydrogen generation is one of the most promising approaches to create clean energy and to overcome the environmental problems associated with use of conventional fossil fuels. Photoelectrochemical (PEC) water splitting generates hydrogen through chemical reactions assisted by photo-generated electrons and holes in semiconductor materials [1-3]. An ideal semiconductor for PEC water splitting requires a small bandgap to capture enough solar light, a high conversion efficiency, a good durability in aqueous environments, as well as low production cost [4]. Compared with the hydrogen evolution at the semiconductor photocathode, the low efficiency of oxygen evolution at the photoanode poses a great challenge to the water splitting process [5]. As a result, great efforts have been made in developing photoanode materials and optimizing their performance. Monoclinic $BiVO_4$ is one of the most promising photoanode materials for PEC water splitting, as it meets

most of the requirements. It has a theoretical conversion efficiency of 9.1% with a bandgap of 2.4 eV. Moreover, it also possesses a favorable conduction band potential that is very close to the reduction potential of water, and a proper valance band that is more positive than the water oxidation potential [6-10].

One of the problems associated with $BiVO_4$ is its relatively short minority carrier diffusion length, which ultimately affects the solar-to-hydrogen efficiency. Nanostructured materials have been often employed to overcome this limitation [11], as they can shorten the carrier collection distance and increase the volume ratio between depletion layer and bulk. In addition, they also offer a high surface area for chemical reactions and enhance light capture due to multiple light scattering within the nanostructures [11-13]. Many research works have been reported for enhanced PEC water splitting performances using nanostructured $BiVO_4$ [5,6,12,14-19]. However, most of them require complex processes. Moreover, there has been no report about a facile process capable of continually adjusting the coating morphology from planar to porous structures for doped $BiVO_4$.

In this study, we report the synthesis of a morphologically controlled W-doped $BiVO_4$ by simply tuning the composition of the precursor solution. Considering the poor electron conductivity of $BiVO_4$, which leads to a poor photoelectrochemical performance (see Figure S1, Supporting Information File 1), we employed tungsten as a doping element because it has a higher valence than vanadium and an ionic radius close to that of vanadium. By changing the solvent ratio, planar and porous nanostructured W-doped $BiVO_4$ thin films were prepared. The photocurrent of the porous W-doped $BiVO_4$ is ca. 50% higher than that of planar W-doped $BiVO_4$. We have analyzed this improvement quantitatively with regard to contributions from light absorption, charge separation and interfacial charge injection. The quantitative analysis provides a powerful insight into the materials potentials and limitations, and is useful for the development of other PEC systems in the future.

Results and Discussion

The synthesis of W-doped $BiVO_4$ thin films was carried out by drop-casting of metal organic precursors with different volume ratios of water to ethylene glycol (EG). The morphologies of the obtained films are shown in Figure 1. An overview of the synthesis conditions and the corresponding sample labels can be found in Table 1. A detailed description of the syntheses can be found in the Experimental section. The films in Figure 1a–c were prepared using EG precursor solutions containing 0.5 mL EG solution of V, 0.5 mL EG solution of Bi, 0.015 mL EG solution of W, and 0.15 mL EG solution of citric acid (CA) to which 2 mL of a mixture of water and EG with different volume ratios was added.

As shown in Figure 1a–c, the films prepared have a largely planar structure. With increasing water content, small pores emerge with a diameter of ca. 50 nm. Films prepared using water precursor solutions (Figure 1d–f) show nanoporous structures. With increasing EG content, the pore size decreases. The film prepared from the water-based solution with the smallest amount of EG (0.5-EG) exhibits cracks in the film (Figure S2, Supporting Information File 1) and has poor adhesion to the substrate.

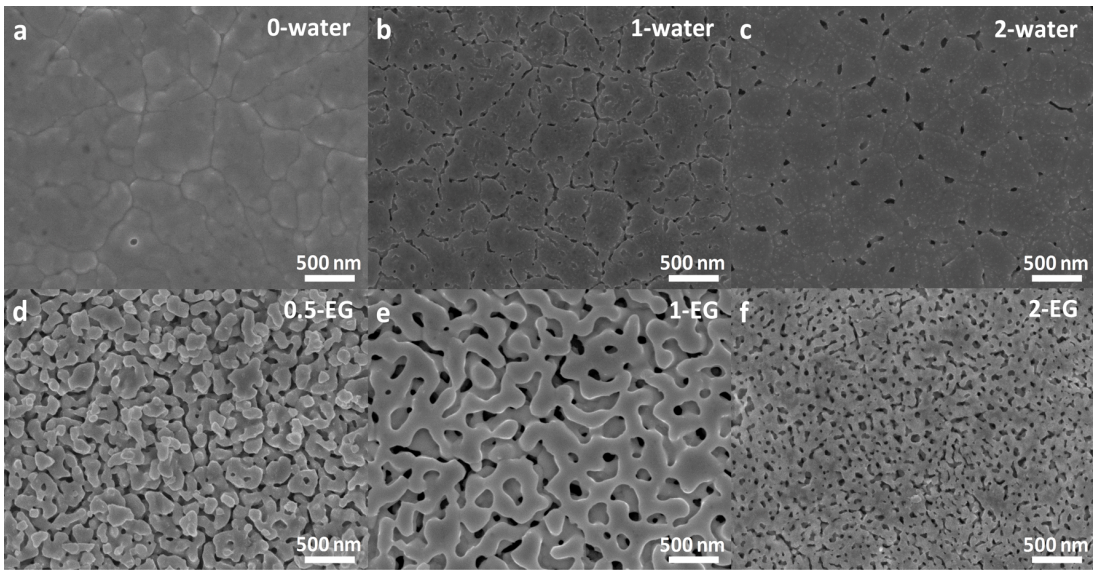

Figure 1: SEM images of W-doped $BiVO_4$ thin films with different ratios of water to EG.

Table 1: Elaboration of all samples with different precursors and water-to-EG ratio.

sample	0.1 M Bi EG solution (μL)	0.1 M V EG solution (mL)	0.1 M W EG solution (mL)	1 M CA EG solution (μL)	water (mL)	EG (mL)
0-water	0.500	0.485	0.015	150	0	2.0
1-water	0.500	0.485	0.015	150	1.0	1.0
2-water	0.500	0.485	0.015	150	2.0	0
	0.1 M Bi water solution (mL)	0.1 M V water solution (mL)	0.1 M W EG solution (mL)	1 M CA water solution (μL)	water (mL)	EG (mL)
0.5-EG	0.500	0.485	0.015	150	1.5	0.5
1-EG	0.500	0.485	0.015	150	1.0	1.0
2-EG	0.500	0.485	0.015	150	0	2.0

The sol–gel method allows reagents to be mixed at the atomic/molecular level, which can increase the reaction rate and, thus, is very suitable for homogenous doping. In this study, it was successfully employed in preparing W-doped $BiVO_4$ films with the following sequences. First, a mixture of cations is formed with the aid of an organic complexing agent, citric acid and EG solution. Second, the cations are chelated and form a polymeric resin when dried. Finally, this resin decomposes at high temperatures and forms the targeted W-doped $BiVO_4$ films [20]. Jaramillo et al. reported that the ambient humidity affects the rate of both hydrolysis and polycondensation reactions and solvent evaporation, which causes a morphology change of the $BiVO_4$ films [18]. We assume that, in our study, the mixture of precursors from different (water or EG) solutions affects the chelate formation and polycondensation, which has great influence on the morphology of the obtained films.

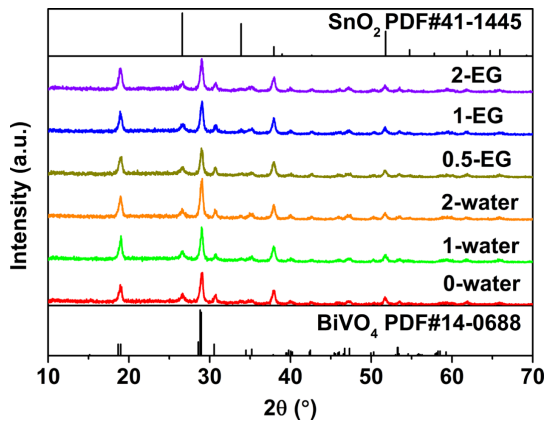

Figure 2: X-ray diffraction patterns of as prepared W-doped $BiVO_4$ films.

X-ray diffraction was used to characterize the crystal structure of the obtained films. Figure 2 shows that all peaks agree well with the ones of $BiVO_4$ (PDF#14-0688). No peaks belonging to other phases were present except the ones from the fluorine-doped tin oxide (SnO_2) substrate. This demonstrates $BiVO_4$ thin films can be successfully synthesized by the sol–gel method. Elemental analysis was also performed to confirm the composition. To simplify the test, two typical samples, 0-water and 1-EG, were selected for the EDX analysis. The results were shown in Table S1 and Table S2 of Supporting Information File 1. Both samples have almost the same composition, the Bi/V/W/O ratio is 1:0.88:0.03:3.45 for the 0-water sample, and Bi/V/W/O is 1:0.88:0.035:3.4 for the 1-EG sample. The stoichiometric ratio agrees with the one for $BiVO_4$, and the dopant concentration is about 3%.

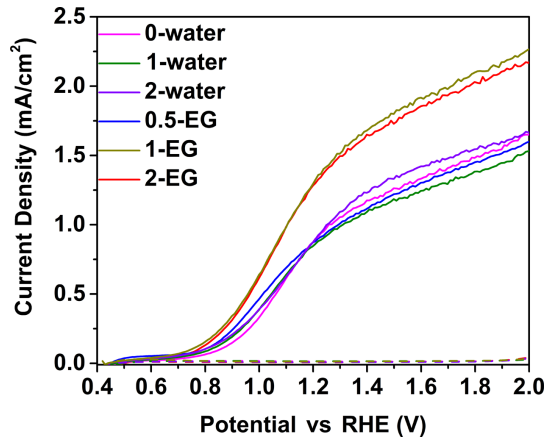

Figure 3: Photocurrents of W-doped $BiVO_4$ thin films with different ratios between water and EG.

Figure 3 shows the photocurrents of W-doped $BiVO_4$ photoanodes with different morphologies according to Figure 1. The samples prepared using EG precursors have lower photocurrents (around 1 mA/cm^2 at 1.23 V vs RHE). This is because they mainly display a planar structure (Figure 1a–c), while the samples prepared using water precursor have a nanoporous structure and a better performance (around 1.5 mA/cm^2 at 1.23 V vs RHE). This corresponds to an increase of ca. 50%.

The exception is sample 0.5-EG. As mentioned before, the sample 0.5-EG has poor adhesion and many cracks leading to a poor connection between the sample and the conductive FTO substrate and a worse performance than the other two samples (1-EG, 2-EG).

In the following, we attempt to quantify the contributions from light absorption, charge separation, and charge injection across the electrode/electrolyte interface. These three factors contribute to the water oxidation photocurrent, which is expressed by Equation 1 [21],

$$J_{H_2O} = J_0 \cdot \eta_{abs} \cdot \eta_{sep} \cdot \eta_{inj} = J_{abs} \cdot \eta_{sep} \cdot \eta_{inj}, \quad (1)$$

where J_{H2O} is the total water splitting photocurrent, J_0 is the theoretical solar photocurrent assuming that all solar energy corresponding to the band edge can be fully converted to fuel energy (7.3 mA/cm^2 for $BiVO_4$), η_{abs} is the light absorption efficiency, η_{sep} is the charge separation efficiency for photogenerated electrons and holes, and η_{inj} is the interfacial charge injection efficiency for water oxidization. J_{abs} is the maximum photocurrent of a given photoanode based on its light absorption efficiency.

In order to quantify the contributions of the nanostructured W-doped $BiVO_4$ in comparison with the planar structure, two representative samples with planar and nanoporous structure, 0-water and 1-EG, were selected. Figure 4 shows the light absorption efficiency of the samples 0-water and 1-EG by measuring the light transmittance and reflectance [12]. The porous structure indeed enhances the light absorption efficiency compared with the planar structure. According to the light absorption efficiencies, J_{abs} is calculated to be 3.86 mA/cm^2 and 4.38 mA/cm^2 for planar and porous W-doped $BiVO_4$, respectively. This means that light absorption enhancement due to the porous structure contributes a 13% increase to J_{abs}.

The oxidation of water is known to have slow oxidation kinetics. To probe the photoelectrochemical properties, an effective hole scavenger, Na_2SO_3, was added to the electrolyte. The interfacial charge injection efficiency can be approximated to be 100% (η_{inj} = 1) due to the fast oxidation kinetics of Na_2SO_3 [21]. Under such an approximation, the photocurrent measured with Na_2SO_3 electrolyte can be determined by [21]:

$$J_{Na_2SO_3} = J_0 \cdot \eta_{abs} \cdot \eta_{sep} = J_{abs} \cdot \eta_{sep}, \quad (2)$$

where J_{Na2SO3} is the oxidation photocurrent using Na_2SO_3. From Equation 1 and Equation 2, we obtain the charge separation efficiency $\eta_{sep} = J_{Na2SO3}/J_{abs}$ and the charge injection efficiency $\eta_{inj} = J_{H2O}/J_{Na2SO3}$.

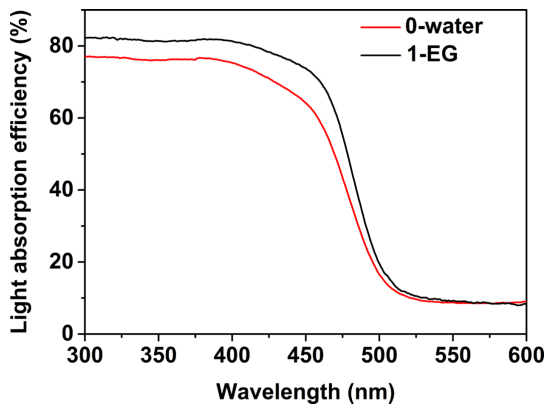

Figure 4: Light absorption efficiency of W-doped $BiVO_4$ with planar (0-water) and nanoporous structure (1-EG).

Figure 5a shows the oxidation photocurrent density of Na_2SO_3 of the sample 1-EG with porous structure at 1.23 V vs RHE (2.06 mA/cm^2) is 30% higher than that of the planar sample 0-water (1.58 mA/cm^2). The calculated values of η_{sep} and η_{inj} of the planar and porous W-doped $BiVO_4$ are shown in Figure 5b and 5c. η_{sep} at 1.23 V vs RHE of the planar and porous W-doped $BiVO_4$ are, respectively, 41% and 47%, representing a 14% increase by the nanostructure formation. η_{inj} at 1.23 V vs RHE of the planar and porous W-doped $BiVO_4$ are, respectively, 55% and 66%, corresponding to a 20% increase by the nanostructure formation. It has been reported that porous structures can shorten the hole diffusion distance to the surface and, thus, enhance the charge separation efficiency close to 60% at 1.23 V vs RHE [12]. Our finding is consistent with the report.

Mott–Schottky plots of W-doped $BiVO_4$ with planar (0-water) or nanoporous structure (1-EG) were obtained to investigate the carrier density (Figure 6a). The positive Mott–Schottky slopes indicate electrons as the majority carriers. The carrier density can be estimated by Equation 3 [22]:

$$N_d = \left(2/e_0 \varepsilon \varepsilon_0 A^2\right)\left[\mathrm{d}\left(1/C^2\right)/\mathrm{d}V\right], \quad (3)$$

where e_0 is the electron charge ($1.60 \cdot 10^{-19}$ C), ε is the dielectric constant of $BiVO_4$ (68) [23,24], ε_0 is the electrical permittivity of vacuum ($8.85 \cdot 10^{-12}$ F·m^{-1}), A is the electrode area, N_d is the donor density, V is the potential applied at the electrode, and C is the surface capacitance calculated from the electrochemical impedance measured in the dark. The carrier densities of W-doped $BiVO_4$ with planar (0-water) and

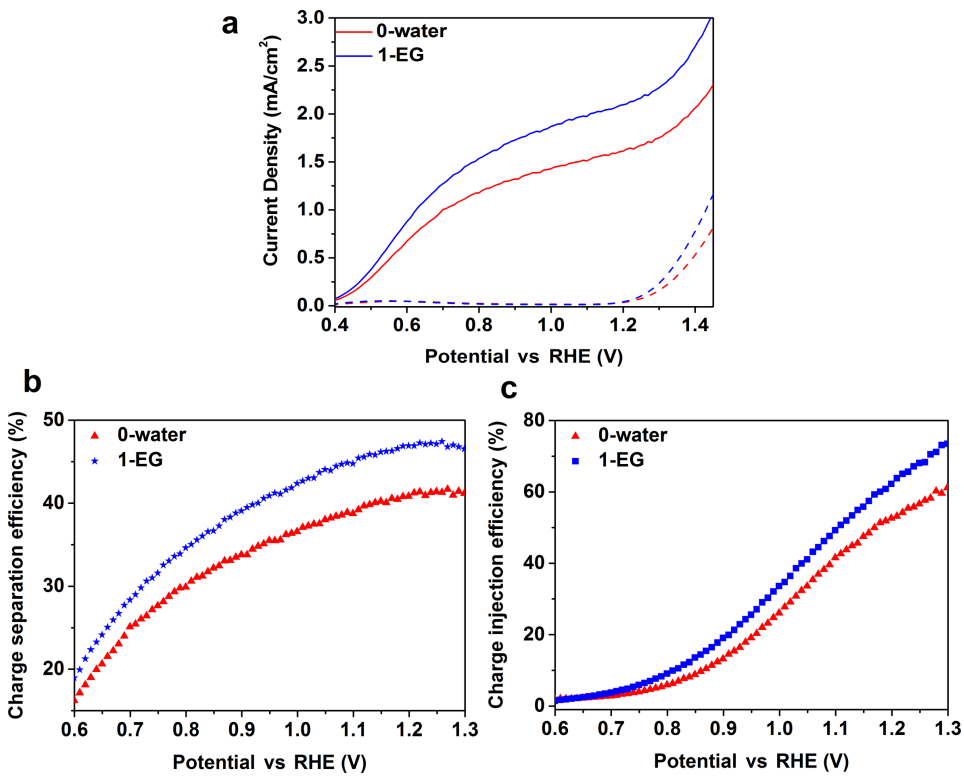

Figure 5: (a) Photocurrents of the samples 0-water and 1-EG measured with hole scavenger Na_2SO_3. Dark currents are shown as dashed lines. (b) Charge separation efficiency and (c) charge injection efficiency of the samples 0-water and 1-EG.

nanoporous (1-EG) structure were found to be $3.7 \cdot 10^{20}$ cm^{-3} and $3.3 \cdot 10^{20}$ cm^{-3}, respectively. This indicates that the structure difference has little effect on the carrier densities, which is understandable since the doping content of W is the same for both samples.

Figure 6b shows the Nyquist plots of W-doped $BiVO_4$ with planar (0-water) and nanoporous (1-EG) structure at the applied potential of 1.23 V vs RHE, which provides information on the charge injection process at the interface. Only one semicircle was observed for both samples, and the radius of the semicircle of the planar sample is larger than that of the nanoporous sample. This indicates that the planar sample has a larger surface resistance. According to a previous report, an equivalent circuit is taken to analyze the surface charge injection (inset in Figure 6b) [25]. In the equivalent circuit, R_s represents the sum of resistance values of the FTO film, the external electrical contacts, and the liquid electrolyte; R_{ct} and C_{bulk} represent, respectively, the direct charge transfer resistance, and a capacitance at the semiconductor/electrolyte interface. The value of R_s, around 40 Ω, is independent of the film structure. The capacitance of the sample 0-water with planar structure is about $2.27 \cdot 10^{-5}$ F, while that of the porous sample 1-EG is about $3.21 \cdot 10^{-5}$ F. The difference in the surface capacitance indicates that porous structure provides more surface area, about 2.13-times that of the planar structure (Figure 6c). This is determined based on the capacitive region of the cyclic voltammograms (Figure S3, Supporting Information File 1) according to Jaramillo's method [26]. The nanoporous structure forms more surface depletion layers, which leads to a higher capacitance. The surface charge transfer resistance of the sample 0-water is about 3783 Ω, while the one of sample 1-EG is smaller at around 2629 Ω. The smaller charge transfer resistance leads to a higher interfacial charge injection efficiency for water oxidation as shown in Figure 5c. It was reported that a porous film with a larger surface area has led to a lower interfacial charge transfer efficiency for water oxidation than its dense counterpart [12]. The current work indicates an opposite trend in that the surface charge injection was improved by the formation of the nanoporous structure. This reason for such an opposite tread remains unknown, and requires further work in the future. We suspect different synthesis methods may have a greater influence on the surface states, which leads to different charge transfer efficiencies.

Conclusion

Morphologically controlled W-doped $BiVO_4$ films with planar and porous structures were prepared by simply tuning the sol-

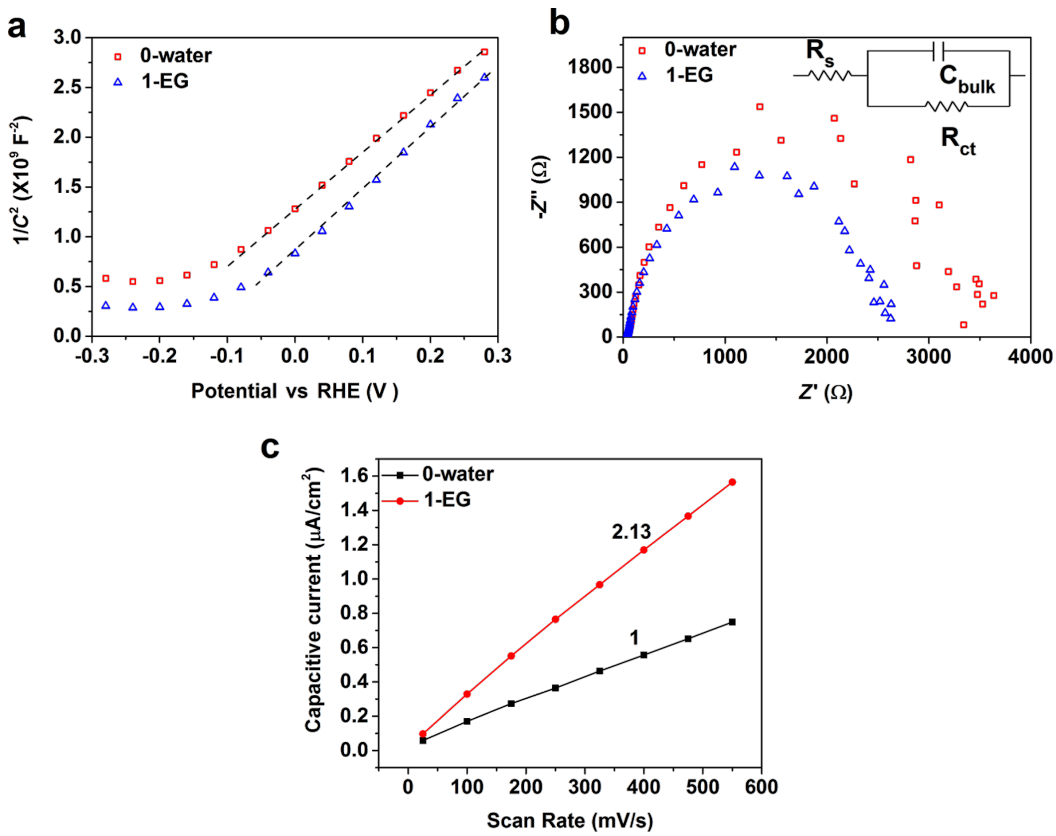

Figure 6: (a) Mott–Schottky plots of W-doped $BiVO_4$ with planar (0-water) and nanoporous (1-EG) structure measured at the frequency of 1 kHz in 0.5 M Na_2SO_4 aqueous solution. (b) Electrochemical impedance spectra of W-doped $BiVO_4$ with planar (0-water) and nanoporous (1-EG) structure at the applied potential of 1.23 V vs RHE under simulated solar illumination in 0.5 M Na_2SO_4 electrolyte. Inset is the equivalent circuit employed to fit the experimental EIS data. (c) Relative electrochemical surface area.

vent composition during the preparation of the precursor solution. A nearly 50% photocurrent enhancement has been observed due to the formation of the porous structure. The porous structure enhances the light absorption as well as the charge separation due to the short hole diffusion path to the surface. The porous structure also provides more surface reaction sites, estimated to be ca. two times that of the planar film. The surface charge transfer resistance of W-doped $BiVO_4$ has been found to decrease for the porous film compared with the planar one, which leads to an enhancement in the interfacial charge injection efficiency. The quantitative analysis shows that three factors contribute to the photoelectrochemical performance enhancement: 13% from enhanced light absorption, 14% from improved charge separation and 20% from increased interfacial charge injection.

Experimental

Sample preparation: Bismuth trioxide, ammonium metavanadate and ammonium tungstate hydrate were dissolved in water or ethylene glycol (EG) with proper amounts of nitric acid to form 0.1 M precursor solutions of Bi, V and W in water or EG. The first three samples were prepared using precursor solutions of Bi, V and W in EG. The solutions were mixed according to the stoichiometric ratio (Bi/V/W = 100:97:3 corresponding to volume a ratio of 500 μL:485 μL:15 μL) for 3% W-doped $BiVO_4$. Citric acid (CA) was also added according to a stoichiometric ratio of CA/M = 1.5:1 (M is the total amount of cations). To the mixture different amounts of water or EG were added as follows: to sample 1 0 mL water and 2 mL EG were added (denoted as 0-water); to sample 2 1 mL water and 1 mL EG solution were added (denoted as 1-water); to sample 3 2 mL water and 0 mL EG solution were added (denoted as 2-water).

Samples 4–6 were prepared using precursors solutions of Bi and V in water and of W in EG. The solutions were mixed first, with a volume ratio of Bi/V/W = 500 μL:485 μL:15 μL. Similar to the case above, to the mixture different amounts of water or EG were added: to sample 4 1.5 mL water and 0.5 mL EG were added (denoted as 0.5-EG); to sample 5 1 mL water and 1 mL EG were added (denoted as 1-EG); to sample 6 0 mL water and 2 mL EG were added (denoted as 2-EG). Detailed information is provided in Table 1. After mixing, 60 μL of the

precursor solution were dropped on 1 × 1 cm^2 FTO substrates (1 cm × 2 cm with half of the length covered by thermal tape). The samples were dried at 120 °C for 30 min, and after tearing off the tape the films were subsequently calcined at 500 °C for 2 h in a furnace.

Characterization: The morphologies were observed using a field-emission scanning electron microscope (FESEM, JEOL JSM-7600F). Crystallinity was identified by X-ray diffraction (XRD) patterns (Shimadzu 6000 X-ray diffractometer) with Cu Kα radiation (λ = 0.154 nm), using a 2θ scan mode with a fixed incidence angle at 5°. Elemental analysis was conducted by energy-dispersive X-ray spectroscopy (EDX) equipped on a field-emission scanning electron microscopy (FESEM, JEOL JSM-7600F). Light absorption was measured using a UV–visible spectrophotometer by measuring the reflectance and transmittance with an integrating sphere (Lambda 950, Perkin-Elmer). Photoelectrochemical performance was evaluated using a three-electrode configuration (PCI4/300™ potentiostat with PHE200™ software, Gamry Electronic Instruments, Inc.), with the W-doped $BiVO_4$ thin film as the working electrode, a Pt foil as a counter electrode, and a Ag/AgCl electrode as a reference electrode. The light source for photoelectrochemical water splitting measurement is a solar simulator (HAL-320, Asahi Spectra Co., Ltd.) with a power intensity of 100 $mW \cdot cm^{-2}$. The photocurrent was measured in a 0.5 M Na_2SO_4 aqueous solution with a scan rate of 30 $mV \cdot s^{-1}$. The photocurrents with hole scavenger was measured in a 0.5 M Na_2SO_4 aqueous solution with 0.1 M Na_2SO_3. Electrochemical impedance spectroscopy (EIS) measurements were carried out under illumination of an AM 1.5G solar simulator in a 0.5 M Na_2SO_4 electrolyte at the applied potential of 1.23 V vs RHE using a PCI4/300™ potentiostat (Gamry Electronic Instruments, Inc.). The Mott–Schottky measurements were carried out using an AUTOLAB Potentiostat-Galvanostat (AUTOLAB PGSTAT302 N) at a fixed frequency of 1 kHz in 0.5 M Na_2SO_4 aqueous solution.

Supporting Information

Supporting Information features photocurrent measurements of pristine BiVO4, an SEM image of the sample 0.5-EG, cyclic voltammograms of porous and planar films, and elemental analyses of the samples 0-water and 1-EG by EDX.

Supporting Information File 1

Additional experimental data.
[http://www.beilstein-journals.org/bjnano/content/supplementary/2190-4286-8-264-S1.pdf]

Acknowledgements

Financial support from Ministry of Education (grant RG15/16), Nanyang Technological University (SUG), and Singapore National Research Foundation through the Singapore-Berkeley Initiative for Sustainable Energy (SINBERISE) CREATE Programme are gratefully acknowledged.

References

1. Walter, M. G.; Warren, E. L.; McKone, J. R.; Boettcher, S. W.; Mi, Q.; Santori, E. A.; Lewis, N. S. *Chem. Rev.* **2010,** *110,* 6446–6473. doi:10.1021/cr1002326
2. Li, Z.; Luo, W.; Zhang, M.; Feng, J.; Zou, Z. *Energy Environ. Sci.* **2013,** *6,* 347–370. doi:10.1039/C2EE22618A
3. Grätzel, M. *Nature* **2001,** *414,* 338–344. doi:10.1038/35104607
4. Sivula, K.; Le Formal, F.; Grätzel, M. *ChemSusChem* **2011,** *4,* 432–449. doi:10.1002/cssc.201000416
5. Rao, P. M.; Cai, L.; Liu, C.; Cho, I. S.; Lee, C. H.; Weisse, J. M.; Yang, P.; Zheng, X. *Nano Lett.* **2014,** *14,* 1099–1105. doi:10.1021/nl500022z
6. Kim, T. W.; Choi, K.-S. *Science* **2014,** *343,* 990–994. doi:10.1126/science.1246913
7. Abdi, F. F.; Han, L.; Smets, A. H. M.; Zeman, M.; Dam, B.; van de Krol, R. *Nat. Commun.* **2013,** *4,* No. 2195. doi:10.1038/ncomms3195
8. Luo, W.; Yang, Z.; Li, Z.; Zhang, J.; Liu, J.; Zhao, Z.; Wang, Z.; Yan, S.; Yu, T.; Zou, Z. *Energy Environ. Sci.* **2011,** *4,* 4046–4051. doi:10.1039/c1ee01812d
9. Chen, F.; Yang, Q.; Li, X.; Zeng, G.; Wang, D.; Niu, C.; Zhao, J.; An, H.; Xie, T.; Deng, Y. *Appl. Catal., B: Environ.* **2017,** *200,* 330–342. doi:10.1016/j.apcatb.2016.07.021
10. Chen, F.; Yang, Q.; Zhong, Y.; An, H.; Zhao, J.; Xie, T.; Xu, Q.; Li, X.; Wang, D.; Zeng, G. *Water Res.* **2016,** *101,* 555–563. doi:10.1016/j.watres.2016.06.006
11. Li, Z.; Feng, J.; Yan, S.; Zou, Z. *Nano Today* **2015,** *10,* 468–486. doi:10.1016/j.nantod.2015.06.001
12. Zhao, X.; Luo, W.; Feng, J.; Li, M.; Li, Z.; Yu, T.; Zou, Z. *Adv. Energy Mater.* **2014,** *4,* 1301785. doi:10.1002/aenm.201301785
13. Cho, I. S.; Chen, Z.; Forman, A. J.; Kim, D. R.; Rao, P. M.; Jaramillo, T. F.; Zheng, X. *Nano Lett.* **2011,** *11,* 4978–4984. doi:10.1021/nl2029392
14. McDonald, K. J.; Choi, K.-S. *Energy Environ. Sci.* **2012,** *5,* 8553–8557. doi:10.1039/c2ee22608a
15. Berglund, S. P.; Flaherty, D. W.; Hahn, N. T.; Bard, A. J.; Mullins, C. B. *J. Phys. Chem. C* **2011,** *115,* 3794–3802. doi:10.1021/jp1109459
16. Su, J.; Guo, L.; Bao, N.; Grimes, C. A. *Nano Lett.* **2011,** *11,* 1928–1933. doi:10.1021/nl2000743
17. Pihosh, Y.; Turkevych, I.; Mawatari, K.; Asai, T.; Hisatomi, T.; Uemura, J.; Tosa, M.; Shimamura, K.; Kubota, J.; Domen, K.; Kitamori, T. *Small* **2014,** *10,* 3692–3699. doi:10.1002/smll.201400276
18. Chakthranont, P.; Seitz, L. C.; Jaramillo, T. F. *J. Phys. Chem. Lett.* **2015,** *6,* 3702–3707. doi:10.1021/acs.jpclett.5b01587
19. Chen, F.; Yang, Q.; Sun, J.; Yao, F.; Wang, S.; Wang, Y.; Wang, X.; Li, X.; Niu, C.; Wang, D.; Zeng, G. *ACS Appl. Mater. Interfaces* **2016,** *8,* 32887–32900. doi:10.1021/acsami.6b12278
20. Vaqueiro, P.; López-Quintela, M. A. *Chem. Mater.* **1997,** *9,* 2836–2841. doi:10.1021/cm970165f
21. Dotan, H.; Sivula, K.; Grätzel, M.; Rothschild, A.; Warren, S. C. *Energy Environ. Sci.* **2011,** *4,* 958–964. doi:10.1039/C0EE00570C

22. Zhao, X.; Feng, J.; Chen, S.; Huang, Y.; Sum, T. C.; Chen, Z. *Phys. Chem. Chem. Phys.* **2017,** *19,* 1074–1082. doi:10.1039/C6CP06410H
23. Valant, M.; Suvorov, D. *J. Am. Ceram. Soc.* **2000,** *83,* 2721–2729. doi:10.1111/j.1151-2916.2000.tb01623.x
24. Wee, S.-H.; Kim, D.-W.; Yoo, S.-I. *J. Am. Ceram. Soc.* **2004,** *87,* 871–874. doi:10.1111/j.1551-2916.2004.00871.x
25. Hernández, S.; Thalluri, S. M.; Sacco, A.; Bensaid, S.; Saracco, G.; Russo, N. *Appl. Catal., A* **2015,** *504,* 266–271. doi:10.1016/j.apcata.2015.01.019
26. Pinaud, B. A.; Vesborg, P. C. K.; Jaramillo, T. F. *J. Phys. Chem. C* **2012,** *116,* 15918–15924. doi:10.1021/jp3041742

License and Terms

This is an Open Access article under the terms of the Creative Commons Attribution License (http://creativecommons.org/licenses/by/4.0), which permits unrestricted use, distribution, and reproduction in any medium, provided the original work is properly cited.

The license is subject to the *Beilstein Journal of Nanotechnology* terms and conditions: (http://www.beilstein-journals.org/bjnano)

The definitive version of this article is the electronic one which can be found at:
doi:10.3762/bjnano.8.264

BEILSTEIN JOURNAL OF NANOTECHNOLOGY

CdSe nanorod/TiO_2 nanoparticle heterojunctions with enhanced solar- and visible-light photocatalytic activity

Fakher Laatar[1,2], Hatem Moussa[3], Halima Alem[4], Lavinia Balan[5], Emilien Girot[3], Ghouti Medjahdi[4], Hatem Ezzaouia[1,2] and Raphaël Schneider[*3]

Full Research Paper

Open Access

Address:
[1]Laboratory of Semiconductors, Nanostructures and Advanced Technology (LSNTA), Center for Research and Technology Energy, Tourist Route Soliman, BP 95, 2050 Hammam-Lif, Tunisia, [2]rue Grandville 54001 Nancy, France, [3]Laboratoire Réactions et Génie des Procédés (LRGP), UMR 7274 CNRS Université de Lorraine, [4]Institut Jean Lamour (IJL), UMR 7198 CNRS Université de Lorraine, BP 70239, 54506 Vandoeuvre-lès-Nancy Cedex, France, and [5]Institut de Science des Matériaux de Mulhouse (IS2M), CNRS UMR 7361, 15 rue Jean Starcky, 68093 Mulhouse, France

Email:
Raphaël Schneider* - raphael.schneider@univ-lorraine.fr

* Corresponding author

Keywords:
CdSe nanorods; heterojunction; photocatalysis; TiO_2

Beilstein J. Nanotechnol. **2017,** *8,* 2741–2752.
doi:10.3762/bjnano.8.273

Received: 28 August 2017
Accepted: 27 November 2017
Published: 19 December 2017

This article is part of the Thematic Series "Energy conversion, storage and environmental remediation using nanomaterials".

Guest Editor: W.-J. Ong

© 2017 Laatar et al.; licensee Beilstein-Institut.
License and terms: see end of document.

Abstract

CdSe nanorods (NRs) with an average length of ≈120 nm were prepared by a solvothermal process and associated to TiO_2 nanoparticles (Aeroxide® P25) by annealing at 300 °C for 1 h. The content of CdSe NRs in CdSe/TiO_2 composites was varied from 0.5 to 5 wt %. The CdSe/TiO_2 heterostructured materials were characterized by XRD, TEM, SEM, XPS, UV–visible spectroscopy and Raman spectroscopy. TEM images and XRD patterns show that CdSe NRs with wurtzite structure are associated to TiO_2 particles. The UV–visible spectra demonstrate that the narrow bandgap of CdSe NRs serves to increase the photoresponse of CdSe/TiO_2 composites until ≈725 nm. The CdSe (2 wt %)/TiO_2 composite exhibits the highest photocatalytic activity for the degradation of rhodamine B in aqueous solution under simulated sunlight or visible light irradiation. The enhancement in photocatalytic activity likely originates from CdSe sensitization of TiO_2 and the heterojunction between these materials which facilitates electron transfer from CdSe to TiO_2. Due to its high stability (up to ten reuses without any significant loss in activity), the CdSe/TiO_2 heterostructured catalysts show high potential for real water decontamination.

Introduction

The development of efficient photocatalysts to address environmental and energy needs, such as degradation of harmful organic compounds in water and in the air or the conversion of solar energy to chemical energy, for example, via water splitting to produce hydrogen, is the topic of numerous current research projects. Titanium dioxide (TiO_2) has been widely in-

vestigated over the last three decades and has been demonstrated to be of high potential [1,2]. However, TiO_2 suffers from two main drawbacks. First, due to its wide bandgap (E_g = 3.2 and 3.0 eV for anatase and rutile, respectively), TiO_2 can only be activated by light with a wavelength of less than 390 nm to trigger the electron–hole separation. Second, TiO_2 exhibits a low quantum efficiency due to the fast recombination of photogenerated charge carriers (electrons and holes).

To address these problems, a number of studies have been devoted to the improvement of light absorption and charge separation by hybridizing TiO_2 with narrow bandgap semiconductors, doping with metal or nonmetal elements, association with noble metal particles, or constructing heterojunctions between TiO_2 and graphene-based materials or carbon nitride (C_3N_4), acting as electron-transport materials [3-5]. All of these strategies have the common goal of decreasing the charge carrier recombination rate by increasing the spatial charge separation.

The interfacial electron transfer between two semiconductors has gained significant interest because the heterojunction improves both the optical absorption in the visible range and the charge separation yield and thus the charge carrier lifetime [3-8]. The photocatalytic activity is enhanced because oxidation of water by holes and reduction of oxygen by electrons are retained at two different sites.

Recently, many groups demonstrated that the creation of a heterojunction between TiO_2 and CdS, CdSe or alloyed CdSeS nanoparticles allows the optical absorption of TiO_2 to be extended into the visible light range and increases the photoconversion efficiency by improving the charge transfer [9-37]. CdSe is one of the most commonly used semiconductors due to its narrow bandgap (1.7 eV) and its band energies are located at relatively low potential. Despite the large number of reports describing the sensitization of TiO_2 (used in the form of spherical particles, films, wires, tubes, etc.) with CdSe nanocrystals (generally quantum dots or spherical nanoclusters) [9-37], very little attention has been devoted to the influence of CdSe crystal morphology on the photocatalytic activity of the CdSe/TiO_2 heterostructured photocatalysts. CdSe nanorods (NRs) and wires are of high interest for use as sensitizers for photocatalytic applications due to their high surface area, higher optical absorption cross section (as compared to spherical particles) and easier charge carrier separation [38]. Only a couple of reports describe the association of CdSe NRs with TiO_2. Luo et al. used chemical vapor deposition to associate CdS, CdSe or CdSeS rods to TiO_2 NRs arrays and demonstrated that the CdSeS/TiO_2 heterostructure exhibits the highest performances as photoelectrode [39]. More recently, small CdSe NRs [40] or type II CdSe/$CdSe_xTe_{1-x}$ NRs [41] were also used as light harvesters to develop TiO_2-based solar cells. Core/shell TiO_2/CdSe NRs were also prepared by growing CdSe quantum dots onto TiO_2 NRs at high temperature [42].

In this paper, we report an investigation on the synthesis of CdSe-NR-sensitized TiO_2 nanoparticles and on the use of these materials for the degradation of rhodamine B (RhB) in aqueous solution. Our results demonstrate that the composite containing 2 wt % CdSe NRs exhibits the optimal photocatalytic activity under solar or visible light irradiation. Moreover, the photocatalytic response was maintained after ten cycles in simulated sunlight. A possible mechanism is also discussed.

Experimental

Chemicals

Cadmium acetate (Cd(OAc), 99.995%, Sigma), sodium selenite (Na_2SeO_3, 99%, Sigma), diethylenetriamine (99%, Sigma), TiO_2 nanoparticles (Sigma-Aldrich, Aeroxide® P25, CAS: 13463-67-7), rhodamine B (RhB, >95%, Sigma), *tert*-butanol (*t*-BuOH, >99.5%, Sigma), *p*-benzoquinone (>98%, Sigma) and ethanol (>99%, anhydrous) were used as received without additional purification. All solutions were prepared using Milli-Q water (18.2 MΩ·cm, Millipore) as the solvent.

Synthesis of CdSe nanorods

CdSe NRs were synthetized via a solvothermal method according to the protocol described by Li et al. [43], with slight modifications. Briefly, diethylenetriamine (34.3 mL) and water (5.8 mL) were mixed in a reaction flask and the mixture stirred for 5 min. Next, $Cd(OAc)_2$ (0.266 g, 1 mmol) and Na_2SeO_3 (0.173 g, 1 mmol) were added and the mixture further stirred for 30 min at room temperature to ensure complete dissolution of precursors. Next, the solution was transferred to a teflon-lined stainless steel autoclave with 100 mL capacity and heated to 180 °C for 12 h. After cooling to room temperature, the CdSe NRs were recovered by centrifugation (4000 rpm for 15 min), washed with water (5 × 10 mL), then with ethanol (2 × 10 mL) and finally dried at 50 °C for 12 h.

Preparation of CdSe/TiO_2 composites

CdSe/TiO_2 composites with a varied content of CdSe NRs (0.5, 1, 2 and 5 wt %) were prepared. For the CdSe (2 wt %)/TiO_2 composite, commercial Aeroxide® P25 TiO_2 nanoparticles (250 mg) and CdSe NRs (5 mg) were dispersed by sonication in 5 mL water for 30 min. Next, the mixture was heated to 70 °C to evaporate water. The solid obtained was washed with water (3 × 10 mL), with ethanol (3 × 5 mL) and then calcined under air at 300 °C for 1 h to couple the CdSe NRs with TiO_2. CdSe/TiO_2 composites with different wt % CdSe NRs were prepared using a similar synthetic procedure.

Photocatalytic activity measurements

The photocatalytic activity of $CdSe/TiO_2$ composites was evaluated by the degradation of RhB in aqueous solution. Sylvania LuxLine FHO T5 neon tubes were used as the simulated solar light source (light intensity = 5 mW/cm^2). A polycarbonate filter was added for experiments conducted under visible light irradiation (light intensity = 10 mW/cm^2).

In a typical experiment, 50 mg of the $CdSe/TiO_2$ composite were dispersed in 50 mL of aqueous solution of RhB (10 mg/L) in a 70 mL glass flask and the mixture was magnetically stirred in the dark under ambient conditions for 45 min to reach a thorough adsorption–desorption equilibrium. After that period, the light was turned on. Aliquots of 2 mL were taken at regular time intervals and centrifuged (4000 rpm for 2 min) to remove the $CdSe/TiO_2$ photocatalyst. The relative concentration of RhB in the solution was determined by comparing its UV−visible absorption at 554 nm with that of the starting solution.

The mechanism of RhB photodegradation in aqueous solution was investigated through the use of scavengers. *t*-BuOH and *p*-benzoquinone, used as hydroxyl and superoxide scavengers, were used at concentrations of 1 and 10 mM, respectively.

Characterization

Transmission electron microscopy (TEM) investigations were performed with a JEOL ARM 200F-Cold FEG TEM/STEM (point resolution 0.19 nm in TEM mode and 0.078 nm in STEM mode) fitted with a GIF Quatum ER. For each sample, one drop of a dispersed solution was deposited on holey carbon grids and imaged.

Scanning electron microscopy (SEM) images were prepared using a JEOL SEM JSM-6490 LV.

The crystalline phase of the powders was determined by powder X-ray diffraction (XRD) on an X'Pert MPD diffractometer (Panalytical AXS) with a goniometer radius of 240 mm, fixed divergence slit module (1/2° divergence slit, 0.04 rd Sollers slits) and an X'Celerator as a detector. The samples were placed on a silicon zero-background sample holder and the XRD patterns were recorded at room temperature using Cu Kα radiation (λ = 0.15418 nm).

XPS analysis was conducted on a Gammadata Scienta (Uppsala, Sweden) SES 200-2 spectrometer under ultra-high vacuum conditions ($P < 10^{-9}$ mbar). For all peak fitting procedures the CASA XPS software (Casa Software Ltd, Teignmouth, UK, http://www.casaxps.com) was used and the areas of each component were modified according to classical Scofield sensitivity factors.

All the optical measurements were performed at room temperature (20 ± 1 °C) under ambient conditions. The absorption spectra of liquid samples were recorded on a Thermo Scientific Evolution 220 UV–visible spectrophotometer. Diffuse reflectance spectra (DRS) were recorded on a Shimadzu 2600 UV−visible spectrophotometer. $BaSO_4$ powder was used as a standard for baseline measurements and spectra were recorded in a range of 250–1400 nm. Raman spectra were recorded using an Xplora spectrometer from Horiba Scientific with 532 nm wavelength incident laser light.

The initial and final total organic carbon (TOC) content was determined using a Shimadzu TOC-V_{CSH} analyzer to evaluate the degree of photomineralization.

Results and Discussion

Synthesis, morphological and structural characterization of $CdSe/TiO_2$ composites

CdSe NRs were prepared by a solvothermal method using diethylenetriamine as structure directing agent [43]. The CdSe rods were associated to TiO_2 nanoparticles by a heat treatment at 300 °C for 1 h to construct a heterojunction between these materials that favors the charge injection from CdSe to TiO_2.

The microstructure of CdSe NRs and $CdSe/TiO_2$ composites was first characterized by SEM (Figure S1, Supporting Information File 1). The small CdSe NRs were found to be strongly associated to each other to form larger particles with sizes varying between 1 and 4 µm. The associated energy dispersive X-ray (EDX) spectrum demonstrates that Cd and Se were the only elements detected in CdSe NRs. Due to the low content of CdSe NRs in $CdSe/TiO_2$ composites, CdSe NRs could only hardly be observed by SEM. Ti, O, Cd and Se elements were detected for all composites, which indicates the successful association of CdSe NRs with TiO_2. All $CdSe/TiO_2$ composites exhibit a non-rigid texture and the pores observed should be beneficial for the diffusion of molecules and thus for an enhanced photocatalytic activity.

The morphology of the particles was further characterized by TEM. Commercial P25 TiO_2 nanoparticles (Aeroxide® P25) are of spherical/ellipsoidal shape and their average diameter is ≈23 ± 6 nm (Figure 1a). CdSe NRs produced after the solvothermal synthesis have an average length and an average diameter of 120 and 12 nm, respectively (Figure 1b). Some nanowires with lengths up to 300 nm could also be detected. A typical TEM image of the CdSe (2 wt %)/TiO_2 composite is given in Figure 1c and demonstrates the coexistence and the association of CdSe NRs and TiO_2 particles. This could be further confirmed by HR-TEM (Figure 1d). The measured lattice spacing was 0.36 and 0.37 nm, corresponding to the (101) plane

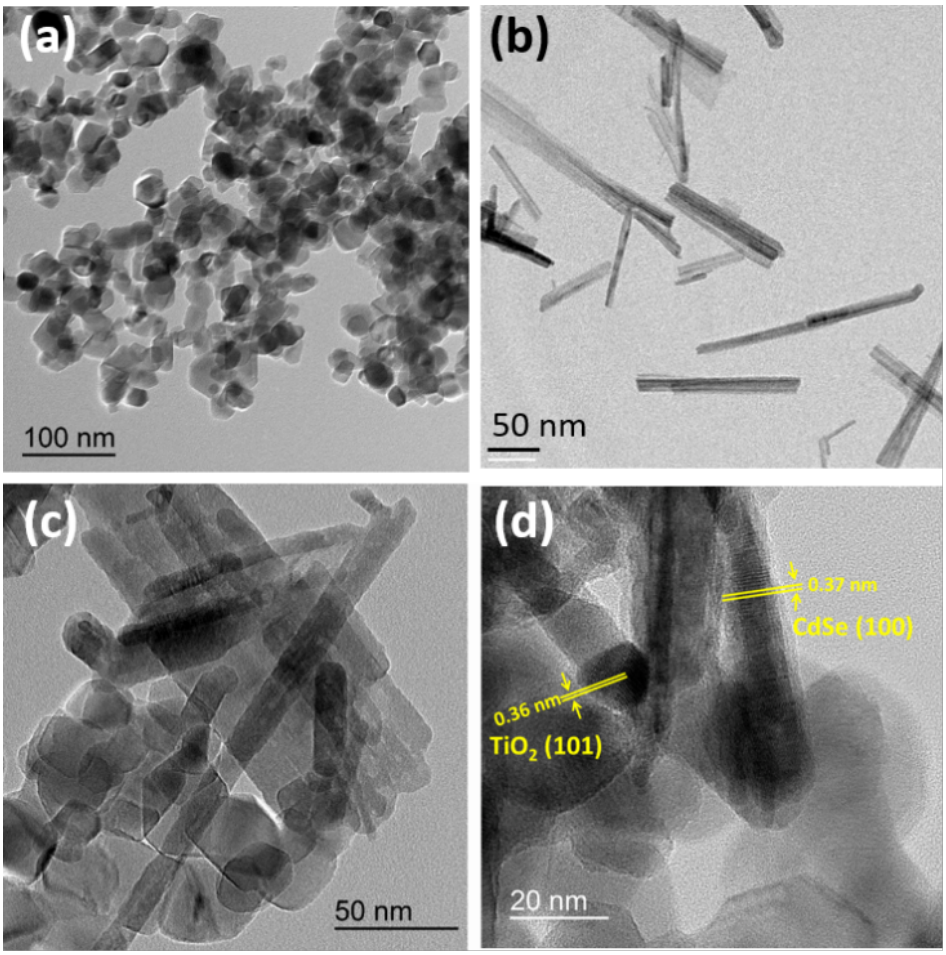

Figure 1: TEM images of (a) TiO_2, (b) CdSe nanorods and (c) the CdSe (2 wt %)/TiO_2 composite. (d) HR-TEM image of CdSe nanorods associated to TiO_2 nanoparticles.

of anatase TiO_2 and to the (100) plane of wurtzite CdSe, respectively.

XRD analysis of CdSe, TiO_2 and CdSe-NR-sensitized TiO_2 is presented in Figure 2. For pure CdSe rods, all peaks could be indexed to the hexagonal wurtzite structure (JCPDS No 77-2307), which is in accordance with the previously described HR-TEM results (Figure 2a). For TiO_2, the diffraction peaks at $2\theta = 25.41$, 37.98, 48.18, 54.12, 55.24, 62.93, 69.03, 70.42 and 75.17° can be indexed to the (111), (004), (200) (105), (211), (204), (310), (116) and (220) crystal planes of anatase TiO_2 (JCPDS No 21-1272), while those located at $2\theta = 27.55$, 36.23, 41.34 and 56.72° belong to rutile TiO_2 (JCPDS No 21-1276) (Figure 2b). The anatase and rutile phases of TiO_2 exhibit a higher catalytic activity than the brookite phase [44]. The anatase/rutile ratio was not affected by the heating at 300 °C (the phase transition occurs at 500 °C). The position of TiO_2 diffraction peaks was not changed after association with CdSe, indicating that CdSe NRs do not affect the lattice structure of TiO_2. The diffraction peaks of CdSe NRs could not be observed in all CdSe/TiO_2 composites due to the low content of CdSe (from 0.5 to 5 wt %) and their dispersion in TiO_2 particles.

Raman spectroscopy was further used to confirm the structures of CdSe/TiO_2 composites. Two peaks located at 206 and 414 cm^{-1} corresponding to the longitudinal optical (LO) phonon and its overtone (2LO) can be observed for CdSe NRs (Figure S2, Supporting Information File 1) [45]. For TiO_2, the E_g, B_{1g}, A_{1g} and E_g peaks located at 143, 397, 514 and 636 cm^{-1}, respectively, are typical of the TiO_2 anatase phase [46] (Figure 3). Due to the weak content in CdSe NRs, the LO signal of CdSe could only be detected for composites containing 2 and 5 wt % CdSe NRs. However, Raman analysis indicates that CdSe NRs are well-associated to TiO_2 particles.

The UV–visible absorption spectra of TiO_2 and CdSe/TiO_2 composites are shown in Figure 4a. The bandgap energies of TiO_2, CdSe and CdSe/TiO_2 composites were determined by

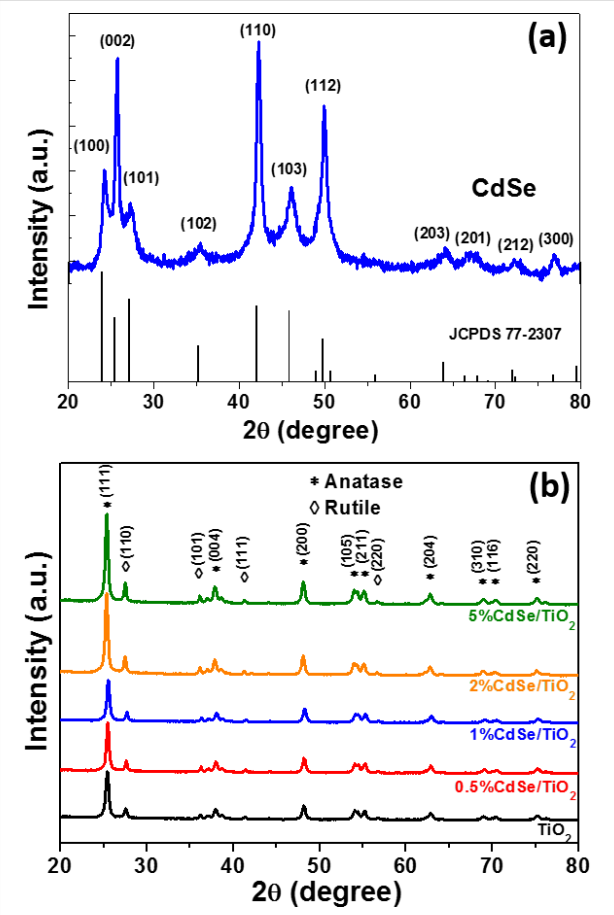

Figure 2: X-ray diffraction patterns of (a) CdSe and (b) TiO_2 and CdSe/TiO_2 composites with varying CdSe wt % from 0.5 to 5 wt %.

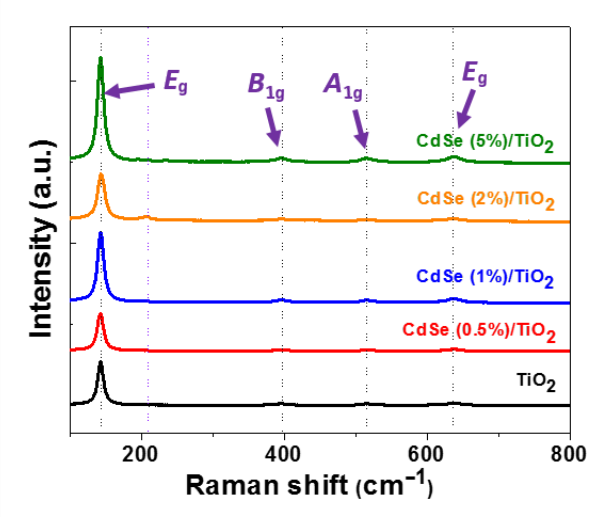

Figure 3: Raman spectra of TiO_2 and CdSe/TiO_2 composites.

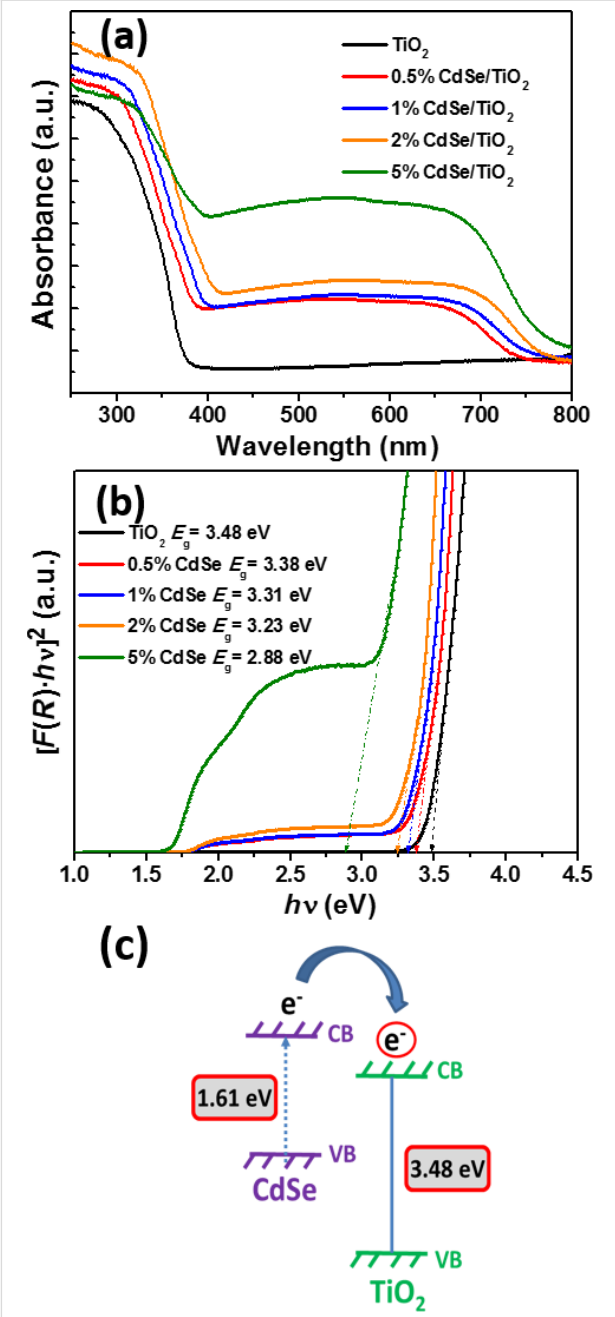

Figure 4: (a) UV–visible absorption spectra of TiO_2 and CdSe/TiO_2 composites, (b) plots of transformed Kubelka–Munk functions $[F(R)\cdot h\nu]^2$ vs $h\nu$ for TiO_2 and CdSe/TiO_2 composites, and (c) energy level diagram for CdSe NRs/TiO_2 composites.

plotting $[F(R)h\nu]^2$ vs photon energy and extrapolating the plots at $[F(R)h\nu]^2 = 0$ ($F(R)$ is the Kubelka–Munk function, h is the Planck constant and ν is the frequency) (Figure 4b). No optical response in the visible region could be detected for TiO_2 due to its wide bandgap (3.48 eV). As can be seen, the absorption increases with the increase of CdSe NRs in the composite from 400 to ≈725 nm, which corresponds to the energy bandgap of CdSe NRs (≈1.61 eV) – a value slightly lower than the standard bandgap of CdSe (1.78 eV) [47]. This enhanced visible light absorption originates from the excitation of CdSe NRs and indicates a decrease of the bandgap with increasing amount of

CdSe (the bandgap of CdSe/TiO_2 composites was found to decrease from 3.38 eV for 0.5 wt % CdSe to 2.88 eV for 5 wt % CdSe) (Figure 4b). Because the conduction band edge of CdSe NRs is higher than that of TiO_2, the results shown in Figure 4 demonstrate that the excited electrons of CdSe NRs can be transferred to TiO_2 nanoparticles due to the heterojunction between these materials (Figure 4c). This should contribute to enhance the photocatalytic activity of CdSe/TiO_2 composites under visible light irradiation (vide infra).

The chemical state of the elements composing the CdSe (2 wt %)/TiO_2 composite was studied by XPS. The high-resolution spectra of the elements Cd $3d_{5/2}$, Se $3p_{3/2}$, Cd $3p_{1/2}$, Ti 2p and O 1s in the CdSe (2 wt %)/TiO_2 composite are provided in Figure 5. The signals of Ti $2p_{3/2}$, Ti $2p_{1/2}$, O 1s (lattice oxygen atoms), and O 1s (surface hydroxyl groups) appear at 458.74, 464.56, 530.0, and 531.76 eV, respectively, which are values in good accordance with those measured for pure TiO_2 [48]. The signals of Cd $3d_{5/2}$ and Se $3p_{3/2}$ and Se $3p_{1/2}$ can be observed at 405.46, 160.26 and 165.91 eV, respectively. These values are typical for CdSe [49] and further confirm that CdSe NRs are associated to TiO_2. Both for CdSe and TiO_2, no significant shift in binding energy was observed after building the heterojunction between these materials (see Supporting Information File 1, Figure S3 for the high-resolution XPS spectra of Cd $3d_{5/2}$ and Se 3p of CdSe NRs). Noteworthy is also that the surface of CdSe NRs was not oxidized into CdO during the calcination step. The signals of Cd $3d_{5/2}$ at ≈403.2 eV for CdO [50] and Se $3p_{3/2}$ at 165.1 eV for SeO_2 [51] were not detected in the XPS spectra of the CdSe (2 wt %)/TiO_2 composite.

Solar light photocatalytic activity of CdSe/TiO_2 composites

The photocatalytic decomposition of RhB at pH 7 over TiO_2 nanoparticles and CdSe/TiO_2 composites under simulated solar light irradiation was first evaluated (light intensity: 5 mW/cm^2). Before illumination, the adsorption/desorption equilibrium was established for 45 min. In the absence of the photocatalyst, the

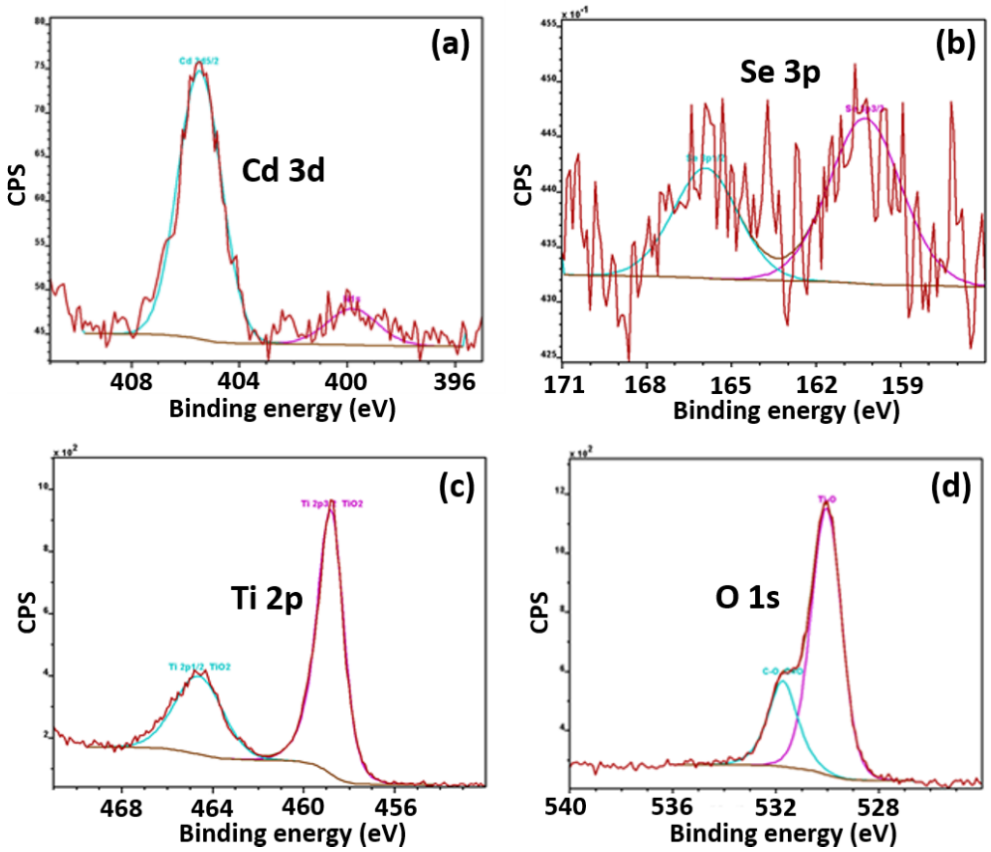

Figure 5: High-resolution XPS spectra of the CdSe (2 wt %)/TiO_2 composite: (a) Cd 3d, where Cd $3d_{5/2}$ (blue) at 405.46 eV comprised 45.18% of the area of the spectra and N 1s (pink) at 399.81 eV comprised 54.82% of the area of the spectra; (b) Se 3p, where Se $3p_{1/2}$ (blue) at 165.91 eV comprised 50.09% of the area of the spectra and Se $3p_{3/2}$ (pink) at 160.26 eV comprised 49.91% of the area of the spectra; (c) Ti 2p, where Ti $2p_{1/2}$ (blue) at 464.56 eV comprised 44.72% of the area of the spectra and Ti $2p_{3/2}$ (pink) at 458.74 eV comprised 55.28% of the area of the spectra and (d) O 1s, where C–O C=O (blue) at 531.72 eV comprised 24.81% of the area of the spectra and Ti–O (pink) at 530.00 eV comprised 75.19% of the area of the spectra. CPS = counts per second.

photodegradation of RhB was found to be negligible. As shown in Figure 6a, the highest photocatalytic activity was reached for the CdSe (2 wt %)/TiO_2 material which fully bleached the dye in 150 min. Thereafter, the activity decreases when increasing the amount of CdSe NRs associated to TiO_2. Because the photocatalytic activity originates from the spatial separation of photogenerated electrons and holes, it is likely that CdSe NRs are not properly associated to TiO_2 and do not contribute to the photocatalytic process.

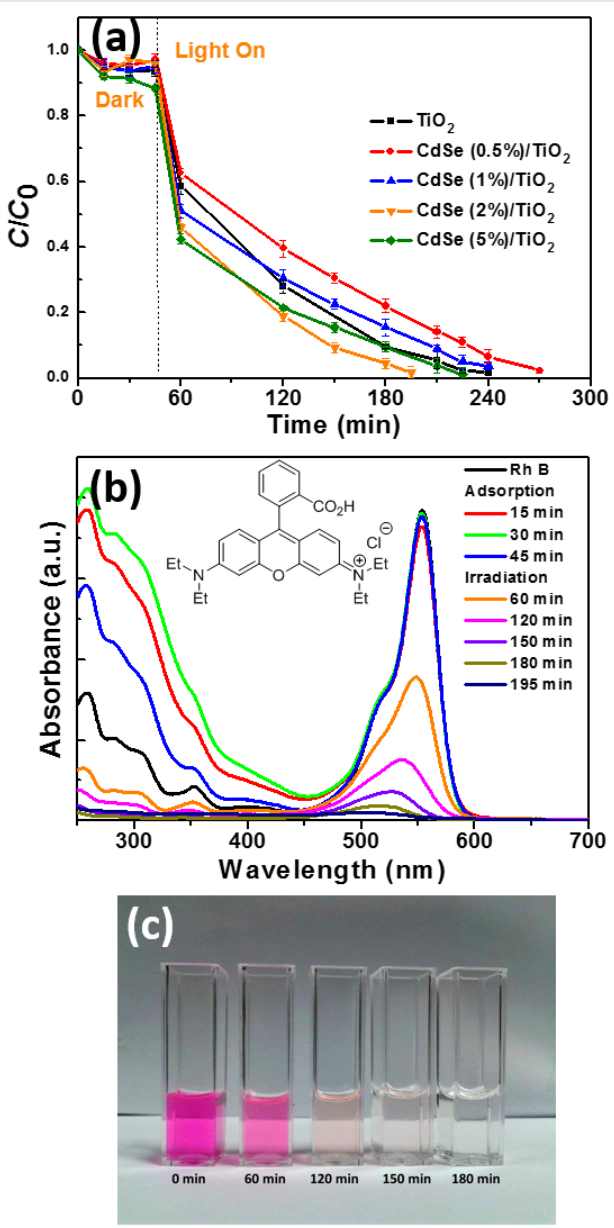

Figure 6: (a) Photocatalytic activity of TiO_2 and CdSe/TiO_2 composites for the degradation of RhB under simulated solar light irradiation, (b) UV–visible absorption spectra of RhB during the photodegradation using the CdSe (2 wt %)/TiO_2 composite (the inset shows the chemical structure of RhB), and (c) a digital photograph of the RhB solution over the course of the photocatalytic degradation.

Total organic carbon (TOC) measurements showed that the RhB solution was discolored during photocatalytic experiments (Figure 6c) and the dye was also partially decomposed (the TOC value decreased from 6.9 ± 0.3 to 2.4 ± 0.2 mg/L after the 150 min of irradiation).

The temporal evolution of the UV–vis absorption spectra is displayed in Figure 6b. The intensity of the RhB absorption from 250 to 600 nm decreases over time. A blue shift (from 553 to 503 nm) of the main absorption peak is also observed, which is indicative of stepwise *N*-de-ethylation of the dye during the photocatalytic process [52]. The plots of $\ln(C_0/C)$ of RhB vs irradiation time indicate that the photodegradation of RhB over CdSe/TiO_2 composites follows a pseudo-first-order kinetic model (C_0 is the initial concentration of RhB and C is the concentration of the dye at time t). The rate constants k determined from the slopes of $\ln(C_0/C)$ vs time were found to be 0.017, 0.012, 0.013, 0.019, and 0.014 min^{-1} for TiO_2 and CdSe/TiO_2 composites loaded with 0.5, 1, 2, and 5 wt % CdSe, respectively (Figure S4, Supporting Information File 1).

Influence of the photocatalyst dosage and rhodamine B concentration

The photodegradation efficiency is generally affected by the amount of catalyst used and by the concentration of the pollutant. First, we investigated the influence of the catalyst concentration (25, 50 or 100 mg in 50 mL of RhB solution) (Figure 7a). Using 25 mg of the CdSe (2 wt %)/TiO_2 photocatalyst, the dye decomposition required 255 min while the degradation could be achieved within 75 min using 100 mg of photocatalyst. As expected, the photocatalytic degradation rates increased with the catalyst dosage, which is linked to the concentration of adsorption sites and photocatalytically active sites (k = 0.010, 0.019 and 0.034 min^{-1} for reactions conducted with 25, 50 and 100 mg of photocatalyst, respectively).

Next, the concentration of the RhB solution was varied from 5, 10 to 25 mg/L while the amount of catalyst was fixed at 50 mg (Figure 7b). The photodegradation rate decreases with increasing RhB concentration (k = 0.028, 0.019 and 0.002 min^{-1} for RhB concentrations of 5, 10 and 25 mg/L, respectively). This originates (i) from the high amount of dye and/or the photodegradation intermediates adsorbed at the photocatalyst surface and (ii) from the decrease of the light penetration in the reactor due to the high absorption of RhB and thus to the decreased amount of reactive oxygen species produced.

Influence of the pH of the rhodamine B solution

The pH of the aqueous solution may play a crucial role on the kinetic of the photodegradation since it influences the surface

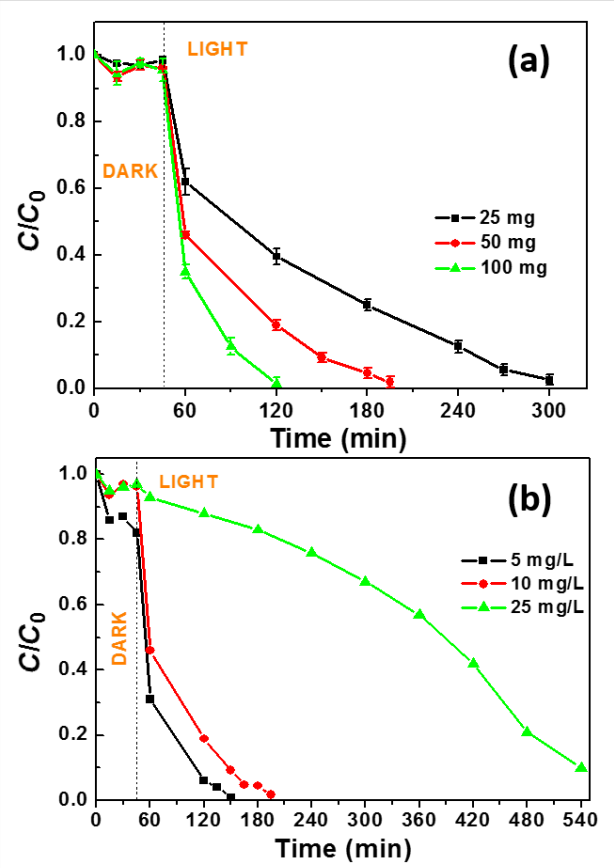

Figure 7: (a) Effect of the catalyst concentration on the photodegradation efficiency (25, 50 or 100 mg of photocatalyst were dispersed in 50 mL of a 10 mg/L RhB solution). (b) Influence of RhB concentration on the photocatalytic efficiency (50 mg of photocatalyst and 50 mL of the dye solution were used).

charge of the catalyst and the structure of the dye in solution. Figure 8 shows that the CdSe (2 wt %)/TiO_2 photocatalyst exhibits the highest activity at pH values varying from 5 to 8

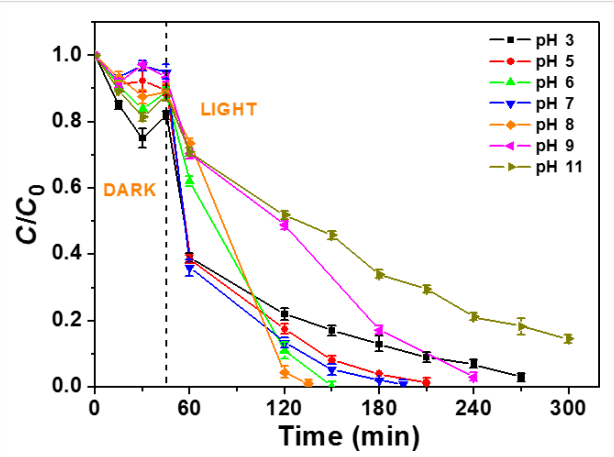

Figure 8: Influence of pH on the degradation of rhodamine B using the CdSe (2 wt %)/TiO_2 photocatalyst.

(k values are varying from 0.017 to 0.031 min^{-1}). At pH 3, the photodegradation kinetic is reduced (k = 0.011 min^{-1}) but the highest inhibition was observed in basic media (k = 0.009 and 0.006 min^{-1} at pH 9 and 11, respectively). The point of zero charge of the TiO_2 nanoparticles is at ≈6.5 [53] and the pK_a of the acid function of RhB is 3.7. At pH ≥ 9, the weak photocatalytic activity probably originates from the strong repellency between the carboxylate function of RhB and the negatively charged catalyst. At pH 3, the positively charged RhB exhibits only a modest affinity for the positively charged catalyst. At pH values ranging from 5 to 8, RhB may associate to the photocatalyst either via interaction involving the carboxylate function or the positively charged diethylamino groups.

Visible light photocatalytic activity of the CdSe (2 wt %)/TiO_2 composite

The CdSe (2 wt %)/TiO_2 composite is also photocatalytically active when the incident light wavelength is greater than 400 nm. The spectral evolution of RhB and the degradation profile are shown in Figure 9. As can be seen, the photodegradation is slower than that initiated by simulated solar light and ≈70% of RhB is bleached after 6.25 h of irradiation. A similar

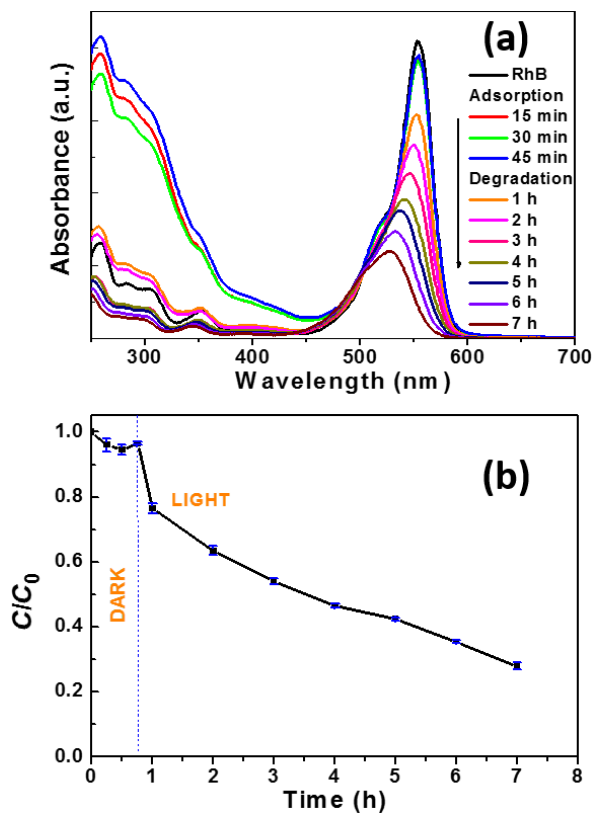

Figure 9: (a) UV–visible spectral evolution of rhodamine B as a function of irradiation time using the CdSe (2 wt %)/TiO_2 catalyst under visible light irradiation (light intensity: 10 mW/cm^2) and (b) evolution of C/C_0 vs irradiation time.

hypsochromic shift of the absorption band at 553 nm to that observed under simulated sunlight irradiation was observed, indicating that photooxidative *N*-de-ethylation of RhB occurred in the early stages of its photodegradation. Finally, although the operating conditions and the structure of the pollutant were different from those used in this study, the CdSe NR/TiO_2 nanoparticle photocatalyst favorably compares with catalysts engineered from CdSe quantum dots and TiO_2 nanoparticles or nanotubes [9,11,12,22,26,31,33,34].

Reusability of the CdSe (2 wt %)/TiO_2 photocatalyst

The CdSe (2 wt %)/TiO_2 photocatalyst was subjected to reuse under simulated solar light irradiation. After the first run, the photocatalyst was recovered by centrifugation (4000 rpm for 15 min) and reused without any treatment. As can be seen from Figure 10, no marked decrease in photocatalytic activity was observed after ten reuses, indicating that byproducts originating from RhB decomposition do not block the active sites on the photocatalyst surface and that the photocatalyst is not photocorroded. Furthermore, XRD patterns of the CdSe (2 wt %)/TiO_2 composite before and after ten reuses and the SEM analysis clearly demonstrate that the photocatalyst is stable during the reaction (Supporting Information File 1, Figure S5). The stability of the CdSe/TiO_2 catalyst is of high importance for real photocatalytic applications.

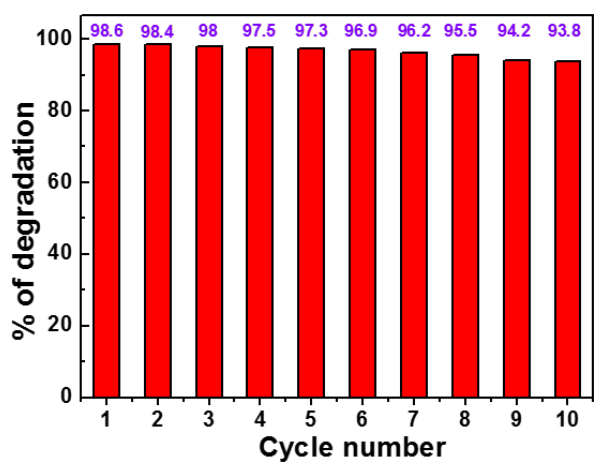

Figure 10: Recycling of the CdSe (2 wt %)/TiO_2 catalyst in the degradation of RhB under simulated solar light irradiation.

Photodegradation mechanism

Under simulated solar light irradiation, electron (e^-)/hole (h^+) pairs are generated both in CdSe NRs and TiO_2 nanoparticles. The holes in the valence band (VB) of TiO_2 are transferred to the VB of CdSe NRs while electrons are transferred from the conduction band (CB) of CdSe NRs to the CB of TiO_2 (Figure 11a). Under visible light illumination, only CdSe can be activated. A CdSe NR electron is promoted from the VB to the CB, leaving a hole in the VB. Then, the electron is transferred to TiO_2 (Figure 11b). All these transfer processes are thermodynamically favorable since both the CB and VB of CdSe NRs lie above that of TiO_2. These charge separations may effectively reduce the probability of recombination and increase the lifetime of charge carriers (e^- and h^+).

Under visible light irradiation, holes in the VB of CdSe may directly oxidize the dye. Meanwhile, the electrons accumulated in TiO_2 can be trapped by dissolved oxygen molecules and generate superoxide $O_2^{\bullet-}$ radicals which are strong oxidants able to decompose organic substances. These $O_2^{\bullet-}$ radicals may also react with an electron and protons to form hydrogen peroxide which is further decomposed into hydroxyl $^{\bullet}OH$ radicals able to oxidize RhB.

To estimate which of these reactive oxygen species plays a key role in the photodegradation of RhB under visible light irradiation, experiments were carried out by adding *t*-BuOH and *p*-benzoquinone, used as $^{\bullet}OH$ and $O_2^{\bullet-}$ radicals scavengers, respectively (Figure 11c). As can be seen, RhB could not be photodegraded in the presence of *p*-benzoquinone, even when used at a low concentration (1 mM), indicating that $O_2^{\bullet-}$ radicals play a key role in the photodegradation. In the presence of *t*-BuOH (10 mM), the reaction rate was markedly decreased ($k = 0.004\ min^{-1}$ vs $0.012\ min^{-1}$ in the absence of *t*-BuOH) but RhB can still be photodegraded. On the basis of these results, the photodegradation catalyzed by CdSe/TiO_2 composites under visible light irradiation occurs mainly via $O_2^{\bullet-}$ radicals and to a lesser extend via $^{\bullet}OH$ radicals. It is therefore likely that the heterojunction between CdSe and TiO_2 favors the transfer of electrons in the CB of TiO_2 followed by the production of $O_2^{\bullet-}$ radicals (Figure 11b).

Conclusion

In this study, CdSe NRs with an average length of ≈120 nm were successfully associated to TiO_2 particles to form heterostructured CdSe/TiO_2 photocatalysts. Due to their structure, the CdSe/TiO_2 composites exhibit full visible and near-infrared light absorption and improved photocatalytic activity via charge separation between CdSe and TiO_2 materials. The CdSe (2 wt %)/TiO_2 composite was demonstrated to be the more efficient for the degradation of rhodamine B both under simulated sunlight or visible light irradiation. This facile approach for the preparation of a CdSe NRs/TiO_2 photocatalyst, along with the high stability and low sensitivity to pH changes, demonstrates the high potential of this material for practical photocatalytic applications. The results described in this work stimulate the idea that CdSe/TiO_2 composites may be of high potential for

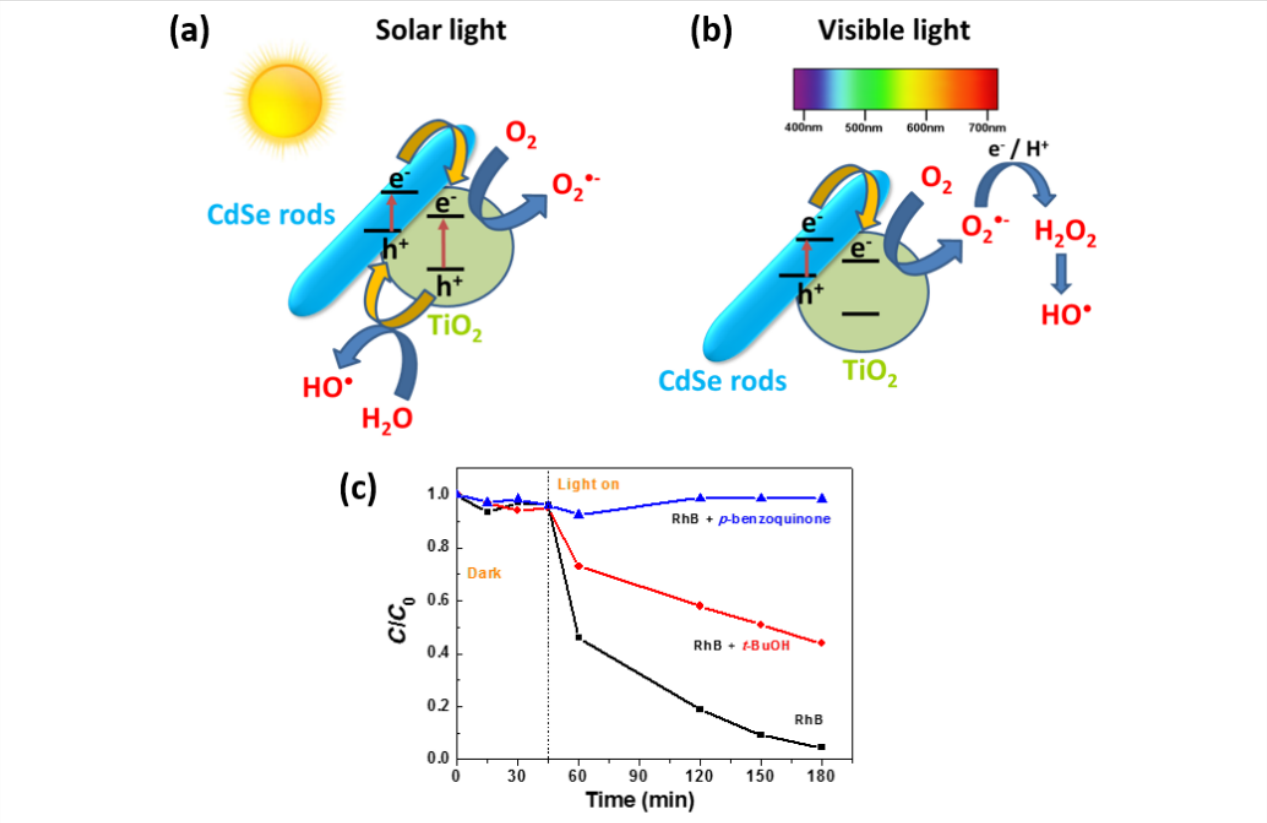

Figure 11: Schematic of the charge separation in the CdSe/TiO_2 photocatalyst under (a) solar light and (b) visible light irradiation. (c) The influence of $O_2^{\bullet-}$ and $^{\bullet}OH$ scavengers on the photocatalytic degradation of rhodamine B under visible light irradiation (*p*-benzoquinone and *t*-BuOH were used at concentrations of 1 mM and 10 mM, respectively).

other applications, such as CdSe-sensitized TiO_2 films for solar cells.

Supporting Information

Supporting Information File 1

Additional figures.
[http://www.beilstein-journals.org/bjnano/content/supplementary/2190-4286-8-273-S1.pdf]

Acknowledgements

This work is supported by the Agence Nationale pour la Recherche (ANR CD2I 2013, project PRUMOS). We also thank Steve Pontvianne (LRGP, Université de Lorraine) for TOC analyses.

ORCID® iDs

Hatem Moussa - https://orcid.org/0000-0001-9744-5599
Halima Alem - https://orcid.org/0000-0002-7918-0504
Lavinia Balan - https://orcid.org/0000-0003-0144-401X
Raphaël Schneider - https://orcid.org/0000-0002-6870-6902

References

1. Nakata, K.; Fujishima, A. *J. Photochem. Photobiol., C: Photochem. Rev.* **2012,** *13,* 169–189. doi:10.1016/j.jphotochemrev.2012.06.001
2. Schneider, J.; Matsuoka, M.; Takeuchi, M.; Zhang, J.; Horiuchi, Y.; Anpo, M.; Bahnemann, D. W. *Chem. Rev.* **2014,** *114,* 9919–9986. doi:10.1021/cr5001892
3. Kumar, S. G.; Den, L. G. *J. Phys. Chem. A* **2011,** *115,* 13211–13241. doi:10.1021/jp204364a
4. Huang, Q.; Tian, S.; Zeng, D.; Wang, X.; Song, W.; Li, Y.; Xiao, W.; Xie, C. *ACS Catal.* **2013,** *3,* 1477–1485. doi:10.1021/cs400080w
5. Chen, H.; Xie, Y.; Sun, X.; Lv, M.; Wu, F.; Zhang, L.; Li, L.; Xu, X. *Dalton Trans.* **2015,** *44,* 13030–13039. doi:10.1039/C5DT01757B
6. Wang, H.; Zhang, L.; Chen, Z.; Hu, J.; Li, S.; Wang, Z.; Liu, J.; Wang, X. *Chem. Soc. Rev.* **2014,** *43,* 5234–5244. doi:10.1039/C4CS00126E
7. Labiadh, H.; Ben Chaabane, T.; Balan, L.; Becheik, N.; Corbel, S.; Medjahdi, G.; Schneider, R. *Appl. Catal., B: Environ.* **2014,** *144,* 29–35. doi:10.1016/j.apcatb.2013.07.004
8. Donat, F.; Corbel, S.; Alem, H.; Pontvianne, S.; Balan, L.; Medjahdi, G.; Schneider, R. *Beilstein J. Nanotechnol.* **2017,** *8,* 1080–1093. doi:10.3762/bjnano.8.110
9. Lo, S.-C.; Lin, C.-F.; Wu, C.-H.; Hsieh, P.-H. *J. Hazard. Mater.* **2004,** *114,* 183–190. doi:10.1016/j.jhazmat.2004.08.007
10. Shen, Q.; Arae, D.; Toyoda, T. *J. Photochem. Photobiol., A: Chem.* **2004,** *164,* 75–80. doi:10.1016/j.jphotochem.2003.12.027

11. Liu, H.; Gao, L. *J. Am. Ceram. Soc.* **2005,** *88,* 1020–1022. doi:10.1111/j.1551-2916.2005.00196.x
12. Ho, W.; Yu, J. C. *J. Mol. Catal. A: Chem.* **2006,** *247,* 268–274. doi:10.1016/j.molcata.2005.11.057
13. Robel, I.; Subramanian, V.; Kuno, M.; Kamat, P. V. *J. Am. Chem. Soc.* **2006,** *128,* 2385–2393. doi:10.1021/ja056494n
14. Lee, J.-C.; Kim, T. G.; Choi, H.-J.; Sung, Y.-M. *Cryst. Growth Des.* **2007,** *7,* 2588–2593. doi:10.1021/cg070588m
15. Robel, I.; Kuno, M.; Kamat, P. V. *J. Am. Chem. Soc.* **2007,** *129,* 4136–4137. doi:10.1021/ja070099a
16. Shen, X.-C.; Zhang, Z.-L.; Zhou, B.; Peng, J.; Xie, M.; Zhang, M.; Pang, D.-W. *Environ. Sci. Technol.* **2008,** *42,* 5049–5054. doi:10.1021/es800668g
17. Kongkanand, A.; Tvrdy, K.; Takechi, K.; Kuno, M.; Kamat, P. V. *J. Am. Chem. Soc.* **2008,** *130,* 4007–4015. doi:10.1021/ja0782706
18. López-Luke, T.; Wolcott, A.; Xu, L.-p.; Chen, S.; Wen, Z.; Li, J.; De La Rosa, E.; Zhang, J. Z. *J. Phys. Chem. C* **2008,** *112,* 1282–1292. doi:10.1021/jp077345p
19. Lee, H.; Wang, M.; Chen, P.; Gamelin, D. R.; Zakeeruddin, S. M.; Grätzel, M.; Nazeeruddin, M. K. *Nano Lett.* **2009,** *9,* 4221–4227. doi:10.1021/nl902438d
20. Zhang, H.; Quan, X.; Chen, S.; Yu, H.; Ma, N. *Chem. Mater.* **2009,** *21,* 3090–3095. doi:10.1021/cm900100k
21. Hensel, J.; Wang, G.; Li, Y.; Zhang, J. Z. *Nano Lett.* **2010,** *10,* 478–483. doi:10.1021/nl903217w
22. Yang, L.; Luo, S.; Liu, R.; Cai, Q.; Xiao, Y.; Liu, S.; Su, F.; Wen, L. *J. Phys. Chem. C* **2010,** *114,* 4783–4789. doi:10.1021/jp910489h
23. Wang, C.; Thompson, R. L.; Baltrus, J.; Matranga, C. *J. Phys. Chem. Lett.* **2010,** *1,* 48–53. doi:10.1021/jz9000032
24. Chi, C.-F.; Liau, S.-Y.; Lee, Y.-L. *Nanotechnology* **2010,** *21,* 025202. doi:10.1088/0957-4484/21/2/025202
25. Xie, Y.; Ali, G.; Yoo, S. H.; Cho, S. O. *ACS Appl. Mater. Interfaces* **2010,** *2,* 2910–2914. doi:10.1021/am100605a
26. Lim, C.-S.; Chen, M.-L.; Oh, W.-C. *Bull. Korean Chem. Soc.* **2011,** *32,* 1657–1661. doi:10.5012/bkcs.2011.32.5.1657
27. Liu, L.; Wang, G.; Li, Y.; Li, Y.; Zhang, J. Z. *Nano Res.* **2011,** *4,* 249–258. doi:10.1007/s12274-010-0076-7
28. Cheng, S.; Fu, W.; Yang, H.; Zhang, L.; Ma, J.; Zhao, H.; Sun, M.; Yang, L. *J. Phys. Chem. C* **2012,** *116,* 2615–2621. doi:10.1021/jp209258r
29. Meng, Z.-D.; Zhu, L.; Ye, S.; Sun, Q.; Ullah, K.; Cho, K.-Y.; Oh, W.-C. *Nanoscale Res. Lett.* **2013,** *8,* 189. doi:10.1186/1556-276X-8-189
30. Lee, S.; Lee, K.; Kim, W. D.; Lee, S.; Shin, D. J.; Lee, D. C. *J. Phys. Chem. C* **2014,** *118,* 23627–23634. doi:10.1021/jp508315m
31. Wang, P.; Li, D.; Chen, J.; Zhang, X.; Xian, J.; Yang, X.; Zheng, X.; Li, X.; Shao, Y. *Appl. Catal., B: Environ.* **2014,** *160–161,* 217–226. doi:10.1016/j.apcatb.2014.05.032
32. Wang, H.; Zhu, W.; Chong, B.; Qin, K. *Int. J. Hydrogen Energy* **2014,** *39,* 90–99. doi:10.1016/j.ijhydene.2013.10.048
33. Zhang, M.; Xu, Y.; Lv, J.; Yang, L.; Jiang, X.; He, G.; Song, X.; Sun, Z. *Nanoscale Res. Lett.* **2014,** *9,* 636. doi:10.1186/1556-276X-9-636
34. Lv, J.; Wang, H.; Gao, H.; Xu, G.; Wang, D.; Chen, Z.; Zhang, X.; Zheng, Z.; Wu, Y. *Surf. Coat. Technol.* **2015,** *261,* 356–363. doi:10.1016/j.surfcoat.2014.10.066
35. Zhou, R.; Niu, H.; Zhang, Q.; Uchaker, E.; Guo, Z.; Wan, L.; Miao, S.; Xu, J.; Cao, G. *J. Mater. Chem. A* **2015,** *3,* 12539–12549. doi:10.1039/C5TA01461A
36. Wang, P.; Li, X.; Fang, J.; Li, D.; Chen, J.; Zhang, X.; Shao, Y.; He, Y. *Appl. Catal., B: Environ.* **2016,** *181,* 838–847. doi:10.1016/j.apcatb.2015.08.046
37. Zhang, G.; Zhou, Y.; Fan, X.; Zou, J.; Dong, W.; Xu, X. *Int. J. Hydrogen Energy* **2017,** *42,* 19877–19884. doi:10.1016/j.ijhydene.2017.06.153
38. Huynh, W. U.; Dittmer, J. J.; Alivisatos, A. P. *Science* **2002,** *295,* 2425–2457. doi:10.1126/science.1069156
39. Luo, J.; Ma, L.; He, T.; Ng, C. F.; Wang, S.; Sun, H.; Fan, H. J. *J. Phys. Chem. C* **2012,** *116,* 11956–11963. doi:10.1021/jp3031754
40. Esparza, D.; Zarazùa, I.; López-Luke, T.; Cerdán-Pasarán, A.; Sánchez-Solis, A.; Torres-Castro, A.; Mora-Sero, I.; De La Rosa, E. *J. Phys. Chem. C* **2015,** *119,* 13394–13403. doi:10.1021/acs.jpcc.5b01525
41. Lee, S.; Flanagan, J. C.; Kang, J.; Kim, J.; Shim, M.; Park, B. *Sci. Rep.* **2015,** *5,* 17472. doi:10.1038/srep17472
42. Hassan, Y.; Chuang, C.-H.; Kobayashi, Y.; Coombs, N.; Gorantla, S.; Botton, G. A.; Winnik, M. A.; Burda, C.; Scholes, G. D. *J. Phys. Chem. C* **2014,** *118,* 3347–3358. doi:10.1021/jp411830u
43. Li, Y.; Hu, Y.; Peng, S.; Lu, G.; Li, S. *J. Phys. Chem. C* **2009,** *113,* 9352–9358. doi:10.1021/jp901505j
44. Mills, A.; Davies, R. H.; Worksky, D. *Chem. Soc. Rev.* **1993,** *22,* 417–423. doi:10.1039/cs9932200417
45. Dzhagan, V. M.; Valakh, M. Ya.; Raevskaya, A. E.; Stroyuk, A. L.; Kuchmiy, S. Ya.; Zahn, D. R. T. *Nanotechnology* **2007,** *18,* 285701. doi:10.1088/0957-4484/18/28/285701
46. Tian, F.; Zhang, Y.; Zhang, J.; Pan, C. *J. Phys. Chem. C* **2012,** *116,* 7515–7519. doi:10.1021/jp301256h
47. Mastai, Y.; Polsky, R.; Koltypin, Yu.; Gedanken, A.; Hodes, G. *J. Am. Chem. Soc.* **1999,** *121,* 10047–10052. doi:10.1021/ja9908772
48. Nawawi, W. I.; Nawi, M. A. *J. Mol. Catal. A: Chem.* **2013,** *374–375,* 39–45. doi:10.1016/j.molcata.2013.03.024
49. Aldeek, F.; Mustin, C.; Balan, L.; Medjahdi, G.; Roques-Carmes, T.; Arnoux, P.; Schneider, R. *Eur. J. Inorg. Chem.* **2011,** 794–801. doi:10.1002/ejic.201000790
50. Vargas-Hernández, C.; Lara, V. C.; Vallejo, J. E.; Jurado, J. F.; Giraldo, O. *Phys. Status Solidi A* **2005,** *242,* 1897–1901. doi:10.1002/pssb.200461717
51. Wagner, C. D.; Gale, L. H.; Raymond, R. H. *Anal. Chem.* **1979,** *51,* 466–482. doi:10.1021/ac50040a005
52. Fu, H.; Pan, C.; Yao, W.; Zhu, Y. *J. Phys. Chem. B* **2005,** *109,* 22432–22439. doi:10.1021/jp052995j
53. Zhao, J.; Hidaka, H.; Takamura, A.; Pelizzetti, E.; Serpone, N. *Langmuir* **1993,** *3,* 1646–1650. doi:10.1021/la00031a008

License and Terms

This is an Open Access article under the terms of the Creative Commons Attribution License (http://creativecommons.org/licenses/by/4.0), which permits unrestricted use, distribution, and reproduction in any medium, provided the original work is properly cited.

The license is subject to the *Beilstein Journal of Nanotechnology* terms and conditions: (http://www.beilstein-journals.org/bjnano)

The definitive version of this article is the electronic one which can be found at:
doi:10.3762/bjnano.8.273

BEILSTEIN JOURNAL OF NANOTECHNOLOGY

Facile synthesis of silver/silver thiocyanate (Ag@AgSCN) plasmonic nanostructures with enhanced photocatalytic performance

Xinfu Zhao[1], Dairong Chen[1,2], Abdul Qayum[1], Bo Chen[*2] and Xiuling Jiao[*1,2]

Full Research Paper

Open Access

Address:
[1]School of Chemistry and Chemical Engineering, Shandong University, Jinan 250100, PR China and [2]National Engineering Research Center for Colloidal Materials, Shandong University, Jinan 250100, PR China

Email:
Bo Chen[*] - sduchenbo@126.com; Xiuling Jiao[*] - jiaoxl@sdu.edu.cn

* Corresponding author

Keywords:
Ag@AgSCN; degradation of oxytetracycline; plasmonic photocatalyst; stability

Beilstein J. Nanotechnol. **2017,** *8,* 2781–2789.
doi:10.3762/bjnano.8.277

Received: 12 August 2017
Accepted: 08 November 2017
Published: 22 December 2017

This article is part of the Thematic Series "Energy conversion, storage and environmental remediation using nanomaterials".

Guest Editor: W.-J. Ong

© 2017 Zhao et al.; licensee Beilstein-Institut.
License and terms: see end of document.

Abstract

A nanostructured plasmonic photocatalyst, silver/silver thiocyanate (Ag@AgSCN), has been prepared by a simple precipitation method followed by UV-light-induced reduction. The ratio of Ag to silver thiocyanate (AgSCN) can be controlled by simply adjusting the photo-induced reduction time. The formation mechanism of the product was investigated based on the time-dependent experiments. Further experiments indicated that the prepared Ag@AgSCN nanostructures with an atomic ratio of Ag/AgSCN = 0.0463 exhibited high photocatalytic activity and long-term stability for the degradation of oxytetracycline (84%) under visible-light irradiation. In addition to the microstructure and high specific surface area, the enhanced photocatalytic activity was mainly caused by the surface plasmon resonance of Ag nanoparticles, and the high stability of AgSCN resulted in the long-term stability of the photocatalyst product.

Introduction

In the past decade, water decontamination technology has attracted great attention due to the increasing health risk that water contamination poses to humankind. The removal of pollutants has been intensively investigated in recent years, and various methods such as adsorption, biodegradation, photocatalytic degradation and chemical oxidation have been developed [1-4]. Among them, photocatalytic degradation is considered as one of the most effective strategies due to its high removal efficiency and environmental friendlessness. For example, as a typical semiconductor, TiO_2 exhibits high photocatalytic degradation performance against a large number of organic pollutants [5-7]. However, it is difficult to obtain a high photocatalytic activity under visible-light irradiation with TiO_2 as a catalyst due to its wide bandgap of 3.2 eV, which limits its practical application. Therefore, the development of new photocatalysts with visible-light catalytic performance, high surface active

sites and long life of separated electron and hole pairs, has become a hot research topic in recent years.

Ag-based semiconductors are well known due to their excellent visible-light catalytic properties, but their easy inactivation limits their utilization in practice. Aimed at this problem, a series of methods, such as doping, surface sensitization, heterojunctions and noble-metal plasma, have been adopted to improve the visible-light catalytic performance of Ag-based materials [8-10]. Among them, plasmonic photocatalysts consisting of Ag/AgX (X = Cl, Br, I) have exhibited improvement in separation of photogenerated electrons and holes [11-18]. However, these Ag-based photocatalysts, Ag/AgX (X = Cl, Br, I), suffer from instability during the recycling application, mainly due to the decomposition of AgX (X = Cl, Br, I) under irradiation [19-22]. Therefore, the development of visible-light catalysts with both high catalytic activity and long-term stability is of great importance.

As one of the Ag-containing semiconductor materials, AgSCN exhibits superior stability under irradiation [23,24]. The relatively large bandgap of AgSCN (3.4 eV) makes it only ultraviolet light active, largely limiting the wide utilization of the solar light energy spectrum. The addition of Ag on AgSCN structures can not only improve the utilization of visible light, but can also trap the photogenerated electrons to enhance the catalytic efficiency and stability. In the present work, a nanostructured Ag@AgSCN plasmonic photocatalyst was achieved by using hydrazine hydrate as a reducing agent, followed by a UV-light-induced reduction, in which the ratio of Ag to AgSCN can be controlled by simply adjusting the photo-induced reduction time. The degradation of a representative contaminate, oxytetracycline, which often exists in contaminated water, was used to test the photocatalytic performance of Ag@AgSCN. Compared with previous reports, the as-prepared product had regular morphology, more active sites and a higher specific surface area [23-28], which led to high photocatalytic activity. More importantly, the activity toward the degradation of oxytetracycline after the fifth cycle was almost the same as for the first cycle, which is notable for a Ag-based catalyst.

Results and Discussion

Ag@AgSCN nanostructures

Ag@AgSCN nanostructures were synthesized by a simple precipitation method, followed by UV-light-induced reduction. As shown in Figure 1a, all the XRD patterns of the Ag@AgSCN nanostructures formed at different irradiation times can be indexed to monoclinic AgSCN (JCPDS file, No. 72-1176). No obvious reflections of face-centered cubic Ag can be observed even with an irradiation time as long as 3 h, mainly due to the small amount of Ag derived from the high stability of AgSCN. An SEM image of the sample M_2 is shown in Figure 1b as a representation. It can be seen that the product is sphere-like nanostructures with uniform size of ≈2.0 µm. Further observation of the high-resolution SEM image (inset of Figure 1b) reveals that the nanostructures are composed of close-packed nanoplates. The large nanoplates with a thickness of tens of nanometers firstly close arrange into crisscross structures, and there are many small plates in the crossed gap to form the sphere-like nanostructures. The corresponding EDS analysis indicates that only elemental Ag, C, N, and S are detected in the sample (Supporting Information File 1, Figure S1), showing the high chemical purity of the product. The selected area electron diffraction (SAED) pattern of a single particle (Figure 1c) displays a set of bright spots, obviously suggesting the high crystallinity of the product. Based on calculations, the spots can be indexed to diffraction from the ($\bar{2}23$) and (332) planes of the monoclinic AgSCN. The SAED pattern also reveals that

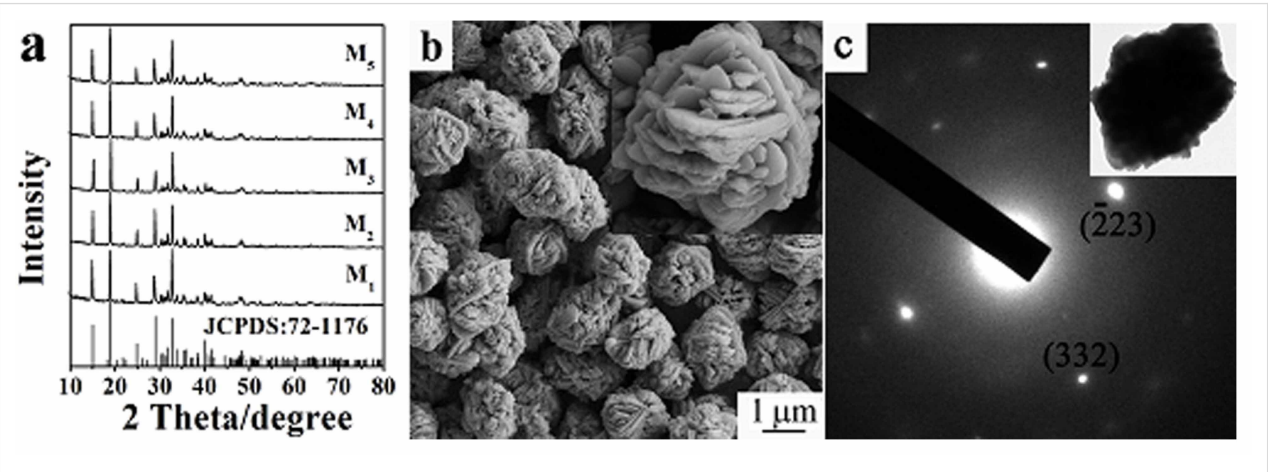

Figure 1: (a) XRD patterns of Ag@AgSCN nanostructures with different molar ratios of Ag to AgSCN. An (b) SEM image and (c) SAED pattern of the Ag@AgSCN nanostructure (sample M_2).

the oriented attachment of the nanoplates composed the Ag@AgSCN nanostructures.

To determine the Ag content in the Ag@AgSCN nanostructures, elemental analysis was conducted, and the results are shown in Table 1. Before UV irradiation, the molar ratio of Ag to AgSCN in the product is 0.024. With the extension of the UV irradiation time, the content of Ag in the product gradually increases, and the molar ratio of Ag to AgSCN reaches 0.0775 after being irradiated for 3 h, indicating the slow reduction of AgSCN under UV irradiation.

UV–vis diffuse reflectance spectra of M_0, M_1, M_2, M_3, M_4, and M_5 are shown in Figure 2a. Here, the characteristic absorption of AgSCN appears at 200–350 nm and that from the surface plasmon resonance of Ag particles is above 350 nm. The absorption peak of silver nanoparticles becomes gradually stronger as the content of Ag increases, indicating that the sunlight utilization efficiency increases steadily. During UV irradiation, many defects are formed in AgSCN, including different interstitial sites and vacancies [29]. The presence of silver particles not only improves the photocatalytic efficiency, but also enhances the electric field strength around AgSCN due to the surface plasmon resonance, which in turn enhances the optical transition of midgap defect states of AgSCN. All these conditions contribute to the strong absorption of Ag@AgSCN in both the UV and visible region, which is beneficial for application as a visible-light catalyst. The bandgap of AgSCN can be determined according to the Kubelka–Munk equation, which is estimated as 3.4 eV for sample M_0 (Figure 2b), and the valence band value of 1.12 eV is obtained from [30]. Therefore, the conduction band position can be determined to be −2.28 eV. The bandgap of sample M_2 is estimated as 3.2 eV, where the change in the value of the bandgap of AgSCN may be due to the surface plasmon resonance of Ag nanoparticles under visible light. In this process, electrons in the metal from the Fermi level directly transfer to the conduction band of AgSCN, and the vacancies remain on the surface of the Ag particles. A dipole-based resonance energy can directly excite semiconductors to produce photogenerated electron–hole pairs

Table 1: Elemental content of the synthesized Ag@AgSCN samples with different reduction times. In all calculation process, the molar value of S was representative of AgSCN.

Sample	Weight of Ag@AgSCN (mg)	Atomic content of S (%)	AgSCN (mol)[a] × 10^{-5}	Ag (mol)[b] × 10^{-7}	Molar ratio, Ag/AgSCN[c]
M_1	2.233	18.987	1.325	3.177	0.024
M_2	2.111	18.719	1.235	5.723	0.0463
M_3	2.557	18.631	1.489	8.014	0.0538
M_4	2.431	18.502	1.406	9.127	0.0649
M_5	3.008	18.358	1.726	13.375	0.0775

[a]Molar content of AgSCN is calculated as the mole of AgSCN = $A{\cdot}B/32$ (where A is the atomic % of S and B is the weight (mg) of Ag@AgSCN. [b]Molar content of Ag is calculated according to Ag = $(B - (A{\cdot}B/32){\cdot}165.95)/107.87$ (where A is the atomic % of S and B is the weight (mg) of Ag@AgSCN. [c]Molar ratio of Ag/AgSCN is calculated as Ag/AgSCN = B/A.

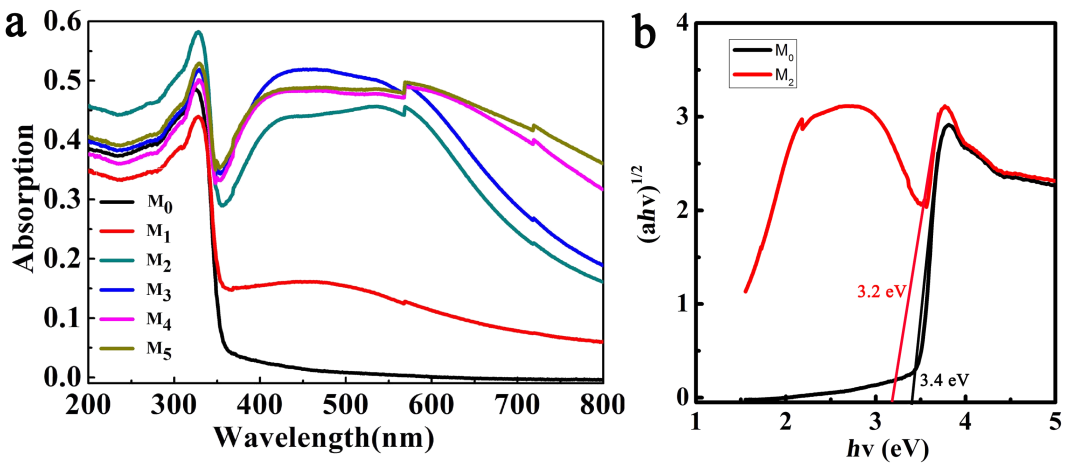

Figure 2: (a) UV–vis diffuse reflectance spectra of M_0, M_1, M_2, M_3, M_4, M_5. (b) Kubelka–Munk plots of M_0 and M_2.

that can improve the visible-light catalytic activity of AgSCN [31,32].

Formation mechanism of Ag@AgSCN nanostructures

To investigate the formation mechanism of Ag@AgSCN nanostructures, a time-dependent precipitation experiment was conducted. It can be seen that small AgSCN nanoplates with size of ≈10 nm were formed in 2 min due to the low solubility product constant (K_{sp}) of AgSCN (Figure 3a). These nanoplates rapidly aggregated due to the high surface energy, and the crystal growth occurred simultaneously (Figure 3b). At this time, the dropwise addition of the $AgNO_3$ solution finished. The oriented-aggregates with a size of ≈1.5 µm were formed in 10 min (Figure 3c). Further extending the reaction time led to the gradual increase in the size of the nanostructures, and the sphere-like nanostructures with size of ≈2 µm were finally obtained (Figure 3d). Certainly, because of the existence of $N_2H_4{\cdot}H_2O$, a small amount of Ag was formed at the same time, but it cannot be distinguished from the TEM image. So the XPS spectra of the samples obtained with and without $N_2H_4{\cdot}H_2O$ were compared (Figure 4a). As to the AgSCN nanostructures formed without $N_2H_4{\cdot}H_2O$, the bonding energy of Ag $3d_{3/2}$ and Ag $3d_{5/2}$ located at 373.35 eV and 367.8 eV with a symmetrical profile, indicated that there was no Ag^0 in the sample. For M_1 (Figure 4b), the peaks of Ag $3d_{5/2}$ and Ag $3d_{3/2}$ can be divided into two different peaks at 368.2, 368.0 eV and 374.3, 373.9 eV, respectively. The peaks at 368.2 and 374.3 eV can be attributed to Ag^0, indicating the presence of Ag^0 [33]. The elemental analysis results shown in Table 1 also indicate the existence of a small amount of Ag^0 in the precipitated products.

Further experiments indicated that $N_2H_4{\cdot}H_2O$ did not affect the morphology of the product. As shown in Figure S2a (see Supporting Information File 1), the phase-pure AgSCN with the same morphology as the precipitated product was formed without the addition of $N_2H_4{\cdot}H_2O$ while other conditions were held constant, indicating the existence of $N_2H_4{\cdot}H_2O$ and the formation of the small amount of Ag had no effect on the morphology of the product. Figure S2b (see Supporting Information File 1) shows the SEM image of the sample obtained without polyvinylpyrrolidone (PVP). The product was composed of nanoparticles with of tens of nanometers in diameter with a large size distribution. This result revealed that the formation of the nanoplate units which composed the Ag@AgSCN nanostructures was directed by PVP. According to the previous

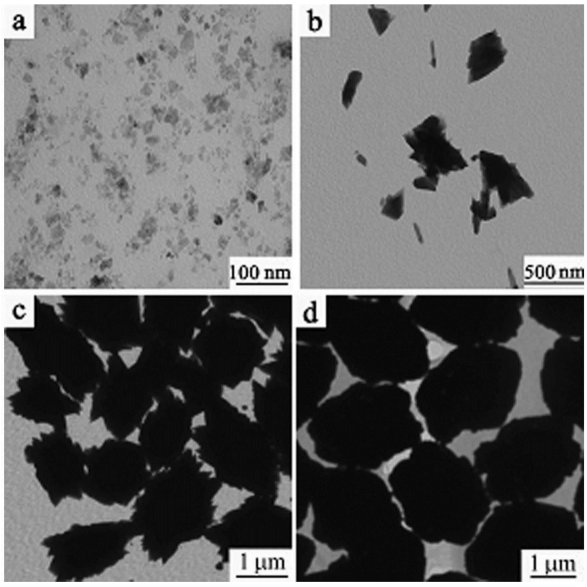

Figure 3: TEM images of precipitated samples formed after addition of the $AgNO_3$ solution after (a) 2 min, (b) 6 min, (c) 10 min, and (d) 20 min.

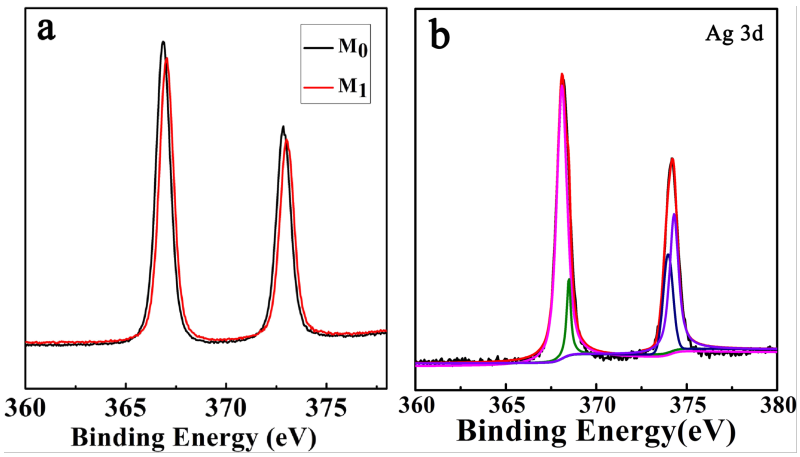

Figure 4: (a) XPS spectra of M_0 and M_1; (b) XPS peaks of Ag $3d_{5/2}$ and Ag $3d_{3/2}$ of M_1.

studies, it was proposed that PVP can selectively adsorb on certain crystal planes and then lead to the formation of AgSCN nanoplates [34]. The rapid addition of the $AgNO_3$ solution (instead of dropwise addition) resulted in the formation of crisscross nanostructures composed of nanoplates without small plates in the cross gap (see Supporting Information File 1, Figure S2c). BET measurements were used to illustrate the specific surface area of the nanostructured Ag@AgSCN, which was 4.04 $m^2 \cdot g^{-1}$, while the BET specific surface area of a sample without PVP (see Supporting Information File 1, Figure S2b) was only 2.88 $m^2 \cdot g^{-1}$.

Based on the above results, the formation process of Ag@AgSCN nanostructures can be summarized. The AgSCN nanoplates were quickly formed under the direction of PVP once the $AgNO_3$ solution was added into the solution (Figure 3a). Then rapid aggregation of the nanoplates occurred to reduce the total surface energy, with the simultaneously growth of the AgSCN plates (Figure 3b). The nanoplates were arranged in a face-to-face stacking manner, and the tetragonal star-shaped Ag@AgSCN nanostructures composed of nanoplates were formed. After that, the addition of the $AgNO_3$ solution finished and the homogeneous nucleation stopped due to the decrease in concentration of the Ag(I) ions. Then, the heterogeneous nucleation on the nanoplate surface occurred and some small nanoplates gradually filled in the crisscross gap of the star-shaped Ag@AgSCN nanostructures. At last, the sphere-like Ag@AgSCN nanostructures composed of nanoplates were formed.

In the following UV-light-induced reduction process, the content of Ag gradually increased with increased irradiation time. Due to the high stability, it is difficult for phase-pure AgSCN to be reduced to Ag by UV-light irradiation, but the existence of a small amount of Ag in the above precipitate can promote the transformation from AgSCN to Ag. Finally, the Ag@AgSCN nanostructures with different Ag content were obtained by adjusting the irradiation time of the UV light.

Visible-light catalytic performance

The visible-light catalytic activity of the samples was evaluated by measuring the degradation rate of oxytetracycline (20 $mg \cdot L^{-1}$) under a halogen lamp (400 W) using phase-pure AgSCN as a reference. The oxytetracycline concentration variation with irradiation time for the M_0, M_1, M_2, M_3, M_4 and M_5 catalysts are shown in Figure 5a. The degradation rates were 29%, 81%, 84%, 61%, 49%, and 30%, respectively, in 60 min according to the absorption intensity at 364 nm. When M_2 was

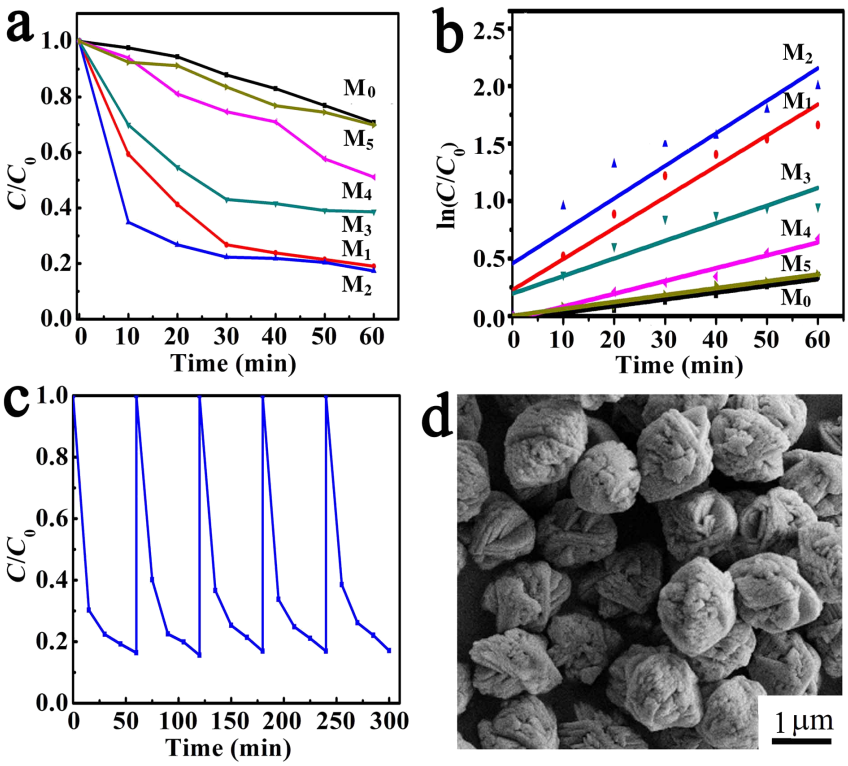

Figure 5: (a) Photocatalytic degradation of oxytetracycline over M_0, M_1, M_2, M_3, M_4, M_5. (b) Kinetic curves for the oxytetracycline degradation with M_0, M_1, M_2, M_3, M_4, M_5. (c) The cycle curves of oxytetracycline degradation using M_2 as a photocatalyst. (d) TEM images of M_2 after five cyclic experiments.

used as a photocatalyst, the maximum degradation rate was obtained. The time-dependent UV–vis spectrum of the oxytetracycline solution over M_2 is shown in Supporting Information File 1, Figure S3. Furthermore, the degradation efficiency of Ag@AgSCN was much higher than that of the pure AgSCN, mainly due to the localized surface plasmon resonance state of Ag particles in the visible-light region. The photogenerated electrons of AgSCN will be captured by Ag particles, rather than recombination with holes. The dipole character of Ag particles in the plasma can promote the separation of electrons and holes in AgSCN under visible light. The electrons will quickly transfer onto the surface of Ag nanoparticles, while the holes will congregate on the surface of AgSCN [35]. On one hand, with increasing Ag content in the product, the recombination of electrons and holes is inhibited, and the catalytic efficiency would be enhanced. But on the other hand, the formation of excess Ag on the surface of AgSCN particles would partially cover the active sites and reduce the adsorption of oxytetracycline on the AgSCN particle surface. Furthermore, the presence of excess Ag particles will decrease the absorption of light and reduce the production of electrons and holes. All of these phenomena led to the decrease of the degradation efficiency [36,37]. Therefore, with the increase of the Ag content in the Ag@AgSCN nanostructures, the degradation efficiency firstly increased and then decreased. The Langmuir–Hinshelwood model was used to investigate the kinetic behaviors of the photocatalyst for degradation of oxytetracycline [38]. Figure 5b showed that the photodegradation process of oxytetracycline nearly complied with the first-order kinetics, and the corresponding reaction rate constants (K_a) with M_0, M_1, M_2, M_3, M_4 and M_5 as catalysts were 0.0058, 0.0269, 0.02832, 0.01531, 0.01115, 0.006 min^{-1}, respectively. The value of K_a for M_2 was 4.8-fold faster than that of the bare AgSCN, so the existence of an appropriate amount of Ag played a prominent role in the photodegradation process. Electrochemical impedance spectrum (EIS) was used to illustrate the rate of charge transfer for the photocatalysts. Nyquist plots of M_0, M_1, M_2, M_3, M_4, M_5 were shown in Figure S4 (see Supporting Information File 1), the circular radius of plot over M_2 in the high-frequency region was much smaller than that of other catalysts, which suggested the smallest charge transfer resistance for M_2, while the charge transfer resistance for M_0 was the largest. That can be attributed to the presence of Ag particles and the promotion of the separation of photogenerated carriers.

The stability of the plasmonic photocatalyst M_2 was investigated by the degradation of oxytetracycline, which was of practical importance for application. As shown in Figure 5c, about 84% oxytetracycline was degraded in 60 min in the fifth cycle, and the efficiency was almost the same as for the first cycle. Further investigations revealed that after five cyclic experiments, the microstructure of Ag@AgSCN had no obvious changes except a somewhat smoother Ag@AgSCN nanostructure surface (Figure 5d). The composition of Ag, S, C, N in M_2 hardly changed in the EDS analysis (see Supporting Information File 1, Figure S5), indicating that AgSCN cannot be reduced in this period of time under visible-light irradiation. Elemental analysis of the Ag@AgSCN after cyclic experiments were also performed. The result showed that the molar ratio of Ag to AgSCN is 0.047, which was near the value in the fresh M_2. All these results indicated that the prepared Ag@AgSCN nanostructures showed long-term stability as a photocatalyst. For Ag@AgSCN, Ag particles coated the surface of AgSCN uniformly, which trapped the photogenerated electrons and protected AgSCN from being reduced. Compared with the previously reported silver halogen photocatalysts (Ag/AgX (X = Cl, Br, I)), the present Ag@AgSCN nanostructures exhibited superior catalytic stability [13,14]. This was mainly due to the higher stability of AgSCN than the AgX (X = Cl, Br, I). Also, the stronger electron affinity of SCN^0 as compared to Br^0 and Cl^0, and the more easy combination of SCN^- with holes as compared to Cl^- and Br^- can improve the photocatalytic stability of Ag@AgSCN nanostructures.

Based on the above discussion, Ag nanoparticles located on AgSCN played a decisive role in the photocatalytic efficiency and stability of Ag@AgSCN. For one, Ag nanoparticles can absorb the visible light, which enhances the utilization of visible light compared with pure AgSCN. On the other hand, the presence of Ag particles effectively reduced the recombination of photogenerated electrons and holes, improving the efficiency and stability of the photocatalyst. The surface plasmon resonance of Ag nanoparticles occurred under visible light, and electrons in the metal from the Fermi level directly transferred to the conduction band of AgSCN, whereas the vacancies were left on the surface of the Ag particles. The dipole-based resonance energy can directly excite semiconductors to produce photogenerated electron–hole pairs. The presence of Ag nanoparticles can not only improve the photocatalytic efficiency, but also can trap photogenerated electrons, slow the reduction of AgSCN, and enhance the stability of Ag@AgSCN. The degradation mechanism suggested that electrons of Ag@AgSCN were prompted to the conduction band and holes were left in the valence band of AgSCN under irradiation (Figure 6a). The electrons were rapidly trapped by Ag nanoparticles, then captured by dissolved O_2, resulting in the formation of $\bullet O_2^-$ radicals, which can decompose oxytetracycline. The photogenerated holes can oxidize H_2O into •OH, which could also oxidize oxytetracycline. To investigate the effect of $\bullet O_2^-$ radicals, 1, 4-benzoquinone (BQ), which was an efficient scavenger for $\bullet O_2^-$ [39], was added to the solution. The degradation efficiency of oxytetracycline was significantly suppressed as shown

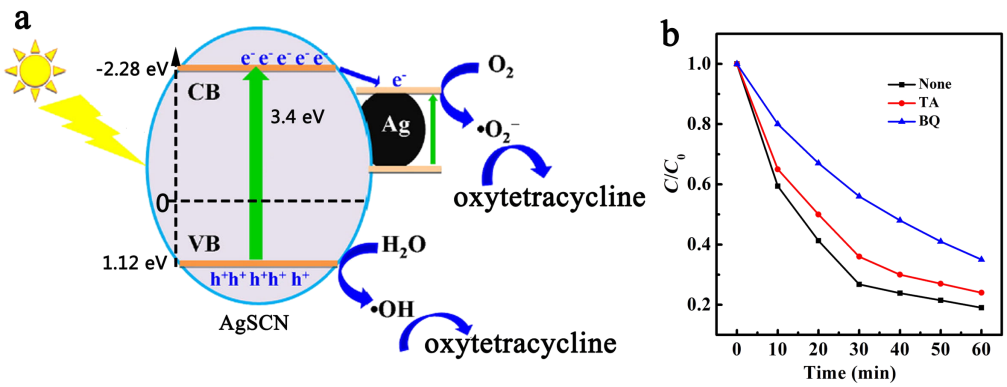

Figure 6: (a) Photocatalysis mechanism of the Ag@AgSCN plasmonic photocatalyst. (b) Photocatalytic degradation of oxytetracycline in the absence and presence of scavengers.

in Figure 6b. Additionally, the presence of •OH was confirmed by addition of terephthalic acid (TA), which was a •OH scavenger [40]. The degradation efficiency of oxytetracycline was also slowed, but was higher than that of the rate with BQ. This revealed that the $•O_2^-$ and •OH both contributed to the decomposition of oxytetracycline, but $•O_2^-$ was the main active species in the photocatalytic process.

Conclusion

Ag@AgSCN nanostructures composed of nanoplates were synthesized through a simple precipitation method, followed by UV-light irradiation. The sphere-like Ag@AgSCN nanostructures went through the formation of AgSCN nanoplates and their oriented aggregation, as well as simultaneous crystal growth. PVP played a critical role in the formation of 2D AgSCN units. The content of Ag in Ag@AgSCN nanostructures can be controlled by simply adjusting the irradiation time of the UV light. The catalytic performance of the nanostructure was evaluated by degradation of oxytetracycline under visible-light irradiation. The Ag@AgSCN nanostructures showed high photocatalytic activity due to their surface plasmon resonance effects. When the molar ratio of Ag/AgSCN was 0.0463, the catalytic rate reached to the maximum and the value of K_a was 4.8-fold faster than that of the bare AgSCN. Most importantly, the prepared Ag@AgSCN nanostructures also exhibited superior photocatalytic stability compared to the previously reported silver halogen plasma catalyst, which make it more suitable for practical application.

Experimental

Chemicals

Silver nitrate ($AgNO_3$, Shanghai Chemical Co.) and ammonium thiocyanate (NH_4SCN, Tianjin Reagent Co.) were used as precursors for the synthesis of silver/silver thiocyanate nanostructures (Ag@AgSCN). Polyvinylpyrrolidone (PVP, K30, Beijing Reagent Co.) and hydrazine hydrate ($N_2H_4·H_2O$, 85 wt %, Shanghai Chemical Co.) were used as stabilizer and reducing agent, respectively. For the photocatalytic test, oxytetracycline was purchased from Sinopharm Chemical Co. Ltd (China). All chemicals were used as received without further purification.

Synthesis of Ag@AgSCN nanostructures

Ag@AgSCN nanostructures were prepared by photoreducing AgSCN nanoparticles. Due to the slow reducing rate of AgSCN under UV–vis light irradiation, the AgSCN nanoparticles (with a small amount of Ag nuclei) were firstly synthesized as follows. At first, 50 mL of deionized water, 5.55 g of PVP, 0.38 g of NH_4SCN and 2 mL $N_2H_4·H_2O$ (85 wt %) were sequentially added to the beaker, and then 10 mL solution of $AgNO_3$ (0.5 M) was injected drop by drop via a pipette. The addition of the $AgNO_3$ solution lasted for ≈6 min, after that the beaker was kept at 30 °C for 30 min under stirring and AgSCN nanostructures with a small amount of Ag nuclei were obtained (labeled as M_1). The precipitate was collected by centrifugation and washed with water several times and then dried at 60 °C for 6 h in a vacuum drying box.

Next, 0.1 g of the above-described nanostructures was dispersed in 50 mL deionized water by ultrasonication. To establish the adsorption–desorption equilibrium, the dispersion was stirred for 30 min under dark prior to the light irradiation. Then the production was performed under UV-light irradiation by using a halogen lamp (400 W). The reaction lasted for 1, 2, 2.5, and 3 h to adjust the ratio of Ag to AgSCN (which are respectively labeled as M_2, M_3, M_4, M_5). The product was collected by centrifugation at 4000 rpm for 5 min and washed with water for three times. In this process, part of AgSCN was transferred to Ag by photoreduction with the color of the solid changing from milk white to pale red, red brown and black. The samples were

dried at 60 °C for 6 h in a vacuum drying box. Then the Ag@AgSCN nanostructures with different molar ratio of Ag:AgSCN were obtained.

As a comparison, the pure AgSCN nanomaterial (labeled as M_0) was also prepared using the same procedure as preparing AgSCN with a small amount of Ag except the addition of $N_2H_4 \cdot H_2O$.

Characterization

The morphology and microstructure of the samples were characterized using a field-emission scanning electron microscope (FE-SEM, JSM-6700F), a transmission electron microscope (TEM, JEM 100-CXII) with an accelerating voltage of 80 kV, and a high-resolution TEM (HRTEM, GEOL-2010) with an accelerating voltage of 200 kV. Also, powder X-ray diffraction (XRD) patterns were collected on an X-ray diffractometer (Rigaku D/Max 2200 PC) with a graphite monochromator and Cu Kα radiation (λ = 0.15148 nm), while the tube voltage and electric current were held at 40 kV and 20 mA. The composition of the samples was tested by Vario EL III organic elemental analyzer (Germany Elmentar Company). Ultraviolet–visible (UV–vis) diffuse reflectance spectra (DRS) were recorded on an Agilent Cary 100 UV–vis spectrophotometer coupled to an integrating sphere with $BaSO_4$ as reference. X-ray photoelectron spectra (XPS) were recorded on a Perkin-Elmer PHI-5300 ESCA spectrometer with a pass energy of 35.75 eV and an Al Kα line excitation source. N_2 adsorption–desorption isotherms were determined by using a Quadrasorb SI apparatus to obtain the Brunauer–Emmett–Teller (BET) surface area. Electrochemical impedance spectroscopy (EIS) was recorded on a CHI660A electrochemical workstation (CH Instrument Company, Shanghai, China).

Photocatalytic performance test

The photocatalytic performance of the Ag@AgSCN nanostructures was evaluated by degradation of oxytetracycline (20 mg/L aqueous solution) at ambient temperature and pressure. To establish the adsorption–desorption equilibrium, the dispersion was stirred for 30 min under dark prior to the light irradiation. The degradation was performed under visible-light irradiation by using a halogen lamp (400 W) with a UV cutoff filter ($\lambda \geq 420$ nm). The halogen lamp spectrum is commonly used to simulate the sunlight spectrum, in which the visible light is about 60–80%. An ≈3 mL aliquot was taken every 10 min and centrifuged to remove the dispersed photocatalyst, and the supernatant was transferred to a quartz cuvette to measure the UV–vis absorption spectrum. The concentration change of oxytetracycline was monitored according to its maximum absorbance at 364 nm (λ_{max}) recorded by a Perkin-Elmer Lambda-35 UV–vis spectrometer.

Supporting Information

Supporting Information File 1

Additional experimental data.
The Supporting Information contains details of the AgSCN characterization, Nyquist plots, EDS spectrum of different Ag/AgSCN samples, and UV–vis absorption spectra of oxytetracycline solutions with M_2 as a catalyst.
[http://www.beilstein-journals.org/bjnano/content/supplementary/2190-4286-8-277-S1.pdf]

Acknowledgements

This work is supported by the National Natural Science Foundation of China (Grant 21771118), and the Taishan Scholars Climbing Program of Shandong Province (tspd20150201).

ORCID® iDs

Dairong Chen - https://orcid.org/0000-0001-6961-9328
Xiuling Jiao - https://orcid.org/0000-0002-4358-7396

References

1. Kelsic, E. D.; Zhao, J.; Vetsigian, K.; Kishony, R. *Nature* **2015,** *521,* 516–519. doi:10.1038/nature14485
2. Cui, W.; Li, J.; Dong, F.; Sun, Y.; Jiang, G.; Cen, W.; Lee, S. C.; Wu, Z. *Environ. Sci. Technol.* **2017,** *51,* 10682–10690. doi:10.1021/acs.est.7b00974
3. Dong, F.; Xiong, T.; Sun, Y.; Lu, L.; Zhang, Y.; Zhang, H.; Huang, H.; Zhou, Y.; Wu, Z. *Appl. Catal., B: Environ.* **2017,** *219,* 450–458. doi:10.1016/j.apcatb.2017.07.082
4. Cui, W.; Li, J.; Cen, W.; Sun, Y.; Lee, S. C.; Dong, F. *J. Catal.* **2017,** *352,* 351–360. doi:10.1016/j.jcat.2017.05.017
5. Cavalcante, R. P.; Dantas, R. F.; Bayarri, B.; González, O.; Giménez, J.; Esplugas, S.; Junior, A. M. *Catal. Today* **2015,** *252,* 27–34. doi:10.1016/j.cattod.2014.09.030
6. Wang, Y.; Feng, C.; Zhang, M.; Yang, J.; Zhang, Z. *Appl. Catal., B* **2010,** *100,* 84–90. doi:10.1016/j.apcatb.2010.07.015
7. Meng, F.; Hong, Z.; Arndt, J.; Li, M.; Zhi, M.; Yang, F.; Wu, N. *Nano Res.* **2012,** *5,* 213–221. doi:10.1007/s12274-012-0201-x
8. Cao, Y.; Li, C.; Li, J.; Li, Q.; Yang, J. *Nanoscale Res. Lett.* **2015,** *10,* 251. doi:10.1186/s11671-015-0952-x
9. Kuai, L.; Geng, B.; Chen, X.; Zhao, Y.; Luo, Y. *Langmuir* **2010,** *26,* 18723–18727. doi:10.1021/la104022g
10. Hou, W.; Cronin, S. B. *Adv. Funct. Mater.* **2013,** *23,* 1612–1619. doi:10.1002/adfm.201202148
11. Wang, P.; Huang, B.; Qin, X.; Zhang, X.; Dai, Y.; Wei, J.; Whangbo, M.-H. *Angew. Chem., Int. Ed.* **2008,** *47,* 7931–7933. doi:10.1002/anie.200802483
12. Chen, Y.-S.; Choi, H.; Kamat, P. V. *J. Am. Chem. Soc.* **2013,** *135,* 8822–8825. doi:10.1021/ja403807f
13. Tang, Y.; Jiang, Z.; Xing, G.; Li, A.; Kanhere, P. D.; Zhang, Y.; Sum, T. C.; Li, S.; Chen, X.; Dong, Z.; Chen, Z. *Adv. Funct. Mater.* **2013,** *23,* 2932–2940. doi:10.1002/adfm.201203379
14. Ma, B.; Guo, J.; Dai, W.-L.; Fan, K. *Appl. Catal., B: Environ.* **2013,** *130–131,* 257–263. doi:10.1016/j.apcatb.2012.10.026

15. Wang, P.; Huang, B.; Qin, X.; Zhang, X.; Dai, Y.; Wei, J.; Whangbo, M.-H. *Angew. Chem.* **2008,** *120,* 8049–8051. doi:10.1002/ange.200802483
16. Wang, H.; Yang, X.; Zi, J.; Zhou, M.; Ye, Z.; Li, J.; Guan, Q.; Lv, P.; Huo, P.; Yan, Y. *J. Ind. Eng. Chem.* **2016,** *35,* 83–92. doi:10.1016/j.jiec.2015.12.023
17. Wang, P.; Huang, B.; Zhang, X.; Qin, X.; Jin, H.; Dai, Y.; Wang, Z.; Wei, J.; Zhan, J.; Wang, S.; Wang, J.; Whangbo, M.-H. *Chem. – Eur. J.* **2009,** *15,* 1821–1824. doi:10.1002/chem.200802327
18. Hu, C.; Peng, T.; Hu, X.; Nie, Y.; Zhou, X.; Qu, J.; He, H. *J. Am. Chem. Soc.* **2010,** *132,* 857–862. doi:10.1021/ja907792d
19. Lou, Z.; Huang, B.; Wang, P.; Wang, Z.; Qin, X.; Zhang, X.; Cheng, H.; Zheng, Z.; Dai, Y. *Dalton Trans.* **2011,** *40,* 4104–4110. doi:10.1039/c0dt01795g
20. Xia, Y.; Xiong, Y.; Lim, B.; Skrabalak, S. E. *Angew. Chem., Int. Ed.* **2008,** *48,* 60–103. doi:10.1002/anie.200802248
21. An, C.; Peng, S.; Sun, Y. *Adv. Mater.* **2010,** *22,* 2570–2574. doi:10.1002/adma.200904116
22. Chen, H.; Xiao, L.; Huang, J. *Mater. Res. Bull.* **2014,** *57,* 35–40. doi:10.1016/j.materresbull.2014.05.032
23. Zhang, S.; Zhang, S.; Song, L.; Wu, X.; Fang, S. *Chem. Eng. J.* **2014,** *243,* 24–30. doi:10.1016/j.cej.2014.01.015
24. Hu, J.-W.; Zhang, X. *Powder Technol.* **2014,** *267,* 240–244. doi:10.1016/j.powtec.2014.07.035
25. Lin, J.-D.; Li, Z.-H.; Li, J.-R.; Du, S.-W. *Polyhedron* **2007,** *26,* 107–114. doi:10.1016/j.poly.2006.07.034
26. Yang, M.; Ma, J. *Appl. Surf. Sci.* **2009,** *255,* 9323–9326. doi:10.1016/j.apsusc.2009.07.028
27. Zurmühl, C.; Wolf, S.; Feldmann, C. *Z. Anorg. Allg. Chem.* **2015,** *641,* 1510–1514. doi:10.1002/zaac.201500107
28. Soofivand, F.; Salavati-Niasari, M.; Mohandes, F. *J. Ind. Eng. Chem.* **2014,** *20,* 3780–3788. doi:10.1016/j.jiec.2013.12.079
29. Amornpitoksuk, P.; Suwanboon, S. *Adv. Powder Technol.* **2014,** *25,* 1026–1030. doi:10.1016/j.apt.2014.02.001
30. Gong, J.; Cao, J.; Zhang, J.; Liao, Q.; Zhang, G.; Wu, X. *Mater. Technol. (Abingdon, U. K.)* **2017**. doi:10.1080/10667857.2017.1336597
31. Wang, P.; Huang, B.; Dai, Y.; Whangbo, M.-H. *Phys. Chem. Chem. Phys.* **2012,** *14,* 9813–9825. doi:10.1039/c2cp40823f
32. Cushing, S. K.; Li, J.; Meng, F.; Senty, T. R.; Suri, S.; Zhi, M.; Li, M.; Bristow, A. D.; Wu, N. *J. Am. Chem. Soc.* **2012,** *134,* 15033–15041. doi:10.1021/ja305603t
33. Liu, Y.; Fang, L.; Lu, H.; Li, Y.; Hu, C.; Yu, H. *Appl. Catal., B: Environ.* **2012,** *115–116,* 245–252. doi:10.1016/j.apcatb.2011.12.038
34. Zeng, J.; Xia, X.; Rycenga, M.; Henneghan, P.; Li, Q.; Xia, Y. *Angew. Chem.* **2011,** *50,* 244–249. doi:10.1002/anie.201005549
35. Wang, P.; Huang, B.; Lou, Z.; Zhang, X.; Qin, X.; Dai, Y.; Zheng, Z.; Wang, X. *Chem. – Eur. J.* **2010,** *16,* 538–544. doi:10.1002/chem.200901954
36. Xiang, Q.; Meng, G. F.; Zhao, H. B.; Zhang, Y.; Li, H.; Ma, W. J.; Xu, J. Q. *J. Phys. Chem. C* **2010,** *114,* 2049–2055. doi:10.1021/jp909742d
37. Gyawali, G.; Adhikari, R.; Joshi, B.; Kim, T. H.; Rodríguez-Gonzalez, V.; Lee, S. W. *J. Hazard. Mater.* **2013,** *263,* 45–51. doi:10.1016/j.jhazmat.2013.03.065
38. Niu, J.; Ding, S.; Zhang, L.; Zhao, J.; Feng, C. *Chemosphere* **2013,** *93,* 1–8. doi:10.1016/j.chemosphere.2013.04.043
39. Stylidi, M.; Kondarides, D. I.; Verykios, X. E. *Appl. Catal., B: Environ.* **2004,** *47,* 189–201. doi:10.1016/j.apcatb.2003.09.014
40. Choudhury, B.; Borah, B.; Choudhury, A. *Photochem. Photobiol.* **2012,** *88,* 257–264. doi:10.1111/j.1751-1097.2011.01064.x

License and Terms

This is an Open Access article under the terms of the Creative Commons Attribution License (http://creativecommons.org/licenses/by/4.0), which permits unrestricted use, distribution, and reproduction in any medium, provided the original work is properly cited.

The license is subject to the *Beilstein Journal of Nanotechnology* terms and conditions: (http://www.beilstein-journals.org/bjnano)

The definitive version of this article is the electronic one which can be found at:
doi:10.3762/bjnano.8.277

BEILSTEIN JOURNAL OF NANOTECHNOLOGY

Review on optofluidic microreactors for artificial photosynthesis

Xiaowen Huang[1,2,3], Jianchun Wang[1], Tenghao Li[2,3], Jianmei Wang[1], Min Xu[1], Weixing Yu[4], Abdel El Abed[5] and Xuming Zhang[*2,3,§]

Review

Open Access

Address:
[1]Energy Research Institute, Shandong Academy of Sciences, Jinan, Shandong 250014, China, [2]Department of Applied Physics, The Hong Kong Polytechnic University, Hong Kong, China, [3]The Hong Kong Polytechnic University Shenzhen Research Institute, Shenzhen 518057, China, [4]Key Laboratory of Spectral Imaging Technology, Xi'an Institute of Optics and Precision Mechanics, Chinese Academy of Sciences, Xi'an, Shaanxi 710119, China, and [5]Laboratoire de Photonique Quantique et Moléculaire, UMR 8537, Ecole Normale Supérieure de Cachan, CentraleSupélec, CNRS, Université Paris-Saclay, 61 avenue du Président Wilson, 94235 Cachan, France

Email:
Xuming Zhang* - apzhang@polyu.edu.hk

* Corresponding author
§ Tel.: +852-34003258; Fax: +852-23337629

Keywords:
artificial photosynthesis; carbon dioxide fixation; coenzyme regeneration; microfluidics; optofluidics; water splitting

Beilstein J. Nanotechnol. **2018,** *9,* 30–41.
doi:10.3762/bjnano.9.5

Received: 20 July 2017
Accepted: 06 December 2017
Published: 04 January 2018

This article is part of the Thematic Series "Energy conversion, storage and environmental remediation using nanomaterials".

Guest Editor: W.-J. Ong

© 2018 Huang et al.; licensee Beilstein-Institut.
License and terms: see end of document.

Abstract

Artificial photosynthesis (APS) mimics natural photosynthesis (NPS) to store solar energy in chemical compounds for applications such as water splitting, CO_2 fixation and coenzyme regeneration. NPS is naturally an optofluidic system since the cells (typical size 10 to 100 µm) of green plants, algae, and cyanobacteria enable light capture, biochemical and enzymatic reactions and the related material transport in a microscale, aqueous environment. The long history of evolution has equipped NPS with the remarkable merits of a large surface-area-to-volume ratio, fast small molecule diffusion and precise control of mass transfer. APS is expected to share many of the same advantages of NPS and could even provide more functionality if optofluidic technology is introduced. Recently, many studies have reported on optofluidic APS systems, but there is still a lack of an in-depth review. This article will start with a brief introduction of the physical mechanisms and will then review recent progresses in water splitting, CO_2 fixation and coenzyme regeneration in optofluidic APS systems, followed by discussions on pending problems for real applications.

Review

Introduction

The emerging energy crisis, the greenhouse effect and food shortage are devastating problems to be solved, and artificial photosynthesis (APS) is considered to be the most promising and viable method [1-9]. As the name implies, APS is the human replication of natural photosynthesis (NPS). NPS is a very important process in plants and other organisms which utilize sunlight, water and CO_2 to synthesize energy-rich carbohydrates [10,11]. The chloroplast is the place where NPS occurs. To clearly introduce this organelle, progressively smaller structures (plant cell, chloroplast, thylakoid membrane) of a general leaf are shown in Figure 1A–D. Each chloroplast (Figure 1C) contains numerous thylakoids. On the thylakoid membrane, the natural light-harvesting antenna complexes, photosystem II (PS II, P680) and photosystem I (PS I, P700), capture the photons and regenerate the coenzyme for carbohydrates synthesis (Figure 1D). However, in APS, sunlight is used to create not only the carbohydrates but also other high-value chemicals from abundant resources [12-21].

Based on the targeted production, three key areas in the field of APS have attracted intense attention including: photocatalytic water splitting [24,25], light-driven CO_2 reduction [26] and photo-coenzyme regeneration [27] (see Figure 2), which are promising solutions to the energy crisis, greenhouse effect and food shortage, respectively [24,26,28-45].

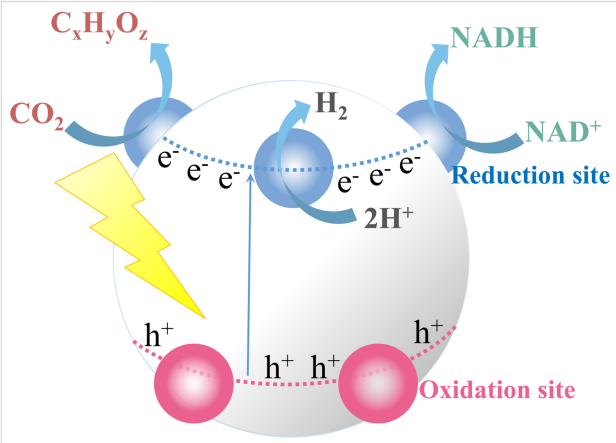

Figure 2: Basic principles and reactions in artificial photosynthesis, in which the processes of water splitting, CO_2 reduction and coenzyme regeneration all utilize electrons on the reduction site.

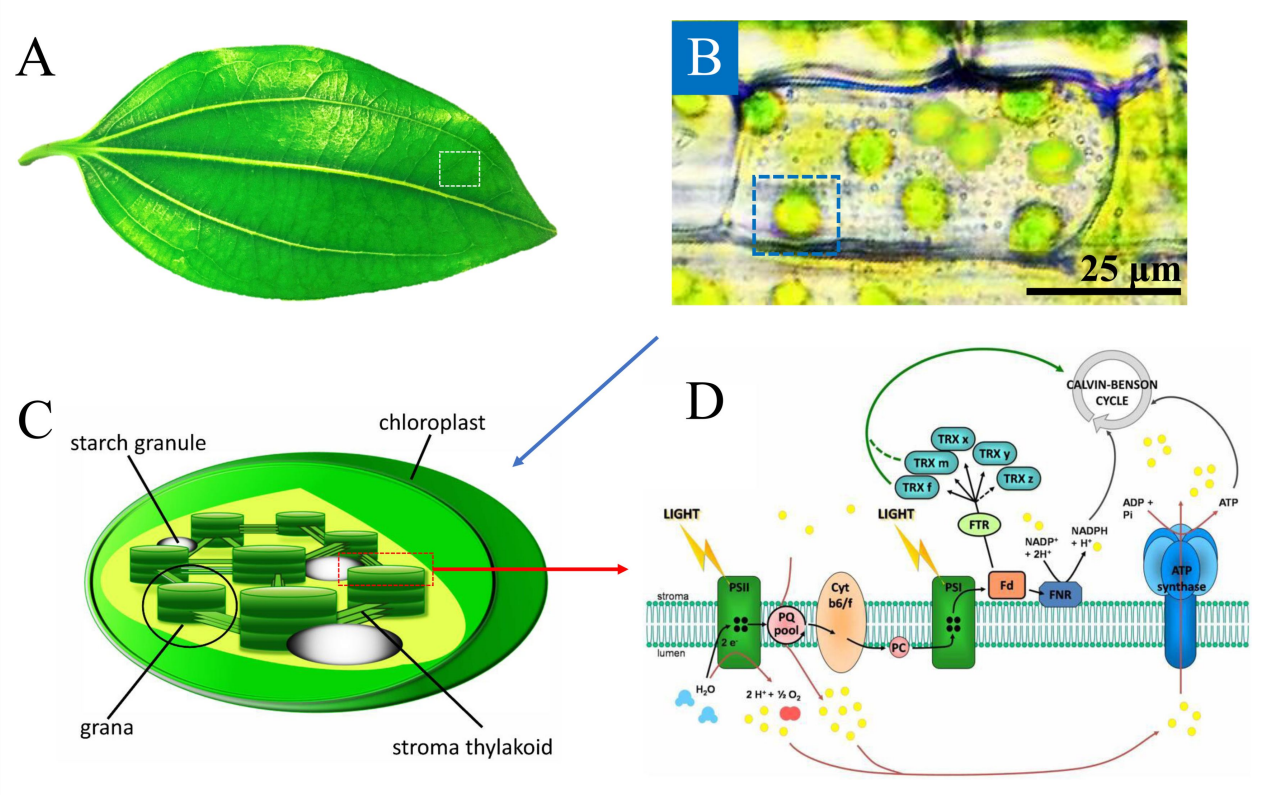

Figure 1: (A) A typical plant leaf. (B) Chloroplasts inside the plant cells. The average size of the chloroplasts is 6 µm (ranging from 3 to 10 µm). (C) Plant cell chloroplast structure. Adapted from [22], copyright BioMed Central Ltd. 2014. (D) Thylakoid membrane containing photosystem II reaction centers P680 and photosystem I reaction centers P700. Adapted from [23], copyright 2013 Michelet, Zaffagnini, Morisse, Sparla, Pérez-Pérez, Francia, Danon, Marchand, Fermani, Trost, and Lemaire.

Photocatalytic water splitting aims to convert water into hydrogen and oxygen. Some studies have focused on only the half-reaction for water splitting, while ignoring the other half-reaction for oxygen production. This is often called photocatalytic hydrogen production (or generation) and can be regarded as a low-configured version of photocatalytic water splitting. As a renewable and nontoxic gas, hydrogen works not only as a clean fuel but also as a feedstock for important chemical production, such as ammonia and methanol. Similarly, light-driven CO_2 reduction has great potential as a clean fuel supplier, especially for the production of methanol or methane [45,46]. Additionally, with the consumption of CO_2, APS possibly provides a solution to the greenhouse effect and global warming. Unlike human beings, plants have no need to use CO_2 as a clean fuel or for to reduce the greenhouse effect. They simply "consume" CO_2 to produce carbohydrates (e.g., sugar, cellulose). The global demand for food is increasing dramatically with the continuous growth of the world population [47]. An increase in population requires more land, water and energy, which in turn decreases the ability to produce food. Meanwhile, the requirement for more land results in the destruction of an increased area of forests, further disrupting the climate change and the greenhouse effect. Thus, in a global perspective, the energy crisis, climate change, greenhouse effect, air pollution and food shortage are interconnected. Food production in the form of crops relies on the famous Calvin cycle, in which the coenzymes – nicotinamide adenine dinucleotide hydride (NADH) and nicotinamide adenine dinucleotide phosphate hydride (NADPH) – play an important role since they work as the reducing power for the biosynthetic reactions. Despite its advantages, NPS still has a very low energy conversion efficiency (typically <1%) to capture sunlight and CO_2 for the production of carbohydrates, even after billions of years of evolution, and it is far from its theoretical limit of 30% [48]. This gives great room to develop an improved scientific solution to produce basic food materials with high energy efficiency while circumventing all the problems.

Optofluidic technology has recently exploded with new concepts to enable fine control of light and liquids in microscale structures [39-41]. In fact, NPS is naturally an optofluidic system as it is carried out in microscale organisms (chloroplasts) filled with fluids (see Figure 1), inferring the feasibility to be mimicked by man-made optofluidic structures. Optofluidics can promote the reaction efficiencies due to its advantages such as large surface-area-to-volume ratio [40], fast reaction rate, high-precision manipulation [38], easy flow control and improved mass and photon transfer in the reaction system [49-53]. The small volume of optofluidic systems reduces the diffusion time, dramatically increases the reaction rate on the photocatalyst surface, and reduces the consumption of expensive photocatalysts and enzymes. Therefore, this platform is also useful for the rapid screening of various photocatalysts [54-59]. Inexpensive, parallel tests are beneficial for the rare or expensive chemical reactions, too [60,61]. Moreover, for enzymatic reactions, the flow-based reaction has the great advantage of avoiding product inhibition and cross-reaction [42]. Furthermore, cascaded reactions can be divided into different areas where each region can be set with their own optimal reaction conditions such as temperature, pH and concentration. The various photocatalytic nanomaterials [62] can be designed in different forms in the microreactor inside the optofluidic device, such as in the form of immobilized nanoparticles, films, plugs, droplets, etc.

Fortunately, many works have contributed to the field of APS. The research efforts have mostly focus on aspects such as development of novel catalytic materials, modification of the existed catalytic materials (e.g., noble-gas doping, co-catalyst impregnation, noble-metal loading, plasmonic sensitization and Z-scheme systems), and optofluidics (or microfluidics) based APS.

It should be noted that many efforts have been made to develop bio-photoreactors to culture microorganisms to produce microalgae, bioenergy and biomass [63]. Broadly speaking, these bio-photoreactors also belong to optofluidics-based APS, but they are not covered in this article since many of them use large reactors and are thus not related to microstructures.

The following review will start with a brief introduction on the mechanisms of photocatalysis-based APS (water splitting, CO_2 reduction and coenzyme regeneration). Then we will introduce the representative designs of these three areas with an emphasis on how they help solve the existing problems in their respective area. Finally, we conclude with a discussion of the technical barriers that hinder their practical application.

Basic mechanisms of artificial photosynthesis

The APS reaction is not a spontaneous reaction, for example, the Gibbs free energy in water splitting increases by 237 $kJ \cdot mol^{-1}$, and the required energy could be offered by external light. In principle, a semiconductor photocatalyst (e.g., TiO_2, C_3N_4) absorbs the appropriate photon ($h\nu \geq E_0$, where E_0 is the bandgap of the semiconductor photocatalyst) to excite an electron in the conduction band, leaving a hole in the valence band. The electron moves to the surface-active sites for surface redox reactions [64]. The activation equations for water splitting, CO_2 photoreduction and coenzyme regeneration are as follows:

$$\mathrm{SC} + h\nu \rightarrow \mathrm{SC}(\mathrm{e_{cb}}^- + \mathrm{h_{vb}}^-) \quad (1)$$

$$2H_2O + 4h^+ \rightarrow 4H^+ + O_2 \quad (2)$$

$$2H^+ + 2e^- \rightarrow H_2 \quad (3)$$

$$CO_2 + 6H^+ + 6e^- \rightarrow CH_3OH + H_2O \quad (4)$$

$$CH_3OH + 2CO \rightarrow CH_3CHO + CO_2 \quad (5)$$

$$CH_3OH + CO_2 + 2H^+ + 2e^- \rightarrow HCOOCH_3 + H_2O \quad (6)$$

$$HCOOCH_3 + CO \rightarrow CH_3CHO + CO_2 \quad (7)$$

$$HCOOCH_3 + 4H^+ + 4e^- \rightarrow 2CH_3OH \quad (8)$$

$$H_2O + CO \rightarrow H_2 + CO_2 \quad (9)$$

$$NAD^+ + H^+ + 2e^- \rightarrow NADH \quad (10)$$

Equation 1 represents the formation of the electron–hole pair. Equation 2 and Equation 3 describe the water splitting process. Equations 4–9 present the CO_2 reduction processes and Equation 10 is the typical NAD^+ regeneration. For clearly uncovering the chemical mechanism from the reactants to products, some intermediate processes are reasonably ignored.

All these three items (i.e., water splitting, CO_2 reduction and coenzyme regeneration) utilize the electrons on the reduction site, as shown in Figure 2. However, recombination of photoexcited electrons and holes may occur. Even after the electrons are moved to the surface of photocatalysts, some of them would be wasted due to recombination if the electrons are not used immediately for the redox reactions [65-67].

The desirable features of a photocatalyst include wide-range absorption, long-term stability, fast electron–hole separation, and strong redox powers. However, it is difficult to have all of these features in a single photocatalyst. Thereby, a simple heterojunction of two or more photocatalysts and artificial Z-scheme photocatalytic systems have been developed [68]. Figure 3A shows the charge carrier transfer in a heterojunction-type photocatalytic system, in which the photo-generated electrons and holes are separated in space to suppress the undesirable recombination. However, when the charge carriers are transferred to lower potentials, the redox ability of these electrons and holes is weakened. Then, another type of photocatalytic system is explored, as shown in Figure 3B. The electron acceptor/donor (A/D) pair is introduced to form the Z-scheme system, known as the PS-A/D-PS system. Since the electron acceptor (A) can react with both the photogenerated electron in PS I and PS II, the electron donor (D) can react with both the photogenerated hole in PS I and PS II, and backward reactions would occur, leading to a significant waste of photogenerated electrons and holes. In another design, the A/D pair is replaced by the conductor (C) to form the PS-C-PS system, as shown in Figure 3C. The inserted conductor acts as the electron mediator and forms the ohmic contact with low contact resistance between PS II and PS I. Through the ohmic contact, the photogenerated electrons from PS II directly recombine with the photogenerated holes from PS I, reducing the electron transfer distance and avoiding the backward reaction in the PS-A/D-PS system. Another simpler design using the solid–solid contact (PS-PS system) is illustrated in Figure 3D. On the contact interface, many defects are easily aggregated, causing the energy levels to be quasi-continuous for the ohmic contact. Besides, the biomimetic or bioinspired strategy showed the most interesting results. Zhou et al. reported a light-harvesting antenna-network inspired polymeric semiconductor-based hybrid nano-system in which water and CO_2 were catalyzed to form H_2 and CO in this integrated system [66]. Jiang et al. showed a thylakoid-inspired multishell g-C_3N_4 nanocapsule with orderly stacked nanostructures, which exhibited enhanced visible-light harvesting and electron-transfer properties for high-efficiency photocatalysis [67].

In summary, the basic mechanism of APS is comprised of three processes: (1) generation of charge carriers (i.e., electrons and holes), (2) separation and transfer of charge carriers, and (3) chemical reactions between surface species and charge carriers. Based on this mechanism, various materials have been developed to improve the photocatalytic efficiency [69-72]. Furthermore, by taking advantage of the properties of optofluidics, many studies with interesting improvements have been reported. We will now review these in terms of water splitting, CO_2 reduction and coenzyme regeneration.

Microreactors for artificial photosynthesis

An optofluidic microreactor is a versatile platform for combining new materials and characterizing their reaction kinetics without expensive bulky setups. Recent developments in optofluidics has allowed for the advancement of APS technology by use of the microreactors.

Water splitting

In the early studies on optofluidic-based water splitting, the optofluidic device often employed sol–gel catalysts on planar channels. For example, Erickson et al. demonstrated a planar setup with TiO_2–Pt to process the water splitting reaction [73].

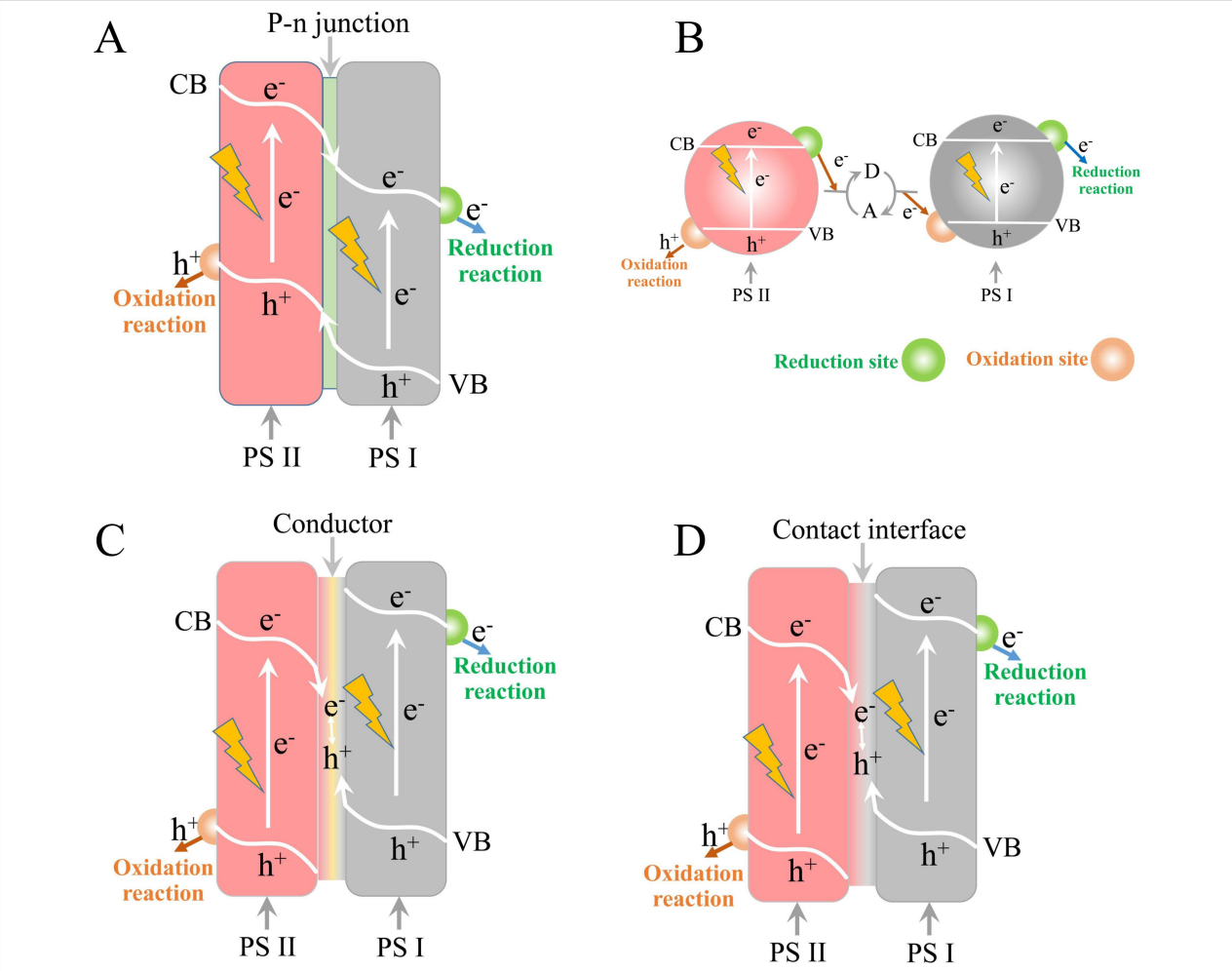

Figure 3: Schematic diagrams of heterojunction and Z-scheme systems. Transfer of charge carriers in (A) the heterojunction-type photocatalytic system, (B) the Z-scheme PS-A/D-PS system, (C) the Z-scheme PS-C-PS system, and (D) the Z-scheme electron PS-PS system. Adapted from [68], copyright 2014 Wiley-VCH Verlag GmbH & Co. KGaA. PS stands for photosystem.

The reaction was mediated by I^-/IO_3^- redox pairs, belonging to the PS-A/D-PS system. After the reaction, the optofluidic device showed ≈2-fold improvement in the reaction rates as compared to the traditional bulk method. Nevertheless, this planar design still showed an unsatisfactory performance of hydrogen generation due to a limited active surface area and low mass transfer rate. In another work, Wang et al. proposed an optofluidic microreactor with staggered micropillars in the reaction microchamber [74], as shown in Figure 4. Such structure has four favorable features: (1) enlarged surface area for loading catalysts; (2) perturbation to the liquid flow for rapid mixing; (3) shortened transfer length and enhanced mass transfer; and (4) increased active surface area. With these advantages, the reaction rate could be increased by 56% as compared to the conventional planar microreactors.

However, a new problem emerges: the direct coating methods are unable to load catalysts firmly and uniformly on the PDMS substrate. Zhang et al. proposed a new casting transfer method for loading catalysts on the PDMS substrate [36], as shown in Figure 5. This method exhibited critically higher durability and better hydrogen production rate than the conventional ones.

CO_2 reduction

Optofluidic microreactors have been firstly applied for water purification [50], water splitting [73], photocatalytic fuel cells [75] and then CO_2 reduction [76]. Chen et al. combined the optofluidics with the TiO_2/carbon paper composite membrane for the photoreduction of CO_2 [76], as shown in Figure 6. Using this device, they studied the factors that affected the methanol yield (such as flow rate, light intensity and catalyst loading) and obtained a high reduction result in comparison to the reported data. Other membrane-based reactors were reported as well, for instance, mesoporous CdS/TiO_2/SBA-15@carbon paper composite membranes [77] and copper-decorated TiO_2 nanorod thin films [78].

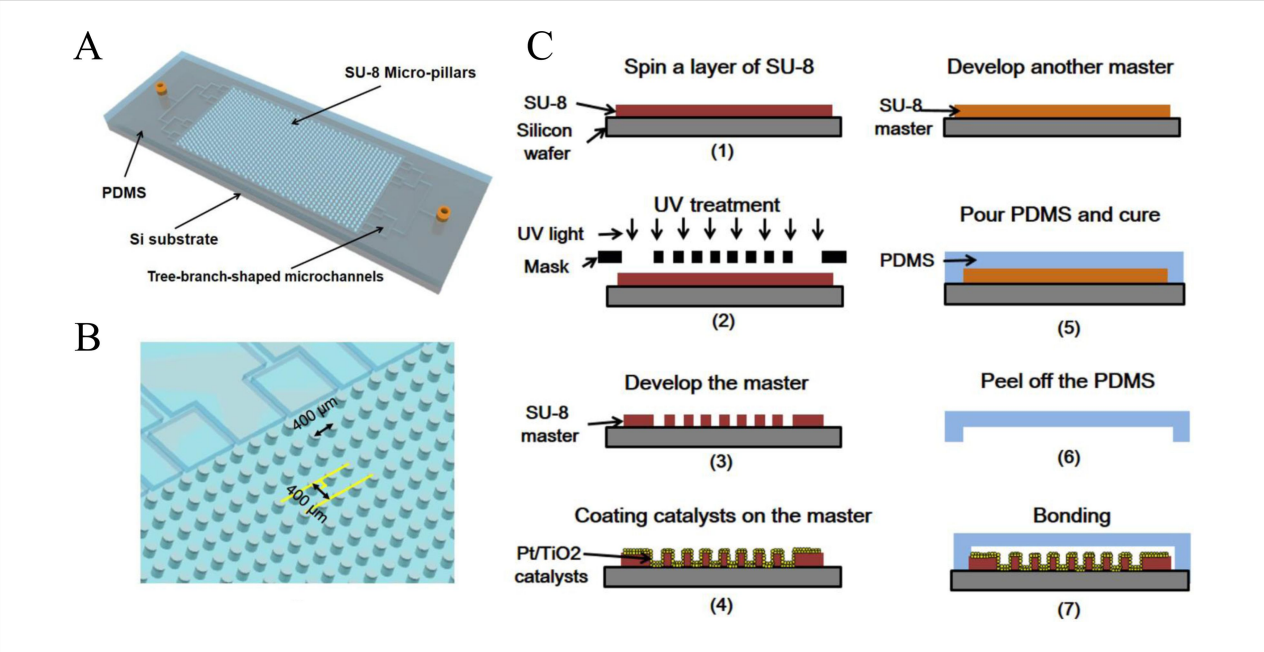

Figure 4: (A) Schematic of the high-surface-area optofluidic microreactor with micropillar structure. (B) Staggered micropillars in the reaction chamber. (C) Fabrication procedure of the optofluidic microreactor with the catalyst-coated micropillars. Reprint with the permission from [74], copyright 2014 Elsevier Ltd.

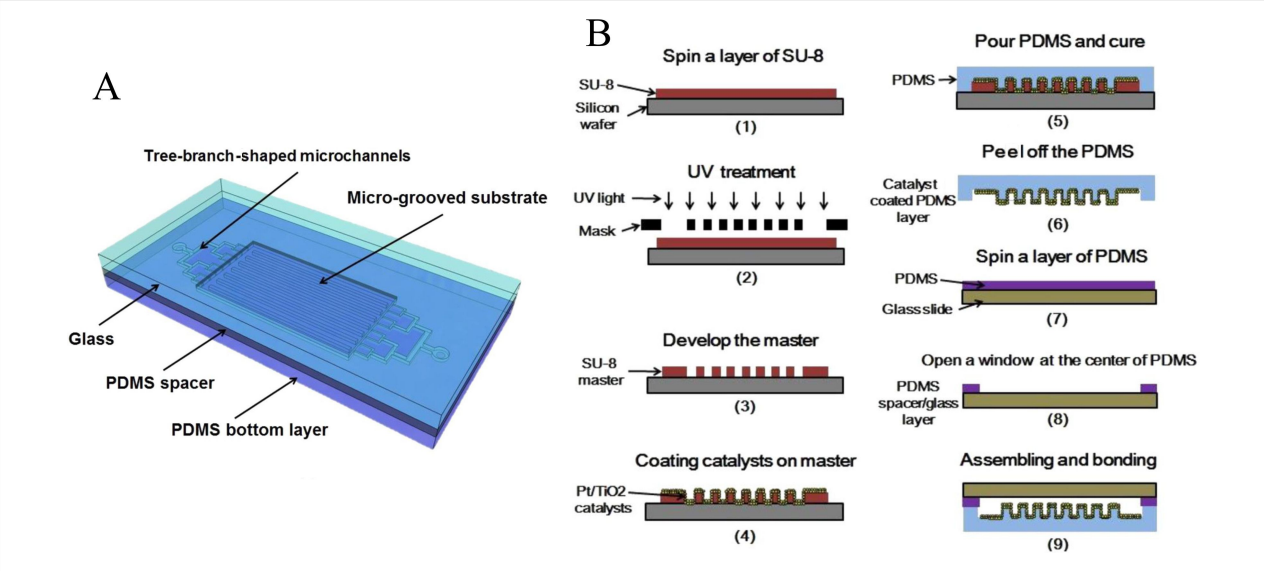

Figure 5: (A) Schematic of the high-surface-area optofluidic microreactor with micro-grooved structure. (B) Fabrication procedure of the optofluidic microreactor with the catalysts on the PDMS substrate. Adapted from [36], copyright 2015 Elsevier Ltd.

In addition to the PDMS/PMMA-based microchannel reactors, bacterium has been shown to be a good microreactor as well. Yang et al. developed a hybrid approach that combined highly efficient light harvesting of inorganic semiconductors with biocatalysts [79]. As shown in Figure 7, they induced a non-photosynthetic bacterium with biologically precipitated CdS nanoparticles, enabling the photosynthesis of acetic acid from CO_2. The CdS nanoparticles functioned as the light harvester. This self-augmented biological system selectively produced acetic acid continuously over several days, demonstrating a novel CO_2 reduction microreactor.

Coenzyme regeneration

APS-based coenzyme regeneration has attracted less attention as compared to water splitting and CO_2 reduction [80], but significant progress had already been made before it was combined

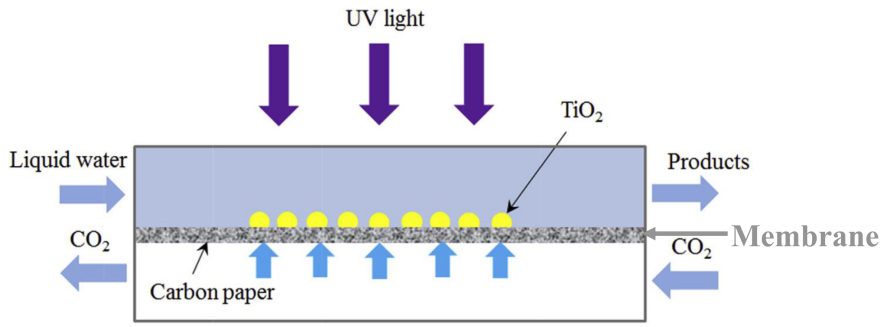

Figure 6: Schematic of the optofluidic membrane microreactor for photocatalytic CO_2 reduction. Adapted from [76], copyright 2016 Elsevier Ltd.

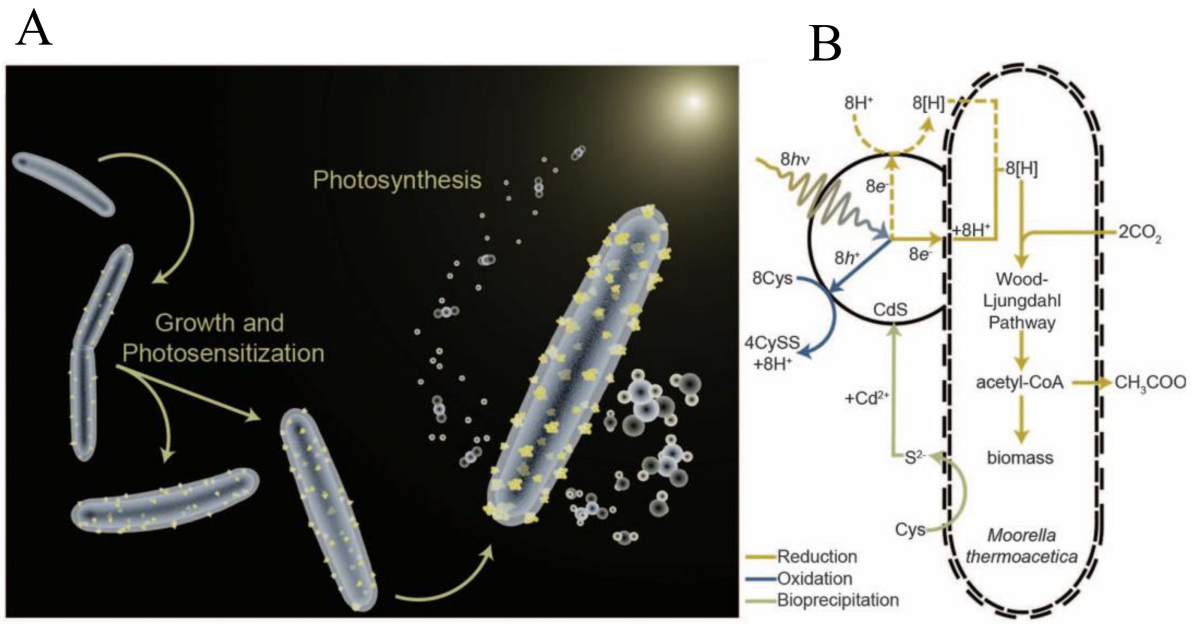

Figure 7: (A) Bacterium–CdS hybrid system that has CdS nanoparticles on the bacterium membrane (yellow particles). (B) Pathway diagram for the light harvesting and the photosynthetic conversion of CO_2 to acetic acid with the bacterial enzyme system. Adapted from [79], copyright 2016 American Association for the Advancement of Science.

with the optofluidics [81]. Park et al. developed CdS quantum-dot-sensitized TiO_2 nanotube arrays for the photo-regeneration of nicotinamide cofactors [82]. They also used SiO_2-supported CdS quantum dots for sustainable NADH regeneration [83]. However, the toxicity and photoinduced instability of CdS limited the application of this material. Liu et al. used carbon nitride (C_3N_4), a stable and environmental friendly material [84], for NADH regeneration [85-87]. For example, one bioinspired method utilized the diatom as the C_3N_4 formation templet, enlarging the specific surface area for enhanced light trapping and scattering and eventually high photocatalytic efficiency [27]. This research is mostly based on the slurry method. Optofluidics-based coenzyme regeneration appeared only in recent years.

Park et al. presented an optofluidic device that incorporated quantum dots and redox enzymes for photo-enzymatic synthesis [88]. As shown in Figure 8, the microchannel was separated into two parts by a valve, the light-dependent reaction zone for NADH regeneration in the upstream of microchannel and the light-independent zone for enzymatic synthesis in the downstream. Our group reported a optofluidic chip-based artificial PS I using a novel one-step fabrication method (see Figure 9), which outperformed the traditional methods in several aspects in terms of facile synthesis, promotion of the combination of g-C_3N_4 and electron mediator through π–π stacking, in addition to a significantly enhanced coenzyme regeneration rate [89]. Coenzyme regeneration is also of great importance in CO_2 reduction with the help of enzymes. Formaldehyde dehydroge-

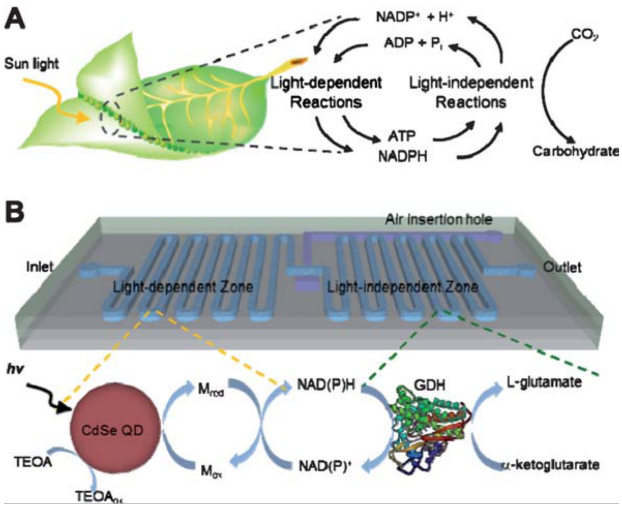

Figure 8: Microfluidic APS platform that incorporates quantum dots and redox enzymes for photoenzymatic synthesis. (A) Concept and (B) besign of microreactor in which the cofactor regeneration takes place in the light-dependent reaction zone and the enzymatic synthesis in the light-independent zone. Adapted from [88], copyright 2011 Royal Society of Chemistry.

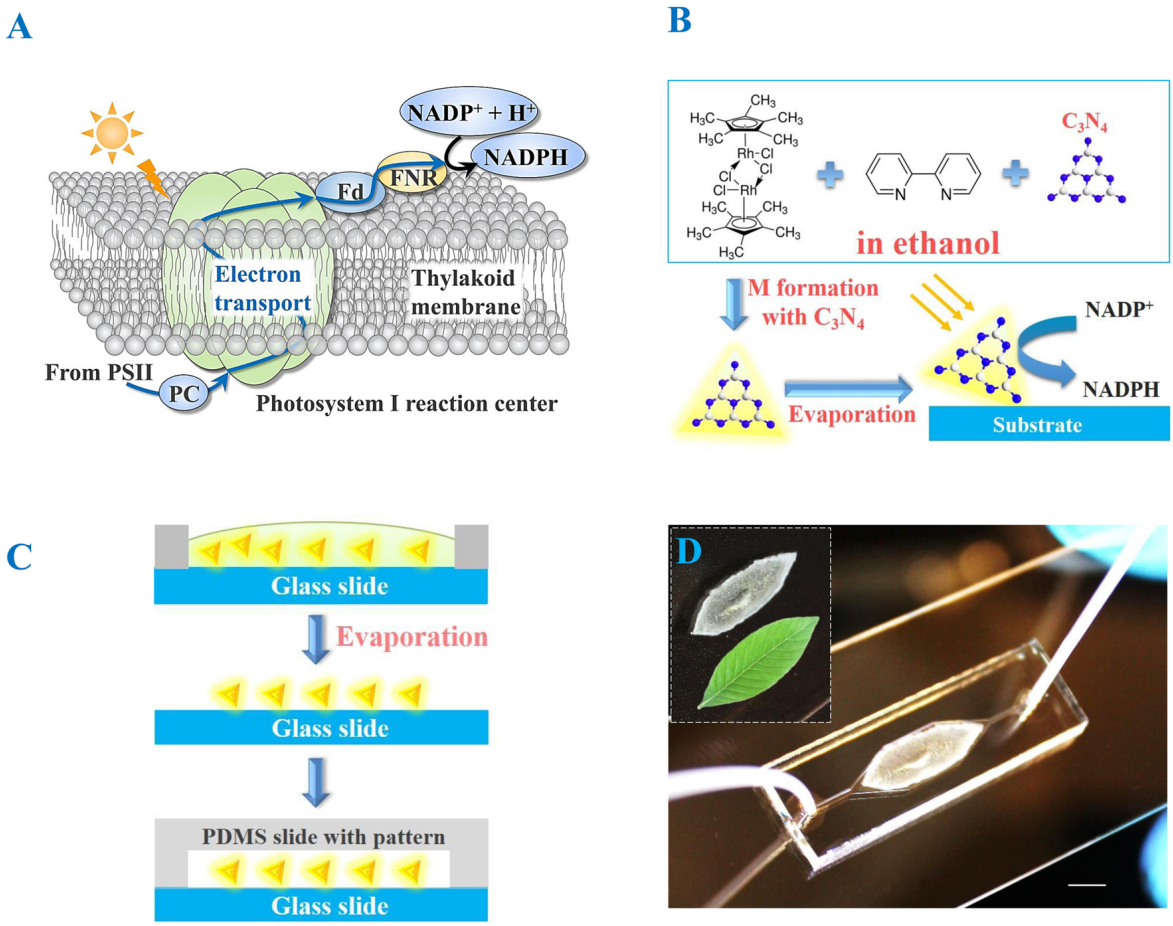

Figure 9: Microfluidic chip based artificial photosystem I. (A) Schematic illustration of the PS I reaction center. (B) One-step fabrication process of the immobilized artificial PS I (IAPSI) in the form of the g-C_3N_4-M film. (C) Simple procedures to fabricate the IAPSI microreactor. (D) Photograph of the as-fabricated IAPSI microreactor, in which the inset presents the leaf-like shape of g-C_3N_4-M. The scale bar is 2 mm. Adapted from [89], copyright 2016 The Royal Society of Chemistry.

nase is a typical one that selectively achieves methanol formation from CO_2 with the depletion of NADH to NAD^+ [46]. The continuous regeneration of NADH enables the continuous reduction of CO_2.

Conclusion

APS is a promising way to utilize solar energy and a prospective solution for the energy crisis, greenhouse effect and coenzyme utilization. An effective photocatalyst is expected to have wide-range absorption, long-term stability, fast electron–hole separation, and strong redox power. The heterojunction and Z-scheme systems are the important most research results to date. Based on these systems, various materials have been developed for the improvement of photocatalytic efficiency [90-94]. Besides, biomimetic or bioinspired strategies for the synthesis of semiconductor materials represents a significant advancement in the development of high-efficiency and cost-effective visible-light photocatalysts for solar energy conversion [65-67]. Given the advantages of optofluidic systems, more studies with significant improvement are expected.

The optofluidic planar microreactor has shown to be a versatile platform for superior performance in water splitting, CO_2 reduction and coenzyme regeneration. However, there are still some problems. One problem is the limited production amount caused by the small volume of the microreactor. For high throughput and adequate production, a feasible solution may involve the combination of two approaches: to parallelize the microreactors to form an array and to enlarge the microchannel in the lateral direction into a planar chamber [50,95-98]. Another problem is the lack of an integrated on-chip detection method. After the reaction, the production products should be collected and then analyzed by the bulky, expensive, traditional off-chip equipment, such as a UV–vis spectrometer or high-performance liquid chromatography and gas chromatography mass spectrometer. As demonstrated by our group in a work on microfluidic water purification [99], on-chip detection would make it convenient to monitor the reaction process in real time, to probe the intermediate reactions/productions and to study the reaction kinetics.

In view of the many merits induced by optofluidics, the microreactors may be also introduced to other APS systems such as nitrogen fixation (e.g., NH_4) [100], CH_4 [101-106], CO [107-111], formaldehyde [112,113], methanol [114-116], and formic acid [117]. More profound and meaningful work is expected to appear in the field of optofluidics-based APS since the optofluidic devices are versatile and can be integrated together with other functions, for instance, deoxygenation, temperature control, electricity/magnetic field and pressure [118-121].

Acknowledgements

This work is supported by Shandong Province Natural Science Foundation (No. ZR2016BB15), The Youth Science Fund of Shandong Academy of Sciences (No. 2016QN006), National Natural Science Foundation of China (no. 61377068, no. 61361166004), Research Grants Council of Hong Kong (N_PolyU505/13, PolyU 5334/12E, PolyU 152184/15E, PolyU 509513 and PolyU 152127/17E), and Hong Kong Polytechnic University (grants G-YN07, G-YBBE, G-YBPR, 4-BCAL, 1-ZVAW, 1-ZE14, A-PM21, 1-ZE27 and 1-ZVGH).

ORCID® iDs

Xuming Zhang - https://orcid.org/0000-0002-9326-5547

References

1. Turek, A. K.; Hardee, D. J.; Ullman, A. M.; Nocera, D. G.; Jacobsen, E. N. *Angew. Chem., Int. Ed.* **2016,** *55,* 539. doi:10.1002/anie.201508060
2. Solis, B. H.; Maher, A. G.; Dogutan, D. K.; Nocera, D. G.; Hammes-Schiffer, S. *Proc. Natl. Acad. Sci. U. S. A.* **2016,** *113,* 485. doi:10.1073/pnas.1521834112
3. Liu, C.; Colón, B. C.; Ziesack, M.; Silver, P. A.; Nocera, D. G. *Science* **2016,** *352,* 1210. doi:10.1126/science.aaf5039
4. Lin, S.; Diercks, C. S.; Zhang, Y.-B.; Kornienko, N.; Nichols, E. M.; Zhao, Y.; Paris, A. R.; Kim, D.; Yang, P.; Chang, C. J.; Yaghi, O. M. *Science* **2015,** *349,* 1208–1213. doi:10.1126/science.aac8343
5. Dou, L.; Wong, A. B.; Yu, Y.; Lai, M.; Kornienko, N.; Eaton, S. W.; Fu, A.; Bischak, C. G.; Ma, J.; Ding, T.; Ginsberg, N. S.; Wang, L.-W.; Alivisatos, A. P.; Yang, P. *Science* **2015,** *349,* 1518. doi:10.1126/science.aac7660
6. Nocera, D. G. *Acc. Chem. Res.* **2017,** *50,* 616. doi:10.1021/acs.accounts.6b00615
7. Zhou, H.; Yan, R.; Zhang, D.; Fan, T. *Chem. – Eur. J.* **2016,** *22,* 9870. doi:10.1002/chem.201600289
8. Tachibana, Y.; Vayssieres, L.; Durrant, J. R. *Nat. Photonics* **2012,** *6,* 511. doi:10.1038/nphoton.2012.175
9. Marshall, J. *Nature* **2014,** *510,* 22. doi:10.1038/510022a
10. Gust, D.; Moore, T. A.; Moore, A. L. *Acc. Chem. Res.* **2009,** *42,* 1890. doi:10.1021/ar900209b
11. Lin, S.; Liu, Y.; Hu, Z.; Lu, W.; Hin Mak, C.; Zeng, L.; Zhao, J.; Li, Y.; Yan, F.; Hong Tsang, Y.; Zhang, X.; Ping Lau, S. *Nano Energy* **2017,** *42,* 26–33. doi:10.1016/j.nanoen.2017.10.038
12. Faunce, T.; Styring, S.; Wasielewski, M. R.; Brudvig, G. W.; Rutherford, A. W.; Messinger, J.; Lee, A. F.; Hill, C. L.; DeGroot, H.; Fontecave, M.; MacFarlane, D. R.; Hankamer, B.; Nocera, D. G.; Tiede, D. M.; Dau, H.; Hillier, W.; Wang, L.; Amal, R. *Energy Environ. Sci.* **2013,** *6,* 1074. doi:10.1039/c3ee40534f
13. Liu, C.; Gallagher, J. J.; Sakimoto, K. K.; Nichols, E. M.; Chang, C. J.; Chang, M. C. Y.; Yang, P. *Nano Lett.* **2015,** *15,* 3634. doi:10.1021/acs.nanolett.5b01254
14. Torella, J. P.; Gagliardi, C. J.; Chen, J. S.; Bediako, D. K.; Colón, B.; Way, J. C.; Silver, P. A.; Nocera, D. G. *Proc. Natl. Acad. Sci. U. S. A.* **2015,** *112,* 2337. doi:10.1073/pnas.1503606112
15. Kornienko, N.; Zhao, Y.; Kley, C. S.; Zhu, C.; Kim, D.; Lin, S.; Chang, C. J.; Yaghi, O. M.; Yang, P. *J. Am. Chem. Soc.* **2015,** *137,* 14129. doi:10.1021/jacs.5b08212

16. Choi, K. M.; Kim, D.; Rungtaweevoranit, B.; Trickett, C. A.; Barmanbek, J. T. D.; Alshammari, A. S.; Yang, P.; Yaghi, O. M. *J. Am. Chem. Soc.* **2017,** *139,* 356. doi:10.1021/jacs.6b11027
17. Cao, Z.; Kim, D.; Hong, D.; Yu, Y.; Xu, J.; Lin, S.; Wen, X.; Nichols, E. M.; Jeong, K.; Reimer, J. A.; Yang, P.; Chang, C. J. *J. Am. Chem. Soc.* **2016,** *138,* 8120. doi:10.1021/jacs.6b02878
18. Kong, Q.; Kim, D.; Liu, C.; Yu, Y.; Su, Y.; Li, Y.; Yang, P. *Nano Lett.* **2016,** *16,* 5675. doi:10.1021/acs.nanolett.6b02321
19. Su, Y.; Liu, C.; Brittman, S.; Tang, J.; Fu, A.; Kornienko, N.; Kong, Q.; Yang, P. *Nat. Nanotechnol.* **2016,** *11,* 609. doi:10.1038/nnano.2016.30
20. Nichols, E. M.; Gallagher, J. J.; Liu, C.; Su, Y.; Resasco, J.; Yu, Y.; Sun, Y.; Yang, P.; Chang, M. C. Y.; Chang, C. J. *Proc. Natl. Acad. Sci. U. S. A.* **2015,** *112,* 11461. doi:10.1073/pnas.1508075112
21. Kornienko, N.; Sakimoto, K. K.; Herlihy, D. M.; Nguyen, S. C.; Alivisatos, A. P.; Harris, C. B.; Schwartzberg, A.; Yang, P. *Proc. Natl. Acad. Sci. U. S. A.* **2016,** *113,* 11750. doi:10.1073/pnas.1610554113
22. Chen, M.-Y.; Zhuo, G.-Y.; Chen, K.-C.; Wu, P.-C.; Hsieh, T.-Y.; Liu, T.-M.; Chu, S.-W. *BMC Plant Biol.* **2014,** *14,* 175. doi:10.1186/1471-2229-14-175
23. Michelet, L.; Zaffagnini, M.; Morisse, S.; Sparla, F.; Pérez-Pérez, M. E.; Francia, F.; Danon, A.; Marchand, C. H.; Fermani, S.; Trost, P.; Lemaire, S. D. *Front. Plant Sci.* **2013,** *4,* 470. doi:10.3389/fpls.2013.00470
24. Hisatomi, T.; Kubota, J.; Domen, K. *Chem. Soc. Rev.* **2014,** *43,* 7520. doi:10.1039/C3CS60378D
25. Liu, J.; Liu, Y.; Liu, N.; Han, Y.; Zhang, X.; Huang, H.; Lifshitz, Y.; Lee, S.; Zhong, J.; Kang, Z. *Science* **2015,** *347,* 970. doi:10.1126/science.aaa3145
26. Liu, C.; Dasgupta, N. P.; Yang, P. *Chem. Mater.* **2014,** *26,* 415. doi:10.1021/cm4023198
27. Liu, J.; Antonietti, M. *Energy Environ. Sci.* **2013,** *6,* 1486. doi:10.1039/c3ee40696b
28. Ma, K.; Yehezkeli, O.; Park, E.; Cha, J. N. *ACS Catal.* **2016,** *6,* 6982. doi:10.1021/acscatal.6b02524
29. Su, J.; Vayssieres, L. *ACS Energy Lett.* **2016,** *1,* 121. doi:10.1021/acsenergylett.6b00059
30. Kim, D.; Sakimoto, K. K.; Hong, D.; Yang, P. *Angew. Chem., Int. Ed.* **2015,** *54,* 3259. doi:10.1002/anie.201409116
31. Gemoets, H. P. L.; Su, Y.; Shang, M.; Hessel, V.; Luque, R.; Noël, T. *Chem. Soc. Rev.* **2016,** *45,* 83. doi:10.1039/C5CS00447K
32. Lin, Y.; Yuan, G.; Liu, R.; Zhou, S.; Sheehan, S. W.; Wang, D. *Chem. Phys. Lett.* **2011,** *507,* 209. doi:10.1016/j.cplett.2011.03.074
33. Lee, S. H.; Kim, J. H.; Park, C. B. *Chem. – Eur. J.* **2013,** *19,* 4392. doi:10.1002/chem.201204385
34. Maciá-Agulló, J. A.; Corma, A.; Garcia, H. *Chem. – Eur. J.* **2015,** *21,* 10940. doi:10.1002/chem.201406437
35. Whipple, D. T.; Finke, E. C.; Kenis, P. J. A. *Electrochem. Solid-State Lett.* **2010,** *13,* B109. doi:10.1149/1.3456590
36. Chen, R.; Li, L.; Zhu, X.; Wang, H.; Liao, Q.; Zhang, M.-X. *Energy* **2015,** *83,* 797. doi:10.1016/j.energy.2015.02.097
37. Simms, R.; Dubinsky, S.; Yudin, A.; Kumacheva, E. *Lab Chip* **2009,** *9,* 2395. doi:10.1039/b904962b
38. Oelgemöller, M.; Shvydkiv, O. *Molecules* **2011,** *16,* 7522. doi:10.3390/molecules16097522
39. Psaltis, D.; Quake, S. R.; Yang, C. *Nature* **2006,** *442,* 381. doi:10.1038/nature05060
40. Elvira, K. S.; Casadevall i Solvas, X.; Wootton, R. C. R.; de Mello, A. J. *Nat. Chem.* **2013,** *5,* 905. doi:10.1038/nchem.1753
41. Erickson, D.; Sinton, D.; Psaltis, D. *Nat. Photonics* **2011,** *5,* 583. doi:10.1038/nphoton.2011.209
42. Shvydkiv, O.; Yavorskyy, A.; Tan, S. B.; Nolan, K.; Hoffmann, N.; Youssef, A.; Oelgemöller, M. *Photochem. Photobiol. Sci.* **2011,** *10,* 1399. doi:10.1039/c1pp05024a
43. Coyle, E. E.; Oelgemöller, M. *Photochem. Photobiol. Sci.* **2008,** *7,* 1313. doi:10.1039/b808778d
44. Zhao, D.; He, Z.; Wang, G.; Wang, H.; Zhang, Q.; Li, Y. *Sens. Actuators, B* **2016,** *229,* 281. doi:10.1016/j.snb.2016.01.125
45. Ji, X.; Su, Z.; Wang, P.; Ma, G.; Zhang, S. *Small* **2016,** *12,* 4753. doi:10.1002/smll.201600707
46. Yadav, R. K.; Oh, G. H.; Park, N.-J.; Kumar, A.; Kong, K.-j.; Baeg, J.-O. *J. Am. Chem. Soc.* **2014,** *136,* 16728. doi:10.1021/ja509650r
47. Godfray, H. C. J.; Beddington, J. R.; Crute, I. R.; Haddad, L.; Lawrence, D.; Muir, J. F.; Pretty, J.; Robinson, S.; Thomas, S. M.; Toulmin, C. *Science* **2010,** *327,* 812. doi:10.1126/science.1185383
48. Blankenship, R. E.; Tiede, D. M.; Barber, J.; Brudvig, G. W.; Fleming, G.; Ghirardi, M.; Gunner, M. R.; Junge, W.; Kramer, D. M.; Melis, A.; Moore, T. A.; Moser, C. C.; Nocera, D. G.; Nozik, A. J.; Ort, D. R.; Parson, W. W.; Prince, R. C.; Sayre, R. T. *Science* **2011,** *332,* 805. doi:10.1126/science.1200165
49. Whitesides, G. M. *Nature* **2006,** *442,* 368. doi:10.1038/nature05058
50. Wang, N.; Zhang, X.; Chen, B.; Song, W.; Chan, N. Y.; Chan, H. L. W. *Lab Chip* **2012,** *12,* 3983. doi:10.1039/c2lc40428a
51. Wang, N.; Zhang, X.; Wang, Y.; Yu, W.; Chan, H. L. W. *Lab Chip* **2014,** *14,* 1074. doi:10.1039/c3lc51233a
52. Gorkin, R.; Park, J.; Siegrist, J.; Amasia, M.; Lee, B. S.; Park, J.-M.; Kim, J.; Kim, H.; Madou, M.; Cho, Y.-K. *Lab Chip* **2010,** *10,* 1758. doi:10.1039/b924109d
53. Zhao, C.; Xie, Y.; Mao, Z.; Zhao, Y.; Rufo, J.; Yang, S.; Guo, F.; Mai, J. D.; Huang, T. J. *Lab Chip* **2014,** *14,* 384. doi:10.1039/c3lc50748c
54. Zhang, H.; Wang, J.-J.; Fan, J.; Fang, Q. *Talanta* **2013,** *116,* 946. doi:10.1016/j.talanta.2013.08.012
55. Sun, M.; Fang, Q. *Lab Chip* **2010,** *10,* 2864. doi:10.1039/c005290f
56. Su, Y.; Zhu, Y.; Fang, Q. *Lab Chip* **2013,** *13,* 1876. doi:10.1039/c3lc00063j
57. Li, Y.; Lin, B.; Ge, L.; Guo, H.; Chen, X.; Lu, M. *Sci. Rep.* **2016,** *6,* 28803. doi:10.1038/srep28803
58. Huang, X.; Hui, W.; Hao, C.; Yue, W.; Yang, M.; Cui, Y.; Wang, Z. *Small* **2014,** *10,* 758. doi:10.1002/smll.201202659
59. Huang, X.; Yue, W.; Liu, D.; Yue, J.; Li, J.; Sun, D.; Yang, M.; Wang, Z. *Sci. Rep.* **2016,** *6,* 23591. doi:10.1038/srep23591
60. Squires, T. M.; Quake, S. R. *Rev. Mod. Phys.* **2005,** *77,* 977. doi:10.1103/RevModPhys.77.977
61. Huang, X.; Zhu, Y.; Zhang, X.; Bao, Z.; Lei, D. Y.; Yu, W.; Dai, J.; Wang, Y. *Sens. Actuators, B* **2016,** *222,* 106. doi:10.1016/j.snb.2015.08.069
62. Liu, J.; He, K.; Wu, W.; Song, T.-B.; Kanatzidis, M. G. *J. Am. Chem. Soc.* **2017,** *139,* 2900. doi:10.1021/jacs.6b13279
63. Das, A. A. K.; Esfahani, M. M. N.; Velev, O. D.; Pamme, N.; Paunov, V. N. *J. Mater. Chem. A* **2015,** *3,* 20698. doi:10.1039/C5TA07112G
64. Li, S.; Yang, L.; Ola, O.; Maroto-Valer, M.; Du, X.; Yang, Y. *Energy Convers. Manage.* **2016,** *116,* 184. doi:10.1016/j.enconman.2016.03.001

65. Sun, J.; Zhang, J.; Zhang, M.; Antonietti, M.; Fu, X.; Wang, X. *Nat. Commun.* **2012,** *3,* 1139. doi:10.1038/ncomms2152
66. Zhou, H.; Li, P.; Liu, J.; Chen, Z.; Liu, L.; Dontsova, D.; Yan, R.; Fan, T.; Zhang, D.; Ye, J. *Nano Energy* **2016,** *25,* 128. doi:10.1016/j.nanoen.2016.04.049
67. Tong, Z.; Yang, D.; Li, Z.; Nan, Y.; Ding, F.; Shen, Y.; Jiang, Z. *ACS Nano* **2017,** *11,* 1103. doi:10.1021/acsnano.6b08251
68. Zhou, P.; Yu, J.; Jaroniec, M. *Adv. Mater.* **2014,** *26,* 4920. doi:10.1002/adma.201400288
69. Cheng, L.; Zheng, Y.; Xu, Q.; Qin, Y. *Adv. Opt. Mater.* **2017,** *5,* 1600623. doi:10.1002/adom.201600623
70. Wang, L.; Liu, S.; Wang, Z.; Zhou, Y.; Qin, Y.; Wang, Z. L. *ACS Nano* **2016,** *10,* 2636. doi:10.1021/acsnano.5b07678
71. Tan, F.; Wang, N.; Lei, D. Y.; Yu, W.; Zhang, X. *Adv. Opt. Mater.* **2017,** *5,* 1600399. doi:10.1002/adom.201600399
72. Tan, F.; Li, T.; Wang, N.; Lai, S. K.; Tsoi, C. C.; Yu, W.; Zhang, X. *Sci. Rep.* **2016,** *6,* 33049. doi:10.1038/srep33049
73. Ahsan, S. S.; Gumus, A.; Erickson, D. *Lab Chip* **2013,** *13,* 409. doi:10.1039/C2LC41129F
74. Li, L.; Chen, R.; Liao, Q.; Zhu, X.; Wang, G.; Wang, D. *Int. J. Hydrogen Energy* **2014,** *39,* 19270. doi:10.1016/j.ijhydene.2014.05.098
75. Li, L.; Wang, G.; Chen, R.; Zhu, X.; Wang, H.; Liao, Q.; Yu, Y. *Lab Chip* **2014,** 3368. doi:10.1039/c4lc00595c
76. Cheng, X.; Chen, R.; Zhu, X.; Liao, Q.; He, X.; Li, S.; Li, L. *Int. J. Hydrogen Energy* **2016,** *41,* 2457. doi:10.1016/j.ijhydene.2015.12.066
77. Chen, R.; Cheng, X.; Zhu, X.; Liao, Q.; An, L.; Ye, D.; He, X.; Wang, Z. *Chem. Eng. J.* **2017,** *316,* 911. doi:10.1016/j.cej.2017.02.044
78. Cheng, M.; Yang, S.; Chen, R.; Zhu, X.; Liao, Q.; Huang, Y. *Int. J. Hydrogen Energy* **2017,** *42,* 9722. doi:10.1016/j.ijhydene.2017.01.126
79. Sakimoto, K. K.; Wong, A. B.; Yang, P. *Science* **2016,** *351,* 74. doi:10.1126/science.aad3317
80. Thomas, A.; Fischer, A.; Goettmann, F.; Antonietti, M.; Müller, J.-O.; Schlögl, R.; Carlsson, J. M. *J. Mater. Chem.* **2008,** *18,* 4893. doi:10.1039/b800274f
81. Lee, M.; Kim, J. H.; Lee, S. H.; Lee, S. H.; Park, C. B. *ChemSusChem* **2011,** *4,* 581. doi:10.1002/cssc.201100074
82. Ryu, J.; Lee, S. H.; Nam, D. H.; Park, C. B. *Adv. Mater.* **2011,** *23,* 1883. doi:10.1002/adma.201004576
83. Lee, S. H.; Ryu, J.; Nam, D. H.; Park, C. B. *Chem. Commun.* **2011,** *47,* 4643. doi:10.1039/c0cc05246a
84. Liu, J.; An, T.; Chen, Z.; Wang, Z.; Zhou, H.; Fan, T.; Zhang, D.; Antonietti, M. *J. Mater. Chem. A* **2017,** *5,* 8933. doi:10.1039/C7TA02923C
85. Liu, J.; Cazelles, R.; Chen, Z. P.; Zhou, H.; Galarneau, A.; Antonietti, M. *Phys. Chem. Chem. Phys.* **2014,** *16,* 14699. doi:10.1039/c4cp01348d
86. Liu, J.; Huang, J.; Zhou, H.; Antonietti, M. *ACS Appl. Mater. Interfaces* **2014,** *6,* 8434. doi:10.1021/am501319v
87. Liu, J.; Wang, H.; Antonietti, M. *Chem. Soc. Rev.* **2016,** *45,* 2308. doi:10.1039/C5CS00767D
88. Lee, J. S.; Lee, S. H.; Kim, J. H.; Park, C. B. *Lab Chip* **2011,** *11,* 2309. doi:10.1039/c1lc20303g
89. Huang, X.; Liu, J.; Yang, Q.; Liu, Y.; Zhu, Y.; Li, T.; Tsang, Y. H.; Zhang, X. *RSC Adv.* **2016,** *6,* 101974. doi:10.1039/C6RA21390A
90. Chen, X.; Li, N.; Kong, Z.; Ong, W.-J.; Zhao, X. *Mater. Horiz.* **2018,** in press. doi:10.1039/c7mh00557a
91. Kibria, M. G.; Mi, Z. *J. Mater. Chem. A* **2016,** *4,* 2801. doi:10.1039/C5TA07364B
92. Kumar, S.; Kumar, A.; Bahuguna, A.; Sharma, V.; Krishnan, V. *Beilstein J. Nanotechnol.* **2017,** *8,* 1571. doi:10.3762/bjnano.8.159
93. Ong, W.-J. *Front. Mater.* **2017,** *4,* No. 11. doi:10.3389/fmats.2017.00011
94. Ong, W.-J.; Tan, L.-L.; Ng, Y. H.; Yong, S.-T.; Chai, S.-P. *Chem. Rev.* **2016,** *116,* 7159. doi:10.1021/acs.chemrev.6b00075
95. Lei, L.; Wang, N.; Zhang, X. M.; Tai, Q.; Tsai, D. P.; Chan, H. L. W. *Biomicrofluidics* **2010,** *4,* 43004. doi:10.1063/1.3491471
96. Liao, W.; Wang, N.; Wang, T.; Xu, J.; Han, X.; Liu, Z.; Zhang, X.; Yu, W. *Biomicrofluidics* **2016,** *10,* 014123. doi:10.1063/1.4942947
97. Wang, N.; Tan, F.; Wan, L.; Wu, M.; Zhang, X. *Biomicrofluidics* **2014,** *8,* 054122. doi:10.1063/1.4899883
98. Wang, N.; Lei, L.; Zhang, X. M.; Tsang, Y. H.; Chen, Y.; Chan, H. L. W. *Microelectron. Eng.* **2011,** *88,* 2797. doi:10.1016/j.mee.2010.12.051
99. Wang, N.; Tan, F.; Zhao, Y.; Tsoi, C. C.; Fan, X.; Yu, W.; Zhang, X. *Sci. Rep.* **2016,** *6,* 28928. doi:10.1038/srep28928
100. Liu, J.; Kelley, M. S.; Wu, W.; Banerjee, A.; Douvalis, A. P.; Wu, J.; Zhang, Y.; Schatz, G. C.; Kanatzidis, M. G. *Proc. Natl. Acad. Sci. U. S. A.* **2016,** *113,* 5530. doi:10.1073/pnas.1605512113
101. Bi, F.; Ehsan, M. F.; Liu, W.; He, T. *Chin. J. Chem.* **2015,** *33,* 112. doi:10.1002/cjoc.201400476
102. Li, M.; Li, P.; Chang, K.; Wang, T.; Liu, L.; Kang, Q.; Ouyang, S.; Ye, J. *Chem. Commun.* **2015,** *51,* 7645. doi:10.1039/c5cc01124h
103. Marcì, G.; García-López, E. I.; Palmisano, L. *Catal. Commun.* **2014,** *53,* 38. doi:10.1016/j.catcom.2014.04.024
104. Vaiano, V.; Iervolino, G.; Sarno, G.; Sannino, D.; Rizzo, L.; Murcia Mesa, J. J.; Hidalgo, M. C.; Navío, J. A. *Oil Gas Sci. Technol.* **2015,** *70,* 891. doi:10.2516/ogst/2014062
105. Wu, T.; Zou, L.; Han, D.; Li, F.; Zhang, Q.; Niu, L. *Green Chem.* **2014,** *16,* 2142. doi:10.1039/C3GC42454E
106. Zhu, S.; Liang, S.; Tong, Y.; An, X.; Long, J.; Fu, X.; Wang, X. *Phys. Chem. Chem. Phys.* **2015,** *17,* 9761. doi:10.1039/C5CP00647C
107. Bonin, J.; Robert, M.; Routier, M. *J. Am. Chem. Soc.* **2014,** *136,* 16768. doi:10.1021/ja510290t
108. Deng, X.-Q.; Zhu, B.; Li, X.-S.; Liu, J.-L.; Zhu, X.; Zhu, A.-M. *Appl. Catal., B: Environ.* **2016,** *188,* 48. doi:10.1016/j.apcatb.2016.01.055
109. Fei, H.; Sampson, M. D.; Lee, Y.; Kubiak, C. P.; Cohen, S. M. *Inorg. Chem.* **2015,** *54,* 6821. doi:10.1021/acs.inorgchem.5b00752
110. Hwang, S.; Lee, M. C.; Choi, W. *Appl. Catal., B: Environ.* **2003,** *46,* 49. doi:10.1016/S0926-3373(03)00162-0
111. Zhang, Y.; Luc, W.; Hutchings, G. S.; Jiao, F. *ACS Appl. Mater. Interfaces* **2016,** *8,* 24652. doi:10.1021/acsami.6b09095
112. Nakata, K.; Ozaki, T.; Terashima, C.; Fujishima, A.; Einaga, Y. *Angew. Chem., Int. Ed.* **2014,** *53,* 871. doi:10.1002/anie.201308657
113. Tu, W.; Zhou, Y.; Zou, Z. *Adv. Mater.* **2014,** *26,* 4607. doi:10.1002/adma.201400087
114. Ma, Y.; Wang, X. L.; Jia, Y. S.; Chen, X. B.; Han, H. X.; Li, C. *Chem. Rev.* **2014,** *114,* 9987. doi:10.1021/cr500008u
115. Qin, S.; Xin, F.; Liu, Y.; Yin, X.; Ma, W. *J. Colloid Interface Sci.* **2011,** *356,* 257. doi:10.1016/j.jcis.2010.12.034
116. Zeng, G.; Qiu, J.; Li, Z.; Pavaskar, P.; Cronin, S. B. *ACS Catal.* **2014,** *4,* 3512. doi:10.1021/cs500697w
117. Li, K.; An, X.; Park, K. H.; Khraisheh, M.; Tang, J. *Catal. Today* **2014,** *224,* 3. doi:10.1016/j.cattod.2013.12.006

118. Chiang, M.-Y.; Hsu, Y.-W.; Hsieh, H.-Y.; Chen, S.-Y.; Fan, S.-K. *Sci. Adv.* **2016,** *2,* e1600964. doi:10.1126/sciadv.1600964
119. Wang, L.; Liu, W.; Wang, Y.; Wang, J.-c.; Tu, Q.; Liu, R.; Wang, J. *Lab Chip* **2013,** *13,* 695. doi:10.1039/c2lc40661f
120. Dunkel, P.; Hayat, Z.; Barosi, A.; Bchellaoui, N.; Dhimane, H.; Dalko, P. I.; El Abed, A. I. *Lab Chip* **2016,** *16,* 1484. doi:10.1039/c6lc00024j
121. Ngo, H. M.; Lai, N. D.; Ledoux-Rak, I. *Nanoscale* **2016,** *8,* 3489. doi:10.1039/C5NR07571H

License and Terms

This is an Open Access article under the terms of the Creative Commons Attribution License (http://creativecommons.org/licenses/by/4.0), which permits unrestricted use, distribution, and reproduction in any medium, provided the original work is properly cited.

The license is subject to the *Beilstein Journal of Nanotechnology* terms and conditions: (http://www.beilstein-journals.org/bjnano)

The definitive version of this article is the electronic one which can be found at:
doi:10.3762/bjnano.9.5

BEILSTEIN JOURNAL OF NANOTECHNOLOGY

Bombyx mori silk/titania/gold hybrid materials for photocatalytic water splitting: combining renewable raw materials with clean fuels

Stefanie Krüger[1], Michael Schwarze[2], Otto Baumann[3], Christina Günter[4], Michael Bruns[5], Christian Kübel[6], Dorothée Vinga Szabó[5], Rafael Meinusch[7], Verónica de Zea Bermudez[8] and Andreas Taubert[*1,§]

Full Research Paper

Open Access

Address:
[1]Institute of Chemistry, University of Potsdam, D-14476 Potsdam, Germany, [2]Institute of Chemistry, Technical University Berlin, D-10623 Berlin, Germany, [3]Institute of Biochemistry and Biology, University of Potsdam, D-14476 Potsdam, Germany, [4]Institute of Earth and Environmental Science, University of Potsdam, D-14476 Potsdam, Germany, [5]Institute for Applied Materials (IAM) and Karlsruhe Nano Micro Facility (KNMF), Karlsruhe Institute of Technology (KIT), D-76344 Eggenstein-Leopoldshafen, Germany, [6]Institute of Nanotechnology (INT) and Karlsruhe Nano Micro Facility (KNMF), Karlsruhe Institute of Technology (KIT), D-76344 Eggenstein-Leopoldshafen, Germany, [7]Institute of Physical Chemistry, Justus-Liebig-University Giessen, D-35392 Giessen, Germany and [8]Department of Chemistry and CQ-VR, University of Trás-os-Montes e Alto Douro, Pt-5001-801 Vila Real, Portugal

Email:
Andreas Taubert[*] - ataubert@uni-potsdam.de

* Corresponding author
§ Tel.: +49 (0) 331 977 5773

Keywords:
Bombyx mori silk; gold; photocatalytic water splitting; titania

Beilstein J. Nanotechnol. **2018,** *9,* 187–204.
doi:10.3762/bjnano.9.21

Received: 06 September 2017
Accepted: 12 December 2017
Published: 17 January 2018

This article is part of the Thematic Series "Energy conversion, storage and environmental remediation using nanomaterials".

Guest Editor: W.-J. Ong

© 2018 Krüger et al.; licensee Beilstein-Institut.
License and terms: see end of document.

Abstract

The synthesis, structure, and photocatalytic water splitting performance of two new titania (TiO_2)/gold(Au)/*Bombyx mori* silk hybrid materials are reported. All materials are monoliths with diameters of up to ca. 4.5 cm. The materials are macroscopically homogeneous and porous with surface areas between 170 and 210 m^2/g. The diameter of the TiO_2 nanoparticles (NPs) – mainly anatase with a minor fraction of brookite – and the Au NPs are on the order of 5 and 7–18 nm, respectively. Addition of poly(ethylene oxide) to the reaction mixture enables pore size tuning, thus providing access to different materials with different photocatalytic activities. Water splitting experiments using a sunlight simulator and a Xe lamp show that the new hybrid materials are effective water splitting catalysts and produce up to 30 mmol of hydrogen per 24 h. Overall the article demonstrates that the combination of a renewable and robust scaffold such as *B. mori* silk with a photoactive material provides a promising approach to new monolithic photocatalysts that can easily be recycled and show great potential for application in lightweight devices for green fuel production.

Introduction

Fossil fuel availability is one of the pressing issues today. Especially in light of a growing world population and the corresponding increasing energy demand worldwide there is a need for alternative, sustainable, and cheap fuels [1,2]. Hydrogen (H_2) is the most attractive fuel for fuel cells to produce "clean" electricity and water as an environmentally friendly reaction product [1,3]. However, one of the limitations of H_2 is the efficient and sustainable H_2 production. Currently, H_2 is mainly produced by steam reforming of gas and oil, by catalytic reforming, or by water electrolysis [3,4].

In 1972 Fujishima and Honda reported that TiO_2 is able to split water [5], a seminal discovery that has led to a wealth of studies on photocatalytic water splitting [6-10]. To be successful, the water splitting catalyst needs to have a certain set of properties. Most prominently, it should have a bandgap of at least 1.23 eV to provide the energy needed to split water. However, the bandgap should not exceed ca. 3 eV to most efficiently use the visible spectral range of the sunlight [6]. As a result, numerous water-splitting catalysts with various efficiencies have been reported [6-8,11-13].

Because of its bandgap of 3.0–3.2 eV (depending on the crystal structure and particle size [14,15]) TiO_2-based water splitting catalysts are among the most popular materials for visible light water splitting [16-20]. Among these, TiO_2/Au nanocomposites have attracted special interest because of their synergistic mode of action between the Au nanoparticle (AuNP) plasmons and the bandgap of the TiO_2 semiconductors [21]. Gallo et al. used amorphous TiO_2 doped with Au and/or platinum (Pt) NPs to split water under ultraviolet (UV)-A light and simulated sunlight. Best results with 1.6 mmol/(h·g) of H_2 production were obtained with $Au_{0.5}Pt_{0.5}/TiO_2$ catalysts [22]. Chen et al. used calcined P25 TiO_2 NPs (TNPs) loaded with 3 wt % of Au for photocatalytic water splitting. Irradiation with UV and visible light combined yielded a higher H_2 and oxygen production after 7 h than with UV or visible light alone [23].

In a more analytical study, Silva et al. [24] investigated the influence of particle size and preparation procedure on the photocatalytic activity of Au/TiO_2 catalysts. Lower Au loadings of 0.25% Au on P25 TiO_2 produced more efficient water splitting catalysts than materials with Au loadings of 1.5% or 2.2%. Moreover, the authors showed that 532 nm laser light is more efficient for water splitting than polychromatic light with wavelengths (λ) > 400 nm. Furthermore they also concluded that small Au particle sizes of around 2 nm and a low calcination temperature of 200 °C also yields materials producing more H_2 than materials with larger Au particles or materials pre-treated at higher temperatures [24].

Following the same general idea, Gärtner et al. investigated the effect of different Au precursors for Au loading via in situ photodeposition with sodium tetrachloridoaurate(III) dihydrate ($NaAuCl_4{\cdot}2H_2O$) providing the most efficient water splitting catalyst. The same authors also showed that methanol is the most efficient sacrificial agent when compared to isopropanol, glycerol, and glucose [25]. A further study by Jose et al. focused on the effect of TiO_2 modification (anatase and/or rutile). These authors observed that TiO_2 P25/Au mixed systems performed best in the entire UV–visible range when the TiO_2 is composed of 75% of anatase and 25% of rutile with identical AuNPs [26].

In an interesting new approach, Zhang et al. found that Janus particles (rather than the core–shell or randomly organized materials described so far) based on large TiO_2 particles with diameters of ca. 440 nm and AuNPs with diameters of ca. 60 nm could split water in the visible range, even at low Au fractions of only 1.8% [27]. Finally, Seh et al. showed that TiO_2/Au Janus nanoparticles have a higher photocatalytic activity than the corresponding core–shell particles [28].

All materials described so far are powders or NPs. As a result, recycling is rather difficult and other photocatalysts that can more easily be recycled and are suited for continuous processes are necessary. For example, Liu et al. used a titanium sheet to make TiO_2 nano-sheet films doped with different amounts of silver (Ag) NPs or TiO_2 nano-grass films with AuNP for photocatalytic water splitting [29,30]. Matsuoka et al. sputtered TiO_2 on a quartz glass plate by radiofrequency (RF) magnetron sputtering deposition followed by Pt deposition to make a TiO_2 thin film photocatalyst for water splitting [31]. Finally, Goutailler et al. deposited an anatase/brookite NP mixture on cellulose from tetrabutylammonium bromide ($N(n\text{-}Bu)_4Br$)/titanium tetraisopropoxide ($Ti(OiPr)_4$) solutions in hexane [32]. These NPs strongly interact via non-covalent interactions (e.g., hydrogen bonds [33,34]) with the cellulose fibers and the resulting material was thus a macroscopic and mechanically robust object that could simply be retrieved and washed before reuse [32].

Another viable approach for the synthesis of larger and mechanically stable objects with photocatalytic activity is the immobilization of TiO_2/Au nanostructures on a scaffold, ideally a scaffold with a high porosity, and good chemical and mechanical stability to enable access of all reactants to the catalytically active sites over extended periods of time. Moreover, a suitable photocatalyst should ideally use a scaffold from renewable materials; ideally the scaffold should be mechanically and chemically stable to withstand the conditions during photocatalysis.

Daoud and Xin [35] coated cotton fibers with 20 nm anatase particles via a sol–gel method. The covalently bonded TiO_2 particles have a 50+ UV protection factor and are stable against washing. In an alternative approach, Zheng et al. used tetrabutylorthotitanate, $Ti(OBu)_4$, and bis(*P*,*P*-bis-ethylhexyldiphosphato)ethanediolatotitanate (BPET, $C_{34}H_{74}O_{16}P_4Ti$) in a cold oxygen plasma to coat *B. mori* silk fabrics with TiO_2 to produce a UV resistant material [36].

The current study also focuses on *B. mori* silk rather than cotton as a scaffold for photocatalyst synthesis. Instead of plasma chemistry, however, we employed a much softer wet chemistry method for materials synthesis.

B. mori silk contains numerous amino acids, predominantly glycine, alanine, serine, and tyrosine [37,38]. As numerous amide and hydroxyl groups are present in *B. mori* silk, a strong interaction of the silk scaffold with the TiO_2 phase can be expected although silkworm silk does not contain specific TiO_2 or Au binding domains [39-48]. Moreover, silk worms can easily be grown in large quantities and the resulting silk is chemically and mechanically rather robust [49]. As a result, the method reported here is a promising approach towards new photocatalytically active materials based on a renewable scaffold.

Experimental

Chemicals

Bombyx mori silk cocoons (http://www.seidentraum.biz, date of access: 14.01.2017), calcium chloride dihydrate ($CaCl_2{\cdot}2H_2O$, ≥99%, Carl Roth), ethanol (EtOH; 99%, VWR), ethyl acetoacetate (EtAcAc, 99%, Alfa Aesar), glutaraldehyde solution (GA, 25% in H_2O, Sigma-Aldrich), hydrogen tetrachloridoaurate(III) trihydrate ($HAuCl_4{\cdot}3H_2O$, 99.99%, Alfa Aesar), poly(ethylene oxide) (PEO_{780}, nominal M_w = 4600 g/mol, Sigma-Aldrich, measured M_w = 780 g/mol), PEO_{8300}, (nominal M_w = 600 g/mol, abcr, measured M_w = 8300 g/mol), sodium carbonate (Na_2CO_3, 99.8%, Carl Roth), titanium isopropoxide ($Ti(OiPr)_4$, TTIP, 98%, abcr), disodium hydrogen phosphate (Na_2HPO_4, ACS reagent, Sigma-Aldrich), magnesium sulfate ($MgSO_4$, AnalaR Normapure, VWR), sodium phosphate monobasic (NaH_2PO_4, ACS reagent, Sigma Aldrich), uranyl acetate (p.a., Merck), ethanol absolute ($EtOH_{abs}$, ≥99.8%, Carl Roth), acetone (≥99.8%, Carl Roth), AGAR Low Viscosity Resin (Plano), and PLANOCARBON (Plano) were used as received. Water-free solvents were stored over 3 Å molecular sieves prior to use. All syntheses were done with Millipore water (18.2 MΩ/cm).

Synthesis

Materials synthesis is based on a significantly modified protocol by Hasegawa et al. [50,51]. The resulting materials are denoted as TS, TS_Au_x, TPS, and TPS_Au_x (Table S1, Supporting Information File 1), where TS represents materials based only on TiO_2 and silk, TPS stands for materials based on TiO_2, PEO, and silk, TS_Au_x and TPS_Au_x denote the respective silk/TiO_2 scaffolds further modified with Au and x denotes the amount of $HAuCl_4{\cdot}3H_2O$ (in mg) used in the synthesis.

Step 1: *Bombyx mori* silk cocoons were treated in 0.1 M aqueous Na_2CO_3 solution for 1 h at reflux temperature to remove the sericin. Subsequently, the cocoons were washed three times in hot water and dried at 40 °C in air.

Step 2: Silk was dissolved in a mixture of $CaCl_2$/EtOH/H_2O (molar ratio 1:2:8) at 60 °C (1 g silk/6.7 g solvent) [52] (solution 1) and 0.2 g of PEO_{780} and 0.2 g of PEO_{8300} were mixed and dissolved in 0.5 mL of water at 90 °C (solution 2). Then, 3.08 g of solution 1 and 2 mL of a 0.5 M $CaCl_2$ solution were added to the hot solution 2. This mixture was briefly shaken at room temperature and then transferred to a 6 cm-diameter Teflon dish.

Step 2a: In an alternative reaction (to evaluate the effect of PEO), a PEO-free synthesis was also studied. In this case 6.16 g of the silk solution 1 and 2 mL of the 0.5 M $CaCl_2$ solution were mixed and transferred to a Teflon dish as described before.

Step 3: 5 mL of $Ti(OiPr)_4$, 4.6 mL of EtAcAc, and 1.4 mL of EtOH were mixed in a beaker. After 30 min 0.5 mL of a 0.5 M $CaCl_2$ solution and 0.5 mL of water were added and the resulting slightly yellow solution was held in an oven at 60 °C for 9 min. This hot TiO_2 precursor solution was immediately added to the (i) PEO/silk (step 2) or (ii) the PEO-free silk solution (step 2a) in the Teflon dish and stirred manually with a wooden spatula until a homogeneous liquid was obtained. The Teflon dish was covered with a glass Petri dish and left on the laboratory bench over night at room temperature.

Step 4: The resulting slightly yellow solid was purified via solvent exchange with EtOH/H_2O (1:1 v/v), EtOH/H_2O (3:7 v/v) each for at least 8 h at 60 °C, and finally with water for 24 h.

Step 5: When a modification with AuNP was desired, the as-prepared wet silk/TiO_2 hybrid materials obtained in step 4 were stored in an aqueous $HAuCl_4$ solution (10, 5, or 2.5 mg in 50 mL of water) overnight. No additional reducing agent was added to this reaction mixture. After 2 days the surface color changed from yellow to purple, indicating the deposition of AuNPs on the surface. The as-prepared Au/TiO_2/silk hybrid material was washed three times with 50 mL of water at room temperature.

Characterization

Samples for all transmission electron microscopy (TEM) investigations were prepared as follows: small pieces (ca. 2 mm^2) of the wet hybrid materials were immersed in a 3% glutaraldehyde solution in 0.1 M phosphate buffer (pH 7) for 30 min followed by washing three times in 0.1 M phosphate buffer, once with water, and once with 50% ethanol for 5 min each. Then the hybrid materials were immersed in 2% uranyl acetate solution in 50% ethanol for 30 min followed by treatment with 70% EtOH, 90% EtOH, 100% EtOH, 2× 100% $EtOH_{abs.}$, and 2× 100% $acetone_{abs.}$ for 15 min each. Finally, the materials were immersed in Agar Low Viscosity Resin/acetone (1:2 wt/wt) mixtures for 2 h, then in resin/acetone (1:1 wt/wt) mixtures for 2 h, and then in pure resin overnight under a rotatory motion. The as-prepared samples were transferred into a mold, covered with resin, and treated at 60 °C for 24 h. After cooling to room temperature, the embedded samples were trimmed and sectioned (100 nm nominal slice thickness, Leica Ultracut UCT with diamond knife at room temperature).

Transmission electron microscopy (TEM) was done on a Philips CM 200 TEM with a LaB_6 cathode operated at 120 kV. High resolution transmission electron microscopy (HRTEM) was done using an aberration corrected Titan 80-300 (FEI, Eindhoven, The Netherlands) with field emission gun, operated at 300 kV. Scanning transmission electron microscopy (STEM) and chemical analysis were done on a Tecnai F20 ST (FEI, Eindhoven, The Netherlands) field emission TEM equipped with an Orius SC600 CCD-camera and a S-UTW EDX detector (EDAX, Mahwah, NJ, USA) operated at 200 kV. For EDXS the instrument was in scanning transmission mode and the α-tilt of the samples was set to 20°.

Scanning electron microscopy (SEM) and energy dispersive X-ray spectroscopy (EDXS) were performed on a JEOL JSM-6510 with a W filament operated at 15 kV and equipped with an Oxford Instruments INCAx-act detector. Dry samples were either ground and deposited as powders on a carbon glue pad followed by sputtering with carbon using a Polaron CC7650 Carbon Coater, or, alternatively, deposited directly on the carbon glue pad using PLANOCARBON and sputtered with Pd/Au using a SC7620 Mini Sputter Coater.

X-ray photoelectron spectroscopy (XPS) measurements were done on a K-Alpha+ XPS instrument (Thermo Fisher Scientific, East Grinstead, UK). Data acquisition and processing using the Thermo Avantage software is described elsewhere [53]. All samples were analyzed using a micro-focused, monochromated Al Kα X-ray source (30–400 µm spot size). The K-Alpha+ charge compensation system was employed during analysis, using 8 eV electrons and low-energy argon ions to prevent any localized charge build-up. The spectra were fitted with one or more Voigt profiles (binding energy uncertainty: ±0.2 eV). The analyzer transmission function, Scofield sensitivity factors [54], and effective attenuation lengths (EALs) for photoelectrons were applied for quantification. EALs were calculated using the standard TPP-2M formalism [55]. All spectra were referenced to the C1s peak of hydrocarbons at 285.0 eV binding energy controlled by means of the well-known photoelectron peaks of metallic Cu, Ag, and Au. Sputter depth profiles were obtained using a raster scanned Ar^+ ion beam at 0.5–3.0 keV and 30° angle of incidence.

X-ray powder diffraction (XRD) was performed on a PANalytical Empyrean Diffractometer in a 2θ range of 4–90°. X-ray wavelength was 1.5408 Å (Cu Kα) and step size was 0.0131°. Data and particle size analysis via Scherrer equation was done using the HighScore Plus V.4.0 (4.0.0.19037) software from PANalytical B.V.

Nitrogen sorption measurements were performed on a BELSORP-max with N_2 at 77 K using 40 measurement points. Prior to all measurements, samples were ground and dried at 90 °C for at least 24 h until the weight differences between two subsequent measurements were less than 10%. Data analysis was done with the BELMaster™ 6.3.0.0 software from BEL Japan, Inc.

Mercury (Hg) intrusion porosimetry was done on a Pascal 140/440 porosimeter (Thermo Fisher Scientific, Rodano, Italy) in a pressure range of 0–400 MPa. The instrument software (Sol.I.D.) was employed for calculations of results supporting Washburn's equation. A mercury surface tension of 0.48 N/m and a contact angle of intruded mercury of 140° were assumed.

Reflection solid-state UV–vis spectrometry was done on a Perkin-Elmer (PE) Lambda 950 UV–vis spectrometer from 200–850 nm with a resolution of 2 nm using a Praying Mantis™ attachment from Harrick Scientific Products Inc. Ground samples were mixed with $MgSO_4$ in a 1:10 w/w ratio prior to measurements. Data analysis was done with the PE UV WinLab V6.03 software.

Fourier transform attenuated total reflection infrared spectroscopy (FT-ATR-IR) was done from 4000–500 cm^{-1} with a resolution of 2 cm^{-1} on an FT-IR NEXUS spectrometer with a ThermoNicolet SmartOrbit ATR attachment with a diamond crystal. Samples were directly deposited on the crystal und fixed in the measurement position via the SmartOrbit attachment. Data analysis was done with the ThermoFisher Omnic 8.1.11 software.

Raman spectroscopy was performed on a WITec alpha300 confocal Raman microscope with an upright optical microscope. Laser wavelength was 532 nm and laser power was 14 mW. The laser was coupled into a single mode optical fiber and focusing on the sample was achieved via an Olympus MPlanFL N (NA = 0.9) 100× objective yielding a probe area of 1.3 μm^2 [56]. Raman spectra were obtained with an integration time of 50 s from 0–1200 cm^{-1} and the grating of the spectrograph was set to 1800 g/nm to avoid laser-induced damage in the samples. Data analysis was done with the WITec Control FOUR 4.1 software.

Thermogravimetric analysis (TGA) was done on a Netzsch TG 209F1 from 30 °C to 1000 °C with a heating rate of 10 K/min in synthetic air. To evaluate the reproducibility of the measurements, one sample was analyzed three times. All data showed the same behavior and the deviations between the individual measurements were below 1%. Elemental analysis (EA) for C, H, and N was performed on a Vario EL III (elementar).

Photocatalysis experiments were done in a planar photoreactor with defined geometry consisting of a stainless steel housing with cooling, a Teflon inlet as reaction chamber, and a 6 cm diameter quartz glass window [57]. The irradiation area is given by the size of the solid sample that was irradiated. A solar simulator (LOT Oriel Quantum Design), which is basically a 300 W Xe-lamp equipped with an AM-1.5G filter, was used at an intensity of about 1000 W/m^2 as light source. For comparison a 300 W Xe-lamp without the AM1.5G filter was also used.

In a typical experiment, the catalyst and a stirring bar were placed in the reactor. Then the setup was evacuated three times and filled with argon (Ar) to remove residual oxygen. Thereafter, 53 mL of a 2:1 mixture of water and ethanol were added under an Ar stream, and the thermostat was set to 25 °C. Both water and ethanol were treated with Ar for at least 10 min to remove dissolved oxygen before injection into to the reaction chamber. The light source was placed at a distance of 10 cm. After reaction (usually 24 h), a sample of the gas phase was analyzed in a gas chromatograph equipped with a Carboxen column (Agilent Technologies 7890A GC System with a jasUNIS Injector System) to determine the amount of H_2.

Results

Two types of materials were made. The first group only contains TiO_2 (T) and silk (S), and will be denoted "TS" throughout the remainder of text. The second group contains TiO_2 (T), PEO (P), and silk (S), and will be denoted "TPS". The respective gold-modified materials are denoted TS_Au_x and TPS_Au_x, respectively, where x is the amount of $HAuCl_4{\cdot}3H_2O$ used for the synthesis in milligrams. Table S1, Supporting Information File 1 summarizes the materials studied in this work.

Figure 1 shows photographs of the hybrid materials. The wet TS and TPS materials are slightly yellow and have a diameter of 4.0–4.5 cm (the Teflon dishes used for synthesis have a diameter of 6 cm). After drying, the samples lose 70–75 % in weight and shrink to a diameter of 2.0–2.5 cm. All samples remain intact and appear macroscopically homogeneous.

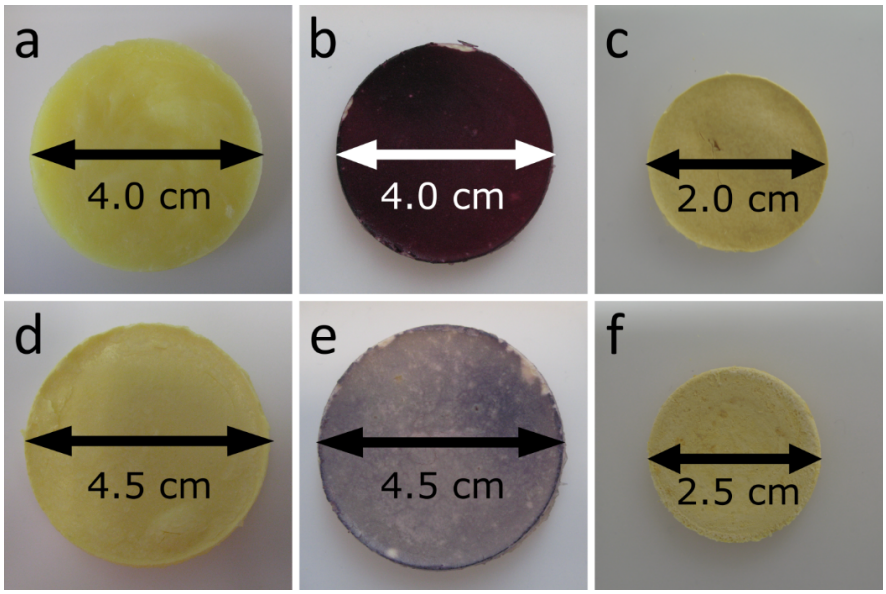

Figure 1: Hybrid materials: a) wet TPS, b) wet TPS_$Au_{2.5}$ c) dry TPS, d) wet TS e) wet TS_$Au_{2.5}$ f) dry TS.

After Au deposition, the surface color of the TPS samples changes to purple. The color depth relates to the amount of $HAuCl_4 \cdot 3H_2O$ used for the synthesis. The surface of TPS_$Au_{1.0}$ is light purple; in the case of TPS_$Au_{2.5}$ it is intense purple (Figure 1). The surface of TPS_$Au_{5.0}$ is dark purple to nearly black, and TPS_$Au_{10.7}$ has a surface with an Au cast. Moreover, light microscopy of cross-sections of the materials (Figure S1, Supporting Information File 1) suggests that the penetration depth of the AuNP reaches up to 120 µm, judging from the purple color visible in the optical micrographs.

The absence of PEO affects the color of the TS samples. TS_$Au_{2.5}$ is light purple but the color is less intense than in TPS_$Au_{2.5}$. Again, the variation of the Au salt concentration leads to a color change. In contrast to TPS_Au_x, however, the surfaces of TS_$Au_{5.6}$ and TS_$Au_{6.1}$ do not show intensification of the purple color, but instead an increasing gray hue. Moreover, the penetration depth of the Au – again judging by the color – is 400 µm; this is larger that observed for TPS_$Au_{2.5}$.

Finally, Au deposition does not influence the shrinking: both the TiO_2/silk and the TiO_2/silk/Au hybrids have roughly the same diameters in the wet and the dry states, respectively. Moreover, no color change is observed on drying.

Figure 2 shows scanning electron microscopy (SEM) and energy dispersive X-ray spectroscopy (EDXS) data obtained from the hybrid materials. TPS has a rough and rather dense surface with large holes up to 16 µm in diameter and some smaller aggregates on the surface. Higher magnification images show smaller holes with diameters ranging between 0.04 and 0.1 µm. These holes are often located around the larger holes described above. EDXS confirms the presence of Ti and O, suggesting the formation of TiO_2. Finally, the samples also exhibit fiber-like features, presumably from the silk.

Au deposition appears to have promoted the opening of the surface of the samples to some extent. As a result, TPS_$Au_{2.5}$ partially exhibits a macroporous structure and an inhomogeneous surface morphology with smaller particles located on the surface, similar to the Au-free sample TPS. Again smaller holes are visible around the larger holes. Moreover, the SEM images of TPS_$Au_{2.5}$ show small spots (highlighted with white circles) that were not observed before Au deposition. These objects are assigned to AuNPs and EDXS indeed confirms the presence of Au in these samples.

The PEO-free hybrid materials (TS) have a different morphology. At lower magnification the sample surface has a grainy appearance but higher magnification images show that the materials consist of tightly connected spherical nanoparticles with significant open volume. The particles have a diameter of ca. 1.5 µm and appear to be composed of smaller particles.

The surface morphology of the gold-containing TS_$Au_{2.5}$ is very similar to the morphology of the TS materials. Unlike the TS materials, however, all TS_$Au_{2.5}$ materials show small, bright dots (highlighted with white circles) in the SEM images. These can again be assigned to AuNP. The presence of Au is again confirmed by EDXS.

EDXS generally only shows C Kα, O Kα, Ti Kα/β, and Ti Lα/β signals. Only the TS samples exhibit Ca Kα and Cl Kα/β signals showing that these samples also contain Ca and Cl. As both these elements are present in the reaction mixture (see Experimental section) it is likely that they are not completely washed out during purification.

Figure 3 shows representative TEM images of the same materials. Lower magnification images reveal significant differences between the TS and TPS materials. The TPS materials exhibit tightly packed pores with diameters ranging between 0.4 and 4.0 µm and rather thin walls between the pores of ca. 0.1–1.8 µm. A few larger pores with diameters up to 50 µm are present as well (Figure S2, Supporting Information File 1). Some of these larger pores have a darker hue, suggesting that they are filled with silk, because the silk was stained with uranyl acetate. The lighter pores are likely filled with resin. The location of the PEO could not be determined.

The TS materials exhibit much less pores than the TPS materials. The pore diameters are larger (10 to 100 µm) than in the TPS materials. The pores are separated from one another by walls with thicknesses between 2–20 µm (highlighted by red lines in Figure 3). All pores show a light gray structure in the TEM images, indicating that they may be filled with silk.

Higher magnification images reveal that the inorganic structure surrounding these large pores is composed of TiO_2 NPs (TNPs) with diameters on the order of 5.5 ± 1.5 nm (Figure 3). Although the primary particles roughly have the same size in all samples, there are differences in the inter-particle distances. While the NPs in the TS samples show a more open, cluster-like structure with small pore-like spaces up to 100 nm, the TPS samples always exhibit very densely packed NPs without further pores in the 10–100 nm range. In spite of their different arrangements, the individual TNPs are essentially identical in all the samples.

Unlike the TNPs, the AuNPs found in the TS and TPS materials are different. For example, in TPS_$Au_{2.5}$ the nanoparticles

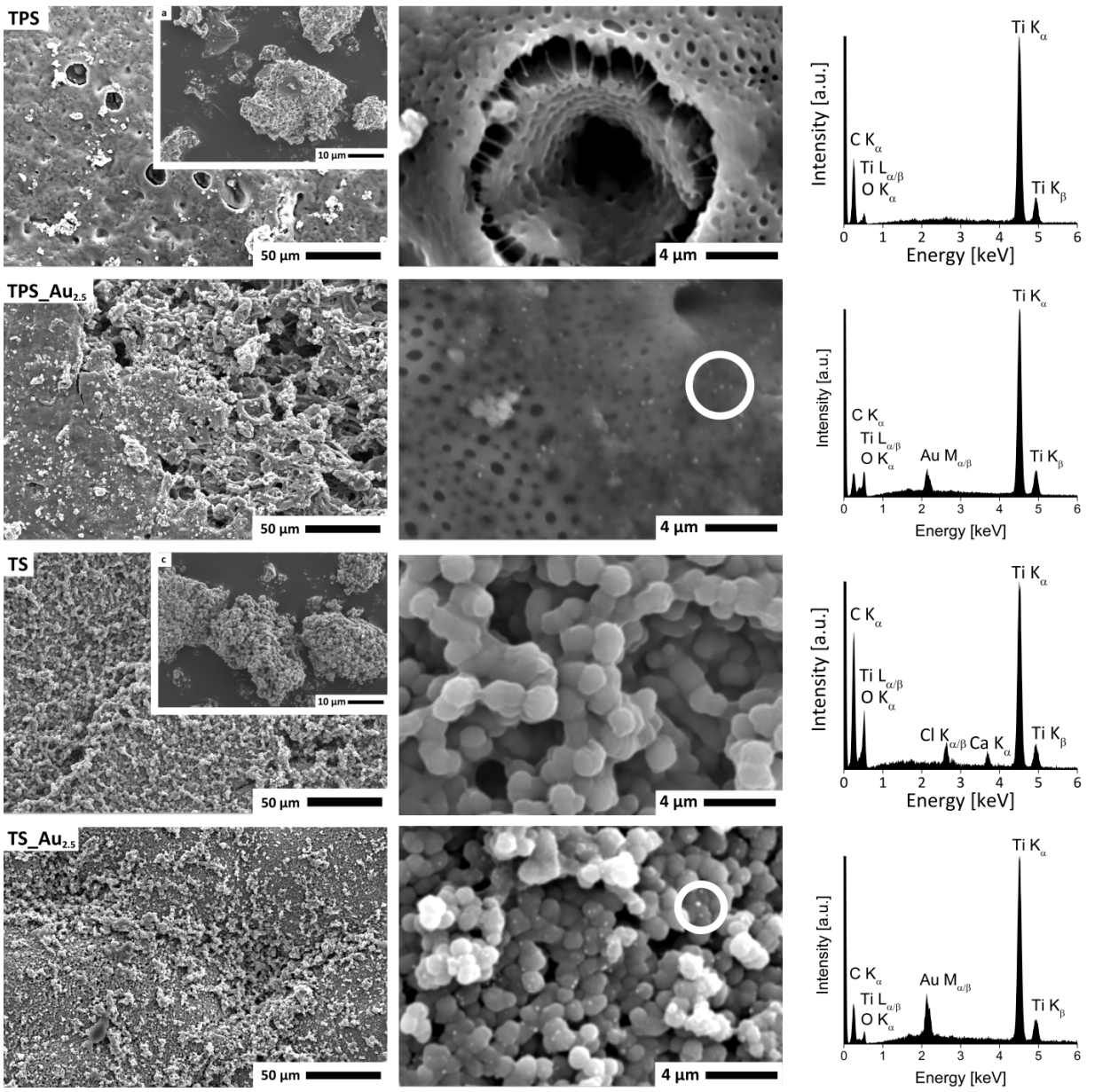

Figure 2: From top to bottom: SEM Images (left) of the surfaces of TPS, TPS_$Au_{2.5}$, TS, and TS_$Au_{2.5}$ at different magnifications, and EDX spectra (right) of the respective samples. Insets show examples of the same material after grinding. Circles highlight some of the bright spots mentioned in the text.

are located at the edge and the pore walls of the hybrid material and are positioned fairly close to each other. The particles have a rather broad size distribution between 4–38 nm, with most particles in the 10–18 nm range (Figure 3).

Judging from the TEM images, TS_$Au_{5.0}$ contains a lower number of AuNPs in spite of the fact that the amount of $HAuCl_4 \cdot 3H_2O$ used for the synthesis was higher than in TPS_$Au_{2.5}$. Furthermore, the particles are more clearly separated from one another. TEM also suggests that the AuNPs have a higher penetration depth in the TS-based materials than in the TPS_Au_x materials, which is consistent with optical microscopy. Moreover, the diameter of the AuNPs in the TS_$Au_{5.0}$ materials is mainly between 7–13 nm, but smaller Au particles are also present. Furthermore, bright field TEM images of TS_$Au_{5.0}$ show a homogeneous AuNP distribution on the TNP.

Dark field STEM images of the HM show a better contrast between Au and TiO_2 (Figure S3, Supporting Information File 1).

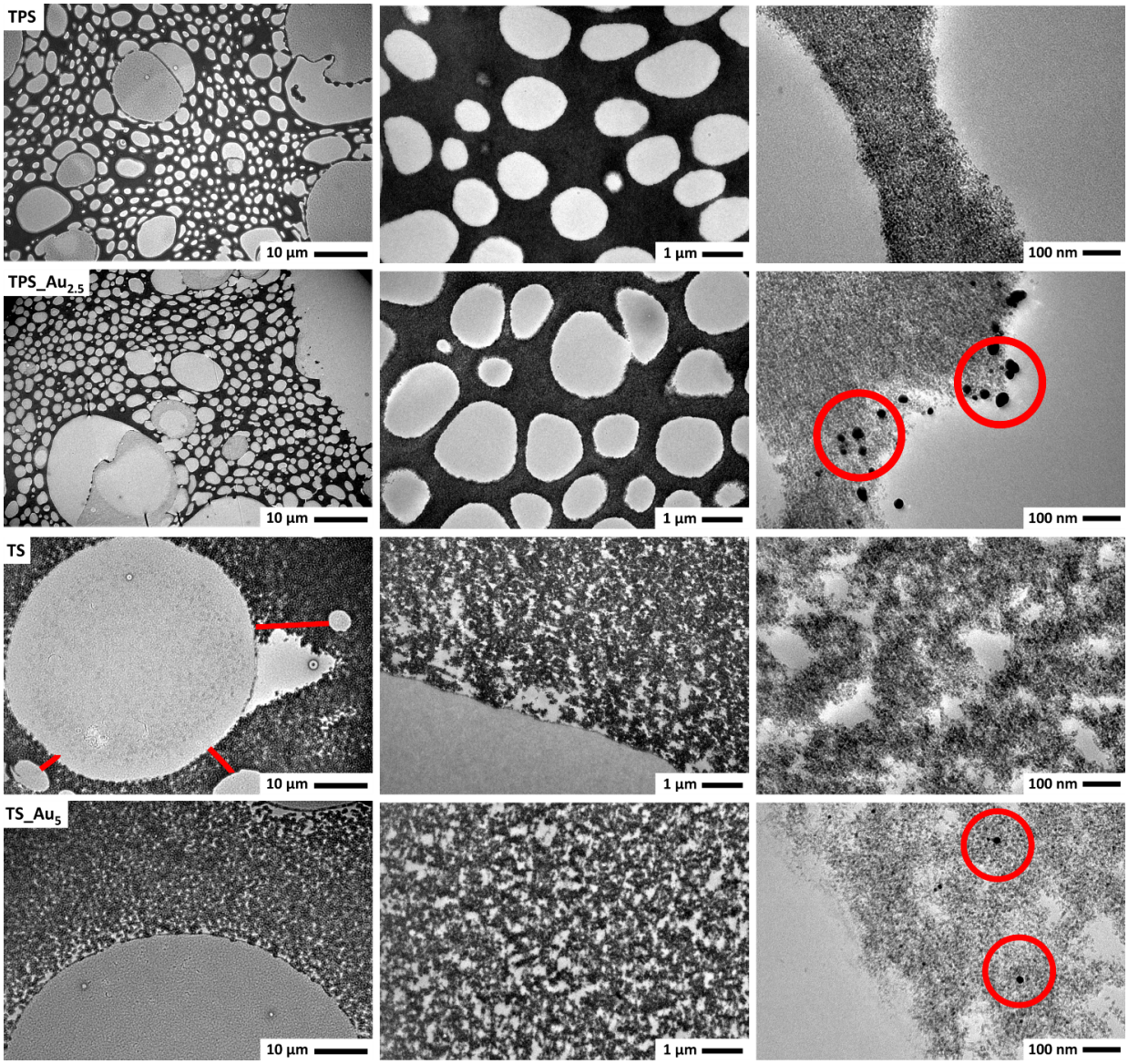

Figure 3: TEM images of TPS, TPS_$Au_{2.5}$, TS, and TS_$Au_{5.0}$ at different magnifications. Red circles highlight the AuNPs and the red bars highlight the walls between two adjacent pores in TS.

The AuNP in TS_$Au_{5.0}$ and TPS_$Au_{2.5}$ are rather homogeneously distributed. Moreover, the images show that the size distribution of the AuNP is quite homogeneous and no overly large or highly aggregated particles are present in the samples. The slight differences between the AuNP distribution in TEM and STEM may be due to variation between sample areas.

Both the AuNPs and the TNPs were further analyzed via HRTEM and fast Fourier transformation (FFT) analysis of the observed lattice fringes along with further EDXS experiments. Figure S4, Supporting Information File 1 shows a representative HRTEM image of a typical AuNP and the surrounding TNP in TS_$Au_{5.0}$. The size of the AuNP (dark spot) is 12 nm. The AuNP is surrounded by different TNPs of about 5 nm in diameter. The size was deduced from the extension of the lattice fringes observed in the HRTEM images (white circles). FFT analysis of the HRTEM image shows a series of reflections that can be assigned to Au and different TiO_2 modifications (brookite and anatase), which are also identified by XRD (Table S2, Supporting Information File 1). Rutile cannot be detected. The EDX spectra were primarily obtained by spot analysis with the electron beam directly placed on one of the dark spherical features; the corresponding spectra show intense Au signals, which confirm HRTEM.

Corresponding data for TPS_$Au_{2.5}$ are displayed in Figure S4, Supporting Information File 1. The AuNP shown here is 15 nm in diameter and the lattice spacings observed in this particle (0.235 nm and 0.204 nm) can again be assigned to (111) and (200) fringes of gold. The TNP observed in these samples have a size of roughly 5 nm in diameter and the lattice spacings obtained from FFT indicates that anatase and brookite are present in the sample. The corresponding EDX spectra prove the presence of Au and Ti.

Figure 4 shows representative XRD patterns of the hybrid materials. All patterns are essentially identical and exhibit a series of broad reflections that can be assigned to anatase (ICDD 98-015-4602). Only one reflection at 30.5°2θ is specifically due to brookite (i.e., the (121) reflection with 90% intensity, ICDD 00-029-1360). The other brookite reflections are located at the same positions as the anatase reflections and can therefore not be distinguished. The very low intensity of the brookite (121) reflection, however, suggests the presence of only a low amount of brookite.

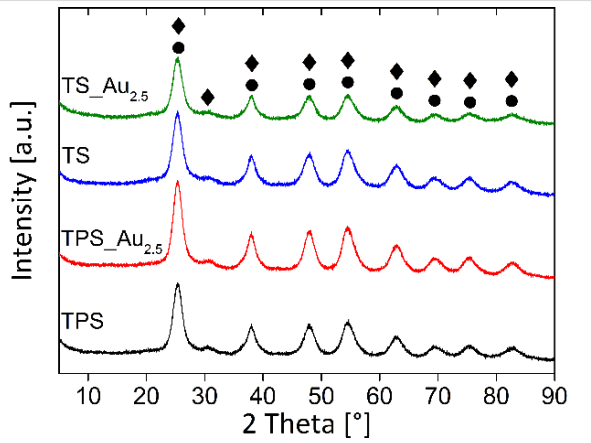

Figure 4: XRD patterns of the hybrid materials. Reflections labeled • are anatase reflections (ICDD: 98-015-4602) and reflections labeled ♦ are brookite reflections (ICDD: 00-029-1360).

Interestingly, the XRD patterns do not display any reflections assigned to Au. In principle, the most intense Au reflection ((111), ICDD 00-004-0784) should be observed at 38.2°. Unfortunately, this position overlaps with the anatase (004) reflection. Therefore, an unambiguous assignment of the observed reflection is not possible. Measurements for longer times and higher count rates for improvement of the signal to noise ratio were thus done from 35–47° (Figure S5a, Supporting Information File 1). The Au (200) reflection at 44.4° (ICDD 00-004-0784) should be clearly visible if high amounts of Au are present in the samples. There is, however, no evidence of this Au reflection. The weak reflection at 42.3° can be attributed to the brookite (221) reflection. Consequently XRD agrees with HRTEM which pointed out the presence of anatase and some brookite.

Scherrer analysis [58] of the XRD patterns yields an average anatase particle size of 4.0 ± 0.5 nm in all samples. This is in good agreement with particle sizes of 5–10 nm evident from the TEM images (Figure 3, Figure S3, Supporting Information File 1).

For photocatalytic water splitting (see below) the wet samples were used. To ensure that there is no drying-induced phase transition in the hybrid materials, XRD was also done on a wet sample (Figure S5b, Supporting Information File 1). Clearly, the wet samples produce a higher X-ray background due to large amounts of water present in these samples. Nevertheless, the data prove that there is no structural change in the material upon drying because XRD patterns are identical to the data obtained from the dry material. Moreover, particle size analysis via Scherrer equation [58] yields exactly the same particle size of 4.1 ± 0.5 nm for the wet samples.

Figure 5 compares the Au 4f, Ti 2p, C 1s, N 1s, and O 1s XP spectra of the TS_$Au_{2.5}$ and TPS_$Au_{2.5}$ surfaces. The respective binding energy assignments (Table S3, Supporting Information File 1) are in a good agreement with literature. The main peak at Au $4f_{7/2}$ = 84.0 ± 0.2 eV is attributed to metallic Au, which proves the formation of Au^0 NPs [59]. The additional weak component at Au $4f_{7/2}$ = 85.1 eV in case of TPS_$Au_{2.5}$ cannot be attributed unambiguously, but is probably due to a local charge-up. The binding energy of Au^{3+} residues would be expected at Au $4f_{7/2}$ = 86.6 eV and, therefore, the presence of Au^{3+} species can be excluded [60].

The Ti $2p_{3/2}$ peak at 459.0 eV and the corresponding O 1s peak at 530.5 eV are attributed to TiO_2 [61]. Furthermore the binding energy of Ti $2p_{3/2}$ at 459.0 eV could possibly also be assigned to Ti–O–C units, possibly stemming from silk, PEO, or residual EtAcAc connected to the TNPs [62]. The O 1s binding energies at 531.8 eV and 533.3 eV can be attributed to Ti–OH motives [63].

The main N 1s peak at 400.1 eV is attributed to the amide and amine groups (peptide bonds) of silk (Table S3, Supporting Information File 1) [64-67]. This assignment is corroborated by the corresponding C 1s peaks at 286.4 eV (C–N) and 288.3 eV (O=C–N, O 1s = 531.8 eV) [66-70]. The weak N 1s component at 402.0 eV is assigned to protonated nitrogen [68]. Note that C–N and C–O contributions cannot be resolved within the C 1s multiplet. In spite of this, the weak O 1s peak at 533.3 eV suggests the presence of C–O groups originating from PEO or synthesis residuals of EtAcAc [66,68]. The C 1s peak at 285.0 eV

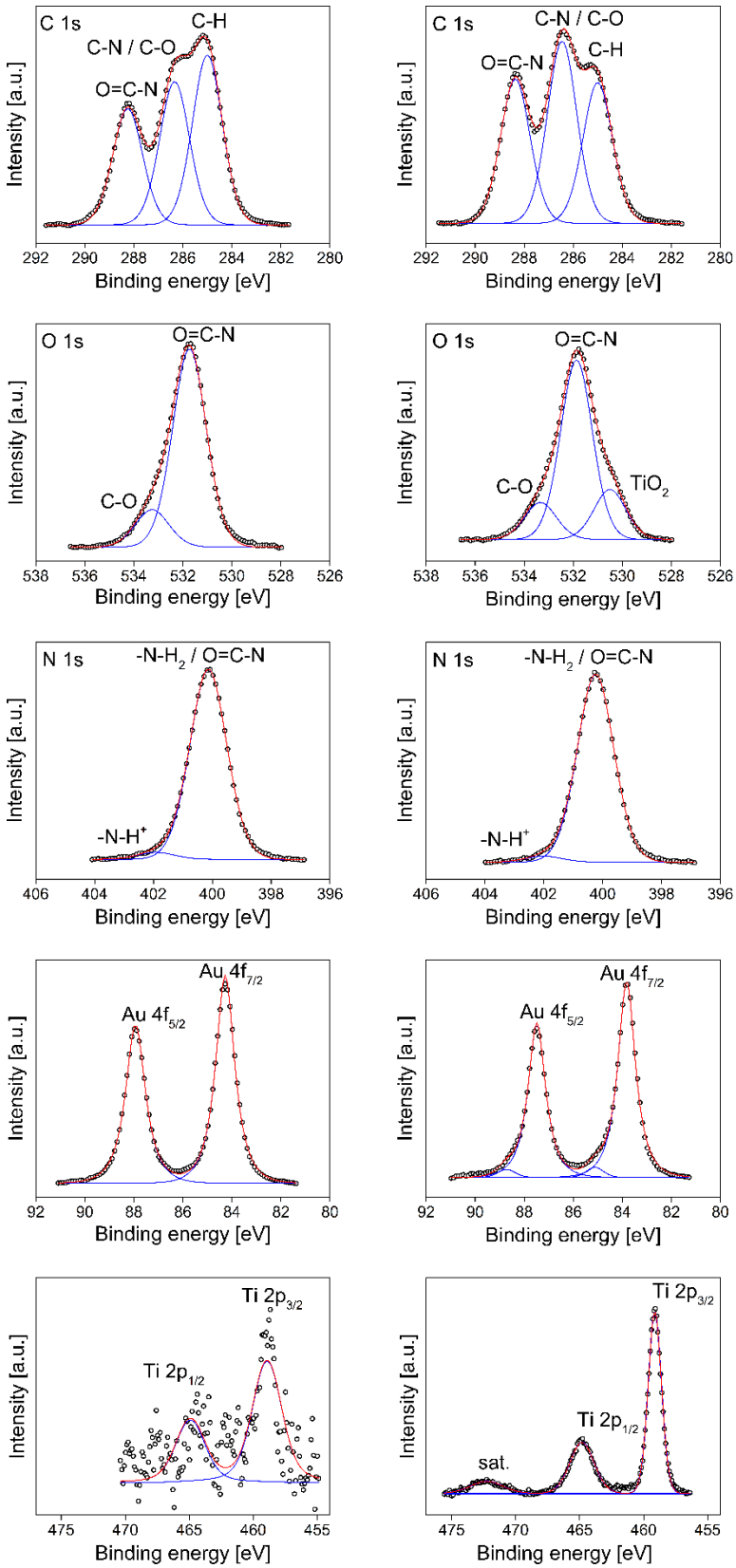

Figure 5: Au 4f, Ti 2p, C 1s, N 1s, and O 1s XP spectra of the TS_$Au_{2.5}$ (left) and TPS_$Au_{2.5}$ (right) surfaces. Open circles are experimental data, red line represents the sum of all fits and blue lines are the single fit components.

is attributed to the C–H groups of PEO and silk and adventitious carbon.

Table S3, Supporting Information File 1 summarizes the XPS binding energies, assignments to the respective binding partners, and atomic concentrations for the samples TS_$Au_{2.5}$ and TPS_$Au_{2.5}$. The chemical composition of all materials is fairly similar except for the fractions of Au and Ti. TS_$Au_{2.5}$ has a higher amount of Au (2.2 atom % vs 1.2 atom %) whereas the amount of titanium (and hence TiO_2) is lower (0.2 vs 2.1 atom %). Conversely, the Au content is lower in TPS_$Au_{2.5}$ and the TiO_2 content is higher.

Furthermore, XPS sputter depth profiles were acquired to obtain information on the chemical composition of the samples vs depth. Figure S6, Supporting Information File 1 shows a representative data set from TPS_$Au_{2.5}$. The fractions of O and Ti increase slightly with increasing sample depth until a plateau is reached at around 500 s. The atomic concentrations of around 30% for Ti and around 60% for O indicate the presence of TiO_2. In contrast the atomic concentrations of C, N, and Au are much lower and further decrease with increasing sample depth, indicating that Au and possibly silk are slightly enriched directly on the surface [71].

EDXS and XPS data (Figure 2 and Figure S4, Supporting Information File 1) were further confirmed by elemental analysis (EA, Table S4, Supporting Information File 1). The overall amount of CHN (indicative of the organic fraction in the materials) is 15.2% in TPS and 14.6% in TPS_$Au_{2.5}$. The fraction of organic material is 21.2% in TS and 20.8% in TS_$Au_{2.5}$.

Figure 6 shows complementary infrared (IR) and Raman spectra. The presence of AuNPs is advantageous, as the signals of chemical species close to the AuNPs are enhanced (surface enhanced Raman effect) [72,73] providing chemical information on the surroundings of the AuNP. In all cases, the addition of Au leads to an increase in the Raman band intensities compared to the Au-free samples. As a result, the Raman spectra of TPS_Au_x and TS_Au_x can be analyzed in detail.

The Raman spectra obtained for "bulk" anatase typically show O–Ti–O vibration bands at 144, 197, and 640 cm^{-1} from the E_g symmetric stretching vibration, at 400 and 519 cm^{-1} from the B_{1g}, symmetric bending vibration, and at 513 cm^{-1} from the A_{1g} asymmetric bending vibration [63,74]. The bands at 519 and 513 cm^{-1} overlap in the current spectra although they are known to be separated below 73 K [63,74]. In the case of nanoparticles (vs bulk TiO_2), broader signals and a red or blue shift in the Raman bands are observed [75]. The O–Ti–O vibration bands observed in Figure 6 are located at 626, 509, 409, 209,

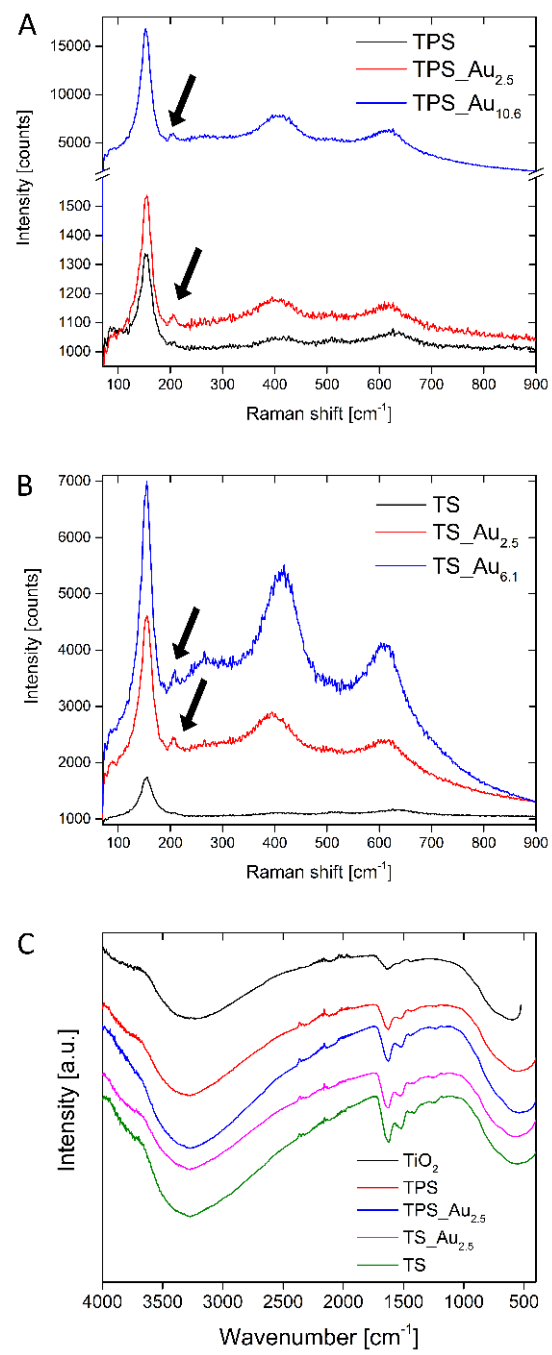

Figure 6: Raman spectra of (A) TPS_Au_x and (B) TS_Au_x. (C) IR spectra of TiO_2 made using the same procedure employed for the hybrid materials (black line), TPS (red), TPS_$Au_{2.5}$ (blue line), TS_$Au_{2.5}$ (violet line), and TS (green line). The signal around 2200 cm^{-1} in the IR spectra stems from the diamond crystal of the ATR-IR spectrometer.

and 151 cm^{-1}. The band at 151 cm^{-1} is the most intense and sharpest signal. The 209 cm^{-1} band is very weak and its intensity increases in the presence of Au. The bands at 409 and 630 cm^{-1} are broad and again their intensity increases in the presence of AuNP. In contrast, the band at 509 cm^{-1} is also

broad, but there is no significant change in intensity upon Au addition. Furthermore, the Raman spectra of TPS_$Au_{10.6}$ and TS_$Au_{6.1}$ show a new weak, broad band at 266 cm^{-1} possibly originating from brookite (RRUFF ID: R50363.3), consistent with XRD.

All FT-IR spectra exhibit a broad band centered at ca. 3300 cm^{-1}, which can be assigned to the stretching vibrations of O–H groups from water and to the symmetric and asymmetric stretching vibrations of the N–H bonds in silk. Symmetric and asymmetric stretching modes of CH_2 groups from silk [76] or from terminal TiO–H groups [77] may also contribute to this broad signal.

Bands at 1620 and 1510 cm^{-1} are the amide I and amide II bands of the β-sheet of *B. mori* silk, respectively [78,79]. The band at 1620 cm^{-1} may also be due to the O–H bending vibration from adsorbed water or TiO–H groups [80]. This signal is more intense in the silk/TiO_2 hybrid materials than in the pure TiO_2 [81]. Finally, Ti–O–Ti and Ti–O vibration bands are observed between 800 and 400 cm^{-1} region [76]. An identification of the crystal phase (anatase, rutile, brookite) is, however, not possible because of the breadth of these bands.

Figure S7, Supporting Information File 1 shows thermogravimetric analysis (TGA) data. The TGA curves of the pure silk show two steps. The first step which spans up to 105 °C with a 4% weight loss, can be assigned to water desorption. The second step is a large weight loss with three overlapping steps between 210 and 640 °C with an overall 97% weight loss with no further weight loss up to 1000 °C.

Pure TiO_2 only shows a broad weight loss of 17% from room temperature to 420 °C, which is assigned to water, ethanol, ethylacetoacetate (EtAcAc), and possibly isopropanol from unreacted TiO_2 precursors [82].

The PEO-containing hybrid materials TPS and TPS_$Au_{2.5}$ essentially exhibit an identical thermal stability. The first weight loss of 9% below 120 °C can be assigned to water and ethanol evaporation. The second step from 120 to 250 °C only shows a minor weight loss of 3% and is likely due to evaporation of more strongly bonded water and ethanol. The third step with an overall weight loss of 20% can again be assigned to silk degradation and combustion of unreacted EtAcAc and TTIP occurring between 250 and 600 °C [82]. No further weight loss is observed up to 1000 °C and the residual 68% can be assigned to TiO_2.

Like the TPS materials, the TS materials essentially exhibit identical TGA curves irrespective of the presence or absence of Au. Again, the first weight loss of 10% up to 120 °C is due to the loss of water and ethanol. A next weight loss of 3% from 120 to 250 °C is from the evaporation of more strongly bound water and ethanol. The third step is a multi-step silk degradation and combustion of unreacted EtAcAc and TTIP from 250 to 580 °C with an overall weight loss of 28% (TS) and 27% (TS_$Au_{2.5}$) indicating a higher amount of organic matter in the TS materials than in the corresponding TPS materials.

In summary, both types of hybrid material contain of ca. 12% of solvent. The TPS materials contain 20% of organic matter (combined silk and PEO) and the TS materials contain ca. 28% of silk. Consequently, the fraction of TiO_2 in TPS is ca. 8% higher than in TS.

Figure 7 shows nitrogen sorption data obtained from the Au-free and Au-modified samples. All samples show a type IV(a) isotherm with a type H2(a) hysteresis loop; the hysteresis loop is typical for materials with pore diameters wider than 4 nm when measuring at 77 K [83]. The vertical slope in the beginning of all measurements indicates the presence of micropores and the remainder of the adsorption and desorption branches indicates the presence of mesopores.

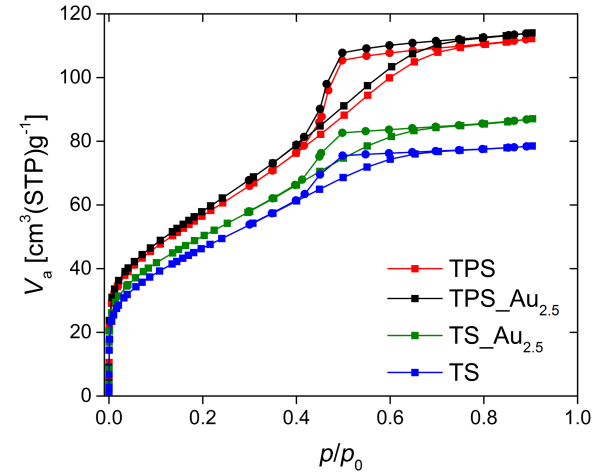

Figure 7: Nitrogen sorption isotherms of TPS (black symbols), TPS_$Au_{2.5}$ (blue symbols), TS_$Au_{2.5}$ (green symbols), and TS (red symbols); ▪ adsorption branch, ● desorption branch.

Pure TiO_2 made by the same synthesis method, but without PEO and silk, has a pore diameter of 2.4 nm and a specific surface area of 280 m^2/g. The TPS and TPS_$Au_{2.5}$ samples have the same pore diameter of 3.2 nm and nearly the same specific surface area of 210 m^2/g. The materials made without PEO (TS and TS_$Au_{2.5}$) have a lower pore diameter of 2.4 nm and a lower specific surface area of 170 m^2/g (TS) and 180 m^2/g (TS_$Au_{2.5}$) respectively. Table 1 summarizes the surface areas and pore volumes.

Table 1: Porosimetry data of the hybrid materials and a TiO_2 control sample made via the same method but without silk and PEO. Surface areas and pore sizes were calculated via the Barrett–Joyner–Halenda (BJH) or Brunauer–Emmett–Teller (BET) method [84,85].

	BJH		BET	Hg intrusion		
sample	Average pore diameter [nm]	Pore volume [mm^3/g]	Total specific surface area [m^2/g]	Average pore diameter [nm]	Pore volume [mm^3/g]	Total pore surface area [m^2/g]
TiO_2	2.4	170	280	–	–	–
TPS powder	3.2	150	210	3.5–5 100–50,000	643	49.5
TPS monolith	–	–	–	3.5–10 100–10,000	332	47.8
TPS_$Au_{2.5}$	3.2	150	210	–	–	–
TS powder	2.4	90	170	500–30,000	517	16.8
TS monolith	–	–	–	3.5–10 500–5,000	344	30.3
TS_$Au_{2.5}$	2.4	110	180	–	–	–

As SEM and TEM also show the presence of macropores, nitrogen sorption was complemented with Hg intrusion porosimetry. Figure 8 shows that TPS ground to a powder prior to the measurements has a very broad pore diameter distribution. The cumulative pore volume indicates a very undefined porosity with pore sizes mainly in the range of 200 nm and 50 µm. In contrast, in the case of monolithic TPS samples (i.e., samples that were not ground prior to analysis), the pore size distribution is different. Pores created between powder particles by grinding (pores bigger than 4–6 µm) cannot be detected here. As a result, the residual porosity appears more distinct, showing pores with a diameter below 10 nm and in the range of 200 nm and ca. 5 µm.

Both TS samples (ground and monolithic) have a narrower pore size distribution than the TPS samples. In the powdered sample, the pores are mainly on the order of 500 nm to 30 µm whereas the monolithic sample shows pores below 10 nm and from

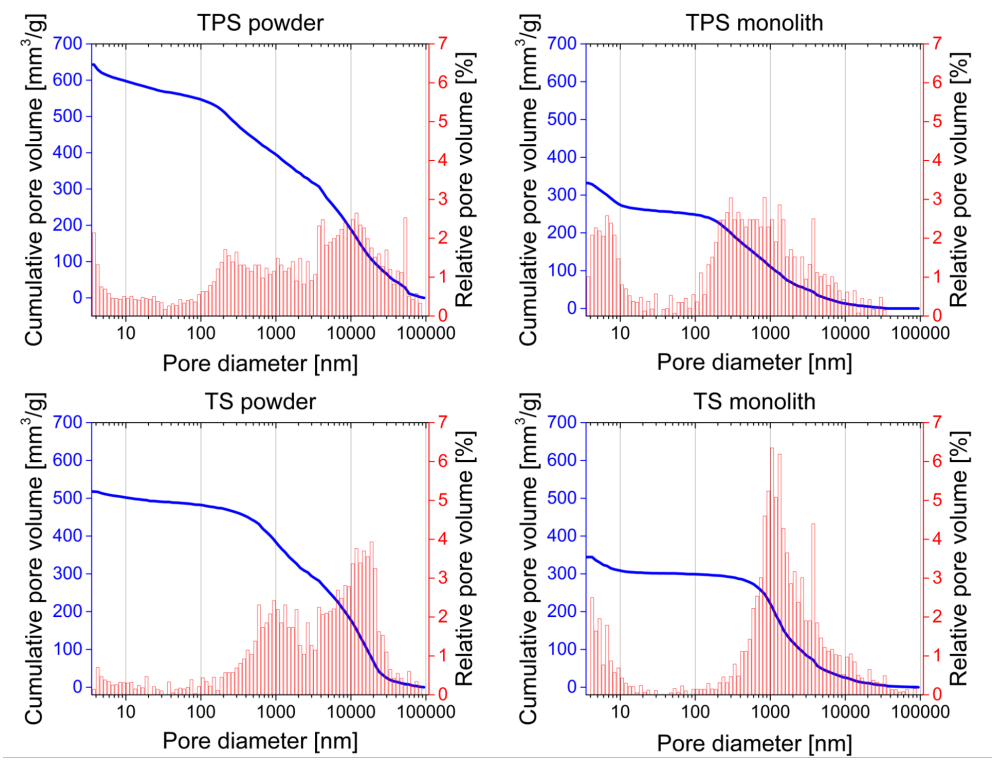

Figure 8: Cumulative (blue) and relative (red) pore volume of TPS (top) and TS (bottom) measured by Hg intrusion.

500 nm to 5 µm with a rather pronounced main pore diameter at 1 µm.

As the purpose of the materials presented here is photocatalytic water splitting, the bandgap is important. It was determined via solid state UV–vis reflection spectroscopy via Kubelka–Munk analysis [61]. The indirect bandgap for all materials is 3.15 ± 0.10 eV, regardless of the presence or absence of Au. This band gap is slightly lower than values found in the literature, which are typically around 3.2 eV for anatase (which is the major component in the current materials) [31,86].

Figure 9 shows the results from photocatalytic water splitting experiments in the presence of ethanol as sacrificial reagent. A possible mechanism of photocatalytic water splitting is shown in Equations S1–S5, Supporting Information File 1. The data reveal a significant influence of the amount of Au present in the samples on the photocatalytic efficiencies. TPS_$Au_{10.7}$ shows the lowest H_2 production of 4 mmol in 24 h (all values are normalized to a catalyst area of 1 m^2). TPS_$Au_{5.8}$ produces 11 mmol of H_2, TPS_$Au_{1.0}$ generates 9 mmol, and TPS_Au_0 produces 16 mmol of H_2. The highest amount (30 mmol) of H_2 is produced with TPS_$Au_{2.5}$.

Replacement of the sun simulator with a 300 W Xenon lamp increases the amount of H_2 produced from TPS_$Au_{5.8}$ by a factor of about 18 from 11 mmol to 200 mmol (Figure S8, Supporting Information File 1). Interestingly, there is no significant difference between materials that were dried before use and those used directly without drying; 16 mmol vs 14 mmol in 24 h.

The TS materials were used as synthesized and show a low H_2 production of 0.3 mmol in 24 h whereas Au modified TS_$Au_{2.5}$ produces 4 mmol in 24 h.

Discussion

H_2 is among the most attractive fuels for a more resource-efficient energy management. As a result, practical and cheap production and delivery strategies for H_2 gas are highly sought after [6-10]. Photocatalytic water splitting is among the most promising technologies for point-of-use H_2 production and therefore a large number of photocatalysts have been developed [8,87-90]. As pointed out in the introduction, however, NP-based photocatalysts have disadvantages, for example in terms of recycling.

The current report therefore focuses on a new hybrid material for water splitting. The main advantage of the current group of materials is that they are available as macroscopic, rather uniform, discs (Figure 1). The macroscopic dimensions enable simple handling of the catalysts. A further advantage that needs to be explored in more detail in the future is the fact that the scaffold is made from silkworm silk, which is – at least in principle – a renewable raw material.

The materials are macroscopically quite uniform. Electron microscopy (Figure 3) and porosimetry (Figure 8) show that all materials exhibit a complex pore architecture. The latter can be tuned by the addition of PEO to the reaction mixture. The specific surface area of TiO_2 without silk and PEO is 280 m^2/g, which is close to the theoretical external surface (315 m^2/g) of 5 nm TNP and consistent with earlier data on 6 nm TNP with a surface area of 250 m^2/g [91].

Generally, the TPS and TS samples have a somewhat lower surface area of 210 m^2/g and 170 m^2/g, respectively. These data clearly show that the approach is flexible and enables the synthesis of materials with a tunable pore size. This may be helpful for optimizing the photocatalytic activity.

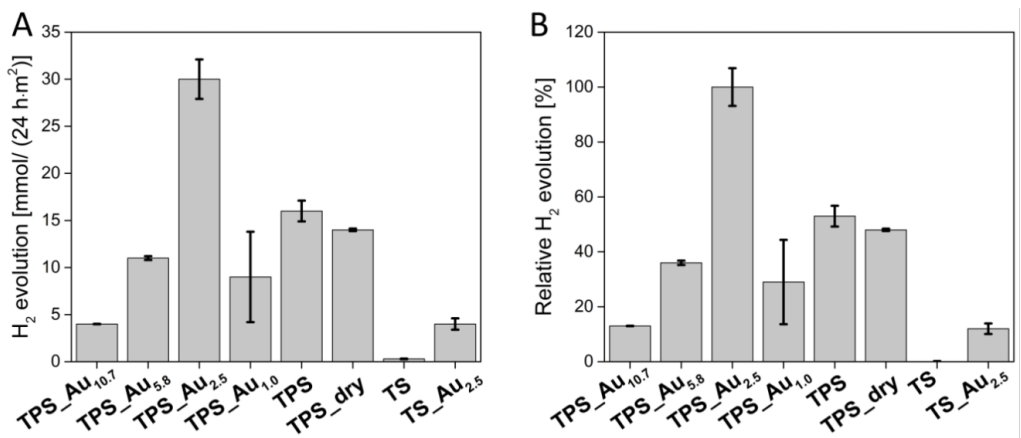

Figure 9: H_2 production of the hybrid materials using a sunlight simulator. A) Numbers are mmol of H_2 produced per 24 h and m^2 of catalyst B) relative H_2 evolution in %.

HRTEM, FFT, and XRD (Figure S4, Supporting Information File 1 and Figure 4) demonstrate that in all cases anatase with traces of brookite forms and that AuNPs are present in the samples. Furthermore, the chemical composition was ascertained via EA, EDXS, XPS, TGA, as well as IR and Raman spectroscopy (Table S4, Supporting Information File 1, Figure 2, Table S3, Supporting Information File 1, Figure S7, Supporting Information File 1, Figure 6) and the data consistently show that the TS samples contain slightly more organic (i.e., silk) material. The deviations in the chemical composition that are observed between the XPS and the EA data are likely due to the fact that EA probes the entire material while XPS solely probes the surface. Indeed XPS sputter profiles (Figure S6, Supporting Information File 1) reveal a carbon-rich surface of the TPS sample suggesting that the surface may be enriched in silk and/or PEO.

Overall, these data prove that: (i) The materials have an open pore structure, (ii) the AuNP and the TNP are in close contact with each other, (iii) the TNPs and the AuNPs are crystalline, and (iv) the materials vary somewhat depending on the synthesis protocols. In spite of this, all materials share the same generic features such as an open porosity and chemical composition suitable for water splitting.

Indeed, all materials are photocatalysts for water splitting. However, Figure 9 clearly shows that there are significant differences between the materials. Expectedly, water splitting is much more efficient under UV irradiation than under simulated sunlight. This is due to the bandgap of 3.15 eV. Indeed it has been pointed out that larger TNP could lead to a higher photocatalytic activity [92] but this aspect is beyond the scope of the current article.

Besides TNP size, the AuNPs play a crucial role. In the current study, samples made with 2.5 mg of $HAuCl_4{\cdot}3H_2O$ yield the best results. Higher Au concentrations possibly lead to an AuNP layer, which is too dense for efficient energy transfer between AuNPs and TNPs. On the other hand, a lower amount of $HAuCl_4{\cdot}3H_2O$ could lead to smaller particles and consequently to very few reaction centers or the reduction of the Au plasmon in the materials, thereby reducing the overall effectiveness of the photocatalytic activation of the reaction.

Comparison of the efficiency of the current materials with other materials is difficult: (i) most photocatalysts described in the literature [22-24] are used as nanoparticles in dispersion. This results in a much higher surface area than those observed in the TS or TPS materials; (ii) the amounts of H_2 produced are often given in µmol/h or µmol/g catalyst. While this is generally viable, solid materials such as the TS and TPS materials are much better characterized by H_2 production in µmol/(h·m^2) as the irradiated area of catalyst is the crucial parameter (and not the mass of catalyst); (iii) there are no standard procedures to quantify the photocatalytic activity and experimental setups show large variations in terms of, e.g., reactor design, feed design, light source, irradiation window, and water/organic solvent mixtures in the reactors [9].

Regardless of this, Silva et al. [24] reported that a higher amount of AuNPs results in a lower H_2 yield, similar to the data presented here. Chen et al. [23] demonstrated that a high amount of AuNP leads to AuNP clusters, which promote the recombination of electron–hole-pairs. The same studies also show an effect of the irradiation wavelength.

Matsuoka et al. [31] deposited TiO_2 on a quartz glass plate. The TiO_2 (columnar rutile) had a height of 1.2 µm and was further sputter-coated with Pt particles. The resulting composites produced 2760 mmol/(24 h·m^2) of H_2 with a 500 W Xe lamp. This is higher than the current materials, which produce 200 mmol/(24 h·m^2) of H_2. It must be noted, however, that these lower numbers were achieved using a 300 W Xe lamp. Moreover, the material used for these experiments (TPS_$Au_{5.8}$) has only ca. 36% of the efficiency of the best material (TPS_$Au_{2.5}$). In addition, Matsuoka et al. used a rutile-based material with a rutile bandgap of ca. 3.02 eV, whereas the current materials are mainly anatase with a bandgap of 3.15 eV; presumably this slightly larger band gap results is a somewhat less effective use of the irradiated light compared to the example by Matsuoka.

As a result, there are differences between these materials making a quantitative comparison between the different approaches difficult. Nevertheless, TiO_2-based composites are highly promising and the current example further broadens the pool of attractive and tunable photocatalysts for water splitting. The performance of the current materials is comparable to other photocatalysts, but they have the additional advantage that they can easily be purified and recycled by simple washing.

Conclusion

We have successfully synthesized two new TiO_2-silk hybrid materials using *B. mori* silk as a renewable and versatile scaffold. The hybrid materials have a complex architecture and are efficient water splitting catalysts. The TPS-based materials are better catalysts than the TS-based materials but more information is necessary to better understand and to optimize these systems. Although the current efficiency of the catalysts is reasonable, the materials presented here are among the first models of complex water splitting catalysts that are at least partly based on renewable materials that can easily be recycled by simple

washing, and are rather efficient at generating H_2, one of the most attractive green energy sources available today.

Supporting Information

Supporting Information File 1

Additional data. A comparison of the different hybrid materials, and further analytic results like (STEM, HRTEM, digital microscope images, XRD, binding energies from XPS measurements and results from TGA and elemental analysis) are shown in the supporting information. Furthermore a comparison between H_2 productions using simulated sunlight vs a xenon lamp and a possible mechanism for photocatalytic water splitting is also shown.
[https://www.beilstein-journals.org/bjnano/content/supplementary/2190-4286-9-21-S1.pdf]

Acknowledgements

We thank Prof. I. Bald and Dr. J. Prinz (U Potsdam) for Raman measurements, Dr. A. M. Schleicher (GFZ Potsdam) for XRD measurements on wet samples, Prof. B. Smarsly (U Giessen) for access to the Hg intrusion porosimetry, Y. Linde (U Potsdam) for EA measurements, Dr. K. Tauer and U. Lubahn (MPI-KG) for TGA measurements. Financial support by the Deutsche Forschungsgemeinschaft (SPP 1569, grant TA571/11-1 and 11-2), the Fundação para a Ciência e Tecnologia (FCT)/ Deutscher Akademischer Austauschdienst (DAAD) Scientific and Technological Cooperation project 2014-2015 (Ref: 6818), the University of Potsdam, and the Fraunhofer-Institute for Applied Polymer Research (FhI-IAP, Golm) is gratefully acknowledged. Purchase of the K-Alpha+ instrument was financially supported by the Federal Ministry of Economics and Technology on the basis of a decision by the German Bundestag.

ORCID® iDs

Christian Kübel - https://orcid.org/0000-0001-5701-4006
Dorothée Vinga Szabó - https://orcid.org/0000-0002-5139-8771
Verónica de Zea Bermudez - https://orcid.org/0000-0002-7577-4938

References

1. Scott, D. S. Back from the Future: To Plan the Best Way Nuclear Can Get Us There. *Nuclear Production of Hydrogen;* Organization for Economic Co-operation and Development (OECD): Paris, France, 2004; p 11.
2. B. P. Company. BP Statistical Review of World Energy June 2016. https://www.bp.com/content/dam/bp/pdf/energy-economics/statistical-review-2016/bp-statistical-review-of-world-energy-2016-full-report.pdf (accessed Oct 24, 2016).
3. Organization for Economic Co-operation and Development (OECD). *Hydrogen and Fuel Cells;* OECD Publishing: Paris, France, 2004.
4. Schnurnberger, W.; Janßen, H.; Wittstadt, U. *Wasserspaltung mit Strom und Wärme. FVS Themen;* 2004; pp 50–59.
5. Fujishima, A.; Honda, K. *Nature* **1972,** *238,* 37–38. doi:10.1038/238037a0
6. Kudo, A.; Miseki, Y. *Chem. Soc. Rev.* **2009,** *38,* 253–278. doi:10.1039/B800489G
7. Osterloh, F. E. *Chem. Soc. Rev.* **2013,** *42,* 2294–2320. doi:10.1039/C2CS35266D
8. Chen, X.; Shen, S.; Guo, L.; Mao, S. S. *Chem. Rev.* **2010,** *110,* 6503–6570. doi:10.1021/cr1001645
9. Hisatomi, T.; Kubota, J.; Domen, K. *Chem. Soc. Rev.* **2014,** *43,* 7520–7535. doi:10.1039/C3CS60378D
10. Maeda, K.; Domen, K. *J. Phys. Chem. Lett.* **2010,** *1,* 2655–2661. doi:10.1021/jz1007966
11. Kudo, A. *Catal. Surv. Asia* **2003,** *7,* 31–38. doi:10.1023/A:1023480507710
12. Youngblood, W. J.; Lee, S.-H. A.; Maeda, K.; Mallouk, T. E. *Acc. Chem. Res.* **2009,** *42,* 1966–1973. doi:10.1021/ar9002398
13. Linic, S.; Christopher, P.; Ingram, D. B. *Nat. Mater.* **2011,** *10,* 911–921. doi:10.1038/nmat3151
14. Mattsson, A.; Österlund, L. *J. Phys. Chem. C* **2010,** *114,* 14121–14132. doi:10.1021/jp103263n
15. Ruzimuradov, O.; Nurmanov, S.; Hojamberdiev, M.; Prasad, R. M.; Gurlo, A.; Broetz, J.; Nakanishi, K.; Riedel, R. *J. Eur. Ceram. Soc.* **2014,** *34,* 809–816. doi:10.1016/j.jeurceramsoc.2013.10.009
16. Kato, H.; Kudo, A. *J. Phys. Chem. B* **2002,** *106,* 5029–5034. doi:10.1021/jp0255482
17. Abe, R.; Sayama, K.; Sugihara, H. *J. Phys. Chem. B* **2005,** *109,* 16052–16061. doi:10.1021/jp052848l
18. Yu, J.; Qi, L.; Jaroniec, M. *J. Phys. Chem. C* **2010,** *114,* 13118–13125. doi:10.1021/jp104488b
19. Ni, M.; Leung, M. K. H.; Leung, D. Y. C.; Sumathy, K. *Renewable Sustainable Energy Rev.* **2007,** *11,* 401–425. doi:10.1016/j.rser.2005.01.009
20. Khan, S. U. M.; Al-Shahry, M.; Ingler, W. B., Jr. *Science* **2002,** *297,* 2243–2245. doi:10.1126/science.1075035
21. Primo, A.; Corma, A.; García, H. *Phys. Chem. Chem. Phys.* **2011,** *13,* 886–910. doi:10.1039/C0CP00917B
22. Gallo, A.; Marelli, M.; Psaro, R.; Gombac, V.; Montini, T.; Fornasiero, P.; Pievo, R.; Santo, V. D. *Green Chem.* **2012,** *14,* 330. doi:10.1039/C2GC16112E
23. Chen, J.-J.; Wu, J. C. S.; Wu, P. C.; Tsai, D. P. *J. Phys. Chem. C* **2011,** *115,* 210–216. doi:10.1021/jp1074048
24. Silva, C. G.; Juárez, R.; Marino, T.; Molinari, R.; García, H. *J. Am. Chem. Soc.* **2011,** *133,* 595–602. doi:10.1021/ja1086358
25. Gärtner, F.; Losse, S.; Boddien, A.; Pohl, M.-M.; Denurra, S.; Junge, H.; Beller, M. *ChemSusChem* **2012,** *5,* 530–533. doi:10.1002/cssc.201100281
26. Jose, D.; Sorensen, C. M.; Rayalu, S. S.; Shrestha, K. M.; Klabunde, K. J. *Int. J. Photoenergy* **2013,** *2013,* 685614. doi:10.1155/2013/685614
27. Zhang, J.; Jin, X.; Morales-Guzman, P. I.; Yu, X.; Liu, H.; Zhang, H.; Razzari, L.; Claverie, J. P. *ACS Nano* **2016,** *10,* 4496–4503. doi:10.1021/acsnano.6b00263
28. Seh, Z. W.; Liu, S.; Low, M.; Zhang, S.-Y.; Liu, Z.; Mlayah, A.; Han, M.-Y. *Adv. Mater.* **2012,** *24,* 2310–2314. doi:10.1002/adma.201104241

29. Liu, E.; Kang, L.; Yang, Y.; Sun, T.; Hu, X.; Zhu, C.; Liu, H.; Wang, Q.; Li, X.; Fan, J. *Nanotechnology* **2014,** *25,* 165401. doi:10.1088/0957-4484/25/16/165401
30. Liu, E.; Fan, J.; Hu, X.; Hu, Y.; Li, H.; Tang, C.; Sun, L.; Wan, J. *J. Mater. Sci.* **2015,** *50,* 2298–2305. doi:10.1007/s10853-014-8793-z
31. Matsuoka, M.; Kitano, M.; Takeuchi, M.; Anpo, M.; Thomas, J. M. *Top. Catal.* **2005,** *35,* 305–310. doi:10.1007/s11244-005-3838-9
32. Goutailler, G.; Guillard, C.; Daniele, S.; Hubert-Pfalzgraf, L. G. *J. Mater. Chem.* **2003,** *13,* 342–346. doi:10.1039/b208738c
33. Galkina, O. L.; Sycheva, A.; Blagodatskiy, A.; Kaptay, G.; Katanaev, V. L.; Seisenbaeva, G. A.; Kessler, V. G.; Agafonov, A. V. *Surf. Coat. Technol.* **2014,** *253,* 171–179. doi:10.1016/j.surfcoat.2014.05.033
34. Galkina, O. L.; Ivanov, V. K.; Agafonov, A. V.; Seisenbaeva, G. A.; Kessler, V. G. *J. Mater. Chem. B* **2015,** *3,* 1688–1698. doi:10.1039/C4TB01823K
35. Daoud, W. A.; Xin, J. H. *J. Sol-Gel Sci. Technol.* **2004,** *29,* 25–29. doi:10.1023/B:JSST.0000016134.19752.b4
36. Zheng, C.; Chen, G.; Qi, Z. *Plasma Chem. Plasma Process.* **2012,** *32,* 629–642. doi:10.1007/s11090-012-9350-7
37. Ude, A. U.; Eshkoor, R. A.; Zulkifili, R.; Ariffin, A. K.; Dzuraidah, A. W.; Azhari, C. H. *Mater. Des.* **2014,** *57,* 298–305. doi:10.1016/j.matdes.2013.12.052
38. Zhou, C.-Z.; Confalonieri, F.; Jacquet, M.; Perasso, R.; Li, Z.-G.; Janin, J. *Proteins: Struct., Funct., Genet.* **2001,** *44,* 119–122. doi:10.1002/prot.1078
39. Dickerson, M. B.; Sandhage, K. H.; Naik, R. R. *Chem. Rev.* **2008,** *108,* 4935–4978. doi:10.1021/cr8002328
40. Durupthy, O.; Bill, J.; Aldinger, F. *Cryst. Growth Des.* **2007,** *7,* 2696–2704. doi:10.1021/cg060405g
41. Kanie, K.; Sugimoto, T. *Chem. Commun.* **2004,** 1584–1585. doi:10.1039/B404220D
42. Dickerson, M. B.; Jones, S. E.; Cai, Y.; Ahmad, G.; Naik, R. R.; Kröger, N.; Sandhage, K. H. *Chem. Mater.* **2008,** *20,* 1578–1584. doi:10.1021/cm071515t
43. Fang, Y.; Poulsen, N.; Dickerson, M. B.; Cai, Y.; Jones, S. E.; Naik, R. R.; Kröger, N.; Sandhage, K. H.; Kroger, N.; Sandhage, K. H. *J. Mater. Chem.* **2008,** *18,* 3871–3875. doi:10.1039/b806797j
44. Kröger, N.; Dickerson, M. B.; Ahmad, G.; Cai, Y.; Haluska, M. S.; Sandhage, K. H.; Poulsen, N.; Sheppard, V. C. *Angew. Chem., Int. Ed.* **2006,** *45,* 7239–7243. doi:10.1002/anie.200601871
45. Sewell, S. L.; Wright, D. W. *Chem. Mater.* **2006,** *18,* 3108–3113. doi:10.1021/cm060342p
46. Puddu, V.; Slocik, J. M.; Naik, R. R.; Perry, C. C. *Langmuir* **2013,** *29,* 9464–9472. doi:10.1021/la401777x
47. Huang, Y.; Chiang, C.-Y.; Lee, S. K.; Gao, Y.; Hu, E. L.; De Yoreo, J.; Belcher, A. M. *Nano Lett.* **2005,** *5,* 1429–1434. doi:10.1021/nl050795d
48. Sarikaya, M.; Tamerler, C.; Jen, A. K.-Y.; Schulten, K.; Baneyx, F. *Nat. Mater.* **2003,** *2,* 577–585. doi:10.1038/nmat964
49. Pérez-Rigueiro, J.; Elices, M.; Llorca, J.; Viney, C. *J. Appl. Polym. Sci.* **2001,** *82,* 1928–1935. doi:10.1002/app.2038
50. Hasegawa, G.; Kanamori, K.; Nakanishi, K.; Hanada, T. *J. Sol-Gel Sci. Technol.* **2010,** *53,* 59–66. doi:10.1007/s10971-009-2056-5
51. Hasegawa, G.; Kanamori, K.; Nakanishi, K.; Hanada, T. *J. Am. Ceram. Soc.* **2010,** *93,* 3110–3115. doi:10.1111/j.1551-2916.2010.03831.x
52. Ajisawa, A. *J. Seric. Sci. Jpn.* **1998,** *67,* 91–94.
53. Parry, K. L.; Shard, A. G.; Short, R. D.; White, R. G.; Whittle, J. D.; Wright, A. *Surf. Interface Anal.* **2006,** *38,* 1497–1504. doi:10.1002/sia.2400
54. Scofield, J. H. *J. Electron Spectrosc. Relat. Phenom.* **1976,** *8,* 129–137. doi:10.1016/0368-2048(76)80015-1
55. Tanuma, S.; Powell, C. J.; Penn, D. R. *Surf. Interface Anal.* **1994,** *21,* 165–176. doi:10.1002/sia.740210302
56. Prinz, J.; Matković, A.; Pešić, J.; Gajić, R.; Bald, I. *Small* **2016,** *12,* 5458–5467. doi:10.1002/smll.201601908
57. Schwarze, M.; Stellmach, D.; Schröder, M.; Kailasam, K.; Reske, R.; Thomas, A.; Schomäcker, R. *Phys. Chem. Chem. Phys.* **2013,** *15,* 3466. doi:10.1039/c3cp50168j
58. Scherrer, P. *Nachr. Ges. Wiss. Goettingen, Math.-Phys. Kl.* **1918,** *2,* 98–100.
59. Joseph, Y.; Besnard, I.; Rosenberger, M.; Guse, B.; Nothofer, H.-G.; Wessels, J. M.; Wild, U.; Knop-Gericke, A.; Su, D.; Schlögl, R.; Yasuda, A.; Vossmeyer, T. *J. Phys. Chem. B* **2003,** *107,* 7406–7413. doi:10.1021/jp030439o
60. Conte, M.; Davies, C. J.; Morgan, D. J.; Davies, T. E.; Carley, A. F.; Johnston, P.; Hutchings, G. J. *Catal. Sci. Technol.* **2013,** *3,* 128–134. doi:10.1039/C2CY20478A
61. Tunc, I.; Bruns, M.; Gliemann, H.; Grunze, M.; Koelsch, P. *Surf. Interface Anal.* **2010,** *42,* 835–841. doi:10.1002/sia.3558
62. Qiu, B.; Zhou, Y.; Ma, Y.; Yang, X.; Sheng, W.; Xing, M.; Zhang, J. *Sci. Rep.* **2015,** *5,* 8591. doi:10.1038/srep08591
63. Yan, J.; Wu, G.; Guan, N.; Li, L.; Li, Z.; Cao, X. *Phys. Chem. Chem. Phys.* **2013,** *15,* 10978–10988. doi:10.1039/c3cp50927c
64. Bruns, M.; Barth, C.; Brüner, P.; Engin, S.; Grehl, T.; Howell, C.; Koelsch, P.; MacK, P.; Nagel, P.; Trouillet, V.; Wedlich, D.; White, R. G. *Surf. Interface Anal.* **2012,** *44,* 909–913. doi:10.1002/sia.4876
65. Tischer, T.; Goldmann, A. S.; Linkert, K.; Trouillet, V.; Börner, H. G.; Barner-Kowollik, C. *Adv. Funct. Mater.* **2012,** *22,* 3853–3864. doi:10.1002/adfm.201200266
66. Engin, S.; Trouillet, V.; Franz, C. M.; Welle, A.; Bruns, M.; Wedlich, D. *Langmuir* **2010,** *26,* 6097–6101. doi:10.1021/la904829y
67. Preuss, C. M.; Tischer, T.; Rodriguez-Emmenegger, C.; Zieger, M. M.; Bruns, M.; Goldmann, A. S.; Barner-Kowollik, C. A. *J. Mater. Chem. B* **2014,** *2,* 36–40. doi:10.1039/C3TB21317J
68. Zydziak, N.; Preuss, C. M.; Winkler, V.; Bruns, M.; Hübner, C.; Barner-Kowollik, C. *Macromol. Rapid Commun.* **2013,** *34,* 672–680. doi:10.1002/marc.201300025
69. Lock, E. H.; Petrovykh, D. Y.; Mack, P.; Carney, T.; White, R. G.; Walton, S. G.; Fernsler, R. F. *Langmuir* **2010,** *26,* 8857–8868. doi:10.1021/la9046337
70. Rodriguez-Emmenegger, C.; Preuss, C. M.; Yameen, B.; Pop-Georgievski, O.; Bachmann, M.; Mueller, J. O.; Bruns, M.; Goldmann, A. S.; Bastmeyer, M.; Barner-Kowollik, C. *Adv. Mater.* **2013,** *25,* 6123–6127. doi:10.1002/adma.201302492
71. Mai, T.; Wolski, K.; Puciul-Malinowska, A.; Kopyshev, A.; Gräf, R.; Bruns, M.; Zapotoczny, S.; Taubert, A. *Biomacromolecules*, in press.
72. Schlücker, S. *Angew. Chem., Int. Ed.* **2014,** *53,* 4756–4795. doi:10.1002/anie.201205748
73. Haynes, C. L.; McFarland, A. D.; van Duyne, R. P. *Anal. Chem.* **2005,** *77,* 338A–346A.
74. Ohsaka, T.; Izumi, F.; Fujiki, Y. *J. Raman Spectrosc.* **1978,** *7,* 321–324. doi:10.1002/jrs.1250070606

75. Swamy, V.; Kuznetsov, A.; Dubrovinsky, L. S.; Caruso, R. A.; Shchukin, D. G.; Muddle, B. C. *Phys. Rev. B: Condens. Matter Mater. Phys.* **2005,** *71,* 184302. doi:10.1103/PhysRevB.71.184302
76. Vasconcelos, D. C. L.; Costa, V. C.; Nunes, E. H. M.; Sabioni, A. C. S.; Gasparon, M.; Vasconcelos, W. L. *Mater. Sci. Appl.* **2011,** *2,* 1375–1382. doi:10.4236/msa.2011.210186
77. Buonsanti, R.; Carlino, E.; Giannini, C.; Altamura, D.; De Marco, L.; Giannuzzi, R.; Manca, M.; Gigli, G.; Cozzoli, P. D. *J. Am. Chem. Soc.* **2011,** *133,* 19216–19239. doi:10.1021/ja208418z
78. Lu, Q.; Hu, X.; Wang, X.; Kluge, J. A.; Lu, S.; Cebe, P.; Kaplan, D. L. *Acta Biomater.* **2010,** *6,* 1380–1387. doi:10.1016/j.actbio.2009.10.041
79. Ming, J.; Zuo, B. *J. Appl. Polym. Sci.* **2012,** *125,* 2148–2154. doi:10.1002/app.36354
80. Musić, S.; Gotić, M.; Ivanda, M.; Popović, S.; Turković, A.; Trojko, R.; Sekulić, A.; Furić, K. *Mater. Sci. Eng., B* **1997,** *47,* 33–40. doi:10.1016/S0921-5107(96)02041-7
81. Zhang, H.; Magoshi, J.; Becker, M.; Chen, J. Y.; Matsunaga, R. *J. Appl. Polym. Sci.* **2002,** *86,* 1817–1820. doi:10.1002/app.11089
82. Rahal, R.; Daniele, S.; Hubert-Pfalzgraf, L. G.; Guyot-Ferréol, V.; Tranchant, J.-F. *Eur. J. Inorg. Chem.* **2008,** *6,* 980–987. doi:10.1002/ejic.200700971
83. Thommes, M.; Kaneko, K.; Neimark, A. V.; Olivier, J. P.; Rodriguez-Reinoso, F.; Rouquerol, J.; Sing, K. S. W. *Pure Appl. Chem.* **2015,** *87,* 1051–1069. doi:10.1515/pac-2014-1117
84. Brunauer, S.; Emmett, P. H.; Teller, E. *J. Am. Chem. Soc.* **1938,** *60,* 309–319. doi:10.1021/ja01269a023
85. Barrett, E. P.; Joyner, L. G.; Halenda, P. P. *J. Am. Chem. Soc.* **1951,** *73,* 373–380. doi:10.1021/ja01145a126
86. Dette, C.; Pérez-Osorio, M. A.; Kley, C. S.; Punke, P.; Patrick, C. E.; Jacobson, P.; Giustino, F.; Jung, S. J.; Kern, K. *Nano Lett.* **2014,** *14,* 6533–6538. doi:10.1021/nl503131s
87. Jaeger, C. D.; Bard, A. J. *J. Phys. Chem.* **1979,** *83,* 3146–3152. doi:10.1021/j100487a017
88. Ong, W. L.; Lim, Y.-F.; Ting Ong, J. L.; Ho, G. W. *J. Mater. Chem. A* **2015,** *3,* 6509–6516. doi:10.1039/C4TA06674J
89. Linsebigler, A. L.; Lu, G.; Yates, J. T., Jr. *Chem. Rev.* **1995,** *95,* 735–758. doi:10.1021/cr00035a013
90. Chen, X.; Mao, S. S. *Chem. Rev.* **2007,** *107,* 2891–2959. doi:10.1021/cr0500535
91. Mendez, V.; Caps, V.; Daniele, S. *Chem. Commun.* **2009,** 3116–3118. doi:10.1039/b902606a
92. Chou, T. P.; Zhang, Q.; Russo, B.; Fryxell, G. E.; Cao, G. *J. Phys. Chem. C* **2007,** *111,* 6296–6302. doi:10.1021/jp068939f

License and Terms

This is an Open Access article under the terms of the Creative Commons Attribution License (http://creativecommons.org/licenses/by/4.0), which permits unrestricted use, distribution, and reproduction in any medium, provided the original work is properly cited.

The license is subject to the *Beilstein Journal of Nanotechnology* terms and conditions: (https://www.beilstein-journals.org/bjnano)

The definitive version of this article is the electronic one which can be found at:
doi:10.3762/bjnano.9.21

BEILSTEIN JOURNAL OF NANOTECHNOLOGY

Sugarcane juice derived carbon dot–graphitic carbon nitride composites for bisphenol A degradation under sunlight irradiation

Lan Ching Sim*[1], Jing Lin Wong[1], Chen Hong Hak[1], Jun Yan Tai[1], Kah Hon Leong[1] and Pichiah Saravanan[2]

Full Research Paper

Open Access

Address:
[1]Department of Environmental Engineering, Faculty of Engineering and Green Technology, Universiti Tunku Abdul Rahman, Jalan Universiti, Bandar Barat, 31900, Kampar, Perak, Malaysia and [2]Environmental Nanotechnology Laboratory, Department of Environmental Science and Engineering, Indian Institute of Technology (ISM), Dhanbad 826004, Jharkhand, India

Email:
Lan Ching Sim* - simcl@utar.edu.my

* Corresponding author

Keywords:
carbon dots; g-C_3N_4; photocatalytic degradation; sugarcane juice; sunlight

Beilstein J. Nanotechnol. **2018,** *9,* 353–363.
doi:10.3762/bjnano.9.35

Received: 28 September 2017
Accepted: 04 January 2018
Published: 30 January 2018

This article is part of the Thematic Series "Energy conversion, storage and environmental remediation using nanomaterials".

Guest Editor: W.-J. Ong

© 2018 Sim et al.; licensee Beilstein-Institut.
License and terms: see end of document.

Abstract

Carbon dots (CDs) and graphitic carbon nitride (g-C_3N_4) composites (CD/g-C_3N_4) were successfully synthesized by a hydrothermal method using urea and sugarcane juice as starting materials. The chemical composition, morphological structure and optical properties of the composites and CDs were characterized using various spectroscopic techniques as well as transmission electron microscopy. X-ray photoelectron spectroscopy (XPS) results revealed new signals for carbonyl and carboxyl groups originating from the CDs in CD/g-C_3N_4 composites while X-ray diffraction (XRD) results showed distortion of the host matrix after incorporating CDs into g-C_3N_4. Both analyses signified the interaction between g-C_3N_4 and CDs. The photoluminescence (PL) analysis indicated that the presence of too many CDs will create trap states at the CD/g-C_3N_4 interface, decelerating the electron (e^-) transport. However, the CD/g-C_3N_4(0.5) composite with the highest coverage of CDs still achieved the best bisphenol A (BPA) degradation rate at 3.87 times higher than that of g-C_3N_4. Hence, the charge separation efficiency should not be one of the main factors responsible for the enhancement of the photocatalytic activity of CD/g-C_3N_4. Instead, the light absorption capability was the dominant factor since the photoreactivity correlated well with the ultraviolet–visible diffuse reflectance spectra (UV–vis DRS) results. Although the CDs did not display upconversion photoluminescence (UCPL) properties, the π-conjugated CDs served as a photosensitizer (like organic dyes) to sensitize g-C_3N_4 and injected electrons to the conduction band (CB) of g-C_3N_4, resulting in the extended absorption spectrum from the visible to the near-infrared (NIR) region. This extended spectral absorption allows for the generation of more electrons for the enhancement of BPA degradation. It was determined that the reactive radical species responsible for the photocatalytic activity were the superoxide anion radical ($O_2^{\bullet-}$) and holes (h^+) after performing multiple scavenging tests.

Introduction

Carbon dots (CDs) predominantly consist of amorphous carbon together with nanocrystalline regions of sp^2-hybridized graphitic carbon [1]. CDs possess upconversion photoluminescence (UCPL) properties [2] and are able to harvest long wavelength light in the visible and near infrared (NIR) region [3,4], rendering them promising candidates as photosensitizers in photocatalysis. Nevertheless, the reported preparation method of CDs has met several limitations including limited spectral efficiency, low product yield and toxic chemicals usage [5]. Thus, the use of renewable bioprecursors such as orange juice [6], soy milk [7], orange waste peels [8], watermelon rinds [9], hair [10] and cow manure [11] to produce CDs has drawn the attention of researchers. Such green CDs are widely applied in bioimaging [6,12], sensing [13] and solar cells [14]. However, the obtained CDs showed superior water solubility, limiting their down-to-earth applicability for photocatalysis in aqueous solution. It is well-known that the organic semiconductor g-C_3N_4 possesses visible light harvesting properties due to its narrow band gap energy (≈2.7 eV) [15]. Thus g-C_3N_4 has emerged as a promising polymeric semiconductor for photocatalytic reduction of carbon dioxide (CO_2) [16-20], hydrogen evolution [21-25], oxidation of NO [26,27], and degradation of pollutants [28-30]. However, the photocatalytic performance of bulk g-C_3N_4 remains unsatisfactory because of the fast recombination rate of electron pairs and narrower light absorption range over the entire solar spectrum. Turning g-C_3N_4 into a mesoporous nanorod structure [31] and the hydrogenation of g-C_3N_4 [32] could be an alternative to increase the light-harvesting ability and charge separation efficiency. Our group has reported the self-modification of g-C_3N_4 structures using alkaline [28] and acid treatment [29] to overcome the limitations of g-C_3N_4. Despite of the positive results, the self-modification consumes concentrated alkali and acid, which is harmful to our environment and health. It has been accepted that the coupling of nanocarbon materials with other semiconductors [21] could induce synergetic effects like photosensitization, electron mediator and acceptor and increasing adsorption [33,34]. Therefore, g-C_3N_4 could be combined with CDs to overcome the solubility problem of CDs and to boost the performance of g-C_3N_4. Besides, the CDs can also act as photosensitizers to harvest a wide spectrum of solar light to achieve efficient daylight-driven photocatalysis. Prasannan and Imae reported a simple and facile one-pot synthesis of fluorescent CDs from orange waste peels using the hydrothermal carbonization method. As prepared CDs were combined with zinc oxide (ZnO) to degrade naphthol blue–black azo dye under UV irradiation, and the superior photocatalytic activity was demonstrated [8]. Guo and co-workers used the electrochemical method to produce CDs from graphite rods. The deposition of CDs onto g-C_3N_4/ZnO heterojunctions enhanced the degradation of tetracycline by absorbing a wider spectrum of visible light and suppressing the recombination of electron–hole pairs [35]. A facile hydrothermal approach was adopted to synthesize CD/g-C_3N_4 using ascorbic acid as precursor to prepare CDs, showing higher hydrogen (H_2) production than pure g-C_3N_4 under UV light irradiation [36]. A similar composite was also reported using 6-aminohexanoic acid [37] and rapeseed flower bee pollen [38] as precursors to produce CDs for the photocatalytic generation of H_2 under visible light irradiation. In addition, Wang and co-workers used citric acid and urea as precursors to prepare N-doped CDs (NCDs). The NCD/g-C_3N_4 composite exhibited better degradation of indomethacin from the UV to NIR spectrum because of the superior electron transfer and extension of visible light absorption region after doping with N atoms [39]. Their group further enhanced the efficiency of CD/g-C_3N_4 through the incorporation of single-atom-dispersed silver. The optimum amount of Ag (3.0 wt %) and CDs (1.0 wt %) resulted in a 10-fold higher degradation rate of naproxen [40]. Much of the work on g-C_3N_4 has been reported for environmental and energy remediation [41,42]. The above-mentioned research works suggested that the enhancement of the photocatalytic performance was attributed to the dual functionality of CDs as electron trapper and photosensitizer. Although some works have been carried out in this field, several insights have yet to be explored to fill the gaps of previous works, including (i) the utilization of harmless solar energy as a resource to irradiate photocatalytic degradation of organic pollutant (since CDs could act as a photosensitizer over the entire solar spectrum) and (ii) acknowledgement that the most reported bioprecursor-derived CDs and g-C_3N_4 composite are limited to the photocatalytic generation of H_2 (instead limited attempts have been performed on the removal of the organic pollutant since foremost discovery by Prasannan and Imae [8]).

Collectively, considering all of the aforementioned problems, it provokes the idea that the combination of g-C_3N_4 with CDs produced from sugarcane juice can be used for the photocatalytic degradation of endocrine disrupting chemicals (EDCs). Bisphenol A (BPA) was chosen as a model pollutant under natural sunlight irradiation. Herein, the structural and optical properties of samples were characterized by X-ray diffraction (XRD), Fourier transform infrared spectroscopy (FTIR), photoluminescence (PL), X-ray photoelectron spectroscopy (XPS), transmission electron microscopy (TEM), etc. The influence of the weight percentage of CDs and a scavenging experiment were carried out to illustrate the potential degradation mechanisms. Overall, the incorporation of CDs into g-C_3N_4 was efficient towards the removal of BPA, mainly because the CDs act as a photosensitizer to extend the light harvesting region.

Results and Discussion

Field emission scanning electron microscopy (FESEM) and transmission electron microscopy (TEM)

Figure 1a shows a field emission scanning electron microscopy (FESEM) image of a lamellar structure of pure g-C_3N_4 with nonuniform, porous folding structures. The surface of the CD/g-C_3N_4 composites were conglomerate and resembled each other in various ways after incorporating different concentration of CDs as shown in Figure 1b–d. The wrinkled structure of g-C_3N_4 provides a great support to attach with CDs. After incorporating the CDs, the CD/g-C_3N_4 composites exhibited a more packed and agglomerated morphological nanostructure compared to that of pure g-C_3N_4. A similar observation was reported in our previous research [28], showing that the clustered effect was attributed to the self-assembly process during the hydrothermal treatment [43]. However, a more porous structure

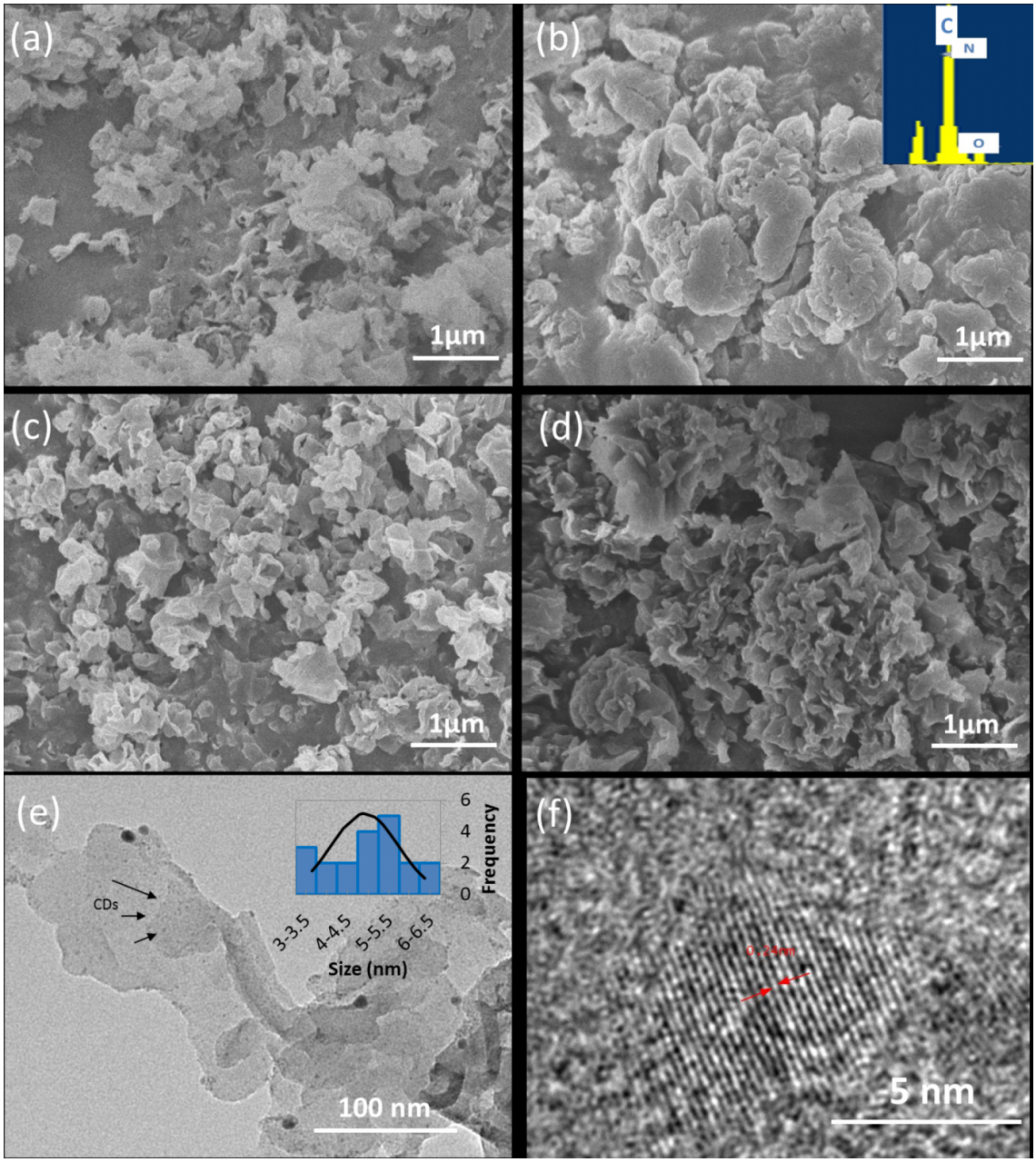

Figure 1: Field emission scanning electron microscopy (FESEM) images of (a) g-C_3N_4, (b) CD/g-C_3N_4(0.1), (c) CD/g-C_3N_4(0.2), and (d) CD/g-C_3N_4(0.5) composites. (e) TEM image and (f) HRTEM image of CD/g-C_3N_4(0.5). The insets of (b) and (e) show the energy-dispersive X-ray spectroscopy (EDS) results and particle size distribution of CDs, respectively.

in the CD/g-C_3N_4(0.5) composite was observed as compared to that of CD/g-C_3N_4(0.1), signifying that the increasing concentration of CDs could reduce the agglomeration effect in the composites. The detection of elemental C and N (inset of Figure 1b) using energy-dispersive X-ray spectroscopy (EDS) was attributed to the presence of pristine g-C_3N_4 and CDs [44]. A small peak of elemental O inevitably appeared due to reaction under ambient conditions. Figure 1e and Figure S2 (Supporting Information File 1) show a TEM image of CD/g-C_3N_4(0.5) and g-C_3N_4, respectively. The observation of CDs (small dark spots) shows that the CDs were well distributed onto the smooth, thin-layered g-C_3N_4 nanosheets. The inset of Figure 1e indicates that the particle size of the CDs falls in the range of 3−6.5 nm. The lattice fringes of the CDs were found to be about 0.24 nm (Figure 1f), which correlated with the (100) in-plane lattice spacing of graphene [45].

X-ray diffraction (XRD) and Fourier-transform infrared spectroscopy (FTIR)

Figure 2a shows the XRD patterns of all CD/g-C_3N_4 composites. A major diffraction peak was found around 27°, representing the graphitic aromatic C–N units. The diffraction angle peak shifted from 27.5° to 27.8° after incorporating 0.2 and 0.5 wt % of CDs into the g-C_3N_4, indicating that the CDs were successfully intercalated into the host matrix and the defects were introduced in the g-C_3N_4 [46]. A low concentration of CDs at 0.1 wt % did not exert significant changes in the host structure. The strong peak at 27.6° was ascribed to the stacking of aromatic units with crystal face (002) with interplanar distance of 0.328 nm [47]. A minor peak at 12.8° was correlated to condensed tri-*s*-triazine units in the sheets (001) with an interplanar distance of 0.665 nm [48]. No extra peaks were detected in the CD/g-C_3N_4 composites due to the insignificant content of CDs [49,50]. In Figure 2b, the peaks at 3150 and 3155 cm^{-1} are attributed to the amide N–H stretch and carboxylic acid O–H stretch, respectively. The presence of N–H stretching vibration modes is due to some uncondensed amine functional groups in the carbon nitride layer [51]. The band in the range of 1230–1650 cm^{-1} corresponded to the stretching of sp^3 C–N and sp^2 C=N in CN heterocycles that exists within the g-C_3N_4 compound [52]. The sharp peak at 811 cm^{-1} corresponded to the alkyne C–H bond (trisubstituted) or the breathing mode of the heptazine arrangement [44]. The alkene C=C bond (conjugated) at 1639 cm^{-1} was due to the connection between heptazine-based g-C_3N_4 [53]. As shown in Figure S1 (Supporting Information File 1), the CDs show the obvious absorption peaks at 2925 cm^{-1}, 1608 cm^{-1} and 670 cm^{-1} which are correlated to the stretching vibrations of C–H, stretching vibrations of C=O, and bending vibration of =C–H, respectively. The three obvious absorption peaks at 2368 cm^{-1}, 1409 cm^{-1} and 1095 cm^{-1} are associated with the stretching and bending vibrations of C≡N, C=C and C−O−C, respectively. This result is consistent with previous reports [54,55]. Similar absorption bands were observed for all CD/g-C_3N_4 composites because the strong peaks from g-C_3N_4 covered the weak absorptions of CDs due to the low CD content.

Optical properties

Figure 3a shows the UV–vis absorption spectra of CDs in an aqueous solution in the range from 200 nm to 750 nm. The obvious peak at about 330 nm could be ascribed to the n–π* transition of C=O bond [56]. The inset of Figure 3a shows that the CD solution emitted a strong blue-green fluorescence under excitation at 365 nm with a UV lamp. The CD solution was tested with different excitation wavelengths to evaluate the ideal excitation spectrum that initiates the photoluminescence (PL)

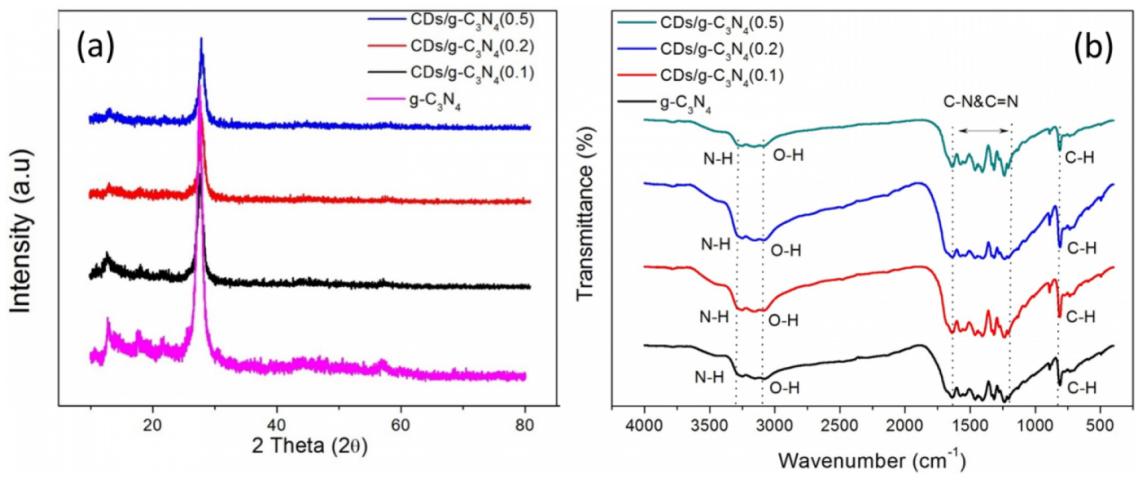

Figure 2: (a) XRD patterns and (b) FTIR spectra of g-C_3N_4, CD/g-C_3N_4(0.1), CD/g-C_3N_4(0.2), and CD/g-C_3N_4(0.5).

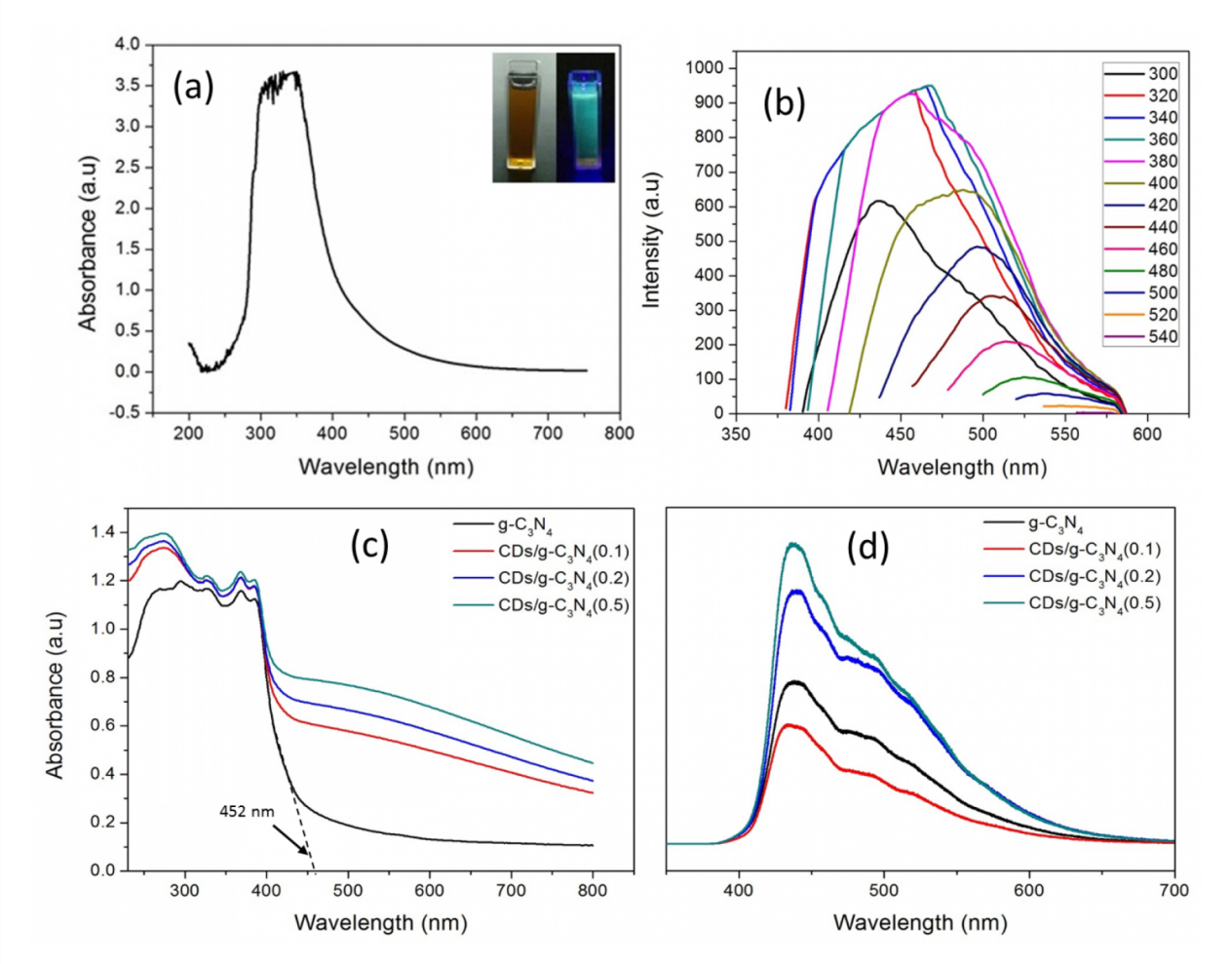

Figure 3: (a) The absorption spectrum of carbon dots (CDs) solution. The inset shows the fluorescence of the CDs under daylight (left) and UV light irradiation at 365 nm (right). (b) The photoluminescence (PL) emission spectrum of CDs at different excitation wavelengths, (c) UV–vis diffuse reflection spectra (DRS) spectra, and (d) PL spectra of the composites.

properties. Figure 3b displays wide, broad PL emission peak across the UV to visible spectrum ranging from 380 to 580 nm. It was found that the optimal excitation and emission wavelengths are ≈320−380 nm and ≈460 nm, respectively. The emission spectrum of the CD solution was red-shifted to longer wavelengths with decreasing intensity when the excitation wavelength increased, which is consistent with previous reports [4,56]. Although the origin of the PL luminescence in CDs is not fully elucidated, the excitation-dependent PL behavior of CDs is usually correlated to the size distribution of CDs, the recombination of photogenerated charges at surface-confined defect states and the different distributions of emissive trap sites [57-59]. The UCPL of CDs only occurs when multiphotons are activated simultaneously, emitting emission wavelengths shorter than the excitation wavelength [60]. In Figure 3b, no emission peak was detected when the excitation wavelength was above 540 nm, which is consistent with previous reports [61]. A recent study by Wen and co-workers suggested that most of the CDs and graphene quantum dots (GQDs) do not have detectable upconversion fluorescence. The frequently cited UCPL properties could originate from the normal fluorescence excited by the leaking component from the second diffraction in the monochromater of the fluorescence spectrophotometer [62].

As shown in Figure 3c, the pure g-C_3N_4 showed expected absorption peaks at 265 nm and 340 nm due to the π–π* or n–π* electronic transitions in the conjugated aromatic s-heptazine ring system of g-C_3N_4 [63]. The onset of the absorption spectra of pure g-C_3N_4 started from 452 nm, showing a band gap of 2.75 eV, which is almost the same as that previously reported [28,46,64]. It is obvious that all CD/g-C_3N_4 composites displayed a broad light absorption in the whole solar spectrum ranging from 200 to 800 nm due to the quantum confinement effect induced by the CDs [65]. This result suggests that CD/g-C_3N_4 composites possess greater potential than that of pure g-C_3N_4 to drive photocatalysis under the irradiation of the en-

tire solar spectrum. In contrary to our earlier work that reported blue-shifted absorption spectra after titanium dioxide (TiO_2) loading [28] and acid treatment [29], the incorporation of CDs into g-C_3N_4 consistently red-shifted the absorption spectra towards the visible and NIR region. However, the photocatalytic performance of the composites is possibly limited under NIR light irradiation because the UCPL properties of CDs (which could overcome the low energy of NIR-light photons to initiate the excitation of electrons) are not detected in Figure 3b. The PL spectra in Figure 3d were evaluated to determine the charge separation efficiency of all composites. The recombination of electron–hole pairs produces emission of photons resulting in photoluminescence. The weaker PL intensity corresponded to a lower recombination rate of excited electron [66]. Among the composites, CD/g-C_3N_4(0.1) (with a lower CD coverage) exhibited the lowest PL intensity, indicating that the minimum coverage of CDs could suppress the recombination of photogenerated carriers in g-C_3N_4. As the CD coverage increased, trap states were created at the CD/g-C_3N_4 interface, thus increasing the trapping events and decelerating the electron transport [67-69]. A similar observation was reported previously and it was concluded that CDs are favorable for the separation of charge carriers, but the increasing concentration of CDs could lead to inefficiency of charge separation [46].

X-ray photoelectron spectroscopy (XPS) analysis

The XPS spectra in Figure 4a–c reveal the surface composition and chemical state of CD/g-C_3N_4(0.5). From the C 1s spectrum of CD/g-C_3N_4(0.5) in Figure 4a, the signals at 284.4 eV and 288.7 eV are found to correspond to graphitic carbon (C–C) and sp^2 carbon (N–C=N) [70]. Compared with the C 1s spectrum of pure g-C_3N_4, three new signals were detected at 284.8 eV (sp^2 C–C), 285.4 eV (C–N) and 288.8 eV (N–C=N) after the incorporation of CDs, revealing the abundant carbonyl and carboxyl groups on the CDs as a result of the significant interaction between g-C_3N_4 and CDs [71-74]. The N 1s spectrum was deconvoluted into three peaks at 398.8 eV, 399.8 eV and 401.1 eV. The strong peak at 398.8 eV corresponds to sp^2 hybridized aromatic N in the triazine units (C=N–C) while the signals at

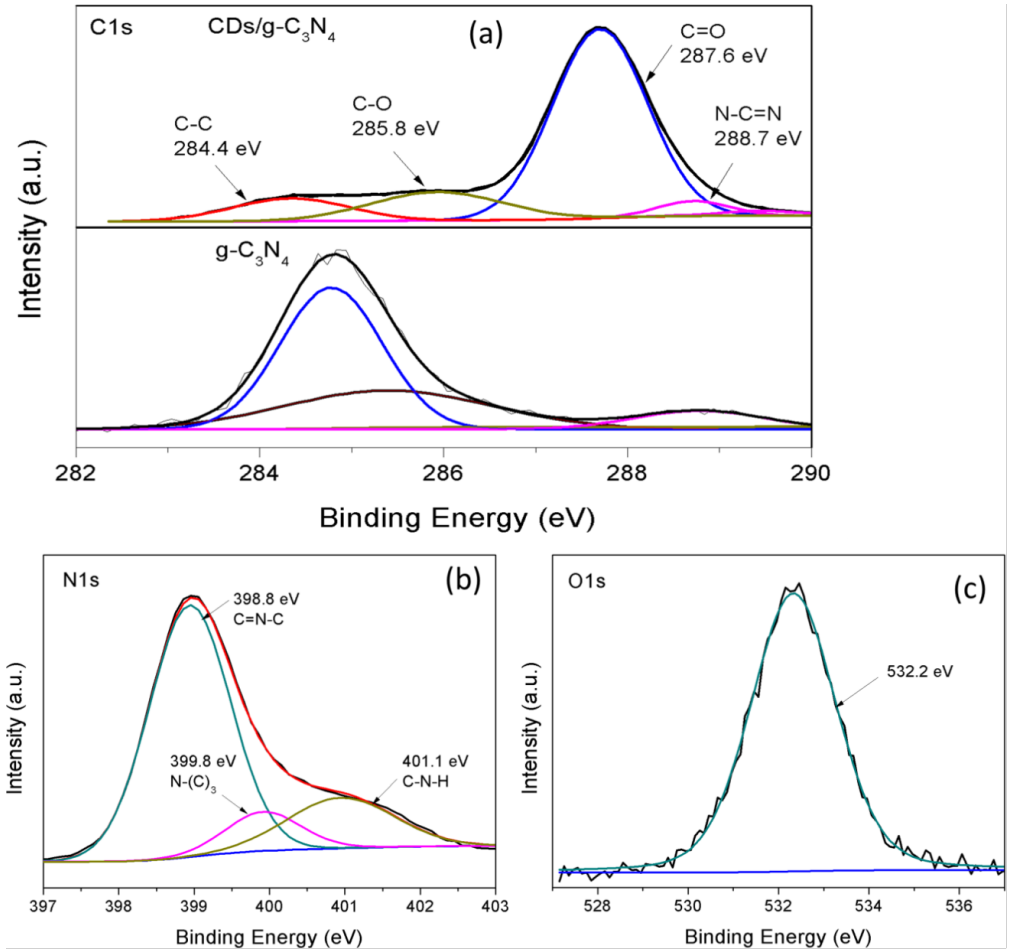

Figure 4: X-rat photoelectron spectroscopy (XPS) of (a) C 1s (b) N 1s, (c) O 1s for CD/g-C_3N_4(0.5), and (d) C 1s for g-C_3N_4.

399.8 eV and 401.1 eV are attributed to tertiary (N– $(C)_3$) groups and amino functional groups (C–N–H) [75]. The sole O 1s binding energy at 532.2 eV is due to absorbed water [37].

Photocatalytic performance under solar irradiation

The photocatalytic performance of the composites was evaluated using BPA as a model pollutant under natural sunlight irradiation. Figure 5a shows that the blank was stable with almost no degradation throughout the experiment, indicating BPA had poor photolysis properties. The CD/g-C_3N_4(0.5) exhibited the best photocatalytic degradation rate with 100% removal of BPA after 90 min of reaction. Pure g-C_3N_4 achieved relatively good degradation efficiency (68.2%) attributed to its visible light absorption capability (Table S1, Supporting Information File 1). A great difference in the degradation rate was observed between CD/g-C_3N_4(0.1) and CD/g-C_3N_4(0.2) in which the degradation efficiency increased to ≈20% with the addition of 0.1 wt % of CDs. Both CD/g-C_3N_4(0.1) and g-C_3N_4 were unable to fully eliminate BPA within the 2 h of reaction time. These results correlated well with the UV DRS results (Figure 3c), in which the increasing concentration of CDs resulted in stronger photosensitizing effect in the composite, thus leading to a broader absorption band in the visible and NIR light region compared to that of pure g-C_3N_4. This indicates that the electrons can be easily excited in each of the CDs and g-C_3N_4 to produce more electron–hole pairs for the reaction of pollutants. The recombination rate of electron–hole pairs was another factor affecting the degradation rate. As shown in the PL analysis (Figure 3d), the separation efficiency of electron–hole pairs will be suppressed if the concentration of CDs is too high. However, the photocatalytic performance did not correlate well with the PL analysis. The remarkable performance of CD/g-C_3N_4(0.5) proved that the intense photosensitizing effect of CDs at higher dosage could overcome the poorer separation efficiency of charge carriers, leading to the enhancement of photocatalytic activity. As a result, the photocatalytic performance followed the sequence of CD/g-C_3N_4(0.5) > CD/g-C_3N_4(0.2) > CD/g-C_3N_4(0.1) > g-C_3N_4 > blank.

A radical scavenging experiment (Figure 5b) was carried out to identify the main radicals involved in the photoreaction. The influence order of the active radical species on the degradation of BPA was $O_2^{\bullet-}$ > h^+ > hydroxyl radical ($^\bullet$OH) > e^-. It is obvious that $O_2^{\bullet-}$ was the main radical species generated since the photodegradation of BPA was significantly inhibited after the addition of benzoquinone (BQ). The addition of ethylenediaminetetraacetic acid disodium salt dihydrate (EDTA-2Na^+) in BPA solution slightly suppressed the degradation rate, showing that h^+ was also one of the active radicals involved in the photoreaction. In contrast, neither $^\bullet$OH nor e^- are the main reactive species because the addition of dimethylsulfoxide (DMSO) and isopropyl alchohol (IPA) did not exert a significant effect on the degradation rate of BPA. Based on the above results, a degradation mechanism is proposed in Figure 6.

The edge potential of the conduction band (CB) and the valence band (VB) of a semiconductor at the point of zero charge was estimated using the following equations:

$$E_{VB} = X - E_c + 0.5E_g \quad (1)$$

$$E_{CB} = E_{VB} - E_g, \quad (2)$$

where E_{VB} and E_{CB} are the VB and CB edge potential respectively, X is the electronegativity of the semiconductor; E_c is the energy of free electrons on the hydrogen scale (≈4.5 eV vs

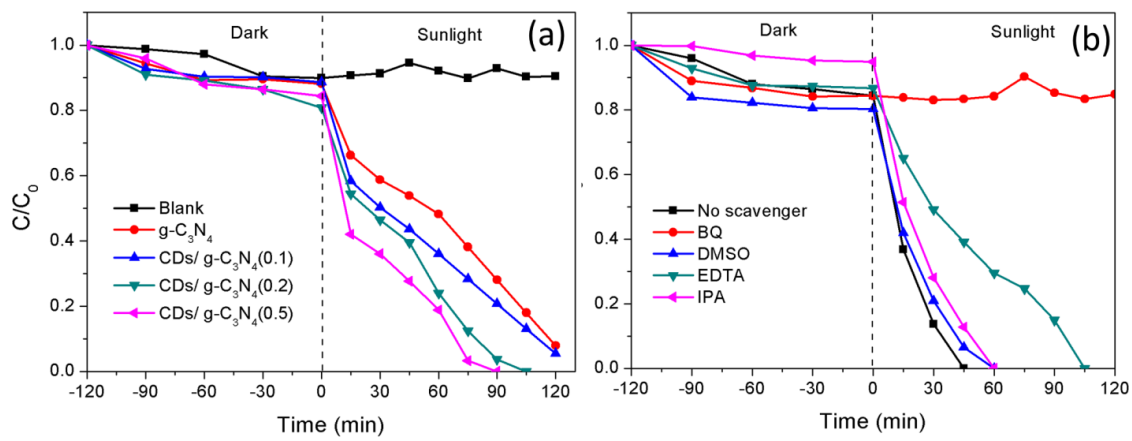

Figure 5: (a) Photocatalytic degradation of bisphenol A (BPA) as a function time under irradiation of natural sunlight, and (b) the effect of different scavengers for CD/g-C_3N_4(0.5) on BPA removal.

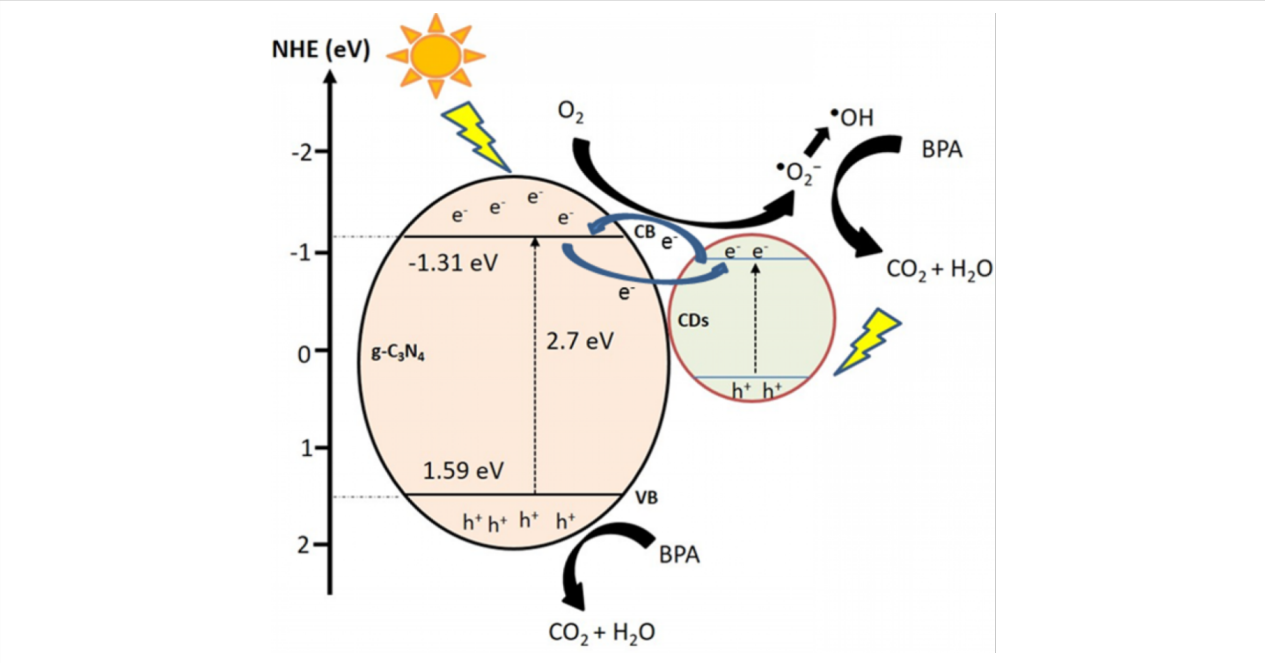

Figure 6: Electron transfer mechanism of CD/g-C_3N_4.

NHE) and E_g is the band gap energy of the semiconductor. The X value of g-C_3N_4 is 4.64 eV [75] while the band gap energy of g-C_3N_4 is 2.75 eV. The VB and CB of g-C_3N_4 were theoretically calculated at 1.52 eV and −1.23 eV, respectively. In g-C_3N_4, the electrons were easily excited from the VB to the CB because of its narrow band gap energy. The trapped h^+ in the VB directly oxidized BPA but cannot react with water (H_2O) and hydroxide (OH^-) to generate $^{\bullet}OH$ because the VB of g-C_3N_4 (+1.52 eV vs NHE) was more negative than the redox potential of $OH^-/^{\bullet}OH$ (+2.4 eV) [76]. With a lower amount of CDs, the CDs facilitated efficient electron transfer from the CB of g-C_3N_4 to adsorbed oxygen (O_2), generating $O_2^{\bullet}$. Meanwhile, $O_2^{\bullet-}$ radicals also reacted with the hydrogen (H^+) ion to further produce a minor portion of $^{\bullet}OH$ radicals. Thus, the $O_2^{\bullet-}$ and $^{\bullet}OH$ could oxidize the BPA simultaneously to enhance the photocatalytic performance. Although the CDs did not display UCPL properties, the π-conjugated CDs served as a photosensitizer (like organic dyes) to sensitize g-C_3N_4 and injected electrons to the CB of g-C_3N_4 [37,38,73], resulting in an extended absorption spectrum from the visible to the NIR region. This results in the generation of more electrons for the enhancement of BPA degradation. It is notable that the photosensitizing effect of CDs serves as a dominant factor for enhancing the photocatalytic activity of CD/g-C_3N_4 composites since the degradation rate of BPA is well consistent with the UV DRS results. Unlike CDs, TiO_2 in combination with g-C_3N_4 for the photocatalytic process [28] was able to trap electrons efficiently due to the favorable band edge potential; however, the material could not absorb visible light. As shown in Table S2 (Supporting Information File 1), CD/g-C_3N_4 composites demonstrated the best degradation efficiency of BPA than that of other composites reported earlier in our previous works [28,29].

Conclusion

The CD/g-C_3N_4 composite photocatalyst was successfully synthesized using hydrothermal treatment. With an increase in the concentration of CDs, the UV–vis DRS results showed a broader and stronger visible and NIR light absorption band while the lattice distortion of g-C_3N_4 was observed in XRD analysis. The minimal coverage of CDs (<0.5 wt %) mediated the electron transfer from the CB of g-C_3N_4 to adsorbed O_2 to produce $O_2^{\bullet-}$. It is evidenced by the scavenger test that both $O_2^{\bullet-}$ and h^+ were the major active species involved in the redox process. The excessive loading of CDs could act as recombination centers to increase the recombination rate of electron–hole pairs, but this did not reduce the photocatalytic performance of CD/g-C_3N_4(0.5). In fact, the degradation rate of BPA in all CD/g-C_3N_4 composites increased with the increasing concentration of CDs, which correlated well with UV–vis DRS results. The higher coverage of CDs exerted a stronger photosensitizing effect in CD/g-C_3N_4(0.5) to overcome its inefficient charge carrier separation, improving the BPA removal efficiency by 3.87-fold as compared to g-C_3N_4. The preparation of CD/g-C_3N_4 is considered cost-effective and environmentally friendly because sugarcane juice was used as a “green” precursor instead of harmful chemicals. The photocatalytic reaction occurred under natural sunlight irradiation, which is renewable and sustainable.

Experimental

Materials and reagents

All the chemical reagents used were of analytical grade and purity. Sugarcane juice was obtained from a night market where the deposit was filtered out. The dichloromethane (≥99.8%), BPA (>99%) and BQ (>98%) were purchased from Sigma-Aldrich. The ethanol (95%) and urea (>99.5%) were purchased from R&M Chemicals. Distilled water was used throughout the experiment for dilution and washing purpose. In addition, IPA (83.5%) and DMSO (99%) was purchased from Bendosen and Univar, respectively. The EDTA-2Na$^+$ (99%) was obtained from ChemSoln.

Preparation of carbon nitride (g-C_3N_4) and carbon dot solutions

Urea was chosen as a starting material to produce g-C_3N_4. It was placed into an alumina crucible with a cover to avoid over-reaction with oxygen. The urea was heated at 550 °C for 3 h to obtain yellowish g-C_3N_4. The synthesis of CDs was similar to the method reported by Sahu and co-workers [6]. To prepare the CD solution, 40 mL of sugarcane juice was mixed with 30 mL ethanol and stirred for 10 min to ensure homogeneity. The mixture was then transferred to a 80 mL teflon-lined stainless-steel autoclave and closed up tightly. It was dried in oven at 120 °C for 8 h with a heating rate of 1 °C/min. A dark brown solution was obtained and it was washed with dichloromethane to remove unreacted organics moieties. The aqueous solution was centrifuged at 3000 rpm for 15 min to separate out the residue and less fluorescent deposit. Two layers of solution formed where the top layer was extracted into a beaker. The acetone solution was added excessively into the solution and centrifuged at 10,000 rpm for 15 min to remove the remaining deposit. A clear yellowish-brown solution was obtained.

Preparation of CD/g-C_3N_4 composites

0.2 g of g-C_3N_4 was mixed with the previously prepared CD solution and then stirred for 24 h using a hot plate magnetic stirrer under room temperature. After the solution mixed homogeneously, it was placed into teflon-lined stainless-steel autoclave and heated at 100 °C for 2 h. It was then centrifuged to remove excessive CDs. The samples were then dried overnight. The synthesis route is illustrated in Figure S3 (Supporting Information File 1). Same preparation steps were repeated to synthesize the composites with 0.1, 0.2 and 0.5 wt % of CDs. The samples obtained were denoted as CD/g-C_3N_4(0.1), CD/g-C_3N_4(0.2) and CD/g-C_3N_4(0.5), respectively.

Characterization of CD/g-C_3N_4 composites

FTIR spectra (Perkin Elmer Spectrum 400 spectrophotometer) were conducted in the range of 400–4000 cm^{-1} with the samples dispersed in KBr. The XRD analyses were performed using the powder XRD (PANalytical-Empyrean) with Cu Kα radiation at a scanning speed of 0.02 s^{-1}. A micro-PL spectroscope (Renishaw, inVia Raman Microscope) was used to acquire the PL spectra with an excitation wavelength of 325 nm. UV–vis DRS was obtained using a Shimadzu UV-2600 spectrophotometer equipped with an integrating sphere attachment with barium sulfate ($BaSO_4$) as a reference. The surface chemical composition of samples was analyzed by XPS (PHI Quantera II, Ulvac-PHI, Inc.) with an Al Kα radiation source. High resolution transmission electron microscope (HRTEM, FEI-TECNAI F20) images were obtained at 200 kV. PL spectra of CDs solution were acquired with a PL spectrophotometer (Perkin Elmer LS 55) with different excitation wavelengths ranging from 300 to 540 nm.

Photocatalytic degradation of BPA

The photocatalytic performance of CD/g-C_3N_4 composites was investigated using BPA under natural sunlight irradiation. All photocatalytic experiments were carried out under sunlight radiation for a duration of 2 h. The initial concentration of BPA was 5 mg/L prepared in a 500 mL beaker with 250 mL solution. Each experiment was carried out for 2 h where a sample was collected at 15 min intervals. Each beaker was stirred well with 0.1 g of photocatalyst. Prior to the photocatalytic degradation, the solutions were magnetically stirred in the dark for 2 h to establish an adsorption–desorption equilibrium. The residual concentration of BPA was analyzed with a high performance liquid chromatography (HPLC, Flexar, Perkin Elmer) equipped with a UV detector (217 nm). An RS pak DE-413L (250 mm × 4.6 mm i.d., Showa Denko Co.) separation column was used. The mobile phase was 40% acetonitrile (ACN), 60% water and the flow rate was 0.7 mL min^{-1}. The experiment was carried out under clear sky conditions at the University Tunku Abdul Rahman, Kampar (latitude 101.1398 °E and longitude 4.3394 °N) between 11:00 a.m. and 1:00 p.m. in May 2017. The solar light intensity was measured using a LT Lutron LX-101 lux meter of 1000 × 100 and the average light intensity over the duration of the clear sky weather conditions was found to be 89,200 lux. Table S3 (Supporting Information File 1) showed the recorded light intensity during the photocatalytic experiment.

Scavenging experiment

CD/g-C_3N_4(0.5) was used as a photocatalyst in the scavenging experiment because of its superior photocatalytic performance among the samples. The scavenger test was used to identify the mechanism of photocatalyst to investigate the involved free radicals. Scavengers like BQ, DMSO, EDTA-2Na$^+$ and IPA were used to conduct this test. BQ was used to trap $O_2^{\bullet-}$ while DMSO functioned as the photoinduced e$^-$ catcher. EDTA-2Na$^+$ caught the h$^+$ left by the excited electron. IPA worked to trap

$^{\bullet}OH$ that was produced by the CD/g-C_3N_4 composites [77]. The scavenging test was carried out for 2 h under the solar radiation and the sample was collected for HPLC analysis.

Supporting Information

Supporting Information File 1

Additional experimental data.
[https://www.beilstein-journals.org/bjnano/content/supplementary/2190-4286-9-35-S1.pdf]

Acknowledgements

This research work was supported by Universiti Tunku Abdul Rahman Research Fund, UTARRF (IPSR/RMC/UTARRF/2017-C1/S04) and (IPSR/RMC/UTARRF/2016-C2-L05).

ORCID® iDs

Lan Ching Sim - https://orcid.org/0000-0003-4002-6726
Pichiah Saravanan - https://orcid.org/0000-0001-8302-9586

References

1. Tian, L.; Ghosh, D.; Chen, W.; Pradhan, S.; Chang, X.; Chen, S. *Chem. Mater.* **2009,** *21,* 2803–2809. doi:10.1021/cm900709w
2. Wang, F.; Chen, Y.-h.; Liu, C.-y.; Ma, D.-g. *Chem. Commun.* **2011,** *47,* 3502–3504. doi:10.1039/C0CC05391K
3. Wang, J.; Ng, Y. H.; Lim, Y.-F.; Ho, G. W. *RSC Adv.* **2014,** *4,* 44117–44123. doi:10.1039/C4RA07290A
4. Martindale, B. C. M.; Hutton, G. A. M.; Caputo, C. A.; Reisner, E. *J. Am. Chem. Soc.* **2015,** *137,* 6018–6025. doi:10.1021/jacs.5b01650
5. Ming, H.; Ma, Z.; Liu, Y.; Pan, K.; Yu, H.; Wang, F.; Kang, Z. *Dalton Trans.* **2012,** *41,* 9526–9531. doi:10.1039/C2DT30985H
6. Sahu, S.; Behera, B.; Maiti, T. K.; Mohapatra, S. *Chem. Commun.* **2012,** *48,* 8835–8837. doi:10.1039/C2CC33796G
7. Zhu, C.; Zhai, J.; Dong, S. *Chem. Commun.* **2012,** *48,* 9367–9369. doi:10.1039/C2CC33844K
8. Prasannan, A.; Imae, T. *Ind. Eng. Chem. Res.* **2013,** *52,* 15673–15678. doi:10.1021/ie402421s
9. Zhou, J.; Sheng, Z.; Han, H.; Zou, M.; Li, C. *Mater. Lett.* **2012,** *66,* 222–224. doi:10.1016/j.matlet.2011.08.081
10. Liu, S.-S.; Wang, C.-F.; Li, C.-X.; Wang, J.; Mao, L.-H.; Chen, S. *J. Mater. Chem. C* **2014,** *2,* 6477–6483. doi:10.1039/C4TC00636D
11. D'Angelis do E. S. Barbara, C.; Corrêa, J. R.; Medeiros, G. A.; Barreto, G.; Magalhães, K. G.; de Oliveira, A. L.; Spencer, J.; Rodrigues, M. O.; Neto, B. A. D. *Chem. – Eur. J.* **2015,** *21,* 5055–5060. doi:10.1002/chem.201406330
12. Rodrigues, C. V.; Correa, J. R.; Aiube, C. M.; Andrade, L. P.; Galvão, P. M.; Costa, P. A.; Campos, A. L.; Pereira, A. J.; Ghesti, G. F.; Felix, J. F.; Weber, I. T. *J. Braz. Chem. Soc.* **2015,** *26,* 2623–2628. doi:10.5935/0103-5053.20150291
13. Guo, Y.; Zhang, L.; Cao, F.; Leng, Y. *Sci. Rep.* **2016,** *6,* 35795. doi:10.1038/srep35795
14. Briscoe, J.; Marinovic, A.; Sevilla, M.; Dunn, S.; Titirici, M. *Angew. Chem., Int. Ed.* **2015,** *54,* 4463–4468. doi:10.1002/anie.201409290
15. Ong, W.-J.; Tan, L.-L.; Ng, Y. H.; Yong, S.-T.; Chai, S.-P. *Chem. Rev.* **2016,** *116,* 7159–7329. doi:10.1021/acs.chemrev.6b00075
16. Qin, J.; Wang, S.; Ren, H.; Hou, Y.; Wang, X. *Appl. Catal., B* **2015,** *179,* 1–8. doi:10.1016/j.apcatb.2015.05.005
17. Ong, W.-J.; Putri, L. K.; Tan, Y.-C.; Tan, L.-L.; Li, N.; Ng, Y. H.; Wen, X.; Chai, S.-P. *Nano Res.* **2017,** *10,* 1673–1696. doi:10.1007/s12274-016-1391-4
18. Wang, S.; Lin, J.; Wang, X. *Phys. Chem. Chem. Phys.* **2014,** *16,* 14656–14660. doi:10.1039/C4CP02173H
19. Wang, S.; Wang, X. *Small* **2015,** *11,* 3097–3112. doi:10.1002/smll.201500084
20. Kuriki, R.; Yamamoto, M.; Higuchi, K.; Yamamoto, Y.; Akatsuka, M.; Lu, D.; Yagi, S.; Yoshida, T.; Ishitani, O.; Maeda, K. *Angew. Chem., Int. Ed.* **2017,** *56,* 4867–4871. doi:10.1002/anie.201701627
21. Wen, J.; Li, X.; Li, H.; Ma, S.; He, K.; Xu, Y.; Fang, Y.; Liu, W.; Gao, Q. *Appl. Surf. Sci.* **2015,** *358,* 204–212. doi:10.1016/j.apsusc.2015.08.244
22. Yu, H.; Xiao, P.; Wang, P.; Yu, J. *Appl. Catal., B* **2016,** *193,* 217–225. doi:10.1016/j.apcatb.2016.04.028
23. Zeng, D.; Xu, W.; Ong, W.-J.; Xu, J.; Ren, H.; Chen, Y.; Zheng, H.; Peng, D.-L. *Appl. Catal., B* **2018,** *221,* 47–55. doi:10.1016/j.apcatb.2017.08.041
24. Zeng, D.; Ong, W.-J.; Zheng, H.; Wu, M.; Chen, Y.; Peng, D.-L.; Han, M.-Y. *J. Mater. Chem. A* **2017,** *5,* 16171–16178. doi:10.1039/C7TA04816E
25. Wu, K.-H.; Huang, Y.-J.; Teng, H. *Part. Part. Syst. Charact.* **2017,** in press. doi:10.1002/ppsc.201700221
26. Li, Y.; Ho, W.; Lv, K.; Zhu, B.; Lee, S. C. *Appl. Surf. Sci.* **2018,** *430,* 380–389. doi:10.1016/j.apsusc.2017.06.054
27. Li, Y.; Lv, K.; Ho, W.; Zhao, Z.; Huang, Y. *Chin. J. Catal.* **2017,** *38,* 321–329. doi:10.1016/S1872-2067(16)62573-1
28. Sim, L. C.; Tan, W. H.; Leong, K. H.; Bashir, M. J. K.; Saravanan, P.; Surib, N. A. *Materials* **2017,** *10,* 28. doi:10.3390/ma10010028
29. Leong, K. H.; Lim, P. F.; Sim, L. C.; Punia, V.; Pichiah, S. *Appl. Surf. Sci.* **2018,** *430,* 355–361. doi:10.1016/j.apsusc.2017.06.169
30. Fang, S.; Lv, K.; Li, Q.; Ye, H.; Du, D.; Li, M. *Appl. Surf. Sci.* **2015,** *358,* 336–342. doi:10.1016/j.apsusc.2015.07.179
31. Liu, X.; Pang, F.; He, M.; Ge, J. *Nano Res.* **2017,** *10,* 3638–3647. doi:10.1007/s12274-017-1574-7
32. Zhou, M.; Hou, Z.; Chen, X. *Part. Part. Syst. Charact.* **2017,** in press. doi:10.1002/ppsc.201700038
33. Cao, S.; Yu, J. *J. Photochem. Photobiol., C: Photochem. Rev.* **2016,** *27,* 72–99. doi:10.1016/j.jphotochemrev.2016.04.002
34. Wen, J.; Xie, J.; Chen, X.; Li, X. *Appl. Surf. Sci.* **2017,** *391,* 72–123. doi:10.1016/j.apsusc.2016.07.030
35. Guo, F.; Shi, W.; Guan, W.; Huang, H.; Liu, Y. *Sep. Purif. Technol.* **2017,** *173,* 295–303. doi:10.1016/j.seppur.2016.09.040
36. Wang, X.; Cheng, J.; Yu, H.; Yu, J. *Dalton Trans.* **2017,** *46,* 6417–6424. doi:10.1039/C7DT00773F
37. Li, K.; Su, F.-Y.; Zhang, W.-D. *Appl. Surf. Sci.* **2016,** *375,* 110–117. doi:10.1016/j.apsusc.2016.03.025
38. Liu, Q.; Chen, T.; Guo, Y.; Zhang, Z.; Fang, X. *Appl. Catal., B* **2016,** *193,* 248–258. doi:10.1016/j.apcatb.2016.04.034
39. Wang, F.; Chen, P.; Feng, Y.; Xie, Z.; Liu, Y.; Su, Y.; Zhang, Q.; Wang, Y.; Yao, K.; Lv, W.; Liu, G. *Appl. Catal., B* **2017,** *207,* 103–113. doi:10.1016/j.apcatb.2017.02.024
40. Wang, F.; Wang, Y.; Feng, Y.; Zeng, Y.; Xie, Z.; Zhang, Q.; Su, Y.; Chen, P.; Liu, Y.; Yao, K.; Lv, W.; Liu, G. *Appl. Catal., B* **2018,** *221,* 510–520. doi:10.1016/j.apcatb.2017.09.055

41. Kumar, S.; Kumar, A.; Bahuguna, A.; Sharma, V.; Krishnan, V. *Beilstein J. Nanotechnol.* **2017,** *8,* 1571–1600. doi:10.3762/bjnano.8.159
42. Ong, W.-J. *Front. Mater.* **2017,** *4,* 11. doi:10.3389/fmats.2017.00011
43. Gao, J.; Zhou, Y.; Li, Z.; Yan, S.; Wang, N.; Zou, Z. *Nanoscale* **2012,** *4,* 3687–3692. doi:10.1039/C2NR30777D
44. Amiri, M.; Salehniya, H.; Habibi-Yangjeh, A. *Ind. Eng. Chem. Res.* **2016,** *55,* 8114–8122. doi:10.1021/acs.iecr.6b01699
45. Tang, L.; Ji, R.; Cao, X.; Lin, J.; Jiang, H.; Li, X.; Teng, K. S.; Luk, C. M.; Zeng, S.; Hao, J.; Lau, S. P. *ACS Nano* **2012,** *6,* 5102–5110. doi:10.1021/nn300760g
46. Fang, S.; Xia, Y.; Lv, K.; Li, Q.; Sun, J.; Li, M. *Appl. Catal., B: Environ.* **2016,** *185,* 225–232. doi:10.1016/j.apcatb.2015.12.025
47. Su, X.; Vinu, A.; Aldeyab, S. S.; Zhong, L. *Catal. Lett.* **2015,** *145,* 1388–1395. doi:10.1007/s10562-015-1537-0
48. Aleksandrzak, M.; Kukulka, W.; Kijowska, E. *Appl. Surf. Sci.* **2017,** *398,* 56–62. doi:10.1016/j.apsusc.2016.12.023
49. Bozetine, H.; Wang, Q.; Barras, A.; Li, M.; Hadjersi, T.; Szunerits, S.; Boukherroub, R. *J. Colloid Interface Sci.* **2016,** *465,* 286–294. doi:10.1016/j.jcis.2015.12.001
50. Rodenas, P.; Song, T.; Sudhagar, P.; Marzari, G.; Han, H.; Badia-Bou, L.; Gimenez, S.; Fabregat-Santiago, F.; Mora-Sero, I.; Bisquert, J.; Paik, U.; Kang, Y. S. *Adv. Energy Mater.* **2013,** *3,* 176–182. doi:10.1002/aenm.201200255
51. Samanta, S.; Martha, S.; Parida, K. *ChemCatChem* **2014,** *6,* 1453–1462. doi:10.1002/cctc.201300949
52. Ge, L.; Zuo, F.; Liu, J.; Ma, Q.; Wang, C.; Sun, D.; Bartels, L.; Feng, P. *J. Phys. Chem. C* **2012,** *116,* 13708–13714. doi:10.1021/jp3041692
53. Gracia, J.; Kroll, P. *J. Mater. Chem.* **2009,** *19,* 3013–3019. doi:10.1039/B821568E
54. Kurdekar, A.; Avinash Chunduri, L. A.; Bulagonda, E. P.; Haleyurgirisetty, M. K.; Kamisetti, V.; Hewlett, I. K. *Microfluid. Nanofluid.* **2016,** *20,* 99. doi:10.1007/s10404-016-1763-9
55. Miao, X.; Ji, Z.; Wu, J.; Shen, X.; Wang, J.; Kong, L.; Liu, M.; Song, C. *J. Colloid Interface Sci.* **2017,** *502,* 24–32. doi:10.1016/j.jcis.2017.04.087
56. Niu, W.-J.; Li, Y.; Zhu, R.-H.; Shan, D.; Fan, Y.-R.; Zhang, X.-J. *Sens. Actuators, B* **2015,** *218,* 229–236. doi:10.1016/j.snb.2015.05.006
57. Wang, X.; Cao, L.; Lu, F.; Meziani, M. J.; Li, H.; Qi, G.; Zhou, B.; Harruff, B. A.; Kermarrec, F.; Sun, Y.-P. *Chem. Commun.* **2009,** *25,* 3774–3776. doi:10.1039/b906252a
58. Cao, L.; Meziani, M. J.; Sahu, S.; Sun, Y.-P. *Acc. Chem. Res.* **2013,** *46,* 171–180. doi:10.1021/ar300128j
59. Wang, L.; Zhu, S.-J.; Wang, H.-Y.; Qu, S.-N.; Zhang, Y.-L.; Zhang, J.-H.; Chen, Q.-D.; Xu, H.-L.; Han, W.; Yang, B.; Sun, H.-B. *ACS Nano* **2014,** *8,* 2541–2547. doi:10.1021/nn500368m
60. Wang, Y.; Hu, A. *J. Mater. Chem. C* **2014,** *2,* 6921–6939. doi:10.1039/c4tc00988f
61. Li, F.; Tian, F.; Liu, C.; Wang, Z.; Du, Z.; Li, R.; Zhang, L. *RSC Adv.* **2015,** *5,* 8389–8396. doi:10.1039/C4RA14865G
62. Wen, X.; Yu, P.; Toh, Y.-R.; Ma, X.; Tang, J. *Chem. Commun.* **2014,** *50,* 4703–4706. doi:10.1039/c4cc01213e
63. Ren, G.; Zhang, Q.; Li, S.; Fu, S.; Chai, F.; Wang, C.; Qu, F. *Sens. Actuators, B* **2017,** *243,* 244–253. doi:10.1016/j.snb.2016.11.149
64. Dong, F.; Wu, L.; Sun, Y.; Fu, M.; Wu, Z.; Lee, S. C. *J. Mater. Chem.* **2011,** *21,* 15171–15174. doi:10.1039/C1JM12844B
65. Dong, F.; Wang, Z.; Sun, Y.; Ho, W.-K.; Zhang, H. *J. Colloid Interface Sci.* **2013,** *401,* 70–79. doi:10.1016/j.jcis.2013.03.034
66. Cao, S.; Low, J.; Yu, J.; Jaroniec, M. *Adv. Mater.* **2015,** *27,* 2150–2176. doi:10.1002/adma.201500033
67. Maloney, F. S.; Poudyal, U.; Chen, W.; Wang, W. *Nanomaterials* **2016,** *6,* 191. doi:10.3390/nano6110191
68. Tvrdy, K.; Frantsuzov, P. A.; Kamat, P. V. *Proc. Natl. Acad. Sci. U. S. A.* **2011,** *108,* 29–30. doi:10.1073/pnas.1011972107
69. Guijarro, N.; Shen, Q.; Giménez, S.; Mora-Seró, I.; Bisquert, J.; Lana-Villarreal, T.; Toyodo, T.; Gómez, R. *J. Phys. Chem. C* **2010,** *114,* 22352–22360. doi:10.1021/jp108499h
70. Yang, S.; Gong, Y.; Zhang, J.; Zhan, L.; Ma, L.; Fang, Z.; Vajtai, R.; Wang, X.; Ajayan, P. M. *Adv. Mater.* **2013,** *25,* 2452–2456. doi:10.1002/adma.201204453
71. Zhang, H.; Zhao, L.; Geng, F.; Guo, L.-H.; Wan, B.; Yang, Y. *Appl. Catal., B: Environ.* **2016,** *180,* 656–662. doi:10.1016/j.apcatb.2015.06.056
72. Xia, X.; Deng, N.; Cui, G.; Xie, J.; Shi, X.; Zhao, Y.; Wang, Q.; Wang, W.; Tang, B. *Chem. Commun.* **2015,** *51,* 10899–10902. doi:10.1039/C5CC02589C
73. Dadigala, R.; Bandi, R.; Gangapuram, B. R.; Guttena, V. *J. Photochem. Photobiol.* **2017,** *342,* 42–52. doi:10.1016/j.jphotochem.2017.03.032
74. Cao, J.; Qin, C.; Wang, Y.; Zhang, H.; Sun, G.; Zhang, Z. *Materials* **2017,** *10,* 604. doi:10.3390/ma10060604
75. Chen, Y.; Huang, W.; He, D.; Situ, Y.; Huang, H. *ACS Appl. Mater. Interfaces* **2014,** *6,* 14405–14414. doi:10.1021/am503674e
76. Cui, Y.; Huang, J.; Fu, X.; Wang, X. *Catal. Sci. Technol.* **2012,** *2,* 1396–1402. doi:10.1039/C2CY20036H
77. Joo, W. J.; Pradhan, D.; Min, B.-K.; Sohn, Y. *Appl. Catal., B* **2014,** *147,* 711–725. doi:10.1016/j.apcatb.2013.10.008

License and Terms

This is an Open Access article under the terms of the Creative Commons Attribution License (http://creativecommons.org/licenses/by/4.0), which permits unrestricted use, distribution, and reproduction in any medium, provided the original work is properly cited.

The license is subject to the *Beilstein Journal of Nanotechnology* terms and conditions: (https://www.beilstein-journals.org/bjnano)

The definitive version of this article is the electronic one which can be found at:
doi:10.3762/bjnano.9.35

BEILSTEIN JOURNAL OF NANOTECHNOLOGY

Photocatalytic and adsorption properties of TiO_2-pillared montmorillonite obtained by hydrothermally activated intercalation of titanium polyhydroxo complexes

Mikhail F. Butman*[1], Nikolay L. Ovchinnikov[1], Nikita S. Karasev[1], Nataliya E. Kochkina[2], Alexander V. Agafonov[2] and Alexandr V. Vinogradov[3]

Full Research Paper

Open Access

Address:
[1]Ivanovo State University of Chemistry and Technology, Sheremetevsky Av. 7, Ivanovo 153000, Russian Federation, [2]G.A. Krestov Institute of Solution Chemistry, Russian Academy of Sciences, Akademicheskaya St. 1, Ivanovo 153045, Russian Federation and [3]ITMO University, Lomonosova St. 9, St. Petersburg 197101, Russian Federation

Email:
Mikhail F. Butman* - butman@isuct.ru

* Corresponding author

Keywords:
adsorption; intercalation; mesoporosity; photocatalytic activity; pillared montmorillonite; titanium oxide

Beilstein J. Nanotechnol. **2018,** *9,* 364–378.
doi:10.3762/bjnano.9.36

Received: 29 September 2017
Accepted: 29 December 2017
Published: 31 January 2018

This article is part of the Thematic Series "Energy conversion, storage and environmental remediation using nanomaterials".

Guest Editor: W.-J. Ong

© 2018 Butman et al.; licensee Beilstein-Institut.
License and terms: see end of document.

Abstract

We report on a new approach for the synthesis of TiO_2-pillared montmorillonite, where the pillars exhibit a high degree of crystallinity (nanocrystals) representing a mixture of anatase and rutile phases. The structures exhibit improved adsorption and photocatalytic activity as a result of hydrothermally activated intercalation of titanium polyhydroxo complexes (i.e., $TiCl_4$ hydrolysis products) in a solution with a concentration close to the sol formation limit. The materials, produced at various annealing temperatures from the intercalated samples, were characterized by infrared spectroscopy, differential scanning calorimetry (DSC)/thermogravimetric analysis (TGA), X-ray diffraction, dynamic light scattering (DLS) measurements, and liquefied nitrogen adsorption/desorption. The photocatalytic activity of the TiO_2-pillared materials was studied using the degradation of anionic (methyl orange, MO) and cationic (rhodamine B, RhB) dyes in water under UV irradiation. The combined effect of adsorption and photocatalysis resulted in removal of 100% MO and 97.5% RhB (with an initial concentration of 40 mg/L and a photocatalyst-sorbent concentration of 1 g/L) in about 100 minutes. The produced TiO_2-pillared montmorillonite showed increased photocatalytic activity as compared to the commercially available photocatalyst Degussa P25.

Introduction

Titanium dioxide in its nanometer-sized form is one of the most promising modern photocatalysts [1]. However, the use of pure TiO_2 nanoparticles is hindered by some limitations such as low adsorption capacity and possibility of particle agglomeration, which reduce its photocatalytic efficiency for the processes of purifying sewage and natural water bodies from pollutants of

organic origin. To overcome these limitations, titanium dioxide nanoparticles are distributed on mineral carriers such as natural clay minerals [2], particularly montmorillonite (MM) [3]. The structure of MM is characterized by a three-layer package (2:1): two layers of silicon–oxygen tetrahedron (T) turned towards each other by their vertices, covering a layer of aluminum hydroxyl octahedra (O) on both sides. Due to isomorphous substitutions (e.g., Al^{3+} for Si^{4+} in a T layer and/or Al^{3+} for Mg^{2+} in an O layer) aluminosilicate layers are negatively charged, so positive charge compensating ions (counter ions) may move within the 2D interlayer space [4]. The weak bond between the layers results in a significant cation exchange capacity. This makes it possible to efficiently intercalate various inorganic cations into the interlayer space of MM, in particular, those possessing photocatalytic activity.

One of promising methods for modifying MM with titanium dioxide, called pillarization, consists in carrying out a reaction of exchanging the interlayer cations of MM for positively charged titanium polyhydroxo complexes or TiO_2 sol particles and subsequent thermal treatment to yield metal oxide nanocrystals (pillars) in the interlayer space of MM [3,5]. Pillarization of MM results in an increase in the distance between aluminosilicate layers in the structure of the clay mineral and the emergence of additional micro- and mesopores. The TiO_2-pillared MM possesses a highly developed specific surface area and improved sorptive capacity, and exhibits high activity in various photocatalytic processes, including photolysis of organic dyes [6].

The main challenge in obtaining TiO_2-pillared MM is the synthesis of intercalants, i.e., large-size multiple charged titanium hydroxo complexes. The structure and formula for polynuclear titanium complexes is still not established exactly. For example, Einaga [7] believes that their main form is the cation $(TiO)_8(OH)_{12}{}^{4+}$. However, based on an analysis of textural properties for TiO_2-pillared MM, Bahranowski et al. [8] call this view into question by favoring polycations with higher amounts of titanium ions.

Two different methods are suggested in the literature for the synthesis of titanium polycations. The first approach is based on adding $TiCl_4$ to HCl followed by dilution with distilled water [9,10]; the second is related to hydrolyzing titanium salts or alkoxides in a solution of HCl or CH_3COOH to give a titania sol. For example, Zhang et al. [11] describes a low-temperature method for pillaring MM using a TiO_2 sol produced by hydrolyzing $TiCl_4$ in strongly acidic medium and subsequent drying at 30–80 °C. Chen et al. [12] shows the results of pillaring MM using titanium tetra-*N*-butoxide hydrolyzed in HCl solution and subsequent annealing at a temperature of 500–900 °C. The improved photocatalytic activity of the obtained TiO_2-pillared MM in comparison with the commercial photocatalyst Degussa P 25 is revealed.

A significant advantage of using a solution prior to sol stems from the possibility of obtaining titanium hydroxo complexes with sizes as small as 1–2 nm, which favors producing pillars with adjustable size [7,12], whereas sol peptization yields particles of about 11–50 nm [13,14], i.e., considerably larger than, for example, $(TiO)_8(OH)_{12}{}^{4+}$. Using a sol as a precursor often leads to the formation of a partially disordered structure in the pillar samples [15] due to (1) the nonuniform size distribution of the sol particles and (2) the formation of a partially delaminated structure [16], whereas the use of titanium hydroxo complexes ensures the formation of well-ordered structures. The use of a transparent intercalating solution makes it possible to effectively control the formation of titanium polycations by the dynamic scattering of a laser beam. Furthermore, applying titanium polycations for the MM intercalation process promotes a more uniform distribution of the precursor on the inner surface of a layered matrix. Recently, we have successfully used this advantage in the preparation of TiO_2 particles by the biotemplate technique while impregnating cellulose with a concentrated solution of titanium polyhydroxo complexes [17].

In order to improve the textural and photocatalytic properties of pillared MM, researchers have used various intensifications at the intercalation stage, for example, performing the process in supercritical CO_2 [18] or under the influence of microwave treatment [19-21]. As a result, it is possible to achieve increased values of specific surface area for the pillared samples and high degree of dispersion and crystallinity for TiO_2 in the MM structure, thus enhancing photocatalytic activity. Ooka et al. [16] report some data demonstrating high efficiency of hydrothermal effects when using a TiO_2 sol as an intercalating agent. They note that the advantage of the hydrothermal treatment stems from imparting higher acid resistance to the pillared MM, which is important when it is used for photocatalysis in highly acidic media. In particular, hydrothermal treatment accelerates crystallization and formation of clusters which grow and produce amorphous TiO_2 nanoparticles in the interlayer space of montmorillonite prior the stage of heat treatment, and significantly improves the transformation of these particles into well-crystallized TiO_2 pillars after further annealing. To the best of our knowledge, the literature data contain no information on hydrothermal synthesis of the pillared MM using a solution of titanium polyhydroxo complexes.

In this paper we propose and successfully apply a method for producing TiO_2-pillared MM with a high degree of crystallinity for the TiO_2 pillars and improved adsorption and photocatalytic

activities by hydrothermally activated intercalation of titanium polyhydroxo complexes, i.e., products of a controlled $TiCl_4$ hydrolysis. A solution of titanium hydroxo complexes representing the borderline between a conventional solution of a titanium salt and a TiO_2 sol was obtained by hydrolyzing $TiCl_4$ in a strongly acidic medium [9]. The effect of hydrothermal treatment and temperature on structural, textural, and adsorption properties and UV photocatalytic activity of the produced TiO_2-pillared MM samples is assessed.

Results and Discussion

Structure and texture of TiO_2-pillared materials

Figure 1 shows small-angle diffractograms for the initial MM sample and that intercalated with titanium polycations, as well as for the TiO_2-pillared materials without treatment and subjected to hydrothermal treatment (see Experimental section), calcined at different temperatures, whereas Table 1 contains their basal distances d_{001}.

Based on an analysis of the diffraction patterns, all the TiO_2-pillared MM samples are observed to possess well-ordered structures. As seen in Figure 1, in the case of intercalation with titanium polycations there is a shift of the characteristic peak of the original MM (2θ = 7.1°) in the direction of small angles. Upon intercalation, the basal distance d_{001} is increased from 1.3 nm to 3.8 nm, which indicates the penetration of polycations into the interlayer space of MM. After calcination, the d_{001} value (Table 1) varies from 4.0 nm for TiO_2-PMM to 4.2 nm for TiO_2-PMMH*x* (for abbreviations see Experimental section). High values of d_{001}, as also observed previously in [22,23], are attributed by Sahel et al. [24] to not just simple intercalation of titanium hydroxo complexes, but also to the existence of a certain porous structure associated with the aggregation of pillars in the interlayer space of MM. Some increase in the basal distance for the hydrothermally treated samples is probably due to the processes of polymerization of the hydroxo complexes mentioned in [25,26] in the interlayer space of MM already at the stage of intercalation. It is interesting to note that the basal distance retains its value both in samples subjected to hydrothermal treatment and those without it even after annealing at 700–800 °C, indicating thermal stability of the structure of the obtained pillared materials.

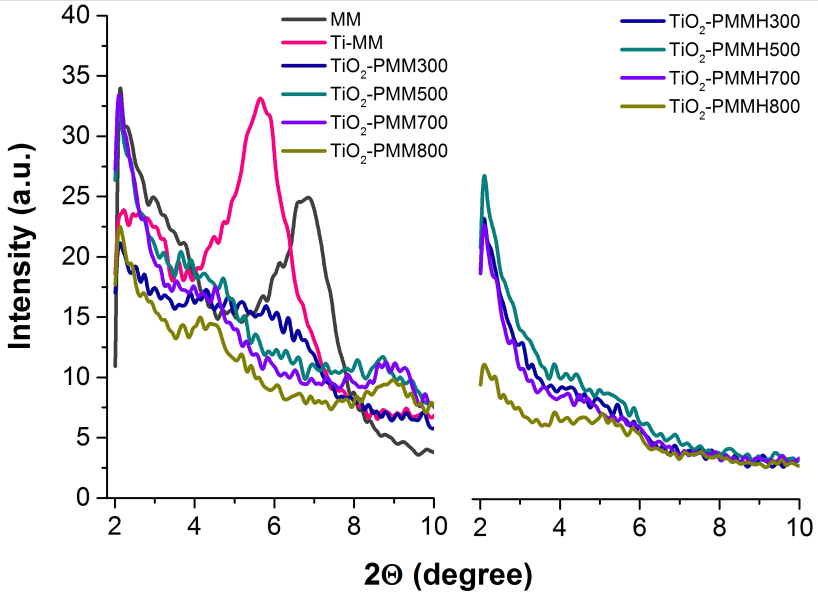

Figure 1: Small-angle XRD patterns of the raw MM, Ti-MM, TiO_2-PMM*x*, and TiO_2-PMMH*x* (see Experimental section for abbreviations).

Table 1: Basal distance d_{001} of the MM, Ti-MM, TiO_2-PMM*x*, and TiO_2-PMMH*x* samples (see Experimental section for abbreviations).

d_{001}, nm					
MM	Ti-MM	TiO_2-PMM300	TiO_2-PMM500	TiO_2-PMM700	TiO_2-PMM800
1.3 ± 0.01	3.8 ± 0.1	4.0 ± 0.1			
–	–	TiO_2-PMMH300	TiO_2-PMMH500	TiO_2-PMMH700	TiO_2-PMMH800
–	–	4.2 ± 0.1			

Figure 2 shows the results of an X-ray analysis. One observes a single montmorillonite phase for the initial MM sample (100% intensity reflex with a basal spacing d_{001} of 1.3 nm). After calcination, the pillared material samples are characterized with peaks corresponding to the montmorillonite (2θ = 19.8°, 35.6°) and cristobalite (2θ = 21.7°) phases. The cristobalite phase which has also been observed in [27], is a secondary product probably produced under the synthesis conditions with a low pH value of the medium. The diffractograms of the TiO_2-pillared samples calcined at 300 °C have shown the absence of the anatase phase, and from 500 °C broad and weak peaks of both anatase (at 2θ = 25.3°, 47.8°, 54.4°) and rutile (at 2θ = 27.7°) could be identified, which is in agreement with the data of [28] where the co-presence of both anatase and rutile phases at calcination temperatures of 450–500 °C has been established.

The TiO_2-PMMH*x* samples (Figure 2) showed significantly more sharp and intense peaks of the anatase and rutile phases at the above mentioned angles. In addition, the anatase peak becomes visible at 2θ = 37.7°. These results demonstrate that in the preparation of the pillared materials employing hydrothermal treatment, the TiO_2 pillars crystallize in the anatase and rutile phases much more readily than in the absence of that treatment.

The mass fraction of rutile crystallites (X_R) in the samples of TiO_2-pillared materials was determined from the radiographs by the ratio of heights of peaks (101) of anatase I_A and (110) of rutile I_R according to the equation [29]:

$$X_R = \frac{1}{1 + 0.794\frac{I_A}{I_R}} \quad (1)$$

The hydrothermally intercalated samples annealed at 300–800 °C are a mixture of the anatase and rutile phases in a ratio that ranges from 86:14 to 72:28 with increasing calcination temperature (Table 2).

Table 2: Average crystallite size and phase composition of the TiO_2-PMMH*x* samples (see Experimental sections for a description of the sample names).

Sample	Average crystallite size, *L* (nm)	Phase composition (%)	
		Anatase	Rutile
TiO_2-PMMH300	5.6	86	14
TiO_2-PMMH500	7.3	80	20
TiO_2-PMMH700	9.1	77	23
TiO_2-PMMH800	12.7	72	28

As seen in Figure 2, the intensity of peaks for anatase and rutile increases with increasing calcination temperature. This suggests that higher temperatures can promote the growth of crystallites. Indeed, the size of the anatase crystallites sequentially increases from 5.6 to 12.7 nm (Table 2) with increasing calcination temperature from 300 to 800 °C. According to the data of Figure 2, the phase transformation of anatase into rutile lies in the temperature range from 500 to 800 °C.

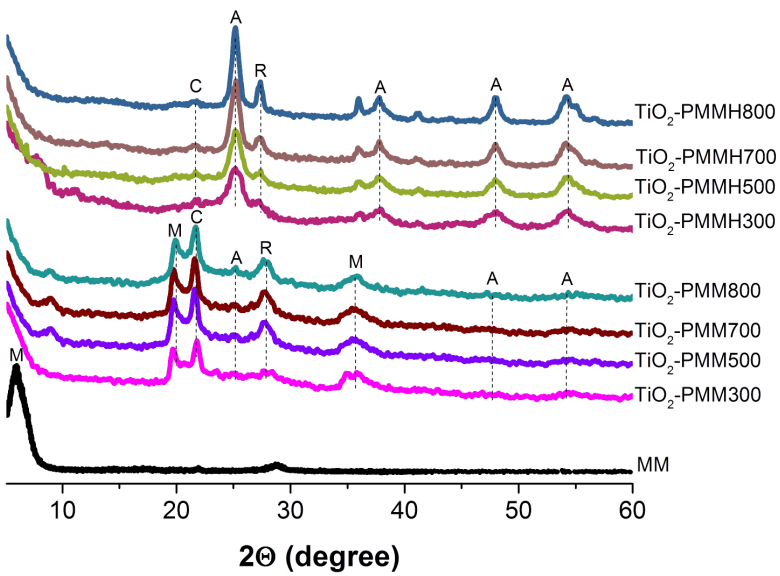

Figure 2: XRD patterns of the raw MM and TiO_2-PMM*x*, and TiO_2-PMMH*x*, where M, C, A, and R represent montmorillonite, cristobalite, anatase, and rutile phases, respectively.

Figure 3 shows the IR spectra of the original MM, TiO_2-PMM500 and TiO_2-PMMH500 samples as an example (because of their identity) of a TiO_2-pillared material. Spectra of all the samples in the region 3700 to 2800 cm^{-1} feature bands due to stretching vibrations of the OH groups. In particular, a wide band centered at about 3440 cm^{-1} is associated with the OH groups of the layered structure [30], which is even further broadened in the spectra of pillared samples. Low-intensity absorption bands at 2920 and 2850 cm^{-1} observed in the spectra of samples TiO_2-PMM500 and TiO_2-PMMH500 is attributed, according to [31], to the isolated OH groups on the surface of TiO_2.The absorption band at 1636 cm^{-1} in the region 1700 to 1500 cm^{-1} results from bending vibrations of the OH groups of adsorbed water molecules. Note that for all the samples of pillared materials the intensity of this band compared to the original MM increases due to the conservation of a larger amount of water molecules during the formation of TiO_2, as noted previously in [32]. The intense band between 800 and 1200 cm^{-1} centered at about 1040 cm^{-1} corresponds to the Si–O stretching vibrations [30,33]. A change in its intensity indicates the formation of cross-links of pillars with silicate layers. Changes in the spectra of the pillared samples between 930 and 400 cm^{-1} may be caused by the formation of both the Si–O–Ti bonds, yielding absorption bands at 920, 780, and 725 cm^{-1} [34], and the Ti–O and Ti–O–Ti bonds, absorption bands of which are located in the region 800 to 400 cm^{-1} [35,36]. Based on an analysis of the IR spectra one should expect that the increased hydroxylation of the surface of pillared MM contributes to increasing adsorption of the reactant and its delivery to the active photocatalytic centers of titanium dioxide.

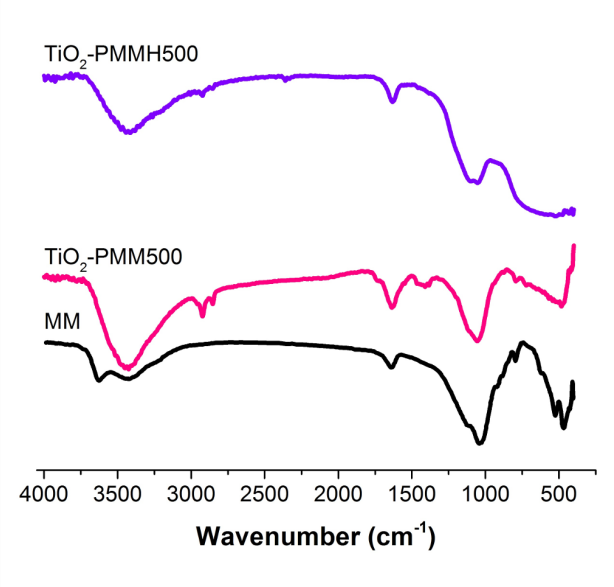

Figure 3: FTIR spectra of the raw MM, and TiO_2-pillared MM.

The results of a synchronous (thermogravimetric analysis (TGA) and differential scanning calorimetry (DSC)) thermal analysis of the samples are shown in Figure 4.

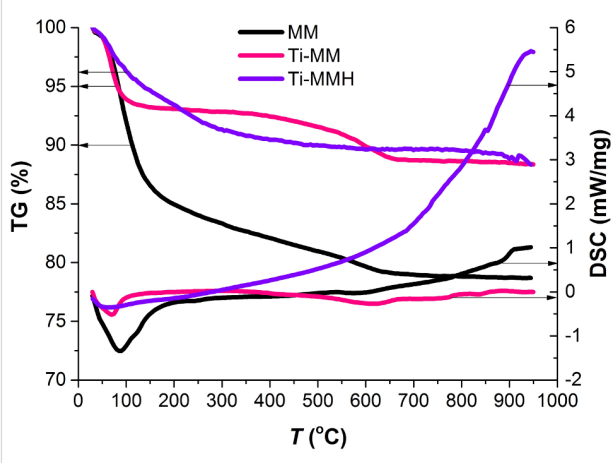

Figure 4: Thermogravimetric analysis (TGA)/differential scanning calorimetry (DSC) curves of the raw MM, Ti-MM, and Ti-MMH.

As seen in Figure 4, the MM, Ti-MM and Ti-MMH samples yield similar thermogravimetric curves, in which the loss of mass for all the samples occurs in two stages [37]. The first stage is observed in the temperature range 70–150 °C (first endothermic effect) and accompanied with 6.7, 17.1, and 6.6% weight losses for the samples MM, Ti-MM, and Ti-MMH, respectively. This weight loss is associated with the release of physically adsorbed water from the interlayer space. Further reduction in mass (4.0, 6.7, and 3.7% for the MM, Ti-MM, and Ti-MMH, respectively) in the range from 260 to 580 °C corresponds to the dehydroxylation of titanium polycations located in the interlayer space of MM, as well as aluminosilicate layers (second endothermic effect). The total weight loss in air-dry conditions for Ti-MM (23.8%) increased compared to the original MM (10.7%) due to the dehydration of intercalated polyhydroxo complexes. However, in the case of Ti-MMH there is a relatively low total weight loss (10.3%) compared to Ti-MM, which is probably a result of the aggregation of hydroxo complexes under hydrothermal conditions.

Data on the zeta potentials for the particles of all samples dispersed in double distilled water are shown in Table 3.

The value of this parameter is often used as a measure of attractive/repulsive electrostatic interaction forces between the particles and provides information on the charge state of the surface of particles in the suspension. It is worth noting that all the samples possess negative values of the zeta potential in water. As is evident from Table 3, the zeta potential values for TiO_2-PMM*x* ranged from −26.4 to −31.5 mV. The TiO_2-PMMH*x* samples

Table 3: Average values of the zeta potential for the samples tested in this work.

Sample	Zeta potential, mV
MM	−29.1
Ti-MM	−24.2
TiO_2-PMM300	−26.4
TiO_2-PMM500	−35.7
TiO_2-PMM700	−33.9
TiO_2-PMM800	−31.5
TiO_2-PMMH300	−5.3
TiO_2-PMMH500	−16.3
TiO_2-PMMH700	−16.0
TiO_2-PMMH800	−17.8

show a decrease in the magnitude of the zeta potential. This result is probably related to the formation of larger particles of TiO_2 on the external surface of MM due to flocculation at high titanium content, which leads to a reduction in their electrophoretic mobility.

In pillared samples, titanium oxide may probably exist both in the interlayer space and on the external surface of pillared MM. Figure 5 shows SEM images of the pillared samples TiO_2-PMM500 and TiO_2-PMMH500. Their morphologies have essential differences. In the case of TiO_2-PMM500 (Figure 5a-1), agglomerates of TiO_2 crystallites with different shapes and sizes dispersed on the surface of MM are clearly seen. On the surface of TiO_2-PMMH500 (Figure 5b-1) there are coral-like formations of titanium oxide, between which the TiO_2 aggregates are distributed. Such a surface profile of a hydrothermally treated sample is consistent with its increased porosity (see Table 5 below). The fact of increasing the amount of titanium on the surface of hydrothermally treated pillared samples compared to the samples without treatment is confirmed by the results of an elemental analysis using EDS spectra (Figure 5a-2 and 5b-2). These results are shown in Table 4.

It is quite difficult to obtain quantitative information on the content of TiO_2 in the interlayer space and on the external surface of pillared MM. However, given that the specific surface area of intraporous space for pillared MM (S_{int} > 200 m^2/g, the BET method) is many times larger than the area of its external surface (S_{ext} = 0.5 m^2/g, the Tovarov method [38]), it is reasonable to assume that TiO_2 will be predominantly in the form of pillars in the interlayer space.

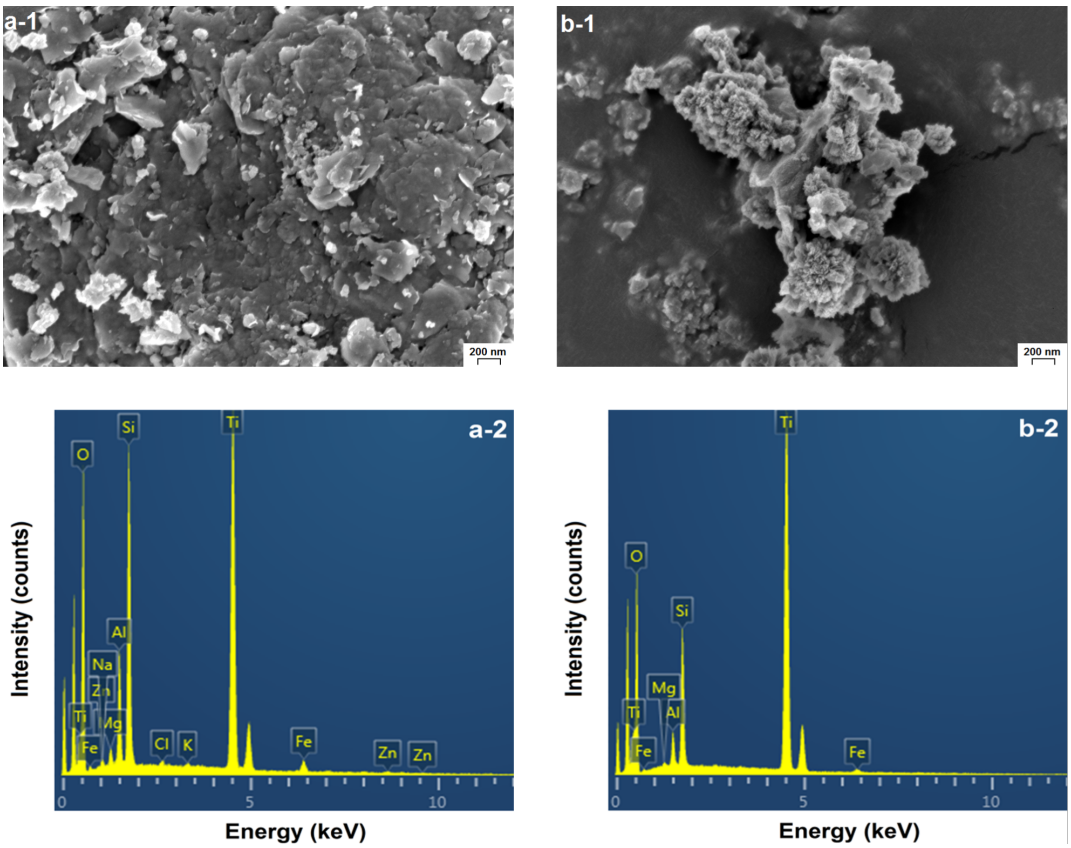

Figure 5: SEM images and EDS spectra of the surface of (a) TiO_2-PMM500, and (b) TiO_2-PMMH500.

Table 4: Elemental analysis of the MM, TiO_2-PMM500, and TiO_2-PMMH500 samples.

Sample	Element, wt %										
	O	Na	Mg	Al	Si	Cl	K	Ca	Ti	Fe	Zn
MM	64.26	1.43	2.06	6.59	21.19	0.18	0.16	0.51	0.30	3.31	–
TiO_2-PMM500	55.16	0.32	0.67	3.79	9.99	0.22	0.14	–	27.58	1.61	0.51
TiO_2-PMMH500	56.47	–	0.19	1.47	5.58	–	–	–	35.75	0.54	–

Low-temperature nitrogen adsorption–desorption isotherms for the obtained samples are shown in Figure 6a.

All the isotherms are characterized by the presence of capillary condensation hysteresis loops and belong to type IV according to IUPAC classification [39], which is typical for materials with mesoporous structure. Furthermore, the shape of the hysteresis loop for these isotherms is of type H3 according to IUPAC [34], indicating the presence of long slit-shaped and plane-parallel pores in the obtained pillared materials. In addition, the desorption branch of the isotherm shows an inflection at about 0.45–0.5 P/P_0, typical for many types of layered materials while using nitrogen as an adsorbent [40,41]. At P/P_0 ratios close to 1 the isotherms of the samples TiO_2-PMMH*x* feature a sharp rise of the sorption curve indicating the presence of large pores in the pillared samples, which is confirmed by the average pore diameter data (D_{av}) (Table 5).

The values of specific surface area according to Brunauer–Emmett–Teller (BET) (S_{BET}) and total pore volume (ΣV_{pore}) (by the Barrett–Joyner–Halenda (BJH) method) are shown in Table 5, revealing that the process of pillarization leads to significant increases in specific surface area and total pore volume compared to the original MM.

As seen from Table 5, the use of hydrothermal treatment causes a decrease in specific surface area and an increase in total pore volume in the TiO_2-PMMH*x* samples.

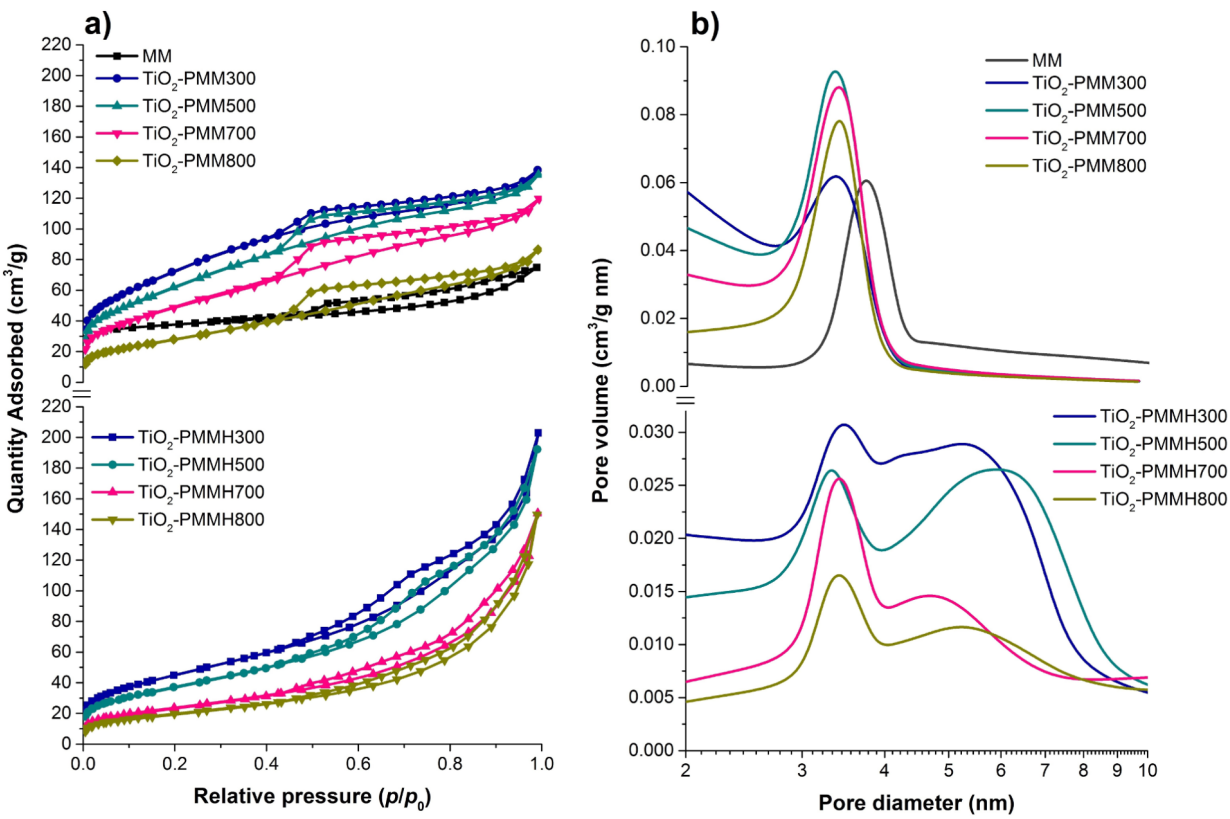

Figure 6: Nitrogen adsorption/desorption isotherms (a) and pore size distribution (b) of the raw MM, TiO_2-PMM*x*, and TiO_2-PMMH*x*.

Table 5: Textural characteristics of TiO_2-pillared MM samples.

Sample	S_{BET}, m^2/g	$\sum V_{pore}$, cm^3/g	D_{av}, nm
MM	96.0	0.170	7.00
TiO_2-PMM300	258.2	0.214	3.79
TiO_2-PMM500	228.5	0.209	3.98
TiO_2-PMM700	177.3	0.185	4.41
TiO_2-PMM800	106.1	0.134	5.02
TiO_2-PMMH300	161.4	0.320	7.85
TiO_2-PMMH500	135.1	0.303	8.34
TiO_2-PMMH700	85.4	0.235	10.09
TiO_2-PMMH800	71.5	0.234	11.72

Increasing calcination temperature from 300 to 800 °C leads to a decrease in specific surface area and pore volume for all pillared samples (Table 5). However, calcination at 800 °C leads to a drastic decrease in specific surface area, which apparently reflects a partial collapse of the pillared structure. Increasing the temperature from 300 to 800 °C causes a gradual increase in D_{av} in the TiO_2-PMM*x* samples. A similar increase was also observed in [42] and related to the growth of TiO_2 anatase crystals.

The pore size distribution curves are shown in Figure 6b. The distribution pattern for the TiO_2-PMM*x* samples is narrow and unimodal. The samples prepared using hydrothermal treatment feature a shift of the distribution curve to larger pore sizes and the broadening of its shape. Furthermore, as seen in Figure 6b, the TiO_2-PMMH*x* samples already demonstrate two peak sat 300 and 500 °C, and 3 peaks above 700 °C. This is due to the aggregation processes in the interlayer space of MM activated under hydrothermal conditions. The phenomenon of pillar enlargement can also be explained by Ostwald ripening [43]. Pillar growth occurs due to recondensation, i.e., via the process of dissolving relatively small TiO_2 pillars in water followed by re-precipitation at high pillars.

The effectiveness of decolorization for the solutions of model dyes (anionic type MO and cationic type RhB) was assessed by measuring a decrease in concentration in the dark and under UV irradiation. It is known that the efficiency of dye removal from aqueous solutions on TiO_2-pillared MM is determined by the additive process of photolysis, adsorption, and photocatalysis [37]. Therefore, we studied the kinetics of adsorption for the MO and RhB dyes (Figure 7, Figure 8) first.

All the samples under study reach adsorption equilibria in about 30 minutes. Adsorption rate for the cationic RhB is significantly higher than that for the anionic MO due to electrostatic interaction (see Table 3). The TiO_2-PMM500 and TiO_2-PMMH500 samples demonstrated maximum adsorption abilities of

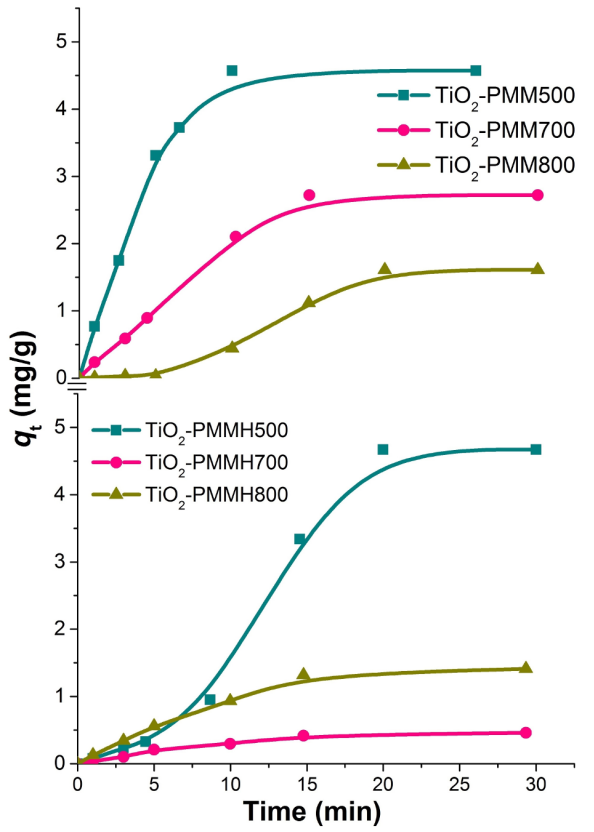

Figure 7: Kinetic curves of methyl orange dye adsorption at 20 °C by the TiO_2-PMM*x*, and TiO_2-PMMH*x* samples.

4.6 mg/g and 34.5 mg/g, respectively, with respect to MO and RhB at removal efficiencies of approximately 14% and 87%. It is interesting to note that TiO_2-PMM500 and TiO_2-PMMH500 had almost identical adsorption efficiencies with respect to both dyes, although their textural characteristics (Table 5) are significantly different. Apparently, a decrease in specific surface area is canceled for this process by an increase in pore volume and size.

When increasing calcination temperature to 700 and 800 °C, one observes a decrease in adsorption abilities of the samples of pillared materials for both dyes, and for the samples obtained using hydrothermal treatment this decrease is faster, which correlates with the results of studying textural characteristics (Table 5).

In order to describe kinetics of the process of adsorbing model anionic and cationic dyes from aqueous solutions on TiO_2-pillared MM, we used well-known pseudo-first order kinetic models of Lagergren [44], pseudo-second order models by Ho and McKay [45], and intraparticle diffusion models by Morris and Weber [46] and others [47], which may be respectively represented by the following equations:

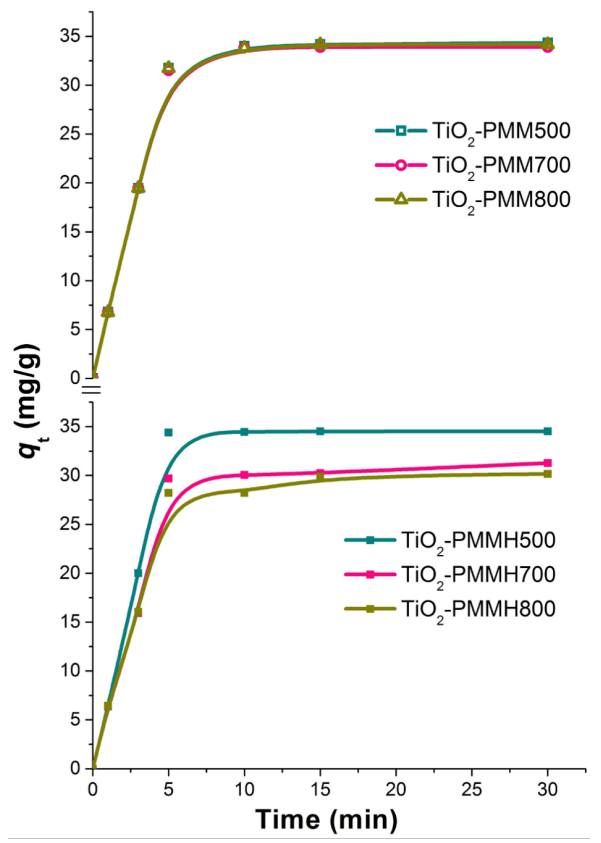

Figure 8: Kinetic curves of rhodamine B dye adsorption at 20 °C by the TiO_2-PMM*x*, and TiO_2-PMMH*x* samples.

$$Q_t = Q_e(1 - \exp^{-k_1 t}) \quad (2)$$

$$Q_t = \frac{k_2 Q_e^2 t}{1 + k_2 Q_e t} \quad (3)$$

$$Q_t = k_i t^{1/2} + C \quad (4)$$

where Q_t and Q_e are the amounts of adsorbed dye per unit weight of adsorbent at a given time t (mg/g) and at equilibrium, respectively; k_1 and k_2 are the adsorption rate constants of pseudo-first (min^{-1}) and pseudo-second order (mg g^{-1} $min^{-1/2}$), respectively; k_i is the constant of intraparticle diffusion rate (mg g^{-1} $min^{-1/2}$), t is the phase contact time (min), C is an y-intercept for the $Q_t = f(t^{1/2})$ function.

The approximation and calculation of kinetic model parameters were performed using the Origin 7.5 software package (OriginLab, USA) with a nonlinear least-squares method. The determination coefficient R^2 served as a criterion for the adequacy of kinetic models. The results of the nonlinear approximation of the experimental data are shown in Figure 7 and Figure 8; the model parameters are given in Table 6.

Table 6: Parameters of methyl orange (MO) and rhodamine B (RhB) dye adsorption kinetics for the obtained TiO_2-pillared MM samples.

Kinetic model	Adsorbents			
	TiO_2-PMM500		TiO_2-PMMH500	
Pseudo-first order	MO	RhB	MO	RhB
Q_e (mg g^{-1})	4.81	35.20	7.61	35.68
k_1 (min^{-1})	0.218	0.312	0.034	0.329
R^2	0.982	0.973	0.891	0.953
Pseudo-second order				
Q_e (mg g^{-1})	5.81	40.63	24.75	41.05
k_2 (g mg^{-1} min^{-1})	0.040	0.009	0.036	0.010
R^2	0.952	0.940	0.898	0.912
Intraparticle diffusion				
k_i, (mg g^{-1} $min^{-1/2}$)	1.023	6.810	1.047	6.853
C (mg g^{-1})	0.381	5.914	1.037	6.345
R^2	0.792	0.702	0.828	0.656

The obtained R^2 values indicate the applicability of kinetic models of pseudo-first and pseudo-second order to describe the adsorption kinetics for MO and RhB on TiO_2-pillaed MM. Preference should be given to the pseudo-first order kinetic model, which indicates that adsorption is preceded by diffusion. The process of adsorption for both dyes on TiO_2-pillared samples is likely to include both physical and chemical sorptions [48]. Given a high degree of adequacy of the pseudo-first order model, one can conclude that the process is significantly affected by film diffusion, and we are dealing with a high initial concentration of sorbate [49].

Figure 9 represents the isotherms of MO and RhB adsorption on TiO_2-PMM500 (Figure 9a) and TiO_2-PMMH500 (Figure 9b), which are related an adsorption model fitting the experimental data in the most appropriate way.

Thereby, the hydrothermal treatment does not significantly influence the adsorption capacity. The curve shape in Figure 9 corresponds the L-type adsorption isotherm, according to the classification of Giles, Smith, and Huitson [50].

Besides, the adsorption isotherms were analysed by the Freundlich, Langmuir, and Sips models [51,52], represented mathematically as follows:

$$Q_e = K_F C_e^{1/n} \quad (5)$$

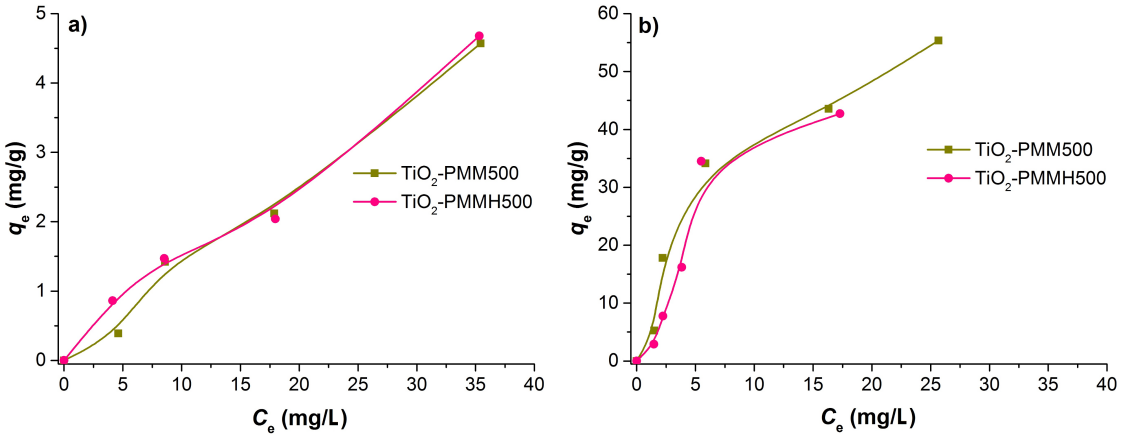

Figure 9: Adsorption isotherms of (a) MO and (b) RhB dyes at T = 20 °C.

$$Q_e = \frac{q_L K_L C_e}{1 + K_L C_E} \quad (6)$$

$$Q_e = \frac{Q_m K_S C_e^{1/n}}{1 + K_S C_e^{1/n}} \quad (7)$$

where C_e (mg/L) is the equilibrium liquid phase concentration of the adsorbate; Q_e (mg/g) the equilibrium solid phase concentration of adsorbate; q_L (mg/g) is the maximum sorption capacity; K_L (L/mg) and K_F (mg/g) are the Langmuir and Freundlich constants, respectively; Q_m (mg/g) and K_S (L/mg) are the Sips constants; 1/n is the empirical parameter. The adsorption parameters and correlation coefficients R^2 are represented in Table 7.

Table 7: Freundlich, Langmuir and Sips constants for MO and RhB adsorption.

	Adsorbents			
	TiO_2-PMM500		TiO_2-PMMH500	
Freundlich	MO	RhB	MO	RhB
K_F	0.13	11.08	0.18	7.51
n	1.00	0.50	0.91	0.63
R^2	0.987	0.948	0.977	0.849
Langmuir				
q_L (mg g^{-1})	4.90	67.47	2.33	72.87
K_L (L mg^{-1})	0.070	0.139	0.381	0.092
R^2	0.820	0.968	0.467	0.891
Sips				
Q_m, (mg g^{-1})	4.73	56.31	2.70	43.91
K_S (L mg^{-1})	0.068	0.114	0.687	0.010
n	1.01	1.42	0.88	3.27
R^2	0.819	0.974	0.443	0.982

According to the R^2 values, the Freundlich model describes MO adsorption more adequately, whereas in the case of RhB, the Sips model is more suitable.

The results for the removal of the MO and RhB dyes in aqueous solution in the presence of produced photocatalysts under UV irradiation are shown in Figure 10 and Figure 11.

These results indicate that the degradation of the MO and RhB dyes upon irradiation for 1 hour in the absence of photocatalysts was only 8% and 4%, respectively, thus that process can be neglected. Prior to obtaining the kinetic curves of photodegradation for the MO and RhB solutions, the photocatalyst samples were exposed to solutions of respective dyes with constant stirring in the dark for 30 min to reach adsorption–desorption equilibrium.

The photocatalytic effect and adsorption for the two types of dyes are substantially different. For example, a total MO removal efficiency of 64% by the TiO_2-PMM500 sample breaks down into 14% adsorption and 86% photocatalytic decomposition, whereas in the case of removing RhB a total efficiency of 91% breaks down into 87% adsorption and 13% photocatalytic decomposition.

Upon increasing calcination temperatures in the photocatalyst series TiO_2-PMM500, TiO_2-PMM700, TiO_2-PMM 800 (Figure 10 and Figure 11) the rate of removing MO and RhB sequentially increases, reaching a maximum value for TiO_2-PMM800 (79% and 94%, respectively), and the lowest efficiency among all photocatalysts under study was shown by the TiO_2-PMM500 sample, which removed about 62% MO and 89% RhB in 120 minutes. The photocatalyst series TiO_2-PMMH500, TiO_2-PMMH700, TiO_2-PMMH800 features a

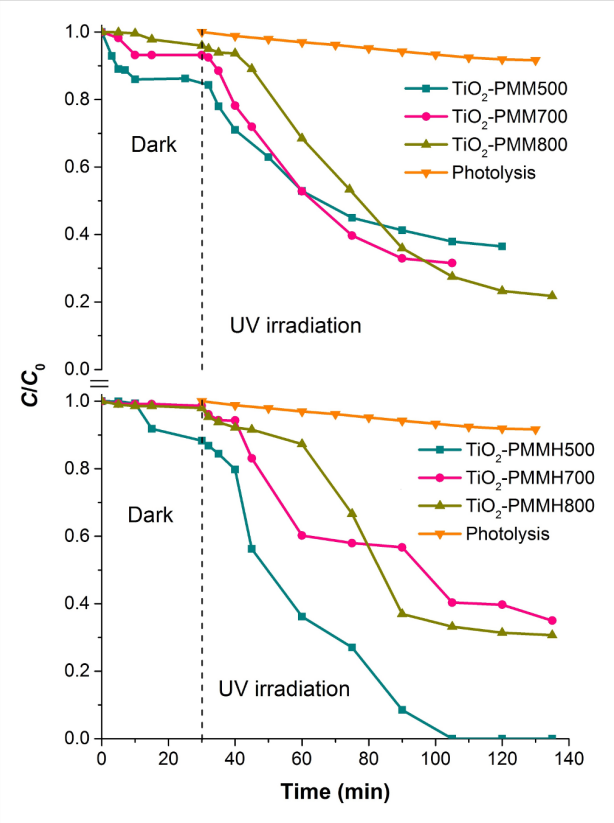

Figure 10: Removal of methyl orange (MO) on the TiO_2-PMM*x*, TiO_2-PMMH*x* samples used as photocatalysts and that without photocatalyst in the dark and under UV irradiation.

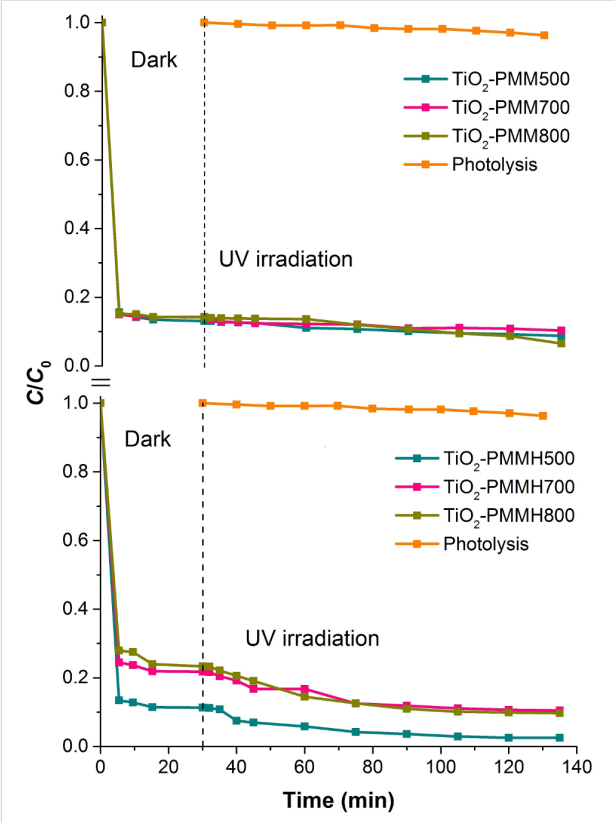

Figure 11: Removal of RhB on the TiO_2-PMM*x*, TiO_2-PMMH*x* samples used as photocatalysts and those without photocatalyst under dark and under UV irradiation conditions.

reverse trend – removal rate decreases for both dyes. The TiO_2-PMMH500 sample removes virtually 100% MO and 97.5% RhB from solution in 100 minutes.

The considerably higher decolorization rate in this case can be explained by the higher degree of crystallinity for pillars and higher porosity (Table 5), which is known to greatly affect the performance of the catalyst [53]. In addition, anatase and rutile phase ratio can play an important role, which, as noted in [54], can significantly affect the rate of photocatalytic decomposition. While interpreting the photocatalytic activity of TiO_2-pillared clays one should keep in mind the formation of cross-links between pillars and silicate layers to give the Ti–O–Si bonds, which constrain the electron–hole recombination [55]. According to this logic, the larger the crystallites of TiO_2, the greater the number of cross-linking bonds and the higher the photocatalytic activity of pillars.

Figure 12 compares the effectiveness of photocatalytic decomposition of anionic and cationic dyes at the best samples of pillared materials obtained in this work, as well as on the commercially available photocatalyst Degussa P25. The synthesized samples show significantly higher photocatalytic activity.

Conclusion

TiO_2-pillared MM was obtained by hydrothermally intensified intercalation of titanium polyhydroxo complexes, i.e., products of $TiCl_4$ controlled hydrolysis. The porous structure of the material is thermally stable due to polymerization of titanium polycations and aggregation of pillars in the interlayer space of MM, as evidenced by high values of basal distance d_{001} and total pore volume. For the hydrothermal treatment it was found that: (1) the pillars of TiO_2, representing a mixture of anatase and rutile phases, possessed a higher degree of crystallinity, and their size is confined to the range 5.6 to 12.7 nm; (2) the highest efficiency in the processes of adsorption and photocatalysis for water-soluble dyes of anionic and cationic types is observed for the samples annealed at 500 °C – a combined adsorption and photocatalytic method made it possible to remove 100% MO and 97.5% RhB in about 100 minutes. The kinetics of dye adsorption on all pillared materials under study is amenable to the pseudo-first order kinetic model. The electrostatic interaction (negative charge of modified clay particles) was found to be related to a high adsorption capacity in removing cationic dyes as compared to anionic ones. The pillared materials prepared using hydrothermal treatment combine sorptive and photocatalytic properties and can be recommended for mineraliza-

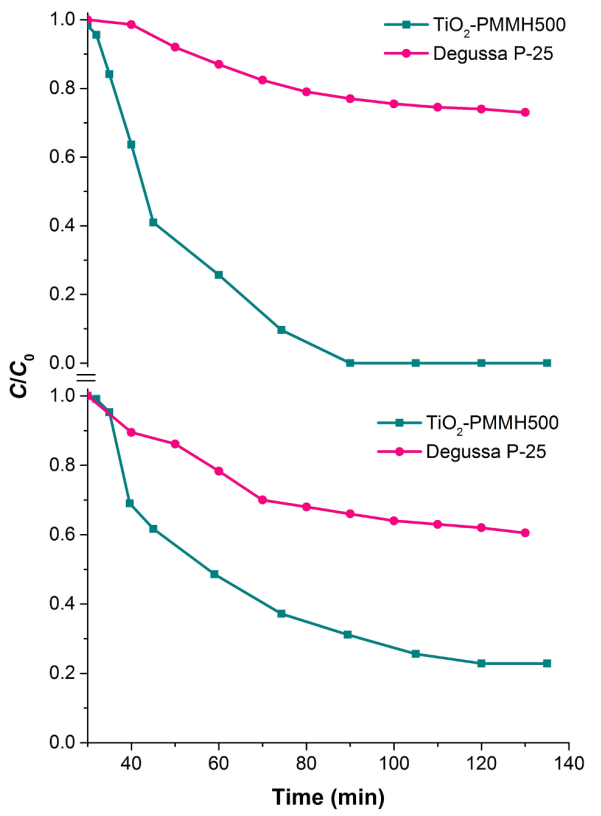

Figure 12: Comparison of photocatalytic activity of TiO_2-pillared MM with the commercial photocatalyst Degussa P25 upon degradation of methyl orange (MO) and rhodamine B (RhB) dyes in aqueous solution.

tion and decomposition of organic contaminants, even in highly acidic media.

Experimental

Montmorillonite

A fraction of MM particles with a size of <2 micrometers, which was isolated by the sedimentation method from natural bentonite of the Dash-Salakhly deposit [56], was used as a starting material. The extracted MM fraction was subjected to drying at a temperature of 60 °C.

Original MM (Figure 13) has a characteristic layered structure and consists of flaky particles with sizes ranging from 100 to 1000 nm, which "stick" to large aggregates.

A MM form enriched with the Na^+ ions was obtained by adding a 1 M solution of NaCl to the MM suspension (10 g of MM per 1 L of solution) under continuous mixing with a magnetic stirrer and heating to 80 °C for 2 hours. The resulting suspension was washed to remove the Cl^- ions with distilled water until a negative reaction with $AgNO_3$ was achieved, then centrifuged and dried at a temperature of 60 °C.

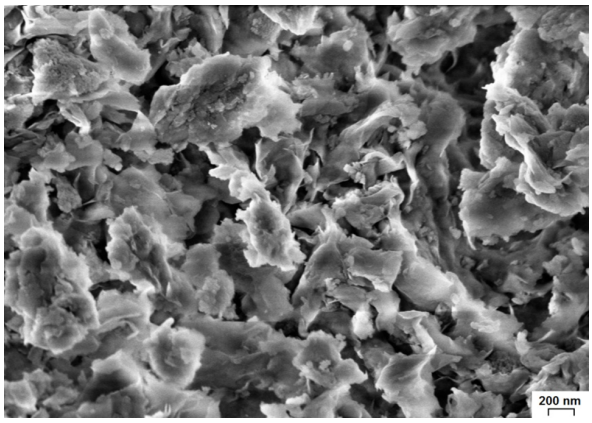

Figure 13: SEM image of the surface of original MM.

Intercalation solutions

Solutions containing titanium polycations were prepared at room temperature by hydrolyzing titanium chloride according to a procedure from [9]. To this end, a 6 M solution of HCl was treated drop wise with $TiCl_4$ (Sigma-Aldrich) to obtain solutions with Ti^{4+} concentrations of 4.92 M (solution concentration of 4.92 M is the upper limit of sol formation). For further intercalation the solutions were diluted by slowly adding deionized water to yield solutions with a residual Ti^{4+} concentration of 0.56 M. Prior to use the intercalation solutions were aged for 3 hours at 20 °C, resulting in the formation of titanium polyhydroxo complexes.

Figure 14 shows the fluorescence spectrum of an intercalation solution (scanning spectrofluorometer Varian Cary Eclipse, wavelength range 200–1000 nm, excitation wavelength 210 nm). Note that the solution spectrum has a peak at 422 nm, which apparently corresponds to polynuclear hydroxo complexes, because it disappears after fivefold dilution of the solution.

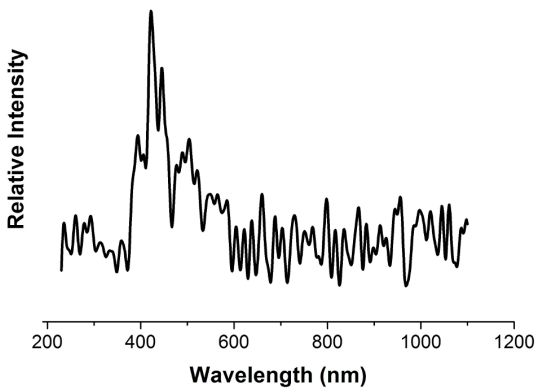

Figure 14: The fluorescence spectrum of an intercalating solution of titanium polyhydroxo complexes.

Figure 15 shows the results of particle size analysis for the intercalation solution using the laser beam dynamic scattering method (analyzer Zetasizer Nano ZS «Malvern Instruments Ltd», He–Ne laser with a wavelength of 633 nm and a recording angle of 173°). The particle size distribution curve features a peak at 1.5 nm, which corresponds to polymeric forms of the $(TiO)_8(OH)_{12}^{4+}$ polycations, as mentioned previously [8,26].

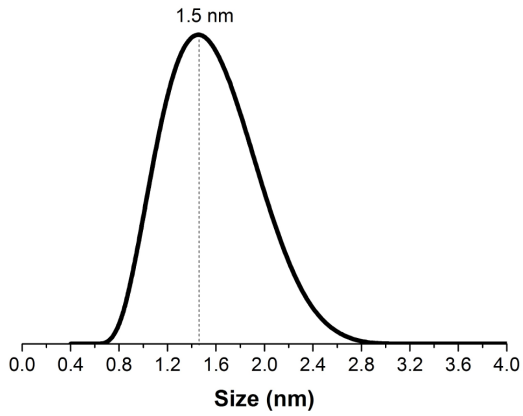

Figure 15: The dynamic light scattering (DLS) spectrum.

Intercalated and TiO_2-pillared montmorillonite

The intercalation of montmorillonite with titanium polyhydroxo complexes was performed by ion exchange in a 1% aqueous suspension by adding the intercalating solution drop wise (10 mmol Ti^{4+}/g MM) and stirring vigorously with a magnetic stirrer for 3 hours at 20 °C. After coagulation for 12 h at room temperature the suspension was washed to remove the Cl^- ions, centrifuged and subjected to drying in an oven at a temperature of 60 °C. The intercalated samples are designated as Ti-MM.

The effectiveness of intercalation was monitored photometrically (spectrophotometer UV-VisU-2001, Hitachi, Japan), with photometric technique based on the formation of a complex titanium(IV) compound with hydrogen peroxide, yellow in color, which was studied at a wavelength of 400–450 nm) determining the total concentration of the Ti^{4+} ions in polycations before and after completion of intercalation. For the applied solution of titanium hydroxo complexes it is found that prior to intercalation the concentration of Ti^{4+} ions was 1075 mg/L, and after that a substantial decrease in their concentration (to 700 mg/L) was observed. The amount of the Ti^{4+} ions in the interlayer space of MM was 187.5 mg/g of MM.

When using hydrothermal treatment at the MM intercalation stage the preparation of intercalating solution and the clay modification process were identical to those described above. In this case the MM and intercalating solution suspensions were subjected to hydrothermal treatment for 5 h at a temperature of 115 °C and a pressure of 170 kPa using a pressurized reactor with teflon tube. The samples intercalated using hydrothermal treatment are designated as Ti-MMH.

The pillared materials were obtained by annealing the samples in an oven at temperatures of 300, 500, 700, and 800 °C for 3 h. Samples of pillared materials without treatment are denoted as TiO_2-PMM*x*, and those subjected to hydrothermal treatment at the intercalation stage as TiO_2-PMMH*x*, where *x* is the calcination temperature.

Sample characterization

XRD analysis and measurements of the basal distance $d_{001}$for the samples by small-angle diffraction was performed using a Bruker D8 Advance X-ray diffractometer (Bruker-AXS, Germany). The average crystallite size (L) of anatase was evaluated using Scherer's equation:

$$L = \frac{k\lambda}{\beta\cos\theta} \quad (8)$$

where k is the dimensionless coefficient of particle shape (0.94), λ is the X-ray wavelength, β is the width of reflex at half height (in units of 2θ), θ is the diffraction angle.

IR spectra of TiO_2-pillared materials were recorded at room temperature using a Fourier transform IR spectrophotometer 360 Avatar ESP in the wavenumber range 400 to 4000 cm^{-1} with a resolution of 2 cm^{-1} and averaging over 64 scans.

A synchronous thermal analysis was performed using a NETZSCH STA 449F3 Jupiter (Netzsch, Germany) at a sample heating rate of 5 K/min.

Porosimetric measurements were carried out by low-temperature nitrogen adsorption–desorption using a specific surface area and porosity analyzer ASAP 2020 (Micromeritics, USA); prior to measurements the samples were degassed at 180 °C and residual pressure of 5–10 Pa for 3.5 h.

An analysis of the sample surface morphology was performed using an IEK-2 scanning electron microscope (Zeiss SUPRA 50VP, Germany) by coating a conductive layer of iridium. Elemental analysis of the surface was carried out on a VEGA 3 SBH scanning electron microscope integrated with a Bruker energy-dispersive microanalyzer.

Photocatalytic activity measurements

The photocatalytic activity of the produced samples of TiO_2-pillared MM was evaluated by studying degradation rates for

dyes of anionic and cationic types, i.e., methyl orange (MO) and rhodamine B (RhB) in aqueous solution. The source of UV irradiation was a high pressure mercury lamp rated at 250 watts with an emission maximum at 365 nm. The lamp was located in a water cooled quartz jacket placed in the center of the reaction vessel with a volume of 800 mL. The bottom of the reactor featured a magnetic stirrer, which ensured effective mixing of the reaction mass. The reaction solution was purged with air at a constant rate to provide a constant concentration of dissolved oxygen therein. In each experiment a dye solution (500 mL) with a concentration of 40 mg/L was treated by synthesized photocatalyst powder in an amount of 1 g/L. The reaction mixture was stirred for a predetermined time (0 to 135 min) at 25 °C. After certain time intervals 1 mL of the suspension was picked. Then, the dye solution was separated from the photocatalyst by centrifugation at 8000 rpm for 15 min. Amount of dye in the solution after centrifugation was determined with a UV-VisU-2001 spectrophotometer (Hitachi, Japan) by measuring absorbance at a wavelength corresponding to the maximum of the absorption spectrum for MO (λ_{max} = 505 nm) and RhB (λ_{max} = 554 nm). Preliminary irradiation of dye solutions for 1 h in the absence of photocatalysts showed that no significant decoloration changes occurred in the meantime.

The study of the adsorption behavior of MO on the obtained samples of photocatalysts was carried out under the same conditions as in the investigation of their photocatalytic activity, but without UV irradiation and air purge of the reaction solution. An amount of adsorbed dye (q_t, mg/g) on the sample at the time t was calculated by the equation:

$$q_t = \frac{(C_0 - C_t)V}{m} \quad (9)$$

where C_0 and C_t (mg/L) are the initial concentration of dye and the dye concentration at time t (min), V is the volume of the dye solution (L), m is the mass of air-dried adsorbent (g).

Acknowledgements

This work was supported by the RFBR foundation (16-03-01016-a). A.V.V. thanks the Ministry of Education and Science of the Russian Federation (Project 11.1706.2017/4.6) for financial support.

ORCID® iDs

Mikhail F. Butman - https://orcid.org/0000-0001-6575-6958
Nikita S. Karasev - https://orcid.org/0000-0002-0540-3808
Nataliya E. Kochkina - https://orcid.org/0000-0002-3558-3715
Alexander V. Agafonov - https://orcid.org/0000-0003-3375-6819

References

1. Yamashita, H.; Li, H., Eds. *Nanostructured Photocatalysts: Advanced Functional Materials;* Springer: Berlin, Germany, 2016. doi:10.1007/978-3-319-26079-2
2. Szczepanik, B. *Appl. Clay Sci.* **2017,** *141,* 227–239. doi:10.1016/j.clay.2017.02.029
3. Vicente, M. A.; Gil, A.; Bergaya, F. Pillared Clays and Clay Minerals. In *Handbook of Clay Science,* 2nd ed.; Bergaya, F.; Lagaly, G., Eds.; Elsevier: Amsterdam, Netherlands, 2013; Vol. 5A, pp 523–557. doi:10.1016/B978-0-08-098258-8.00017-1
4. Brigatti, M. F.; Galán, E.; Theng, B. K. G. Structure and Mineralogy of Clay Minerals. In *Developments in Clay Science,* 2nd ed.; Bergaya, F.; Lagaly, G., Eds.; Handbook of Clay Science, Vol. 5; Elsevier: Amsterdam, Netherlands, 2013; pp 21–81. doi:10.1016/B978-0-08-098258-8.00002-X
5. Kon'kova, T. V.; Alekhina, M. B.; Mikhailichenko, A. I.; Kandelaki, G. I.; Morozov, A. N. *Prot. Met. Phys. Chem. Surf.* **2014,** *50,* 326–330. doi:10.1134/S2070205114030083
6. Fatimah, I. *J. Mater. Environ. Sci.* **2012,** *3,* 983–992.
7. Einaga, H. *J. Chem. Soc., Dalton Trans.* **1979,** 1917–1919. doi:10.1039/dt9790001917
8. Bahranowski, K.; Włodarczyk, W.; Wisła-Walsh, E.; Gaweł, A.; Matusik, J.; Klimek, A.; Gil, B.; Michalik-Zym, A.; Dula, R.; Socha, R. P.; Serwicka, E. M. *Microporous Mesoporous Mater.* **2015,** *202,* 155–164. doi:10.1016/j.micromeso.2014.09.055
9. Sterte, J. *Clays Clay Miner.* **1986,** *34,* 658–664. doi:10.1346/CCMN.1986.0340606
10. Bernier, A.; Admaiai, L. F.; Grange, P. *Appl. Catal.* **1991,** *77,* 269–281. doi:10.1016/0166-9834(91)80071-4
11. Zhang, G. K.; Ding, X. M.; He, F. S.; Yu, X. Y.; Zhou, J.; Hu, Y. J.; Xie, J. W. *Langmuir* **2008,** *24,* 1026–1030. doi:10.1021/la702649v
12. Chen, D.; Du, G.; Zhu, Q.; Zhou, F. *J. Colloid Interface Sci.* **2013,** *409,* 151–157. doi:10.1016/j.jcis.2013.07.049
13. Galkina, O. L.; Vinogradov, V. V.; Agafonov, A. V.; Vinogradov, A. V. *Int. J. Inorg. Chem.* **2011,** 108087. doi:10.1155/2011/108087
14. Xu, N.; Shi, Z.; Fan, Y.; Dong, J.; Shi, J.; Hu, M. Z.-C. *Ind. Eng. Chem. Res.* **1999,** *38,* 373–379. doi:10.1021/ie980378u
15. Sun, S.; Jiang, Y.; Yu, L.; Li, F.; Yang, Z.; Hou, T.; Hu, D.; Xia, M. *Mater. Chem. Phys.* **2006,** *98,* 377–381. doi:10.1016/j.matchemphys.2005.09.047
16. Ooka, C.; Akita, S.; Ohashi, Y.; Horiuchi, T.; Szuki, K.; Komai, S.-i.; Yoshida, H.; Hattori, T. *J. Mater. Chem.* **1999,** *9,* 2943–2952. doi:10.1039/a901421g
17. Kochkina, N. E.; Agafonov, A. V.; Vinogradov, A. V.; Karasev, N. S.; Ovchinnikov, N. L.; Butman, M. F. *ACS Sustainable Chem. Eng.* **2017,** *5,* 5148–5155. doi:10.1021/acssuschemeng.7b00504
18. Yoda, S.; Sakurai, Y.; Endo, A.; Miyata, T.; Otake, K.; Yanagishita, H.; Toshio, T. *Chem. Commun.* **2002,** 1526–1527. doi:10.1039/b202589b
19. Damardji, B.; Khalaf, H.; Duclaux, L.; David, B. *Appl. Clay Sci.* **2009,** *44,* 201–205. doi:10.1016/j.clay.2008.12.010
20. Damardji, B.; Khalaf, H.; Duclaux, L.; David, B. *Appl. Clay Sci.* **2009,** *45,* 98–104. doi:10.1016/j.clay.2009.04.002
21. Martínez-Ortiz, M. J.; Fetter, G.; Domínguez, J. M.; Melo-Banda, J. A.; Ramos-Gómez, R. *Microporous Mesoporous Mater.* **2003,** *58,* 73–80. doi:10.1016/S1387-1811(02)00592-9
22. Ooka, C.; Yoshida, H.; Suzuki, K.; Hattori, T. *Microporous Mesoporous Mater.* **2004,** *67,* 143–150. doi:10.1016/j.micromeso.2003.10.011

23. Kaneko, T.; Shimotsuma, H.; Kajikawa, M.; Hatamachi, T.; Kodama, T.; Kitayama, Y. *J. Porous Mater.* **2001,** *8,* 295–301. doi:10.1023/A:1013165014982
24. Sahel, K.; Bouhent, M.; Belkhadem, F.; Ferchichi, M.; Dappozze, F.; Guillard, C.; Figueras, F. *Appl. Clay Sci.* **2014,** *95,* 205–210. doi:10.1016/j.clay.2014.04.014
25. Zheng, Y.; Shi, E.; Li, W.; Chen, Z.; Zhong, W.; Hu, X. *Sci. China, Ser. E: Technol. Sci.* **2002,** *45,* 273–281.
26. Schoonheydt, R. A.; Jacobs, K. Y. Studies in Surface Science and Catalysis. In *Introduction to Zeolite Science and Practice;* Jacobs, P. A.; Flanigen, E. M.; Jansen, J. C.; van Bekkum, H., Eds.; Elsevier Science B.V.: Amsterdam, Netherlands, 2001; Vol. 137, pp 299–343. doi:10.1016/S0167-2991(01)80249-4
27. Zuo, S.; Ding, M.; Tong, J.; Feng, L.; Qi, C. *Appl. Clay Sci.* **2015,** *105–106,* 118–123. doi:10.1016/j.clay.2014.12.033
28. Ding, Z.; Zhu, H. Y.; Lu, G. Q.; Greenfield, P. F. *J. Colloid Interface Sci.* **1999,** *209,* 193–199. doi:10.1006/jcis.1998.5857
29. Spurr, R. A.; Myers, H. *Anal. Chem.* **1957,** *29,* 760–762. doi:10.1021/ac60125a006
30. Blanco, C.; González, F.; Pesquera, C.; Benito, I.; Mendioroz, S.; Pajares, J. A. *Spectrosc. Lett.* **1989,** *22,* 659–673. doi:10.1080/00387018908053926
31. Baraton, M.-I. *Open Nanosci. J.* **2011,** *5,* 64–77. doi:10.2174/1874140101105010064
32. Kurian, M.; Sugunan, S. *Indian J. Chem.* **2003,** *42A,* 2480–2486.
33. Farmer, V. C. *The Infrared Spectra of Minerals;* Mineralogical Society: London, United Kingdom, 1974; Vol. 4. doi:10.1180/mono-4
34. Ninness, B. J.; Bousfield, D. W.; Tripp, C. P. *Colloids Surf., A* **2003,** *214,* 195–204. doi:10.1016/S0927-7757(02)00390-4
35. Castellano, F. N.; Stipkala, J. M.; Friedman, L. A.; Meyer, G. J. *Chem. Mater.* **1994,** *6,* 2123–2129. doi:10.1021/cm00047a037
36. Vasconcelos, D. C. L.; Costa, V. C.; Nunes, E. H. M.; Sabioni, A. C. S.; Gasparon, M.; Vasconcelos, W. L. *Mater. Sci. Appl.* **2011,** *2,* 1375–1382. doi:10.4236/msa.2011.210186
37. Djellabi, R.; Ghorab, M. F.; Cerrato, G.; Morandi, S.; Gatto, S.; Oldani, V.; Di Michele, A.; Bianchi, C. L. *J. Photochem. Photobiol., A: Chem.* **2014,** *295,* 57–63. doi:10.1016/j.jphotochem.2014.08.017
38. Nikitin, Yu. I.; Petasyuk, G. A. *J. Superhard Mater.* **2008,** *30,* 58–70.
39. Sing, K. S. W.; Everett, D. H.; Haul, R. A. W.; Moscou, L.; Pierotti, R. A.; Rouquérol, J.; Siemieniewska, T. *Pure Appl. Chem.* **1985,** *57,* 603–619. doi:10.1351/pac198557040603
40. Cool, P.; Zhu, H. Y.; Cassiers, K.; Vansant, E. F. *Stud. Surf. Sci. Catal.* **2004,** *154,* 789–796. doi:10.1016/S0167-2991(04)80886-3
41. Auerbach, S. M.; Carrado, K. A.; Dutta, P. K., Eds. *Handbook of Layered Materials;* Marcel-Dekker Inc.: New York, NY, U.S.A., 2004.
42. Chen, D.; Zhu, Q.; Zhou, F.; Deng, X.; Li, F. *J. Hazard. Mater.* **2012,** *235–236,* 186–193. doi:10.1016/j.jhazmat.2012.07.038
43. Buckley, H. E. *Crystal Growth;* John Wiley & Sons: New York, NY, U.S.A., 1951.
44. Lagergren, S. *K. Sven. Vetenskapsakad. Handl.* **1898,** *24,* 1–39.
45. Ho, Y. S.; Mckay, G. *Can. J. Chem. Eng.* **1998,** *76,* 822–827. doi:10.1002/cjce.5450760419
46. Weber, W. J.; Morris, J. C. *J. Sanit. Eng. Div., Am. Soc. Civ. Eng.* **1963,** *89,* 31–60.
47. Allen, S. J.; McKay, G.; Khader, K. Y. H. *Environ. Pollut. (Oxford, U. K.)* **1989,** *56,* 39–50. doi:10.1016/0269-7491(89)90120-6
48. Ho, Y. S.; McKay, G. *Process Biochem. (Oxford, U. K.)* **1999,** *34,* 451–465. doi:10.1016/S0032-9592(98)00112-5
49. Azizian, S. *J. Colloid Interface Sci.* **2004,** *276,* 47–52. doi:10.1016/j.jcis.2004.03.048
50. Giles, C. H.; Smith, D.; Huitson, A. *J. Colloid Interface Sci.* **1974,** *47,* 755–765. doi:10.1016/0021-9797(74)90252-5
51. Rangabhashiyam, S.; Anu, N.; Nandagopal, M. S. G.; Selvaraju, N. *J. Environ. Chem. Eng.* **2014,** *2,* 398–414. doi:10.1016/j.jece.2014.01.014
52. Petkovska, M. *Adsorption* **2014,** *20,* 385–395. doi:10.1007/s10450-013-9571-y
53. Alsawat, M.; Altalhi, T.; Shapter, J. G.; Losic, D. *Catal. Sci. Technol.* **2014,** *4,* 2091–2098. doi:10.1039/C3CY01100C
54. Yan, M.; Chen, F.; Zhang, J.; Anpo, M. *J. Phys. Chem. B* **2005,** *109,* 8673–8678. doi:10.1021/jp046087i
55. Son, H.-J.; Wang, X.; Prasittichai, C.; Jeong, N. C.; Aaltonen, T.; Gordon, R. G.; Hupp, J. T. *J. Am. Chem. Soc.* **2012,** *134,* 9537–9540. doi:10.1021/ja300015n
56. Nasedkin, V. V.; Shirinadze, N. A. *Dash-Salakhly Bentonite Deposit (Establishment and Development Prospects);* GEOS: Moscow, Russia, 2008.

License and Terms

This is an Open Access article under the terms of the Creative Commons Attribution License (http://creativecommons.org/licenses/by/4.0), which permits unrestricted use, distribution, and reproduction in any medium, provided the original work is properly cited.

The license is subject to the *Beilstein Journal of Nanotechnology* terms and conditions: (https://www.beilstein-journals.org/bjnano)

The definitive version of this article is the electronic one which can be found at:
doi:10.3762/bjnano.9.36

BEILSTEIN JOURNAL OF NANOTECHNOLOGY

Facile synthesis of $ZnFe_2O_4$ photocatalysts for decolourization of organic dyes under solar irradiation

Arjun Behera[1], Debasmita Kandi[1], Sanjit Manohar Majhi[2], Satyabadi Martha[*1,§] and Kulamani Parida[*1]

Full Research Paper

Open Access

Address:
[1]Centre for Nano Science and Nano Technology, Institute of Technical Education and Research, Siksha 'O' Anusandhan (deemed to be university), Bhubaneswar-751030, India and [2]Department of Electronic Information Materials Engineering, Division of Advanced Materials Science and Engineering, Chonbuk National University, Jeonju, 561-756, Republic of Korea

Email:
Satyabadi Martha* - martha.satyabadi@gmail.com;
Kulamani Parida* - kulamaniparida@soa.ac.in

* Corresponding author
§ Fax: +91674-2350642

Keywords:
Congo red; electrochemical study; phenol; photocatalyst; rhodamine B (Rh B); $ZnFe_2O_4$

Beilstein J. Nanotechnol. **2018,** *9,* 436–446.
doi:10.3762/bjnano.9.42

Received: 08 August 2017
Accepted: 17 January 2018
Published: 05 February 2018

This article is part of the Thematic Series "Energy conversion, storage and environmental remediation using nanomaterials".

Guest Editor: W.-J. Ong

© 2018 Behera et al.; licensee Beilstein-Institut.
License and terms: see end of document.

Abstract

$ZnFe_2O_4$ was fabricated by a simple solution-combustion method. The structural, optical and electronic properties are investigated by XRD, TEM, FESEM, UV–vis DRS, PL, FTIR and photocurrent measurements. The photocatalytic activity of the prepared material is studied with regard to the degradation of rhodamine B (Rh B) and Congo red under solar irradiation. The kinetic study showed that the material exhibits zeroth and first order reaction kinetics for the degradation of Rh B and Congo red, respectively. The photocatalytic behaviour of $ZnFe_2O_4$ was systematically studied as a function of the activation temperature. $ZnFe_2O_4$ prepared at 500 °C showed the highest activity in degrading Rh B and Congo red. The highest activity of $ZnFe_2O_4$-500 °C correlates well with the lowest PL intensity, highest photocurrent and lowest particle size.

Introduction

Photocatalysis is a "green" technology for the treatment of environmental pollutants with solar energy [1]. It is important to develop a suitable environmentally friendly material that can absorb the full range of the solar spectrum for solving energy and environmental challenges. Since last decade, ternary transition metal oxides (TTMOs) have gained tremendous popularity in the field of photocatalysis by the scientific community. To exploit solar light more efficiently, photocatalysts with narrow band gap (e.g., $ZnSnO_3$ [2], Bi_2WO_6 [3], $Ce(MoO_4)_2$ [4] and $ZnFe_2O_4$ [5]) have been used, for absorbance of solar light in the visible region. Among ternary metal oxides, transition metal ferrites have drawn a great attention in the field of photocataly-

sis. The reasons are the absorption of a maximum fraction of solar light, and specific optoelectronic and magnetic properties [6-9]. Metal ferrites exhibit a spinel-like structure having the general formula of MFe_2O_4 (M = Zn, Cu, Ni, Mn, Co) and are magnetic in nature [10-13]. Among different metal ferrite materials, zinc ferrite ($ZnFe_2O_4$) plays a significant role because of its low band gap (1.88 eV), high thermal conductivity, good chemical stability, higher specific strength, magneto-resistive and magneto optical properties and low fabrication cost [14]. $ZnFe_2O_4$ is an n-type semiconductor having a direct band gap with suitable band edge positions for various photocatalytic processes. It is a solid solution of ferric oxide and zinc oxide, which greatly enhances the charge carrier separation. To date, various methods such as refluxing, hydrothermal [15-17] solid-state combustion, sol–gel, co-precipitation, mechanochemical [18] and microwave-hydrothermal assisted ionic liquids have been reported for the synthesis of metal ferrite [10,13,19]. Recently, Sharma et al. reported the synthesis of $ZnFe_2O_4$ nanoparticles by an urea combustion method that was controlled at 400 °C for 6 h and followed by calcination at 900 °C for 6 h [20]. Yang and co-workers synthesized $ZnFe_2O_4$ nano-octahedrons by one-step hydrothermal reaction at 180 °C for 14 h followed by drying in an oven at 60 °C for 12 h [21]. Dom et al. reported the preparation of $ZnFe_2O_4$ by different physical (SSR and μW) and chemical (PC and SPC) methods with the formation of different structures [22]. Ponhan et al. prepared $ZnFe_2O_4$ nanofibres by electrospinning at room temperature. The resultant $ZnFe_2O_4$/PVP composite nano-fibres were calcined at 500, 600 and 700 °C for 2 h in a furnace at heating and cooling rates of 5 $°C·min^{-1}$ [23]. Most of these preparation processes require various reaction steps or high temperature, which is the major drawback of the prepared materials. The prepared ferrite materials have been widely applied in the field of photocatalysis to degrade most of the organic dyes (i.e., Congo red, Rh B, malachite green methylene blue) to CO_2, H_2O and the corresponding mineral acids [19,24]. Movahedi et al. have prepared $ZnFe_2O_4$ through precipitation tested the photocatalytic activity of $ZnFe_2O_4$ in the degradation of 5 ppm Congo red obtaining 64% degradation in 120 min [19]. The photocatalytic activity of $ZnFe_2O_4$ has also been tested in the degradation of Rh B [24]. Zhao et al. have synthesized $ZnFe_2O_4$ through chemical etching followed by calcination and reported a degradation rate of 31% in 3 h [24]. Doong and co-workers have prepared $ZnFe_2O_4$ through a non-aqueous hydrothermal method obtaining 15% degradation of Rh B [25]. The above mentioned reports give an idea about that Rh B and Congo red degradation takes a long time. Hence, our objective is to degrade these harmful organic dyes as fast as possible.

In order to obtain the required phase without impurities, we have synthesized $ZnFe_2O_4$ by a simple solution-combustion method with varying activation temperatures. The effect of the activation temperature has been systematically studied. The property of the material has been examined by various characterisation techniques. Electrochemical studies have been carried out to investigate the photocatalytic decolourization of organic dyes (Congo red and Rh B) under solar light irradiation.

Experimental

$Fe(NO_3)_3·9H_2O$ (98%, Merck), $Zn(NO_3)_2·6H_2O$ (98%, Lobachemie) and urea (99.5%, Spectrochem) were used directly without any further purification.

Synthesis of $ZnFe_2O_4$ by solution combustion method

In a typical experiment, 10 mmol of $Fe(NO_3)_3·9H_2O$, 5 mmol of $Zn(NO_3)_2·6H_2O$ and 30 mmol of urea were collectively added to 30mL distilled water and stirred for 30 min at room temperature. The solution was transferred to a 100 mL alumina crucible and calcined at 500 °C for 10 min in muffle furnace. The calcined sample was cooled to room temperature and ground with mortar and pestle. The obtained powder was calcined at various temperatures such as 400, 500, 600 and 700 °C for 2 h. The samples were subsequently designated as ZFO-400, ZFO-500, ZFO-600 and ZFO-700 [26].

Photocatalytic decolourization process

The activity in the photo-decolourization of organic dyes such as Rh B and Congo red was evaluated under solar light irradiation for 60 min and 30 min, respectively. The average solar light intensity during the reaction is 100000 lx and the reaction is carried out under broad solar light. For the experiments, 0.02 g of ZFO samples was added to 20 mL of 5 ppm Rh B or 10 ppm Congo red. The obtained suspensions were kept in the dark with stirring for 30 min to develop an adsorption–desorption equilibrium. After that the solutions were exposed to solar light. At regular time intervals, 2 mL of the reaction solution was drawn from the conical flask with the help of a syringe followed by centrifugation to separate the photocatalyst. The solution was then analysed using a UV–vis spectrometer (JASCO 750) at 497 and 554 nm for Rh B and congo red, respectively.

Sample characterization

The phase composition, crystal structure and crystallinity were examined by a Rigaku Miniflex XRD instrument using Cu Kα radiation (λ = 1.54056 Å). The UV–vis diffused reflectance spectra were analysed by a UV–vis spectrophotometer (JASCO 750) using $BaSO_4$ as the reflectance reference. The photoluminescence (PL) emission spectra were investigated by a JASCO-FP-8300 fluorescence spectrometer with an excitation wavelength of 330 nm. The chemical composition and vibrational modes of the ZFO samples were analysed by JASCO FTIR-

4600. A ZEISS SUPRA 55 was used for FESEM analysis. Morphology and microstructure of the prepared catalysts were investigated by a TEM-JEOL-2010 200 kV instrument. The electrochemical analysis was carried out using an Ivium potentiostat. Photoelectrochemical (PEC) measurements were performed in a Pyrex electrochemical set up, which includes ZFO samples (deposited on FTO) as working photo anode, Ag/AgCl as reference electrode and Pt as counter electrode. The electrolyte chosen for the study was 0.1 M Na_2SO_4 aqueous solution of pH 6.8. A 400 nm cut-off filter was used for the light irradiation during linear sweep voltammetry (LSV) analysis.

Results and Discussion

XRD analysis

XRD is carried out to identify the crystal structure, phase purity and crystallinity of the materials. Figure 1 presents the XRD patterns of the $ZnFe_2O_4$ samples calcined at different temperatures. The material prepared at 400 °C did not $ZnFe_2O_4$ nanocrystals because the activation temperature is not sufficient. The materials prepared at 500–700 °C are well crystalline and the formation of pure $ZnFe_2O_4$ is confirmed corresponding to JCPDS file no (82-1049). The figure shows strong intensity and narrow peak width, which indicates the formation of crystalline ZFO samples. With increasing reaction temperature, the crystallinity of the prepared ZFO materials increases. The crystallite size has been calculated by using the Scherrer equation, $D = K\lambda/\beta \cos\theta$ (K is a constant having value 0.9, θ is the Bragg diffraction angle, λ is the wavelength of the X-rays used (1.5406 Å) and β is the full-width at half-maximum of the diffraction peak) [27]. The XRD pattern of the ZFO mixed oxide shows peaks at 2θ values of 29.7, 35.1, 42.7, 53.7, 56.4, 62.0, and 73.4° which correspond to (220), (311), (400), (422), (333), (440) and (533) crystal planes of ZFO crystal structure.

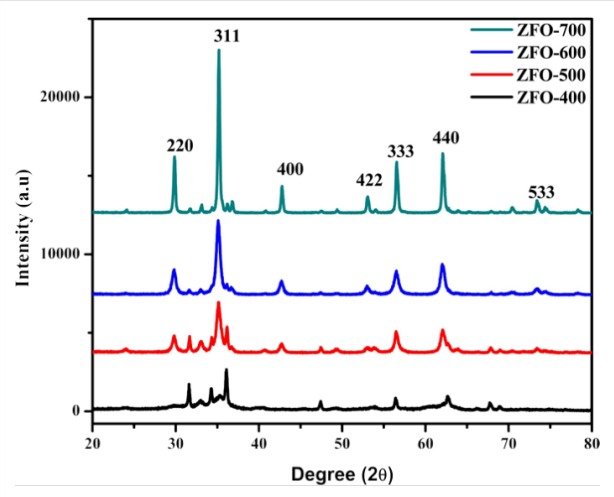

Figure 1: XRD patterns of ZFO samples with different calcination temperatures.

FESEM

Field-emission scanning electron microscopy (FESEM) provides surface morphology and topography of the prepared materials. Figure 2 shows the surface topography of ZFO-500. The sample consists of agglomerated nanoparticles with smooth surface. The agglomeration of ZFO-500 is accompanied with the formation of small crystallites [28].

TEM

The internal morphology of ZFO-500 was investigated by TEM analysis. The TEM images are shown in Figure 3. ZFO-500 NPs are a mixture of spherical and quasi-spherical particles as shown in Figure 3b. However, most of the ZFO-500 NPs are agglomerated with an average particle size of 50 nm [29].

UV–vis DRS analysis

UV–vis diffuse reflectance spectra (DRS) were measured to determine the optical absorption properties of the ZFO samples.

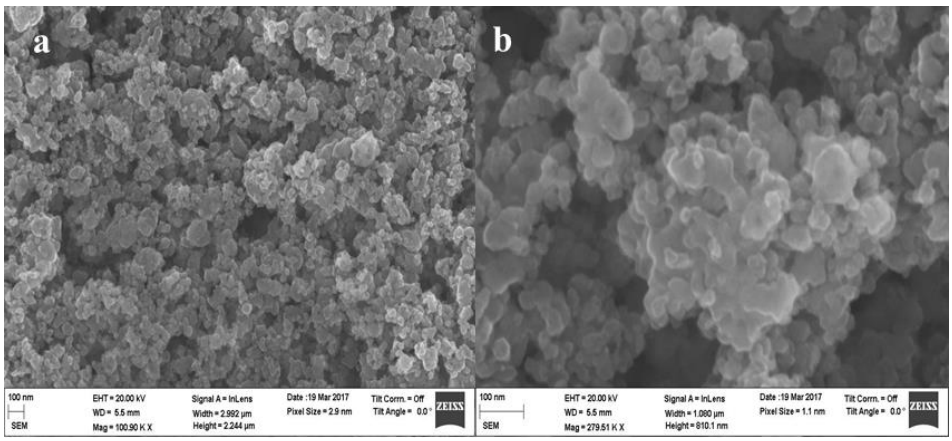

Figure 2: (a) FESEM image and (b) enlarged view of ZFO-500.

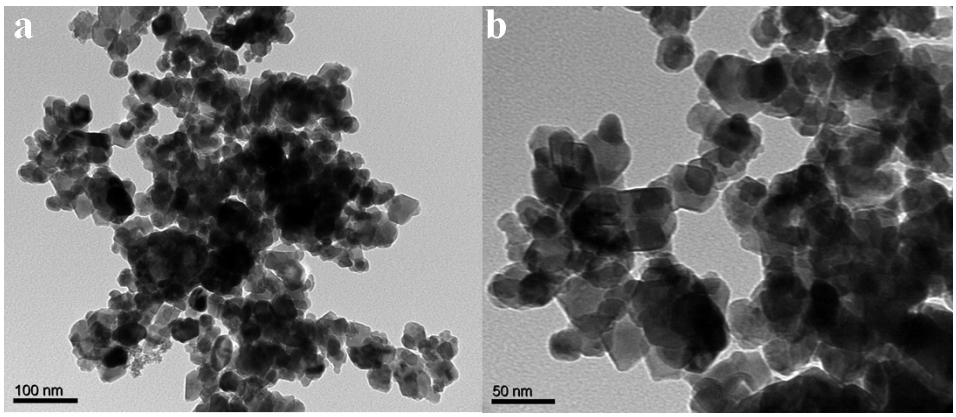

Figure 3: (a) TEM image and (b) magnified TEM image of ZFO-500.

The samples show a wide absorption range from 200 to 700 nm as depicted in Figure 4a, and among them ZFO-500 shows the highest absorption. With increasing calcination temperature the absorption of the materials shifted towards higher wavelengths. The band-gap energy of ZFO-500 has been calculated with the help of Tauc plots using Equation 1 [30]:

$$\alpha h\nu = A\left(h\nu - E_g\right)^n, \quad (1)$$

where α, h, ν, E_g, and A are absorption coefficient, Plancks constant, frequency of light, band-gap energy and a proportionality constant, respectively. In the above equation, n determines the transition in a semiconductor, i.e., $n = 1/2$ for a direct transition and $n = 2$ for an indirect transition. Figure 4b shows that the band-gap energy of ZFO-500 C is 1.81 eV.

PL analysis

The PL emission can be used to investigate the charge separation process and the fate of photoinduced electron–hole pair. Figure 5 shows the photoluminescence spectra of the ZFO samples calcined at different temperatures. The most intense PL band of ZFO is centred around 400–410 nm when excited at

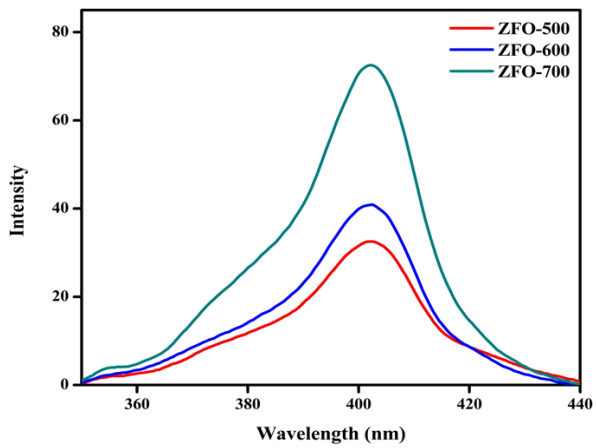

Figure 5: Photoluminescence spectra of ZFO samples excited at 330 nm.

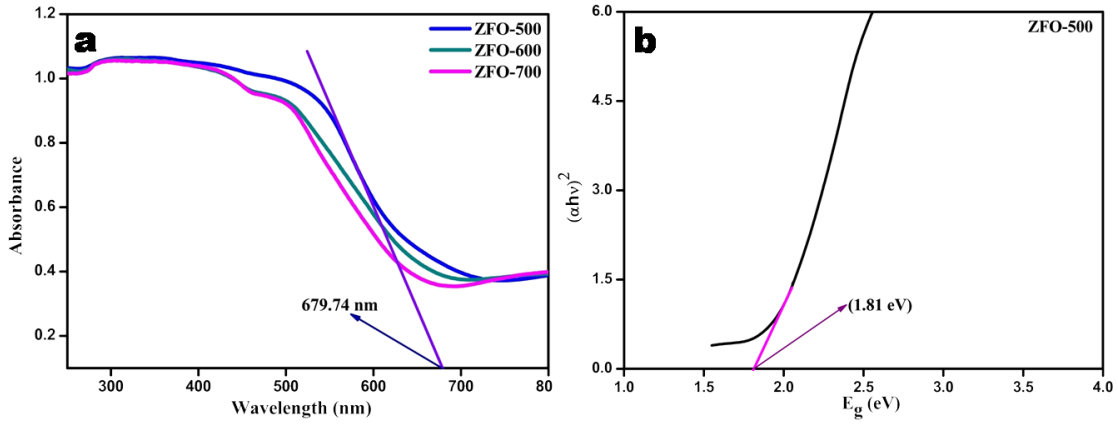

Figure 4: (a) Diffuse reflectance spectra of ZFO samples with different calcinantion temperatures with ZFO-500 showing the highest absorbance; (b) Tauc plot of ZFO-500.

330 nm. PL spectra with low-emission intensity correlate with a low recombination rate of photo-excited charge carriers and vice versa [31].

ZFO-700 exhibits an intense peak indicating higher electron–hole recombination rate. ZFO-500 exhibits low PL intensity indicating a high electron–hole separation efficiency. It can be concluded that ZFO-500 should possess the highest photocatalytic activity, which is in good agreement with the experimental photocatalytic activity (degradation of Congo red and Rh B) discussed later.

FTIR analysis

FTIR spectra of the ZFO samples were measured in the range of 4000–400 cm^{-1} (Figure 6). The bands in the region of 3600–3300 cm^{-1} and in the region of 1650–1550 cm^{-1} (red lines) represent the stretching vibration and deformation vibration of surface-adsorbed hydroxy groups. The peak centred at 2350 cm^{-1} is characteristic for anti-symmetrical stretching mode of dissolved carbon dioxide [32]. The stretching band in the region of 590–540 cm^{-1} is due to stretching vibrations of M–O bonds (Zn-O and Fe-O).

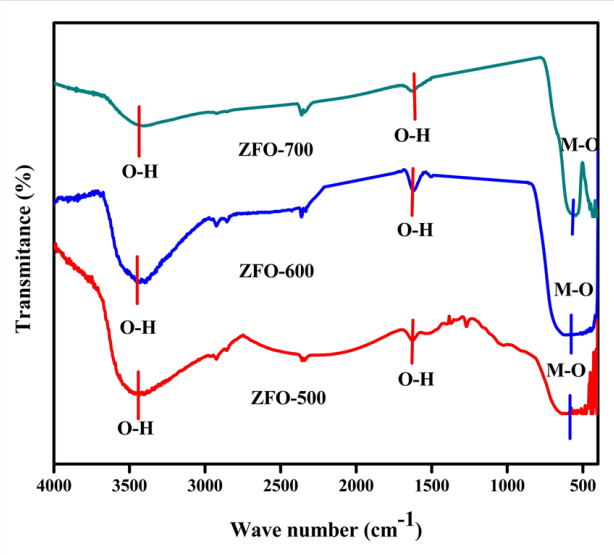

Figure 6: FTIR spectra of ZFO samples.

Electrochemical studies

Linear-sweep voltammetry

In order to know the photocurrent response of the prepared catalysts, linear-sweep voltammetry was carried out in the range of 0–1.1 V in 0.1 M Na_2SO_4 at a scan rate of 10 $mV{\cdot}s^{-1}$. Figure 7 shows photocurrent measurements. Under dark conditions, ZFO-500 could generate a current of 0.25 mA/cm^2. Under light illumination of the rear side of ZFO-coated FTO, the current is significantly increased up to 0.54 mA/cm^2.

Mott–Schottky analysis

Mott–Schottky analysis was performed to obtain the band edge of the prepared materials. The Mott–Schottky graphs were plotted according to Equation 2:

$$C^{-2} = \frac{2\left(V_{\text{app}} - V_{\text{fb}} - \frac{kT}{e}\right)}{N_{\text{D}}\varepsilon\varepsilon_0 e A^2}, \quad (2)$$

where C, V_{fb}, k, T, e, N_D, ε, ε_0 and A are capacitance of the sample, flat-band potential, Boltzmann constant, absolute temperature, electron charge, donor density, semiconductor dielectric constant, dielectric constant in vacuum and area, respectively. C^{-2} was plotted as a function of the applied potential, V_{app}. The extrapolation of the graph leads to the intersection point at the Y-axis, which gives the flat-band potential of the sample [33].

Figure 8 shows the Mott–Schottky plot of ZFO-500. The material is an n-type semiconductor and the flat-band potential (E_{fb})

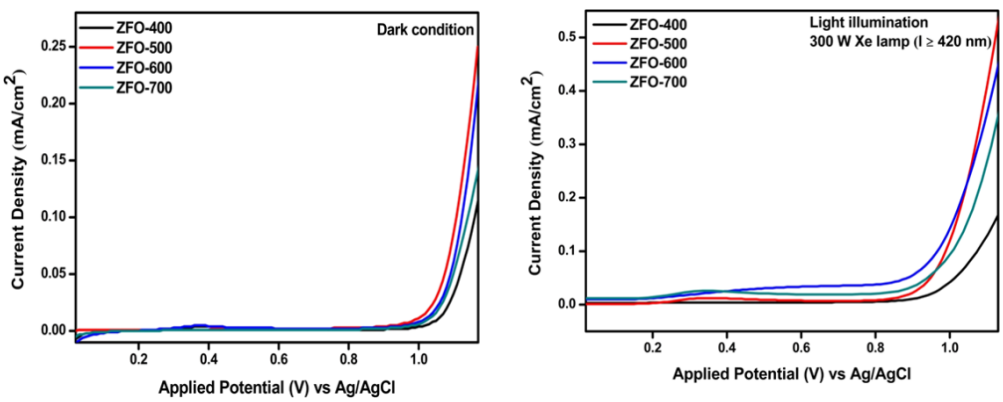

Figure 7: Linear-sweep voltammograms of ZFO-400 to ZFO-700 (a) under dark conditions, (b) under visible-light illumination.

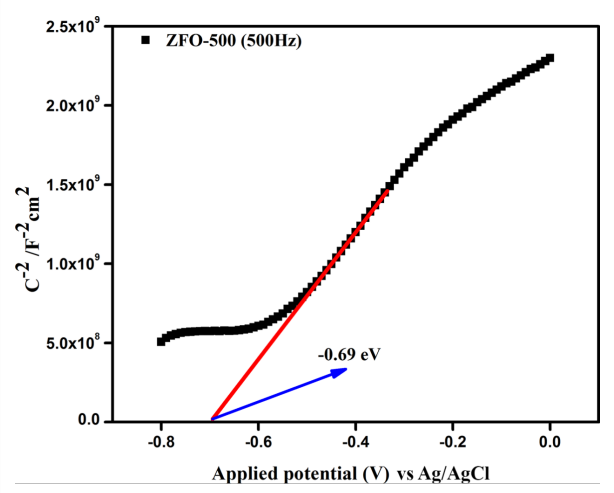

Figure 8: Mott–Schottky plot yielding the flat-band potential of ZFO-500.

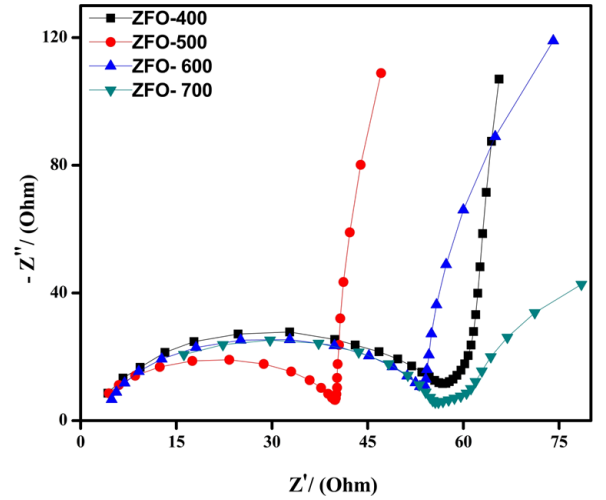

Figure 9: Nyquist plot of ZFO-400 to ZFO-700 photo anode in a frequency range from 50 to 10^5 Hz.

was calculated to be −0.69 eV (vs Ag/AgCl) or −0.09 eV (vs RHE). From UV–vis DRS measurements, the band gap of was found to be 1.81 V. So, the valence band position of ZFO is calculated as +1.72 eV (vs RHE). By considering the calculated band-edge potential, a mechanism of the photocatalytic reaction has been proposed which is discussed later.

Electrochemical impedance study

Impedance measurements are commonly used to determine the charge transfer, resistance, and effective charge separation processes occurring at electrode–electrolyte interface. In general, the radius of the semicircle in the Nyquist plots yields information about the resistance and interfacial charge migration, i.e., a smaller radius reflects a better flow of charge or low interfacial resistance compared to larger radii. ZFO-500 offered the fastest interfacial charge transfer, effective charge separation and high conductivity (Figure 9). This result is well supported by PL measurements and photocatalytic activity.

Photocatalytic activity

Decolourization of Congo red under solar-light irradiation

The photocatalytic activity in the decolourization of 10 ppm Congo red (CR) under solar irradiation was determined. To know the self-degradation of the dye, a control experiment was carried out by exposing Congo red solution to the light source for 30 min. The results showed that the Congo red solution could not be photo-degraded in the absence of the photocatalyst. In the next step, the adsorption ability of the catalyst was studied under dark conditions for 30 min. It was confirmed that the adsorption effect of the catalyst is negligible regarding the decolourization of a Congo red solution. Then 0.02 g of photocatalyst was used to decolourize 20 mL of 10 ppm of Congo red solution under solar irradiation for 30 min. The decolourization rate of Congo red solution is presented in Figure 10a and the corresponding spectral changes are represented in Figure 10b. A decolourization of 95% was obtained in the first 30 min with ZFO-500 (Figure 10c), more than with the other prepared materials. The order of decolourization efficiency is ZFO-500 > ZFO-600 > ZFO-700 > ZFO-400. For ZFO-400, ZFO-600 and ZFO-700 the decolourization rate is 59%, 82% and 73%, respectively (Figure 10c). ZFO-500 has a higher stability (up to three cycles as shown in Figure 10d) than the other ZFO samples. The results for decolourization activity are in good agreement with the results obtained from the other measurements.

The values of BET surface area of ZFO-400, ZFO-500, ZFO-600 and ZFO-700 are 34 m^2/g, 17 m^2/g, 14.5 m^2/g, 6.9 m^2/g. This result shows that the surface area has no effect towards photocatalytic degradation process [34].

Kinetics of the decolourization of Congo red

The kinetics involved in the decolourization of Congo red are shown in Figure 10e. The data obtained from the experiment was fitted with the model for first-order reactions, i.e., $\ln C_0/C = kt$) and the fitted parameters are given in Table 1.

Table 1: First-order fitting results of Congo red decolourization over ZFO samples.

catalyst	R^2	k_{obs} (min^{-1})	$t_{1/2}$ (min)	% decolourization after 30 min
ZFO-400	0.83	$34 \cdot 10^{-3}$	20.38	59
ZFO-500	0.97	$117 \cdot 10^{-3}$	5.92	95
ZFO-600	0.93	$64 \cdot 10^{-3}$	10.82	82
ZFO-700	0.90	$50 \cdot 10^{-3}$	13.86	73

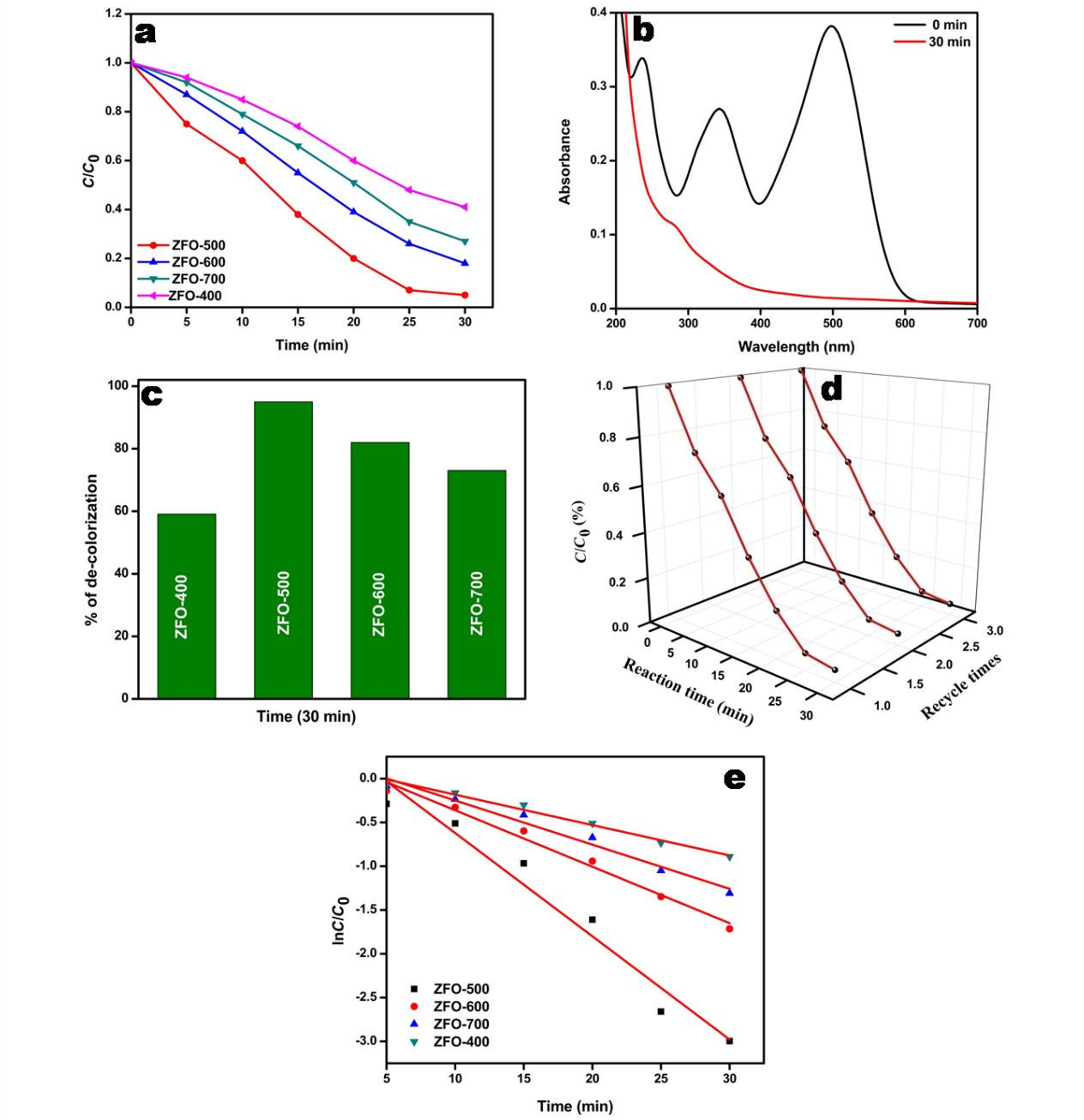

Figure 10: (a) Photocatalytic decolourization of Congo red over different ZFO samples; (b) spectral changes of the Congo red solution over ZFO-500; (c) rate of decolourization of Congo red over various ZFO samples and (d) repeated stability test of the photocatalytic activity of ZFO-500; (e) kinetics linear fit in this process.

Scavenger test for the radicals involved in the process

In order to analyse the mechanism of degradation, the most active species formed during the decomposition of Congo red were examined by scavenging experiments. The active species responsible for the decolourization of Congo red can be detected by using trapping reagents such as dimethyl sulfoxide, isopropyl alcohol, ethylenediaminetetraacetic acid, *p*-benzoquinone for electrons, hydroxyl radicals (•OH), holes (h^+), and superoxide ($•O_2^-$) radicals, respectively [35]. Figure 11b,c clearly shows that hydroxyl and superoxide radicals play a major role in the decolourization of Congo red solution. When isopropyl alcohol, a •OH scavenger, was added to the Congo red solution, the rate of decolourization was decreased. When *p*-benzoquinone was added, the same behaviour was observed. Thus, it can be concluded that •OH and $•O_2^-$ are the active species in the decolourization process. The confirmation of the active species is studied in next section.

Confirmatory test for •OH radical

In order to confirm the major role of •OH radicals, terephthalic acid (TA) was utilised as a probe reagent because it does not react with other radicals and molecules in the solution ($•O_2^-$, $•HO_2$, H_2O_2). TA readily reacts with •OH and forms 2-hydroxyterephthalic acid (HTA) via the reaction shown in Scheme 1.

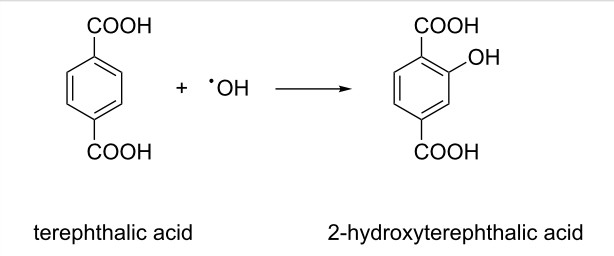

Scheme 1: Formation of luminescent 2-hydroxyterephthalic acid from terephthalic acid.

In a typical procedure, 5 mM of TA was mixed with the required amount of catalyst and an equimolar ratio of NaOH, as TA is not soluble in acidic or neutral medium. The whole solution was then exposed to solar light for 30 min, and then PL analysis was carried out. HTA can be detected by PL measurements. It shows emission at λ = 426 nm under excitation at λ = 315 nm, while TA does not fluoresce. The emission peak at 424 nm in Figure 11b proves the formation of HTA. The more •OH radicals are formed, the higher will be the intensity of the PL peak. The results confirm that •OH radicals are the active species in the decolourization of Congo red over ZFO samples.

Confirmatory test for $•O_2^-$ radicals

In order to confirm the formation of $•O_2^-$ radicals, a $5·10^{-5}$ M solution of nitroblue tetrazolium (NBT) was taken as molecular probe. 0.01 g of ZFO was dispersed in 10 mL of the prepared NBT solution and irradiated under solar light for 1 h. After reaction, the catalyst was separated and the solution analysed in an UV spectrophotometer. Figure 11c shows the results and it suggests the generation of $•O_2^-$ radical through ZFO-500. By the end of reaction the concentration of NBT was found to be decreased which clearly indicates the formation of $•O_2^-$ during the decolourization process. This confirms the contribution of $•O_2^-$ in the decolourization of Congo red.

Decolourization of rhodamine B under solar light irradiation

The photocatalytic activity of as prepared ZFO samples was also tested in the decolourization of Rh B. ZFO-500 has also

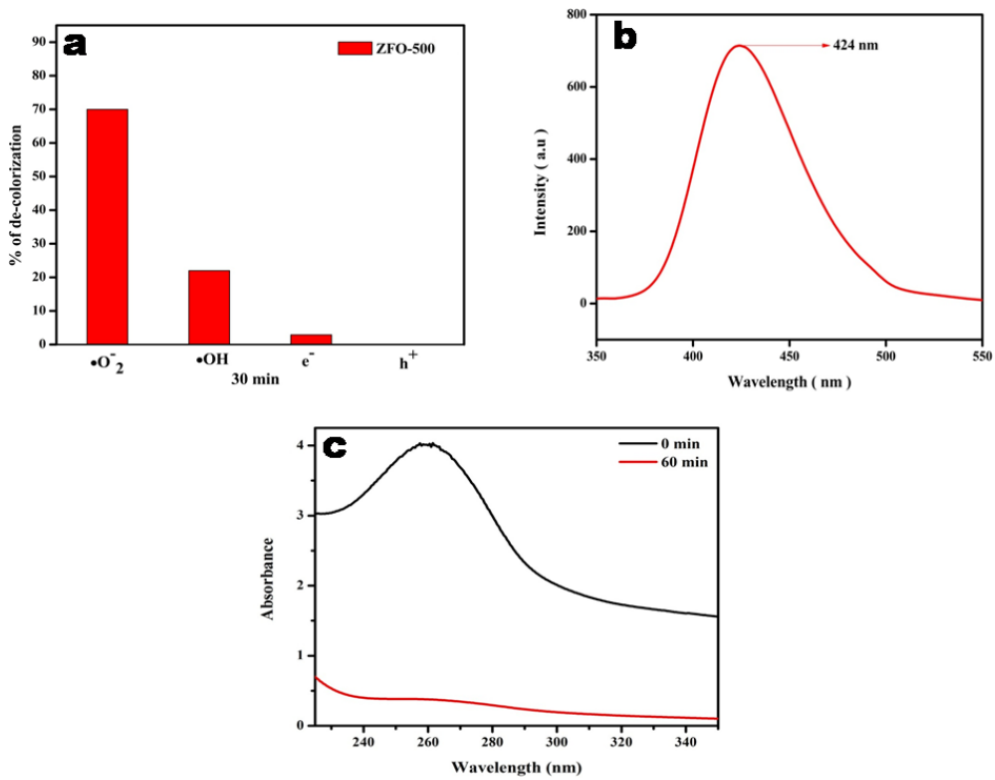

Figure 11: (a) Histogram representing the role of active species in the decolourization of Congo Red; (b) fluorescence spectra of ZFO-500 solution with TA; (c) absorbance spectra of nitroblue tetrazolium solution with ZFO-500 before and after experiment.

proven to be a good photocatalyst in decolourization of 5 ppm Rh B in 1 h. The experimental procedure was similar to that in the decolourization of Congo red. The results show that among the prepared ZFO samples, ZFO-500 could decolourize 93.6% in 1 h. The percentage of decolourization over all ZFO samples follows the order ZFO-500 (94%) > ZFO-600 (90%) > ZFO-700 (62%) > ZFO-400 (43%). The decolourization as a function of the time is presented in Figure 12a. Figure 12b shows the absorption spectrum of the Rh B solution containing ZFO-500 as function of the time.

The obtained resulted data indicates that decolourization process follows zero-order kinetics (Figure 12c) and the derived parameters are listed in Table 2. The zero-order rate constant for ZFO-500 is found to be 0.064 $mg{\cdot}L^{-1}min^{-1}$ which is lowest among all ZFO samples. The stability was also tested by repeating the decolourization experiment using the same ZFO-500 sample. ZFO-500 could retain its activity up to three cycles (Figure 12d).

Table 2: Zero-order fitting parameters of Rh B decolourization over ZFO samples.

catalyst	R^2	k_{obs} ($mg{\cdot}L^{-1}{\cdot}min^{-1}$)	$t_{1/2}$ (min)	% decolourization
ZFO-400	0.84	0.026	96.15	43
ZFO-500	0.98	0.064	39.06	94
ZFO-600	0.95	0.062	40.32	90
ZFO-700	0.90	0.040	62.5	62

Proposed mechanism for the decolourization of Congo red and Rh B

Based upon the above results, the mechanism of the photocatalytic decolourization of Congo red and Rh B is illustrated in Figure 13. Electron and holes generated in ZFO are the agents for the production of the main active species in the photodegradation. CB and VB position of ZFO were determined at −0.09 and +1.72 eV, respectively, from the Mott–Schotky plots. The conduction band of ZFO is more negative than E_0 of $\bullet O_2^-$

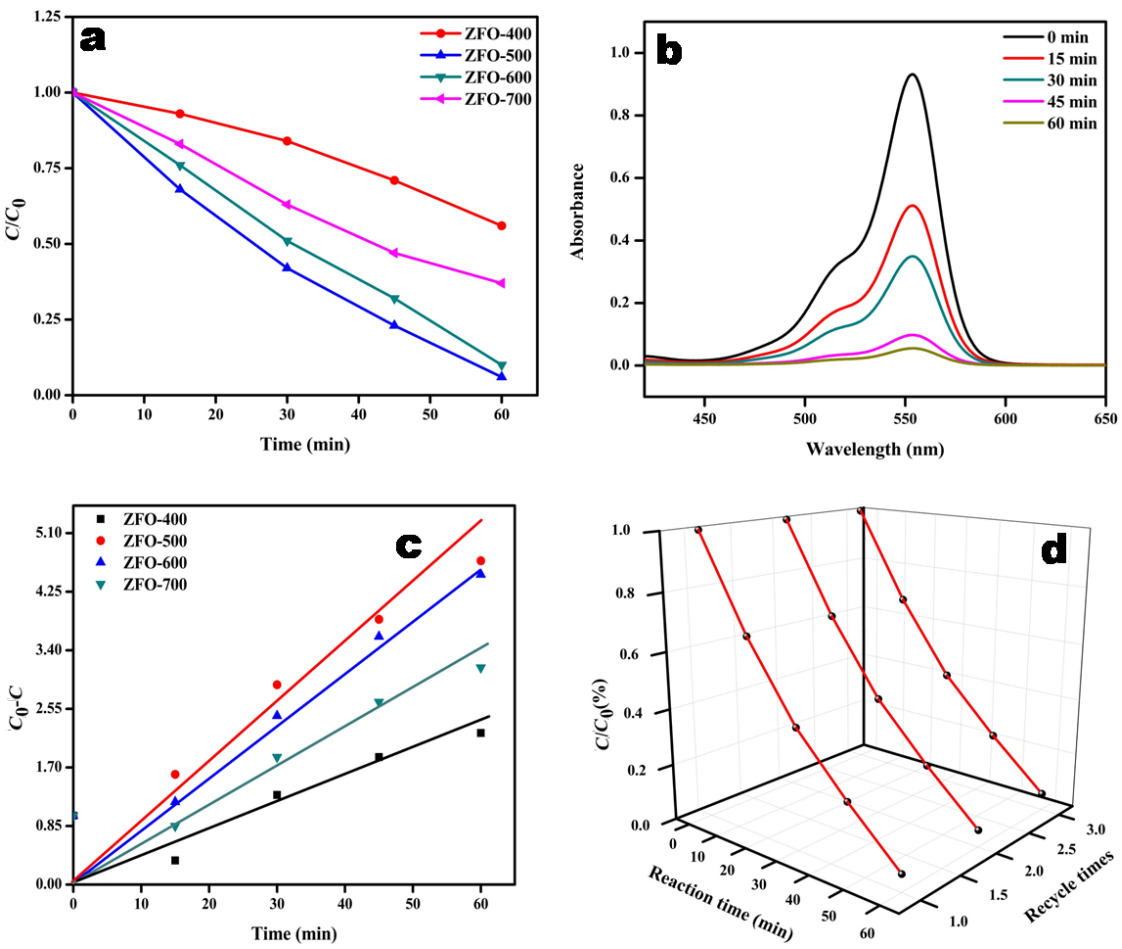

Figure 12: (a) Rate of decolourization of 5 ppm Rh B over ZFO samples; (b) spectral changes of Rh B over ZFO-500 after different time intervals; (c) zero-order kinetics plot of Rh B decolourization over ZFO samples; (d) stability graph of ZFO-500.

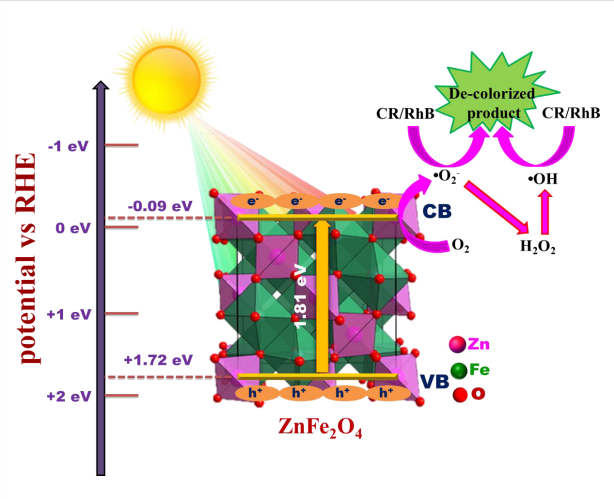

Figure 13: Reaction mechanism of the decolourization of Congo red and Rh B over ZFO-500.

(−0.046 eV vs NHE) [36]. Hence, electrons from the CB of ZFO are able to produce $\bullet O_2^-$ from dissolved oxygen. According to the scavenger tests, •OH radicals play an important role [37]. However, from the band gap positions of ZFO it can be derived that the direct formation of •OH is not possible from the photogenerated holes since E_0 of $\bullet OH/OH^-$ = +1.99 eV vs NHE. Instead, the radicals are generated indirectly from H_2O_2. The entire decolourization process can be described by the following equations:

$$\mathrm{ZFO} + h\nu \longrightarrow \mathrm{ZFO}\left(e^-\right) + \mathrm{ZFO}\left(h^+\right),$$

$$\mathrm{ZFO}\left(e^-\right) + \mathrm{O_2} \longrightarrow \bullet\mathrm{O_2^-},$$

$$\mathrm{H_2O} \rightleftharpoons \mathrm{H^+} + \mathrm{OH^-},$$

$$\mathrm{OH^-} + h^+_{\mathrm{VB}} \longrightarrow \bullet\mathrm{OH},$$

$$\mathrm{ZFO}\left(e^-\right) + \bullet\mathrm{O_2^-} + 2\mathrm{H^+} \longrightarrow \mathrm{H_2O_2},$$

$$\mathrm{ZFO}\left(e^-\right) + \mathrm{H_2O_2} \longrightarrow \bullet\mathrm{OH} + \mathrm{OH^-},$$

$$\mathrm{ZFO}\left(h^+\right) + \mathrm{H_2O} \longrightarrow \bullet\mathrm{OH} + \mathrm{H^+},$$

$$\mathrm{Rh\ B/CR} + \bullet\mathrm{OH} \longrightarrow \mathrm{decolourization},$$

$$\mathrm{Rh\ B/CR} + \bullet\mathrm{O_2^-} \longrightarrow \mathrm{decolourization}.$$

Hence the net reaction is Rh B/CR + $\bullet OH$ + $\bullet O_2^-$ → decolourization.

Degradation of phenol

In order to show its versatility, the ZFO-500 photocatalyst was also tested in degradation of colourless organic pollutants. We have used phenol as a model pollutant. The photocatalytic degradation rate of 10 ppm phenol was found to be 60% after 60 min over ZFO-500. The degradation procedure of phenol is similar to the degradation of Rh B and Congo red [35]. Photodegradation of phenol was performed by using 20 mL of a 10 ppm phenol solution containing 0.02 g of photocatalyst in a 100 mL conical flask kept under dark conditions for 30 min to ensure adsorption–desorption equilibrium. Then the photo degradation reaction was carried out for 1 h under 250 W visible light and stirring for 60 min. Then the catalyst was removed and the residual phenol was analysed with JASCO 750 UV–vis spectrophotometer. Figure 14 shows the spectral changes after degradation for 60 min. Utilizing the Beer–Lambert law, the degradation was found to be 60% for ZFO-500.

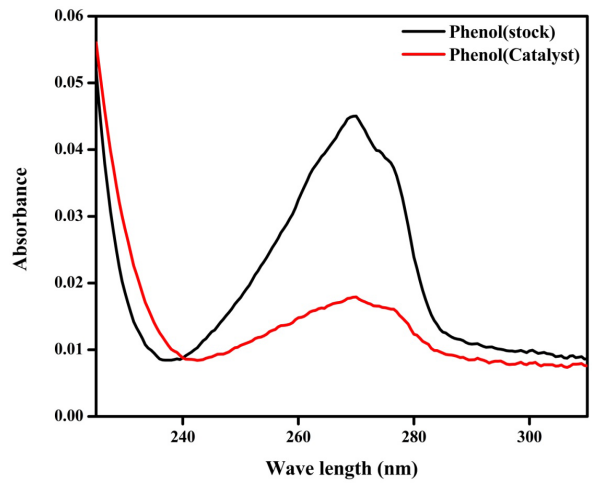

Figure 14: Adsorption spectra of the phenol solution before and after photodegradation over ZFO-500.

Conclusion

$ZnFe_2O_4$ photocatalysts were successively fabricated by a facile solution-combustion method. XRD showed the formation of cubic $ZnFe_2O_4$. TEM showed the particles are spherical with an average size of 50 nm. PL study reveals that $ZnFe_2O_4$-500 has lowest PL intensity, which means the electron–hole recombination is minimum leading to the generation of a high photocurrent. From the degradation study it is concluded that ZFO-500 is able to degrade Congo red and Rh B. The active species •OH and $\bullet O_2^-$ play a major role in the photocatalytic decolourization process. This work will provide new ways for the further improvement of semiconductor materials for energy and environmental applications.

Acknowledgements

The authors are very much thankful to SOA management for their encouragement and support. The author Dr. S. Martha is greatly acknowledged to YSRA SERB project (YSS/2015/

001949) for the financial support for the research work. The author Mr. A. Behera is also thankful to SERB for giving opportunity to carry out the project work.

ORCID® iDs

Sanjit Manohar Majhi - https://orcid.org/0000-0002-3088-3727
Satyabadi Martha - https://orcid.org/0000-0001-6529-6154
Kulamani Parida - https://orcid.org/0000-0001-7807-5561

References

1. Zhuang, J.; Dai, W.; Tian, Q.; Li, Z.; Xie, L.; Wang, J.; Liu, P.; Shi, X.; Wang, D. *Langmuir* **2010,** *26,* 9686. doi:10.1021/la100302m
2. Guo, R.; Guo, Y.; Duan, H.; Li, H.; Liu, H. *ACS Appl. Mater. Interfaces* **2017,** *19,* 8271. doi:10.1021/acsami.6b16629
3. Huang, Y.; Kang, S.; Yang, Y.; Qin, H.; Ni, Z.; Yang, S.; Li, X. *Appl. Catal., B* **2016,** *196,* 89. doi:10.1016/j.apcatb.2016.05.022
4. Karthik, R.; Kumar, J. V.; Chen, S.-M.; Karuppiah, C.; Cheng, Y.-H.; Muthuraj, V. *ACS Appl. Mater. Interfaces* **2017,** *28,* 6547. doi:10.1021/acsami.6b14242
5. Chen, X.; Dai, Y.; Guo, J.; Liu, T.; Wang, X. *Ind. Eng. Chem. Res.* **2016,** *55,* 568. doi:10.1021/acs.iecr.5b03690
6. Tatarchuk, T.; Bououdina, M.; Macyk, W.; Shyichuk, O.; Paliychuk, N.; Yaremiy, I.; Al-Najar, B.; Pacia, M. *Nanoscale Res. Lett.* **2017,** *12,* 141. doi:10.1186/s11671-017-1899-x
7. Vadivel, M.; Babu, R. R.; Ramamurthi, K.; Arivanandhan, M. *Ceram. Int.* **2016,** *42,* 19320. doi:10.1016/j.ceramint.2016.09.101
8. Franco, A., Jr.; Pessoni, H. V. S.; Neto, F. O. *J. Alloys Compd.* **2016,** *680,* 198. doi:10.1016/j.jallcom.2016.04.110
9. Jesudoss, S. K.; Vijaya, J. J.; Kennedy, L. J.; Rajan, P. I.; Al-Lohedan, H. A.; Ramalinga, R. J.; Kaviyarasu, K.; Bououdina, M. *J. Photochem. Photobiol., B* **2016,** *165,* 121. doi:10.1016/j.jphotobiol.2016.10.004
10. Dom, R.; Chary, A. S.; Subasri, R.; Hebalka, N. Y.; Borse, P. H. *Int. J. Energy Res.* **2015,** *39,* 1378. doi:10.1002/er.3340
11. Huang, S.; Xu, Y.; Xie, M.; Xu, H.; He, M.; Xia, J.; Huang, L.; Li, H. *Colloids Surf., A* **2015,** *478,* 71. doi:10.1016/j.colsurfa.2015.03.035
12. Kaviyarasu, K.; Geetha, N.; Kanimozhi, K.; Magdalane, C. M.; Sivaranjani, S.; Ayeshamariam, A.; Kennedy, J.; Maaza, M. *Mat. Sci. Eng. C* **2017,** *74,* 325. doi:10.1016/j.msec.2016.12.024
13. Li, J.; Huang, Z.; Wu, D.; Yin, G.; Liao, X.; Gu, J.; Han, D. *J. Phys. Chem. C* **2010,** *114,* 1586. doi:10.1021/jp907107s
14. Kasinathan, K.; Kennedy, J.; Elayaperumal, M.; Henini, M.; Malik, M. *Sci. Rep.* **2016,** *3,* 38064. doi:10.1038/srep38064
15. Han, L.; Zhou, X.; Wan, L.; Deng, Y.; Zhan, S. *J. Environ. Chem. Eng.* **2014,** *2,* 123. doi:10.1016/j.jece.2013.11.031
16. Chen, Z. P.; Fang, W. Q.; Zhang, B.; Yang, H. G. *J. Alloys Compd.* **2013,** *550,* 348. doi:10.1016/j.jallcom.2012.10.105
17. Köseoğlu, Y.; Baykal, A.; Toprak, M. S.; Gözüak, F.; Başaran, A. C.; Aktaş, B. *J. Alloys Compd.* **2008,** *462,* 209.
18. Lazarević, Z. Ž.; Jovalekić, Č.; Lvanoveski, V. N.; Rečnik, A.; Milutinović, A.; Cekić, B.; Romčević, N. Ž. *J. Phys. Chem. Solids* **2014,** *75,* 869. doi:10.1016/j.jpcs.2014.03.004
19. Movahedi, M.; Cheryani, F. K.; Rasouli, N.; Salavati, H. *Iran. Chem. Commun.* **2015,** *3,* 166.
20. Sharma, Y.; Sharma, N.; Subba Rao, G. V.; Chowdari, B. V. R. *Electrochim. Acta* **2008,** *53,* 2380. doi:10.1016/j.electacta.2007.09.059
21. Xing, Z.; Ju, Z.; Yang, J.; Xu, H.; Qian, Y. *Nano Res.* **2012,** *5,* 477. doi:10.1007/s12274-012-0233-2
22. Dom, R.; Subasri, R.; Hebalkar, N. Y.; Sadananda Chary, A.; Borsel, P. H. *RSC Adv.* **2012,** *2,* 12782. doi:10.1039/C2RA21910G
23. Ponhan, W.; Swatsitang, E.; Maensiri, S. *Mater. Sci. Technol.* **2010,** *26,* 1298. doi:10.1179/026708310X12798718274115
24. Liu, H.; Hao, H.; Xing, J.; Dong, J.; Zhang, Z.; Zheng, Z.; Zhao, K. *J. Mater. Sci.* **2016,** *51,* 5872. doi:10.1007/s10853-016-9888-5
25. Nguyena, T. B.; Doong, R.-a. *RSC Adv.* **2016,** *6,* 103428. doi:10.1039/c6ra21002c
26. Pradhan, G. K.; Martha, S.; Parida, K. M. *ACS Appl. Mater. Interfaces* **2012,** *4,* 707. doi:10.1021/am201326b
27. Martha, S.; Reddy, K. H.; Biswal, N.; Parida, K. *Dalton Trans.* **2012,** *41,* 14107. doi:10.1039/C2DT31949G
28. Dayakar, T.; Rao, K. V.; Chakra, C. S. *Int. J. Nano Sci. Technol.* **2013,** *1,* 1.
29. Abbas, M.; Torati, S. R.; Rao, B. P.; Abdel-Hamed, M. O.; Kim, C. *J. Alloys Compd.* **2015,** *644,* 774. doi:10.1016/j.jallcom.2015.05.101
30. Mansingh, S.; Padhi, D. K.; Parida, K. M. *Catal. Sci. Technol.* **2017,** *7,* 2772. doi:10.1039/C7CY00499K
31. Mansingh, S.; Padhi, D. K.; Parida, K. M. *Int. J. Hydrogen Energy* **2016,** *41,* 14133. doi:10.1016/j.ijhydene.2016.05.191
32. Ashwini, K.; Pandurangappa, C.; Nagabhushana, B. M. *Phys. Scr.* **2012,** *85,* 065706. doi:10.1088/0031-8949/85/06/065706
33. Yengantiwar, A.; Palanivel, S.; Archana, P. S.; Ma, Y.; Pan, S.; Gu, A. *J. Phys. Chem. C* **2017,** *121,* 5914. doi:10.1021/acs.jpcc.6b12710
34. Parida, K. M.; Nashim, A.; Mahanta, S. K. *Dalton Trans.* **2011,** *40,* 12839. doi:10.1039/C1DT11517K
35. Kandi, D.; Martha, S.; Thirumurugan, A.; Parida, K. M. *J. Phys. Chem. C* **2017,** *121,* 4834. doi:10.1021/acs.jpcc.6b11938
36. Tian, N.; Huang, H.; Liu, C.; Dong, F.; Zhang, T.; Du, X.; Yu, S.; Zhang, Y. *J. Mater. Chem. A* **2015,** *3,* 17120. doi:10.1039/C5TA03669K
37. Luo, J.; Yan, Z.; Liu, R.; Xu, J.; Wang, X. *RSC Adv.* **2017,** *7,* 23246. doi:10.1039/c7ra02083j

License and Terms

This is an Open Access article under the terms of the Creative Commons Attribution License (http://creativecommons.org/licenses/by/4.0), which permits unrestricted use, distribution, and reproduction in any medium, provided the original work is properly cited.

The license is subject to the *Beilstein Journal of Nanotechnology* terms and conditions: (https://www.beilstein-journals.org/bjnano)

The definitive version of this article is the electronic one which can be found at:
doi:10.3762/bjnano.9.42

BEILSTEIN JOURNAL OF NANOTECHNOLOGY

Influence of the preparation method on the photocatalytic activity of Nd-modified TiO_2

Patrycja Parnicka[1], Paweł Mazierski[1], Tomasz Grzyb[2], Wojciech Lisowski[3], Ewa Kowalska[4], Bunsho Ohtani[4], Adriana Zaleska-Medynska[*1] and Joanna Nadolna[*1]

Full Research Paper

Open Access

Address:
[1]Department of Environmental Technology, University of Gdansk, 80-308 Gdansk, Poland, [2]Department of Rare Earths, Faculty of Chemistry, Adam Mickiewicz University in Poznan, 60-780 Poznan, Poland, [3]Institute of Physical Chemistry, Polish Academy of Sciences,01-224 Warsaw, Poland and [4]Institute for Catalysis, Hokkaido University, Sapporo 001-0021, Japan

Email:
Adriana Zaleska-Medynska* - adriana.zaleska@ug.edu.pl;
Joanna Nadolna* - joanna.nadolna@ug.edu.pl

* Corresponding author

Keywords:
heterogeneous photocatalysis; hydrothermal method; modified TiO_2; neodymium; sol–hydrothermal method

Beilstein J. Nanotechnol. **2018,** *9,* 447–459.
doi:10.3762/bjnano.9.43

Received: 29 September 2017
Accepted: 08 January 2018
Published: 06 February 2018

This article is part of the Thematic Series "Energy conversion, storage and environmental remediation using nanomaterials".

Guest Editor: W.-J. Ong

© 2018 Parnicka et al.; licensee Beilstein-Institut.
License and terms: see end of document.

Abstract

Nd-modified TiO_2 photocatalysts have been obtained via hydrothermal (HT) and sol–hydrothermal (SHT) methods. The as-prepared samples were characterized by X-ray diffraction (XRD), BET surface area measurements, scanning electron microscopy (SEM), diffuse reflectance spectroscopy (DRS), luminescence spectroscopy and X-ray photoelectron spectroscopy (XPS). The photocatalytic activity of the synthesized samples was evaluated by the degradation of phenol in aqueous solution under irradiation with UV–vis ($\lambda > 350$ nm) and vis ($\lambda > 420$ nm) light, as well as by the degradation of gaseous toluene under irradiation with vis ($\lambda_{max} = 415$ nm) light. It was found that Nd-modified TiO_2 is an efficient photocatalyst for the degradation of phenol and toluene under visible light. XPS analysis revealed that the photocatalyst prepared via HT method contains a three-times higher amount of hydroxy groups at the surface layer and a two-times higher amount of surface defects than that obtained by the SHT method. The photocatalytic efficiency of phenol and toluene degradation under vis irradiation in the presence of 0.25% Nd-TiO_2(HT) reached 0.62 and 3.36 $\mu mol \cdot dm^{-1} \cdot min^{-1}$, respectively. Photocatalytic activity tests in the presence of Nd-TiO_2 and scavenger confirm that superoxide radicals were responsible for the visible light-induced degradation of the model pollutant in aqueous solution.

Introduction

Heterogeneous photocatalysis based on titanium dioxide (TiO_2) has become the focus of numerous studies due to its possible applications in the treatment of air, water and wastewater [1-5] after the photocatalytic splitting of water on TiO_2 electrodes was discovered by Fujishima and Honda in 1972 [6]. However, serious disadvantages of TiO_2 are its wide band gap, which

requires the use of ultraviolet light irradiation for excitation (the band gap of anatase is about 3.2 eV) and low quantum yield (due to the fast recombination of electron–hole pairs) [7]. These restrictions on its application could be overcome by modifying TiO_2, which results in increased activity and ability to work under visible light irradiation [8-10].

In recent years, the modification with rare earth (RE) metals has proven to be an efficient method to improve the photocatalytic properties of TiO_2 and to broaden its absorption to the solar spectrum [8,11,12]. Various Lewis bases can form complexes with RE-modified TiO_2, which leads to enhanced surface adsorption properties of TiO_2 and indirectly increases the photocatalytic activity of the photocatalysts [13,14]. Moreover, it has been reported that the presence of RE ions slowed down the rate of the charge-carrier recombination processes [15]. Besides, RE ions, due to the 4f electron structure, can act as conversion luminescent media [14,16-18]. Neodymium (Nd^{3+}) ions are well known as one of the more interesting lanthanides due to unique electronic and optical properties [19,20]. Several reports suggested that the transformation of light from near-infrared and visible spectral ranges into ultraviolet wavelengths can be responsible for the photocatalytic activity of RE-modified TiO_2 [21,22]. In our previous paper, based on action spectra analysis we revealed that Nd-modified TiO_2 could be excited under visible light in the range of 400 to 480 nm. Nevertheless, it has been proven that the up-conversion process was not responsible for the degradation of phenol under vis irradiation [23]. A similar conclusion based on action spectra analysis was also formulated by us for other RE-TiO_2 systems activated by visible light [11,14,24].

The photocatalytic activity is strictly affected by physical properties such as crystalline structure and size, specific surface area, and the density of surface hydroxy groups [7]. The impact of the synthesis of TiO_2 nanoparticles (NPs) on properties and morphology is important for understanding, creating and improving materials for various applications. According to the literature, RE-modified TiO_2 could be prepared through a wide spectrum of methods, such as sol–gel [18,25], hydrothermal [23,26,27], solvothermal [28], electrospinning [29], co-precipitation [30] and electrochemical [8] methods.

In our previous papers, we presented experimental studies concerning the effect of synthesis methods on lanthanide-modified TiO_2. In these studies we compared hydrothermal and sol–gel method. The synthesis method significantly affects the structure, optical, luminescence and photocatalytic properties. It was found that all samples (TiO_2 modified with Y^{3+}, Pr^{3+}, Er^{3+} and Eu^{3+}) obtained through the hydrothermal method approach exhibited a higher photocatalytic activity, while the samples prepared via the sol–gel method approach yielded more luminescence when irradiated with 980 nm photons [24].

Meanwhile, the hydrothermal treatments in combination with the sol–gel method (sol–hydrothermal method) provide an alternative approach for preparing TiO_2. During the preparation, before the hydrothermal process, a sol is obtained, which may prevent the agglomeration of the nanocrystals [26]. However, information regarding the photocatalytic activity of Nd-modified TiO_2 NPs preparated by the sol–hydrothermal method is still lacking in the literature.

In view of this, in the present study, we proposed to combine the effects of synthesis route and neodymium modification to improve the photocatalytic activity of TiO_2 under visible light. The Nd-modified TiO_2 photocatalysts have been prepared using two different preparation routes, namely hydrothermal and sol–hydrothermal methods. The surface properties of these photocatalysts have been correlated with the preparation method as well as with the photoactivity in two model reactions, degradation of phenol in aqueous solution and degradation of gaseous toluene. Moreover, the photocatalytic mechanism of the Nd-modified photocatalysts was explored using a scavenger test.

Results and Discussion

Table 1 contains the description of all prepared photocatalysts, including preparation method, content of Nd, BET surface area and crystallite sizes. The amount of Nd precursor (0.25 mol %) was selected based on previous research [10,24].

Structural properties

The X-ray diffraction (XRD) technique was used to determined the crystalline phase of pristine TiO_2 and Nd-modified TiO_2

Table 1: Sample label and physicochemical characterization of pristine and Nd- modified TiO_2 photocatalysts.

sample label	preparation method	content of Nd (mol %)	S_{BET} (m^2/g)	crystallite size (nm)
pristine-TiO_2(SHT)	sol–hydrothermal	0	106	16.3
0.25% Nd-TiO_2(SHT)	sol–hydrothermal	0.25	137	14.3
pristine-TiO_2(HT)	hydrothermal	0	117	8.9
0.25% Nd-TiO_2(HT)	hydrothermal	0.25	126	7.4

NPs. The XRD patterns of the examined samples are shown in Figure 1. In all synthesized photocatalysts, the diffraction pattern presents a group of lines at 2θ values of 25.4, 37.9, 48.1, 54.1, 55.1 and 62.9°, which are characteristic of anatase phase. The phase transformation to rutile has not occurred despite the heat treatment at 450 °C. The absence of peaks corresponding to Nd_2O_3 in the XRD patterns can be ascribed to the following phenomena: The content of Nd^{3+} ions was too small or highly dispersed and was below the detection limit of the diffractometer, Nd^{3+} was present in the form of an amorphous phase or Nd^{3+} ions adsorbed either on the titania surface or Nd^{3+} cations were placed inside the titania lattice (titania doping) [24,31].

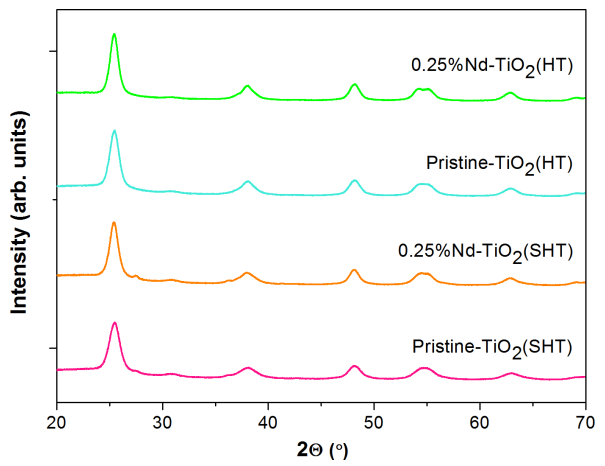

Figure 1: X-ray diffraction patterns of pristine TiO_2 and Nd-modified TiO_2 prepared by sol–hydrothermal and hydrothermal methods.

Using the Scherrer equation, the average crystallite size of anatase was determined and presented in Table 1. For modified samples, 0.25% Nd-TiO_2(SHT) and 0.25% Nd-TiO_2(HT) the crystallite sizes were 14.3 and 7.4 nm, respectively. While, for pristine samples, pristine-TiO_2(SHT) and pristine-TiO_2(HT) the crystallite sizes were equal to 16.3 and 8.9 nm, respectively. This indicates that the neodymium ions can inhibit the growth of crystallite size of TiO_2. The photocatalysts prepared by the hydrothermal method showed a higher contraction of crystallites than those obtained by the sol–hydrothermal method. The present study reveals that loading with neodymium ions hindered the increase in grain size of TiO_2 during hydrothermal synthesis. Our findings correlate with some other reports. A similar average particle size of anatase (compared to the HT samples) was observed by Thomas and co-workers [31]. In their study, NPs of Nd-TiO_2 were prepared by using titanium(IV) isopropoxide and $NdCl_3$ as the titanium and neodymium source in the hydrothermal reaction at 180 °C for 2 h. The surface area of all as-prepared samples ranged from 106 to 137 m^2/g (Table 1). All Nd-modified photocatalysts showed higher BET surface area than the pristine samples. The highest BET surface area was observed for the 0.25% Nd-TiO_2(SHT) sample. According to literature data and our previous investigation, the presence of lanthanides in the obtained samples contributed to a decrease in size of the crystallites, which probably caused an increase in the specific surface area of photocatalysts [24,32,33].

The difference in ion radii (0.99 Å for Nd^{3+} and 0.75 Å for Ti^{4+}) suggests that Nd^{3+} ions cannot be effectively incorporated into the TiO_2 lattice. Additionally, a full inclusion of Nd^{3+} ions may be hindered by the low coordination number of Ti^{4+} ions (CN = 6), because Nd^{3+} ions prefer sites with CN = 8 or 9. Therefore, it is reasonable to assume that Nd-containing species are localized at the surface of TiO_2 [34]. Xie et al. [35] have reported that during the hydrothermal reaction, Nd^{3+} and O^{2-} ions could form a Nd–O oxide on the superficial layer of the TiO_2 particle by a chemical bonding process and Nd^{3+} ions mainly occur in the form of Ti–O–Nd in the Nd-TiO_2 compound. The formation of Ti–O–Nd bonds probably restricts direct contact between TiO_2 crystallites and stabilizes the anatase phase and crystallite growth [25,35].

Morphology

Surface morphology of the obtained photocatalysts was studied using scanning electron microscopy (SEM). Figure 2 shows a SEM image of pristine TiO_2 and Nd-modified TiO_2, and an irregular shape of particles can be clearly observed. Moreover, aggregation occurred in all samples. These images show no change in particle morphology due to Nd loading. The shape of particles does not show much difference between the synthesis methods. However, it seems that for photocatalysts obtained by the SHT method the agglomerates are a bit smaller.

Optical and photoluminescence properties

To study the optical absorption properties of the as-prepared photocatalysts, diffuse reflectance spectra (DRS) in the range of 200–850 nm were investigated, and the results are shown in Figure 3.

The optical absorption of TiO_2 in the UV region below 400 nm can be mainly attributed to the charge transfer, related to electron excitation from the valence band to the conduction band (band-to-band transition, $O_{2p} \rightarrow Ti_{3d}$) [30]. Modification of TiO_2 with neodymium significantly affected the light absorption of the photocatalysts. A redshift of the absorption edge toward the visible region was observed for the Nd-modified samples. The optical absorption edge was shifted further when the SHT method was applied. Nassuko et al. reported that the redshift can be ascribed to the new energy level in the band gap and

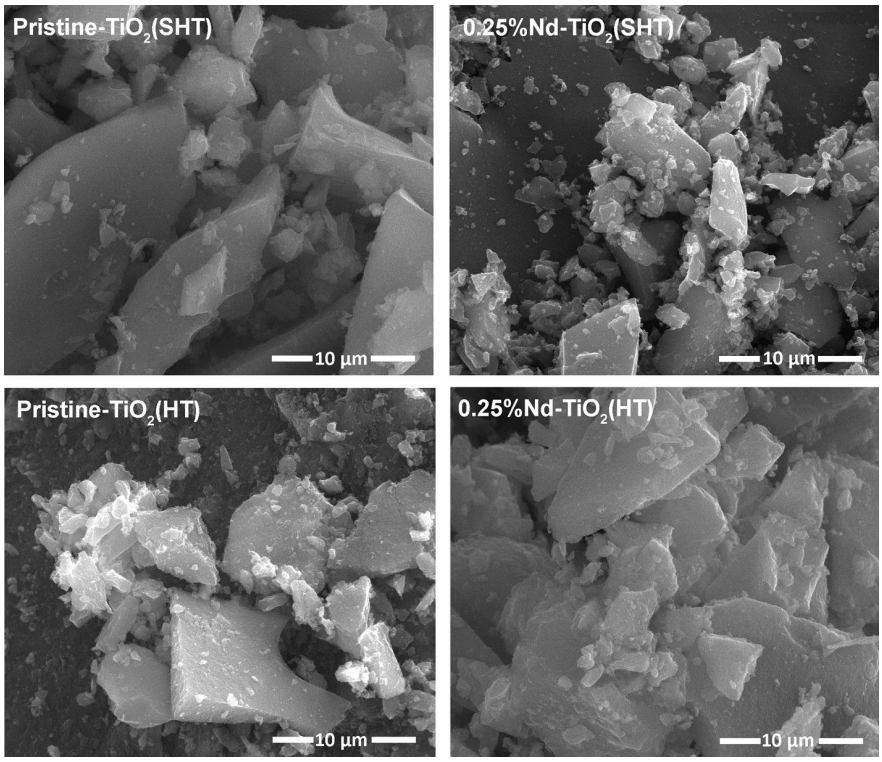

Figure 2: SEM images of TiO_2 and Nd-modified TiO_2.

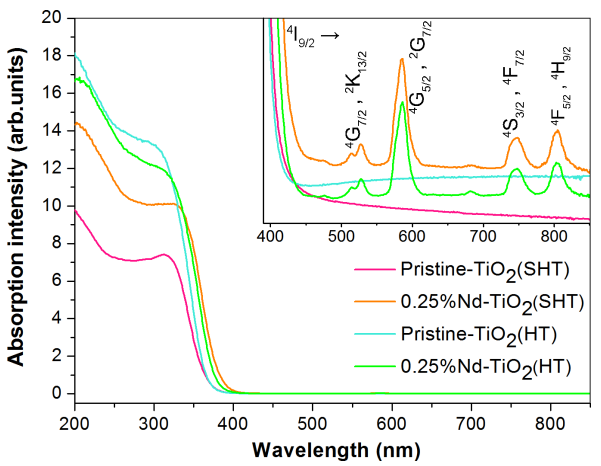

Figure 3: UV–vis diffuse reflectance spectra of Nd-modified TiO_2 photocatalysts and pristine TiO_2.

charge transfer between the TiO_2 valence band and Nd^{3+} ion levels [36]. Furthermore, there are four absorption bands in the vis region typical for neodymium located at 520, 585, 745 and 805 nm. They correspond to transitions from the $^4I_{9/2}$ ground state to the excited states of $^4G_{7/2}$ and $^2K_{13/2}$, $^4G_{5/2}$ and $^2G_{7/2}$, $^4S_{3/2}$ and $^4F_{7/2}$, $^4F_{5/2}$ and $^2H_{9/2}$ [30,37]. In all of the studied Nd-modified samples, the intensity of these absorption bands was similar.

To understand the rate of electron–hole recombination, photoluminescence (PL) spectroscopy was applied. Figure 4 shows the PL spectra of pristine and Nd-modified TiO_2 under excitation by light at λ_{ex} = 315 nm.

The photoluminescence spectra show a weak broad emission band with a maximum intensity at around 350–700 nm. Khalid et al. [38] and Raja et al. [39] reported that emission in that

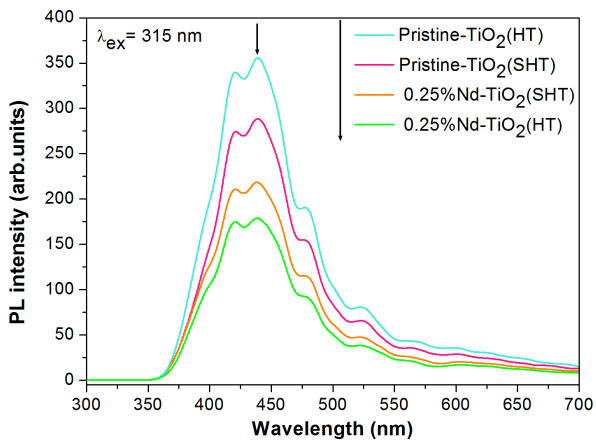

Figure 4: Photoluminescence spectra under UV light (λ_{ex} = 315 nm) of pristine TiO_2 and Nd-modified TiO_2 prepared by sol–hydrothermal and hydrothermal methods.

range is characteristic for direct (band–band) or indirect (via a band-gap state) recombination of excited electrons and holes [38]. The Nd-TiO_2 photocatalysts were characterized by a better separation ability of the photogenerated electrons and holes compared to pristine samples. In addition, the Nd-modified photocatalyst prepared by the HT method exhibited the lowest photoluminescence intensity, which suggests that the prepared material significantly inhibited the recombination of photogenerated charge carriers, which can improve the photocatalytic performance. A possible reason is the occurrence of numerous Ti–O–Nd bonds increasing the content of surface oxygen vacancies and defects [31,40]. These electron trapping sites can enhance the separation of photogenerated electron–hole pairs [24]. Furthermore, both pristine and Nd-TiO_2 NPs exhibit obvious excitonic PL signals with a similar curve shape. The observed phenomena can be explained by the spectroscopic properties of the Nd^{3+} ions caused by the transition of electrons within the 4f subshell and the shielding properties of the 5s and 5p outer orbitals. The 4f inner shell transitions can generate different arrangements of new energy levels, improving the transfer and photogenerated lifetime of the carriers, and finally increasing the formation of highly reactive and oxidative radicals during the photocatalytic degradation [15]. The Nd-TiO_2 NPs showed intense emission of Nd^{3+} ions under excitation by laser radiation with λ_{ex} = 350 nm (Figure 5).

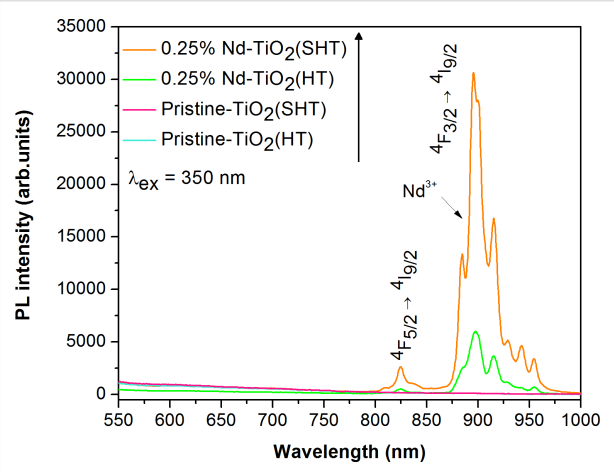

Figure 5: Photoluminescence spectra under laser light excitation (λ_{ex} = 350 nm) of pristine TiO_2 and Nd-modified TiO_2 prepared by sol–hydrothermal and hydrothermal methods.

The characteristic transition bands appeared in the near infrared range, with a maximum at around 900 nm ($^4F_{3/2}\rightarrow{}^4I_{9/2}$ transition) and a less intense peak at 850 nm ($^4F_{5/2}\rightarrow{}^4I_{9/2}$ transition) [41]. The observed emission occurred because of a direct excitation of Nd^{3+} ions into the $^4I_{9/2}\rightarrow{}^4D_{1/2},{}^4D_{3/2},{}^4D_{5/2}$ absorption peak [42]. The sample prepared by the HT method showed lower emission intensity than the one prepared by the SHT method. This is a result of the differences in morphology between these two samples. According to Table 1, the 0.25% Nd-TiO_2(HT) sample exhibited crystals that are roughly half the size, which increases the number of quenching processes of Nd^{3+} on the NP surfaces. The emission of NPs is more sensitive to interactions with the surrounding environment as a larger fraction of Nd^{3+} ions can be placed on the surface in comparison to bulk material. What is more, the surface of NPs usually exhibits more defects than, which also affects the luminescence [43]. The XPS results showed a lower concentration of Nd^{3+} ions in the sample prepared by the HT method, which may be another factor responsible for its reduced emission (see below in Table 2). Furthermore, the carbon content determined by XPS is the highest for the 0.25% Nd-TiO_2(HT) sample. Hence, organic impurities might be considered as another factor quenching the luminescence of Nd^{3+} ions. The Nd^{3+}-doped samples were also irradiated with 590, 750 and 808 nm laser light, however up-conversion luminescence was not detected. The Nd^{3+} ions have dense packaged energy levels, which limits the possible efficiency of up-conversion processes [20]. To obtain up-conversion of Nd^{3+} ions, good crystallization of the host material, revealing also low phonon energy is required [20]. The presence of Nd^{3+} ions in the Nd_2O_3 phase or in an environment that is highly defected and contaminated by organic impurities can also hinder the up-conversion process or even make it impossible to occur.

Chemical composition

To correlate the surface properties with the photoactivity of the obtained Nd-TiO_2, the surface layer of pristine TiO_2 and Nd-modified TiO_2 prepared by SHT and HT methods was examined by XPS. The existence of the titanium, oxygen and carbon has been proven in all samples and the corresponding amounts as well as the chemical character are presented in Figure 6 and in Table 2 and Table 3. The presence of neodymium was confirmed in both types of Nd-modified samples.

Elemental surface composition and chemical character of detected elements were identified by using high-resolution (HR) XPS of the Ti 2p, O 1s, C 1s and Nd 4d orbitals. The chemical character of elements is similar to that reported in our previously published paper [23].

The neodymium content (in wt %) is consistent with the nominal amount of Nd introduced into the Nd-TiO_2 samples during preparation via the SHT method, while it is slightly lower in the sample obtained by the HT method (Table 2). Probably, the relatively large surface content of carbon species in the last sample results in a smaller Nd concentration (compare the C/Ti and Nd/Ti atomic concentration values in Table 2). The inspection of the XPS data in Table 3 reveals that the contribution of

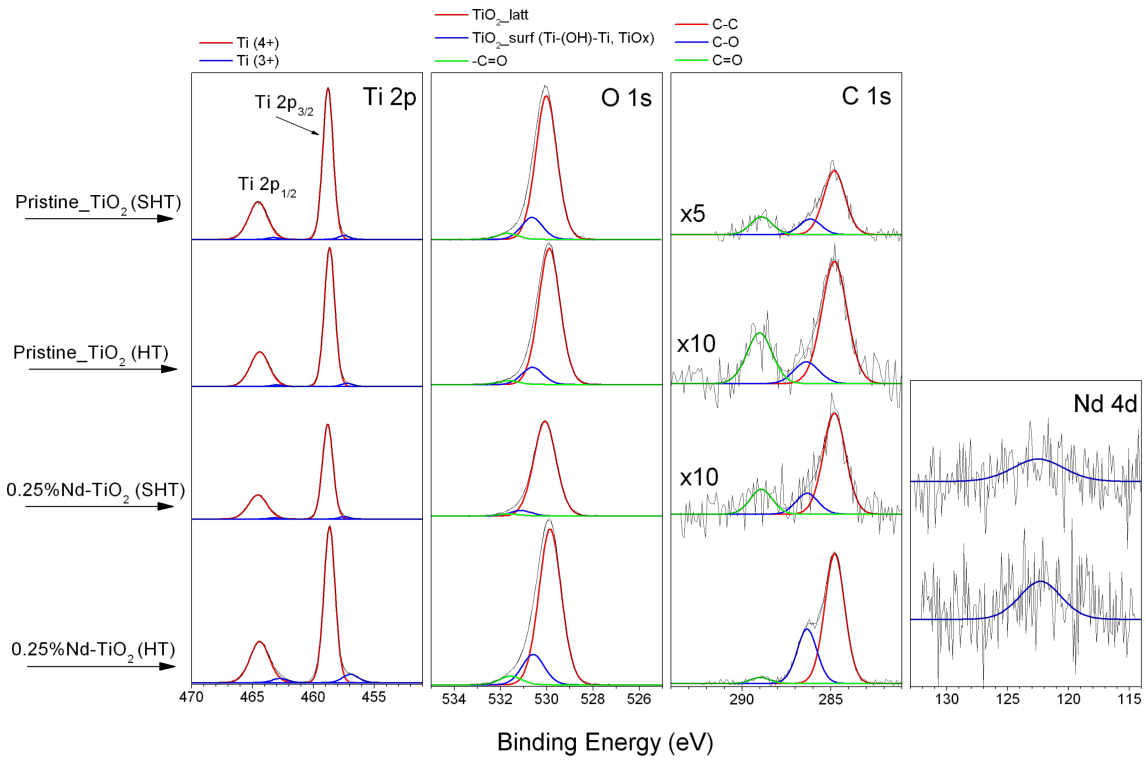

Figure 6: XPS spectra of pristine TiO_2 and Nd-modified TiO_2.

Table 2: Chemical composition of pristine and Nd-modified TiO_2 photocatalysts based on XPS analysis.

sample	Ti (wt %)	O (wt %)	C (wt %)	Nd (wt %)	C/Ti	Nd/Ti
pristine_TiO_2(SHT)	53.34	45.10	1.56	0	0.116	0
0.25% Nd-TiO_2(SHT)	54.01	44.84	0.89	0.24	0.065	0.0014
pristine_TiO_2(HT)	53.44	45.48	1.07	0	0.080	0
0.25% Nd-TiO_2(HT)	51.19	44.11	4.54	0.17	0.353	0.0012

Table 3: XPS analysis data for pristine and Nd-modified TiO_2.

sample	Ti fraction (%)		O fraction (%)			C fraction (%)		
	Ti(4+)	Ti(3+)	Ti–O_{latt}	Ti–O_{surf}	–C=O	C–C	C–OH	–C=O
pristine_TiO_2(SHT)	97.11	2.89	83.50	12.88	3.62	65.50	16.07	18.43
0.25% Nd-TiO_2(SHT)	97.48	2.52	92.59	5.40	2.01	68.80	14.25	16.95
pristine_TiO_2(HT)	97.31	2.69	86.58	10.96	2.46	62.62	11.21	26.17
0.25% Nd-TiO_2(HT)	92.74	7.26	79.83	15.63	4.54	68.13	28.66	3.21

Ti–O_{surf} (Ti–(OH)–Ti, TiO*x*) and C–OH fractions in the surface region of 0.25% Nd-TiO_2(HT) is larger than in other samples.

This clearly indicates the higher amount of hydroxy groups on the surface of the Nd-TiO_2 sample prepared via the HT method. The presence of the Ti–O_{surf} species can initiate the formation of Ti–O–Nd bonds. In addition, the Ti^{3+} fraction in the surface region of the 0.25% Nd-TiO_2(HT) sample is significantly larger than in the corresponding 0.25% Nd-TiO_2(SHT) sample (Table 3). The XPS data correspond well with the highest photocatalytic activity exhibited by the 0.25% Nd-TiO_2 photocata-

lyst prepared via HT method (described in detail in the next section).

Photocatalytic properties

The photocatalytic properties of pristine and Nd-modified TiO_2 were investigated using the photocatalytic degradations of phenol in aqueous solution and of gaseous toluene. Kinetics and degradation rate of model pollutants are presented in Figure 7 and Table 4.

The photodegradation of phenol was performed in aqueous solution under UV–vis ($\lambda > 350$ nm) and vis ($\lambda > 420$ nm) light irradiation. The data showed that the photocatalytic activitiy of Nd-modified TiO_2 NPs were lower than that of pristine TiO_2 under UV–vis irradiation. The highest activity was observed for pristine TiO_2 prepared via the HT method, with the phenol degradation rate reaching 1.59 $\mu mol \cdot dm^{-1} \cdot min^{-1}$. In the case of Nd-modified samples, the photocatalysts prepared via the HT method also showed higher activity (the degradation rate was equal to 1.22 $\mu mol \cdot dm^{-1} \cdot min^{-1}$). It should be pointed out that samples prepared by the HT process revealed the highest inhibition of recombination of the photogenerated charge carriers (see Figure 4). The observed decrease of photocatalytic activity of Nd-modified TiO_2 is due to the presence of Nd^{3+} ions on the surface of the TiO_2 NPs, which lowered the excitation under UV irradiation. The UV irradiation does not yield sufficiently high energy of photons to penetrate deeper into the surface of the material [11]. This phenomenon can also be explained by the spectroscopic properties of rare earth ions. In our previous paper [23], it has been proven that Nd^{3+} ions are prone to cross-relaxation (energy migration between Nd^{3+} ions). Therefore, Nd^{3+} ions could absorb UV irradiation and emit energy in radiative transitions (luminescence). The photocatalytic properties of the as-prepared samples in the aqueous phase were also investigated under visible light irradiation (Figure 6b). The Nd-modified TiO_2 has the ability to degrade effectively phenol under visible light, while pristine TiO_2 shows only weak activity. The photocatalyst 0.25%Nd-TiO_2(HT) exhibited the highest photocatalytic activity with a phenol degradation rate of 0.62 $\mu mol \cdot dm^{-1} \cdot min^{-1}$. Moreover, the lower photocatalytic activity of Nd-TiO_2 sample prepared via the SHT method under UV–vis and vis irradiation (0.99 and 0.31 $\mu mol \cdot dm^{-1} \cdot min^{-1}$, respectively), is the consequence of a small amount of surface adsorbed hydroxy groups. A similar decrease of photoactivity for RE-modified TiO_2 was reported in our previous paper [24]. It was shown that photocatalysts prepared by the sol–gel method contain less OH groups than the powders obtained via the hydrothermal method, and the latter exhibited lower activity under UV–vis light irradiation. This behaviour was also observed by Tobaldi and co-workers [44]. They concluded that the overall photocatalytic activity is strongly influenced by surface hydroxyl groups helping to generate reactive oxygen species, such as hydroxyl radicals.

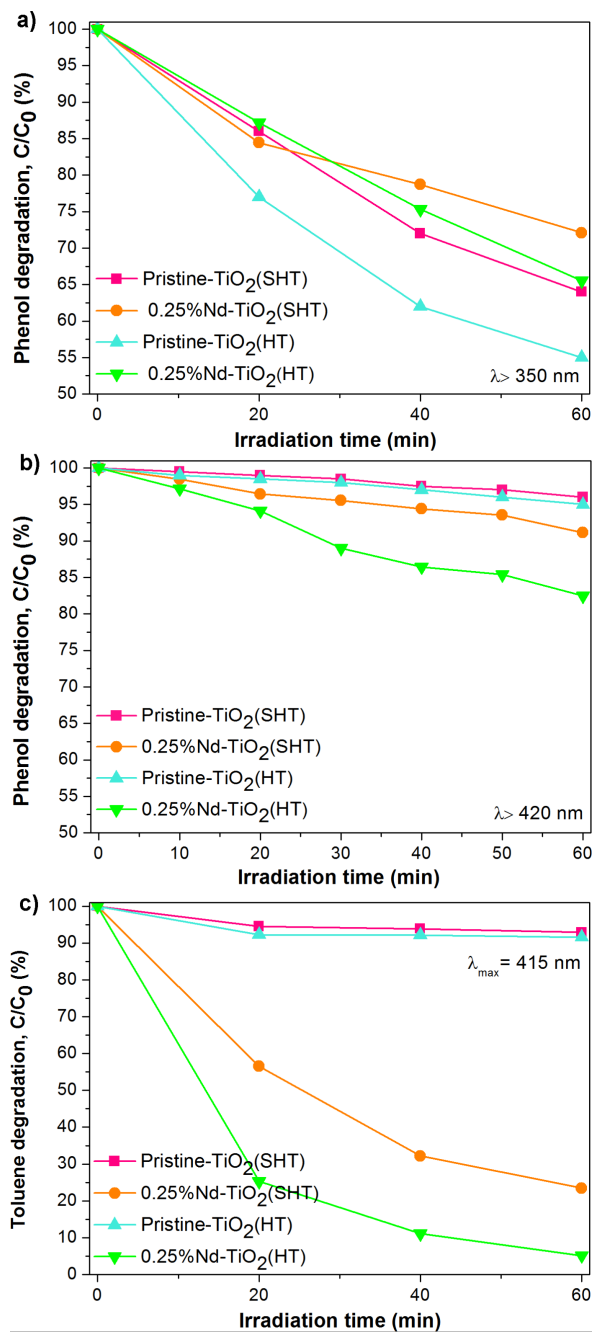

Figure 7: Photocatalytic activity of pristine and Nd-modified TiO_2 NPs. Degradation of phenol in aqueous solution under (a) UV–vis and (b) vis irradiation, and degradation of gaseous toluene under (c) vis irradiation.

The photocatalytic degradation of toluene was carried out under LED irradiation (λ_{max} = 415 nm). A high photocatalytic activity was exhibited by all the neodymium-modified photocatalysts (Figure 6c). The rate of toluene degradation was

Table 4: Photocatalytic activity under UV–vis and vis irradiation of pristine and Nd-modified TiO_2 photocatalysts.

sample label	toluene degradation rate (μmol·dm^{-1}·min^{-1}) under vis (λ_{max} = 415 nm) irradiation	phenol degradation rate (μmol·dm^{-1}·min^{-1})		phenol degradation rate (μmol·dm^{-1}·min^{-1}) with added scavenger under vis (λ > 420 nm) irradiation			
		under UV–vis (λ > 350 nm) irradiation	under vis (λ > 420 nm) irradiation	silver nitrate	ammonium oxalate	benzoquinone	*tert*-butanol
pristine-TiO_2(SHT)	0.25	1.28	0.14	—	—	—	—
0.25% Nd-TiO_2(SHT)	2.71	0.99	0.31	0.12	0.30	0.22	0.30
pristine-TiO_2(HT)	0.30	1.59	0.18	—	—	—	—
0.25% Nd-TiO_2(HT)	3.36	1.22	0.62	0.15	0.58	0.21	0.57

3.36 μmol·dm^{-1}·min^{-1} for HT-prepared TiO_2 modified with Nd, while the photodegradation efficiency decreased in SHT-prepared TiO_2 down to 2.71 μmol·dm^{-1}·min^{-1}. Pristine TiO_2 exhibits only low activity (Figure 6c). As photolysis of toluene was not observed and the toluene concentration decreased in the dark experiment by approximately 6.5% for all samples, probably pollutant was adsorbed on the surface of TiO_2 and on the walls of the reactor. A correlation between photocatalytic activity measured in both model reactions and the BET surface area was not observed. Based on XPS analysis, it can be seen that photocatalysts prepared via the HT method had a higher amount of hydroxy groups on the surface than those obtained by the SHT method. The hydroxy groups can act as adsorption centres on which the degradation of pollutants takes place [45]. Moreover, a high amount of oxygen vacancies and defects was found on the surface of the 0.25% Nd-TiO_2(HT) sample. As previously mentioned, the presence of oxygen deficient centres on the surface and surface defects such as Ti^{3+} can reduce the rate of electron–hole pair recombination [45-47]. Further, the light adsorption ability could be strongly related to the band-gap structure, which is affected by defects. With a reduced band gap or addition of sub-bands, TiO_2 can respond to visible light, increasing its light absorption efficiency [48]. A schematic illustration showing impact of the preparation methods on the surface properties and the charge carrier recombination processes is presented in Figure 8.

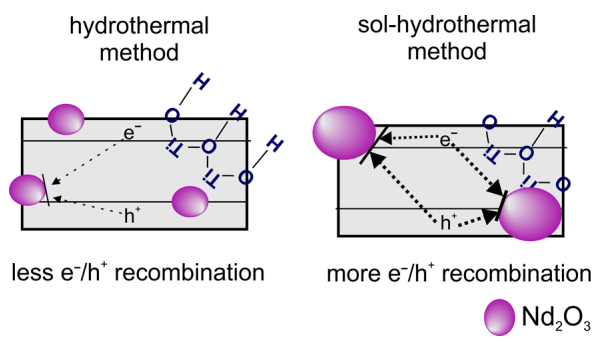

Figure 8: Schematic illustration showing the impact of preparation methods on the surface properties and the charge carrier recombination processes.

The results of the photodegradation significant differences between aqueous solution and gas phase. The quantum yield of

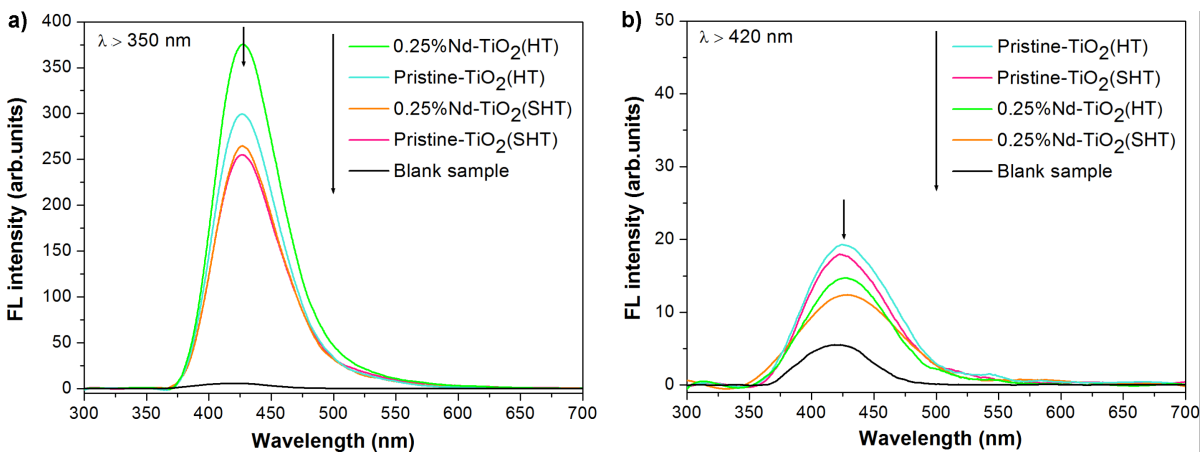

Figure 9: Fluorescence spectral changes in a solution of terephthalic acid under (a) UV–vis (λ > 350 nm) and (b) vis (λ > 420 nm) light irradiation.

the reaction in the gas phase is much higher than that one in aqueous solution due to lower light scattering. Also, a lower irradiation intensity is required to perform the photocatalytic reaction in the gas phase [8,49].

Degradation mechanism

Based on the obtained results, it can be stated that the Nd-modified TiO_2 could be effectively excited by irradiation with visible light. To explore which active species are responsible for the degradation of phenol under vis irradiation, hydroxyl radical generation tests with terephthalic acid (TPA) were performed. Figure 9 shows the fluorescence of 2-hydroxyterephthalic acid after 60 min in the presence of pristine and Nd-modified TiO_2 under UV–vis and vis light. The increase in intensity of the fluorescent peak indicates the formation of $^{\bullet}OH$ radicals produced in the aqueous solution.

As shown in Figure 9a, the presence of Nd^{3+} increases the intensity of the peaks. This indicates that Nd^{3+} effectively leads to an increase in the production of hydroxyl radicals on the surface of the photocatalysts under UV–vis light irradiation. Moreover, the obtained results showed that the intensity of the FL spectra increases for the HT series of photocatalysts. The obtained results correlate with photocatalytic activity under UV–vis light. It should be mentioned that the number of hydroxyl radicals is increased under the influence of UV–vis irradiation in the presence of Nd-modified TiO_2 compared to pristine TiO_2. However, the observed efficiency of phenol degradation in presence of Nd-TiO_2 was much lower. The difference is caused by the different reaction paths of phenol photodegradation and formation of 2-hydroxyterephthalic acid from TPA through generated $^{\bullet}OH$ radicals. Based on the available literature, the TPA formation depends only on the amount of $^{\bullet}OH$ radicals generated at the surface of the excited semiconductor. The phenol degradation can result from: (i) the reaction of $^{\bullet}OH$ with phenol, (ii) the reaction of phenol with photogenerated holes in TiO_2, and (iii) by direct oxidation of phenol through oxygen dissolved in water [50]. When the TPA test was carried out under vis irradiation (Figure 9b), the FL intensity was close to zero for all samples. Based on the presented results it can be stated that the modification of TiO_2 with Nd ions does not increase the production of hydroxyl radicals under visible light irradiation. According to our previous paper, the photodegradation of phenol under vis light irradiation occurs through the other forms of reactive oxygen species such as $O_2^{\bullet-}$, $HO_2^{\bullet}$ and H_2O_2 [8,23].

In order to better understand which reactive oxygen species may be important in the photocatalytic process, the photocatalytic activity tests in aqueous solution have been carried out in the presence of Nd-TiO_2 and different scavengers (Figure 10).

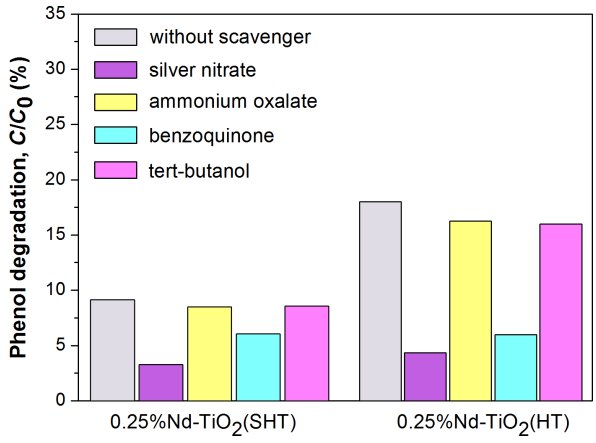

Figure 10: Photocatalytic decomposition of phenol in the presence of Nd-modified TiO_2 and scavengers after 60 min of visible (λ > 420 nm) irradiation.

Silver nitrate was used as electron scavenger, ammonium oxalate as hole scavenger, benzoquinone for $O_2^{\bullet-}$ and *tert*-butanol for $^{\bullet}OH$ radicals. After 60 min of visible light irradiation in the presence of SHT photocatalyst, the degradation rate declined from 0.31 to 0.30 $\mu mol \cdot dm^{-1} \cdot min^{-1}$ due to addition of ammonium oxalate and *tert*-butanol (Table 4). While, after the addition of silver nitrate and benzoquinone, the degradation rate decreased from 0.31 to 0.12 and 0.22 $\mu mol \cdot dm^{-1} \cdot min^{-1}$, respectively, suggesting that photogenerated electrons and superoxide radicals are the main active species responsible for the degradation of the model pollutants. In the presence of HT photocatalyst with scavengers similar phenomena were observed. The photocatalytic system with added ammonium oxalate and *tert*-butanol showed congruous degradation rates (0.58 and 0.57 $\mu mol \cdot dm^{-1} \cdot min^{-1}$, respectively) compared to the system without scavengers (0.62 $\mu mol \cdot dm^{-1} \cdot min^{-1}$), suggesting a limited role played by holes in the photocatalytic process. The addition of silver nitrate and benzoquinone significantly reduced the phenol degradation rate (from 0.62 to 0.15 and 0.21 $\mu mol \cdot dm^{-1} \cdot min^{-1}$, respectively), indicating that superoxide radical is the major active species in this system. These experiments also showed that for the photodegradation of phenol with the photocatalyst prepared via HT method, a larger suppression was noted upon the addition of benzoquinone, compared to the photocatalyst prepared via SHT method. This suggests that 0.25% Nd-TiO2(HT) generates a bigger amount of $O_2^{\bullet-}$. The reaction of electrons in the conduction band of TiO_2 is probably responsible for the formation of $O_2^{\bullet-}$. Electrons from the conduction band of TiO_2, generated by the excitation of the Nd^{3+}, migrate to the surface of the semiconductor where they are involved in the formation of $O_2^{\bullet-}$ and then H_2O_2 and $HO_2^{\bullet}$, as presented in the following reactions [8]:

$$\text{Nd-modified TiO}_2 + h\nu \longrightarrow e^-$$
$$e^- + O_2 \longrightarrow O_2^{\bullet -}$$
$$e^- + O_2^{\bullet -} + 2H^+ \longrightarrow H_2O_2$$
$$O_2^{\bullet -} + H^+ \longrightarrow HO_2^{\bullet}$$
$$O_2^{\bullet -}, H_2O_2, HO_2^{\bullet} + \text{phenol/toluene} \longrightarrow \text{byproducts} + CO_2 + H_2O.$$

The proposed photocatalytic mechanism under visible light can be explained by the energy diagram shown in Figure 11.

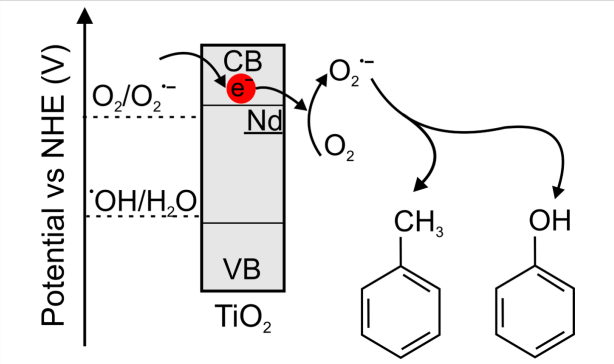

Figure 11: Proposed photocatalytic mechanism of Nd-modified TiO_2 under visible light.

Conclusion

We have observed how the spectroscopic properties of Nd^{3+} ions on the surface of TiO_2 NPs can be conveniently exploited for a variety of environmental purification processes. We presented the experimental studies concerning the effect of synthesis methods on the photocatalytic activity of Nd-modified TiO_2. Nanocrystalline anatase-phase TiO_2 NPs were successfully prepared via hydrothermal and sol–hydrothermal methods. Both Nd-modified samples can achieve the photocatalytic degradation of phenol and toluene under visible light, and Nd-TiO_2 has a higher activity than pristine TiO_2 (2.25- and 6.3-times higher activity for 0.25% Nd-TiO_2(SHT), and 3.6- and 7.1-times higher activity for 0.25% Nd-TiO_2(HT), respectively). This is mainly due to the increase of the BET surface area, the decrease of the anatase crystallite size and the prevention of recombination of charge carriers. The surface properties of the Nd-TiO_2 NPs obtained via hydrothermal method yield a significantly higher photocatalytic activity compared to Nd-TiO_2 NPs prepared via sol–hydrothermal process. The photocatalyst prepared via HT method has three times more hydroxy groups on its surface layer and a two times higher amount of surface defects than the powder obtained by SHT method. According to the photocatalytic degradation experiments, the Nd-modified TiO_2 photocatalyst preparated via HT method can be effectively used for air purification using LED irradiation (the degradation rate of toluene reached 3.36 μmol·dm^{-1}·min^{-1}). Furthermore, photocatalytic activity test in the presence of Nd-TiO_2 and scavengers confirm that superoxide radicals were responsible for the visible-light degradation of the model pollutant in aqueous solution.

Experimental

Materials

Titanium(IV) butoxide (97%, TBOT) and $Nd(NO_3)_3{\cdot}6H_2O$ (99.99%) were purchased from Sigma-Aldrich, Poland. Nitric acid (65%) and hydrochloric acid (31–38%) were purchased from STANLAB, Poland. Ethanol, phenol and terephthalic acid were purchased from POCh S.A, Poland. P25 from Evonik, Germany was used as a standard and for comparison of the photocatalytic activity. Deionised water (0.05 μS) was used for all reactions and treatment processes. All the chemicals were used as received without further purification.

Preparation of Nd-TiO_2

Nd-TiO_2 NPs were synthesized by two methods, i.e., hydrothermal (HT) and sol–hydrothermal (SHT).

HT method

In a typical procedure, 15 mL of TBOT was dissolved in 80 mL of ethanol. Then, 40 mL water (pH 3 adjusted with HCl) was added dropwise. Next, a certain amount of solid $Nd(NO_3)_3{\cdot}6H_2O$ was added. The mixture was stirred for 30 min at room temperature and treated at 180 °C for 6 h in a 200 mL autoclave.

SHT method

In the first step, 24 mL TBOT was dissolved in 48 mL ethanol (solution A), and stirred for 15 min. Then, to 48 mL ethanol, 20 mL water, and 1.90 mL HNO_3 was added a certain amount of solid $Nd(NO_3)_3{\cdot}6H_2O$ (solution B). In the next step, solution B was added to solution A dropwise and stirred for 30 min at room temperature. The obtained sol was treated at 160 °C for 3 h in a 200 mL autoclave.

The samples obtained from both methods were separated by centrifugation, washed three times with deionised water and ethanol, and dried at 35 °C for 16 h and ground. Crystallization of titania was performed at a temperature of 450 °C for 2 h in a muffle furnace under air atmosphere with a heating rate of 2 °C/min followed by grinding to obtain the Nd-TiO_2 powders. For comparison, TiO_2 without Nd was prepared likewise. A description of the prepared photocatalysts is shown in Table 1.

Characterization of Nd-TiO_2

X-ray diffraction (XRD) was used to determine and verify the crystalline structure of the obtained photocatalysts. XRD

patterns were recorded on a Rigaku diffractometer (RINT Ultima+) equipped with a graphite monochromator using Cu Kα radiation (40 kV tube voltage and 20 mA tube current). Measurements were performed in a 2θ range of 5–90°. Based on the results obtained, the particle sizes of photocatalysts and XRD data were calculated using the Scherrer equation.

Nitrogen adsorption–desorption isotherms were measured at −196 °C (liquid nitrogen temperature) using a Micromeritics Gemini V (model 2365). The surface area was determined according to the standard Brunauer–Emmet–Teller (BET) method. All samples were degassed at 200 °C prior to nitrogen adsorption measurements.

The morphology of obtained Nd-TiO_2 was determined using scanning electron microscopy (SEM, FEI Quanta 250 FEG).

UV–vis diffuse reflectance spectra of the synthesized materials were recorded in the range of 200–850 nm with a scanning speed of 200 nm/min at room temperature using a Shimadzu UV–vis spectrophotometer (UV 2600) equipped with an integrating sphere. $BaSO_4$ was used as the reference.

Photoluminescence (PL) properties in the range of 300–700 nm were measured on a Perkin Elmer limited LS50B spectrophotometer equipped with a xenon discharge lamp as an excitation source and an R928 photomultiplier as a detector. The spectra were recorded with an excitation wavelength of 315 nm directed on the sample surface at an angle of 90°. PL spectra in the range covering Nd^{3+} emission (550–1000 nm) were measured with a Princeton Instrument PIXIS:256E digital CCD camera, equipped with a SP-2156 Imaging Spectrograph and an Opolette 355LD UVDM tunable laser as the excitation source.

X-ray photoelectron spectroscopy (XPS) measurements were used for chemical characterization of the Nd-TiO_2 composites surface. The high-resolution (HR) XPS spectra were recorded on PHI 5000 VersaProbe (ULVAC-PHI) spectrometer with monochromatic Al Kα radiation ($h\nu$ = 1486.6 eV). The binding energy (BE) scales of all detected HR spectra were calibrated by centering the aliphatic carbon peak (C–C) at 284.8 eV.

Measurement of photocatalytic activity

The photocatalytic activity of the obtained Nd-TiO_2 samples was studied in two model processes, namely decomposition of phenol in aqueous solution and degradation of gaseous toluene. In addition, to determine which reactive oxygen species participate in the degradation mechanism, a hydroxyl radical test using terephthalic acid and a reactive oxygen species formation test using benzoquinone, silver nitrate, ammonium oxalate and *tert*-butanol as scavengers were carried out.

Measurements of phenol decomposition and generation of $^{\bullet}OH$ radicals were carried out for two irradiation ranges, UV–vis (λ > 350 nm) and vis (λ > 420 nm), while scavenger test was carried under vis (λ > 420 nm) light irradiation, using a 1000 W Xenon lamp (Oriel 66021). The optical path included a water filter to cut off IR irradiation. For the test of UV–vis and vis light-induced activity the light beam passed through GG350 or GG420 filters to cut-off wavelengths shorter than 350 or 420 nm, respectively. The experimental procedure was as follows: Nd-TiO_2 powder (125 mg) was suspended in aqueous solutions of phenol (0.21 mM) or terephthalic acid (0.5 mM) or in an aqueous solution of scavenger and phenol in a quartz photoreactor (working volume of about 25 mL). After 30 min of mixing (550 rpm) and aeration (5 dm^3/h) in the dark, the suspension was irradiated with a cut-off spectrum of light. The temperature of the suspension during photoirradiation was maintained at 10 °C using a thermostatically controlled water bath (to avoid the stripping process). Samples of 0.5 mL reaction mixture were collected after regular time periods during irradiation and filtered through syringe filters (diameter 0.2 μm) to remove the suspended photocatalyst particles. Kinetics of phenol degradation were determined by high-performance liquid chromatography (HPLC, Shimadzu). The HPLC system was equipped with a Kinetex C18 column (150 mm × 3 mm; particle size of 2.6 μm; pore diameter 100 Å) and the SPD-M20A diode array detector (λ = 205 nm). The flow rate was maintained at 0.4 mL/min with a mobile phase composed of acetonitrile and water (7.5/92.5 v/v). The injection volume was 30 μL. For fluorescnece measurements, 2 mL of the reaction mixture of terephthalic acid were collected after 60 min irradiation and filtered through syringe filters (diameter 0.2 μm) to remove the suspended photocatalyst particles. Fluorescence spectra were measured at room temperature using a Perkin Elmer limited LS50B spectrophotometer equipped with a xenon discharge lamp as an excitation source and an R928 photomultiplier as a detector. The obtained solution was measured with an excitation wavelength of 315 nm.

Decomposition of toluene in the gas phase was carried out in a flat stainless steel reactor with the working volume of about 35 mL equipped with a quartz window, two valves and a septum. An array of five LEDs (λ_{max} = 415 nm) was used as an irradiation source. A glass plate covered by Nd-modified TiO_2 was placed at the bottom side of the reactor followed by closing the reactor with a quartz window. Subsequently, the gaseous mixture was passed through the reaction chamber for 1 min. After closing the valves, the reactor was kept in dark for 30 min in order to achieve adsorption equilibrium. A reference of 200 μL sample was taken just before starting irradiation and further samples were collected after regular time periods during irradiation. The analysis of toluene concentration in the gas

phase was performed using a gas chromatograph (Trace 1300, Thermo Scientific) equipped with a flame ionization detector (FID) and Elite-5 capillary column.

Acknowledgements

This research was financially supported by Polish National Science Centre (grant No. NCN 2015/17/D/ST5/01331 and No. NCN 2017/24/T/ST5/00221) and supported by the Foundation for Polish Science (FNP).

ORCID® iDs

Patrycja Parnicka - https://orcid.org/0000-0002-2953-2663
Paweł Mazierski - https://orcid.org/0000-0002-8674-0151
Tomasz Grzyb - https://orcid.org/0000-0002-2947-6366
Ewa Kowalska - https://orcid.org/0000-0003-0955-9268
Adriana Zaleska-Medynska - https://orcid.org/0000-0003-3817-296X
Joanna Nadolna - https://orcid.org/0000-0001-7933-6663

References

1. Kowalska, E.; Janczarek, M.; Rosa, L.; Juodkazis, S.; Ohtani, B. *Catal. Today* **2014,** *230,* 131–137. doi:10.1016/j.cattod.2013.11.021
2. Scuderi, V.; Zimbone, M.; Miritello, M.; Nicotra, G.; Impellizzeri, G.; Privitera, V. *Beilstein J. Nanotechnol.* **2017,** *8,* 190–195. doi:10.3762/bjnano.8.20
3. Klein, M.; Nadolna, J.; Gołabiewska, A.; Mazierski, P.; Klimczuk, T.; Remita, H.; Zaleska-Medynska, A. *Appl. Surf. Sci.* **2016,** *378,* 37–48. doi:10.1016/j.apsusc.2016.03.191
4. Leong, K. H.; Chu, H. Y.; Ibrahim, S.; Saravanan, P. *Beilstein J. Nanotechnol.* **2015,** *6,* 428–437. doi:10.3762/bjnano.6.43
5. Lu, D.; Yang, M.; Fang, P.; Li, C.; Jiang, L. *Appl. Surf. Sci.* **2017,** *399,* 167–184. doi:10.1016/j.apsusc.2016.12.077
6. Fujishima, A.; Honda, K. *Nature* **1972,** *238,* 37–38. doi:10.1038/238037a0
7. Zaleska, A. *Recent Pat. Eng.* **2008,** *2,* 157–164. doi:10.2174/187221208786306289
8. Mazierski, P.; Lisowski, W.; Grzyb, T.; Winiarski, M. J.; Klimczuk, T.; Mikołajczyk, A.; Flisikowski, J.; Hirsch, A.; Kołakowska, A.; Puzyn, T.; Zaleska-Medynska, A.; Nadolna, J. *Appl. Catal., B: Environ.* **2017,** *205,* 376–385. doi:10.1016/j.apcatb.2016.12.044
9. Mazierski, P.; Nadolna, J.; Nowaczyk, G.; Lisowski, W.; Winiarski, M. J.; Klimczuk, T.; Kobylański, M. P.; Jurga, S.; Zaleska-Medynska, A. *J. Phys. Chem. C* **2017,** *121,* 17215–17225. doi:10.1021/acs.jpcc.7b03895
10. Reszczynska, J.; Esteban, D. A.; Gazda, M.; Zaleska, A. *Physicochem. Probl. Miner. Process.* **2014,** *50,* 515–524. doi:10.5277/ppmp140208
11. Reszczyńska, J.; Grzyb, T.; Sobczak, J. W.; Lisowski, W.; Gazda, M.; Ohtani, B.; Zaleska, A. *Appl. Surf. Sci.* **2014,** *307,* 333–345. doi:10.1016/j.apsusc.2014.03.199
12. Reszczynska, J.; Iwulska, A.; Sliwinski, G.; Zaleska, A. *Physicochem. Probl. Miner. Process.* **2012,** *48,* 201–208.
13. Dominguez, R. D.; Alarcón-Flores, G.; Aguilar-Frutis, M.; Sánchez-Alarcón, R. I.; Falcony, C.; Dorantes-Rosales, H. J.; González-Velázquez, J. L.; Rivas-López, D. I. *J. Alloys Compd.* **2016,** *687,* 121–129. doi:10.1016/j.jallcom.2016.06.083
14. Reszczyńska, J.; Grzyb, T.; Sobczak, J. W.; Lisowski, W.; Gazda, M.; Ohtani, B.; Zaleska, A. *Appl. Catal., B: Environ.* **2015,** *163,* 40–49. doi:10.1016/j.apcatb.2014.07.010
15. Trujillo-Navarrete, B.; Haro-Vázquez, M. d. P.; Félix-Navarro, R. M.; Paraguay-Delgado, F.; Alvarez-Huerta, H.; Pérez-Sicairos, S.; Reynoso-Soto, E. A. *J. Rare Earths* **2017,** *35,* 259–270. doi:10.1016/S1002-0721(17)60909-8
16. Grzyb, T.; Tymiński, A. *J. Alloys Compd.* **2016,** *660,* 235–243. doi:10.1016/j.jallcom.2015.11.122
17. Tymiński, A.; Grzyb, T. *J. Lumin.* **2017,** *181,* 411–420. doi:10.1016/j.jlumin.2016.09.028
18. Grzyb, T.; Gruszeczka, A.; Lis, S. *J. Lumin.* **2016,** *175,* 21–27. doi:10.1016/j.jlumin.2016.02.021
19. Dias, J. D. M.; Melo, G. H. A.; Lodi, T. A.; Carvalho, J. O.; Façanha Filho, P. F.; Barboza, M. J.; Steimacher, A.; Pedrochi, F. *J. Rare Earths* **2016,** *34,* 521–528. doi:10.1016/S1002-0721(16)60057-1
20. Ramakrishna, P. V.; Pammi, S. V. N.; Samatha, K. *Solid State Commun.* **2013,** *155,* 21–24. doi:10.1016/j.ssc.2012.10.043
21. Castañeda-Contreras, J.; Marañón-Ruiz, V. F.; Chiu-Zárate, R.; Pérez-Ladrón de Guevara, H.; Rodriguez, R.; Michel-Uribe, C. *Mater. Res. Bull.* **2012,** *47,* 290–295. doi:10.1016/j.materresbull.2011.11.021
22. Wang, J.; Xie, Y.; Zhang, Z.; Li, J.; Chen, X.; Zhang, L.; Xu, R.; Zhang, X. *Sol. Energy Mater. Sol. Cells* **2009,** *93,* 355–361. doi:10.1016/j.solmat.2008.11.017
23. Parnicka, P.; Mazierski, P.; Grzyb, T.; Wei, Z.; Kowalska, E.; Ohtani, B.; Klimczuk, T.; Nadolna, J. *J. Catal.* **2017,** *353,* 211–222. doi:10.1016/j.jcat.2017.07.017
24. Reszczyńska, J.; Grzyb, T.; Wei, Z.; Klein, M.; Kowalska, E.; Ohtani, B.; Zaleska-Medynska, A. *Appl. Catal., B: Environ.* **2016,** *181,* 825–837. doi:10.1016/j.apcatb.2015.09.001
25. Sun, D.; Wang, K.; Xu, Z.; Li, R. *J. Rare Earths* **2015,** *33,* 491–497. doi:10.1016/S1002-0721(14)60446-4
26. Qin, Y.; Hu, Z.; Lim, B. H.; Chang, W. S.; Chong, K. K.; Zhang, P.; Zhang, H. *J. Alloys Compd.* **2016,** *686,* 803–809. doi:10.1016/j.jallcom.2016.06.179
27. Liu, Y.; Fang, P.; Cheng, Y.; Gao, Y.; Chen, F.; Liu, Z.; Dai, Y. *Chem. Eng. J.* **2013,** *219,* 478–485. doi:10.1016/j.cej.2012.12.098
28. Zhang, H.; Sheng, Y.; Song, Y.; Li, H.; Huang, J.; Zheng, K.; Huo, Q.; Xu, X.; Zou, H. *Powder Technol.* **2013,** *239,* 403–408. doi:10.1016/j.powtec.2013.02.010
29. Cacciotti, I.; Bianco, A.; Pezzotti, G.; Gusmano, G. *Chem. Eng. J.* **2011,** *166,* 751–764. doi:10.1016/j.cej.2010.07.008
30. Yuan, M.; Zhang, J.; Yan, S.; Luo, G.; Xu, Q.; Wang, X.; Li, C. *J. Alloys Compd.* **2011,** *509,* 6227–6235. doi:10.1016/j.jallcom.2011.03.010
31. Thomas, J.; Radhika, S.; Yoon, M. *J. Mol. Catal. A: Chem.* **2016,** *411,* 146–156. doi:10.1016/j.molcata.2015.10.021
32. Luo, X.; Zhu, S.; Wang, J.; Wang, C.; Wu, M. *Int. J. Environ. Res. Public Health* **2017,** *14,* 1471. doi:10.3390/ijerph14121471
33. Qu, X.; Yan, X.; Hou, Y.; Wang, P.; Song, H.; Du, F. *J. Sol-Gel Sci. Technol.* **2015,** *76,* 699–707. doi:10.1007/s10971-015-3823-0
34. Wojcieszak, D.; Mazur, M.; Kurnatowska, M.; Kaczmarek, D.; Domaradzki, J.; Kepinski, L.; Chojnacki, K. *Int. J. Photoenergy* **2014,** *2014,* No. 463034. doi:10.1155/2014/463034
35. Xie, Y.; Yuan, C.; Li, X. *Colloids Surf., A* **2005,** *252,* 87–94. doi:10.1016/j.colsurfa.2004.10.061

36. Nassoko, D.; Li, Y.-F.; Li, J.-L.; Li, X.; Yu, Y. *Int. J. Photoenergy* **2012,** *2012,* No. 716087. doi:10.1155/2012/716087
37. Kasim, A. Absorption and upconversion of (Nd3+/Er3+) doped tellurite glass. In *2012 IEEE Business Engineering and Industrial Applications Colloquium (BEIAC),* Kuala Lumpur, Malaysia, April 7–8, 2012; IEEE Publishing: Piscataway, NJ, U.S.A., 2012; pp 38–42. doi:10.1109/BEIAC.2012.6226090
38. Khalid, N. R.; Ahmed, E.; Hong, Z.; Zhang, Y.; Ullah, M.; Ahmed, M. *Ceram. Int.* **2013,** *39,* 3569–3575. doi:10.1016/j.ceramint.2012.10.183
39. Raja, R.; Govindaraj, M.; Antony, M. D.; Krishnan, K.; Velusamy, E.; Sambandam, A.; Subbaiah, M.; Rayar, V. W. *J. Solid State Electrochem.* **2017,** *21,* 891–903. doi:10.1007/s10008-016-3437-7
40. Liqiang, J.; Xiaojun, S.; Baifu, X.; Baiqi, W.; Weimin, C.; Honggang, F. *J. Solid State Chem.* **2004,** *177,* 3375–3382. doi:10.1016/j.jssc.2004.05.064
41. Balabhadra, S.; Debasu, M. L.; Brites, C. D. S.; Nunes, L. A. O.; Malta, O. L.; Rocha, J.; Bettinelli, M.; Carlos, L. D. *Nanoscale* **2015,** *7,* 17261–17267. doi:10.1039/c5nr05631d
42. Li, H.; Wang, G.; Zhang, L.; Huang, Y.; Wang, G. *CrystEngComm* **2010,** *12,* 1307–1310. doi:10.1039/B914641E
43. Tian, Y.; Tian, B.; Cui, C.; Huang, P.; Wang, L.; Chen, B. *RSC Adv.* **2015,** *5,* 14123–14128. doi:10.1039/C4RA13204A
44. Tobaldi, D. M.; Pullar, R. C.; Škapin, A. S.; Seabra, M. P.; Labrincha, J. A. *Mater. Res. Bull.* **2014,** *50,* 183–190. doi:10.1016/j.materresbull.2013.10.033
45. Araña, J.; Alonso, A. P.; Rodríguez, J. M. D.; Colón, G.; Navío, J. A.; Peña, J. P. *Appl. Catal., B: Environ.* **2009,** *89,* 204–213. doi:10.1016/j.apcatb.2008.11.027
46. Kongsuebchart, W.; Praserthdam, P.; Panpranot, J.; Sirisuk, A.; Supphasrirongjaroen, P.; Satayaprasert, C. *J. Cryst. Growth* **2006,** *297,* 234–238. doi:10.1016/j.jcrysgro.2006.09.018
47. Tryba, B.; Tygielska, M.; Colbeau-Justin, C.; Kusiak-Nejman, E.; Kapica-Kozar, J.; Wróbel, R.; Żołnierkiewicz, G.; Guskos, N. *Mater. Res. Bull.* **2016,** *84,* 152–161. doi:10.1016/j.materresbull.2016.07.035
48. Zhao, H.; Pan, F.; Li, Y. *J. Materiomics* **2017,** *3,* 17–32. doi:10.1016/j.jmat.2016.12.001
49. Mazierski, P.; Bajorowicz, B.; Grabowska, E.; Zaleska-Medynska, A. Photoreactor Design Aspects and Modeling of Light. In *Heterogeneous Photocatalysis: From Fundamentals to Green Applications;* Colmenares, J.; Xu, Y. J., Eds.; Springer: Berlin, Germany, 2016; pp 211–248. doi:10.1007/978-3-662-48719-8_7
50. Sobczyński, A.; Duczmal, L.; Zmudziński, W. *J. Mol. Catal. A: Chem.* **2004,** *213,* 225–230. doi:10.1016/j.molcata.2003.12.006

License and Terms

This is an Open Access article under the terms of the Creative Commons Attribution License (http://creativecommons.org/licenses/by/4.0), which permits unrestricted use, distribution, and reproduction in any medium, provided the original work is properly cited.

The license is subject to the *Beilstein Journal of Nanotechnology* terms and conditions: (https://www.beilstein-journals.org/bjnano)

The definitive version of this article is the electronic one which can be found at:
doi:10.3762/bjnano.9.43

BEILSTEIN JOURNAL OF NANOTECHNOLOGY

Fabrication and photoactivity of ionic liquid–TiO_2 structures for efficient visible-light-induced photocatalytic decomposition of organic pollutants in aqueous phase

Anna Gołąbiewska[1], Marta Paszkiewicz-Gawron[1], Aleksandra Sadzińska[2], Wojciech Lisowski[3], Ewelina Grabowska[1], Adriana Zaleska-Medynska[*1] and Justyna Łuczak[*2]

Full Research Paper

Open Access

Address:
[1]University of Gdansk, Faculty of Chemistry, Department of Environmental Technology, Wita Stwosza 63, 80-308 Gdansk, Poland, [2]Gdansk University of Technology, Chemical Faculty, Department of Chemical Technology, Narutowicza 11/12, 80-233 Gdansk, Poland, and [3]Institute of Physical Chemistry, Polish Academy of Sciences, 01-224 Warsaw, Poland

Email:
Adriana Zaleska-Medynska* - adriana.zaleska@ug.gda.pl;
Justyna Łuczak* - justyna.luczak@pg.gda.pl

* Corresponding author

Keywords:
heterogeneous photocatalysis; ionic liquids; TiO_2; visible light catalysis

Beilstein J. Nanotechnol. **2018,** *9,* 580–590.
doi:10.3762/bjnano.9.54

Received: 10 October 2017
Accepted: 19 January 2018
Published: 14 February 2018

This article is part of the Thematic Series "Energy conversion, storage and environmental remediation using nanomaterials".

Guest Editor: W.-J. Ong

© 2018 Gołąbiewska et al.; licensee Beilstein-Institut.
License and terms: see end of document.

Abstract

To investigate the effect of the ionic liquid (IL) chain length on the surface properties and photoactivity of TiO_2, a series of TiO_2 microspheres have been synthesized via a solvothermal method assisted by 1-methyl-3-octadecylimidazolium chloride ([ODMIM][Cl]) and 1-methyl-3-tetradecylimidazolium chloride ([TDMIM][Cl]). All as-prepared samples were characterized by X-ray powder diffraction (XRD), X-ray photoelectron spectroscopy (XPS), diffuse reflectance spectroscopy (DRS), scanning transmission microscopy (STEM) and the Brunauer–Emmett–Teller (BET) surface area method, whereas the photocatalytic activity was evaluated by the degradation of phenol in aqueous solution under visible light irradiation ($\lambda > 420$ nm). The highest photoefficiency (four times higher than pristine TiO_2) was observed for the TiO_2 sample obtained in the presence of [TDMIM][Cl] for a IL to TiO_2 precursor molar ratio of 1:3. It was revealed that interactions between the ions of the ionic liquid and the surface of the growing titanium dioxide spheres results in a red-shift of absorption edge for the IL–TiO_2 semiconductors. In this regard, the direct increase of the photoactivity of IL–TiO_2 in comparison to pristine TiO_2 was observed. The active species trapping experiments indicated that $O_2^{\bullet-}$ is the main active species, created at the surface of the IL–TiO_2 material under visible-light illumination, and is responsible for the effective phenol degradation.

Introduction

The development of heterogeneous photocatalysis to degrade organic pollutants in aqueous and gas phases requires visible-light responsive, stable materials and a basic understanding of these materials [1-4]. Although various semiconductors are considered for environmental pollution abatement, titanium dioxide (TiO_2) is still the most promising due to its stability, low cost, nontoxicity and availability [5]. Despite many advantages, the commercial application of TiO_2 to solve environmental problems is still limited. The main obstacle is the relatively wide band gap of 3.2 eV for anatase that limits the photoexcitation wavelength needed to activate photocatalytic reactions to ultraviolet (UV) irradiation [6]. To break through the aforementioned drawbacks, semiconductor coupling [7], sensitization by inorganic complexes or organic dyes [8,9], as well as metal nanoparticle (NP) deposition [10] and metal doping [11] have been applied and have revealed potential to achieve visible-light-activated photocatalysts.

Another, actually surprising, way to improve the efficiency of solar-driven photocatalysis appeared in an application of ionic liquids (ILs) for TiO_2 preparation [12-14]. Sometimes referred to as "solvents of the future", ILs have induced a large and still growing interest from the scientific community and continuously find new areas of application. This scientific interest comes from the many interesting properties such as negligible vapor pressure, high thermal and electrochemical stability, and inflammability, providing a neoteric media for nano- and microstructure preparation with novel properties [15]. Especially, their polarity and affinity towards particles and precursors, transport and surface properties seem to be crucial for formation of the protective layer at the particle surface, thus electrosteric, solvation and viscous stabilization of growing particles [15-18].

The initial works on the application of ILs for semiconductor (including TiO_2) preparation were focused mainly on the usage of these salts as solvents (reaction medium) [19-21] or components of the reaction system [22-25]. Their role was devoted to control the crystallization process and formation of the final particle structure (structuring agent). In this regard, various interesting structures were obtained and their properties are described in the literature. However, the more advanced works presented examples of the practical usage of the IL–TiO_2 composites, for example, for photo-electrochemical water splitting [26,27], photo-oxidation of benzyl alcohol [12], phenol [28], degradation of chlorophenol [17,29], reduction of Cr^{6+} to Cr^{3+} [30] and the photocatalytic desulfurization of diesel oil [31]. Nevertheless, in most of these publications the photoactivity of TiO_2 was determined under UV–vis irradiation [17,26,27,29,31-35]. Much less attention, in contrast, has been paid towards the enhancement of the visible light photoactivity of TiO_2 by ILs and the elucidation of the role of ILs in the mode of action of photocatalysts [12,13,36-38]. Interestingly, in all mentioned publications [12,13,36-38] the same ionic liquid, 1-butyl-3-methylimidazolium tetrafluoroborate ([BMIM][BF_4]), was used. However, the proposed mechanisms were different. The photoactivity enhancement under visible-light irradiation was proposed to be due to: (i) doping of nonmetal elements (e.g., N, B, F) derived from the IL structure, inducing a narrower band gap and improving the separation efficiency of the photogenerated electron/hole pairs [13,36,37]; (ii) enhancement of Ti^{3+} species formation in the TiO_2 lattice (being a source of the electronic charge required for O_2 adsorption and intermediate energy level) [12,36]; (iii) promoting TiO_2 hollow structure formation, thereby shortening the diffusion length of the charge carriers as well as increasing the number of reactive sites [12]; and (iv) direct sensitization of TiO_2 photocatalysts [38]. The only exception is our previous work [14], where three ILs composed of 1-butyl-3-methylimidazolium cation [BMIM] and bromide, hexafluorophosphate [PF_6] and octylsulphate [$OctSO_4$] anions were used. In contrast to [BMIM][BF_4], the improved TiO_2 photoactivity under visible-light irradiation originated from the interaction of the bromide anion and molecular oxygen with the TiO_2 surface with formation of surface complex [14]. Therefore, taking into account the ease of modification of the cation and anion structure of the IL, and as a consequence, the altering of their physicochemical properties, the mechanism of the visible-light activity improvement may vary depending on the IL composition. However, the relation between the IL structure and visible-light photoactivity as well as its mode of action is still not known.

In this regard, in this comparative study, we have continued the elucidation of the role of the IL (alkyl chain length in the imidazolium cation) as well as the effect of the IL structure on the formation of TiO_2 photocatalysts with improved activity towards visible irradiation. The structures of the ILs used in this study, 1-methyl-3-tetradecylimidazolium ([TDMIM][Cl]) and 1-methyl-3-octadecylimidazolium chlorides ([ODMIM][Cl]), are shown in Figure 1. This study gave us better phenomenolog-

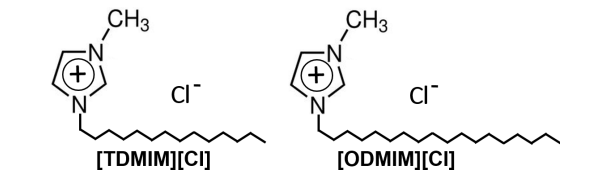

Figure 1: Structures of ionic liquids used in the ionic liquid assisted solvothermal synthesis of TiO_2–1-methyl-3-tetradecylimidazolium ([TDMIM][Cl]) and TiO_2–1-methyl-3-octadecylimidazolium chlorides ([ODMIM][Cl]).

ical insight into the performance of the IL–TiO_2 photocatalysts and better prospects for optimizing the IL of choice. The results form a part of a very broad, but hardly touched issue in the field of IL–TiO_2 composites, that is, which structural descriptors of ILs are crucial for the preparation of visible-light-active photocatalysts with desired morphology and properties and how to predict the properties of the IL–TiO_2 material on the basis of the structure and properties of IL.

Results and Discussion

Twelve novel TiO_2 photocatalysts prepared in the presence of two ionic liquids containing different alkyl chain lengths in the imidazolium cation ([ODMIM][Cl] and [TDMIM][Cl]) were obtained by the solvothermal method. All samples were prepared in six different molar ratios IL:TBOT (see Table 1). First of all, the samples were analyzed in terms of specific surface area, optical and photocatalytic properties (in a model reaction of phenol degradation in the aqueous phase under visible-light irradiation). The description of all prepared photocatalysts, including the selected physicochemical and photocatalytic properties, is shown in Table 1. To understand the nature of the visible-light-induced activity (IL:TBOT molar ratio equal to 1:3 and 1:10), the photocatalysts possessing the highest and lowest activity have been selected for further detailed study (SEM, XPS and XRD). Moreover, for the two samples with the highest photoactivity (TiO_2_T(1:3) and TiO_2_O(1:3)), the active species involved in the photocatalytic reaction were also determined.

Morphology and phase structure

The crystal structure of the selected IL–TiO_2 samples was characterized by XRD, as shown in Figure 2. The typical diffraction peaks corresponding to anatase phase of TiO_2 (2θ = 25.3°, 37.8°, 48.1°, 54°, 54.9°, 62.7°, 68.5°, 70.2°, 75°, 82.6°) were observed for all photocatalysts. The analysis confirmed that the samples do not contain any impurities and anatase phase of high quality was formed. Based on the line width analysis of the anatase (101) reflection peak, the average crystal size of the crystallites (*d*) forming photocatalysts with the highest (IL:TBOT molar ratio 1:3) and the lowest photoactivity (IL:TBOT molar ratio 1:10), estimated by the Scherrer equation, were determined and summarized in Table 2.

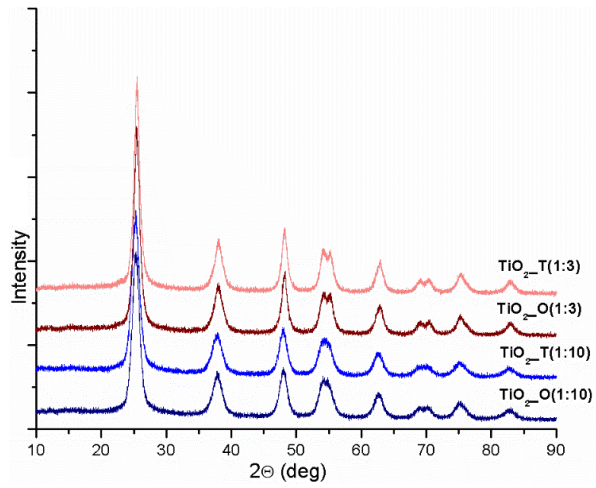

Figure 2: The X-ray diffraction patterns of composite TiO_2–IL photocatalysts.

The average crystal size values of the IL–TiO_2 composites generally increased with the addition of ILs in comparison to pristine TiO_2. This could suggest that the addition of ILs during the preparation of TiO_2 affects the growth of the anatase nanocrystals, forming microparticles. Similar results were reported by Li

Table 1: Specific surface area (S_{BET}), pore volume and the efficiency of phenol degradation after 60 min visible-light irradiation of the samples tested in this study.

Sample label	Ionic liquid	Molar ratio (IL:TBOT)	Specific surface area ($m^2 \cdot g^{-1}$)	Pore volume ($cm^3 \cdot g^{-1}$)	Efficiency of phenol degradation (%)
Pristine_TiO_2	–	–	199	0.10	14
TiO_2_T(1:10)	[TDMIM][Cl]	1:10	211	0.10	23
TiO_2_T(1:8)	[TDMIM][Cl]	1:8	178	0.08	59
TiO_2_T(1:5)	[TDMIM][Cl]	1:5	164	0.08	58
TiO_2_T(1:3)	[TDMIM][Cl]	1:3	156	0.06	61
TiO_2_T(1:2)	[TDMIM][Cl]	1:2	140	0.07	56
TiO_2_T(1:1)	[TDMIM][Cl]	1:1	119	0.05	45
TiO_2_O(1:10)	[ODMIM][Cl]	1:10	193	0.09	23
TiO_2_O(1:8)	[ODMIM][Cl]	1:8	184	0.09	53
TiO_2_O(1:5)	[ODMIM][Cl]	1:5	166	0.08	57
TiO_2_O(1:3)	[ODMIM][Cl]	1:3	157	0.07	59
TiO_2_O(1:2)	[ODMIM][Cl]	1:2	137	0.06	54
TiO_2_O(1:1)	[ODMIM][Cl]	1:1	122	0.05	49

Table 2: Lattice parameters and average crystallite size of the IL–TiO_2 photocatalysts. The values in parenthesis represent the error in measurement.

Sample label	*a* (Å)	*c* (Å)	*V* (Å^3)	*d* (Å)
TiO_2	3.7890(3)	9.497(1)	136.34(4)	63
TiO_2_O(1:10)	3.7816(1)	9.520(8)	136.15(3)	57
TiO_2_O(1:3)	3.7692(9)	9.522(8)	135.29(6)	78
TiO_2_T(1:10)	3.7760(8)	9.530(3)	135.89(1)	74
TiO_2_T(1:3)	3.7687(7)	9.518(2)	135.19(3)	81

et al. [37] who suggest that [BMIM][BF_4] acted as a growth inhibitor of the anatase crystal. The addition of ILs to the TiO_2 preparation route also influenced the length of the cell edges – a decrease of *a* and increase of *c* lengths in comparison to pristine TiO_2 was detected. These observations can be related to changes in the crystalline structure, i.e., generation of Ti^{3+} as will be described below in the next section. Comparing the IL–TiO_2 samples, the photocatalysts with the highest activity were characterized by the shorter length of both cell edges as well as the lowest cell volume (Table 2).

The surface morphology and microstructure of the IL–TiO_2 composites were characterized by SEM. The morphology of four selected samples prepared with different IL concentrations (IL:TBOT molar ratio equal to 1:3 and 1:10) which revealed the highest and the lowest photoactivity under visible-light irradiation is presented in Figure 3. The average size of the microspheres, calculated based on the statistical average size of 100 microstructures, is also included in this figure. The four main fractions of TiO_2 microspheres have been recognized. Generally, for all the samples, the dominant fraction were the microspheres with an average diameter ranging from 3 to 5 µm. Based on these results, as well as our previous study [28], we

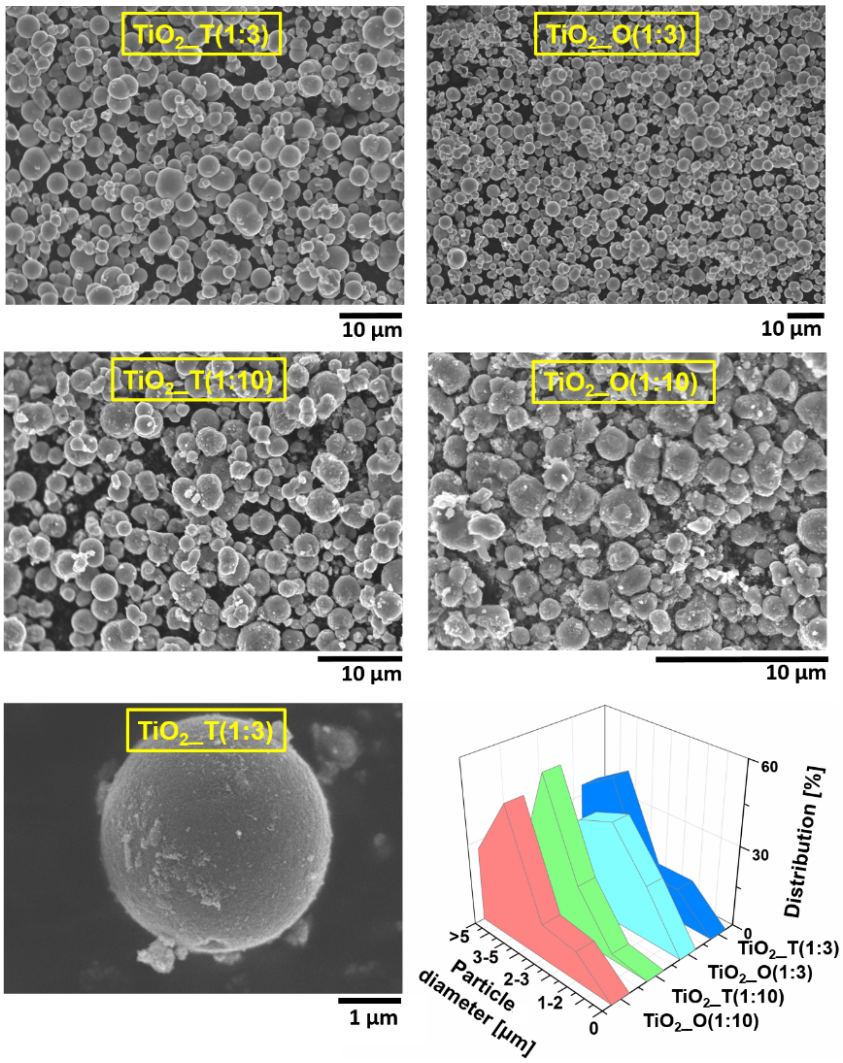

Figure 3: SEM images and particles size distribution of ILs assisted TiO_2microspheres.

can conclude that longer alkyl chains in the imidazolium cation lead to a larger particle size. Recently we examined the influence of two ionic liquids with four and ten atoms of carbon in the alkyl chain of the imidazolium cation (i.e., 1-butyl- and 1-decyl-3-methylimizadolium chlorides, [BMIM][Cl] and [DMIM][Cl], respectively) on the selected properties and photoactivity of TiO_2 particles under UV irradiation. For [BMIM][Cl] (IL:TBOT molar ratio 1:10), the highest contribution (44%) had structures with diameter 0.5–1 µm, whereas for [DMIM][Cl], up to 50% were particles of 1–2 µm. For comparison, IL–TiO_2 structures prepared in this study in the presence of [TDMIM][Cl] and [ODMIM][Cl], for a IL:TBOT molar ratio equal to 1:10, yielded mainly particles with a diameter of 3–5 µm, in an amount of 54% and 49%, respectively. It was also observed that synthesis in the presence of low IL content in the reaction mixture (i.e., IL:TBOT molar ratio of 1:10) provided TiO_2 structures with deformations (Figure 3), whereas the photocatalysts prepared using a IL:TBOT molar ratio equal to 1:3 (TiO_2_T(1:3) and TiO_2_O(1:3)) had a more uniform, spherical shape and smoother surface. Moreover, increasing the concentration of IL resulted in formation of particles with a higher contribution of smaller particles in comparison to samples obtained using IL:TBOT with a molar ratio equal to 1:10. [TDMIM][Cl] and [ODMIM][Cl] are salts consisting of a large, asymmetric, amphiphilic imidazolium cation and a small single-atomic chloride anion. Based on our previous research we can assume that ILs interact with the TiO_2 surface, making a protective layer due to a combination of electrostatic and steric stabilization. 1-Methyl-3-octadecylimidazolium chloride is probably less firmly packed on the TiO_2 surface due to the longer alkyl chain. As a result, the [ODMIM][Cl] ionic liquid may limit smaller particle deposition during Ostwald ripening, thus inhibiting further growth and agglomeration. For the TiO_2_O(1:3) sample, the dominant fraction were microspheres with diameter ranging from 2–3 µm (38%), whereas for TiO_2_T(1:3), the main fraction was particles with an average diameter of 3–5 µm (42%).

Diffuse reflectance spectroscopy, UV–vis spectroscopy and BET analysis

The Brunauer–Emmett–Teller (BET) specific surface area (S_{BET}) of the IL–TiO_2 photocatalysts ranged from 119 to 211 $m^2 \cdot g^{-1}$ (see Table 1). For comparison, pristine TiO_2 obtained by the same method but without IL, has a S_{BET} equal to 199 $m^2 \cdot g^{-1}$. In this regard, all samples (except TiO2_T(1:10)) had a smaller S_{BET} as compared to TiO_2 unmodified by ILs. Taking into account the type and the amount of IL used in the experiments, the largest S_{BET} was detected for the IL–TiO_2 samples obtained with the IL:TBOT molar ratio of 1:10, that is, the lowest amount of IL used for TiO_2 synthesis. The specific surface area determined for these samples was 211 $m^2 \cdot g^{-1}$ and 193 $m^2 \cdot g^{-1}$ for [TDMIM][Cl] and [ODMIM][Cl], respectively. Further increase of the IL content in the reaction mixture resulted in decrease of S_{BET}. The results obtained for both IL are similar (Table 1), therefore influence of the chain length in the imidazolium cation on the surface properties of IL–TiO_2 was not observed. However, the comparison of S_{BET} of samples described in this work with values previously presented by Paszkiewicz [28] for ILs containing shorter chain lengths in the imidazolium cation (C4 and C10) revealed that elongation of the alkyl substituent provided photocatalysts with smaller surface area. This property may be related to formation of the protecting layer by the IL at the TiO_2 surface, resulting therefore in higher steric hindrance for salts with longer alkyl chains influencing the final pore volume, and thus, the surface area. The total pore volume ranged from 0.05 to 0.1 $cm^3 \cdot g^{-1}$ depending on the IL type used in the experiments and its concentration. A higher BET surface area was also related to higher pore volume values and could lead to improved efficiency of the photocatalytic reactions [39].

The diffuse reflection (DR)/UV–vis spectra of the photocatalysts as well as for the pure ionic liquids used in this study are shown in Figure 4. The pristine TiO_2 obtained by the solvothermal method showed the expected bandgap of 3.2 eV and very weak visible-light absorption. However, the visible-light absorption of the TiO_2 photocatalysts appeared when the selected ionic liquids, [ODMIM][Cl] and [TDMIM][Cl], were applied in the TiO_2 synthesis reaction. Moreover, with increasing IL:TBOT molar ratio, the optical absorption of the composites in the viible-light region was also greatly increased (compare for example spectra for IL–TiO_2 obtained at IL:TBOT molar ratio of 1:10 and 1:3). Therefore, this enhanced absorbance of the light in the visible spectrum is expected to enhance the photocatalytic activity in the visible region for the target reaction. This observation is well verified by the photocatalytic tests of the IL–TiO_2 composites for the phenol degradation under visible light irradiation (Table 1).

Additionally, to understand why the obtained microparticles exhibited a strong light absorption over the visible range pure ILs were also examined as shown in Figure 4. The shape and nature of the imidazolium ionic liquid spectra are consistent with literature data [40,41]. A clear maximum is observable above 220 nm and a long tail of the absorption extended even beyond 350 nm and 500 nm for [ODMIM][Cl] and [TDMIM][Cl], respectively. The intense absorption in the UV region can be assigned to the π–π^* transition of the imidazolium ring. On the other hand, the long tail of the absorption spectra could be due to (i) the energy structure of the cation as well as the spatial arrangement of the anion and (ii) the presence of an impurity resulting from the IL synthesis [42-44].

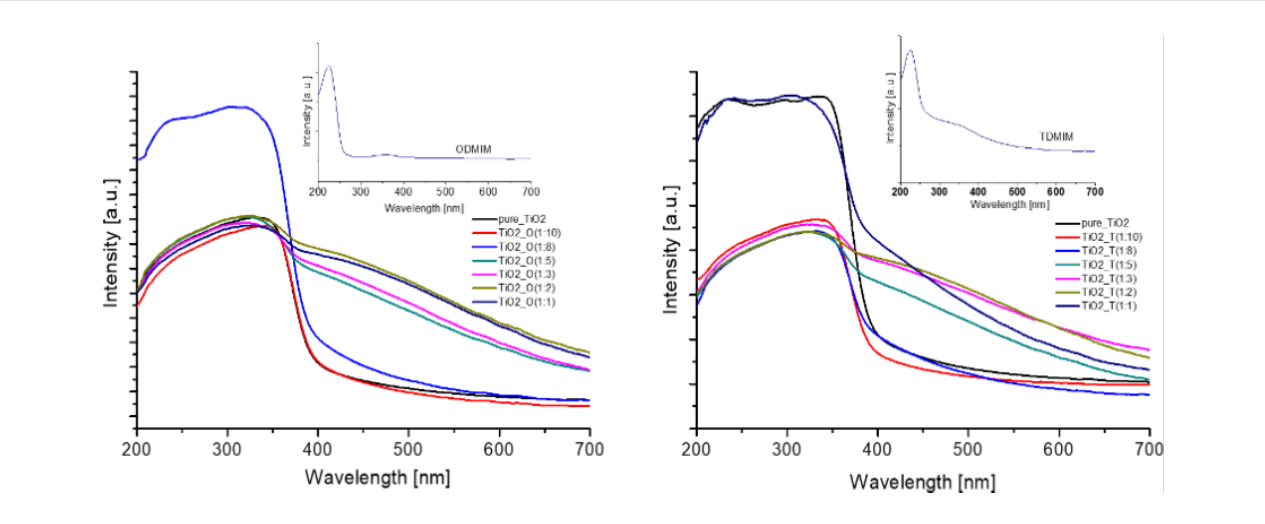

Figure 4: The diffuse reflectance and UV–vis spectra for the samples ODMIM_Cl_TiO_2 (left) and TDMIM_Cl_TiO_2 (right).

Considering the above results the improvement of the optical absorption of the composites in the visible-light region could be associated with the synergic effect of its two main components, that is, TiO_2 and ILs. Binetti et al. [42] stated that the absorbance of IL–TiO_2 materials increased with the modification of TiO_2 with 1-hexyl-3-methylimidazolium tetrafluoroborate ([HMIM][BF_4]), and concomitantly, a tail appears in the visible region due to absorption by IL. Moreover, taking into account that both ILs used in this study have a high number of carbon atoms in the structure (Figure 1), thus high carbon content, the absorption of IL–TiO_2 in the visible region can be attributed to the existence of carbon species on the surface of the photocatalysts [45].

Chemical composition of ionic liquid/TiO_2 composites

The photocatalytic degradation is based on chemical reactions on the surface of the photocatalyst [46-48]. In this context, XPS measurements have been chosen to analyze the surface of the IL–TiO_2 composites. Both [ODMIM][Cl]–TiO_2 and [TDMIM][Cl]–TiO_2 samples modified with a IL:TBOT molar ratio of 1:3 and 1:10 were investigated. The elemental surface composition of all IL–TiO_2 specimens analyzed is shown in Table 3. The titanium, oxygen, carbon, nitrogen and chlorine atoms were detected. The last two elements evidenced successful interaction between the IL and the surface of TiO_2. The chemical character of these elements was identified from corresponding Ti 2p, O 1s, C 1s, N 1s and Cl 2p high-resolution XPS spectra, respectively. The deconvoluted spectra are shown in Figure 5. The carbon fraction at binding energy (BE) close to 286.2 eV is characteristic for C–Cl and C–N bonds [49]. Two nitrogen states can be distinguished in the N 1s spectra recorded on the IL–TiO_2 composites (see Figure 5 and Table 3). The signal at BE = 400 eV can be assigned to nitrogen states formed by Ti–O–N and C–N bonds [50]. The last one can be from superposition of C–NH–C and C=N–C bonds attributed to pyrrole- and pyridine-type interactions [49,51,52]. The peaks at BEs above 401.4 eV can be due to the positively charged nitrogen (N^+) caused by pyridine-type nitrogen bonds and oxidized nitrogen species [53]. It should be noted that this nitrogen state appears for both types of IL–TiO_2 with a molar ratio of IL:TBOT of 1:3. No signals located at BEs lower than 399 eV, characteristic for Ti–N bond formation [28], were detected. The XPS data collected in Table 3 showed that the amount of carbon, nitrogen and chlorine were higher for the samples with molar ratio 1:3 than for those with molar ratio 1:10. In addition, the surface concentration of these elements for the TiO_2_O(1:3) sample with longer alkyl substituents is smaller than corresponding values evaluated for TiO_2_T(1:3) samples containing ILs with shorter substituents (see the C/Ti and N/Ti entries in Table 3). Thus, the lower coverage of the [ODMIM] cations seems to be the result of the larger steric effect induced by this ion. The C/N ratios, evaluated for all samples, were estimated to be higher than nominal values related to the respective IL cations (see Table 3). This may be caused by adsorption of additional carbon contaminants on the finally prepared IL-assisted TiO_2 because of the exposure of the samples to air prior to the XPS analysis or during synthesis and preparation.

Photocatalytic activity

The photocatalytic activity of the IL–TiO_2 samples was evaluated by phenol degradation induced by visible-light irradiation (using an optical filter with $\lambda > 420$ nm). All photocatalysts exhibited better photocatalytic properties than the reference TiO_2 sample (Table 1 and Figure 6).

Table 3: Elemental composition (in atom %) and chemical characteristics of titanium, oxygen, carbon and nitrogen states in the surface layer of [ODMM][Cl] and [TDMM][Cl] IL-modified TiO_2 particles, evaluated by X-ray photoelectron analysis.

Sample	TiO_2_O(1:10)	TiO_2_O(1:3)	TiO_2_T(1:10)	TiO_2_T(1:3)
∑Ti	26.97	24.38	25.66	23.79
$Ti^{(4+)}$ 458.9 ± 0.2 eV	96.18	94.95	94.87	94.55
$Ti^{(3+)}$ 457.2 ± 0.2 eV	3.82	5.05	5.13	5.45
∑O	69.22	64.05	67.05	61.79
Ti–O_{latt} 530.0 ± 0.1 eV	74.98	67.79	79.14	71.77
Ti–O_{surf} 530.6 ± 0.2 eV	18.36	23.18	14.35	19.17
C=O 531.6 ± 0.2 eV	4.53	6.72	5.26	7.06
–OH 532.6 ± 0.2 eV	2.12	2.31	1.25	2
∑C	3.51	9.84	7	12.22
C–C 284.8 ± 0.1 eV	66.09	65.54	56.57	66.8
C–OH, C–Cl, C–N 286.2 ± 0.1 eV	10.9	25.49	29.71	29.22
–C=O, N–C=O 289.0 ± 0.1 eV	23	8.96	13.72	3.99
∑N	0.26	0.52	0.24	0.72
“A” 400.0 ± 0.4 eV	100	59.42	100	41.39
“B” 401.4 ± 0.1 eV	0	40.58	0	58.61
∑Cl	0.05	1.21	0.06	1.48
C/N	13.5	18.9	29.2	17
N/Ti	0.01	0.021	0.009	0.03
C/Ti	0.13	0.4	0.27	0.51
Cl/N	0.19	2.33	0.25	2.06

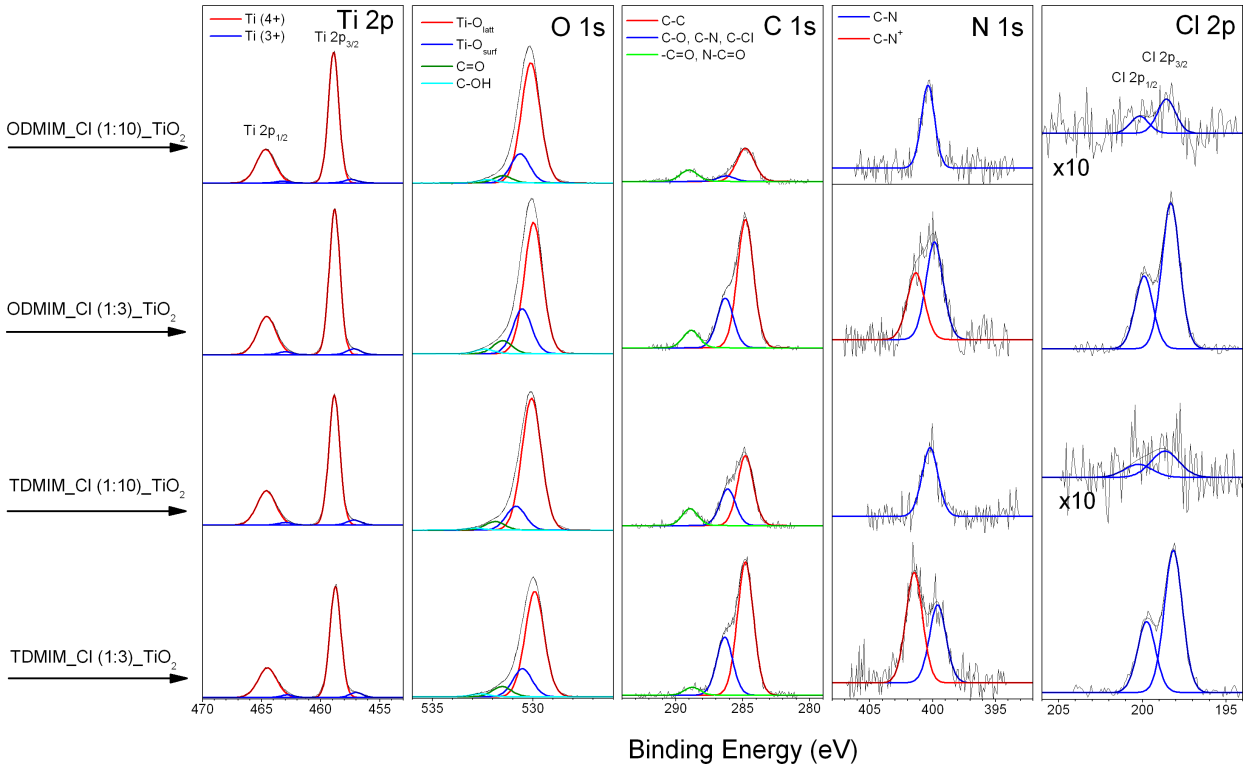

Figure 5: High-resolution XPS spectra of elements detected in the [ODMIM][Cl]–TiO_2 and [TDMIM][Cl]–TiO_2 samples.

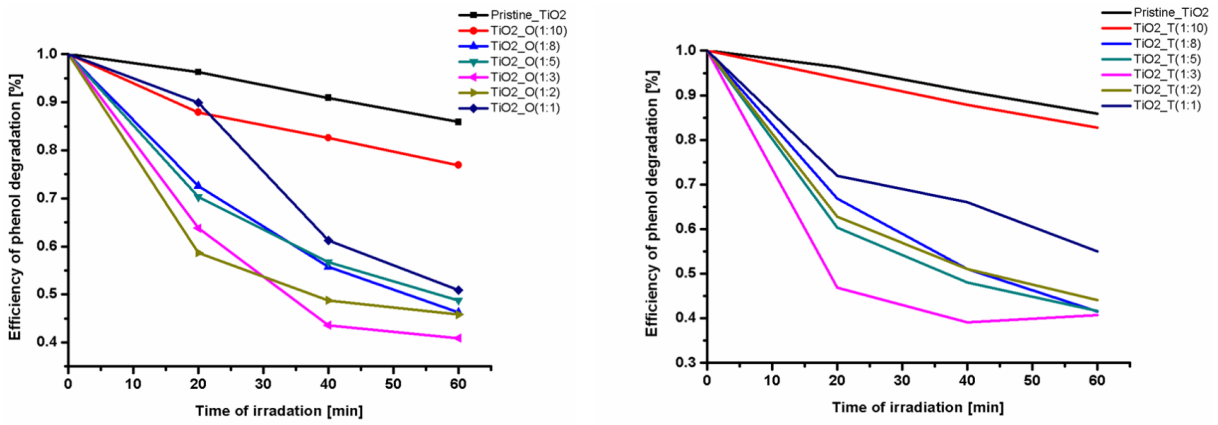

Figure 6: The efficiency of phenol degradation for ODMIM_Cl_TiO_2 (left) and TDMIM_Cl_TiO_2 (right) photocatalyst samples.

Before the photocatalytic activity tests, phenol adsorption on the surface of the photocatalyst was tested for the samples possessing the highest photoactivity. It was observed that the concentration of phenol after 120 min in dark conditions practically did not change. The samples with the highest photoactivity were prepared using a IL:TBOT molar ratio of 1:3. The efficiency of phenol degradation increased from 14 to 59% and 61% for pristine TiO_2, TiO_2_O(1:3) and TiO_2_T(1:3) samples, respectively. Moreover, for both ionic liquids the phenol degradation efficiency increased with increasing IL:TBOT molar ratio from 1:10 to 1:3. However, a further increase in the IL concentration in the reaction system resulted in an opposite relation. These results corresponded well with SEM and XRD results. Particles prepared using a IL:TBOT molar ratio equal to 1:10 were poorly formed and had highly irregular shapes, which resulted in lower photocatalytic activity. Based on the literature data, it is known that regularly shaped TiO_2 microspheres show a higher photoefficiency due to their low density, high surface-to-volume ratio, high surface area and good surface permeability [54-56]. Thus, it could be expected that the higher photocatalytic activity could be achieved by using TiO_2 microspheres with uniform and spherical shape.

According to the DRS UV–vis spectra shown in Figure 4, the incorporation of ILs into TiO_2 microspheres significantly extended the absorption spectrum of the titanium dioxide in the visible region. Therefore, the enhanced photocatalytic activity of IL–TiO_2 can be attributed to the improved optical absorption. Moreover, the XPS data showed that the amount of carbon, nitrogen and chlorine were higher for the samples with molar ratio 1:3 in comparison to 1:10, which corresponds well with changes in photoactivity. It should be noticed that the total amount of C, N and Cl was higher for TiO_2_T(1:3) than TiO_2_O(1:3) despite that the [ODMIM] cation contained a longer alkyl chain than [TDMIM]. This is probably due to the higher steric hindrance created by [ODMIM][Cl] at the TiO_2 surface, hence a probably less firmly packed organic protection layer. Additionally, the XPS analysis also confirmed that C, N and Cl atoms are located solely on the surface of the semiconductors. Hereby, the possible mechanism of the TiO_2 photoactivity improvement under visible-light irradiation by doping of nonmetal elements derived from IL structures was rejected.

Therefore, to further elucidate the mechanisms of the photocatalytic reaction, the role of the generated reactive species in the photocatalytic process under visible irradiation was investigate using *t*-BuOH, $AgNO_3$, *p*-benzoquinone (BQ) and ammonium oxalate (AO) as the scavengers of $^{\bullet}OH$, e^-, $O_2^{-\bullet}$ and h^+, respectively. These measurements have been performed for the IL–TiO_2 samples possessing the highest activity, that is, TiO_2_T(1:3) and TiO_2_O(1:3), and the obtained results are presented in Table 4. It was observed that application of $AgNO_3$ as a scavenger of e^- for the both samples (TiO_2_T(1:3) and TiO_2_O(1:3) did not affect the effectiveness of the photocatalytic process compared to that carried out without scavengers.

Table 4: Percent efficiency of phenol degradation under visible light in the presence of scavengers.

Sample ID	$AgNO_3$	$C_2H_8N_2O_4$	C_4H_9OH	$C_6H_4O_2$
TiO_2_T(1:3)	68	54	63	22
TiO_2_O(1:3)	77	53	85	11

Participation of $O_2^{\bullet}$ in the photodegradation process was investigated by adding BQ, which is capable of trapping $O_2^{\bullet}$ [57]. It

was observed that the addition of BQ to both samples (TiO_2_O(1:3) and TiO_2_O(1:3)) caused inhibition of phenol degradation, as presented in Table 4. The degradation rate was largely suppressed to 22 and 11% for the TiO_2_T(1:3) and TiO_2_O(1:3) photocatalysts, respectively. It is deduced that the oxidation inhibition of phenol is due to the suppression of the superoxide anion formation by the BQ addition. Addition of AO (holes scavenger) resulted in a slight inhibition of the photodegradation process under visible-light irradiation for both samples, indicating that h^+ might play a negligible role in the phenol photo-oxidation process. Probably the positively charged hole could catch OH^- to yield hydroxyl radicals [58]. In the case of the TiO_2_T(1:3) sample, when *tert*-butyl alcohol ($^{\bullet}OH$ scavenger) was added to the phenol solution, 63% of phenol was degraded, indicating that OH radicals play an insignificant role in the degradation process. Interestingly, for the TiO_2_O(1:3) photocatalyst, the addition of $AgNO_3$ and *tert*-butyl alcohol increased the effectiveness of the photocatalytic process. As explained by Liu et al., $AgNO_3$ may be capable of enhancing the separation of electrons and holes, resulting in a greater amount of holes and following active species generated, which promotes the degradation rate [59].

Conclusion

The results presented in this study revealed that visible-light-responsive TiO_2 microspheres could be successfully obtained by a solvothermal method assisted by ionic liquids, such as 1-methyl-3-tetradecylimidazolium or 1-methyl-3-octadecylimidazolium chlorides. The ionic liquids introduced into the reaction environment work as structure-controlling agents, providing TiO_2 microparticles (composed of nanocrystals) with a large specific surface area ranging from 119 to 211 m^2/g. However, more importantly, application of ionic liquids during TiO_2 synthesis enabled formation of visible-light-induced photocatalysts. It was found that the amount of the ionic liquid used for the synthesis is crucial and significantly affects the photoresponse of the IL–TiO_2 materials toward visible irradiation, thus photoactivity. The highest photoactivity was observed for samples prepared using a IL:TBOT molar ratio of 1:3, as observed for both ILs. From 59% to 61% of phenol used as a model compound was degraded after 60 min of irradiation by visible light ($\lambda > 420$ nm) in the presence of suspended TiO_2 that was modified by [ODMIM][Cl] and [TDMIM][Cl], respectively. The enhanced photocatalytic activity of IL–TiO_2 can be attributed to the presence of the ionic liquid cation and anion at the TiO_2 surface, resulting in the improved optical absorption of visible light by the photocatalysts. The phenol degradation was realized mainly by radical anions $O_2^{\bullet-}$, whereas the contribution of the other active species was limited in the reaction mechanism. In this regard, the role of the ionic liquid in TiO_2 photoexcitation requires further investigation.

Experimental

Chemicals

Titanium(IV) *n*-butoxide (TBOT), (≥97%) as a precursor of TiO_2, hydrochloric acid (36%) as a pH stabilizer and ethanol (99.9%) as the reaction medium were provided by Sigma-Aldrich. The ionic liquids, 1-methyl-3-octadecylimidazolium chloride [ODMIM][Cl] and 1-methyl-3-tetradecylimidazolium chloride [TDMIM][Cl] were purchased from Ionic Liquids Technologies GmbH. Ammonium oxalate, silver nitrate (≥99%), benzoquinone and *tert*-butyl alcohol from Sigma-Aldrich were used as scavengers.

Photocatalyst preparation

TiO_2 was modified by ILs using a solvothermal method. First of all, the titania precursor, Ti(IV) *n*-butoxide, was dissolved in absolute ethanol under stirring. Then the hydrochloric acid, distilled water and selected ionic liquid were added. Vigorous stirring of the solution was continued for 10 min to obtain a transparent solution. In the final step, the homogeneous mixture was transferred to a 200 mL teflon-lined stainless steel autoclave and the solvothermal reaction was performed at 180 °C for 24 h [28]. The reaction product was washed with ethanol and deionized water, respectively, followed by drying at 60 °C for 6 h. The obtained powder was calcinated at 200 °C for 2 h (heating rate 2 °C/min). Various molar ratios of ILs to TBOT were selected as listed in Table 1.

Sample characterization

The morphology and size distribution of the TiO_2 powders were observed using a Jeol SEM microscope operated at 12 kV and Cs-corrected STEM (high angle annular darkfield, HAADF).

X-ray photoelectron spectroscopy (XPS) experiments were performed on a PHI 5000 VersaProbeTM (ULVAC-PHI) spectrometer with monochromatic Al Kα radiation ($h\nu$ = 1486.6 eV). The high-resolution (HR) XPS spectra were collected by the hemispherical analyzer at a pass energy of 23.5 eV and an energy step size of 0.1 eV. CasaXPS software was used to evaluate the XPS data. The binding energy (BE) scale of all detected spectra was referenced by setting the BE of the aliphatic carbon peak (C–C) signal to 284.8 eV.

The UV–vis reflectance and absorbance spectra of TiO_2 photocatalysts were recorded using a Shimadzu UV–vis spectrophotometer (UV 2600) equipped with an integrating sphere and $BaSO_4$ was used as the reference sample.

BET surface area and total pore volume of the photocatalysts (physical adsorption and desorption of nitrogen at 77 K) was measured using a Micromeritics Gemini V200 instrument. The

photocatalyst samples were dried and degassed in a sample cell at 200 °C for at least 2 h before the adsorption. The specific surface area of the photocatalysts was determined by the BET method.

Powder X-ray diffraction (XRD) studies of the photocatalyst samples were carried out using a RigakuMiniFlex 600 XRD system equipped an X-ray generator with a copper target (operated at 40 kV and 30 mA). The average TiO_2 crystallite size was calculated using the Scherrer equation.

Photocatalytic activity test

For determination of the photoactivity under visible-light irradiation, the aqueous phase containing 125 mg of the photocatalyst (5 g/dm^3), 24 cm^3 of deionized water and 1 cm^3 of phenol as a model compound (Co = 500 mg/dm^3) was used. The suspension was stirred and aerated (V = 5 dm^3/h) for 30 min in the dark to obtain equilibrium and then the content of the reactor was photoirradiated with a 1000 W Xe lamp (Oriel, light flux 6.5–7.5 mW/cm^2) which emitted both UV and visible-light irradiation. The photoreactor (V = 25 cm^3, i.d. 37 mm, length 30 mm) was equipped with a quartz window and exposure layer thickness was 3 cm. The optical path included a water filter and a glass filter (GG 420) which cut-off wavelengths shorter than 420 nm. The temperature of the aqueous phase during irradiation was kept at 10 °C using a water bath. During the irradiation, the suspension (1 cm^3) was collected and filtered through syringe filters (diameter 0.2 µm) to remove the photocatalyst particles. The phenol concentration was estimated by means of the colorimetric method (λ = 480 nm) after derivatization with diazo-*p*-nitroaniline using a UV–vis spectrophotometer (Thermo Evolution 220). The photocatalytic degradation runs were preceded by a blind test in the absence of a photocatalyst or illumination. No degradation of phenol was observed in the absence of either the photocatalyst or illumination.

Determination of reactive species

To clarify which active species are involved in the photodegradation of the model compound, the phenol irradiation process was preceded by analogous experiments performed in the presence of different radicals scavengers (ammonium oxalate as a scavenger for photogenerated holes, $AgNO_3$ as scavenger for electrons, benzoquinone (BQ) as scavenger for superoxide radical species, and *tert*-butyl alcohol as a scavenger for hydroxyl radical species). The procedure of the photocatalytic measurements was carried out similar to the above-described photocatalytic degradation of phenol, except that the radical scavengers were added to the reaction system. The scavenger concentration was equal to 0.21 mmol dm^{-3}. No adsorption of phenol was observed in the presence of the photocatalyst in the phenol/scavenger solution and absence of illumination.

Acknowledgements

The authors acknowledge funding from the National Science Center within the program SONATA 8, research grant: "Influence of the ionic liquid structure on interactions with TiO_2 particles in ionic liquid assisted hydrothermal synthesis", contract No.2014/15/D/ST5/02747. The authors also acknowledge Karina Kacperska for her support.

ORCID® iDs

Anna Gołąbiewska - https://orcid.org/0000-0002-1787-9934
Adriana Zaleska-Medynska - https://orcid.org/0000-0003-3817-296X
Justyna Łuczak - https://orcid.org/0000-0001-9939-7156

References

1. Zhong, J.; Li, J.; Zeng, J.; He, X.; Huang, S.; Jiang, W.; Li, M. *Appl. Phys. A: Mater. Sci. Process.* **2014,** *115,* 1231–1238. doi:10.1007/s00339-013-7965-z
2. Chen, J.; Zhong, J.; Li, J.; Huang, S.; Hu, W.; Li, M.; Du, Q. *Mol. Catal.* **2017,** *435,* 91–98. doi:10.1016/j.mcat.2017.03.026
3. Zhang, L.-S.; Wong, K.-H.; Yip, H.-Y.; Hu, C.; Yu, J. C.; Chan, C.-Y.; Wong, P.-K. *Environ. Sci. Technol.* **2010,** *44,* 1392–1398. doi:10.1021/es903087w
4. Meng, S.; Li, D.; Sun, M.; Li, W.; Wang, J.; Chen, J.; Fu, X.; Xiao, G. *Catal. Commun.* **2011,** *12,* 972–975. doi:10.1016/j.catcom.2011.02.026
5. Fujishima, A.; Rao, T. N.; Tryk, D. A. *J. Photochem. Photobiol., C* **2000,** *1,* 1–21. doi:10.1016/S1389-5567(00)00002-2
6. Ohtani, B. *J. Photochem. Photobiol., C* **2010,** *11,* 157–178. doi:10.1016/j.jphotochemrev.2011.02.001
7. Xu, J.; Wang, W.; Sun, S.; Wang, L. *Appl. Catal., B* **2012,** *111–112,* 126–132. doi:10.1016/j.apcatb.2011.09.025
8. Choi, S. K.; Yang, H. S.; Kim, J. H.; Park, H. *Appl. Catal., B* **2012,** *121–122,* 206–213. doi:10.1016/j.apcatb.2012.04.011
9. Yin, M.; Li, Z.; Kou, J.; Zou, Z. *Environ. Sci. Technol.* **2009,** *43,* 8361–8366. doi:10.1021/es902011h
10. Długokęcka, M.; Łuczak, M.; Polkowska, Ż.; Zaleska-Medynska, A. *Appl. Surf. Sci.* **2017,** *405,* 220–230. doi:10.1016/j.apsusc.2017.02.014
11. Choi, W.; Termin, A.; Hoffmann, M. R. *J. Phys. Chem.* **1994,** *98,* 13669–13679. doi:10.1021/j100102a038
12. Chen, Y.; Li, W.; Wang, J.; Gan, Y.; Liu, L.; Ju, M. *Appl. Catal., B* **2016,** *191,* 94–105. doi:10.1016/j.apcatb.2016.03.021
13. Ramanathan, R.; Bansal, V. *RSC Adv.* **2015,** *5,* 1424–1429. doi:10.1039/C4RA14510K
14. Łuczak, J.; Paszkiewicz-Gawron, M.; Długokęcka, M.; Lisowski, W.; Grabowska, E.; Makurat, S.; Rak, J.; Zaleska-Medynska, A. *ChemCatChem* **2017,** *9,* 4377–4388. doi:10.1002/cctc.201700861
15. Łuczak, J.; Paszkiewicz, M.; Krukowska, A.; Malankowska, A.; Zaleska-Medynska, A. *Adv. Colloid Interface Sci.* **2016,** *230,* 13–28. doi:10.1016/j.cis.2015.08.006
16. Chang, S.-m.; Lee, C.-y. *Appl. Catal., B* **2013,** *132–133,* 219–228. doi:10.1016/j.apcatb.2012.11.026
17. Choi, H.; Kim, Y. J.; Varma, R. S.; Dionysiou, D. D. *Chem. Mater.* **2006,** *18,* 5377–5384. doi:10.1021/cm0615626
18. Łuczak, J.; Paszkiewicz, M.; Krukowska, A.; Malankowska, A.; Zaleska-Medynska, A. *Adv. Colloid Interface Sci.* **2016,** *227,* 1–52. doi:10.1016/j.cis.2015.08.010
19. Nakashima, T.; Kimizuka, N. *J. Am. Chem. Soc.* **2003,** *125,* 6386–6387. doi:10.1021/ja034954b

20. Zhou, Y.; Antonietti, M. *J. Am. Chem. Soc.* **2003,** *125,* 14960–14961. doi:10.1021/ja0380998
21. Hu, S.; Wang, H.; Cao, J.; Liu, J.; Fang, B.; Zheng, M.; Ji, G.; Zhang, F.; Yang, Z. *Mater. Lett.* **2008,** *62,* 2954–2956. doi:10.1016/j.matlet.2008.01.082
22. Lin, H.; de Oliveira, P. W.; Grobelsek, I.; Haettich, A.; Veith, M. *Z. Anorg. Allg. Chem.* **2010,** *636,* 1947–1954. doi:10.1002/zaac.201000073
23. Verma, Y. L.; Singh, M. P.; Singh, R. K. *Mater. Lett.* **2012,** *86,* 73–76. doi:10.1016/j.matlet.2012.07.025
24. Verma, Y. L.; Tripathi, A. K.; Shalu; Singh, V. K.; Balo, L.; Gupta, H.; Singh, S. K.; Singh, R. K. *Mater. Sci. Eng., B* **2017,** *220,* 37–43. doi:10.1016/j.mseb.2017.03.010
25. Liu, Y.; Li, J.; Wang, M.; Li, Z.; Liu, H.; He, P.; Yang, X.; Li, J. *Cryst. Growth Des.* **2005,** *5,* 1643–1649. doi:10.1021/cg050017z
26. Nagaraju, G.; Ravishankar, T. N.; Manjunatha, K.; Sarkar, S.; Nagabhushana, H.; Goncalves, R.; Dupont, J. *Mater. Lett.* **2013,** *109,* 27–30. doi:10.1016/j.matlet.2013.07.031
27. Jing, L.; Wang, M.; Li, X.; Xiao, R.; Zhao, Y.; Zhang, Y.; Yan, Y.-M.; Wu, Q.; Sun, K. *Appl. Catal., B* **2015,** *166–167,* 270–276. doi:10.1016/j.apcatb.2014.11.046
28. Paszkiewicz, M.; Łuczak, J.; Lisowski, W.; Patyk, P.; Zaleska-Medynska, A. *Appl. Catal., B* **2016,** *184,* 223–237. doi:10.1016/j.apcatb.2015.11.019
29. Liu, H.; Liang, Y.; Hu, H.; Wang, M. *Solid State Sci.* **2009,** *11,* 1655–1660. doi:10.1016/j.solidstatesciences.2009.06.011
30. Ravishankar, T. N.; Nagaraju, G.; Dupont, J. *Mater. Res. Bull.* **2016,** *78,* 103–111. doi:10.1016/j.materresbull.2016.02.017
31. Wang, X.-j.; Li, F.-t.; Liu, J.-x.; Kou, C.-g.; Zhao, X.; Hao, Y.-j.; Zhao, D. *Energy Fuels* **2012,** *26,* 6777–6782. doi:10.1021/ef301337y
32. Qi, L.; Yu, J.; Jaroniec, M. *Adsorption* **2013,** *19,* 557–561. doi:10.1007/s10450-013-9478-7
33. Shahi, S. K.; Kaur, N.; Singh, V. *Appl. Surf. Sci.* **2016,** *360,* 953–960. doi:10.1016/j.apsusc.2015.11.092
34. Wang, B.; Guo, L.; He, M.; He, T. *Phys. Chem. Chem. Phys.* **2013,** *15,* 9891–9898. doi:10.1039/c3cp50862e
35. An, J.; Wang, D.; Luo, Q.; Yuan, X. *Mater. Sci. Eng., C* **2009,** *29,* 1984–1989. doi:10.1016/j.msec.2009.03.015
36. Yu, J.; Li, Q.; Liu, S.; Jaroniec, M. *Chem. – Eur. J.* **2013,** *19,* 2433–2441. doi:10.1002/chem.201202778
37. Li, F.-t.; Wang, X.-j.; Zhao, Y.; Liu, J.-x.; Hao, Y.-j.; Liu, R.-h.; Zhao, D.-s. *Appl. Catal., B* **2014,** *144,* 442–453. doi:10.1016/j.apcatb.2013.07.050
38. Mirhoseini, F.; Salabat, A. *RSC Adv.* **2015,** *5,* 12536–12545. doi:10.1039/C4RA14612C
39. Elsayed, M. A.; Gobara, M.; Elbasuney, S. *J. Photochem. Photobiol., A* **2017,** *344,* 121–133. doi:10.1016/j.jphotochem.2017.05.008
40. Mandal, P. K.; Paul, A.; Samanta, A. *J. Photochem. Photobiol., A* **2006,** *182,* 113–120. doi:10.1016/j.jphotochem.2006.01.003
41. Mandal, P. K.; Sarkar, M.; Samanta, A. *J. Phys. Chem. A* **2004,** *108,* 9048–9053. doi:10.1021/jp047250c
42. Binetti, E.; Panniello, A.; Tommasi, R.; Agostiano, A.; Fantini, S.; Curri, M. L.; Striccoli, M. *J. Phys. Chem. C* **2013,** *117,* 12923–12929. doi:10.1021/jp312266s
43. Paul, A.; Mandal, P. K.; Samanta, A. *Chem. Phys. Lett.* **2005,** *402,* 375–379. doi:10.1016/j.cplett.2004.12.060
44. Paul, A.; Mandal, P. K.; Samanta, A. *J. Phys. Chem. B* **2005,** *109,* 9148–9153. doi:10.1021/jp0503967
45. Wu, Z.; Dong, F.; Zhao, W.; Wang, H.; Liu, Y.; Guan, B. *Nanotechnology* **2009,** *20,* 235701. doi:10.1088/0957-4484/20/23/235701
46. Nakata, K.; Fujishima, A. *J. Photochem. Photobiol., C* **2012,** *13,* 169–189. doi:10.1016/j.jphotochemrev.2012.06.001
47. Hoffmann, M. R.; Martin, S. T.; Choi, W.; Bahnemann, D. W. *Chem. Rev.* **1995,** *95,* 69–96. doi:10.1021/cr00033a004
48. Linsebigler, A. L.; Lu, G.; Yates, J. T., Jr. *Chem. Rev.* **1995,** *95,* 735–758. doi:10.1021/cr00035a013
49. Xue, G.; Dai, Q.; Jiang, S. *J. Am. Chem. Soc.* **1988,** *110,* 2393–2395. doi:10.1021/ja00216a009
50. Cong, Y.; Zhang, J.; Chen, F.; Anpo, M. *J. Phys. Chem. C* **2007,** *111,* 6976–6982. doi:10.1021/jp0685030
51. Bhargava, G.; Ramanarayanan, T. A.; Bernasek, S. L. *Langmuir* **2010,** *26,* 215–219. doi:10.1021/la9020355
52. Lázaro Martínez, J. M.; Rodríguez-Castellón, E.; Sánchez, R. M. T.; Denaday, L. R.; Buldain, G. Y.; Campo Dall' Orto, V. *J. Mol. Catal. A: Chem.* **2011,** *339,* 43–51. doi:10.1016/j.molcata.2011.02.010
53. Naumkin, A. V.; Kraut-Vass, A.; Gaarenstroom, S. W.; Powell, C. J. NIST X-ray Photoelectron Spectroscopy Database 20, Version 4.1, 2012. http://srdata.nist.gov/xps/
54. Wang, R.; Cai, X.; Shen, F. *Ceram. Int.* **2013,** *39,* 9465–9470. doi:10.1016/j.ceramint.2013.05.064
55. Zheng, Z.; Huang, B.; Qin, X.; Zhang, X.; Dai, Y. *Chem. – Eur. J.* **2010,** *16,* 11266–11270. doi:10.1002/chem.201001280
56. Zheng, Y.; Cai, J.; Lv, K.; Sun, J.; Ye, H.; Li, M. *Appl. Catal., B* **2014,** *147,* 789–795. doi:10.1016/j.apcatb.2013.10.011
57. Palominos, R.; Freer, J.; Mondaca, M. A.; Mansilla, H. D. *J. Photochem. Photobiol., A* **2008,** *193,* 139–145. doi:10.1016/j.jphotochem.2007.06.017
58. An, G.; Ma, W.; Sun, Z.; Liu, Z.; Han, B.; Miao, S.; Miao, Z.; Ding, K. *Carbon* **2007,** *45,* 1795–1801. doi:10.1016/j.carbon.2007.04.034
59. Liu, X.; Lv, J.; Wang, S.; Li, X.; Lang, J.; Su, Y.; Chai, Z.; Wang, X. *J. Alloys Compd.* **2015,** *622,* 894–901. doi:10.1016/j.jallcom.2014.11.005

License and Terms

This is an Open Access article under the terms of the Creative Commons Attribution License (http://creativecommons.org/licenses/by/4.0), which permits unrestricted use, distribution, and reproduction in any medium, provided the original work is properly cited.

The license is subject to the *Beilstein Journal of Nanotechnology* terms and conditions: (https://www.beilstein-journals.org/bjnano)

The definitive version of this article is the electronic one which can be found at:
doi:10.3762/bjnano.9.54

BEILSTEIN JOURNAL OF NANOTECHNOLOGY

Mechanistic insights into plasmonic photocatalysts in utilizing visible light

Kah Hon Leong[1], Azrina Abd Aziz[2], Lan Ching Sim[1], Pichiah Saravanan[*3], Min Jang[4] and Detlef Bahnemann[5]

Review

Open Access

Address:
[1]Department of Environmental Engineering, Faculty of Engineering and Green Technology, Universiti Tunku Abdul Rahman, Jalan Universiti, Bandar Barat, 31900, Kampar, Perak, Malaysia, [2]Faculty of Engineering Technology, Universiti Malaysia Pahang, Lebuhraya Tun Razak, Gambang, 26300 Kuantan, Pahang, Malaysia, [3]Environmental Nanotechnology Laboratory, Department of Environmental Science and Engineering, Indian Institute of Technology (ISM) Dhanbad 826004, Jharkhand, India, [4]Department of Environmental Engineering, Kwangwoon University, 447-1 Wolgye-Dong, Nowon-Gu, Seoul, South Korea and [5]Institut für Technische Chemie, Leibniz Universität Hannover, Callinstrasse 3, 30167 Hannover, Germany

Email:
Pichiah Saravanan* - pichiahsaravanan@gmail.com

* Corresponding author

Keywords:
localized surface plasmon resonance (LSPR); noble metal; plasmonic photocatalyst; reactive radicals; Schottky junctions; visible light

Beilstein J. Nanotechnol. **2018,** *9,* 628–648.
doi:10.3762/bjnano.9.59

Received: 28 September 2017
Accepted: 17 January 2018
Published: 19 February 2018

This article is part of the Thematic Series "Energy conversion, storage and environmental remediation using nanomaterials".

Guest Editor: W.-J. Ong

© 2018 Leong et al.; licensee Beilstein-Institut.
License and terms: see end of document.

Abstract

The utilisation of sunlight as an abundant and renewable resource has motivated the development of sustainable photocatalysts that can collectively harvest visible light. However, the bottleneck in utilising the low energy photons has led to the discovery of plasmonic photocatalysts. The presence of noble metal on the plasmonic photocatalyst enables the harvesting of visible light through the unique characteristic features of the noble metal nanomaterials. Moreover, the formation of interfaces between noble metal particles and semiconductor materials further results in the formation of a Schottky junction. Thereby, the plasmonic characteristics have opened up a new direction in promoting an alternative path that can be of value to the society through sustainable development derived through energy available for all for diverse applications. We have comprehensively prepared this review to specifically focus on fundamental insights into plasmonic photocatalysts, various synthesis routes, together with their strengths and weaknesses, and the interaction of the plasmonic photocatalyst with pollutants as well as the role of active radical generation and identification. The review ends with a pinnacle insight into future perspectives regarding realistic applications of plasmonic photocatalysts.

Review

Introduction

Photocatalysts have played and will continue to play a pivotal role in environmental and energy applications in order to fulfil the needs of the current and future generation. They cleverly tackle the various limitations in the aforementioned field to satisfy the requirements of clean and green energy, and sustainable treatment of water and air. Indeed, years of research have been directed towards developing this sustainable process for a profound, promising and reliable approach towards energy generation and environmental remediation [1,2]. In line with this, the identification of photocatalysts capable of harvesting energy from the wider electromagnetic spectrum has become the focus of most researchers. The ability to harvest such a wide spectrum will lead to a pathway for better utilization of the solar spectrum. The invention and progression of plasmonic photocatalysts laid a foundation for the successful utilisation of longer wavelengths, known as "visible light photocatalysis".

The localised surface plasmon resonance (LSPR) is a unique characteristic of a plasmonic material, which can extend the absorption of light towards the visible light spectrum. Thus, LSPR greatly supports the utilisation of the solar spectrum, which comprises a considerable portion (≈43%) of these wavelengths. The resonance appears when the photons interact with the metal nanoparticle surface conduction electrons [3]. This phenomenon enables these photocatalysts to concentrate the light energy surrounding it and leads to a strong improvement and activation of electron movement within the metal (i.e, noble metals) and semiconductor material [4].

Besides this, another distinguishing characteristic of plasmonic photocatalysts is that they also behave as an electron trap. The incorporation of a noble metal with semiconductors in the formation of Schottky junctions contributes to this behaviour [5]. This barrier formation prevents the recombination of electrons with the holes at the valance bands by trapping the electrons excited to the conduction bands. The LPSR, along with this distinctive characteristic feature, strengthens and contributes to the improvement of the plasmonic photocatalyst.

All these distinctive characteristics of plasmonic photocatalysts have motivated researchers in the field of light-driven nanomaterials, resulting in abundant findings on the successful application of this phenomenon through the support of noble metal. Hence, we deemed a comprehensive and timely review on this topic beneficial to its development, especially in the context of promoting sustainable photocatalysts. This review exclusively discusses the recent advances with regards to synthesis, the mechanism behind the plasmonic phenomenon, quantum efficiency, identification of active radicals and future perspectives.

Fundamentals of plasmonic photocatalysts

An amalgamation of noble and semiconductor metal forms an exclusive "plasmonic photocatalyst" classification. The term "plasmonic" is mainly in reference to the unique characteristics of LSPR and induced effects [6]. However, the formation of a Schottky junction does not classify as plasmonic or resonant effects. This formation is a result of notable contact between noble metal nanoparticles with a semiconductor. Plasmonic effects have been verified to increase the photocatalytic performance due to the intrinsic influences on the semiconductor photocatalyst. Plasmonic effects work to improve harvesting of visible light, prolong the lifetime of the charge carriers, improve activation of electron–hole pairs and enhance the redox reaction potential [7]. Moreover, the excitation of excess electrons and holes increases the rate of redox reaction through the heat generated. The distinct characteristic features of plasmonics are portrayed in Figure 1.

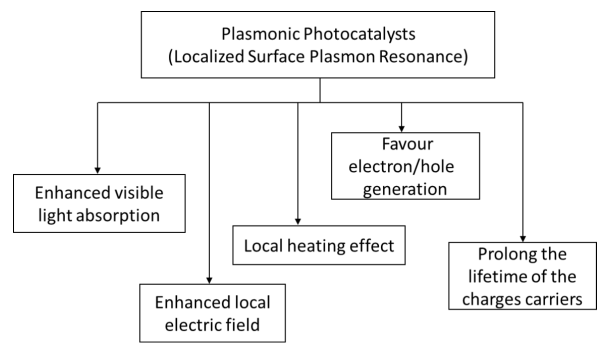

Figure 1: Distinctive features of plasmonics contributing to improved photocatalyst performance.

Noble metals such as Au, Ag, Pt, Pd in the form of nanoparticles are a novel candidate for high absorption of visible light owing to their strong optical absorption in the entire solar region [8,9]. The unique characteristics of the LSPR effect in noble metal allow the enhanced absorption of photon energy from the visible light spectrum. Larger metallic nanoparticles (>5 nm) produce a robust surface plasmon emission in the visible spectrum [10]. The intensity of the plasmon band is highly dependent on the morphology, surrounding medium dielectric constant, and electronic interactions between the stabilizing ligands and nanoparticles [11]. Besides, the creation of a Schottky junction with a noble metal and a semiconductor acts to retard the recombination rate of electrons and holes [12].

LSPR takes place when noble metal NPs are excited by the oscillating electric field of the light. The photon frequency is designed to match with the natural frequency of the noble metal

throughout the oscillation. This reduces the field on one side of the electron while increasing it on the other side of the noble metal. The development of this nonequilibrium condition results in the rearrangement of the charge density and builds an opposing electric field within the noble metal NPs. This further leads to the establishment of a coulombic restoring force and the noble metal NP electrons then experience harmonic oscillation [1,5,13,14]. These oscillating charges trigger the LSPR effects when the excited surface electric field frequency is sufficient, and the noble metal resonance leads to dynamic utilisation of visible light. A schematic representation of the phenomenon is illustrated in Figure 2. Hence, it is clear that absorption of photons emitted by the visible spectrum was promoted through LSPR and is very well ascribed to the electric polarization effect. Moreover, LSPR also speeds up the electron movement from the photoexcited noble metal to the semiconductor [5].

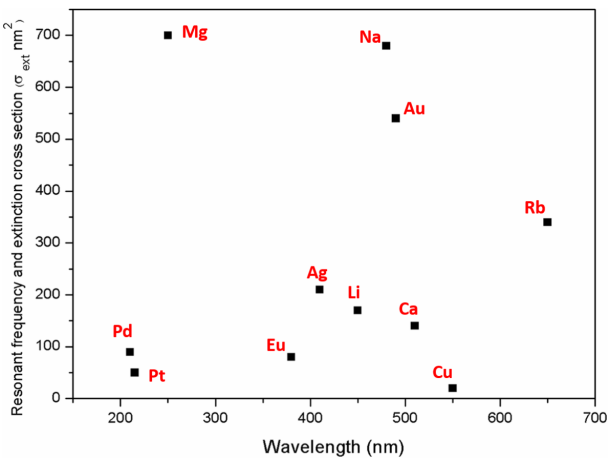

Figure 3: The metallic equivalent resonant wavelength for 10 nm diameter nanoparticles. Reprinted with permission from [27], copyright 2011 IOP Publishing.

The morphology, interparticle interactions and the local dielectric environment of noble metal nanoparticles is significantly influenced by the LSPR frequency [17-20]. It must be noted that not all noble metal nanoparticles of 10 nm diameter are able to utilize visible light, as shown in Figure 3. Ag and Au NPs are relatively good at harvesting visible light as compared to the others. These two noble metals can generate a stable, high electron–hole pair density [21]. However, the lower cost of Ag makes it more desirable to be utilized for broader applications as compared to Au, and therefore, most studies utilize Ag as a plasmonic inducer [22-24]. Moving away from Au one can find that palladium (Pd) in the form of NPs with a diameter of <10 nm is limited to the UV spectrum [25]. Nevertheless, the larger particle size and agglomeration of palladium particles contribute to the enhanced absorption of visible light. Mohapatra and coworkers demonstrated this where they successfully improved the harvesting potential of visible light for Pd NPs with a particle size in the range of ≈80 nm [25]. Similar results were also obtained by Kwak et al. where Pd NPs particles of ≈15 nm diameter were integrated onto TiO_2 [26].

The plasmon-assisted physico-chemical interrelation between the noble metal and semiconductor is the key for understanding electron generation and excitation. Once sufficient photon

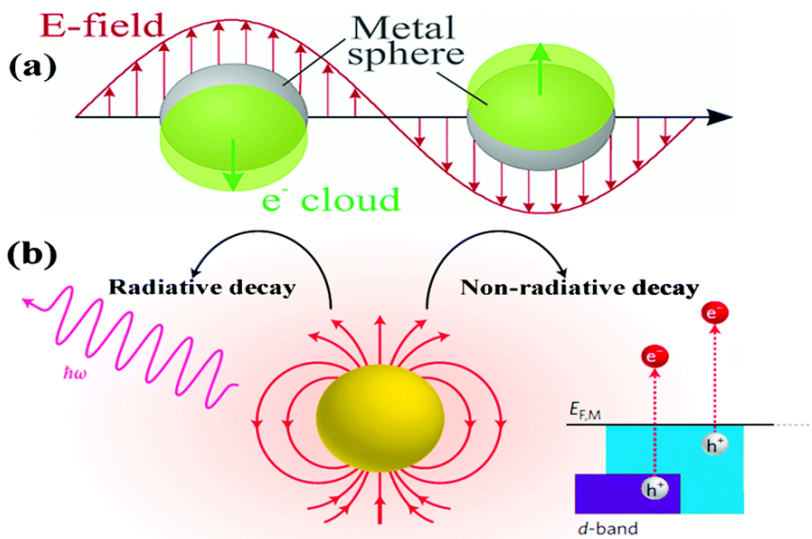

Figure 2: (a) Representation of localized surface plasmon resonance (LSPR) evolution in a noble metal particle irradiated by a light source. Reprinted with permission from [15], copyright 2003 American Chemical Society. (b) LSPR decay processes. Reprinted with permission from [16], copyright 2014 Nature Publishing Group.

energy is obtained, it will excite the free electrons present in the noble metal to a higher Fermi level [28,29]. This movement of electrons leads to the redistribution of energy through non-equilibrium Fermi–Dirac statistics. During this redistribution, the excited electrons are transferred from the noble metal to the semiconductor and the phenomenon leads to the formation of a Schottky junction. The formed Schottky junction enables electron movement towards the semiconductor through the LSPR decay effect as illustrated in Figure 4 and Figure 5 [30], leaving behind positively charged holes at the valence band or their transfer to the counter electrode preventing recombination [16,31-35]. Figure 4a demonstrates the excited electron mobility from the thermal equilibrium to the upper energy state. Meanwhile Figure 4b illustrates the redistribution of the Fermi–Dirac distribution in a metal nanoparticle achieved through the collision. Figure 4c demonstrates the movement of excited electrons to the ordinary distribution and different regions [3,6].

Moreover, noble metals offer a rapid path for charge movement through the interface as electron–hole trap centres and allow more energetic spots for photoreactions to occur. Thus the combined traits act to readily suppress the electron–hole recombination.

Synthesis routes for plasmonic photocatalysts

There are quite a number of ways to synthesize plasmonic photocatalysts. The most important step in their fabrication is the incorporation or deposition of noble metals onto the surface of a semiconductor. The most commonly studied semiconductor is TiO_2, which exhibits superior photocatalysis efficiency.

Such materials have already been applied in various environmental and energy conversion applications [36]. Recently, the evolution of a metal-free semiconductor, graphitic carbon nitride (g-C_3N_4), has been discovered as an alternative for plasmonic photocatalysts. This metal-free semiconductor by itself has the ability to extend the absorption of visible light [37-44]. Moreover, future studies on other semiconductors such as metal chalcogenides and metal phosphides could lead to further developments for plasmonic photocatalysts to address current environmental and energy issues [45-49].

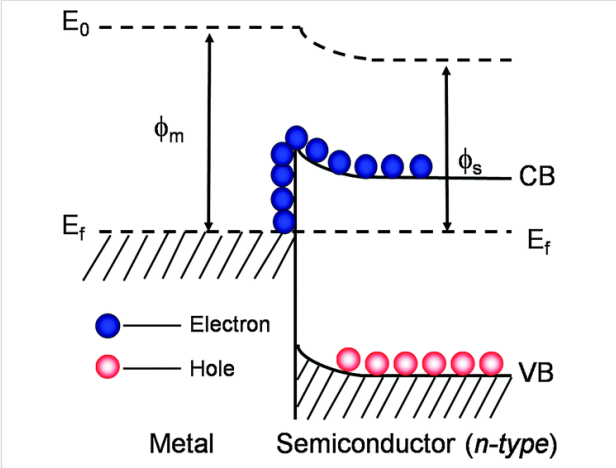

Figure 5: Schematic of the Schottky junction mechanism. Reprinted with permission from [35], copyright 2014 Royal Society of Chemistry.

Synthesis routes such as sol–gel, hydrothermal, microwave hydrothermal, impregnation, electrochemical deposition, chemical deposition, deposition-precipitation, UV photodeposition and direct sunlight photodeposition have been reported [23,50-86]. The conventional and most frequently used methods are the sol–gel and deposition–precipitation methods. These are mostly widely preferred due to the relatively facile and direct synthesis for obtaining the target composite. However, the deposition concentration of noble metal is moderately low [3]. Meanwhile, the hydrothermal method often suffers from major metal nanoparticle aggregation issues [3]. Similarly, chemical methods result in aggregation of nanoparticles throughout the adsorption stage and thus decrease the efficiency during photocatalysis [3].

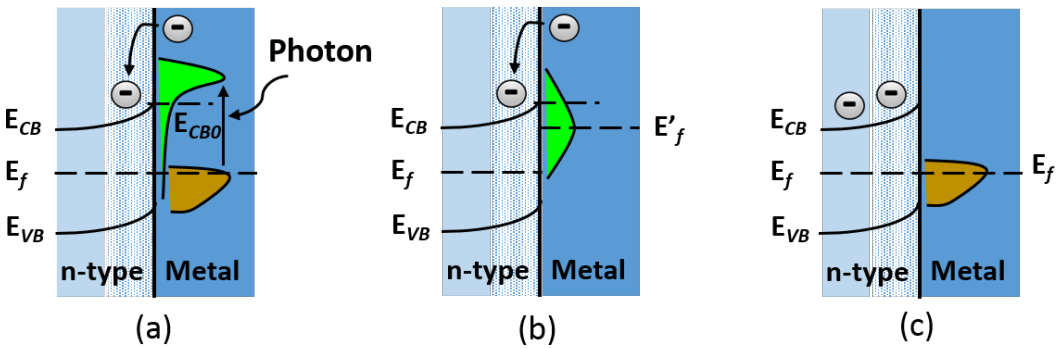

Figure 4: Pictorial representation of the localized surface plasmon resonance principle. Reprinted with permission from [31], copyright 2016 Springer.

The photodeposition method has overcome these disadvantages and produces a higher concentration of incorporated noble metal into the semiconductor composite [1]. This method is assisted by light whereby the deposition of noble metal nanoparticles takes place on the semiconductor surface. The most common light source used is a UV lamp producing a high-energy spectrum. Since most contemporary research promotes sustainable and green synthesis routes, replacing the UV lamp as the source of photons with renewable energy could be an alternative. Moreover, researchers have proven the possibility of using direct sunlight as an alternative to artificial UV light for such noble metal deposition. In a study by Leong and co-workers, they successfully achieved the deposition of Ag and Pd onto the surface of TiO_2 via this renewable route. They also used sunlight to synthesize the LPSR-induced photocatalyst through the electron formation and mobility mechanism. Thus, the fabricated photocatalyst exhibited pronounced efficiency in generating reactive oxygen species [50,51]. In general, this specific deposition mechanism functions similar to that of TiO_2 which has a distinctive electronic configuration structure (filled valence band and an empty conduction band). When exposed to direct sunlight irradiation, the UV light breaks the band gap energy of TiO_2 (3.2 eV) and then activates the electrons in the valence band. Thus, activated electrons move to the conduction band, leaving behind enriched holes in the valance band. The free electrons in the conduction band are then free to react with specific precursors through the support of reducing agents, resulting uniform metallic nanoparticles deposited on the surface. The holes then react with ethylene glycol to form aldehyde. Table 1 comprehensively presents the various synthesis routes for fabrication of LPSR-induced photocatalysts. Interestingly, the fabrication of plasmonic photocatalysts using sustainable approaches showed better performance as compared to the conventional synthesis methods. The mechanism of nanoparticle formation and deposition using an sustainable approach is illustrated in Figure 6.

Interaction of noble metals with semiconductor materials

Most of the literature claims that the incorporation of plasmonic nanoparticles with semiconductors can extend light absorption towards the visible and near infrared (NIR) spectrum. But in order to show enhanced plasmonic photocatalysis performance, the understanding of the material system plays a vital role. This includes the type of noble metal and semiconductor photocatalyst together with their morphology, porosity, crystallinity, contact form, etc. Although many semiconductor metal oxides such as N-doped TiO_2 [88], Fe_2O_3 [89], CdS [90] and Bi_2O_3 [91,92] have been reported, this section will mainly focus on TiO_2, which is the most widely studied. Au or Ag nanoparticles can be employed to produce an outstanding plasmonic effect in the visible and UV range [93-96]. Additionally, other noble metals such as Pt and Pd also exhibited a similar photocatalytic performance [97,98].

Ag, Au, Pt and Pd nanoparticles

Ag and Au are the most preferred noble metals for interaction with various types of semiconductors due to the strong LSPR produced; however, this phenomenon is mainly affected by morphology, size, and composition of the NPs as well as the dielectric properties of the surrounding medium [99,100]. Xu et al. reported that the content of metallic Ag and the extent of metallic Ag dispersion were factors which can be controlled to improve photocatalytic efficiency [101]. The LSPR of Ag in a Ag/AgCl composite was found to enhance the local inner electromagnetic field and prolong the lifetime of the charge carriers. Wang et al. observed that Ag@AgBr exhibited enhanced photocatalytic activity as compared to Ag/AgCl by a factor of 1.5.

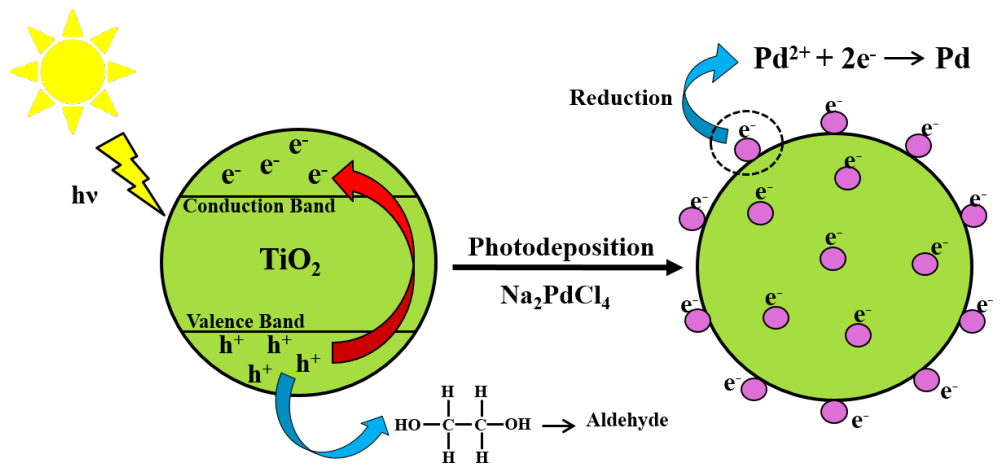

Figure 6: Synthesis of Pd/TiO_2 photocatalyst via sunlight-assisted photodeposition [50].

Table 1: Summary of various synthesis routes for preparation of plasmonic photocatalysts.

Plasmonic photocatalyst	Preparation method	Light source	Photocatalysis performance	Ref.
Ag-TiO_2	UV photodeposition	visible light (457 nm) and sunlight	enhanced H_2 production of 90 µmol (artificial visible light) and 105 µmol (sunlight) as compared to TiO_2 (70 µmol, artificial visible light and 80 µmol, sunlight)	[52]
Ag-TiO_2	wet chemical	sunlight	increase in Ag NP loading increased the photocatalysis efficiency: 97% degradation for 10 µM MB in 60 min and 93% for 5 µM MO in 40 min	[53]
Ag-TiO_2	ultrasound	visible light (400–700 nm)	20 wt % Ag-TiO_2 showed acetone degradation rate of 0.57 mg m^{-3} min^{-1} as compared to almost 0 mg m^{-3} min^{-1} for TiO_2	[54]
Ag-TiO_2	sol–gel process	visible light (18 W fluorescence TL-D tube light)	complete removal of indigo carmine (2.5×10^{-5} M) was achieved in 3 h	[55]
Ag-TiO_2	hydrothermal	visible light (400–500 nm)	complete removal of rhodamine B (2 mg/L) in 180 min by Ag-TiO_2 arrays; 55% for TiO_2	[56]
Ag-TiO_2	electrochemical deposition	visible light (>420 nm)	photocatalysis of Ag-TiO_2 achieved about 80% removal of methyl blue (2×10^{-5} M) in 2.5 h against TiO_2	[57]
Ag-TiO_2	electrodeposition	visible light (400–700 nm)	complete decomposition of methyl blue with Ag/TiO_2 core–shell nanowires within 40 min and 10 min for UV and visible light, respectively	[58]
Ag-TiO_2	sulfydryl-assisted	visible light (>400 nm)	almost complete degradation (98%) of methyl orange was achieved by Ag/TiO_2 as compare to TiO_2 (30%)	[59]
Ag-TiO_2	photodeposition	visible light (200 W halogen lamp)	TiO_2 with 2% Ag obtained improved photodegradation of rhodamine B (10^{-5} M) with ≈30% improvement under visible light irradiation	[60]
Ag-TiO_2	photoreduction by artificial UV light	visible light (>400 nm)	complete degradation of rhodamine B was achieved for TiO_2 with 1 wt % Ag with initial dye concentration of 10 mg L^{-1} in 30 min	[61]
Ag-C_3N_4	reflux treatment	visible light (>420 nm)	enhanced photocurrent intensity (a factor of 4), photodegradation of methylene blue (by 1.8 times) and hydrogen production (by 30 times) as compared with C_3N_4	[62]
Ag-TiO_2	photoreduction by direct sunlight	visible light (>420 nm)	0.3 wt % Ag/TiO_2 showed clear photodegradation of amoxicillin and 2,4-dichlorophenol in contrast to TiO_2	[51]
Ag-TiO_2	photochemical reduction under Xe lamp	visible light (>400 nm)	incorporation of Ag onto TiO_2 resulted in significant photodegradation of rhodamine B as compared to TiO_2 (by a factor of more than 2)	[63]
Au-TiO_2	impregnation	visible light (460–700 nm)	complete decolourization of methylene blue (1.0×10^{-5} M) in a short duration (10 min); complete degradation was reported for rhodamine B (2 min) and ≈25% degradation of 4-chlorophenol in 180 min	[64]
Au-TiO_2	impregnation	visible light (LED green light)	significant enhancement was achieved with complete conversion of formaldehyde of 83.3% under visible light at 44% relative humidity	[65]
Au-TiO_2	sol–gel	UV light (200 W Hg lamp)	Au deposition over TiO_2 enhanced the conversion of CO_2 to CO with a rate of 4144 µmol g^{-1} h^{-1} which is 345-fold higher than pure TiO_2	[66]
Au-TiO_2	deposition–precipitation	visible light (>420 nm)	the presence of Au enhanced the photocatalytic activity of both methylene orange removal and hydrogen production	[67]
Au-TiO_2	deposition–precipitation	visible light (400–700 nm)	improved charge separation and transfer resulted to an enhanced H_2 evolution rate	[68]
Au-TiO_2	deposition–precipitation	sunlight	highest degradation efficiency of 97% in 50 min was reported for Safranin O dye after the incorporation of Au nanoparticles	[69]
Au-TiO_2	deposition–precipitation	simulated solar light (Abet Technologies, Sun 2000)	H_2 production increased up to 5–6 mmol ($g^{-1}h^{-1}$) under simulated solar irradiation and further increased with increased Au concentration	[70]
Au-TiO_2	deposition–precipitation	sunlight	mesoporous Au/TiO_2 with 4 wt % Au resulted in 99% removal of alizarin as compared to P25 (65%) in 80 min	[71]

Table 1: Summary of various synthesis routes for preparation of plasmonic photocatalysts. (continued)

Au-TiO_2	chemical precipitation method	visible light (>305 nm)	the surface deposition approach significantly improved the photoactivity by 5–10-fold for the studied micropollutant	[72]
Au-TiO_2	microwave–chemical reduction	visible light (>420 nm)	H_2 production rate for Au/TiO_2 reached 4.3 μmol cm^{-2} h^{-1} as compared to 0.47 μmol cm^{-2} h^{-1} for TiO_2	[73]
Pd-TiO_2	impregnation	UV and visible light (400–700 nm)	Pd activates SPR which escalates hydrogen production (by a factor of 4); the reaction requires the presence of both UV and visible light to achieve 800 μmol/g	[74]
Pd-TiO_2	sol–gel	UV light (8 W UV lamp)	Pd-doped TiO_2 enhanced the degradation of NO_x (88%) and CO (74%) as compared to un-doped TiO_2 (59% and 56%)	[75]
Pd-TiO_2	hydrothermal	visible light (>400 nm)	optimal photocatalytic performance of p-nitrophenol reduction was achieved by loading 1.0 mol % Pd onto titania nanotubes; a rate constant of 0.7072 min^{-1} was reported for the photocatalytic oxidation	[76]
Pd-TiO_2	glucose reduction	UV light (150 W Hg lamp)	Pd NPs on the TiO_2 surface substantially increase the electron movement and act as vital sites for adsorption to promote CO_2 hydrogenation; as a result, 1.0 wt % Pd loading yielded 355.62, 46.35, and 39.69 μmol/g for CH_4, CO and C_2H_6, respectively	[77]
Pd-TiO_2	reduction	UV light (100 W UV lamp)	photocatalytic activity of TiO_2 impregnated with 1 wt % Pd performed well compared to TiO_2; almost 90% conversion of n-hexane, n-octane, cyclohexane and isooctane achieved within 27, 28, 34 and 36 s, respectively	[78]
Pd-TiO_2	chemical reduction	solar stimulator (50 mW cm^{-2}, 300 W Xe lamp)	immense improvement in photocatalytic activity with enhanced H_2 production as compared to TiO_2; TiO_2 decorated with 0.18 wt % Pd NPs showed an H_2 production rate of 3096 μmol $g^{-1}h^{-1}$	[79]
Pd-TiO_2	chemical photodeposition	solar simulator	higher decolourization (32%) for rhodamine B	[80]
Pd-TiO_2	solar deposition	sunlight	complete degradation (97.5%) of amoxicillin was obtained within 5 h by optimum loading of 0.5 wt % Pd onto the surface of TiO_2	[50]
Pt-loaded g-C_3N_4	polyol	15 W energy saving daylight	2 wt % Pt on g-C_3N_4 showed highest CH_4 yield of 13.02 μmol g^{-1} as compared to unloaded g-C_3N_4 (2.55 μmol g^{-1}) after 10 h of irradiation	[81]
Pt-TiO_2	sol–gel	18 W daylight lamp	better formaldehyde degradation (98.3%) as compared to TiO_2 (75.2%)	[82]
Pt-TiO_2	impregnation–reduction	visible light (>450 nm)	improved catalytic performance of aniline oxidation was achieved for 2 wt % Pt particles with 12 h of photoreaction	[83]
Pt-TiO_2	impregnation–reduction	UV light (350 W high-pressure Hg)	optimal Pt loading of 1.2 wt % exhibited increased (125-fold) H_2 production rate compared to unmodified TiO_2 microspheres	[84]
Pt-TiO_2	chemical deposition	visible light (>420 nm)	rate constant of Pt-TiO_2 for 10 mg/L nitrobenzene degradation was 2× larger than with TiO_2	[85]
Pt-TiO_2	UV-assisted photodeposition	visible light (>420 nm)	3 mM H_2PtCl_6 yielded highest photodegradation (84.27%) for methyl orange	[86]
AgCl-CN	deposition–precipitation	15 W energy saving daylight	2.5-fold increase in methane yield of was achieved for the AgCl-CN compared to CN	[87]

This achievement was attributed to the lower electron affinity of Br^- compared to Cl^-. The variation in shape and diameter of the Ag NPs resulted in an increased frequency range of plasmonic oscillation and thus Ag@AgBr was found to readily absorb a wide range of the visible spectrum [102]. Purbia et al. incorporated Au as a secondary noble metal in a Ag@AgBr heterostructure in which the LSPR of Au NPs remained in the visible region. The resulting bimetallic (Ag–Au) coupling boosted the photocatalytic efficiency by 16-fold as compared to mono-metallic (AgBr). The increase of the resonance-excited hot-electron density on the surface of Ag and Au NPs escalated the Fermi energy level of Ag and Au, enabling the electrons to be easily injected to the conduction band of AgBr. Simultaneously, the difference in work function between the bimetallic and AgBr formed a Schottky junction to facilitate the electron transfer until a Fermi equilibrium was achieved. The schematic of the mechanism of the bimetallic Au/AgBr-Ag heterostructure and the reactive oxygen species (ROS) formation reaction as reported by Purbia et al. is depicted in Figure 7 [103].

Another such similar finding was reported on the photoreduction of graphene oxide (GO) to graphene or reduced graphene oxide (rGO) by Wu et al. Their study revealed the photocatalytic Ag NP reduction at λ > 390 nm [95]. The schematic diagram representing the interaction of GO with Ag is shown in Figure 8. The LSPR effect on the Ag NPs generated a strong oscillating local electric field that enhanced the excitation of metallic charge carriers. The subsequently excited electrons were transferred to the conduction band of GO, yielding GO reduction and oxidation of Ag NPs [6].

Sun et al. described the role of Ag in the Ag@C composite. The composite displayed a broad LSPR absorption band at ≈630 nm [93]. The Ag@C nanocomposite exhibited excellent removal of aqueous rhodamine B and gaseous acetaldehyde (CH_3CHO) under visible light irradiation. There have been some research reports on the combination of either Pd or Pt (considered to induce a reduced plasmonic effect) with Au or Ag, (considered to induce an enhanced plasmonic effect) in which the former acts as an electron sinker for more efficient electron–hole pair separation [6]. For instance, Shuang et al. studied one such combination where they decorated TiO_2 nanopillar arrays with both Au and Pt NPs and achieved a photocatalysis efficiency of 21 and 13 times higher than for pure TiO_2. Their excellent results were attributed to the synergistic effect of Pt NPs which act as an electron trapper and the SPR of Au NPs [104].

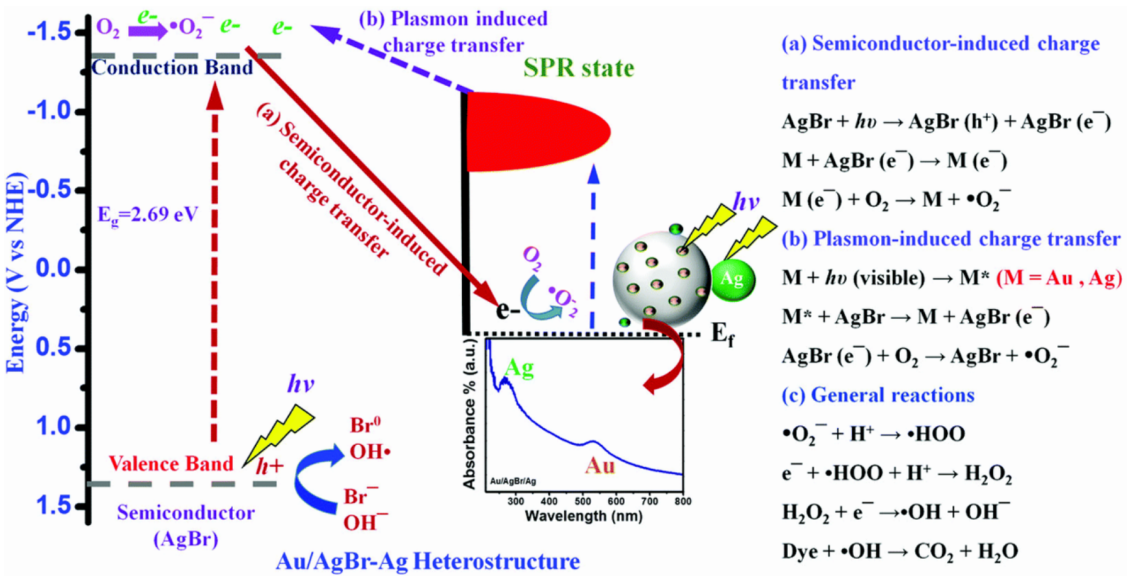

Figure 7: Schematic of Au/AgBr-Ag heterostructure mechanism for improved photocatalytic performance. (a) Semiconductor-excited (AgBr) electron transfer to metal (Au or Ag) NPs. (b) Plasmon-excited electron (Au or Ag) transfer to semiconductor (AgBr) NPs (e^- = electron, h^+ = hole, E_f = Fermi energy, M = Au or Ag). (c) General reaction involved in mechanism of Au/AgBr-Ag heterostructure. Reprinted with permission from [103], copyright 2017 Royal Society of Chemistry.

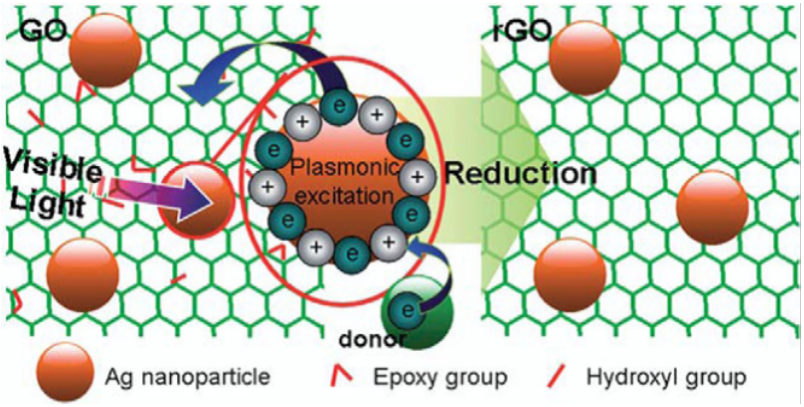

Figure 8: Photodegradation of GO in the presence of an electron donor (Ag NPs). Reprinted with permission from [95], copyright 2011 Royal Society of Chemistry.

Interactive plasmonic photocatalytic systems

The various plasmonic photocatalytic systems differ with respect to the type of interaction between the noble metal and the semiconductor. The taxonomy of the plasmonic photocatalytic systems together with their interaction patterns are schematically explained in Figure 9 [6].

Figure 9c clearly shows the embedded form of the noble metal/semiconductor system in which the metal is completely embedded into the semiconductor. This type of system benefits from the full advantages of Schottky junction formation with enhanced electron mobility as compared to partially embedded structures (Figure 9b). In addition, noble metal NPs that are embedded inside the semiconductor layer are less likely to dissolve, aggregate and detach. These advantages are helpful to increase the scattering of the NPs in the semiconductor and to confirm the stability of the photocatalysis reaction. However, noble metal NPs do not interact with the surrounding environment in this system (as do organic molecules in the solution) and thus lack the potential for redox reactions to occur. The generated charge carriers are trapped by the presence of noble metal. This leads to saturation when accumulating charge carrier reaches it limits. Thus, the gathered charges are finally trapped and allow a slow dispersion across the Schottky junction. However, in order to understand the mechanism of the LSPR effect, the Schottky junction, and the Fermi and mobilisation of electron/holes across the noble metal and semiconductor, either advanced characterisation tools or a theoretical simulation is necessary for detailed understanding of the circumstances.

Advanced characterization and theoretical simulation

The electron transfer mechanisms of plasmonic/semiconductor hybrid systems have been reported elsewhere. However, the principal mechanism that governs the plasmon excitation and electron injection into the semiconductor are still unclear. The verification that plasmon-excited electrons in Au NPs possess sufficient energy to overcome the Schottky junction to be injected into TiO_2 was confirmed using high-resolution X-ray absorption spectroscopy (HR-XAS) [105]. The adopted experimental setup is depicted in Figure 10. The significant spectral variations observed by X-ray absorption spectroscopy (XAS) and resonant inelastic X-ray scattering (RIXS) suggest that electrons injected from Au NPs upon LSPR excitation could survive longer and become trapped at a Ti site near the surface of TiO_2 [106]. More detailed work needs to be carried out to identify the individual contributions from different plasmonic effects such as hot-electron injection, generation of electromagnetic field and plasmon-induced heating [107]. The measurement of plasmonic photoelectrodes with polarized irradiation along various axes was combined with theoretical simulations based on the finite element method (FEM). In situ XAS was used to understand the electronic structural changes caused by the electromagnetic field upon the surface of plasmonic materials [108]. Designing the physical parameters of plasmonic metal nanostructures such as particle size, work function, surface facet and plasmonic band is a challenging task that demands numerical

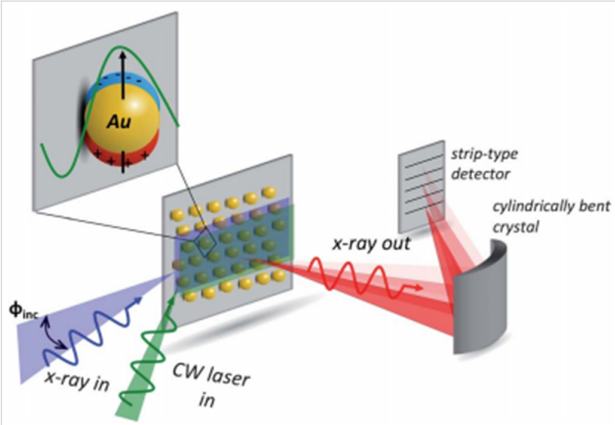

Figure 10: High-resolution X-ray absorption spectroscopy (HR-XAS) experiment used to determine the changes in the Au L_{III}-edge induced by 100 mW continuous wave laser excitation of the localized surface plasmon at 532 nm. Reprinted with permission from [105], copyright 2013 Royal Society of Chemistry.

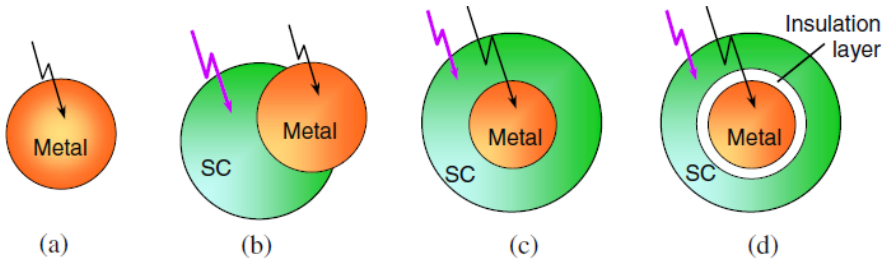

Figure 9: (a) Pure metal nanoparticles (NPs) without any semiconductor. (b) Metal NPs partially embedded into the semiconductor and partially exposed to the environment. (c) Metal NPs having a direct electrical contact by being fully embedded within the semiconductor without being exposed to the environment. (d) Metal NPs isolated from the semiconductor by a non-conducting layer to prevent direct electric contact. Reprinted with permission from [6], copyright 2013 IOP Publishing.

simulation. It is known that the photocatalysis performance is affected by the noble metal particle size and thus finite difference time domain (FDTD) simulations were studied to reveal spectral and spatial features of the plasmonic field [109,110]. The FDTD simulations probe the effect of the particle size for optimizing the performance of catalytic systems. Some research groups have performed FDTD simulations to elucidate the contribution of the LSPR feature in the Cu_7S_4@Pd catalyst. They found that Pd NPs showed weak LSPR absorption at 808, 980 and 1500 nm, while Cu_7S_4 exhibited obvious electrical field enhancement at these wavelengths; thus Cu_7S_4 was found to be the dominant contributor to the LSPR feature [111]. Using a similar simulation method, it was claimed that the enhanced photo-electrochemical water splitting performance of Pd@$BiVO_4$ was attributed to the hot-electron injection from Pd NPs upon SPR excitation in the vis–NIR region [112].

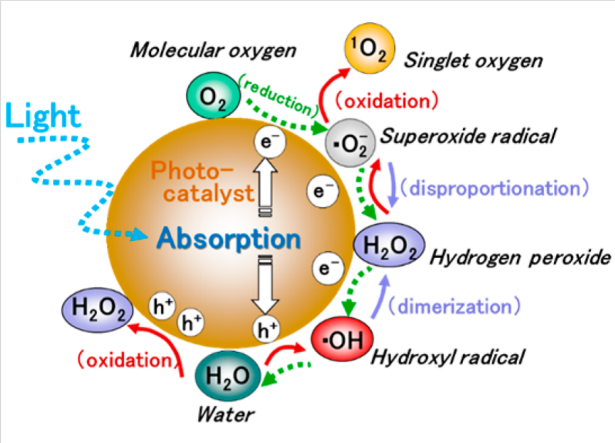

Figure 11: Generation of reactive oxygen species (ROSs) in the photocatalytic reduction and oxidation of O_2 and H_2O. Reprinted with permission from [115], copyright 2017 American Chemical Society.

Identification of reactive radicals

It is quite obvious that photocatalysis is supported by redox reactions caused by photo-induced formation of electrons (e^-) and holes (h^+). Several reactive species are produced on the heterogeneous solid surfaces of photocatalysts during the oxidative and reductive reactions in photocatalysis. Thus photocatalysis can be practically employed with water vapour under aerobic conditions, whereby photocatalysis involving oxygen (O_2) and water (H_2O) as reaction species is vital. The species to which oxygen converts with high reactivity are generally called reactive oxygen species (ROSs) and four such major ROSs are recognized, namely hydroxyl radical (•OH), superoxide anion radical ($\cdot O_2^-$), singlet oxygen ($^1O_2$) and hydrogen peroxide (H_2O_2). Since the redox reaction takes place during the photocatalysis reaction, ROSs are produced sequentially both from O_2 and H_2O as illustrated in Figure 11 [113-115]. In general ROSs of •OH, H_2O_2, $\cdot O^{2-}$ and $^1O^2$ would be generated in this order by the stepwise oxidation of H_2O. On the other hand, the stepwise reduction of O_2 generates $\cdot O^{2-}$, H_2O_2 and •OH.

The detection or quantification of these ROSs in the presence of a reactant pollutant is crucial for practical applications and such quantification can be correlated to the quantum efficiency (i.e., formation of ROSs for incident photon). Direct phosphorescence detection during the photocatalytic reaction would be beneficial for detection of $^1O_2$. For •OH, probing in solution could be observed from the surface reaction by perceiving the location of the probe molecules. In some cases the detection of $\cdot O_2^-$ and H_2O_2 after the photocatalytic reaction could be also possible. This review covers various studied detection methods used to identify the active radicals (quantum analysis) involved in the photocatalysis along with the uncertainties involved. Most of the reports of the present review concern ROSs in aqueous suspensions of photocatalyst powders. However, in some cases, reactions under gaseous conditions, whose behaviour might be different from those in aqueous suspensions, were involved.

Quantification methods for H_2O_2

Although the generated ROSs subsequently decay, H_2O_2 is the most stable of the molecules and can be detected separately. As of now, various methods have been employed for its quantification in photocatalysis reactions and could be classified as (1) direct optical absorption in UV and IR regions, (2) coloration and (3) fluorescence probe.

Direct optical absorption

The direct detection of H_2O_2 in solution by measuring UV spectra is difficult due to the weak molar absorption coefficient of H_2O_2 (0.01 M^{-1} cm^{-1}) at 360 nm, which gradually increases up to 13 M^{-1} cm^{-1} at the wavelength of 260 nm [115]. Meanwhile, the optical absorption in the IR region can be detected by observing the peak of O–O stretching of H_2O_2. Figure 12 shows three plausible types of structural formation of adsorbed H_2O_2 on to the surface of TiO_2. A side-on peroxide structure (Figure 12c) appeared for the absorption band on rutile at

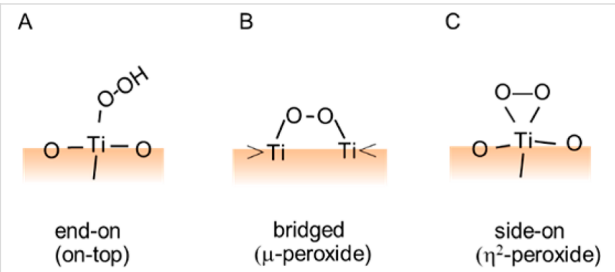

Figure 12: Plausible structural formation of adsorbed H_2O_2 on TiO_2 surface (a) end-on (b) bridged and (c) side-on. Reprinted with permission from [115], copyright 2017 American Chemical Society.

820–940 cm^{-1} [113]. The peaks at 838 and 877 cm^{-1} were assigned to the end-on peroxide (see Figure 12a), and that at 812 cm^{-1} was assigned to the bridged peroxide (see Figure 12b) [115]. The signal observed at 928 cm^{-1} was tentatively assigned to the triangle peroxide (see Figure 12c) [115].

Coloration methods

Coloration is another common method adopted for the quantification of H_2O_2. In this method, iodide [116,117], Ti^{4+} ions [118] and *N*,*N*-dimethyl-*p*-phenylenediamine (DPD) [119,120] were used to detect H_2O_2 during photocatalysis. For the iodide method, the solution was mixed with KI and sodium acetate buffer containing a few drops of catalyst (ammonium dimolybdate) for the oxidation of I^- by H_2O_2. Thus, I^{3-} was obtained in the solution and was measured at 360 nm. Alternatively, when Ti^{4+} ions were used as indicators, yellow-coloured metal complexes with H_2O_2 were formed and examined at 410 nm. [118]. The DPD method is based on the oxidation of DPD by H_2O_2 catalysed with horseradish peroxidase. The radical cation DPD^+ exhibits a fairly stable colour with an absorption peak at 551 nm [119,120].

Fluorescent probe

In this method a fluorescent dimer is created by reacting determining species (H_2O_2) with p-hydroxyphenyl- acetic acid mediated with horseradish peroxidase as a catalyst. The complete reaction scheme is explained in Figure 13a [115]. The intensity of the generated fluorescence is analysed using a fluorescence spectrophotometer with an emission wavelength of 408.5 nm excited at 316.5 nm. The concentration of the peroxide is directly proportional to the intensity of the created fluorescence as explained by the Beer–Lambert law [121-123]. Alternatively, a fluorescence probe reagent, dihydrorhodamine 123 was also reported to detect H_2O_2 in photocatalytic systems where dihydrorhodamine 123 is oxidized to a fluorescent molecule, rhodamine 123, by the reaction with H_2O_2 and peroxidase as shown in Figure 13b [115].

Detection methods for $^1O_2$

$^1O_2$ is singlet oxygen, which is an excited state of O_2. It can be deactivated to the original stable O_2 without being involved in chemical reactions or electron transfer. The detection methods of $^1O_2$ are focussed on (1) electron magnetic resonance and (2) fluorescence probe methods.

Electron spin resonance detection with probe reagents

For the detection of singlet oxygen in photocatalysis, 4-hydroxy-2,2,6,6-tetramethylpiperidine (HTMP), a well-known stable nitroxide radical (4-hydroxy-2,2,6,6-tetramethylpiperidine 1-oxyl, TEMPOL) is used to generate the corresponding 1-oxyl radical by the reaction with $^1O_2$ [124]. The final product is subjected to electron spin resonance (ESR) for the quantification of $^1O_2$ as shown in Figure 14a.

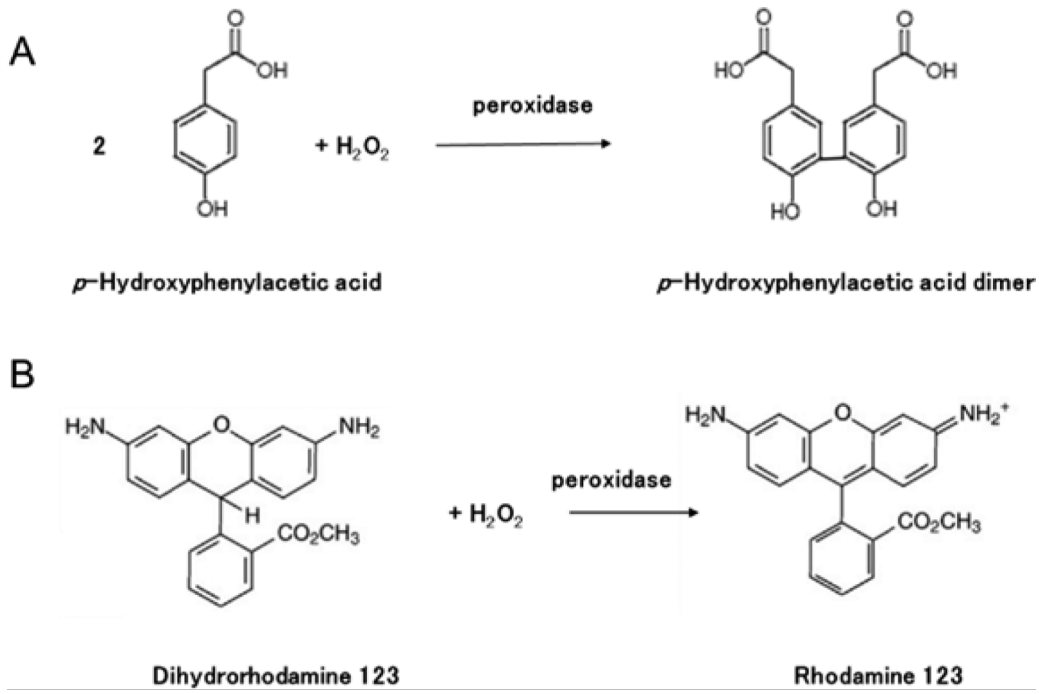

Figure 13: Reactions involved in the detection method of H_2O_2 with fluorescence probes (a) p-hydroxyphenylacetic acid (HPA) and (b) dihydrorhodamine 123. Reprinted with permission from [115], copyright 2017 American Chemical Society.

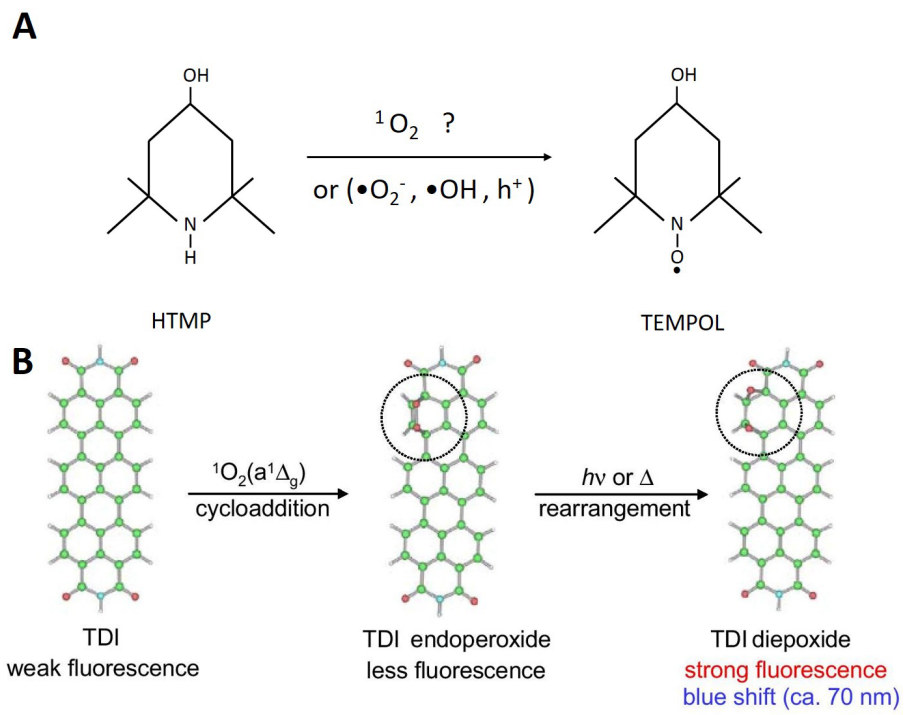

Figure 14: (a) Reaction of HTMP to TEMPOL. Reprinted with permission from [115], copyright 2017 American Chemical Society. (b) Fluorescence detection of $^1O_2$ with TDI. Reprinted with permission from [125], copyright 2007 Springer Science + Business Media.

A terrylene diimide (TDI) derivative that can produce fluorescent diepoxide through cycloaddition (Figure 14b) was adopted to detect $^1O_2$ generated in air. This TDI derivative is usually coated on a glass plate and faced the photocatalyst with an air gap through which $^1O_2$ diffuses. The detection of single-molecule fluorescence can be observed using a light microscope [125,126].

Finally, since the $^1O_2$ species possess paramagnetic properties caused by the orbital angular momentum, they can be quantified by direct ESR detection [127]. Therefore, an ESR spectrometer with a microwave frequency of about 9 GHz (X-band) could be used to observe the quartet signal of $^1O_2$ in the gas phase at 950 mT. Nevertheless, this detection method has not yet been applied to detect $^1O_2$ produced during photocatalysis.

Detection methods of •OH

The •OH radical is often regarded as the most effective reactant for photocatalytic decomposition. Among the various ROSs, the rate constant of •OH is almost at the diffusion limit and hence the reactivity of •OH is considerably high. The detection methods utilized for •OH in photocatalysis are focussed on (1) laser-induced fluorescence (LIF), (2) spin-trapping ESR and (3) fluorescent probe methods.

Laser-induced fluorescence methods

This highly sensitive method is employed to detect an low concentration of •OH radicals in the atmosphere. Figure 15a shows the experimental framework to measure the •OH radicals generated from irradiated TiO_2 [128]. A dye laser, which acts as a source of the emission wavelength at 310 nm, was used to calculate the intensity of the fluorescence emitted from •OH radicals. The •OH radicals emitted from the photoexcited TiO_2 surface to the gas phase were confirmed by the LIF spectrum (see Figure 15b) with the characteristic rotational structure of the transition energies [115].

Spin-trapping electron spin resonance

Spin-trapping ESR is a conventional method and most often utilized to detect the •OH generated in biological systems with the support of a spin-trapping reagent, namely 5,5-dimethyl-1-pyrroline *N*-oxide (DMPO) [129,130]. The unstable •OH radicals released during the photocatalysis react with DMPO to convert stable DMPO–OH radicals and are detected by ESR spectroscopy. There is a high probability that the valence-band holes might alternatively oxidize the spin-trapping reagents before the formation of •OH radicals. Figure 16 shows a three-step process for DMPO–OH radical formation in photocatalysis.

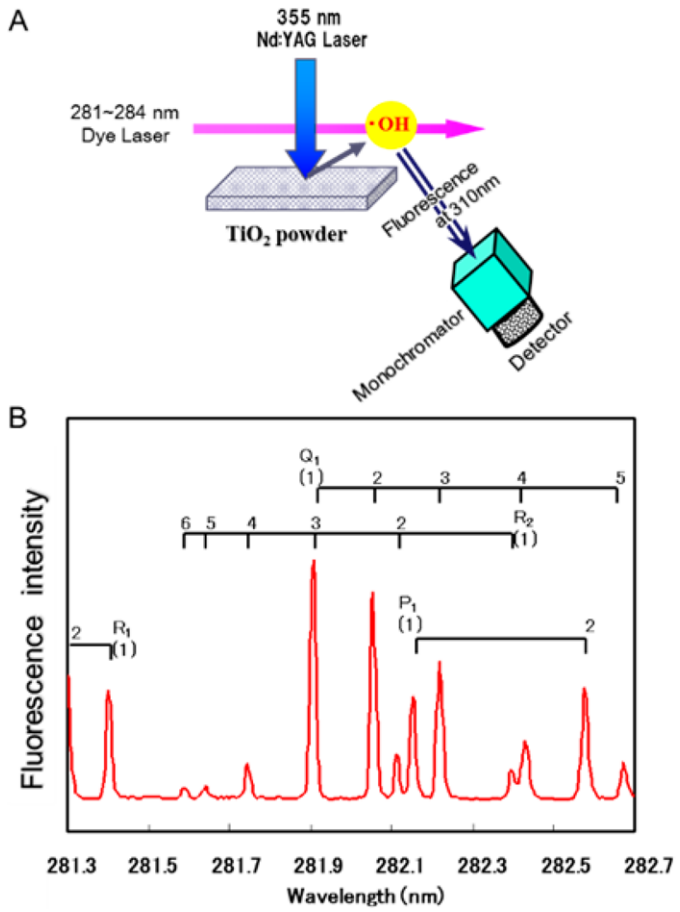

Figure 15: (a) Laser-induced fluorescence detection of •OH released from an irradiated TiO_2 surface. Reprinted with permission from [128], copyright 2007 American Chemical Society. (b) Obtained excitation spectrum of •OH radicals. Reprinted with permission from [115], copyright 2017 American Chemical Society.

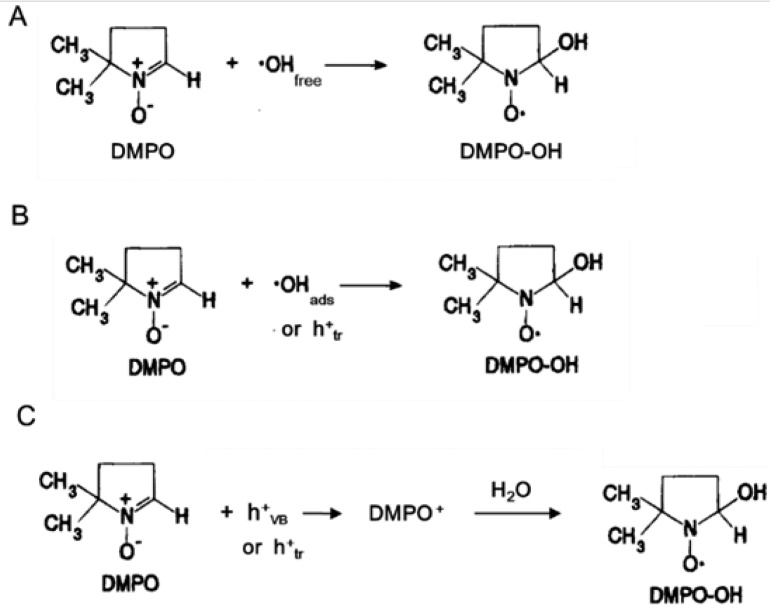

Figure 16: Reaction routes for detection of •OH radicals with a DMPO spin-trapping reagent. Reactions with •OH radicals (a) in solution, (b) at the surface, and (c) indirect reaction via oxidation of DMPO. Reprinted with permission from [115], copyright 2017 American Chemical Society.

Fluorescent probe

The fluorescein, 3-(*p*-hydroxyphenyl)fluorescein (HPF) and 3-(*p*-aminophenyl)fluorescein (APF) dyes have been used as reagents in photocatalytic reactions [131]. A strongly emissive fluorescein molecule, as shown in Figure 17a, was formed when HPF selectively reacts with •OH radicals. However, it does not react with the other ROSs, such as $•O_2^-$, $^1O_2$, and H_2O_2. A fluorescein-coated glass plate supported with HPF molecules is employed and a silanol group separates the TiO_2 coating glass plate with a spacer, as shown in Figure 17b. Polyimide films were used to control the distance between the two glass plates, and the space was filled with air-saturated water. In this way, it was confirmed that the •OH generated on the photocatalysts could diffuse to the HPF-coated glass.

Detection methods of $•O_2^-$

Spin-trapping electron paramagnetic resonance

The detection the $•O_2^-$ in aqueous solution by EPR can be performed with the presence of DMPO as the trapping agent (Figure 18a). Unfortunately the reaction rates of DMPO with $•O_2^-$ and $•O_2H$ are extremely small as compared with the •OH radical. In addition, the $•O_2^-$, which is drawn to DMPO, is unstable and it converts to •OH adducts (Figure 18a).Thus, the detection of $•O_2^-$ with DMPO is not facile [115].

Spin-trapping reagents such as 5-diethoxyphosphoryl-5-methyl-1-pyrroline *N*-oxide (DEPMPO) [132] and 5-*tert*-butoxycarbonyl-5-methyl-1-pyrroline *N*-oxide (BMPO) [133] and 5-(2,2-dimethyl-1,3-propoxycyclophosphoryl)-5-methyl-1-pyrroline *N*-oxide (CYPMPO) [134] have been reported. The chemical structures of these reagents are explained in Figure 18b.

Future perspective

Even though remarkable progress has been achieved in this area of research, some challenges are still to be met. The future perspective on the realistic application of plasmonic photocatalysts will focus on the scalability, cost and sustainability from the perspective of synthesis route to application. In addition, the

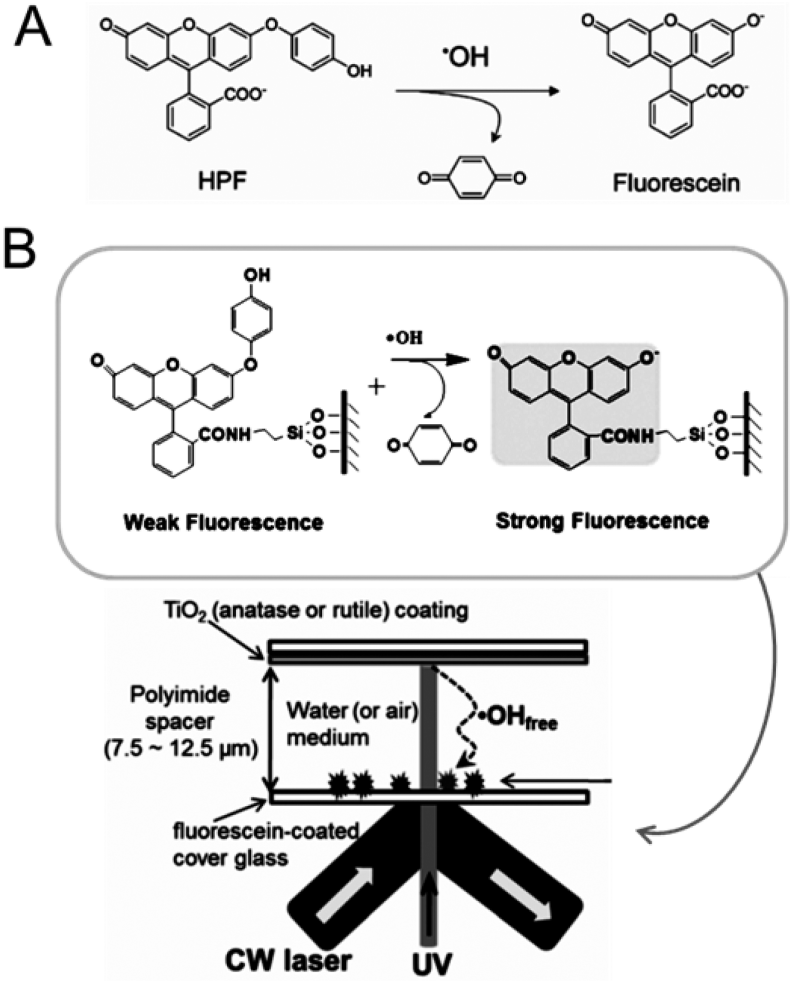

Figure 17: (a) Usage of fluorescence probe HPF to detect •OH radicals. (b) Experimental setup for the single-molecule detection of photogenerated •OH in H_2O. Reprinted with permission from [131], copyright 2014 Wiley-VCH Verlag GmbH & Co.

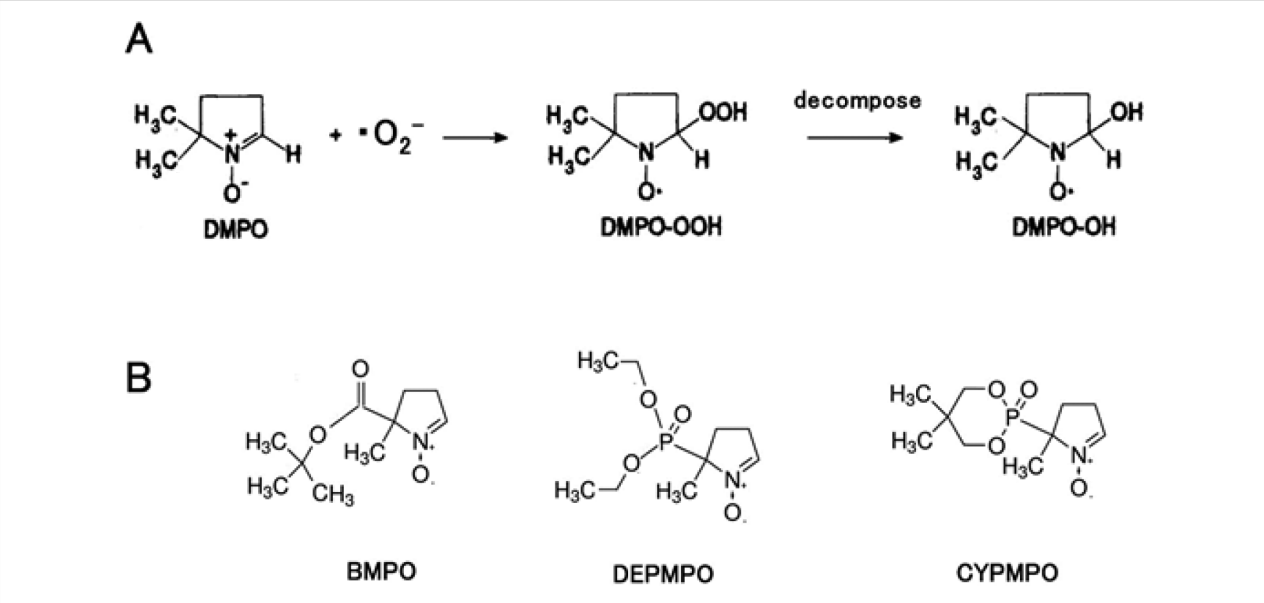

Figure 18: (a) Reactions involved in the detection of $\bullet O_2^-$ with DMPO. (b) Chemical structures of the spin-trapping reagents for $\bullet O_2^-$, BMPO, DEPMPO and CYPMPO. Reprinted with permission from [115], copyright 2017 American Chemical Society.

theory behind the plasmonic-induced electron transfer mechanism still remains questionable and thus necessitates the advanced characterization and theoretical simulation at the electronic level.

Near-infrared plasmonic materials for optimized solar absorption

In the preceding decades, much research was focused on the application of Au and Ag as plasmonic metals for utilising the visible region that consists of ≈43% of the solar spectrum against NIR [135]. The high carrier concentration (≈5.9×10^{22} cm^{-3}) of Au and Ag enables their intense LSPR excitations in the visible region [136]. The resonance in both Au and Ag can be controlled, but their high resistive loss, earth rarity and high cost are all disadvantages which limit them from being produced in large scale for real-world applications [21]. It is well-known that NIR wavelengths (760–3000 nm) account for ≈54% of the solar spectrum compared to the visible, which necessitates the search for plasmonic materials capable of utilising photons across the NIR region [137]. Compared to Au and Ag, conducting oxides and semiconductor nanomaterials possess lower carrier concentrations that are useful for their resonance in the NIR range [16]. For example, when coupled with Pd, copper chalcogenide (Cu_7S_4) utilizes NIR range photons through LSPR, and Pd traps the hot-holes for photocatalysis reactions, including oxidation of benzyl alcohol, hydrogenation of nitrobenzene and the Suzuki coupling reaction. The strong electrical field intensity at 1500 nm (Figure 19) reveals that the LSPR is more significant when the irradiation wavelength is near to the Cu_7S_4 LSPR peak [111]. Likewise, tungsten oxide ($WO_{3-\delta}$) nanocrystals showed intense NIR absorption with an LSPR peak at ≈900 nm [138]. The plasmonic resonance of semiconductors could be manipulated by tuning the stoichiometric composition, dopant concentration, or phase transitions [139,140]. The manipulation of the stoichiometric ratio of semiconductors could increase the free-charge density and promote the LSPR arising from collective oscillations of excess free charges on semiconductor surface, thus enhancing the NIR absorption abilities [141,142]. Interestingly, $Cu_{2-x}Se$ nanocrystals (NCs) showed distinct NIR plasmon band due to the formation of copper vacancies in the material through exposure to oxygen or to a Ce(IV) complex [143]. Similarly, the LSPR band in stoichiometric $Cu_{2-x}S$, $Cu_{2-x}Se$ and $Cu_{2-x}Te$ was improved by converting them into their nonstoichiometric counterparts via oxidation/reductive reactions [142]. Besides, the carrier concentration of aluminium-doped zinc oxide (AZO) can be shifted from 0.5 to 10×10^{20} cm^{-3} by varying the concentration of Al, thus contributing to the wide-range SPR (2200–880 nm) [144]. Despite the tunable plasmonic features of semiconductors, some plasmonic semiconductors are photocatalytically inert due to their unfavourable band edge position compared to the redox potential of targeted species. An effective approach to overcome this restriction was to integrate the nonstoichiometric materials (tungsten oxide ($W_{18}O_{49}$)) with graphitic carbon nitride (g-C_3N_4). The g-C_3N_4 was used to effectively capture the LSPR-excited hot electrons from $W_{18}O_{49}$, enabling an efficient photocatalytic reaction [145]. Similarly, TiO_2 was coupled with $W_{18}O_{49}$ for effective photocatalysis under full solar spectrum conditions. Another advantage of such hybrid nanostructures is their ability to facilitate the spatial charge separation of photoin-

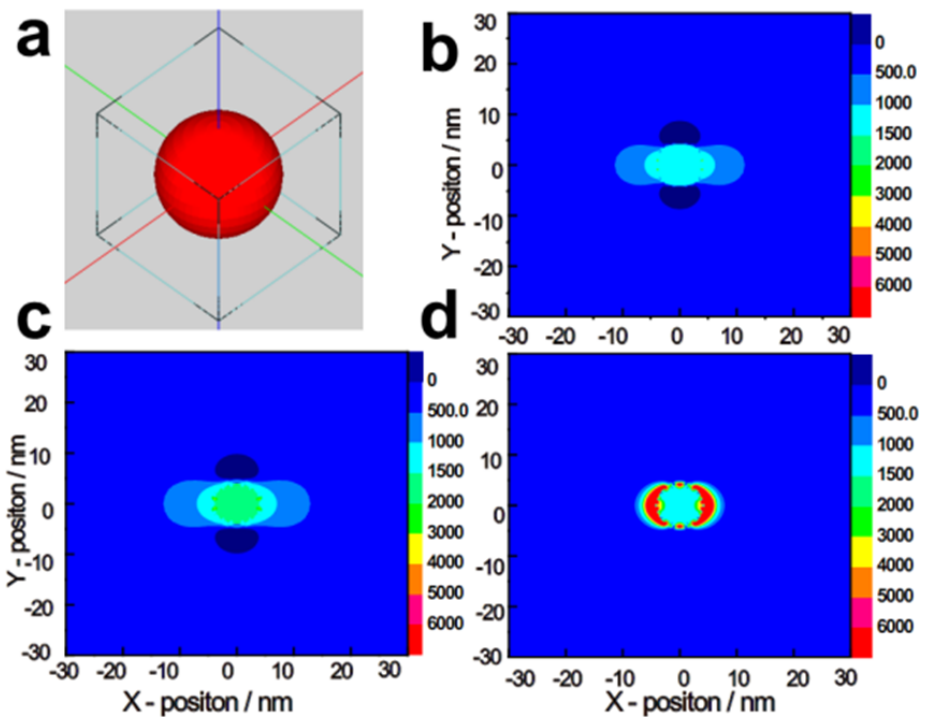

Figure 19: (a) FDTD simulation set up for Cu_7S_4. (b–d) 2D contour map of the electric field intensities around the Cu_7S_4 nanocrystal under illumination at 808 nm (b), 980 nm (c) and 1500 nm (d), respectively. Reprinted with permission from [111], copyright 2015 American Chemical Society.

duced carriers by creating an alternate permutation of band edges at the interface [146]. Some researchers found that both titanium nitride (TiN) and zirconium nitride (ZrN) displayed similar optical properties as Au and can replace Au NPs for vis–NIR light absorption [147,148].

Bio-inspired plasmonic nanostructures/architectures

The pioneering works of several research groups have revealed that by mimicing biological systems, such as butterfly wings [149] and snake skin [150], systems can be designed that are cable of absorbing NIR light due to their distinctive nanoarchitectures with underlying mechanisms. For example, the velvet black scales on snake skins have been shown to demonstrate four times better absorbance than other scales in the UV–NIR spectrum range due to their hierarchical pattern of leaf-like microstructures with nanoridges [150]. In other case, the geometry of the scales of a butterfly promote a light trapping effect from the UV to NIR range, which significantly increases the light absorption compared to a non-patterned system [149]. These works inspired the combination of bismuth vanadate ($BiVO_4$) with the 3D architecture design of a butterfly wing, in addition to gold nanorods (NRs) as plasmonic nanoantennas for an effective far red-to-NIR photocatalytic conversion. The electron–hole pairs were formed in some parts of BVO when $BiVO_4$ encountered intense SPR-induced electric fields localized at Au NRs, and hence the entire photocatalytic system could function under red-to-NIR irradiation [151]. All these studies provide new insight into using plasmonic nanoarchitectures for photocatalysis applications in the future. Similarly, biomimetic assembly methods can also be used to arrange plasmonic metals (Au and Ag) with molecular-level precision to achieve tunable light absorption and emission. Prior works reported the use of DNA oligonucleotides [152,153] and virus capsids [154] as tunable spacers to control the distance between Au NPs and fluorophores. The assembly hierarchy of the plasmonic photocatalysts were carried out using both MS2 virus capsids and DNA origami as biological scaffolds to increase fluorescence intensity by tuning the distance between capsid and Au NPs [155]. In recent years, the phytochemicals present in plant-based and waste materials have been used as reducing and stabilizing agents to prepare plasmonic metals (Au and Ag). The so called green synthesis of Au and Ag are suitably used in clinical and biomedical fields because it is free of toxic chemicals and non-polar solvents. Numerous researches have proved that Au and Ag NPs can be synthesized from the chemicals extracted from plants and microorganisms such as fungi, algae, bacteria and yeasts [156-161]. Different types of biomolecules available in plants, for example, polysaccharides, phenolics, or flavonoids are capable of producing metal nanoparticles of different sizes and shapes [162]. This phytosynthesis is more favourable than that which occurs in microorganisms because it is fast and cost effective and can be readily scaled for realistic

applications [163]. A very recent study demonstrated that Ag/AgCl can be synthesized using ash gourd peel extract without using organic toxic solvents [157]. Bovine serum albumin (BSA) and Neem extract were used to prepare Ag-ZnO nanostructures, in which both green extracts acted as a shape controllers and reducing agents of Ag^+ to overcome the self-nucleation problem of Ag NPs [164,165].

Direct photocatalysis by plasmonic metals

Plasmonic catalyst systems have almost exclusively focused on the coupling of plasmonic metals (Au and Ag) with semiconductors. Recent reports found that plasmonic metals can be utilised to motivate direct photocatalysis where both light harvesting and activation of reactants take place on the plasmonic metals. It is observed that, unlike semiconductors, the photocatalytic quantum efficiency on plasmonic metal enhances the light intensity and thermal energy absorption. This result shows that plasmonic metals are effective at coupling thermal and photonic stimuli for driving chemical transformations [166]. The rapid recombination of plasmon charge carriers restricted the direct photocatalysis reaction on metal surfaces; however, the energy obtained as a result of recombination facilitated thermal reaction and resolved this drawback [167]. Since the foremost discovery of primary photocatalysis by Au NPs through LSPR [168], numerous reactions have been performed on Ag, Au, and Cu surfaces, showing that low intensity visible photon irradiation significantly enhances the rate of chemical reactions. A pioneering work showed that Au NPs have potential in degrading volatile organic compounds, HCHO to CO_2, under 600–700 nm red light irradiation [168]. The same group also reported the use of Ag NPs to remove phenol and drive oxidation of benzyl alcohol to benzaldehyde under UV light. This verifies the role of the LSPR effect and interband transition of Ag NPs in activating organic molecules for oxidation under UV–vis irradiation [169]. Au NPs are more suitable for immediate plasmonic photocatalysis compared to other plasmonic metals because they are more chemically resistant and stable to standard atmosphere [170]. Under LED excitation at 530 nm in the presence of air or oxygen, Au NPs could promote the oxidation reaction of 9- anthraldehyde to form anthraquinone as the dominant product [171]. As compared to semiconductors like TiO_2, the ability of Au NPs to conduct plasmonic-induced reductions at lower temperature and pressure enable the selection of unstable intermediates of a thermal reaction as the product (e.g., aromatic azo compounds). These findings show the potential of Au NPs in utilizing the solar spectrum, also in temperature-sensitive synthesis [172]. Most reported works on direct photocatalysis are limited only to plasmon-induced chemical transformations. Very few have moved away from this traditional route to demonstrate the feasibility of electrocatalytic oxidation adopting glucose accelerated by Au NPs upon LSPR excitation under a suitable voltage bias. The hot electrons injected from Au NPs can be driven into the external circuit to deliver appreciable current, while the holes facilitate the electrocatalytic oxidation of glucose owing to their equal energy levels. This constructive finding propelled the potential applications of electrochemical energy conversion, electroanalysis and electrochemical devices [173]. Overall, it is clear that the plasmonic metals are able to concentrate and channel the energy of low intensity visible light into adsorbed molecules to promote significant enhancement in the rate of chemical transformation. Furthermore, there are certain cases that have showed primary evidence for direct plasmon-driven photocatalysis capable of controlling catalytic selectivity through different reaction mechanisms. Gold NPs on CeO_2 were found to be efficient at reducing a wide range of epoxides, azo compounds, and ketones at ambient temperature under visible light. Their reduction potential highly depends on the incident wavelength [174]. The team revealed the selectivity tuning by plasmon-mediated photo-switching and demonstrated the same for propylene epoxidation on Cu NPs in which the reduction of the Cu_2O shell was brought on by the plasmon-excited Cu [175].

Conclusion

This review explicitly detailed insight into plasmonic photocatalysts as a potential candidate for enhanced utilisation of the solar spectrum. The topic of the review was detailed through fundamental explanations together with the various synthesis routes. The review also clarified the mechanism of LSPR for the various noble metal nanoparticles in addition to the Schottky phenomenon on the studied metal oxide photocatalysts. An in-depth analysis on the formation and identification of ROSs and their interaction with pollutants was clearly presented. The future prospects of these sustainable photocatalysts with real-time applications for energy storage and environmental remediation were thoroughly reviewed. The present review also revealed the potential of plasmonic photocatalysts as an alternative sustainable approach and new direction for effectively harnessing sunlight to fulfil global environmental issues and aid to the energy crisis.

Acknowledgements

The corresponding author is grateful to Science and Engineering Research Board [SERB], Department of Science and Technology for the financial support received under the Early Career Research Award with grant code ECR/2016/001400. This work was also supported by Universiti Tunku Abdul Rahman Research Fund, UTARRF (IPSR/RMC/UTARRF/2016-C2-L05), (IPSR/RMC/UTARRF/2017-C1/S04) and Universiti Malaysia Pahang Internal Grant, RDU 160317 and RDU 1603137.

ORCID® iDs

Pichiah Saravanan - https://orcid.org/0000-0001-8302-9586

References

1. Zhou, X.; Liu, G.; Yu, J.; Fan, W. *J. Mater. Chem.* **2012,** *22,* 21337–21354. doi:10.1039/C2JM31902K
2. Ong, W.-J.; Tan, L.-L.; Chai, S.-P.; Yong, S.-T.; Mohamed, A.-R. *ChemSusChem* **2014,** *7,* 690–719. doi:10.1002/cssc.201300924
3. Kochuveedu, S. T.; Jang, Y. H.; Kim, D. H. *Chem. Soc. Rev.* **2013,** *42,* 8467–8493. doi:10.1039/C3CS60043B
4. Chen, H.; Sun, Z.; Ni, W.; Woo, K. C.; Lin, H.-Q.; Sun, L.; Yan, C.; Wang, J. *Small* **2009,** *5,* 2111–2119. doi:10.1002/smll.200900256
5. Wang, P.; Huang, B.; Dai, Y.; Whangbo, M.-H. *Phys. Chem. Chem. Phys.* **2012,** *14,* 9813–9825. doi:10.1039/C2CP40823F
6. Zhang, X.; Chen, Y. L.; Liu, R.-S.; Tsai, D. P. *Rep. Prog. Phys.* **2013,** *76,* 046401. doi:10.1088/0034-4885/76/4/046401
7. Wang, Z.; Liu, Y.; Huang, B.; Dai, Y.; Lou, Z.; Wang, G.; Zhang, X.; Qin, X. *Phys. Chem. Chem. Phys.* **2014,** *16,* 2758–2774. doi:10.1039/C3CP53817F
8. Cushing, S. K.; Li, J.; Meng, F.; Senty, T. R.; Suri, S.; Zhi, M.; Li, M.; Bristow, A. D.; Wu, N. *J. Am. Chem. Soc.* **2012,** *134,* 15033–15041. doi:10.1021/ja305603t
9. Linic, S.; Christopher, P.; Ingram, D. B. *Nat. Mater.* **2011,** *10,* 911–921. doi:10.1038/nmat3151
10. Shin, D. O.; Jeong, J.-R.; Han, T. H.; Koo, C. M.; Park, H.-J.; Lim, Y. T.; Kim, S. O. *J. Mater. Chem.* **2010,** *20,* 7241–7247. doi:10.1039/C0JM01319F
11. Moores, A.; Goettmann, F. *New J. Chem.* **2006,** *30,* 1121–1132. doi:10.1039/B604038C
12. Wang, X.; Zhu, M.; Sun, Y.; Fu, W.; Gu, Q.; Zhang, C.; Zhang, Y.; Dai, Y.; Sun, Y. *Part. Part. Syst. Charact.* **2016,** *33,* 140–149. doi:10.1002/ppsc.201500139
13. Sarina, S.; Waclawik, E. R.; Zhu, H. *Green Chem.* **2013,** *15,* 1814–1833. doi:10.1039/C3GC40450A
14. Wang, C.; Astruc, D. *Chem. Soc. Rev.* **2014,** *43,* 7188–7216. doi:10.1039/C4CS00145A
15. Kelly, K. L.; Coronado, E.; Zhao, L. L.; Schatz, G. C. *J. Phys. Chem. B* **2003,** *107,* 668–677. doi:10.1021/jp026731y
16. Clavero, C. *Nat. Photonics* **2014,** *8,* 95–103. doi:10.1038/nphoton.2013.238
17. Galian, R. E.; Pérez-Prieto, J. *Energy Environ. Sci.* **2010,** *3,* 1488–1498. doi:10.1039/C0EE00003E
18. Barnes, W. L.; Dereux, A.; Ebbesen, T. W. *Nature* **2003,** *424,* 824–830. doi:10.1038/nature01937
19. Chen, Y.; Xin, X.; Zhang, N.; Xu, Y.-J. *Part. Part. Syst. Charact.* **2017,** *34,* 1600357. doi:10.1002/ppsc.201600357
20. Stahl, S. S. *Science* **2005,** *309,* 1824–1826. doi:10.1126/science.1114666
21. Boltasseva, A.; Atwater, H. A. *Science* **2011,** *331,* 290–291. doi:10.1126/science.1198258
22. Choi, M.; Shin, K.-H.; Jang, J. *J. Colloid Interface Sci.* **2010,** *341,* 83–87. doi:10.1016/j.jcis.2009.09.037
23. Tada, H.; Kiyonaga, T.; Naya, S.-i. *Chem. Soc. Rev.* **2009,** *38,* 1849–1858. doi:10.1039/B822385H
24. Xie, Y.; Kum, J.; Zhao, X.; Cho, S. O. *Semicond. Sci. Technol.* **2011,** *26,* 085037. doi:10.1088/0268-1242/26/8/085037
25. Mohapatra, S. K.; Kondamudi, N.; Banerjee, S.; Misra, M. *Langmuir* **2008,** *24,* 11276–11281. doi:10.1021/la801253f
26. Kwak, B.-S.; Chae, J.-H.; Kim, J.-Y.; Kang, M.-S. *Bull. Korean Chem. Soc.* **2009,** *30,* 1047–1053. doi:10.5012/bkcs.2009.30.5.1047
27. Garcia, M. A. *J. Phys. D: Appl. Phys.* **2011,** *44,* 283001. doi:10.1088/0022-3727/44/28/283001
28. Kale, M. J.; Avanesian, T.; Christopher, P. *ACS Catal.* **2014,** *4,* 116–128. doi:10.1021/cs400993w
29. Molina, R. A.; Weinmann, D.; Jalabert, R. A. *Phys. Rev. B* **2002,** *65,* 155427. doi:10.1103/PhysRevB.65.155427
30. White, T. P.; Catchpole, K. R. *Appl. Phys. Lett.* **2012,** *101,* 073905. doi:10.1063/1.4746425
31. Leong, K. H.; Sim, L. C.; Saravanan, P.; Ibrahim, S. Light Driven Nanomaterials for Removal of Agricultural Toxins. In *Nanoscience in Food and Agriculture 3;* Ranjan, S.; Dasgupta, N.; Lichtfouse, E., Eds.; Sustainable Agriculture Reviews, Vol. 23; Springer: Berlin, Germany, 2016; pp 225–242. doi:10.1007/978-3-319-48009-1_9
32. Bumajdad, A.; Madkour, M. *Phys. Chem. Chem. Phys.* **2014,** *16,* 7146–7158. doi:10.1039/C3CP54411G
33. Qu, Y.; Duan, X. *Chem. Soc. Rev.* **2013,** *42,* 2568–2580. doi:10.1039/C2CS35355E
34. Liu, S.; Han, C.; Tang, Z.-R.; Xu, Y.-J. *Mater. Horiz.* **2016,** *3,* 270–282. doi:10.1039/C6MH00063K
35. Wang, H.; Zhang, L.; Chen, Z.; Hu, J.; Li, S.; Wang, Z.; Liu, J.; Wang, X. *Chem. Soc. Rev.* **2014,** *43,* 5234–5244. doi:10.1039/C4CS00126E
36. Ong, W.-J.; Tan, L.-L.; Chai, S.-P.; Yong, S.-T.; Mohamed, A.-R. *Nanoscale* **2014,** *6,* 1946–2008. doi:10.1039/C3NR04655A
37. Wang, J.; Tang, L.; Zeng, G.; Liu, Y.; Zhou, Y.; Deng, Y.; Wang, J.; Peng, B. *ACS Sustainable Chem. Eng.* **2017,** *5,* 1062–1072. doi:10.1021/acssuschemeng.6b02351
38. Rajender, G.; Choudhury, B.; Giri, P. K. *Nanotechnology* **2017,** *28,* 395703. doi:10.1088/1361-6528/aa810a
39. Ong, W.-J.; Putri, L. K.; Tan, L.-L.; Chai, S.-P.; Yong, S.-T. *Appl. Catal., B: Environ.* **2016,** *180,* 530–543. doi:10.1016/j.apcatb.2015.06.053
40. Ong, W.-J.; Putri, L. K.; Tan, Y.-C.; Tan, L.-L.; Li, N.; Ng, Y. H.; Wen, X.; Chai, S.-P. *Nano Res.* **2017,** *10,* 1673–1696. doi:10.1007/s12274-016-1391-4
41. Zeng, D.; Xu, W.; Ong, W.-J.; Xu, J.; Ren, H.; Chen, Y.; Zheng, H.; Peng, D.-L. *Appl. Catal., B: Environ.* **2018,** *221,* 47–55. doi:10.1016/j.apcatb.2017.08.041
42. Zeng, D.; Ong, W.-J.; Zheng, H.; Wu, M.; Chen, Y.; Peng, D.-L.; Han, M.-Y. *J. Mater. Chem. A* **2017,** *5,* 16171–16178. doi:10.1039/C7TA04816E
43. Ong, W.-J.; Tan, L.-L.; Ng, Y. H.; Yong, S.-T.; Chai, S.-P. *Chem. Rev.* **2016,** *116,* 7159–7329. doi:10.1021/acs.chemrev.6b00075
44. Ong, W.-J. *Front. Mater.* **2017,** *4,* 11. doi:10.3389/fmats.2017.00011
45. Yu, S.; Wilson, A. J.; Kumari, G.; Zhang, X.; Jain, P. K. *ACS Energy Lett.* **2017,** *2,* 2058–2070. doi:10.1021/acsenergylett.7b00640
46. Rahmanian, E.; Malekfar, R.; Pumera, M. *Chem. – Eur. J.* **2018,** *24,* 18–31. doi:10.1002/chem.201703434
47. Zeng, D.; Xiao, L.; Ong, W.-J.; Wu, P.; Zheng, H.; Chen, Y.; Peng, D.-L. *ChemSusChem* **2017,** *10,* 4624–4631. doi:10.1002/cssc.201701345
48. Zhang, Z.; Zheng, T.; Li, X.; Xu, J.; Zeng, H. *Part. Part. Syst. Charact.* **2016,** *33,* 457–472. doi:10.1002/ppsc.201500243
49. Chen, X.; Li, N.; Kong, Z.; Ong, W.-J.; Zhao, X. *Mater. Horiz.* **2018,** *5,* 9–27. doi:10.1039/C7MH00557A

50. Leong, K. H.; Chu, H. Y.; Ibrahim, S.; Saravanan, P. *Beilstein J. Nanotechnol.* **2015,** *6,* 428. doi:10.3762/bjnano.6.43
51. Leong, K. H.; Gan, B. L.; Ibrahim, S.; Saravanan, P. *Appl. Surf. Sci.* **2014,** *319,* 128–135. doi:10.1016/j.apsusc.2014.06.153
52. Rather, R. A.; Singh, S.; Pal, B. *Sol. Energy Mater. Sol. Cells* **2017,** *160,* 463–469. doi:10.1016/j.solmat.2016.11.017
53. Singh, J.; Satpati, B.; Mohapatra, S. *Plasmonics* **2017,** *12,* 877–888. doi:10.1007/s11468-016-0339-6
54. Stucchi, M.; Bianchi, C. L.; Argirusis, C.; Pifferi, V.; Neppolian, B.; Cerrato, G.; Boffito, D. C. *Ultrason. Sonochem.* **2018,** *40,* 282–288. doi:10.1016/j.ultsonch.2017.07.016
55. Suwanchawalit, C.; Wongnawa, S.; Sriprang, P.; Meanha, P. *Ceram. Int.* **2012,** *38,* 5201–5207. doi:10.1016/j.ceramint.2012.03.027
56. Zhao, C.; Zhu, D.-c.; Cheng, X.-y.; Cao, S.-x. *Front. Mater. Sci.* **2017,** *11,* 241–249. doi:10.1007/s11706-017-0386-8
57. Chen, Z.; Fang, L.; Dong, W.; Zheng, F.; Shen, M.; Wang, J. *J. Mater. Chem. A* **2014,** *2,* 824–832. doi:10.1039/C3TA13985A
58. Eom, H.; Jung, J.-Y.; Shin, Y.; Kim, S.; Choi, J.-H.; Lee, E.; Jeong, J.-H.; Park, I. *Nanoscale* **2014,** *6,* 226–234. doi:10.1039/C3NR04388F
59. Xia, H.; Wu, S.; Bi, J.; Zhang, S. *Nanotechnology* **2017,** *28,* 465604. doi:10.1088/1361-6528/aa8d94
60. Sung-Suh, H. M.; Choi, J. R.; Hah, H. J.; Koo, S. M.; Bae, Y. C. J. *J. Photochem. Photobiol., A* **2004,** *163,* 37–44. doi:10.1016/S1010-6030(03)00428-3
61. Chen, D.; Chen, Q.; Ge, L.; Yin, L.; Fan, B.; Wang, H.; Lu, H.; Xu, H.; Zhang, R.; Shao, G. *Appl. Surf. Sci.* **2013,** *284,* 921–929. doi:10.1016/j.apsusc.2013.08.051
62. Kumar, S.; Kumar, A.; Bahuguna, A.; Sharma, V.; Krishnan, V. *Beilstein J. Nanotechnol.* **2017,** *8,* 1571–1600. doi:10.3762/bjnano.8.159
63. Xiang, Q.; Yu, J.; Cheng, B.; Ong, H. C. *Chem. – Asian J.* **2010,** *5,* 1466–1474. doi:10.1002/asia.200900695
64. Bian, Z.; Tachikawa, T.; Zhang, P.; Fujitsuka, M.; Majima, T. *J. Am. Chem. Soc.* **2014,** *136,* 458–465. doi:10.1021/ja410994f
65. Zhu, X.; Jin, C.; Li, X.-S.; Liu, J.-L.; Sun, Z.-G.; Shi, C.; Li, X.; Zhu, A.-M. *ACS Catal.* **2017,** *7,* 6514–6524. doi:10.1021/acscatal.7b01658
66. Tahir, B.; Tahir, M.; Amin, N. A. S. *Clean Technol. Environ. Policy* **2016,** *18,* 2147–2160. doi:10.1007/s10098-016-1181-4
67. Ding, D.; Liu, K.; He, S.; Gao, C.; Yin, Y. *Nano Lett.* **2014,** *14,* 6731–6736. doi:10.1021/nl503585m
68. Priebe, J. B.; Radnik, J.; Lennox, A. J.; Pohl, M.-M.; Karnahl, M.; Hollmann, D.; Grabow, K.; Bentrup, U.; Junge, H.; Beller, M.; Brückner, A. *ACS Catal.* **2015,** *5,* 2137–2148. doi:10.1021/cs5018375
69. Bumajdad, A.; Madkour, M.; Abdel-Moneam, Y.; El-Kemary, M. *J. Mater. Sci.* **2014,** *49,* 1743–1754. doi:10.1007/s10853-013-7861-0
70. Puga, A. V.; Forneli, A.; García, H.; Corma, A. *Adv. Funct. Mater.* **2014,** *24,* 241–248. doi:10.1002/adfm.201301907
71. Mehta, A.; Sharma, M.; Kumar, A.; Basu, S. *Gold Bull.* **2017,** *50,* 33–41. doi:10.1007/s13404-016-0191-7
72. Nalbandian, M. J.; Greenstein, K. E.; Shuai, D.; Zhang, M.; Choa, Y.-H.; Parkin, G. F.; Myung, N. V.; Cwiertny, D. M. *Environ. Sci. Technol.* **2015,** *49,* 1654–1663. doi:10.1021/es502963t
73. Liu, E.; Fan, J.; Hu, X.; Hu, Y.; Li, H.; Tang, C.; Sun, L.; Wan, J. *J. Mater. Sci.* **2015,** *50,* 2298–2305. doi:10.1007/s10853-014-8793-z
74. Khan, M. A.; Sinatra, L.; Oufi, M.; Bakr, O. M.; Idriss, H. *Catal. Lett.* **2017,** *147,* 811–820. doi:10.1007/s10562-017-1998-4
75. Seifvand, N.; Kowsari, E. *Ind. Eng. Chem. Res.* **2016,** *55,* 10533–10543. doi:10.1021/acs.iecr.6b02783
76. Kalarivalappil, V.; Divya, C. M.; Wunderlich, W.; Pillai, S. C.; Hinder, S. J.; Nageri, M.; Kumar, V.; Vijayan, B. K. *Catal. Lett.* **2016,** *146,* 474–482. doi:10.1007/s10562-015-1663-8
77. Li, N.; Liu, M.; Yang, B.; Shu, W.; Shen, Q.; Liu, M.; Zhou, J. *J. Phys. Chem. C* **2017,** *121,* 2923–2932. doi:10.1021/acs.jpcc.6b12683
78. Fujimoto, T. M.; Ponczek, M.; Rochetto, U. L.; Landers, R.; Tomaz, E. *Environ. Sci. Pollut. Res.* **2017,** *24,* 6390–6396. doi:10.1007/s11356-016-6494-7
79. Wu, J.; Lu, S.; Ge, D.; Zhang, L.; Chen, W.; Gu, H. *RSC Adv.* **2016,** *6,* 67502–67508. doi:10.1039/C6RA10408H
80. Yilmaz, P.; Lacerda, A. M.; Larrosa, I.; Dunn, S. *Electrochim. Acta* **2017,** *231,* 641–649. doi:10.1016/j.electacta.2017.02.035
81. Ong, W.-J.; Tan, L.-L.; Chai, S.-P.; Yong, S.-T. *Dalton Trans.* **2015,** *44,* 1249–1257. doi:10.1039/c4dt02940b
82. Zhu, Z.; Wu, R.-J. *J. Taiwan Inst. Chem. Eng.* **2015,** *50,* 276–281. doi:10.1016/j.jtice.2014.12.022
83. Shiraishi, Y.; Sakamoto, H.; Fujiwara, K.; Ichikawa, S.; Hirai, T. *ACS Catal.* **2014,** *4,* 2418–2425. doi:10.1021/cs500447n
84. Wei, P.; Liu, J.; Li, Z. *Ceram. Int.* **2013,** *39,* 5387–5391. doi:10.1016/j.ceramint.2012.12.045
85. Wang, W.-K.; Chen, J.-J.; Li, W.-W.; Pei, D.-N.; Zhang, X.; Yu, H.-Q. *ACS Appl. Mater. Interfaces* **2015,** *7,* 20349–20359. doi:10.1021/acsami.5b06161
86. Lv, J.; Gao, H.; Wang, H.; Lu, X.; Xu, G.; Wang, D.; Chen, Z.; Zhang, X.; Zheng, Z.; Wu, Y. *Appl. Surf. Sci.* **2015,** *351,* 225–231. doi:10.1016/j.apsusc.2015.05.139
87. Putri, L. K.; Ong, W.-J.; Chang, W. S.; Chai, S.-P. *Catal. Sci. Technol.* **2016,** *6,* 744–754. doi:10.1039/C5CY00767D
88. Ingram, D. B.; Linic, S. *J. Am. Chem. Soc.* **2011,** *133,* 5202–5205. doi:10.1021/ja200086g
89. Thomann, I.; Pinaud, B. A.; Chen, Z.; Clemens, B. M.; Jaramillo, T. F.; Brongersma, M. L. *Nano Lett.* **2011,** *11,* 3440–3446. doi:10.1021/nl201908s
90. Torimoto, T.; Horibe, H.; Kameyama, T.; Okazaki, K.-i.; Ikeda, S.; Matsumura, M.; Ishikawa, A.; Ishihara, H. *J. Phys. Chem. Lett.* **2011,** *2,* 2057–2062. doi:10.1021/jz2009049
91. Chai, S. Y.; Kim, Y. J.; Jung, M. H.; Chakraborty, A. K.; Jung, D.; Lee, W. I. *J. Catal.* **2009,** *262,* 144–149. doi:10.1016/j.jcat.2008.12.020
92. Wang, C.; Shao, C.; Liu, Y.; Zhang, L. *Scr. Mater.* **2008,** *59,* 332–335. doi:10.1016/j.scriptamat.2008.03.038
93. Sun, S.; Wang, W.; Zhang, L.; Shang, M.; Wang, L. *Catal. Commun.* **2009,** *11,* 290–293. doi:10.1016/j.catcom.2009.09.026
94. Christopher, P.; Xin, H.; Linic, S. *Nat. Chem.* **2011,** *3,* 467–472. doi:10.1038/nchem.1032
95. Wu, T.; Liu, S.; Luo, Y.; Lu, W.; Wang, L.; Sun, X. *Nanoscale* **2011,** *3,* 2142–2144. doi:10.1039/C1NR10128E
96. Chen, X.; Zhu, H.-Y.; Zhao, J.-C.; Zheng, Z.-F.; Gao, X.-P. *Angew. Chem., Int. Ed. Engl.* **2008,** *47,* 5353. doi:10.1002/anie.200800602
97. Langhammer, C.; Yuan, Z.; Zorić, I.; Kasemo, B. *Nano Lett.* **2006,** *6,* 833–838. doi:10.1021/nl060219x
98. Langhammer, C.; Kasemo, B.; Zorić, I. *J. Chem. Phys.* **2007,** *126,* 194702. doi:10.1063/1.2734550
99. Tabor, C.; Murali, R.; Mahmoud, M.; El-Sayed, M. A. *J. Phys. Chem. A* **2009,** *113,* 1946–1953. doi:10.1021/jp807904s
100. Zhang, Q.; Tan, Y. N.; Xie, J.; Lee, J. Y. *Plasmonics* **2009,** *4,* 9–22. doi:10.1007/s11468-008-9067-x

101. Xu, H.; Li, H.; Xia, J.; Yin, S.; Luo, Z.; Liu, L.; Xu, L. *ACS Appl. Mater. Interfaces* **2011,** *3,* 22–29. doi:10.1021/am100781n
102. Wang, P.; Huang, B.; Zhang, X.; Qin, X.; Jin, H.; Dai, Y.; Wang, Z.; Wei, J.; Zhan, J.; Wang, S.; Wang, J.; Whangbo, M.-H. *Chem. – Eur. J.* **2009,** *15,* 1821–1824. doi:10.1002/chem.200802327
103. Purbia, R.; Paria, S. *Dalton Trans.* **2017,** *46,* 890–898. doi:10.1039/C6DT03723B
104. Shuang, S.; Lv, R.; Xie, Z.; Zhang, Z. *Sci. Rep.* **2016,** *6,* No. 26670. doi:10.1038/srep26670
105. Sá, J.; Tagliabue, G.; Friedli, P.; Szlachetko, J.; Rittmann-Frank, M. H.; Santomauro, F. G.; Milne, C. J.; Sigg, H. *Energy Environ. Sci.* **2013,** *6,* 3584–3588. doi:10.1039/C3EE42731E
106. Amidani, L.; Naldoni, A.; Malvestuto, M.; Marelli, M.; Glatzel, P.; Dal Santo, V.; Boscherini, F. *Angew. Chem.* **2015,** *127,* 5503–5506. doi:10.1002/ange.201412030
107. Furube, A.; Du, L.; Hara, K.; Katoh, R.; Tachiya, M. *J. Am. Chem. Soc.* **2007,** *129,* 14852–14853. doi:10.1021/ja076134v
108. Chen, H. M.; Chen, C. K.; Chen, C.-J.; Cheng, L.-C.; Wu, P. C.; Cheng, B. H.; Ho, Y. Z.; Tseng, M. L.; Hsu, Y.-Y.; Chan, T.-S.; Lee, J.-F.; Liu, R.-S.; Tsai, D. P. *ACS Nano* **2012,** *6,* 7362–7372. doi:10.1021/nn3024877
109. Wei, Z.; Rosa, L.; Wang, K.; Endo, M.; Juodkazis, S.; Ohtani, B.; Kowalska, E. *Appl. Catal., B* **2017,** *206,* 393–405. doi:10.1016/j.apcatb.2017.01.043
110. Zhang, L.; Herrmann, L. O.; Baumberg, J. J. *Sci. Rep.* **2015,** *5,* No. 16660. doi:10.1038/srep16660
111. Cui, J.; Li, Y.; Liu, L.; Chen, L.; Xu, J.; Ma, J.; Fang, G.; Zhu, E.; Wu, H.; Zhao, L.; Wang, L.; Huang, Y. *Nano Lett.* **2015,** *15,* 6295–6301. doi:10.1021/acs.nanolett.5b00950
112. Yang, W.; Xiong, Y.; Zou, L.; Zou, Z.; Li, D.; Mi, Q.; Wang, Y.; Yang, H. *Nanoscale Res. Lett.* **2016,** *11,* 283. doi:10.1186/s11671-016-1492-8
113. Ohno, T.; Masaki, Y.; Hirayama, S.; Matsumura, M. *J. Catal.* **2001,** *204,* 163–168. doi:10.1006/jcat.2001.3384
114. Nakamura, R.; Nakato, Y. *J. Am. Chem. Soc.* **2004,** *126,* 1290–1298. doi:10.1021/ja0388764
115. Nosaka, Y.; Nosaka, Y. A. *Chem. Rev.* **2017,** *117,* 11302–11336. doi:10.1021/acs.chemrev.7b00161
116. Diesen, V.; Jonsson, M. *J. Phys. Chem. C* **2014,** *118,* 10083–10087. doi:10.1021/jp500315u
117. Hirakawa, T.; Koga, C.; Negishi, N.; Takeuchi, K.; Matsuzawa, S. *Appl. Catal., B* **2009,** *87,* 46–55. doi:10.1016/j.apcatb.2008.08.027
118. Sahel, K.; Elsellami, L.; Mirali, I.; Dappozze, F.; Bouhent, M.; Guillard, C. *Appl. Catal., B* **2016,** *188,* 106–112. doi:10.1016/j.apcatb.2015.12.044
119. Wu, T.; Liu, G.; Zhao, J.; Hidaka, H.; Serpone, N. *J. Phys. Chem. B* **1999,** *103,* 4862–4867. doi:10.1021/jp9846678
120. Chen, C.; Lei, P.; Ji, H.; Ma, W.; Zhao, J.; Hidaka, H.; Serpone, N. *Environ. Sci. Technol.* **2004,** *38,* 329–337. doi:10.1021/es034384f
121. Lippert, A. R.; Van De Bittner, G. C.; Chang, C. J. *Acc. Chem. Res.* **2011,** *44,* 793–804. doi:10.1021/ar200126t
122. Fu, X.; Tang, Y.; Dickinson, B. C.; Chang, C. J.; Chang, Z. *Biochem. Biophys. Res. Commun.* **2015,** *458,* 896–900. doi:10.1016/j.bbrc.2015.02.055
123. Wang, D.; Zhao, L.; Guo, L.-H.; Zhang, H. *Anal. Chem.* **2014,** *86,* 10535–10539. doi:10.1021/ac503213m
124. Nakamura, K.; Ishiyama, K.; Ikai, H.; Kanno, T.; Sasaki, K.; Niwano, Y.; Kohno, M. *J. Clin. Biochem. Nutr.* **2011,** *49,* 87–95. doi:10.3164/jcbn.10-125
125. Tachikawa, T.; Majima, T. *J. Fluoresc.* **2007,** *17,* 727–738. doi:10.1007/s10895-007-0181-5
126. Tachikawa, T.; Majima, T. *Chem. Soc. Rev.* **2010,** *39,* 4802–4819. doi:10.1039/B919698F
127. Yagi, M.; Takemoto, S.; Sasase, R. *Chem. Lett.* **2004,** *33,* 152–153. doi:10.1246/cl.2004.152
128. Murakami, Y.; Endo, K.; Ohta, I.; Nosaka, A. Y.; Nosaka, Y. *J. Phys. Chem. C* **2007,** *111,* 11339–11346. doi:10.1021/jp0722049
129. Sawada, T.; Yoshino, F.; Kimoto, K.; Takahashi, Y.; Shibata, T.; Hamada, N.; Sawada, T.; Toyoda, M.; Lee, M.-C. *J. Dent. Res.* **2010,** *89,* 848–853. doi:10.1177/0022034510370806
130. Naito, K.; Tachikawa, T.; Fujitsuka, M.; Majima, T. *J. Phys. Chem. C* **2008,** *112,* 1048–1059. doi:10.1021/jp076335l
131. Kim, W.; Tachikawa, T.; Moon, G.-h.; Majima, T.; Choi, W. *Angew. Chem., Int. Ed.* **2014,** *53,* 14036–14041. doi:10.1002/anie.201406625
132. Hawkins, C. L.; Davies, M. J. *Biochim. Biophys. Acta, Gen. Subj.* **2014,** *1840,* 708–721. doi:10.1016/j.bbagen.2013.03.034
133. Zhao, H.; Joseph, J.; Zhang, H.; Karoui, H.; Kalyanaraman, B. *Free Radical Biol. Med.* **2001,** *31,* 599–606. doi:10.1016/S0891-5849(01)00619-0
134. Saita, M.; Kobatashi, K.; Yoshino, F.; Hase, H.; Nonami, T.; Kimoto, K.; Lee, M.-C.-i. *Dent. Mater. J.* **2012,** *31,* 458–464. doi:10.4012/dmj.2011-192
135. Zhou, P.; Yu, J.; Jaroniec, M. *Adv. Mater.* **2014,** *26,* 4920–4935. doi:10.1002/adma.201400288
136. Kittel, C. *Introduction to Solid State Physics,* 5th ed.; John Wiley & Sons Inc.: New York, NY, U.S.A., 1976.
137. Wu, X.; Yin, S.; Dong, Q.; Liu, B.; Wang, Y.; Sekino, T.; Lee, S. W.; Sato, T. *Sci. Rep.* **2013,** *3,* No. 2918. doi:10.1038/srep02918
138. Manthiram, K.; Alivisatos, A. P. *J. Am. Chem. Soc.* **2012,** *134,* 3995–3998. doi:10.1021/ja211363w
139. Zhao, Y.; Burda, C. *Energy Environ. Sci.* **2012,** *5,* 5564–5576. doi:10.1039/C1EE02734D
140. Naik, G. V.; Shalaev, V. M.; Boltasseva, A. *Adv. Mater.* **2013,** *25,* 3264–3294. doi:10.1002/adma.201205076
141. Zhou, D.; Liu, D.; Xu, W.; Yin, Z.; Chen, X.; Zhou, P.; Cui, S.; Chen, Z.; Song, H. *ACS Nano* **2016,** *10,* 5169–5179. doi:10.1021/acsnano.6b00649
142. Kriegel, I.; Jiang, C.; Rodríguez-Fernandez, J.; Schaller, R. D.; Talapin, D. V.; Da Como, E.; Feldmann, J. *J. Am. Chem. Soc.* **2012,** *134,* 1583–1590. doi:10.1021/ja207798q
143. Dorfs, D.; Härtling, T.; Miszta, K.; Bigall, N. C.; Kim, M. R.; Genovese, A.; Falqui, A.; Povia, M.; Manna, L. *J. Am. Chem. Soc.* **2011,** *133,* 11175–11180. doi:10.1021/ja2016284
144. Mendelsberg, R. J.; Lim, S. H. N.; Zhu, Y. K.; Wallig, J.; Milliron, D. J.; Anders, A. *J. Phys. D: Appl. Phys.* **2011,** *44,* 232003. doi:10.1088/0022-3727/44/23/232003
145. Zhang, Z.; Huang, J.; Fang, Y.; Zhang, M.; Liu, K.; Dong, B. *Adv. Mater.* **2017,** *29,* 1606688. doi:10.1002/adma.201606688
146. Li, J.; Li, W.; Li, X.; Li, Y.; Bai, H.; Li, M.; Xi, G. *RSC Adv.* **2017,** *7,* 23846–23850. doi:10.1039/C7RA03389C
147. Naik, G. V.; Schroeder, J. L.; Ni, X.; Kildishev, A. V.; Sands, T. D.; Boltasseva, A. *Opt. Mater. Express* **2012,** *2,* 478–489. doi:10.1364/OME.2.000478
148. Guler, U.; Kildishev, A. V.; Boltasseva, A.; Shalaev, V. M. *Faraday Discuss.* **2015,** *178,* 71–86. doi:10.1039/C4FD00208C
149. Van Hooijdonk, E.; Vandenbem, C.; Berthier, S.; Vigneron, J. P. *Opt. Express* **2012,** *20,* 22001–22011. doi:10.1364/OE.20.022001

150. Spinner, M.; Kovalev, A.; Gorb, S. N.; Westhoff, G. *Sci. Rep.* **2013,** *3,* 1846. doi:10.1038/srep01846
151. Yan, R.; Chen, M.; Zhou, H.; Liu, T.; Tang, X.; Zhang, K.; Zhu, H.; Ye, J.; Zhang, D.; Fan, T. *Sci. Rep.* **2016,** *6,* 20001. doi:10.1038/srep20001
152. Chhabra, R.; Sharma, J.; Wang, H. N.; Zou, S. L.; Lin, S.; Yan, H.; Lindsay, S.; Liu, Y. *Nanotechnology* **2009,** *20,* 485201. doi:10.1088/0957-4484/20/48/485201
153. Cheng, W.; Campolongo, M. J.; Cha, J. J.; Tan, S. J.; Umbach, C. C.; Muller, D. A.; Luo, D. *Nat. Mater.* **2009,** *8,* 519–525. doi:10.1038/NMAT2440
154. Capehart, S. L.; Coyle, M. P.; Glasgow, J. E.; Francis, M. B. *J. Am. Chem. Soc.* **2013,** *135,* 3011–3016. doi:10.1021/ja3078472
155. Wang, D.; Capehart, S. L.; Pal, S.; Liu, M.; Zhang, L.; Schuck, P. J.; Liu, Y.; Yan, H.; Francis, M. B.; De Yoreo, J. J. *ACS Nano* **2014,** *8,* 7896–7904. doi:10.1021/nn5015819
156. Akhtar, M. S.; Panwar, J.; Yun, Y.-S. *ACS Sustainable Chem. Eng.* **2013,** *1,* 591–602. doi:10.1021/sc300118u
157. Devi, T. B.; Ahmaruzzaman, M. *Environ. Sci. Pollut. Res.* **2016,** *23,* 17702–17714. doi:10.1007/s11356-016-6945-1
158. Huang, J.; Li, Q.; Sun, D.; Lu, Y.; Su, Y.; Yang, X.; Wang, H.; Wang, Y.; Shao, W.; He, N.; Hong, J.; Chen, C. *Nanotechnology* **2007,** *18,* 105104. doi:10.1088/0957-4484/18/10/105104
159. Joerger, R.; Klaus, T.; Granqvist, C. G. *Adv. Mater.* **2000,** *12,* 407–409. doi:10.1002/(SICI)1521-4095(200003)12:6<407::AID-ADMA407>3.0.CO;2-O
160. Bhainsa, K. C.; D'souza, S. F. *Colloids Surf., B* **2006,** *47,* 160–164. doi:10.1016/j.colsurfb.2005.11.026
161. Gardea-Torresdey, J. L.; Parsons, J. G.; Gomez, E.; Peralta-Videa, J.; Troiani, H. E.; Santiago, P.; Yacaman, M. J. *Nano Lett.* **2002,** *2,* 397–401. doi:10.1021/nl015673+
162. Palanco, M. E.; Mogensen, K. B.; Gühlke, M.; Heiner, Z.; Kneipp, J.; Kneipp, K. *Beilstein J. Nanotechnol.* **2016,** *7,* 834–840. doi:10.3762/bjnano.7.75
163. Shankar, S. S.; Rai, A.; Ahmad, A.; Sastry, M. *J. Colloid Interface Sci.* **2004,** *275,* 496–502. doi:10.1016/j.jcis.2004.03.003
164. Gao, S.; Jia, X.; Yang, S.; Li, Z.; Jiang, K. *J. Solid State Chem.* **2011,** *184,* 764–769. doi:10.1016/j.jssc.2011.01.025
165. Patil, S. S.; Mali, M. G.; Tamboli, M. S.; Patil, D. R.; Kulkarni, M. V.; Yoon, H.; Kim, H.; Al-Deyab, S. S.; Yoon, S. S.; Kolekar, S. S.; Kale, B. B. *Catal. Today* **2016,** *260,* 126–134. doi:10.1016/j.cattod.2015.06.004
166. Christopher, P.; Xin, H.; Marimuthu, A.; Linic, S. *Nat. Mater.* **2012,** *11,* 1044–1050. doi:10.1038/NMAT3454
167. Xiao, Q.; Jaatinen, E.; Zhu, H. *Chem. – Asian J.* **2014,** *9,* 3046–3064. doi:10.1002/asia.201402310
168. Chen, X.; Zhu, H.-Y.; Zhao, J.-C.; Zheng, Z.-F.; Gao, X.-P. *Angew. Chem.* **2008,** *120,* 5433–5436. doi:10.1002/ange.200800602
169. Chen, X.; Zheng, Z.; Ke, X.; Jaatinen, E.; Xie, T.; Wang, D.; Guo, C.; Zhao, J.; Zhu, H. *Green Chem.* **2010,** *12,* 414–419. doi:10.1039/B921696K
170. Cheng, H.; Fuku, K.; Kuwahara, Y.; Mori, K.; Yamashita, H. *J. Mater. Chem. A* **2015,** *3,* 5244–5258. doi:10.1039/C4TA06484D
171. Wee, T.-L.; Schmidt, L. C.; Scaiano, J. C. *J. Phys. Chem. C* **2012,** *116,* 24373–24379. doi:10.1021/jp308956y
172. Zhu, H.; Ke, X.; Yang, X.; Sarina, S.; Liu, H. *Angew. Chem.* **2010,** *122,* 9851–9855. doi:10.1002/ange.201003908
173. Wang, C.; Nie, X.-G.; Shi, Y.; Zhou, Y.; Xu, J.-J.; Xia, X.-H.; Chen, H.-Y. *ACS Nano* **2017,** *11,* 5897–5905. doi:10.1021/acsnano.7b01637
174. Ke, X.; Sarina, S.; Zhao, J.; Zhang, X.; Chang, J.; Zhu, H. *Chem. Commun.* **2012,** *48,* 3509–3511. doi:10.1039/C2CC17977F
175. Marimuthu, A.; Zhang, J.; Linic, S. *Science* **2013,** *339,* 1590–1593. doi:10.1126/science.1231631

License and Terms

This is an Open Access article under the terms of the Creative Commons Attribution License (http://creativecommons.org/licenses/by/4.0), which permits unrestricted use, distribution, and reproduction in any medium, provided the original work is properly cited.

The license is subject to the *Beilstein Journal of Nanotechnology* terms and conditions: (https://www.beilstein-journals.org/bjnano)

The definitive version of this article is the electronic one which can be found at:
doi:10.3762/bjnano.9.59

BEILSTEIN JOURNAL OF NANOTECHNOLOGY

Optimisation of purification techniques for the preparation of large-volume aqueous solar nanoparticle inks for organic photovoltaics

Furqan Almyahi[1,2], Thomas R. Andersen[*2], Nathan A. Cooling[2], Natalie P. Holmes[2], Matthew J. Griffith[2], Krishna Feron[2,3], Xiaojing Zhou[2], Warwick J. Belcher[2] and Paul C. Dastoor[2]

Full Research Paper

Open Access

Address:
[1]Department of Physics, College of Science, University of Basrah, Iraq, [2]Centre for Organic Electronics, University of Newcastle, University Drive, Callaghan, NSW 2308, Australia and [3]CSIRO Energy Technology, Newcastle, NSW 2300, Australia

Email:
Thomas R. Andersen[*] - Thomas.andersen@newcastle.edu.au

* Corresponding author

Keywords:
aqueous nanoparticle; crossflow ultrafiltration; miniemulsion; organic photovoltaic; SDS surfactant; surface tension

Beilstein J. Nanotechnol. **2018,** *9,* 649–659.
doi:10.3762/bjnano.9.60

Received: 12 October 2017
Accepted: 22 January 2018
Published: 20 February 2018

This article is part of the Thematic Series "Energy conversion, storage and environmental remediation using nanomaterials".

Guest Editor: W.-J. Ong

© 2018 Almyahi et al.; licensee Beilstein-Institut.
License and terms: see end of document.

Abstract

In this study we have optimised the preparation conditions for large-volume nanoparticle inks, based on poly(3-hexylthiophene) (P3HT):indene-C_{60} multiadducts (ICxA), through two purification processes: centrifugal and crossflow ultrafiltration. The impact of purification is twofold: firstly, removal of excess sodium dodecyl sulfate (SDS) surfactant from the ink and, secondly, concentration of the photoactive components in the ink. The removal of SDS was studied in detail both by a UV–vis spectroscopy-based method and by surface tension measurements of the nanoparticle ink filtrate; revealing that centrifugal ultrafiltration removed SDS at a higher rate than crossflow ultrafiltration even though a similar filter was applied in both cases (10,000 Da M_w cut-off). The influence of SDS concentration on the aqueous solar nanoparticle (ASNP) inks was investigated by monitoring the surface morphology/topography of the ASNP films using atomic force microscopy (AFM) and scanning electron microscopy (SEM) and photovoltaic device performance as a function of ultrafiltration (decreasing SDS content). The surface morphology/topography showed, as expected, a decreased number of SDS crystallites on the surface of the ASNP film with increased ultrafiltration steps. The device performance revealed distinct peaks in efficiency with ultrafiltration: centrifuge purified inks reached a maximum efficiency at a dilution factor of 7.8×10^4, while crossflow purified inks did not reach a maximum efficiency until a dilution factor of 6.1×10^9. This difference was ascribed to the different wetting properties of the prepared inks and was further corroborated by surface tension measurements of the ASNP inks which revealed that the peak efficiencies for both methods occurred for similar surface tension values of 48.1 and 48.8 mN m^{-1}. This work demonstrates that addressing the surface tension of large-volume ASNP inks is key to the reproducible fabrication of nanoparticle photovoltaic devices.

Introduction

Organic photovoltaics (OPV) are a promising energy technology that utilizes large-scale roll-to-roll (R2R) fabrication techniques (such as slot-die coating, flexographical printing and screen printing) for high-speed production due to the solution-processable nature of the device materials [1,2]. The application of high throughput R2R equipment produces devices which have a short energy payback time and which deliver power at a low levelised cost of electricity [3,4]. In state of the art large scale OPV, the organic materials (polymers, fullerene or other macromolecules) comprising the active layer are dissolved in organic solvents, i.e., chloroform or chlorobenzene [5]. The application of these solvents can be an issue for the large-scale production of OPV due to their toxicity as they are harmful towards both environmental and human health. In reality, water is the eco-friendly solvent and is therefore a more sustainable solvent for upscaling of OPVs [6]. Some low molecular weight alcohols are also frequently used as green solvents in the printing industry, whereas they do have advantages such as ease of process primarily due to much easier removal, they all remain human and environmental exposure limits and are flammable. Currently, it is difficult to synthesise water-soluble semiconducting macromolecules suitable for OPV active layers [7]. Therefore, two methods have been developed for transferring currently utilized semiconducting macromolecules into green solvents: Method 1: The reprecipitation method, herein the semiconductive materials are dissolved in organic solvent which is added to a vigorously stirring alcohol causing the semiconductive materials to precipitation into nanoparticles. OPV prepared from this method have shown great efficiency by reaching 4% [8], however, this method have so far only proven efficient on one donor–acceptor pair. The low versatility of this method as well as with a poor stability of the prepared suspension [9] greatly limits the industrial potential of this method. Method 2: The mini-emulsion method: This method involves ultrasonic mixing of the two-phase organic–aqueous system in the presence of a surfactant, which is commonly sodium dodecyl sulfate (SDS), to produce the mini-emulsion [10]. The presence of free (unbound) SDS in the aqueous solar nanoparticle (ASNP) inks affects several aspects of the fabrication of nanoparticle (NP)-OPV devices; including the packing density of the photoactive particles in the nanoparticle films and thus the formation of cracks or de-wetting areas [11-13]. Previous studies have reported nanoparticle films prepared from inks without purification have exhibited a higher degree of trap states than inks where the excess free SDS has been removed [14]. Residual SDS is generally removed by dialysis which is also applied for concentrating the ASNP inks. A centrifugal ultrafiltration process is a common purification method for preparing small-volume ASNP inks [12,15]. However, this technique is not suitable for preparing the large volumes of inks required to fabricate OPV devices on the roll-to-roll (R2R) scale (for instance, to just fill the reservoir of a typical R2R coating head requires 50 mL of ink with a solids content of 60 mg mL^{-1} before even a centimetre has been coated [16]). Since the supernatant volume loss in any individual centrifuge separation step is large and the removal of SDS requires significant dilution and purification steps, the continual manual intervention required to renew the solvent and continue separation makes this technique impractical for large scale material preparation. In an earlier study, ASNP inks with large volume (100 mL) from 500 mL dispersions were prepared, with the purification of ASNPs from excess-surfactant conducted using a commercial crossflow Millipore filtration system [13,17]. However, the fabrication of NP-OPVs using slot-die coating of these purified inks on a roll-to-roll setup required the addition of an fluorosurfactant (FSO) to improve the wetting of the NP ink onto the substrate [17], indicating that the SDS content had not been optimized in the flow purification study. In principle, it should be possible to control the wetting properties of ASNP inks by tailoring the free-SDS surfactant concentration. However, to date it has been difficult to determine the SDS content of aqueous solar nanoparticle inks, even though it is known that the SDS content has an effect on the performance of resulting NP-OPVs [13,18,19].

In this paper, we investigate how the purification method (centrifuge or crossflow ultrafiltration) influences the wetting of ASNP inks and the performance of the corresponding OPV devices. The purification was monitored by measuring both the concentration of free SDS and the surface tension of the ASNP ink. The effects of these factors are correlated with device efficiencies for both small and large volume ASNP ink purification processes. We demonstrate that it is the surface tension of the resultant ink that is the key factor to determine the efficiency of nanoparticle photovoltaic devices independent of the purification method.

Results and Discussion

The important parameters when upscaling can be summarized into three areas; size of nanoparticles [20], free SDS concentration [21], and internal morphology of nanoparticles [22] (herein evaluated by solar cell performance).

Particle size distribution

The size of the nanoparticles has an impact on the overall number of layers of particles in an OPV device active layer (as 100 nm thick active layer has been found to be optimal), i.e., smaller particles allow for a more densely packed film, assuming an optimal hexagonal packing of particles [23], which in turn lowers the risk of short circuiting through the active layer. The particle size also influences the overall domain size

of donor and acceptor assuming a core–shell structure [15] and therefore greatly influences the efficiency of the prepared devices [24]. Aggregation and sedimentation of ASNP inks as a function of free SDS concentration and applied forces were investigated by measuring the particle size at different dilution factors for inks from both centrifugal and crossflow ultrafiltration methods, as shown in (Figure 1A). There is no evidence of large aggregate formation within the ASNP inks as the particle sizes indicated by the *Z*-average are constant at approximately 41 ± 9 nm as a function of dilution factor (defined in section 'Preparation of aqueous solar nanoparticle inks'). As such, the particle sizes of the formulated ASNP inks are independent of both dilution factor and ultrafiltration method. The shape of the prepared ASNPs is predominately spherical with a few elongated particles as observed by SEM (Figure 1B).

Free SDS concentration determination of ASNP inks

The main purpose of the purification of ASNP inks is the removal of excess SDS. For 0.5 mL small-scale nanoparticle inks, the excess SDS is removed by a centrifuge process, which due to volume restrictions is not feasible for large-scale ink preparation where volumes exceed 100 mL. Large-scale ink preparation is therefore conducted by the crossflow ultrafiltration technique with a flow-cartridge. In order to determine the effectiveness of removal of free SDS from the P3HT:ICxA NP inks with increasing dilution factor, the SDS concentration in the filtrates from the purification of P3HT:ICxA NP inks have been determined for both ultrafiltration processes by a UV–vis spectrophotometric method as shown in Figure 2. Figure 2A shows the absorbance values of methylene blue (MB) at 664 nm for the filtrates of ASNP inks that were purified by the centrifugal and the crossflow ultrafiltration techniques with dilution factors of 1–1.2 × 10^9 and 1–3.1 × 10^{10}, respectively. Commonly for both techniques the graphs can be divided into three regions, initially (low dilution factor) the curves appear flat with an absorption of 0.2–0.25 due to an SDS concentration higher than 1 mg mL^{-1}, which saturates the coordination complex chemistry and thus provides an upper limit for detection with this technique. This stage is followed by an increase from an absorption of 0.25 to 0.5–0.6; corresponding to an SDS concentration of 0.30–0.35 mg mL^{-1} for centrifuge and crossflow ultrafiltration, respectively (Supporting Information File 1, Figure S1A). In the third region, the curves once again appear flat indicating that we are continuously removing filtrate with a fixed SDS concentration of 0.3–0.35 mg mL^{-1} even when dialysing high dilution factor inks. This result is not a measurement detection limit as observed for the saturation at high SDS content as the calibration samples (Supporting Information File 1, Figure S1B) clearly show detection of SDS at much higher absorbance (lower SDS content) than where the ASNP ink saturate. Thus it is clear the samples reach a fixed SDS content of 0.3–0.35 mg mL^{-1} beyond which no further SDS can be removed with ultrafiltration. Furthermore, as a comparison, surface tension (ST) measurements have been used to determine the free SDS concentration in the filtrates of P3HT:ICxA NP inks with varying dilution factors for each of the purification techniques, as shown in Figure 2B. For the centrifugal and crossflow ultrafiltration, the filtrates with low dilution factors have lower constant surface tensions, which then increase sharply with increasing dilution factors before plateauing at high dilution factor. Using the calibration curve for absorption vs SDS concentration (Supporting Information File 1, Figure S1A) and surface tension vs free SDS concentration curve (Supporting Information File 1, Figure S1B), we created Figure 2C, which show the concentration of SDS in the filtrate as a func-

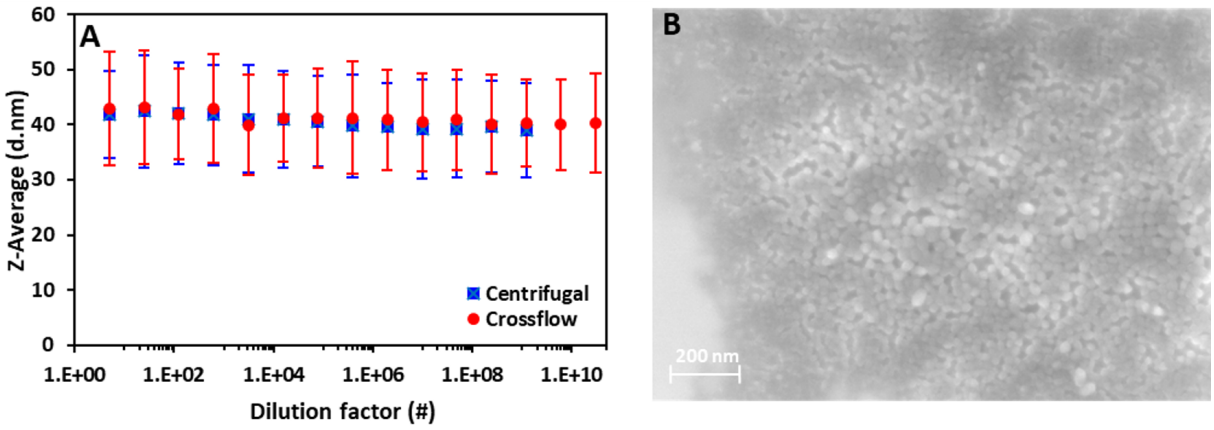

Figure 1: (A) The *Z*-average size of poly(3-hexylthiophene) (P3HT):indene-C_{60} multiadducts (ICxA) NPs dialysed by crossflow and centrifugal ultrafiltration processes vs varying dilution factor. The error bars makes the standard deviation in particle size for the particle population in the sample. (B) SEM image of P3HT:ICxA NPs.

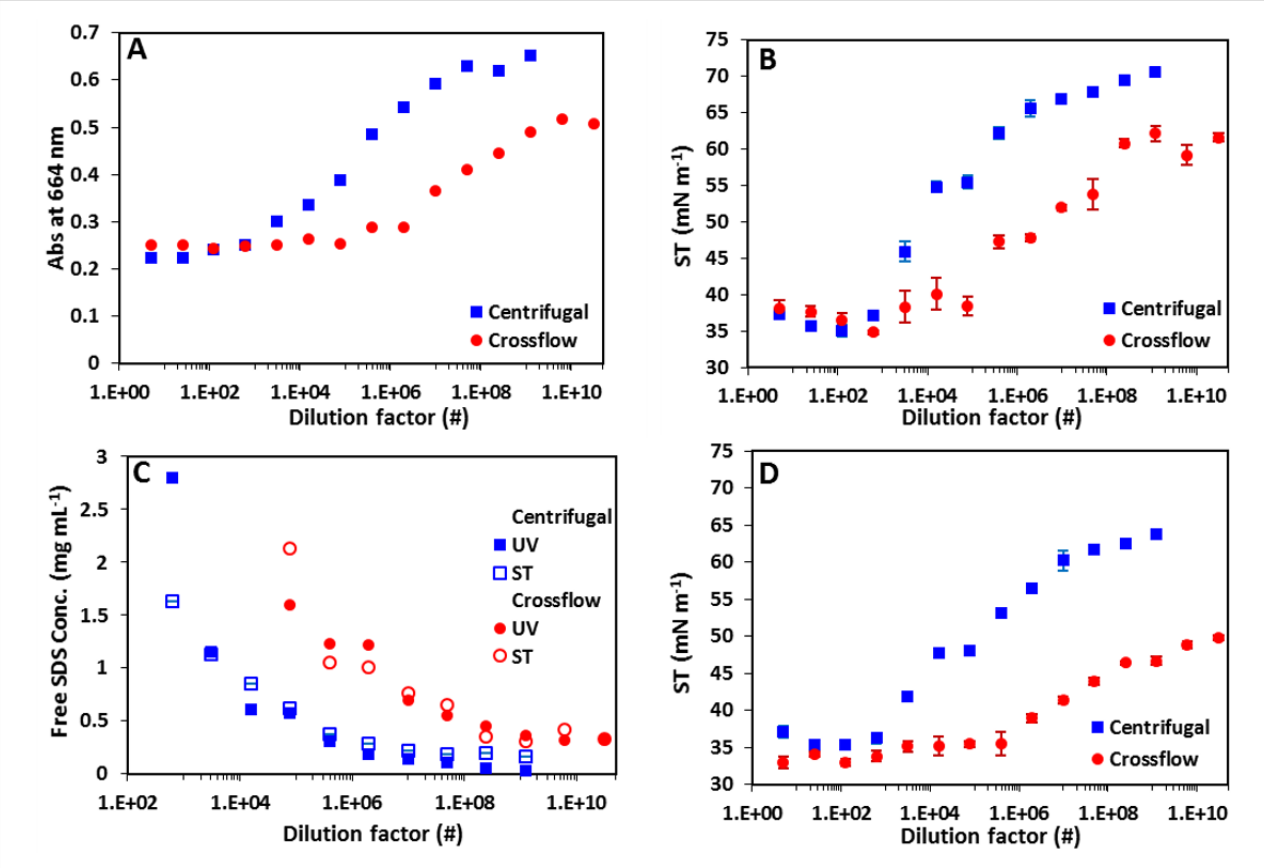

Figure 2: The absorbance at 664 nm of the filtrates of P3HT:ICxA NP inks (A), and surface tension (ST) (B) of the filtrates of P3HT:ICxA NP inks with different dilution factors for centrifugal (blue squares) and crossflow (red circles) ultrafiltration processes. (C) Free SDS concentrations in filtrates vs dilution factor for centrifugal (squares) and crossflow (circles) ultrafiltration processes. (D) The surface tension of NP inks with varying dilution factor for centrifugal (squares) and crossflow (circles) ultrafiltration processes.

tion of dilution factor for both methods. As seen from Figure 2C the concentration values determined using the UV absorption and surface tension methods are in good agreement. Moreover, both methods clearly show that the purification of ASNP inks using centrifugal ultrafiltration proceeds faster than using crossflow ultrafiltration, indicating a higher physical partition coefficient for separation at the filtration membrane using the centrifuge process.

Figure S2 and Figure S3 (see Supporting Information File 1) show photographs of films coated from ASNP ink with the various dilution factors. It is clear that ASNP inks with low dilution factor (1–625) and (1–3.9 × 10^5) exhibit poor wetting properties on pre-cleaned glass slides. Moving towards higher dilution factors leads to an improvement in the wetting properties of ASNP inks, however, with excessive SDS removal the wetting properties of the ASNP inks again decreases. Further investigation (Figure 2D) shows that the surface tension of ASNP inks with lower dilution factors than 625 were roughly constant (33.6–36 mN m^{-1}) for both purifications. With higher dilution factors, we observe an increase in surface tension, indicating that the concentration of free SDS is reduced. The maximal surface tension of ASNP inks reached was 64 and 50 mN m^{-1} for the centrifugal and the crossflow purifications, respectively.

Influence of free-SDS surfactant on the surface morphology/topography of ASNP films

Optical microscopy and atomic force microscopy (AFM) were conducted for ASNP films with low, medium and high dilution factors; photographs illustrating the film forming ability for all inks can be seen in Supporting Information File 1, Figure S2 and Figure S3. Figure 3A–C shows the optical microscopy images of the as spun ASNP films with dilution factors of 625, 7.8 × 10^4 and 9.8 × 10^6 following centrifugal ultrafiltration. The large aggregates present in the film prepared from an ink with a dilution factor of 625 are no longer observed once a highly purified ink with a dilution factor of 9.8 × 10^6 is utilized and thus we ascribe the observed aggregates to SDS crystallites which are eliminated with SDS removal. When using crossflow ultrafiltration, the ASNP films with dilution factors of 1.6 × 10^4, 9.8 × 10^6 and 6.1 × 10^9 all show aggregates on their surfaces

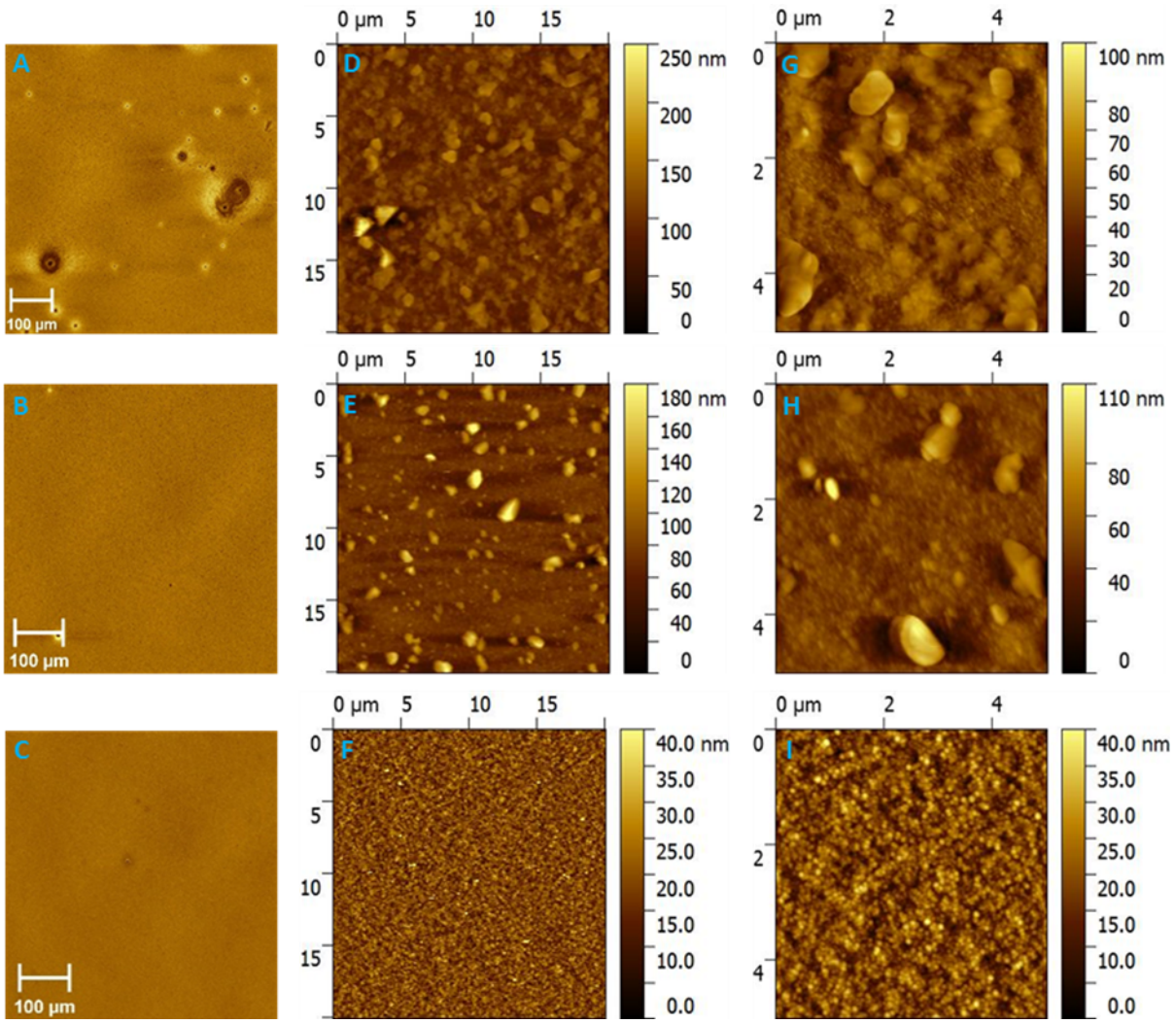

Figure 3: Optical microscopy (A–C), scale bar 100 µm, AFM images with scale bar 20 × 20 µm (D–F) and 5 × 5 µm (G–I) of P3HT:ICxA NP films with dilution factors 625 (A,D,G), 7.8 × 10^4 (B,E,H) and 9.8 × 10^6 (C,F,I) for centrifugal ultrafiltration.

(Figure 4A–C). These aggregates were analysed by energy dispersion X-ray spectroscopy (EDX, Supporting Information File 1, Figure S4). It is evident that the aggregates on the surfaces consist of sulphur, sodium, oxygen and carbon which are the building blocks for SDS, whereas a region with no aggregates show no peak for sodium. Thus, the aggregates are attributed to SDS, since this is the only chemical species present in the ink that contains sodium and oxygen. To further investigate the insights into the nanoscale surface morphologies, AFM was conducted on the same ASNP films, the investigations were conducted on homogenous regions of the NP films rather than on regions dominated by SDS aggregates. The AFM images of P3HT:ICxA NP films are presented in Figure 3D–F with scale 20 × 20 µm and Figure 3G–I with scale 5 × 5 µm for ASNP with centrifugal ultrafiltration. The ASNP films with dilution factor of 625 and 7.8 × 10^4 revealed multiple SDS aggregates and nanoparticle regions whereas increasing the dilution factor to 9.8 × 10^6 leads to a NP surfaces without SDS aggregates. With the crossflow purification, the AFM images of ASNP films with dilution factors of 1.6 × 10^4, 9.8 × 10^6 and 6.1 × 10^9 are shown in Figure 4D–F and Figure 4G–I with a scale of 20 × 20 µm and 5 × 5 µm, respectively. In contrast with centrifugal filtration, it is difficult to distinguish the NP regions in the AFM images of the crossflow filtered films prepared with dilution factors of 1.6 × 10^4; suggesting that the high SDS content of these films is obscuring almost all of the film surface. However, with higher dilution factors of up to 6.1 × 10^9, the NP regions in the film are more clearly distinguishable and dominate the surface. Thus, although increasing the dilution factor leads to a reduction of the surface SDS concentration for both ultrafiltration processes, centrifugal purification removes SDS much more efficiently than crossflow purification.

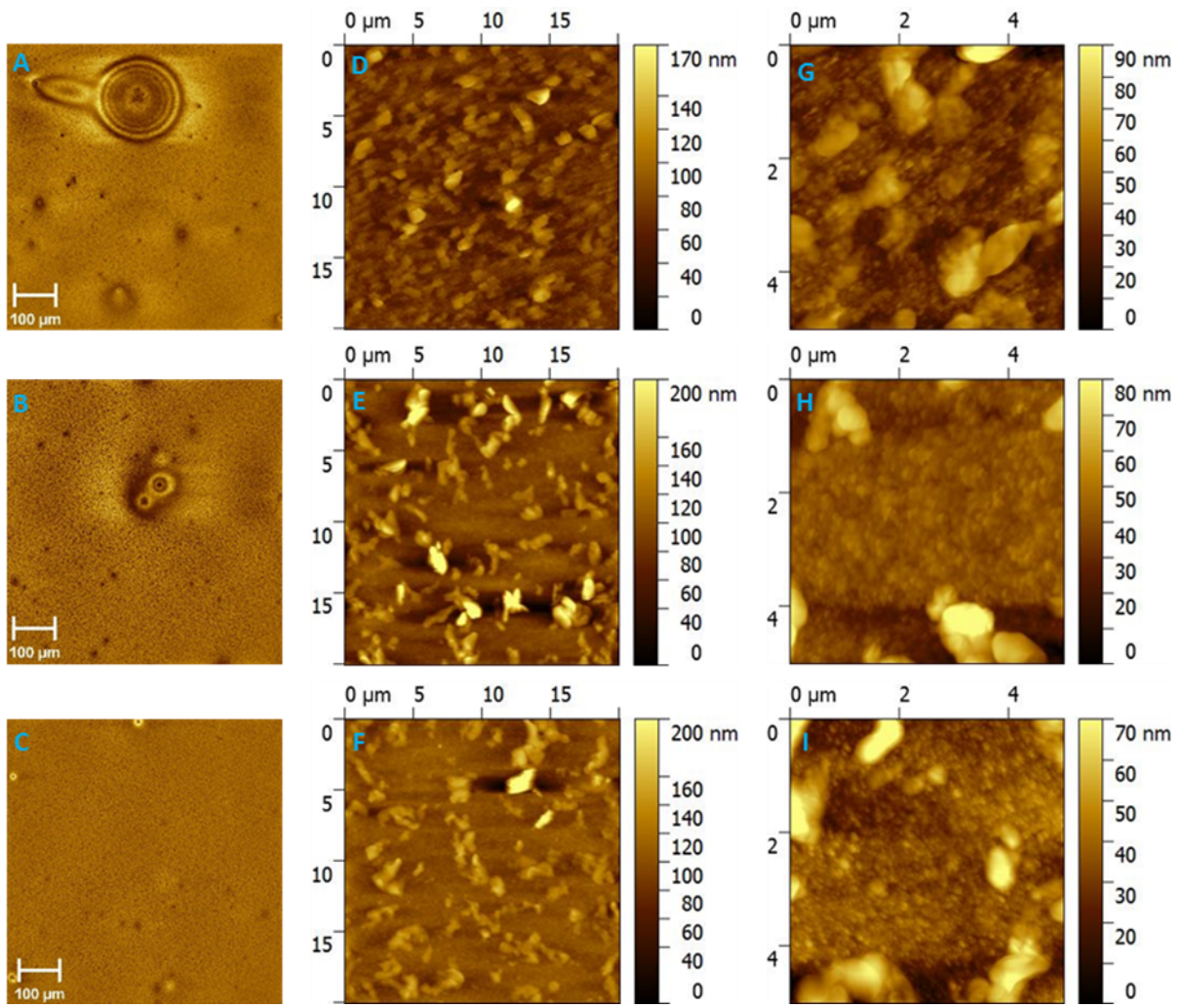

Figure 4: Optical microscopy (A–C), scale bar 100 µm, AFM images with scale bar 20 × 20 µm (D–F) and 5 × 5 µm (G–I) of P3HT:ICxA NPs with dilution factors 1.6 × 10^4 (A,D,G), 9.8 × 10^6 (B,E,H) and 6.1 × 10^9 (C,F,I) for crossflow ultrafiltration.

Effect of the ASNP ink purification on NP-OPV performance

NP-OPV devices were successfully fabricated from P3HT:ICxA ASNP inks with dilution factors of 1–1.2 × 10^9 and 3.9 × 10^5–3.1 × 10^{10} for centrifugal and crossflow ultrafiltration inks, respectively. The device was prepared in normal geometry in order to determine the optimal SDS concentration based on OPV device performance. Supporting Information File 1, Figure S5A–D shows the *J*–*V* characteristics for dried and annealed NP-OPV devices for the centrifugal and the crossflow ultrafiltration techniques (summarized in Supporting Information File 1, Table S1).

Previous work by Bag et al. has suggested that lower SDS concentration for ASNP inks should lead to more efficient devices due to SDS hindering hole transport [14]. By contrast, in this study, plotting the OPV characteristics (power conversion efficiency (PCE), open-circuit voltage (V_{OC}), short-circuit current (J_{SC}) and fill factor (FF)) versus dilution factor (Figure 5A–D) reveals a clear peak in efficiency as a function of dilution factor for inks purified using centrifugal ultrafiltration. A maximum efficiency is observed at a dilution factor 7.8 × 10^4 with a PCE of 0.65%, while efficiencies for dilution factors of 1.6 × 10^4 and 3.9 × 10^5 drop to 0.55% and 0.49%, respectively, and continue to decrease when moving towards both dilution extremes. A similar pattern is obtained for the inks purified by the crossflow ultrafiltration with a low PCE of 0.16% observed for a dilution factor of 3.9 × 10^5 rising to a peak performance of 0.67% at a dilution factor 6.1 × 10^9, after which performance decreases slightly to 0.62% at 3.1 × 10^{10}. Furthermore, the observation that similar peak efficiencies are obtained at two very different dilution factors is consistent with the earlier observation that SDS is removed at different rates using the two ultrafiltration processes, but may indicate that both techniques produce

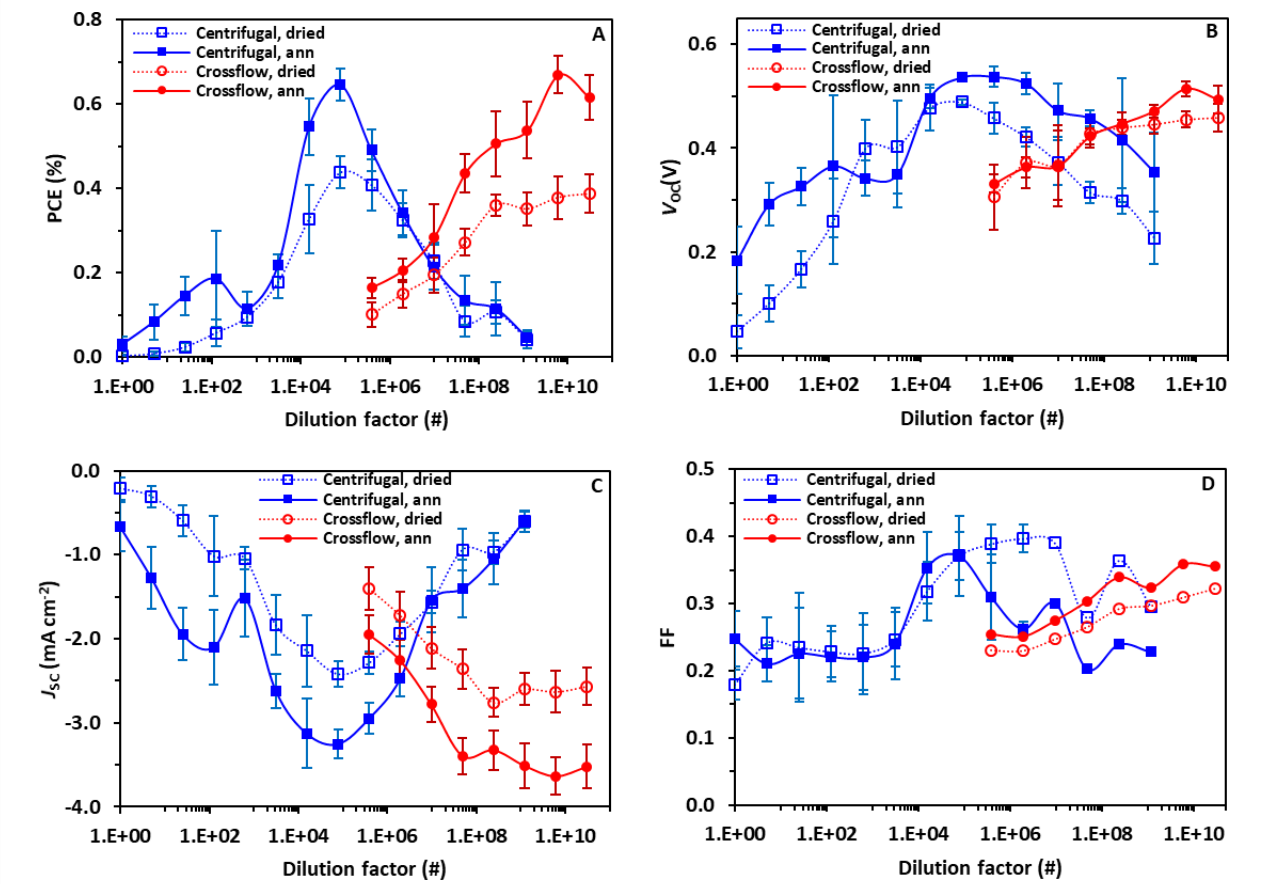

Figure 5: The performance parameters (PCE, V_{OC}, J_{sc} and FF) of P3HT:ICxA NP OPV devices for crossflow and centrifugal ultrafiltration methods plotted as red and blue lines, respectively. Solid line refers to annealed devices (140 °C, 4 min), and dotted line refers to dried (110 °C, 10 min) devices. The error bars represent the standard deviation of an average of 12 devices per sample.

inks with similar optimized properties at different dilution factors.

To evaluate whether this effect is due to the ink or the purification technique, the efficiency parameters (PCE, V_{OC}, J_{SC} and FF) were plotted as a function of surface tension instead of dilution factor (Figure 6A–D). Figure 6A shows the PCEs of NP-OPV devices versus surface tension of ASNP inks for both purification methods and a clear correlation can be observed, with device efficiencies for inks from both purification processes peaking at a surface tension of approximately 48 mN m^{-1}. In contrast, low surface tension of ASNP inks with high free SDS concentrations result in less wetting and less uniform films. The increased surface tension of ASNP inks towards 48 mN m^{-1} were caused by decreasing the free-SDS concentration of inks, and the enhanced efficiency of NP-OPV devices can be attributed to improved wetting properties between ASNP inks and the underlying PEDOT:PSS layer. The efficiency drop observed at higher surface tensions are ascribed to a reduction in the ink wetting properties as observed in Supporting Information File 1, Figure S2 and Figure S3.

The observation that there is an optimal surface tension of 48–49 mN m^{-1} for peak device performance regardless of purification technique is important and reveals that controlling the wetting properties is the dominant parameter in determining the performance of NP-OPV devices at scale. The changing wetting properties for each DF required the spin coating procedure for each device type to be optimized in order to achieve similar layer thicknesses of 105 ± 5 nm. The uniformity of active layer thicknesses was investigated by measuring the reflectance of the prepared devices (seen in Supporting Information File 1, Figure S6). The reflectance measurements illustrate uniform absorption across devices with very different current densities, meaning that the J_{SC} trends are clearly not a function of reduced absorption.

The real challenge in the OPV community is the upscaling of devices from small area lab-scale devices prepared by spin-coating to large area R2R prepared devices. We have chosen to utilize HTL Solar as our PEDOT:PSS for this study as it has a PEDOT to PSS ratio of 1:2.5 which is the same as PH1000 which are being used frequently for R2R prepared large area

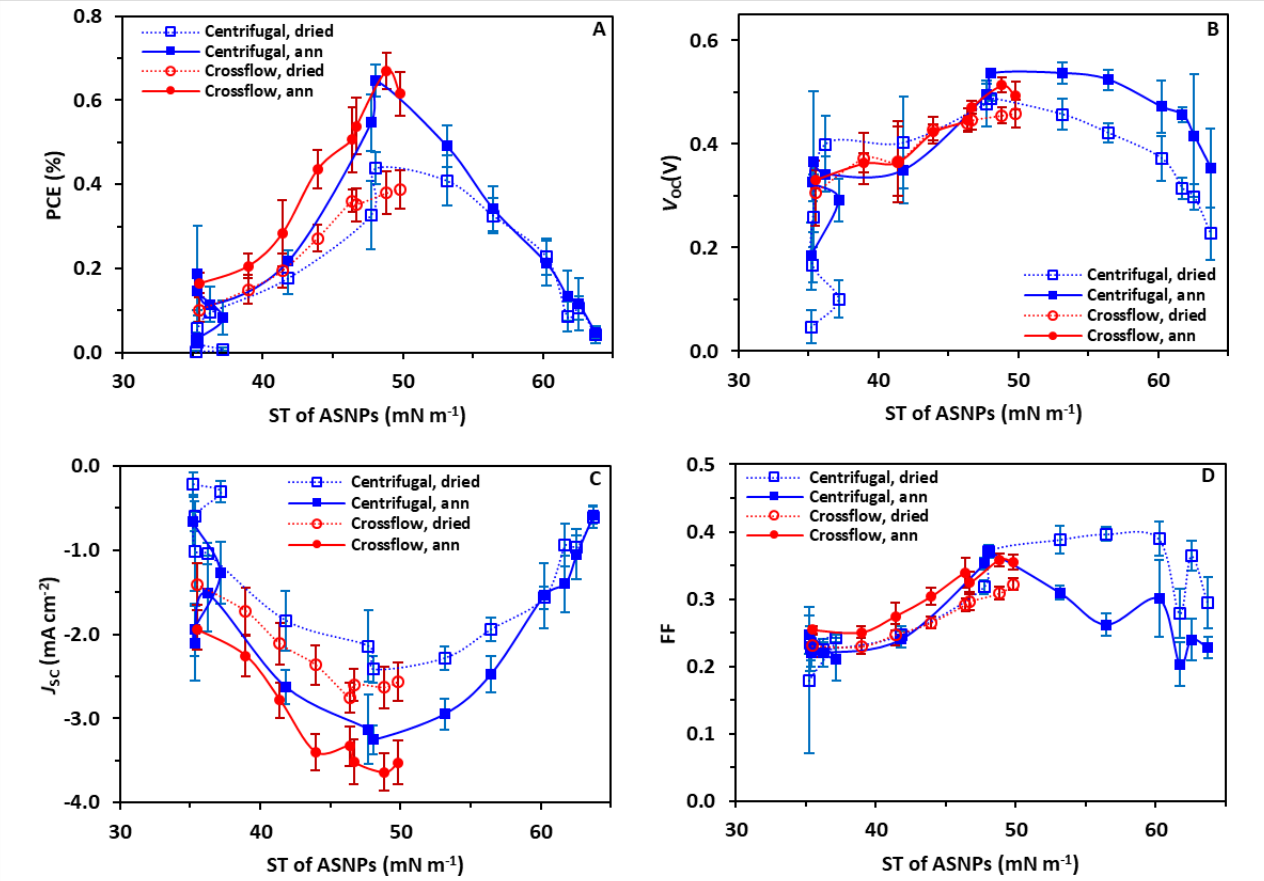

Figure 6: OPV performance showing (A) PCE, (B) V_{oc}, (C) J_{sc} and (D) FF values of NP-OPVs versus surface tension (ST) of P3HT:ICxA NPs dialysed by crossflow and centrifugal process (A–D), respectively. Solid line refers to annealed devices, and dot line refer to dried devices.

devices [16,25-27]. Moreover, HTL Solar has a lower conductivity than PH1000 which reduces/eliminates cross-over between cells on the same substrate. Based on the PEDOT/PSS ratio being the same, we expect, the wetting properties to be similar for our NP-inks on both types of PEDOT:PSSes. During upscaling the deposition technique would also be changed from spin-coating to slot-die coating which might also have an impact on film quality.

Conclusion

Herein we have demonstrated ASNP purification through two different ultrafiltration processes (centrifuge and crossflow-based techniques). It is clearly demonstrated that the rate for free-SDS removal varies between the two techniques even though a similar filter was used (10,000 M_w cut-off). In particular, inks purified by centrifuge ultrafiltration reached an optimal surface tension of 48 mN m^{-1} at a dilution factor of 7.8×10^4 whereas ink purified by crossflow reached an optimal surface tension of 48.8 mN m^{-1} at a dilution factor of 6.1×10^9. It has been shown that the efficiencies of NP-OPV devices vary with the dilution factor and is governed by the wetting properties of ASNP inks. We find that P3HT:ICxA NP inks having a surface tension of 48 and 48.8 mN m^{-1} produce NP-OPV devices having a masked average PCE of 0.65 and 0.67% (0.70 and 0.73% maximum) for centrifugal and crossflow purification, respectively. Therefore, efficient preparation conditions for either purification process of ASNP inks can be simply monitored through the surface tension of the ASNP inks as the key parameter.

Experimental

Materials and equipment

Poly(3-hexylthiophene) (P3HT) (M_n 20 kDa) and ICxA were synthesised in house according to the literature [28], with this batch of ICxA consisting of a mixture of 36% ICMA, 51% ICBA and 13% ICTA [16,27,28]. Sodium dodecyl sulphate (SDS) with 98% purity was purchased from Sigma-Aldrich. Poly(ethylenedioxythiophene):poly(styrene sulfonate) (PEDOT:PSS) Clevios HTL Solar was purchased from Heraeus. For the ultrafiltration process, centrifugal filter tubes (for small-volume) and Vivaflow 200 crossflow cassette (for large-volume) were supplied by Vivaproducts and Sartorius, respectively, each equipped with a poly(ethersulfone) (PES) membrane with a cut-off at 10 kDa (MWCO). A Hielscher ultra-

sound type UIP1000hdT (1000 W, 20 kHz) with a 22 mm diameter sonotrode was used to prepare the mini-emulsion for large-volume nanoparticle inks. Layer thicknesses were measured by a KLA–Tencor Alpha step 500 surface profilometer.

Preparation of aqueous solar nanoparticle inks

In accordance with the modified mini-emulsion process [10,11], the formulation of ASNP inks based on P3HT:ICxA (1:0.8) in large batch (100 mL) comprised several procedural steps. The first step is preparation of the organic phase (≈170 g) by dissolving 6 g of P3HT:ICxA in 112 mL of chloroform (CF) (≈54 mg mL^{-1}) at 35 °C and 700 rpm on hotplate, and independently 6.6 g of SDS surfactant is dissolved in 560 mL of Milli-Q water (≈12 mg mL^{-1}) to form the aqueous phase (≈566 g). The second step is macro-emulsion formation (≈736 g), which is the vigorous mixing of organic and aqueous solutions with stirring at 1200 rpm and 33 °C for 60 min. The third step is formation of a mini-emulsion (≈736 g) by ultrasonic treatment of the macro-emulsion (10 min, 60% amplitude and 450–500 W). As a fourth step, removal of chloroform was conducted at 65 °C and 1200 rpm for 4 h to produce aqueous nanoparticle P3HT:ICxA dispersions (≈500 g). The final step is the ultrafiltration process to remove excess surfactant using two types of purification methods, and to concentrate to 6 wt % solids content. In this step, the small-volume ultrafiltration (2.5 mL) was conducted by centrifuge (3550 rpm with controlling the time to concentrate ASNP inks to 0.5 mL) called a centrifugal ultrafiltration process, whilst the crossflow ultrafiltration process that is comprised of a Vivaflow 200 system involving pump with 1.25 bar pressure was used for large-volume inks (250 mL). The ultrafiltration process was performed in a series of sequential steps, with each step increasing the dilution of SDS by refreshing the ink solution with pure solvent such that each purification step was commenced with an identical initial dilution and completed with an identical volume to provide a constant dilution factor. The initial volume of ASNP dispersions were 250 mL or 2.5 mL for inks purified by the crossflow and centrifugal ultrafiltration processes, respectively. In any single filtration step, these volumes were then purified through ultrafiltration until final volumes of 50 mL and 0.5 mL were obtained, providing a dilution factor of 5. This process was then continually re-iterated with the addition of fresh solvent to provide a series of ASNP ink samples where the dilution factors (DF) varied exponentially, with the exponent being the number of dilution steps (DF = 5^0, 5^1, 5^2 …, 5^{15}), where dilution factor of 5 is the ratio between the initial volume and the concentrated volume. Through this repeated dilution procedure, P3HT:ICxA nanoparticle inks with dilution factor of (1 to 1.2×10^9 (5^{13})) and (1 to 3.1×10^{10} (5^{15})) were prepared and purified by centrifugal and crossflow methods, respectively. The removal of SDS and concentration of NP inks therefore occurred in the same equivalent volumes for both purification methods, even though the crossflow technique provided a much larger final sample. For large volume NP ink production, 3 mL of ASNP ink was collected at each dilution step for surface tension measurements, the reduced total ink volume was taken into account when adding water by reducing the volume of added water before the next ultrafiltration step. In addition to the preparation of ASNP inks, filtrates were collected at each dilution step for both purification methods. For small volume, 0.5 mL of ASNP inks were collected at each dilution step while the collected filtrate was 2 mL.

Nanoparticle characterisation

Particle size

Particle sizes were determined by dynamic light scattering (DLS) (Zetasiser Nano-ZS ZEN3500, Malvern Instruments) with a 633 nm laser and a backscatter detector angle of 173°. Samples for DLS were prepared by diluting 5 µL of NP ink in 10 mL Milli-Q water in order to reduce the solids content from 6 to 0.003%.

Free SDS concentration

UV-vis spectroscopy: An ultraviolet–visible absorption spectrophotometer (UV–vis, Varian Cary 6000i) was used to determine the free SDS concentration. This method works by measuring the absorption of methylene blue (MB) and monitoring its reduced absorption after forming a complex with free SDS [29]. Measurements were conducted on samples consisting of 1 mL of filtrate mixed with 2 mL of a 22.5 µM MB stock solution. The UV–vis spectra of the reference (1 mL of water and 2 mL MB stock solution) and calibration standards (SDS solutions with concentrations 0.01, 0.05, 0.1, 0.5, 1,.., 3.5 mg mL^{-1}) are shown in Supporting Information File 1, Figure S1A. The absorbance of MB at 664 nm decreased when increasing the SDS surfactant concentration, as shown in the calibration curve in Supporting Information File 1, Figure S1B. Hence free SDS concentration for unknowns were calculated from this calibration curve.

Surface tension: An Attension Theta optical tensiometer (Bionic Scientific Co.) was used to record drop images and automatically analyse the drop shape (pendant drop method using OneAttension software) of ASNP inks and their filtrates in order to measure their surface tension.

Film inspection: An Asylum Research Cypher atomic force microscope (AFM) operated in AC mode was used to probe the nanoparticle films. Film samples for AFM were spin-coated on quartz glass substrates at 2000 rpm for 1 min. A Zeiss Sigma ZP field-emission scanning electron microscope (FESEM) was

used to image the nanoparticle films (operating at accelerating voltage of 2 kV and magnification ranges of 10,000–100,000×), with concurrent energy dispersive X-ray spectroscopy (EDX) measurements. For SEM, NP films were coated on conductive silicon substrates by spin coating, where 2.5 µL of NP ink was diluted in 12.5 µL of water and spun at 3000 rpm speed with 112 rpm/s acceleration for 1 min.

Device fabrication

On pre-cleaned (water, acetone and isopropanol) patterned ITO glass substrates PEDOT:PSS (HTL Solar) films were spin-coated at 5000 rpm for 1 min and baked for 30 min at 140 °C (film thickness of 35 ± 5 nm). On top of the PEDOT:PSS layer, the P3HT:ICxA ASNP inks (dilution factor of 625–1.2×10^9 and 3.9×10^5–3.1×10^{10} for centrifugal and crossflow ultrafiltration, respectively) were used to fabricate films with thickness of 105 ± 6 nm. These films were spin-coated and dried at 110 °C for 5 min in air, followed by an additional drying step at 110 °C for 5 min in nitrogen glove box. Under vacuum (2×10^{-6} Torr) calcium (film thickness ≈30 nm) and aluminium (film thickness ≈100 nm) electrodes (Ca/Al) were thermally evaporated.

Film thickness

The Film thickness of the active layer was determined based on an average of 4 scans by profilometry (KLA-Tencor Alpha-step 500 surface profilometer) over a scratch on annealed (140 °C for 4 min) spin coated samples on a glass substrate. The spin coating recipe was adjusted for each sample to obtain the desired thickness.

Reflectance of the prepared devices was measured on a Varian Cary 6000i with an integrating sphere.

Device testing

The NP-OPV devices had a masked area of 3.8 mm^2 and were tested under a nitrogen atmosphere in glovebox before and after annealing at 140 °C for 4 min. Current density–voltage (J–V) measurements were performed using Keithley 2400 source meter under illumination of a Newport Class AAA solar simulator with an AM 1.5 spectrum filter. The light intensity was calibrated to 100 mW cm^{-2} using a silicon reference solar cell (FHG-ISE).

Supporting Information

Supporting Information File 1

Supporting Information.
[https://www.beilstein-journals.org/bjnano/content/supplementary/2190-4286-9-60-S1.pdf]

Acknowledgements

Furqan Almyahi gratefully acknowledges the Office of the Prime Minister of Iraq through the Higher Committee for Education Development (HCED) for funding support. The work was performed in part at the Materials node of the Australian National Fabrication Facility, a company established under the National Collaborative Research Infrastructure Strategy to provide nano- and microfabrication facilities for Australia's researchers. The authors thank the University of Newcastle Electron Microscopy and X-ray Unit.

ORCID® iDs

Furqan Almyahi - https://orcid.org/0000-0003-0765-2995
Thomas R. Andersen - https://orcid.org/0000-0003-0180-1443

References

1. Brabec, C. J. *Sol. Energy Mater. Sol. Cells* **2004,** *83,* 273–292. doi:10.1016/j.solmat.2004.02.030
2. Krebs, F. C.; Gevorgyan, S. A.; Alstrup, J. *J. Mater. Chem.* **2009,** *19,* 5442–5451. doi:10.1039/b823001c
3. Roes, A. L.; Alsema, E. A.; Blok, K.; Patel, M. K. *Prog. Photovoltaics* **2009,** *17,* 372–393. doi:10.1002/pip.891
4. Mulligan, C. J.; Bilen, C.; Zhou, X.; Belcher, W. J.; Dastoor, P. C. *Sol. Energy Mater. Sol. Cells* **2015,** *133,* 26–31. doi:10.1016/j.solmat.2014.10.043
5. Andersen, T. R.; Dam, H. F.; Andreasen, B.; Hösel, M.; Madsen, M. V.; Gevorgyan, S. A.; Søndergaard, R. R.; Jørgensen, M.; Krebs, F. C. *Sol. Energy Mater. Sol. Cells* **2014,** *120,* 735–743. doi:10.1016/j.solmat.2013.07.006
6. Søndergaard, R.; Helgesen, M.; Jørgensen, M.; Krebs, F. C. *Adv. Energy Mater.* **2011,** *1,* 68–71. doi:10.1002/aenm.201000007
7. Duan, C.; Cai, W.; Hsu, B. B. Y.; Zhong, C.; Zhang, K.; Liu, C.; Hu, Z.; Huang, F.; Bazan, G. C.; Heeger, A. J.; Cao, Y. *Energy Environ. Sci.* **2013,** *6,* 3022–3034. doi:10.1039/c3ee41838c
8. Gärtner, S.; Christmann, M.; Sankaran, S.; Röhm, H.; Prinz, E.-M.; Penth, F.; Pütz, A.; Türeli, A. E.; Penth, B.; Baumstümmler, B.; Colsmann, A. *Adv. Mater.* **2014,** *26,* 6653–6657. doi:10.1002/adma.201402360
9. Darwis, D.; Holmes, N.; Elkington, D.; Kilcoyne, A. L. D.; Bryant, G.; Zhou, X.; Dastoor, P.; Belcher, W. *Sol. Energy Mater. Sol. Cells* **2014,** *121,* 99–107. doi:10.1016/j.solmat.2013.10.010
10. Landfester, K.; Montenegro, R.; Scherf, U.; Güntner, R.; Asawapirom, U.; Patil, S.; Neher, D.; Kietzke, T. *Adv. Mater.* **2002,** *14,* 651–655. doi:10.1002/1521-4095(20020503)14:9<651::AID-ADMA651>3.0.CO;2-V
11. Kietzke, T.; Neher, D.; Landfester, K.; Montenegro, R.; Güntner, R.; Scherf, U. *Nat. Mater.* **2003,** *2,* 408–412. doi:10.1038/nmat889
12. Bag, M.; Gehan, T. S.; Renna, L. A.; Algaier, D. D.; Lahti, P. M.; Venkataraman, D. *RSC Adv.* **2014,** *4,* 45325–45331. doi:10.1039/C4RA07463G
13. Andersen, T. R.; Larsen-Olsen, T. T.; Andreasen, B.; Böttiger, A. P. L.; Carlé, J. E.; Helgesen, M.; Bundgaard, E.; Norrman, K.; Andreasen, J. W.; Jørgensen, M.; Krebs, F. C. *ACS Nano* **2011,** *5,* 4188–4196. doi:10.1021/nn200933r

14. Bag, M.; Gehan, T. S.; Algaier, D. D.; Liu, F.; Nagarjuna, G.; Lahti, P. M.; Russell, T. P.; Venkataraman, D. *Adv. Mater.* **2013,** *25,* 6411–6415. doi:10.1002/adma.201301302
15. Holmes, N. P.; Marks, M.; Kumar, P.; Kroon, R.; Barr, M. G.; Nicolaidis, N.; Feron, K.; Pivrikas, A.; Fahy, A.; Diaz de Zerio Mendaza, A.; Kilcoyne, A. L. D.; Müller, C.; Zhou, X.; Andersson, M. R.; Dastoor, P. C.; Belcher, W. J. *Nano Energy* **2016,** *19,* 495–510. doi:10.1016/j.nanoen.2015.11.021
16. Andersen, T. R.; Cooling, N. A.; Almyahi, F.; Hart, A. S.; Nicolaidis, N. C.; Feron, K.; Noori, M.; Vaughan, B.; Griffith, M. J.; Belcher, W. J.; Dastoor, P. C. *Sol. Energy Mater. Sol. Cells* **2016,** *149,* 103–109. doi:10.1016/j.solmat.2016.01.012
17. Larsen-Olsen, T. T.; Andreasen, B.; Andersen, T. R.; Böttiger, A. P. L.; Bundgaard, E.; Norrman, K.; Andreasen, J. W.; Jørgensen, M.; Krebs, F. C. *Sol. Energy Mater. Sol. Cells* **2012,** *97,* 22–27. doi:10.1016/j.solmat.2011.08.026
18. Pedersen, E. B. L.; Pedersen, M. C.; Simonsen, S. B.; Brandt, R. G.; Böttiger, A. P. L.; Andersen, T. R.; Jiang, W.; Xie, Z. Y.; Krebs, F. C.; Arleth, L.; Andreasen, J. W. *J. Mater. Chem. A* **2015,** *3,* 17022–17031. doi:10.1039/C5TA04980F
19. Stapleton, A.; Vaughan, B.; Xue, B.; Sesa, E.; Burke, K.; Zhou, X.; Bryant, G.; Werzer, O.; Nelson, A.; Kilcoyne, A. L. D.; Thomsen, L.; Wanless, E.; Belcher, W.; Dastoor, P. *Sol. Energy Mater. Sol. Cells* **2012,** *102,* 114–124. doi:10.1016/j.solmat.2012.03.016
20. Parrenin, L.; Laurans, G.; Pavlopoulou, E.; Fleury, G.; Pecastaings, G.; Brochon, C.; Vignau, L.; Hadziioannou, G.; Cloutet, E. *Langmuir* **2017,** *33,* 1507–1515. doi:10.1021/acs.langmuir.6b04496
21. Colberts, F. J. M.; Wienk, M. M.; Janssen, R. A. J. *ACS Appl. Mater. Interfaces* **2017,** *9,* 13380–13389. doi:10.1021/acsami.7b00557
22. Holmes, N. P.; Nicolaidis, N.; Feron, K.; Barr, M.; Burke, K. B.; Al-Mudhaffer, M.; Sista, P.; Kilcoyne, A. L. D.; Stefan, M. C.; Zhou, X.; Dastoor, P. C.; Belcher, W. J. *Sol. Energy Mater. Sol. Cells* **2015,** *140,* 412–421. doi:10.1016/j.solmat.2015.04.044
23. Vaughan, B.; Stapleton, A.; Sesa, E.; Holmes, N. P.; Zhou, X.; Dastoor, P. C.; Belcher, W. J. *Org. Electron.* **2016,** *32,* 250–257. doi:10.1016/j.orgel.2016.02.022
24. Al-Mudhaffer, M. F.; Griffith, M. J.; Feron, K.; Nicolaidis, N. C.; Cooling, N. A.; Zhou, X.; Holdsworth, J.; Belcher, W. J.; Dastoor, P. C. *Sol. Energy Mater. Sol. Cells* **2018,** *175,* 77–88. doi:10.1016/j.solmat.2017.09.007
25. Hösel, M.; Søndergaard, R. R.; Jørgensen, M.; Krebs, F. C. *Energy Technol.* **2013,** *1,* 102–107. doi:10.1002/ente.201200029
26. Krebs, F. C.; Hösel, M.; Corazza, M.; Roth, B.; Madsen, M. V.; Gevorgyan, S. A.; Søndergaard, R. R.; Karg, D.; Jørgensen, M. *Energy Technol.* **2013,** *1,* 378–381. doi:10.1002/ente.201300057
27. Andersen, T. R.; Almyahi, F.; Cooling, N. A.; Elkington, D.; Wiggins, L.; Fahy, A.; Feron, K.; Vaughan, B.; Griffith, M. J.; Mozer, A. J.; Sae-kung, C.; Wallace, G. G.; Belcher, W. J.; Dastoor, P. C. *J. Mater. Chem. A* **2016,** *4,* 15986–15996. doi:10.1039/C6TA06746H
28. Cooling, N. A.; Barnes, E. F.; Almyahi, F.; Feron, K.; Al-Mudhaffer, M. F.; Al-Ahmad, A.; Vaughan, B.; Andersen, T. R.; Griffith, M. J.; Hart, A. S.; Lyons, A. G.; Belcher, W. J.; Dastoor, P. C. *J. Mater. Chem. A* **2016,** *4,* 10274–10281. doi:10.1039/C6TA04191D
29. Carroll, M. K.; Unger, M. A.; Leach, A. M.; Morris, M. J.; Ingersoll, C. M.; Bright, F. V. *Appl. Spectrosc.* **1999,** *53,* 780–784. doi:10.1366/0003702991947568

License and Terms

This is an Open Access article under the terms of the Creative Commons Attribution License (http://creativecommons.org/licenses/by/4.0), which permits unrestricted use, distribution, and reproduction in any medium, provided the original work is properly cited.

The license is subject to the *Beilstein Journal of Nanotechnology* terms and conditions: (https://www.beilstein-journals.org/bjnano)

The definitive version of this article is the electronic one which can be found at:
doi:10.3762/bjnano.9.60

BEILSTEIN JOURNAL OF NANOTECHNOLOGY

Perovskite-structured $CaTiO_3$ coupled with g-C_3N_4 as a heterojunction photocatalyst for organic pollutant degradation

Ashish Kumar, Christian Schuerings, Suneel Kumar, Ajay Kumar and Venkata Krishnan*

Full Research Paper

Open Access

Address:
School of Basic Sciences and Advanced Materials Research Center, Indian Institute of Technology Mandi, Kamand, Mandi 175005, Himachal Pradesh, India

Email:
Venkata Krishnan* - vkn@iitmandi.ac.in

* Corresponding author

Keywords:
$CaTiO_3$; graphitic carbon nitride (g-C_3N_4); heterojunction photocatalyst; pollutant degradation

Beilstein J. Nanotechnol. **2018,** *9,* 671–685.
doi:10.3762/bjnano.9.62

Received: 07 October 2017
Accepted: 25 January 2018
Published: 21 February 2018

This article is part of the Thematic Series "Energy conversion, storage and environmental remediation using nanomaterials".

Guest Editor: W.-J. Ong

© 2018 Kumar et al.; licensee Beilstein-Institut.
License and terms: see end of document.

Abstract

A novel graphitic carbon nitride (g-C_3N_4)–$CaTiO_3$ (CTCN) organic–inorganic heterojunction photocatalyst was synthesized by a facile mixing method, resulting in the deposition of $CaTiO_3$ (CT) nanoflakes onto the surface of g-C_3N_4 nanosheets. The photocatalytic activity of the as-synthesized heterojunction (along with the controls) was evaluated by studying the degradation of an aqueous solution of rhodamine B (RhB) under UV, visible and natural sunlight irradiation. The CTCN heterojunction with 1:1 ratio of g-C_3N_4/CT showed the highest photocatalytic activity under sunlight irradiation and was also demonstrated to be effective for the degradation of a colorless, non-photosensitizing pollutant, bisphenol A (BPA). The superior photocatalytic performance of the CTCN heterojunction could be attributed to the appropriate band positions, close interfacial contact between the constituents and extended light absorption (both UV and visible region), all of which greatly facilitate the transfer of photogenerated charges across the heterojunction and inhibit their fast recombination. In addition, the two-dimensional (2D) morphology of g-C_3N_4nanosheets and CT nanoflakes provides enough reaction sites due to their larger surface area and enhances the overall photocatalytic activity. Furthermore, the active species trapping experiments validate the major role played by superoxide radicals ($O_2^{-\bullet}$) in the degradation of pollutants. Based on scavenger studies and theoretically calculated band positions, a plausible mechanism for the photocatalytic degradation of pollutants has been proposed and discussed.

Introduction

Photocatalysis is recognized as an attractive approach for environmental remediation and energy generation applications due to its potential towards utilization of solar energy [1-3]. Therefore, extensive efforts have been made for the design and synthesis of highly efficient and stable photocatalyst systems over the past few decades [4-7]. Hence, the development of such photocatalysts with high stability and good activity is desirable. The physical and chemical properties of a photocatalyst are

related to its photocatalytic performance as three crucial factors of photocatalysis (i.e., photon absorption, charge carrier transfer and catalytic surface reactions) are dependent on them [8,9]. Two-dimensional (2D) layered heterojunctions are of great interest in the photocatalysis domain for achieving environmental sustainability [10,11]. These nanocomposites are known for their greater photogenerated electron–hole mobility across the heterojunction interface, which reduces the distance and time of charge transport to impede their recombination rate [12,13]. The 2D–2D heterojunctions exhibit larger face-to-face contact area as compared with the line-to-face contact (1D–2D) and point-to-face contact (0D–2D) photocatalysts, which is responsible for their enhanced photocatalytic activity [14]. It is worth mentioning here that 2D–2D nanocomposites could effectively improve the specific surface area and provide abundant reaction sites to adsorb reactant species on their surface, which can significantly enhance the photocatalytic activity [15,16].

Recently, graphitic carbon nitride (g-C_3N_4), which is a metal-free polymeric organic semiconductor with tri-s-triazine units, has drawn huge attention from researchers due to its excellent photocatalytic performance and unique properties such as appropriate band structure, visible light absorption and high chemical and thermal stability [2,4]. In addition, g-C_3N_4 consists of earth-abundant carbon and nitrogen elements and the low cost of the initial precursors promotes it as a promising photocatalytic material for diverse applications, such as energy generation [17-19], sensor [20], and fuel cell applications [21], as well as environmental remediation [22]. The band gap of g-C_3N_4 lies between 2.4–2.8 eV and therefore it has the capability to absorb visible light irradiation [23]. However, the photocatalytic efficiency of bare g-C_3N_4 is truncated by the high recombination rate of photogenerated charges (electrons and holes), insufficient light absorption and low specific surface area [24]. In this regard, various attempts have been made by researchers to eliminate these issues in recent times. Several strategies such as synthesis of mesoporous g-C_3N_4 [25], synthesis of 2D nanosheets [26], coupling with conductive materials [23], heterostructure formation with other semiconductor materials [27,28] and synthesis of carbon nitride like materials [29] have been explored to improve its photocatalytic activity.

Another attractive strategy to enhance the photocatalytic activity and to reduce the electron–hole recombination in a photocatalyst involves the coupling of a wide band gap material with a low band gap material [30]. Natarajan et al. have demonstrated the enhanced degradation of isoniazid (a pharmaceutical pollutant) over the g-C_3N_4–TiO_2 nanocomposite via a direct Z-scheme charge transfer mechanism [31]. The enhanced photocatalytic activity has been attributed to the exact positions of energy band offsets of the coupled materials, which facilitates the photogenerated charge transfer and effectively suppresses their recombination. Moreover, perovskite materials are also potential candidates for environmental remediation applications and are well-explored in the literature [32,33]. Xian and coworkers have studied the photocatalytic degradation of MO under simulated solar light irradiation in $BaTiO_3$–g-C_3N_4 composites with an efficient charge separation of photogenerated charge carriers at the interfaces [30]. Leong et al. have successfully made a promising amalgamated g-C_3N_4–$SrTiO_3$ photocatalyst by a simple thermal method. The as-prepared composites showed exceptional properties for photocatalytic degradation of bisphenol A (BPA) under intense sunlight due to the enhanced migration of photogenerated charges over the close interfacial connections between g-C_3N_4 and $SrTiO_3$ [34]. Thus, wide band gap materials can play an important role in maximizing the photocatalytic activity of g-C_3N_4 by suppressing the photogenerated charge recombination.

$CaTiO_3$ (CT) is a well-known titanium-based perovskite material with a wide band gap of ≈3.5 eV and its activity is limited to UV excitation only [35]. Recently, our group has reported a novel RGO–N–$CaTiO_3$ (RGO-NCT) bifunctional photocatalyst which comprises both adsorption and photocatalytic properties [36]. The photocatalytic activity of RGO-NCT photocatalysts was evaluated by studying the degradation of methylene blue (MB) and thiabendazole (TBZ) under visible light irradiation. Another attractive strategy for enhancement of photocatalytic performance is the coupling of a wide band gap material with a low band gap material, which allows the charge transfer via suitably arranged band edge positions in both materials [37]. Thus, the fabrication of a binary heterojunction of CT with a narrow band gap semiconductor like g-C_3N_4 can enhance the photocatalytic activity by effective charge separation and transfer across the heterojunction. Moreover, a sheet-like morphology can promote the photocatalytic activity, as such materials possess a large surface area, providing abundant active sites for reaction, and the short bulk diffusion length reduces the probability of recombination of the photogenerated charges. Herein, we report the optimized synthesis of sheet-like 2D CT nanoflakes for the first time via the polyacrylamide gel route. Furthermore, we made a promising 2D–2D heterojunction of CT nanoflakes and g-C_3N_4 nanosheets by a facile mixing method. The photocatalytic performance of the as-prepared CT–g-C_3N_4 (CTCN) heterojunction photocatalyst and the controls was evaluated by monitoring the degradation of rhodamine B (RhB) dye under UV, visible and natural sunlight irradiation. Also, the degradation of a non-photosensitizing colorless pollutant, BPA, was also studied under sunlight to eliminate the doubt of RhB photosensitization in the photocatalytic activity. The CTCN heterojunction offers enhanced light

absorption both in the UV and visible light regions, leading to the formation of a higher number of charge carriers, their suppressed recombination, efficient separation and transfer over layered interface. Thus, we anticipate that the CTCN heterojunction can be used for the efficient removal of detrimental pollutants from water very effectively.

Experimental

Materials

Both titanium diisopropoxide bis(acetylacetonate) and dicyandiamide were purchased from Sigma-Aldrich, India. Calcium nitrate ($Ca(NO_3)_2{\cdot}4H_2O$), acrylamide and D-glucose were supplied by MP Biomedicals, India. Ammonia solution (NH_3 about 25%), nitric acid (HNO_3) and tartaric acid were supplied by Merck, India. All chemicals were used as received. Deionized (DI) water obtained from a double-stage water purifier (ELGA PURELAB Option-R7) was used for all experimental work.

Synthesis of $CaTiO_3$ nanoflakes

$CaTiO_3$ nanoflakes were synthesized by adopting a reported procedure with some modifications [38]. In brief, equimolar ratio of $Ca(NO_3)_2{\cdot}4H_2O$ and titanium diisopropoxide bis(acetylacetonate) (0.0075 mol) were dissolved in 20 mL of dilute HNO_3 aqueous solution with a concentration of 1.6 mol L^{-1}. To this solution, 0.0225 mol of tartaric acid, 20 g of glucose and 0.135 mol of acrylamide were successively added with constant stirring. The thus-obtained viscous solution was made up to 100 mL by adding distilled water, and aqueous ammonia was added dropwise to get a final pH of 2. This solution was heated at 70 °C on a hot plate to initiate the polymerization reaction and was kept at 120 °C for 24 h in an oven to obtain a black mass. The obtained xerogel was grounded into a powder and calcinated at 700 °C for 8 h, finally yielding white-colored CT nanoflakes.

Synthesis of g-C_3N_4 nanosheets

The g-C_3N_4 nanosheets were synthesized by heating dicyandiamide at 550 °C with a temperature ramp of 3 °C/min for 4 h in static air and allowed to cool naturally to room temperature. The resultant yellow mass was well ground to form a fine powder. The thus-obtained powder was subjected to thermal oxidation etching in static air at 500 °C for 2 h with a ramp rate of 5 °C/min to get a pale yellow powder of g-C_3N_4 nanosheets upon cooling [16,39].

Synthesis of $CaTiO_3$–g–C_3N_4 2D–2D heterojunction

The binary heterojunction photocatalyst (CTCN) was prepared by mixing both the organic (g-C_3N_4) and inorganic ($CaTiO_3$) semiconductor materials in a 1:1 ratio by using a modified facile heating method [34]. In the typical procedure, 100 mg of as-prepared g-C_3N_4 nanosheets was ultrasonically dispersed in 20 mL of DI water. A similar dispersion of 100 mg of CT nanoflakes was also prepared in 20 mL of DI water and both solutions were mixed and stirred for 1 h. The final mixture was subjected to heating at 80 °C with constant stirring to get a thick suspension. The resulting suspension was then washed with DI water, centrifuged and dried overnight at 70 °C. The resultant material was finally ground into a fine powder employing a mortar and pestle and used for further experiments.

Characterization

The purity, phase composition and structure of the resultant samples were identified by utilizing powder X-ray diffraction (XRD) studies using a Rigaku SmartLab 9 kW rotating anode diffractometer working in Bragg configuration with Ni-filtered Cu Ka irradiation (λ = 0.1542 nm) at 45 kV and 100 mA. The scans were collected over a 2θ range of 10–90° with a scan rate of 2° per minute. Fourier transform infrared (FTIR) spectra were recorded for functional group analysis by using an Agilent K8002AA Carry 660 instrument. Thermogravimetric analysis (TGA) was carried out in order to ascertain the stability of the as-prepared samples under nitrogen atmosphere by using a Netzsch STA 449 F1 Zupiter instrument. The samples were heated from room temperature to 800 °C at a heating rate of 10 °C min^{-1} with a flow rate of 40 mL min^{-1} in all experiments. Field-emission scanning electron microscopy (FE-SEM) was employed to explore the morphology and surface features of the resultant samples by using a FEI Nova Nano SEM-450 instrument. The samples were sputter-coated with a 2 nm Au layer before measurements in order to make them conducting. Energy dispersive X-ray spectroscopic analysis (EDAX) measurements were performed by using the same SEM instrument in order to find the elemental constituents of the samples. More detailed investigations on the morphology were obtained by transmission electron microscopy (TEM) and high-resolution TEM (HRTEM) studies. Images were recorded on a Technai G 20 (FEI) S-twin microscope operating at 200 kV (accelerating voltage). Elemental mapping was also carried out by using the same instrument in order to study the presence and spatial distribution of expected elements in all prepared samples. The light harvesting ability of the resultant samples as a dry-pressed disk was measured by diffuse reflectance spectroscopy (DRS). DRS studies were performed on a Perkin Elmer UV–visible–NIR Lambda 750 spectrophotometer by utilizing polytetrafluoroethylene (PTFE) polymer as a diffuse reflectance standard in the wavelength range 200–800 nm. Photoluminescence (PL) spectroscopy measurements were carried out by using an Agilent Technologies Cary Eclipse fluorescence spectrophotometer. The Brunauer–Emmett–Teller (BET) surface area and nitrogen adsorption–desorption isotherms were measured at 77 K on a Quantachrome Autosorb-iQ-MP-XR system.

Photocatalytic degradation study

The evaluation of the photocatalytic performance of CTCN heterojunction and control samples was performed by monitoring the degradation of a model dye, RhB, which is a carcinogenic organic pollutant and is used illegally in the food industries in many countries [40]. The photocatalytic degradation ability tests were performed in a 50 mL glass conical flask by taking 25 mL of 1×10^{-5} M aqueous solution of RhB under UV light irradiation by using a Luzchem LZC 4V UV irradiation chamber equipped with 12 UV lamps (λ = 365 nm with intensity of approximately 32000 lux), under visible light irradiation by using a homemade photoreactor setup consisting of two 14 W white light LED bulbs (intensity approximately 55000 lux) and under intense sunlight on a full sunny day, separately. For each experiment, 25 mg of the photocatalyst was dispersed in 25 mL of aqueous solution of RhB and then stirred magnetically for 1 h in the dark to establish complete equilibrium of adsorption/desorption between the photocatalyst and the RhB dye before being subjected to irradiation. Blank experiments were also performed in the absence of any photocatalyst to observe the stability of RhB. During the photocatalytic reaction, 1 mL aliquots of the dispersion were extracted after 15 min regular intervals and centrifuged to separate the residual photocatalyst particulates. The photocatalytic degradation ability was examined by monitoring the change in the absorbance of the characteristic wavelength of RhB at 554 nm by using the UV–vis spectrophotometer. The photocatalytic degradation percentage (%) of the catalyst was calculated from the following relation [41,42]: Degradation (%) = $(1 - C/C_0) - 100$, where C_0 refers to the absorbance of RhB after adsorption equilibrium, achieved prior to the light irradiation, and C is the absorbance of RhB at the different time intervals under visible light illumination. For the BPA degradation study, it was dissolved in DI water with the help of probe sonication and the concentration of the final solution was kept at 5×10^{-5} M. Prior to irradiation, 25 mL of BPA solution mixed with 25 mg of CTCN heterojunction photocatalyst was kept in the dark for one hour under stirring conditions to attain adsorption–desorption equilibrium. Subsequently, the solution was kept under natural sunlight and aliquots of samples were collected at regular intervals of time by following the same procedure as performed in the case of RhB dye.

Results and Discussion

Synthesis and structural studies

The heterojunction of g-C_3N_4 and $CaTiO_3$ in a 1:1 ratio has been prepared by using a facile mixing method with well-defined 2D interfacial contacts. The powder XRD patterns of g-C_3N_4, CT and CTCN heterojunction were recorded to analyze the crystal phase structure and are presented in Figure 1. g-C_3N_4 nanosheets exhibit a weak diffraction peak at

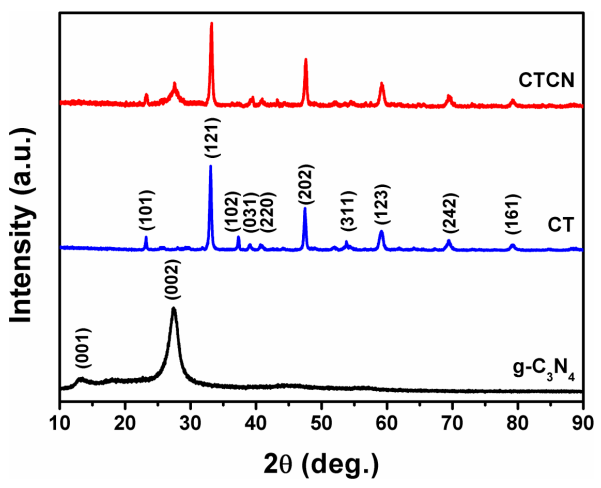

Figure 1: Powder X-ray diffraction patterns of g-C_3N_4, CT and CTCN heterojunction.

2θ = 13.10° (001) and an intense peak at 2θ = 27.34° (002), which corresponds to the in-plane structural motif packing and interplanar stacking of aromatic systems, respectively, and are consistent with literature [16,34]. The diffraction pattern of CT nanoflakes shows peaks at 2θ = 23.20°, 33.05°, 37.30°, 39.08°, 40.68°, 47.49°, 53.78°, 59.18°, 69.43° and 79.20°, corresponding to the (101), (121), (102), (031), (220), (202), (311), (123), (242) and (161) planes, respectively, and are well indexed to the orthorhombic phase with high purity (JCPDS card no. 42−0423, a = 5.442 Å, b = 7.642 Å, c = 5.381 Å) [36]. All the peaks corresponding to CT could be identified in the powder XRD pattern of the CTCN heterojunction, illustrating the predominant presence and phase purity of CT. Although the (002) peak of g-C_3N_4 could be evidenced in the diffraction pattern of the CTCN heterojunction, the (001) peak of g-C_3N_4 could not be seen, which could be attributed to its weak diffraction intensity in comparison to the other peaks.

Furthermore, FTIR spectroscopy has been employed for functional group analysis and the obtained spectra are shown in Figure 2. For g-C_3N_4, the sharp band around 807 cm^{-1} arises due to the presence of heptazine rings; the peaks at 1228 cm^{-1} and 1310 cm^{-1} can be assigned to the stretching vibrations of trigonal C–N(–C)–C or bridging C–NH–C units. The peaks at 1398 cm^{-1}, 1540 cm^{-1} and 1636 cm^{-1} correspond to the stretching vibration of aromatic C–N bonds [16,34]. The broad peak from 3000–3600 cm^{-1} can be assigned to the terminal NH or NH_2 groups of the aromatic rings and O–H stretching of surface hydroxyl groups [20]. The FTIR spectrum of CT nanoflakes shows three distinct peaks at 435 cm^{-1}, 540 cm^{-1} and 1420 cm^{-1} corresponding to the stretching vibrations of Ti–O, bridging stretching modes of Ti–O–Ti and bending vibration of CO_3^{2-} ions which is consistent with the literature [43]. The

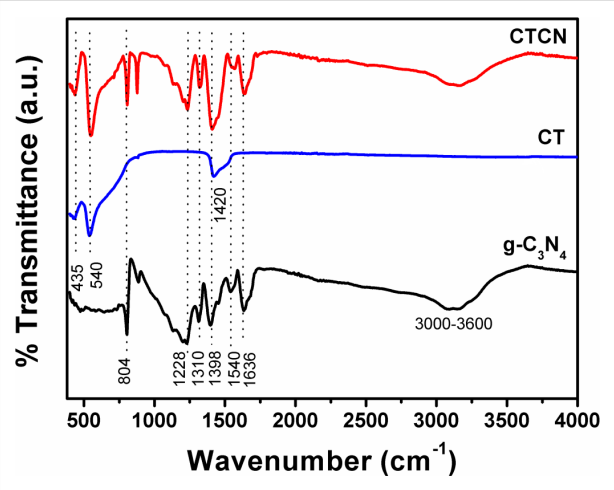

Figure 2: FTIR spectra of g-C_3N_4, CT and CTCN heterojunction.

FTIR spectrum of the CTCN heterojunction comprises of all the peaks of g-C_3N_4 and CT, indicating that the addition of g-C_3N_4 has not altered the structural properties of CT, which is in agreement with the XRD results.

Thermogravimetric studies

To investigate the thermal stability of g-C_3N_4, CT and CTCN heterojunction, thermogravimetric (TGA) analysis was carried out from ambient temperature to 800 °C, at a heating rate of 10 °C min^{-1} under nitrogen atmosphere. The corresponding results are presented in Figure 3. For pure g-C_3N_4 nanosheets, the rapid decay of the TGA curve from 520 °C to 740 °C represents the typical thermal decomposition and indicates its intrinsic thermal instability in this temperature range [44]. CT nanoflakes show very high thermal stability in comparison to g-C_3N_4 and no significant weight loss is observed in the TGA curve of pure CT, even at 800 °C [36]. The relative content of

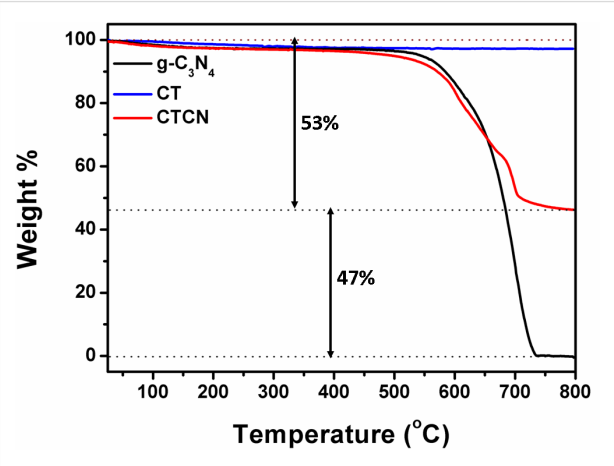

Figure 3: Thermogravimetric analysis plots of g-C_3N_4, CT and CTCN heterojunction.

the g-C_3N_4 in the CTCN heterojunction could also be verified from its TGA curve, which shows about 50% of each of the constituents, as expected from the preparation procedure. Overall, TGA analysis reveals that the as-prepared CTCN heterojunction possesses good thermal stability.

Morphological and compositional studies

The morphology of g-C_3N_4, CT and CTCN heterojunction were investigated by using SEM and TEM microscopic techniques. The SEM images of g-C_3N_4 are presented in Figure 4a and 4b, which shows an aggregated sheet-like morphology for bare g-C_3N_4. The SEM images of CT are presented in Figure 4c and 4d, which shows flake-like morphology. The SEM images of the CTCN heterojunction presented in Figure 4e and 4f shows the CT flakes deposited on g-C_3N_4 sheets, hence confirming the successful heterojunction formation with the 2D interface with face-to-face contact. The EDAX spectra of g-C_3N_4, CT and CTCN heterojunction presented in Figure S1, Supporting Information File 1 show the presence of all the constituent elements.

The TEM images of g-C_3N_4, CT and CTCN heterojunction are presented in Figure 5. Pure g-C_3N_4 exhibits a 2D lamellar sheet-like morphology (Figure 5a). The HRTEM image of g-C_3N_4 shows lattice fringes with 0.325 nm distance, which corresponds to its characteristic (002) plane (Figure 5b) [45]. The lattice fringes are not uniformly seen, which is due to the semi-crystalline nature of g-C_3N_4 as previously reported in the literature [46]. It can be seen from Figure 5c that CT has a thin sheet-like morphology joined together to form an aggregated flake-like structure. Furthermore, lattice fringes with 0.267 nm distance corresponding to the (121) plane of CT are observed in Figure 5d [47]. A TEM image of the CTCN sample presented in Figure 5e shows well-anchored CT nanoflakes on the g-C_3N_4 sheets, which form a heterojunction due to their close interfacial contact. The heterojunction formation can be confirmed in Figure 5f as the presence of CT is confirmed with 0.267 nm (121) and 0.385 nm (101) lattice fringes along with g-C_3N_4 sheets clearly marked [48]. The lattice fringes of g-C_3N_4 are not observed in the heterojunction, which could be due to its poor crystallinity [46]. This interfacial contact favors the charge transfer between CT and g-C_3N_4, which suppress the recombination of photogenerated charge carriers and enhance the photocatalytic activity. Furthermore, the elemental mapping of g-C3N4, CT and CTCN was also carried out in order to study the presence and spatial distribution of expected elements and corresponding maps are provided in Figure S2, S3 and S4, Supporting Information File 1, respectively. The mapping results show the uniform distribution and co-existence of expected elements in the selected area. Moreover, these results also show that the CTCN heterojunction is not simply a physical mixture of separate CT and g-C_3N_4 entities [49].

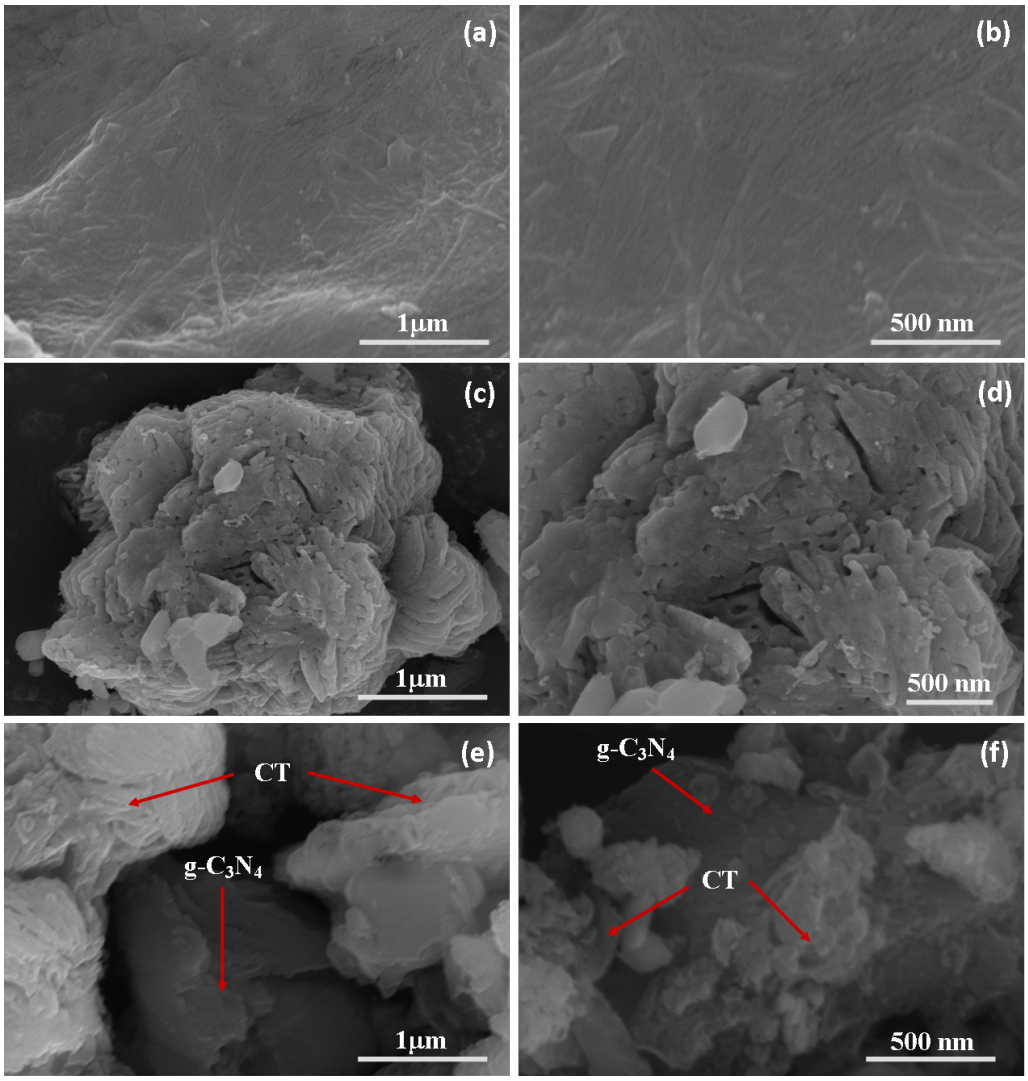

Figure 4: SEM images of (a, b) g-C_3N_4 sheets, (c, d) CT flakes and (e, f) CTCN heterojunctions.

Optical properties study

The band gap energy of a material is directly related to its light harvesting capability. To gain insight into the band structure of heterojunction, a DRS study has been performed with all prepared catalysts. The DRS plots for g-C_3N_4, CT and CTCN heterojunction are depicted in Figure 6a. The band gap values of g-C_3N_4, CT and CTCN heterojunction are calculated from the transformed Kubelka–Munk plots (Figure 6b–d). Bare g-C_3N_4 nanosheets unveil a distinct absorption edge in the visible region corresponding to the band gap of 2.75 eV resulting from the transfer of electrons from the valence band to the conduction band [50]. The absorption edge for CT nanoflakes lies in the UV region exhibiting a band gap of 3.45 eV. The DRS profile of CTCN heterojunction presents a combination of the spectral features of g-C_3N_4 and CT, showing absorption both in the UV (3.22 eV) and visible regions (2.79 eV). The combination of these two materials may result in an effective photocatalyst that can absorb a larger part of the solar light spectrum, encompassing both the UV and visible light regions.

In addition, photoluminescence (PL) spectroscopy studies were carried out in order to study the separation and migration of photogenerated charge carriers in the CTCN heterojunction. It is well-reported in literature that recombination of electrons and holes give rise to intense PL emissions [51]. The g-C_3N_4 nanosheets show high PL emission, which is an indication of a high recombination rate of photogenerated charge carriers produced during light irradiation. However, the formation of the CTCN heterojunction allows the migration of photogenerated charges across the 2D–2D interface, which results in the prolongation of their lifetime. This is evident from the reduced PL emission in-

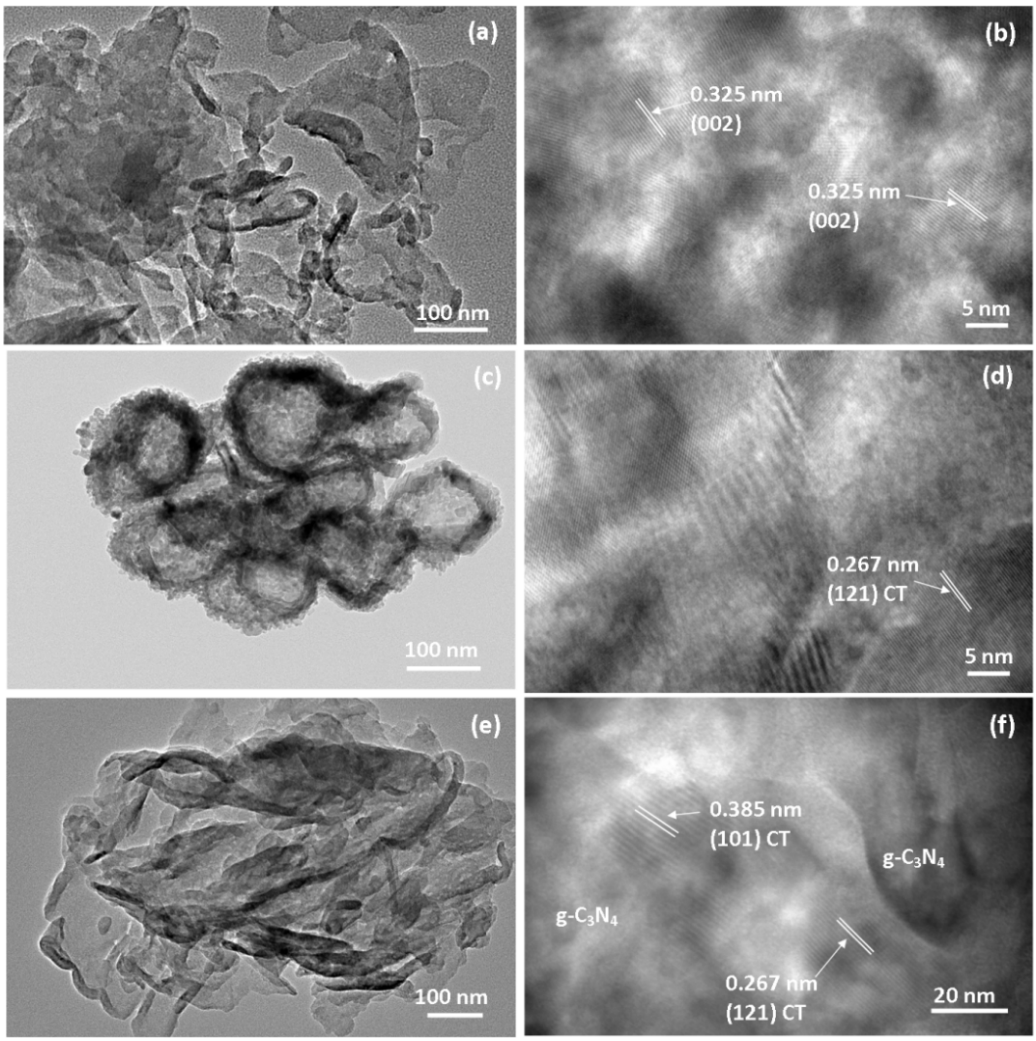

Figure 5: TEM images of (a, b) g-C_3N_4 nanosheets, (c, d) CT flakes and (e, f) CTCN heterojunction.

tensity of CTCN heterojunction as compared to the bare g-C_3N_4 nanosheets as shown in Figure 7.

Surface area studies

In order to explore the influence of g-C_3N_4 nanosheets on the surface area of CT flakes and to investigate the effect of g-C_3N_4 on enhancing the photocatalytic activity of the CTCN heterojunction, the BET surface area of bare CT, g-C_3N_4 and CTCN heterojunction has been investigated. Figure 8a–c represents the N_2 adsorption–desorption isotherms for g-C_3N_4, CT and CTCN heterojunction, respectively. The corresponding BET surface area plots and values are presented in Figure 8d–f. It can be seen that the BET surface area of bare CT flakes was estimated to be 29.3 m^2g^{-1} and the pure g-C_3N_4 nanosheets was 41.0 m^2g^{-1}. However, upon coupling of g-C_3N_4 nanosheets with CT flakes, the BET surface area of the resulting CTCN composite was enhanced to 50.7 m^2g^{-1}, which is larger in comparison to that of bare samples. This enhancement could be due to the exfoliation of g-C_3N_4 nanosheets and CT nanoflakes due to the ultrasonication process adopted in the synthesis of the CTCN heterojunction. Thus, the high surface area of CTCN heterojunction photocatalyst provides more reaction sites for the adsorption and degradation of pollutant molecule and hence results in the enhancement of photocatalytic activity.

Photocatalytic activity studies

The photocatalytic activity of the CTCN heterojunction and the corresponding control samples was investigated by studying the degradation of a model dye pollutant, rhodamine B (RhB) under UV, visible and natural sunlight irradiations. The prominent absorption peak of RhB at 554 nm was monitored by employing UV–vis spectroscopy to quantify the amount of dye degraded. The time-dependent absorption spectra of RhB solutions degraded by the CTCN heterojunction photocatalyst under

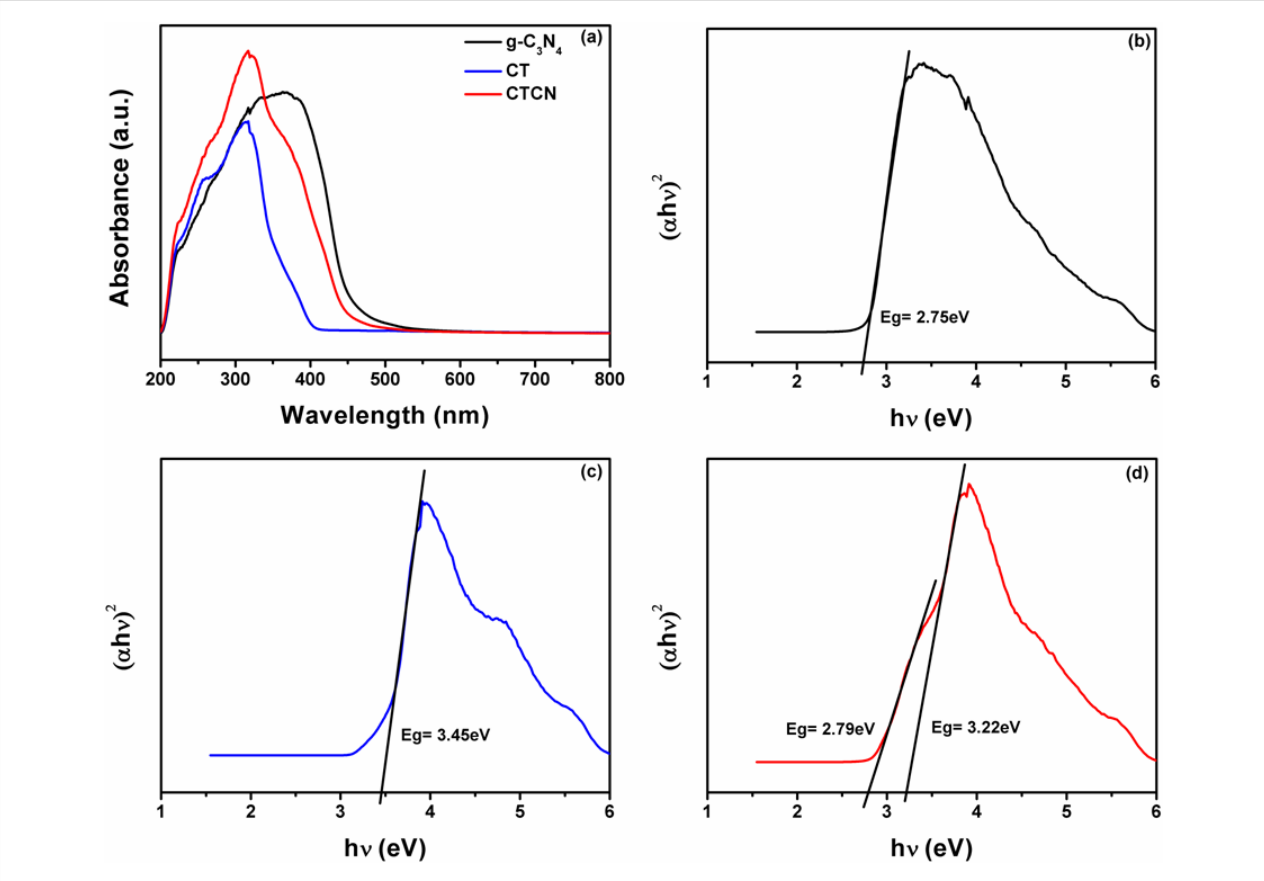

Figure 6: (a) UV–visible diffuse reflectance spectroscopy (DRS) spectra for g-C_3N_4, CT and CTCN heterojunction; Plot of transformed Kubelka–Munk function vs energy for (b) g-C_3N_4, (c) CT and (d) CTCN heterojunction.

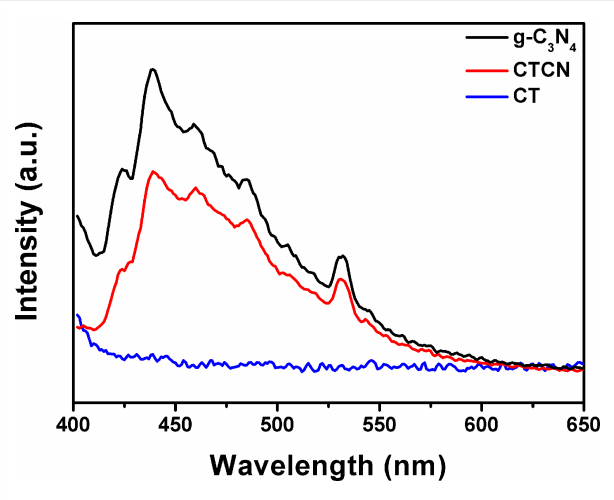

Figure 7: Photoluminescence spectra of g-C_3N_4, CT and CTCN heterojunction.

different light sources are depicted in Figure 9a–c and those for bare g-C_3N_4 and CT, including the control experiments performed without catalyst, are provided in Figure S5, Supporting Information File 1. It can be seen from the absorption plots presented in Figure 9a–c and Figure S5a–c, Supporting Information File 1, that a shift in the absorption maximum of RhB along with the decrease in intensity is observed upon irradiation under any light source [52]. Generally, the degradation of RhB takes place either by destruction of the chromophore or by *N*-deethylation of RhB, resulting in the decrease in absorption at λ_{max} = 554 nm. *N*-Deethylation of RhB leads to a steady blue shift toward 495 nm with increase in the irradiation time in the presence of g-C_3N_4, which could be due to the formation of *N*-deethylated intermediates. However, direct chromophore destruction leads to the formation of low molecular weight fragments, which does not have absorption in the lower visible region [53]. In our study, we observed a distinguishable blue shift in the λ_{max} of RhB solution containing the bare g-C_3N_4 or CTCN heterojunction, under all three types of irradiation. Thus, we can say that degradation of RhB takes place via *N*-deethylation processes in this case. However, in case of bare CT nanoflakes, no blue shift was observed in the λ_{max} which infers direct destruction of the chromophore of RHB during the degradation process. Control experiments for the degradation of RhB without any catalyst reflect its high stability under different light irradiation conditions, as no significant decrease in the

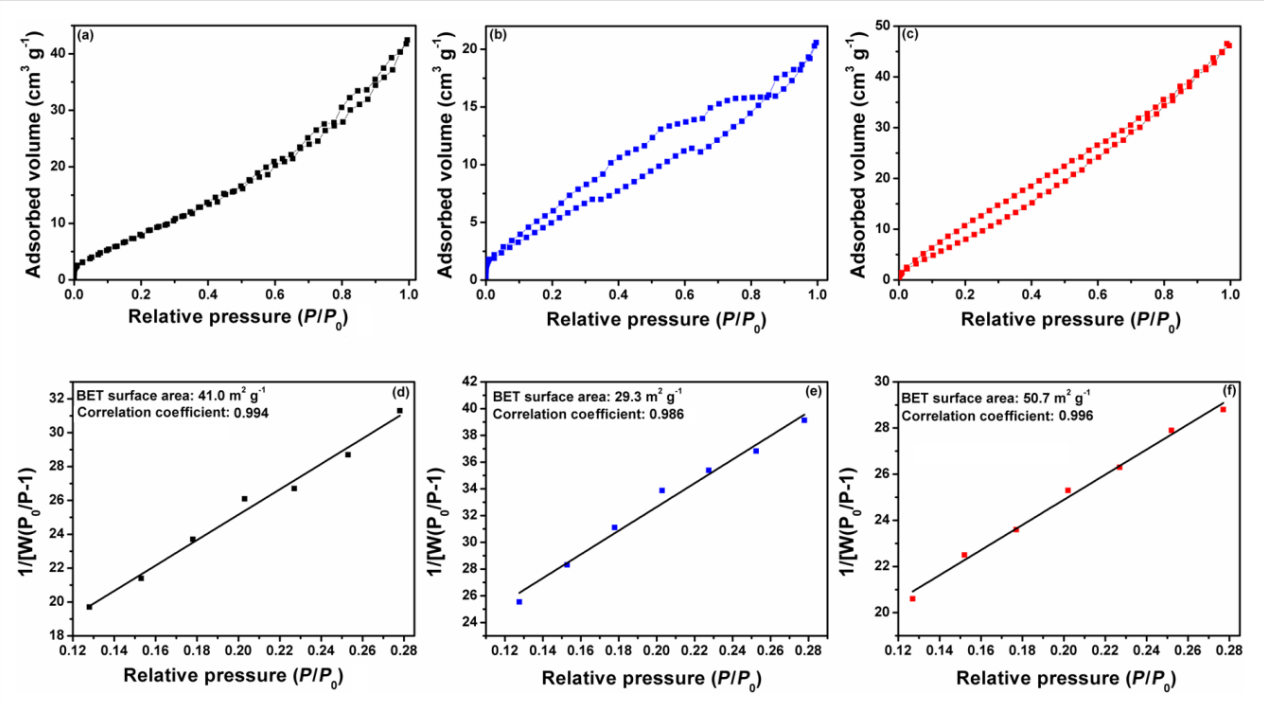

Figure 8: Nitrogen adsorption–desorption curves for (a) g-C_3N_4 (b) CT and (c) CTCN heterojunction; BET surface area plots for (d) g-C_3N_4 (e) CT and (f) CTCN heterojunction.

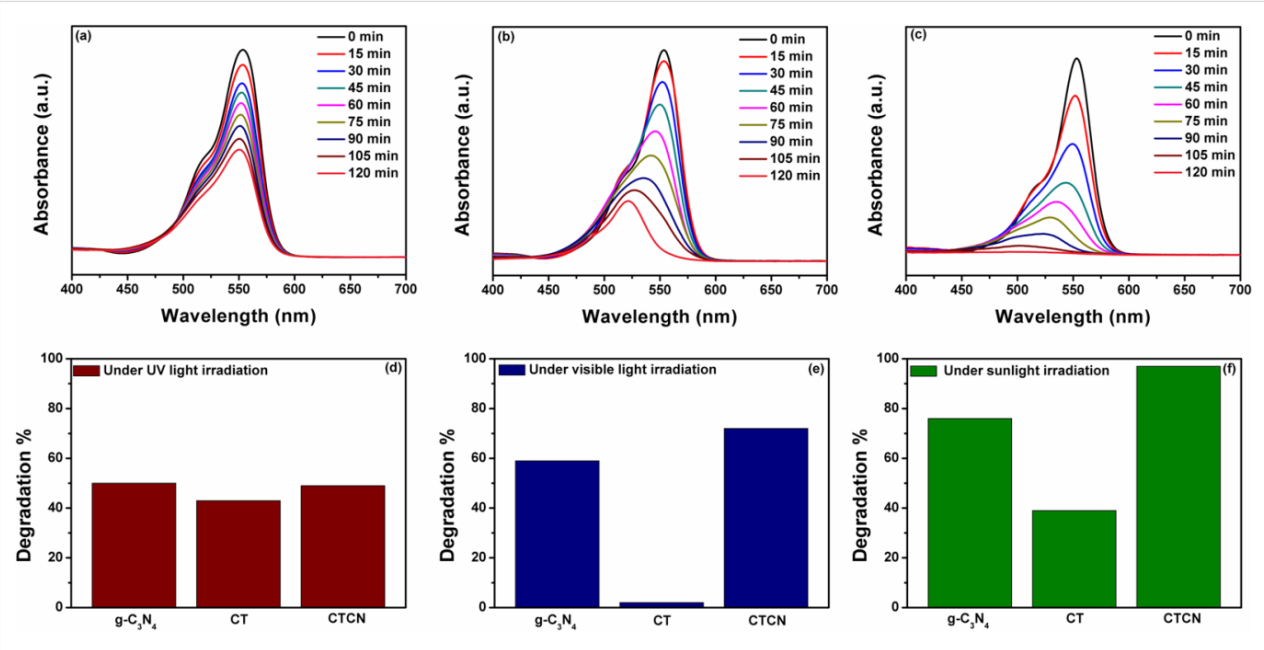

Figure 9: Time-dependent absorption spectra of RhB degradation with the CTCN heterojunction under (a) UV light, (b) visible light and (c) sunlight irradiation; degradation percentage plots of RhB with different samples under (d) UV light, (e) visible light and (f) sunlight irradiation after 120 min of irradiation.

absorption was observed. Figure 9d–f represents the degradation percentage of RhB upon irradiation under different light sources. It can be seen from Figure 8d that in the presence of UV light irradiation, bare g-C_3N_4 degrades ≈50% of the RhB dye. This degradation is obvious because high-energy UV light can also cause excitation of electrons from the valence band to the conduction band of g-C_3N_4. In the presence of bare CT nanoflakes, ≈43% degradation of RhB could be achieved. The

CTCN heterojunction also degraded only ≈50% of RhB, indicating that it is only as good as the bare g-C_3N_4 under UV irradiation. However, under visible light irradiation (Figure 8e), the CTCN heterojunction performed better by degrading ≈72% of RhB, while bare g-C_3N_4 could degrade only ≈59% of RhB. On the other hand, the RhB degradation achieved using bare CT nanoflakes was almost negligible as visible light did not have any effect on this wide band gap material. In addition, another set of control experiments performed on a simple physical mixture of CT and g-C_3N_4 showed substantially lower photocatalytic activity compared to the CTCN heterojunction. This indicates that the coupling of CT with g-C_3N_4 results in the formation of a heterojunction between them and enhances the photocatalytic performance under visible-light irradiation. The CTCN heterojunction provides a platform for the quick transfer of the photogenerated charge carriers from g-C_3N_4 to CT, thereby preventing their recombination and increasing their lifetime. This heterojunction formation also played a crucial role under natural sunlight irradiation (Figure 9f), wherein the CTCN heterojunction showed ≈97% degradation of RhB, much higher than bare g-C_3N_4 (≈76%) and CT (≈39%). The enhanced photocatalytic activity observed for a CTCN heterojunction under sunlight irradiation as compared to UV and visible light irradiation could be attributed to the following three reasons: (i) extended light absorption by the CTCN heterojunction both in the UV and visible region of solar energy, (ii) greater number of photoinduced charge carriers generation due to g-C_3N_4 and CT excitation by sunlight and (iii) fast charge transfer across a 2D interface to produce active species, which causes mineralization of pollutants. Therefore, our photocatalytic activity studies illustrate that the CTCN heterojunction formed by coupling CT with g-C_3N_4 performs well in comparison to its bare counterparts under all three irradiation conditions (i.e., UV, visible and sunlight).

To demonstrate the photocatalytic performance of the as-prepared catalysts more precisely, the kinetics of the photodegradation of RhB aqueous solutions was studied by fitting the obtained degradation results to a pseudo-first-order reaction model [54,55] and modified Freundlich model [56,57], utilizing the following integral equation respectively:

$$\ln\left(C / C_0\right) = -kt$$

$$\ln\left(1 - C / C_0\right) = \ln k + b \ln t$$

In these equations, C_0 is the absorbance of RhB after attaining the adsorption equilibrium, achieved prior to light illumination, C is the absorbance of RhB at time interval t under light illumination and k is the degradation rate constant. The kinetic plots corresponding to a pseudo-first-order reaction model are presented in Figure S6, Supporting Information File 1. Figure S6a–c represents the C/C_0 vs time plots for the catalysts under UV, visible and sunlight irradiation, respectively. The corresponding logarithmic plots are presented in Figure 10a–c under UV, visible and sunlight irradiation, respectively, according to

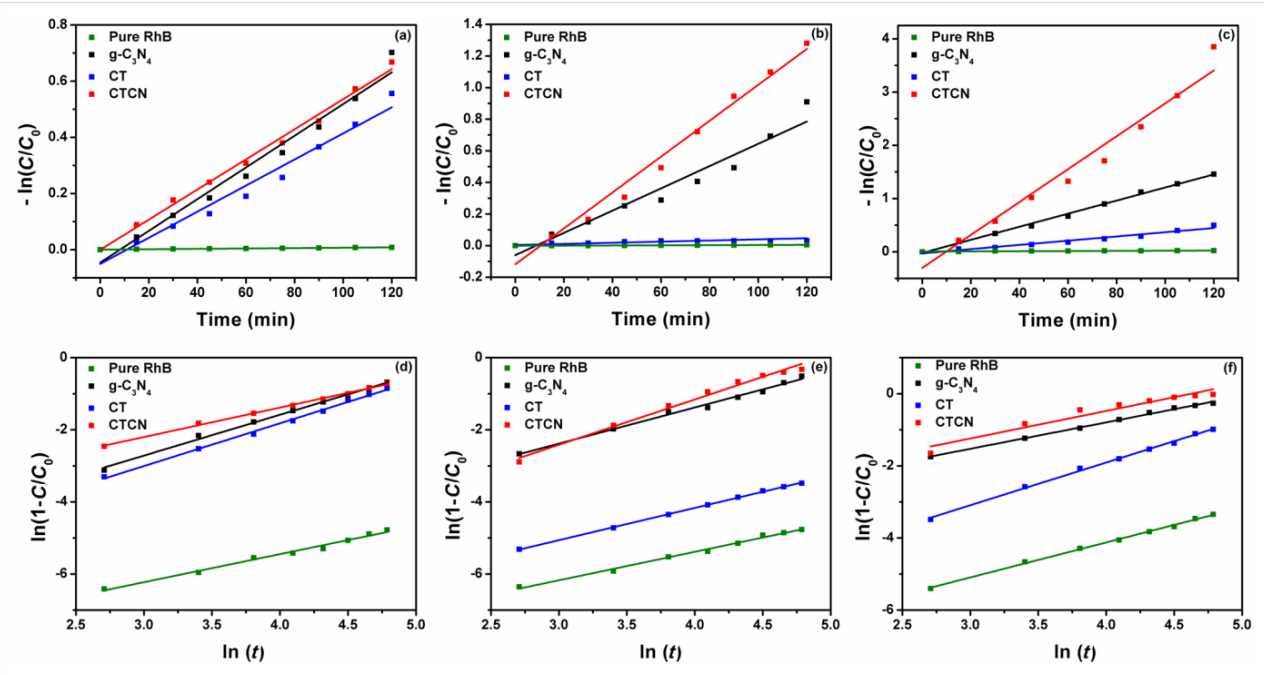

Figure 10: Kinetic curves obtained by applying (a, b, c) pseudo-first-order and (d, e, f) the modified Freundlich model for RhB degradation with different photocatalysts under (a, d) UV light, (b, e) visible light and (c, f) sunlight irradiation.

the pseudo-first-order reaction model. The degradation rate constants (k) acquired from the slope of the plot of $-\ln(C/C_0)$ vs time are presented in Table S1 (Supporting Information File 1) along with corresponding linear regression coefficients (R^2). The kinetic plots obtained by fitting the experimental data to the modified Freundlich model are presented in Figure 10d–f. The calculated k and R^2 values are provided in Table S2 in Supporting Information File 1. From the analysis of the kinetic plots and corresponding R^2 values obtained from both kinetic models, it can be concluded that degradation of RhB follows the modified Freundlich model more appropriately. The removal of RhB from its aqueous solution is controlled by adsorption of the dye molecules on the photocatalyst surface followed by their successive degradation as per the modified Freundlich model [56]. Therefore, the photocatalytic degradation reaction happens on the surface of the photocatalysts only. Also, the analysis of the degradation constants suggests that the CTCN heterojunction offers the best degradation of RhB under different light irradiation conditions, with sunlight showing the highest activity.

Furthermore, we have also studied the degradation of a non-photosensitizing colorless pollutant, BPA, against the CTCN heterojunction under natural sunlight irradiation. BPA is an industrially important compound used in the production of polycarbonates and other plastics. It comes under the class of endocrine disruptors and is known to mainly causes damage to the reproductive system and fertility in human beings [58]. The absorption peak at 275 nm was monitored as presented in the degradation plot of BPA shown in Figure 11. After 120 min of irradiation under sunlight ≈47% degradation of BPA could be observed using the CTCN heterojunction as catalyst, while the control experiments performed without any catalyst showed no degradation. Thus, it can be concluded that the as-prepared heterojunction photocatalyst has favorable solar light harvesting capability and can be utilized for the degradation of various water pollutants. We have also quantified the adsorption of both RhB and BPA over different prepared photocatalysts. The adsorption percentage of both the pollutants was very low, which infers that the photocatalytic action is solely due to the degradation of adsorbed molecules (Figure S7, Supporting Information File 1). From Figure S7a, it can be seen that the difference in the absorbance of pure RhB solution and after attaining adsorption–desorption equilibrium is much less, which corresponds to about 6% adsorption of dye molecules on the surface of the CTCN heterojunction, while for BPA, only 7% adsorption was observed over the CTCN heterojunction, as depicted in Figure S7b, Supporting Information File 1.

Photocatalyst reusability studies

It is of immense importance to explore the photostability and recyclability of the photocatalyst materials as it could appreciably reduce the costs of the photocatalytic process and reveals the most promising photocatalysis candidates. Hence, we carried out three successive cycles of photodegradation of RhB in order to comment on the reusability of the CTCN heterojunction as an efficient photocatalyst. The results obtained are presented in Figure 12a. Analysis of the recyclability results shows only an indiscernible decrease (≈7%) in the photocatalytic performance of the CTCN heterojunction, even after three successive cycles under natural sunlight illumination, which could be due to the unavoidable catalyst loss in the recycling process. Powder XRD spectra of the as-prepared and recycled CTCN heterojunction are also presented in Figure 12b. It can be seen from the PXRD pattern that there is no apparent change in the structure of the catalyst following the three successive cycles of photocatalytic degradation. Thus, the recycling results reflect the commendable stability of the CTCN heterojunction and support its potential for environmental remediation applications.

Mechanism of photocatalytic activity

The attainment of high efficiency of charge separation during a photocatalytic reaction plays an important role in the signifi-

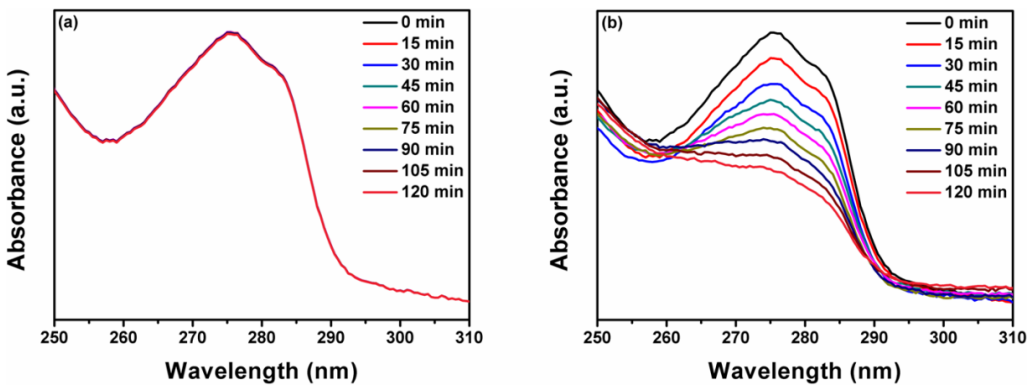

Figure 11: Time-dependent absorption spectra of BPA degradation under sunlight irradiation (a) pure BPA (without catalyst) and (b) using CTCN heterojunction.

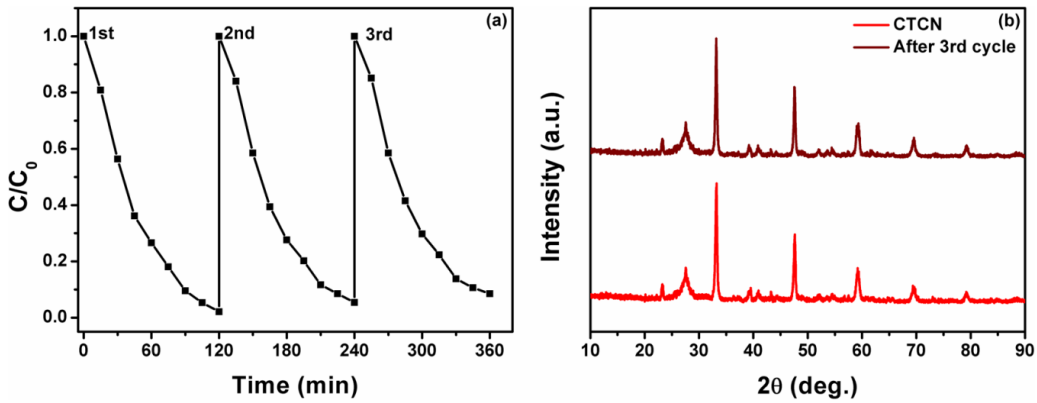

Figure 12: (a) Photocatalyst reusability up to three cycles and (b) powder XRD pattern of a CTCN heterojunction before and after the third cycle.

cant enhancement of the photocatalytic activity of heterojunction photocatalysts. However, the separation of photoinduced charge carriers totally relies on the appropriate band edge positions of the two constituent materials of the heterojunction photocatalyst, which are responsible for the separation and migration of photogenerated charges. The appropriate band positions of the semiconductor materials produce space charge accumulation/depletion at the interfaces, which helps in the effective separation of photogenerated charge carriers [59]. In this regard, the valence band (VB) and conduction band (CB) edge potentials of g-C_3N_4 and CT can be calculated by using following equations [36,54]:

$$E_{VB} = c - E_e + 0.5E_g$$

$$E_{CB} = E_{VB} - E_g,$$

where E_{VB} *and* E_{CB} are the VB and CB edge potentials and E_g is the bandgap of the semiconductor materials. The band gap values for g-C_3N_4 and CT are 2.75 eV and 3.45 eV respectively, obtained from DRS measurements. χ is the Sanderson electronegativity with values 4.64 eV and 5.40 eV for g-C_3N_4 and CT, respectively [34,36]. E_e is the energy of free electrons on the hydrogen scale (4.5 eV vs NHE). Based on this information, the calculated E_{CB} values for g-C_3N_4 and CT are −1.23 eV and −0.83 eV vs NHE, respectively, and E_{VB} values are 1.52 eV and 2.62 eV vs NHE, respectively. The appropriate band gap positions and close interfacial contact between g-C_3N_4 nanosheets and CT nanoflakes inhibit the fast recombination of electron–hole pairs, resulting in an enhanced photocatalytic activity for the degradation of the pollutant (RhB and BPA in this case). Based on these facts, a reasonable mechanism for the enhanced photocatalytic activity of the CTCN heterojunction under sunlight irradiation has been proposed as schematically presented in Figure 13, which involves the promotion of the charge transfer efficiency at the g-C_3N_4-CT interface.

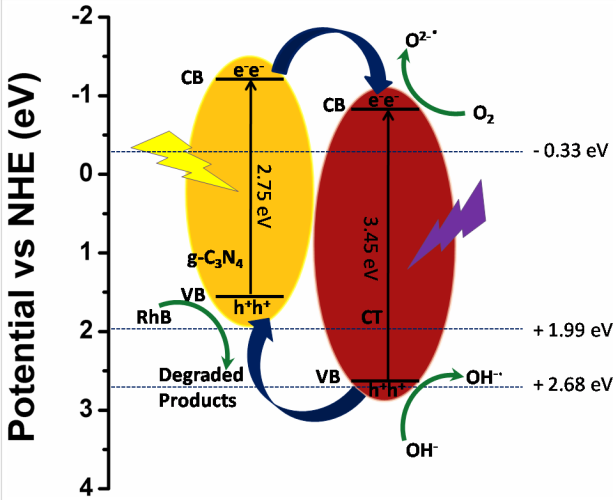

Figure 13: Plausible mechanism of degradation of pollutants under sunlight irradiation using the CTCN heterojunction photocatalyst.

In the case of the bare photocatalysts, CT (being UV light active, 3.45 eV) can undergo excitation under sunlight irradiation to generate electrons and holes. Also, g-C_3N_4 (2.75 eV) absorbs in the sunlight to induce photogenerated electron–hole pairs. Unfortunately, due to the fast recombination of photogenerated charges, a small fraction of them implicated in the photocatalytic degradation process which leads to the relatively low activity of the g-C_3N_4. In addition, CT could not be excited under visible light irradiation because of its wide band gap and it exhibits a weaker photocatalytic activity. When CT is coupled with g-C_3N_4, the formation of an effective heterojunction (CTCN) takes place, which facilitates the transfer of photogenerated electrons from the CB of g-C_3N_4 to that of CT through the intimate interface as governed by their band edge positions and hinders the charge recombination. This electron transfer is thermodynamically highly favored as charge flows from higher negative potential value to the lower negative potential values [34,60]. Thus, the formation of $O_2^{-\bullet}$ radicals is facilitated here

as the reduction potential of O_2/O_2^- (−0.33 eV vs NHE) is less negative in comparison with the CB edge potential of CT (−0.83 eV). Therefore, the transferred electrons react with O_2 to reduce it into $O_2^{-\bullet}$ radical anions. In comparison to the standard redox potentials of $^\bullet OH/H_2O$ (2.68 eV vs NHE) and $^\bullet OH/OH^-$ (1.99 eV vs NHE), the h^+ species left on the VB of g-C_3N_4 cannot react with OH^- or H_2O to produce $^\bullet OH$ radicals due to the more negative VB potential of g-C_3N_4 (1.52 eV vs NHE). However, the h^+ on the VB of CT (2.62 eV) can react with the OH^- ions to generate $^\bullet OH$ radicals due to more positive potential as compared to $OH^-/^\bullet OH$ (1.99 eV vs NHE) but cannot react with H_2O directly according to the band potential values ($^\bullet OH/H_2O$ = 2.68 eV vs NHE) [54]. Also the migration of h^+ from the VB of CT to the VB of g-C_3N_4 is also possible as holes can migrate upwards [61,62]. Therefore, it can be concluded that $O_2^{-\bullet}$, h^+ and $^\bullet OH$ species participate in the photodegradation of the pollutant. The entire photocatalytic reaction mechanism under sunlight irradiation can be summarized as follows:

$$\text{CTCN} + h\nu(\text{sunlight}) \rightarrow \text{CTCN}\left(h^+\text{VB} + e^-\text{CB}\right)$$

$$\text{g-}C_3N_4\left(e^-\text{CB}\right) \rightarrow CaTiO_3\left(e^-\text{CB}\right)$$

$$CaTiO_3\left(h^+\text{VB}\right) \rightarrow \text{g-}C_3N_4\left(h^+\text{VB}\right)$$

$$CaTiO_3\left(e^-\text{CB}\right) + O_2 \rightarrow O_2^{-\bullet}$$

$$HO^- + CaTiO_3(h^+\text{VB}) \rightarrow {}^\bullet OH$$

$$O_2^{-\bullet} + h^+ + {}^\bullet OH + \text{pollutants} \rightarrow \text{degradation products}$$

To validate the proposed mechanism and to gain insight into the role played by active species, radical trapping experiments were performed for RhB degradation under natural sunlight illumination using the CTCN heterojunction as the photocatalyst. In this study, benzoquinone (BQ), isopropanol (IPA) and triethanolamine (TEA) were used as scavengers for superoxide radicals ($O_2^{-\bullet}$), hydroxyl radicals ($^\bullet OH$) and photoexcited holes (h^+), respectively, and the corresponding results are depicted in Figure 14 [54]. It can be seen from the Figure 14 that the photodegradation of RhB solution was drastically quenched in the presence of BQ showing the dominance of $O_2^{-\bullet}$ radical anions in the degradation process. Also, a significant decrease in degradation percentage is also observed in the presence of TEA pointing towards the active role of h^+ species in the degradation of RhB. However, $^\bullet OH$ radicals do not contribute much as the addition of IPA and had only a small effect on the degradation process of RhB. Thus, the trapping experiment results also confirm that $O_2^{-\bullet}$ and h^+ were the dominant reactive species and the involvement of $^\bullet OH$ was less important in the decomposition of RhB.

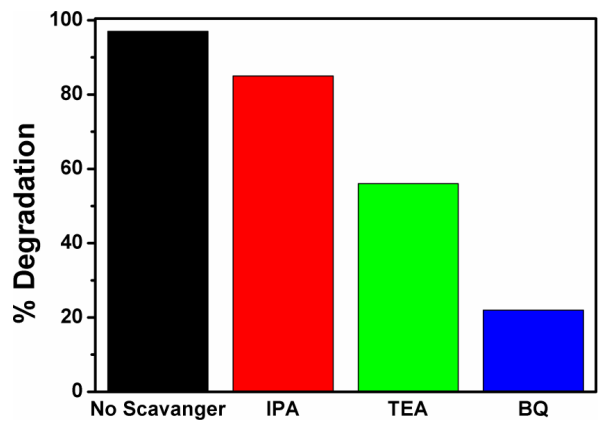

Figure 14: Effect of scavengers on the photocatalytic degradation of RhB using the CTCN heterojunction photocatalyst under natural sunlight illumination.

The above proposed mechanism holds true for UV light irradiation as well, as per our experimental observations, because g-C_3N_4 also shows significant degradation of RhB under UV light irradiation, which cannot be attributed to the dye photosensitization alone. High energy UV radiation can also cause excitation of electrons from the VB of g-C_3N_4 to its CB. However, this mechanism may not be applicable for visible light irradiation, as CT does not absorb at all in the visible region and excitation of electrons from the VB of CT to the CB is not possible. The role of each of the semiconductor material (CT and g-C_3N_4) in the heterojunction is clearly elucidated by these experiments.

Conclusion

In conclusion, a promising CTCN heterojunction photocatalyst with intimate interfacial contact was successfully prepared by a facile low temperature mixing of g-C_3N_4 nanosheets and CT nanoflakes in a 1:1 ratio. The photocatalytic activity of the CTCN heterojunction photocatalyst was investigated by studying the degradation of an aqueous solution of RhB under UV, visible and sunlight irradiation conditions. The prepared CTCN heterojunction exhibited the highest photocatalytic activity in comparison to the bare g-C_3N_4 and CT samples. The prepared CTCN heterojunction has also been proven effective to degrade a non-photosensitizing, colorless pollutant, bisphenol A, under sunlight irradiation. The enhanced photocatalytic performance could be attributed to the appropriate band positions, close interfacial contact between g-C_3N_4 nanosheets and CT nanoflakes, excellent heterojunction formation and high specific surface area, which provides larger surface active sites for the reaction and facilitates the transfer of photogenerated charges across the heterojunction by inhibiting their fast recombination. Superoxide radicals ($O_2^{-\bullet}$) were found to contribute as the main active species in trapping experiments for the decomposition of

RhB under sunlight irradiation. A plausible mechanism for the enhanced photocatalytic activity of the CTCN heterojunction photocatalyst has been proposed based on our experimental results and theoretically calculated band potential values. Therefore, in our understanding, this study can provide insights into the design, development and mechanistic study of two-dimensional heterojunction photocatalysts with enhanced photocatalytic activity.

Supporting Information

Supporting Information File 1

Additional experimental results.
EDAX spectra of g-C_3N_4, CT and CTCN heterojunction (Figure S1). Elemental mapping of g-C_3N_4, CT and CTCN composite (Figure S2–S4). Time-dependent absorption spectra of RhB degradation under different light irradiation conditions for control samples and pure RhB (Figure S5). C/C_0 vs time plots for the photocatalytic degradation of RhB under UV, visible and sunlight irradiation (Figure S6). Summary of the kinetic data of photocatalytic degradation of RhB (Table S1 and S2). Absorption curves for the calculation of adsorption percentage of RhB and BPA (Figure S7).
[https://www.beilstein-journals.org/bjnano/content/supplementary/2190-4286-9-62-S1.pdf]

Acknowledgements

We thank the Advanced Materials Research Center (AMRC), IIT Mandi for the laboratory and characterization facilities. Venkata Krishnan acknowledges financial support from the Department of Science and Technology (DST), India under Young Scientist Scheme (YSS/2014/000456). Suneel Kumar is thankful to UGC, India for his senior research fellowship. Ajay Kumar acknowledges a scholarship from MHRD, India.

ORCID® iDs

Ashish Kumar - https://orcid.org/0000-0003-3527-4952
Christian Schuerings - https://orcid.org/0000-0002-2325-7963
Suneel Kumar - https://orcid.org/0000-0002-5259-1792
Venkata Krishnan - https://orcid.org/0000-0002-4453-0914

References

1. Cao, S.; Low, J.; Yu, J.; Jaroniec, M. *Adv. Mater.* **2015,** *27,* 2150–2176. doi:10.1002/adma.201500033
2. Ong, W.-J.; Tan, L.-L.; Ng, Y. H.; Yong, S.-T.; Chai, S.-P. *Chem. Rev.* **2016,** *116,* 7159–7329. doi:10.1021/acs.chemrev.6b00075
3. Zhang, G.; Li, G.; Lan, Z.-A.; Lin, L.; Savateev, A.; Heil, T.; Zafeiratos, S.; Wang, X.; Antonietti, M. *Angew. Chem., Int. Ed.* **2017,** *56,* 13445–13449. doi:10.1002/anie.201706870
4. Kumar, S.; Kumar, A.; Bahuguna, A.; Sharma, V.; Krishnan, V. *Beilstein J. Nanotechnol.* **2017,** *8,* 1571–1600. doi:10.3762/bjnano.8.159
5. Zhao, Z.; Sun, Y.; Dong, F. *Nanoscale* **2015,** *7,* 15–37. doi:10.1039/C4NR03008G
6. Zhang, G.; Lan, Z.-A.; Lin, L.; Lin, S.; Wang, X. *Chem. Sci.* **2016,** *7,* 3062–3066. doi:10.1039/C5SC04572J
7. Xu, Q.; Cheng, B.; Yu, J.; Liu, G. *Carbon* **2017,** *118,* 241–249. doi:10.1016/j.carbon.2017.03.052
8. Sun, Z.; Kim, J. H.; Zhao, Y.; Bijarbooneh, F.; Malgras, V.; Lee, Y.; Kang, Y.-M.; Dou, S. X. *J. Am. Chem. Soc.* **2011,** *133,* 19314–19317.
9. Cao, S.; Yu, J. *J. Phys. Chem. Lett.* **2014,** *5,* 2101–2107. doi:10.1021/jz500546b
10. Jiang, D.; Wang, T.; Xu, Q.; Li, D.; Meng, S.; Chen, M. *Appl. Catal., B: Environ.* **2017,** *201,* 617–628. doi:10.1016/j.apcatb.2016.09.001
11. Ong, W.-J. *Front. Mater.* **2017,** *4,* 11. doi:10.3389/fmats.2017.00011
12. Hou, Y.; Laursen, A. B.; Zhang, J.; Zhang, G.; Zhu, Y.; Wang, X.; Dahl, S.; Chorkendorff, I. *Angew. Chem., Int. Ed.* **2013,** *52,* 3621–3625. doi:10.1002/anie.201210294
13. Cheng, H.; Hou, J.; Takeda, O.; Guo, X.-M.; Zhu, H. *J. Mater. Chem. A* **2015,** *3,* 11006–11013. doi:10.1039/C5TA01864A
14. Zhang, Z.; Huang, J.; Zhang, M.; Yuan, Q.; Dong, B. *Appl. Catal., B: Environ.* **2015,** *163,* 298–305. doi:10.1016/j.apcatb.2014.08.013
15. Xiang, Q.; Yu, J. *J. Phys. Chem. Lett.* **2013,** *4,* 753–759. doi:10.1021/jz302048d
16. Niu, P.; Zhang, L.; Liu, G.; Cheng, H.-M. *Adv. Funct. Mater.* **2012,** *22,* 4763–4770. doi:10.1002/adfm.201200922
17. Zhang, Y.; Liu, J.; Wu, G.; Chen, W. *Nanoscale* **2012,** *4,* 5300–5303. doi:10.1039/C2NR30948C
18. Zhang, G.; Lan, Z.-A.; Wang, X. *Chem. Sci.* **2017,** *8,* 5261–5274. doi:10.1039/C7SC01747B
19. Cheng, F.; Yin, H.; Xiang, Q. *Appl. Surf. Sci.* **2017,** *391,* 432–439. doi:10.1016/j.apsusc.2016.06.169
20. Barman, S.; Sadhukhan, M. *J. Mater. Chem.* **2012,** *22,* 21832–21837. doi:10.1039/C2JM35501A
21. Zheng, Y.; Liu, J.; Liang, J.; Jaroniec, M.; Qiao, S. Z. *Energy Environ. Sci.* **2012,** *5,* 6717–6731. doi:10.1039/C2EE03479D
22. Wang, H.; Yuan, X.; Wu, Y.; Zeng, G.; Chen, X.; Leng, L.; Li, H. *Appl. Catal., B: Environ.* **2015,** *174–175,* 445–454. doi:10.1016/j.apcatb.2015.03.037
23. Tong, Z.; Yang, D.; Shi, J.; Nan, Y.; Sun, Y.; Jiang, Z. *ACS Appl. Mater. Interfaces* **2015,** *7,* 25693–25701. doi:10.1021/acsami.5b09503
24. Guo, S.; Deng, Z.; Li, M.; Jiang, B.; Tian, C.; Pan, Q.; Fu, H. *Angew. Chem., Int. Ed.* **2016,** *55,* 1830–1834. doi:10.1002/anie.201508505
25. Shi, L.; Liang, L.; Wang, F.; Liu, M.; Zhong, S.; Sun, J. *Catal. Commun.* **2015,** *59,* 131–135. doi:10.1016/j.catcom.2014.10.014
26. Lin, Q.; Li, L.; Liang, S.; Liu, M.; Bi, J.; Wu, L. *Appl. Catal., B: Environ.* **2015,** *163,* 135–142. doi:10.1016/j.apcatb.2014.07.053
27. Li, Q.; Zhang, N.; Yang, Y.; Wang, G.; Ng, D. H. L. *Langmuir* **2014,** *30,* 8965–8972. doi:10.1021/la502033t
28. Jiang, Z.; Jiang, D.; Yan, Z.; Liu, D.; Qian, K.; Xie, J. *Appl. Catal., B: Environ.* **2015,** *170–171,* 195–205. doi:10.1016/j.apcatb.2015.01.041
29. Savateev, A.; Pronkin, S.; Epping, J. D.; Willinger, M. G.; Wolff, C.; Neher, D.; Antonietti, M.; Dontsova, D. *ChemCatChem* **2017,** *9,* 167–174. doi:10.1002/cctc.201601165

30. Xian, T.; Yang, H.; Di, L. J.; Dai, J. F. *J. Alloys Compd.* **2015,** *622,* 1098–1104. doi:10.1016/j.jallcom.2014.11.051
31. Jo, W.-K.; Natarajan, T. S. *Chem. Eng. J.* **2015,** *281,* 549–565. doi:10.1016/j.cej.2015.06.120
32. Reddy, J. R.; Kurra, S.; Guje, R.; Palla, S.; Veldurthi, N. K.; Ravi, G.; Vithal, M. *Ceram. Int.* **2015,** *41,* 2869–2875. doi:10.1016/j.ceramint.2014.10.109
33. Subramanian, V.; Roeder, R. K.; Wolf, E. E. *Ind. Eng. Chem. Res.* **2006,** *45,* 2187–2193. doi:10.1021/ie050693y
34. Leong, K. H.; Tan, Z. Z.; Sim, L. C.; Saravanan, P.; Bahnemann, D.; Jang, M. *ChemistrySelect* **2017,** *2,* 84–89.
35. Zhang, H.; Chen, G.; Li, Y.; Teng, Y. *Int. J. Hydrogen Energy* **2010,** *35,* 2713–2716. doi:10.1016/j.ijhydene.2009.04.050
36. Kumar, A.; Kumar, S.; Bahuguna, A.; Kumar, A.; Sharma, V.; Krishnan, V. *Mater. Chem. Front.* **2017,** *1,* 2391–2404. doi:10.1039/C7QM00362E
37. Wang, W.; Tadé, M. O.; Shao, Z. *Chem. Soc. Rev.* **2015,** *44,* 5371–5408. doi:10.1039/C5CS00113G
38. Xian, T.; Yang, H.; Huo, Y. S. *Phys. Scr.* **2014,** *89,* 115801. doi:10.1088/0031-8949/89/11/115801
39. Kumar, S.; Reddy, N. L.; Kumar, A.; Shankar, M. V.; Krishnan, V. *Int. J. Hydrogen Energy* **2017,** in press. doi:10.1016/j.ijhydene.2017.09.113
40. Cheng, Y.-Y.; Tsai, T.-H. *J. Agric. Food Chem.* **2017,** *65,* 1078–1085. doi:10.1021/acs.jafc.6b04975
41. Kumar, S.; Sharma, V.; Bhattacharyya, K.; Krishnan, V. *New J. Chem.* **2016,** *40,* 5185–5197. doi:10.1039/C5NJ03595C
42. Sharma, V.; Harith, G.; Kumar, S.; Sharma, R.; Reddy, K. L.; Bahuguna, A.; Krishnan, V. *Mater. Technol.* **2017,** *32,* 461–471. doi:10.1080/10667857.2016.1271861
43. Wang, Y.; Niu, C.-G.; Wang, L.; Wang, Y.; Zhang, X.-G.; Zeng, G.-M. *RSC Adv.* **2016,** *6,* 47873–47882. doi:10.1039/C6RA06435C
44. Liu, H.; Jin, Z.; Xu, Z.; Zhang, Z.; Ao, D. *RSC Adv.* **2015,** *5,* 97951–97961. doi:10.1039/C5RA17028A
45. Di, J.; Xia, J.; Yin, S.; Xu, H.; Xu, L.; Xu, Y.; He, M.; Li, H. *J. Mater. Chem. A* **2014,** *2,* 5340–5351. doi:10.1039/C3TA14617K
46. Fu, M.; Liao, J.; Dong, F.; Li, H.; Liu, H. *J. Nanomater.* **2014,** 2014.
47. Lee, S.-W.; Lozano-Sánchez, L. M.; Rodríguez-González, V. *J. Hazard. Mater.* **2013,** *263,* 20–27. doi:10.1016/j.jhazmat.2013.08.017
48. Lewis, C. S.; Liu, H.; Han, J.; Wang, L.; Yue, S.; Brennan, N. A.; Wong, S. S. *Nanoscale* **2016,** *8,* 2129–2142. doi:10.1039/C5NR06697B
49. Tian, Y.; Chang, B.; Lu, J.; Fu, J.; Xi, F.; Dong, X. *ACS Appl. Mater. Interfaces* **2013,** *5,* 7079–7085. doi:10.1021/am4013819
50. Liu, C.; Zhang, Y.; Dong, F.; Reshak, A. H.; Ye, L.; Pinna, N.; Zeng, C.; Zhang, T.; Huang, H. *Appl. Catal., B: Environ.* **2017,** *203,* 465–474. doi:10.1016/j.apcatb.2016.10.002
51. Bhirud, A.; Sathaye, S.; Waichal, R.; Park, C.-J.; Kale, B. *J. Mater. Chem. A* **2015,** *3,* 17050–17063. doi:10.1039/C5TA03955J
52. Liu, C.; Huang, H.; Du, X.; Zhang, T.; Tian, N.; Guo, Y.; Zhang, Y. *J. Phys. Chem. C* **2015,** *119,* 17156–17165. doi:10.1021/acs.jpcc.5b03707
53. Zhang, X.-S.; Hu, J.-Y.; Jiang, H. *Chem. Eng. J.* **2014,** *256,* 230–237. doi:10.1016/j.cej.2014.07.012
54. Kumar, S.; Sharma, V.; Bhattacharyya, K.; Krishnan, V. *Mater. Chem. Front.* **2017,** *1,* 1093–1106. doi:10.1039/C6QM00274A
55. Sharma, V.; Kumar, S.; Krishnan, V. *ChemistrySelect* **2016,** *1,* 2963–2970. doi:10.1002/slct.201600671
56. Uddin, M. J.; Islam, M. A.; Haque, S. A.; Hasan, S.; Amin, M. S. A.; Rahman, M. M. *Int. Nano Lett.* **2012,** *2,* 19. doi:10.1186/2228-5326-2-19
57. Gu, Z.; Thomas, A. C.; Xu, Z. P.; Campbell, J. H.; Lu, G. Q. *Chem. Mater.* **2008,** *20,* 3715–3722. doi:10.1021/cm703602t
58. Ohko, Y.; Ando, I.; Niwa, C.; Tatsuma, T.; Yamamura, T.; Nakashima, T.; Kubota, Y.; Fujishima, A. *Environ. Sci. Technol.* **2001,** *35,* 2365–2368. doi:10.1021/es001757t
59. Jiang, F.; Yan, T.; Chen, H.; Sun, A.; Xu, C.; Wang, X. *Appl. Surf. Sci.* **2014,** *295,* 164–172. doi:10.1016/j.apsusc.2014.01.022
60. Zang, Y.; Li, L.; Xu, Y.; Zuo, Y.; Li, G. *J. Mater. Chem. A* **2014,** *2,* 15774–15780. doi:10.1039/C4TA02082K
61. Min, Y.; He, G.; Xu, Q.; Chen, Y. *J. Mater. Chem. A* **2014,** *2,* 2578–2584. doi:10.1039/C3TA14240J
62. Wang, D.; Xu, Y.; Sun, F.; Zhang, Q.; Wang, P.; Wang, X. *Appl. Surf. Sci.* **2016,** *377,* 221–227. doi:10.1016/j.apsusc.2016.03.146

License and Terms

This is an Open Access article under the terms of the Creative Commons Attribution License (http://creativecommons.org/licenses/by/4.0), which permits unrestricted use, distribution, and reproduction in any medium, provided the original work is properly cited.

The license is subject to the *Beilstein Journal of Nanotechnology* terms and conditions: (https://www.beilstein-journals.org/bjnano)

The definitive version of this article is the electronic one which can be found at:
doi:10.3762/bjnano.9.62

BEILSTEIN JOURNAL OF NANOTECHNOLOGY

A review of carbon-based and non-carbon-based catalyst supports for the selective catalytic reduction of nitric oxide

Shahreen Binti Izwan Anthonysamy, Syahidah Binti Afandi, Mehrnoush Khavarian and Abdul Rahman Bin Mohamed*§

Review

Open Access

Address:
School of Chemical Engineering, Universiti Sains Malaysia, Engineering Campus, 14300 Nibong Tebal, Penang, Malaysia

Email:
Abdul Rahman Bin Mohamed* - chrahman@usm.my

* Corresponding author
§ Tel.: +604 599 6410; Fax: +604 599 6908

Keywords:
carbon-based catalyst support; Eley–Riedeal mechanism; Langmuir–Hinshelwood mechanism; nitric oxide; non-carbon-based catalyst support; selective catalytic reduction

Beilstein J. Nanotechnol. **2018,** *9,* 740–761.
doi:10.3762/bjnano.9.68

Received: 30 September 2017
Accepted: 18 January 2018
Published: 27 February 2018

This article is part of the Thematic Series "Energy conversion, storage and environmental remediation using nanomaterials".

Guest Editor: W.-J. Ong

© 2018 Anthonysamy et al.; licensee Beilstein-Institut.
License and terms: see end of document.

Abstract

Various types of carbon-based and non-carbon-based catalyst supports for nitric oxide (NO) removal through selective catalytic reduction (SCR) with ammonia are examined in this review. A number of carbon-based materials, such as carbon nanotubes (CNTs), activated carbon (AC), and graphene (GR) and non-carbon-based materials, such as Zeolite Socony Mobil–5 (ZSM-5), TiO_2, and Al_2O_3 supported materials, were identified as the most up-to-date and recently used catalysts for the removal of NO gas. The main focus of this review is the study of catalyst preparation methods, as this is highly correlated to the behaviour of NO removal. The general mechanisms involved in the system, the Langmuir–Hinshelwood or Eley–Riedeal mechanism, are also discussed. Characterisation analysis affecting the surface and chemical structure of the catalyst is also detailed in this work. Finally, a few major conclusions are drawn and future directions for work on the advancement of the SCR-NH_3 catalyst are suggested.

Review

Introduction

Nowadays, air pollution has become a major environmental problem, which affects the natural characteristics of the atmosphere (gaseous constituents, water vapour that determines humidity and ozone layer) and adversely impacts the environment and human health. Nitrogen oxides (NO_x, $x = 1, 2$) are irritant gases that cause problems such as photochemical smog, formation of fine particles (PM), acid rain, ozone depletion, and the release of greenhouse gases to the environment [1]. NO is considered to be the most difficult gas to remove from the atmosphere because it behaves like a supercritical fluid at room temperature. On the other hand, NO_2 can easily be removed because of its propensity to dissolve in water. Thus, the difficulty in NO elimination is the main challenge in NO_x gas removal. In fact, NO is the main pollutant, representing about

90% of total NO_x [2]. The main source of NO_x emissions is dominated by stationary sources, which originate from industrial processes, energy production and distribution, transportation, and agriculture. In large cities where motor vehicle traffic is high, a huge amount of NO_x is released into the environment. This phenomenon can significantly cause detriment to public health. To overcome this problem, maximum standards for NO_x emissions have been reinforced in the transportation sector. These guidelines and regulations must be adhered to and numerous efforts taken in order to reduce NO_x emissions in the atmosphere. However, more beneficial and economic ways to remove NO are still lacking and are yet to be practically evaluated.

In recent years, many abatement technologies including dry and wet techniques have been utilised in industrial boilers and power plants to control NO_x emissions. Post-combustion such as selective catalytic reduction (SCR), non-selective catalytic reduction (NSCR), adsorption, corona discharge, electrochemical cell, radiation, and the wet system are examples of the dry technique while the scrubber is an example of the wet technique [3]. Of these technologies, due to its effectiveness, low cost, and high selectivity, the SCR of NO has emerged as the most promising method and has been widely applied over several decades to meet the stringent regulation of NO emissions from stationary sources [4]. Meanwhile, the three-way catalyst with carbon monoxide (CO) and hydrocarbon is also used in mobile sources to remove NO from gasoline, but this technology is limited to diesel and lean-burn gasoline engines. In the SCR of NO, a reducing agent must be introduced into the system in order to successfully convert NO into nitrogen (N_2), inert gases such as ammonia (NH_3), and urea [5]. The reaction system reduces the Gibbs free energy values initiated by the reducing agent; the introduction of oxygen also contributes to this occurrence. According to results from the literature, NH_3 is the most practical reducing agent in the SCR of NO, as it results in high NO removal. The catalyst plays an important role in enhancing NO-SCR technology. The most widely used catalyst is V_2O_5–WO_3/TiO_2 due to its excellent catalytic activity and its high resistance to sulphur poisoning [6]. However, some problems are still evident with the use of this catalyst, e.g., the vanadium species is highly toxic to humans and the environment, and excessive dust pollution will usually result from the upstream flue gas, which can cause the deactivation of the catalyst. In addition, the catalyst also has a limited temperature window (300–400 °C) and poor thermal stability [7,8]. Hence, there is an urgent need to find other catalysts that can overcome these drawbacks and also have high resistance to water (H_2O) and oxidation of SO_2 to SO_3, so that high activity and selectivity, high thermal stability, and a temperature lower than 300 °C can be achieved, thus increasing the lifetime of the catalyst. Lower-temperature SCR is foremost in importance to ensure the complete removal of NO. This is because of the wide temperature window of 150–500 °C in a diesel engine as well as the low energy consumption and economy of NH_3-SCR [9].

In the literature, abundant catalysts at low temperature have been explored such as transitional metals (Mn, Cu, Ce, Fe, Co, Mo) [10-13], novel metals (Pt, Pd) [14], and metal ion-exchange zeolite catalysts [15]. The Mn-based catalyst is one of the most active metal oxide catalysts for high N_2 selectivity at low temperature and is recognised by many researchers as a potential alternative for the common catalyst. Jin et al. [16] successfully used a Mn-based catalyst with the addition of Ce to improve the activity and stability of SCR performance. It is well known that Ce is a good additive that can provide enough oxygen groups with the ability to release or store oxygen, thus improving the catalytic activity of SCR. In addition, over the last few years, the use of carbon-based catalysts have been widely studied due to their high surface area, porosity, ability to regenerate and be reused, and good support properties [17]. Several metal oxides were impregnated with carbon-based materials such as carbon nanotubes (CNTs), activated carbon (AC), activated carbon nanofibres (ACNFs), and graphene (GR). It is highly favourable to use these carbon-based materials as a catalyst support in the SCR system, as they can provide sites for active metals and protect the metals from sintering. However, they are also significantly affected by H_2O and SO_2 poisoning.

There are various methods for preparing a catalyst such as impregnation, sol–gel, incipient-wetness, co-precipitation, electroplating, and the polyol process. Some of the catalysts prepared via these methods can achieve low temperatures of SCR with content resistance of H_2O and SO_2. Each method is different from the other, and thus each affects the structure and physical and chemical properties of the catalyst. In fact, choosing the best method for catalyst preparation is crucial in order to increase the interaction between the metal and support, and to obtain a desirable catalyst particle size. Lázaro et al. [17] summarised the carbon-based catalysts for SCR at low temperature and compared it with commercial catalysts. A good example can be seen in Chuang et al. [18], where a comparative study was made between the preparation of AC-supported Cu catalysts through impregnation, the polyol process, and microwave-heated polyol process using $Cu(NO_3)\cdot 3H_2O$ as the copper precursor.

To date, many researchers have reviewed the SCR of NO at low temperature. Li et al. [9] reviewed low-temperature SCR on metal oxide and zeolite catalysts with a focus on catalyst performance and taking into account other possible mechanisms.

Meanwhile, Mrad et al. [5] reviewed and summarised the use of a hydrocarbon catalyst in the SCR of NO. However, not much effort has been made to summarise the progress of catalyst synthesis methods to achieve catalytic activity at low-temperature SCR. Therefore, this paper addresses this gap by reviewing the development of catalyst preparation methods.

In this paper, the current progress in research on low-temperature SCR of NO over metal and bi-metallic oxides with carbon-based catalysts is reviewed. Furthermore, this review provides a comprehensive focus on the methods of catalyst preparation that can provide high activity, high stability, and convey good resistance towards H_2O and SO_2. The reaction mechanism for NO removal is also discussed. Finally, major conclusions and future directions for research on the SCR of NO are presented.

Mechanism of NO removal

The adsorption behaviour of gas on the catalyst surface is known to be an important factor for understanding the chemical nature of SCR. In NH_3-SCR, NO is targeted and reduced to N_2, which can then be safely released into the surroundings. The typical mechanism for the SCR-NH_3 of NO, which involves O_2, is outlined in Equation 1 [19].

$$4NO + O_2 + 4NH_3 = 4N_2 + 6H_2O \quad (1)$$

In the absence of O_2, the reaction mechanism follows Equation 2.

$$6NO + 4NH_3 = 5N_2 + 6H_2O \quad (2)$$

Equation 1 is recommended as the standard reaction for NH_3-SCR of NO, as more than 90% of NO is present among the NO_x species and thus controlling the reaction stoichiometry. In the standard SCR mechanism of Equation 1, one molecule of NH_3 is required to reduce one molecule of NO with the excess O_2.

However, fast SCR may also occur in the presence of O_2 with NO and NO_2 over active components. In the presence of O_2, NO_2 can be formed when NO is being oxidised by active oxygen. The general reactions are described by Equation 3 and Equation 4 [20].

$$2NO_2 + O_2 + 4NH_3 = 3N_2 + 6H_2O \quad (3)$$

$$2NO_2 + 2NO + 4NH_3 = 4N_2 + 6H_2O \quad (4)$$

Fast SCR and standard SCR can be distinguished according to the formation of NO_2. In fast SCR, nitrous acid (HNO_2) and nitric acid (HNO_3) are formed from the dimerisation of NO_2 [2]. Then, an ammonium nitrate (H_4NNO_3) intermediate is formed when NH_3 reacts with HNO_3 and subsequently decomposes to N_2O and H_2O by NO at higher temperature [20].

It is noted that NO_2 is highly crucial in the fast SCR reaction, as NO_2 is a more powerful oxidising agent compared to O_2. Thus, the reaction between NO and HNO_3 is significant in determining the rate-limiting step of fast SCR. According to Nova et al. [20], a ratio of NO/NH_3 approaching 1 is good for increasing the reaction rate, whereby the formation of NO_2 will be inhibited when the NH_3 concentration is increased, which restrains the formation of HNO_3. Indeed, Nova et al. [20] also addressed the mechanism of fast SCR reaction over V_2O_5–WO_3/TiO_2 catalysts. They concluded that NO_2 is vital for attaining faster reoxidation of the vanadium sites.

There are two surface reactions that are usually involved in the NO removal system: the Langmuir–Hinshelwood and Eley–Rideal mechanisms [9]. It is believed that NH_3 is first adsorbed by both Lewis acid sites and Brønsted acid sites followed by NO and O_2.

Langmuir–Hinshelwood mechanism

The Langmuir–Hinshelwood mechanism occurs when two molecules of NO and NH_3 are adsorbed to the catalyst surface and then bonded together to form N_2 and H_2O. Liu et al. [21] examined the Langmuir–Hinshelwood mechanism over a MnO_x-CeO_2 catalyst reaction. The adsorbed NH_3 on the Lewis acid sites formed activated NH_3, which is a NH_2^- species, in the oxidation dehydrogenation process. The NO that was oxidised to NO_2 on the catalyst surface reacted with NH_2^- to produce intermediate nitrosamine (NH_2NO). The proposed Langmuir–Hinshelwood reaction scheme is outlined by Equation 5–9.

$$NO(g) \rightarrow NO(ad) \quad (5)$$

$$NH_3(g) \rightarrow NH_3(ad) \quad (6)$$

$$NH_3^-{*} + O^-{*} \rightarrow NH_2^-{*} + OH^-{*} \quad (7)$$

$$NO + 1/2\,O_2 \rightarrow NO_2^-{*} \quad (8)$$

$$NH_2^-{*} + NO \rightarrow NH_2NO^-{*} \rightarrow N_2 + H_2O + {*} \quad (9)$$

where $*$ represents the Lewis acid sites on the catalyst surface.

Firstly, gaseous NO and NH_3 are adsorbed on the catalyst surface, as per Equation 5 and Equation 6. As the reaction starts with NH_3, NH_3 will be adsorbed on the Lewis acid sites and Brønsted acid sites and then oxidised into coordinated NH_3 species and ionic NH_4^+, while NO is oxidised into NO_2 via

Equation 7 and Equation 8, respectively. The manganese and ceria cations used in this reaction contribute to the large amount of Lewis acid sites. It is noted that the NH_4^+ formed on the Brønsted acid sites are not necessary in the SCR reaction at low temperature. Furthermore, the oxidised NO reacts with adjacent activated NH_3 species to form intermediate NH_2NO^-. After that, it will decompose into N_2 and H_2O, as per Equation 9.

Eley–Rideal mechanism

The Eley–Rideal mechanism suggests that only one molecule will adsorb on the catalyst surface and the second molecule will react with it directly from the gas phase (van der Waals force) to form a new product. Liu et al. [22] found that the Fe_2O_3 catalyst forms amide species (NH_2^-) in the presence of NH_3 on the Lewis acid sites and reacted directly with gaseous NO to form N_2 and H_2O, as per Equation 10–12, respectively:

$$NH_3(g) \rightarrow NH_3(ad) \quad (10)$$

$$NH_3 + * \rightarrow NH_2^-* + H \quad (11)$$

$$NH_2^-* + NO \rightarrow N_2 + H_2O \quad (12)$$

In addition, Cha et al. [19] also proposed the Eley–Rideal mechanism involving CeO_2. The higher quantity of Ce^{3+} ions over the Ce^{4+} ions facilitated the oxidation of NH_3 to N_2 and H_2O for NO reduction in the SCR reaction. High Ce^{3+} ion concentration contributed to the high amount of chemisorbed oxygen, which increased the redox cycle and enhanced the reducibility of hydrogen. This is because the Ce^{3+} ions will assist the migration of O_2 from gas phase to the surface of the catalyst [8,23]. Afterwards, Wei et al. [24] explained that NO_x removal using FeCu/zeolite catalyst followed both Eley–Rideal and Langmuir–Hinshelwood mechanisms. First, NO_x directly reacted with oxidised NH_3 to express the Eley–Rideal mechanism, and the NO species reacted with NH_3 species adsorbed to the Fe^{2+} and Cu^{2+} ions, following the Langmuir–Hinshelwood mechanism. Shi et al. [25] used DRIFT to investigate the chemical reaction of reactants with the Lewis acid site and Brønsted acid site to improve activity at low temperature. Chen et al. [26] found that CeO_2 provided both acid sites, while WO_3 helped in increasing the Brønsted acid sites in the CeO_2-WO_3 mixed oxide catalyst.

Generally, chemical reactions that occurr in the NO adsorption system involve a redox reaction on the surface of the catalyst and adsorption of NO, NH_3, and O_2. The rate of a chemical reaction normally depends on the catalyst, which speeds up the reaction with less energy being required. Thus, the addition of a support for the catalyst will only increase the rate of reaction for NO removal. A redox reaction is a chemical reaction that involves the simultaneous occurrence of the oxidation and reduction process. This reaction occurs during the preparation of the catalyst between the active components and selected support. According to Liu et al. [27], the electronic inductive interaction between Fe^{3+} (metal) and Ti^{4+} (support) species will increase the oxidation ability of Fe^{3+} to Fe^{2+} species, which will then lead to the enhancement of surface active sites to readily react with NO. The synergetic effect of the metal cations present is important to increase the catalytic activity in the SCR of NO.

Catalyst preparation

The success of nitric oxide removal in a SCR reaction depends entirely on catalyst stability and activity [28]. The synthesis method is one of the key factors that contribute towards an even distribution of the active component and good particle properties [29]. Different preparation methods have been carried out by modifying the current SCR catalyst to achieve high NO selectivity in the NH_3-SCR system. Impregnation is one of the most commonly used techniques due to its simplicity [30]. This method starts with the inclusion of metals (Zn, Cu, Ni, Co, Fe or Mn) into the catalyst support material. A metal solution precursor is commonly added together with the support material. After mixing, the surface material is allowed to fully submerge with the selection of metals through continuous mixing. Sonication or stirring methods are applied to assure the upmost dispersion of metal in the solution precursor [31]. In the end, the precursor supported material is dried followed by consecutive heat treatment with inert gas in order to further enhance and stabilise the metal catalyst [32]. Owing to its ease of metal loading control as well as high utilisation of the active component with less metal precursor dosage, the impregnation method is profoundly known as one of the well established procedures for SCR catalyst preparation [32,33]. Jeong et al. [34] applied the impregnation technique to study the characteristics of graphene-supported tungsten (WO_3) catalyst in a selective catalytic reduction system. The transmission electron microscopy energy-dispersive X-ray spectroscopy (TEM-EDS) measurements in their study showed that the WO_3 particles were very well distributed over GR and the catalyst surface. The use of a precursor solution (ammonium metatungstate) further enhanced the dispersion of GR, resulting in high catalyst dispersion. Thus, huge amounts of NO could be successfully removed via the catalytic reaction. Qi et al. [35] used the impregnation method to prepare Ce-modified Mn-based catalysts with the aim of studying the effect of a different calcination atmosphere (N_2, air and O_2) on the performance of SCR-NH_3 of NO. Both Ce and Mn particles were well distributed onto the catalyst surface. Nam et al. [36] proposed an impregnation method to investigate the promotional effects of tungsten-modified Mn/Ce/Ti catalysts for a low-temperature SCR reaction. It was found that

introduction of W metal into the catalyst helped promote the conversion of NO to gaseous NO_2, thereby promoting a "fast SCR" reaction to improve low-temperature SCR activity.

The sol–gel method has been used quite frequently for the development of nano-based catalysts. Basically, certain chemical solutions together with a foaming agent (citric acid) is mixed vigorously by stirring under room temperature to produce a homogeneous mixture. Subsequently, the produced sols are dried at a specific temperature for 24 hours in order to obtain xerogel. Then, the xerogel is crushed before being calcined at a desired atmosphere condition and temperature [37]. In the case of catalyst preparation, many researchers have adopted the sol–gel method because: (i) it can form a more even distribution of metal component onto the support material, (ii) it can alter the catalyst porous structure using various foaming agents, (iii) it is able to synthesise the metal-supported catalyst in a single-step process, leading to a unique metal oxide interaction and oxide–oxide interactions that are unreachable otherwise [38]. Xiong et al. [39] prepared magnetic iron–cerium–tungsten mixed oxide pellets using a citric acid sol–gel process assisted by microwave irradiation for the SCR-NH_3 of NO. They found that the dispersion of both cerium oxide and tungsten oxide onto iron the oxide was improved. In addition, the surface absorbtion capacity of oxygen concentration was enhanced, thus increasing selective catalytic reduction activity. Yao et al. [40] investigated certain physiochemical properties and found that SCR-NH_3 catalytic performance is influenced by the function of support materials. In their study, SiO_2 was synthesised using the sol–gel method. Zeng et al. [41] implemented the sol–gel technique to prepare CuO–TiO_2 catalysts for the selective catalytic oxidation of NO. Based on the results, the CuO–TiO_2 catalysts demonstrated higher catalytic activity than the $Cu_{0.07}$/Ti catalyst prepared using the impregnation method. The CuO–TiO_2 catalyst possessed more highly dispersed CuO species as well as many oxygen vacancy active sites, which enhanced the NO gas and made it easily attachable during the catalytic reaction. Similar to previous work, Zhu et al. [42] applied the sol-gel method to study the effect of a particular synthesis method on the catalytic activities of CoO_x–TiO_2 at low-temperature SCR-NH_3. In comparison, the CoO_x–TiO_2 catalyst was also prepared using the impregnation approach. They found that the Co–TiO_2 catalyst prepared using the sol–gel method had better catalytic activity than that of the impregnation method. Besides that, a huge amount of oxygen vacancies and superoxide ions was observed when cobalt metal was introduced via the sol–gel method, thereby enhancing the SCR performance.

On the other hand, the co-precipitation method has also been applied in the preparation of the SCR catalyst. This technique is much more preferable due to its simple handling procedure and time-saving process. In addition, particle size and composition of the catalyst structure is easy to control [43]. In general, the preparation method starts by initially dissolving a certain amount of metal chemical forms into a homogenous solution. An ammonia solution is then added gradually to the earlier mixture until the pH reaches 10. Then, the slurry is filtered, washed, and dried overnight in the oven before undergoing the activation procedure in the furnace at a specified reaction temperature. Many researchers have used the co-precipitation technique for catalyst preparation to investigate the SCR reaction of NO. For instance, Zhang et al. [44] prepared Mn–FeO_x/CNT catalysts through redox co-precipitation to investigate NO reduction with NH_3 at low operating temperatures. Excellent SCR activity was observed since the Mn-FeO_x/CNT catalysts possessed high-stability morphology, high chemisorbed oxygen content, as well as strong reducibility at low SCR temperature. Zhang et al. [45] used the co-precipitation method to produce a high loading Zn- (Fe-, Ni-, Cu- or Ag-) promoted Co/Al_2O_3 catalyst to study the effect of additive metals on the SCR of NO. From the experimental studies, it was found that this technique definitely contributes towards a good homogeneous dispersion and helps prevent aggregation of highly deposited cobalt on alumina. Moreover, a uniform morphology of the catalyst was obtained and small-sized deposited cobalt was sustained under the presence of Fe, Ni, Cu, Zn or Ag. Meanwhile, Sun et al. [46] planned to enhance the performance of MnO_x catalyst for the SCR-NH_3 of NO reaction by modifying it with Eu using the co-precipitation method. An enhanced performance of the MnO_x catalyst was observed due to the strong interaction between Mn and Eu, which hinders the MnO_x crystallisation process.

Overall, there are various types of synthesis methods (impregnation, sol–gel, co-precipitation, incipient wetness, and pyridine thermal) that can be used to prepare the SCR catalyst for NO removal. Some of the previously mentioned preparation methods are among the most commonly applied techniques for the SCR-NH_3 of NO. However, traditional catalyst preparation methods (such as impregnation and co-precipitation) usually result in poor dispersion of the active component and pore blocking on the catalyst surface, thereby decreasing the removal activity of NO [32,47]. Hence, the sol–gel method is seen as the best method for catalyst preparation since it helps achieve better physiochemical properties of SCR catalysts [48].

Typical characterisation techniques for catalysts

The importance of the characterisation of catalysts for the SCR-NH_3 reaction for the removal of nitric oxide can be linked specifically to the inner structure of the catalyst. The characteristic features are highly associated with the deposition of car-

bon onto the catalyst surface, changes of phase, behavior of the catalyst support and active sites, catalyst morphology, type of carbon present on the catalyst, as well as the catalyst chemistry. A broad mixture of characterisation techniques have been applied to characterise the SCR-NH_3 catalyst, as summarized in the the following [49].

In particular, the catalyst active phases before and after SCR-NH_3 reaction are typically characterised by:

- atomic absorption spectroscopy (AAS)
- X-ray fluorescence spectroscopy (XRF)
- electron paramagnetic resonance (EPR)
- X-ray photoelectron spectroscopy (XPS)
- temperature-programmed reduction (TPR)
- X-ray diffraction (XRD)

The dispersion of metal, particle size of the catalyst and original state of the metal on the SCR-NH_3 supported catalysts can be characterised by the following techniques:

- transmission electron microscopy (TEM)
- scanning electron microscopy (SEM)
- X-ray diffraction (XRD)
- CO chemisorption

The behaviour of the SCR-NH_3 catalyst deposition is typically characterised by:

- temperature-programmed surface reaction (TPSR)
- mass spectroscopy (MS)
- differential thermal analysis (DTA)
- thermogravimetric analysis (TGA)
- temperature-programmed hydrogenation (TPH)
- temperature-programmed oxidation (TPO)

Table 1 summarises the typical characterisation approach for SCR-NH_3 catalysts.

Carbon-based materials as catalyst supports for NO removal

Carbonious materials have rich physical and chemical properties, which lend to their high porosity and good surface chemistry. In line with this, carbon-based materials are found suitable for use in most catalytic process applications. Although carbonious materials have traditionally been used as supports for catalysts in heterogeneous catalytic processes, they are becoming more familiar as catalysts of their own [63-65]. Carbon nanotubes (CNTs), activated carbon (AC), and graphene (GR) are among the most typical choices for carbon-based supports.

Several features can be seen when applying carbon-based materials as a catalyst support. The dispersion of the active phase over the support increases due to the large surface area and high porosity [64,66]. The pore size distribution can be altered to suit the requirements of a specific type of reaction. The surface chemistry of a carbon-based catalyst also plays a significant role, as it influences catalytic performance especially during the synthesis stage. In terms of interactions, carbon-based materials are known to be hydrophobic in nature. These materials normally show a low affinity against polar solvents, such as water, and in other cases, have a high affinity against non-polar solvents, such as acetone. Although the essence of carbon-based materials are mostly likely to be hydrophobic, which will eventually agitate the uniform distribution of the active component onto the carbon support, the surface chemistry of the carbon material could be simply adjusted, for instance, by undergoing an oxidation process, in order to increase the hydrophilicity of the carbon materials. Aside from the easy modification of the porous structure and surface chemistry, carbon-based materials also portray other distinct advantages [64]: (i) easier reduction of metals on the support; (ii) resistance towards acids and bases resulting in best carbon structure; (iii) firm at high working temperature (>750 °C) due to sturdy carbon composition; (iv) able to be produced in different physical shape (granules, pellets, fibres, and cloth) as carbon-based catalyst is very much porous in structure; (v) the cost of carbon-based supports is usually lower and more economical as compared to the conventional supports (silica and alumina) [67].

In recent years, many industrial applications have used carbon as a support material for catalysts. These catalysts are applied during the reaction process of oxidising organic compounds, desulphurisation, halogenation, and as fuel cells [64,66,67]. Unfortunately, all these industrial processes result in an unhealthy environment. Nowadays, treating the emission of nitric oxide, especially from industrial exhaust gas, has become a great concern [54,68-70].

Various types of metal species have been incorporated onto the surface of carbon materials. In order to integrate carbon materials with metal or metal oxide, a functionalisation process known as pre-treatment is required since the surface of pristine CNTs is hydrophobic and inert in nature. Unfortunately, existing preparation methods suffer from scarce deposition, catalyst particle aggregation, and unwanted large-sized metal particles. After attaching the oxide functional group onto the CNTs, the main properties of CNTs are usually affected. As a result, the performance of the as-prepared hybrid material will be impaired. Therefore, more preparation methods with less impact on the properties of CNTs have to be developed. This process is also important for the purification of pristine CNTs from amor-

Table 1: Summary of typical characterisation approach for SCR-NH_3 catalysts.

Characterisation techniques	Catalyst	Aspects characterised or investigated	Refs.
XRD & TEM	Mn/CNT Mn/ZSM-5	average size of active particles on the catalyst surface	[50,51]
NH_3-TPD	CuO/CNT CeO_2/CNT	adsorption state of NH_3 on the surface of the catalyst	[52,53]
TPD	V_2O_5/CNT	effect of different catalysts surface on SO_2 adsorption	[54]
H_2-TPR	Mn/CNT Mn/ZSM-5 CeO_2/CNT MnO_x/CNT Fe–Cu–O_x/CNT–TiO_2 CuCe/ZSM-5 $CeMo_xO_y/Al_2O_3$	reducibility of the catalysts	[50,51, 53,55-60]
TGA	Mn–Ce/CNT MnO_x/CNT	thermal stability	[55] [57]
XPS	Mn/CNT Mn/ZSM-5 CeO_2/CNT	surface chemical states and amount of the active component	[50,51, 53]
Raman	Mn/CNT	interaction between confined metal species and support material	[50]
NO-TPD & DRIFT spectra	Mn/CNT	interaction of NO with the surface of the catalysts	[50]
XRD	Fe–Cu–O_x/CNT–TiO_2 V_2O_5–WO_3/CNT Mn–Ce/CNT MnO_x/TiO_2	crystalline phase and structure of catalyst	[47,56, 57,61]
SEM	Fe–Cu–O_x/CNT–TiO_2 V_2O_5–WO_3/CNT	characterise the morphologies of the samples	[56,61]
XPS	Fe–Cu–O_x/CNT–TiO_2 Mn–Ce/CNT Ce–MnO_x/TiO_2 M_xO_y–V_2O_5–WO_3/TiO_2 $CeMo_xO_y/Al_2O_3$	peak intensity of active metal	[56-60]
NH_3-TPD	Fe–Cu–O_x/CNT–TiO_2 V_2O_5–WO_3/CNT M_xO_y–V_2O_5–WO_3/TiO_2 Ce–MnO_x/TiO_2 CuCe/ZSM-5	acidic sites in the catalyst	[56,58, 59,61, 62]
NOx-TPD	Fe–Cu–O_x/CNT–TiO_2	record the NO and NO_2 signals	[56]
TEM	Fe–Cu–O_x/CNT–TiO_2 V_2O_5–WO_3/CNT Mn–Ce/CNT CuCe/ZSM-5	support diameter and metal species particle size	[56,57, 61,62]
BET	Mn/ZSM-5 Mn–Ce/CNT Ce–MnO_x/TiO_2 MnO_x/TiO_2 M_xO_y–V_2O_5–WO_3/TiO_2	textural properties of the catalyst (specific surface area, pore volume, and pore size of catalysts)	[47,51, 57-59]
TPR	Ce–MnO_x/TiO_2	influence of metal content on the oxidation states of catalyst	[58]
XRD	M_xO_y–V_2O_5–WO_3/TiO_2	crystalline phases of the supports and catalysts	[59]
SEM & TEM	M_xO_y–V_2O_5–WO_3/TiO_2	morphologies and textural features of the catalyst	[59]

phous carbon, fullerenes, coal, and catalyst particles by means of their production. The wet chemical method is considered to be one of the most efficient methods for purification, activation, and functionalisation of CNTs. In this method, CNTs are immersed in a solution containing an oxidising agent for a few hours. A certain amount of heat is also applied to accelerate the oxidation process. The most commonly used technique for surface oxidation is acid treatment such as nitric acid or preferably nitric/sulphuric acid, as this results in the formation of oxygen-containing groups (OH, C=O and COOH) on the surface of the CNTs. The amount of oxygen-containing groups formed depends on the treatment method used. The chemical modification of the surface of (MWCNTs) multiwall carbon nanotubes is required via the oxygenated functional groups for the attach-

ment of metal nanoparticles. It is believed that the oxidative treatment may create defects to the hexagonal or pentagonal structures of the GR sheet in the nanotubes. The functional groups can be introduced at the bent parts, defect sites, and at the sidewall of the MWCNTs. Acid treatment enables the covalent attachment of oxygenated groups on the surface and the open ends of the CNTs. After undergoing pre-treatment, the treated-CNTs will be dispersed with the choice of metal species. In the next step, several synthesis methods are applied such as impregnation, pyridine thermal, sol–gel, and incipient wetness in order to enhance the dispersion of metal element onto the carbon surface. Therefore, a proper preparation technique for the carbon-based catalyst is important to obtain good catalytic performance.

Carbon nanotubes as a catalyst support

Nowadays, CNTs are recognised as an attractive catalyst support for SCR catalysts due to their electronic properties and unique nanostructure [71-73]. CNT-supported metal oxide catalysts are well-known in the adsorption field and present interesting properties for the denitrification of NO_x species [74,75]. Ma et al. [56] investigated the NO activity at low operating temperatures on iron-copper-oxide TiO_2 and CNT (Fe–Cu–O_x/CNT-TiO_2) catalyst supports prepared via the sol–gel method. The Fe–Cu–O_x/CNT-TiO_2 catalyst demonstrates the highest (90%) nitric oxide conversion at a reaction temperature of 175 to 275 °C. It is observed that the active component was highly dispersed onto the TiO_2 and CNT surface because the copper oxide was not detectable by XRD measurements. CNTs play a significant role in the catalyst structure, as they promote the distribution of metal oxides. The XPS analysis shows that the intensity peak of Cu and Fe reduces when the CNTs are added into the catalyst, thus enhancing the conversion of nitric oxide. Moreover, Fe–Cu–O_x/CNT–TiO_2 catalysts show high resistance towards H_2O and SO_2. With the introduction of 10% H_2O into the inlet gas at 225 °C, the NO_x conversion rapidly decreased from 99% to 65% over the $Cu_3Fe_1Ti_{85}C_5$ catalyst, and then slowly recovered and kept constant at 85%. On the contrary, the activity of NO_x completely recovered and remained consistent during 6 hours of testing, as soon as the H_2O flow stopped. It was found that the competitive adsorption between the H_2O molecule and NH_3 reactant is the cause of reduction in the conversion of NO_x [76]. Meanwhile, the NO_x conversion immediately reduced from 99% to 84% when SO_2 was present in the inlet gas at 225 °C. Even after the SO_2 introduction had stopped, the efficiency was still kept low (70%), implying the phenomenon of catalyst deactivation. At 250 °C reaction temperature, NO_x removal also decreased to 81–84%. However, when the SO_2 supply was switched off, the NO_x recovered up to 88.34%, suggesting a partial recovery of the catalyst deactivation. Phil et al. [77] and Li et al. [78] justified the possible reasons for catalyst deactivation. According to them, this was mostly due to the deposition of sulphates and bisulphates on the catalyst surface. By applying activated carbon (AC) as the catalyst support, the decomposition temperature of these species was reduced [79]. Correspondingly, in the study, the decomposition temperature of both sulphates and bisulphates were reduced with the introduction of CNTs as the support material for the catalyst. Hence, recovery of SO_2 deactivation was achieved at 250 °C.

Fang et al. [53] found that CeO_2 particles are highly dispersed on the surface of CNTs when prepared using the pyridine-thermal (PT) route compared to other methods such as impregnation (IM) and physical mixture (PM). The CeO_2/CNT-PT has smaller and narrower ceria particle size distribution (2 to 14 nm) than CeO_2/CNT-IM (6 to 20 nm) based on the TEM and HRTEM analysis. In addition, NH_3-TPD analysis was carried out in order to determine the surface acid amount and strength in the prepared catalysts. It was found that CeO_2/CNT-PT had much stronger acid sites since the desorption peaks shifted to a higher temperature range, as compared to CeO_2/CNT-IM and CeO_2/CNT-PM catalysts [80]. In this moment, the largest area of the desorption peaks can be observed in CeO_2/CNT-PT, signifying that the amount of NH_3 adsorbed on the surface of CeO_2/CNT-PT is greater than on CeO_2/CNT-IM and CeO_2/CNT-PM [80,81]. Meanwhile, the XPS analysis indicates that there was more oxygen surface vacancy in the CeO_2/CNT-PT catalyst, thus, enhancing the NH_3-SCR reaction. In comparison, Fang et al. [53] studied the performance of the catalysts via the impregnation and physical mixture methods. More than 90% of NO was removed at a reaction temperature between 250 °C and 370 °C for the CeO_2/CNT-PT catalyst compared to CeO_2/CNT-IM and CeO_2/CNT-PM with only 85% and 80% of NO conversion at a reaction temperature below 380 °C, respectively. This suggests that the CeO_2/CNT-PT catalyst has better catalytic activity.

Wang et al. [57] investigated the use of mixed Mn–Ce oxides-supported CNTs (Mn-Ce/CNT) for NO removal. An array of Mn–Ce/CNT catalysts with different molar ratios (0.6 to 1.8%) were prepared via the incipient-wetness method. During the preparation of the catalysts, the CNTs were pre-treated with concentrated nitric acid for roughly 16 hours. This procedure is advantegous since it helps with the dispersion of mixed oxides onto the surface of CNTs. More than 90% conversion of NO at a reaction temperature between 120 °C to 180 °C was recorded by all Mn(0.4)–Ce/CNT catalysts. Diffraction peaks corresponding to CNTs were the only pattern detected by XRD for all Mn(0.4)–Ce/CNT catalysts. Beside that, negative peaks were observed in the CeO_2 and MnO_2 crystalline phase at high loading (1.8%). This suggests that the Mn–Ce particles were

evenly distributed on the CNTs. The TEM images specified that the size of Mn–Ce particles were very small crystals and well dispersed on the surface of the MWCNTs. Further analysis was conducted using HRTEM in order to determine the exact sizes and distribution of metal particles. The mixed metal was well distributed with Mn–Ce particle sizes ranging from 2 to 4 nm on the CNT surface. Su et al. [82] investigated the effect of the position of MnO_x particles inside and outside of CNT cavities on the NO activity in the SCR reaction. It is found that the MnO_x particles inside the CNTs displayed higher NO activity in the SCR reaction compared to when the MnO_x particles were introduced outside of the CNT surface. In line with this research, Wang et al. [57] found that the high catalytic performance by Mn–Ce/CNT catalyst was partly attributed to the Mn–Ce particles found inside the cavity of the CNTs.

Wang et al. [83] reported high NO conversion (≈90%) at a relatively high reaction temperature of 200 to 300 °C on the Mn–Ce/CNT catalyst prepared using the incipient-wetness method. To improve the nitric oxide activity, especially at lower temperature, an alternative approach known as the liquid-phase method was applied in preparing the Mn–CeO_x/CNT catalyst [83]. Interestingly, excellent NO activity at low reaction temperatures was demonstrated by the developed catalysts. Even at a low catalytic temperature of 80 °C, the 63–85% NO conversion was still achieved. Soon after, the NO conversion started to rise significantly, nearly up to 100%, as the reaction temperature increased from 120 to 180 °C. The authors also investigated the Mn-CeO_x/CNT catalysts at different Mn/(Mn + Ce) molar ratios (0.4 to 0.6) on the NO removal activity. 0.5 Mn/(Mn + Ce) molar ratio was found to be the optimum loading amount for Mn–CeO_x/CNT catalyst preparation. From the HRTEM images, an uneven shape and fuzzy crystal lattice was identified on the metal nanoflakes suggesting that the Mn–CeO_x/CNT catalyst is amorphous in structure. The XRD result confirms only the presence of typical CNT peaks. Both of these features highly contribute towards high NO activity at low SCR temperature. This conclusion is in agreement with the research work of Tang et al. [84], where amorphous oxides showed greater NO activity compared to oxides with a crystalline structure in SCR at low temperature.

The effect of thermal treatment condition over MnO_x/CNT catalysts for the SCR of NO was investigated by Wang et al. [55]. The conventional method for CNT-based catalyst preparation always takes place in an inert atmosphere at a high calcination temperature. However, this condition is undesirable since it could disturb the NO activity due to the catalyst mass loss at high calcination temperature [57]. Hence, Wang et al. [55] prepared the MnO_x/CNT catalysts based on three different thermal conditions; MnO_x/CNT-A1 (calcined in air, 250 °C for 2 h), MnO_x/CNT-A2 (calcined in air, 300 °C for 50 min), and MnO_x/CNT-N3 (calcined in N_2, 300 °C for 2 h) to examine their catalytic activity in the NO removal reaction. It was found that MnO_x/CNT-A1 (calcined in air at 250 °C for 2 h) demonstrated the highest catalytic activity compared to the sample calcined in air at 300 °C for 50 min and the MnO_x/CNT catalysts (calcined in N_2 at 300 °C for 2 h) throughout the entire temperature window. Even at a low reaction temperature of 80 °C, the recorded NO conversion was up to 60%. However, the NO activity declined in both the MnO_x/CNT-A2 (calcined in air at 300 °C for 50 min) and MnO_x/CNT-N3 (calcined in N_2 at 300 °C for 2 h) catalysts. This is greatly associated with the CNTs reducing MnO_x to a lower valence state during the calcination process. Thus, thermal treatment condition plays a vital role in obtaining the best NO removal for CNT-based catalysts in the SCR reaction.

Su et al. [50] modified the catalytic properties of (Mn) species by introducing MnO_x either on the outer CNT surface or on the inner and outer CNT surface for the SCR of NO with NH_3. The recorded NO_x conversion was very low over blank CNTs at a reaction temperature ranging from 80 °C to 300 °C. By introducing a small amount of Mn (3%) to the CNTs, the catalytic activity of MnO_x/CNTs was improved tremendously at a reaction temperature between 150 and 250 °C. This positive performance may be greatly associated with the oxidation state of Mn species as well as the interaction type present between the MnO_x species and the surface of CNTs due to the unique structure of the CNTs [85]. According to the H_2-TPR result, MnO_x/CNTs with Mn content of 3% showed a two-step reduction process, as some of the MnO_x was introduced inside the CNT cavities. Meanwhile, the reduction temperature was identified to be at 219 °C and 418 °C. Meanwhile, the 3% Mn-out-$CNTs_{400}$ peaks were around 440 to 520 °C. Generally, the valance state and electron environment of manganese are two key components that affect the reduction steps and reduction temperature [50]. Previous work done by Cao et al. [86] showed that the amount of electrons found on the inner part of the CNT surface was insufficient compared to the one located on the outside surface. When the metal oxide species are introduced at the side, which lacks electrons, metal oxide will tend to donate more electrons, leading towards easier reduction activity. Other reports by Chen et al. [87,88] reveal that the reduction of Fe_2O_3 nanoparticles, which are located inside the cavity, occur at 600 °C while the reduction of the outer surface of the MWCNTs occur at 800 °C. Therefore, the difference in reduction activity may be associated with the strong interaction between MnO_x nanoparticles with the inner and outer CNT surface. Concurrently, the number of oxygen molecules could be supplied when MnO_x is introduced onto the CNT surface, promoting high SCR activity.

In another work, Zhang et al. [70] compared the catalytic activity of Mn–Ce species on CNT using an in situ (reflux) method. In this method, poly(sodium 4-styrenesulonate) (PSS) was used as surfactant during the synthesis of the catalyst in order to assist with the dispersion of CNTs in aqueous solution and to maintain its stability. From the experimental activities, it was found that the MnCe@CNTs-R catalyst showed the highest (>90%) NO conversion and most comprehensive reaction temperature (200–350 °C) in comparison with other catalysts prepared using impregnation and mechanically mixed methods. Both MnCe@CNTs-I and MnCe@CNT-M prepared by impregnation and mechanically mixed methods showed a NO conversion of only up to 90% and 85%, respectively, at a 170 °C and 200 °C temperature window. Upon undergoing the characterisation study, the XRD and TEM results showed that prepared MnCe@CNTs-R afforded an excellent dispersion amount of active species on the CNT surface. This phenomenon could be one of the main reasons favouring the outstanding NO activity. Meanwhile, the XPS analysis revealed that the prepared MnCe@CNTs-R catalyst had more active sites, which promoted the NH_3-SCR reaction since more Mn atoms were exposed onto the CNT surface. Besides that, the oxidation process helped oxidised NO to NO_2. This was due to the interaction present between the MnO_x and CeO_x species, resulting in more oxygen vacancy in the MnCe@CNTs-R catalyst. This rapidly enhanced the SCR reaction, making it faster. The NH_3-TPD analysis shows that the MnCe@CNTs-R catalyst was not only able to demonstrate a large amount of acid content, but also a stronger acid strength. In terms of stability, the MnCe@CNTs-R activity remained constant during the test period (300 °C). However, the NO conversion for both MnCe@CNTs-I and MnCe@CNTs-M slowly reduced over time. Furthermore, MnCe@CNTs-R exhibited high tolerance towards SO_2 and H_2O.

Bai et al. [52] studied CuO supported on CNTs. The catalyst was developed to better understand the catalytic behaviour of CNT-based catalysts especially in reducing the amount of nitric oxide in an SCR reaction. Different amounts of CuO loadings were studied at a 200 °C reaction temperature. Apparently, the catalytic activity of the CuO/CNT catalyst was observed to rise as the CuO loading increased from 1 to 10 wt %. About 88.5% of NO was converted when 10 wt % of CuO loading was introduced into the CNT. Unfortunately, the NO conversion decreased as the amount of CuO loading became higher than 10 wt %. It is surmised that the reduction in NO activity is mostly due to the aggregation of CuO particles on top of the CNT surface [54]. The catalytic performance of 10 wt % CuO/CNT was also studied over a 120 to 150 °C temperature window. The NO conversion over 10 wt % CuO/CNT catalyst increased as the reaction temperature increased. Approximately 88.5% of NO was converted when the reaction temperature increased to up to 200 °C. However, the conversion activity of NO reduced to 70.5% when the reaction temperature increased to 250 °C. This result is in accordance with the tendency of NH_3 to oxidise at high reaction temperature, leading to a lower reduction of NO activity [54]. In terms of stability, 10 wt % CuO/CNT catalyst was highly stable at 200 °C temperature where a great NO conversion efficiency of 88.5% as well as outstanding catalytic activity at 72 h of running was also observed. All the features above are just some of the main advantages of using the CuO/CNT catalyst in the SCR of NO at low temperature.

Bai et al. [54] investigated the activity of V_2O_5/CNT catalysts at a low SCR reaction temperature. They found that V_2O_5/CNT catalysts have higher catalytic activity compared to V_2O_5 particles supported on AC (V_2O_5/AC) at 200 °C reaction temperature. The BET analysis confirms that the CNTs have a lower (220 m^2/g) surface area than AC (615 m^3/g), indicating that the catalytic properties in CNTs are better than AC because of the former's special structural features [54]. Meanwhile, a study on the effect of SO_2 shows that there was no significant conversion of nitric oxide by V_2O_5/AC either with or without the presence of SO_2 in the reaction stream. However, the conversion of nitric oxide momentously increased and became almost linear at a high level of SCR reaction by V_2O_5/CNT (0.1–1 wt %) catalysts in the presence of SO_2. This trend implies that the presence of SO_2 has helped increase the reduction of NO over V_2O_5/CNT catalysts, especially at low SCR temperature. Bai et al. [54] added that the V_2O_5 loading is the sole factor influencing the promotional effect of SO_2 in the system. Hence, there was a synergistic connection among CNTs and the vanadium species in the catalyst. Unlike in any other study, SO_2 usually displays a poisoning rather than a promoting effect. In this study, the SO_2 promoting effect is more likely associated with the formation of SO_4^{2-} species on the catalyst surface. These SO_4^{2-} species would act as new acidic sites that help improve NH_3 adsorption, thereby promoting the activity of the catalyst. Similar observations were also reported elsewhere [89-91]. Therefore, the V_2O_5/CNT catalyst is justified as one of the most promising catalytic materials for SCR at low temperature due to the unique promoting effect of SO_2.

Wu et al. [61] introduced the idea of implementing CNTs, a by-product obtained from the prior hydrogen production, as supports for the V_2O_5–WO_3 catalyst. In their study, the catalysts were prepared via the impregnation method, while ammonia was used as a reducing agent. A characterisation study conducted using TEM analysis revealed that the diameter of the CNTs was around 50 nm, whereas the V_2O_5–WO_3 particle size was about 8 nm. A similar observation was found by Su et al.

[50]. In their study, Mn/CNT catalysts were used in the SCR activity. The size of the Mn particles was found to be around 8 nm, while the CNT diameters were around 50 nm. Huang et al. [92] used V_2O_5 supported on CNTs as the SCR catalyst. Upon study, the size of the metal particle was found to be around 10 nm, while the diameter of the CNTs was between 10 to 100 nm. Meanwhile, the XRD analysis showed that tungsten oxides could not be identified because their particle size was too small to be determined [93]. This indicates that the WO_3 particles were evenly dispersed on top of the catalyst surface [94]. In terms of NO_x reduction efficiency, the V_2O_5–WO_3/CNT catalyst achieved more than 95% conversion in reaction temperatures of 340 to 400 °C. However, low NO_x activity was observed when the reaction temperature went below 200 °C, which is probably due to the lack of Lewis active sites. Hence, further investigations into lowering the SCR reaction temperature with high NO_x productivity were proposed. A summary of the reaction conditions and NO activity for CNT-based catalyst supports is shown in Table 2.

Activated carbon and activated carbon fibre as a catalyst support

The discovery of CNTs, AC, and activated carbon fibre (ACF) as catalysts and catalyst supports has been the focus of researchers in NO removal application [95,96]. The adsorption ability of both AC and ACF depends highly on its surface area, internal pore structure, surface characteristics, and the presence of functional groups on the pore surface [97]. Tsen et al. [95] evaluated the catalyst performance of coconut shell AC as a support with several active metals such as Cu, Ni, Co, and Fe. The results conclude that NO conversion increased with an increasing atomic number of active components. Sumathi et al. [2] prepared palm shell AC impregnated with several metal oxides (Ce, Ni, Fe, and V). The palm shell support was found to be capable of removing NO gas and further loading with metal oxides increased the conversion reaction due to the increased micropore volume of the palm shell AC. Yoon et al. [98] studied the effect of propellant waste on ACF by impregnation and heat treatment methods. The introduction of a nitrogen functional group by propellant waste promoted the activity removal of NO two-fold to that of the unmodified ACF at low temperature. The SEM analysis reveals that propellant waste was fully oxidised on the ACF surface after being treated at 500 °C. Meanwhile, Zhu et al. [96] modified ACF through low-temperature oxygen plasma and nitric acid, which are respectively denoted as activated carbon modified by plasma (ACFP) and activated carbon modified by nitric acid (ACFN). The results indicate that the CeO_2 species on ACFN produced higher activity than those on ACFP. This is because the surface of CeO_2/ACFN is more acidic as it was treated with nitric acid and the reaction between NO and the catalyst surface became more active. Using several characterisation techniques, such as Fourier transform infrared spectroscopy (FTIR), X-ray photoelectron spectroscopy (XPS), and temperature-programmed desorption (TPD), the comparison of the properties for both ACFP and ACFN was clarified. Chuang et al. [18] considered three different methods, i.e., impregnation, polyol, and microwave-heated polyol methods for the synthesis of an economical Cu/AC catalyst. Among these methods, the microwave-heated polyol method showed the highest catalytic activity for the Cu/AC catalyst with 80.1% conversion of NO. Analysis using FESEM verified that the Cu particles on the AC surface were better dispersed compared to the catalysts prepared using the other two methods. Interestingly, the MnO_2/ACF catalyst prepared by the co-precipitation method appeared to be a promising catalyst, as it can reduce NO at a temperature as low as 25 °C [1]. A similar finding was reported by Sousa et al. [99], where the melamine/AC catalyst prepared by impregnation removed NO at a reaction temperature of 25 °C with a high conversion of 88%. This suggests that the NO removal by AC and ACF could be a serious contributor to sustainable economic growth by offering cost-effective low energy consumption. Although AC and ACF are extremely effective at removing NO due to the combination with certain active components, the investigation into carbon-based supports is still in progress due to some limitations such as the presence of O_2, reactivity at low temperature, and also the components of the carbon itself.

Other unique catalyst modifications have also be implemented, especially improvements in the quality of supporting materials. Klinik et al. [100] treated activated carbons with N-compounds and further enhanced the catalyst surface chemical properties with manganase oxides. It was observed that the addition of water into the SCR system reduced NO activity by 10 to 20% but increased the selectivity of N_2. The N-AC/MnO_x catalyst can be justified as one of the promising catalysts for SCR-NH_3 reaction since it yields the highest amount of NO conversion (≈100%) at an operating temperature between 180 to 220 °C. Boyano et al. [101] prepared a series of vanadium-loaded carbon-coated monoliths treated with different concentrations of acids. The aim was to investigate the effect of distinct oxidative treatment conditions on the NH_3-SCR catalytic environment including chemical surface and texture properties. HNO_3 treatment resulted in the most outstanding performance. The vanadium-loaded carbon treated with HNO_3 acid achieved the highest NO reduction activity, as there was a large amount of carboxyls and lactones present on the catalyst surface. Acid treatment is an important factor that could enhance the performance of NO activity since it is closely related to the density of the surface oxygen group obtained during the oxidation process. Muniz et al. [102] implemented Nomex-based carbon fibres and Kevlar-based carbon fibres for the SCR of NO with NH_3 at low

Table 2: Summary of the reaction conditions and NO activity for CNT-supported catalysts.

Catalyst	Preparation method Activation condition									
	Reaction condition							Best NO removal		Refs.
	NO (ppm)	NH_3 (ppm)	O_2 (%)	SO_2 (%)	Balance (gas)	Flow rate (mL/min)	GSHV (h^{-1})	Conversion (%)	Temperature (°C)	
Fe–Cu–O_x/CNT–TiO_2	sol–gel calcination: 500 °C/4 h (N_2)									
	550	550	5	–	N_2	500	36,000	99	175–250	[56]
V_2O_5–WO_3/CNT	impregnation calcination: 450 °C/3 h (N_2)									
	0.06 (vol %)	0.06 (vol %)	3	–	N_2	300	–	>95	340–420	[61]
CeO_2/CNT-PT CeO_2/CNT-IM CeO_2/CNT-PM	PT-pyridine thermal route (main), IM-impregnation, PM-physical mixture calcination: 500 °C/4 h (N_2)									
	500	500	3	100	N_2	250	20,000	>90	250–370	[53]
Mn-Ce/CNT	incipient wetness calcination: 300 °C/1 h (air)									
	500	500	5	–	N_2	700	84,000	>90	120–180	[57]
MnCe@CNT-R MnCe@CNT-I MnCe@CNT-M	R-reflux (main), I-impregnation, M-mechanical calcination: 500 °C/6 h (N_2)									
	500	500	3	100	N_2	–	10,000	>90	200–350	[70]
Mn–CeO_x/CNT	liquid-phase vacuum drying: 120 °C/12 h									
	500	500	5	–	N_2	700	30,000	≈100	120–180	[83]
MnO_x/CNT-A1 MnO_x/CNT-A2 MnO_x/CNT-N3	incipient wetness A1 – calcination: 250 °C/2 h (air), A2 – calcination: 300 °C/50 min (air), N3 – calcination: 300 °C/2 h (N_2)									
	500	500	5	–	N_2	700	38,000	>60	80–180	[55]
Mn-in-CNTs Mn-out-CNTs Mn-both-CNTs	wet chemical in – ethanol; ultrasonic treatment/4 h; calcination: 300–400 °C (N_2), out – xylene; ultrasonic treatment/3 h; calcination: 300–400 °C (N_2), both – xylene; ultrasonic treatment/1 h; calcination: 300–400 °C (N_2)									
	0.08 (%)	0.08 (%)	5	–	Ar	600	35,000	>90	200–250	[50]
CuO/CNT	pore volume impregnation calcination: 250 °C/2 h (Ar)									
	450	500	5	–	N_2	–	30,000	88.5	200	[52]
V_2O_5/CNT	pore volume impregnation calcination: 500 °C/5 h (argon steam)									
	450 (μ/L)	500 (μ/L)	5	–	N_2	–	30,000	≈100	250	[54]

reaction temperature. It was found that the Nomex-based carbon fibres demonstrated a higher degree of NO reduction compared to Kevlar-based carbon fibres due to the presence of the oxygen surface group, which enhances the conversion activity of NO. Lazaro et al. [103] applied vanadium supported onto various forms of AC (powder, briquettes, and monoliths) catalysts via the impregnation method for the SCR of NO with NH_3. All these AC-based catalysts are porous in structure, which plays an important role for achieving high NO removal activity. Galvez et al. [104] prepared a series of activated carbons doped with vanadium compounds, which successfully achieved considerable reduction activity of NO in the presence of NH_3 at a reaction temperature between 100–300 °C. A higher NO reduction activity was observed when using a pre-oxidised (SCA750) carbon support. Huang et al. [105] prepared various samples of carbon catalysts from phenol-formaldehyde resins. Each catalyst sample was impregnated with different amounts of *m*-phenyl-enediamine (MPDA) in order to enhance the performance of NO reduction. Upon impregnation of the carbon catalysts with nitrogen, it was observed that the NO catalytic activity increased significantly at operating temperatures below 140 °C. Table 3 summarises the reaction conditions and NO activity for

activated carbon and activated carbon fibre-based catalyst supports.

Graphene as a catalyst support

Graphene (GR) is a new outstanding carbon nanomaterial, which demonstrates excellent physiochemical properties such as good thermal conductivity, chemical stability, large surface area, high electron exchange, and a flexible structure [6]. Therefore, GR is considered to have good conductivity at room temperature due to the freely moving electrons on the surface, which can improve the redox performance of the catalyst as well as the catalytic activity in de-NO_x [113]. You et al. [6] verified that high NO conversion can be achieved over GR at low reaction temperature. A MnO_x–CeO_2/GR catalyst prepared

Table 3: Summary on the reaction conditions and NO activity for activated carbon and activated carbon fiber supported based catalysts.

Catalyst	Preparation method Activation conditions								Refs.
	Reaction conditions						Best NO removal		
	NO (ppm)	NH_3 (ppm)	O_2 (%)	Balance (gas)	Flow rate (mL/min)	GSHV (h^{-1})	Conversion (%)	Temperature (°C)	
CuO_x/AC	wet impregnation calcination: 400 °C/2 h (N_2)								
	700	700	6	N_2	500	7,500	62	250	[78]
Fe/AC	volume impregnation calcination: 450 °C/4 h (N_2)								
	600	–	6	N_2	500	40,000	95	250	[95]
CeO_2/ACFP[a]	impregnation calcination: 350 °C/6 h (N_2)								
	1000	1000	5	N_2	–	11,000	86	180	[96]
CeO_2/ACFN[b]	impregnation calcination: 350 °C/6 h (N_2)								
	1000	1000	5	N_2	–	11,000	94	180	[96]
V_2O_5/AC	impregnation calcination: 500 °C/5 h (Ar)								
	450	500	5	N_2	1200	–	94	150	[106]
Cu/AC	impregnation, polyol, microwave heated calcination: 300 °C/4 h								
	400	400	6	N_2	500	43,750	52.7 79.3 80.1	200 200 200	[18]
Cu/AC	co-precipitation calcination: 800 °C/30 min (N_2)								
	1500	–	5	N_2	–	6,000	>80	300	[107]
MnO_2/ACF[c]	co-precipitation calcination: 200 °C/2 h (N_2)								
	50	–	21	N_2	–	–	30.6	25	[1]
N-AC[e]/MnO_x	impregnation calcination: 220 °C/50 min (He)								
	800	800	3	He	100	–	≈100	180–220	[100]
CeO_2/ACF[c] La_2O_3/ACF[c]	Impregnation Calcination: 360 °C/2 h								
	500	–	21	N_2	266.7	–	70 90	150 350	[108]
Ce/ACF[c]	impregnation calcination: 500 °C/4 h (Ar)								
	150	150	5.6	N_2	250	–	80	300	[109]
Pd/AC	impregnation reduction: 50 °C/30 min (He)								
	500	–	–	N_2	–	15,000	>90	100	[110]

Table 3: Summary on the reaction conditions and NO activity for activated carbon and activated carbon fiber supported based catalysts. (continued)

melamin/AC	impregnation								
	calcination: 600 °C/50 min (N_2)								
	1000	–	20	N_2	–	–	88	25	[99]
propellant/ACF[c]	impregnation								
	calcination: 500 °C/1 h (N_2)								
	900	–	10	N_2	500	–	>90	30	[98]
NH_3/AC	impregnation								
	calcination: 750 °C/1 h (N_2)								
	300	–	20	N_2	–	–	70	450	[111]
CeO_2−Cu−CNF[d]ACF[c]	impregnation								
	calcination: 200 °C/4 h (N_2)								
	500	–	20	N_2	–	–	80	30	[112]
Nomex-based carbon fibres Kevlar-based carbon fibres	carbonization								
	carbonized: 700 °C/1 h (N_2)								
	700	800	3	Ar	300	–	40–80	300–400	[102]
V/AC-powder V/AC-briquettes V/AC-monolith	impregnation								
	activation: 750 °C/2 h (H_2O or CO_2)								
	800	800	3	He	100	–	28–88	150	[103]
carbon-SCA750/V_2O_5	stirring								
	stirring: ambient temperature/4 h								
	1000	1500	3.5	Ar	–	–	>80	200	[104]
PFC[f]	impregnation								
	heating in vacuum: 60 °C/2 h to 120 °C/12 h								
	500	640	1	He	–	–	11	<140	[105]

[a]Activated carbon modified by plasma; [b]activated carbon modified by nitric acid; [c]activated carbon fiber; [d]carbon nanofiber; [e]nitrogen promoted activated carbon; [f]carbon catalysts from phenol-formaldehyde resins.

via the hydrothermal method yielded high catalytic activity of almost 100% at 120 °C. The Raman spectra reveal that GR offers more active sites and improves the interaction between MnO_x and CeO_2 particles on the flexible GR surface. In fact, Guo et al. [114] explains that the removal of NO can be conducted at room temperature with the addition of graphene oxide (GO) onto carbon nanofibres (CNFs). Xiao et al. [115] used GR to obtain high NO conversion at low reaction temperature. Their results indicate that the MnO_x–CeO_2/GR catalyst achieved higher NO conversion compared to pure MnO_x/GR and CeO_2/GR. The XPS analysis revealed that the addition of GR could change the composition of the Mn species, which plays an important role in electron mobility and thus leading to low reaction temperature in SCR. Moreover, MnO_x–CeO_2/GR (0.3%) at 180 °C also showed high catalytic activity when 10 vol % H_2O and 200 ppm SO_2 were added to the system. The same catalytic properties, which convey good resistance towards H_2O and SO_2 poisoning, was also reported by Lu et al. [116]. The researchers employed Ce–Mn/TiO_2–GE catalysts prepared via the sol–gel and ultrasonic impregnation methods. It was noted that the hydrophobic groups present on the GR surface are not favourable for H_2O adsorption. Although some researchers achieved good results for catalyst stability and high H_2O and SO_2 resistance, further investigation is still needed to ensure the long-term activity of the prepared catalysts. In addition, there are still limited reports that focus on GR applications for low-temperature SCR. Therefore, there is still a crucial need for more research on catalysts that can provide a reaction temperature as low as room temperature with high NO conversion. Table 4 shows a summary of the reaction conditions and NO activity for graphene-based catalyst supports.

Non-carbon-based materials as catalyst supports for NO removal

Apart from carbon-based supports, non-carbonious-based materials have also been applied as catalyst supports for nitric oxide removal, especially in the SCR process. Carbon supported materials tend to vaporise easily. This phenomenon would retard the material capability especially during oxidation and hydrogenation reactions [67]. The reproducibility of AC-based catalysts is low since different batches of materials would result in different amounts of ash content [120]. Today, researchers tend to focus on different compound oxides for catalyst support since they possess great features that would result in the higher removal of nitric oxide. Zeolite Socony Mobil–5 (ZSM-5) [62], TiO_2 [37,47,58,59], and Al_2O_3 [60] are some of the examples of the most frequently used catalyst supports. The ZSM-5 support is reported to have a remarkable ion-exchange capacity

Table 4: Summary on the reaction conditions and NO activity for graphene supported based catalysts.

Catalyst	Preparation method Activation conditions								
	Reaction conditions						Best NO removal		Refs.
	NO (ppm)	NH_3 (ppm)	O_2 (%)	Balance (gas)	Flow rate (mL/min)	GSHV (h^{-1})	Conversion (%)	Temperature (°C)	
CuO_x/graphite	wet impregnation calcination: 400 °C/2 h (N_2)								
	700	700	6	N_2	500	7,500	45	250	[78]
GE/CNF (PGCNF)[a]	electro-spinning activation: 850 °C/10 min (NH_3)								
	50	–	21	N_2	–	–	32.83	30	[114]
ACNF[b] GPNF-1900[c] GPNF-2400[c]	electro-spinning activation: 800 °C/30 min (N_2) graphitized: 1900 °C/10 min (N_2) graphitized: 2400 °C/10 min (N_2)								
	20	–	21	N_2	–	–	11 38 45	30 30 30	[117]
MnO_x/TiO_2−GE[d]	ultrasonic impregnation calcination: 450 °C/6 h (N_2)								
	500	500	7	Ar	–	67,000	>93	180	[113]
MnO_x-CeO_2/GR[d]	hydrothermal calcination: 400 °C/2 h (Air)								
	500	500	5	N_2	–	24,000	≈100	120	[6]
CeO_x–MnO_x/TiO_2–GE[d]	ultrasonic Impregnation calcination: 450 °C/6 h (N_2)								
	500	500	7	Ar	–	67,000	>99	180	[116]
MnO_x/TiO_2–GO[e]	ultrasonic Impregnation calcination: 450 °C/3 h (N_2)								
	500	500	7	Ar	600	67,000	>95	180	[118]
MnO_x–CeO_2/GR[d] MnO_x/GR[d] CeO_2/GR[d]	hydrothermal (130 °C/12 h) calcination: 400 °C/2 h (N_2)								
	500	500	5	N_2	–	24,000	100 80 20	140 140 140	[115]
MnO_x/GR[d]	hydrothermal (160 °C/24 h) calcination: 400 °C/2 h (N_2)								
	0.06%	0.06%	3	Ar	500	45,000	>90	190	[119]

[a]Polyacrylonitrile graphene oxide nanofibers; [b]activated carbon nanofibers; [c]graphite carbon nanofibers; [d]graphene; [e]graphene oxide.

[121]. Furthermore, the TiO_2 support is known for its high resistance to sulphur poisoning and sulphates, which are much more stable on the TiO_2 surface compared to other oxides [47]. In the next sections, a comprehensive review on the non-carbon-based catalyst focusing on the types of supports for SCR reaction is discussed in detail.

ZSM-5 as a catalyst support

Nowadays, researchers prefer to modify a currently popular ZSM-5 catalyst support by introducing a second metal in order to broaden the temperature window for the SCR reaction. Usually, a second metal is used as an additive. It was found that the interaction between both metals would significantly influence the catalyst surface physiochemical structure [122,123]. Ceria is one of the most popular promoters used in metal-containing ZSM-5 catalysts. Many studies have implemented ceria due to its exceptional properties, such as: (i) strong metal-support interaction that helps increase the dispersion and stability of the metal catalyst; (ii) formation of oxide ion storage and labile oxygen vacancies; (iii) enabling the easy exchange of oxygen molecule with the medium, as the redox couple between the trivalent and tetravalent oxidation states of the ceria ions are present [124,125]. Pang et al. [126] reported the high activity and stability of the Ce–Cu/ZSM-5 catalyst. However,

no attention has been given towards the investigation of redox properties, surface state, or the synergistic effects between Cu and Ce supported on ZSM-5 in the SCR reaction. Recently, Dou et al. [63] modified Cu/ZSM-5 by introducing Ce into the catalyst. Their main target was to actually develop a catalyst that can broaden the temperature window by focusing on the influence of cerium introduction onto the catalyst structure, acid sites, redox property, and chemical state of Cu and Ce species before and after the SCR reaction takes place. The influence of cerium content on the Cu/ZSM-5 catalyst was evaluated by setting the copper content to 2.0 wt %, and varying the cerium content from 0, 0.5, 1.0, 1.5 to 2.0 wt %, corresponding to Cu-Z, CuCe1-Z, CuCe2-Z, CuCe3-Z, and CuCe4-Z, respectively. The experimental results confirm that the temperature window widened to low and high level temperatures when Ce was introduced into the Cu/ZSM-5 sample. Of all the CuCe/ZSM-5 catalysts, CuCe4-Z (where 4 refers to 2.0 wt % of cerium) demonstrated the best catalytic activity with 95% NO being reduced at a 149–427 °C reaction temperature. In terms of catalytic behaviour, the addition of cerium also helped increase the dispersion of copper onto the support surface (ZSM-5) and also prevented crystallisation, which is prone to happen in SCR reactions. In addition, the redox properties of CuCe/ZSM-5 catalysts were also improved with the addition of cerium as the second metal. CuCe/ZSM-5 also showed a higher amount of Cu valence and lattice oxygen compared to the Cu/ZSM-5 catalyst, which are shown from the XPS and H_2-TPR analysis.

Lou et al. [51] developed a series of Mn/ZSM-5 catalysts for the SCR of NO with ammonia via the precipitation method. The catalysts were prepared at various calcination temperatures (200 to 700 °C), denoted as MnZ-2 (200 °C), MnZ-3 (300 °C), MnZ-4 (400 °C), MnZ-5 (500 °C), MnZ-6 (600 °C), and MnZ-7 (70 °C), respectively. The calcination temperature was found to have a significant effect on the NO catalytic activity. If the calcination temperature is too low, the metal salts will tend to decompose incompletely, resulting in a decrease in the amount of active component on the catalyst surface. On the other hand, if the calcination temperature is too high, sintering could occur in the catalyst, which later leads to a serious decrease in the catalyst surface area as well as reduction in the even distribution of active component onto the catalyst [51]. Generally, the calcination temperature is considered to be associated with the manganese oxide final oxidation states, crystallinity, and surface area, which can help determine the success of the NO reduction activity [51]. Limited studies have been done to explore the influences of calcination temperature on Mn/ZSM-5 catalysts. Still, detailed studies on how calcination temperature affects the formation of different MnO_x species in SCR activities have not yet been reported. Therefore, Lou et al. [51] studied the variation of calcination temperature of Mn/ZSM-5 catalysts in order to analyse its effects on the physical and chemical properties of Mn/ZSM-5 catalysts. Mn/ZSM-5 catalysts that were prepared at lower calcination temperatures (<500 °C) resulted in higher Mn surface and lattice oxygen concentration, as well as a larger surface area. Moreover, lower calcination temperatures (<500 °C) promote the SCR Mn/ZSM-5 catalyst activity since the formation of Mn_3O_4 species and amorphous MnO_2 species will react together in the NO reduction process. On the contrary, a higher calcination temperature (600 to 700 °C) reduced the number of Mn concentration, resulting in smaller surface area and increased crystallinity of the catalysts. This phenomenon will lead to the formation of crystalline Mn_2O_3 species, thus reducing the SCR process. Overall, the MnZ-3 (calcined at 300 °C) catalyst demonstrated the best performance of NO reduction out of all the Mn/ZSM-5 catalysts. Almost 100% of NO was converted at a reaction temperature of 150 to 390 °C.

TiO_2 as a catalyst support

Recently, investigations into bimetallic catalysts such as Fe–Mn/TiO_2 [47,58], Mn–Ni/TiO_2 [127], Ce–W/TiO_2 [128], and ternary mixed-oxide catalysts such as Nb–Ce–W/TiO_2 [129] and Zr–V–W/TiO_2 [130] supported on TiO_2 have increased in popularity among scientists. These research studies imply that all these catalysts demonstrate high catalytic activities. For example, the Mn–Ni/TiO_2 [127] and Fe–Mn/TiO_2 [47,58] catalysts showed almost 100% conversion of NO at low temperature (200 °C) reaction conditions. In addition, the remarkable thermal stability of bimetallic and ternary catalysts has also been recognised. Shi et al. [130] found that the aged Zr–V–W/TiO_2 catalyst is more active than the fresh catalyst at a reaction temperature of 150 to 400 °C, after undergoing thermal aging at 750 °C for 12 h. Lee et al. [131] outlined the applications and synthesis of advanced metal oxide catalysts. They reported that the SCR activities and selectivity were greatly improved with the addition of cerium. This is due to the good thermal stabilities as well as high activities portrayed by the catalysts. Zhang et al. [59] studied the ternary mixed-oxide catalysts for the SCR-NH_3 of NO reaction. A partial substitution method of metal oxide (M_xO_y, M = Fe, Co, Ni, Cu, Sr, La, and Ce) for V_2O_5 in the V_2O_5–WO_3/TiO_2 catalyst was prepared in accordance to the preparation of ternary mixed-oxide catalysts. The developed M_xO_y–V_2O_5–WO_3/TiO_2 catalysts were then tested for SCR-NH_3 reaction. At a reaction temperature of above 400 °C, the M_xO_y–V_2O_5–WO_3/TiO_2 catalysts increased NO reduction activity. On the other hand, at a reaction temperature below 400 °C, only cobalt oxide substitution increased the NO reduction performance. Of all the partial substitution catalysts, the Co-VW catalyst demonstrated excellent NO reduction activity in SCR-NH_3 and resulted in a low yield of N_2O. The Co-VW supported on TiO_2 catalyst displayed over 90% NO

conversion at 350 to 495 °C reaction temperature under a high gas hourly space velocity (GHSV) of 300,000 h^{-1}. In terms of inhibition effect of H_2O and SO_2 on the SCR activity, the substitution of cobalt into the VW/TiO_2 catalyst enhanced the H_2O and SO_2 resistance significantly. From the characterisation studies, the active Co and V species and W promoter are observed to be well dispersed on the TiO_2 support, after partial substitution of the catalyst. An increase in the amount of surface absorbed oxygen, and Brønsted and Lewis acid sites was observed when Co was introduced into the VW/TiO_2 catalyst. Both the Brønsted and Lewis acid sites were involved in the SCR-NH_3 of NO reaction. The activity of SCR-NH_3 within the reaction temperature range was improved, as there was an increment in the number of Lewis and Brønsted acid sites, which is attributed to the Co substitution of V in the catalyst. Hence, unique bimetallic and ternary mixed oxide catalyst has the promising potential as a catalyst for controlling the emission of NO_x from diesel engines.

Generally, low-temperature SCR reactions usually implement manganese oxides (MnO_x)-based catalysts, as they show different types of labile oxygens, which are important for completing the NO catalytic cycle [58]. MnO_x/TiO_2 [132,133] and Mn deposited over carbon-ceramic cellular monolith were reported to be active at low SCR temperature in the presence of oxygen for the successful removal of NO with NH_3 [134]. Ceria (CeO_2), on the other hand, is known to be inexpensive and non-toxic. It is potentially advantageous compared to many catalytic applications since it has two stable oxidation states, Ce^{4+} and Ce^{3+}. The redox shift that occurs between Ce^{4+} and Ce^{3+} could increase the ease of storing and release of oxygen in ceria. In addition, ceria could also increase the catalyst activity for the SCR-NH_3 of NO by promoting the oxidisation of NO to NO_2 [135]. Therefore, the mixed oxide Mn–Ce catalyst is considered to be one of the potential catalysts for high NO reduction activity at low SCR-NH_3 temperature. Recently, Carja et al. [136] developed a Mn–Ce/ZSM-5 catalyst in aqueous phase. They reported that 75% to nearly 100% of NO was converted within a 240 to 500 °C temperature window. Qi et al. [137] also studied the Mn–Ce mixed oxide catalyst, which achived 100% NO conversion at a reaction temperature of 150 °C. Recently, Wu et al. [58] prepared a series of cerium-modified MnO_x supported onto TiO_2 using the sol–gel method. The main objective of the study was to determine the possible catalysts that would result in higher catalytic activities at low operating temperature (<100 °C). It was found that Ce–MnO_x/TiO_2 catalysts demonstrated a high level of NO activity at low SCR-NH_3 temperature. Of all the cerium-modified MnO_x catalysts, Ce(0.07)MnTi showed a high (80%) NO conversion at low (80 °C) SCR-NH_3 temperature with a GHSV of 40,000 h^{-1}. In terms of characterisation studies, the pore volume and BET surface area in the Ce(0.07)MnTi catalyst is 50% larger than that of the Ce(0)MnTi catalyst. The XPS results confirm that by introducing the Ce into the catalyst, the chemisorbed oxygen concentration on the catalyst surface could doubly increase. Besides that, the TPR results indicate that the activity of MnO_x/TiO_2 could be enhanced, the catalyst oxygen storage improved, and facilitation of oxygen mobility over the catalysts achieved, when Ce is present together with MnO_x/TiO_2. NH_3-TPD justifies that the cerium-modified MnO_x/TiO_2 catalyst provides better NH_3 chemisorption ability, which improves the SCR activity.

As mentioned previously, the existence of ceria helps in the process of oxidising NO to NO_2, thereby increasing the NO reduction activity [58,138,139]. Unfortunately, pure ceria usually tends to lose its oxygen storage capacity (OSC), ending up in catalyst deactivation, as it is known to be poorly thermostable and undergoes rapid sintering at high reaction temperatures [140,141]. Hence, numerous efforts have been made to address this problem by incorporating another type of metal oxide into the ceria lattice. This would facilitate the formation of mixed oxides or solid solutions [141-143]. Moreover, the catalytic performance of the two mixed oxides will be improved, and a new stable compound with different physiochemical properties and catalytic behaviour can be obtained [140]. Xu et al. [144] developed a CeO_2–TiO_2 mixed oxide catalyst for the SCR of NO with NH_3 in the presence of oxygen using the impregnation method. It was found that the catalyst was able to convert only up to 92% of NO within a 275 to 400 °C working temperature. Gao et al. [37], on the other hand, applied the sol–gel method to prepare the CeO_2–TiO_2 catalysts for SCR-NH_3 of NO. The main focus of the study was to enhance the catalyst performance by achieving better dispersion of ceria onto the TiO_2 support. From the activity results, it could be summarised that the CeO_2–TiO_2 catalyst prepared by the sol–gel method was highly active in the presence of oxygen. The CeO_2–TiO_2 catalyst with a 0.6 mass ratio was found to be the most optimum metal loading value that would result in a high conversion of NO. About 93.4 to 98.6% of NO was converted at a reaction temperature of 250–450 °C over the Ce(0.6)Ti catalyst. The remarkable performance portrayed by this catalyst is attributed to the strong interaction between Ce and Ti component. Besides that, the high concentration level of amorphous Ce on the catalyst surface as well as the increment in the chemisorbed oxygen or/and weakly bonded species, which is a result of the existence of Ce^{3+} after the introduction of Ce, are also some of the main factors that contribute towards the high catalytic activity.

Al_2O_3 as a catalyst support

Nowadays, gamma alumina (γ-Al_2O_3) has also been used as one of the main supports for SCR catalysts. This material has

good physiochemical properties such as high specific area, high temperature resistance to inertia in both acid and alkali media, as well as excellent dispersion of the active component [60]. The γ-Al_2O_3 support is highly suitable for the SCR reaction since SCR is closely associated with the acidity of the catalyst, whereas the γ-Al_2O_3 surface occupied with both Brønsted and Lewis acid sites can easily absorb alkaline gas [145,146]. Recently, numerous types of Ce-based catalysts have been reported, such as CeO_2/Al_2O_3 [147], MnO_x–CeO_y/γ-Al_2O_3 [148], and copper-modified Al–Ce-PILC [149]. Unfortunately, some of the Ce-based catalyst supported on Al_2O_3 have poor resistance against sulphur poisoning, which limits their application, especially in marine diesel engines [60]. Recently, many studies have implemented MoO_3 as a second metal in the catalyst. MoO_3 has a high compatibility with SO_2, excellent resistance to arsenic poisoning, promotes the adsorption of ammonia, and has a strong solid acid content that enhances the acidity of the catalyst [150,151]. Liu et al. [152] found that high NO conversion was achieved at a broad temperature range of 300 to 450 °C, when 5% of MoO_3 was loaded onto the CeO_2/TiO_2 catalyst. Lietti et al. [153] reported that the NO conversion improved as Mo was added onto the V_2O_5/TiO_2 catalyst. Wang et al. [154] suggested that a high NO conversion could be obtained when MoO_3 is impregnated with the HZSM-5 zeolite catalyst. Hence, Yan et al. [60] worked on developing a series of CeO_2/Al_2O_3 and $CeMo_xO_y/Al_2O_3$ catalysts using an extrusion method in order to study the best catalytic performance of NO_x activity. It was found that the molybdenum additives ($CeMo_xO_y/Al_2O_3$) portrayed more excellent catalytic activity than the CeO_2/Al_2O_3 catalyst. About 95% of NO was converted over 250 to 430 °C

Table 5: Summary on the reaction conditions and NO activity for non-carbon supported catalysts.

Catalyst	Preparation method Activation conditions									
	Reaction conditions							Best NO removal		Refs.
	NO (ppm)	NH_3 (ppm)	O_2 (%)	SO_2 (ppm)	Balance (gas)	Flow rate (mL/min)	GSHV (h^{-1})	Conversion (%)	Temperature (°C)	
CuCe/ZSM-5	conventional ion-exchange calcination: 600 °C/4 h									
	1000	1000	10	–	N_2	–	15,000	95	148–427	[63]
Mn/CeTi Mn/CeSn	inverse co-precipitation calcination: 550 °C/5 h									
	500	500	5	100	N_2	–	60,000	>90	175–300	[155]
M_xO_y–V_2O_5–WO_3/TiO_2	impregnation calcination: 550 °C/3 h (Air)									
	1000	1000	10	–	N_2	2.51	60,000	>90	350–495	[59]
Ce–MnO_x/TiO_2	sol-gel calcination: 500 °C/6 h (Air)									
	1000	1000	3	–	N_2	–	40,000	84	80	[58]
$CeMo_xO_y/Al_2O_3$	extrusion calcination: 550 °C/2 h (Air)									
	930	930	10	475	N_2	1200	7,200	>95	250–430	[60]
CeO_2–TiO_2	sol–gel calcination: 500 °C/5 h (Air)									
	1000	1000	3	200	N_2	–	–	98.6	300–400	[124]
Mn/ZSM-5-t	precipitation calcination: 200-700 °C									
	600	600	4.5	–	N_2	300	36,000	≈100	150–390	[51]
γ-Fe_2O_3 α-Fe_2O_3	co-precipitation calcination: 250 °C/2 h (γ-Fe_2O_3), 500 °C/5 h (α-Fe_2O_3)									
	500	500	3	–	N_2	300	47,000	90	200–300	[156]
Ce–Sn–Ti	inverse co-precipitation calcination: 500 °C/6 h									
	800	800	5	200	N_2	500	50,000	>90	280–400	[157]
Fe–Mn/TiO_2	incipient wetness impregnation calcination: 500 °C/6 h (Air)									
	1000	1000	2	100	N_2	100	30,000	≈100	120	[125]

working temperature under a GHSV of 7200 h^{-1}. The best calcination temperature for $CeMo_xO_y/Al_2O_3$ catalyst was at 550 °C. The catalyst also demonstrated high resistance towards H_2O and SO_2 poisoning. The following reasons are some of the best features that reflect the promotional effect of molybdenum additives on the SCR-NH_3 catalytic performance of NO_x: (a) the amount of surface acidity increases when molybdenum is used as additive in the catalyst; (b) the specific surface area increases as molybdenum is applied as additive; (c) a higher proportion of $Ce^{3+}/(Ce^{4+} + Ce^{3+})$ and $O_\alpha/(O + O_\beta)$ on the catalyst surface is produced, which leads to an increment in catalyst activity. Therefore, the $CeMo_xO_y/Al_2O_3$ catalyst can also be applied to control the emission of NO_x in the SCR-NH_3 of NO reaction. Table 5 summarises the reaction conditions and NO activity of non-carbon-based catalyst supports.

Conclusion

Carbon-based and non-carbon-based materials as catalyst supports for the selective catalytic reduction (SCR)-NH_3 of NO have been comprehensively studied over the past few decades. The mechanism of SCR is acknowledged as a complex process that follows both the Langmuir–Hinshelwood and the Eley–Rideal mechanisms. The standard SCR usually has a lower reaction rate than the fast SCR, where the high formation of NO_2 in the latter contributes more efficiently as an oxidising agent in the redox reaction. The modification of catalyst supports, focusing on their physiochemical properties, was thoroughly reviewed. The preparation method is one of the most crucial factors that affect the nature and dispersion of metal loading onto the catalyst surface. Several methodological procedures such as sol–gel, impregnation, extrusion, reflux, and pyridine-thermal are among the more frequently used methods for achieving high catalytic performance. In this review, the performance of carbon-based materials as catalyst supports, including carbon nanotubes, activated carbon, activated carbon fibre, and graphene on the SCR-NH_3 of NO activity was discussed in detailed. In comparison, non-carbon-based catalyst supports such as ZSM-5, TiO_2, and Al_2O_3 were also reviewed. In summary, carbon nanotube-based catalyst supports were found to yield the best NO conversion, even at low operating temperatures, out of all of the catalyst supports studied. Pure CNTs yield low NO conversion and have poor resistance to H_2O and SO_2. However, catalyst modification with other metal oxides (CeO_x, MnO_x, FeO_x, CuO_x) has been proven to be promising in attaining novel catalysts with high NO reduction activity. Even though many attempts have previously been made, scientists need to conduct more in-depth and far-reaching studies in order to achieve the best NO conversion for actual industrial and power emission applications. Moreover, other suggestions of a technical nature are also important to produce high-end research projects. Further recommendations that can be considered are:

1. Implementing the microwave irradiation technique for activation of CNT-based catalyst supports.
2. Performing a research study on simultaneous removal of SO_2 and NO using the best CNT-based supported catalyst.
3. Fundamental study on the electronic interaction between CNTs and metal oxides in the SCR-NH_3 system using a density functional theory (DFT) approach.

Acknowledgements

This work was supported through the Fundamental Research Grant Scheme (FRGS): 203/PJKIMIA/6071335, and USM-NanoMITE Grant (LRGS): 203/PJKIMIA/6720009.

ORCID® iDs

Abdul Rahman Bin Mohamed - https://orcid.org/0000-0002-5418-5456

References

1. Wang, M.; Liu, H.; Huang, Z.-H.; Kang, F. *Chem. Eng. J.* **2014,** *256,* 101–106. doi:10.1016/j.cej.2014.06.108
2. Sumathi, S.; Bhatia, S.; Lee, K. T.; Mohamed, A. R. *J. Hazard. Mater.* **2010,** *176,* 1093–1096. doi:10.1016/j.jhazmat.2009.11.037
3. Liu, C.; Shi, J.-W.; Gao, C.; Niu, C. *Appl. Catal., A* **2016,** *522,* 54–69. doi:10.1016/j.apcata.2016.04.023
4. Valdes, S.; Marban, G.; Fuertes, A. B. *Appl. Catal., B: Environ.* **2003,** *46,* 261–271. doi:10.1016/S0926-3373(03)00217-0
5. Mrad, R.; Aissat, A.; Cousin, R.; Courcot, D.; Siffert, S. *Appl. Catal., A* **2015,** *504,* 542–548. doi:10.1016/j.apcata.2014.10.021
6. You, X.; Sheng, Z.; Yu, D.; Yang, L.; Xiao, X.; Wang, S. *Appl. Surf. Sci.* **2017,** *423,* 845–854. doi:10.1016/j.apsusc.2017.06.226
7. Pan, S.; Luo, H.; Li, L.; Wer, Z.; Huang, B. *J. Mol. Catal. A: Chem.* **2013,** *377,* 154–161. doi:10.1016/j.molcata.2013.05.009
8. Shan, W.; Song, H. *Catal. Sci. Technol.* **2015,** *5,* 4280–4288. doi:10.1039/C5CY00737B
9. Li, J.; Chang, H.; Ma, L.; Hao, J.; Yang, R. T. *Catal. Today* **2011,** *175,* 147–156. doi:10.1016/j.cattod.2011.03.034
10. Cao, F.; Su, S.; Xiang, J.; Wang, P.; Hu, S.; Sun, L.; Zhang, A. *Fuel* **2015,** *139,* 232–239. doi:10.1016/j.fuel.2014.08.060
11. Li, Y.; Wan, Y.; Li, Y.; Zhan, S.; Guan, Q.; Tian, Y. *ACS Appl. Mater. Interfaces* **2016,** *8,* 5224–5233. doi:10.1021/acsami.5b10264
12. Rahmaninejad, F.; Gavaskar, V. S.; Abbasian, J. *Appl. Catal., B: Environ.* **2012,** *119–120,* 297–303. doi:10.1016/j.apcatb.2012.03.005
13. Shen, B.; Wang, Y.; Wang, F.; Liu, T. *Chem. Eng. J.* **2014,** *236,* 171–180. doi:10.1016/j.cej.2013.09.085
14. Macleod, N.; Lambert, R. M. *Appl. Catal., B: Environ.* **2002,** *35,* 269–279. doi:10.1016/S0926-3373(01)00264-8
15. Pereira, M. V. L.; Nicolle, A.; Berthout, D. *Catal. Today* **2015,** *258,* 424–431. doi:10.1016/j.cattod.2015.03.027
16. Jin, R.; Liu, Y.; Wu, Z.; Wang, H.; Gu, T. *Chemosphere* **2010,** *78,* 1160–1166. doi:10.1016/j.chemosphere.2009.11.049
17. Lázaro, M. J.; Ascaso, S.; Pérez-Rodríguez, S.; Calderón, J. C.; Gálvez, M. E.; Nieto, M. J.; Moliner, R.; Boyano, A.; Sebastián, D.; Alegre, C.; Calvillo, L.; Celorrio, V. *C. R. Chim.* **2015,** *18,* 1229–1241. doi:10.1016/j.crci.2015.06.006

18. Chuang, K.-H.; Lu, C.-Y.; Wey, M.-Y.; Huang, Y.-N. *Appl. Catal., A* **2011,** *397,* 234–240. doi:10.1016/j.apcata.2011.03.003
19. Cha, W.; Ehrman, S. H.; Jurng, J. *J. Environ. Chem. Eng.* **2016,** *4,* 556–563. doi:10.1016/j.jece.2015.10.033
20. Nova, I.; Ciardelli, C.; Tronconi, E.; Chatterjee, D.; Bandl-Konrad, B. *Catal. Today* **2006,** *114,* 3–12. doi:10.1016/j.cattod.2006.02.012
21. Liu, Z.; Yi, Y.; Zhang, S.; Zhu, T.; Zhu, J.; Wang, J. *Catal. Today* **2013,** *216,* 76–81. doi:10.1016/j.cattod.2013.06.009
22. Liu, Z.; Su, H.; Chen, B.; Li, J.; Woo, S. I. *Chem. Eng. J.* **2016,** *229,* 255–262. doi:10.1016/j.cej.2016.04.100
23. Xu, H.; Wang, Y.; Cao, Y.; Fang, Z.; Lin, T.; Gong, M.; Chen, Y. *Chem. Eng. J.* **2014,** *240,* 62–73. doi:10.1016/j.cej.2013.11.053
24. Wei, Z. S.; Zeng, G. H.; Xie, Z. R.; Ma, C. Y.; Liu, X. H.; Sun, J. L.; Liu, L. H. *Fuel* **2011,** *90,* 1599–1603. doi:10.1016/j.fuel.2010.11.021
25. Shi, Y.; Chen, S.; Sun, H.; Shu, Y.; Quan, X. *Catal. Commun.* **2013,** *42,* 10–13. doi:10.1016/j.catcom.2013.07.036
26. Chen, L.; Li, J.; Ge, M.; Ma, L.; Chang, H. *Chin. J. Catal.* **2011,** *32,* 836–841. doi:10.1016/S1872-2067(10)60195-7
27. Liu, F.; Asakura, K.; He, H.; Liu, Y.; Shan, W.; Shi, X.; Zhang, C. *Catal. Today* **2011,** *164,* 520–527. doi:10.1016/j.cattod.2010.10.008
28. Zhang, D.; Zhang, L.; Fang, C.; Gao, R.; Qian, Y.; Shi, L.; Zhang, J. *RSC Adv.* **2013,** *3,* 8811–8819. doi:10.1039/c3ra41400k
29. Sohrabi, S.; Akhlaghian, F. *J. Nanostruct. Chem.* **2016,** *6,* 93–102. doi:10.1007/s40097-015-0182-x
30. Chong, S.; Zhang, G.; Zhang, N.; Liu, J.; Zhu, Y.; Huang, T.; Fang, S. *Ultrason. Sonochem.* **2016,** *32,* 231–240. doi:10.1016/j.ultsonch.2016.03.019
31. Zhang, H.; Chu, W.; Zou, C.; Huang, Z.; Ye, Z.; Zhu, L. *Catal. Lett.* **2011,** *141,* 438–444. doi:10.1007/s10562-010-0536-4
32. Yang, Y.; Chiang, K.; Burke, N. *Catal. Today* **2011,** *178,* 197–205. doi:10.1016/j.cattod.2011.08.028
33. Dong, Y.; Ren, X.; Wang, M.; He, Q.; Chang, L.; Bao, W. *J. Energy Chem.* **2013,** *22,* 783–789. doi:10.1016/S2095-4956(13)60104-7
34. Jeong, B.; Ye, B.; Kim, E.-S.; Kim, H.-D. *Catal. Commun.* **2017,** *93,* 15–19. doi:10.1016/j.catcom.2017.01.022
35. Qi, K.; Xie, J.; Fang, D.; Li, F.; He, F. *Chin. J. Catal.* **2017,** *38,* 845–852. doi:10.1016/S1872-2067(17)62814-6
36. Nam, K. B.; Kwon, D. W.; Hong, S. C. *Appl. Catal., A* **2017,** *542,* 55–62. doi:10.1016/j.apcata.2017.05.017
37. Gao, X.; Jiang, Y.; Zhong, Y.; Luo, Z.; Cen, K. *J. Hazard. Mater.* **2010,** *174,* 734–739. doi:10.1016/j.jhazmat.2009.09.112
38. Yeoh, W.-M.; Lee, K.-Y.; Chai, S.-P.; Lee, K.-T.; Mohamed, A. R. *J. Phys. Chem. Solids* **2013,** *74,* 1553–1559. doi:10.1016/j.jpcs.2013.05.023
39. Xiong, Z.-b.; Peng, B.; Zhou, F.; Wu, C.; Lu, W.; Jin, J.; Ding, S.-f. *Powder Technol.* **2017,** *319,* 19–25. doi:10.1016/j.powtec.2017.06.037
40. Yao, X.; Chen, L.; Kong, T.; Ding, S.; Luo, Q.; Yang, F. *Chin. J. Catal.* **2017,** *38,* 1423–1430. doi:10.1016/S1872-2067(17)62868-7
41. Zeng, Y.; Wang, T.; Zhang, S.; Wang, Y.; Zhong, Q. *Appl. Surf. Sci.* **2017,** *411,* 227–234. doi:10.1016/j.apsusc.2017.03.107
42. Zhu, L.; Zeng, Y.; Zhang, S.; Deng, J.; Zhong, Q. *J. Environ. Sci.* **2017,** *54,* 227–287. doi:10.1016/j.jes.2016.09.014
43. Noor Azeerah, A.; Haliza, A. A.; Zulina, A. M.; Zainab, I. *Co-precipitation technology for preparation of solid catalyst in oleochemical processes;* MPOB Information Series, Vol. TT-524; 2012.
44. Zhang, Y.; Zheng, Y.; Wang, X.; Lu, X. *Catal. Commun.* **2015,** *62,* 57–61. doi:10.1016/j.catcom.2014.12.023
45. Zhang, F.; Zhang, S.; Guan, N.; Schreier, E.; Richter, M.; Eckelt, R.; Fricke, R. *Appl. Catal., B: Environ.* **2007,** *73,* 209–219. doi:10.1016/j.apcatb.2006.12.009
46. Sun, P.; Guo, R.-t.; Liu, S.-m.; Wang, S.-x.; Pan, W.-g.; Li, M.-y. *Appl. Catal., A* **2017,** *531,* 129–138. doi:10.1016/j.apcata.2016.10.027
47. Qi, G.; Yang, R. T. *Appl. Catal., B: Environ.* **2003,** *44,* 217–225. doi:10.1016/S0926-3373(03)00100-0
48. Debecker, D. P.; Hulea, V.; Mutin, P. H. *Appl. Catal., A* **2013,** *451,* 192–206. doi:10.1016/j.apcata.2012.11.002
49. Fan, M.-S.; Abdullah, A. Z.; Bhatia, S. *ChemCatChem* **2009,** *1,* 192–208. doi:10.1002/cctc.200900025
50. Su, Y.; Fan, B.; Wang, L.; Liu, Y.; Huang, B.; Fu, M.; Chen, L.; Ye, D. *Catal. Today* **2013,** *201,* 115–121. doi:10.1016/j.cattod.2012.04.063
51. Lou, X.; Liu, P.; Li, J.; Li, Z.; He, K. *Appl. Surf. Sci.* **2014,** *307,* 382–387. doi:10.1016/j.apsusc.2014.04.041
52. Bai, S.; Li, H.; Wang, L.; Guan, Y.; Jiang, S. *Catal. Lett.* **2014,** *144,* 216–221. doi:10.1007/s10562-013-1157-5
53. Fang, C.; Zhang, D.; Shi, L.; Gao, R.; Li, H.; Ye, L.; Zhang, J. *Catal. Sci. Technol.* **2013,** *3,* 803–811. doi:10.1039/C2CY20670F
54. Bai, S.; Jiang, S.; Li, H.; Guan, Y. *Chin. J. Chem. Eng.* **2015,** *23,* 516–519. doi:10.1016/j.cjche.2014.07.003
55. Wang, X.; Zheng, Y.; Xu, Z.; Liu, X.; Zhang, Y. *Catal. Commun.* **2014,** *50,* 34–37. doi:10.1016/j.catcom.2014.02.016
56. Ma, Z.; Yang, H.; Li, Q.; Zheng, J.; Zhang, X. *Appl. Catal., A* **2012,** *427–428,* 43–48. doi:10.1016/j.apcata.2012.03.028
57. Wang, X.; Zheng, Y.; Lin, J. *Catal. Commun.* **2013,** *37,* 96–99. doi:10.1016/j.catcom.2013.03.035
58. Wu, Z.; Jin, R.; Liu, Y.; Wang, H. *Catal. Commun.* **2008,** *9,* 2217–2220. doi:10.1016/j.catcom.2008.05.001
59. Zhang, Q.-m.; Song, C.-l.; Lv, G.; Bin, F.; Pang, H.-t.; Song, J.-o. *J. Ind. Eng. Chem.* **2015,** *24,* 79–86. doi:10.1016/j.jiec.2014.09.012
60. Yan, W.; Shen, Y.; Zhu, S.; Jin, Q.; Liu, Y.; Li, X. *Catal. Lett.* **2016,** *146,* 1221–1230. doi:10.1007/s10562-016-1739-0
61. Wu, C.; Sun, X.; Shen, B.; Williams, P. T. *J. Energy Inst.* **2014,** *87,* 367–371. doi:10.1016/j.joei.2014.03.024
62. Dou, B.; Lv, G.; Wang, C.; Hao, Q.; Hui, K. *Chem. Eng. J.* **2015,** *270,* 549–556. doi:10.1016/j.cej.2015.02.004
63. Muradov, N.; Smith, F.; T-Raissi, A. *Catal. Today* **2005,** *102–103,* 225–233. doi:10.1016/j.cattod.2005.02.018
64. Rodgiguez-Reinoso, F. *Carbon* **1998,** *36,* 159–175. doi:10.1016/S0008-6223(97)00173-5
65. Santos, A.; Yustos, P.; Quintanilla, A.; García-Ochoa, F. *Top. Catal.* **2005,** *33,* 181–192. doi:10.1007/s11244-005-2524-2
66. Auer, E.; Freund, A.; Pietsch, J.; Tacke, T. *Appl. Catal., A* **1998,** *173,* 259–271. doi:10.1016/S0926-860X(98)00184-7
67. Stüber, F.; Font, J.; Fortuny, A.; Bengoa, C.; Eftaxiaz, A.; Fabregat, A. *Top. Catal.* **2005,** *33,* 3–50. doi:10.1007/s11244-005-2497-1
68. Li, X.; Dong, Z.; Dou, J.; Yu, J.; Tahmasebi, A. *Fuel Process. Technol.* **2016,** *148,* 91–98. doi:10.1016/j.fuproc.2016.02.030
69. Samojeden, B.; Grzybek, T. *Energy* **2016,** *116,* 1481–1491. doi:10.1016/j.energy.2016.04.059
70. Zhang, D.; Zhang, L.; Shi, L.; Fang, C.; Li, H.; Gao, R.; Huang, L.; Zhang, J. *Nanoscale* **2013,** *5,* 1127–1136. doi:10.1039/c2nr33006g
71. Planeix, J. M.; Coustel, N.; Coq, B.; Brotons, V.; Kumbhar, P. S.; Dutarte, R.; Geneste, P.; Bernier, P.; Ajayan, P. M. *J. Am. Chem. Soc.* **1994,** *116,* 7935–7936. doi:10.1021/ja00096a076
72. Santillan-Jimenez, E.; Miljković-Kocić, V.; Crocker, M.; Wilson, K. *Appl. Catal., B: Environ.* **2011,** *102,* 1–8. doi:10.1016/j.apcatb.2010.09.032

73. Santillan-Jimenez, E.; Crocker, M.; Bueno-López, A.; Salinas-Martínez de Lecea, C. *Ind. Eng. Chem. Res.* **2011,** *50,* 7191–7200. doi:10.1021/ie200054u
74. Luo, J. Z.; Gao, L. Z.; Leung, Y. L.; Au, C. T. *Catal. Lett.* **2000,** *66,* 91–97. doi:10.1023/A:1019035220233
75. Long, R. Q.; Yang, R. T. *Ind. Eng. Chem. Res.* **2001,** *40,* 4288–4291. doi:10.1021/ie000976k
76. Huang, Z.; Zhu, Z.; Liu, Z.; Liu, Q. *J. Catal.* **2003,** *214,* 213–219. doi:10.1016/S0021-9517(02)00157-4
77. Phil, H. H.; Reddy, M. P.; Kumar, P. A.; Ju, L. K.; Hyo, J. S. *Appl. Catal., B: Environ.* **2008,** *78,* 301–308. doi:10.1016/j.apcatb.2007.09.012
78. Li, Q.; Yang, H.; Ma, Z.; Zhang, X. *Catal. Commun.* **2012,** *17,* 8–12. doi:10.1016/j.catcom.2011.10.008
79. Zhu, Z.; Niu, H.; Liu, Z.; Liu, S. *J. Catal.* **2000,** *195,* 268–278. doi:10.1006/jcat.2000.2961
80. Shen, Y.; Zhu, S. *Catal. Sci. Technol.* **2012,** *2,* 1806–1810. doi:10.1039/c2cy20238g
81. Jang, S.; Li, J.; Wang, C.; Chen, J.; Ma, L.; Chang, H.; Chen, L.; Peng, Y.; Yan, N. *Appl. Catal., B: Environ.* **2012,** *117–118,* 73–80. doi:10.1016/j.apcatb.2012.01.001
82. Wang, L.; Huang, B.; Su, Y.; Zhaou, G.; Wang, K.; Luo, H.; Ye, D. *Chem. Eng. J.* **2012,** *192,* 232–241. doi:10.1016/j.cej.2012.04.012
83. Wang, X.; Zheng, Y.; Xu, Z.; Liu, Y.; Wang, X. *Catal. Sci. Technol.* **2014,** *4,* 1738–1741. doi:10.1039/C4CY00026A
84. Tang, X.; Hao, J.; Xu, W.; Li, J. *Catal. Commun.* **2007,** *8,* 329–334. doi:10.1016/j.catcom.2006.06.025
85. Kijlstra, W. S.; Brands, D. S.; Smit, H. I.; Poels, E. K.; Bliek, A. *J. Catal.* **1997,** *171,* 219–230. doi:10.1006/jcat.1997.1789
86. Cao, F.; Zhong, K.; Gao, A.; Chen, C.; Li, Q.; Chen, Q. *J. Phys. Chem. B* **2007,** *111,* 1724–1728. doi:10.1021/jp0661037
87. Chen, W.; Pan, X.; Willinger, M.-G.; Su, D. S.; Bao, X. *J. Am. Chem. Soc.* **2006,** *128,* 3136–3137. doi:10.1021/ja056721l
88. Chen, W.; Pan, X.; Bao, X. *J. Am. Chem. Soc.* **2007,** *129,* 7421–7426. doi:10.1021/ja0713072
89. Zhu, Z.; Liu, Z.; Niu, H.; Liu, S.; Hu, T.; Xie, Y. *J. Catal.* **2001,** *197,* 6–16. doi:10.1006/jcat.2000.3052
90. Chen, J. P.; Yang, R. T. *J. Catal.* **1990,** *125,* 411–420. doi:10.1016/0021-9517(90)90314-A
91. Chen, J. P.; Yang, R. T. *J. Catal.* **1993,** *139,* 277–288. doi:10.1006/jcat.1993.1023
92. Huang, B.; Huang, R.; Jin, D.; Ye, D. *Catal. Today* **2007,** *126,* 279–283. doi:10.1016/j.cattod.2007.06.002
93. Buitrago, R.; Ruiz-Martínez, J.; Serrano-Ruiz, J. C.; Rodríguez-Reinoso, F.; Sepúlved-Escribano, A. *J. Colloid Interface Sci.* **2012,** *383,* 148–154. doi:10.1016/j.jcis.2012.06.026
94. Zhang, S.; Li, Q.; Zhong, H. *Appl. Catal., A: Gen.* **2012,** *435–436,* 156–162. doi:10.1016/j.apcata.2012.05.049
95. Tsen, H.-H.; Lub, C.-Y.; Chang, F.-Y.; Weyd, M.-Y.; Chang, H.-T. *Chem. Eng. J.* **2011,** *169,* 135–143. doi:10.1016/j.cej.2011.02.069
96. Zhu, L.; Huang, B.; Wang, W.; Wei, Z.; Ye, D. *Catal. Commun.* **2011,** *12,* 394–398. doi:10.1016/j.catcom.2010.10.028
97. Mochida, I.; Koraia, Y.; Shirahama, M.; Kawano, S.; Hada, T.; Seo, Y.; Yoshikawa, M.; Yasutake, A. *Carbon* **2000,** *38,* 227–239. doi:10.1016/S0008-6223(99)00179-7
98. Yoon, K. S.; Ryu, S. K. *Korean J. Chem. Eng.* **2010,** *27,* 1882–1886. doi:10.1007/s11814-010-0294-4
99. Sousa, J. P. S.; Pereira, M. F. R.; Figueiredo, J. L. *Fuel Process. Technol.* **2013,** *106,* 727–733. doi:10.1016/j.fuproc.2012.10.008
100. Klinik, J.; Samojeden, B.; Grzybek, T.; Suprun, W.; Papp, H.; Gläser, R. *Catal. Today* **2011,** *176,* 303–308. doi:10.1016/j.cattod.2010.12.009
101. Boyano, A.; Iritia, M. C.; Malpartida, I.; Larrubia, M. A.; Alemany, L. J.; Moliner, R.; Lázaro, M. J. *Catal. Today* **2008,** *137,* 222–227. doi:10.1016/j.cattod.2008.02.010
102. Muñiz, J.; Marbán, G.; Fuertes, A. B. *Appl. Catal., B: Environ.* **1999,** *23,* 25–35. doi:10.1016/S0926-3373(99)00063-6
103. Lázaro, M. L.; Boyano, A.; Gálvez, M. E.; Izquierdo, M. T.; Garcia-Bordejé, E.; Ruiz, C.; Juan, R.; Moliner, R. *Catal. Today* **2008,** *137,* 215–221. doi:10.1016/j.cattod.2007.11.007
104. Gálvez, M. E.; Lázaro, M. J.; Moliner, R. *Catal. Today* **2005,** *102–103,* 142–147. doi:10.1016/j.cattod.2005.02.020
105. Huang, M.-C.; Teng, H. *Carbon* **2003,** *41,* 951–957. doi:10.1016/S0008-6223(02)00436-0
106. Gao, X.; Liu, S.; Zhang, Y.; Du, X.; Luo, Z.; Cen, K. *Catal. Today* **2011,** *175,* 164–170. doi:10.1016/j.cattod.2011.03.058
107. Yang, N.; Yu, J.-l.; Dou, J.-x.; Tahmasebi, A.; Song, H.; Moghtaderi, B.; Lucas, J.; Wall, T. *Fuel Process. Technol.* **2016,** *152,* 102–107. doi:10.1016/j.fuproc.2016.06.010
108. Lua, P.; Li, C.; Zenga, G.; Heb, L.; Penga, D.; Cuia, H.; Li, S.; Zhai, Y. *Appl. Catal., B: Environ.* **2010,** *96,* 157–161. doi:10.1016/j.apcatb.2010.02.014
109. Athappan, A.; Sattler, M. L.; Sethupathi, S. *J. Environ. Chem. Eng.* **2015,** *3,* 2502–2513. doi:10.1016/j.jece.2015.08.028
110. Castegnaro, M. V.; Killian, A. S.; Baibich, I. M.; Alves, M. C. M.; Morais, J. *Langmuir* **2013,** *29,* 7125–7133. doi:10.1021/la401460c
111. Rathrore, R. S.; Srivastava, D. K.; Agarwal, A. K.; Verma, N. *J. Hazard. Mater.* **2010,** *173,* 211–222. doi:10.1016/j.jhazmat.2009.08.071
112. Talukdar, P.; Bhaduri, B.; Verma, N. *Ind. Eng. Chem. Res.* **2014,** *53,* 12537–12547. doi:10.1021/ie502043e
113. Lu, X.; Song, C.; Chang, C.-C.; Yeng, Y.; Tong, Z.; Tang, X. *Ind. Eng. Chem. Res.* **2014,** *53,* 11601–11610. doi:10.1021/ie5016969
114. Guo, Z.; Wang, M.; Huang, Z.-H.; Kang, F. *Carbon* **2015,** *87,* 282–291. doi:10.1016/j.carbon.2015.02.037
115. Xiao, X.; Sheng, Z.; Yang, L.; Dong, F. *Catal. Sci. Technol.* **2016,** *6,* 1507–1514. doi:10.1039/C5CY01228G
116. Lu, X.; Song, S.; Jia, C.; Tong, Z.; Tang, X.; Teng, Y. *Chem. Eng. J.* **2015,** *260,* 776–784. doi:10.1016/j.cej.2014.09.058
117. Wang, M.-X.; Huang, Z.-H.; Shen, K.; Kang, F.; Liang, K. *Catal. Today* **2013,** *201,* 109–114. doi:10.1016/j.cattod.2012.05.050
118. Su, W.; Lu, X.; Jia, S.; Wang, J.; Ma, H.; Xing, Y. *Catal. Lett.* **2015,** *145,* 1446–1456. doi:10.1007/s10562-015-1550-3
119. Jiao, J.-Z.; Li, S.-H.; Huang, B.-C. *Acta Phys.-Chim. Sin.* **2015,** *31,* 1383–1390. doi:10.3866/PKU.WHXB201504292
120. Fidalgo, B.; Menéndez, J. A. *Chin. J. Catal.* **2011,** *32,* 207–216. doi:10.1016/S1872-2067(10)60166-0
121. Greenhalgh, B.; Fee, M.; Dobri, A.; Moir, J.; Burich, R.; Charland, J.-P.; Stanciulescu, M. *J. Mol. Catal. A: Chem.* **2010,** *333,* 121–127. doi:10.1016/j.molcata.2010.10.008
122. Liu, F.; He, H.; Ding, Y.; Zhang, C. *Appl. Catal., B: Environ.* **2009,** *93,* 194–204. doi:10.1016/j.apcatb.2009.09.029
123. Picasso, G.; Gutiérrez, M.; Pina, M. P.; Herguido, J. *Chem. Eng. J.* **2007,** *126,* 119–130. doi:10.1016/j.cej.2006.09.005

124. Katta, L.; Sudarsanam, P.; Thrimurthulu, G.; Reddy, B. M. *Appl. Catal., B: Environ.* **2010,** *101,* 101–108. doi:10.1016/j.apcatb.2010.09.012
125. Laguna, O. H.; Sarria, F. R.; Centeno, M. A.; Odriozola, J. A. *J. Catal.* **2010,** *276,* 360–370. doi:10.1016/j.jcat.2010.09.027
126. Pang, L.; Fan, C.; Shao, L.; Song, K.; Yi, J.; Cai, X.; Wang, J.; Kang, M.; Li, T. *Chem. Eng. J.* **2014,** *253,* 394–401. doi:10.1016/j.cej.2014.05.090
127. Thirupathi, B.; Smirniotis, P. G. *Catal. Lett.* **2011,** *141,* 1399–1404. doi:10.1007/s10562-011-0678-z
128. Shan, W.; Liu, F.; He, H.; Shi, X.; Zhang, C. *Appl. Catal., B: Environ.* **2012,** *115–116,* 100–106. doi:10.1016/j.apcatb.2011.12.019
129. Ma, Z.; Weng, D.; Wu, X.; Si, Z.; Wang, B. *Catal. Commun.* **2012,** *27,* 97–100. doi:10.1016/j.catcom.2012.07.006
130. Shi, A.; Wang, X.; Yu, T.; Shen, M. *Appl. Catal., B: Environ.* **2011,** *106,* 359–369. doi:10.1016/j.apcatb.2011.05.040
131. Lee, D. W.; Yoo, B. R. *J. Ind. Eng. Chem.* **2014,** *20,* 3947–3959. doi:10.1016/j.jiec.2014.08.004
132. Wu, Z.; Jiang, B.; Liu, Y.; Zhao, W.; Guan, B. *J. Hazard. Mater.* **2007,** *145,* 488–494. doi:10.1016/j.jhazmat.2006.11.045
133. Ettireddy, P. R.; Ettireddy, N.; Mamedov, S.; Boolchand, P.; Smirniotis, P. G. *Appl. Catal., B: Environ.* **2007,** *76,* 123–134. doi:10.1016/j.apcatb.2007.05.010
134. Valdés-Solís, T.; Marbán, G.; Fuertes, A. B. *Catal. Today* **2001,** *69,* 259–264. doi:10.1016/S0920-5861(01)00378-9
135. Qi, G.; Yang, R. T.; Chang, R. *Appl. Catal., B: Environ.* **2004,** *51,* 93–106. doi:10.1016/j.apcatb.2004.01.023
136. Carja, G.; Kameshima, Y.; Okada, L.; Madhusoodana, C. D. *Appl. Catal., B: Environ.* **2007,** *73,* 60–64. doi:10.1016/j.apcatb.2006.06.003
137. Qi, G.; Yang, R. T. *J. Catal.* **2003,** *217,* 434–441. doi:10.1016/S0021-9517(03)00081-2
138. Long, R. Q.; Yang, R. T. *Appl. Catal., B: Environ.* **2000,** *27,* 87–95. doi:10.1016/S0926-3373(00)00140-5
139. Long, R. Q.; Tang, R. T. *J. Am. Chem. Soc.* **1999,** *121,* 5595–5596. doi:10.1021/ja9842262
140. Reddy, N. M.; Khan, A.; Yamada, Y.; Kobayashi, T.; Loridant, S.; Volta, J.-C. *J. Phys. Chem. B* **2003,** *107,* 5162–5167. doi:10.1021/jp0344601
141. Luo, M.; Chen, J.; Chen, L.; Lu, L.; Feng, Z.; Li, C. *Chem. Mater.* **2001,** *13,* 197–202. doi:10.1021/cm000470s
142. Reddy, B. M.; Laskmanan, P.; Khan, A. *J. Phys. Chem. B* **2004,** *108,* 16855–16863. doi:10.1021/jp047217q
143. Wu, Z.; Jiang, B.; Liu, Y.; Wang, H.; Jin, R. *Environ. Sci. Technol.* **2007,** *41,* 5812–5817. doi:10.1021/es0700350
144. Xu, W.; Yu, Y.; Zhang, C.; He, H. *Catal. Commun.* **2008,** *9,* 1453–1457. doi:10.1016/j.catcom.2007.12.012
145. Yan, S.; Wang, X.; Wang, W.; Liu, Z.; Niu, J. *J. Nat. Gas Chem.* **2012,** *21,* 332–338. doi:10.1016/S1003-9953(11)60373-3
146. Tonetto, G. M.; Damiani, D. E. *J. Mol. Catal. A: Chem.* **2003,** *202,* 289–303. doi:10.1016/S1381-1169(03)00214-0
147. Shen, Y.; Zhu, S.; Qiu, T.; Shen, S. *Catal. Commun.* **2009,** *11,* 20–23. doi:10.1016/j.catcom.2009.08.001
148. Qu, L.; Li, C.; Zeng, G.; Zhang, M.; Fu, M.; Ma, J.; Zhan, F.; Luo, D. *Chem. Eng. J.* **2014,** *242,* 76–85. doi:10.1016/j.cej.2013.12.076
149. Lin, Q.; Hao, J.; Li, J.; Ma, Z.; Lin, W. *Catal. Today* **2007,** *126,* 351–358. doi:10.1016/j.cattod.2007.06.007
150. Djerad, S.; Crocoll, M.; Kureti, S.; Tifouti, L.; Weisweiler, W. *Catal. Today* **2006,** *113,* 208–214. doi:10.1016/j.cattod.2005.11.067
151. Djerad, S.; Tifouti, L.; Crocoll, M.; Weisweiler, W. *J. Mol. Catal. A: Chem.* **2004,** *208,* 257–265. doi:10.1016/j.molcata.2003.07.016
152. Liu, Z.; Zhang, S.; Li, J.; Ma, L. *Appl. Catal., B: Environ.* **2014,** *144,* 90–95. doi:10.1016/j.apcatb.2013.06.036
153. Lietti, L.; Nova, I.; Ramis, G.; Dall'Acqua, L.; Busca, G.; Giamello, E.; Forzatti, P.; Bregani, F. *J. Catal.* **1999,** *187,* 419–435. doi:10.1006/jcat.1999.2603
154. Wang, X.; Yu, S.; Yang, H.; Zhang, S. *Appl. Catal., B: Environ.* **2007,** *71,* 246–253. doi:10.1016/j.apcatb.2006.09.014
155. Xiong, Y.; Tang, C.; Tao, X.; Zhang, L.; Li, L.; Wang, X.; Deng, Y.; Gao, F.; Dong, L. *Appl. Catal., A* **2015,** *495,* 206–216. doi:10.1016/j.apcata.2015.01.038
156. Liu, C.; Yang, S.; Ma, L.; Peng, Y.; Hamidreza, A.; Chang, H.; Li, J. *Catal. Lett.* **2013,** *143,* 697–704. doi:10.1007/s10562-013-1017-3
157. Yu, M.; Li, C.; Zeng, G.; Zhou, Y.; Zhang, X.; Xie, Y. *Appl. Surf. Sci.* **2015,** *342,* 174–182. doi:10.1016/j.apsusc.2015.03.052

License and Terms

This is an Open Access article under the terms of the Creative Commons Attribution License (http://creativecommons.org/licenses/by/4.0), which permits unrestricted use, distribution, and reproduction in any medium, provided the original work is properly cited.

The license is subject to the *Beilstein Journal of Nanotechnology* terms and conditions: (https://www.beilstein-journals.org/bjnano)

The definitive version of this article is the electronic one which can be found at:
doi:10.3762/bjnano.9.68

BEILSTEIN JOURNAL OF NANOTECHNOLOGY

Heavy-metal detectors based on modified ferrite nanoparticles

Urszula Klekotka[1], Ewelina Wińska[1], Elżbieta Zambrzycka-Szelewa[1], Dariusz Satuła[2] and Beata Kalska-Szostko[*1]

Full Research Paper

Open Access

Address:
[1]Institute of Chemistry, University of Białystok, Ciołkowskiego 1K, 15-245, Białystok Poland and [2]Faculty of Physics, University of Białystok, Ciołkowskiego 1L, 15-245, Białystok, Poland

Email:
Beata Kalska-Szostko[*] - kalska@uwb.edu.pl

* Corresponding author

Keywords:
ferrite nanoparticles; heavy metal detection; materials characterization; water purification

Beilstein J. Nanotechnol. **2018,** *9,* 762–770.
doi:10.3762/bjnano.9.69

Received: 13 October 2017
Accepted: 30 January 2018
Published: 28 February 2018

This article is part of the Thematic Series "Energy conversion, storage and environmental remediation using nanomaterials".

Guest Editor: W.-J. Ong

© 2018 Klekotka et al.; licensee Beilstein-Institut.
License and terms: see end of document.

Abstract

In this work, we analyze artificial heavy-metal solutions with ferrite nanoparticles. Measurements of adsorption effectiveness of different kinds of particles, pure magnetite or magnetite doped with calcium, cobalt, manganese, or nickel ions, were carried out. A dependence of the adsorption efficiency on the composition of the inorganic core has been observed. Ferrites surfaces were modified by phthalic anhydride (PA), succinic anhydride (SA), acetic anhydride (AA), 3-phosphonopropionic acid (3-PPA), or 16-phosphohexadecanoic acid (16-PHDA) to compare the adsorption capability of the heavy metals Cd, Cu and Pb. The obtained nanoparticles were structurally characterized by transmission electron microscopy (TEM), X-ray diffraction (XRD), Fourier transform infrared spectroscopy (FTIR) and Mössbauer spectroscopy. The amounts of Cd, Cu and Pb were measured out by atomic absorption spectroscopy (AAS) and energy dispersive X-ray (EDX) as comparative techniques. The performed study shows that SA linker appears to be the most effective in the adsorption of heavy metals. Moreover, regarding the influence of the composition of the inorganic core on the detection ability, the most effective ferrite $Mn_{0.5}Fe_{2.5}O_4$ was selected for discussion. The highest heavy-metal adsorption capability and universality was observed for SA as a surface modifier.

Introduction

Many research reports show that magnetic nanoparticles can be widely used in medicine for drug delivery, implants manufacture, as components of contrast agents in magnetic resonance imaging (MRI) as well as active centers in hyperthermia treatment [1]. The use of magnetic nanoparticles in drug delivery allows for a significant reduction of the amount of applied medications [2]. Also, one can imagine sensors based on nanostructures possessing very high sensitivity towards particular species due to the high surface area and specific reactivity [3,4]. However, very often not only surface termination but also core composition is of crucial importance for the required functionality.

In food industry or water purification, nanotechnology has begun to play a non-negligible role. However, to date it is considered to be a relatively new application area. Currently,

nanostructures are mostly used to improve the quality of food, prolong its storage life, detect contaminants [5] and receive intelligent packaging [6]. A lot of research is focused on the reduction of the amount of fat in the products through the use of nanotechnological solutions. The idea to use fat in the forms of nanoemulsions, e.g., in cream or mayonnaise, became very popular in a novel production process [7]. Moreover, many studies are carried out on sensors based on nanostructures in the detection and removal of toxins, chemical compounds and other pathogens from food. Some nanosensors are designed to improve food–body assimilation by blocking cholesterol or allergens, which are frequently encountered in groceries [8]. Nanomaterials are also widely tested as constituents in the production of modern functional packaging. Packages enriched by nanostructures are not only stronger but also often become "intelligent" and sometimes they can fix themselves after a slight damage. Changing the package color informs that food is not suitable for consumption because either its expiry date passed or packed edibles started to emit harmful compounds [9].

Recent studies show that nanoparticles can be widely used as heavy-metal detectors. Among others, silver [10,11], gold [12] and also magnetic nanoparticles [13,14] usually doped with other elements (e.g., Ca, Mn) [15,16] have been tested for this purpose. Therefore, detailed studies on adsorption efficiency on doped magnetite nanoparticles are very interesting and innovative in order to understand the importance of core composition and surface modification.

The aim of the study is to examine the efficiency of adsorption of heavy metals in artificial solutions on doped magnetite nanoparticles (Ca, Co, Mn, Ni) surface-modified with PA, SA, AA, 3-PPA or 16-PHDA linkers.

Experimental

Reagents and solutions

Chemicals used in this work were of analytical grade and they were used without any purification. $FeCl_2{\cdot}4H_2O$, $FeCl_3{\cdot}6H_2O$, NH_3 (25%), $CaCl_2$ (anhydrous), $MnCl_2$ (anhydrous), $NiCl_2$ (anhydrous), $CuSO_4$ (anhydrous), $PbCl_2$ (anhydrous), $Cd(NO_3)_2{\cdot}4H_2O$, and acetic anhydride (AA) were purchased from Polish Chemical Reagents (POCH). $CoCl_2$ (anhydrous), tetrabutylammonium hydroxide (TBAOH) (40% in water), phthalic anhydride (PA), 3-phosphonopropionic acid (3-PPA), 16-phosphonohexadecanoic acid (16-PHDA) and phosphate-buffered saline (PBS) were received from Sigma-Aldrich.

Apparatus

The structure and morphology of nanoparticles used in the detection experiments were analyzed by X-ray diffraction (XRD) (Agilent Technologies SuperNova diffractometer with micro-focused Mo $K\alpha_2$ (λ = 0.713067 Å) radiation and transmission electron microscopy (TEM) (FEI Tecnai G2 X-TWIN 200 kV microscope). For TEM imaging the nanoparticles after dissolution in ethanol were drop-cast on a carbon-covered 400 mesh Cu grid. The XRD apparatus requires the placement of a small amount of powder on a nylon loop coated with high-viscosity synthetic oil. Infrared spectra (IR) were collected in a spectral range between 400 and 4000 cm^{-1} and were attained by a Nicolet 6700 spectrometer working in transmission mode as a series of 32 repetitive runs. Here, a small amount of powder was directly placed and squeezed into a diamond window for measurement. Mössbauer spectra (MS) were obtained in constant acceleration mode with a ^{57}Co in Cr matrix source. The spectra were calibrated using α-Fe foil at room temperature. MS absorbers were prepared by mixing a proper amount of particles with BN filler to obtain 1 cm^2 tablets.

The amount of Pb, Cu, and Cd elements in the tested solutions was measured by atomic absorption spectrometry (AAS). Measurements were performed using a high-resolution continuum-source atomic absorption spectrometer ContrAA 700 (Analytik Jena AG, Jena, Germany) equipped with a flame atomizer (burner length: 100 mm). The optical system comprises a continuum light source 300 W high-pressure xenon short-arc lamp XBO 301 (GLE, Berlin, Germany) operating in a ”hot-spot” mode, suitable for all the determination of all elements in the wavelength range from 185 to 900 nm. An air–acetylene flame was used for the determination of Pb, Cd, and Cu under optimized conditions, namely a) Pb: burner height: 7 mm, air–C_2H_2 flow rate: 75 $L{\cdot}h^{-1}$; b) Cu: burner height: 4 mm, air–C_2H_2 flow rate: 65 $L{\cdot}h^{-1}$; c) Cd: burner height: 5 mm, air–C_2H_2 flow rate: 55 $L{\cdot}h^{-1}$. Absorbance signals of all analytes were obtained using three pixels (central pixel ± 1) for each element. All absorbance values are the mean values based on three repetitive measurements. The dynamic background correction technique with reference was used. The quantitative determination of Pb, Cd, and Cu was carried out by the external calibration graph technique.

Synthesis of ferrite nanoparticles doped with Ca^{2+}, Co^{2+}, Mn^{2+}, or Ni^{2+}

To obtain doped ferrite nanoparticles, a modified co-precipitation synthesis of iron(II) and iron(III) chlorides was used [17-19]. As a reference, pure magnetite nanoparticles were also synthesized by the method described below.

In the first step of the synthesis, into each of two three-necked flasks, 0.5% NH_3 solution was placed and deoxygenated with argon for 20 min. Then, TBAOH was injected to each flask and one solution was heated and stirred (40 °C, 20 min) while the

other one was deoxygenated at room temperature. In the next step, a proper amount of $FeCl_3 \cdot 6H_2O$ was added to the heated up flask, and $FeCl_2 \cdot 4H_2O$ to the other one. After 15 min, $FeCl_2$, $CaCl_2$, $CoCl_2$, $MnCl_2$, or $NiCl_2$, were additionally added to the second flask in respective amounts. The resultant solution was finally poured into the flask with $FeCl_3 \cdot 6H_2O$, and the whole mixture was kept at 80 °C for 40 min. Thereafter, the solution was cooled down, removed from the supernatant and washed with deoxygenated acetone. Rinsing was repeated two more times and, finally, the sample was dried by rotary evaporation until a powder was obtained [20,21].

Modification of nanoparticles with phthalic anhydride, succinic anhydride and acetic anhydride

The application of Ca ferrite nanoparticles modified with SiO_2 and phthalic anhydride for the detection of Pb in water and food products was described in the literature [15]. The role of the selected inorganic core, however, was not discussed. The modified nanoparticles used in this study had a selectivity for Pb ions twice of that for other metals. In this paper, we will compare the efficiency of PA with other proposed linkers. For this purpose, every type of prepared ferrite nanoparticles was modified with PA, SA and AA. For the modification solutions of PA, SA or AA in ethanol with a concentration of 100 mM were added to about 8 mg of nanoparticles and stirred for 4 h at room temperature. Then, the functionalized nanoparticles were separated from the solutions using a permanent magnet, washed three times with ethanol and left overnight for drying.

Modification of nanoparticles with 3-PPA and 16-PHDA

Another group of compounds tested and selected for the studies as potential heavy-metal detectors are 3-phosphonopropionic acid (3-PPA) and 16-phosphonohexadecanoic (16-PHDA). Before the modification with 3-PPA or 16-PHDA, nanoparticles were washed firstly in acetone and then ethanol, and placed for about 30 s in an ultrasonic bath to ensure proper particles separation. In the next step, 1 mL of 1 mM solution of 3-PPA or 16-PHDA, respectively, were added to the nanoparticles and left at room temperature for 18 h. After this time the mixture was placed in an ultrasonic bath for 1 min, then the supernatant was removed and the nanoparticles were washed three times with PBS and allowed to dry at room temperature [22]. Figure 1A presents the proposed most probable models of linker adsorption. However, the authors do not exclude other configurations.

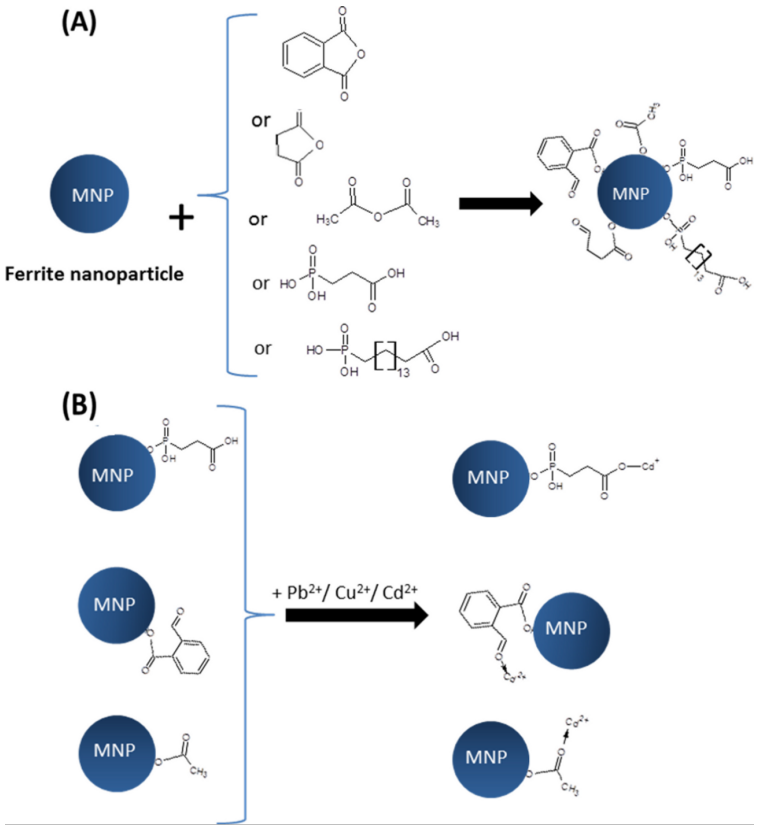

Figure 1: (A) Schematic presentation of the attachment of selected anhydrides and organophosphorus acids to the nanoparticles surface; (B) adsorption of Cu^{2+}, Cd^{2+} or Pb^{2+} to the nanoparticles surface via linkers (B).

Attachment of Pb^{2+}, Cu^{2+} and Cd^{2+} ions

In order to verify if modified nanoparticles are able to detect/select some ions from liquids, aqueous model solutions were prepared. The solutions and particles were analyzed by IR spectroscopy, EDX and AAS measurements after the tests.

For this purpose, approx. 8 mg of surface-modified nanoparticles were added to a 0.1 M aqueous solution of Pb^{2+}, Cu^{2+} and Cd^{2+}. This mixture was stirred for 10 min by a magnetic stirrer. After this time, the liquid was removed and analyzed by AAS to determine the amount of remaining elements. Nanoparticles were left to dry for 4 h at room temperature. A proposed scheme for the binding of heavy metal ions is presented in Figure 1B.

Results and Discussion

Transmission electron microscopy

Prior to any modification of the nanoparticles, their morphology and structural quality was determined. The most informative method is transmission electron microscopy, by which the morphology of the prepared ferrite nanoparticles was analyzed before surface modification. The obtained images for each kind of fabricated ferrites are presented in Figure 2.

The TEM images show that regardless of doping (Ca^{2+}, Co^{2+}, Mn^{2+} or Ni^{2+}), the studied nanoparticles exhibit a similar round shape and average size. In Table 1, diameters of every type of synthesized nanoparticles estimated from TEM images are collected. The obtained average particle sizes are close to those calculated for pure magnetite nanoparticles, which implies that proposed ions do not disturb the crystallization process and used synthesis constituents fulfill the same growth regimes [23].

X-ray diffraction

The fabrication of nonstochiometric compounds affects crystal growth, which is reflected in the crystalization degree. Therefore, examination of the crystallinity of the ferrite nanoparticles was performed by X-ray diffraction. The presence of well-defined sharp patterns proves the incorporation of Ca, Co, Mn and Ni elements into the primary magnetite structure. The obtained diffractograms are depicted in Figure 3.

The XRD patterns show peaks typical for magnetite regardless of the nature of added elements. The 2θ values and the relative intensities unequivocally state the presence of dominate magnetite phase. The most intense reflexes were recognized and indexed to (220), (311), (400), (422), (511), (440), respectively, typical for magnetite [24]. The peak widths, however, are different among the presented samples. This can be caused by chemical modification of the crystallites related to the different ionic radii of the added elements and a resulting slight distortion of the crystal phase. Substitution can take place as a random distribution of particular atoms or as ordered process. Such changes in the structure will cause different modifications of the XRD patterns. The estimation of an average diffraction zone which is related to the crystal size and, therefore, the parti-

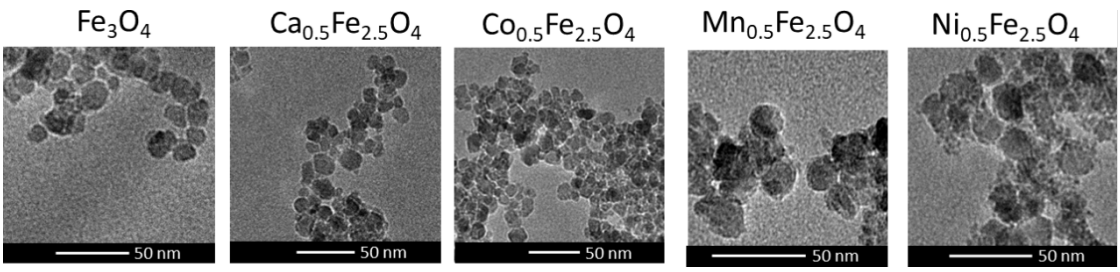

Figure 2: TEM images of prepared ferrite nanoparticles.

Table 1: Table with average crystallite sizes of ferrite nanoparticles estimated from TEM images sizes and calculated from the XRD data.

type of nanoparticles	nanoparticle size [nm] (TEM)	average crystallite size [nm] (XRD)
Fe_3O_4	13 ± 2	13 ± 2
$Ca_{0.5}Fe_{2.5}O_4$	10 ± 2	13 ± 2
$Co_{0.5}Fe_{2.5}O_4$	13 ± 2	13 ± 2
$Mn_{0.5}Fe_{2.5}O_4$	12 ± 2	10 ± 2
$Ni_{0.5}Fe_{2.5}O_4$	14 ± 2	12 ± 2

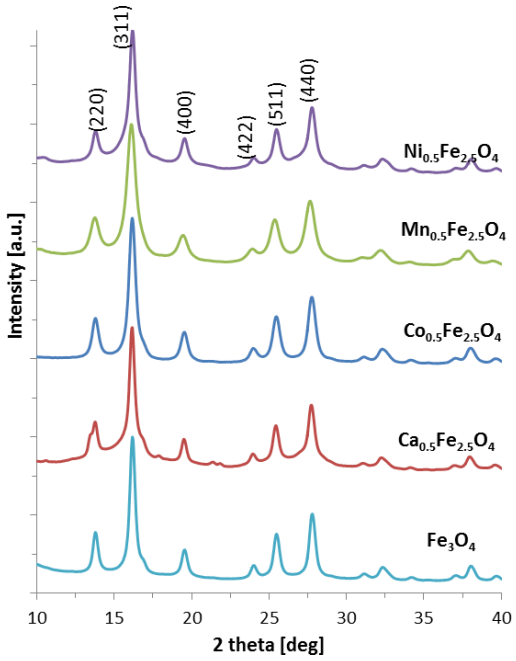

Figure 3: XRD patterns of ferrite nanoparticles.

cle diameter can be calculated by the Scherrer equation (Equation 1). The obtained values are given together with TEM values in Table 1.

$$D = \frac{0.9\lambda}{B_{1/2} \cdot \cos\theta}, \quad (1)$$

where D is the grain size [Å], λ is the wavelength (here 0.7136 Å), $B_{1/2}$ is the full width at half maximum intensity of the (311) peak [rad], and Θ is the diffraction angle [rad]. The average crystallite sizes of nanoparticles presented in Table 1 are similar to each other within the error margin. At the same time, the obtained results of the average grain size estimated on the basis of the TEM images agree with the values calculated from XRD. A numerical analysis of XRD patterns also allows for the assessment of crystal cell parameters, which can be found in Table 2. There, literature bulk values are compared with our findings and both are in satisfactory agreement, which also confirms the successful fabrication of requested structures.

Table 2: Lattice constants (theoretical and calculated from diffraction patterns) [25-29].

	theoretical [Å]	experimental [Å] ±0.05
γ-Fe_2O_3	8.34	8.36
Fe_3O_4	8.39	
$Ca_{0.5}Fe_{2.5}O_4$	—	8.37
$Co_{0.5}Fe_{2.5}O_4$	8.38	8.43
$Mn_{0.5}Fe_{2.5}O_4$	8.51	8.40
$Ni_{0.5}Fe_{2.5}O_4$	8.33	8.36

Infrared spectroscopy

All samples were measured by IR spectroscopy to see if the surface of nanoparticles changes after core modification and surface functionalization. This method was also expected to serve as a reference for the detection of heavy metals. However, the obtained results show that it is not sufficient in every case. Selected results of modified $Mn_{0.5}Fe_{2.5}O_4$ with different linkers and after the detection of Cd^{2+}, Cu^{2+} or Pb^{2+} are presented in Figure 4. This core composition was selected as representative sample for the following tests. Nevertheless, all types of particles were analyzed in the same way.

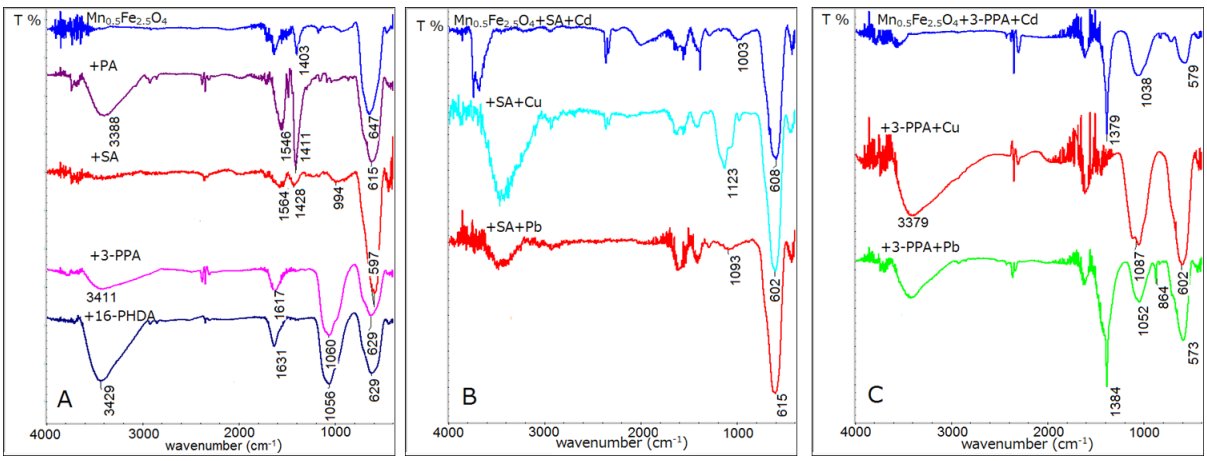

Figure 4: The IR spectra of $Mn_{0.5}Fe_{2.5}O_4$ nanoparticles A) with various linkers used in the experiment, B) with attached SA and Cd, Cu and Pb; and C) with attached 3-PPA and Cd, Cu and Pb.

Figure 4A shows the IR spectra of ferrite nanoparticles before and after linker modification. It can be seen that spectra after modification with PA and SA have increased signals (in comparison to unmodified one) in the range of 1393–1591 cm^{-1}, which indicates the presence of C–C bonds in the rings of PA and SA [30]. The spectra after functionalization with 3-PPA or 16-PHDA show the presence of signals around 1060 and 1105 cm^{-1}, which proves the presence of P–O and P–O–Fe stretching bonds [31]. Bands at 650–590 cm^{-1} are typical for Fe–O in magnetite/maghemite [32]. This observation confirms a successful modification of the surface of the nanoparticles. The spectra in Figure 4B were collected after the exposition of nanoparticles modified with SA to Cd, Cu and Pb ions. As a result, signals in the range of 1003–1123 cm^{-1} appear in addition to those previously observed. In the last series (Figure 4C) the presence of sharp signals at 1379–1384 cm^{-1} in case of Cd and Pb attachment can be found. In this region modifications in the reference system were also observed after interaction with heavy metal [15]. Therefore, the origin of these signals is most probable due to heavy ion adsorption. However, due to a lack of reference information, it is the only speculation on the origin of appearing new signals.

Raman spectroscopy

After every step (synthesis, surface modification, and heavy metal attachment) powdered samples of nanoparticles were analyzed using Raman spectroscopy giving additional information to IR spectroscopy. In Figure 5 selected spectra are presented.

The Raman spectra show a set of peaks that are typical for inorganic cores (magnetite, maghemite/hematite) with accordingly modified organic shells. In Figure 5A only spectra of unmodified particles are collected. One can see that these spectra are dominated by signals centered around 600–700 cm^{-1}. This signal can be attributed both to magnetite and maghemite. The position closer to the middle value of 673–683 cm^{-1} suggests a magnetite-dominated contribution to the signal, while deviation to lower or higher values indicates more maghemite-like contributions [33]. The presence of signals below 670 cm^{-1} implies surface oxidation to maghemite or hematite (for details see Table 3). Signals at a wave number higher than 700 cm^{-1} indicate the presence of an organic shell. Co-doped ferrite nanoparticles have an evidentially dominating peak moved to 600 cm^{-1}, which is in good agreement with the doublet observed in Mössbauer spectra, which, in turn, suggests the presence of maghemite. Ni ferrite also shows a similar trend, which is a hint that local Fe surrounding becomes maghemite-like.

Table 3: Positions of the most intensive lines in the Raman spectra of tested samples [34].

peak position [cm^{-1}]	assignment
524, 673–683	Fe_3O_4
322–335, 704–715	γ-Fe_2O_3
224, 604	α-Fe_2O_3
1335–1383	C–C aliphatic chain/γ-Fe_2O_3
1049, 1166, 1415, 1585	C–C, aromatic ring chain vibrations

In Figure 5B, the spectra of SA-modified $Mn_{0.5}Fe_{2.5}O_4$ nanoparticles after the adsorption of different ions are depicted. The comparison of spectra collected in Figure 5B with unmodified particles (Figure 5A) indicates that surface functionalization by SA causes the presence of a band at 1592 cm^{-1}, and that the

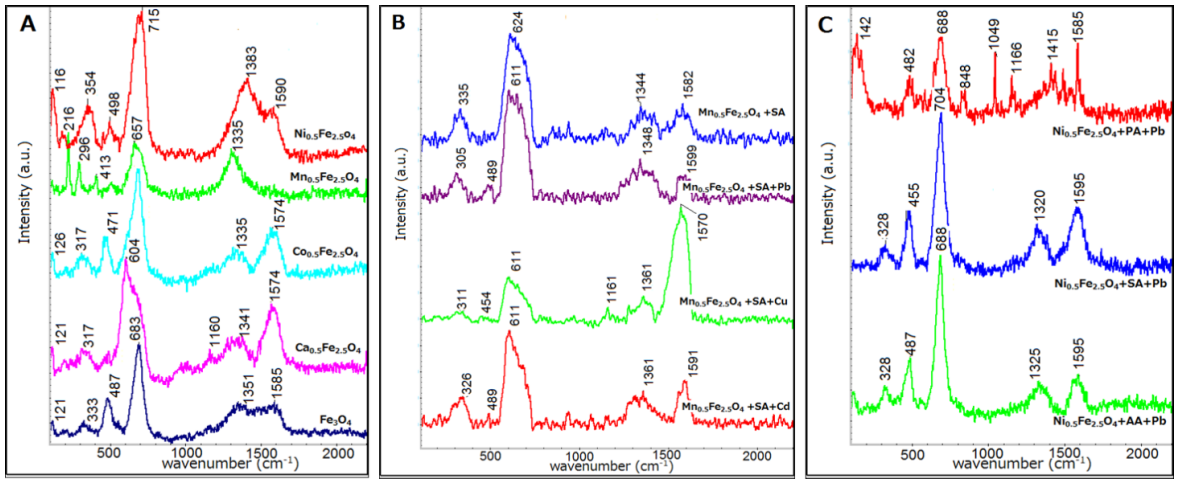

Figure 5: Raman spectra of A) ferrite nanoparticles; B) SA-modified nanoparticles with attached heavy-metal ions; C) various anhydride-modified nanoparticles with attached Pb ions.

adsorption of heavy-metal ions causes further alternation of the signals in the range of 1200–1700 cm^{-1}, which is connected to the interaction of the metal ions with SA and the nanoparticles. A shift of IR signals after heavy-metal adsorption was reported previously [15].

Figure 5C shows the modulation of Raman spectra by different compounds at the surface. A number of additional bands seen in case of PA are due to its specific chemical structure (Table 3). Considering all above-mentioned findings, Raman spectroscopy confirms the surface modification of the nanoparticles and the attachment of heavy-metal ions.

Mössbauer spectroscopy

The magnetic properties of obtained ferrite nanoparticles were examined by Mössbauer spectroscopy at room temperature. The obtained spectra are presented in Figure 6. All spectra show mostly the same features. The first one is the presence of a sextet with broadened lines, which is actually a superposition of sextets corresponding to Fe atoms at the A and B sites of the magnetite structure [35]. The broadening depends on the type of dopant atoms. In the case of Co ions, the full width at half maximum of the spectral lines is much smaller than in the other cases. An especially wide spectrum is observed in the case of magnetite doped by Mn atoms. The value of the average hyperfine magnetic field on the iron atoms is highest on the sample with Co dopant. The second characteristic feature is the presence of a doublet in the central part of the spectrum, which is connected to the superparamagnetic behavior of Fe magnetic moments in the studied samples. The relative intensity of the doubles depends on the kind of dopant. The most intensive doublet is observed for magnetite doped by Ca (more than 50%) and the smallest one in the case of Co dopant. These results show that the superparamagnetic blocking temperature for the Ca doping is below room temperature whereas for the other cases it is slightly above. Taking both features of the measured spectra into account, the mean values of the hyperfine field are equal to 43 T, 44 T, 39 T, 30 T and 20 T for pure magnetite and Co-, Ni-, Mn- and Ca-doped magnetite, respectively. This value strongly depends on the ferrite composition, particle size, surface modification and proximity to superparamagnetic blocking temperature.

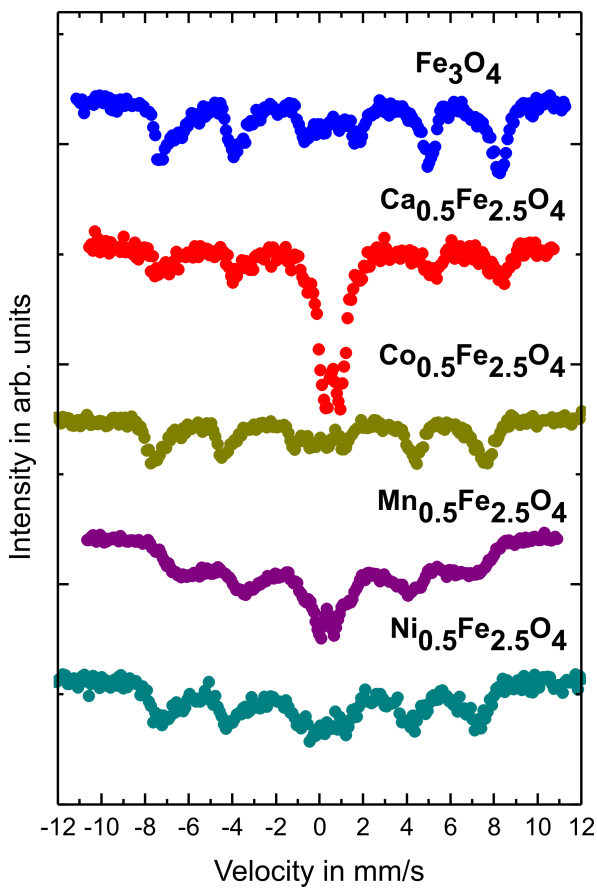

Figure 6: Mössbauer spectra of Fe_3O_4, $Ca_{0.5}Fe_{2.5}O_4$, $Co_{0.5}Fe_{2.5}O_4$, $Mn_{0.5}Fe_{2.5}O_4$ and $Ni_{0.5}Fe_{2.5}O_4$ nanoparticles.

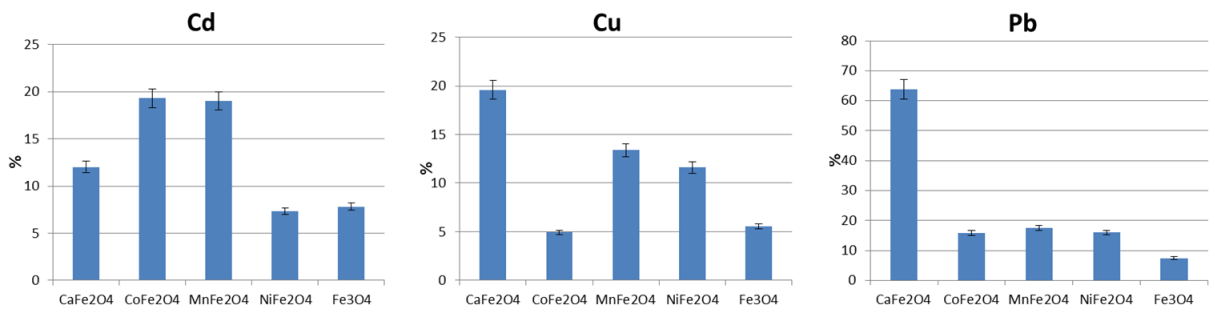

Figure 7: EDX measurements of different types of nanoparticles after exposure to Cd, Cu and Pb solutions.

Attachment of Cu^{2+}, Cd^{2+} and Pb^{2+} ions to unmodified nanoparticles

In the first attempt, we have tested the effectiveness of attachment of metal ions to the unmodified surface of the nanoparticles. This test gives us a reference value and shows if inorganic core additional functionalization affects the interaction with ions. Therefore, ferrite nanoparticles were added to the aqueous heavy-metal solutions and stirred. The liquids were separated from the solid particles, which were dried at room temperature. Powdered samples after the adsorption experiment were examined by EDX and the results are given in Figure 7.

It can be seen that pure magnetite has the lowest capability of interaction with the tested ions. $Mn_{0.5}Fe_{2.5}O_4$ and $Co_{0.5}Fe_{2.5}O_4$ nanoparticles have a similar adsorption tendency of about 20% in case of Cd and Pb ions. Ni ferrite has an adsorption efficiency for Pb similar to that of the previous ferrites, but a very low adsorption efficiency for Cd^{2+}. In case of Cu^{2+}, the situation is different. Here, $Mn_{0.5}Fe_{2.5}O_4$ and $Ni_{0.5}Fe_{2.5}O_4$ show similar values of about 12%, while $Co_{0.5}Fe_{2.5}O_4$ exhibits the worst performance. Interestingly, Ca ferrite adsorbs the most Pb^{2+} up to more than 60%. It seems that $Mn_{0.5}Fe_{2.5}O_4$ has the most similar adsorption properties regarding all types of heavy metals. Hence, for further examination nanoparticles doped with Mn were used. Other ferrite particles will be a subject of further studies (not presented here).

Adsorption of Cu, Cd, and Pb on nanoparticles with modified surfaces

Aqueous solutions of Cu, Cd, or Pb were prepared and added to the nanoparticles. The mixtures were vigorously mixed on a magnetic stirrer. Then, nanoparticles were removed and the concentrations of Cu, Cd, or Pb in the obtained solutions were analyzed using AAS. The data collected in Table 4 show the percentage values of adsorbed heavy-metal ions. It indicates that the best and most universal linker enhancing the adsorption of heavy-metal ions is SA. The PA linker is not selective for Cu ions, but rather good for Pb and Cd. We are aware that adsorption efficiency can be tuned by many other parameters, for example such as linker concentration, heavy ions concentration, pH value, or inorganic core composition, and such studies are in progress and will be a subject of subsequent papers.

Table 4: Percentage of ions adsorbed by $Mn_{0.5}Fe_{2.5}O_4$ nanoparticles modified with different linkers measured by AAS. As a reference, unmodified nanoparticles were used.

	percentage of ions adsorbed		
	Pb	Cu	Cd
NPs	26.1 ± 0.2	22.9 ± 0.2	6.5 ± 0.2
NPs + PA	36.8 ± 0.2	3.2 ± 0.2	27.5 ± 0.2
NPs + SA	38.1 ± 0.2	23.8 ± 0.2	32.3 ± 0.2
NPs + AA	15.9 ± 0.2	14.4 ± 0.2	12.1 ± 0.2
NPs + 3-PPA	25.7 ± 0.2	12.3 ± 0.2	14.9 ± 0.2
NPs + 16-PHDA	1.9 ± 0.2	11.8 ± 0.2	7.6 ± 0.2

Conclusion

Ferrite nanoparticles doped with calcium, cobalt, nickel, or manganese show differences in ion adsorption depending on the type of core. This indicates that the strength of the interparticle interaction can be one of the parameters governing the adsorption capability. It has been confirmed that calcium-modified ferrite is the most effective in Pb case, but only when the core is modified by PA. In any other case its role is average. IR measurements have proved a successful connection of the tested linkers to all nanoparticles, which entails that particles become a proper platform to further studies. AAS tests clearly confirmed the attachment of heavy metals to the selected nanoparticles ($Mn_{0.5}Fe_{2.5}O_4$), with variable efficiency depending on the type of ions. SA appears to be the most effective and universal linker. The use of other types of compounds such as 3-PPA or 16-PHDA improved adsorption in selected cases, but they are not as versatile as succinic anhydride. Other anhydrides (PA and AA) also improve the adsorption of heavy metals in comparison to unmodified particles, but not as efficiently as SA. To conclude, succinic anhydride may be a good potential modifier of the $Mn_{0.5}Fe_{2.5}O_4$ particles to enhance the selective adsorption of heavy metal ions from aqueous solutions. Therefore, in future, experiments with real food samples or a richer solution matrix will be performed. The adsorption efficiency strongly depends on core composition as well as surface modification, and only a complex analysis of the system allows one to draw adequate conclusions.

Acknowledgements

Mössbauer spectroscopy was performed in close collaboration with the Department of Physics of the University of Bialystok. The work was partially financed by the EU funds via the project with a contract number POPW.01.03.00-20-034/09-00, POPW.01.03.00-20-004/11-00, and by NCN funds 2014/13/N/ST5/00568.

ORCID® iDs

Elżbieta Zambrzycka-Szelewa - https://orcid.org/0000-0002-1164-4747

References

1. Akbarzadeh, A.; Samiei, M.; Davaran, S. *Nanoscale Res. Lett.* **2012,** *7,* 144. doi:10.1186/1556-276X-7-144
2. Singh, R.; Lillard, J. W., Jr. *Exp. Mol. Pathol.* **2009,** *86,* 215–223. doi:10.1016/j.yexmp.2008.12.004

3. Feng, L.; Cao, M.; Ma, X.; Zhu, Y.; Hu, C. *J. Hazard. Mater.* **2012,** *217–218,* 439–446. doi:10.1016/j.jhazmat.2012.03.073
4. Laurent, S.; Forge, D.; Port, M.; Roch, A.; Robic, C.; Vander Elst, L.; Muller, R. N. *Chem. Rev.* **2008,** *108,* 2064–2110. doi:10.1021/cr068445e
5. Sharifpour, E.; Khafri, H. Z.; Ghaedi, M.; Asfaram, A.; Jannesar, R. *Ultrason. Sonochem.* **2018,** *40,* 373–382. doi:10.1016/j.ultsonch.2017.07.030
6. Gaikwad, K. K. Active and Intelligent Packaging: Future Need. In *Food Processing and technology: New emerging areas;* Bhatt, D. K.; Kumar, S., Eds.; Shree Publishers & Distributors: New Delhi, 2014.
7. Mason, T. G.; Graves, S. M.; Wilking, J. N.; Lin, M. Y. *Condens. Matter Phys.* **2006,** *9,* 193–199. doi:10.5488/CMP.9.1.193
8. Berekaa, M. M. *Int. J. Curr. Microbiol. Appl. Sci.* **2015,** *4,* 345–357.
9. The Role of Packaging in Minimising Food Waste in the Supply Chain of the Future. http://mams.rmit.edu.au/ie9rn2ifqca.pdf (accessed Jan 30, 2018).
10. Hung, Y.-L.; Hsiung, T.-M.; Chen, Y.-Y.; Huang, Y.-F.; Huang, C.-C. *J. Phys. Chem. C* **2010,** *114,* 16329–16334. doi:10.1021/jp1061573
11. Maiti, S.; Barman, G.; Konar Laha, J. *Appl. Nanosci.* **2016,** *6,* 529–538. doi:10.1007/s13204-015-0452-4
12. Sugunan, A.; Thanachayanont, C.; Dutta, J.; Hilborn, J. G. *Sci. Technol. Adv. Mater.* **2005,** *6,* 335–340. doi:10.1016/j.stam.2005.03.007
13. Predescu, A.; Matei, E.; Berbecaru, A.; Vidu, R. Synthesis of Magnetic Nanoparticles for the Removal of Heavy Metal Ions from Wastewaters. In *Proceedings of the 38th Annual Congress of the American Romanian Academy of Arts and Sciences,* Pasadena, CA, USA, July 23–27, 2014; ARA Publisher, 2014; pp 37–42.
14. Dil, E. A.; Ghaedi, M.; Asfaram, A.; Mehrabi, F. *Ultrason. Sonochem.* **2017,** *36,* 409–419. doi:10.1016/j.ultsonch.2016.12.016
15. Pirouz, M. J.; Beyki, M. H.; Shemirani, F. *Food Chem.* **2015,** *170,* 131–137. doi:10.1016/j.foodchem.2014.08.046
16. Kong, J.; Coolahan, K.; Mugweru, A. *Anal. Methods* **2013,** *5,* 5128. doi:10.1039/c3ay40359a
17. Kalska-Szostko, B.; Wykowska, U.; Piekut, K.; Zambrzycka, E. *Colloids Surf., A* **2013,** *416,* 66–72. doi:10.1016/j.colsurfa.2012.10.019
18. Kandpal, N. D.; Sah, N.; Loshali, R.; Joshi, R.; Prasad, J. *J. Sci. Ind. Res.* **2014,** *73,* 87–90.
19. Kalska-Szostko, B.; Kropiewnicka, K. *Curr. Appl. Phys.* **2012,** *12,* 896–902. doi:10.1016/j.cap.2011.12.003
20. Satuła, D.; Kalska-Szostko, B.; Szymański, K.; Dobrzyński, L.; Kozubowski, J. *Acta Phys. Pol., A* **2008,** *114,* 1615–1621. doi:10.12693/APhysPolA.114.1615
21. Kalska-Szostko, B.; Wykowska, U.; Satula, D.; Nordblad, P. *Beilstein J. Nanotechnol.* **2015,** *6,* 1385–1396. doi:10.3762/bjnano.6.143
22. Kalska-Szostko, B.; Rogowska, M.; Satuła, D. *Colloids Surf., B* **2013,** *111,* 656–662. doi:10.1016/j.colsurfb.2013.07.004
23. Krishnan, K. M. *Fundamentals and Applications of Magnetic Materials;* Oxford University Press, 2016. doi:10.1093/acprof:oso/9780199570447.001.0001
24. Mahadevan, S.; Gnanaprakash, G.; Philip, J.; Rao, B. P. C.; Jayakumar, T. *Physica E* **2007,** *39,* 20–25. doi:10.1016/j.physe.2006.12.041
25. Blaney, L., "Magnetite (Fe_3O_4): Properties, Synthesis, and Applications". http://preserve.lehigh.edu/cas-lehighreview-vol-15/5 (accessed Jan 30, 2018).
26. Goss, C. J. *Phys. Chem. Miner.* **1988,** *16,* 164–171.
27. Thang, P. D.; Rijnders, G.; Blank, D. H. A. *J. Magn. Magn. Mater.* **2005,** *295,* 251–256. doi:10.1016/j.jmmm.2005.01.011
28. Farooq, H.; Ahmad, M. R.; Jamil, Y.; Hafeez, A.; Mahmood, Z.; Mahmood, T. *J. Basic Appl. Sci.* **2012,** *8,* 597–601. doi:10.6000/1927-5129.2012.08.02.53
29. Nabiyouni, G.; Jafari Fesharaki, M.; Mozafari, M.; Amighian, J. *Chin. Phys. Lett.* **2010,** *27,* 126401. doi:10.1088/0256-307X/27/12/126401
30. Coates, J. Interpretation of Infrared Spectra, A Practical Approach. *Encyclopedia of Analytical Chemistry;* Wiley, 2006. doi:10.1002/9780470027318.a5606
31. Kalska-Szostko, B.; Orzechowska, E.; Wykowska, U. *Colloids Surf., B* **2013,** *111,* 509–516. doi:10.1016/j.colsurfb.2013.05.033
32. Subramanian, N. D.; Moreno, J.; Spivey, J. J.; Kumar, C. S. S. R. *J. Phys. Chem. C* **2011,** *115,* 14500–14506. doi:10.1021/jp202215k
33. Slavov, L.; Abrashev, M. V.; Merodiiska, T.; Gelev, C.; Vandenberghe, R. E.; Markova-Deneva, I.; Nedkov, I. *J. Magn. Magn. Mater.* **2010,** *322,* 1904–1911. doi:10.1016/j.jmmm.2010.01.005
34. Chourpa, I.; Douziech-Eyrolles, L.; Ngaboni-Okassa, L.; Fouquenet, J.-F.; Cohen-Jonathan, S.; Soucé, M.; Marchais, H.; Dubois, P. *Analyst* **2005,** *130,* 1395–1403. doi:10.1039/b419004a
35. Kalska-Szostko, B.; Satuła, D.; Olszewski, W. *Curr. Appl. Phys.* **2015,** *15,* 226–231. doi:10.1016/j.cap.2014.12.011

License and Terms

This is an Open Access article under the terms of the Creative Commons Attribution License (http://creativecommons.org/licenses/by/4.0), which permits unrestricted use, distribution, and reproduction in any medium, provided the original work is properly cited.

The license is subject to the *Beilstein Journal of Nanotechnology* terms and conditions: (https://www.beilstein-journals.org/bjnano)

The definitive version of this article is the electronic one which can be found at: doi:10.3762/bjnano.9.69

BEILSTEIN JOURNAL OF NANOTECHNOLOGY

Facile synthesis of a ZnO–BiOI p–n nano-heterojunction with excellent visible-light photocatalytic activity

Mengyuan Zhang[1], Jiaqian Qin[*2,3], Pengfei Yu[1], Bing Zhang[1], Mingzhen Ma[1], Xinyu Zhang[*1] and Riping Liu[1]

Full Research Paper

Open Access

Address:
[1]State Key Laboratory of Metastable Materials Science and Technology, Yanshan University, Qinhuangdao 066004, P. R. China, [2]Metallurgy and Materials Science Research Institute, Chulalongkorn University, Bangkok 10330, Thailand, and [3]Research Unit of Advanced Materials for Energy Storage, Chulalongkorn University, Bangkok, Thailand

Email:
Jiaqian Qin* - jiaqian.q@chula.ac.th;
Xinyu Zhang* - xyzhang@ysu.edu.cn

* Corresponding author

Keywords:
BiOI; photocatalytic degradation; p–n heterojunction; ZnO

Beilstein J. Nanotechnol. **2018,** *9,* 789–800.
doi:10.3762/bjnano.9.72

Received: 23 November 2017
Accepted: 30 January 2018
Published: 05 March 2018

This article is part of the Thematic Series "Energy conversion, storage and environmental remediation using nanomaterials".

Guest Editor: W.-J. Ong

© 2018 Zhang et al.; licensee Beilstein-Institut.
License and terms: see end of document.

Abstract

In this paper, an efficient method to produce a ZnO/BiOI nano-heterojunction is developed by a facile solution method followed by calcination. By tuning the ratio of Zn/Bi, the morphology varies from nanoplates, flowers to nanoparticles. The heterojunction formed between ZnO and BiOI decreases the recombination rate of photogenerated carriers and enhances the photocatalytic activity of ZnO/BiOI composites. The obtained ZnO/BiOI heterostructured nanocomposites exhibit a significant improvement in the photodegradation of rhodamine B under visible light ($\lambda \geq 420$ nm) irradiation as compared to single-phase ZnO and BiOI. A sample with a Zn/Bi ratio of 3:1 showed the highest photocatalytic activity (≈99.3% after 100 min irradiation). The photodegradation tests indicated that the ZnO/BiOI heterostructured nanocomposites not only exhibit remarkably enhanced and sustainable photocatalytic activity, but also show good recyclability. The excellent photocatalytic activity could be attributed to the high separation efficiency of the photoinduced electron–hole pairs as well as the high specific area.

Introduction

The development of semiconductor photocatalysis has opened a new horizon for environmental pollution remediation and provides a potential solution to the global energy problem given the abundance and sustainability of solar energy. The incredible potential of these materials, which has attracted great enthusiasm from researchers in the past a few decades, renders them strong candidates for a variety of applications that range from photocatalytic water splitting [1,2], organic pollution deg-

radiation [3-6], nitrogen fixation [7,8], to solar fuel production [9]. The metal oxides, such as CdO [10], Al_2O_3 [11], and CuO [12,13], has attracted a lot of interest in photocatalytic applications. And among all of these metal oxides, it is titanium dioxide and zinc oxide (TiO_2 and ZnO) that are the most widely exploited by taking advantage of their long-term stability and environmental non-toxicity, in addition to providing a low-cost alternative to the n-type semiconductor photocatalysts [14-16]. However, further application of these metal oxides is usually significantly limited by the poor utilization of visible light, which accounts for 45% of the solar radiation spectrum, because of their wide band gap. Some effort must be paid to extend their working spectrum efficiently.

As is known to all, it is metal orbitals which contribute to the conduction band (CB) of the metal-containing semiconductor's band gap. Bismuth(III)-containing semiconductors (such as bismuth oxide [17], bismuth vanadate [18,19], bismuth tungstate [20], bismuth perovskite [21], bismuth molybdate [22], etc.) have been extensively researched as a broad hybrid orbital composed of Bi 6s in the field of photocatalysis. Recently, bismuth oxyhalides have been proposed as a new kind of narrow band gap p-type semiconductor photocatalyst material whose general formula is BiOX, where X represents Cl, Br or I. They crystallize in the tetragonal matlockite structure with space group P4/NMMS. In the crystal structure of all these ternary compounds, $[Bi_2O_2]^{2+}$ slabs are interweaved with double layers of halide atoms [23]. Calculated and experimental evidence has proven that the band gap of BiOX materials decreases with increasing ionic radii of X (from Cl to I) [24,25]. Hence, BiOI, with a band gap around 1.8 eV, has a strong response to visible light. Though widely investigated, BiOI suffers from its high recombination rate of photoinduced electron–holes and low charge transfer ability. Therefore, the strategies to improve the efficiency of this kind of semiconductor photocatalyst are in need.

Heterogeneous processes are becoming a key focus area for the design of novel and multifunctional materials in the field of photocatalysis. To date, unremitting efforts have been devoted to improving the photocatalysis efficiency [26-29]. Furthermore, coupling n-type semiconductor photocatalysts to p-type to form p–n heterojunctions could promote increased photocatalytic activity efficiency. Once the p–n junction has been formed, the inner electric field between the inner surface of two semiconductors will promote the separation efficiency of photoinduced electron–hole pairs [30,31].

Consequently, coupling an n-type metal oxide to a p-type BiOX to form a p–n heterojunction is an effective method to optimize the photocatalytic activity (summarized in Table S1, Supporting Information File 1). By now, several works have been published in this area. In 2009, Zhang et al. reported a low-temperature route to prepare TiO_2/BiOI photocatalysts which showed higher activity than single-phase BiOI or TiO_2 and 50% BiOI possessed the best performance [32]. Jiang and co-workers used a chemical bath to produce ZnO/BiOI heterostructures. By tuning the ratio of Zn/Bi, they could rationally control the morphology, constituents and optical properties [33]. In 2014, spin-coating was utilized to prepare ZnO nanowire arrays with tunable band gap, layered BiOBr–BiOI composites onto them. It showed that the BiOBr/BiOI composites played the role of sensitizer in the heterojunctions and were tunable by varying the BiOBr/BiOI ratio [34]. Kuang et al. described the synthesis of p–n heterostructures where p-type BiOI nanoplates decorated on n-type ZnO nanorod arrays which were synthesized through a solvothermal route. The high-contact areas provided by the fast charge transfer channel of BiOI and ZnO create the efficient photocatalyst [35]. Tong et al. [36] reported ZnO-embedded BiOI hybrid nanoflakes fabricated by using $Zn_5(CO_3)_2(OH)_6$ ultrathin nanosheets for BiOI deposition followed by calcination. The obtained ZnO-embedded BiOI hybrid nanoflakes show good photocatalytic activity and recyclability. Jiang et al. [37] prepared the BiOI/ZnO photocatalysts by a two-step synthetic method. The improved photocatalytic degradation of phenol could be achieved under simulated solar light irradiation.

Herein, we report a new, facile method to produce the ZnO/BiOI heterojunction by a solution method followed by calcination. Using a milder precipitant NH_4HCO_3 can homogenize the constituent in a relatively smaller range of pH. By tuning the ratio of Zn/Bi, the morphology, which also plays a vital role in photocatalytic dye degradation, varied from nanoplates, to flowers to nanoparticles. The obtained ZnO/BiOI heterostructured nanocomposites showed a significant improvement in the degradation of rhodamine B under visible light ($\lambda \geq 420$ nm) irradiation as compared to ZnO and BiOI. The obtained catalysts with a Zn/Bi ratio of 3:1 exhibited the highest photocatalytic activity. The band gap structure and charge transfer properties are investigated by XPS in detail. With the addition of different kinds of sacrificial agents, the possible ZnO/BiOI heterojunction mechanism of photodegradation is preliminarily discussed.

Results and Discussion

Structure and morphology characterization

The composition of as-prepared ZnO/BiOI heterojunction nanocomposites was examined by X-ray diffraction (XRD) analysis as shown in the Figure 1. It is obvious that all the XRD patterns are in good agreement with the tetragonal BiOI (JCPDS card 73-2062) and the hexagonal ZnO (JCPDS card 36-1451)

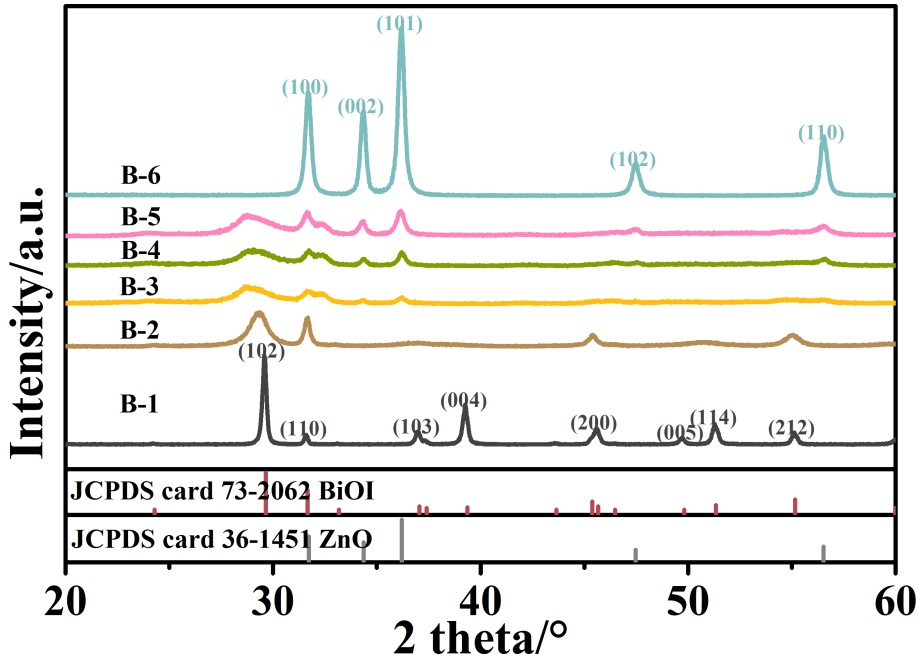

Figure 1: The X-ray diffraction patterns of all of the as-synthesized samples with different Bi/Zn molar ratios (with reference ZnO and BiOI XRD patterns as comparison). All peaks are in good agreement with the tetragonal BiOI and/or the hexagonal ZnO phases.

phases. Moreover, for ZnO/BiOI nanocomposites, the diffraction peaks of BiOI tend to decrease while the ZnO diffraction peaks gradually increase, which is consistent with the composite variation from B-2 to B-5. It is worth noting that the (102) diffraction peaks corresponding to BiOI shift to lower angles as well as become weaker and broader, while the Zn/Bi ratio increases (from B-2 to B-5). To give more details on ZnO's impact on the crystallization of BiOI, the (102) diffraction peak is chosen to roughly estimate the average BiOI crystal size of samples B-2 through B-5 by the Scherrer equation (Table S2, Supporting Information File 1). The estimates show that the average crystal size of BiOI decreases with increasing ZnO, which indicates that the existence of ZnO may impede the crystallization and lead to the exfoliation of BiOI [33]. Y. Tong [36] also reported the broadening and shifting of the (102) diffraction peak of ZnO/BiOI composite samples, which is never mentioned in the previous studies without post-annealing treatment [33]. It is reasonable to believe that the bonding between ZnO and BiOI is stronger after the calcination and can be beneficial to the charge transfer in the photocatalytic activity process.

Figure 2a–c shows the morphology of samples B-1, B-4 and B-6 from scanning electron microscopy (SEM). In Figure 2a, pure BiOI shows a smooth plate-like shape with thickness varying from 100 to 500 nm and particle diameter of around 2 µm. For sample B-2 (Figure S1a, Supporting Information File 1), either the thickness or the size of the particle has remarkably decreased. The particle size further diminishes with the addition of ZnO (B-3, Figure S1b, Supporting Information File 1). When the Zn/Bi ratio becomes 1:3 (Figure 2b), the exfoliated BiOI ultrathin layers assemble together to spontaneously form a hierarchical microsphere to reduce the surface energy. Coupling the elemental distribution displayed by the energy-dispersive spectroscopy (EDS) mapping (Figure 2d–h) and EDS (Figure 2i), it is clear to see that in this 3D nanoflower structure of B-4 sample the ZnO nanoparticles are uniformly embedded on the architecture built up by erect BiOI layers. However, when the Bi/Zn ratio turns to 1:4 (B-5, Figure S1c, Supporting Information File 1), the morphology of the sample has greatly deviated from that of samples B-1–B4, which is characterized as irregular agglomerate nanoparticles. This indicates that a large amount of ZnO particles take the place of BiOI nanolayers. As pure ZnO, sample B-6 (Figure 2c) presents nanospheres with a highly smooth surface, which is possibly caused by calcination [38].

In order to make further investigations on the ZnO/BiOI heterostructure, TEM and HRTEM analysis were applied. Figure S2a, Supporting Information File 1, shows the transmission electron microscopy (TEM) image of pure BiOI. It is clear to see that the as-synthesized BiOI forms into irregular nanoplates with smooth edges. Figure S2b, Supporting Information File 1, shows the TEM image of sample B-3 whose Bi/Zn molar ratio

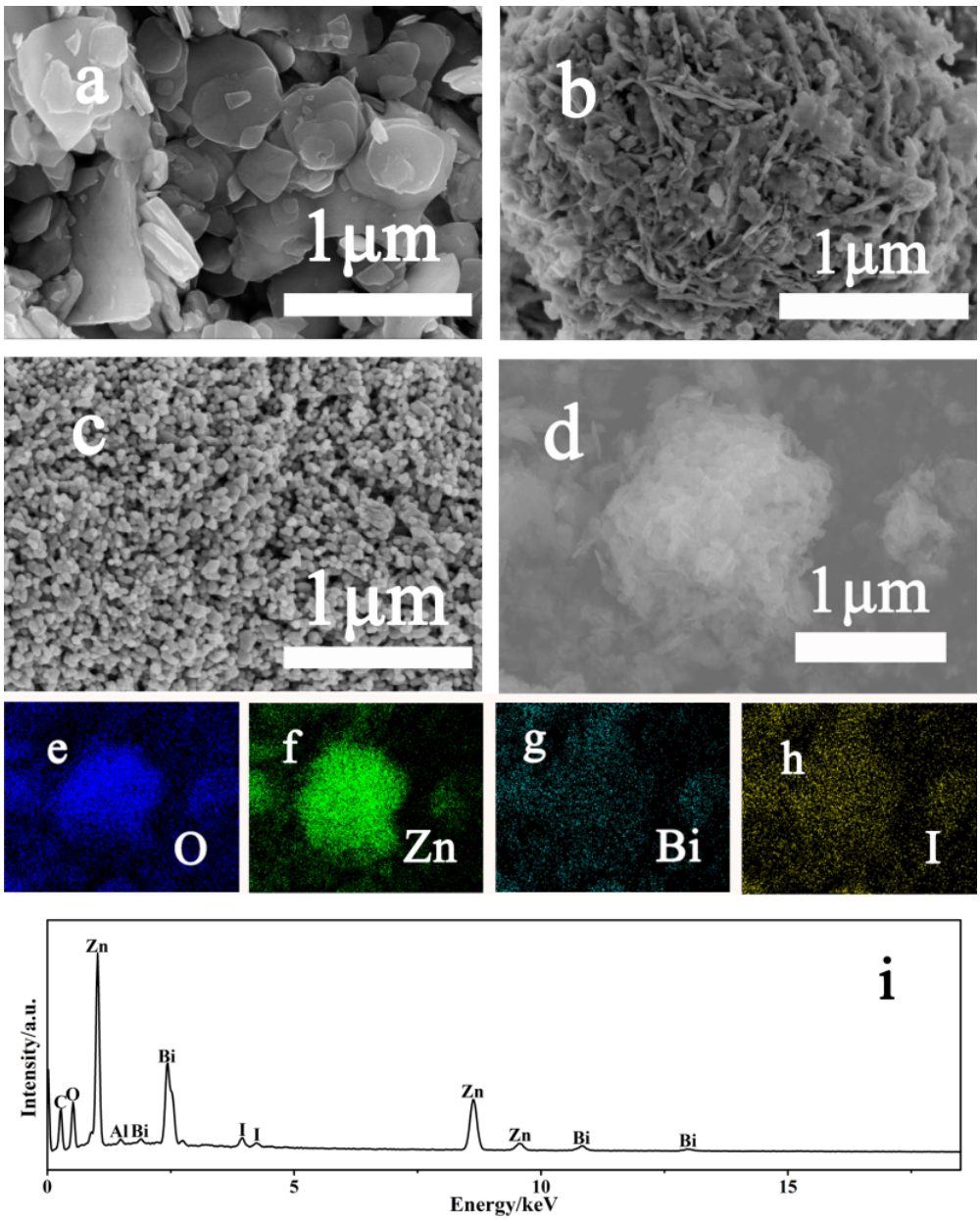

Figure 2: SEM images of sample B-1 (a), B-4 (b), B-6 (c), and B-4, (d). Energy-dispersive spectroscopy (EDS) elemental mapping of (e) O, (f) Bi, (g) Zn, (h) I, and (i) EDS of sample B-4.

equals to 1:2. The morphology of the sample particle displayed here highly agrees with the results of the SEM image, where ZnO aggregates are decorated on the exfoliated BiOI nanolayers. The selected area electron diffraction (SAED) pattern of BiOI (Figure S2c, Supporting Information File 1) reveals that the sample is highly crystalline, as proved by representative SAED pattern of single crystalline with bright spots. The diffraction spots corresponding to (110) and (200) planes are indexed to the {001} facets of tetragonal phase BiOI, which is consistent with the XRD results [39].The concentric circles in the SAED pattern of B-3 (Figure S2d, Supporting Information File 1) illustrate the polycrystalline nature of sample B-3 and the coexistence of BiOI and ZnO. Two bright inner rings, which are indexed to BiOI (106) and ZnO (004) facets, indicate the high crystalline degree and echo the previous XRD study to a great extent. The TEM and HRTEM images on the different edges of sample B-3 are displayed in Figure 3a–c, where lattice fringe spacings are 0.30 and 0.28 nm, respectively, matching well with the interplanar distances of the (102) plane in BiOI and the (100) plane in ZnO. These results further validate the formation of heterostructured nanocomposites of ZnO and BiOI.

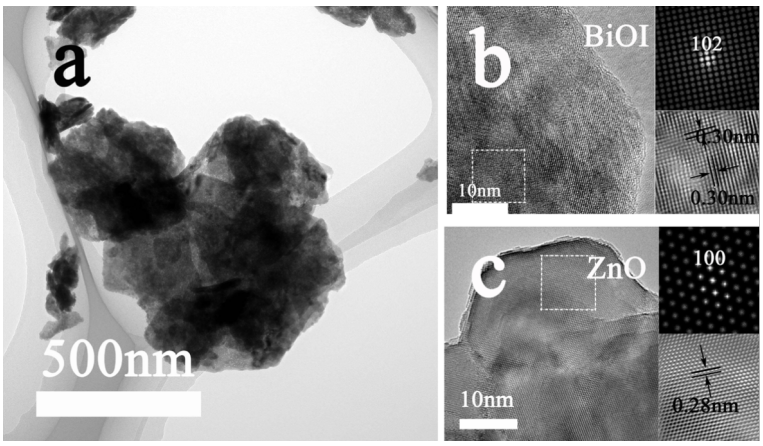

Figure 3: (a) TEM image of sample B-3 and high-resolution images further confirm that a heterostructured ZnO (b) and BiOI (c) nanocomposite is obtained.

The structural characteristics of the as-prepared ZnO/BiOI composites were revealed by nitrogen adsorption–desorption isotherms shown in Figure S3, Supporting Information File 1. The isotherm of sample B-4, with a unique hysteresis loop and a classical two capillary condensation step, undoubtedly corresponds to a type IV isotherm according to the Brunauer–Deming–Derning–Teller (BDDT) classification, indicating the mesoporous nature of sample B-4 [40]. The isotherm has a loop with the shape of H3, which demonstrates that the pores in the sample are mainly made up of slit-like cracks attributed to the aggregation of ultrathin BiOI layers and is consistent to the SEM image of the sample B-4 in Figure 2b. The Brunauer–Emmett–Teller (BET) analysis also illustrated that the specific area (listed in Table S2, Supporting Information File 1) of the B-4 sample is 20.83 cm^2/g, which is significantly improved from the pure BiOI (5.23 cm^2/g) and ZnO (16 cm^2/g) materials. This may lead ZnO/BiOI to have more active bonding sites than pure BiOI and ZnO, which is beneficial for the photodegradation activity.

Chemical state analysis

X-ray photoelectron spectroscopy (XPS) was carried out for the chemical composition and valence state analysis of various species. The foreign impurity C at 284.6 eV is used to calibrate peak positions in all the XPS results. High-resolution narrow-scan spectra of O, Bi, Zn and I are also conducted for the study of surface chemical state in detail.

The O 1s spectra of B-1, B-4 and B-6 are recorded in Figure 4a. The spectrum of O 1s for pure BiOI can be fitted with two peaks that are centered at a binding energy of 532 eV and 530 eV. The dominant peak at 532 eV is attributed to I–O bonds in BiOI, and the peak located at 530 eV is assigned to oxygen species of lattice oxygen (O^{2-}) [22,41,42] which is related to Bi–O in $[Bi_2O_2]$ slabs of BiOI. In the typical ZnO/BiOI heterostructured composite B-4, the high-resolution spectrum of O 1s can be deconvoluted into three components. The I–O peak which is centered at around 532.3 eV is the same as pure BiOI, while the peak that belongs to lattice oxygen could be further deconvoluted into two peaks located at 530.5 eV and 529.5 eV, respectively. It is noticeable that in the previous study, the peak with high energy is ascribed to Zn–O bonds whereas the lower energy peak is attributed to Bi–O bonds [32,33]. However, in the O 1s spectra of the B-6 sample (pure ZnO), the O lattice peak is at 529.6 eV, corresponding to the Zn–O bonds in ZnO [43]. Combining the O 1s high-resolution XPS results of B-1, the peak in the B-4 sample with higher energy at 530.5 eV should be Bi–O [44] and the peak at a lower energy of 529.5 eV should be Zn–O. The subtle deviation between the peak positions in the O 1s spectra of the ZnO/BiOI sample and pure ZnO and BiOI confirms the formation of the heterojunction and the charge transfer from Bi–O bonds to Zn–O bonds in the nanocomposite sample [45].

The high-resolution scan of Bi 4f is displayed in Figure 4b. Both pure BiOI and the nanocomposite sample consist of a doublet which can be well-assigned to Bi $4f_{5/2}$ at 164.5 eV and Bi $4f_{3/2}$ at 159.2 eV with an energy difference of 5.3 eV [39,46], revealing that +3 is the main valence state of the Bi element in B-1 and the nanocomposite sample [17]. A pair of satellite peaks centered at about 1.8 eV higher than the main peaks can be identified as Bi^{5+} defects and agreed well with the reported values [30,32]. As shown in Figure 4c, there are two separate peaks with a difference of 23 eV in Zn 2p region of B-4 and B-6 samples. They are characteristics of Zn $2p_{1/2}$ at 1043 eV and Zn $2p_{3/2}$ at 1020 eV ascribed to the Zn^{2+} state [47]. In the Zn 2p core level of B-4, a pair of satellite peaks are observed with binding energy of 1045.65 and 1022.65 eV,

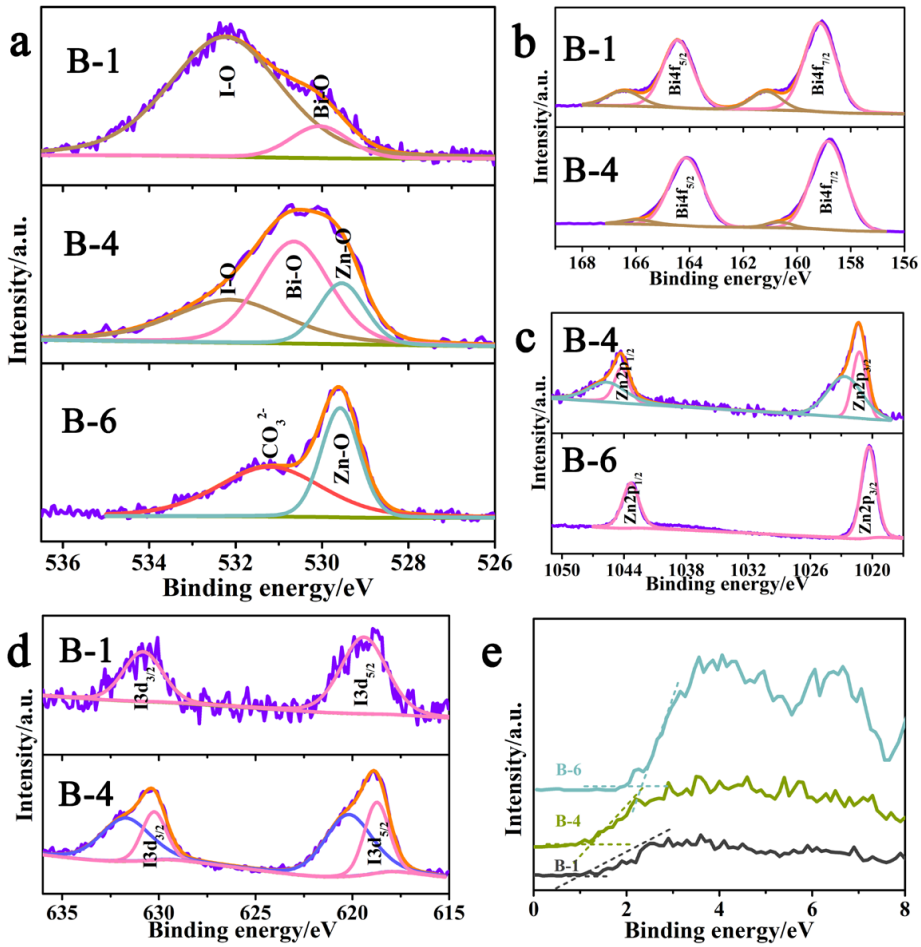

Figure 4: The high-resolution XPS spectrum for: (a) O 1s core energy of B-1, B-4 and B-6; (b) Bi 4f of B-1 and B-4 samples; (c) Zn 2p of B-4 and B-6 samples; (d) I 3d of B-1 and B-4 samples; and (e) XPS valence band spectrum of samples B-1, B-4 and B-6.

which are probably caused by the change of chemical state of Zn attributed to ZnO compositing to BiOI. Interestingly, in Figure 4b,c, the Bi 4f and Zn 2p peaks of the nanocomposite sample are more or less shifted to higher energy as compared with the single phase, but maintain the spin-orbit splitting at about 5.3 and 23 eV, respectively. This indicates that the main states of Bi and Zn are +3 and +2 in the ZnO/BiOI heterostructured composite [48].

Figure 4d exhibits the high-resolution results of I 3d XPS spectra. Two peaks located at 619.4 eV and 630.8 eV can be assigned to I $3d_{5/2}$ and I $3d_{3/2}$ according to the previous works for pure BiOI [46]. After coupling with ZnO, however, the satellite peaks appeared in the B-4 sample, demonstrating the chemistry state of I is changed. This probably resulted from the partial substitution of I for oxidic sites in the ZnO framework [49]. The density of electronic state (DOS) of the valence band was also characterized by XPS, yielding information pertaining to the bonding properties of different samples, as displayed in Figure 4e. The B-1 and B-6 samples show typical valence band DOS characteristics of BiOI and ZnO, with edge cutoff values of 0.96 eV and 2.27 eV, respectively [50]. For the B-4 sample, the edge cutoff value is about 1.22 eV. The change in the state, along with the difference in the shape from pure BiOI and ZnO, is probably due to the band bending attributed to the formation of ZnO–BiOI heterojunctions, as its Bi/Zn molar ratio is 1:3.

Optical properties

To investigate the photo-induced charge carrier separation efficiency, photoluminescence (PL) emission spectra was carried out and the results are displayed in Figure S4, Supporting Information File 1. Generally speaking, stronger PL intensity indicates a higher photoinduced hole–electron recombination rate, which is not in the photocatalysts favor. As can be clearly seen, B-1 and B-6 exhibited an extremely strong intensity, demonstrating the lower charge separation efficiency of pure BiOI and ZnO. The intensity greatly decreased as the BiOI/ZnO ratio equals 1:3, revealing that the formation of the ZnO/BiOI

heterostructured composite is beneficial for improving the charge separation ability.

The light adsorption ability and the band gap structure are some of the decisive factors for photocatalysis. Therefore, the UV–vis diffuse reflection spectra (UV-DRS) is worthy of study to explore their optical properties. The UV-DRS results are shown in Figure 5a (inset is the colors of the B-1–B-6 samples which vary from orange-red to white) for the wavelength range 300–800 nm. Pure ZnO (B-6) shows a cut-off at about 400 nm, and pure BiOI (B-1) has an absorbance edge at about 660 nm. The other samples with the Bi/Zn molar ratio varying from 1:1 to 1:4 displayed a gradually decreasing adsorption edge from the visible light range to the ultraviolet region. To determine the conduction positions, the Tauc relation is utilized to estimate the optical band gap. According to the following relational expression proposed by Tauc, Davis and Mott:

$$(\alpha h\nu)^{1/n} = A(h\nu - E_g), \quad (1)$$

where h is Plank's constant, ν is the frequency of vibration, α is the adsorption coefficient, E_g is the optical band gap and A is a proportionality constant [51,52]. The value of the constant n denotes the characteristics in the transition of a semiconductor. For the case that both ZnO and BiOI indirectly allow the transition, n equals 2. The plots that depict the value of the photoenergy against $(\alpha h\nu)^{1/2}$ and respective tangents, based on the relation mentioned above, is shown in Figure 5b. The points of the intersections of the tangents to the x-axis become the approximate values of the band gap energy of the as-prepared samples, as listed in Table 1. This further illustrates that the band gaps of the samples improve with the increase of the amount of ZnO. It is particularly noteworthy that the band gap of as-synthesized ZnO is 3.16 eV, which is smaller than the band gap of conventional bulk ZnO, probably a result of the quantum confinement effect in the nanometer-sized ZnO particles.

Photocatalytic degradation

To test the as-synthesized samples' ability to remove organic pollutants from waste water, the photodegradation of RhB was carried out under illumination by visible light from a 300 W Xe lamp with a 420 nm cut-off filter. In order to make a valid comparison of the degradation effectiveness of the as-prepared samples, the initial adsorption in the dark is ruled out. The adsorption–desorption equilibrium is displayed in Figure S5, Supporting Information File 1. For a comprehensive comparison, the blank group was conducted under the same conditions. The results can be intuitively observed in Figure 6a, where C_0 represents the initial dye concentration and C is the concentration

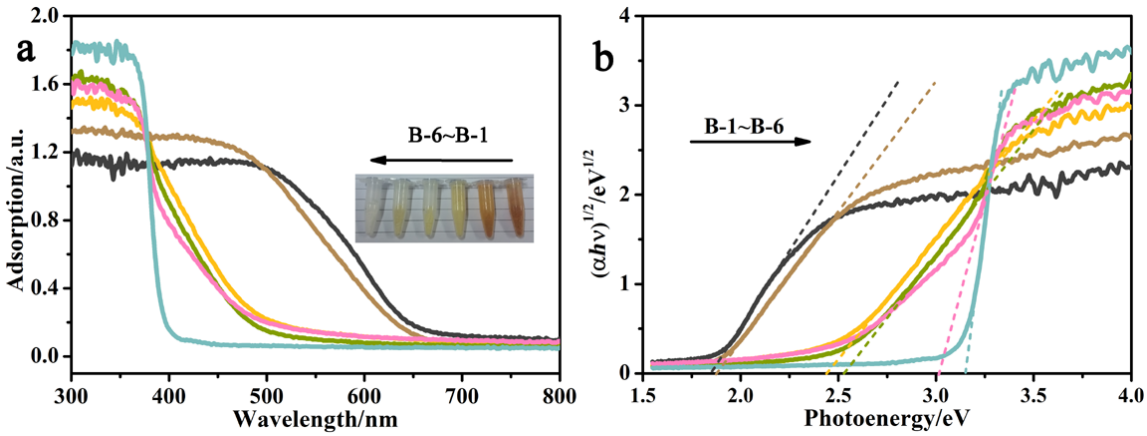

Figure 5: Optical properties of the as-prepared samples (a) UV–vis DRS spectra where the inset shows the physical color of the samples. (b) The plot of $(\alpha h\nu)^2$ vs photon energy ($h\nu$).

Table 1: The optical band gap, degree of degradation for 100 min and the reaction rate coefficient of the as-prepared samples as compared to the reference samples (blanks).

Sample	B-1	B-2	B-3	B-4	B-5	B-6	blank
optical band gap (eV)	1.85	1.90	2.46	2.52	2.96	3.16	–
degradation degree after 100 min (%)	74.0	96.9	96.1	99.3	92.7	21.2	1.6
K ($\times 10^{-4}$ min^{-1})	129.5	303.1	297	462	266.1	23.5	1.17

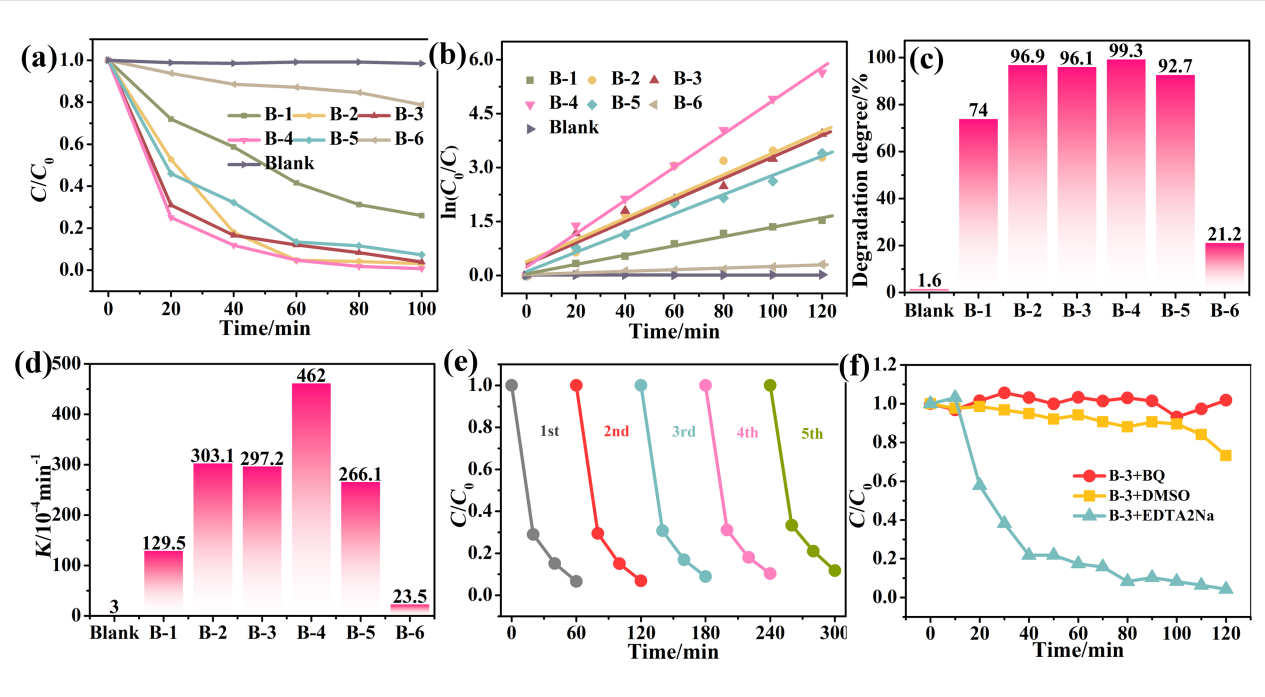

Figure 6: Photocatalytic activity under visible light illumination. (a) The rhodamine B (RhB) solution degradation of the as-prepared samples with sample with no catalyst and P25 as comparison. (b) The linear fitting of the pseudo-first kinetic model. (c) Photodegradation degree within 100 min of the as-synthesized sample. (d) Photocatalytic rate of all the samples. (e) Recycling tests for the B-4 sample whose Bi/Zn molar ratio is 13. (f) The effect of sacrificial agents on the RhB photodegradation of the B-3 sample (Bi/Zn 1:2).

after the photocatalytic testing. The results show that the degradation performance of ZnO and BiOI are quite unsatisfactory, while no concentration difference is visible without the catalyst, demonstrating the self-degradation of RhB is negligible. All of the ZnO–BiOI heterostructured nanocomposites exhibit remarkably improved photocatalytic activity in terms of both the efficiency and the degradation degree for 100 min (Table 1). With reducing the Bi/Zn molar ratio, the degradation degree for 100 min of the sample becomes higher. After the most optimal point has been reached by B-4 sample (with the Bi/Zn ratio of 1:3), the performance of sample B-5 drops off, which is likely to be triggered by the reduction of the heterojunction with further increasing amount of ZnO.

To exploit the kinetic process of the photocatalytic reaction, the RhB degradation data can be fitted to the pseudo-first order reaction kinetic model $\ln(C_0/C) = Kt$ in Figure 6b, where K is the reaction rate coefficient (Table 1). The photodegradation degree within 100 min and the photocatalytic rates of the as-synthesized samples compared with blank controls are shown in Figure 6c,d. Among all the samples and the control groups, B-4, with the highest degradation degree, also displays the highest reaction rate coefficient, confirming that the Bi/Zn molar ratio of 1:3 is the most optimal sample for photocatalytic performance. Other very critical criteria of the photocatalyst for practical application are stability and reusability. Figure 6e presents the recycling test results of the B-4 sample. After being circularly used for five times, the degradation degree still remains at 95% photocatalytic activity compared to the result of the first cycle, indicating the stability and the reuse ability are considerably high.

It is known that the degradation of organic dye is realized through redox reactions, which are mainly dependent on the oxidative and/or reductive species. To obtain a clear consensus of the reactive species and to further explore the photocatalytic degradation mechanism in detail, an examination was carried out by adding different sacrificial agents at a calculated amount. Benzoquinone (BQ), dimethyl sulfoxide (DMSO) and ethylene diamine tetraacetic acid sodium (EDTA sodium) were adopted as scavengers of $O_2^{\bullet-}$ [53], $^{\bullet}OH$ [54] radicals and holes [55], respectively. From the results displayed in Figure 6f, it is obvious that while the addition of BQ significantly inhibits the photocatalytic activity, DMSO has less effect on the degradation degree. EDTA sodium has little impact on the photodegradation of RhB solution under visible light. Thus, although produced in the photocatalytic processes, the photoinduced holes do not play an important role in the degradation reaction. Therefore, the decomposition of RhB solution is mainly attributed to the oxidation reaction of $O_2^{\bullet-}$ and the $^{\bullet}OH$ radicals. Based on the results of the experiments, the probable processes of the mechanism can be proposed as follows:

$$\mathrm{BiOI} \xrightarrow{h\nu(\lambda \geq 420\ \mathrm{nm})} \mathrm{BiOI}\left(h_{VB^+} + e_{CB^+}\right) \quad (2)$$

$$\mathrm{BiOI}\left(e_{CB^-}\right) \xrightarrow{\text{transfer}} \mathrm{ZnO}\left(e_{CB^-}\right) \quad (3)$$

$$\mathrm{ZnO}\left(e_{CB^-}\right) + O_2 \rightarrow \mathrm{ZnO} + O_2^{\cdot -} \quad (4)$$

$$O_2^{\cdot -} + H^+ \rightarrow {}^{\cdot}\mathrm{OH} \quad (5)$$

$$O_2^{\cdot -} \text{ and } {}^{\cdot}\mathrm{OH} + \mathrm{RhB} \rightarrow \text{degradation products} \quad (6)$$

Photocatalytic mechanism

On the basis of above results, it is firmly believed that the photocatalytic degradation ability of ZnO/BiOI nanocomposites was greatly improved due to the p–n heterojunction structure between ZnO and BiOI. Further insight into the mechanism is illustrated as follow. Figure 7a shows the simplified energy band structure of BiOI and ZnO. The valence band maximum energies of BiOI and ZnO as obtained in XPS measurements are 0.96 and 2.27 eV, and the band gaps calculated from UV–vis spectra are 1.83 eV for BiOI and 3.16 eV for ZnO. Thus, the conduction band minimum energy should occur at –0.87 eV and –0.89 eV for BiOI and ZnO, respectively. While BiOI possesses a p-type semiconductor material nature whose Femi level is located not far from the valence band, ZnO is a typical n-type material with the Femi level near the conduction band. When BiOI was hybridized by ZnO, the construction of a p–n heterojunction realigned the Femi levels of the two materials to the same energy to form an equilibrium state, hence the band bending and the electric field are created consequently [56] and photoinduced electrons are transferred to the conduction band of ZnO and leave the holes in the valence band of BiOI (Figure 7b). This indicates that the separation efficiency of the ZnO/BiOI nanocomposite is remarkably improved, thus the photocatalytic degradation ability of the heterostructure sample is better than the single phase.

Conclusion

ZnO–BiOI heterostructured nanocomposites were successfully synthesized via a facile solution method followed by calcination, resulting in different morphology, optical properties and band gap structures by tuning the Bi/Zn molar ratio to 1:0, 1:1, 1:2, 1:3, 1:4 to 0:1. The results of the photocatalytic degradation of rhodamine B under visible-light irradiation demonstrate that the as-synthesized ZnO/BiOI heterostructured nanocomposites exhibit the superior photocatalytic ability as compared to pure BiOI and ZnO, which could be attributed to the synergistic effects of higher specific area and the enhanced separation efficiency of photoinduced electron–hole pairs.

Experimental

Chemicals

Zinc acetate ($Zn(CH_3COO)_2{\cdot}2H_2O$), bismuth nitrate ($Bi(NO_3)_3{\cdot}5H_2O$), potassium iodine (KI), ammonium hydrogen carbonate (NH_4HCO_3), rhodamine B (RhB), benzoquinone (BQ), dimethyl sulfoxide (DMSO) and ethylenediamine teraacetic acid sodium (EDTA sodium) were directly used without any further purification.

Synthesis of ZnO–BiOI nanocomposites

Generally, 0.05 mol NH_4HCO_3 were added into 50 mL DI water to form solution A, and 0.025 mol $Zn(CH_3COO)_2{\cdot}2H_2O$ was dissolved in 25 mL DI water which was denoted as solution B. After the 30 min of stirring, solution B was slowly poured into solution A with continuous stirring for about 1 h. Subsequently, the required amount of $Bi(NO_3)_3{\cdot}5H_2O$ (Bi/Zn

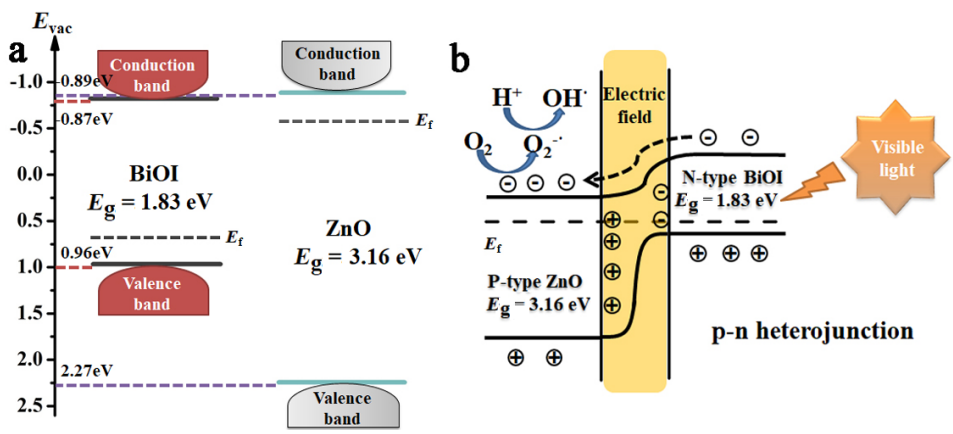

Figure 7: Schematic band energy diagram of BiOI and ZnO before (a) and after (b) interfacial contact.

molar ratios which range from 1:0, 1:1, 1:2, 1:3, 1:4 to 0:1 denoted as B-1, B-2, B-3, B-4, B-5 and B-6, respectively), dissolved in acetic acid, was added dropwise to the above-mentioned mixture of solution A and B. KI at an appropriate amount was added as the iodine source. The solution was stirred at 80 °C for 2 h. The resulting samples were centrifuged, washed thoroughly with distilled water, and then dried at 65 °C for 12 h. Finally, the heterostructured ZnO/BiOI nanocomposites were obtained after calcination at 300 °C for 2 h in air. For comparison, the pure ZnO was prepared by the same procedure but without using the BiOI precursor, and the preparation of pure BiOI was also fabricated without using ZnO precursor, based on the method described by Yu et al. [57].

Characterization

X-ray diffraction (XRD) was conducted on a Rigaku A/MAX-Rb system operated at 40 kV and 100 mA with Cu Kα radiation, with a scanning rate of 4°/min in the range of from 10 to 90°. A Hitachi S4800 scanning electron microscope (SEM) was used to investigate the morphology with an accelerating voltage of 15 kV. The elemental analysis was also performed on an energy-dispersive spectrometer (EDS) with the same instrument. Transmission electron microscopy (TEM) was employed to observe the microstructure of the as-synthesized ZnO/BiOI heterojunction nanocomposites under the operating voltage of 120 kV on a JEOL-ARM200F device. The surface area and the pore distribution were tested by the nitrogen adsorption–desorption isotherms recorded on a ASAP 2020 HD88 using the Brunauer–Emmett–Teller (BET) method at liquid nitrogen temperature 77 K.

The optical absorption properties of the samples were measured by UV–vis spectra on a Hitachi U-4100 spectrophotometer equipped with an integrating sphere at room temperature in the region of 200–800 nm. The photoluminence (PL) spectra were recorded by a Horiba Floruomax-4_1188D-4513-FM instrument with an emission wavelength of 320 nm. X-ray photoelectron spectroscopy (XPS) measurements were performed at 150 W with a monochromatic Al Kα (1486.6 eV) X-ray source on an ESCALAB 250 instrument. The binding energy correction was carried out using the C 1s peak of 284.6 eV as reference.

Photocatalytic tests

The photocatalytic activity of ZnO–BiOI nanocomposites was evaluated by degradation of rhodamine B (RhB) under irradiation by a 300 W Xe lamp with a 420 nm cut-off filter at ambient temperature. 0.1 g of sample was added to 100 mL of 10 mg/L RhB DI water solution in the reactor. To achieve the balance of adsorption–desorption in the uniform suspension, the system was sonicated and magnetic stirred for 30 min in the dark. After the irradiation was introduced into the system, the concentration of RhB was periodically detected by the UV–vis spectrum to determine the photodegradation degree with continuous stirring. For reactive species investigation, specific scavengers were introduced into the reaction system by following the same procedures as described in the photodegradation experiments.

Supporting Information

Supporting Information File 1

Additional experimental information.
[https://www.beilstein-journals.org/bjnano/content/supplementary/2190-4286-9-72-S1.pdf]

Acknowledgements

This research is financially supported by the Thailand Research Fund (RSA6080017). We also gratefully acknowledge the NSFC (grant 51421091), and National Science Foundation for Distinguished Young Scholars for Hebei Province of China (grant E2016203376). JQ would like to acknowledge the support from the Thai Government Budget (2017), Chulalongkorn University (GB_B_60_114_62_03), Ratchadapisek Sompoch Endowment Fund, Chulalongkorn University, granted to the Surface Coatings Technology for Metals and Materials Research Unit (GRU 60-001-62-001-1), and State Key Laboratory of Metastable Materials Science and Technology, Yanshan University.

ORCID® iDs

Jiaqian Qin - https://orcid.org/0000-0002-9166-3533

References

1. Fujishiima, A.; Honda, K. *Nature* **1972,** *238,* 37–38. doi:10.1038/238037a0
2. Kumar, S.; Kumar, A.; Bahuguna, A.; Sharma, V.; Krishnan, V. *Beilstein J. Nanotechnol.* **2017,** *8,* 1571–1600. doi:10.3762/bjnano.8.159
3. Zhang, X. Y.; Qin, J. Q.; Hao, R. R.; Wang, L. M.; Shen, X.; Yu, R. C.; Limpanart, S.; Ma, M. Z.; Liu, R. P. *J. Phys. Chem. C* **2015,** *119,* 20544–20554. doi:10.1021/acs.jpcc.5b07116
4. He, H. B.; Xue, S. S.; Wu, Z.; Yu, C. L.; Yang, K.; Peng, G. M.; Zhou, W. Q.; Li, D. H. *Chin. J. Catal.* **2016,** *37,* 1841–1850. doi:10.1016/S1872-2067(16)62515-9
5. Pathania, D.; Gupta, D.; Al-Muhtaseb, A. H.; Sharma, G.; Kumar, A.; Naushad, M.; Ahamad, T.; Alshehri, S. M. *J. Photochem. Photobiol., A* **2016,** *329,* 61–68. doi:10.1016/j.jphotochem.2016.06.019
6. Han, W. W.; Li, Z.; Li, Y.; Fan, X.; Zhang, F.; Zhang, G.; Peng, W. *Front. Chem. (Lausanne, Switz.)* **2017,** *5,* 84. doi:10.3389/fchem.2017.00084
7. Schrauzer, G. N.; Guth, T. D. *J. Am. Chem. Soc.* **1977,** *99,* 7189–7193. doi:10.1021/ja00464a015
8. Chen, X. Z.; Li, N.; Kong, Z. Z.; Ong, W. J.; Zhao, X. J. *Mater. Horiz.* **2018,** *5,* 9–27. doi:10.1039/C7MH00557A

9. Tran, P. D.; Wong, L. H.; Barber, J.; Loo, J. S. C. *Energy Environ. Sci.* **2012,** *5,* 5902–5918. doi:10.1039/c2ee02849b
10. Saravanan, R.; Shankar, H.; Prakash, T.; Narayanan, V.; Stephen, A. *Mater. Chem. Phys.* **2011,** *125,* 277–280. doi:10.1016/j.matchemphys.2010.09.030
11. Pathania, D.; Katwal, R.; Sharma, G.; Naushad, M.; Khan, M. R.; Al-Muhtaseb, A. H. *Int. J. Biol. Macromol.* **2016,** *87,* 366–374. doi:10.1016/j.ijbiomac.2016.02.073
12. Pandiyarajan, T.; Saravanan, R.; Karthikeyan, B.; Gracia, F.; Mansilla, H. D.; Gracia-Pinilla, M. A.; Mangalaraja, R. V. *J. Mater. Sci.: Mater. Electron.* **2017,** *28,* 2448–2457. doi:10.1007/s10854-016-5817-2
13. Gnanasekaran, L.; Hemamalini, R.; Saravanan, R.; Ravichandran, K.; Gracia, F.; Agarwal, S.; Gupta, V. K. *J. Photochem. Photobiol., B* **2017,** *173,* 43–49. doi:10.1016/j.jphotobiol.2017.05.027
14. Novokreshchenova, M. N.; Yukhin, Y.; Bokhonov, B. B. *Chemistry for Sustainable Develoment;* Springer: Dordrecht, 2005.
15. Chen, X. B.; Mao, S. S. *Chem. Rev.* **2007,** *107,* 2891–2959. doi:10.1021/cr0500535
16. Yu, J. G.; Yu, X. X. *Environ. Sci. Technol.* **2008,** *42,* 4902–4907. doi:10.1021/es800036n
17. Yu, C. L.; Zhou, W. Q.; Zhu, L. H.; Li, G.; Yang, K.; Jin, R. C. *Appl. Catal., B: Environ.* **2016,** *184,* 1–11. doi:10.1016/j.apcatb.2015.11.026
18. Kudo, A.; Omori, K.; Kato, H. *J. Am. Chem. Soc.* **1999,** *121,* 11459–11467. doi:10.1021/ja992541y
19. Zhao, X.; Chen, Z. *Beilstein J. Nanotechnol.* **2017,** *8,* 2640–2647. doi:10.3762/bjnano.8.264
20. Tang, J. W.; Zou, Z. G.; Ye, J. H. *Catal. Lett.* **2004,** *92,* 53–56. doi:10.1023/B:CATL.0000011086.20412.aa
21. Tang, J. W.; Zou, Z. G.; Ye, J. H. *Angew. Chem., Int. Ed.* **2004,** *43,* 4463–4466. doi:10.1002/anie.200353594
22. Yu, C. L.; Wu, Z.; Liu, R. Y.; Dionysiou, D. D.; Yang, K.; Wang, C. Y.; Liu, H. *Appl. Catal., B: Environ.* **2017,** *209,* 1–11. doi:10.1016/j.apcatb.2017.02.057
23. Xiao, X.; Zhang, W. D. *J. Mater. Chem.* **2010,** *20,* 5866–5870. doi:10.1039/c0jm00333f
24. An, H. Z.; Du, Y.; Wang, T. M.; Wang, C.; Hao, W. C.; Zhang, J. Y. *Rare Met.* **2008,** *27,* 243–250. doi:10.1016/S1001-0521(08)60123-0
25. Huang, W. L. *J. Comput. Chem.* **2009,** *30,* 1882–1891. doi:10.1002/jcc.21191
26. Yu, C. L.; Zhou, W. Q.; Yu, J. C.; Liu, H.; Wei, L. F. *Chin. J. Catal.* **2014,** *35,* 1609–1618. doi:10.1016/S1872-2067(14)60170-4
27. Qin, J. Q.; Yang, C. W.; Cao, M.; Zhang, X. Y.; Rajendran, S.; Limpanart, S.; Ma, M. Z.; Liu, R. P. *Mater. Lett.* **2017,** *189,* 156–159. doi:10.1016/j.matlet.2016.12.007
28. Ong, W. J. *Front. Mater.* **2017,** *4,* 11. doi:10.3389/fmats.2017.00011
29. Zeng, D. Q.; Xiao, L.; Ong, W. J.; Wu, P. Y.; Zheng, H. F.; Chen, Y. Z.; Peng, D. L. *ChemSusChem* **2017,** *10,* 4624–4631. doi:10.1002/cssc.201701345
30. Lv, C. D.; Chen, G.; Zhou, X.; Zhang, C. M.; Wang, Z. K.; Zhao, B. R.; Li, D. Y. *ACS Appl. Mater. Interfaces* **2017,** *9,* 23748–23755. doi:10.1021/acsami.7b05302
31. Zhang, K. H. L.; Rui, W.; Tang, F.; Li, W.; Oropeza, F. E.; Liang, Q.; Lazarov, V. K.; Du, Y.; Payne, D. J.; MacManus-Driscoll, J. L.; Blamire, M. G. *ACS Appl. Mater. Interfaces* **2017,** *9,* 26549–26555. doi:10.1021/acsami.7b06025
32. Zhang, X.; Zhang, L. Z.; Xie, T. F.; Wang, D. J. *J. Phys. Chem. C* **2009,** *113,* 7371–7378. doi:10.1021/jp900812d
33. Jiang, J.; Zhang, X.; Sun, P. B.; Zhang, L. Z. *J. Phys. Chem. C* **2011,** *115,* 20555–20564. doi:10.1021/jp205925z
34. Yu, Y. X.; Ouyang, W. X.; Zhang, W. D. *J. Solid State Electrochem.* **2014,** *18,* 1743–1750. doi:10.1007/s10008-014-2402-6
35. Kuang, P.-Y.; Ran, J.-R.; Liu, Z.-Q.; Wang, H.-J.; Li, N.; Su, Y.-Z.; Jin, Y.-G.; Qiao, S.-Z. *Chem. – Eur. J.* **2015,** *21,* 15360–15368. doi:10.1002/chem.201501183
36. Tong, Y. H.; Zheng, C.; Lang, W. J.; Wu, F.; Wu, T.; Luo, W. Q.; Chen, H. F. *Mater. Des.* **2017,** *122,* 90–101. doi:10.1016/j.matdes.2017.02.033
37. Jiang, J. J.; Wang, H. T.; Chen, X. D.; Li, S.; Xie, T. F.; Wang, D. J.; Lin, Y. H. *J. Colloid Interface Sci.* **2017,** *494,* 130–138. doi:10.1016/j.jcis.2017.01.064
38. Al-Gaashani, R.; Radiman, S.; Daud, A. R.; Tabet, N.; Al-Douri, Y. *Ceram. Int.* **2013,** *39,* 2283–2292. doi:10.1016/j.ceramint.2012.08.075
39. Reddy, K. H.; Martha, S.; Parida, K. M. *Inorg. Chem.* **2013,** *52,* 6390–6401. doi:10.1021/ic400159m
40. Sing, K. S. W.; Everett, D. H.; Haul, R. A.; Moscou, L.; Pierotti, R. A.; Rouquérol, J.; Siemieniewska, T. *Pure Appl. Chem.* **1985,** *57,* 603–619. doi:10.1351/pac198557040603
41. Dimitrov, V.; Komatsu, T. *J. Solid State Chem.* **2002,** *163,* 100–112. doi:10.1006/jssc.2001.9378
42. Sun, J. J.; Li, X. Y.; Zhao, Q. D.; Tadé, M. O.; Liu, S. M. *Appl. Catal., B: Environ.* **2017,** *219,* 259–268. doi:10.1016/j.apcatb.2017.07.052
43. Zhang, X.; Qin, J.; Xue, Y.; Yu, P.; Zhang, B.; Wang, L.; Liu, R. *Sci. Rep.* **2014,** *4,* 4596. doi:10.1038/srep04596
44. Gurunathan, K. *Int. J. Hydrogen Energy* **2004,** *29,* 933–940. doi:10.1016/j.ijhydene.2003.04.001
45. Sambandam, B.; Surenjan, A.; Philip, L.; Pradeep, T. *ACS Sustainable Chem. Eng.* **2015,** *3,* 1321–1329. doi:10.1021/acssuschemeng.5b00044
46. Ye, L. Q.; Tian, L. H.; Peng, T. Y.; Zan, L. *J. Mater. Chem.* **2011,** *21,* 12479–12484. doi:10.1039/c1jm11005e
47. Jing, L. Q.; Xu, Z. L.; Shang, J.; Sun, X. J.; Cai, W. M.; Guo, H. C. *Mater. Sci. Eng., A* **2002,** *332,* 356–361. doi:10.1016/S0921-5093(01)01801-9
48. Zhang, Z. Y.; Shao, C. L.; Li, X. H.; Wang, C. H.; Zhang, M. Y.; Liu, Y. C. *ACS Appl. Mater. Interfaces* **2010,** *2,* 2915–2923. doi:10.1021/am100618h
49. Wang, Y.; Fang, H. B.; Ye, R. Q.; Zheng, Y. Z.; Li, N.; Tao, X. *RSC Adv.* **2016,** *6,* 24430–24437. doi:10.1039/C6RA00903D
50. Ansari, S. A.; Khan, M. M.; Kalathil, S.; Nisar, A.; Lee, J.; Cho, M. H. *Nanoscale* **2013,** *5,* 9238–9246. doi:10.1039/c3nr02678g
51. Tauc, J. *Mater. Res. Bull.* **1968,** *3,* 37–46. doi:10.1016/0025-5408(68)90023-8
52. Davis, E. A.; Mott, N. F. *Philos. Mag.* **1970,** *22,* 0903–0922. doi:10.1080/14786437008221061
53. Wang, L.; Ouyang, S.; Ren, B.; Ye, J.; Wang, D. *APL Mater.* **2015,** *3,* 104414. doi:10.1063/1.4928702
54. Li, T. B.; Chen, G.; Zhou, C.; Shen, Z. Y.; Jin, R. C.; Sun, J. X. *Dalton Trans.* **2011,** *40,* 6751–6758. doi:10.1039/c1dt10471c
55. Liu, Y. F.; Yao, W. Q.; Liu, D.; Zong, R. L.; Zhang, M.; Ma, X. G.; Zhu, Y. F. *Appl. Catal., B: Environ.* **2015,** *163,* 547–553. doi:10.1016/j.apcatb.2014.08.039
56. Yoon, H. J.; Choi, Y. I.; Jang, E. S.; Sohn, Y. *J. Ind. Eng. Chem.* **2015,** *32,* 137–152. doi:10.1016/j.jiec.2015.08.010
57. Yu, C. L.; Fan, C. F.; Yu, J. C.; Zhou, W. Q.; Yang, K. *Mater. Res. Bull.* **2011,** *46,* 140–146. doi:10.1016/j.materresbull.2010.08.013

License and Terms

This is an Open Access article under the terms of the Creative Commons Attribution License (http://creativecommons.org/licenses/by/4.0), which permits unrestricted use, distribution, and reproduction in any medium, provided the original work is properly cited.

The license is subject to the *Beilstein Journal of Nanotechnology* terms and conditions: (https://www.beilstein-journals.org/bjnano)

The definitive version of this article is the electronic one which can be found at:
doi:10.3762/bjnano.9.72

BEILSTEIN JOURNAL OF NANOTECHNOLOGY

Noble metal-modified titania with visible-light activity for the decomposition of microorganisms

Maya Endo[1], Zhishun Wei[1,2], Kunlei Wang[1,3], Baris Karabiyik[1], Kenta Yoshiiri[1,3], Paulina Rokicka[1,4], Bunsho Ohtani[1,3], Agata Markowska-Szczupak[*1,4] and Ewa Kowalska[*1,3]

Full Research Paper

Open Access

Address:
[1]Institute for Catalysis, Hokkaido University, N21 W10, 001-0021 Sapporo, Japan, [2]School of Materials and Chemical Engineering, Hubei University of Technology, 430068 Wuhan, China, [3]Graduate School of Environmental Science, N10 W5, 060-0810 Sapporo, Japan and [4]Institute of Inorganic Technology and Environment Engineering, West Pomeranian University of Technology, Szczecin, Pulaskiego 10, 70-322 Szczecin, Poland

Email:
Agata Markowska-Szczupak[*] - agata@erb.pl; Ewa Kowalska[*] - kowalska@cat.hokudai.ac.jp

* Corresponding author

Keywords:
antifungal properties; antimicrobial properties; bactericidal effect; noble-metal nanoparticles; plasmonic photocatalysis

Beilstein J. Nanotechnol. **2018,** *9,* 829–841.
doi:10.3762/bjnano.9.77

Received: 01 October 2017
Accepted: 02 February 2018
Published: 07 March 2018

This article is part of the Thematic Series "Energy conversion, storage and environmental remediation using nanomaterials".

Guest Editor: W.-J. Ong

© 2018 Endo et al.; licensee Beilstein-Institut.
License and terms: see end of document.

Abstract

Commercial titania photocatalysts were modified with silver and gold by photodeposition, and characterized by diffuse reflectance spectroscopy (DRS), X-ray powder diffraction (XRD), X-ray photoelectron spectroscopy (XPS) and scanning transmission electron microscopy (STEM). It was found that silver co-existed in zero valent (core) and oxidized (shell) forms, whereas gold was mainly zero valent. The obtained noble metal-modified samples were examined with regard to antibacterial (*Escherichia coli* (*E. coli*)) and antifungal (*Aspergillus niger* (*A. niger*), *Aspergillus melleus* (*A. melleus*), *Penicillium chrysogenum* (*P. chrysogenum*), *Candida albicans* (*C. albicans*)) activity under visible-light irradiation and in the dark using disk diffusion, suspension, colony growth ("poisoned food") and sporulation methods. It was found that silver-modified titania, besides remarkably high antibacterial activity (inhibition of bacterial proliferation), could also decompose bacterial cells under visible-light irradiation, possibly due to an enhanced generation of reactive oxygen species and the intrinsic properties of silver. Gold-modified samples were almost inactive against bacteria in the dark, whereas significant bactericidal effect under visible-light irradiation suggested that the mechanism of bacteria inactivation was initiated by plasmonic excitation of titania by localized surface plasmon resonance of gold. The antifungal activity tests showed efficient suppression of mycelium growth by bare titania, and suppression of mycotoxin generation and sporulation by gold-modified titania. Although, the growth of fungi was hardly inhibited through disc diffusion (inhibition zones around discs), it indicates that gold does not penetrate into the media, and thus, a good stability of plas-

monic photocatalysts has been confirmed. In summary, it was found that silver-modified titania showed superior antibacterial activity, whereas gold-modified samples were very active against fungi, suggesting that bimetallic photocatalysts containing both gold and silver should exhibit excellent antimicrobial properties.

Introduction

Environmental pollution and the lack of clean potable water are main issues facing human development. Although, various methods of efficient control and monitoring of waste management have been successfully applied in developed countries, pollution in low-income countries is still a major environmental and public health challenge. It is thought that in developing countries, the quest for poverty reduction and economic development results in little consideration for environmental issues. Although, weak environmental regulatory institutions often undermine conventional command-and-control policies in these countries [1], various techniques and methods of water purification, such as disinfection, have already been applied. During disinfection, vegetative forms of microorganisms are destroyed or deactivated through interfering with cell activity (e.g., changes in cell permeability, enzyme activity and cell division). It is believed that in the history of humanity, disinfection is one of the most important achievements in the health protection [2]. Improvements in sanitation facilities and water-treatment methods have reduced the spread of many infectious diseases (e.g., cholera and dysentery), whereas the sterilization practices in hospitals have prevented the transition of infectious pathogens to patients. Water disinfection is usually carried out by chlorination, and sometimes by more expensive methods, such as UV irradiation and ozonation. Although, chlorine can inactivate some microorganisms completely, it may also negatively influence water environment, and even animal and human health, e.g., the chlorination by-products are mutagenic and carcinogenic [3]. Moreover, chlorine disinfection has only a low effect on some pathogenic protozoa (e.g., *Cryptosporidium sp.* responsible for diarrhoea and even the death of immunocompromised patients) and viruses (e.g., norovirus). In contrast, UV disinfection is highly efficient against various microorganisms (even viruses) since absorption of UV light (λ = 253.7 nm) by nucleic acids induces the damage of genetic information and inactivation. However, it should be pointed out that chlorine disinfection is often complementary used because: (i) some viruses have low sensitivity to UV irradiation (e.g., adenovirus), and (ii) the lack of residual disinfection of UV irradiation (only during treatment/direct irradiation). Ozone disinfection is also efficient for the degradation of microorganisms, either directly by ozone molecules or by formed oxidative radicals. However, it should be reminded that ozone itself is harmful and can initiate the formation of toxic compounds. Moreover, ozonation and UV irradiation are quite expensive technologies considering both investment and exploration costs.

Accordingly, inorganic antimicrobial agents have been extensively investigated for water purification since they are stable and environmentally safe. Historically, noble metals such as gold, silver and copper have been used since ancient times for the treatment of many diseases and illnesses or for the disinfection of water. In ancient Greece and Rome, the silver or gold dishes left in the sun were believed to protect people against pathogenic microorganisms, and silver coins thrown into the water prolonged its freshness [4-6]. Recent advances in nanotechnology enable to utilize size-dependent properties of nanomaterials, such as high specific surface area, high reactivity, quantum-size effects and plasmonic properties. Nanosilver and nanogold have already been used for various antimicrobial applications, such as (i) ionization techniques, (ii) membrane technologies to reduce biofouling of sanitation devices, (iii) development of sensors with high sensitivity and selectivity for pathogen detection, (iv) everyday products (cosmetics, shoes, clothes and dental treatment). For example, slowly released nanosilver has been used in a variety of domestic appliances, such as washing machines (e.g., Samsung SilverNanoHealth technology). Moreover, antibacterial properties of noble metals have been applied for medical purposes, including healing of burn wounds (bandage and dressing), and protection against infection (braces and catheters).

Photocatalysis is considered as one of the best methods for environmental purification since additional chemical compounds, such as strong oxidants (ozone, hydrogen peroxide or chlorine) [7-14], are not introduced into the environment [15,16]. The energy consumption is also much lower than that of other advanced oxidation technologies (AOTs), e.g., wet air oxidation [17], supercritical water oxidation [18], or H_2O_2/UV-C [19]. That is because UV-A lamps or even solar radiation can be used for photocatalyst activation [20]. Titanium(IV) oxide (titania) is the most widely used semiconductor photocatalyst used in treatment of water/wastewater and air [21]. The major barrier for common application of titania photocatalysis is the low activity under solar radiation (mainly due to wide band gap of titania of 3.0–3.2 eV and the recombination of charge carriers). There are various ways to improve photocatalytic performance of titania photocatalysts: (1) to inhibit the recombination of charge carriers, and (2) to extend its working abilities to the visible-light region, for example, by morphology design [22-26], surface modification [27-32], doping [33-36], or the formation of heterojunctions with other semiconductors [37-

40]. Modification with noble metals seems the most promising as it is well known that under UV irradiation, noble metals work as an electron pool retarding the recombination of charge carriers [41-43], whereas under visible-light irradiation titania is activated by the plasmonic properties of noble metals ("plasmonic photocatalysis") [44,45]. Accordingly, it has been proposed that the combination of the antimicrobial properties of noble metals with the high photocatalytic activity of modified titania should result in a high purification efficiency of noble metal-modified titania [6,46-52]. Indeed, in our recent study, noble metal-modified faceted anatase titania (octahedral anatase particles; OAP) have shown high activity in both the decomposition of organic compounds and of microorganisms (*E. coli* and *C. albicans*) [48]. It has been found that both the intrinsic properties of silver and the photocatalytic activity of silver-modified titania are responsible for the high antibacterial activity under visible-light irradiation, whereas the size and shape of silver nanoparticles (NPs) and the aspect ratio of titania affect the antifungal activity [29]. In the present study, antimicrobial properties of commercial titania samples modified with noble metals have been investigated in order to further clarify (1) the mechanism of antimicrobial action of plasmonic photocatalysts, (2) key factors of the high activity against various microorganisms, (3) the correlation between the inactivation and complete decomposition of bacteria, (4) the inhibition of filamentous fungal growth and sporulation by using a new evaluation method.

Results and Discussion

Characterization of titania samples modified with NPs of silver and gold

Six commercial titania samples were modified with gold or silver by photodeposition [53,54]. In brief, during photodeposition, metal cations were reduced by photogenerated electrons on irradiated titania. To enable a efficient deposition of metals on titania, photodeposition was carried out in 50 vol % methanol as a hole scavenger and under anaerobic conditions to avoid electron scavenging by oxygen. To find the key factors of antimicrobial activity, various titania samples modified with noble metal NPs (NMNPs) were investigated. The NMNPs differ in crystallographic composition, crystallite sizes and specific surface area. It was confirmed that properties of titania influenced the resultant properties of NMNPs [53], as shown in Table 1. Min et al. proposed that gold clusters were preferentially deposited on surface defects of the support [55]. Therefore, fine titania with a high number of defects (electron traps, ETs) induced the formation of fine and well-dispersed NMNPs on titania surface, as shown in Figure 1 (top). In contrast, titania with large crystals (low number of ETs) induced the aggregation of NMNPs on its well-crystallized surface (Figure 1 (bottom)). It was found that silver formed smaller NPs than gold, as shown in Figure 1 (left and right, respectively).

To investigate the surface properties of the deposited noble metals, XPS analysis was performed, and exemplary data are shown in Figure 2. XPS peaks of Au $4f_{7/2}$ and Ag $3d_{5/2}$ were assigned to two and/or three components, i.e., $Au^{\delta+}$, Au^0 and $Au^{\delta-}$ for binding energies (BE) of ca. 83.0, 82.5 and 82.0 eV, respectively, and Ag^0, Ag^+ and Ag^{2+} for BE of ca. 368.4, 367.4 and 366.3 eV, respectively. It was found that gold existed mainly in zero valent form, whereas silver existed in both zero valent and oxidized forms (mainly as Ag^+). It is proposed that although zero valent silver NPs were formed during photodeposition (brown colour of suspension, which is characteristic for spherical silver NPs with localized surface plasmon resonance (LSPR) at ca. 410–430 nm), they were easily oxidized under ambient conditions, and the resultant silver deposits on titania were composed of a zero valent silver core and a silver oxide shell. XRD analysis confirmed XPS data showing silver in three oxidation states (Ag(0), Ag(I) and Ag(II)), as shown in Figure 3.

All modified titania samples were coloured due to LSPR of NMNPs. Gold-modified samples were violet (light violet for larger titania and gold NPs (Au/TiO_2(ST41), Au/TiO_2(FP6)) and dark violet for smaller particle sizes (Au/TiO_2(TIO12),

Table 1: Properties of titania photocatalysts used for metal deposition and crystallite sizes of gold and silver NPs.

titania	phase[a]	size[b]/nm	ET[c]/mmol·g^{-1}	BET[d]/m^2·g^{-1}	NP size[e]/nm	
					Au	Ag
ST01	anatase	8[f]	84[f]	298[f]	8	0.9[g]
ST41	anatase	205[f]	25[f]	11[f]	29	20
TIO12	anatase	6[f]	111[f]	290[f]	14	—
FP6	anatase/r	12	—	97	—	6
TIO6	rutile	15[f]	242[f]	100[f]	14	—
STF10	rutile/a	102	71[f]	12[f]	23	22

[a]crystal phase (r: small content of rutile and a: small content of anatase), [b]crystallite size of the dominant titania phase, [c]content of electron traps, [d]specific surface area, [e]crystallite size of metal NPs, [f,g]data reported previously in [56,57], respectively.

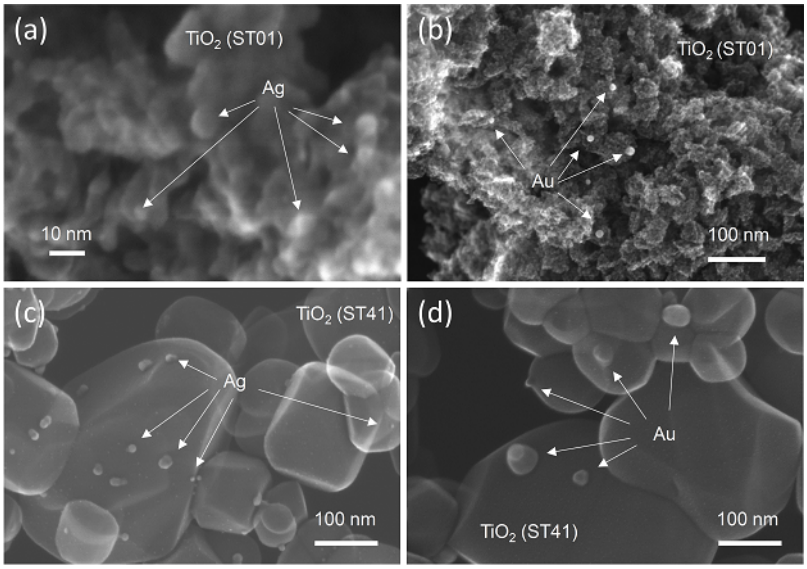

Figure 1: STEM images of modified titania samples: (a) Ag/TiO_2(ST01), (b) Au/TiO_2(ST01), (c) Ag/TiO_2(ST41) and (d) Au/TiO_2(ST41).

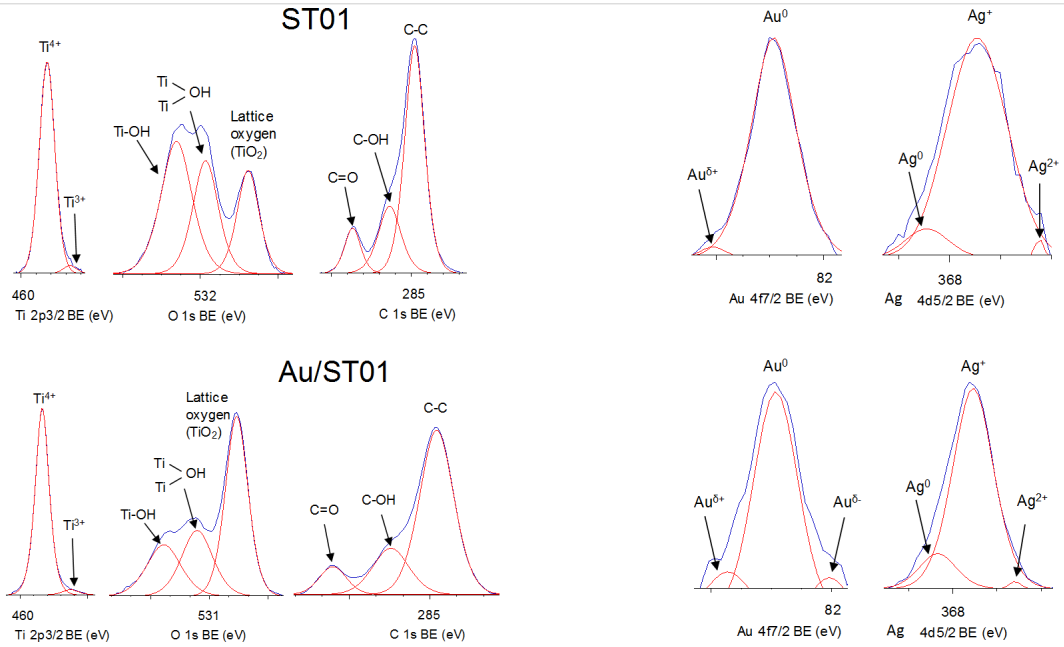

Figure 2: XPS spectra for bare (top left) and gold-modified (bottom left) TiO_2(ST01) sample, and deconvoluted peaks of Au $4f_{7/2}$ (center) and Ag $3d_{5/2}$ (right) for metal-modified ST01 (top) and ST41 (bottom).

Au/TiO_2(ST01)), and silver-modified samples were brown-violet. Exemplary diffuse reflectance spectra (DRS) are shown in Figure 4. It should be pointed out that LSPR of silver could overlap with photoabsorption of titania, and thus to obtain clear LSPR peak of silver, DRS taken with bare titania as reference is recommended (Figure 4 (right)). The intrinsic absorption of anatase titania was observed at wavelengths shorter than 400 nm (E_g > 3 eV), and LSPR peaks appeared at longer wavelengths for gold NPs (λ_{max} at ca. 560 nm) than for silver NPs (λ_{max} at ca. 450 nm), correlating well with reported data for spherical NPs of gold and silver [58].

Antibacterial activities of plasmonic photocatalysts

At first, the antibacterial properties of bare titania samples were investigated, and data are presented in Supporting Information File 1 (Table S1). In the dark, antibacterial properties of bare titania samples were very low reaching 15.4%, 16.4% and

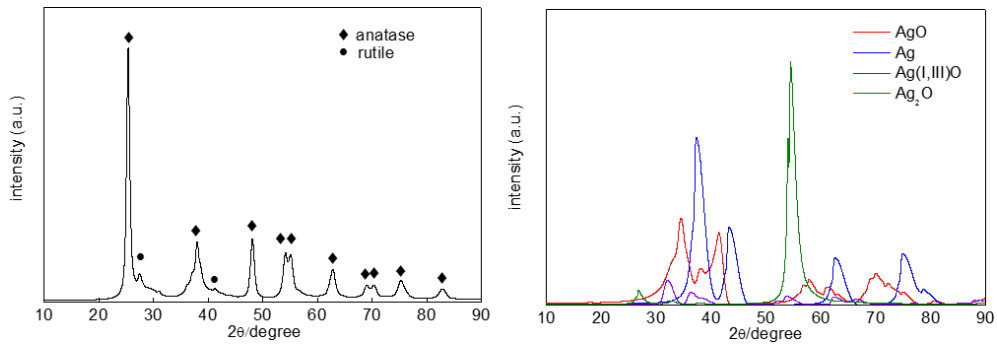

Figure 3: XRD patterns of Ag/TiO_2(FP6): (left) original pattern, and (right) after subtraction of titania peaks.

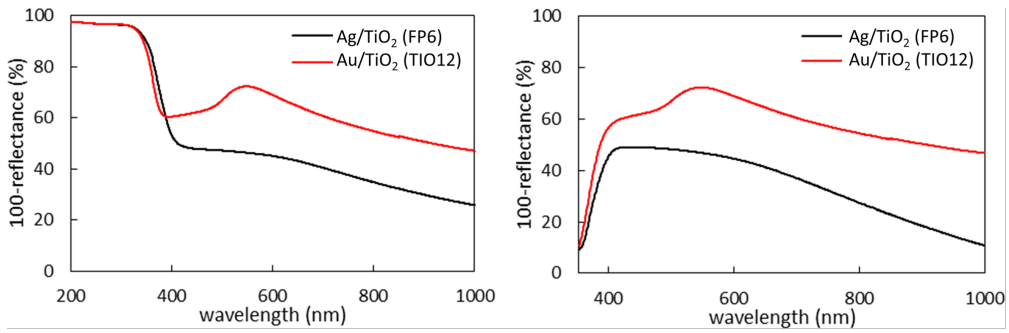

Figure 4: DRS spectra of Ag/TiO_2(FP6) and Au/TiO_2(TIO12) taken with $BaSO_4$ (left) and respective bare titania (right) as a reference.

23.7% of mortality after 45 min of treatment with TiO_2(ST01), TiO_2(ST41) and TiO_2(TIO6) samples, respectively. Under irradiation with visible light, an increase in antibacterial properties was noticed reaching 23.2%, 25.8% and 27.9%, respectively. Under UV irradiation, significant increase in activity was observed, especially for the fine anatase sample (ST01, 93.1%). Modification with gold caused a slight increase in activity under UV irradiation reaching 96.2%, 94.2% and 77.5%, respectively. An increase in photocatalytic activity after titania modification with NPs of NMs is not surprising, due to a decrease in charge-carrier recombination since noble metals work as an electron sink [54]. The most interesting finding was a significant enhancement of activity under vis irradiation and in the dark. Under vis irradiation the antibacterial activity was increased four times for ST01 and TIO6 samples and three times for ST41 sample, and in the dark it was increased two, three and four times for TIO6, ST01 and ST41, respectively. It is proposed that inactivation of bacteria under visible light irradiation is mainly caused by plasmonic photocatalysis, i.e., the activation of titania by LSPR of gold with a probable electron transfer from gold NPs to the conduction band (CB) of titania and subsequent reduction of oxygen resulting in the formation of reactive oxygen species (ROS). It is also possible that bacteria could be easier adsorbed on positively charged (electron-deficient) gold NPs, and then directly oxidized with simultaneous electron transfer to gold NPs keeping them in the initial zero valent state. A similar mechanism was proposed for decomposition of organic compounds under vis irradiation [53]. The increase in dark activity of titania samples after modification with gold could be caused by an extracellular electron transfer between bacteria and gold, i.e., the surface of gold-modified titania could abstract respiration-active electrons from bacteria, inducing bacterial death [59]. In addition, silver and gold could affect proper transport through the plasma membrane by alteration of the membrane viscosity and disruption of ionic pumps [60]. It is assumed that fine gold NPs more effectively clogged the channels (called porins), which allowed for passive transports of various ions, amino acids and other important molecules. This mechanism is independent on light action [61-63]. In this mechanism, the photocatalyst properties such as particle shape, size and content of NPs could influence the efficiency on interaction between NPs and bacteria [64].

To evaluate the difference between dark activity and plasmonic photocatalysis, decomposition of bacterial cells in titania suspension with simultaneous measurements of evolved carbon dioxide was studied for bare and modified titania with gold or silver. Our preliminary studies on TiO_2(ST41) photocatalyst

showed that although inactivation of bacterial cells was similar for bare and silver-modified samples (eight orders of decrease after three hours of vis irradiation and one order in the dark), only the silver-modified samples under vis irradiation caused continuous evolution of carbon dioxide suggesting a mineralization of bacterial cells [54]. To check if bacterial cells were really decomposed, scanning electron microscopy (SEM) observations were performed and the obtained data are shown in Figure 5. It was found that 1 h of vis irradiation was sufficient to initiate the destruction of bacterial cell walls, and 3 h of irradiation resulted in the decomposition of bacterial cells with clear formation of protoplast.

For the other silver-modified samples (Ag/TiO_2(FP6) and Ag/TiO_2(ST01)) a similar tendency was observed, i.e., continuous evolution of carbon dioxide was observed for silver-modified samples under vis irradiation as shown in Figure 6. Carbon dioxide also evolved on silver-modified samples in the dark, but only during the first two hours. In contrast to Ag/TiO_2(ST41), for which similar inactivation of bacteria was observed in the dark and under vis irradiation [35], a significantly larger activity for silver-modified samples was noticed under vis irradiation than that in the dark. The higher activity of Ag/TiO_2(FP6) compared to Ag/TiO_2(ST01) in the dark is presumably caused by larger NPs of silver in Ag/TiO_2(FP6) (Table 1), because there is a tendency that antibacterial activity increases with an increase in the size of silver NPs [65]. Indeed, the highest activity in the dark was obtained for the large NPs of silver in the Ag/TiO_2(ST41) sample. There are two possible explanations for the larger activity under vis irradiation: (1) bacteria inactivation by plasmonic photocatalysis (generation of ROS under vis irradiation) or (2) formation of larger amounts of positively charged silver and its subsequent release into bacteria–titania suspension (also through a plasmonic mechanism, as discussed above for gold). In order to clarify the exact mechanism under vis irradiation, the dependence of activity on the irradiation wavelength should be scrutinized, which is presently done. At the moment, it is clear that the activity of bare titania in the dark

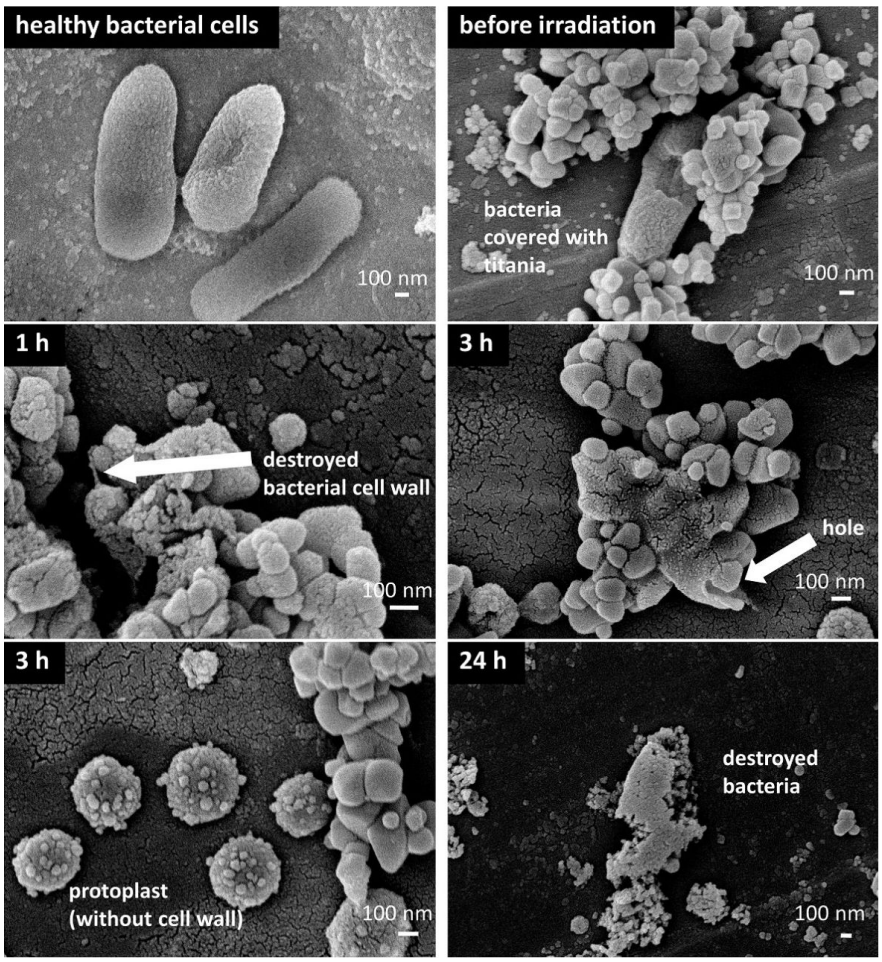

Figure 5: SEM images of the decomposition of bacterial cells under vis (λ > 420 nm) irradiation on Ag/TiO_2(ST41) photocatalyst.

and under vis irradiation is negligible compared to the high activity of the silver-modified samples. For comparison, a gold-modified sample (Au/TiO_2(TIO12)) was also tested, and the obtained data are shown in Supporting Information File 1 (Figure S1). For bare titania (TIO12, fine anatase), similar to other titania samples (ST01 and FP6 (Figure 6)), negligible activities under vis irradiation and in the dark, were noticed. A negligible activity of the gold-modified sample under dark conditions was observed, which was even lower than that of bare titania. It is proposed that very fine gold NPs on titania could disturb the binding of titania to the bacterial cells as a result of active site blocking by gold [66]. Thus a lower antibacterial activity was obtained. Under vis irradiation, a high antibacterial activity was observed, but significantly lower than that of the silver-modified samples (two to four orders of magnitude). Although, the activity of the gold-modified sample was lower, it is clear that it originated from plasmonic activation of titania. Probably, this is the first evidence proving antibacterial activity of plasmonic photocatalysts under visible-light irradiation (λ > 420 nm), resulting only from plasmonic activation of titania. There was no activity in the dark and an inactivity of bare titania. Plasmonic activity of other photocatalysts has been reported, but silver-modified samples, also exhibit activity in the dark due to the antimicrobial effect of silver [26,48,67,68]. Although, gold-modified titania exhibited antibacterial activity under visible-light irradiation, the bacteria killing rate was much slower than that of the silver-modified samples (due to the high silver activity in the dark). Accordingly, it is proposed that silver-modified samples are more promising as antibacterial agents, due to high efficiency (both in the dark and under vis irradiation) as well as the lower price of silver.

Antifungal activity of plasmonic photocatalysts

High humidity, positive temperature and lack of proper ventilation are significant factors affecting the growth of mould fungi in indoor environment. Some moulds produce spores that pose a serious threat to human health, e.g., chronic fatigue and allergic asthma. Long-term exposure to indoor moulds aggravates mentioned symptoms and can promote new ones. Moreover, fungi as more complex microorganisms than bacteria and viruses are much more resistant to antimicrobial agents. Therefore, there is a great need to develop new efficient antifungal materials. Regarding this, the antifungal properties of plasmonic photocatalysts have been tested. At first, experiments were performed by disc diffusion, as exemplary shown in Supporting Information File 1 (Figures S2–S5). Small (0–5 mm) inhibition zones were observed only for *Candida albicans* for paper discs impregnated with Ag/TiO_2(ST41) under vis irradiation. Consequently, it can be assumed that silver and gold ions are not releases from modified titania to the medium. All paper discs impregnated with silver-modified titania (Ag/TiO_2(ST41) and Ag/TiO_2(ST01)) and gold-modified titania (Au/TiO_2(ST41) and Au/TiO_2(ST01)) were avoided by all tested mould fungi under vis irradiation. This suggests that the antifungal effect is mainly associated with photocatalytic action. This effect was not observed for bare titania samples.

Mycelia of mould fungi, e.g., *Aspergillus melleus*, displayed a colour change in direct contact with paper discs impregnated with Ag/TiO_2(ST01) and Ag/TiO_2(ST41) in the dark and under vis irradiation due to inhibited sporulation. That effect was not observed for paper discs impregnated with bare and gold-modi-

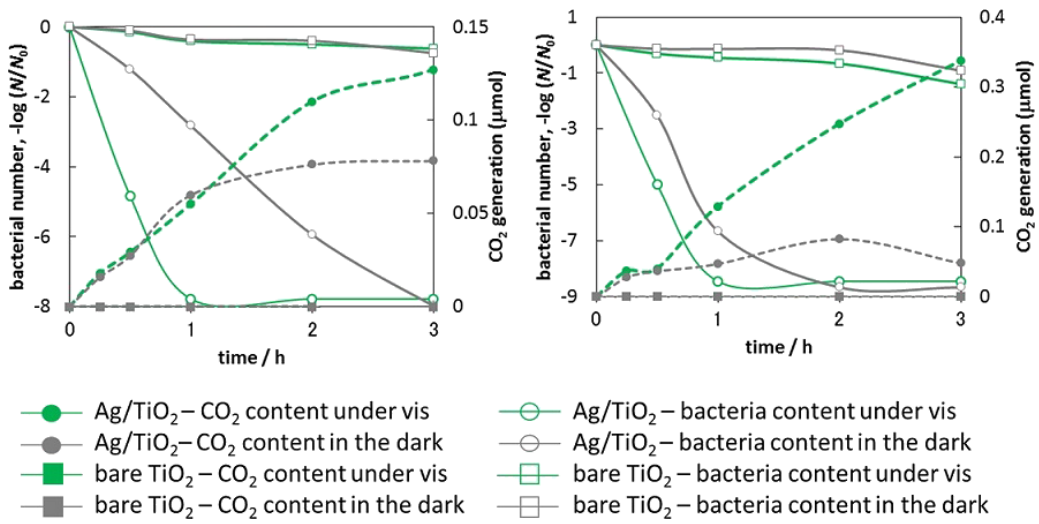

Figure 6: Number of *E. coli* bacteria (closed symbols) and evolution of CO_2 (open symbols) during inactivation of bacterial cells in the dark (grey symbols) and under vis irradiation (λ > 420 nm; green symbols) on bare (squares) and modified titania (circles): (left) TiO_2(ST01) and Ag/TiO_2(ST01), (right) TiO_2(FP6) and Ag/TiO_2(FP6).

fied titania. The antifungal study based on disc diffusion showed ambiguous results for silver- and gold-modified titania samples. It may be concluded that a concentration of 1 g/L of Ag- and Au-modified titania is not sufficient to observe a biocidal effect, regardless of the experimental conditions. As it was shown in our previous studies [69,70], the photocatalytic degradation of fungi was much lower than that of bacteria, because of differences in inactivation mechanism and cell-wall structure. The potent activity of Ag-modified titania against yeast (*C. albicans*) was caused by its different morphology and taxonomy group. It is well known that yeast are unicellular fungi, and do not produce mycelia and spores, which makes them the most vulnerable object, i.e., a few times more sensitive towards antifungal agents than other fungi. Auyeung et al. found that only metallic and ZnO NPs showed a potent antimould activity against *A. niger* and *P. chrysogenum* [71].

Despite the low antifungal activity of silver-modified titania, the inhibition zones around paper disks may be considered as positive results indicating a high stability of photocatalysts. However, it should be concluded that the antifungal properties of silver-modified titania are not attractive for commercial application. Moreover, the small inhibition zones around discs were difficult to evaluate quantitatively. Therefore, the "poisoned food" method (fungal growth on titania/MEA support) with gold-modified titania was used for further investigations. At first, bare titania samples were examined, and obtained data are shown in Supporting Information File 1 (Figure S6). It was found that fungi, especially *A. melleus*, were sensitive to photocatalysis, and the highest activity was obtained for fine titania samples especially under vis irradiation. Interestingly, for *P. chrysogenum* and *A. niger* the same activity of bare titania FP6 was observed in the dark and under irradiation. It should be mentioned that both titania samples (ST01 and FP6) are highly active photocatalysts for various photocatalytic reactions, e.g., oxidative decomposition of acetic acid and dehydrogenation of methanol [72]. FP6 has larger crystals (smaller specific surface area), and thus its lower activity under irradiation is reasonable. Not only the diameter of the mycelium, but also the level of sporulation should be estimated for antifungal activity tests, and summarized data for mycelium growth and sporulation are shown in Supporting Information File 1 (Table S2**,** and exemplary photographs of fungal growth in Figure S7). It was confirmed that titania ST01 was more efficient than titania FP6. Next, gold-modified samples were examined, and antifungal properties of gold were confirmed in the dark, as shown in Figure 7 and in Supporting Information File 1 (Table S3).

Surprisingly, under fluorescent irradiation bare titania was more active than gold-modified titania. Noble metal-modified titania samples are usually more active under both UV and visible light irradiation than bare titania samples (see studies for sixteen commercial titania samples modified with gold [53] and silver [43,54]). However, in the near-UV range and in some cases, bare titania shows larger photocatalytic activity [45]. It should be reminded that the titania samples here are commercial samples, and thus with small content of impurities and defects, which can increase the visible-light activity of titania by narrowing of the band gap. The adsorbed gold on the titania surface would disturb this intrinsic vis response at 390–420 nm. Moreover, it should be clarified that the lower inhibition of mycelium growth does not unequivocally mean a lower antifungal action, since sporulation and possible mycotoxin generation must be also considered. Therefore, a decrease in sporulation and the inhibition of droplet formation (with possible presence of mycotoxins) on gold-modified titania indicate that gold-modified titania could be used as efficient antifungal agent.

Antifungal properties were also confirmed for other gold-modified titania samples (TIO12 and STF10), as shown in Supporting Information File 1 (Figures S8–S9). Although, the antifungal effect was clear, the evaluation of the overall antifungal activity was quite troublesome, due to the difficult differentiation between the colours of mycelium and support (modified-titania). Therefore, a new method, namely "spore counting" was applied (Supporting Information File 1, Figure S10), and the obtained data are shown in Figure 8. In the literature, contradictory opinions on the influence of light on fungi have been presented. Light can stimulate or inhibit fungal growth or be without any effect [73]. Most filamentous fungi are photophobic [74]. Light could limit (or even completely inhibit) germination, probably due to an increase in temperature during irradiation [75]. The inhibition effect increases with an increase in light energy, i.e., UVB (280–320 nm) is more harmful than UVA (320–400 nm). UV light in the solar spectrum is considered to be responsible for inhibition of mycotoxin generation [75]. It is known that fungi are heterotrophic organisms, and thus light is not necessary for their growth. However, it has been also reported that light may act on enzyme levels and metabolite secretion in fungal cells [75]. Our results clearly demonstrate that irradiation does not influence the sporulation of *A. melleus* and *P. chrysogenum* in the absence of titania. However, a significant effect on sporulation was observed for bare titania. Moreover, gold slightly enhanced this effect depending on the fungi species. *P. chrysogenum* was sensitive to light, which stimulated its growth, whereas irradiation almost did not influence the groth of *A. melleus*.

To the best of our knowledge, this is the first report on the effect of gold-modified titania on sporulation of mould fungi. It is clear that although a negligible inhibition of mycelium

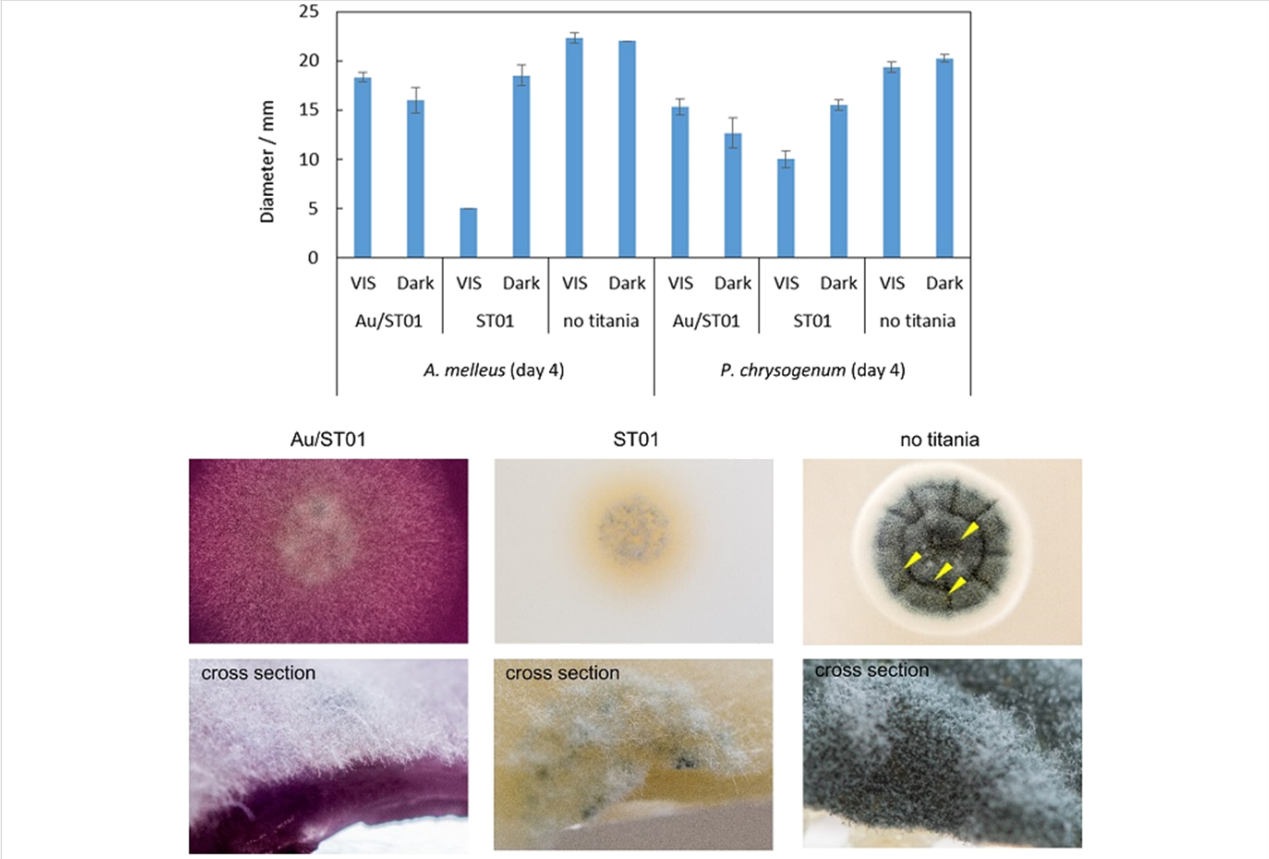

Figure 7: (top) Antifungal properties of bare and gold-modified titania ST01 by a comparison of diameters of colonies after four days of growth (n = 6, mean ± S. D.), and (bottom) representative photograph of *P. chrysogenum* cultivated for four days under fluorescent-light irradiation. Arrowheads indicate the droplets.

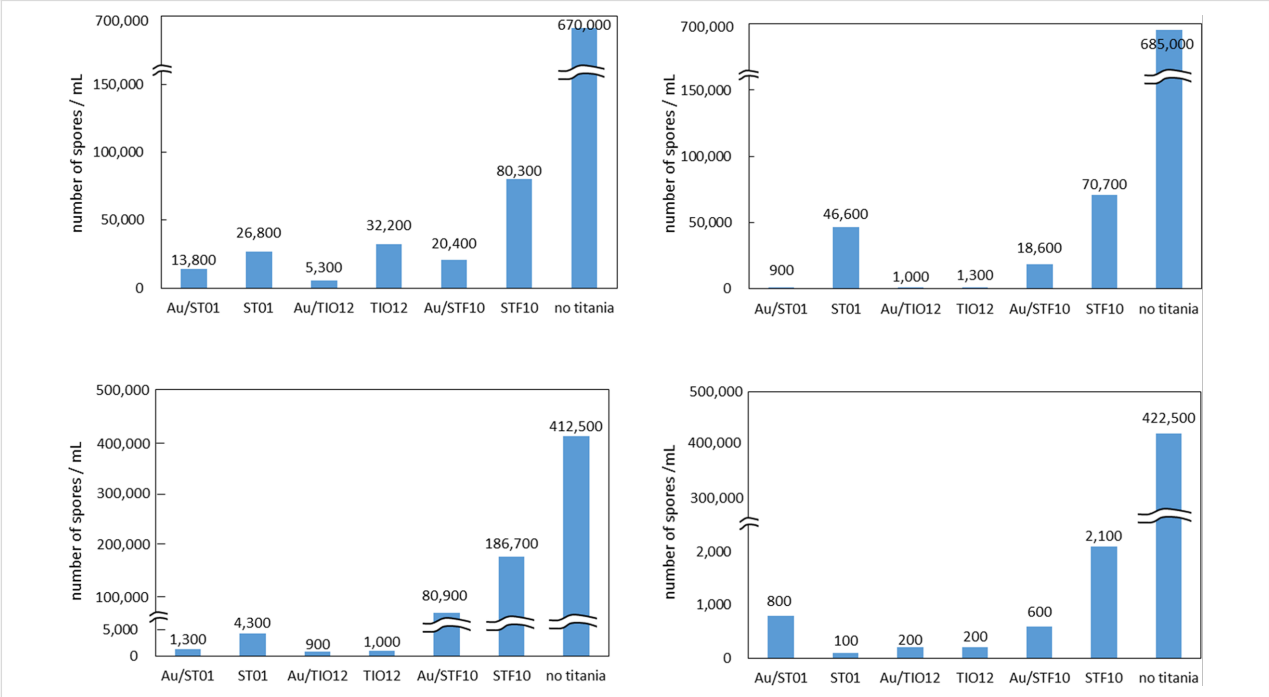

Figure 8: Sporulation after five days of growth of *P. chrysogenum* (top) and *A. melleus* (bottom) under vis light (left) and in the dark (right).

growth was observed (Figure 7, and Figure S8 and Figure S9 and Table S3 in Supporting Information File 1), sporulation was inhibited almost completely (99.8%) on slants supplemented with Au/TiO_2. In order to understand the function of Au NPs in the inhibition of sporulation, colloidal Au NPs (ca. 12 nm) were investigated by the same method (Figure S11, Supporting Information File 1). It was found that unsupported Au NPs did not show inhibition of sporulation in the dark, and only a slight inhibition under visible-light irradiation for *A. melleus.* Accordingly, it is proposed that Au NPs do not intrinsically inhibit sporulation. It may be concluded that the Au–TiO_2 heterojunction is necessary to influence the formation of sporangia and/or spores during the growth of mycelium. Although, further investigation is necessary for the mechanism clarification, it is proposed that titania could change the availability of nutrients from media. Suberkropp has already reported that the nutrient availability and allocation of resources are main factors determining fungal reproduction (sporulation) [76]. It is proposed that the main reason of a decrease in media nourishment for mould fungi is probably caused by sorption of macromolecules (e.g., proteins and sugars) on titania, as suggested by Raffaini and Ganzoli [77] and Ellingsen [78].

On the other hand, our previous study showed that Au-modified faceted titania was inactive against *C. albicans*, in contrast to the Ag-modified sample [29]. It is assumed that different results could originate from different structures of the fungi. *C. albicans* is a dimorphic fungus since it grows as yeast, and it neither forms a mycelium nor produces reproductive cells (spores). It is proposed that Ag could penetrate the cell envelope easily and cause significant changes in survival rate, due to the simple cell structure of *C. albicans*. Accordingly, it is proposed that the bactericidal mechanism could be similar to the anti-"candida" mechanism, and different from antifungal mechanism for mould fungi.

Rogawansamy et al. have proposed that the best antifungal agent should inhibit the growth of various fungal genera, whereas less active antifungal agents could only inhibit sporulation or the growth of a limited range of fungi [79]. However, it should be reminded that spores are essential for fungal reproduction by expanding into the environment, and thus causing various allergies and respiratory diseases. Therefore, it is proposed that Au/TiO_2, which exhibits effective inhibition of sporulation, can be a promising material for reducing health-threatening factors in indoor environment.

Conclusion

Noble metal-modified titania photocatalysts exhibit good antimicrobial properties in the dark and under visible-light irradiation due to antimicrobial properties of noble metals and plasmonic photocatalysis. The surface properties of photocatalysts are crucial for the antimicrobial effect, and generally, a decrease in particle sizes results in an activity increase, due to a larger interface between microorganisms and photocatalysts. Silver-modified samples show high antibacterial activity (complete decomposition of bacterial cells), whereas gold-modified samples are very active against fungi, especially in the inhibition of sporulation. Therefore, it is expected that bimetallic (Au/Ag) titania photocatalysts should exhibit broad antimicrobial properties. The lack of inhibition zones around disks supplemented with photocatalysts confirms the high stability of photocatalysts and their commercial applicability.

Experimental

Preparation of silver- and gold-modified TiO_2

2 wt % of silver and gold were deposited on six commercial titania samples: ST01 (Ishihara, ST-01), ST41 (Ishihara, ST-41), TIO12 (TAYCA, JRC-TIO-12), FP6 (Showa Denko Ceramics, FP-6), TIO6 (Catalysis Society of Japan, JRC-TIO-6) and STF10 (Showa Denko Ceramics, ST-F10). In brief, TiO_2 samples were suspended in a 50 vol % aqueous solution of methanol, to which either $AgNO_3$ aqueous solution or $HAuCl_4{\cdot}H_2O$ aqueous solution was added, suspensions were purged with argon for 15 min, and irradiated with a 400 W mercury lamp in a thermostatic water bath at 298 K under stirring (500 rpm). The obtained noble metal-modified TiO_2 samples were centrifuged, washed twice with methanol and twice with Milli-Q water and dried at 378 K.

Antibacterial activity test

50 mg of the sample was dispersed in 7.0 mL of *E. coli* K12 (ATCC29425) suspension at a concentration of ca. 0.180 Abs at 630 nm (ca. 1–5 × 10^8 cells/mL) in a test tube with stirring bar and irradiated with a xenon lamp (with CM1 and Y-45 filter; $\lambda > 420$ nm) or kept in the dark. Serial dilutions (10^{-1} to 10^{-6}) were prepared and aliquots of suspensions were inoculated on Plate Count Agar (Becton, Dickinson and Company, USA) media after 0, 0.5, 1, 2 and 3 h. Media were incubated at 37 °C overnight and then colonies were counted. Simultaneously, generated CO_2 was measured by FID-gas chromatography.

For SEM observation, 0.1 mL of the mixture of *E. coli* K12 and sample before and after reaction was collected, diluted 10 times with sterile Milli-Q water and mounted on a piece of copper tape. The bacterial cells were fixed by 2.0% glutaraldehyde and 2.0% paraformaldehyde in 30 mM HEPES buffer for 1 h. After fixation, cells were washed with 30 mM HEPES buffer for 1 min, dehydrated by a graded series of ethanol (30, 50, 70, 90, 95 and 99.5% (v/v)) for 10 min each. Then, samples were washed with *tert*-butyl alcohol three times, soaked in it and dried under vacuum. Samples were sputtered with platinum for

60 s from three directions and observed by SEM (JSM-7400F, JEOL).

Antifungal activity test

The antifungal tests were performed with the following microorganisms: the yeast *Candida albicans*, isolated from patients (throat smear) with immunodeficiency disorders that cause candidiasis (IIT&EE ZUT collection), and mould fungi *Aspergillus niger*, *Aspergillus melleus* and *Penicillium chrysogenum*, isolated from damp basement air (IIT&EE ZUT collection). The antimicrobial activity of the photocatalysts was tested by using disc diffusion [80]. Culture plates were prepared with 20 mL of two solid media: Sabouraud Glucose Agar SGA (BIOCORP, Poland) for *C. albicans* and Malt Extract Agar (Merck, Germany) for mould fungi. Sterilized culture media were poured in Petri dishes and, after solidification of the medium, 0.25 mL of fungal suspension was spread on the plate using an L-rod. The concentration of microorganisms was ca. 10^6 CFU/mL. The sterile paper discs (Whatman No.1, diameter 5 mm) impregnated with photocatalyst suspension (1 g/L 10 µL/disc) were placed at different locations on the culture plates. The control discs were impregnated with saline solution (0.9% NaCl). One part of the plates was incubated in the dark, while another part was exposed to the indoor light. The natural indoor light from windows (intensity of ca. 120 lx) was strengthened by 8 h of exposure to a halogen lamp (intensity of ca. 400–500 lx). The distance from three halogen lamps to the plates was ca. 50 cm. The temperature was maintained at ca. 30 °C for *C. albicans* and 25 °C for *A. niger*, *A. melleus* and *P. chrysogenum*. The incubation periods were 48 h for *C. albicans* and 72 h for mould fungi. After incubation, the zones of inhibition around the paper discs were investigated.

Colony growth test

20 g/L of the sample was dispersed in Malt Extract Agar (MEA) medium, sonicated for 1 min, autoclaved at 121 °C for 10 min and poured in Petri dishes. The spores of *A. niger*, *A. melleus* and *P. chrysogenum* were collected with 8.5 g/L NaCl aqueous solution, and the suspension was inoculated on the Petri dishes. Dishes were irradiated with fluorescence light or kept in dark. After three and eight days of exposure the diameters of colonies were measured and the appearances were checked visually.

Sporulation test

20 g/L of the sample was dispersed in MEA medium, sonicated for 1 min, autoclaved at 121 °C for 10 min and dispensed to the slants. The spores of *A. melleus* and *P. chrysogenum* were collected with 8.5 g/L NaCl aqueous solution, the number of spores were counted by Thoma hemacytometers and 10,000 spores/mL of the suspension was inoculated on the slants. The slants were irradiated with fluorescence light or kept in dark. Triton X-100 (0.05%) in 8.5 g/L NaCl aqueous solution was added to the culture after five days and mixed with a vortex mixer. Collected spores were diluted 10–50 times with 8.5 g/L NaCl aqueous solution, and then counted.

Supporting Information

Supporting Information File 1

Additional experimental data.
[https://www.beilstein-journals.org/bjnano/content/supplementary/2190-4286-9-77-S1.pdf]

Acknowledgements

This research was supported by a Grand Challenges Explorations Grant (GCE R8, OPP1060234) from Bill and Melinda Gates Foundation. We also thank Yuji Kimura for preparation of Au/TiO_2(TIO6) sample.

ORCID® iDs

Zhishun Wei - https://orcid.org/0000-0001-7436-6409
Ewa Kowalska - https://orcid.org/0000-0003-0955-9268

References

1. Blackman, A. *Rev. Environ. Econ. Policy* **2010,** *4,* 234–253. doi:10.1093/reep/req005
2. Blancou, J. *Rev. Sci. Tech. (OIE)* **1995,** *14,* 31–39.
3. Yang, H.; Cheng, H. *Sep. Purif. Technol.* **2007,** *56,* 392–396. doi:10.1016/j.seppur.2007.05.036
4. Zhang, L.; Gu, F. X.; Chan, J. M.; Wang, A. Z.; Langer, R. S.; Farokhzad, O. C. *Clin. Pharmacol. Ther. (Hoboken, NJ, U. S.)* **2008,** *83,* 761–769. doi:10.1038/sj.clpt.6100400
5. Pradeep, T.; Anshup. *Thin Solid Films* **2009,** *517,* 6441–6478. doi:10.1016/j.tsf.2009.03.195
6. Qu, X.; Alvarez, P. J. J.; Li, Q. L. *Water Res.* **2013,** *47,* 3931–3946. doi:10.1016/j.watres.2012.09.058
7. Arslan, I.; Balcioglu, I. A.; Tuhkanen, T. *Environ. Technol.* **1999,** *20,* 921–931. doi:10.1080/09593332008616887
8. Kowalska, E.; Janczarek, M.; Hupka, J.; Grynkiewicz, M. *Water Sci. Technol.* **2004,** *49,* 261–266.
9. Barbeni, M.; Minero, C.; Pelizzetti, E.; Borgarello, E.; Serpone, N. *Chemosphere* **1987,** *16,* 2225–2237. doi:10.1016/0045-6535(87)90281-5
10. Artuna, E.; Hupka, J. *Cent. Eur. J. Public Health* **2000,** *8,* 88–89.
11. Mozia, S.; Tomaszewska, M.; Morawski, A. W. *Desalination* **2006,** *190,* 308–314. doi:10.1016/j.desal.2006.03.001
12. King, C. H.; Shotts, E. B., Jr.; Wooley, R. E.; Porter, K. G. *Appl. Environ. Microbiol.* **1988,** *54,* 3023–3033.
13. Mokrini, A.; Ousse, D.; Esplugas, E. *Water Sci. Technol.* **1997,** *35,* 95–102.
14. Tomova, D.; Iliev, V.; Rakovsky, S.; Anachkov, M.; Eliyas, A.; Li Puma, G. *J. Photochem. Photobiol., A* **2012,** *231,* 1–8. doi:10.1016/j.jphotochem.2011.12.012

15. Hoffmann, M. R.; Martin, S. T.; Choi, W.; Bahnemann, D. W. *Chem. Rev.* **1995,** *95,* 69–96. doi:10.1021/cr00033a004
16. Cunningham, J.; Fox, M. A.; Pelizzetti, E.; Pichat, P.; Serpone, N. Photocatalytic treatment of waters. *Aquatic and surface photochemistry;* Lewis Publishers: Boca Raton, FL, U.S.A., 1994; pp 261–316.
17. Duffy, J. E.; Anderson, M. A.; Hill, C. G.; Zeltner, W. A. *Ind. Eng. Chem. Res.* **2000,** *39,* 3698–3706. doi:10.1021/ie990941o
18. Sánchez-Oneto, J.; Mancini, F.; Portela, J. R.; Nebot, E.; Cansell, F.; Martínez de la Ossa, E. J. *Chem. Eng. J.* **2008,** *144,* 361–367. doi:10.1016/j.cej.2008.01.041
19. Legrini, O.; Oliveros, E.; Braun, A. M. *Chem. Rev.* **1993,** *93,* 671–698. doi:10.1021/cr00018a003
20. Malato, S.; Blanco, J.; Richter, C.; Curco, D.; Gimenez, J. *Water Sci. Technol.* **1997,** *35,* 157–164.
21. Paz, Y. *Appl. Catal., B* **2010,** *99,* 448–460. doi:10.1016/j.apcatb.2010.05.011
22. Murakami, N.; Kurihara, Y.; Tsubota, T.; Ohno, T. *J. Phys. Chem. C* **2009,** *113,* 3062–3069. doi:10.1021/jp809104t
23. Yang, H. G.; Sun, C. H.; Qiao, S. Z.; Zou, J.; Liu, G.; Smith, S. C.; Cheng, H. M.; Lu, G. Q. *Nature* **2008,** *453,* 638–U4. doi:10.1038/nature06964
24. Wu, J.-J.; Yu, C.-C. *J. Phys. Chem. B* **2004,** *108,* 3377–3379. doi:10.1021/jp0361935
25. Janczarek, M.; Kowalska, E.; Ohtani, B. *Chem. Eng. J.* **2016,** *289,* 502–512. doi:10.1016/j.cej.2016.01.008
26. Wei, Z.; Kowalska, E.; Verrett, J.; Colbeau-Justin, C.; Remita, H.; Ohtani, B. *Nanoscale* **2015,** *7,* 12392–12404. doi:10.1039/C5NR02386F
27. Kouamé, N. A.; Alaoui, O. T.; Herissan, A.; Larios, E.; José-Yacaman, M.; Etcheberry, A.; Colbeau-Justin, C.; Remita, H. *New J. Chem.* **2015,** *39,* 2316–2322. doi:10.1039/C4NJ01979B
28. Jaffrezic-Renault, N.; Pichat, P.; Foissy, A.; Mercier, R. *J. Phys. Chem.* **1986,** *90,* 2733–2738. doi:10.1021/j100403a035
29. Ząbek, P.; Eberl, J.; Kisch, H. *Photochem. Photobiol. Sci.* **2009,** *8,* 264–269. doi:10.1039/b812798k
30. Janus, M.; Tryba, B.; Inagaki, M.; Morawski, A. W. *Appl. Catal., B: Environ.* **2004,** *52,* 61–67. doi:10.1016/j.apcatb.2004.03.011
31. Yang, D.; Sun, Y.; Tong, Z.; Tian, Y.; Li, Y.; Jiang, Z. *J. Phys. Chem. C* **2015,** *119,* 5827–5835. doi:10.1021/jp511948p
32. Chen, Q.; Wu, S.; Xin, Y. *Chem. Eng. J.* **2016,** *302,* 377–387. doi:10.1016/j.cej.2016.05.076
33. Asahi, R.; Morikawa, T.; Ohwaki, T.; Aoki, K.; Taga, Y. *Science* **2001,** *293,* 269–271. doi:10.1126/science.1061051
34. Zaleska, A. *Recent Pat. Eng.* **2008,** *2,* 157–164. doi:10.2174/187221208786306289
35. Ohno, T.; Akiyoshi, M.; Umebayashi, T.; Asai, K.; Mitsui, T.; Matsumura, M. *Appl. Catal., A* **2004,** *265,* 115–121. doi:10.1016/j.apcata.2004.01.007
36. Dozzi, M. V.; Selli, E. *J. Photochem. Photobiol., C* **2013,** *14,* 13–28. doi:10.1016/j.jphotochemrev.2012.09.002
37. Li, G.; Dimitrijevic, N. M.; Chen, L.; Rajh, T.; Gray, K. A. *J. Phys. Chem. C* **2008,** *112,* 19040–19044. doi:10.1021/jp8068392
38. Marschall, R. *Adv. Funct. Mater.* **2014,** *24,* 2421–2440. doi:10.1002/adfm.201303214
39. Barreca, D.; Fornasiero, P.; Gasparotto, A.; Gombac, V.; Maccato, C.; Montini, T.; Tondello, E. *ChemSusChem* **2009,** *2,* 230–233. doi:10.1002/cssc.200900032
40. Wang, G.; Chen, Q.; Xin, Y.; Liu, Y.; Zang, Z.; Hu, C.; Zhang, B. *Electrochim. Acta* **2016,** *222,* 1903–1913. doi:10.1016/j.electacta.2016.11.182
41. Kraeutler, B.; Bard, A. J. *J. Am. Chem. Soc.* **1978,** *100,* 4317–4318. doi:10.1021/ja00481a059
42. Kowalska, E.; Remita, H.; Colbeau-Justin, C.; Hupka, J.; Belloni, J. *J. Phys. Chem. C* **2008,** *112,* 1124–1131. doi:10.1021/jp077466p
43. Kowalska, E.; Yoshiiri, K.; Wei, Z.; Zheng, S.; Kastl, E.; Remita, H.; Rau, S.; Ohtani, B. *Appl. Catal., B: Environ.* **2015,** *178,* 133–143. doi:10.1016/j.apcatb.2014.10.003
44. Tian, Y.; Tatsuma, T. *J. Am. Chem. Soc.* **2005,** *127,* 7632–7637. doi:10.1021/ja042192u
45. Verbruggen, S. W.; Keulemans, M.; Goris, B.; Blommaerts, N.; Bals, S.; Martens, J. A.; Lenaerts, S. *Appl. Catal., B* **2016,** *188,* 147–153. doi:10.1016/j.apcatb.2016.02.002
46. Lemire, J. A.; Harrison, J. J.; Turner, R. J. *Nat. Rev. Microbiol.* **2013,** *11,* 371–384. doi:10.1038/nrmicro3028
47. Rodríguez-Chueca, J.; Ormad, M. P.; Mosteo, R.; Sarasa, J.; Ovelleiro, J. L. *Water Environ. Res.* **2015,** *87,* 281–288. doi:10.2175/106143014X13987223590362
48. Wei, Z.; Endo, M.; Wang, K.; Charbit, E.; Markowska-Szczupak, A.; Ohtani, B.; Kowalska, E. *Chem. Eng. J.* **2017,** *318,* 121–134. doi:10.1016/j.cej.2016.05.138
49. Benabbou, A. K.; Derriche, Z.; Felix, C.; Lejeune, P.; Guillard, C. *Appl. Catal., B* **2007,** *76,* 257–263. doi:10.1016/j.apcatb.2007.05.026
50. Guillard, C.; Bui, T.-H.; Felix, C.; Moules, V.; Lina, B.; Lejeune, P. *C. R. Chim.* **2008,** *11,* 107–113. doi:10.1016/j.crci.2007.06.007
51. Zielińska, A.; Kowalska, E.; Sobczak, J. W.; Łącka, I.; Gazda, M.; Ohtani, B.; Hupka, J.; Zaleska, A. *Sep. Purif. Technol.* **2010,** *72,* 309–318. doi:10.1016/j.seppur.2010.03.002
52. Zielińska-Jurek, A.; Wei, Z.; Wysocka, I.; Szweda, P.; Kowalska, E. *Appl. Surf. Sci.* **2015,** *353,* 317–325. doi:10.1016/j.apsusc.2015.06.065
53. Kowalska, E.; Mahaney, O. O. P.; Abe, R.; Ohtani, B. *Phys. Chem. Chem. Phys.* **2010,** *12,* 2344–2355. doi:10.1039/b917399d
54. Kowalska, E.; Wei, Z.; Karabiyik, B.; Herissan, A.; Janczarek, M.; Endo, M.; Markowska-Szczupak, A.; Remita, H.; Ohtani, B. *Catal. Today* **2015,** *252,* 136–142. doi:10.1016/j.cattod.2014.10.038
55. Min, B. K.; Wallace, W. T.; Goodman, D. W. *Surf. Sci.* **2006,** *600,* L7. doi:10.1016/j.susc.2005.10.024
56. Ohtani, B.; Mahaney, O. O. P.; Amano, F.; Murakami, N.; Abe, R. *J. Adv. Oxid. Technol.* **2010,** *13,* 247–261. doi:10.1515/jaots-2010-0303
57. Zheng, S.; Wang, K.; Wei, Z.; Yoshiiri, K.; Braumuller, M.; Rau, S.; Ohtani, B.; Kowalska, E. *J. Adv. Oxid. Technol.* **2016,** *19,* 208–217.
58. Xia, Y.; Xiong, Y.; Lim, B.; Skrabalak, S. E. *Angew. Chem., Int. Ed.* **2008,** *48,* 60–103. doi:10.1002/anie.200802248
59. Wang, G.; Feng, H.; Gao, A.; Hao, Q.; Jin, W.; Peng, X.; Li, W.; Wu, G.; Chu, P. K. *ACS Appl. Mater. Interfaces* **2016,** *8,* 24509–24516. doi:10.1021/acsami.6b10052
60. Zeyons, O.; Thill, A.; Chauvat, F.; Menguy, N.; Cassier-Chauvat, C.; Oréar, C.; Daraspe, J.; Auffan, M.; Rose, J.; Spalla, O. *Nanotoxicology* **2009,** *3,* 284–295. doi:10.3109/17435390903305260
61. Soloviev, A.; Zholos, A.; Ivanova, I.; Novokhatska, T.; Tishkin, S.; Raevska, A.; StroyukC, A.; Yefanov, V. *Vasc. Pharmacol.* **2015,** *72,* 190–196. doi:10.1016/j.vph.2015.05.016
62. Chin, C.; Park, Y. S. *Cardiol. Ther.* **2016,** *5,* 101–108. doi:10.1007/s40119-016-0060-8
63. Halawani, E. M. *Int. J. Curr. Microbiol. Appl. Sci.* **2016,** *5,* 397–414. doi:10.20546/ijcmas.2016.502.045

64. Wang, L. L.; Hu, C.; Shao, L. Q. *Int. J. Nanomed.* **2017,** *12,* 1227–1249. doi:10.2147/IJN.S121956
65. Cao, H.; Qiao, Y.; Liu, X.; Lu, T.; Cui, T.; Meng, F.; Chu, P. K. *Acta Biomater.* **2013,** *9,* 5100–5110. doi:10.1016/j.actbio.2012.10.017
66. Mogyorósi, K.; Kmetykó, A.; Czirbus, N.; Veréb, G.; Sipos, P.; Dombi, A. *React. Kinet. Catal. Lett.* **2009,** *98,* 215–225. doi:10.1007/s11144-009-0052-y
67. Rtimi, S.; Baghriche, O.; Sanjines, R.; Pulgarin, C.; Bensimon, M.; Kiwi, J. *J. Photochem. Photobiol., A* **2013,** *256,* 52–63. doi:10.1016/j.jphotochem.2013.02.005
68. Rtimi, S.; Pascu, M.; Sanjines, R.; Pulgarin, C.; Ben-Simon, M.; Houas, A.; Lavanchy, J.-C.; Kiwi, J. *Appl. Catal., B* **2013,** *138–139,* 113–121. doi:10.1016/j.apcatb.2013.01.066
69. Markowska-Szczupak, A.; Ulfig, K.; Morawski, A. W. *J. Adv. Oxid. Technol.* **2012,** *15,* 30–33. doi:10.1515/jaots-2012-0103
70. Markowska-Szczupak, A.; Janda, K.; Wang, K.; Morawski, A. W.; Kowalska, E. *Cent. Eur. J. Public Health* **2015,** *23,* 267–271. doi:10.21101/cejph.a4054
71. Auyeung, A.; Casillas-Santana, M. A.; Martínez-Castañón, G. A.; Slavin, Y. N.; Zhao, W.; Asnis, J.; Häfeli, U. O.; Bach, H. *PLoS One* **2017,** *12,* e0169940. doi:10.1371/journal.pone.0169940
72. Prieto-Mahaney, O.-O.; Murakami, N.; Abe, R.; Ohtani, B. *Chem. Lett.* **2009,** *38,* 238–239. doi:10.1246/cl.2009.238
73. Nielsen, K. F. *Fungal Genet. Biol.* **2003,** *39,* 103–117. doi:10.1016/S1087-1845(03)00026-4
74. Fargues, J.; Rougier, M.; Goujet, R.; Smits, N.; Coustere, C.; Itier, B. *J. Invertebr. Pathol.* **1997,** *69,* 70–78. doi:10.1006/jipa.1996.4637
75. Willocquet, L.; Colombet, D.; Rougier, M.; Fargues, J.; Clerjeau, M. *Eur. J. Plant Pathol.* **1996,** *102,* 441–449. doi:10.1007/BF01877138
76. Suberkropp, K. *Can. J. Bot.* **1995,** *73,* S1361–S1369. doi:10.1139/b95-398
77. Raffaini, G.; Ganazzoli, F. *Philos. Trans. R. Soc. London, Ser. A* **2012,** *370,* 1444–1462. doi:10.1098/rsta.2011.0266
78. Ellingsen, J. E. *Biomaterials* **1991,** *12,* 593–596. doi:10.1016/0142-9612(91)90057-H
79. Rogawansamy, S.; Gaskin, S.; Taylor, M.; Pisaniello, D. *Int. J. Environ. Res. Public Health* **2015,** *12,* 6319–6332. doi:10.3390/ijerph120606319
80. Markov, S. L.; Vidaković, A. M. *Acta Period. Technol.* **2014,** 141–152. doi:10.2298/APT1445141M

License and Terms

This is an Open Access article under the terms of the Creative Commons Attribution License (http://creativecommons.org/licenses/by/4.0), which permits unrestricted use, distribution, and reproduction in any medium, provided the original work is properly cited.

The license is subject to the *Beilstein Journal of Nanotechnology* terms and conditions: (https://www.beilstein-journals.org/bjnano)

The definitive version of this article is the electronic one which can be found at:
doi:10.3762/bjnano.9.77

BEILSTEIN JOURNAL OF NANOTECHNOLOGY

Semi-automatic spray pyrolysis deposition of thin, transparent, titania films as blocking layers for dye-sensitized and perovskite solar cells

Hana Krýsová[1], Josef Krýsa[*2] and Ladislav Kavan[1]

Full Research Paper

Open Access

Address:
[1]J. Heyrovský Institute of Physical Chemistry of the CAS, v. v. i., Dolejškova 2155/3, 182 23 Prague 8, Czech Republic, and
[2]University of Chemistry and Technology Prague, Technická 5, 166 28 Prague 6, Czech Republic

Email:
Josef Krýsa[*] - josef.krysa@vscht.cz

* Corresponding author

Keywords:
blocking films; FTO; solar cells; spray pyrolysis deposition; titanium dioxide

Beilstein J. Nanotechnol. **2018,** *9,* 1135–1145.
doi:10.3762/bjnano.9.105

Received: 05 October 2017
Accepted: 13 March 2018
Published: 10 April 2018

This article is part of the Thematic Series "Energy conversion, storage and environmental remediation using nanomaterials".

Guest Editor: W.-J. Ong

© 2018 Krýsová et al.; licensee Beilstein-Institut.
License and terms: see end of document.

Abstract

For proper function of the negative electrode of dye-sensitized and perovskite solar cells, the deposition of a nonporous blocking film is required on the surface of F-doped SnO_2 (FTO) glass substrates. Such a blocking film can minimise undesirable parasitic processes, for example, the back reaction of photoinjected electrons with the oxidized form of the redox mediator or with the hole-transporting medium can be avoided. In the present work, thin, transparent, blocking TiO_2 films are prepared by semi-automatic spray pyrolysis of precursors consisting of titanium diisopropoxide bis(acetylacetonate) as the main component. The variation in the layer thickness of the sprayed films is achieved by varying the number of spray cycles. The parameters investigated in this work were deposition temperature (150, 300 and 450 °C), number of spray cycles (20–200), precursor composition (with/without deliberately added acetylacetone), concentration (0.05 and 0.2 M) and subsequent post-calcination at 500 °C. The photo-electrochemical properties were evaluated in aqueous electrolyte solution under UV irradiation. The blocking properties were tested by cyclic voltammetry with a model redox probe with a simple one-electron-transfer reaction. Semi-automatic spraying resulted in the formation of transparent, homogeneous, TiO_2 films, and the technique allows for easy upscaling to large electrode areas. The deposition temperature of 450 °C was necessary for the fabrication of highly photoactive TiO_2 films. The blocking properties of the as-deposited TiO_2 films (at 450 °C) were impaired by post-calcination at 500 °C, but this problem could be addressed by increasing the number of spray cycles. The modification of the precursor by adding acetylacetone resulted in the fabrication of TiO_2 films exhibiting perfect blocking properties that were not influenced by post-calcination. These results will surely find use in the fabrication of large-scale dye-sensitized and perovskite solar cells.

Introduction

Dye-sensitized solar cells (DSSCs), solid state dye-sensitized solar cells (SSDSSCs) and perovskite solar cells (PSCs) are attractive alternatives to solid state photovoltaics at competitive cost. The general concept of a DSSC is based on a liquid junction photo-electrochemical cell with a nanocrystalline TiO_2 photoanode that is sensitized with a dye. This is in contact with an electrolyte solution with a redox mediator which transports holes from the photo-oxidized dye towards the counter electrode. In SSDSSCs or PSCs, the photogenerated holes are transported by a solid conductive material (e.g., spiro-OMeTAD) [1,2]. This is accompanied by the undesirable back reaction of photoinjected electrons with the hole-transporting medium or the oxidized mediator. This reaction occurs both at the TiO_2 surface and at the exposed areas of the F-doped SnO_2 (FTO) conducting glass that are not covered by the titanium dioxide nanoparticles. In liquid-type DSSCs there is a relatively small recombination current as compared to FTO, which becomes critical in SSDSSCs and perovskite solar cells [3].

For proper function of these solar cells, a semiconducting nonporous blocking layer of oxide (usually TiO_2 or SnO_2) must be deposited on top of FTO to prevent recombination on this surface [3-5]. Blocking layers (BLs) can be fabricated by spray pyrolysis [3,6], magnetron sputtering [7], electrochemical deposition [8] spin coating [9,10], dip coating [11] and atomic layer deposition (ALD) [3].

From the viewpoint of low-cost processing and easy upscaling, spray pyrolysis deposition (SPD) is the most practical option for the fabrication of solar cells. 120–200 nm thick, compact, TiO_2 layers were found to be optimal for SSDSSCs [12]. The same layers (with optimized thickness of 30–35 nm) turned out to be useful for PSCs, where they clearly outperformed the layers made by spin coating [9]. Matteocci et al. [13] used a modified precursor solution which was obtained by addition of acetylacetone to the conventional formulation (i.e., titanium diisopropoxide bis(acetylacetonate)) in ethanol. They fabricated compact TiO_2 blocking layers (via SPD) for poly(3-hexylthiophene) SSDSSCs. Their optimised BLs showed an overall increase in the solar cell efficiency, but the blocking function was not quantified, for example, by analysis of the pinhole area [13]. This was one of the motivations for this work.

The blocking properties are often significantly impaired by calcination at 500 °C (which is mandatory for the subsequent fabrication of mesoporous TiO_2 thick films). Even though SPD is a popular technique for the fabrication of BLs and the resulting TiO_2 films are less sensitive to calcination, the blocking properties are inferior to those with films prepared by electrodeposition or ALD for example [3,8]. Therefore the central motivation for this work was SPD fabrication of blocking TiO_2 films using conventional [6] and novel [13] spray protocols using a semi-automatic spray device, enabling reproducible and uniform thin transparent titania films to be achieved with good blocking properties and low sensitivity to calcination at the same time. Such fabricated BL TiO_2 films were characterized by photo-electrochemical measurements in aqueous electrolyte solution. The blocking ability was quantified by cyclic voltammetry with a $K_3[Fe(CN)_6]/K_4[Fe(CN)_6]$ model redox probe [3].

Experimental

Two types of FTO glass supports were used with the same nominal sheet resistivity (as declared by the supplier, 8 Ω/sq) and thickness (2.2 mm): TEC 8 from Libbey-Owens-Ford, labelled as FTO(A) and TEC 8 from Dyesol labelled as FTO(B). Our own measurement of the sheet resistivity showed 12.5 Ω/sq and 7.9 Ω/sq for FTO(A) and FTO(B), respectively. FTO glass slides were cleaned in ethanol and acetone. TiO_2 layers were deposited by semi-automatic spray coating set up using two different precursors (i) an ethanolic solution of titanium diisopropoxide bis(acetylacetonate) (abbreviated TAA [6], at concentrations of 0.05 M and 0.2 M) and (ii) an ethanolic solution of titanium diisopropoxide bis(acetylacetonate) with added acetylacetone with total molar ratio Ti/acetylacetone 1:2.4 (abbreviated TAA-AcAc) [13]. Spraying was carried out by semi-automatic spray device consisting of a nozzle (EST 616, Czech Republic) fed with compressed air (3 bar) and a solution of precursor (flux of 2.7 cm^3/min). The nozzle was mounted on a linear stage (velocity 20 cm/s) and the precursor solution was delivered downwards to a heated support (150, 300 or 450 °C). The working area of deposition was up to 20 × 30 cm, whereby upscaling is technically feasible. During each spray process (lasting approximately 0.5 s) a significant decrease of the temperature of the heating plate occurred for several seconds. To avoid this undesired cooling, the next spraying was performed at regular time intervals (30 s) which were necessary for complete layer formation and restoration of the original substrate temperature. This technique allows for the fabrication of films using various numbers of spray cycles (SCs). During the coating procedure, a narrow area at the edge of the FTO glass substrate was protected against deposition of the TiO_2 by a mask. This allowed for an ohmic contact to the electrode for subsequent electrochemical and photo-electrochemical tests. Table 1 gives a summary of the fabricated samples. The variable growth parameters were: FTO type (A, B), precursor concentration, deposition temperature, number of spray cycles and influence of the post-calcination step (in air at 500 °C for 1 h).

The produced titania films were characterized by X-ray diffraction (XRD) (PANanalytical X'Pert PRO, Cu Kα radiation,

Table 1: Overview of the experimental conditions for spray deposition of titania blocking layers deposited on top of FTO conducting glass.

Precursor type and concentration	FTO glass	Substrate temperature/ °C	Number of spray cycles
0.05 M TAA	A	150	100
	A	450	100
0.05 M TAA	A,B	450	50
	A,B	450	100
	A,B	450	200
0.2 M TAA	B	450	20
	B	450	30
	B	450	40
	B	450	50
	B	450	60
	B	450	70
0.2 M TAA- AcAc	B	450	20
	B	450	30
	B	450	40
	B	450	50
	B	450	60
	B	450	70

1D XCelerator detector, PANanalytical B.V., Almelo, Netherlands), scanning electron microscopy (SEM) (Hitachi FE SEM S-4800 microscope), and UV–vis spectroscopy (Varian CARY 100 with integrating sphere DRA-CA-30I and 8° reflectance geometry, Varian, USA). X-ray fluorescence spectroscopy (XRF) analysis was performed on an ARL 9400 XP sequential WD-XRF spectrometer (Thermo ARL, Switzerland) equipped with a Rh anode end window and a 4GN-type X-ray tube fitted with a 50 µm Be window. The obtained data were evaluated by Uniquant 4 software.

Photo-electrochemical and electrochemical experiments were carried out in a one-compartment three-electrode cell using an Autolab Pgstat 101 instrument controlled by the NOVA software. The TiO_2 thin film on FTO was the working electrode, the reference electrode was Ag/AgCl (3 M KCl) and a platinum rod was used as the counter electrode. The TiO_2 films were illuminated from the front side by a Hg lamp (Oriel), and the TiO_2 film area (1 cm^2) was defined by a Teflon tape mask. Optical filters were used to select the wavelength range of 320–380 nm. Intermittent light was applied at 10 s dark/light intervals and the working electrode potential was swept with a scan rate of 5 mV s^{-1}. 0.1 M Na_2SO_4 (pH 10) was used as the electrolyte solution for photo-electrochemical experiments [14]. The blocking properties of the deposited layers were evaluated by cyclic voltammetry (CV) in aqueous electrolyte solution composed of 0.5 mM $K_4[Fe(CN)_6]$, 0.5 mM $K_3[Fe(CN)_6]$ in 0.5 M KCl, pH 2.5.

Results and Discussion

To optimize the SPD conditions, we initially tested the effect of deposition temperature. Our TiO_2 films were grown using 100 spray cycles (SCs) using a TAA solution of concentration 0.05 M, and the temperature of the FTO substrates was held at 150, 300 and 450 °C, respectively. Figure 1a shows the UV-photo-electrochemical scan of a TiO_2 film deposited at 150 °C. Without post-calcination at 500 °C, the photocurrent density is negligible. The photoresponse was similarly negligible for the deposition temperature of 300 °C (data not shown). Only after calcination at 500 °C will the low-temperature-grown films become photoactive, where the photocurrent onset was observed at around −0.35 V (Figure 1a). In the applied potential range of 0.25–1.2 V there is a photocurrent plateau at ≈14 µA/cm^2 at the UV illumination intensity applied (7.5 mW/cm^2).

For the deposition temperature of 450 °C, our titania films are photoactive already in the as-grown state (see Figure 1b). These TiO_2 films exhibit the photocurrent onset at around –0.3 V but there is no plateau at larger potentials. Instead, the photocurrent increases monotonically with the applied potential. The effect of post-calcination is opposite compared to the low-temperature films deposited at 150 °C (cf. Figure 1a). For instance, at the potential of 1.2 V, we observe a photocurrent density of ≈300 µA/cm^2 for the as-grown film (at 450 °C) but only ≈240 µA/cm^2 for the same film, but post-calcined at 500 °C.

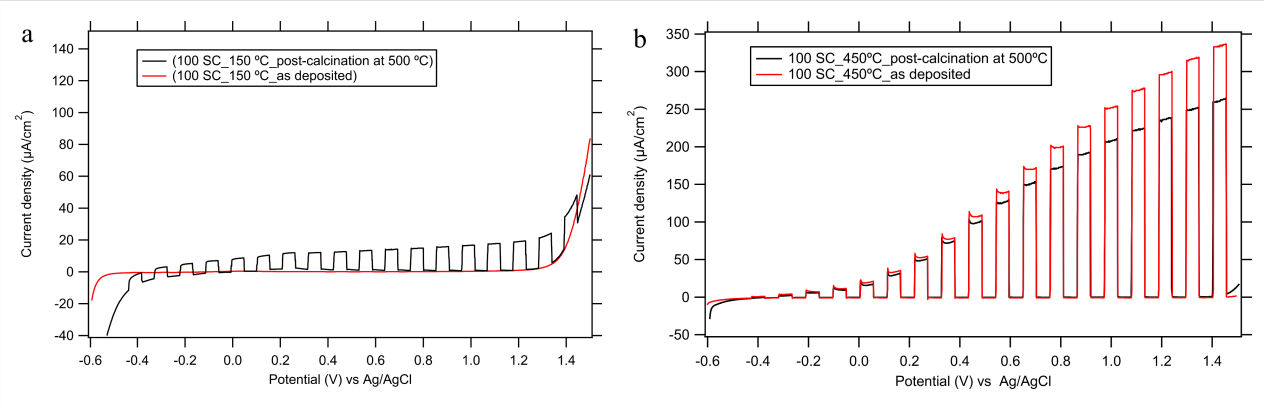

Figure 1: Linear sweep voltammetry under intermittent UV light excitation (Hg lamp 320–380 nm) of intensity 7.5 mW/cm^2. Comparison of TiO_2 films (100 SCs) deposited on FTO (A) at 150 °C (a) and 450 °C (b) with and without subsequent calcination. The electrolyte solution was 0.1 M Na_2SO_4 (pH 10), dark/light intervals of 10 s were applied.

The onset of anodic dark current for a TiO_2 film deposited at 450 °C occurs at a potential of ≈1.45 V. On the other hand the onset potential of the dark anodic current is downshifted to ≈1.3 V for TiO_2 films deposited at 150 °C. A similar dark current onset potential (of ≈1.3 V) was observed on bare FTO under comparable experimental conditions [15,16]. This suggests that the TiO_2 films deposited at 150 °C and post-calcined at 500 °C contain pinholes and cracks through which the electrolyte can reach the FTO surface. As TiO_2 is under strong depletion at these potentials, no anodic current of, for example, water oxidation, is expected to flow at the perfectly compact titania electrode in dark.

The blocking quality of our layers was tested in the pH-independent aqueous model redox system $K_3[Fe(CN)_6]/K_4[Fe(CN)_6]$ [3]. Nernstian pH-dependence is demonstrated by the flat-band potential, φ_{FB}, of a single-crystal anatase electrode (Equation 1) [17]:

$$\varphi_{FB} = -0.36 - 0.059\,\text{pH (in V vs Ag/AgCl)}. \quad (1)$$

As compared to this TiO_2 (anatase) flat-band potential, the redox potential of $[Fe(CN)]_6^{3-}/[Fe(CN)]_6^{4-}$ (0.24 V vs Ag/AgCl) is sufficiently positive in aqueous electrolyte solutions at all pH values. As a result, a rectifying interface, at which no anodic current of $[Fe(CN)_6]^{4-}$ oxidation flows, is obtained with high-quality titania (anatase) blocking layers because at these potentials titania is in the depletion regime. The cathodic current onset (beginning $[Fe(CN)_6]^{3-}$ reduction) appears at potentials negative to the φ_{FB} when the titania electrode is in the accumulation regime, mimicking metallic behaviour. Defects, such as cracks in the blocking layer are thus sensitively identified by the occurrence of anodic voltammetric current assigned to the $[Fe(CN)_6]^{4-}$ oxidation at the exposed FTO areas in pinholes [3].

Figure 2 shows cyclic voltammograms of $Fe(CN)_6^{3-/4-}$ redox couple at a bare FTO(A) substrate and that for a sample coated with TiO_2 films (100 SCs) of different deposition. Our TiO_2 film deposited at 150 °C without post-calcination displays perfect blocking properties, although it is photo-electrochemically inactive (cf. Figure 1a). Post-calcination of this film causes severe deterioration of its blocking function. The cyclic voltammogram $Fe(CN)_6^{3-/4-}$ is similar to that of pure FTO. The

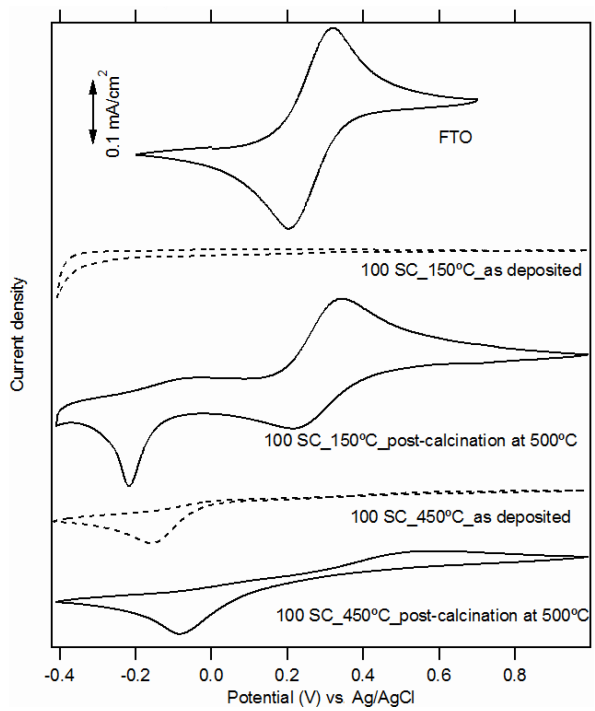

Figure 2: Cyclic voltammograms on an uncoated FTO(A) electrode and one covered by TiO_2 films consisting of 100 SCs of TAA (0.05 M). Scan rate 50 mV/s. Electrolyte solution was 0.5 mM $Fe(CN)_6^{3-/4-}$ in aqueous 0.5 M KCl, pH 2.5. The voltammograms (except for FTO) are offset for clarity but the current density scale is identical for all plots.

presence of TiO_2 manifests itself solely by a cathodic peak at ≈−0.2 V which is assigned to the reduction of ferricyanide at the TiO_2 surface [3]. On the other hand, the as-grown TiO_2 film deposited at 450 °C has perfect barrier properties, which are less perturbed by the post-calcination.

As a next step, we investigated in detail the influence of layer thickness, which was adjusted by the number of spray cycles (SC, 50–200) of 0.05 M TAA solution. We have chosen the deposition temperature of 450 °C and have also investigated the influence of the respective FTO glass substrates (A or B, see Experimental section). Figure 3 shows that the photocurrent density increases with the number of SCs for both the FTO substrates.

The onset potential of the dark anodic current (≥1.4 V) suggests a rather compact character of our films deposited at 450 °C. The onset potential of photocurrent is very similar (around −0.3 V) on both our FTO supports and for various layer thicknesses. There is very small slope of the photocurrent/potential curve around the photocurrent onset and then an almost linear increase of the photocurrent. A similar shape in the polarization curve was observed previously for rutile TiO_2 films [18]. However, SPD titania films are likely to be of anatase structure as shown by our XRD analysis (see Figure S1 and Figure S2 in Supporting Information File 1) and confirmed by others [3,6,13].

Figure 3a,b shows that the type of FTO substrate used significantly influences the photocurrent on the as-deposited TiO_2 films. On the FTO(A) substrate, there is a strong increase of photocurrent between 50 and 100 SCs and a less-pronounced increase between 100 and 200 SCs. On the other hand, for FTO(B), the photocurrent increases proportionally with the increase of the number of spray cycles (between 50 and 200 SCs). This FTO-specific behaviour greatly diminishes after post calcination at 500 °C (Figure 3c,d), which results in a very similar influence of the number of SCs on the photocurrent for both the FTO supports.

Cyclic voltammograms of $Fe(CN)_6^{3-/4-}$ redox couple on pure FTO substrates (A or B) are almost identical (cf. Figure 2 for FTO(A)). Figure 4a shows the corresponding cyclic voltammograms on TiO_2 films deposited at 450° on FTO(A) substrates (50–200 SCs). All TiO_2 films have good blocking properties; there is a slight improvement with an increase of the number of SCs, i.e., with the layer thickness. However, after post-calcination, there is a significant deterioration of the blocking properties, and the positive influence of increased SCs on the blocking properties is more apparent (see Figure 4c).

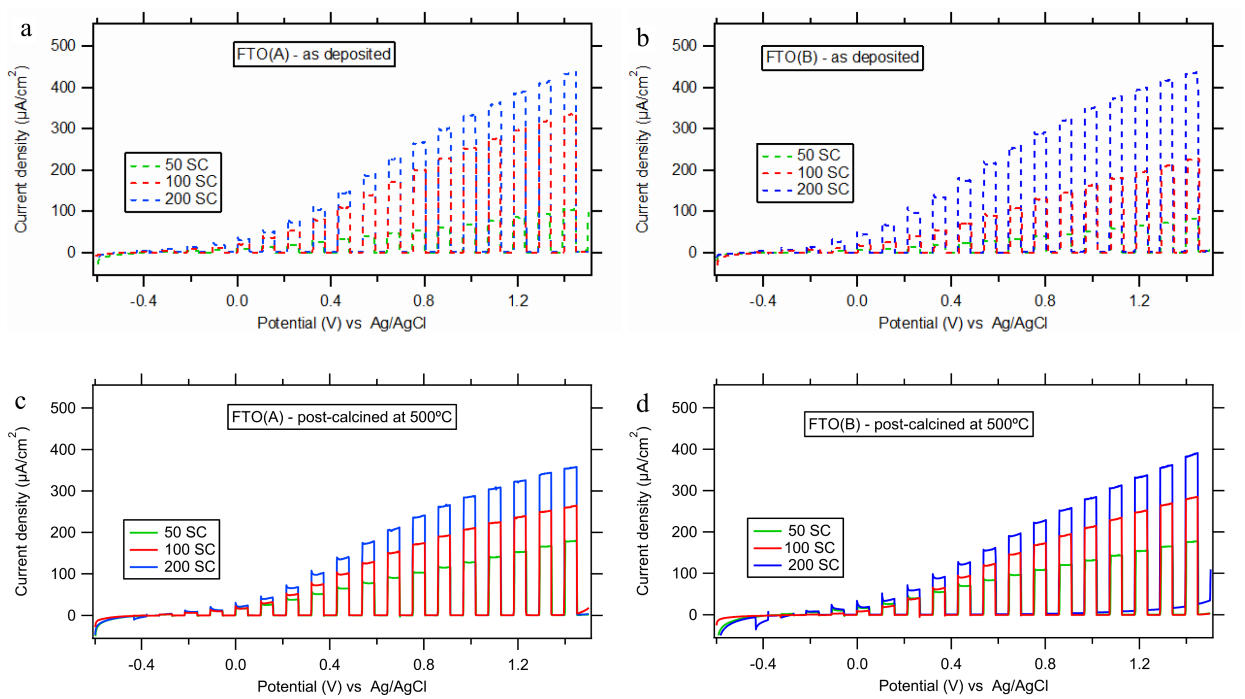

Figure 3: Linear sweep voltammetry under intermittent UV light (Hg lamp 320–380 nm; intensity 7.5 mW/cm^2). Precursor: 0.05M TAA, deposition temperature: 450 °C, electrolyte solution: 0.1 M Na_2SO_4 (pH 10), dark/light interval: 10 s. (a,c) Films deposited on FTO(A) 50, 100 and 200 SCs. (b,d) Films deposited on FTO(B) 50, 100 and 200 SCs.

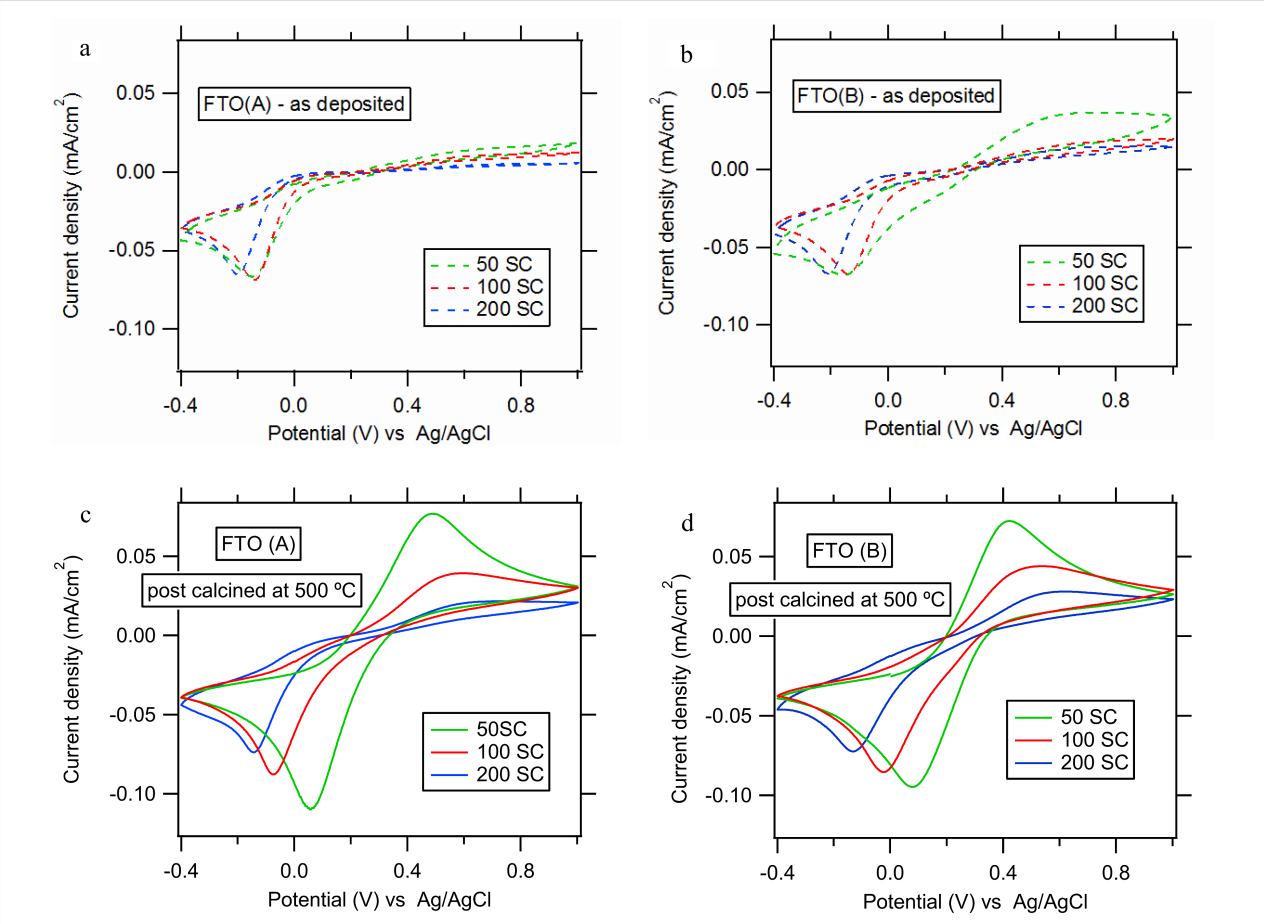

Figure 4: Cyclic voltammograms for TiO_2 films; precursor: 0.05M TAA, deposition temperature: 450 °C, scan rate: 50 mV/s, electrolyte solution: 0.5 mM $Fe(CN)_6^{3-/4-}$ in aqueous 0.5 M KCl, pH 2.5. (a,c) films deposited on FTO(A) 50, 100 and 200 SCs, (b,d) films deposited on FTO(B) 50, 100 and 200 SCs.

A similar behaviour was observed for the TiO_2 films deposited on the FTO(B) substrate, but the blocking properties were not as good as than those for TiO_2 films deposited on FTO(A), especially for the lowest thickness (50 SCs), see Figure 4b. Also, the post calcination at 500 °C results in a significant deterioration of the blocking properties, see Figure 4d.

Although the used substrates (FTO(A) and FTO(B)) are nominally identical (TEC 8; differing solely by the supplier, see Experimental section) we observed a surprisingly strong influence of the substrate type on the blocking properties of titania films which were sprayed over them. More specifically, FTO(A) provides considerably better blocking properties of the corresponding titania films. To address this peculiarity, we investigated these substrates in more detail and the results are summarized below.

Figure 5 shows the top surface morphology of both our FTO substrates. The grain size is between 100 and 200 nm for FTO(A), but between 300 and 500 nm for FTO(B). Furthermore, FTO(B) is less transparent than FTO(A), whereby the optical transmittance in the range of wavelengths from 350 to 550 nm is by about 15–20% lower, which is consistent with the difference in the structure. The coherent domain size calculated from X-ray line broadening by the Scherrer equation was 24 nm for FTO(A) and 36 nm for FTO(B). These values are consistent with the difference in the grain size for both the FTO samples. Our own measurement of sheet resistivity provided the following values. FTO(A), TEC8, Libbey-Owens-Ford: 12.5 Ω/sq and FTO (B), TEC 8, Dyesol: 7.9 Ω/sq. This finding is quite surprising and implies that FTO(B) has a higher resistivity (by about 50%) than that declared by the supplier.

The larger grain size of the FTO(B) substrate is the apparent reason for its incomplete coverage by titania film. Figure 4a illustrates this finding, which is particularly expressed for the smallest thicknesses (50 SCs). For a larger number of SCs (100 and 200) the differences between our FTO substrates are damped. The evaluation of the fraction coverage of FTO by the titania blocking layer is based on the voltammetric current den-

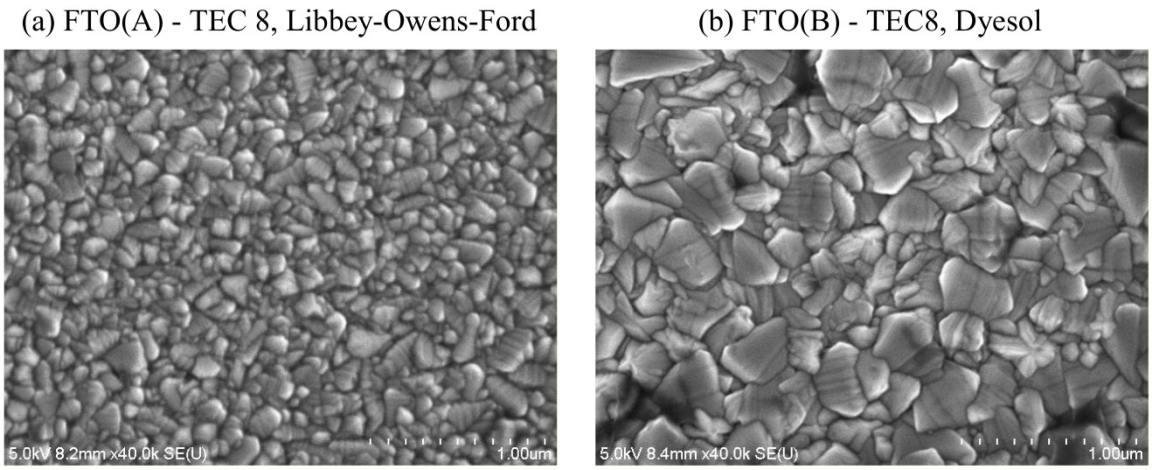

Figure 5: Top view SEM images of FTO glass substrates, (a) FTO(A) and (b) FTO(B).

sity peak, j_p, which follows the Randless−Sevcik equation [3]. The effective pinhole area (EPA) can be expressed by Equation 2 as

$$\mathrm{EPA} = \frac{A_u}{A_0} = \frac{j_p}{j_{p,FTO}}(\%), \quad (2)$$

where j_p is the peak current density (with reference to the projected electrode area, A_0) measured at the actual blocking electrode, A_u is the uncovered area of FTO and $j_{p,FTO}$ is the current density peak measured at a bare FTO electrode. The actual values are listed in Table 2. As suggested in a previous work [3], there are two types of defects in the barrier film: (i) "defect A" – the partially blocked electrode behaves like a "clean" FTO but with a relatively smaller effective area. The relative increase of voltammetric peaks separation (ΔE_{pp}) on the BL normalized to that for pure FTO is smaller than 3. (ΔE_{pp} is defined as the difference between the peak potentials for the $Fe(CN)_6^{4-}$ oxidation and $Fe(CN)_6^{3-}$ reduction). (ii) "defect B" – a more complex situation, where the defect causes not only the delamination of the titania film from FTO, but also the slowdown of charge transfer kinetics (accompanied by a strong increase in ΔE_{pp}).

The barrier properties after post calcination were fairly good for the 0.05 M TAA precursor and the largest layer thickness (200 SCs), but still ≈10–13% of the FTO surface was uncovered by TiO_2 (Table 2). Therefore, in the next step, the concentration of TAA was increased to 0.2 M to achieve a larger film thickness per one spray cycle. FTO(B) was chosen as a substrate due to the conformity of its measured/declared sheet resistivity and also as a solution for the reduced blocking performance of thin TiO_2 films deposited on it (cf. Figure 4a,c and

Table 2: Analysis of the effective pinhole area for our as-deposited and post-calcined TiO_2 films. Data from cyclic voltammetry of $Fe(CN)_6^{3-/4-}$; scan rate 50 mV/s (experimental conditions same as in Figure 2).

Substrate	Precursor	No. of SCs	j_p (mA cm^{-2})		EPA (%)		Defect type
			as dep.	calcined	as dep.	calcined	
FTO(A)	–	–	0.15	–	100	–	–
FTO(A)	0.05 TAA	50	0.020	0.075	13	50	A
FTO(A)	0.05 TAA	100	0.013	0.035	9	23	A+B
FTO(A)	0.05 TAA	200	0.006	0.02	4	13	B
FTO(B)	0.05 TAA	50	0.040	0.07	27	47	A
FTO(B)	0.05 TAA	100	0.017	0.03	11	20	A+B
FTO(B)	0.05 TAA	200	0.010	0.015	7	10	B
FTO(B)	0.2 TAA	20	0.010	0.02	7	13	B
FTO(B)	0.2 TAA	50	0.005	0.01	3	7	B
FTO(B)	0.2 TAA	70	0.002	0.005	1	3	B
FTO(B)	0.2 TAA-AcAc	70	0.002	0.002	1	1	B

Figure 4b,d). The actual TiO_2 films were deposited by 20 to 70 spray cycles at 450 °C and again the influence of the post-calcination was investigated. The photocurrent response was measured similarly as in Figure 3. For the as-deposited films as well as the calcined films, the photocurrent density slightly increases with increasing number of SCs (from 20 to 40), but remains constant for higher SCs (between 50 and 70). The observed photocurrent density at a potential of 1.2 V was 460 μA/cm^2 for the calcined TiO_2 film from 0.2 M TAA (50 SCs). Figure 3b and Figure 3d illustrate that this photocurrent is roughly comparable to that on the calcined thick film from diluted solution (0.05 M-TAA; 200 SCs), i.e., 350 μA/cm^2.

Figure S3 in Supporting Information File 1 shows the cyclic voltammograms of FTO(B) covered by TiO_2 films deposited by 20 SCs of 0.2M TAA. There is a large improvement of the blocking properties when compared to the previous set of samples (Figure 4b,d). More detailed CV data are shown in Figure 6 for the TiO_2 films consisting of 20, 50 and 70 SCs. In all cases, post-calcination causes a strong deterioration of the blocking properties. The difference between as-deposited TiO_2 films and those after post-calcination is a dampening with increasing number of SCs. For instance, at 70 SCs, the difference is almost negligible.

Figure 7 shows the top surface morphology of our FTO(B) and that of the substrate covered by TiO_2 films consisting of various SCs. A thin TiO_2 film (20 SCs) is barely visible on top of FTO (Figure 7b), where the image is dominated by the substrate morphology. With increasing number of SCs, the grains of FTO become covered by small TiO_2 particles, which provide the blocking function of the electrode (Figure 7c). Interestingly, post-calcination does not result in any significant increase of the TiO_2 particle size, as seen in Figure 7d.

From the comparison of Figure 6 and Figure 4b,d it follows that the as-deposited and post-calcined TiO_2 films consisting of 20 SCs (0.2 TAA) have comparable blocking properties to the TiO_2 film consisting of 200 SCs (0.05 TAA). With increasing number of SCs (from 20 to 70), the negative influence of post-calcination on the blocking properties of TiO_2 films further diminishes (cf. Figure 6 and the EPA values in Table 2).

In the last step, we investigated the influence of the precursor solution composition. Figure 8 compares the cyclic voltammograms of $Fe(CN)_6^{3-/4-}$ on FTO(B) covered by TiO_2 films consisting of 70 SCs by two precursors, 0.2 M TAA and 0.2 M TAA-AcAc, where the latter was enriched with added acetylacetone (see Experimental section). Although the 70 SC TAA film has already quite good blocking properties even after post-calcination, examination of the details in the curves shows that the TAA-AcAc films are still better. The shift of the electroreduction peak, or in some cases the missing electroreduction (at −0.2 V), is a sign of good coverage of the electroactive FTO by the TiO_2 film, which has properties comparable to those of a perfect anatase single crystal. The latter has a flat band potential (φ_{FB}) (cf. Equation 1) at ≈−0.5 V at the given experimental conditions (as in Figure 8). Hence, no electroreduction of ferricyanide to ferrocyanide is expected to occur at −0.2 V, because anatase is in the depletion regime. This is indeed observed for our TAA-AcAc films. Actually, the occurrence of the electroreduction peak at −0.2 V at some other compact (pinhole-free) TiO_2 layers (cf. Figure 6) is less clear from this point of view. A tentative interpretation could consider the fact that certain TiO_2 films (e.g., those grown by ALD) do show their φ_{FB} significantly upshifted (by ≈0.3 V), see e.g. [3].

Our conclusion concerning a significant difference in the properties of the BL resulting from the two compositions of spray pyrolysis precursors is a bit empirical, and the comparison of

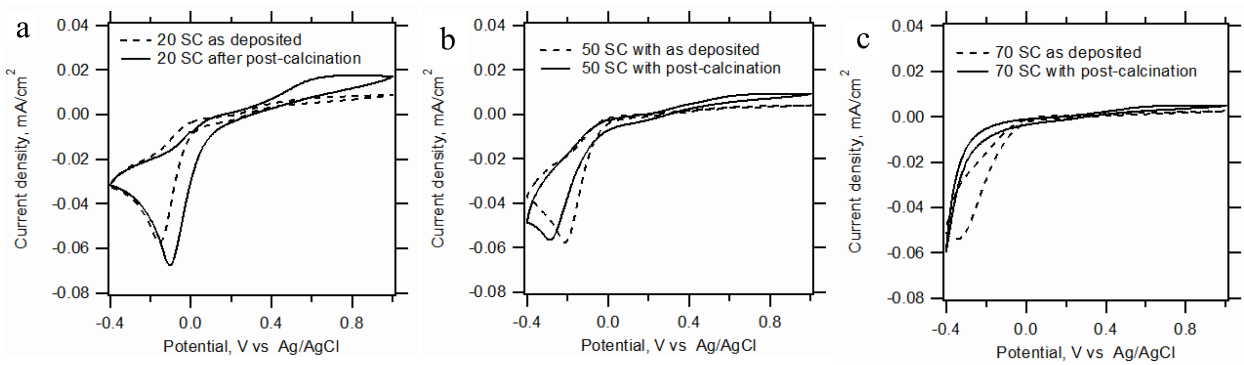

Figure 6: Cyclic voltammograms on a FTO(B) substrate covered by TiO_2 films of (a) 20 SCs, (b) 50 SCs and (c) 70 SCs of 0.2 M TAA. Scan rate 50 mV/s. Electrolyte solution was 0.5 mM $Fe(CN)_6^{3-/4-}$ in aqueous 0.5 M KCl, pH 2.5.

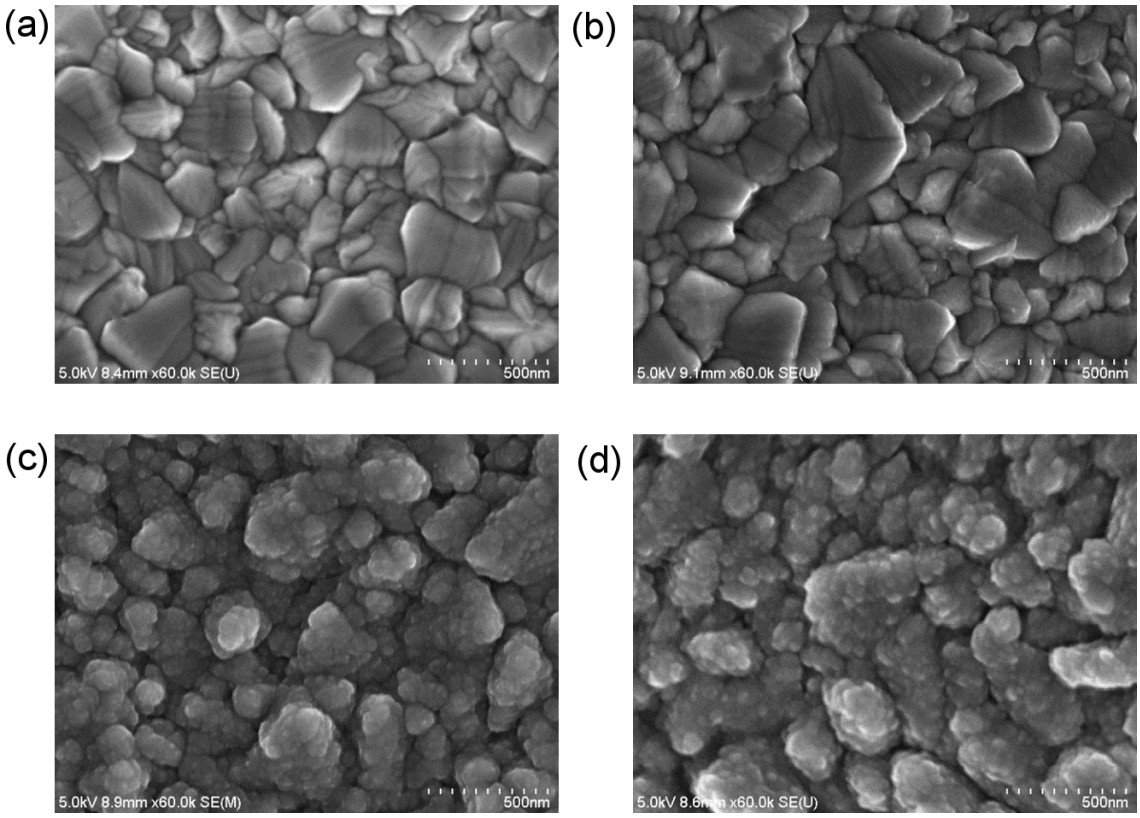

Figure 7: Top view SEM images of a) bare FTO(B), b) FTO(B) covered by 20 SCs of 0.2 M TAA, c) FTO(B) covered by 70 SCs of 0.2 M TAA and d) FTO(B) covered by 70 SCs of 0.2 M TAA with post-calcination at 500 °C.

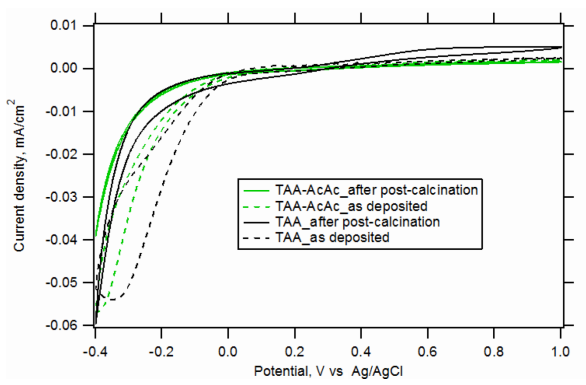

Figure 8: Cyclic voltammograms of FTO(B) covered by sprayed TiO_2 films made of 70 SCs of 0.2 M TAA and of 0.2 M TAA-AcAc. Scan rate 50 mV/s. Electrolyte solution was 0.5 mM $Fe(CN)_6^{3-/4-}$ in aqueous 0.5 M KCl, pH 2.5.

TAA vs TAA-AcAc is not reinforced by deeper discussion of the growth mechanism and structure of the products. Matteocci et al. [13] assumed that acetylacetone can induce functionalization of FTO, aiding in turn an efficient anchoring of TiO_2 to FTO. This hypothesis is rationalized by the well-known chelating effect of acetylacetone on both organometallic complexes and on oxidic surfaces. The optimization through compositional variation is limited by the growth of complicated species, particularly if the acetylacetone concentration is too high [13]. In a closely related study, Boland et al. [19] used IR spectroscopy to confirm that the precursor solution made by mixing of titanium (IV) isopropoxide with acetylacetone contains an excess of unchelated acetylacetone for the Ti/AcAc ratio ≥3. Hence, we (in accord with the cited works and references therein) assume that our used precursor solution has the optimal composition already.

From the XRD analysis, an anatase crystalline structure was not detected for any as-deposited TiO_2 films even those consisting of 70 SCs (0.2 M TAA), see Figure S1 in Supporting Information File 1. For post-calcined TiO_2 films, anatase can be detected only for films consisting of 70 SCs (only one band (θ = 25.4°), see Figure S1 in Supporting Information File 1. Similarly, XRD analysis of the 70 SC TAA-AcAc film shows that the anatase band (θ = 25.4°) is visible only after post-calcination.

Surface XRF analysis of the TiO_2 film consisting of 50 SCs (0.2 M TAA) shows the content of Ti equal to 8.1 μg/cm^2.

Assuming that the film contains only TiO_2 we obtain the mass of our TiO_2 to be 13.3 μg/cm^2 and the corresponding thickness of the TiO_2 film (using the density of 3.8 mg/cm^3) equal to 36 nm. Analogously, the thicknesses of our TiO_2 films consisting of 20, 50 and 70 SCs (0.2 M TAA) are 14, 36 and 50 nm, respectively. This rather low layer thickness together with the very small size of the sprayed TiO_2 particles (see Figure 7c,d) is responsible for the very weak XRD response.

We should note that our layer thicknesses are considerably smaller than those reported previously for dye-sensitised solar cells (the thicknesses were typically 100–200 nm) [6,13], and are in the thickness region which was optimized previously for perovskite solar cells (30–35 nm) [9,11]. However, the cited work used solely the stoichiometric titanium diisopropoxide bis(acetylacetonate) without any added acetylacetone. Our results support the earlier finding by Matteocci et al. [13], that the addition of extra acetylacetone for BL fabrication is beneficial for the efficiency of poly(3-hexylthiopene) solar cells. Here we extended this finding by an analysis of the blocking function of these layers. To the best of our knowledge, this analysis as well as the systematic screening of deposition conditions is carried out in this work for the first time.

Conclusion

Transparent TiO_2 films were prepared by spray pyrolysis using precursors consisting of an ethanolic solution of titanium diisopropoxide bis(acetylacetonate) (TAA) with or without additional acetylacetone added. The films were deposited on FTO glass substrates at temperatures of 150, 300 and 450 °C using a semi-automatic spray device, enabling control of the film homogeneity and thickness over a large area. The minimal deposition temperature of 450 °C was identified for obtaining the photo-electrochemically active, as-grown films. An increase in the precursor concentration affords the corresponding increase of layer thickness normalized to the number of the deposition cycles. The need of careful selection of an FTO substrate is highlighted by a comparison of two nominally identical products from two suppliers. The as-deposited TiO_2 films (at 450 °C) of thickness ≈15 nm prepared from precursor TAA exhibit good blocking properties with an effective pinhole area (EPA) smaller than 10%. However, post-calcination of the as-grown films at 500 °C had a negative influence on the blocking properties. The problem could be addressed by increasing the number of spray cycles (thickness ≈50 nm) so that an EPA of ≈3% is achieved. The negative influence of the post-calcination is further minimized by deliberate addition of acetylacetone to the precursor solution. In this way, high-quality barrier films were fabricated (EPA ≈1%) which do not suffer from any loss in blocking function after subsequent post-calcination. To the best of our knowledge, the unperturbed blocking utility of our calcined films is shown here for the first time. Furthermore, good blocking is observed for calcined films, which are similar or thinner than those reported earlier by spray pyrolysis deposition. This finding is significant for the fabrication of DSSCs, SSDSSCs and perovskite solar cells.

Supporting Information

Supporting Information File 1

Additional experimental data.
[https://www.beilstein-journals.org/bjnano/content/supplementary/2190-4286-9-105-S1.pdf]

Acknowledgements

This work was supported by the Grant Agency of the Czech Republic (contracts No. 17-20008S and 18-08959S). This work was also supported by the Ministry of Education, Youth and Sports of the Czech Republic and The European Union - European Structural and Investments Funds in the frame of Operational Programme Research Development and Education - project Pro-NanoEnviCz (Reg. No. CZ.02.1.01/0.0/0.0/16_013/0001821). The authors would like to thank to Martin Zlamal (UCT Prague) for the set-up of the spray pyrolysis device.

ORCID® iDs

Ladislav Kavan - https://orcid.org/0000-0003-3342-4603

References

1. Hagfeldt, A.; Boschloo, G.; Sun, L.; Kloo, L.; Pettersson, H. *Chem. Rev.* **2010,** *110,* 6595–6663. doi:10.1021/cr900356p
2. Kavan, L. *Curr. Opin. Electrochem.* **2017,** *2,* 88–96. doi:10.1016/j.coelec.2017.03.008
3. Kavan, L.; Tétreault, N.; Moehl, T.; Grätzel, M. *J. Phys. Chem. C* **2014,** *118,* 16408–16418. doi:10.1021/jp4103614
4. Cameron, P. J.; Peter, L. M. *J. Phys. Chem. B* **2003,** *107,* 14394–14400. doi:10.1021/jp030790+
5. Cameron, P. J.; Peter, L. M. *J. Phys. Chem. B* **2005,** *109,* 930–936. doi:10.1021/jp0405759
6. Kavan, L.; Grätzel, M. *Electrochim. Acta* **1995,** *40,* 643–652. doi:10.1016/0013-4686(95)90400-W
7. Braga, A.; Baratto, C.; Colombi, P.; Bontempi, E.; Salvinelli, G.; Drera, G.; Sangaletti, L. *Phys. Chem. Chem. Phys.* **2013,** *15,* 16812–16818. doi:10.1039/c3cp52250d
8. Kavan, L.; O'Regan, B.; Kay, A.; Grätzel, M. *J. Electroanal. Chem.* **1993,** *346,* 291. doi:10.1016/0022-0728(93)85020-H
9. Wang, P.; Shao, Z.; Ulfa, M.; Pauporté, T. *J. Phys. Chem. C* **2017,** *121,* 9131–9141. doi:10.1021/acs.jpcc.7b00979
10. Jeong, I.; Park, Y. H.; Bae, S.; Park, M.; Jeong, H.; Lee, P.; Ko, M. J. *ACS Appl. Mater. Interfaces* **2017,** *9,* 36865–36874. doi:10.1021/acsami.7b11901
11. Masood, M. T.; Weinberger, C.; Sarfraz, J.; Rosqvist, E.; Sandén, S.; Sandberg, O. J.; Vivo, P.; Hashmi, G.; Lund, P. D.; Österbacka, R.; Smått, J.-H. *ACS Appl. Mater. Interfaces* **2017,** *9,* 17906–17913. doi:10.1021/acsami.7b02868

12. Peng, B.; Jungmann, G.; Jäger, C.; Haarer, D.; Schmidt, H.-W.; Thelakkat, M. *Coord. Chem. Rev.* **2004,** *248,* 1479–1489. doi:10.1016/j.ccr.2004.02.008
13. Matteocci, F.; Mincuzzi, G.; Giordano, F.; Capasso, A.; Artuso, E.; Barolo, C.; Viscardi, G.; Brown, T. M.; Reale, A.; Di Carlo, A. *Org. Electron.* **2013,** *14,* 1882–1890. doi:10.1016/j.orgel.2013.03.037
14. Krysa, J.; Lee, K.; Pausova, S.; Kment, S.; Hubicka, Z.; Ctvrtlik, R.; Schmuki, P. *Chem. Eng. J.* **2017,** *308,* 745–753. doi:10.1016/j.cej.2016.09.112
15. Waldner, G.; Krýsa, J.; Jirkovský, J.; Grabner, G. *Int. J. Photoenergy* **2003,** *5,* 115–122. doi:10.1155/S1110662X03000229
16. Krýsa, J.; Baudys, M.; Zlámal, M.; Krýsová, H.; Morozová, M.; Klusoň, P. *Catal. Today* **2014,** *230,* 2–7. doi:10.1016/j.cattod.2014.01.008
17. Kavan, L.; Grätzel, M.; Gilbert, S. E.; Klemenz, C.; Scheel, H. J. *J. Am. Chem. Soc.* **1996,** *118,* 6716–6723. doi:10.1021/ja954172l
18. Waldner, G.; Krýsa, J. *Electrochim. Acta* **2005,** *50,* 4498–4504. doi:10.1016/j.electacta.2005.02.028
19. Boland, S. W.; Pillai, S. C.; Yang, W.-D.; Haile, S. M. *J. Mater. Res.* **2004,** *19,* 1492–1498. doi:10.1557/JMR.2004.0199

License and Terms

This is an Open Access article under the terms of the Creative Commons Attribution License (http://creativecommons.org/licenses/by/4.0), which permits unrestricted use, distribution, and reproduction in any medium, provided the original work is properly cited.

The license is subject to the *Beilstein Journal of Nanotechnology* terms and conditions: (https://www.beilstein-journals.org/bjnano)

The definitive version of this article is the electronic one which can be found at:
doi:10.3762/bjnano.9.105

BEILSTEIN JOURNAL OF NANOTECHNOLOGY

Understanding the performance and mechanism of Mg-containing oxides as support catalysts in the thermal dry reforming of methane

Nor Fazila Khairudin, Mohd Farid Fahmi Sukri, Mehrnoush Khavarian and Abdul Rahman Mohamed*§

Review

Open Access

Address:
School of Chemical Engineering, Universiti Sains Malaysia, 14300 Nibong Tebal, Pulau Pinang, Malaysia

Email:
Abdul Rahman Mohamed* - chrahman@usm.my

* Corresponding author
§ Tel.: +604 599 6410; Fax: +604 599 6908

Keywords:
carbon formation; catalyst development; dry reforming of methane; magnesium catalyst; mechanism

Beilstein J. Nanotechnol. **2018,** *9,* 1162–1183.
doi:10.3762/bjnano.9.108

Received: 29 September 2017
Accepted: 16 February 2018
Published: 13 April 2018

This article is part of the Thematic Series "Energy conversion, storage and environmental remediation using nanomaterials".

Guest Editor: W.-J. Ong

© 2018 Khairudin et al.; licensee Beilstein-Institut.
License and terms: see end of document.

Abstract

Dry reforming of methane (DRM) is one of the more promising methods for syngas (synthetic gas) production and co-utilization of methane and carbon dioxide, which are the main greenhouse gases. Magnesium is commonly applied in a Ni-based catalyst in DRM to improve catalyst performance and inhibit carbon deposition. The aim of this review is to gain better insight into recent developments on the use of Mg as a support or promoter for DRM catalysts. Its high basicity and high thermal stability make Mg suitable for introduction into the highly endothermic reaction of DRM. The introduction of Mg as a support or promoter for Ni-based catalysts allows for good metal dispersion on the catalyst surface, which consequently facilitates high catalytic activity and low catalyst deactivation. The mechanism of DRM and carbon formation and reduction are reviewed. This work further explores how different constraints, such as the synthesis method, metal loading, pretreatment, and operating conditions, influence the dry reforming reactions and product yields. In this review, different strategies for enhancing catalytic activity and the effect of metal dispersion on Mg-containing oxide catalysts are highlighted.

Review

Introduction

Global warming is a present critical issue resulting from the excessive production of greenhouse gases, particularly carbon dioxide and methane (CO_2 and CH_4). This phenomenon is attributed to human dependence on fossil fuels to meet the high energy demands of the rapidly increasing world population. Therefore, one of the solutions to mitigate the emission of

greenhouse gases is to utilize these gases to yield new products, such as hydrogen or syngas (synthetic gas) [1-4]. Three principal technologies used for the production of syngas are steam reforming [5-7], partial oxidation [8-10], and dry reforming of methane (DRM) [11-13]. Among these technologies, DRM has attracted a growing body of research because of its potential to simultaneously utilize both carbon dioxide and methane gases. DRM is the most promising approach because the H_2/CO ratio for this reaction favors the Fischer–Tropsch synthesis [14,15]. DRM is yet to be commercialized on an industrial scale, as this method still has several issues and limitations, including the following: (i) the endothermic nature of the DRM reaction, (ii) catalyst deactivation, and (iii) the H_2/CO product ratio is lower than unity due to the occurrence of a reverse water–gas shift (RWGS) reaction, $CO_2 + H_2 \leftrightarrow CO + H_2O$. However, the major obstacle in implementing this technology is catalyst deactivation, which is defined as the susceptibility to carbon deposition and sintering of both support and active metal particles [16-18]. The loss of catalytic activity or selectivity over time of production affects the cost of catalyst replacement, process shutdown, and product quality and quantity. Numerous researchers have reported that noble metal-based catalysts, such as Pt, Rh, Pd, Ru, and Ir, exhibit high activity and resistance toward carbon formation [19-21]. However, these noble metals are associated with high cost and low availability, so non-noble metals, such as Ni [18,22-24], Fe [25-28], and Co [29,30] are most often used. Among the non-noble metals, Ni has been frequently chosen as an active catalyst metal owing to its vast availability, excellent activity, substantial redox characteristic, and relatively low cost [31]. However, Ni-based catalysts suffer from significant carbon deposition, which leads to carbon deactivation [32,33]. Recently, numerous attempts have been made to minimize carbon deposition on the catalyst surface in a DRM reaction. A high dispersion of active metal over the support is an effective approach to decrease carbon deposition by producing catalysts of small particle size [19,28,31,34-40]. In addition, a high dispersion of metal particles enhances the interaction between metal and support, consequently reducing carbon deposition [40-44].

One other alternative for inhibiting carbon deposition, as suggested by researchers, is the application of a second metal oxide, such as alkali or alkaline earth metal oxides, to the DRM catalyst to alter the catalyst acidity [39,45-48]. Numerous publications have reported on the ability of Mg-containing oxide catalysts to decrease the rate of carbon formation in a DRM reaction [18,19,49-54]. MgO exhibits superior surface and catalytic characteristics as a catalyst support combined with a high dispersion of small active particles for suppressing carbon formation [55]. The decreased carbon formation in DRM is due to the high basicity of MgO to capture CO_2, thereby accelerating the overall reaction [34,49,51]. Furthermore, its characteristics such as high thermal stability, high melting point, and low cost make MgO a promising component in endothermic reactions, especially in the DRM process [18,34,49].

Therefore, this review discusses the research regarding the DRM reaction over Mg-containing oxide catalysts as conducted by numerous researchers to assist in the reaction for decreasing carbon formation and to improve catalyst activity, selectivity, and stability. To date, an incorporated mechanism for carbon deposition and removal has yet to be proposed and is still being debated among researchers. The present review mainly focuses on the mechanism of DRM, carbon formation and removal, the role of Mg-containing oxide catalysts in resistance to catalyst deactivation, Mg-containing oxide catalyst development, and the effect of reaction conditions on catalyst performance.

Thermodynamic analysis

Thermodynamic analysis of a reaction is important for the theoretical study on the behavior of the process and the possible reaction conditions. A thermodynamic study could provide a basis for experimental investigation of the DRM reaction because the chemical reactions are conducted under equilibrium conditions [13,56]. Pressure, temperature and the composition of reactants (CH_4 and CO_2) are emphasized the most in thermodynamic studies using Gibbs free energy minimization technique [13,57,58].

Effect of temperature and pressure in DRM

In a DRM reaction, the conversion of CH_4 and CO_2 increases with an increase in temperature. This is because the DRM reaction is endothermic. In addition the reaction temperature in the DRM is the most important factor compared to pressure and reactant composition. As the temperature increases, the reaction approximately reaches complete conversion and equilibrium is achieved. Nikoo et al. [56] investigated the effect of temperature on the equilibrium conversion of CH_4 and CO_2 in a DRM reaction using Gibbs free energy minimization method. They showed that at low temperatures, $T_{rxn} < 800$ °C (1073 K), the equilibrium conversion of CH_4 was different for different ratios of CO_2/CH_4. However, when the temperature increased, $T_{rxn} \geq 800$ °C, for ratios of 2 and 3, the equilibrium conversion of CH_4 was 100% and for ratios 0.5 and 1, the conversion reached 95% and later increased up to 100% at a temperature of 1200 °C. They also found that the equilibrium conversion of CO_2 decreased as the temperature was increased from 300 °C (573 K) to 600 °C (873 K). This was due to the reaction of CO_2 with two moles of H_2 (Equation 1) to produce a large amount of carbon deposits and water since the reaction is exothermic and favorable at lower temperature.

$$CO_2(g)+2H_2 \leftrightarrow C+2H_2O \quad \Delta H_{298K} = -90\,kJ/mol \quad (1)$$

However, the equilibrium conversion of CO_2 increased as the temperature was increased to above 600 °C (873 K), as Equation 2 and Equation 3 are favorable at high temperature. The results obtained for the equilibrium conversion of CH_4 and CO_2 showed that the ratio of unity was the best ratio to obtain a balanced conversion between CH_4 and CO_2. As the ratio of CO_2/CH_4 increased, CH_4 became the limiting reactant and CO_2 was the excess reactant, so the limiting reactant was consumed more and the consumption of excess reactant was not completed.

$$CH_4+CO_2 \leftrightarrow 2CO+2H_2 \quad \Delta H_{298K} = 247\,kJ/mol \quad (2)$$

$$CO_2+H_2 \leftrightarrow CO+H_2O \quad \Delta H_{298K} = 41.4\,kJ/mol \quad (3)$$

In terms of catalytic performance, pressure is one of the factors which influences the activity of the catalyst in a DRM reaction because as the pressure increases, carbon deposition increases significantly. In addition, according to Chein et al. [13], the carbon deposit could increase to approximately 50% from atmospheric to 10 bar. It has been reported that as the conversion of reactants (CH_4 and CO_2) decreased, the yield of H_2 and CO also decreased and the carbon deposition increased with an increase in pressure, which indicates that the DRM reaction is not favored at high pressure [13,59,60]. This is probability because the collision of gas molecule and the active site surface of the catalyst increases and the surface concentration along with residence time for the CH_x species also increase as the pressure increases. The increase in pressure leads to a synchronization of carbon deposition and consumption whereby the rate of carbon deposition is higher than the consumption rate, resulting in catalyst deactivation due to carbon deposition [61].

In the DRM reaction, the carbon deposition and side reactions, especially the RWGS reaction, are known as a major problem to the stability of the catalyst and prevent a high yield of syngas production (H_2 and CO) [62]. Jafarbegloo et al. [63] also reported that the mole fraction of H_2O increased as the pressure in the DRM reaction was increased. Even at atmospheric pressure, the formation of H_2O was observed which indicates the occurrence of the RWGS reaction. This shows that the RWGS in the DRM reaction can be reduced but it cannot be eliminated according to thermodynamic equilibrium.

Role of inert gas in DRM

The use of inert gases such as N_2 can affect the DRM reaction especially in methane cracking (Equation 4). Figure 1 shows the relationship between CH_4, H_2, inert gas, and temperature in a ternary composition diagram [64]. The dotted line represents the presence of inert gas in the equilibrium mixture of CH_4 and H_2 at 500 °C. As the mole fraction of the inert gas increases, the reaction will increasingly favor thermodynamic CH_4 decomposition. Furthermore, it can be said that at higher temperature, the inert gas does not affect the DRM reaction in terms of carbon deposition, so the effect of inert gas at high temperature could be negligible.

$$CH_4 \leftrightarrow C+2H_2 \quad \Delta H_{298K} = 74.9\,kJ/mol \quad (4)$$

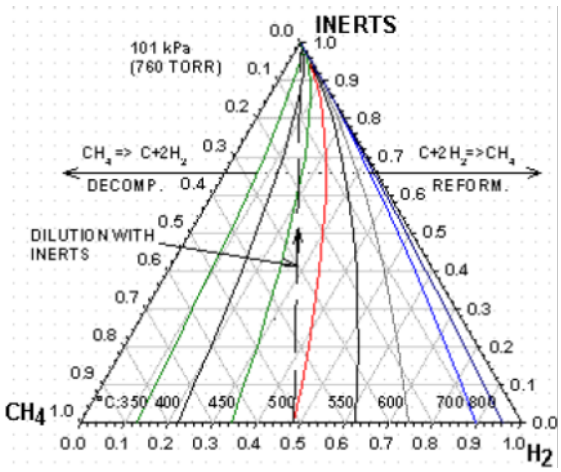

Figure 1: Methane decomposition equilibrium in the presence of inert gas at different temperatures. Reprinted with permission from [64], copyright 2002 Taylor and Francis Group.

DRM reaction mechanism

DRM is an endothermic reaction favored at high temperature and a low pressure. The reaction mechanism is extremely important for understanding the involved processes or for determining a solution to overcome catalyst deactivation. In general, the reaction mechanism depends on the choice of catalyst and all reactions involved in the DRM process. The overall proposed mechanism of the DRM reaction in the literature [57,65,66] follows three main steps: i) adsorption of CH_x (x = 0–4) and H, and decomposition of CH_4, ii) adsorption and activation of CO_2 and iii) oxidation of CH and C.

The role of the various catalyst constituents is important for the adsorption of reactants onto the catalyst surface and for the weakening of the chemical bonds of the reactant for the dissociation process. In one proposal, CH_4 activation was found to take place on the active sites. Niu et al. [66] proposed the mechanism of DRM over a Pt catalyst as shown in Equation 5. Equation 5 shows the adsorption of methane on the metal catalyst followed by dehydrogenation to produce hydrogen and a hydrocarbon species CH_x (x = 0–3). When x = 0, carbon deposition

occurs on the metal surface. Equation 6 describes the dissociation of CO_2 into CO and O. The produced atomic H from the dehydrogenation process activates CO_2 to form COOH before decomposition into CO and OH, as displayed in Equation 7. The H adsorbed by the catalyst surface activates CO_2 to form HCOO*, which then dissociates into CHO* and H* (Equation 8). Then, in the following step (Equation 9), CH* is oxidized to produce CHO*/COH* and subsequently decomposes to CO* and H*. Equation 10 depicts the oxidation of CH* by OH*, becoming CHOH* as an intermediate before dissociating into CHO*/COH* and H*. Finally, Equation 11 shows the oxidation of C* by O* and OH*, resulting in CO* and COH*, respectively. The large majority of the adsorbed hydrogen species are then recombined to produce the hydrogen molecules that subsequently desorb into the gaseous phase. In the following equations, the symbol (*) indicates the surface of the catalyst active site in the reactions.

$$CH_{x(x=1-4)^*} + * \rightarrow CH_{x(x=0-3)^*} + H^* \quad (5)$$

$$CO_2^* + * \rightarrow CO^* + O^* \quad (6)$$

$$CO_2^* + H^* \rightarrow COOH^* + * \rightarrow CO^* + OH^* \quad (7)$$

$$CO_2^* + H^* \rightarrow HCOO^* + * \rightarrow CHO^* + O^* \quad (8)$$

$$CH^* + O^* \rightarrow CHO^* / COH^* + * \rightarrow CO^* + H^* \quad (9)$$

$$CH^* + OH^* \rightarrow CHOH^* + * \rightarrow CHO^* / COH^* + H^* \quad (10)$$

$$C^* + O^* / OH^* \rightarrow CO^* / COH^* \quad (11)$$

Another reaction mechanism, in which the activation of CO_2 takes place on the surface of the support rather than the metal active site, was proposed by Fan et al. [65] for catalysts with basic supports, such as MgO. In this mechanism, CO_2 is adsorbed on the catalyst support in the vicinity of the metal particles, CO_2 (g) ↔ CO_2 (support), to form carbonate species, CO_2 (support) + O^{2-} ↔ CO_3^{2-} (support). Then, the carbonate was reduced by the adsorbed hydrogen (CO_3^{2-} (support) + 2H ↔ HCO_2^- (support) + OH^-) to form CO [65,67,68]. When Mg or MgO are added as promoters, CO_2 is supposedly adsorbed onto the promoter and dissociated into CO and O (Equation 4). Then, the surface reaction occurs between the adsorbed oxygen on the promoter followed by deposition of carbon from CH_4 decomposition on the catalyst active sites to form CO(O* + C* → CO*).

Mechanism of carbon formation/removal in DRM

Catalyst deactivation is usually influenced by metal sintering and carbon deposition. Metal sintering may be caused by exothermic reactions and/or local overheating [69]. Carbon deposition is the major problem in the DRM; carbon deposition originates from reactions such as CH_4 decomposition (Equation 4), the Boudouard reaction (Equation 12), and CO reduction reaction (Equation 13).

$$2CO \rightarrow C + CO_2 \quad \Delta H_{298K} = -172.4\,\text{kJ/mol} \quad (12)$$

$$CO + H_2 \rightarrow H_2O + C \quad \Delta H_{298K} = -131.0\,\text{kJ/mol} \quad (13)$$

Several studies have attempted to discover the phenomena of carbon deposition in terms of its formation and variations in chemical structure with the applied catalysts, feed gas ratio, and other process conditions [24,68,70-76]. In the past decade, most researchers have focused on catalyst development to decrease or eliminate carbon formation and have struggled to understand the mechanism of carbon formation. Different mechanisms according to reactant activation and type of applied catalyst have been proposed for the growth of carbon on the catalyst surface. Lobo et al. [77] suggested the basic idea for the mechanism of carbon formation based on three main steps: i) carbon formation from the surface reaction occurring from the decomposition of hydrocarbons on the metal surface; (ii) dispersion of carbon atoms through the bulk of active metal; and (iii) the progression of the deposited carbon. Wang et al. [73] proposed conducting the DRM reaction over Ni metal through four main pathways, namely, CH_4 dissociation, CO_2 dissociation, C oxidation, and CH oxidation, as shown in Figure 2. Interestingly, carbon formed only through the C oxidation pathway; meanwhile, CH was transformed to CO through CHO in the CH oxidation pathway, which bypasses the formation of carbon from CH_4. Furthermore, carbon formation from methane dissociation could decrease if the rate of CH oxidation exceeded that of C oxidation. In contrast, carbon formed from the CO_2 dissociation pathway could be related to the energy barrier in CO. First, CO_2 dissociates on the catalyst into CO and O. Then, CO dissociates into C and O and forming carbon. Thus, the high energy barrier of CO could prevent the formation of carbon.

Djaidja et al. [78] highlighted that the inhibition of carbon deposition over a Ni–M/MgO catalyst is a result of increasing the adsorption of CO_2 on the support surface, enhancing the rate of surface reaction and decreasing the rate of methane decomposition. Meanwhile, Theofanidis et al. [28] stated that carbon deposition could be solved with a higher distribution of active metal on the support surface, high basicity of catalyst surface to

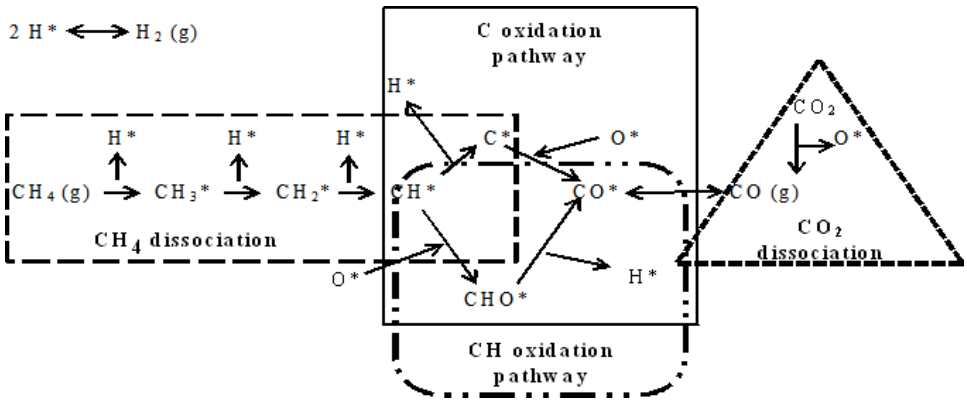

Figure 2: A schematic diagram of the DRM reaction on Ni metal. Adapted from [73].

capture acidic CO_2, and the addition of resources that offer an oxygen atom through their redox properties.

Theofanidis et al. [28] proposed a mechanism for carbon removal using Fe–Ni/$MgAl_2O_4$ in a DRM reaction. They focused on the mechanism of carbon species removal by CO_2. They proposed that the carbon removal mechanism involved two parallel processes, as clearly depicted in Figure 3a. First, CO_2 was dissociated over Ni metal followed with the surface oxygen (O_s) originating from O_2 dissociation or by direct interaction with gas phase O_2. Then, O_s combined with the carbon deposited on the Ni metal (C_m) to form CO. The second process commenced with the oxidation of Fe by CO_2 to form iron oxide (Fe_3O_4). Next, the lattice oxygen (O_L) obtained from the reduction of Fe_3O_4 was pooled with carbon deposited on the metal (C_m) to form CO. However, carbon located far from the active sites (C_s) does not directly intermingle with CO_2. Based on the results of this study, the application of $MgAl_2O_4$ as support could help the adsorption of more CO_2 on the catalyst surface because of its alkaline property and consequently increase the rate of elimination of carbon deposited on the catalyst as a result of the dehydrogenation of CH_4. Figure 3b exhibits the proposed mechanisms of carbon removal by Khavarian et al. [69], who demonstrated carbon removal by active surface oxygen produced from CO_2 dissociation over active metal particles supported by multiwalled carbon nanotubes (MWCNTs). Interestingly, the active sites of the catalyst were regenerated, and stable conversions were accomplished. In brief, development of a reliable surface reaction mechanism is a complex process. However, there are various elementary mechanisms developed for the DRM reaction, which should be measured in the absence of heat and mass transfer limitations [29].

Kinetic study in DRM

Several research studies have investigated how to inhibit or remove carbon formation at the early stages. It is believed that the development of a coke-resistant catalyst may lie in a detailed understanding of catalytic processes and kinetic studies. The reaction kinetics in the DRM depends on the type of catalysts and the involvement of reactants in the reaction. Even though the type of catalyst, the nature of the support and the reaction temperature range affect the reaction kinetics in DRM, there is still no available universal expression for the reaction kinetics in this process. Many studies have been carried out especially on developing elementary and microkinetic analyses for the understanding of reactions that occur in DRM

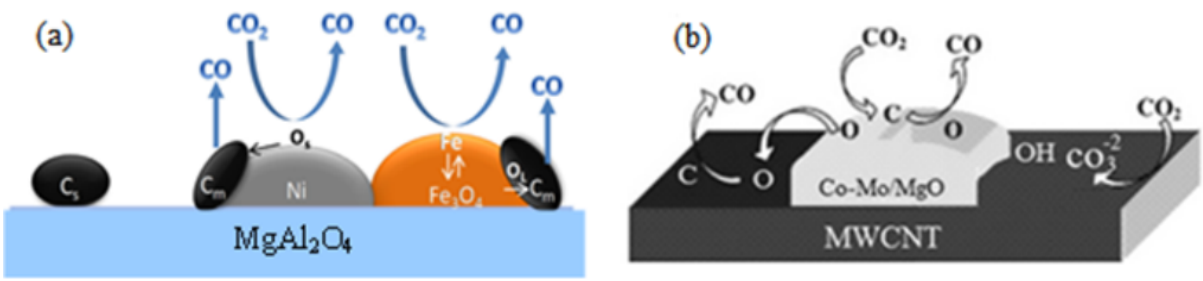

Figure 3: Schematic diagram of carbon species removal by CO_2 over (a) Fe–Ni catalyst [28] and (b) Co–Mo–MgO/MWCNT nanocomposite. [69]. (C_s: deposited carbon far from metals, O_s: surface oxygen, O_L: lattice oxygen, C_m: carbon deposited on metals). Reprinted with permissions from [28] and [69], copyright 2016 and 2014, respectively, Elsevier.

[79-82]. Microkinetic analysis is an investigation based on elementary chemical reactions on the catalytic surface and their relationship with each other and with the surface during a catalytic cycle. Commonly, the kinetic parameters involved in reactions are extracted from experimental and theoretical studies using several methods, which include adsorption, surface reaction and desorption [82].

Fan et al. [3] performed a kinetic study over Ni–Co/MgO–ZrO_2 at various partial pressures (45–360 kPa) and temperatures (700–800 °C). In this study, the effects of CH_4 and CO_2 partial pressure on the reforming rate were observed respectively. The results obtained emphasized that the partial pressure of CO_2 showed a positive effect on the reforming rate compared to CH_4, as shown clearly in Figure 4a,b. The authors declared that this is due to more CO_2 being attracted and adsorbed to the surface of the catalyst, which has a higher basicity support and strong metal-support interaction compared to CH_4.

Table 1 displays a comparison of the activation energies found in the literature using various catalysts for DRM [3]. The CO_2 activation energy in this study recorded a lower value, which is 48.1 kJ/mol compared to that of CH_4 and CO_2 of previous studies. This is might be due to the existence of Mg, which is known to be a strong Lewis base, making it easier for CO_2 to activate on the Ni–Co/MgO–ZrO_2 catalyst.

The effect of the presence of MgO in maintaining the stability of the catalyst was clearly exhibited in the X-ray photoelectron spectroscopy (XPS) results, as shown in Figure 5. Based on a study by Fan et al. [52], Figure 5 shows a high binding energy of 531.5 eV. This indicates the high intensity of the hydroxyl group by the Ni–Co/MgO–ZrO_2 catalyst, which reflects high surface basicity.

Kinetic studies of DRM over Ni–Co/Al–Mg-O have been carried out by Zhang et al. [86]. From this study, it was found that the rate of reforming is more prone to CH_4 partial pressure rather than CO_2 partial pressure, which is clearly displayed in Figure 6a,b. The authors mention that this might be due to a high amount of CH_4 being adsorbed to the catalyst surface compared to CO_2 at higher partial pressure.

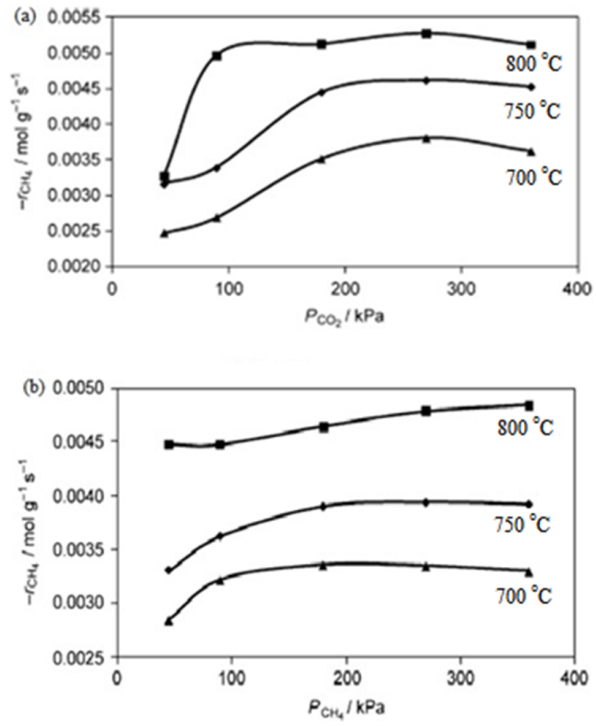

Figure 4: The partial pressure effect of (a) CO_2 and (b) CH_4 on the rate of CH_4 reforming; P_{CO2} = 90 kPa. Reprinted with permission from [3], copyright 2011 Elsevier.

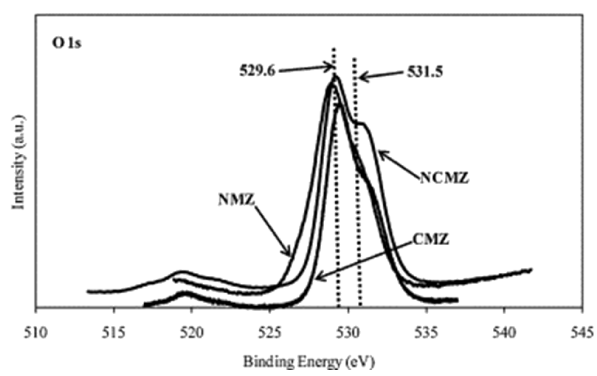

Figure 5: XPS spectra of O 1s of the catalysts. (NCMZ = Ni–Co/MgO–ZrO_2, NMZ = Ni/MgO–ZrO_2, CMZ = Co/MgO–ZrO_2). Reprinted with permission from [52], copyright 2010 Elsevier.

Table 1: Activation energies of various catalysts for DRM [3].

Catalyst	*T* (°C)	Activation energy of CH_4 (kJ/mol)	Activation energy of CO_2 (kJ/mol)	Ref.
Ni–Co/MgO–ZrO_2	700–800	52.9	48.1	[3]
Ni/Al_2O_3	500–700	50.9	56.1	[83]
Ni/MgO	450–550	92.1	87.9	[84]
Ni/CaO–Al_2O_3	620–690	106.8	98.8	[85]

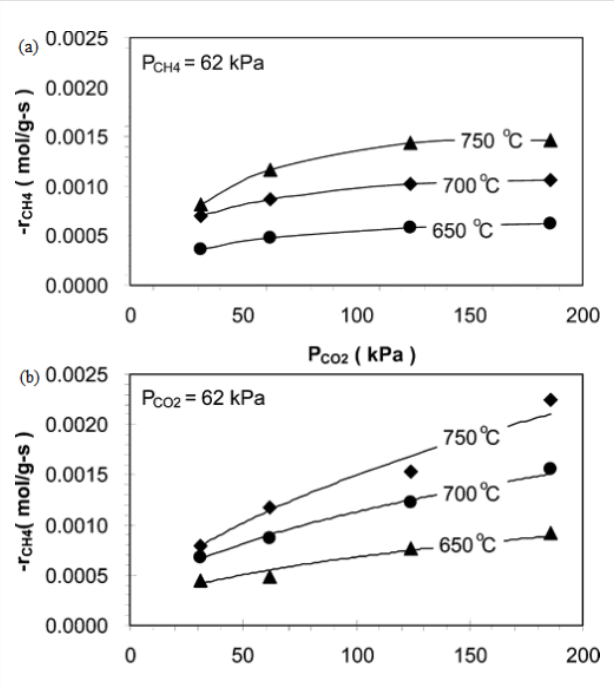

Figure 6: The reforming rates of DRM over the Ni–Co/Al–Mg-O catalyst affected by the (a) CO_2 partial pressure and (b) CH_4 partial pressure at different temperatures. Reprinted from [86], copyright 2009 American Chemical Society.

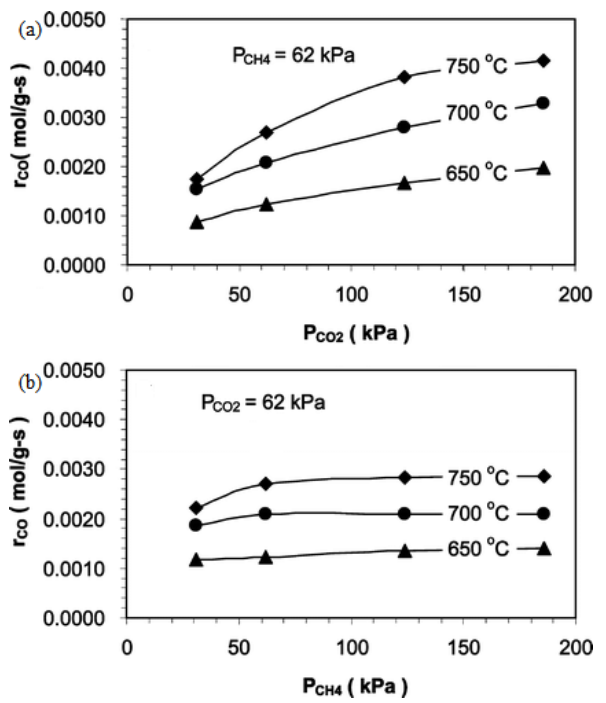

Figure 7: The formation rates of CO affected by (a) CH_4 partial pressure and (b) CO_2 partial pressure at different temperatures. Reprinted from [86], copyright 2009 American Chemical Society.

Zhang et al. [86] also studied the formation rate of products influenced by the partial pressure of the reactants. Figure 7a,b shows that the rate of CO formation is more sensitive towards CO_2 partial pressure compared to CH_4 partial pressure. This could be attributed to the reverse water–gas shift (RWGS) reaction. Moreover, the H_2 formation is relatively stable in both CO_2 partial pressure and CH_4 partial pressure due to the simultaneously occurrence of DRM and RWGS reactions. Figure 8a,b displays the effect of reactant partial pressure on H_2 formation rates.

Table 2 outlines the values of activation energy for CO_2, CH_4, H_2 and CO_2 for various catalysts. The authors highlighted that the lowest activation energies were recorded by CO_2. This is probably due to the existence of MgO, which is a strong Lewis base that acts as a support in this study, and can also activate CO_2. The activation energy of H_2 is greater than CO because of the occurrence of the RWGS reaction.

Development of Mg-containing oxide catalysts

The use of Mg or MgO, as either a promoter or a support in catalyst components, has attracted considerable interest [50-52,78]. Catalyst supports and promoters perform different roles in chemical reactions. Catalyst supports are normally applied to increase the catalyst surface area for active metal dispersion and

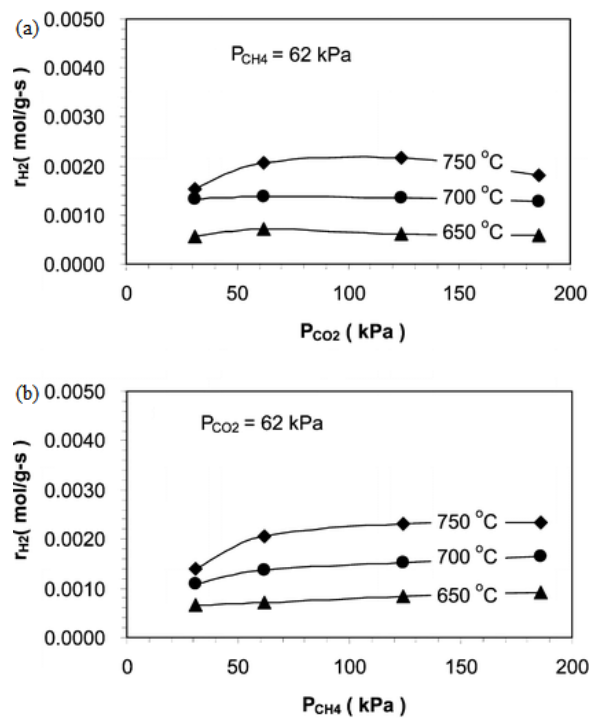

Figure 8: The formation rates of H_2 affected by (a) CH_4 partial pressure and (b) CO_2 partial pressure at different temperatures. Reprinted from [86], copyright 2009 American Chemical Society.

Table 2: Activation energies of various catalysts [86].

Catalyst	*T* (°C)	Activation energy of CH_4 (kJ/mol)	Activation energy of CO_2 (kJ/mol)	Activation energy of CO (kJ/mol)	Activation energy of H_2 (kJ/mol)	Ref.
Ni–Co/Al–Mg–O	650–750	69.4	25.9	61.8	85.1	[86]
Ni/Al_2O_3	500–700	50.9	56.1	80.5	–	[83]
$Ni/CaO–Al_2O_3$	620–690	106.8	98.8	103	147.4	[85]

to enhance the properties of the catalyst [65,87,88]. However, supports sometimes act as a transportation medium for the active sites while remaining catalytically inactive during the reaction [65]. Park and Song [89] stated that conventional supports could stabilize active metal and prevent the occurrence of leaching or metal agglomeration. The authors further mention that supports can not only transport the reactants to the reaction center, but can also control diffusion rates of reactants and products and donate protons or electrons to alter total reactivity. Promoters can be classified as small amounts of additives to active metals or support. The promoter of supports is used to prevent unwanted catalyst activity, such as carbon deposition, while promoters are added to active components to enhance reaction activity [90].

The activity and stability of catalysts prepared by various preparation methods have been observed by numerous researchers [91-94]. The catalyst preparation technique is an alternative approach to achieve carbon inhibition by controlling particle size and metal loading during catalyst preparation. The pivotal factors determining the activity and the selectivity of the catalysts are the dispersion and the physico-chemical characteristics of active metals on the support catalyst. Three general approaches are applied for the catalyst preparation, including (i) deposition of active metals onto a support; (ii) precipitation of materials with significant properties; and (iii) preparation of compact, nonporous compounds, or alloys with an active component, followed by the extraction of inactive particles, leaving a porous, high-surface-area active phase [95]. Arora [96] further highlighted that strong metal–support interactions were observed at low metal loadings (<12%), and a small particle size (<6 nm) could prevent carbon accumulation on the catalyst surface. The effects of operating conditions were investigated by adjusting the reaction temperature, feed ratio, space velocity, and temperature. The following sections investigate the influence of these variables on catalytic activity and morphology of deposited carbon. The target product compositions are also outlined.

Application of MgO as a support

Djaidja et al. [78] prepared a Ni/MgO catalyst via an impregnation method to test the performance in a DRM reaction. The conversion of CO_2 and CH_4 with MgO using 5 mol % of Ni loading were 98.1% and 97.1%, respectively, and a H_2/CO ratio of 1.1 was recorded with a low quantity of deposited carbon. Notably, a slightly higher coke deposition was recorded in the catalyst without Mg. Thus, this finding proves that coke could be minimized with an increase in MgO concentration in the catalyst because MgO exhibits alkaline characteristics. Its high basicity and similar crystal structure with NiO render MgO as highly suitable for Ni-based catalyst supports. Strong metal–support interaction between MgO and NiO formed a basic solid solution ($Ni_xMg_{(1-x)}O$) and could consequently enhance CO_2 adsorption and Ni particle size. Moreover, the reduced Ni/MgO catalysts may result in a high distribution of Ni particles and may prevent the occurrence of particle sintering during DRM reactions. Therefore, this catalyst exhibits the potential for long-term reaction and resistance to carbon formation. As highlighted, 15 wt % of Ni metal loading is required for substantial metal–support interaction and high catalytic activity in DRM [97].

Hua et al. [36] synthesized a Ni/MgO catalyst via a dielectric barrier discharge plasma and compared the catalyst with the ones prepared via the conventional impregnation method. The Ni/MgO catalyst prepared using a dielectric barrier discharge plasma presented a smaller particle size, higher dispersion, and higher specific surface area. Moreover, the recorded CO_2 and CH_4 conversions were 20% higher than that of the conventionally prepared catalyst. The plasma treatment method is suggested to be more appropriate for the preparation of Ni/MgO, offering high activity and stability, and a lesser amount of deposited carbon on the catalyst compared to using the Ni/MgO catalyst prepared via impregnation. Zanganeh et al. [34] used the co-precipitation method to prepare a NiO–MgO nanocrystalline solid solution catalyst. High Ni (25 wt %) content negatively affected the supression of carbon deposition on the solid solution catalyst. However, high Ni dispersion and the basicity of the support surface could inhibit carbon formation in DRM on the reduced $Ni_{0.03}Mg_{0.97}O$ solid solution catalyst.

DBD plasma, also known as silent discharge, is a conventional cold plasma phenomenon that has been widely applied in the preparation of multi-oxide catalysts. This method can over-

come the problem that arises from the use of thermal calcination techniques at high temperature. This plasma treatment is the most well-known technique because of its requirement for a low operation temperature with greatly energetic electrons for catalyst preparation. Thus, this method is very friendly towards heat sensitive substrates. Rapid reactions occur between the active plasma species and catalyst precursors compared to the thermal decomposition technique. Therefore, this may encourage the rapid nucleation of the crystals under plasma treatment. The application of low temperature may result in slow crystal growth, which contributes to the production of a catalyst with a small particle size or high metal dispersion. Furthermore, plasma treatment has been proven to show superb performance in surface treatment and modification. Moreover, this technique is able to efficiently decompose precursors at low temperature. Greater dispersion of oxide nanoparticles on another oxide support can be obtained via plasma treatment without any additional chemicals. [98]

According to previous studies [36,99,100], plasma-treated catalysts have a smaller particle size, enhanced metal dispersion and increased specific surface area. Moreover, Yan et al. [101] confirmed that plasma treated catalysts can improve the interaction between Ni and the SiO_2 support and produces less defect sites on the Ni particles. The authors further remarked that this plasma treatment could suppress inactive carbon deposition and enhance catalyst performance. Yan et. al [102] studied the preparation methods of the Ni catalyst, which are the DBD plasma and thermal decomposition. It is interesting to note that plasma treatment produces more Ni (111) surface with fewer defects, which is most suitable for suppressing carbon deposition. Meanwhile, the structure for Ni catalysts were treated via thermal decomposition recorded with a great number of defect sites, which consist of Ni (100) and Ni (101) surfaces. These surfaces could increase carbon deposition rate. Table 3 summarizes the development and process conditions of Mg-containing oxide catalysts used in DRM.

Application of MgO as a co-support

Abdollahifar et al. [49] investigated catalyst performance by applying the ultrasound-assisted impregnation (sonochemistry) method in the synthesis of a Ni/Al_2O_3–MgO catalyst for a DRM reaction. The measured surface area for the Ni/Al_2O_3–MgO catalyst was 53.25 m^2/g. Ni nanoparticles with a diameter of 21.4 nm were dispersed on the support. For the catalyst performance, at a reaction temperature range of 750 °C to 800 °C was used and CO_2 conversion and H_2/CO ratios almost achieved thermodynamic equilibrium. At the reaction temperature range of 500 °C to 800 °C, the recorded CO_2 is markedly higher than CH_4 conversion and the H_2/CO ratio reaches unity. The Ni/Al_2O_3–MgO catalyst was stable without deactivation for up to 53 h at a reaction temperature of 700 °C.

Table 3: Literature summary on the development and process conditions of Mg-containing oxide catalysts in DRM. PM: Preparation method; W: metal loading; CC: calcination conditions; RC: reaction conditions; SV: space velocity.

Catalyst	PM	W (wt %)	CC	RC	Conversion				
					CH_4 (%)	CO_2 (%)	H_2/CO	Carbon	Ref.
Ni–Ce/Mg–Al	carbonate co-precipitation	Ni/Mg: 2/1[a]	T = 500 °C, t = 16 h	T = 500–800 °C, CH_4/CO_2 1:1[a], SV = 30 L/h·g	90	95	1.2–1.5	–	[50]
Ni/MgO	impregnation	Ni: 5–10 wt %	T = 600–900 °C	T = 800 °C, CH_4/CO_2 1:1[a]	97.15	98.1	1.1	–	[78]
Ni/MgO	dielectric barrier discharge plasma	Ni: 10 wt %	T = 700 °C, t = 4 h	P = 1 atm, T = 700 °C, $CH_4/CO_2/NO_2$ 1:1:2[a], SV = 96 L/h·g	46	52	0.84	3.9 wt %	[36]
Pt–Ni–Mg/Ceria–zirconia	co-precipitation; incipient wetness impregnation	Pt/Ni/Mg: (0.2–2)/8/8 wt %	T = 800 °C, t = 4 h	P = 1 atm, T = 430–470 °C, CH_4/CO_2 1:1[a], SV = 68,000 h^{-1}	≈10	≈20	0.23	no coke deposited	[51]
Ni–Co/MgO–ZrO_2	surfactant-assisted impregnation; impregnation	Ni: 3, Co: 3 wt %	T = 800 °C, t = 3 h	P = 1 atm, T = 750 °C, CH_4/CO_2 1:1[a], SV = 125 L/h·g	80	84	0.97	0.89 $mg_C/g_{catalyst}$	[52]

Table 3: Literature summary on the development and process conditions of Mg-containing oxide catalysts in DRM. PM: Preparation method; W: metal loading; CC: calcination conditions; RC: reaction conditions; SV: space velocity. (continued)

Ni/ZrO_2–MgO	co-precipitation; wet impregnation	MgO: 1–5 wt %	*T* = 700 °C, *t* = 3 h, rate = 5 °C/min	*P* = 1 atm, *T* = 600 °C, CH_4/CO_2 1:1[a]	30	32	–	0.26–0.31 $mg_C/mg_{catalyst}$	[103]
Ni–Mg/Al_2O_3	reverse microemulsion	Ni/Mg: 10[a]	*T* = 800 °C, *t* = 2 h, rate = 10 °C/min	*P* = 1 atm, *T* = 400–700 °C, CH_4/CO_2/He 20:20:60[a], SV = 6,000 h^{-1}	58	69	0.67	0.5 wt %	[19]
Ni/Al_20_3–MgO	sol–gel	Ni: 10 wt %	*T* = 600 °C, *t* = 5 h	*P* = 1 atm, *T* = 550–850 °C, CH_4/CO_2 0.5–2.0[a], SV = 24–60 L/h·g	93–95	97–99	0.5–0.98	–	[37]
Ni/Al_20_3–MgO	impregnation	Ni: 10 wt %	*T* = 500 °C, *t* = 2 h	*P* = 1 atm, *T* = 550–850 °C, CH_4/CO_2 0.5–2.0[a], SV = 24–60 L/h·g	83–85	85–87	0.38–0.78	–	[37]
Ni–MgO–Al_2O_3	sol–gel	Ni: 15 wt %, MgO/(MgO+Al_2O_3) 0–1[a] optimum ratio 0.44–0.86[a]	*T* = 750 °C, *t* = 5 h	*P* = 1 atm, *T* = 800 °C, *t* = 40 h, CH_4:CO_2:N_2 1:1:1[a], SV = 36 L_{CH4}/h·g	83.6–90	88.8–92	–	13 wt %	[104]
Ni–MgO–Al_2O_3	co-precipitation	Ni: 15 wt %, MgO/(MgO+Al_2O_3) 0–1[a] optimum ratio 0.44–0.86[a]	*T* = 750 °C, *t* = 5 h	*P* = 1 atm, *T* = 800 °C, *t* = 40 h, CH_4:CO_2:N_2 1:1:1[a], SV = 36 L_{CH4}/h·g	83.6	88.8	–	–	[104]
Ni–Mg/SiO_2	impregnation	Ni: 10 wt %, Mg: 5 wt %	*T* = 800 °C, *t* = 5 h	*P* = 1 atm, *T* = 800 °C, *t* = 10 h, CH_4/CO_2 1:1[a]	74.6	78.6	1.49	6.56 wt %	[105]
Ni/MgO/γ-Al_2O_3	cold plasma	Ni: 12 wt %, MgO: 2 wt %	*T* = 550 °C, *t* = 4 h	*P* = 1 atm, *T* = 800 °C, *t* = 400 h, CH_4/CO_2 4:6[a], SV = 30 L/h·g	78–97	74	–	5 wt %	[106]
NiO/MgO	impregnation	NiO/MgO 20:100[b]	*T* = 600–800 °C, *t* = 1.5 h	*P* = 0.1 MPa, *T* = 800 °C, *t* = 5 h, CH_4/CO_2 1:1[a], SV = 20 L/h·g	85–92	90–94	–	–	[94]
Ni–Mg–Al	co-precipitation	Ni/Mg 1–5[a]	*T* = 400–800 °C, *t* = 6 h	*P* = 1 atm, *T* = 700 °C, $CH_4/CO_2/N_2$ 1:2:9[a], SV = 45 L/h·g	95–96	49–50	–	2.8–3.7 wt %	[92]
Ni/MgO	wet impregnation	Ni: 8.8 wt %	*T* = 400–950 °C, *t* = 5 h	*P* = 0.1 MPa, *T* = 750 °C, CH_4/CO_2 1:1[a], SV = 16–240 L/h·g	84	–	–	–	[23]

Table 3: Literature summary on the development and process conditions of Mg-containing oxide catalysts in DRM. PM: Preparation method; W: metal loading; CC: calcination conditions; RC: reaction conditions; SV: space velocity. (continued)

La–NiMgAl	co-precipitation	Ni: 2.1 wt % Mg/Al 1.7[a]	*T* = 250–750 °C, *t* = 2 h	*T* = 700 °C, *t* = 50 h, CH_4/CO_2 1:1[a]	25–31	32.5–55	–	0–0.06 $g_C/g_{catalyst}\cdot h$	[107]
$NiCoMg/Al_2O_3$	co-impregnation	Ni: 3, Co: 3, Mg: 3 wt %	*T* = 500 °C, *t* = 5 h	*P* = 1 atm, *T* = 850 °C, *t* = 3000 h, $CH_4/CO_2/N_2$ 1:1:1[a], SV = 80,000 h^{-1}	95.1	96.2	0.982	1.3 wt %	[54]
Ni/MgO	wetness impregnation	Ni: 5–15 wt % Optimum 15 wt %	*T* = 500 °C, *t* = 4 h	*P* = 1 atm, *T* = 500–700 °C, *t* = 5 h, CH_4/CO_2 2:1–1:2[a], SV = 6–24 L/h·g	25–86.29	27–86.77	0.64–0.91	–	[108]
Ni/MgO (111)	impregnation	Ni: 2–20 wt %	*T* = 650 °C, *t* = 5 h	*P* = 1 atm, *T* = 450–650 °C, *t* = 10 h, CH_4/CO_2 1:1[a], SV = 36 L/h·g	28–60	40–65	–	–	[109]
$Ni–CeO_2/MgO$	surfactant-assisted precipitation	Ni: 5–15 wt % optimum 10 wt %	*T* = 500 °C, *t* = 4 h	*P* = 1 atm, *T* = 550–700 °C, *t* = 20 h, CH_4/CO_2 4:1–1:2[a], SV = 6–18 L/h·g	27–95	30–97	–	–	[110]
Ni/MgO	surfactant-assisted precipitation	Ni: 5–15 wt %, Mg/Al 1:1[a] optimum 7 wt % Ni	*T* = 500 °C, *t* = 2 h	*P* = 1 atm, *T* = 550–700 °C, *t* = 5 h, CH_4/CO_2 2:1–1:3[a], SV = 6–24 L/h·g	67.5–97.2	62.4–97.4	0.58–0.97	–	[111]
NiMgAl	sol–gel	Ni: 5 wt %, Mg/Al 5:1–1:5[a]	*T* = 600 °C, *t* = 4 h	*P* = 1 atm, *T* = 550–700 °C, *t* = 5 h, CH_4/CO_2 1:1[a], SV = 12 L/h·g	55	80	1.2	–	[112]
$Ni_{0.5}Mg_{2.5}Al_{0.9}La_{0.1}O_{4.5}$	co-precipitation	La: 0.04–0.15[a]	*T* = 500 °C, *t* = 16 h	*P* = 1 atm, *T* = 600–700 °C, *t* = 13 h, CH_4/CO_2 1:1[a], SV = 7200 h^{-1}	96	90	1.1	20.8 wt %	[113]

[a]molar ratio; [b]weight ratio.

The recorded performance might be influenced by the high surface area of Al_2O_3 and the high alkaline properties and thermal stability of MgO, which is more suitable for CO_2 and CH_4 adsorption. In fact, MgO offers low surface area, which could further be improved, and yields optimum texture properties with a combination of alumina [45,114-117].

Based on the investigation of the morphology, structure, and catalytic properties of the Ni–Ce/Mg–Al catalyst in DRM by Daza et al. [50], Ce and Mg are concluded to exert a synergistic effect on CO_2 adsorption. Although the basic properties of Ce exert a significant effect on catalyst basicity, the bulk CeO_2 possesses low basic properties. Therefore, the combination of

Ce with Mg improves the catalyst basicity site. CeO_2, commonly known for its oxygen storage capacity, contains a great concentration of highly mobile oxygen vacancies which could reduce the deposition of carbon on the catalyst surface [76]. In fact, CO_2 molecules are more attracted to the base center (–Mg–OH group) and then dissociate on Ce_2O_3 via electron transfer to CO_2 through oxygen vacancies to form CO_2 and CeO_2. Thus, the base center is most suitable for adsorbing the largest amount of CO_2. The catalyst was stable for up to 50 h of reaction at 700 °C with an equal feed CO_2/CH_4 ratio. The conversion of CO_2 and CH_4 was in the range of 70 to 80% when the obtained H_2/CO ratio was between 1 and 1.5.

The influence of the synthesis method on the Ni/Al_2O_3–MgO catalyst by sol–gel and impregnation techniques was investigated by Hassani Rad et al. [37]. A higher specific surface area (178 m^2/g) was recorded with the MgO-doped catalyst obtained by the sol–gel method than that obtained using the impregnation method (70 m^2/g). As a consequence, the preparation technique significantly affected the catalytic performance of the Ni/Al_2O_3–MgO catalyst and the Ni/Al_2O_3–MgO catalyst prepared using the sol–gel method, exhibiting large yields for H_2, CO, and H_2/CO, which were 90%, 98%, and 98%, respectively, at a reaction temperature of 850 °C. Evidently, the application of the sol–gel method and MgO as a support promoter improved the surface area and Ni dispersion and resulted in highly homogeneous morphology and small particle size but affected the adsorption of reactants on the catalyst. This research study is associated with the work of Sajjadi et al. [38], who used the sol–gel method to prepare a Ni–Co/Al_2O_3–MgO–ZrO_2 catalyst. The findings showed that application of the sol–gel method with the addition of MgO as a support promoter produced considerable homogeneity of metal composition, small particle size, and enhanced the particle distribution and surface area.

In the study conducted by Min et al. [104], a comparative study was conducted between the sol–gel and co-precipitation methods for the preparation of a Ni–MgO–Al_2O_3 catalyst. The Ni particle size was uniformly distributed in the catalysts prepared via sol–gel. TGA results clearly showed that 13% and 7.7% carbon was deposited on the catalysts prepared via the sol–gel method and the co-precipitation method, respectively. Therefore, they concluded that the sol–gel method is preferable for Ni–MgO–Al_2O_3 catalyst preparation and possibly for inhibiting the formation of carbon. Xu et al. [106] prepared a Ni/MgO/γ-Al_2O_3 catalyst via the cold plasma technique and discovered an enhanced distribution of Ni particles. Moreover, the addition of MgO in this catalyst prevented the agglomeration of Ni particles and increased the basicity of the catalyst; consequently, more CO_2 was adsorbed on the catalyst surface. The adsorption and activation of CO_2 decreased the carbon deposition. Notably, the catalyst performance showed high stability for up to 400 h of reaction. Fan et al. [52] carried out DRM over a Ni–Co/MgO–ZrO_2 catalyst synthesized by applying impregnation and surfactant-assisted impregnation methods. Reportedly, MgO stabilized *t*-ZrO_2 and influenced the particle size. Furthermore, the addition of MgO to the ZrO_2 support suppressed carbon deposition, which occurred between the crystallites of *t*-ZrO_2 and prohibited a shift of the zirconia support from the tetragonal phase to the monoclinic phase. This catalyst tends to survive with low carbon formation (0.89 $mg/g_{catalyst}/h$ for 40 h with CO_2 and CH_4 conversion of 80% and 84%, respectively). García et al. [103] studied the effects of MgO on the basicity and performance of the Ni/ZrO_2 catalyst in DRM. The catalyst was synthesized using two methods, wet impregnation and co-precipitation. A high carbonaceous residue (0.8 mg C/mg catalyst) was discovered on the catalyst surface with the absence of Mg in comparison to the amount of carbon deposition of 0.26 mg C/mg catalyst on the catalyst with an additional of 2.3% and 0.4% MgO. The conversion for CO_2 and CH_4 was 30% and 32%, respectively. The presence of MgO in the catalyst resulted in increased thermal stability in stabilizing the zirconia tetragonal phase, improved basicity sites for the support, and decreased reducibility of Ni^{2+}.

Li et al. [118] designed a Ni@Ni–Mg phyllosilicate core–shell catalyst using the hydrothermal treatment of Ni@SiO_2 with $Mg(NO_3)_2$. The alkalinity and porosity of the catalyst can be controlled during various hydrothermal treatment durations applied (such as 2.5, 10, and 24 h). Interestingly, the optimum hydrothermal treatment time for this catalyst was 10 h, resulting in good catalytic performance of 80% and 78% CO_2 and CH_4 conversion, respectively. Moreover, the increase in hydrothermal treatment time enhanced the basicity of the catalyst from the high exposure to the Mg phase. The strong basicity properties of Mg enhanced CO_2 adsorption and suppressed carbon deposition via the reverse Boudouard reaction ($C + CO_2 \leftrightarrow 2CO$). However, the core–shell structure became unstable when the catalyst was exposed to an excessively long treatment time.

Wang et al. [119] prepared and analyzed a MgO-SBA-15 catalyst via two different methods, which are the one-pot synthesis method and impregnation method as shown in Figure 9a. As a result, the catalyst prepared using the one-pot synthesis showed a better order of MgO-coated sample in the mesostructure of SBA-15, a larger BET surface area, and formed more basic sites compared to the conventional impregnation method. The authors further impregnated the basic sites with nickel metal and tested it in DRM. The MgO-coated Ni/SBA-15 catalysts showed greater catalyst performance and stability compared to the Ni/SBA-15 sample. Figure 9b depicts the total petroleum

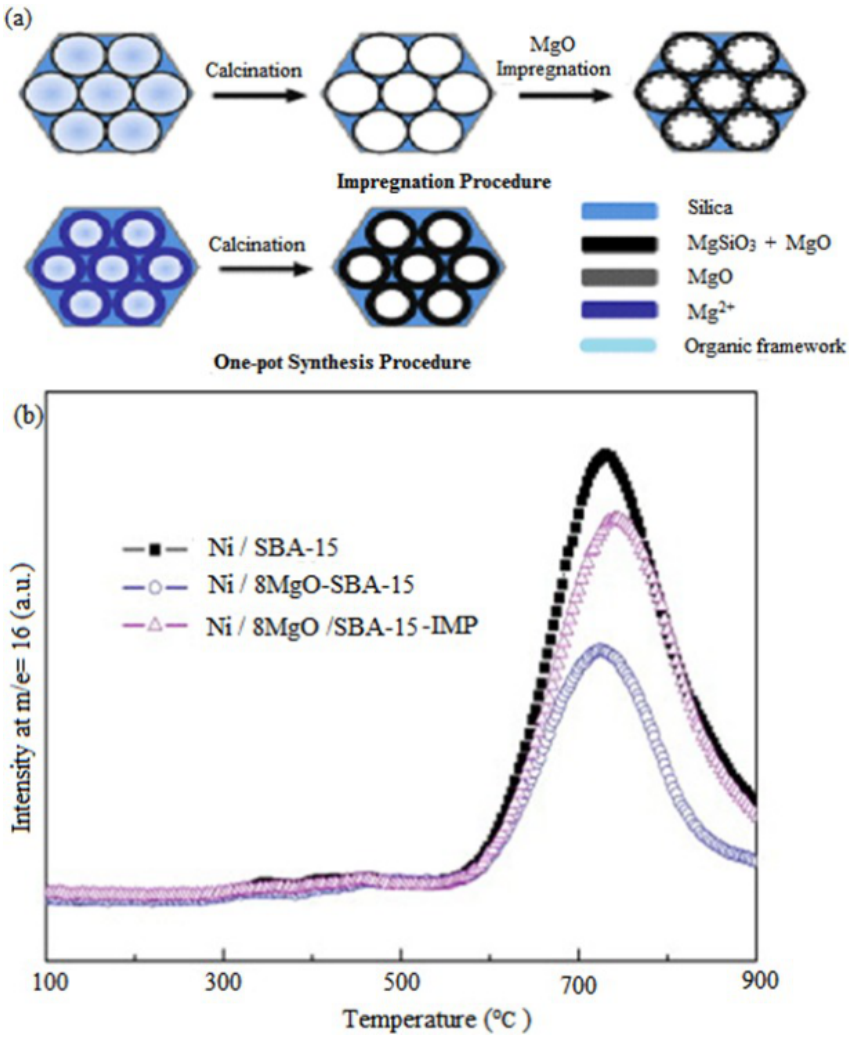

Figure 9: (a) Schematic illustration of the two synthesis methods for the MgO basic sites formation on SBA-15, (b) TPH profiles of spent catalysts after 40 h stability test. Reprinted with permission from [119], copyright 2013 Elsevier.

hydrocarbons (TPH) profiles of spent catalyst after 40 h of stability. It is interesting to note that 8 wt % of MgO loading exhibited excellent catalytic activity. The SBA-15 supported catalyst showed that the confinement of pore walls inhibited the Ni particle aggregation. Meanwhile, the MgO coating showed a higher dispersion of Ni metal and highly basic sites than the MgO impregnated method. It was also found that this structure improved stability and could inhibit the formation of filamentous and encapsulating carbon. Deactivation of the catalyst occurs over the Ni/SBA-15 sample since a large amount of graphitic carbon species were formed.

Application of Mg as a promoter of active metal

Elsayed et al. [51] demonstrated DRM over Pt–Ni–Mg/ceria–zirconia synthesized via precipitation and the incipient wetness method. The largest amount of basic sites were found in the Ni–Mg/$(Ce_{0.6}Zr_{0.4})O_2$ catalyst, but the basicity site characteristics decreased with the addition of Pt to the catalyst. Consequently, the lowest CO_2 and CH_4 conversions were obtained and no carbon was deposited on the catalyst surface. Moreover, the catalyst was of a good composition, given that the DRM process could be performed within the low temperature range of 430 °C to 470 °C. The catalyst was stable for up to 100.5 h without carbon deposition.

García-Diéguez et al. [19] developed a Ni–Mg active metal material supported on alumina via the reverse microemulsion method and impregnation method in a comparative study. Mg was proven to stabilize Ni on the catalyst surface by preventing the diffusion of Ni particles into the alumina lattice, indirectly suppressing carbon deposition. Table 4 shows the average particle size of Ni and carbon content in the catalysts after the reac-

Table 4: The average particle diameter, D_p, of Ni^0 and the carbon content in the catalysts after reaction [19]. ME = microemulsion method; IM = impregnation method. DRM = dry reforming of methane; DRP = dry reforming of propane.

Catalyst	DRM		DRP	
	D_p Ni^0 (nm)[a]	C content (wt %)[b]	D_p Ni^0 (nm)[a]	C content (wt %)[b]
$NiMg/Al_2O_3$ IM	20	13	25	26
$NiMg/Al_2O_3$ ME	16	0.5	16	5

[a]Calculated by the Scherrer equation; [b]Obtained by elemental analysis.

tion. The $NiMg/Al_2O_3$ catalyst synthesized using the microemulsion method recorded a lower particle size (16 nm) and carbon content (0.5 wt %) compared with that of the $NiMg/Al_2O_3$ catalyst prepared via the impregnation method (20 nm for and 13 wt %, respectively). Based on the reactivity in DRM, both $NiMg/Al_2O_3$ catalysts prepared via different methods showed similar CO_2 conversion of 27% at a reaction temperature of 600 °C, whereas the $NiMg/Al_2O_3$ catalyst prepared via the impregnation method showed a slightly higher CO_2 conversion of 71% at a reaction temperature of 700 °C. The $NiMg/Al_2O_3$ catalyst synthesized via reverse microemulsion showed a CH_4 conversion of 58%, which was higher than that of the catalyst prepared via other methods. The obtained ratios of H_2/CO for the catalysts prepared using both methods were not markedly different, at 0.66–0.67. In terms of the preparation method, the reverse microemulsion method was preferable for the DRM process, owing to the good activity and stability of the catalyst, which minimized carbon deposition and caused considerable interaction between Ni and Mg.

Macedo Neto et al. [120] studied the synthesis of Ce in Ni–Mg–Al layered double hydroxides by co-precipitation using ultrasonication. Sonication significantly increased not only the specific surface area but also the incorporation of Ce in the structure. In fact, the ultrasonication method guarantees a uniform distribution of nanoparticles on the catalyst support without aggregation. Zhu et al. [105] introduced Mg as a promoter to the Ni/SiO_2 catalyst synthesized via the impregnation method. The $Ni–Mg/SiO_2$ catalyst was deactivated after a 30 h of reaction time due to the deposition of inert carbon, which is difficult to oxidize. However, the addition of Mg caused the reduction of the RWGS reaction; thus, a high H_2 production was obtained.

Yan et al. [121] investigated the effects of the addition of MgO on the Ni catalyst in the DRM. In their investigation, a good dispersion of nickel oxide and MgO promoter was reported over a γ-Al_2O_3 support. In addition, the MgO promoter remarkably retarded the formation of the $NiAl_2O_4$ phase during the reaction. The addition of MgO to the catalyst in the presence of CeO_2 inhibited self-dispersion and promoted Ni dispersion on the catalysts. Alipour et al. [68] reported that the addition of MgO to the Ni catalysts supported on nanocrystalline Al_2O_3 decreased the surface area of the catalysts. MgO has the most beneficial effect for catalytic activity and suppressed the carbon formation in comparison with other alkaline earth promoters such as CaO and BaO investigated in this work. In fact, adding MgO to the catalyst decreased the reduction temperature of the NiO species and increased the catalyst reducibility.

Influence of metal loading

Khajenoori et al. [110] conducted the DRM reaction over a $Ni–CeO_2/MgO$ catalyst with various Ni loadings (5–15 wt %) at a temperature of 550 °C to 700 °C. Thus, the CO_2 and CH_4 conversions showed significant increments when the Ni loading increased up to 10 wt %. However, the catalyst performance decreased with Ni loading greater than wt % because of the formation of large Ni crystals and, consequently, low dispersion. Moreover, the 10% Ni–7% CeO_2/MgO catalyst was highly stable for 20 h of reaction without a decrease in CH_4 conversion for the CO_2 reforming reaction.

Meshkani et al. [111] studied the effect of Ni loading on the catalytic activity of a Ni/MgO catalyst in the DRM reaction. The CO_2 and CH_4 conversion, H_2/CO ratio, and H_2 and CO yields showed a progressive increase as the Ni loading increased from 5 wt % to 7 wt %. In contrast, the conversion yields decreased with higher Ni loading of 10 and 15 wt %. The conversion yields decreased because of low Ni dispersion. Meanwhile, the H_2/CO ratio was reduced due to the occurrence of RWGS. In terms of stability, carbon deposition was observed at the Ni/MgO catalyst with 15 wt % Ni loading. However, this deposition could not deactivate the catalyst, and high stability was recorded up to a reaction time of 300 min. Furthermore, the reduced NiO–MgO solid solution catalysts could inhibit carbon deposition owing to the strong synergistic effect between high Ni dispersion and basicity of the MgO support. In contrast, Meshkani et al. [108] reported that low Ni loading results in low conversion of CO_2 and CH_4 over the Ni/MgO catalyst as shown in Figure 10. This finding is due to fewer NiO species being

reduced to metallic species, thus minimizing the amount of active sites for the reaction. Stable conversion of CO_2 and CH_4 at 70% and 55%, respectively, were observed for the Ni/MgO catalyst with 5 wt % of Ni loading for long-term reactions up to 50 h.

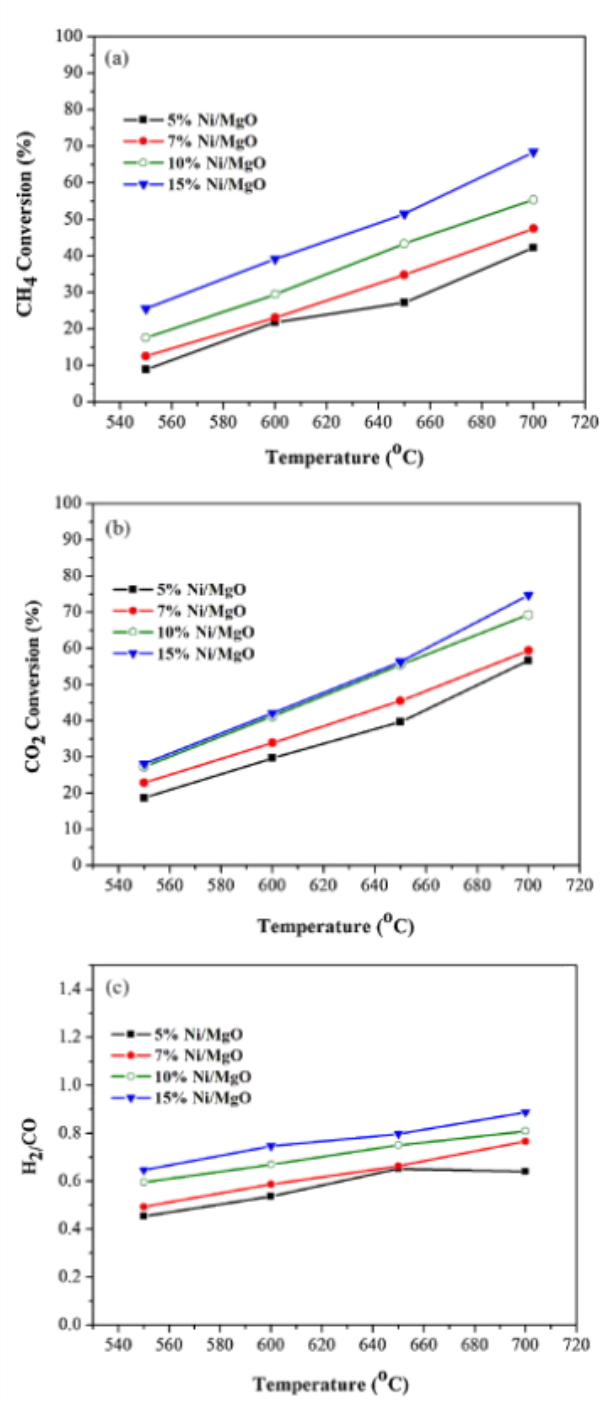

Figure 10: (a) CH_4 conversion, (b) CO_2 conversion, (c) H_2/CO ratio of catalysts with different nickel loadings in the DRM reaction, CH_4/CO_2 1:1 and gas hourly space velocity (GHSV) of 1.8 × 10^4 mL/h·$g_{cat.}$ Reprinted with permission from [108], copyright 2014 Elsevier.

The high stability is due to the high basicity of the support and the formation of solid solution, thus inhibiting carbon deposition. Figure 11 shows the stability of the DRM reaction on the Ni/MgO catalysts with various nickel loadings at 700 °C.

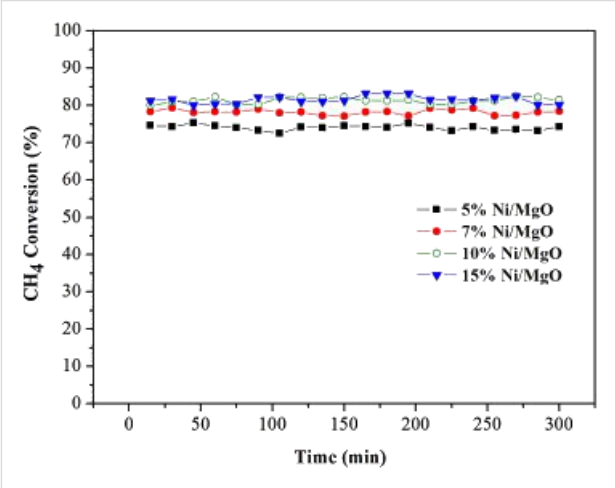

Figure 11: Stability of CH_4 conversion over Ni/MgO catalysts with different Ni loadings (5% to 15%) in a DRM reaction at 700 °C, CH_4/CO_2 1:1, and gas hourly space velocity (GHSV) of 1.8 × 104 mL/h·g_{cat}. Reprinted with permission from [108], copyright 2014 Elsevier.

Lin et al. [109] inspected the effect of Ni loading (2–20 wt %) on the Ni/MgO (111) catalyst prepared via the impregnation method. According to the morphology results, the 6 wt % Ni/MgO (111) catalyst showed a high Ni dispersion of 21.3% and a small particle size of 4.7 nm. The catalytic performance of the Ni/MgO(111) catalyst increased as the Ni loading increased from 2% to 10%; however, adverse effects were observed for the applied catalyst with 20% Ni loading. This finding may be explained by the decrease in metal dispersion and formation of large particles when the highest Ni loading was employed. Moreover, the 2 wt % Ni/MgO (111) catalyst produced a small particle size catalyst and was more easily oxidized during the reaction, possibly causing catalyst sintering. Meanwhile, Ni loading exceeding 6% may result in a larger particle size and poor oxidizability, thereby yielding high stability and consequent carbon deposition.

Sajjadi et al. [38] investigated the influence of MgO loading to feed conversion, product yield, H_2/CO ratio, and stability over a Ni–Co/Al_2O_3–MgO–ZrO_2 catalyst. The findings showed that the feed conversion increased as the metal loading of MgO increased. Notably, a 25 wt % of MgO loading showed the highest conversion of CO_2 and CH_4 with all applied reaction temperatures ranging from 550 °C to 850 °C as exhibited in Figure 12. This finding indicates a small particle size distribution, good morphology, and high surface area of the catalyst, as well as high diffusion of active metal without agglomeration

during the reaction. Moreover, the average particle size was 11.6 nm, which was small enough to suppress carbon formation. Meanwhile, the product yield appeared to be markedly affected by the increment in MgO loading. The optimum yield of H_2 and CO of 96.9 and 97.1, respectively, were recorded over the Ni–Co/Al_2O_3–MgO–ZrO_2 catalyst containing 25 wt % MgO loading at a reaction temperature of 850 °C. This excellent performance is due to the properties of MgO, which provides a highly alkaline surface for CO_2 adsorption. The stable yield with a H_2/CO ratio close to unity was observed with the Ni–Co/Al_2O_3–MgO–ZrO_2 catalyst with 25 wt % MgO loading. The catalyst was highly stable in the 24 h reaction time without deposition of carbon. MgO promotion enhanced the metal distribution when exposed to the highly basic surface and decreased the particle size.

Min et al. [104] studied the effect of Mg/Al ratio on catalytic activity and stability over a Ni–MgO–Al_2O_3 catalyst and found that the conversion of CO_2 and CH_4 showed improved results when MgO was introduced. The best catalytic performance was detected for a catalyst with a ratio of MgO/(MgO+Al_2O_3) of approximately 0.44 to 0.86. This outcome is due to the capability of MgO in enhancing the interaction between metal and support. Moreover, the compound improved the alkalinity of the catalyst surface, leading to increased adsorption of CO_2. They proposed that the adsorbed CO_2 reacted with deposited carbon to stimulate the catalyst. In a different study by Zhu et al. [112], different Mg/Al molar ratios of 5:1, 3:1, 1:1, 1:3, and 1:5 were applied for the preparation of a $NiMg_xAl_y$ catalyst. The optimum Mg/Al molar ratio of 1:1 yielded the highest CO_2 and CH_4 conversions of 90% and 83%, respectively. These results are due to the formation of the hydrotalcite precursor for the NiMgAl catalyst. Moreover, MgO played an important role for improved catalyst performance; thus, a high Mg/Al molar ratio corresponded to the highest conversion in the order of $NiMg_5Al_1$ > $NiMg_3Al_1$ > $NiMg_1Al_3$ > $NiMg_1Al_5$. Furthermore, low carbon formation of 3.3 mg/g_{cat}·h was observed with the $NiMg_5Al_1$ catalyst. Overall, the formation of hydrotalcite and a high ratio of Mg could improve the performance of Ni metal and enhance the catalytic activity and stability.

Alipour et al. [122] successfully investigated the effect of alkaline earth metals, such as MgO, CaO, and BaO, as support modifiers for a Ni/Al_2O_3 catalyst. The addition of basic support modifiers resulted in the reduction of the surface area of the Ni/Al_2O_3 catalyst. However, these modifiers could enhance the catalyst performance and inhibit carbon deposition. Interestingly, MgO showed an excellent effect on catalytic activity and carbon deposition. Furthermore, they analyzed the effect of different MgO loadings (1.5%–6%) on the Ni/Al_2O_3 catalyst. A moderate amount of MgO, that is, 3 wt %, was suitable for the

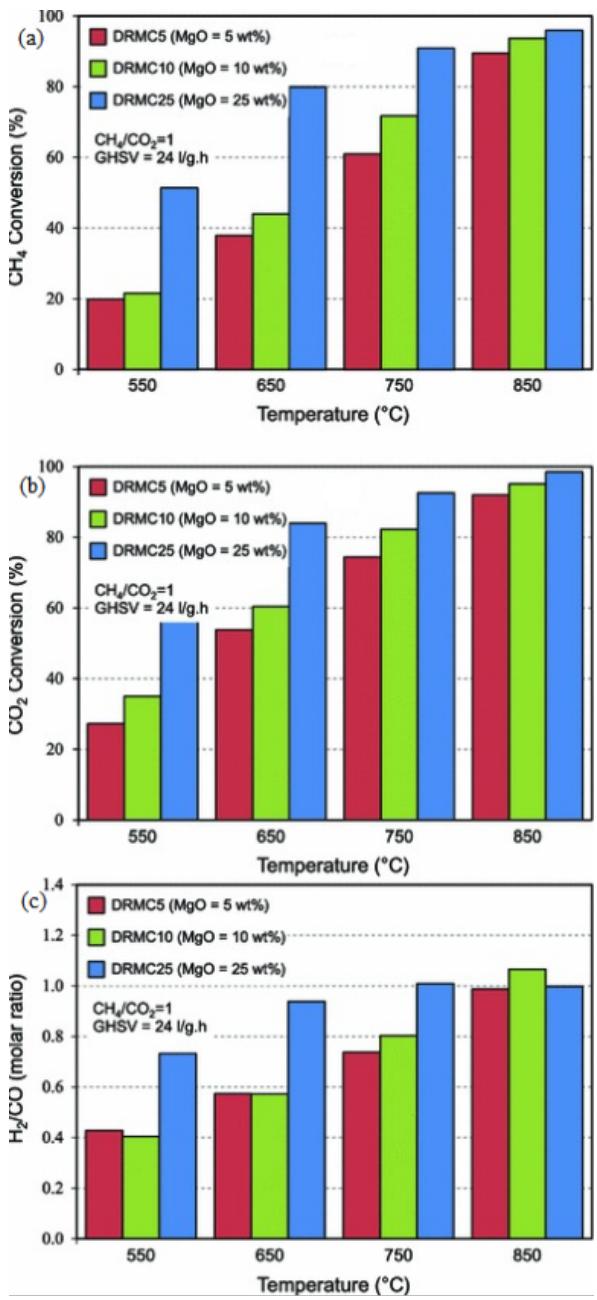

Figure 12: Effect of MgO loading on (a) CH_4, (b) CO_2 conversion and (c) H_2/CO molar ratio over various MgO loadings (5, 10, 25 wt %). Reprinted from [38], copyright 2014, Springer Nature.

Ni/Al_2O_3 catalyst because of stable catalytic activity and H_2/CO ratio. Yu et al. [113] studied the effect of La as a promoter to a NiMgAl catalyst and found that the addition of La enhanced the basic surface of the catalyst and improved Ni metal distribution. Moreover, the catalytic activity increased, and the stability of the NiMgAl catalyst considerably improved. The combination of La and Mg suppressed carbon formation. The investigation using a La molar ratio ranging from

0.04 to 0.15 yielded the highest catalytic activity over the $Ni_{0.5}Mg_{2.5}Al_{0.9}La_{0.1}O_{4.5}$ catalyst.

Effect of catalyst pretreatment

Pretreatment, such as calcination, is mainly conducted to eliminate and volatilize various catalyst precursors that are used during catalyst preparation, including hydroxides, nitrates, or carbonates, which are unnecessary for the final catalyst. High temperature treatment is typically conducted for this elimination. Notably, overheating of the solid catalyst results in high pressure because of trapped H_2O molecules in the micropores, which may crack particulate carriers [95]. Feng et al. [94] investigated the influence of calcination temperature (between 600 °C to 800 °C) on the adsorption and dissociation of CO_2 by applying DRM over the NiO/MgO catalyst. High performance and strong interactions between metal and support were observed with the calcination of the NiO/MgO catalyst at 800 °C. In addition, the catalyst calcined at 800 °C exhibited more active sites, which are strong enough to absorb CO_2 on the metal surface. Moreover, CO_2 was not directly adsorbed on the Ni metal, and dissociated H from CH_4 cracking assisted the dissociation of CO_2 into CO. This result was in an agreement with Wang et al. [23]. Wang et al. [23] stated that the activity and stability of the NiO/MgO catalyst was strongly dependent on calcination temperature. The calcination temperature influenced the metal/support interaction, which performs an important role in hindering sintering and carbon deposition. Moreover, the strong Lewis base property of MgO enabled the adsorption of more CO_2 on the catalyst, consequently enhancing the conversion of reactants and minimizing the carbon deposition via a reverse Boudouard reaction (Equation 12).

In contrast, Perez-Lopez et al. [92] studied the effect of calcination temperature (400 °C, 600 °C, and 800 °C) in a DRM reaction over a Ni–Mg–Al catalyst. They stated that the increase in calcination temperature from 400 °C to 800 °C yielded a decrease in surface area values from 250 m^2/g to 150 m^2/g, respectively. Figure 13a,b shows the conversion of CO_2 and CH_4 of the NiMg (loading of Ni 55 mol %; Mg 11 mol %) catalyst influenced by calcination temperature. As evidently seen from the results, the catalyst activity was independent of calcination temperature. However, significant differences in catalyst activity were observed, possibly as a result of the surface area of the catalyst. Moreover, this catalyst displayed high suppression of coke formation because of the synergetic effect of Ni and Mg, as proven by the highest concentration of basic sites obtained from the sample with lower Mg compared with Ni contents. However, they proposed a Ni/Mg ratio of lower than 5 for the best result. These results further highlighted higher carbon deposition for the catalyst calcined at 400 °C compared with those at other temperatures.

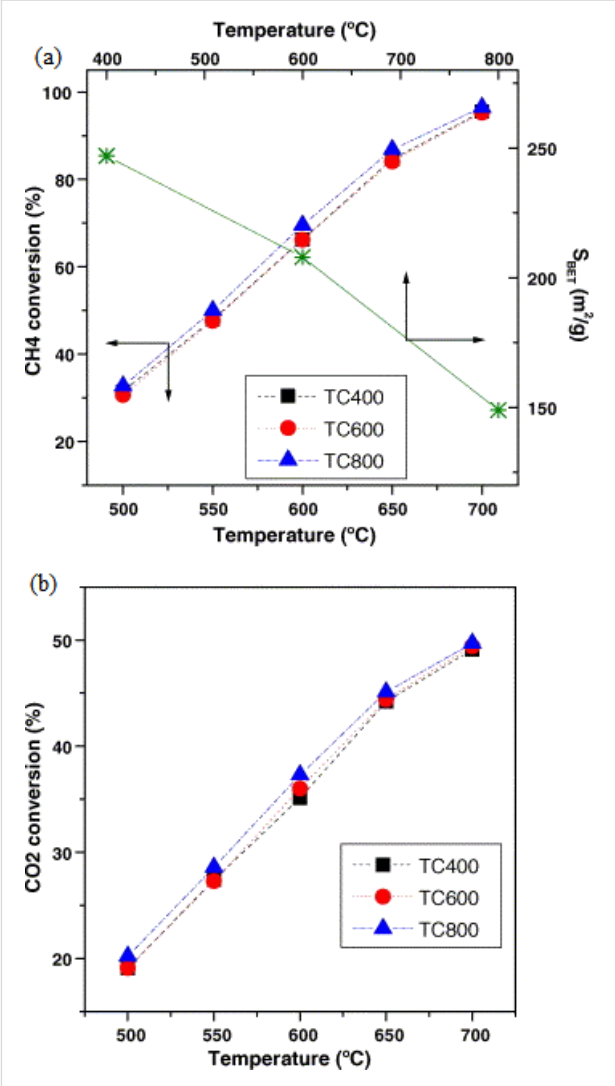

Figure 13: Conversion of methane (a) and carbon dioxide (b) on N55M11 calcined at different temperatures (■) 400 °C, (●) 600 °C and (▲) 800 °C and reduced at 700 °C. S_{BET} as a function of the calcination temperature. Reprinted with permission from [92], copyright 2006 Elsevier.

Serrano-Lotina et al. [107] investigated the influence of calcination temperature of a La–NiMgAl catalyst for biogas reforming. The catalyst was calcined at different temperatures between 250 °C and 750 °C. As a result, the grain size and cell parameter values increased with calcination temperature. The calcination temperature is extremely crucial, possibly affecting the activity and stability of the catalyst, as evidently proven by the significant decrease in activity at higher calcination temperature. An increased interaction inside the Mg(Ni,Al)O solid solution leads to agglomeration, which is inefficient for the catalytic reaction. The optimized calcination temperature was 550 °C for the La–NiMgAl catalyst to yield large catalytic activity. However, the La–NiMgAl catalyst calcined at 750 °C was reportedly the most preferable for coke suppression. To en-

hance catalytic performance, Son et al. [54] performed steam pretreatment over a $NiCoMg/Al_2O_3$ catalyst. During the treatment, $MgAl_2O_4$ was formed on the catalyst when the unstable aluminum leached out and moved to MgO. Aluminum leaching stimulated the acidic sites, leading to carbon deposition. Thus, the formation of $MgAl_2O_4$ on the catalyst enhanced the CO_2 adsorption or desorption and consequently suppressed carbon deposition. From this study, long-term stability was achieved for 3000 h at a reaction temperature of 850 °C with high selectivity of H_2 (93.8%) and CO (95.5%) and low carbon deposition (1.3 wt %) at a rate of 0.0003 ($mg_c/g_{cat}\cdot h$).

Influence of reaction conditions

Meshkani et al. [108] carried out a DRM reaction at various temperatures from 500 °C to 700 °C for various Ni loadings on a Ni/MgO catalyst. The catalytic activity and H_2/CO ratio were significantly affected by Ni loading ranging between 5–15 wt % as the reaction temperature increased. Excellent catalyst performance was recorded for the Ni/MgO catalyst with 15 wt % Ni loading. Lin et al. [109] investigated the influence of the reaction temperature of 450 °C to 650 °C for various Ni loadings as displayed in Figure 14. The study found that the CO_2 and CH_4 conversions gradually increased with a reaction temperature of up to 650 °C. The highest conversion of CO_2 and CH_4 of 65% and 60%, respectively, was recorded at a reaction temperature of 650 °C.

Meshkani et al. [111] investigated the effect of CO_2/CH_4 feed ratios of 3:1, 2:1, 1:1, and 1:2 on the catalytic activity and H_2/CO ratio over a 5 wt % Ni/MgO catalyst at a reaction temperature of 700 °C. Table 5 shows the effect of feed ratio on the catalytic performance over a 5% Ni/MgO catalyst in the DRM. It could be concluded that the conversion of CH_4 increased considerably as the feed ratio increased. However, the CO_2 conversion and H_2/CO ratio showed adverse effects.

Meshkani et al. [108] further studied the effect of CO_2/CH_4 feed ratios of 1:2, 1:1, 1.5:1, and 2:1 on a 10 wt % Ni/MgO catalyst as shown in Table 6. The same pattern as in their previous study in [111] was observed. The highest CH_4 conversion of 86.29% was obtained at a CO_2/CH_4 feed ratio of 2:1. Meanwhile, the highest CO_2 conversion and H_2/CO ratio of 81.95% and 0.91, respectively, were obtained at CO_2/CH_4 feed ratio at 1:2. Mirzaei et al. [123] found that CH_4 conversion increased as the CO_2/CH_4 feed ratio increased from 0.5 to 2 over a 10 wt % CoMgO catalyst. However, the CO_2 conversion and H_2/CO ratio decreased with increasing CO_2/CH_4 feed ratio.

The catalytic performance of a $Ni/MgO–Al_2O_3$ catalyst was examined for the application of various gas hourly space velocity measurements between 6 and 18 $L/h\cdot g_{cat}$ by keeping the

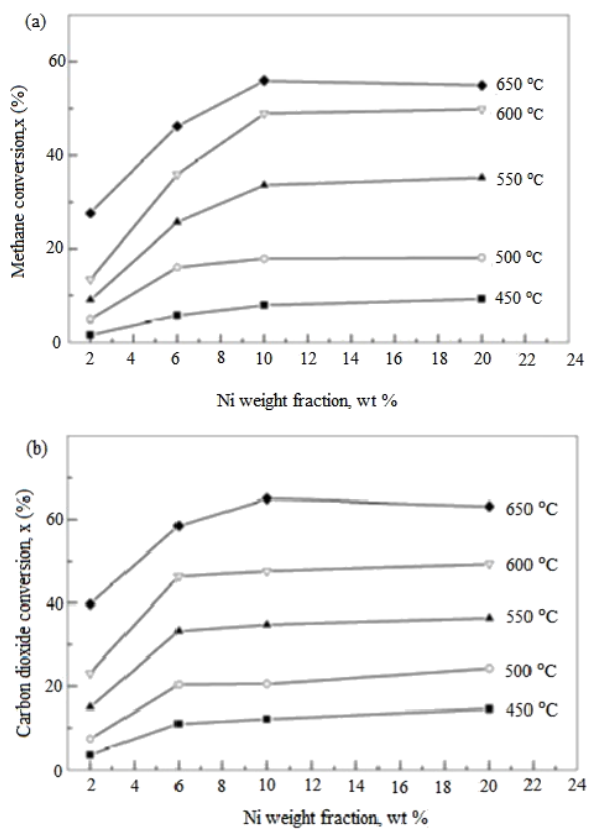

Figure 14: The effect of reaction temperature on catalyst performance: (a) CH_4 conversion, (b) CO_2 conversion, at feed ratio CH_4/CO_2 1:1, gas hourly space velocity (GHSV) of 36000 mL/h·g, $P = 1.01 \times 10^5$ Pa. Reprinted with permission from [109], copyright 2015 Elsevier.

Table 5: Influence of feed ratio on the catalytic performance of 5 wt % Ni/MgO catalysts in DRM reaction at 700 °C and gas hourly space velocity (GHSV) of 1.0×10^4 $mL/h\cdot g_{cat}$ [111].

Feed ratio CO_2/CH_4	CH_4 conversion (%)	CO_2 conversion (%)	H_2/CO
3:1	97.2	62.4	0.58
2:1	89.3	69.3	0.65
1:1	81.6	83.8	0.80
1:2	67.5	89.5	0.97

Table 6: Influence of feed ratio on the activity of a 10 wt % Ni/MgO catalyst in the DRM reaction at 700 °C and gas hourly space velocity (GHSV) of 1.8×10^4 $mL/h\cdot g_{cat}$ [108].

Feed ratio CO_2/CH_4	CH_4 conversion (%)	CO_2 conversion (%)	H_2/CO
1:2	60.42	81.95	0.91
1:1	69.07	77.35	0.80
1.5:1	78.40	66.13	0.77
2:1	86.29	59.56	0.64

reaction temperature and feed ratio in the system constant (T = 650 °C, CH_4/CO_2 1:1) [70]. The CO_2 and CH_4 conversion decreased as the space velocity increased, as exhibited in Figure 15. This is due to the insufficient contact time for the reactant on the surface of catalyst, which leads to a decrease in catalytic activity.

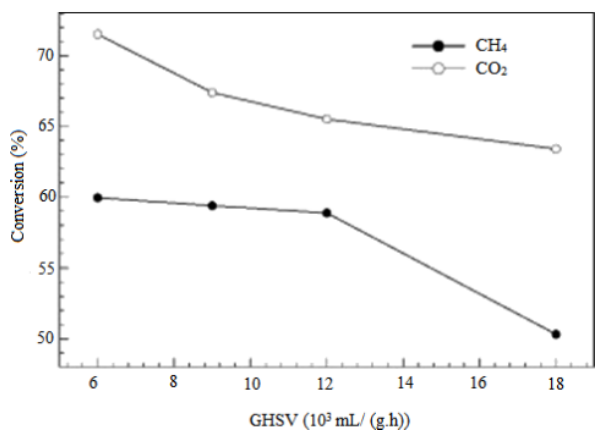

Figure 15: Influence of gas hourly space velocity (GHSV) on the catalyst performance of 20 wt % Ni/3 wt % MgO–Al_2O_3 catalyst at a feed ratio CH_4/CO_2 1:1, T = 650 °C. Reprinted with permission from [70], copyright 2014 Elsevier.

Meshkani et al. [108] also reported the reduction of CO_2 and CH_4 conversion yields as the space velocity increased from 6 L/h·g_{cat} to 24 L/h·g_{cat} over a 10 wt % Ni/MgO catalyst. Table 7 displays the effect of gas hourly space velocity (GHSV) on the activity of a 10 wt % Ni/MgO catalyst in a DRM reaction at 700 °C and molar ratio of CH_4/CO_2 1:1. The pattern of the CH_4 conversion versus space velocity appeared similar to that of the study by Mirzaei et al. [123] over Co–MgO. Khajenoori et al. [110] investigated the space velocity of 6–18 L/h·g_{cat} on 10 wt % Ni–7 wt % CeO_2/MgO catalyst at a reaction temperature of 700 °C and a feed ratio of CH_4/CO_2 2:1. Conversions of CO_2 and CH_4 showed a negative effect with increasing gas hourly space velocity. This phenomenon was in agreement with the findings obtained by Meshkani et al. [108].

Table 7: Effect of gas hourly space velocity (GHSV) on the activity of a 10 wt % Ni/MgO catalyst in DRM reaction at 700 °C and molar ratio of CH_4/CO_2 1:1 [108].

GHSV 10^4 (mL/h·g_{cat})	CH_4 conversion (%)	CO_2 conversion (%)
0.6	83.75	86.77
0.9	80.16	84.33
1.2	75.60	80.36
1.5	66.14	70.75
1.8	63.36	68.99
2.4	58.88	64.61

Conclusion

This review reported on the mechanism reaction for the DRM, mechanism of carbon formation and removal, development of Mg-containing oxide catalysts, and the effect of reaction conditions on catalytic performance. This work can be used as a reference for future works on the improvement of catalytic activity, selectivity, and stability. Through the mechanism, researchers can understand the reactions occurring in DRM, carbon deposition, and catalyst regeneration. This understanding can assist researchers in designing new multifunctional catalysts for DRM.

Two main issues requiring increased attention in catalyst development include pretreatment and the preparation method of the catalyst. First, in the catalyst preparation method for Mg as a promoter, the sol–gel method is more preferable, whereas cold plasma is highly suitable for synthesizing Mg as a support catalyst. Secondly, this review focused on the calcination temperature for catalyst pretreatment. Most researchers applied a high temperature range of 500 °C to 800 °C for markedly improving catalytic activity and minimizing carbon deposition. The analysis of the effect of reaction temperature on catalytic performance suggested that high temperatures of 800 °C and 950 °C were suitable for high CO_2 and CH_4 conversion reaching 99% and could inhibit carbon deposition. Given that methane decomposition and the Boudouard reaction contribute to carbon formation, a feed ratio (CH_4/CO_2) lower than unity should be used to suppress carbon deposition on the catalyst. All previous studies agree that the lowest space velocity is preferable for a DRM reaction to enhance catalytic activity. Optimization of metal loading for Mg-containing oxide catalysts also led to improved catalyst morphology and performance.

Despite considerable achievements by Mg-containing oxide catalysts as a support or promoter, the activity of Mg should be clearly specified and justified. Therefore, future investigations should focus on studying Mg-containing oxide catalysts at the molecular level to justify the capability of this highly basic catalyst for inhibiting carbon deposition in the dry reforming of methane reactions. Moreover, information on the effect of reduction on the prepared catalyst is lacking; thus, further research to analyze the effect of catalyst reduction on catalytic performance would prove highly beneficial. Reduction studies should include the composition of medium and time applied to the catalyst. Besides that, regeneration of the spent catalyst during dry reforming of methane reactions has yet to be studied extensively. This information would be extremely useful for im-

proving catalyst performance and could be beneficial for decreasing the cost of preparing new dry reforming catalysts.

Acknowledgements

The authors express great gratitude to the Fundamental Research Grant Scheme (FRGS) – Malaysia's Rising Star Award 2015 (No: 203/PJKIMIA/6071335) from the Ministry of Higher Education of Malaysia to support this research work.

ORCID® iDs

Mehrnoush Khavarian - https://orcid.org/0000-0002-4282-8258
Abdul Rahman Mohamed - https://orcid.org/0000-0002-5418-5456

References

1. Zhang, A.-J.; Zhu, A.-M.; Guo, J.; Xu, Y.; Shi, C. *Chem. Eng. J.* **2010,** *156,* 601–606. doi:10.1016/j.cej.2009.04.069
2. Zhang, K.; Kogelschatz, U.; Eliasson, B. *Energy Fuels* **2001,** *15,* 395–402. doi:10.1021/ef000161o
3. Fan, M.-S.; Abdullah, A. Z.; Bhatia, S. *ChemSusChem* **2011,** *4,* 1643–1653. doi:10.1002/cssc.201100113
4. Rahemi, N.; Haghighi, M.; Babaluo, A. A.; Allahyari, S.; Jafari, M. F. *Energy Convers. Manage.* **2014,** *84,* 50–59. doi:10.1016/j.enconman.2014.04.016
5. Anderson, D. M.; Kottke, P. A.; Fedorov, A. G. *Int. J. Hydrogen Energy* **2014,** *39,* 17985–17997. doi:10.1016/j.ijhydene.2014.03.127
6. Angeli, S. D.; Turchetti, L.; Monteleone, G.; Lemonidou, A. A. *Appl. Catal., B: Environ.* **2016,** *181,* 34–46. doi:10.1016/j.apcatb.2015.07.039
7. Oyama, S. T.; Hacarlioglu, P.; Gu, Y.; Lee, D. *Int. J. Hydrogen Energy* **2012,** *37,* 10444–10450. doi:10.1016/j.ijhydene.2011.09.149
8. de Lima, S. M.; da Silva, A. M.; da Costa, L. O. O.; Graham, U. M.; Jacobs, G.; Davis, B. H.; Mattos, L. V.; Noronha, F. B. *J. Catal.* **2009,** *268,* 268–281. doi:10.1016/j.jcat.2009.09.025
9. Dedov, A. G.; Loktev, A. S.; Komissarenko, D. A.; Parkhomenko, K. V.; Roger, A.-C.; Shlyakhtin, O. A.; Mazo, G. N.; Moiseev, I. I. *Fuel Process. Technol.* **2016,** *148,* 128–137. doi:10.1016/j.fuproc.2016.02.018
10. Pantaleo, G.; La Parola, V.; Deganello, F.; Singha, R. K.; Bal, R.; Venezia, A. M. *Appl. Catal., B: Environ.* **2016,** *189,* 233–241. doi:10.1016/j.apcatb.2016.02.064
11. Abasaeed, A. E.; Al-Fatesh, A. S.; Naeem, M. A.; Ibrahim, A. A.; Fakeeha, A. H. *Int. J. Hydrogen Energy* **2015,** *40,* 6818–6826. doi:10.1016/j.ijhydene.2015.03.152
12. Ay, H.; Üner, D. *Appl. Catal., B: Environ.* **2015,** *179,* 128–138. doi:10.1016/j.apcatb.2015.05.013
13. Chein, R. Y.; Chen, Y. C.; Yu, C. T.; Chung, J. N. *J. Nat. Gas Sci. Eng.* **2015,** *26,* 617–629. doi:10.1016/j.jngse.2015.07.001
14. Usman, M.; Wan Daud, W. M. A.; Abbas, H. F. *Renewable Sustainable Energy Rev.* **2015,** *45,* 710–744. doi:10.1016/j.rser.2015.02.026
15. Budiman, A. W.; Song, S.-H.; Chang, T.-S.; Shin, C.-H.; Choi, M.-J. *Catal. Surv. Asia* **2012,** *16,* 183–197. doi:10.1007/s10563-012-9143-2
16. García-Vargas, J. M.; Valverde, J. L.; Díez, J.; Dorado, F.; Sánchez, P. *Int. J. Hydrogen Energy* **2015,** *40,* 8677–8687. doi:10.1016/j.ijhydene.2015.05.032
17. Hadian, N.; Rezaei, M. *Fuel* **2013,** *113,* 571–579. doi:10.1016/j.fuel.2013.06.013
18. Hadian, N.; Rezaei, M.; Mosayebi, Z.; Meshkani, F. *J. Nat. Gas Chem.* **2012,** *21,* 200–206. doi:10.1016/S1003-9953(11)60355-1
19. García-Diéguez, M.; Herrera, C.; Larrubia, M. Á.; Alemany, L. J. *Catal. Today* **2012,** *197,* 50–57. doi:10.1016/j.cattod.2012.06.019
20. Roy, P. S.; Park, C. S.; Raju, A. S. K.; Kim, K. *J. CO2 Util.* **2015,** *12,* 12–20. doi:10.1016/j.jcou.2015.09.003
21. Yasyerli, S.; Filizgok, S.; Arbag, H.; Yasyerli, N.; Dogu, G. *Int. J. Hydrogen Energy* **2011,** *36,* 4863–4874. doi:10.1016/j.ijhydene.2011.01.120
22. Rezaei, M.; Meshkani, F.; Ravandi, A. B.; Nematollahi, B.; Ranjbar, A.; Hadian, N.; Mosayebi, Z. *Int. J. Hydrogen Energy* **2011,** *36,* 11712–11717. doi:10.1016/j.ijhydene.2011.06.056
23. Wang, Y.-H.; Liu, H.-M.; Xu, B.-Q. *J. Mol. Catal. A: Chem.* **2009,** *299,* 44–52. doi:10.1016/j.molcata.2008.09.025
24. Zhao, X.; Li, H.; Zhang, J.; Shi, L.; Zhang, D. *Int. J. Hydrogen Energy* **2016,** *41,* 2447–2456. doi:10.1016/j.ijhydene.2015.10.111
25. de Llobet, S.; Pinilla, J. L.; Moliner, R.; Suelves, I. *Fuel* **2015,** *139,* 71–78. doi:10.1016/j.fuel.2014.08.031
26. Tsoukalou, A.; Imtiaz, Q.; Kim, S. M.; Abdala, P. M.; Yoon, S.; Müller, C. R. *J. Catal.* **2016,** *343,* 208–214. doi:10.1016/j.jcat.2016.03.018
27. Theofanidis, S. A.; Galvita, V. V.; Poelman, H.; Marin, G. B. *ACS Catal.* **2015,** *5,* 3028–3039. doi:10.1021/acscatal.5b00357
28. Theofanidis, S. A.; Batchu, R.; Galvita, V. V.; Poelman, H.; Marin, G. B. *Appl. Catal., B: Environ.* **2016,** *185,* 42–55. doi:10.1016/j.apcatb.2015.12.006
29. San-José-Alonso, D.; Juan-Juan, J.; Illán-Gómez, M.; Román-Martínez, M. *Appl. Catal., A* **2009,** *371,* 54–59. doi:10.1016/j.apcata.2009.09.026
30. Luisetto, I.; Tuti, S.; Di Bartolomeo, E. *Int. J. Hydrogen Energy* **2012,** *37,* 15992–15999. doi:10.1016/j.ijhydene.2012.08.006
31. Gallego, G. S.; Batiot-Dupeyrat, C.; Barrault, J.; Florez, E.; Mondragón, F. *Appl. Catal., A* **2008,** *334,* 251–258. doi:10.1016/j.apcata.2007.10.010
32. Daza, C. E.; Gallego, J.; Mondragón, F.; Moreno, S.; Molina, R. *Fuel* **2010,** *89,* 592–603. doi:10.1016/j.fuel.2009.10.010
33. Xiancai, L.; Min, W.; Zhihua, L.; Fei, H. *Appl. Catal., A* **2005,** *290,* 81–86. doi:10.1016/j.apcata.2005.05.021
34. Zanganeh, R.; Rezaei, M.; Zamaniyan, A. *Int. J. Hydrogen Energy* **2013,** *38,* 3012–3018. doi:10.1016/j.ijhydene.2012.12.089
35. Cai, W.-J.; Qian, L.-P.; Yue, B.; Chen, X.-Y.; He, H.-Y. *Chin. Chem. Lett.* **2013,** *24,* 777–779. doi:10.1016/j.cclet.2013.05.034
36. Hua, W.; Jin, L.; He, X.; Liu, J.; Hu, H. *Catal. Commun.* **2010,** *11,* 968–972. doi:10.1016/j.catcom.2010.04.007
37. Hassani Rad, S. J.; Haghighi, M.; Alizadeh Eslami, A.; Rahmani, F.; Rahemi, N. *Int. J. Hydrogen Energy* **2016,** *41,* 5335–5350. doi:10.1016/j.ijhydene.2016.02.002
38. Sajjadi, S. M.; Haghighi, M.; Rahmani, F. *J. Sol-Gel Sci. Technol.* **2014,** *70,* 111–124. doi:10.1007/s10971-014-3280-1
39. Dębek, R.; Motak, M.; Duraczyska, D.; Launay, F.; Galvez, M. E.; Grzybek, T.; Da Costa, P. *Catal. Sci. Technol.* **2016,** *6,* 6705–6715. doi:10.1039/C6CY00906A
40. Singha, R. K.; Yadav, A.; Shukla, A.; Iqbal, Z.; Pendem, C.; Sivakumar, K.; Bal, R. *ChemistrySelect* **2016,** *1,* 3075–3085. doi:10.1002/slct.201600685
41. Djaidja, A.; Libs, S.; Kiennemann, A.; Barama, A. *Catal. Today* **2006,** *113,* 194–200. doi:10.1016/j.cattod.2005.11.066

42. Dong, W.-S.; Jun, K.-W.; Roh, H.-S.; Liu, Z.-W.; Park, S.-E. *Catal. Lett.* **2002,** *78,* 215–222. doi:10.1023/A:1014905318290
43. Pino, L.; Vita, A.; Cipitì, F.; Laganà, M.; Recupero, V. *Appl. Catal., B: Environ.* **2011,** *104,* 64–73. doi:10.1016/j.apcatb.2011.02.027
44. Zhang, S.; Muratsugu, S.; Ishiguro, N.; Tada, M. *ACS Catal.* **2013,** *3,* 1855–1864. doi:10.1021/cs400159w
45. Frusteri, F.; Arena, F.; Calogero, G.; Torre, T.; Parmaliana, A. *Catal. Commun.* **2001,** *2,* 49–56. doi:10.1016/S1566-7367(01)00008-5
46. Snoeck, J.-W.; Froment, G.; Fowles, M. *Ind. Eng. Chem. Res.* **2002,** *41,* 4252–4265. doi:10.1021/ie010666h
47. Bachiller-Baeza, B.; Mateos-Pedrero, C.; Soria, M. A.; Guerrero-Ruiz, A.; Rodemerck, U.; Rodríguez-Ramos, I. *Appl. Catal., B: Environ.* **2013,** *129,* 450–459. doi:10.1016/j.apcatb.2012.09.052
48. Zarei, M.; Meshkani, F.; Rezaei, M. *Adv. Powder Technol.* **2016,** *27,* 1963–1970. doi:10.1016/j.apt.2016.06.028
49. Abdollahifar, M.; Haghighi, M.; Babaluo, A. A. *J. Ind. Eng. Chem.* **2014,** *20,* 1845–1851. doi:10.1016/j.jiec.2013.08.041
50. Daza, C. E.; Moreno, S.; Molina, R. *Int. J. Hydrogen Energy* **2011,** *36,* 3886–3894. doi:10.1016/j.ijhydene.2010.12.082
51. Elsayed, N. H.; Roberts, N. R. M.; Joseph, B.; Kuhn, J. N. *Appl. Catal., B: Environ.* **2015,** *179,* 213–219. doi:10.1016/j.apcatb.2015.05.021
52. Fan, M.-S.; Abdullah, A. Z.; Bhatia, S. *Appl. Catal., B: Environ.* **2010,** *100,* 365–377. doi:10.1016/j.apcatb.2010.08.013
53. García-Vargas, J. M.; Valverde, J. L.; Díez, J.; Sánchez, P.; Dorado, F. *Appl. Catal., B: Environ.* **2015,** *164,* 316–323. doi:10.1016/j.apcatb.2014.09.044
54. Son, I. H.; Kwon, S.; Park, J. H.; Lee, S. J. *Nano Energy* **2016,** *19,* 58–67. doi:10.1016/j.nanoen.2015.11.007
55. Xu, B.-Q.; Wei, J.-M.; Wang, H.-Y.; Sun, K.-Q.; Zhu, Q.-M. *Catal. Today* **2001,** *68,* 217–225. doi:10.1016/S0920-5861(01)00303-0
56. Nikoo, M. K.; Amin, N. *Fuel Process. Technol.* **2011,** *92,* 678–691. doi:10.1016/j.fuproc.2010.11.027
57. Wang, S.; Lu, G.; Millar, G. J. *Energy Fuels* **1996,** *10,* 896–904. doi:10.1021/ef950227t
58. Li, Y.; Wang, Y.; Zhang, X.; Mi, Z. *Int. J. Hydrogen Energy* **2008,** *33,* 2507–2514. doi:10.1016/j.ijhydene.2008.02.051
59. Shamsi, A.; Johnson, C. D. *Catal. Today* **2003,** *84,* 17–25. doi:10.1016/S0920-5861(03)00296-7
60. Sun, Y.; Ritchie, T.; Hla, S. S.; McEvoy, S.; Stein, W.; Edwards, J. H. *J. Nat. Gas Chem.* **2011,** *20,* 568–576. doi:10.1016/S1003-9953(10)60235-6
61. Zhang, Y.; Zhang, G.; Zhang, B.; Guo, F.; Sun, Y. *Chem. Eng. J.* **2011,** *173,* 592–597. doi:10.1016/j.cej.2011.08.008
62. Jafarbegloo, M.; Tarlani, A.; Mesbah, A. W.; Sahebdelfar, S. *Int. J. Hydrogen Energy* **2015,** *40,* 2445–2451. doi:10.1016/j.ijhydene.2014.12.103
63. Jafarbegloo, M.; Tarlani, A.; Mesbah, A. W.; Sahebdelfar, S. *J. Nat. Gas Sci. Eng.* **2015,** *27,* 1165–1173. doi:10.1016/j.jngse.2015.09.065
64. Klein, J. E. *Fusion Sci. Technol.* **2002,** *41,* 998–1003. doi:10.13182/FST02-A22734
65. Fan, M.-S.; Abdullah, A. Z.; Bhatia, S. *ChemCatChem* **2009,** *1,* 192–208. doi:10.1002/cctc.200900025
66. Niu, J.; Du, X.; Ran, J.; Wang, R. *Appl. Surf. Sci.* **2016,** *376,* 79–90. doi:10.1016/j.apsusc.2016.01.212
67. Nakamura, J.; Aikawa, K.; Sato, K.; Uchijima, T. *Catal. Lett.* **1994,** *25,* 265–270. doi:10.1007/BF00816306
68. Alipour, Z.; Rezaei, M.; Meshkani, F. *J. Ind. Eng. Chem.* **2014,** *20,* 2858–2863. doi:10.1016/j.jiec.2013.11.018
69. Khavarian, M.; Chai, S.-P.; Mohamed, A. R. *Chem. Eng. J.* **2014,** *257,* 200–208. doi:10.1016/j.cej.2014.05.079
70. Alipour, Z.; Rezaei, M.; Meshkani, F. *J. Energy Chem.* **2014,** *23,* 633–638. doi:10.1016/S2095-4956(14)60194-7
71. Angeli, S. D.; Pilitsis, F. G.; Lemonidou, A. A. *Catal. Today* **2015,** *242,* 119–128. doi:10.1016/j.cattod.2014.05.043
72. Schulz, L. A.; Kahle, L. C. S.; Delgado, K. H.; Schunk, S. A.; Jentys, A.; Deutschmann, O.; Lercher, J. A. *Appl. Catal., A* **2015,** *504,* 599–607. doi:10.1016/j.apcata.2015.03.002
73. Wang, Z.; Cao, X. M.; Zhu, J.; Hu, P. *J. Catal.* **2014,** *311,* 469–480. doi:10.1016/j.jcat.2013.12.015
74. Saqib, N.; Porter, J. M. *Sens. Actuators, B* **2016,** *224,* 755–763. doi:10.1016/j.snb.2015.10.112
75. Singha, R. K.; Yadav, A.; Agrawal, A.; Shukla, A.; Adak, S.; Sasaki, T.; Bal, R. *Appl. Catal., B: Environ.* **2016,** *191,* 165–178. doi:10.1016/j.apcatb.2016.03.029
76. Luisetto, I.; Tuti, S.; Battocchio, C.; Lo Mastro, S.; Sodo, A. *Appl. Catal., A* **2015,** *500,* 12–22. doi:10.1016/j.apcata.2015.05.004
77. Lobo, L. S.; Figueiredo, J. L.; Bernardo, C. A. *Catal. Today* **2011,** *178,* 110–116. doi:10.1016/j.cattod.2011.07.030
78. Djaidja, A.; Messaoudi, H.; Kaddeche, D.; Barama, A. *Int. J. Hydrogen Energy* **2015,** *40,* 4989–4995. doi:10.1016/j.ijhydene.2014.12.106
79. Istadi, I.; Anggoro, D. D.; Amin, N. A. S.; Ling, D. H. W. *Bull. Chem. React. Eng. Catal.* **2011,** *6,* 129–136. doi:10.9767/bcrec.6.2.1213.129-136
80. Wei, J.; Iglesia, E. *J. Catal.* **2004,** *224,* 370–383. doi:10.1016/j.jcat.2004.02.032
81. Aparicio, L. M. *J. Catal.* **1997,** *165,* 262–274. doi:10.1006/jcat.1997.1468
82. Dehimi, L.; Benguerba, Y.; Virginie, M.; Hijazi, H. *Int. J. Hydrogen Energy* **2017,** *42,* 18930–18940. doi:10.1016/j.ijhydene.2017.05.231
83. Wang, S. *Ind. Eng. Chem. Res.* **1999,** *38,* 2615–2625. doi:10.1021/ie980489t
84. Bradford, M. C. J.; Vannice, M. A. *Catal. Rev.* **1999,** *41,* 1–42. doi:10.1081/CR-100101948
85. Lemonidou, A. A.; Vasalos, I. A. *Appl. Catal., A* **2002,** *228,* 227–235. doi:10.1016/S0926-860X(01)00974-7
86. Zhang, J.; Wang, H.; Dalai, A. K. *Ind. Eng. Chem. Res.* **2009,** *48,* 677–684. doi:10.1021/ie801078p
87. Joyner, R. W.; Pendry, J. B.; Saldin, D. K.; Tennison, S. R. *Surf. Sci.* **1984,** *138,* 84–94. doi:10.1016/0039-6028(84)90497-7
88. Julkapli, N. M.; Bagheri, S. *Rev. Inorg. Chem.* **2016,** *36,* 1–41. doi:10.1515/revic-2015-0010
89. Park, J. C.; Song, H. *Nano Res.* **2011,** *4,* 33–49. doi:10.1007/s12274-010-0039-z
90. Richardson, J. T. *Principles of Catalyst Development;* Springer : US, 1989.
91. Wang, H. Y.; Ruckenstein, E. *Appl. Catal., A* **2001,** *209,* 207–215. doi:10.1016/S0926-860X(00)00753-5
92. Perez-Lopez, O. W.; Senger, A.; Marcilio, N. R.; Lansarin, M. A. *Appl. Catal., A* **2006,** *303,* 234–244. doi:10.1016/j.apcata.2006.02.024
93. Serrano-Lotina, A.; Rodríguez, L.; Muñoz, G.; Daza, L. *J. Power Sources* **2011,** *196,* 4404–4410. doi:10.1016/j.jpowsour.2010.10.107

94. Feng, J.; Ding, Y.; Guo, Y.; Li, X.; Li, W. *Fuel* **2013,** *109,* 110–115. doi:10.1016/j.fuel.2012.08.028
95. Bartholomew, C. H.; Farrauto, R. J. *Fundamentals of Industrial Catalytic Processes,* 2nd ed.; John Wiley & Sons, Inc.: Hoboken, New Jersey, 2011.
96. Arora, S.; Prasad, R. *RSC Adv.* **2016,** *6,* 108668–108688. doi:10.1039/C6RA20450C
97. Ni, J.; Chen, L.; Lin, J.; Schreyer, M. K.; Wang, Z.; Kawi, S. *Int. J. Hydrogen Energy* **2013,** *38,* 13631–13642. doi:10.1016/j.ijhydene.2013.08.041
98. Liu, C.; Li, M.; Wang, J.; Zhou, X.; Guo, Q.; Yan, J.; Li, Y. *Chin. J. Catal.* **2016,** *37,* 340–348. doi:10.1016/S1872-2067(15)61020-8
99. Zou, J.-J.; Liu, C.-J.; Zhang, Y.-P. *Langmuir* **2006,** *22,* 2334–2339. doi:10.1021/la052135u
100. Liu, G.; Li, Y.; Chu, W.; Shi, X.; Dai, X.; Yin, Y. *Catal. Commun.* **2008,** *9,* 1087–1091. doi:10.1016/j.catcom.2007.10.013
101. Yan, X.; Liu, Y.; Zhao, B.; Wang, Z.; Wang, Y.; Liu, C.-j. *Int. J. Hydrogen Energy* **2013,** *38,* 2283–2291. doi:10.1016/j.ijhydene.2012.12.024
102. Yan, X.; Zhao, B.; Liu, Y.; Li, Y. *Catal. Today* **2015,** *256,* 29–40. doi:10.1016/j.cattod.2015.04.045
103. García, V.; Fernández, J. J.; Ruíz, W.; Mondragón, F.; Moreno, A. *Catal. Commun.* **2009,** *11,* 240–246. doi:10.1016/j.catcom.2009.10.003
104. Min, J.-E.; Lee, Y.-J.; Park, H.-G.; Zhang, C.; Jun, K.-W. *J. Ind. Eng. Chem.* **2015,** *26,* 375–383. doi:10.1016/j.jiec.2014.12.012
105. Zhu, J.; Peng, X.; Yao, L.; Shen, J.; Tong, D.; Hu, C. *Int. J. Hydrogen Energy* **2011,** *36,* 7094–7104. doi:10.1016/j.ijhydene.2011.02.133
106. Xu, Y.; Long, H.; Wei, Q.; Zhang, X.; Shang, S.; Dai, X.; Yin, Y. *Catal. Today* **2013,** *211,* 114–119. doi:10.1016/j.cattod.2013.03.007
107. Serrano-Lotina, A.; Rodríguez, L.; Muñoz, G.; Martin, A. J.; Folgado, M. A.; Daza, L. *Catal. Commun.* **2011,** *12,* 961–967. doi:10.1016/j.catcom.2011.02.014
108. Meshkani, F.; Rezaei, M.; Andache, M. *J. Ind. Eng. Chem.* **2014,** *20,* 1251–1260. doi:10.1016/j.jiec.2013.06.052
109. Lin, L.; Zhang, L.-m.; Zhang, Y.-h.; Li, J.-l. *J. Fuel Chem. Technol. (Beijing, China)* **2015,** *43,* 315–322. doi:10.1016/S1872-5813(15)30007-4
110. Khajenoori, M.; Rezaei, M.; Meshkani, F. *J. Ind. Eng. Chem.* **2015,** *21,* 717–722. doi:10.1016/j.jiec.2014.03.043
111. Meshkani, F.; Rezaei, M. *J. Nat. Gas Chem.* **2011,** *20,* 198–203. doi:10.1016/S1003-9953(10)60169-7
112. Zhu, Y.; Zhang, S.; Chen, B.; Zhang, Z.; Shi, C. *Catal. Today* **2016,** *264,* 163–170. doi:10.1016/j.cattod.2015.07.037
113. Yu, X.; Wang, N.; Chu, W.; Liu, M. *Chem. Eng. J.* **2012,** *209,* 623–632. doi:10.1016/j.cej.2012.08.037
114. Sengupta, S.; Deo, G. *J. CO2 Util.* **2015,** *10,* 67–77. doi:10.1016/j.jcou.2015.04.003
115. Charisiou, N. D.; Baklavaridis, A.; Papadakis, V. G.; Goula, M. A. *Waste Biomass Valorization* **2016,** *7,* 725–736. doi:10.1007/s12649-016-9627-9
116. Akbari, E.; Alavi, S. M.; Rezaei, M. *Fuel* **2017,** *194,* 171–179. doi:10.1016/j.fuel.2017.01.018
117. Jabbour, K.; Massiani, P.; Davidson, A.; Casale, S.; El Hassan, N. *Appl. Catal., B: Environ.* **2017,** *201,* 527–542. doi:10.1016/j.apcatb.2016.08.009
118. Li, Z.; Kathiraser, Y.; Ashok, J.; Oemar, U.; Kawi, S. *Langmuir* **2014,** *30,* 14694–14705. doi:10.1021/la503340s
119. Wang, N.; Yu, X.; Shen, K.; Chu, W.; Qian, W. *Int. J. Hydrogen Energy* **2013,** *38,* 9718–9731. doi:10.1016/j.ijhydene.2013.05.097
120. Macedo Neto, O. R.; Ribeiro, N. F. P.; Perez, C. A. C.; Schmal, M.; Souza, M. M. V. M. *Appl. Clay Sci.* **2010,** *48,* 542–546. doi:10.1016/j.clay.2010.02.015
121. Yan, Z.-F.; Ding, R.-G.; Liu, X.-M.; Song, L.-H. *Chin. J. Chem.* **2001,** *19,* 738–744. doi:10.1002/cjoc.20010190806
122. Alipour, Z.; Rezaei, M.; Meshkani, F. *Fuel* **2014,** *129,* 197–203. doi:10.1016/j.fuel.2014.03.045
123. Mirzaei, F.; Rezaei, M.; Meshkani, F.; Fattah, Z. *J. Ind. Eng. Chem.* **2015,** *21,* 662–667. doi:10.1016/j.jiec.2014.03.034

License and Terms

This is an Open Access article under the terms of the Creative Commons Attribution License (http://creativecommons.org/licenses/by/4.0), which permits unrestricted use, distribution, and reproduction in any medium, provided the original work is properly cited.

The license is subject to the *Beilstein Journal of Nanotechnology* terms and conditions: (https://www.beilstein-journals.org/bjnano)

The definitive version of this article is the electronic one which can be found at:
doi:10.3762/bjnano.9.108

BEILSTEIN JOURNAL OF NANOTECHNOLOGY

Ag_2WO_4 nanorods decorated with AgI nanoparticles: Novel and efficient visible-light-driven photocatalysts for the degradation of water pollutants

Shijie Li*[1], Shiwei Hu[1], Wei Jiang[1], Yanping Liu[2], Yu Liu[1], Yingtang Zhou*[1], Liuye Mo[1] and Jianshe Liu[3]

Full Research Paper

Open Access

Address:
[1]Key Laboratory of Health Risk Factors for Seafood of Zhejiang Province, Institute of Innovation & Application, Zhejiang Ocean University, Zhoushan, Zhejiang Province, 316022, China, [2]Department of Environmental Engineering, Zhejiang Ocean University, Zhoushan, Zhejiang Province, 316022, China, and [3]State Environmental Protection Engineering Center for Pollution Treatment and Control in Textile Industry, College of Environmental Science and Engineering, Donghua University, Shanghai 201620, China

Email:
Shijie Li* - lishijie@zjou.edu.cn; Yingtang Zhou* - zhouyingtang@zjou.edu.cn

* Corresponding author

Keywords:
AgI/Ag_2WO_4; nanocomposites; photocatalysis; visible light

Beilstein J. Nanotechnol. **2018,** *9,* 1308–1316.
doi:10.3762/bjnano.9.123

Received: 02 January 2018
Accepted: 29 March 2018
Published: 27 April 2018

This article is part of the Thematic Series "Energy conversion, storage and environmental remediation using nanomaterials".

Guest Editor: W.-J. Ong

© 2018 Li et al.; licensee Beilstein-Institut.
License and terms: see end of document.

Abstract

To develop efficient and stable visible-light-driven (VLD) photocatalysts for pollutant degradation, we synthesized novel heterojunction photocatalysts comprised of AgI nanoparticle-decorated Ag_2WO_4 nanorods via a facile method. Various characterization techniques, including XRD, SEM, TEM, EDX, and UV–vis DRS were used to investigate the morphology and optical properties of the as-prepared AgI/Ag_2WO_4 catalyst. With AgI acting as the cocatalyst, the resulting AgI/Ag_2WO_4 heterostructure shows excellent performance in degrading toxic, stable pollutants such as rhodamine B (RhB), methyl orange (MO) and *para*-chlorophenol (4-CP). The high performance is attributed to the enhanced visible-light absorption properties and the promoted separation efficiency of charge carriers through the formation of the heterojunction between AgI and Ag_2WO_4. Additionally, AgI/Ag_2WO_4 exhibits durable stability. The active species trapping experiment reveals that active species ($O_2^{\bullet-}$ and h^+) dominantly contribute to RhB degradation. The AgI/Ag_2WO_4 heterojunction photocatalyst characterized in this work holds great potential for remedying environmental issues due to its simple preparation method and excellent photocatalytic performance.

Introduction

The development of high-performance novel photocatalysts for the degradation of pollutants has received great interest due to the worsening of environmental pollution [1-11]. However, achieving high efficiency for photocatalytic conversion under natural sunlight irradiation is still a great challenge because many catalysts only respond to ultraviolet (UV) light [5,12]. Exploring photocatalysts that can be driven by visible light, which comprises 43% of solar energy, is important for practical application [13-20].

Silver-containing compounds such as AgI, Ag_2CrO_4, Ag_2O, Ag_3PO_4 etc., have proven to be efficient VLD photocatalysts [21-35]. Among these photocatalysts, Ag_2WO_4 presents good photocatalytic performance for dye degradation under light irradiation [30,31,36,37]. Unfortunately, due to its wide bandgap of about 3.1 eV, Ag_2WO_4 has limited photocatalytic activity under sunlight, which severely limits its application and illustrates the urgency for optimization of Ag_2WO_4 to overcome these disadvantages [38-42].

The integration of VLD components with wide bandgap semiconductors having well-matched energy bands has provided a new opportunity for the development of VLD photocatalysts [12]. As a consequence, some Ag_2WO_4-based composites containing VLD components such as Ag_2S/Ag_2WO_4 [40], C_3N_4/Ag_2WO_4 [39], $Bi_2MoO_6/Ag_2WO_4/Ag$ [42] etc., have been reported to show improved VLD performance in the degradation of pollutants. To the best of our knowledge, application of AgI/Ag_2WO_4 as a VLD photocatalyst for the degradation of toxic pollutants remains unreported.

In this study, to enhance the photocatalytic performance of Ag_2WO_4, AgI (possessing matched energy band levels) was chosen as a suitable component to combine with Ag_2WO_4, AgI/Ag_2WO_4 heterojunctions at different mole ratios. These heterojunctions were prepared via an in situ ion-exchange approach, utilizing Ag_2WO_4 nanorods as the Ag source. The as-prepared AgI/Ag_2WO_4 heterojunctions exhibited remarkably higher photocatalytic activity than pure Ag_2WO_4 toward the degradation of rhodamine B (RhB), methyl orange (MO) and *para*-chlorophenol (4-CP) under visible light. Based on a systematic characterization and study, a possible photocatalytic mechanism over AgI/Ag_2WO_4 was also elucidated in this work.

Results and Discussion

Preparation and characterization of catalysts

Ag_2WO_4 nanorods decorated with AgI nanoparticles were prepared via an in situ anion-exchange method. Ag_2WO_4 nanorods were first synthesized by mixing $AgNO_3$ and Na_2WO_4 aqueous solutions at room temperature [37]. Subsequently, AgI nanoparticles were readily anchored onto Ag_2WO_4 nanorods via an in situ anion-exchange between I^- in the solution and the lattice $W_2O_4^{2-}$ in Ag_2WO_4. The resulting catalysts were denoted as $0.1AgI/Ag_2WO_4$, $0.2AgI/Ag_2WO_4$, $0.3AgI/Ag_2WO_4$, and $0.4AgI/Ag_2WO_4$, respectively.

The XRD patterns of pure Ag_2WO_4, pure AgI, and AgI/Ag_2WO_4 heterojunctions are displayed in Figure 1. Pure Ag_2WO_4 is in its orthorhombic structure (JCPDS no. 70-1719) and exhibits several strong peaks at 30.3°, 31.8°, 33.1, 45.6°, 54.8° and 58.3°, which can be indexed to (002), (231), (400), (402), (361) and (333) diffraction planes, respectively [31,41]. The diffraction peaks of pure AgI match well with those of the standard hexagonal phase (JCPS no 29-1154) [43]. It can be seen that all the AgI/Ag_2WO_4 composites display both Ag_2WO_4 and AgI phases. Of note is that the diffraction peak intensity of AgI becomes stronger with increasing AgI content, confirming the formation of AgI/Ag_2WO_4 heterojunctions.

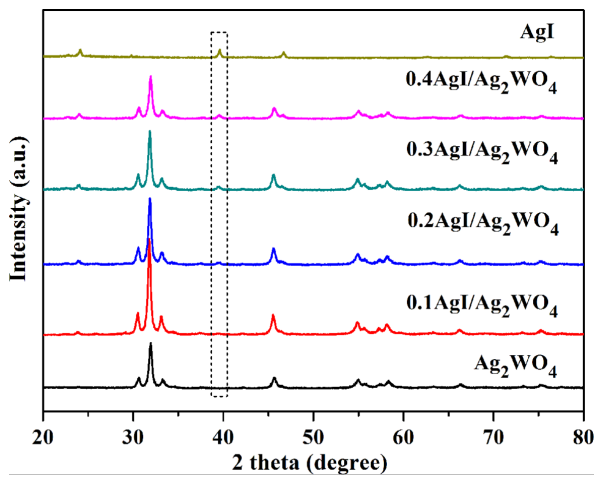

Figure 1: XRD patterns of Ag_2WO_4, AgI, $0.1AgI/Ag_2WO_4$, $0.2AgI/Ag_2WO_4$, $0.3AgI/Ag_2WO_4$, and $0.4AgI/Ag_2WO_4$.

Scanning electron microscopy (SEM) and transmission electron microscopy (TEM) were used to investigate the morphology and microstructure of AgI/Ag_2WO_4 heterojunctions (Figure 2). Figure 2a–d presents the SEM images of Ag_2WO_4 (Figure 2a,b) and the representative $0.3AgI/Ag_2WO_4$ (Figure 2c,d). It can be seen that bare Ag_2WO_4 consists of nanorods (length: 0.3–0.8 μm) with smooth surfaces (Figure 2a,b). After in situ anion-exchange between I^- and the lattice $W_2O_4^{2-}$, small AgI nanoparticles (diameter: 20–40 nm) are uniformly coated on the surface of Ag_2WO_4 nanorods, signifying the formation of the AgI/Ag_2WO_4 core–shell heterostructure. To more clearly observe the microstructure of the AgI/Ag_2WO_4 composite, the TEM and high-resolution TEM

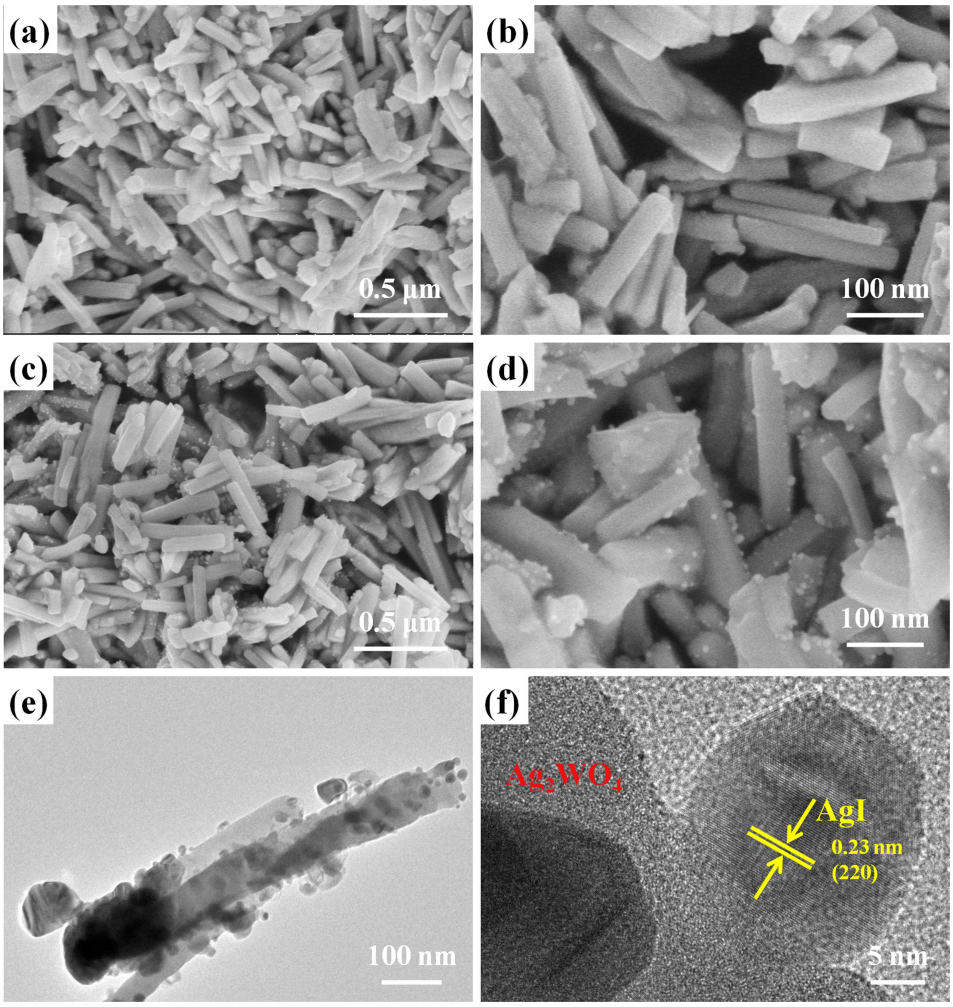

Figure 2: SEM (a, b) images of Ag_2WO_4; SEM (c, d), TEM (e), and HRTEM (f) images of $0.3AgI/Ag_2WO_4$.

(HRTEM) images are shown in Figure 2e,f. It can be seen that many nanoparticles are deposited on the surface of the Ag_2WO_4 nanorods (Figure 2e). The HRTEM image (Figure 2f) shows that one set of lattice fringes can be observed. The lattice fringe of 0.23 nm matches well with the (220) plane of AgI. No lattice fringe correlated to Ag_2WO_4 can be distinguished, which is in accordance with the previous reports [40].

In addition, the composition of $0.3AgI/Ag_2WO_4$ was further identified by energy-dispersive X-ray spectroscopy (EDX). As shown in Figure 3, $0.3AgI/Ag_2WO_4$ is composed of Ag, I, W and O elements. The results further confirm the formation of the AgI/Ag_2WO_4 heterojunctions, thereby facilitating the charge transfer between them [12].

Subsequently, the optical properties of as-prepared photocatalysts were investigated by UV–vis diffuse reflectance spectroscopy (DRS) analysis (Figure 4). As indicated from Figure 4,

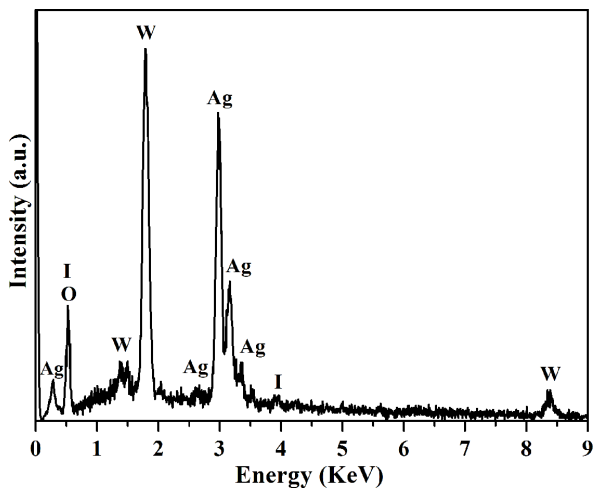

Figure 3: Energy-dispersive X-ray (EDX) spectrum of $0.3AgI/Ag_2WO_4$.

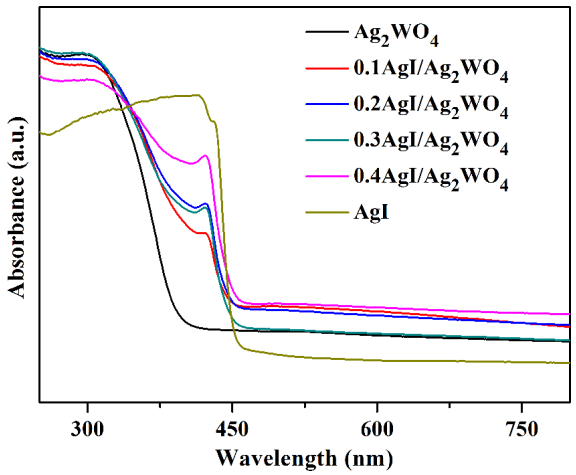

Figure 4: UV–vis diffuse reflectance spectra of Ag_2WO_4, AgI, $0.1AgI/Ag_2WO_4$, $0.2AgI/Ag_2WO_4$, $0.3AgI/Ag_2WO_4$, and $0.4AgI/Ag_2WO_4$.

pure Ag_2WO_4 has a clear absorption edge at about 400 nm [31], while AgI has a broader absorption band with the absorption edge located at around 460 nm [22]. For AgI/Ag_2WO_4 heterojunctions, a pronounced enhancement in visible-light absorption range is achieved when AgI content was progressively increased. This suggests that the introduction of AgI nanoparticles can optimize the light absorption capacity owing to the formation of a nanojunction between AgI and Ag_2WO_4. These facts indicate that AgI/Ag_2WO_4 heterojunctions can harvest more light and thus can be expected to be efficient VLD photocatalysts.

Photocatalytic performance

RhB, MO, and 4-CP, three types of toxic pollutants with stable chemical structures, were used to evaluate the activity of AgI/Ag_2WO_4 heterojunctions. Figure 5a shows the visible-light degradation results of RhB (10 mg L^{-1}) over as-prepared samples. Bare Ag_2WO_4 exhibits poor visible-light photocatalytic activity with an RhB degradation rate of 16.2% after 60 min irradiation due to the unsatisfactory visible-light absorption and fast recombination of photoinduced charge carriers [31,38,44,45]. After hybridization of AgI, all AgI/Ag_2WO_4 heterojunctions ($0.1AgI/Ag_2WO_4$, $0.2AgI/Ag_2WO_4$, $0.3AgI/Ag_2WO_4$, and $0.4AgI/Ag_2WO_4$) show greatly improved photocatalytic activity compared with pure Ag_2WO_4, and their degradation efficiency (within 60 min of reaction) are 56.8%, 72.7%, 91.3% and 85.6%, respectively. Among these composites, $0.3AgI/Ag_2WO_4$ shows the highest performance. Apparently, the introduction of a proper amount of AgI can markedly facilitate the separation of electron–hole pairs, leading to the marked photocatalytic activity, which is in accordance

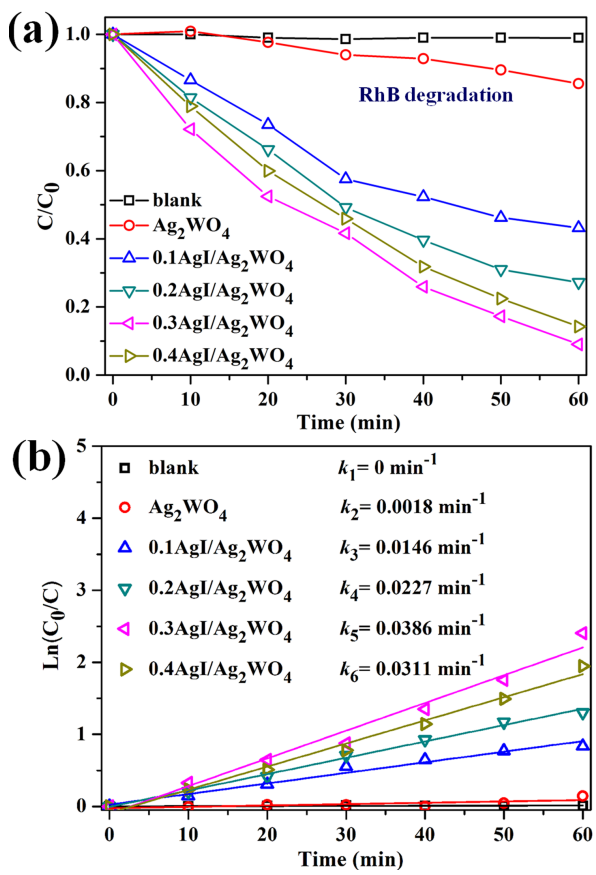

Figure 5: (a) The photocatalytic degradation and (b) degradation rate constants of RhB using different catalysts (10 mg) under visible light.

with previous reports. As the amount of AgI is further increased, the activity of $0.4AgI/Ag_2WO_4$ decreases, indicating that excessive AgI is unfavorable for photocatalytic reaction. The possible reason is that a large amount of AgI particles having a larger diameter could interfere with the light absorption of reactive sites. It has also been found that the degradation process of RhB can be fitted well with the apparent first-order model (Figure 5b). As we can see, the k value for RhB decomposition over $0.3AgI/Ag_2WO_4$ is about 0.0386 min^{-1}, which is much higher than those over other samples.

Besides RhB, MO (Figure 6a) and 4-CP (Figure S1, Supporting Information File 1) also could be efficiently degraded by $0.3AgI/Ag_2WO_4$ under visible light, indicating the outstanding photocatalytic activity of $0.3AgI/Ag_2WO_4$. In addition, the degradation rate constant of MO (Figure 6b) and 4-CP (Figure S1b, Supporting Information File 1) over catalysts were also calculated by the pseudo-first-order model. It is found that $0.3AgI/Ag_2WO_4$ still achieves the highest apparent rate constant (0.0292 min^{-1} for MO degradation and 0.0129 min^{-1} for 4-CP degradation) among all these samples.

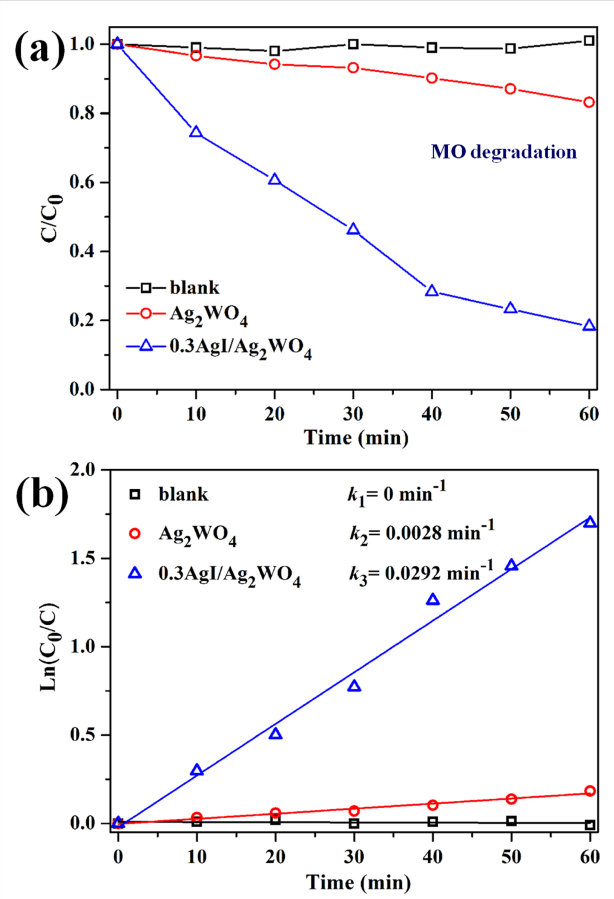

Figure 6: (a) The photocatalytic degradation and (b) degradation rate constants of MO (100 mL, 5 mg L^{-1}) using the catalysts (10 mg).

The mineralization of organic pollutants is crucial for pollutant treatment [46]. Thus, the total organic carbon (TOC) removal efficiency of RhB over $0.3AgI/Ag_2WO_4$ was examined (Figure 7). After 360 min of reaction, the TOC removal efficiency reached 67.2%, signifying that $0.3AgI/Ag_2WO_4$ can effectively mineralize RhB.

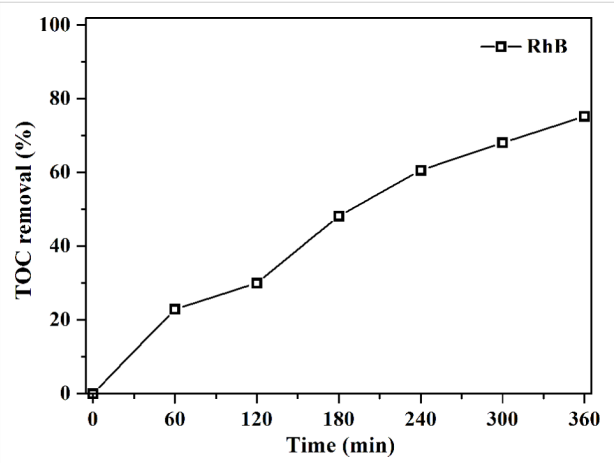

Figure 7: Total organic carbon (TOC) removal during the photocatalytic degradation of RhB in the presence of $0.3AgI/Ag_2WO_4$.

The operational lifetime of the photocatalysts is crucial for practical application [47]. To reveal the durability of $0.3AgI/Ag_2WO_4$, the cycling photocatalytic degradation of RhB was performed. As shown in Figure 8a, no apparent activity decrease was observed after five successive runs, demonstrating the good stability of the catalyst. Furthermore, the XRD pattern of the used $0.3AgI/Ag_2WO_4$ is similar to that of the fresh one (Figure 8b). These facts suggest that $0.3AgI/Ag_2WO_4$ possesses long-term stability for photocatalytic reaction.

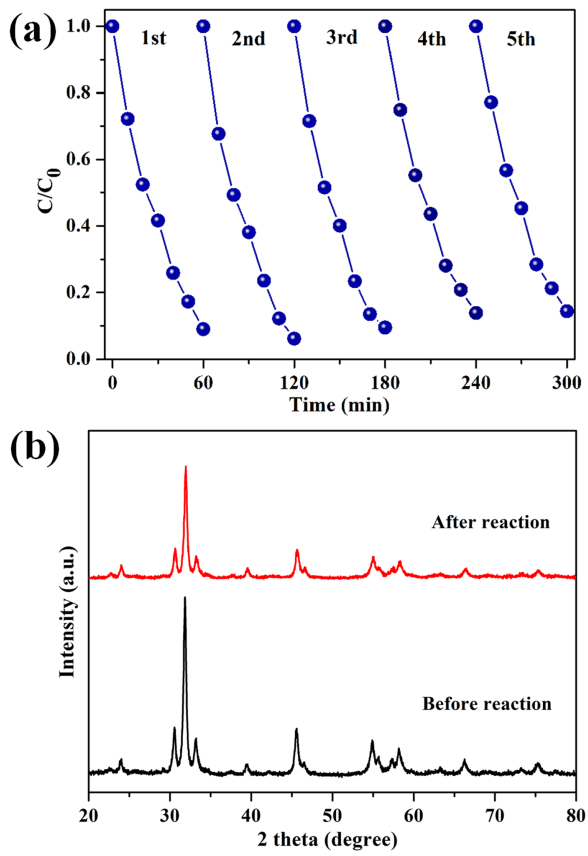

Figure 8: (a) The cycled photocatalytic degradation of RhB over $0.3AgI/Ag_2WO_4$; (b) XRD patterns of the fresh and used $0.3AgI/Ag_2WO_4$.

Photocatalytic mechanism

To elucidate the degradation mechanism, active-species trapping tests were performed during RhB degradation over $0.3AgI/Ag_2WO_4$ (Figure 9) [13,48]. Figure 9 shows the effects of various trapping agents on the RhB degradation efficiency under visible-light irradiation. When IPA was introduced, the RhB degradation efficiency slightly reduced from 91.3 % to 70.7%, suggesting that very little •OH was involved in the reac-

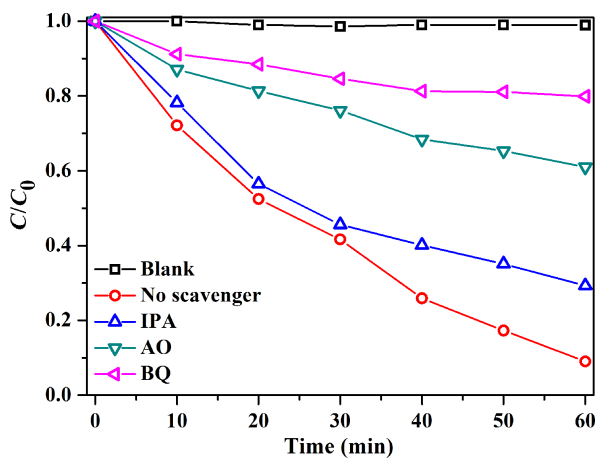

Figure 9: Active-species trapping tests over 0.3AgI/Ag_2WO_4.

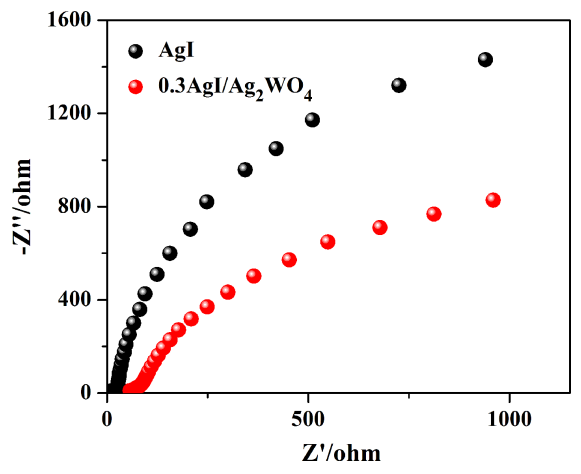

Figure 10: Electrochemical impedance spectroscopy (EIS) Nyquist plots of AgI and 0.3AgI/Ag_2WO_4.

tion. However, when benzoquinone (a superoxide radical ($\bullet O_2^-$) scavenger) or ammonium oxalate (a hole radical (h^+) scavenger) was introduced, the degradation rate of RhB was severely depressed. That is, $\bullet O^{2-}$, •OH, and h^+ were generated in the 0.3AgI/Ag_2WO_4 mediated degradation system, but $\bullet O^{2-}$ and h^+ played a more crucial role in RhB degradation.

Electrochemical impedance spectroscopy (EIS) measurement was applied to study the charge transport and separation [49]. A smaller arc radius commonly signifies a higher charge transport rate. As displayed in Figure 10, the arc radius of 0.3AgI/Ag_2WO_4 is smaller than that of AgI, suggesting that 0.3AgI/Ag_2WO_4 holds a higher charge transfer rate and a more effective separation of charge carriers.

On the basis of the above discussion, the excellent photocatalytic activity of AgI/Ag_2WO_4 is concluded to be due to the broadening of the photo-absorption range from the ultraviolet to the visible light range (Figure 4) and the formation of a heterojunction between AgI and Ag_2WO_4. The matched band alignments lead to a fascinating separation and transfer of the photo-generated electrons and holes (Figure 11) [50-52]. A heterostructure is well constructed after the in situ growth of AgI on Ag_2WO_4. Under visible light irradiation, AgI is excited to produce electrons and holes. Given the negative potential of conduction band (CB) of AgI to that of Ag_2WO_4, electrons tend to migrate from the CB of AgI to that of Ag_2WO_4, whereby the separation rate of electron–hole pairs is boosted. Consequently, the accu-

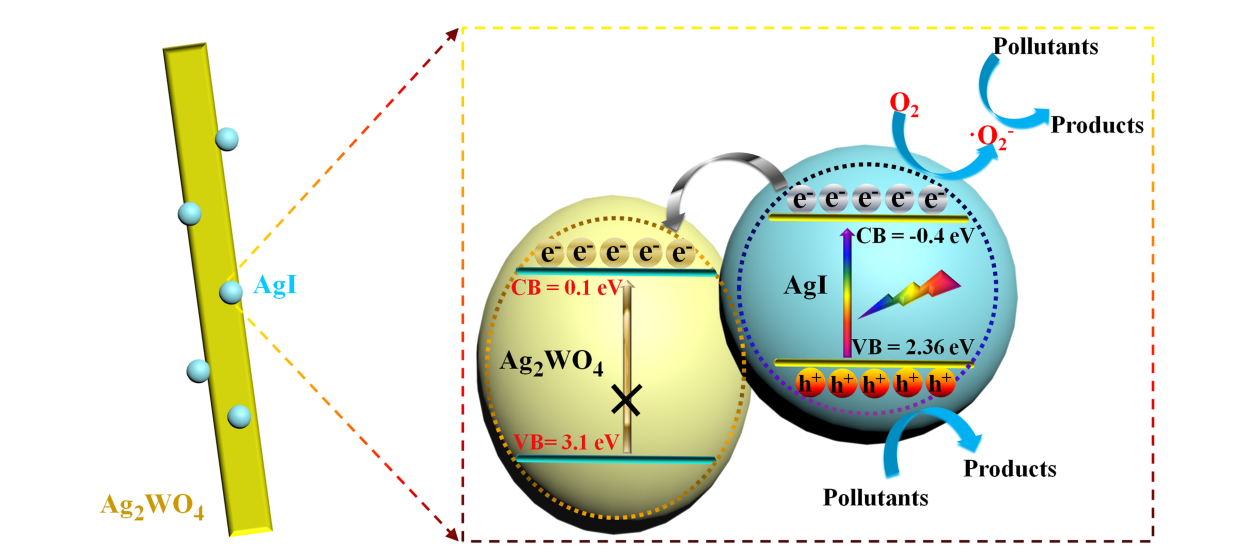

Figure 11: Schematic diagram of electron–hole pair separation and the possible reaction mechanism over the AgI/Ag_2WO_4 heterojunction under visible-light irradiation.

mulated electrons in the CB of AgI (and more holes left behind in the valence band (VB)) could readily attack the pollutant molecules, resulting in the remarkable photocatalytic performance of AgI/Ag_2WO_4.

Conclusion

In summary, a novel heterojunction photocatalyst comprised of AgI nanoparticle-decorated Ag_2WO_4 nanorods exhibiting remarkable photocatalytic performance has been prepared via a facile method. This resulting AgI/Ag_2WO_4 catalyst exhibits exceptionally high and stable photocatalytic activity for the degradation of RhB, MO and 4-CP due to its extended light absorption range and the formation of a heterojunction between AgI and Ag_2WO_4. This work not only offers a high-efficiency AgI/Ag_2WO_4 heterojunction photocatalyst, but also provides new inspiration for the development of visible-light-driven Ag-based heterojunction photocatalysts.

Experimental

Photocatalyst synthesis

All reagents were purchased from Shanghai Sinopharm Chemical Reagent Ltd. and used as received.

Ag_2WO_4 nanorods were prepared according to a previous report [41]. Briefly, $AgNO_3$ (0.01 mol L^{-1}, 100 mL) and Na_2WO_4 (0.005 mol L^{-1}, 100 mL) aqueous solutions were first prepared. Then, the $AgNO_3$ aqueous solution was slowly poured into Na_2WO_4 aqueous solution and incubated at room temperature for 12 h in the dark. Finally, the white precipitate was collected, washed successively with distilled water, and dried in vacuum at 60 °C for 12 h.

The AgI/Ag_2WO_4 nanorods were prepared by an in situ anion-exchange reaction of Ag_2WO_4 nanorods in KI aqueous solution at a temperature of 60 °C in the dark. In a typical reaction, KI (0.1 mmol, 0.2 mmol, 0.3 mmol, 0.4 mmol) was dissolved separately in 60 mL distilled water and stirred to obtain a clear solution. Then, the as-prepared Ag_2WO_4 nanorods (1 mmol) were dispersed respectively in each of the above solutions at 60 °C under stirring for 5 h. After reaction, the products with different amounts of KI (0.1 mmol, 0.2 mmol, 0.3 mmol, 0.4 mmol) were collected, washed, and finally dried in vacuum at 60 °C for 12 h. The products prepared with different amounts of KI (0.1 mmol, 0.2 mmol, 0.3 mmol, 0.4 mmol) were denoted as $0.1AgI/Ag_2WO_4$, $0.2AgI/Ag_2WO_4$, $0.3AgI/Ag_2WO_4$, and $0.4AgI/Ag_2WO_4$, respectively.

Characterization

The crystalline structure of the samples was studied by using a Bruker D8 Advance X-ray diffractometer (XRD). The images of the morphological structure were observed by a field emission scanning electron microscope (FE-SEM, Hitachi S–4800) and a high-resolution transmission electron microscope (HRTEM, JEOL JEM–2010F). Energy-dispersive X-ray (EDX) spectroscopy coupled with SEM was employed to identify the chemical composition of the sample. UV–vis diffuse reflectance spectra (UV–vis DRS) were recorded on an UV–vis spectrophotometer (Shimadzu, UV-2600).

Photocatalytic tests

The photocatalytic activity of the as-prepared samples was evaluated by the removal of RhB, MO or 4-CP under visible-light irradiation. A 300 W Xe lamp with a cut-off filter ($\lambda > 400$ nm) was used as the light source during the reaction. In each experiment, 10 mg of catalyst was dispersed in RhB (100 mL, 10 mg L^{-1}), MO (100 mL, 5 mg L^{-1}) or 4-CP (100 mL, 5 mg L^{-1}) aqueous solution. Before light illumination, the suspensions were first magnetically stirred in the dark for 1 hour. Then 2 mL of the suspension was collected and the light was switched on. With the light on and under magnetic stirring, 2 mL of the suspension was sampled at given time intervals. All suspensions were centrifuged to remove the catalyst particles. The RhB and MO concentrations were monitored by a UV-2600 spectrometer. The 4-CP concentrations were monitored by high-performance liquid chromatography (HPLC, Agilent 110 series).

The total organic carbon (TOC) experiment was carried out by dispersing 100 mg of $0.3AgI/Ag_2WO_4$ in RhB (50 mg L^{-1}, 100 mL) solution. During the reaction, a 10 mL suspension was sampled every hour and monitored by a TOC analyzer (Shimadzu TOC-VCPH).

Radical trapping experiments were conducted by introducing diverse scavengers (1 mM ammonium oxalate, 1 mM *p*-benzoquinone or 1 mM isopropanol) into the RhB (100 mL, 10 mg L^{-1}) solution.

Supporting Information

Supporting Information File 1

Additional figure.
Degradation of *para*-chlorophenol (4-CP) by 0.3AgI/Ag2WO4 under visible light and the degradation rate constants 4-CP.
[https://www.beilstein-journals.org/bjnano/content/supplementary/2190-4286-9-123-S1.tif]

Acknowledgements

This work has been financially supported by the National Natural Science Foundation of China (51708504 and

31501573), the Public Projects of Zhejiang Province (2017C32079 and LGN18E080003), the Science and Technology project of Zhoushan (2017C41006, 2016C41012, 2015C21014, 2015C21013) and the Research Startup Foundation of Zhejiang Ocean University (12215090117).

References

1. Li, S.; Zhang, L.; Wang, H.; Chen, Z.; Hu, J.; Xu, K.; Liu, J. *Sci. Rep.* **2014,** *4,* 3978. doi:10.1038/srep03978
2. Jing, P.; Lan, W.; Su, Q.; Xie, E. *Beilstein J. Nanotechnol.* **2015,** *6,* 1281–1286. doi:10.3762/bjnano.6.132
3. Zhang, G.; Liu, G.; Wang, L.; Irvine, J. T. S. *Chem. Soc. Rev.* **2016,** *45,* 5951–5984. doi:10.1039/c5cs00769k
4. Zhang, G.; Lan, Z.-A.; Wang, X. *Angew. Chem., Int. Ed.* **2016,** *55,* 15712–15727. doi:10.1002/anie.201607375
5. Ong, W.-J.; Tan, L.-L.; Ng, Y. H.; Yong, S.-T.; Chai, S.-P. *Chem. Rev.* **2016,** *116,* 7159–7329. doi:10.1021/acs.chemrev.6b00075
6. Han, W.; Li, Z.; Li, Y.; Fan, X.; Zhang, F.; Zhang, G.; Peng, W. *Front. Chem. (Lausanne, Switz.)* **2017,** *5,* 84. doi:10.3389/fchem.2017.00084
7. Ong, W.-J. *Front. Mater.* **2017,** *4,* 11. doi:10.3389/fmats.2017.00011
8. Kumar, S.; Kumar, A.; Bahuguna, A.; Sharma, V.; Krishnan, V. *Beilstein J. Nanotechnol.* **2017,** *8,* 1571–1600. doi:10.3762/bjnano.8.159
9. Huang, X.; Wang, J.; Li, T.; Wang, J.; Xu, M.; Yu, W.; Abed, A. E.; Zhang, X. *Beilstein J. Nanotechnol.* **2018,** *9,* 30–41. doi:10.3762/bjnano.9.5
10. Chen, X.; Li, N.; Kong, Z.; Ong, W.-J.; Zhao, X. *Mater. Horiz.* **2018,** *5,* 9–27. doi:10.1039/C7MH00557A
11. Zeng, S.; Kar, P.; Thakur, U. K.; Shankar, K. *Nanotechnology* **2018,** *29,* 052001. doi:10.1088/1361-6528/aa9fb1
12. Wang, H.; Zhang, L.; Chen, Z.; Hu, J.; Li, S.; Wang, Z.; Liu, J.; Wang, X. *Chem. Soc. Rev.* **2014,** *43,* 5234–5244. doi:10.1039/C4CS00126E
13. Li, S.; Shen, X.; Liu, J.; Zhang, L. *Environ. Sci.: Nano* **2017,** *4,* 1155–1167. doi:10.1039/c6en00706f
14. Li, S.; Hu, S.; Zhang, J.; Jiang, W.; Liu, J. *J. Colloid Interface Sci.* **2017,** *497,* 93–101. doi:10.1016/j.jcis.2017.02.069
15. Zhang, L.; Zhang, Q.; Xie, H.; Guo, J.; Lyu, H.; Li, Y.; Sun, Z.; Wang, H.; Guo, Z. *Appl. Catal., B* **2017,** *201,* 470–478. doi:10.1016/j.apcatb.2016.08.056
16. Laatar, F.; Moussa, H.; Alem, H.; Balan, L.; Girot, E.; Medjahdi, G.; Ezzaouia, H.; Schneider, R. *Beilstein J. Nanotechnol.* **2017,** *8,* 2741–2752. doi:10.3762/bjnano.8.273
17. Chen, C.; Ma, W.; Zhao, J. *Chem. Soc. Rev.* **2010,** *39,* 4206–4219. doi:10.1039/b921692h
18. Moniz, S. J. A.; Shevlin, S. A.; Martin, D. J.; Guo, Z.-X.; Tang, J. *Energy Environ. Sci.* **2015,** *8,* 731–759. doi:10.1039/C4EE03271C
19. Zhang, G.; Li, G.; Lan, Z.-A.; Lin, L.; Savateev, A.; Heil, T.; Zafeiratos, S.; Wang, X.; Antonietti, M. *Angew. Chem., Int. Ed.* **2017,** *129,* 13630–13634. doi:10.1002/ange.201706870
20. Zhang, G.; Lan, Z.-A.; Wang, X. *Chem. Sci.* **2017,** *8,* 5261–5274. doi:10.1039/C7SC01747B
21. Martin, D. J.; Liu, G.; Moniz, S. J. A.; Bi, Y.; Beale, A. M.; Ye, J.; Tang, J. *Chem. Soc. Rev.* **2015,** *44,* 7808–7828. doi:10.1039/C5CS00380F
22. Wang, X.; Yang, J.; Ma, S.; Zhao, D.; Dai, J.; Zhang, D. *Catal. Sci. Technol.* **2016,** *6,* 243–253. doi:10.1039/C5CY00787A
23. Liu, B.; Li, X.; Zhao, Q.; Ke, J.; Tadé, M.; Liu, S. *Appl. Catal., B* **2016,** *185,* 1–10. doi:10.1016/j.apcatb.2015.12.003
24. Yang, S.-F.; Niu, C.-G.; Huang, D.-W.; Zhang, H.; Liang, C.; Zeng, G.-M. *Environ. Sci.: Nano* **2017,** *4,* 585–595. doi:10.1039/C6EN00597G
25. Wang, X.; Li, S.; Yu, H.; Yu, J.; Liu, S. *Chem. – Eur. J.* **2011,** *17,* 7777–7780. doi:10.1002/chem.201101032
26. Xu, D.; Cheng, B.; Cao, S.; Yu, J. *Appl. Catal., B* **2015,** *164,* 380–388. doi:10.1016/j.apcatb.2014.09.051
27. Yu, C.; Li, G.; Kumar, S.; Yang, K.; Jin, R. *Adv. Mater.* **2014,** *26,* 892–898. doi:10.1002/adma.201304173
28. Jiao, Z.; Zhang, Y.; Yu, H.; Lu, G.; Ye, J.; Bi, Y. *Chem. Commun.* **2013,** *49,* 636–638. doi:10.1039/C2CC37324F
29. Zhu, X.; Wang, P.; Li, M.; Zhang, Q.; Rozhkova, E. A.; Qin, X.; Zhang, X.; Dai, Y.; Wang, Z.; Huang, B. *Catal. Sci. Technol.* **2017,** *7,* 2318–2324. doi:10.1039/C7CY00393E
30. Wang, X.; Fu, C.; Wang, P.; Yu, H.; Yu, J. *Nanotechnology* **2013,** *24,* 165602. doi:10.1088/0957-4484/24/16/165602
31. Xu, D.; Cheng, B.; Zhang, J.; Wang, W.; Yu, J.; Ho, W. *J. Mater. Chem. A* **2015,** *3,* 20153–20166. doi:10.1039/C5TA05248C
32. Li, S.; Hu, S.; Jiang, W.; Liu, Y.; Liu, J.; Wang, Z. *Mol. Catal.* **2017,** *435,* 135–143. doi:10.1016/j.mcat.2017.03.027
33. Li, J.; Yu, C.; Zheng, C.; Etogo, A.; Xie, Y.; Zhong, Y.; Hu, Y. *Mater. Res. Bull.* **2015,** *61,* 315–320. doi:10.1016/j.materresbull.2014.10.018
34. Ong, W.-J.; Putri, L. K.; Tan, L.-L.; Chai, S.-P.; Yong, S.-T. *Appl. Catal., B* **2016,** *180,* 530–543. doi:10.1016/j.apcatb.2015.06.053
35. Tang, H.; Fu, Y.; Chang, S.; Xie, S.; Tang, G. *Chin. J. Catal.* **2017,** *38,* 337–347. doi:10.1016/S1872-2067(16)62570-6
36. Dutta, D. P.; Singh, A.; Ballal, A.; Tyagi, A. K. *Eur. J. Inorg. Chem.* **2014,** *2014,* 5724–5732. doi:10.1002/ejic.201402612
37. Chen, H.; Xu, Y. *Appl. Surf. Sci.* **2014,** *319,* 319–323. doi:10.1016/j.apsusc.2014.05.115
38. Pirhashemi, M.; Habibi-Yangjeh, A. *J. Colloid Interface Sci.* **2017,** *491,* 216–229. doi:10.1016/j.jcis.2016.12.044
39. Li, Y.; Jin, R.; Fang, X.; Yang, Y.; Yang, M.; Liu, X.; Xing, Y.; Song, S. *J. Hazard. Mater.* **2016,** *313,* 219–228. doi:10.1016/j.jhazmat.2016.04.011
40. Wang, X.; Zhan, S.; Wang, Y.; Wang, P.; Yu, H.; Yu, J.; Hu, C. *J. Colloid Interface Sci.* **2014,** *422,* 30–37. doi:10.1016/j.jcis.2014.02.009
41. Wang, X.; Li, S.; Yu, H.; Yu, J. *J. Mol. Catal. A: Chem.* **2011,** *334,* 52–59. doi:10.1016/j.molcata.2010.10.022
42. Lv, J.; Dai, K.; Zhang, J.; Lu, L.; Liang, C.; Geng, L.; Wang, Z.; Yuan, G.; Zhu, G. *Appl. Surf. Sci.* **2017,** *391,* 507–515. doi:10.1016/j.apsusc.2016.05.001
43. Chen, J.; Li, S.; Hu, S.; Jiang, W. *Mater. Lett.* **2017,** *191,* 123–127. doi:10.1016/j.matlet.2016.12.096
44. Liu, X.; Hu, J.; Li, J.; Hu, Y.; Shao, Y.; Yang, H.; Tong, G.; Qian, H. *Mater. Lett.* **2013,** *91,* 129–132. doi:10.1016/j.matlet.2012.09.078
45. Pirhashemi, M.; Habibi-Yangjeh, A. *Ceram. Int.* **2017,** *43,* 13447–13460. doi:10.1016/j.ceramint.2017.07.049
46. Li, S.; Hu, S.; Jiang, W.; Liu, Y.; Liu, J.; Wang, Z. *J. Colloid Interface Sci.* **2017,** *501,* 156–163. doi:10.1016/j.jcis.2017.04.057
47. Li, S.; Hu, S.; Xu, K.; Jiang, W.; Liu, J.; Wang, Z. *Nanomaterials* **2017,** *7,* 22–34. doi:10.3390/nano7010022
48. Li, S.; Hu, S.; Xu, K.; Jiang, W.; Liu, Y.; Leng, Z.; Liu, J. *J. Colloid Interface Sci.* **2017,** *504,* 561–569. doi:10.1016/j.jcis.2017.06.018

49. Zhang, J.; Ma, Z. *J. Taiwan Inst. Chem. Eng.* **2017,** *78,* 212–218. doi:10.1016/j.jtice.2017.06.002
50. Marschall, R. *Adv. Funct. Mater.* **2014,** *24,* 2421–2440. doi:10.1002/adfm.201303214
51. Li, H.; Zhou, Y.; Tu, W.; Ye, J.; Zou, Z. *Adv. Funct. Mater.* **2015,** *25,* 998–1013. doi:10.1002/adfm.201401636
52. Shi, J. *Chem. Rev.* **2013,** *113,* 2139–2181. doi:10.1021/cr3002752

License and Terms

This is an Open Access article under the terms of the Creative Commons Attribution License (http://creativecommons.org/licenses/by/4.0), which permits unrestricted use, distribution, and reproduction in any medium, provided the original work is properly cited.

The license is subject to the *Beilstein Journal of Nanotechnology* terms and conditions: (https://www.beilstein-journals.org/bjnano)

The definitive version of this article is the electronic one which can be found at:
doi:10.3762/bjnano.9.123

BEILSTEIN JOURNAL OF NANOTECHNOLOGY

Cr(VI) remediation from aqueous environment through modified-TiO_2-mediated photocatalytic reduction

Rashmi Acharya*, Brundabana Naik and Kulamani Parida*

Review

Open Access

Address:
Centre for Nano Science and Nano Technology, Siksha 'O' Anusandhan University, Bhubaneswar 751030, India

Email:
Rashmi Acharya* - rashmiacharya@soauniversity.ac.in;
Kulamani Parida* - kulamaniparida@soauniversity.ac.in

* Corresponding author

Keywords:
charge transfer; Cr(VI) reduction; heterojunction; modified TiO_2; photocatalysis; spinel oxides

Beilstein J. Nanotechnol. **2018,** *9,* 1448–1470.
doi:10.3762/bjnano.9.137

Received: 31 October 2017
Accepted: 19 April 2018
Published: 16 May 2018

This article is part of the Thematic Series "Energy conversion, storage and environmental remediation using nanomaterials".

Guest Editor: W.-J. Ong

© 2018 Acharya et al.; licensee Beilstein-Institut.
License and terms: see end of document.

Abstract

Cr(VI) exhibits cytotoxic, mutagenic and carcinogenic properties; hence, effluents containing Cr(VI) from various industrial processes pose threat to aquatic life and downstream users. Various treatment techniques, such as chemical reduction, ion exchange, bacterial degradation, adsorption and photocatalysis, have been exploited for remediation of Cr(VI) from wastewater. Among these, photocatalysis has recently gained considerable attention. The applications of photocatalysis, such as water splitting, CO_2 reduction, pollutant degradation, organic transformation reactions, N_2 fixation, etc., towards solving the energy crisis and environmental issues are briefly discussed in the Introduction of this review. The advantages of TiO_2 as a photocatalyst and the importance of its modification for photocatalytic reduction of Cr(VI) has also been addressed. In this review, the photocatalytic activity of TiO_2 after modification with carbon-based advanced materials, metal oxides, metal sulfides and noble metals towards reduction of Cr(VI) was evaluated and compared with that of bare TiO_2. The photoactivity of dye-sensitized TiO_2 for reduction of Cr(VI) was also discussed. The mechanism for enhanced photocatalytic activity was highlighted and attributed to the resultant properties, namely, effective separation of photoinduced charge carriers, extension of the light absorption range and intensity, increase of the surface active sites, and higher photostability. Advantages and limitations for photoreduction of Cr(VI) over modified TiO_2 are depicted in the Conclusion. The various challenges that restrict the technology from practical applications in remediation of Cr(VI) from wastewater were addressed in the Conclusion section as well. The future perspectives of the field presented in this review are focused on the development of whole-solar-spectrum responsive, TiO_2-coupled photocatalysts which provide efficient photocatalytic reduction of Cr(VI) along with their good recoverability and recyclability.

Review

Introduction

The increase in the global population demands rapid growth of industrialization and urbanization, which in turn act to increase the level of environmental pollution [1-3]. Heavy metals contribute to a significant extent towards environmental pollution because of their toxicity, bio-accumulation and non-biodegradable nature. They also release large quantities of hazardous waste during their extraction. Hence, removal of toxic heavy metal ions from wastewater is considered as one of the most important environmental issues worldwide.

Among the toxic heavy metals, chromium has been a major environmental concern in wastewater treatment. It exists in various oxidation states starting from Cr(II) to Cr(VI). The aqueous environment mostly contains Cr(III) and different Cr(VI) species like $HCrO_4^-$, $Cr_2O_7^{2-}$, CrO_4^{2-} and H_2CrO_4. The speciation of these Cr(VI) species depends on pH and concentration of the solution [4,5]. Figure 1 shows the speciation of Cr(VI) at different concentration and pH. It is evident from Figure 1 that $HCrO_4^-$ and $Cr_2O_7^{2-}$ are the stable Cr(VI) species between pH 1.0 and 6.0 whereas CrO_4^{2-} predominates above pH 6.0 [6].

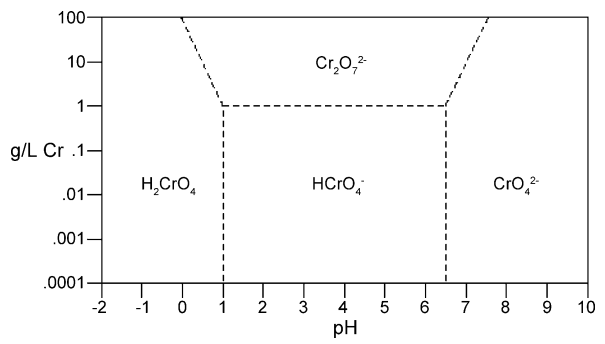

Figure 1: Speciation diagram of Cr(VI). Reprinted from [6], copyright 2016 Thermo Fisher Scientific Inc.

Cr(VI) compounds are corrosion inhibitors and are toxic and are thus mostly used in different industrial processes such as metal plating, leather tanning and pigment manufacturing. Effluents containing a high Cr(VI) concentration from these industries are undesirably discharged into the aquatic environment [7-9]. The chrome tanning process is the most preferred among 80% of tannery industries in India and most of them discharge untreated wastewater into nearby water bodies [4]. The Ganges River at Kanpur city of Uttar Pradesh contains 12.5 mg L^{-1} of Cr(VI) and the concentration of Cr(VI) in surface water in the Ranipet industrial area of Tamilnadu varies from 2.1 to 214 mg L^{-1} because of a number of tanneries are operated in and around these areas [10]. Moreover, accidental leakage and improper disposal at mining sites are also sources of Cr(VI) contamination in natural water ecosystems [11,12].

Being a strong oxidizing agent with cytotoxic, mutagenic and carcinogenic properties, Cr(VI) causes a wide range of clinical/health hazards like damage to liver and kidney, lung carcinoma, nausea, skin dermatitis, nasal membrane inflammation, ulceration, irritation of the gastro-intestinal tract and renal damage, when consumed above the permissible limit. The US Environment Protection Agency (USEPA) has placed it on the priority list of toxic pollutants and has mandated a maximum acceptable concentration of 50 μg L^{-1} in potable water [13-15].

Therefore, it is now of great importance to explore the efficient and economical ways for the treatment of Cr(VI)-rich wastewater. Various techniques, such as chemical reduction, ion exchange, bacterial degradation and adsorption, have been exploited to treat Cr(VI) [16-19]. Among these technologies, chemical reduction has extensively been investigated because it involves conversion of toxic Cr(VI) species to less toxic Cr(III) ions, which are precipitated as green precipitates of $Cr(OH)_3$ in neutral or alkaline solutions ($Ksp_{(Cr(OH)3)} = 6.3 \times 10^{-31}$] and are removed as solid wastes [20,21]. However, use of this traditional technique is restricted due to high cost and generation of secondary waste as it requires a large amount of reducing agent such as ferrous sulfate, sodium hydrogen sulfite, sodium pyrosulfite, hydrazine hydrate or sulfur dioxide [22-25].

In contrast, semiconductor-based photocatalysis has received considerable attention worldwide for its diversified potential applications to solve the global energy crisis and environmental issues in a sustainable and ecologically friendly manner [26-29]. This process involves: (i) generation of renewable energy such as H_2 and O_2 by photoelectrochemical water splitting [30-32], (ii) photocatalytic CO_2 conversion [33-37], (iii) photocatalytic nitrogen (N_2) fixation [38], (iv) selective organic transformation for the fine chemical synthesis [39-42] and (v) photodegradation of pollutants [43-49]. Semiconductor-based photocatalysis proceeds through following three steps: (1) absorption of light; (2) separation and transport of charge carriers; and (3) redox reactions on the surface of the semiconductor.

When photons with energy greater than the band gap energy of the semiconductor photocatalyst (SP) are absorbed, photogenerated electrons are excited to conduction band (CB) leaving behind holes at the valence band (VB) as per Equation 1:

$$SP \xrightarrow{h\nu} h_{VB}^{+} + e_{CB}^{-}. \quad (1)$$

These photogenerated species (electrons (e_{CB}^-) and holes (h_{VB}^+)) must be effectively separated before they can carry out appropriate redox reactions at the semiconductor surface.

Photoelectrochemical water splitting

Hydrogen (H_2) is considered as a sustainable, clean and renewable energy source to provide a solution to the global energy crisis [50]. The conventional processes, such as steam reforming, partial oxidation, coal gasification, etc. used for production of H_2 from fossil fuels (natural gas and coal), are limited because of high cost and stringent environmental regulations [51]. Photocatalytic water splitting for the production of H_2 is recognized as a green technology since it uses abundantly available water resources and inexhaustible solar energy. Therefore, substantial research in this field has been carried out since the pioneering work of Fujishima and Honda over titanium dioxide (TiO_2) electrodes under irradiation of ultraviolet (UV) light in 1972 [52]. In photocatalytic water splitting, h_{VB}^+ in the VB oxidize H_2O to produce O_2 as shown in Equation 2 only when the band edge potential at the VB is more positive than the oxidation potential of O_2 evolution ($E^0_{O2/H2O}$ = 1.23 V vs NHE).

$$2H_2O + 4h_{VB}^+ \rightarrow O_2 + 4H^+. \quad (2)$$

On the other hand, H_2 gas is produced (Equation 3) at the CB after the reduction reaction carried out by e_{CB}^- when the CB potential is more negative than the redox potential of H_2 ($E^0_{H+/H2}$ = 0 V vs NHE at pH 0.0) .

$$2H^+ + 2e_{CB}^- \rightarrow H_2 \quad (3)$$

Photocatalytic CO_2 conversion

The increasing concentration of greenhouse gases (particularly CO_2) in the atmosphere has caused environmental issues such as global warming and climate changes. The technologies used to reduce the CO_2 concentration are energy consuming and expensive [36,37]. In recent years, semiconductor-based visible-light-induced photocatalytic reduction of CO_2 has emerged as an attractive and viable approach for not only decreasing the concentration of atmospheric CO_2 but also producing energy fuels such as CH_4 [53]. In the process of photocatalytic CO_2 conversion, H_2O and CO_2 adsorbed on the surface of the semiconductor are converted to CH_4 and O_2 under irradiation of suitable light energy as shown in the following equation.

$$CO_2 + 2\,H_2O \xrightarrow{h\nu} CH_4 + 2\,O_2 \quad (4)$$

The mechanism of photocatalytic reduction of CO_2 involves the production of e_{CB}^- and h_{VB}^+ in the CB and VB, respectively, under irradiation of suitable light energy. CO_2 is reduced with the help of e_{CB}^- to CH_4 at the CB if the minimum CB potential is more negative than the reduction potential of CO_2/CH_4 (−0.24 V vs NHE) [54]. Similarly, the oxidation of water takes place by h_{VB}^+ in the VB, only when the maximum VB potential is more positive than the oxidation potential of H_2O/H^+ (+0.82 V vs NHE at pH 7.0) [55].

Photocatalytic nitrogen (N_2) fixation

The fixation of N_2 to NH_3 through semiconductor photocatalysis is gaining attention mostly due to the use of a relatively clean, cheap and easily accessible driving force (light) and ingredients (water and air). During photocatalytic N_2 fixation, e_{CB}^- are promoted to the CB, leaving h_{VB}^+ in the VB, upon irradiation with suitable light energy on the semiconductor surface. The h_{VB}^+ so formed in the VB, oxidizes H_2O to liberate O_2 with the production of protons (H^+ ions) if the VB has a more positive potential than that of the potential of O_2 evolution. With the help of these protons, e_{CB}^- in the CB, reduces N_2 molecules adsorbed on the surface of the semiconductor to NH_3 through a number of step reactions. This occurs only when the CB potential is more negative than the reduction potential of the N_2/NH_3 redox couple [38]. The overall photocatalytic N_2 fixation reaction is shown in Equation 5.

$$N_2 + 3H_2O \xrightarrow{h\nu} NH_3 + 1.5O_2 \quad (5)$$

Selective organic transformation for fine chemical synthesis

Photocatalytic, selective, organic transformations are currently preferred over the conventional processes for synthesis of fine chemicals basically due to two reasons. The first one is to restrict the use of environmentally detrimental chemical reagents such as heavy metal catalysts, oxidizing agents (Cr(VI), MnO_4^-, ClO^-, Cl_2 etc.) and reducing agents (H_2, CO). Secondly, energy consuming conditions such as high temperature and high pressure processes are to be avoided [39-42]. In semiconductor-mediated photocatalysis, the e_{CB}^- in the CB combines with molecular O_2 as shown in Equation 6 to form a superoxide anion ($O_2^{\bullet-}$), which acts as a strong oxidizing agent. Similarly, strongly oxidizing hydroxyl radicals (•OH) are produced in the VB by the reaction of h_{VB}^+ with either surface hydroxy groups (–OH) or adsorbed water molecules (Equation 7).

$$e_{CB}^- + O_2 \rightarrow O_2^{\bullet-} \quad (6)$$

$$h_{VB}^{+} + OH\ (\text{or } H_2O) \rightarrow \bullet OH \quad (7)$$

The reaction of these active species with given organic compounds under suitable reaction conditions facilitates the selective organic transformations. For example, Hu et al. demonstrated that photocatalytic, selective oxidation of alcohol to aldehyde can be carried out by h_{VB}^{+} and $O_2^{\bullet-}$ on the surface of CdS/TiO_2 nanocomposites under visible-light irradiation. The authors have also reported that $\bullet CO_2^{-}$ radicals (produced by the reaction of h_{VB}^{+} with HCO_2NH_4) and e_{CB}^{-} are responsible for the reduction of 4-nitroaniline to *p*-phenylenediamine over CdS/TiO_2 photocatalysts [56].

Photodegradation of pollutants

The principle of photocatalysis for degradation of pollutants was first applied by Frank and Bard in 1977 to reduce CN^{-} in water [57,58]. Thereafter, significant research on photocatalytic degradation of hazardous organic compounds and reduction of toxic heavy metal ions (Cr(VI)) was carried out over various semiconductors upon irradiation of suitable light energy. The mechanism of photodegradation of organic pollutants involves the formation of reactive species like $O_2^{\bullet-}$ and $^{\bullet}OH$ as per Equation 6 and Equation 7. Some of the $O_2^{\bullet-}$ species combine with H^{+} ions to form $^{\bullet}OOH$ as represented in Equation 8.

$$O_2^{\bullet-} + H^{+} \rightarrow {}^{\bullet}OOH \quad (8)$$

These active species ($^{\bullet}OH$, $O_2^{\bullet-}$ and $^{\bullet}OOH$) decompose the organic pollutants to less harmful compounds like H_2O and CO_2 (Equation 9).

$$^{\bullet}OOH + \text{dye} \rightarrow CO_2 + H_2O \quad (9)$$

Photocatalytic reduction of Cr(VI)

The semiconductor-mediated photocatalytic reduction of aqueous Cr(VI) has also recently gained tremendous importance because of its simple operation under ambient conditions, low cost, high efficiency and reusability. It uses renewable and pollution-free solar energy and produces minimal secondary waste without using toxic chemicals that follow the rules of green chemistry [59-61]. Various semiconductor photocatalysts such as CdS, ZnO, WO_3, SnO_2, and TiO_2 have been used for the photocatalytic reduction of aqueous Cr(VI) in recent years. Among them TiO_2 has extensively been investigated [62-68] due to its nontoxicity, excellent photochemical stability, great oxidizing power, chemical inertness, high abundance, low cost and environmentally friendly nature [69-72]. Moreover, photo-excited TiO_2 surfaces possess super hydrophilic properties which are evident from their excellent anti-fogging and self-cleaning abilities [73]. The unique feature of TiO_2 among other semiconductors is that the reduction of Cr(VI) occurs at its CB since the redox potential of Cr(VI) ($E^0_{Cr(VI)/Cr(III)}$ = 1.33 V in acidic medium) is more positive than the CB potential and the oxidation of water takes place simultaneously at its VB due to the more negative redox potential of H_2O ($E^0_{O2/H2O}$) = 1.23 V) than the VB potential (Figure 2) [74].

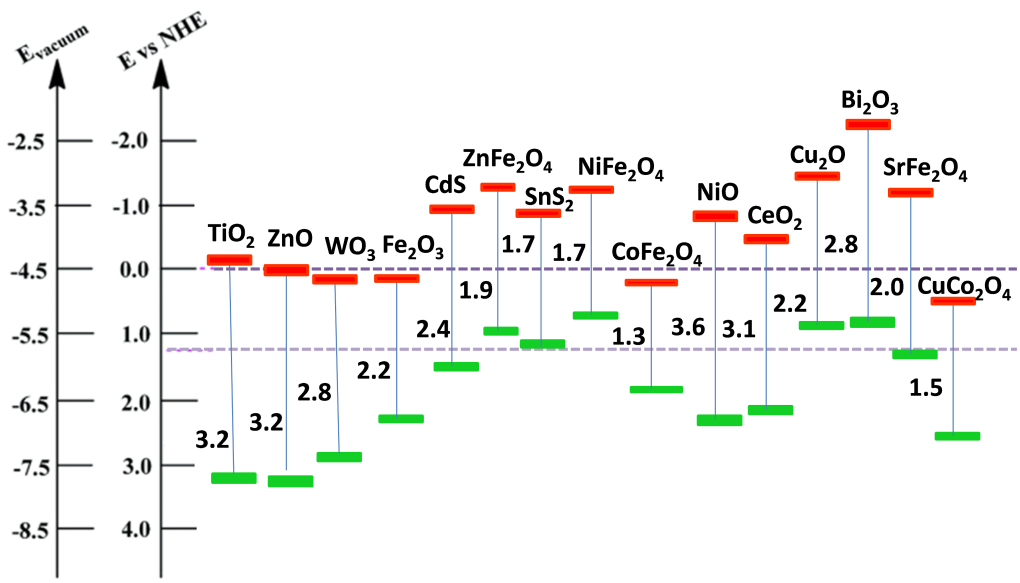

Figure 2: The band edge potentials and band gaps of different semiconductors that combine with TiO_2 for enhanced photocatalytic reduction of Cr(VI).

Therefore, TiO_2 has widely been accepted by the research community as a green photocatalyst [75]. Irradiation using UV light on TiO_2 results in the formation of e_{CB}^- and h_{VB}^+ at its CB and VB, respectively. The e_{CB}^- reduces Cr(VI) species to Cr(III) as per Equation 10 and h_{VB}^+ oxidizes water to O_2 (Equation 11).

$$Cr_2O_7^{2-} + 14H^+ + 6\,e_{CB}^- \rightarrow 2Cr^{3+} + 7H_2O \qquad E^0_{Cr(VI)/Cr(III)} = 1.33\ V \tag{10}$$

$$2H_2O + 4\,h_{VB}^+ \rightarrow O_2 + 4H^+ \qquad E^0_{O_2/H_2O} = 1.23\ V \tag{11}$$

In some cases, hole scavengers are used to facilitate the electron–hole separation process. However, application of TiO_2 in photocatalysis is largely restricted mainly due to the following reasons. (i) The wide band gap of 3.2 eV causes excitation of electrons from the valence band under irradiation of UV light, which is only 3% of the total solar radiation, resulting in limited use of pure TiO_2 in solar energy conversion [76-78]. (ii) The recombination of excited charge carriers in bare TiO_2 takes place at such a high rate that more than 90% of the recombination processes occur in 10 ns [79], leaving behind a small fraction of the excited carriers to be transferred to the surface of TiO_2. This low electron transfer rate on the interface and fast recombination of photoinduced charge carriers causes its poor photocatalytic and photoelectrochemical efficiency [80-83]. (iii) The tendency of nanostructured TiO_2 to agglomerate results in difficulties during the separation process [84]. The detailed mechanism for photocatalytic reduction of Cr(VI) by neat TiO_2 is presented in Figure 3.

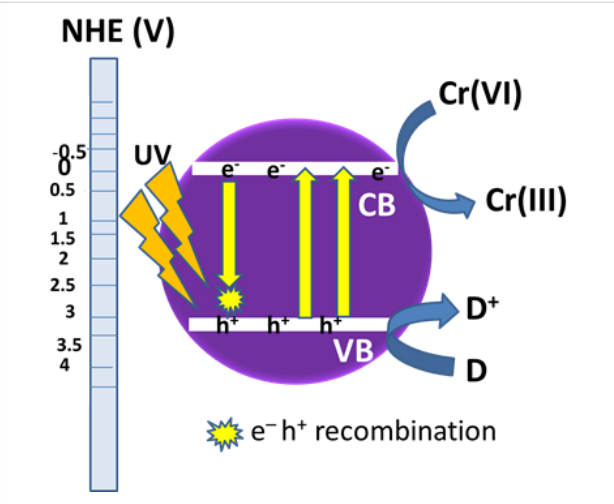

Figure 3: Mechanism of photocatalytic reduction of Cr(VI) over neat TiO_2. (D = donor, D^+ = oxidized product).

To overcome these limitations, researchers have adopted several modifications such as (i) doping with metals, nonmetals and co-doping [85-88], (ii) coupling of photosensitized nanomaterials [89], (iii) combination of heterojunction materials [90] and (iv) introduction of plasmonic photocatalysts for hot electron generation [62,76]. The modification of TiO_2 induces the enhancement of photocatalytic activity by achieving a more efficient charge separation, increasing the lifetime of the charge carriers, inhibiting the recombination of electron–hole pairs and facilitating interfacial charge transfer to adsorbed substrates [91,92]. In this review we have focused on modification of nanostructured TiO_2 with carbon-based advanced materials, noble metals, oxides and sulfides of transition metals for enhanced photocatalytic activity towards degradation of Cr(VI). The photocatalytic reduction of Cr(VI) over dye-sensitized TiO_2 is also briefly discussed. The present review article has been divided into six sections. The optical and electrochemical characteristics of modified TiO_2 photocatalysts are discussed in the first section. In the second section, we have reviewed how carbon-based advanced materials like reduced graphene oxide (RGO), carbon nanotubes (CNTs) and carbon dots (CDs) improve the photocatalytic activity and light absorption range of TiO_2 towards reduction of Cr(VI). The importance of the combination of metal oxides with TiO_2 for photocatalytic reduction of Cr(VI) was discussed in section three. Section four highlights the enhancement of photocatalytic activity and the light absorption range of TiO_2 by modification with metal sulfides. The enhancement in photocatalytic reduction of Cr(VI) over noble-metal-modified TiO_2 is depicted in section five whereas section six includes the use of dye-sensitized TiO_2 for photoreduction of Cr(VI).

Optical and electrochemical characteristics of modified TiO_2 photocatalysts

The photocatalytic activity of a photocatalyst is characterized by its optical and electrochemical properties. Modifications of titania can hinder the recombination of charge carriers and extend the light absorption range, which are evident from optical and photoelectrochemical studies. Optical studies such as ultraviolet–visible diffuse reflectance spectroscopy (UV–vis DRS) and photoluminescence spectroscopy (PL) explain the shift of the absorption range to the visible region and prohibition of recombination of charge carriers, respectively. The doping of nonmetals such as N, S, or B narrows the band gap either by creating a mid-band gap or shifting the valence band to upper positions, resulting in a redshift. Even modification of titania with semiconductor oxides or sulfides improves the light absorption. It was evident from UV–vis DRS spectra that light absorption is shifted to longer wavelengths when TiO_2 is combined with SnS_2 [93]. Moreover, it is seen that modification with sulfates induces a redox couple which facilitates the

electron transfer, and hence, better photocatalytic activity. Naik et al. have shown S and N modified titania where electron shuffle takes place by the sulfate redox couple attached to nitrogen-doped TiO_2 [63]. Hydrogenated defect-promoted black titania exhibits much higher absorption and photocatalytic activity [94,95].

The recombination and charge transfer efficiency can be understood from PL spectra. The PL emission intensity is related to the recombination of excited electrons and holes. The reduction of the PL emission peak indicates less recombination and higher charge transfer. Modified titania has a greater ability to capture the photogenerated charge carriers for enhanced photocatalytic activity. Figure 4 suggests a higher charge transfer (lower PL peak) of Cu_2O-modified TiO_2 than the pure TiO_2 [96].

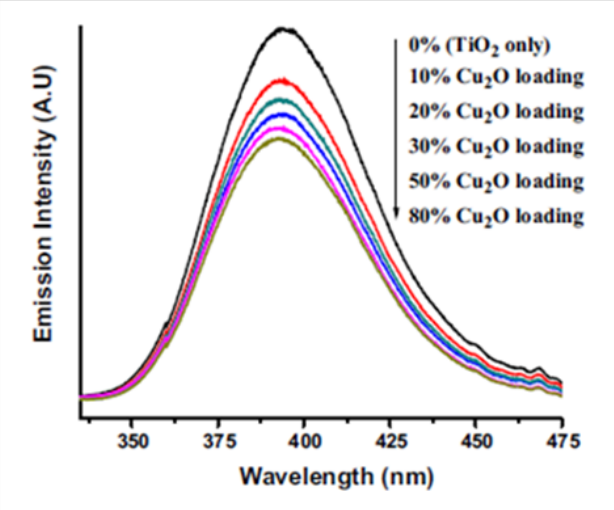

Figure 4: Photoluminescence spectra of bare TiO_2 and Cu_2O–TiO_2 samples. Reprinted from [96], copyright 2016 Springer Science+Business Media.

The enhanced charge transport efficiency can be found from photoelectrochemical studies using a three electrode system (working electrode, counter electrode and reference electrode). A current intensity–applied voltage (*I*–*V*) curve (Figure 5) obtained from linear sweep voltammetry (LSV) gives the photocurrent generation by an applied bias; the higher the current density, the better the separation of photogenerated charge carriers [97,98]. It has been shown that a more negative open circuit potential (V_{oc}), results in higher charge carrier separation and transfer [99-101]. Electrochemical impedance studies (EIS) explore the resistance of a material through a Nyquist plot. A smaller arc radius of the Nyquist plot suggests better transfer of charge carriers with lower resistance. The modification of TiO_2 with ferrites (e.g., MFe_2O_4) results in a smaller arc radius of the Nyquist plot, as shown in Figure 6, and hence, better charge transport is observed [97].

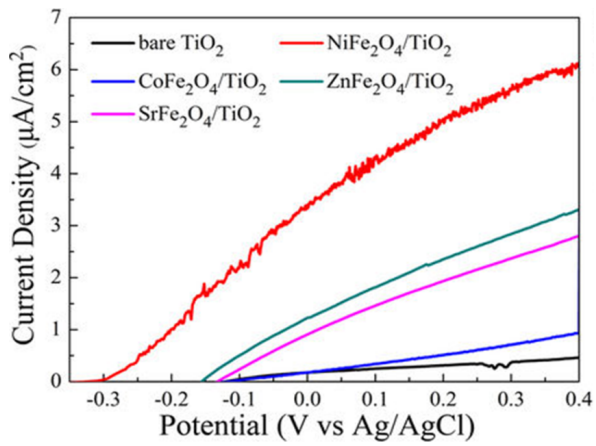

Figure 5: *I*–*V* (current intensity–applied voltage) curve. Reprinted from [97], an article distributed under the Creative Commons Attribution 4.0 license http://creativecommons.org/licenses/by/4.0/ copyright the authors of [97].

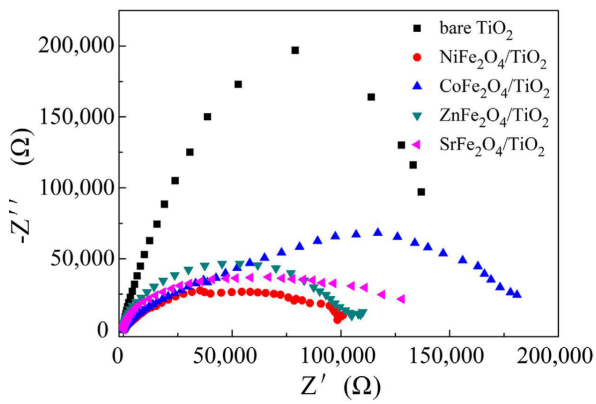

Figure 6: Comparison of arc radius of Nyquist plot between bare TiO_2 and modified TiO_2 (MFe_2O_4/ TiO_2) samples (M = Ni^{2+}, Co^{2+}, Zn^{2+}, Sr^{2+}). Reprinted from [97], an article distributed under the Creative Commons Attribution 4.0 license, http://creativecommons.org/licenses/by/4.0/, copyright the authors of [97].

Modification of TiO_2 with carbon-based advanced materials

Advanced carbon nanomaterials, such as graphene and its derivatives, carbon nanotubes (CNTs) and carbon dots (CDs), have been used to modify semiconductor photocatalysts in order to promote the separation of photoinduced species and extend the light absorption range, which are crucial for enhanced photoactivity [102-105]. In this section, we have discussed photoreduction of Cr(VI) over TiO_2 modified with reduced graphene oxides (RGOs), CNTs and CDs. The various preparation methods of modified photocatalysts, conditions for photocatalytic reduction, source of illumination, percentage of Cr(VI) reduction and the superior performance of the composite photocatalysts in comparison with TiO_2 are listed in Table 1.

Table 1: Preparation methods of modified photocatalysts, experimental conditions for photocatalytic reduction of Cr(VI), source of illumination, percentage of Cr(VI) reduction and comparison of the composite modified-photocatalyst performance with TiO_2. Reduced graphene oxide (RGO), carbon nanotubes (CNTs), carbon dots (CDs), nanorod arrays (NRAs), reduced graphene oxide hydrogel (rGH), TiO_2 hollow-core–shell microspheres (TGHMs), visible light spectrum (vis), ultraviolet light spectrum (UV).

Photocatalyst	Preparation method	pH	Initial Cr(VI) concentration (mg/L)	Dose (g/L)	Irradiation time (min)	Irradiation source	Cr(VI) reduction (%)	Comparison of performance	Ref.
Carbon-based advanced materials for TiO_2 modification									
TiO_2–RGO	microwave assisted reduction	–	10.0	1.0	–	UV	91	1.09 times more than pure TiO_2; 1.3 times more than P25	[125]
TiO_2–RGO	sol–gel combustion	2.6	12.0	0.2	240	vis	86.5	1.6 times more than pure TiO_2	[131]
TiO_2–rGH	vitamin C assisited sol–gel	5.5	5.0	1.0	30	UV	100	1.6 times more than pure TiO_2	[132]
TGHMs	hydrothermal etching reaction	–	50.0	1.0	150	vis	50	≈5 times more than pure TiO_2	[134]
TiO_2–xRGO	one-step solvothermal	2.0	20.0	0.8	210	vis	96	–	[135]
TiO_2/CNTs	hydrothermal method	3.0	20.0	1.0	180	UV	67.5	–	[139]
CDs–TNs	hydrothermal method	3.0	10.0	1.0	150	vis	100	≈7 times more than P25	[143]
Semiconductor-oxide-modified TiO_2									
ZnO–TiO_2	precipitation	3.0	20.0	1.0	120	UV	99.99	1.16 times more than pure TiO_2	[92]
ZnO–TiO_2	wetness impregnation method	5.5	20.0	1.0	–	UV	–	–	[155]
TiO_2–Fe_3O_4	polymerizable sol–gel approach	3.0	7.0	0.3	30	UV	100	–	[158]
WO_3–TiO_2 NTs	electrochemical synthesis	2.0	20.0	–	130	vis	100	1.58 times more than TiO_2 NTs	[159]
Bi_2O_3–TiO_2	sol–gel and hydrothermal methods	3.0	20.0	1.0	180	vis	73.9	reduction by TiO_2 was negligible	[178]
TiO_2–Cu_2O	sol–gel	–	5.0	0.2	90	vis	100	1.8 times more than pure TiO_2	[96]
NiO–TiO_2	sol–gel	3.5	9.6	1.0	120	vis	95	1.5 times more than pure TiO_2	[161]
$CuBi_2O_4$–TiO_2	nitrate route	4.0	30.0	1.0	<240	sunlight	98	–	[182]
$ZnFe_2O_4$–TiO_2	nitrate route	3.0	–	1.0	–	vis	–	–	[186]
$NiFe_2O_4$–TiO_2 NRAs	hydrothermal	–	12.5	–	180	vis	94.18	2.0 times more than pure TiO_2	[97]
$ZnFe_2O_4$ –TiO_2 NRAs	hydrothermal	–	12.5	–	180	vis	94.086	2.0 times more than pure TiO_2	[97]
$SrFe_2O_4$–TiO_2 NRAs	hydrothermal	–	12.5	–	180	vis	92.39	2.0 times more than pure TiO_2	[97]
Semiconductor sulfide-modified TiO_2									
CdS@TiO_2	two-step solvothermal method	–	–	–	30	vis	100	–	[198]
CdS NSPs@TiO_2	facile interfacial self-assembly strategy	–	20.0	0.333	40	vis	–	–	[199]

Table 1: Preparation methods of modified photocatalysts, experimental conditions for photocatalytic reduction of Cr(VI), source of illumination, percentage of Cr(VI) reduction and comparison of the composite modified-photocatalyst performance with TiO_2. Reduced graphene oxide (RGO), carbon nanotubes (CNTs), carbon dots (CDs), nanorod arrays (NRAs), reduced graphene oxide hydrogel (rGH), TiO_2 hollow-core–shell microspheres (TGHMs), visible light spectrum (vis), ultraviolet light spectrum (UV). (continued)

TiO_2–CdS films	one-step microwave assisted chemical bath deposition method	–	10.0	–	240	vis	93	3 times more than TiO_2 film	[200]
SnS_2–TiO_2	solvothermal reactions	–	–	–	–	vis	100	6.6 times more than pure TiO_2	[206]
Noble-metal-modified TiO_2									
Ag–TiO_2	sol–gel method	2.0	10.0	0.2	240	vis	99.8	–	[217]
Ag–Ag_2S/TiO_2	hydrothermal	3.0	10.0	1.0	360	vis	100	3 times more than pure TiO_2	[219]
Au/N–TiO_2	modified sol–gel method	–	10.0	1.0	240	vis	90	2.6 times more than pure TiO_2	[220]
Au/TiO_2−Pt	–	2.0	103.99	10.0	1440	vis	99	–	[221]
TiO_2–Au/Pt	–	≈2.5	5.0	0.25	25	UV–vis LED	100	–	[222]
TiO_2@Au@CeO_2	hydrothermal route	4.03	5.0	0.3	300	vis	95	2.96 times more than Degussa P25 TiO_2	[223]
TiO_2@Pt@CeO_2	sacrificial template route	–	2.49	0.3	150	vis	99	1.66 times more than TiO_2	[225]
Dye-sensitized TiO_2									
(Cu) PP-TiO_2	–	–	7.06	1.0	400	vis	99	–	[228]
N719 dye–TiO_2 films	–	2.0	7.06	–	60	vis	99.5	–	[229]

Photocatalytic reduction of Cr(VI) over reduced graphene oxide modified TiO_2

Graphene is a single layer of two-dimensional carbon material with graphite structure. Because of its low cost, excellent conductivity, superior chemical stability and exceptionally high specific surface area, graphene and its derivatives have attracted significant attention for various applications like photocatalysis, energy storage, nano-electronics and photovoltaics [106-110]. In photocatalytic water treatment, these are considered as promising candidates to combine with semiconductors as they have good electron collector and transporter properties. These materials suppress the recombination of charge carriers by effectively transporting the photoinduced electrons of the semiconductor, resulting in high photocatalytic activity [111-116]. In addition to this, graphene support on TiO_2 results in higher transport of photogenerated charge carriers, enrichment of light harvesting, increase of surface active sites and chemical stability of photocatalysts, which are essentially needed for a good photocatalyst [117-119]. The transport of electrons is facilitated from the semiconductor to graphene only when the work function of graphene is greater than the conduction band energy of the semiconductor. Since the work function of graphene (≈4.42 eV) [120,121] is greater than the conduction band potential of TiO_2 (−4.21 V vs vacuum) [122-124], photogenerated electrons from TiO_2 are efficiently transported to graphene, leading to enhanced photocatalytic activity (Figure 7).

Liu et al. reported that TiO_2–RGO composites exhibited enhanced photocatalytic performance for the reduction of Cr(VI) by UV light illumination as compared to pure TiO_2 and commercial P25 [125]. The enhancement in the photocatalytic activity is mainly due to two reasons: (i) inhibition in recombination of electron–hole pairs by the effective transport of photoinduced electrons from the CB of TiO_2 to RGO [126,127], and (ii) higher light absorption due to the development in surface electric charge of the oxides [128]. In addition, the red shift in the absorption edge of the TiO_2 –RGO composite as compared to pure TiO_2 is ascribed to the formation of C–O–Ti bonds [126]. It was further observed by Liu et al. that the photocatalytic reduction of Cr(VI) by the TiO_2 –RGO composite increases with increasing RGO content and reaches a maximum value of 91% for a sample containing 0.8 wt % of RGO. However, upon further increase of the RGO content, the photocatalytic perfor-

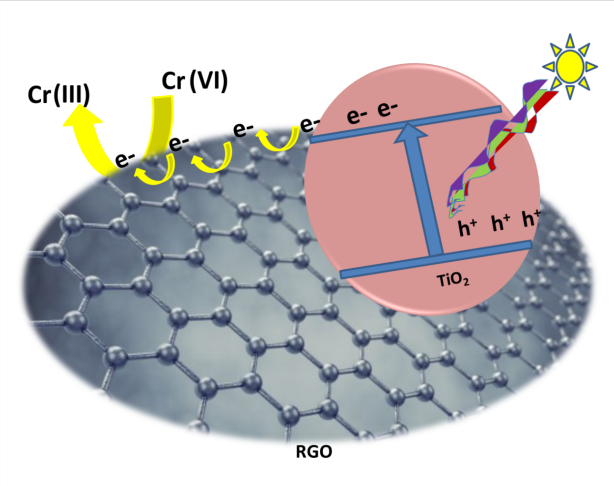

Figure 7: Transport of photoinduced electrons from the conduction band of TiO_2 through an RGO sheet, resulting in suppression of the recombination of charge carriers, which facilitates enhanced photocatalytic reduction of Cr(VI).

mance deteriorated [125]. This may be due to formation of recombination centers by excess RGO, which facilitates recombination of electron–hole pairs instead of providing an electron pathway [129,130] and maximizes the light harvesting competition between TiO_2 and RGO [128]. Zhao et al. prepared TiO_2–RGO composites with large specific surface area (104.9 m^2/g) [131]. At low pH, the large surface of the composite becomes positively charged, which adsorbed negatively charged Cr(VI) species effectively through electrostatic attraction. This facilitated the photocatalytic reduction of Cr(VI). In addition to this, the grafting of TiO_2 onto RGO forms C–O–Ti bonds, which extends light absorption of TiO_2 to longer wavelengths (visible region) for generation of photoelectrons as well as favors the effective transfer of these photoinduced electrons for enhanced photocatalytic activity towards reduction of Cr(VI). About 86.5% of Cr(VI) was photoreduced by TiO_2–RGO composites, while TiO_2 photoreduced only 54.2% of Cr(VI). They proposed following mechanism for photocatalytic reduction of Cr(VI) by the TiO_2–RGO composite. At first, negatively charged Cr(VI) species are bound with the protonated surfaces of TiO_2–RGO through electrostatic attraction. Then there a photocatalytic reduction of Cr(VI) to Cr(III) occurs under irradiation with visible light, in the second step. Third step involves either release of Cr(III) species into the solution due to their electrostatic repulsion from the protonated surfaces of TiO_2–RGO or their adsorption by deprotonated surfaces.

Li et al. fabricated a composite of TiO_2 and reduced graphene oxide hydrogel (rGH). The 3D macrostructures of rGH enhanced the accessible surface area and possessed highly porous structures with a pore size distribution of several micrometers, which enabled the use of the composite for the fast adsorption of Cr(VI) through π–π interactions and a nonporous surface adsorption technique. Moreover, the combination of rGH with TiO_2 nanospheres suppressed the recombination of photoinduced charges and facilitated the transport of photoelectrons for efficient photocatalytic reduction of Cr(VI) under irradiation with UV radiation. Thus, the fabricated photocatalyst exhibited superior synergetic performance of adsorption and photocatalysis by removing 100% Cr(VI) from a solution containing 5 mg L^{-1} of Cr(VI) within 30 minutes. Under continuous flow conditions, the percentage removal was maintained at 100% till the breakthrough point was achieved [132]. Halloysite–polyaniline core–shell nanotubes exhibited higher Cr(VI) oxyanion reduction and adsorption. The activity could be varied with concentration, pH and dopant acid [133].

Graphene-wrapped differently faceted (001 and 101) TiO_2 hollow-core–shell microspheres (TGHMs) have been fabricated by Liu et al. and were applied for efficient photocatalytic Cr(VI) reduction [134]. They prepared the photocatalyst using a direct-wrapped route followed by hydrothermal etching. The high charge separation efficiency and redox ability are due to the synergetic effect of formation of a Z scheme photocatalytic process and its facilitation by a RGO nanosheets, as shown in Figure 8.

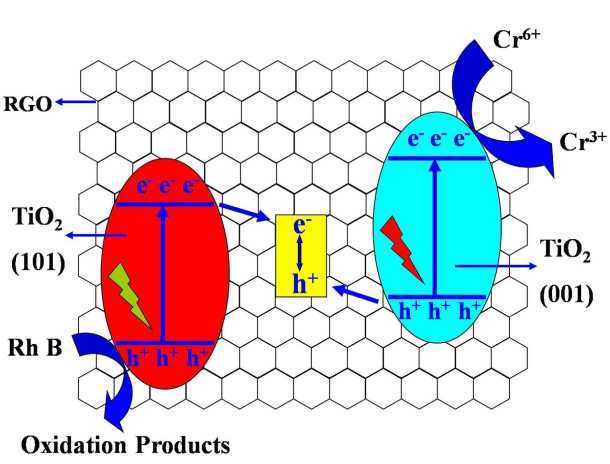

Figure 8: RGO–TiO_2 core–shell Z scheme for photocatalytic reduction of Cr(VI). Reprinted from [134], an article distributed under the Creative Commons Attribution 4.0 license, http://creativecommons.org/licenses/by/4.0/, copyright the authors of [134].

Shaikh et al. synthesized TiO_2–RGO nanocomposites with uniformly dispersed 4–9 nm diameter TiO_2 nanoparticles by a one-step solvothermal technique and evaluated its photocatalytic activity towards reduction of Cr(VI). The use of 1 wt % of RGO at acidic pH (pH 2) exhibited higher photoreduction due to the interfacial charge transfer by RGO [135]. A maximum of

96% Cr(VI) reduction was achieved. An RGO–TiO_2 composite photocatalyst was prepared by a wet impregnation route followed by surface complexation with a simple glucose molecule. The prepared photocatalyst reduced 100% of 30 mg L^{-1} Cr(VI) within 60 minutes under illumination with visible light. The role of glucose is to enhance the light absorption and separation of charge carriers through complex formation with RGO/TiO_2. This leads to the increase in photocatalytic reduction of Cr(VI) [136].

Chen et al. fabricated Mn-doped TiO_2–RGO photocatalysts through a one-pot hydrothermal method and studied the photocatalytic reduction of Cr(VI) under solar illumination. The high photocatalytic activity is attributed to the Mn doping and synergetic effect of adsorption and photocatalysis by the RGO support. The photogenerated electrons are transported from the Mn-doped TiO_2 through RGO and were found to reduce the adsorbed Cr(VI) [137]. A Ti–SBA-15–g-C_3N_4 material was also shown to exhibit higher Cr(VI) photoreduction under visible light illumination. The Ti moiety in Ti–SBA-15 can extract the conduction band electrons of g-C_3N_4 after visible light irradiation followed by transfer of electrons to Cr(VI) to produce Cr(III) [138].

Photocatalytic reduction of Cr(VI) using CNT-modified TiO_2

Carbon nanotubes (CNTs) have also been shown to possess excellent electronic and conductive properties. Waldmann et al. studied photocatalytic reduction of Cr(VI) over TiO_2-coupled CNTs. The reduction rate of Cr(VI) increased due to transfer of photogenerated electrons through CNT surfaces in the absence of sacrificial agents [139]. Huang et al. reported that a simultaneous photocatalytic degradation of Cr(VI) and phenol occurs over CNT-modified TiO_2.The high photoactivity of CNT–TiO_2 may be attributed to the synergistic effect of adsorption and electron trap properties of the CNTs [140].

Photocatalytic reduction of Cr(VI) using carbon-dot-modified TiO_2

Carbons dots (CDs) are now being widely investigated as co-catalysts because of their intriguing properties such as small size, high dispersion, abundant surface functional groups, unique photoluminescence and good electron transfer ability [141,142]. Carbon dot–TiO_2 (CD–TiO_2) nanosheet composites synthesized by a hydrothermal route were studied for photoreduction of Cr(VI) under sunlight illumination [143]. Its enhanced photoreduction capacity over TiO_2 nanosheets, P25 and CD–P25 was attributed to the better charge transfer as well as higher light absorption properties of CDs. The in situ formation of H_2O_2 promotes the photoactivity to a great extent. Zhang et al. synthesized CDs coupled with TiO_2 mesocrystals (CD/MT) in which the CDs acted as both the electron collectors and the active sites [144]. The negatively charged Cr(VI) species adsorbed effectively onto the positively charged surface of the CD/MT followed by photoreduction of Cr(VI) to Cr(III) ions that could be desorbed easily from the surface. Therefore, the selective adsorption–desorption phenomena facilitated the recycling ability of CD/MT and enhanced its photoreduction efficiency by 5.4 fold as compared to that of TiO_2.

Modifications of TiO_2 with semiconductor oxides for photocatalytic reduction of Cr(VI)

Modification of TiO_2 with semiconductor oxides having a suitable band gap is a novel approach for significant charge separation, long lifetime of the charge carriers and effective interfacial charge transfer, which are properties that lead to enhanced photocatalytic activity. This also enhances the light absorption range towards longer wavelengths. The band edge potentials and band gaps of different semiconductor oxides and sulfides are given in Figure 2.

Photocatalytic reduction of Cr(VI) over TiO_2 modified with simple transition metal oxides under UV irradiation

Transition metal oxides such as ZnO have been combined with TiO_2 to form composite photocatalysts, which are used efficiently for photocatalytic reduction of Cr(VI). ZnO has been recognized as a potential photocatalyst for extensive environmental applications because of its availability and low cost. It also possesses intriguing optical and electric properties [145-148]. Studies involving ZnO-mediated photoreduction of Cr(VI) have been carried out under illumination with UV radiation [149]. Since the conduction band edge potential for TiO_2 is more positive than that of ZnO (Figure 2), the combination of ZnO with TiO_2 can cause transfer of electrons from the CB of ZnO to that of TiO_2 and holes from the VB of TiO_2 to that of ZnO, upon UV irradiation. This leads to effective separation of photoinduced charge carriers, which was shown to enhance the photocatalytic activity of a ZnO/TiO_2 composite [150]. Hence, ZnO is considered as a suitable semiconductor to be coupled with TiO_2 [151-153].

Joubani and coworkers reported that a ZnO/TiO_2 composite photocatalysts exhibited superior photocatalytic performance by reducing a maximum of 99.99% of Cr(VI) as compared to TiO_2 and ZnO, which reduced 86.07% and 82.33% of Cr(VI), respectively. Its better performance was also evident from the consumption of the lowest electrical energy per order of magnitude for photocatalytic reduction of Cr(VI) as compared to that in UV/ZnO and UV/TiO_2 systems [92]. The rate of photocatalytic reduction of Cr(VI) was increased by increasing the photocatalyst dose [154]. Ku et al. reported that the combination of

ZnO on the surface of TiO_2 at a higher calcination temperature (>500 °C) prevents the transformation of anatase to rutile phase. It also enhances the specific surface area of the ZnO/TiO_2 composite by inhibiting aggregation and agglomeration of particles. On increasing ZnO content in the ZnO/TiO_2 composite, the rate of reduction of Cr(VI) was increased and the sample containing 2.0 mol % ZnO exhibited a maximum photocatalytic reduction of Cr(VI) in aqueous solution as the recombination of charge carriers is suppressed by the effective transfer of electrons from ZnO to TiO_2 [155]. Further increase in ZnO content created new recombination centers of electron–hole pairs by abundantly available ZnO particles, resulting in a decrease in the degradation rate [156]. The photocatalytic reduction of Cr(VI) was decreased with further increase in the calcination temperature because of the decrease in the specific surface area induced by the aggregation and agglomeration of particles [157].

TiO_2/Fe_3O_4 composite photocatalysts were synthesized through a polymerizable sol−gel route to investigate the photocatalytic reduction of Cr(VI) under UV light irradiation. The anchoring of TiO_2 over Fe_3O_4 resulted in (i) high dispersion of the active site, which is important for achieving higher reaction rate, (ii) enhancement of the photoreduction rate by decreasing the recombination of electron−hole pairs due to significant overlap of the TiO_2 band with that of Fe_3O_4 and (iii) efficient separation and recyclability of the catalyst under application of an external magnetic field because of the presence of magnetic Fe_3O_4. Therefore, the composite photocatalysts exhibited a higher rate of photoreduction of Cr(VI) as compared to the nonsupported bulk TiO_2 as well as calcined Fe_3O_4. In fact, 30% TiO_2/Fe_3O_4 has shown the highest Cr(VI) photoreduction rate due to formation of effective heterojunction by the loading of 30% TiO_2 over Fe_3O_4 [158].

Visible-light responsive, transition metal oxide modified TiO_2 for photocatalytic reduction of Cr(VI)

Two types of transition metal oxides have been combined with TiO_2 for photocatalytic reduction of Cr(VI). One type are simple metal oxides with the common formula MO_x and the other are mixed metal oxides of general formula $MM'O_x$, where M and M′ represent transition metal ions and x represents an integer.

Photocatalytic reduction of Cr(VI) by TiO_2 modified with simple metal oxides: The coupling of TiO_2 with simple metal oxides such as Bi_2O_3, WO_3, or Cu_2O is a promising strategy to design highly efficient photocatalysts [86,159,160]. The recombination of the photogenerated charge carriers is not only suppressed but also the spectral response of TiO_2 is extended to the visible spectrum by combining these metal oxides [159,161]. Moreover, formation of a p–n heterojunction is another strategy to facilitate the effective separation of electron–hole pairs and to extend light absorption to the red end of the solar spectrum [162-164]. The p–n junction is formed by coupling a p-type (hole-rich) semiconductor with n-type (electron-rich) TiO_2. As a result, the photoelectrons are diffused to the p-type semiconductor and holes are diffused to n-type TiO_2 to create an inner electric field at the interface of electron–hole diffusion. The inner electric field thus formed acts as a potential barrier to inhibit the recombination of these charge carriers by escalating the transport of electrons from p-type to n-type and that of holes from n-type to p-type semiconductors. Several studies have been reported on photocatalytic reduction of Cr(VI) by TiO_2–p-type semiconductor metal oxide heterojunctions. The mechanism for visible-light-driven photocatalytic reduction of Cr(VI) on TiO_2–p-type metal oxide heterojunctions is explained in Figure 9.

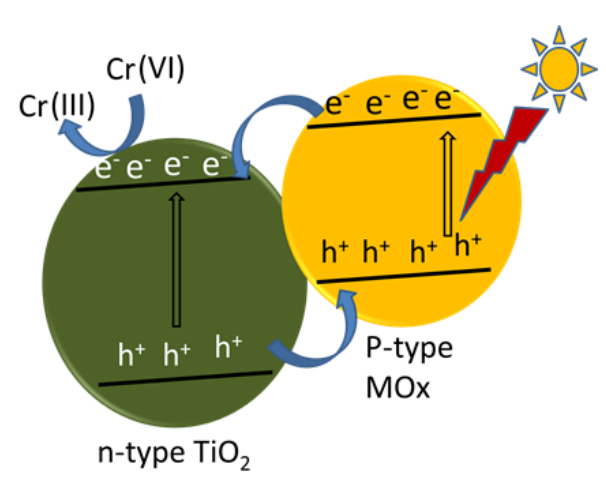

Figure 9: Mechanism for photocatalytic reduction of Cr(VI) by TiO_2–MO_x under irradiation of visible light.

Cuprous oxide (Cu_2O) is a p-type semiconductor having band gap energy of 2.17 eV. It possesses a high absorption coefficient over the whole visible region, and hence, is used as a suitable solar energy converter [160]. Moreover, it is nontoxic and highly abundant in the earth's crust [163]. Abdullah and co-investigators deposited p-type Cu_2O on TiO_2 nanoparticles to form TiO_2/Cu_2O nanocomposites, a p–n nano-heterojunction having a built-in electric field at the interfaces. This built-in electric field largely prevented the recombination of photoexcited charge carriers, resulting in increased lifetime of photocarriers, induced higher quantum efficiency and a largely enhanced photocatalytic performance. It also caused a drift of photogenerated electrons to the CB of TiO_2 for reduction of Cr(VI) to Cr(III) and that of holes to the VB of Cu_2O for oxidation of water to oxygen under visible-light irradiation. Since green colored precipitates of $Cr(OH)_3$ are formed on the sur-

faces of TiO_2/Cu_2O nanocomposites, the possibility of re-oxidation of Cr(III) to Cr(VI) was avoided although the reduction potential of Cr(III) was more negative than that of water [96]. The oxidation of water to O_2 was confirmed from the photocatalytic oxidation of water [165]. Upon increasing the content of Cu_2O in TiO_2/Cu_2O nanocomposites, photoreduction increased and reached a maximum for 30% Cu_2O. This is because 30% Cu_2O might be an appropriate amount for the formation of a p–n junction between TiO_2 and Cu_2O nanoparticles, which could efficiently separate photogenerated charge carriers for higher photoactivity under visible light. Almost 100% of a 10 ppm $K_2Cr_2O_7$ solution was degraded in 90 min. A further increase in the concentration of Cu_2O would cover the surface of TiO_2 and retard the transfer of photoelectrons to outer surface. The percentage photoreduction of Cr(VI) decreases with the increase in number of cycles, mainly due to deposition of $Cr(OH)_3$ on the surfaces of the nanocomposites. Cu_2O with several crystal structures such as octahedrons, rhombic, dodecahedrons and cubes with different facets were synthesized and their efficiency towards photocatalytic reduction of Cr(VI) was investigated by Qin et al. [166]. Zhong and co-workers fabricated Cu-decorated TiO_2 nanotube photoelectrodes by a facile hydrothermal method. The optoelectronic coupling between Cu nanoparticles and TiO_2 nanotubes enhanced the rate of transfer of electrons and subsequently suppressed the electron/hole pair recombination due to which photoreduction of Cr(VI) was increased [167]. Cu/Cu_2O-decorated TiO_2/alginate beads synthesized by a novel, environmentally friendly polyol process exhibited excellent photoreduction of Cr(VI). The superior performance may be attributed to the homogeneous TiO_2 dispersion, presence of Cu nanoparticles for facilitating charge separation processes, synergetic effect of the TiO_2/Cu_2O heterojunction and the small size of the photocatalyst [168].

Velegraki et al. fabricated 3D mesoporous networks of assembled CoO nanoparticles (CoO MNAs) to study its photocatalytic behavior towards reduction of Cr(VI) under UV and visible light irradiation. The enhanced photocatalytic performance may be attributed to its accessible pore volume, appropriate band edge positions and specific reactivity of the crystal phase. Photocatalytic reduction of Cr(VI) proceeds with simultaneous formation of molecular oxygen and hydroxyl radicals at the CoO surface [169]. NiO is a p-type semiconductor, which can conveniently be combined with different photocatalysts and the composite photocatalysts exhibit higher activity [170-172]. The introduction of nickel oxide into the TiO_2 matrix restricts the transformation of anatase to rutile phase possibly because of the presence of Ni^{2+} ions that stabilize the anatase phase. Further, the presence of NiO would hinder the aggregation of TiO_2 particles, resulting in increase of surface area and decrease of particle size of the photocatalyst [173]. An increase in the surface area of NiO/TiO_2 will lead to an increase of active sites, which enhances the photocatalytic activity. Ku et al. reported that coupling of p-type NiO with n-type TiO_2 resulted in the development of an NiO/TiO_2 photocatalyst with the formation of a p–n junction [161]. The inner electric field developed by the thus formed p–n junction separated the photogenerated holes and electrons effectively by transferring the holes into NiO and electrons into TiO_2. As a result, the coupled photocatalyst exhibited a higher photovoltage intensity and enhanced photocatalytic activity towards reduction of Cr(VI). However, the photoactivity was reduced with increasing NiO dosage because excess NiO acted as the recombination centers for photogenerated charge carriers. Therefore, a photocatalyst containing 0.1% NiO and calcined at 500 °C exhibited maximum Cr(VI) reduction. In addition to this, the introduction of NiO resulted in good contact between NiO and TiO_2, and as a consequence, the Ti 3d and Ni 3d sates are overlapped to form a modified conduction band. This caused band gap reduction resulting in a red shift of the absorption. Hence, the coupling of NiO with TiO_2 not only retards the recombination of photogenerated electrons and holes, but also extends the absorption edge towards the visible region. Moreover, an increase in the Ni content hinders aggregation of TiO_2 because an appreciable amount of NiO restricts the growth of TiO_2 particles. The inhibition in aggregation resulted in an increase of the surface area, which improves the active sites that promote the photocatalytic activity of NiO/TiO_2 particles [161].

Since the ionic radius of W^{6+} is similar to that of Ti^{4+}, coupling of TiO_2 with WO_3 forms a well-doped WO_3/TiO_2 composite, which can be applied for photocatalytic degradation of pollutants under visible light irradiation. Yang et al. reported that the photoreduction of Cr(VI) by WO_3-doped TiO_2 nanotube (NT) arrays was found to be greater than that of neat TiO_2 NT arrays [159]. This is because the incorporation of WO_3 with TiO_2 facilitates the separation of photoinduced charge carriers and shifts the absorption edge to the visible region by reducing the band gap of TiO_2 [162,174]. The highest photoreduction efficiency of Cr(VI) was obtained with WO_3/TiO_2 NTs containing 1% tungsten (W) as it provides highest photocurrent and creates photogenerated carriers with the longest lifetime. On further increasing the W content, photocurrents are decreased because excess WO_3 nanoparticles serve as the recombination centers. Moreover, the decrease of the interfacial charge space of the WO_3/TiO_2 NTs with increasing W content was also responsible for the reduction of photocurrent. Dozzi et al. synthesized a series of titanium–tungsten mixed oxides through coupling of TiO_2 with varying WO_3 percentage by a base-catalyzed sol–gel method [175]. WO_3 plays a vital role in inhibiting charge recombination for efficient charge transfer to enhance the Cr(VI) reduction.

Bi_2O_3 possesses a narrow band gap (2.8 eV), appropriate valence band position, and similar photocatalytic mechanism to that of TiO_2. Hence, it can conveniently be coupled with TiO_2 [176,177]. Yang and co-workers prepared Bi_2O_3/TiO_2 coupled photocatalysts by a sol–gel method followed by a hydrothermal technique. The coupling of Bi_2O_3 not only hindered the transformation of anatase phase to rutile but also facilitated the extension of the absorption range to the visible region. It also escalated the interfacial charge transfer between Bi_2O_3 and TiO_2. The maximum photocatalytic activity under irradiation of visible light for reduction of Cr(VI) was exhibited by 2.0% Bi_2O_3/TiO_2. A further increase in Bi_2O_3 dosage may create new recombination centers of photoinduced charge carriers, which in turn decreased the photocatalytic activity [178].

Photocatalytic reduction of Cr(VI) by TiO_2 modified with spinel metal oxides: Spinel types of metal oxides with the general formula AB_2O_4 (where A is a divalent metal ion and B is a trivalent metal ion) possess narrow band gaps which enable them to absorb throughout the visible region [179]. In addition, these materials have a high tendency for conduction of electrons because the hopping of electrons takes place between different valence states of metals in O-sites. This caused efficient transfer of charge carriers [180]. Hence, spinel oxides are being recognized as the potential photocatalysts.

The modification of TiO_2 with these metal oxides has shown promising behavior in photocatalytic Cr(VI) reduction. Gherbi et al. reported the visible-light-driven photoreduction of Cr(VI) over $CuAl_2O_4/TiO_2$ [181] with 95% reduction after 3 h irradiation at pH 2. The photoreduction follows first order kinetics with a half-life of ≈1 h and a quantum yield of 0.11%. Photocatalytic reduction of chromate ions under sunlight over $CuBi_2O_4/TiO_2$ has also been reported by Lahamar et al. A remarkable performance of 98% reduction is obtained in less than 4 h for a Cr(VI) concentration of 30 mg L^{-1} at pH ≈4 by using 1 g L^{-1} catalyst. The kinetics of chromate photoreduction is well described by the Langmuir–Hinshelwood model [182]. The heterosystem $CuCo_2O_4/TiO_2$ for the removal of Cr(VI) by photocatalytic reduction under visible light has been reported by Kebir et al. [183]. The synergetic effect of adsorption and photocatalytic reduction with proper band alignment are attributed to enhanced Cr(VI) removal from tannery wastewater.

Transition metal ferrites have also been combined with TiO_2 for photocatalytic reduction of Cr(VI) not only due to their efficient visible-light-induced photocatalytic activity, but also due to their high photostability, good super-paramagnetic behavior, nontoxicity, facile fabrication, enhanced adsorption ability, low cost and abundant availability [184,185]. The Trari group also reported photocatalytic reduction of Cr(VI) by spinel $ZnFe_2O_4$. The photoelectrons generated in $ZnFe_2O_4$ are injected into TiO_2 and subsequently transferred to Cr(VI), which is reduced to a trivalent state [186]. Gao et al. fabricated MFe_2O_4 (M = Ni^{2+}, Zn^{2+}, Co^{2+} and Sr^{2+}) modified TiO_2 nanorod arrays (NRAs) to compare their photoelectrochemical and photocatalytic activity with that of bare TiO_2 NRAs towards reduction of Cr(VI) [97]. All the modified TiO_2 NRAs exhibited strong visible light absorption due to the intrinsic band gap absorption of MFe_2O_4. Since the CB of MFe_2O_4 is more positive than that of TiO_2, the excited electrons can move from MFe_2O_4 to the CB of TiO_2, whereas the generated holes are accumulated in the VB of MFe_2O_4. This leads to an effective charge transfer, leading to longer lifetime. As a result, $NiFe_2O_4/TiO_2$ NRAs, $ZnFe_2O_4/TiO_2$ NRAs and $SrFe_2O_4/TiO_2$ NRAs exhibited enhanced photocatalytic activity as compared to bare TiO_2 NRAs. On the other hand, the CB of $CoFe_2O_4$ is more positive than that of TiO_2, while its VB is more negative than that of TiO_2 [50,187]. This made the $CoFe_2O_4/TiO_2$ heterojunction nonconductive, resulting in inefficient separation of photoexcited charge carriers and hence poor photocatalytic activity was achieved.

Metal-sulfide-modified TiO_2 as visible-light-responsive photocatalysts for photoreduction of Cr(VI)

Metal sulfides such as CdS and SnS_2 are considered as potential candidates for harvesting light in the visible region due to their narrow band gap and are being used as visible-light-responsive photocatalysts in wastewater treatment for degradation of pollutants [188-191]. These can also act as promising sensitizers for wide band gap semiconductors such as TiO_2 [192]. In this section, we discuss the photocatalytic activity of metal sulfide modified TiO_2 towards reduction of Cr(VI).

Cadmium sulfide (CdS) is an important semiconductor with a direct band gap of 2.4 eV that corresponds well with the visible region of the electromagnetic spectrum. Thus, it is considered as an excellent visible-light induced photocatalyst. Moreover, it has a more negative conduction band edge potential with respect to H^+/H_2 redox potential. However, its application is greatly limited in photocatalysis due to the very fast rate of recombination of photogenerated charge carriers and high photocorrosion affinity in the presence of solar light [193-195]. The coupling of CdS with another semiconductor is a suitable strategy to overcome these restrictions [196]. When CdS is loaded onto TiO_2, the surrounding matrix of the later prevents the former from photocorroding [197]. In addition, CdS acts as a photosensitizer to absorb visible radiation and transfers e_{CB}^- to the CB of TiO_2 by retaining h_{VB}^+ at its VB. As a result, the recombination of photoinduced species is appreciably inhibited [70]. Therefore, it is often combined with TiO_2 for enhanced

photocatalytic reduction of Cr(VI). A one-dimensional CdS–TiO_2 core–shell (CdS@TiO_2) nano-photocatalyst possessed higher reduction and selectivity of Cr(VI) due to the core–shell structure where h_{VB}^+ are trapped by the TiO_2 shell [198]. Ultrathin TiO_2-coated CdS core–shell spheres have also been prepared by Chen et al. A coating of an ultrathin TiO_2 layer on CdS nanoparticles imparts good light harvesting properties, enhanced adsorption capacity, effective charge transport and longer lifetime of excitons, for which the core–shell spheres exhibited higher efficiency for photoreduction of Cr(VI) [199]. Liu et al. reported that CdS sensitization can enhance the photocatalytic performance of TiO_2 films with a maximum reduction rate of 93% for 240 min under white LED light irradiation as compared to that of pure TiO_2 film (31%). This was attributed to an increase in light absorption and reduction in the recombination of injected electrons from CdS to TiO_2 [200].

SnS_2 is a p-type semiconductor with a band gap of 2.2 eV, which is suitable for visible light absorption ($\lambda > 420$ nm). It is harmless, chemically stable and of low cost [201]. It also exhibits relatively higher stability against oxidation and photocorrosion as compared to CdS. Hence, SnS_2 is considered as a promising photocatalyst among the semiconductor metal sulfides [202,203]. Mondal et al. have synthesized shape oriented SnS_2 nanostructures by a facile fabrication route on a large scale [204]. The nanoyarn and nanoflower materials were investigated for photoreduction of Cr(VI) under visible light. The enhanced photoactivity of nanoflowers compared to nanoyarn is attributed to a higher surface area and higher photoabsorption. Qu et al. fabricated a corallite-like nanocomposite by surface modification of SnS_2 and spirobenzopyran derivative (SPNH) with macroporous ordered siliceous foam (MOSF). SnS_2 nanocrystals exhibited enhanced photocatalytic reduction of Cr(VI) under visible light irradiation after being encapsulated into the matrix of MOSF. On the other hand, SPNH decorated on the surface of MOSF generated phenoxy groups by a ring opening reaction in the presence of UV light. The phenoxy groups thus formed could chelate soluble Cr(III) selectively through ligand coordination. As a result, the corallite-like nanocomposite detoxified Cr(VI) from the contaminated solution through visible-light-induced photocatalysis followed by adsorption of Cr(III). Furthermore, the photocatalyst is stable after three cycles of Cr(VI) degradation [205]. A heterojunction structure of SnS_2/TiO_2 nanocomposites was prepared by Zhang et al. [206]. Both VB and CB potentials of SnS_2 are more negative than those of TiO_2 due to which photogenerated electrons are transferred efficiently from the CB of SnS_2 to that of TiO_2 under irradiation of visible light, and the photogenerated holes remain on the VB of SnS_2 [207]. This leads to effective separation of photogenerated electrons and holes in SnS_2. Therefore, the lifetime of the charge carriers is increased owing to interfacial charge transfer to the adsorbed substrates [208-210]. Moreover, TiO_2 can be sensitized due to this electron transfer process. As a result, the photogenerated electrons reduced $Cr_2O_7^{2-}$ to Cr(III) and the holes oxidized water to O_2 in the absence of extra reducing agents or hole scavengers [211-213]. Hence, the nanocomposite photocatalyst (SnS_2/TiO_2) exhibited higher visible-light-driven photocatalytic activity in reduction of Cr(VI) as compared to individual SnS_2 and TiO_2. Furthermore, the composition of the composite plays an important role in obtaining high photocatalytic efficiency. When the TiO_2 content is less, the surfaces of SnS_2 nanoparticles are insufficiently covered with TiO_2 nanoparticles, resulting in inhibition of interfacial electron transfer from SnS_2 to TiO_2. This leads to poor photocatalytic activity. On the other hand, excess TiO_2 on the SnS_2 surface possibly blocked the light irradiation on SnS_2 and hindered the contact of SnS_2 with aqueous Cr(VI), due to which the rate of photoreduction is decreased. Therefore, the SnS_2/TiO_2 nanocomposite containing an adequate amount of TiO_2 (44.5%) possessed the highest photocatalytic activity for reduction of Cr(VI). It also exhibited higher photocatalytic activity in comparison with the materials prepared by simple physical mixing of SnS_2 and TiO_2 nanoparticles with the same composition. This suggested that SnS_2 and TiO_2 nanoparticles were well-mixed and closely contacted with one another in the composite. As a result, the composite provided a better heterojunction interface for effective charge transfer and decreased self-agglomeration [206]. Similar observations were obtained for SnS_2/TiO_2 nanocomposites prepared by depositing smaller nanocrystals of TiO_2 on the surface of larger SnS_2 nanocrystals [93].

Photocatalytic reduction of Cr(VI) using noble-metal-modified TiO_2

The modification of TiO_2 by noble metals such as Ag, Au, Pt and Pd facilitates photocatalytic activity due to the significant visible light absorption ability and prominent efficiency in separation of photogenerated charge carriers of these metals. Ag-loaded TiO_2 photocatalysts were prepared by Liu et al. through the photochemical impregnation method for photocatalytic reduction of Cr(VI) and the enhanced activity was attributed to the co-catalytic behavior of Ag and Ti^{3+} species formed after Ag modification [214]. Noble metal (Ag, Pd, Pt) deposited TiO_2 with oxygen vacancies were fabricated by Pan and Xu for visible-light-active photocatalytic reduction of Cr(VI). The deposition of noble metal can effectively facilitate the charge transfer efficiency of TiO_2 and oxygen vacancy creation enhances the light absorption [215]. Magnesium and silver co-impregnated TiO_2 nanoparticles were prepared by Eskandarloo et al. for photoreduction of Cr(VI) [216]. Lei et al. reported that the surface plasmon absorption of spatially confined electrons in Ag nanoparticles extends the light absorp-

tion of Ag-doped TiO_2 nanomaterials to the visible region. Furthermore, the presence of Ag ions inhibits the recombination of photoinduced species in TiO_2. As a result, Ag–TiO_2 exhibited enhanced visible light induced photoactivity towards reduction of Cr(VI) [217]. Co_3O_4/Ag/TiO_2 nanotubes arrays synthesized via photodeposition of Ag and modification of Co_3O_4 for enhancement in visible-light photoelectrochemical performance have been studied by Zhang et al. [218]. Photoreduced Ag acted as a bridge that transferred the electrons from Co_3O_4 to TiO_2 for simultaneous Cr(VI) reduction and pollutant oxidation. Hollow spherical Ag–Ag_2S–TiO_2 was prepared through in situ chemical transformation of sacrificial Cu_2S templates with $AgNO_3$ solution [219]. The enhanced photoreduction of Cr(VI) is attributed to the synergetic effect of the heterojunction and Schottky barrier that transfer the photogenerated electrons more efficiently. The introduction of Au facilitates the transfer of photogenerated electrons from the CB of TiO_2 to the Au surface, resulting in the effective separation of charge carriers and easy availability of electrons for Cr(VI) reduction. It was also reported that about 90% Cr(VI) reduction was achieved by the photocatalyst containing 0.3 wt % Au. Further increases in Au content decreased the photoreduction because an excess amount of Au can create recombination centers for electron–hole pairs and can cause a light harvesting competition between N-TiO_2 and Au [220]. Tanaka et al. investigated the reduction of Cr(VI) over the functionalized plasmonic photocatalyst Au/TiO_2−Pt under irradiation with visible light. The mechanism of photoreduction is explained in the Figure 10. Owing to the surface plasmon resonance (SPR) phenomenon, Au nanoparticles absorb photons from visible light and release electrons. These electrons are transferred from Au to the Pt co-catalyst through the CB of TiO_2, since the Fermi level of Pt is lower than that of Au. The photogenerated electrons on Pt reduce Cr(VI) to Cr(III). In the meantime, electron-deficient Au particles are converted to their original metallic state by oxidizing H_2O to O_2 [221].

The role of Au and Pt on the photocatalytic activity of anatase TiO_2 nanosheets of {001} through {101} surface heterojunction for reduction of Cr(VI) was explained by Wang et al. [222]. The conduction power of TiO_2 was greatly increased on excitation with a UV LED. Au nanoparticles deposited on the {101} facet produced hot electrons in the presence of green LED illumination due to the SPR effect. These hot electrons are transported to the Pt surface through the {101} facet, resulting in effective separation of electron–hole pairs. The photoelectrons at the surface of Pt reduced Cr(VI) to Cr(III). Overall, the {001} through {101} surface heterojunction, effective excitation of TiO_2 and the synergistic effects of selectively deposited Au and Pt significantly improved the photocatalytic reduction of Cr(VI). A TiO_2–CeO_2 multilayer-shell-based core–shell photocatalyst was prepared by Cai et al. through a hydrothermal route using polystyrene as a template, and its photocatalytic activity was evaluated [223]. Au loading into TiO_2–CeO_2 core–shell nanostructures enhanced the photoactivity owing to the sandwich nanostructure of multishells of both the oxides and Au as a co-catalyst. A similar observation has also been reported by Pandikumar et al. in the case of silicate-supported Au–TiO_2 nanotubes, where the role of Au is to enhance the charge transport by acting as a co-catalyst [224]. Li et al. studied the Pt@TiO_2@CeO_2 system for Cr(VI) photoreduction, where Pt acts as co-catalyst for better charge transport [225].

Dye-sensitized TiO_2 photocatalysts for Cr(VI) reduction

To enrich the light harvesting properties of wide band gap semiconductors, dye sensitization is a useful technique and gained huge attention after the discovery of Gratzel's dye-sensitized solar cell. The mechanism involves the excitation of dye molecules in the visible range and then charge transfer to the surface of the semiconductor. Methylene blue, erythrosin B, thioine and xanthane are some of the dyes which are commonly used in the sensitization process [226]. The Selli group have studied the

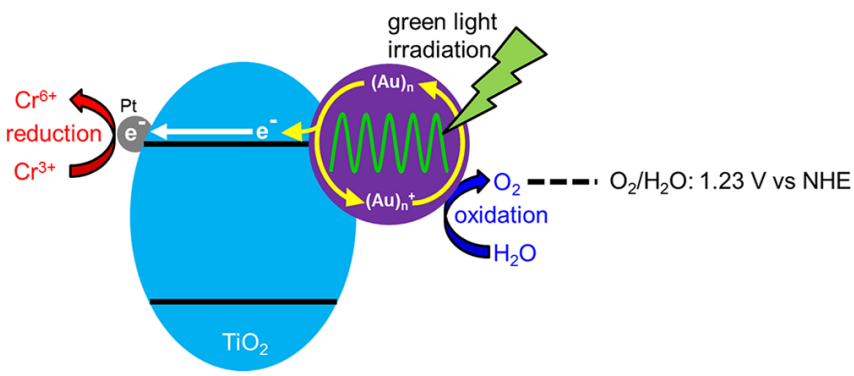

Figure 10: Mechanism of reduction of Cr(VI) using a Au/TiO_2−Pt plasmonic photocatalyst under visible-light irradiation. Reprinted with permission from [221], copyright 2013 American Chemical Society.

photocatalytic reduction of Cr(VI) by taking dye-sensitized Au-deposited TiO_2. The mechanism of the dye-sensitized TiO_2 photocatalysis for Cr(VI) reduction is illustrated in Figure 11 [227]. The extra absorption bands of porphyrin dye make it a potential dye-sensitized visible-light-active material for photocatalytic applications. Kar et al. have loaded copper (II) ion in a protoporphyrin IX–TiO_2 microsphere mixture and studied the effective photoreduction of Cr(VI) under visible light [228].

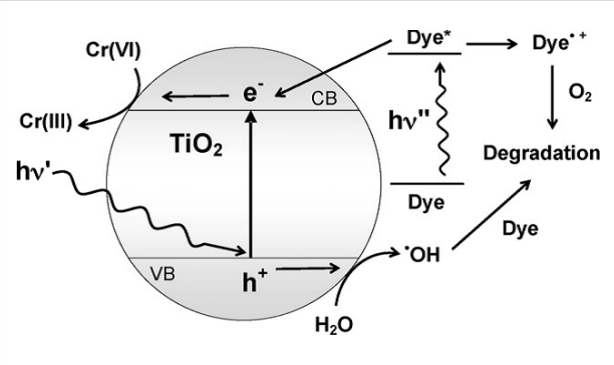

Figure 11: Mechanism for the photocatalytic Cr(VI) reduction by a dye-sensitized TiO_2 nanocatalyst.

Cr(VI) photoreduction by a TiO_2 film and a platinum anode was investigated by Wu et al. [229]. The TiO_2 film consists of two zones: a dye-sensitized zone and a catalysis zone. In the dye-sensitized zone, light absorption and charge separation are accomplished, while in the catalysis zone, the electrons convert Cr(VI) to Cr(III). Copper azomethyn-bridged phenolic phthalocyanine dye functionalized on TiO_2 was investigated for visible-light-active Cr(VI) reduction by Albay et al. [230] and an enhanced performance was observed in the presence of nanometer-sized TiO_2.

A highly effective iron metal-framework photocatalyst (MIL-68(Fe)) has been successfully prepared by Jing et al. via a facile solvothermal method under acidic conditions [231]. The metal organic framework acts as an effective photocatalyst for Cr(VI) reduction and can remove different aqueous contaminants with malachite green (MG) as a scavenger.

Stability of TiO_2-modified photocatalysts

The stability of a photocatalyst is considered as an important aspect for its industrial application. A photocatalyst can be highly stable and can efficiently be industrially applied only when it is conveniently recovered from wastewater and reused effectively without any change in crystal structure, phase or weight. Hence, it is most essential to study the recoverability and recyclability of the photocatalyst. In this section, the stability of different TiO_2-modified photocatalysts in terms of their regeneration ability and reusability in wastewater treatment for potential application in remediation of Cr(VI) has been addressed.

Liu et al. have studied recycle tests up to five cycles for a RGO–TiO_2 photocatalyst by taking fresh rhodamine B and Cr(VI) solution under stimulated solar light irradiation. Even after five cycles, there was no decrease of the performance of the catalyst, showing its high photostability [134]. RGO–Mn–TiO_2 exhibited excellent stability with the high Cr(VI) removal efficiency of 96.61%, even after three cycles [137]. Wang and co-workers reported that graphene foam/TiO_2 nanosheet hybrids could be promising in practical water treatment applications for removal of both Cr(VI) ions and organic dyes as these exhibited excellent recycle stability and easy recoverability [232]. The percentage removal of Cr(VI) was found to be 93%, 88%, and 80% for the first, second and third cycles, respectively, for TiO_2/CdS films, indicating its high photostability [200]. Challagulla et al. reported that TiO_2/Fe_3O_4 composite photocatalysts retained their efficiency towards reduction of Cr(VI) after the fourth cycle [158]. About 84% of it was recovered at the end of the fourth cycle. The recyclability of TiO_2/Fe_3O_4 up to the fourth cycle towards photoreduction of Cr(VI) and its magnetic separation is shown in Figure 12.

The regeneration of the catalyst was confirmed by XRD for the original crystal structure, XPS for the oxidation state and binding energy of the core level elements, Raman spectroscopy for retention of phases, SEM-EDS for morphology and VSM analysis for saturation magnetization. Therefore, this photocatalyst can be considered as highly stable under reaction conditions for potential applications in wastewater treatment.

Conclusion

The surface area, light absorption range, separation ability and transportation of photogenerated carriers are the parameters for controlling the performance of a photocatalyst in the remediation of Cr(VI). The modification of TiO_2 results in the enhancement of the surface area, an increase in the light absorption range and the escalation of electron–hole pair separation, which in turn tremendously promote photoactivity towards reduction of Cr(VI). The high surface area of RGO causes fast adsorption of Cr(VI) onto RGO-modified TiO_2 and facilitates transport of photoinduced electrons from TiO_2 through the surface of RGO to suppress recombination of photogenerated charge carriers effectively. This results in an enhanced photocatalytic activity towards reduction of Cr(VI). The modification of TiO_2 with RGO also extends the absorption range towards the red end of the visible spectrum. The concept of CDs in combination with TiO_2 leads to better separation of photocarriers through the consumption of holes by in-situ-formed H_2O_2. Modifications with wide band gap semiconductor oxides like ZnO provide

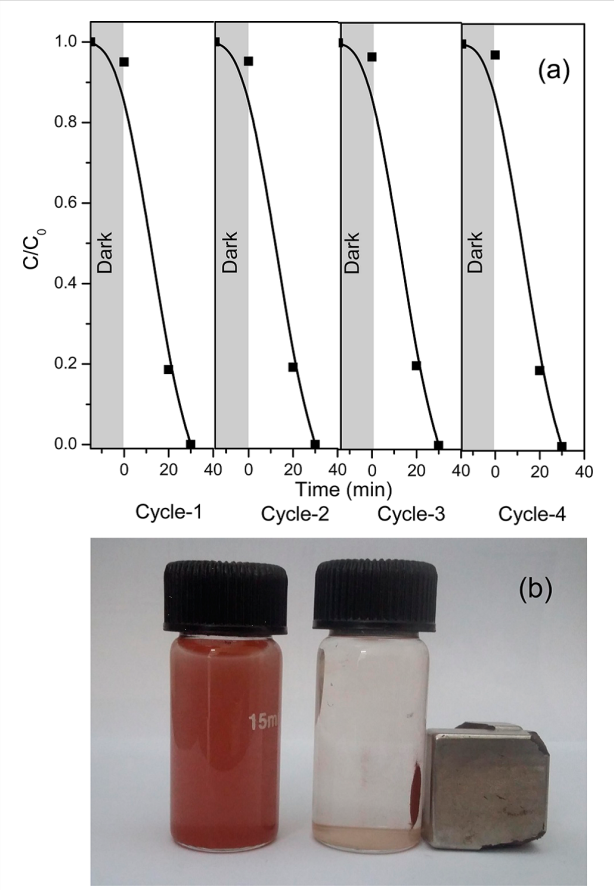

Figure 12: (a) Recyclability of TiO_2/Fe_3O_4 towards photoreduction of Cr(VI) up to 4 cycles, and (b) images of the magnetic separation of TiO_2/Fe_3O_4. Reprinted with permission from [158], copyright 2016 American Chemical Society.

good contact with TiO_2 and photocatalytic reduction of Cr(VI) was increased to a significant extent due to effective separation of charge carriers. However, the reaction is restricted to only the UV range. Narrow band gap semiconductors like metal oxides (e.g., Cu_2O), mixed metal oxides (e.g., $NiFe_2O_4$) and metal sulfides (e.g., CdS, SnS_2) form p–n heterojunctions upon coupling with TiO_2 that created an inner electric field at the interface. The inner electric field formed provides a potential barrier which suppresses the recombination of charge carriers and facilitates the transport of photoelectrons for reduction of Cr(VI). As a result, the degree of photoreduction of Cr(VI) was remarkably increased. Furthermore, the heterojunction lowered the band gap energy between Ti 3d and O 2p states of TiO_2 due to which light absorption of the coupled photocatalyst was extended to the visible region of the solar spectrum.

Dyes are used for sensitization of solar light to the surfaces of TiO_2-based semiconductors to enrich light harvesting. In this review, porphyrin, xanthane and azo dye based sensitization with TiO_2 catalysts are briefly discussed. The most effective method which was recently implemented is surface plasmon resonance metal induction in TiO_2 through hot electron transition. Au, Ag and Pt metals having plasmonic properties coupled on TiO_2-based plasmonic photocatalysts are discussed. Enhanced photoactivity has been reported when bimetallic (plasmonic and other metals) catalysts are utilized.

The photocatalytic reduction of Cr(VI) also depends on controlling experimental parameters like the pH of the solution, concentration of Cr(VI), catalyst dose and irradiation time of the photocatalyst. It was evident from Table 1 that the optimum conditions for maximum reduction of Cr(VI) varied from catalyst to catalyst, and hence, photocatalytic activity cannot be compared. However, a range of optimum conditions for maximum reduction can be listed for further research in this field. These optimal conditions are as follows: pH ≤ 5.5, initial Cr(VI) concentration 5.0–50.0 mg L^{-1}, catalyst dose 0.2–1.0 g L^{-1} and irradiation time 15–360 min. A complete reduction of Cr(VI) was carried out over WO_3/TiO_2 NTs,TiO_2/Cu_2O, CdS@TiO_2, RGO–(CdS nanowire)–TiO_2, SnS_2/TiO_2 and Ag–Ag_2S/TiO_2 composite photocatalysts by harvesting visible light. In addition, the stability of the photocatalyst is an important factor as far as industrialization of the process is concerned. A few studies revealed the adequate stability of a modified TiO_2 photocatalyst for efficient regeneration and reusability. $NiFe_2O_4$-modified TiO_2 can also be considered as a promising photocatalyst not only due to its high photocatalytic activity towards reduction of Cr(VI) under visible light illumination, but also due to its good magnetic behavior that facilitates its separation from treated solution by the application of an external magnetic field. Figure 13 represents the combination of narrow band gap semiconductors with TiO_2 for effective photocatalytic reduction of Cr(VI) under solar energy conversion.

The combination of excess RGO, metal oxides, mixed metal oxides and metal sulfides with TiO_2 resulted in the development of new recombination centers, which facilitates recombination of electron–hole pairs leading to poor photocatalytic activity.

Although photocatalytic reduction of Cr(VI) over modified TiO_2 aims to be an environmentally benign and energy sustainable process, it faces some challenges regarding its practical applicability. These are described as follows.

1. Despite the extension of the light absorption range of TiO_2 from the UV to the visible region by its modification with carbon-based smart materials, metal sulfides, noble metals or the formation of p–n junctions using narrow bandgap metal oxides, the utilization of the com-

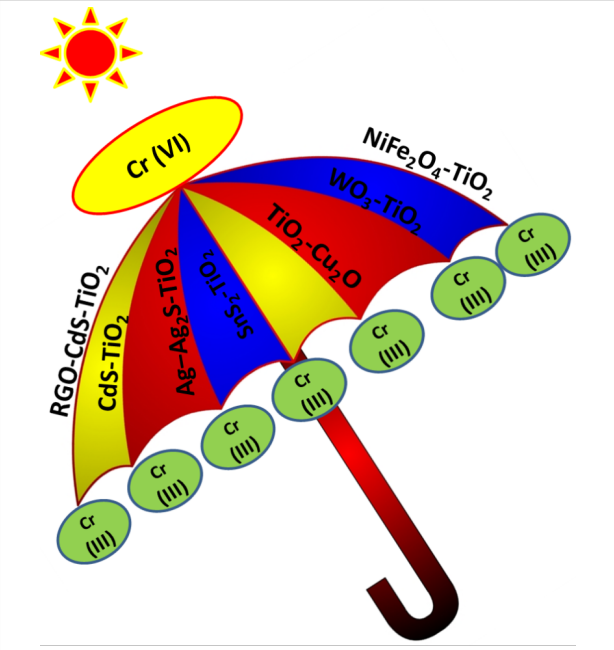

Figure 13: Summary of narrow band gap semiconductors that can be combined with TiO_2 for effective photocatalytic reduction of Cr(VI) through solar energy conversion.

plete solar spectrum is yet to be achieved for harnessing solar light for the photoreduction of Cr(VI).

2. The use of noble metals such as Ag, Au, Pt are costly, and hence, their use in designing the photocatalyst will be expensive. It is a challenge to modify TiO_2 with relatively low cost metals with the retention of the light absorption ability and properties of separation of charge carriers.
3. The remediation of Cr(VI) through photocatalysis is restricted because of loss of weight during recycling of the photocatalyst. Although a few studies reported stability of modified TiO_2 up to five cycles, the number of reuse cycles must be increased without loss in weight in order for widespread commercialization of the process.
4. During photocatalytic reduction, Cr(VI) species are converted to Cr(III) ions, which are deposited on the surface of the photocatalyst; the resulting $Cr(OH)_3$ shields the active surface sites and hinders the rate of reduction of Cr(VI). As a result, the efficiency of the photocatalyst is largely deteriorated during the recycling process. Therefore, the major challenge in photocatalytic reduction of Cr(VI) is to remove/inhibit the formation of $Cr(OH)_3$ on the photocatalyst surface.
5. Attention must be given to investigate remediation of Cr(VI) from wastewater, whereby the pH normally lies above that of the synthetic solution that is commonly used for photocatalytic reduction.

The future prospective of this review depends on the selection of appropriately modified TiO_2-based photocatalysts for enhanced photoactivity in the complete solar spectrum. The modification of TiO_2 with surface plasmon materials induces hot electron generation and injection to the CB of TiO_2 semiconductors for better charge separation as well as light harvesting, leading to higher photocatalytic efficiency. The focus on cost effectiveness should be emphasized for use of plasmonic photocatalysts such as Al, Bi, and Cu instead of Pt, Au etc. Another alternative is to couple a RGO hydrogel and $NiFe_2O_4$ with TiO_2 to set up a photocatalytic system with a low charge recombination rate and fast photoreduction of Cr(VI) by harvesting solar energy. This system will have the major advantage of easy magnetic separation of the catalyst from the treated solution. Efforts must also be given to increase the stability of the photocatalyst for long run without decrease in efficiency. Overall, a comprehensive attempt by the research community in the relevant fields should be made to overcome the differences in results between lab-scale research and large-scale industrial applications. Hopefully, the present review will provide a stepping stone to accelerate research in developing highly efficient photocatalysts with significant stability for remediation of Cr(VI) from wastewater through photocatalysis.

Acknowledgements

Authors are tankful to the management of SOA University, Bhubaneswar for their constant co-operation.

References

1. Sun, Z.; Yao, G.; Zhang, X.; Zheng, S.; Frost, R. L. *Appl. Clay Sci.* **2016,** *129,* 7–14. doi:10.1016/j.clay.2016.04.003
2. Rafatullah, M.; Sulaiman, O.; Hashim, R.; Ahmad, A. *J. Hazard. Mater.* **2010,** *177,* 70–80. doi:10.1016/j.jhazmat.2009.12.047
3. Ahmaruzzaman, M. *Adv. Colloid Interface Sci.* **2008,** *143,* 48–67. doi:10.1016/j.cis.2008.07.002
4. Dubey, R.; Bajpai, J.; Bajpai, A. K. *J. Water Process Eng.* **2015,** *5,* 83–94. doi:10.1016/j.jwpe.2015.01.004
5. Acharya, R.; Martha, S.; Parida, K. M. Remediation of Cr(VI) using clay minerals, biomasses and industrial wastes as adsorbents. In *Advanced Materials for Waste water Treatment;* Islam, S., Ed.; John Wiley & Sons, Inc.: New York, NY, U.S.A., 2017; pp 129–170. doi:10.1002/9781119407805.ch5
6. Dionex. *Determination of Cr(VI) in water, wastewater and solid waste extracts, Technical Note 26 LPN 34398-01 1M 7/96;* Dionex Corporation: Sunnyvale, CA, U.S.A., 1996. https://tools.thermofisher.com/content/sfs/brochures/TN-26-LC-Chromium-Water-Wastewater-Waste-TN71432-EN.pdf
7. Zhao, D.; Gao, X.; Wu, C.; Xie, R.; Feng, S.; Chen, C. *Appl. Surf. Sci.* **2016,** *384,* 1–9. doi:10.1016/j.apsusc.2016.05.022
8. Wan Ngah, W. S.; Hanafiah, M. A. K. M. *Bioresour. Technol.* **2008,** *99,* 3935–3948. doi:10.1016/j.biortech.2007.06.011
9. Demirbas, A. *J. Hazard. Mater.* **2008,** *157,* 220–229. doi:10.1016/j.jhazmat.2008.01.024

10. Gowd, S. S.; Govil, P. K. *Environ. Monit. Assess.* **2008,** *136,* 197–207. doi:10.1007/s10661-007-9675-5
11. Kotaś, J.; Stasicka, Z. *Environ. Pollut.* **2000,** *107,* 263–283. doi:10.1016/S0269-7491(99)00168-2
12. Kumar, A. R.; Riyazuddin, P. *Environ. Monit. Assess.* **2011,** *176,* 647–662. doi:10.1007/s10661-010-1610-5
13. Du, Y.; Wang, L.; Wang, J.; Zheng, G.; Wu, J.; Dai, H. *J. Environ. Sci.* **2015,** *29,* 71–81. doi:10.1016/j.jes.2014.06.047
14. Huang, J.; Zhang, X.; Bai, L.; Yuan, S. *J. Environ. Sci.* **2012,** *24,* 1433–1438. doi:10.1016/S1001-0742(11)60948-0
15. Sun, X.; Yang, L.; Li, Q.; Zhao, J.; Li, X.; Wang, X. *Chem. Eng. J.* **2014,** *241,* 175–183. doi:10.1016/j.cej.2013.12.051
16. Ma, H.-L.; Zhang, Y.; Hu, Q.-H.; Yan, D.; Yu, Z.-Z.; Zhai, M. *J. Mater. Chem.* **2012,** *22,* 5914–5916. doi:10.1039/c2jm00145d
17. Zheng, W.; Hu, J.; Han, Z.; Wang, Z.; Zheng, Z.; Langer, J.; Economy, J. *Chem. Commun.* **2015,** *51,* 9853–9856. doi:10.1039/C5CC02695D
18. Kathiravan, M. N.; Karthick, R.; Muthukumar, K. *Chem. Eng. J.* **2011,** *169,* 107–115. doi:10.1016/j.cej.2011.02.060
19. Fang, J.; Gu, Z.; Gang, D.; Liu, C.; Ilton, E. S.; Deng, B. *Environ. Sci. Technol.* **2007,** *41,* 4748–4753. doi:10.1021/es061969b
20. Liu, W.; Ni, J.; Yin, X. *Water Res.* **2014,** *53,* 12–25. doi:10.1016/j.watres.2013.12.043
21. Lu, A.; Zhong, S.; Chen, J.; Shi, J.; Tang, J.; Lu, X. *Environ. Sci. Technol.* **2006,** *40,* 3064–3069. doi:10.1021/es052057x
22. Ma, H.; Shen, J.; Shi, M.; Lu, X.; Li, Z.; Long, Y.; Li, N.; Ye, M. *Appl. Catal., B* **2012,** *121–122,* 198–205. doi:10.1016/j.apcatb.2012.03.023
23. Chen, G.; Sun, M.; Wei, Q.; Ma, Z.; Du, B. *Appl. Catal., B* **2012,** *125,* 282–287. doi:10.1016/j.apcatb.2012.06.001
24. Pandikumar, A.; Ramaraj, R. *J. Hazard. Mater.* **2012,** *203–204,* 244–250. doi:10.1016/j.jhazmat.2011.12.019
25. Qamar, M.; Gondal, M. A.; Yamani, Z. H. *J. Hazard. Mater.* **2011,** *187,* 258–263. doi:10.1016/j.jhazmat.2011.01.007
26. Ong, W.-J. *Front. Mater.* **2017,** *4,* 11. doi:10.3389/fmats.2017.00011
27. Ong, W.-J.; Tan, L.-L.; Ng, Y. H.; Yong, S.-T.; Chai, S.-P. *Chem. Rev.* **2016,** *116,* 7159–7329. doi:10.1021/acs.chemrev.6b00075
28. Xu, Y.; Li, A.; Yao, T.; Ma, C.; Zhang, X.; Shah, J. H.; Han, H. *ChemSusChem* **2017,** *10,* 4277–4305. doi:10.1002/cssc.201701598
29. Chen, Y.; Xin, X.; Zhang, N.; Xu, Y.-J. *Part. Part. Syst. Charact.* **2017,** *34,* 1600357. doi:10.1002/ppsc.201600357
30. Zeng, D.; Xiao, L.; Ong, W.-J.; Wu, P.; Zheng, H.; Chen, Y.; Peng, D.-L. *ChemSusChem* **2017,** *10,* 4624–4631. doi:10.1002/cssc.201701345
31. Zeng, D.; Ong, W.-J.; Zheng, H.; Wu, M.; Chen, Y.; Peng, D.-L.; Han, M.-Y. *J. Mater. Chem. A* **2017,** *5,* 16171–16178. doi:10.1039/c7ta04816e
32. Putri, L. K.; Ng, B.-J.; Ong, W.-J.; Lee, H. W.; Chang, W. S.; Chai, S.-P. *ACS Appl. Mater. Interfaces* **2017,** *9,* 4558–4569. doi:10.1021/acsami.6b12060
33. Ong, W.-J.; Tan, L.-L.; Chai, S.-P.; Yong, S.-T.; Mohamed, A. R. *Nano Res.* **2014,** *7,* 1528–1547. doi:10.1007/s12274-014-0514-z
34. Ong, W.-J.; Gui, M. M.; Chai, S.-P.; Mohamed, A. R. *RSC Adv.* **2013,** *3,* 4505–4509. doi:10.1039/C3RA00030C
35. Tan, L.-L.; Ong, W.-J.; Chai, S.-P.; Mohamed, A. R. *Chem. Commun.* **2014,** *50,* 6923–6926. doi:10.1039/c4cc01304b
36. Tan, L.-L.; Ong, W.-J.; Chai, S.-P.; Mohamed, A. R. *Chem. Eng. J.* **2016,** *283,* 1254–1263. doi:10.1016/j.cej.2015.07.093
37. Tan, L.-L.; Ong, W.-J.; Chai, S.-P.; Mohamed, A. R. *Chem. Eng. J.* **2017,** *308,* 248–255. doi:10.1016/j.cej.2016.09.050
38. Chen, X.; Li, N.; Kong, Z.; Ong, W.-J.; Zhao, X. *Mater. Horiz.* **2018,** *5,* 9. doi:10.1039/c7mh00557a
39. Liu, S.; Zhang, N.; Xu, Y.-J. *Part. Part. Syst. Charact.* **2014,** *31,* 540–556. doi:10.1002/ppsc.201300235
40. Zhao, J.; Ke, X.; Liu, H.; Huang, Y.; Chen, C.; Bo, A.; Sheng, X.; Zhu, H. *Part. Part. Syst. Charact.* **2016,** *33,* 628–634. doi:10.1002/ppsc.201600049
41. Prier, C. K.; Rankic, D. A.; MacMillan, D. W. C. *Chem. Rev.* **2013,** *113,* 5322–5363. doi:10.1021/cr300503r
42. Lang, X.; Chen, X.; Zhao, J. *Chem. Soc. Rev.* **2014,** *43,* 473–486. doi:10.1039/C3CS60188A
43. Ong, W.-J.; Voon, S.-Y.; Tan, L.-L.; Goh, B. T.; Yong, S.-T.; Chai, S.-P. *Ind. Eng. Chem. Res.* **2014,** *53,* 17333–17344. doi:10.1021/ie5027088
44. Pattnaik, S. P.; Behera, A.; Martha, S.; Acharya, R.; Parida, K. *J. Nanopart. Res.* **2018,** *20,* 10. doi:10.1007/s11051-017-4110-5
45. Kandi, D.; Martha, S.; Thirumurugan, A.; Parida, K. M. *ACS Omega* **2017,** *2,* 9040–9056. doi:10.1021/acsomega.7b01250
46. Wang, H.; Lang, X.; Hao, R.; Guo, L.; Li, J.; Wang, L.; Han, X. *Nano Energy* **2016,** *19,* 8–16. doi:10.1016/j.nanoen.2015.11.022
47. Song, H.; Son, S.-Y.; Kim, S. K.; Jung, G. Y. *Nano Res.* **2015,** *8,* 3553–3561. doi:10.1007/s12274-015-0855-2
48. Zhou, K.-G.; McManus, D.; Prestat, E.; Zhong, X.; Shin, Y.; Zhang, H.-L.; Haigh, S. J.; Casiraghi, C. *J. Mater. Chem. A* **2016,** *4,* 11666–11671. doi:10.1039/C5TA09152G
49. Behera, A.; Kandi, D.; Majhi, S. M.; Martha, S.; Parida, K. *Beilstein J. Nanotechnol.* **2018,** *9,* 436–446. doi:10.3762/bjnano.9.42
50. Kudo, A.; Miseki, Y. *Chem. Soc. Rev.* **2009,** *38,* 253–278. doi:10.1039/B800489G
51. Qu, Y.; Duan, X. *Chem. Soc. Rev.* **2013,** *42,* 2568–2580. doi:10.1039/C2CS35355E
52. Fujishima, A.; Honda, K. *Nature* **1972,** *238,* 37–38. doi:10.1038/238037a0
53. Habisreutinger, S. N.; Schmidt-Mende, L.; Stolarczyk, J. K. *Angew. Chem., Int. Ed.* **2013,** *52,* 7372–7408. doi:10.1002/anie.201207199
54. Zhu, S.; Liang, S.; Tong, Y.; An, X.; Long, J.; Fu, X.; Wang, X. *Phys. Chem. Chem. Phys.* **2015,** *17,* 9761–9770. doi:10.1039/C5CP00647C
55. Liu, Q.; Zhou, Y.; Kou, J.; Chen, X.; Tian, Z.; Gao, J.; Yan, S.; Zou, Z. *J. Am. Chem. Soc.* **2010,** *132,* 14385–14387. doi:10.1021/ja1068596
56. Hu, Z.; Quan, H.; Chen, Z.; Shao, Y.; Li, D. *Photochem. Photobiol. Sci.* **2018,** *17,* 51–59. doi:10.1039/C7PP00256D
57. Frank, S. N.; Bard, A. J. *J. Am. Chem. Soc.* **1977,** *99,* 303–304. doi:10.1021/ja00443a081
58. Frank, S. N.; Bard, A. J. *J. Phys. Chem.* **1977,** *81,* 1484–1488. doi:10.1021/j100530a011
59. Wang, Y.; Yang, W.; Zhang, L.; Hu, Y.; Lou, X. W. D. *Nanoscale* **2013,** *5,* 10864–10867. doi:10.1039/c3nr03909a
60. Padhi, D. K.; Parida, K. *J. Mater. Chem. A* **2014,** *2,* 10300–10312. doi:10.1039/C4TA00931B
61. Padhi, D. K.; Pradhan, G. K.; Parida, K. M.; Singh, S. K. *Chem. Eng. J.* **2014,** *255,* 78–88. doi:10.1016/j.cej.2014.06.039
62. Naik, B.; Kim, S. M.; Jung, C. H.; Moon, S. Y.; Kim, S. H.; Park, J. Y. *Adv. Mater. Interfaces* **2014,** *1,* 1300018. doi:10.1002/admi.201300018
63. Naik, B.; Parida, K. M.; Gopinath, C. S. *J. Phys. Chem. C* **2010,** *114,* 19473–19482. doi:10.1021/jp1083345

64. Ku, Y.; Jung, I.-L. *Water Res.* **2001,** *35,* 135–142. doi:10.1016/S0043-1354(00)00098-1
65. Yang, J.-K.; Lee, S.-M. *Chemosphere* **2006,** *63,* 1677–1684. doi:10.1016/j.chemosphere.2005.10.005
66. Parida, K. M.; Sahu, N. *J. Mol. Catal. A: Chem.* **2008,** *287,* 151–158. doi:10.1016/j.molcata.2008.02.028
67. Das, D. P.; Parida, K.; De, B. R. *J. Mol. Catal. A: Chem.* **2006,** *245,* 217–224. doi:10.1016/j.molcata.2005.10.001
68. Mohapatra, P.; Samantaray, S. K.; Parida, K. *J. Photochem. Photobiol., A: Chem.* **2005,** *170,* 189–194. doi:10.1016/j.jphotochem.2004.08.012
69. Pelaez, M.; Nolan, N. T.; Pillai, S. C.; Seery, M. K.; Falaras, P.; Kontos, A. G.; Dunlop, P. S. M.; Hamilton, J. W. J.; Byrne, J. A.; Oshea, K.; Entezari, M. H.; Dionysiou, D. D. *Appl. Catal., B* **2012,** *125,* 331–349. doi:10.1016/j.apcatb.2012.05.036
70. Daghrir, R.; Drogui, P.; Robert, D. *Ind. Eng. Chem. Res.* **2013,** *52,* 3581–3599. doi:10.1021/ie303468t
71. Asahi, R.; Morikawa, T.; Irie, H.; Ohwaki, T. *Chem. Rev.* **2014,** *114,* 9824–9852. doi:10.1021/cr5000738
72. Luo, C.; Ren, X.; Dai, Z.; Zhang, Y.; Qi, X.; Pan, C. *ACS Appl. Mater. Interfaces* **2017,** *9,* 23265–23286. doi:10.1021/acsami.7b00496
73. Wang, R.; Hashimoto, K.; Fujishima, A.; Chikuni, M.; Kojima, E.; Kitamura, A.; Shimohigoshi, M.; Watanabe, T. *Nature* **1997,** *431–432,* 388. doi:10.1038/41233
74. Bard, A. J.; Parsons, R.; Jordan, J. *Standard Potentials in Aqueous Solution;* CRC Press: Cambridge, MA, U.S.A., 1985; Vol. 6.
75. Yuan, R.; Chen, T.; Fei, E.; Lin, J.; Ding, Z.; Long, J.; Zhang, Z.; Fu, X.; Liu, P.; Wu, L.; Wang, X. *ACS Catal.* **2011,** *1,* 200–206. doi:10.1021/cs100122v
76. Park, J. Y.; Kim, S. M.; Lee, H.; Naik, B. *Catal. Lett.* **2014,** *144,* 1996–2004. doi:10.1007/s10562-014-1333-2
77. Wang, Q.; Yang, X.; Liu, D.; Chi, L.; Hou, J. *Electrochim. Acta* **2012,** *83,* 140–145. doi:10.1016/j.electacta.2012.07.092
78. DeSario, P. A.; Pietron, J. J.; DeVantier, D. E.; Brintlinger, T. H.; Stroud, R. M.; Rolison, D. R. *Nanoscale* **2013,** *5,* 8073–8083. doi:10.1039/c3nr01429k
79. Chen, X.; Mao, S. S. *Chem. Rev.* **2007,** *107,* 2891–2959. doi:10.1021/cr0500535
80. Pany, S.; Naik, B.; Martha, S.; Parida, K. *ACS Appl. Mater. Interfaces* **2014,** *6,* 839–846. doi:10.1021/am403865r
81. Naik, B.; Moon, S. Y.; Kim, S. H.; Park, J. Y. *Appl. Surf. Sci.* **2015,** *354,* 347–352. doi:10.1016/j.apsusc.2015.05.102
82. Choi, W.; Termin, A.; Hoffmann, M. R. *Angew. Chem.* **1994,** *106,* 1148–1149. doi:10.1002/ange.19941061014
83. Wang, H.; You, T.; Shi, W.; Li, J.; Guo, L. *J. Phys. Chem. C* **2012,** *116,* 6490–6494. doi:10.1021/jp212303q
84. Yao, Y.; Qin, J.; Chen, H.; Wei, F.; Liu, X.; Wang, J.; Wang, S. *J. Hazard. Mater.* **2015,** *291,* 28–37. doi:10.1016/j.jhazmat.2015.02.042
85. Parida, K. M.; Naik, B. *J. Colloid Interface Sci.* **2009,** *333,* 269–276. doi:10.1016/j.jcis.2009.02.017
86. Naik, B.; Parida, K. M.; Behera, G. C. *ChemCatChem* **2011,** *3,* 311–318. doi:10.1002/cctc.201000233
87. Naik, B.; Parida, K. M. *Ind. Eng. Chem. Res.* **2010,** *49,* 8339–8346. doi:10.1021/ie100889m
88. Naik, B.; Martha, S.; Parida, K. M. *Int. J. Hydrogen Energy* **2011,** *36,* 2794–2802. doi:10.1016/j.ijhydene.2010.11.104
89. Grätzel, M. *J. Photochem. Photobiol., C: Photochem. Rev.* **2003,** *4,* 145–153. doi:10.1016/S1389-5567(03)00026-1
90. Yu, H.; Chen, S.; Quan, X.; Zhao, H.; Zhang, Y. *Environ. Sci. Technol.* **2008,** *42,* 3791–3796. doi:10.1021/es702948e
91. Fresno, F.; Hernández-Alonso, M. D.; Tudela, D.; Coronado, J. M.; Soria, J. *Appl. Catal., B* **2008,** *84,* 598–606. doi:10.1016/j.apcatb.2008.05.015
92. Naimi-Joubani, M.; Shirzad-Siboni, M.; Yang, J.-K.; Gholami, M.; Farzadkia, M. *J. Ind. Eng. Chem. (Amsterdam, Neth.)* **2015,** *22,* 317–323. doi:10.1016/j.jiec.2014.07.025
93. Li, J.; Wang, T.; Du, X. *Sep. Purif. Technol.* **2012,** *101,* 11–17. doi:10.1016/j.seppur.2012.09.014
94. Chen, X.; Liu, L.; Peter, Y. Y.; Mao, S. S. *Science* **2011,** *331,* 746–750. doi:10.1126/science.1200448
95. Naldoni, A.; Allieta, M.; Santangelo, S.; Marelli, M.; Fabbri, F.; Cappelli, S.; Bianchi, C. L.; Psaro, R.; Dal Santo, V. *J. Am. Chem. Soc.* **2012,** *134,* 7600–7603. doi:10.1021/ja3012676
96. Abdullah, H.; Kuo, D.-H.; Chen, Y.-H. *J. Mater. Sci.* **2016,** *51,* 8209–8223. doi:10.1007/s10853-016-0096-0
97. Gao, X.; Liu, X.; Zhu, Z.; Wang, X.; Xie, Z. *Sci. Rep.* **2016,** *6,* 30543. doi:10.1038/srep30543
98. Baker, D. R.; Kamat, P. V. *Adv. Funct. Mater.* **2009,** *19,* 805–811. doi:10.1002/adfm.200801173
99. Subramanian, V.; Wolf, E. E.; Kamat, P. V. *J. Phys. Chem. B* **2003,** *107,* 7479–7485. doi:10.1021/jp0275037
100. Jakob, M.; Levanon, H.; Kamat, P. V. *Nano Lett.* **2003,** *3,* 353–358. doi:10.1021/nl0340071
101. Wood, A.; Giersig, M.; Mulvaney, P. *J. Phys. Chem. B* **2001,** *105,* 8810–8815. doi:10.1021/jp011576t
102. Li, M.; Lu, B.; Ke, Q.-F.; Guo, Y.-J.; Guo, Y.-P. *J. Hazard. Mater.* **2017,** *333,* 88–98. doi:10.1016/j.jhazmat.2017.03.019
103. Woan, K.; Pyrgiotakis, G.; Sigmund, W. *Adv. Mater.* **2009,** *21,* 2233–2239. doi:10.1002/adma.200802738
104. Huang, Q.; Tian, S.; Zeng, D.; Wang, X.; Song, W.; Li, Y.; Xiao, W.; Xie, C. *ACS Catal.* **2013,** *3,* 1477–1485. doi:10.1021/cs400080w
105. Li, Y.; Cui, W.; Liu, L.; Zong, R.; Yao, W.; Liang, Y.; Zhu, Y. *Appl. Catal., B* **2016,** *199,* 412–423. doi:10.1016/j.apcatb.2016.06.053
106. Chen, P.; Li, N.; Chen, X.; Ong, W.-J.; Zhao, X. *2D Mater.* **2018,** *5,* 014002. doi:10.1088/2053-1583/aa8d37
107. Kumar, S.; Kumar, A.; Bahuguna, A.; Sharma, V.; Krishnan, V. *Beilstein J. Nanotechnol.* **2017,** *8,* 1571–1600. doi:10.3762/bjnano.8.159
108. Han, W.; Li, Z.; Li, Y.; Fan, X.; Zhang, F.; Zhang, G.; Peng, W. *Front. Chem. (Lausanne, Switz.)* **2017,** *5,* 84. doi:10.3389/fchem.2017.00084
109. Li, Y.; Wang, H.; Xie, L.; Liang, Y.; Hong, G.; Dai, H. *J. Am. Chem. Soc.* **2011,** *133,* 7296–7299. doi:10.1021/ja201269b
110. Kemp, K. C.; Seema, H.; Saleh, M.; Le, N. H.; Mahesh, K.; Chandra, V.; Kim, K. S. *Nanoscale* **2013,** *5,* 3149–3171. doi:10.1039/c3nr33708a
111. Williams, G.; Seger, B.; Kamat, P. V. *ACS Nano* **2008,** *2,* 1487–1491. doi:10.1021/nn800251f
112. Williams, G.; Kamat, P. V. *Langmuir* **2009,** *25,* 13869–13873. doi:10.1021/la900905h
113. Loh, K. P.; Bao, Q.; Eda, G.; Chhowalla, M. *Nat. Chem.* **2010,** *2,* 1015–1024. doi:10.1038/nchem.907
114. Bang, J. H.; Suslick, K. S. *Adv. Mater.* **2010,** *22,* 1039–1059. doi:10.1002/adma.200904093
115. Su, C.; Acik, M.; Takai, K.; Lu, J.; Hao, S.-j.; Zheng, Y.; Wu, P.; Bao, Q.; Enoki, T.; Chabal, Y. J.; Loh, K. P. *Nat. Commun.* **2012,** *3,* 1298. doi:10.1038/ncomms2315

116. Liang, Y. T.; Vijayan, B. K.; Gray, K. A.; Hersam, M. C. *Nano Lett.* **2011,** *11,* 2865–2870. doi:10.1021/nl2012906
117. Kim, S. R.; Parvez, M. K.; Chhowalla, M. *Chem. Phys. Lett.* **2009,** *483,* 124–127. doi:10.1016/j.cplett.2009.10.066
118. Zhang, X.-F.; Xi, Q. *Carbon* **2011,** *49,* 3842–3850. doi:10.1016/j.carbon.2011.05.019
119. Wiedmann, S.; van Elferen, H. J.; Kurganova, E. V.; Katsnelson, M. I.; Giesbers, A. J. M.; Veligura, A.; van Wees, B. J.; Gorbachev, R. V.; Novoselov, K. S.; Maan, J. C.; Zeitler, U. *Phys. Rev. B* **2011,** *84,* 115314. doi:10.1103/PhysRevB.84.115314
120. Czerw, R.; Foley, B.; Tekleab, D.; Rubio, A.; Ajayan, P. M.; Carroll, D. L. *Phys. Rev. B* **2002,** *66,* 033408. doi:10.1103/PhysRevB.66.033408
121. Guo, C. X.; Yang, H. B.; Sheng, Z. M.; Lu, Z. S.; Song, Q. L.; Li, C. M. *Angew. Chem., Int. Ed.* **2010,** *49,* 3014–3017. doi:10.1002/anie.200906291
122. Li, Y.; Sasaki, T.; Shimizu, Y.; Koshizaki, N. *J. Am. Chem. Soc.* **2008,** *130,* 14755–14762. doi:10.1021/ja805077q
123. Xu, Y.; Schoonen, M. A. A. *Am. Mineral.* **2000,** *85,* 543–556. doi:10.2138/am-2000-0416
124. Zhu, G.; Pan, L.; Xu, T.; Zhao, Q.; Sun, Z. *J. Alloys Compd.* **2011,** *509,* 7814–7818. doi:10.1016/j.jallcom.2011.05.043
125. Liu, X.; Pan, L.; Lv, T.; Zhu, G.; Lu, T.; Sun, Z.; Sun, C. *RSC Adv.* **2011,** *1,* 1245–1249. doi:10.1039/c1ra00298h
126. Zhang, H.; Lv, X.; Li, Y.; Wang, Y.; Li, J. *ACS Nano* **2010,** *4,* 380–386. doi:10.1021/nn901221k
127. Shen, J.; Yan, B.; Shi, M.; Ma, H.; Li, N.; Ye, M. *J. Mater. Chem.* **2011,** *21,* 3415–3421. doi:10.1039/c0jm03542d
128. Xu, T.; Zhang, L.; Cheng, H.; Zhu, Y. *Appl. Catal., B* **2011,** *101,* 382–387. doi:10.1016/j.apcatb.2010.10.007
129. Yang, N.; Zhai, J.; Wang, D.; Chen, Y.; Jiang, L. *ACS Nano* **2010,** *4,* 887–894. doi:10.1021/nn901660v
130. Zhu, G.; Xu, T.; Lv, T.; Pan, L.; Zhao, Q.; Sun, Z. *J. Electroanal. Chem.* **2011,** *650,* 248–251. doi:10.1016/j.jelechem.2010.10.011
131. Zhao, Y.; Zhao, D.; Chen, C.; Wang, X. *J. Colloid Interface Sci.* **2013,** *405,* 211–217. doi:10.1016/j.jcis.2013.05.004
132. Li, Y.; Cui, W.; Liu, L.; Zong, R.; Yao, W.; Liang, Y.; Zhu, Y. *Appl. Catal., B* **2016,** *199,* 412–423. doi:10.1016/j.apcatb.2016.06.053
133. Zhou, T.; Li, C.; Jin, H.; Lian, Y.; Han, W. *ACS Appl. Mater. Interfaces* **2017,** *9,* 6030–6043. doi:10.1021/acsami.6b14079
134. Liu, H.; Liu, S.; Zhang, Z.; Dong, X.; Liu, T. *Sci. Rep.* **2016,** *6,* 33839. doi:10.1038/srep33839
135. Shaikh, A.; Mishra, S. P.; Mohapatra, P.; Parida, S. *J. Nanopart. Res.* **2017,** *19,* 206. doi:10.1007/s11051-017-3894-7
136. Karthik, P.; Neppolian, B. *J. Environ. Chem. Eng.*, in press. doi:10.1016/j.jece.2017.05.028
137. Chen, Z.; Li, Y.; Guo, M.; Xu, F.; Wang, P.; Du, Y.; Na, P. *J. Hazard. Mater.* **2016,** *310,* 188–198. doi:10.1016/j.jhazmat.2016.02.034
138. Liu, F.; Yu, J.; Tu, G.; Qu, L.; Xiao, J.; Liu, Y.; Wang, L.; Lei, J.; Zhang, J. *Appl. Catal., B* **2017,** *201,* 1–11. doi:10.1016/j.apcatb.2016.08.001
139. Shaham-Waldmann, N.; Paz, Y. *Chem. Eng. J.* **2013,** *231,* 49–58. doi:10.1016/j.cej.2013.07.021
140. Huang, L.; Chan, Q.; Wu, X.; Wang, H.; Liu, Y. *J. Ind. Eng. Chem.* **2012,** *18,* 574–580. doi:10.1016/j.jiec.2011.11.060
141. Li, L.; Wu, G.; Yang, G.; Peng, J.; Zhao, J.; Zhu, J.-J. *Nanoscale* **2013,** *5,* 4015–4039. doi:10.1039/c3nr33849e
142. Lim, S. Y.; Shen, W.; Gao, Z. *Chem. Soc. Rev.* **2014,** *44,* 362–381. doi:10.1039/C4CS00269E
143. Li, Y.; Liu, Z.; Wu, Y.; Chen, J.; Zhao, J.; Jin, F.; Na, P. *Appl. Catal., B* **2018,** *224,* 508–517. doi:10.1016/j.apcatb.2017.10.023
144. Zhang, Y.; Xu, M.; Li, H.; Ge, H.; Bian, Z. *Appl. Catal., B* **2018,** *226,* 213–219. doi:10.1016/j.apcatb.2017.12.053
145. Georgekutty, R.; Seery, M. K.; Pillai, S. C. *J. Phys. Chem. C* **2008,** *112,* 13563–13570. doi:10.1021/jp802729a
146. Lin, D.; Wu, H.; Zhang, R.; Pan, W. *Chem. Mater.* **2009,** *21,* 3479–3484. doi:10.1021/cm900225p
147. Shifu, C.; Wei, Z.; Sujuan, Z.; Wei, L. *Chem. Eng. J.* **2009,** *148,* 263–269. doi:10.1016/j.cej.2008.08.039
148. Tak, Y.; Yong, K. *J. Phys. Chem. B* **2005,** *109,* 19263–19269. doi:10.1021/jp0538767
149. Liu, X.; Lv, T.; Pan, L.; Sun, Z.; Sun, C. Q. *Desalin. Water Treat.* **2012,** *42,* 216–221. doi:10.1080/19443994.2012.683161
150. Serpone, N.; Maruthamuthu, P.; Pichat, P.; Pelizzetti, E.; Hidaka, H. *J. Photochem. Photobiol., A: Chem.* **1995,** *85,* 247–255. doi:10.1016/1010-6030(94)03906-B
151. Wang, X.; Pehkonen, S. O.; Ray, A. K. *Ind. Eng. Chem. Res.* **2004,** *43,* 1665–1672. doi:10.1021/ie030580j
152. Wang, L.; Wang, N.; Zhu, L.; Yu, H.; Tang, H. *J. Hazard. Mater.* **2008,** *152,* 93–99. doi:10.1016/j.jhazmat.2007.06.063
153. Wang, N.; Zhu, L.; Deng, K.; She, Y.; Yu, Y.; Tang, H. *Appl. Catal., B* **2010,** *95,* 400–407. doi:10.1016/j.apcatb.2010.01.019
154. Yang, J. K.; Lee, S. M.; Siboni, M. S. *Environ. Technol.* **2012,** *33,* 2027–2032. doi:10.1080/09593330.2012.655325
155. Ku, Y.; Huang, Y.-H.; Chou, Y.-C. *J. Mol. Catal. A: Chem.* **2011,** *342–343,* 18–22. doi:10.1016/j.molcata.2011.04.003
156. Wang, H.; Wu, Z.; Liu, Y.; Sheng, Z. *J. Mol. Catal. A: Chem.* **2008,** *287,* 176–181. doi:10.1016/j.molcata.2008.03.010
157. Zou, J.-J.; Zhu, B.; Wang, L.; Zhang, X.; Mi, Z. *J. Mol. Catal. A: Chem.* **2008,** *286,* 63–69. doi:10.1016/j.molcata.2008.01.045
158. Challagulla, S.; Nagarjuna, R.; Ganesan, R.; Roy, S. *ACS Sustainable Chem. Eng.* **2016,** *4,* 974–982. doi:10.1021/acssuschemeng.5b01055
159. Yang, L.; Xiao, Y.; Liu, S.; Li, Y.; Cai, Q.; Luo, S.; Zeng, G. *Appl. Catal., B* **2010,** *94,* 142–149. doi:10.1016/j.apcatb.2009.11.002
160. Liu, L.; Yang, W.; Sun, W.; Li, Q.; Shang, J. K. *ACS Appl. Mater. Interfaces* **2015,** *7,* 1465–1476. doi:10.1021/am505861c
161. Ku, Y.; Lin, C.-N.; Hou, W.-M. *J. Mol. Catal. A: Chem.* **2011,** *349,* 20–27. doi:10.1016/j.molcata.2011.08.006
162. Kobayashi, M.; Miyoshi, K. *Appl. Catal., B* **2007,** *72,* 253–261. doi:10.1016/j.apcatb.2006.11.007
163. Susman, M. D.; Feldman, Y.; Vaskevich, A.; Rubinstein, I. *ACS Nano* **2014,** *8,* 162–174. doi:10.1021/nn405891g
164. Ma, D.-K.; Guan, M.-L.; Liu, S.-S.; Zhang, Y.-Q.; Zhang, C.-W.; He, Y.-X.; Huang, S.-M. *Dalton Trans.* **2012,** *41,* 5581–5586. doi:10.1039/c2dt30099k
165. Navío, J. A.; Colón, G.; Trillas, M.; Peral, J.; Domènech, X.; Testa, J. J.; Padrón, J.; Rodríguez, D.; Litter, M. I. *Appl. Catal., B* **1998,** *16,* 187–196. doi:10.1016/S0926-3373(97)00073-8
166. Qin, B.; Zhao, Y.; Li, H.; Qiu, L.; Fan, Z. *Chin. J. Catal.* **2015,** *36,* 1321–1325. doi:10.1016/S1872-2067(15)60877-4
167. Zhong, J. S.; Wang, Q. Y.; Zhou, J.; Chen, D. Q.; Ji, Z. G. *Appl. Surf. Sci.* **2016,** *367,* 342–346. doi:10.1016/j.apsusc.2016.01.189

168. Athanasekou, C.; Romanos, G. E.; Papageorgiou, S. K.; Manolis, G. K.; Katsaros, F.; Falaras, P. *Chem. Eng. J.* **2017,** *318,* 171–180. doi:10.1016/j.cej.2016.06.033
169. Velegraki, G.; Miao, J.; Drivas, C.; Liu, B.; Kennou, S.; Armatas, G. S. *Appl. Catal., B* **2018,** *221,* 635–644. doi:10.1016/j.apcatb.2017.09.064
170. Kudo, A.; Domen, K.; Maruya, K.-i.; Onishi, T. *Chem. Phys. Lett.* **1987,** *133,* 517–519. doi:10.1016/0009-2614(87)80070-2
171. Hwang, D. W.; Kim, H. G.; Kim, J.; Cha, K. Y.; Kim, Y. G.; Lee, J. S. *J. Catal.* **2000,** *193,* 40–48. doi:10.1006/jcat.2000.2875
172. Kato, H.; Asakura, K.; Kudo, A. *J. Am. Chem. Soc.* **2003,** *125,* 3082–3089. doi:10.1021/ja027751g
173. Mohammadi, M. R.; Fray, D. J. *Solid State Sci.* **2010,** *12,* 1629–1640. doi:10.1016/j.solidstatesciences.2010.07.015
174. Akurati, K. K.; Vital, A.; Dellemann, J.-P.; Michalow, K.; Graule, T.; Ferri, D.; Baiker, A. *Appl. Catal., B* **2008,** *79,* 53–62. doi:10.1016/j.apcatb.2007.09.036
175. Dozzi, M. V.; Marzorati, S.; Longhi, M.; Coduri, M.; Artiglia, L.; Selli, E. *Appl. Catal., B* **2016,** *186,* 157–165. doi:10.1016/j.apcatb.2016.01.004
176. Shamaila, S.; Sajjad, A. K. L.; Chen, F.; Zhang, J. *Appl. Catal., B* **2010,** *94,* 272–280. doi:10.1016/j.apcatb.2009.12.001
177. Bian, Z.; Zhu, J.; Wang, S.; Cao, Y.; Qian, X.; Li, H. *J. Phys. Chem. C* **2008,** *112,* 6258–6262. doi:10.1021/jp800324t
178. Yang, J.; Dai, J.; Li, J. *Environ. Sci. Pollut. Res.* **2013,** *20,* 2435–2447. doi:10.1007/s11356-012-1131-6
179. Harish, K. N.; Bhojya Naik, H. S.; Prashanth Kumar, P. N.; Viswanath, R. *ACS Sustainable Chem. Eng.* **2013,** *1,* 1143–1153. doi:10.1021/sc400060z
180. Zhu, H.; Zhang, S.; Huang, Y.-X.; Wu, L.; Sun, S. *Nano Lett.* **2013,** *13,* 2947–2951. doi:10.1021/nl401325u
181. Gherbi, R.; Nasrallah, N.; Amrane, A.; Maachi, R.; Trari, M. *J. Hazard. Mater.* **2011,** *186,* 1124–1130. doi:10.1016/j.jhazmat.2010.11.105
182. Lahmar, H.; Benamira, M.; Akika, F. Z.; Trari, M. *J. Phys. Chem. Solids* **2017,** *110,* 254–259. doi:10.1016/j.jpcs.2017.06.021
183. Kebir, M.; Trari, M.; Maachi, R.; Nasrallah, N.; Bellal, B.; Amrane, A. *J. Environ. Chem. Eng.* **2015,** *3,* 548–559. doi:10.1016/j.jece.2014.12.024
184. Cui, B.; Lin, H.; Li, J.-B.; Li, X.; Yang, J.; Tao, J. *Adv. Funct. Mater.* **2008,** *18,* 1440–1447. doi:10.1002/adfm.200700982
185. Yanguang, L.; Panitat, H.; Yiying, W. *Adv. Mater.* **2010,** *22,* 1926–1929. doi:10.1002/adma.200903896
186. Rekhila, G.; Trari, M.; Bessekhouad, Y. *Appl. Water Sci.* **2017,** *7,* 1273–1281. doi:10.1007/s13201-015-0340-9
187. Singh, S.; Khare, N. *RSC Adv.* **2015,** *5,* 96562–96572. doi:10.1039/C5RA14889H
188. Li, X.; Zhu, J.; Li, H. *Appl. Catal., B* **2012,** *123–124,* 174–181. doi:10.1016/j.apcatb.2012.04.009
189. Park, J.; Park, S.; Selvaraj, R.; Kim, Y. *RSC Adv.* **2015,** *5,* 52737–52742. doi:10.1039/C5RA07620J
190. Yuan, Y.-J.; Chen, D.-Q.; Shi, X.-F.; Tu, J.-R.; Hu, B.; Yang, L.-X.; Yu, Z.-T.; Zou, Z.-G. *Chem. Eng. J.* **2017,** *313,* 1438–1446. doi:10.1016/j.cej.2016.11.049
191. Kwak, B. S.; Lee, H.; Kang, M. *Chem. Eng. J.* **2014,** *255,* 613–622. doi:10.1016/j.cej.2014.05.103
192. Basu, M.; Sinha, A. K.; Pradhan, M.; Sarkar, S.; Negishi, Y.; Pal, T. *Environ. Sci. Technol.* **2010,** *44,* 6313–6318. doi:10.1021/es101323w
193. Xu, X.; Lu, R.; Zhao, X.; Xu, S.; Lei, X.; Zhang, F.; Evans, D. G. *Appl. Catal., B* **2011,** *102,* 147–156. doi:10.1016/j.apcatb.2010.11.036
194. Wang, Q.; Li, J.; Bai, Y.; Lian, J.; Huang, H.; Li, Z.; Lei, Z.; Shangguan, W. *Green Chem.* **2014,** *16,* 2728–2735. doi:10.1039/C3GC42466A
195. Bao, N.; Shen, L.; Takata, T.; Domen, K. *Chem. Mater.* **2008,** *20,* 110–117. doi:10.1021/cm7029344
196. Zong, X.; Yan, H.; Wu, G.; Ma, G.; Wen, F.; Wang, L.; Li, C. *J. Am. Chem. Soc.* **2008,** *130,* 7176–7177. doi:10.1021/ja8007825
197. Bessekhouad, Y.; Chaoui, N.; Trzpit, M.; Ghazzal, N.; Robert, D.; Weber, J. V. *J. Photochem. Photobiol., A* **2006,** *183,* 218–224. doi:10.1016/j.jphotochem.2006.03.025
198. Liu, S.; Zhang, N.; Tang, Z.-R.; Xu, Y.-J. *ACS Appl. Mater. Interfaces* **2012,** *4,* 6378–6385. doi:10.1021/am302074p
199. Chen, Z.; Xu, Y.-J. *ACS Appl. Mater. Interfaces* **2013,** *5,* 13353–13363. doi:10.1021/am4043068
200. Liu, X.; Pan, L.; Lv, T.; Sun, Z. *J. Alloys Compd.* **2014,** *583,* 390–395. doi:10.1016/j.jallcom.2013.08.193
201. Zhang, Y. C.; Du, Z. N.; Li, K. W.; Zhang, M.; Dionysiou, D. D. *ACS Appl. Mater. Interfaces* **2011,** *3,* 1528–1537. doi:10.1021/am200102y
202. Yella, A.; Mugnaioli, E.; Therese, H. A.; Panthöfer, M.; Kolb, U.; Tremel, W. *Chem. Mater.* **2009,** *21,* 2474–2481. doi:10.1021/cm900277j
203. Zhang, Y. C.; Du, Z. N.; Li, S. Y.; Zhang, M. *Appl. Catal., B* **2010,** *95,* 153–159. doi:10.1016/j.apcatb.2009.12.022
204. Mondal, C.; Ganguly, M.; Pal, J.; Roy, A.; Jana, J.; Pal, T. *Langmuir* **2014,** *30,* 4157–4164. doi:10.1021/la500509c
205. Qu, J.; Chen, D.; Li, N.; Xu, Q.; Li, H.; He, J.; Lu, J. *Appl. Catal., B* **2017,** *207,* 404–411. doi:10.1016/j.apcatb.2017.02.050
206. Zhang, Y. C.; Li, J.; Xu, H. Y. *Appl. Catal., B* **2012,** *123–124,* 18–26. doi:10.1016/j.apcatb.2012.04.018
207. Yang, C.; Wang, W.; Shan, Z.; Huang, F. *J. Solid State Chem.* **2009,** *182,* 807–812. doi:10.1016/j.jssc.2008.12.018
208. Mu, J.; Shao, C.; Guo, Z.; Zhang, Z.; Zhang, M.; Zhang, P.; Chen, B.; Liu, Y. *ACS Appl. Mater. Interfaces* **2011,** *3,* 590–596. doi:10.1021/am101171a
209. Liu, B.; Khare, A.; Aydil, E. S. *ACS Appl. Mater. Interfaces* **2011,** *3,* 4444–4450. doi:10.1021/am201123u
210. Huang, Y.; Wei, Y.; Wu, J.; Guo, C.; Wang, M.; Yin, S.; Sato, T. *Appl. Catal., B* **2012,** *123–124,* 9–17. doi:10.1016/j.apcatb.2012.04.010
211. Yang, Q.-L.; Kang, S.-Z.; Chen, H.; Bu, W.; Mu, J. *Desalination* **2011,** *266,* 149–153. doi:10.1016/j.desal.2010.08.018
212. Tuprakay, S.; Liengcharernsit, W. *J. Hazard. Mater.* **2005,** *124,* 53–58. doi:10.1016/j.jhazmat.2005.03.027
213. Zhang, K.; Kemp, K. C.; Chandra, V. *Mater. Lett.* **2012,** *81,* 127–130. doi:10.1016/j.matlet.2012.05.002
214. Liu, S. X.; Qu, Z. P.; Han, X. W.; Sun, C. L. *Catal. Today* **2004,** *93–95,* 877–884. doi:10.1016/j.cattod.2004.06.097
215. Pan, X.; Xu, Y.-J. *J. Phys. Chem. C* **2013,** *117,* 17996–18005. doi:10.1021/jp4064802
216. Eskandarloo, H.; Badiei, A.; Behnajady, M. A.; Ziarani, G. M. *RSC Adv.* **2014,** *4,* 28587–28596. doi:10.1039/c4ra03418j
217. Lei, X. F.; Xue, X. X.; Yang, H. *Appl. Surf. Sci.* **2014,** *321,* 396–403. doi:10.1016/j.apsusc.2014.10.045
218. Zhang, Y.; Nie, J.; Wang, Q.; Zhang, X.; Wang, Q.; Cong, Y. *Appl. Surf. Sci.* **2018,** *427,* 1009. doi:10.1016/j.apsusc.2017.09.008
219. Zhang, D.; Xu, G.; Chen, F. *Appl. Surf. Sci.* **2015,** *351,* 962–968. doi:10.1016/j.apsusc.2015.06.044
220. Liu, X.; Pan, L.; Lv, T.; Sun, Z.; Sun, C. *RSC Adv.* **2012,** *2,* 3823–3827. doi:10.1039/c2ra01107g

221. Tanaka, A.; Nakanishi, K.; Hamada, R.; Hashimoto, K.; Kominami, H. *ACS Catal.* **2013,** *3,* 1886–1891. doi:10.1021/cs400433r
222. Wang, W.; Lai, M.; Fang, J.; Lu, C. *Appl. Surf. Sci.* **2018,** *439,* 430–438. doi:10.1016/j.apsusc.2017.12.249
223. Cai, J.; Wu, S.; Li, S.; Zhang, F. *Appl. Catal., B* **2017,** *201,* 12–21. doi:10.1016/j.apcatb.2016.08.003
224. Pandikumar, A.; Ramasamy, R. *Mater. Chem. Phys.* **2013,** *141,* 629–635. doi:10.1016/j.matchemphys.2013.05.026
225. Lia, S.; Cai, J.; Wu, X.; Liu, B.; Chen, Q.; Li, Y.; Zheng, F. *J. Hazard. Mater.* **2018,** *346,* 52–61. doi:10.1016/j.jhazmat.2017.12.001
226. O'Regan, B.; Grätzel, M. *Nature* **1991,** *353,* 737–740. doi:10.1038/353737a0
227. Dozzi, M. V.; Saccomanni, A.; Selli, E. *J. Hazard. Mater.* **2012,** *211–212,* 188–195. doi:10.1016/j.jhazmat.2011.09.038
228. Kar, P.; Maji, T. K.; Sarkar, P. K.; Lemmens, P.; Pal, S. K. *J. Mater. Chem. A* **2018,** *6,* 3674–3683. doi:10.1039/C7TA11138J
229. Wu, Q.; Zhao, J.; Qin, G.; Wang, C.; Tong, X.; Xue, S. *Appl. Catal., B* **2013,** *142–143,* 142–148. doi:10.1016/j.apcatb.2013.04.056
230. Albay, C.; Koç, M.; Altın, İ.; Bayrak, R.; Değirmencioğlu, İ.; Sökmen, M. *J. Photochem. Photobiol., A: Chem.* **2016,** *324,* 117–125. doi:10.1016/j.jphotochem.2016.03.024
231. Jing, F.; Liang, R.; Xiong, J.; Chen, R.; Zhang, S.; Li, Y.; Wu, L. *Appl. Catal., B* **2017,** *206,* 9–15. doi:10.1016/j.apcatb.2016.12.070
232. Wang, W.; Wang, Z.; Liu, J.; Zhang, Z.; Sun, L. *Sci. Rep.* **2017,** *7,* 43755. doi:10.1038/srep43755

License and Terms

This is an Open Access article under the terms of the Creative Commons Attribution License (http://creativecommons.org/licenses/by/4.0), which permits unrestricted use, distribution, and reproduction in any medium, provided the original work is properly cited.

The license is subject to the *Beilstein Journal of Nanotechnology* terms and conditions: (https://www.beilstein-journals.org/bjnano)

The definitive version of this article is the electronic one which can be found at:
doi:10.3762/bjnano.9.137

BEILSTEIN JOURNAL OF NANOTECHNOLOGY

Controllable one-pot synthesis of uniform colloidal TiO_2 particles in a mixed solvent solution for photocatalysis

Jong Tae Moon[1], Seung Ki Lee[2] and Ji Bong Joo[*1]

Full Research Paper

Open Access

Address:
[1]Department of Chemical Engineering, Konkuk University, 120 Neungdong-ro, Gwangjin-gu, Seoul 05029, Republic of Korea and [2]Department of Life Science, University of Seoul, 163 Seoul Siripdae-ro, Dondaemun-gu, Seoul 02504, Republic of Korea

Email:
Ji Bong Joo* - jbjoo@konkuk.ac.kr

* Corresponding author

Keywords:
mixed solvent; one-pot synthesis; photocatalysts; rhodamine B degradation; sol–gel synthesis; spherical TiO_2 particles

Beilstein J. Nanotechnol. **2018,** *9,* 1715–1727.
doi:10.3762/bjnano.9.163

Received: 15 January 2018
Accepted: 08 May 2018
Published: 08 June 2018

This article is part of the Thematic Series "Energy conversion, storage and environmental remediation using nanomaterials".

Guest Editor: W.-J. Ong

© 2018 Moon et al.; licensee Beilstein-Institut.
License and terms: see end of document.

Abstract

This study reports on the controllable synthesis of uniform colloidal titanium dioxide (TiO_2) particles and their photocatalytic applications toward rhodamine B (RhB) degradation. The monodispersed TiO_2 particles were synthesized under mixed solvent conditions by sol–gel chemistry in a one-pot process. Varying the ratio of solvent composition, the concentration of surfactant and TiO_2 precursor was used to control the particle diameter, degree of monodispersity and morphology. The modification of the calcination temperature affected the crystallinity and crystalline phase of the colloidal TiO_2 particles. When uniform, amorphous TiO_2 particles were calcined at an optimal temperature (500 °C), the final sample exhibited beneficial characteristics such as high anatase crystallinity with a mixed phase of anatase and rutile and relatively high surface area. The photocatalytic efficiency of the uniform TiO_2 sample with high anatase crystallinity with mixed phase and high surface area was dramatically enhanced towards RhB degradation under UV–vis irradiation. We systemically discuss the relationship between the synthetic parameters in our synthesis and the properties of the final TiO_2 products, as well as the crystalline properties and performance enhancement of TiO_2 photocatalysts calcined at different temperatures.

Introduction

Titanium dioxide (TiO_2) is a widely explored semiconducting material that exists in abundance from natural resources. It has a wide range of applications including bio-separation, sensors, energy storage, catalysis and photocatalysis [1-11]. Due to its wide band gap energy (3.0–3.2 eV) between the conduction and valance bands, TiO_2 can absorb photons in the ultraviolet (UV) portion of the light spectrum. This leads to the sequential generation of electron–hole pairs that can induce a variety of surface redox reactions. Photocatalytic water splitting via a TiO_2 electrode under UV irradiation was first reported by Honda and

Fujishima [12]. Over the past decade, there have been many attempts to fabricate highly active TiO_2-based photocatalysts for enhanced photocatalytic efficiency [13-17].

It is well-known that photocatalysis over a semiconductor photocatalyst occurs in the following sequential steps. First, the semiconductor photocatalyst can absorb photon energy that is greater than its band gap and electrons in the valance band can be exited to the conduction band, resulting in photoexcited electron–hole pairs. Then, the photo-exited electron–hole can move to the surface of the photocatalyst without charge recombination. Finally, each charge carrier can be consumed for surface redox reactions [9,15]. To achieve high performance in the overall photocatalysis system, the efficiency of each step should be improved [13]. Regarding the point of light absorption, the band gap energy range of the photocatalyst must be narrow in order to facilitate the facile adsorption of the low energy photon and high harvesting efficiency under visible-light irradiation conditions [11]. To enhance charge separation efficiency and extend the lifetime of photoexcited electron–hole pairs, properties such as a crystalline phase or high crystallinity are essential. Highly crystallized TiO_2 is generally considered to not only reduce the recombination of electron–hole pairs, but to also extend the lifetime of photogenerated charges that result in the enhancement of photocatalytic activity [7]. During photocatalysis, it is well-known that photo-generated electrons can transfer to the bulk in a TiO_2 crystallite, while the hole can move towards the interface between the TiO_2 and solution [18,19]. Once the TiO_2 has a well-crystallized structure, electrons can easily move toward the bulk and freely exist in the bulk of the crystallite, which results in a charge delocalization that leads to a decreasing chance of electron–hole recombination [19]. In addition, even though the well-crystallized anatase phase is superior for photocatalysis under UV conditions due to its intrinsic properties (e.g., low recombination rate of photoexcited electron–hole pairs), it is also well-known that a mixed anatase and rutile crystalline phase can lead to enhanced photocatalysis performance. In particular, the exceptional activity of commercial P25 TiO_2 is often explained to originate from its unique crystalline properties, i.e., its mixed anatase/rutile phase with high anatase crystallinity. As shown in both a previous study and our later discussion, a mixed crystalline phase of anatase and rutile in P25 TiO_2 can have several beneficial effects such as improved light adsorption in the low energy UV range and separation of photoexcited charge carriers which can result in significantly enhanced photocatalysis performance [20,21]. From the surface reaction point of view, a large surface area of the TiO_2 photocatalyst is important for increasing the number density of redox reaction sites [22]. Thus, it is critically essential to synthesize TiO_2 photocatalysts with controlled crystallinity while maintaining a high surface area.

Since many photocatalysis reactions are a liquid phase reaction, a well-dispersible colloidal TiO_2 nanostructure should be one of the most ideal forms. In order to maximize the active surface area as well as improve dispersion in a reactant solution, one can consider the direct use of TiO_2 nanocrystals [23,24]. However, nanocrystals synthesized by a conventional solution-based method are strongly stabilized with organic capping agents, which limit the accessibility of the reactant molecule to the nanocrystal surface and prevent surface reactions, and in turn, hamper the photocatalytic activity [25]. In order to address the above issues, TiO_2 photocatalysts are often synthesized in the form of a porous colloidal particle in sub-micrometer dimensions [8,26,27]. They can be calcined at high temperature, which results in well-developed crystalline properties and clean active sites with a suitable high surface area. Sub-micrometer photocatalysts are usually stabilized by electrostatic charges from their surface so that no additional stabilizers are necessary for maintaining dispersion stability in a reaction solution [8]. In addition, the relatively larger size of the sub-micrometer photocatalysts compared to typical nanocrystal forms makes them easier to recycle from the reaction solution through simple centrifugation.

With continued development of synthetic chemistry, a variety of methods was suggested for preparing colloidal nanostructures and many colloidal TiO_2 porous particles have been demonstrated [13,15,26]. Among the various colloidal TiO_2 nanostructures, there has been increasing interest in uniform, colloidal TiO_2 spheres due to their advantageous characteristics including facile functionalization, large surface area, uniform photocatalytic activity for each particle, and improved accessibility for the reactant molecules. To fabricate the uniform, colloidal TiO_2 spheres, several synthetic methods have been reported including hydrothermal, solvothermal, and sol–gel processes [10,26,28,29]. Although hydrothermal or solvothermal process are simple and convenient, they are typically conducted under high pressure and high temperature conditions for an elongated reaction time in a sealed reactor which requires high energy and large expense. In addition, it is difficult to monitor the overall synthetic progress of the formation and growth of the particle and to control the properties of the final products. On the other hand, the sol–gel process, which is carried out under atmospheric pressure conditions at near room temperature, is well known as a suitable method for producing colloidal metal oxide particles, such as SiO_2, ZrO_2 and TiO_2 that have well-controlled characteristics [15,30,31].

We have previously reported a reproducible sol–gel coating method for producing SiO_2@TiO_2 core–shell nanostructures in the presence of a surfactant in pure ethanol solution [7,8]. In addition, another robust sol–gel coating process in a mixed sol-

vent of ethanol–acetonitrile (EtOH/ACN) for producing polymer@TiO_2 core–shell nanostructures was reported [14]. Since the solubility of the TiO_2 precursor, titanium butoxide (TBOT), is different in the two different solvents (ethanol and acetonitrile), the nucleation/growth rate of TBOT and its hydrolysate is finely controlled by regulating the ethanol–acetonitrile ratio. The spherical curvature and smoothness of the TiO_2 layers was also tuned using the ethanol–acetonitrile solvent conditions that resulted from the controlled diffusion rate of TBOT and its hydrolysate in a mixed solvent [14,32,33]. Without a sacrificial core material, it should be noted that this sol–gel strategy allows the colloidal TiO_2 particles to have finely tuned properties due to the well-controlled nucleation/growth rate of TBOT in mixed solvent conditions. Although this sol–gel coating strategy using a mixed solvent was successfully applied for synthesizing core–shell nanostructures, to the best of our knowledge, there is no obvious report on sol–gel synthesis of uniform colloidal metal oxide particles such as TiO_2 in a mixed solvent solution of ethanol–acetonitrile.

In this study, the synthesis of uniform TiO_2 colloidal particles with controllable properties and their photocatalytic application towards the degradation of rhodamine B is discussed. More specifically, uniform TiO_2 colloidal particles were synthesized by a sol–gel process in a well-controlled mixed solvent of ethanol and acetonitrile, and the relationship between the synthetic parameters and the properties of the final TiO_2 products were systemically studied. The resulting TiO_2 particles exhibited beneficial properties towards the liquid phase photocatalysis, including uniform particle dimensions, well-developed mesoporous structure, and a mixed crystalline phase of anatase and rutile. The final uniform TiO_2 particles displayed significantly improved photocatalytic activity. By controlling the calcination conditions, the crystalline phase and crystallinity of the uniform TiO_2 particles can be fine-tuned and the catalyst activity can be optimized for further enhanced activity. To the best of our knowledge, this is first report on the synthesis and systemic study of uniform colloidal TiO_2 particles using sol–gel synthesis in mixed solvent conditions using ethanol–acetonitrile.

Results and Discussion

Uniform colloidal TiO_2 particles can be synthesized by a modified sol–gel synthesis followed by calcination under atmospheric conditions. The synthesis is conducted in the ethanol–acetonitrile mixed solvent phase in the presence of a surfactant and base catalysts for the hydrolysis and condensation of the TiO_2 precursor. Specifically, a typical synthesis involves three steps, as illustrated in Scheme 1: 1) the formation of TiO_2 nucleates and subsequent growth of amorphous TiO_2 spheres by a sol–gel reaction of titanium butoxide (TBOT) in the mixed solvent with hydroxypropylcellulose (HPC) as a surfactant; 2) aging step of the spherical TiO_2 particles in the water-containing solvent to make the surface of TiO_2 particles condensed; and 3) calcination to crystallize amorphous TiO_2 particles into their crystallized counterparts.

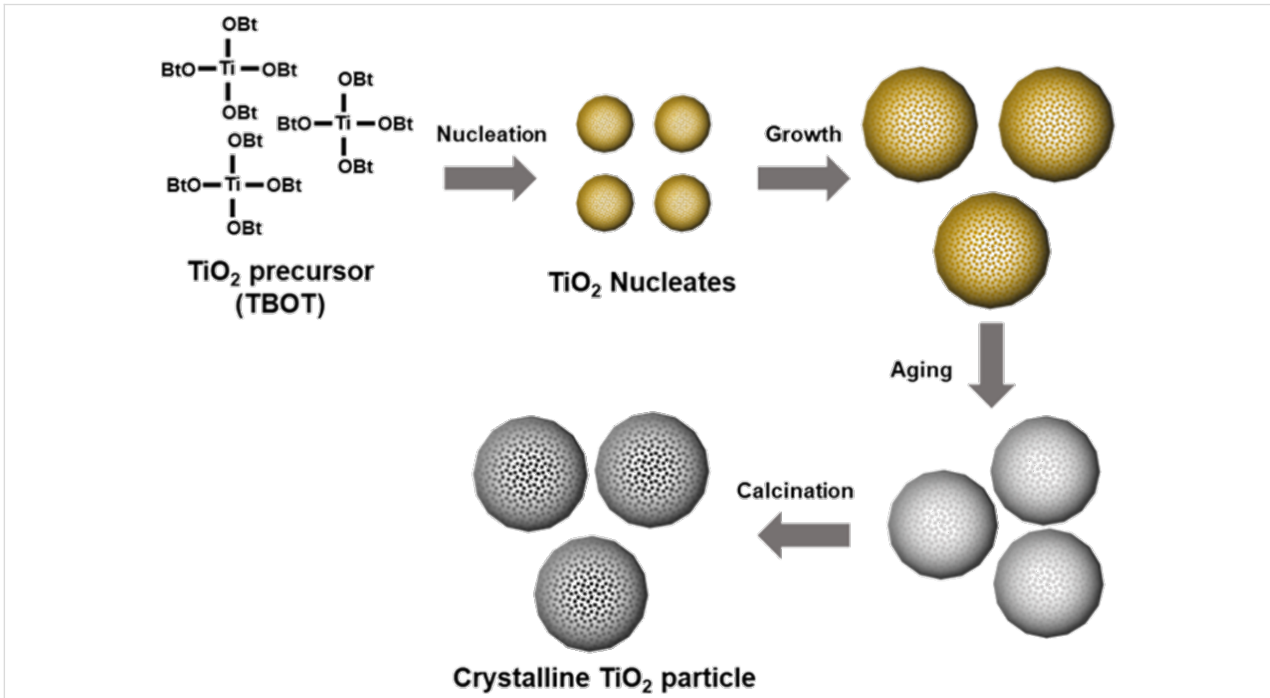

Scheme 1: Schematic illustration of the synthesis of uniform TiO_2 particles using a sol–gel reaction in mixed solvent conditions.

The hydrolysis and condensation of the TBOT precursor are highly influenced by several factors such as the solvent environment, concentration of surfactant, and the amount of precursor used [13-15,31]. The precise tuning of these factors allows the convenient control of the physical–chemical properties of the final colloidal TiO_2 particles such as particle size and macroscopic morphology. In this study, we optimized these factors to control the size of the TiO_2 particles and prevent particle agglomeration.

Figure 1 compares the as-synthesized amorphous TiO_2 particles prepared by varying the solvent composition. As shown in Figure 1a, when only pure ethanol was used as the solvent, the resulting TiO_2 sample exhibited large TiO_2 particles (≈400–500 nm) and the particles were quite aggregated. With the addition of acetonitrile into the synthesis, the particle size and tendency for particle aggregation dramatically changed. When the volume ratio of EtOH/ACN was 3:1, the particle diameter decreased to ≈340 nm and most of the particles

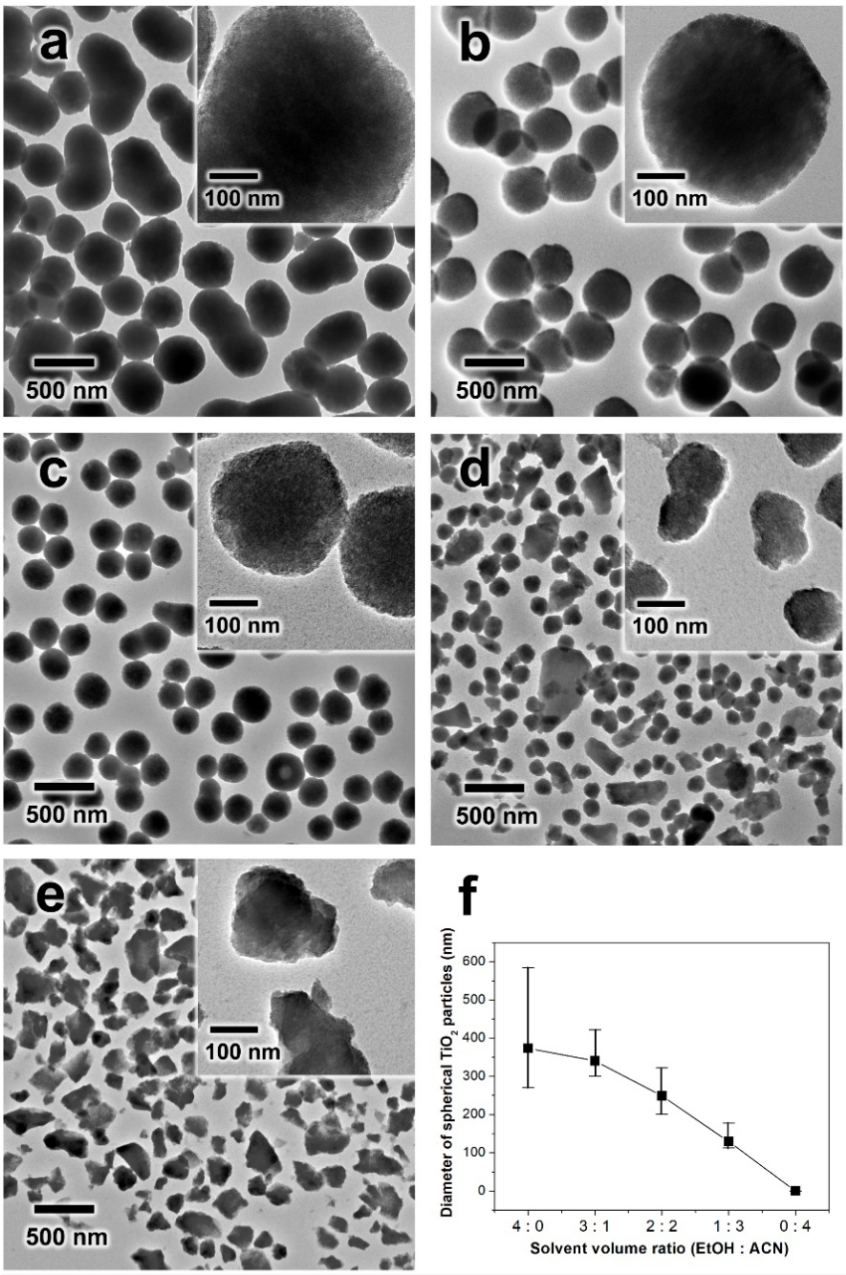

Figure 1: (a–e) TEM images of as-synthesized TiO_2 with different volume ratios of ethanol to acetonitrile used as the solvent: (a) ethanol/ACN 4:0 (b) ethanol/ACN 3:1 (c) ethanol/ACN 2:2 (d) ethanol/ACN 1:3 and (e) ethanol/ACN 0:4. (f) The relationship between the solvent volume ratio and the average diameter of the spherical TiO_2 particles.

were individually isolated without particle agglomeration (Figure 1b). When the volume ratio of EtOH/ACN was 2:2, the particle size of the spherical TiO_2 particles became even smaller, reducing to ≈250 nm without apparent particle aggregation (Figure 1c). As the volume ratio of EtOH/ACN was decreased to 1:3, the particle diameter dramatically decreased and the shape of the TiO_2 particles became irregular (Figure 1d). When pure ACN was used as a solvent, the resulting TiO_2 sample displayed irregular particles without spherical shape. In addition, the particle size of the sample was not uniform and the surface of the particle was not smooth (Figure 1e). As shown in Figure 1f, the particle diameter of the spherical TiO_2 sample continuously decreased from 380 to 340, 250, 130 and 0 nm with the change in the solvent volume ratio of EtOH/ACN from 4:0 to 3:1, 2:2, 1:3 and 0:4, respectively. A reported in other works, the solvent environment can significantly affect the particle size and morphology of the TiO_2 sample [14,32]. As the ACN ratio increased, it was noted that the particle diameter of the spherical TiO_2 continuously decreased and the particle shape became irregular.

These phenomena can be explained by not only the solubility of TBOT and the surfactant, but also by the nucleation-growth kinetics of TBOT in different solvent conditions. It is well-known that acetonitrile is more hydrophobic than ethanol [14]. As the relative ACN ratio increased in the mixed solvent, the precursor (TBOT) and surfactant (HPC), which have many hydrophilic hydroxy groups, were not stable in the mixed solvent. TBOT is not miscible and results in a separated phase, and HPC does not dissolve in the ACN solution. HPC (10 mg) could not be dissolved in ACN solution (10 mL) in the range of solvent conditions used in our works (Supporting Information File 1, Figure S1a). However, HPC (10 mg) can completely be dissolved in 10 mL of ethanol (Supporting Information File 1, Figure S1b). In addition, when we tried to dissolve TBOT in pure acetonitrile solution, TBOT (5 mL) and ACN (5 mL) cannot be mixed, resulting in a separated phase, as shown in Supporting Information File 1, Figure S1c. When TBOT (5 mL) is mixed with ethanol (5 mL), it shows the homogeneously mixed solution (Supporting Information File 1, Figure S1d).

According to a previous study, TBOT molecules have a high solubility in ethanol but not in acetonitrile [14]. As a result, when the concentration of ACN increases, the TBOT and its hydrolysate molecules are forced to form nucleates rapidly and to precipitate out of the solution [32,33]. This rapid nucleation and precipitation induces the formation of relatively small particles in the ACN-rich solvent. In addition, since the HPC was not dissolved and existed in the form of an undissolved solid in the ACN-rich solvent, the HPC molecules could not be positioned on the interface between the surface of the particle and the solvent. As a result, the HPC molecules could not interact with either the surface of the TiO_2 particles or hydrolyzed TiO_2 species (e.g., TBOT hydrolysate) in the ACN-rich solvent. Thus, it neither exhibited a stabilization effect on the TBOT hydrolysate nor any steric hindrance on the surface of the TiO_2 particles, which resulted in the rapid formation of irregular, small TiO_2 particles.

In contrast, when ethanol was used as a solvent, both TBOT and HPC were easily dissolved. Since the HPC surfactant contains many hydroxy and ether groups which can form hydrogen bonds with not only the hydroxy group of TBOT hydrolysate but also those of the TiO_2 surface, the hydrolyzed TiO_2 species should have been relatively stable in the ethanol solvent. In addition, the HPC molecules could also be positioned on the surface of the TiO_2 particle, which displayed enough steric hindrance effects on the deposition of the hydrolyzed TiO_2 species. Thus, the deposition kinetics of the hydrolyzed TiO_2 species was controlled and the growth of the TiO_2 particles preferentially occurred by the deposition of the hydrolyzed TiO_2 species once the TiO_2 nucleates were formed, which resulted in the formation of large TiO_2 particles with a spherical curvature.

When a certain amount of ACN was added to the ethanol to form EtOH/ACN mixed solvent conditions, the TBOT molecules and their hydrolysates were less stable compared to the case of the pure ethanol solvent, and they were likely to precipitate [14,33]. The TBOT molecules and their hydrolysates formed the self-nucleated TiO_2 particles, which could be grown by the controlled diffusion and deposition of TBOT and their hydrolysates on the surface of the TiO_2 particles in the mixed solvent conditions. In addition, since HPC could also be dissolved in the mixed solvent, the dissolved HPC molecules not only tuned the stability of the TBOT molecules and their hydrolysates but also controlled deposition kinetics. The HPC molecules should also be positioned on the surface of the nucleated TiO_2 particles, which resulted in the controlled deposition rate of the TBOT molecules and their hydrolysates, adjusted growth kinetics of the TiO_2 particles, and prevention of particle aggregation. Thus, as-synthesized TiO_2 particles, which were synthesized in the EtOH/ACN mixed solvent, displayed uniform spherical morphology with isolated particles. Since the TiO_2 particles prepared under mixed solvent conditions (EtOH/ACN 3:1) showed great uniformity in size and morphology, the sample in Figure 2b was used for further control. The subsequent discussion will focus on the sample prepared in mixed solvent conditions with a ratio of EtOH/ACN of 3:1.

As mentioned in the previous section, the hydrolysis and condensation of the TBOT precursor were highly influenced by the

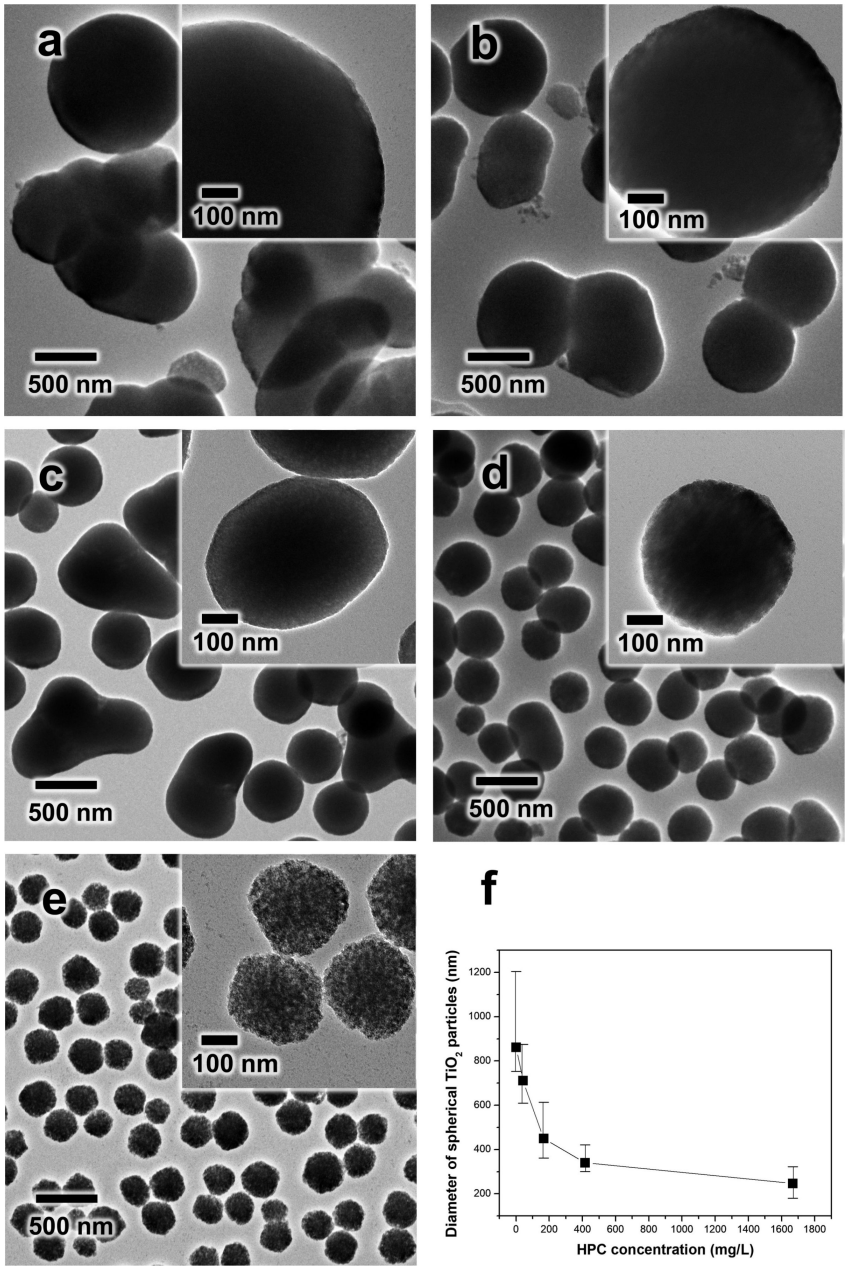

Figure 2: (a–e) TEM images of as-synthesized TiO_2 with different concentrations of HPC: (a) 0 (b) 41.67 (c) 166.67 (d) 416.67 and (e) 1666.67 mg/L. (f) The relationship between HPC concetnration and average diameter of spherical TiO_2 particles.

concentration of HPC as a surfactant. Figure 2 compares the morphology of the TiO_2 particles synthesized by using different concentrations of HPC in the mixed solvent conditions (EtOH/ACN 3:1). As shown in Figure 2a, without HPC, the as-synthesized TiO_2 particles were severely aggregated with large particles. With an increased concentration of HPC, the tendency for particle aggregation dramatically decreased and the size of the primary TiO_2 particle was reduced (Figure 2b,c). When the concentration of HPC was increased to 416.67 mg/L, isolated TiO_2 particles were eventually produced and the particle size decreased to 340 nm (Figure 2d). As the concentration of HPC was increased further (1666.67 mg/L), the particle size became even smaller (250 nm), as shown in Figure 2e. The average diameter of the TiO_2 particles was estimated to be approximately 860, 710, 450, 340 and 250 nm for the samples prepared with 0, 41.67, 166.67, 416.67, and 1666.67 mg/L of HPC, respectively (Figure 2f). As shown in both the previous literature and this study, the surfactant molecules (e.g., HPC) which contain many hydroxyl and ether groups create a strong interaction with the TiO_2 surface via hydrogen bonding [9,31].

In addition, the TBOT hydrolysates were stabilized by the surfactant, which resulted in the controlled deposition on the growing TiO_2 surface and produced small particles. Moreover, the binding of HPC prevented close contact the TiO_2 particles, and therefore, suppressed interparticle agglomeration.

Consistent with other syntheses, synthesizing uniform TiO_2 particles was also controlled by changing the concentration of the precursor [14,31]. When 1 mL of TBOT was used, the as-synthesized TiO_2 particles formed as small particles of about 110–120 nm diameter with a rough surface. As the concentration of the TBOT was increased, the particle size continuously increased (Figure 3b–e). The average diameter of the TiO_2 particle was estimated to be approximately 120, 230, 340, 660, and 900 nm for the samples prepared using 1, 2, 4, 6, and 8 mL of TBOT, respectively (Figure 3f). Based on these results, we can control the monodispersity and uniformity of TiO_2 particles by tuning either the solvent composition, concentration of surfac-

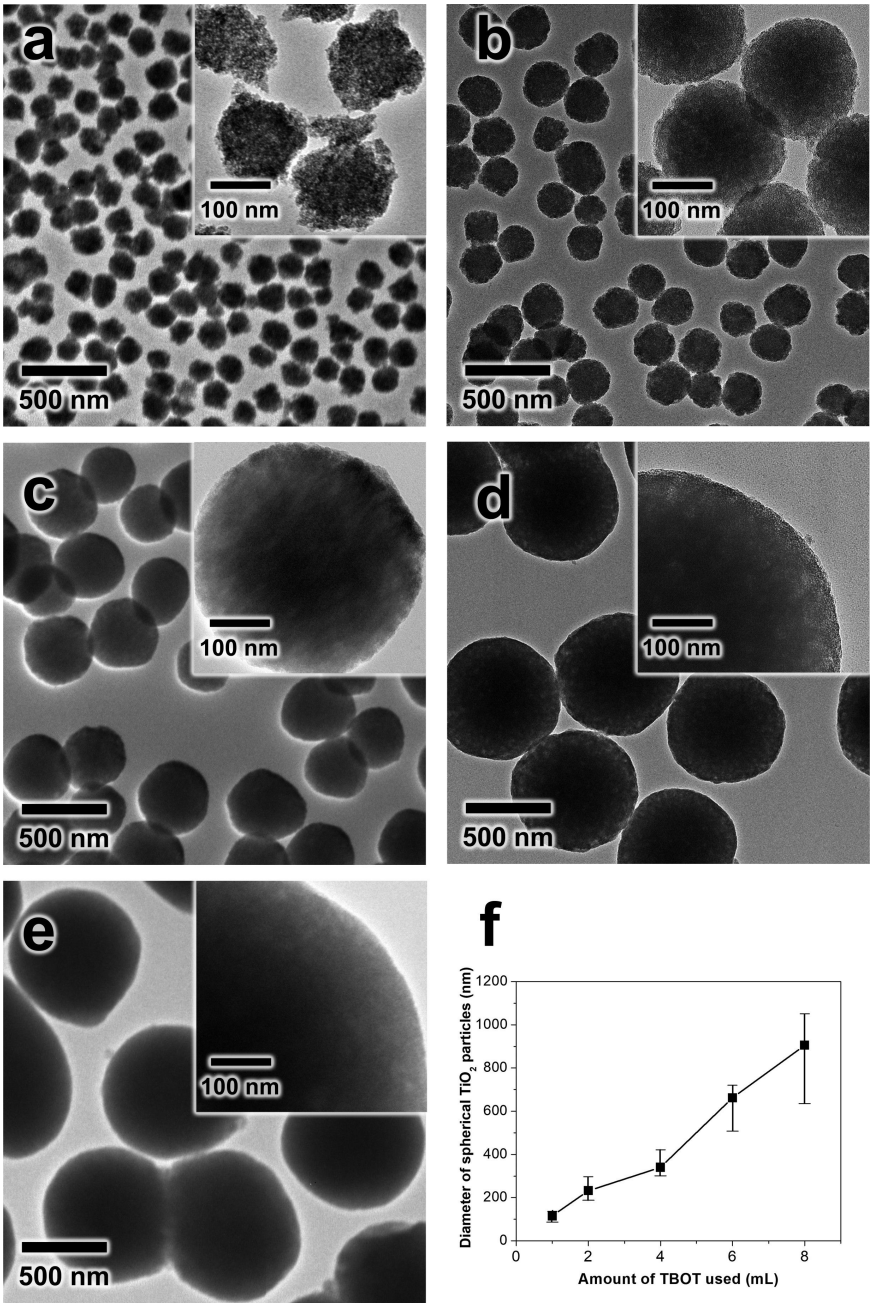

Figure 3: (a–e) TEM images of as-synthesized TiO_2 with different amounts of TBOT: (a) 1 (b) 2 (c) 4 (d) 6 and (e) 8 mL. (f) The relationship between the amount of TBOT used and the average diameter of the spherical TiO_2 particles.

tant or concentration of TBOT. To confirm the particle size and uniformity of as-synthesized TiO_2, we conducted SEM under low magnification and dynamic light scattering (DLS) analysis. Supporting Information File 1, Figure S2 shows low magnification SEM images and the DLS results of as-synthesized amorphous TiO_2 particles which were prepared by using a volume ratio of EtOH/ACN of 3:1, and calcination at 500 °C (labeled as TiO_2-500). Even though the particle diameter is reduced due to the calcination at 500 °C, the spherical morphology of the particle is well maintained with uniform size (Supporting Information File 1, Figure S2a,b). In addition, DLS data showed that the amorphous TiO_2 sample presented in Figure 1b displayed a sharp particle distribution peak centered at ≈350 nm. The calculated particle diameter of the TiO_2 sample is ≈347 ± 75 nm, which is similar to the SEM results. TiO_2-500 samples calcined at 500 °C also showed a sharp particle distribution peak at ≈262 ± 7 nm. Based on the SEM and DLS results, it can be concluded that our TiO_2 particles are uniform (Supporting Information File 1, Figure S2c and inset table). To crystallize the TiO_2 particles and improve the photocatalysis activity, the TiO_2 particles were subjected to calcination at different temperatures. Because the sample shown in Figure 3c displayed a suitable particle size, morphological uniformity and no aggregation, we focus the subsequent discussion by using the TiO_2 sample and its calcined derivatives.

The crystalline characteristics of the TiO_2 particles calcined at different temperatures were investigated by X-ray diffraction (XRD). As shown in Figure 4, the TiO_2 sample calcined at 350 °C (TiO_2-350) showed relatively broad diffraction peaks at 2θ = 25.4, 37.9, 48.1, 54 and 55° which were attributed to the (101), (004), (200), (105) and (211) planes, respectively, indicating an anatase phase. As the calcination temperature increased, the peak sharpness increased, indicating enhanced crystallinity. The TiO_2 sample calcined at 500 °C (TiO_2-500) exhibited not only the obvious anatase peaks but also new peaks at 2θ = 27.6, 36.6, 38.0, 41.4 and 54.5° corresponding to the (110), (101), (111), (210) and (211) planes of the rutile TiO_2 phase, respectively. When the sample was calcined at an even higher temperature of 650 °C (TiO_2-650), the peaks related to the rutile phase were more obvious. In addition, the relative intensity of the rutile phase was much stronger than that of the anatase phase. Upon further increases of the calcination temperature to over 800°C, all of anatase peaks disappeared and only the strong peaks related to the rutile phase were observed, which indicated that the meta-stable anatase phase was completely converted to rutile by the thermal phase transformation. The average anatase crystallite sizes of the TiO_2 samples, which were determined from the widths of the anatase (101) peaks in the XRD results by using the Scherrer equation, were estimated to be approximately 7, 10, 20, 29.7 and 0 nm for samples calcined at 350, 400, 500, 650, and 800 °C, respectively. In addition, the rutile grain sizes of the TiO_2 samples calcined at 500, 650, and 800 °C were calculated as approximately 26, 45, and 48 nm, respectively, by using the rutile (110) peaks.

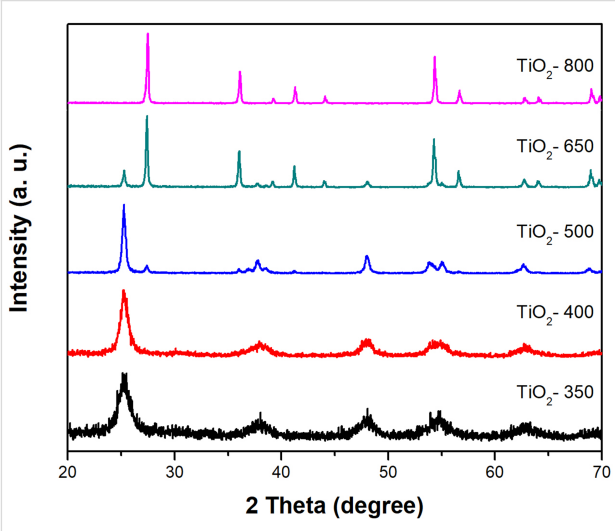

Figure 4: X-ray diffraction patterns of TiO_2 particles calcined at different temperatures (≈350–800 °C).

We also investigated the pore characteristics of the TiO_2 samples calcined at different temperatures. Figure 5 provides the nitrogen adsorption/desorption isotherm and corresponding Barrett–Joyner–Halenda (BJH) pore size distributions of the TiO_2 samples. The TiO_2 sample calcined at 400 °C (TiO_2-400) displayed a typical type IV isotherm with a well-developed hysteresis loop that indicated mesoscale porosity (Figure 5a). The TiO_2 sample (TiO_2-400) calcined at a relatively low temperature (400 °C) had a large adsorption capacity in the range of monolayer adsorption ($0.1 < P/P_0 < 0.25$), which indicated highly porous structures with a large BET surface area. However, the amount of monolayer adsorption of the TiO_2 samples continuously decreased, which indicated decreasing porosity and BET surface area, as the calcination temperature increased. When the TiO_2 samples were calcined at temperatures greater than 650 °C, they showed negligible N_2 adsorption volumes over all of the P/P_0 range, indicating a small BET surface area (Figure 5a). The measured surface area for the TiO_2 samples calcined at 400, 500, 650, 800 °C were 123, 62, 5 and 5 m^2/g respectively. Figure 5b provides the pore size distribution of the TiO_2 sample calcined at different temperatures as calculated by the BJH method using the adsorption branch of the N_2 adsorption isotherm. The TiO_2 particles calcined at 400 °C displayed an obvious distribution in the range of 0–5 nm with a peak in the range of 10–25 nm, which indicated the presence of a mesopore. When the TiO_2 particle was calcined at 500 °C, it exhibited an obvious peak in the range of 10–25 nm, although there

were no sharp peaks in the BJH pore size distribution curves. However, once the TiO_2 sample was calcined at high temperatures, e.g. more than 650 °C, they did not show any obvious peaks in the range related to mesopores, which indicated an almost non-porous characteristic.

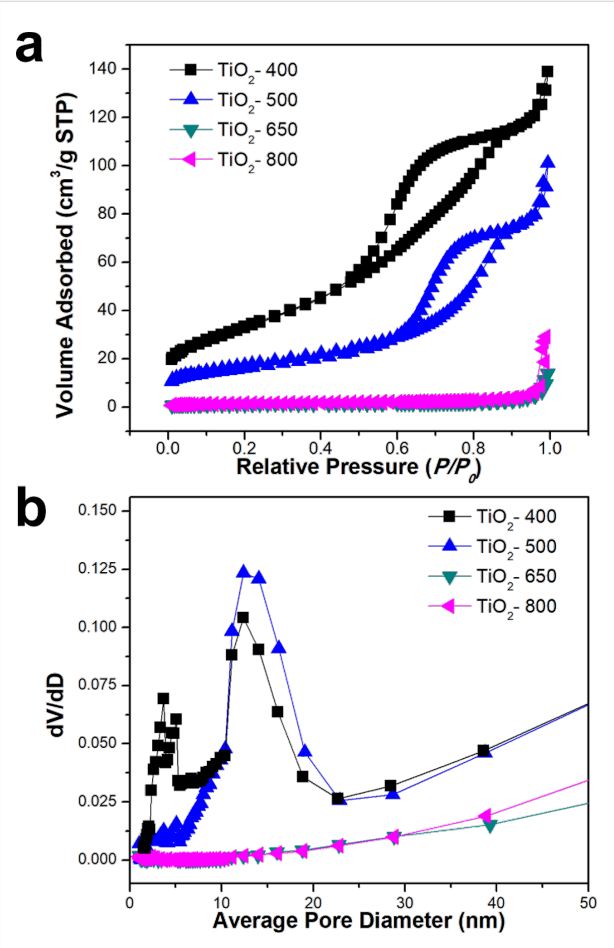

Figure 5: (a) N_2 adsorption/desorption isotherm and (b) pore size distribution of TiO_2 particles calcined at different temperatures (≈400–800 °C).

It is well-known that the amorphous TiO_2 layer has a non-porous or microporous characteristic [14,26]. As the calcination temperature was increased, it should be noted that the amorphous TiO_2 layer was locally aggregated, fused and crystallized into small grains which resulted in the appearance of mesoporosity. When the TiO_2 samples were subjected to calcination at high temperatures, small TiO_2 crystallites were grown, severely fused and finely shirked, which resulted in decreased mesoporosity and a small BET surface area but increased crystallinity.

To estimate the carbon content and thermal behavior of the TiO_2 samples, TGA analysis was conducted. Since only a surfactant (HPC), titanium precursor (TBOT) and solvent were used during the synthesis, the final TiO_2 sample should mainly consist of elements such as Ti, O, H and C, respectively. Therefore, weight loss during a thermogravimetric analysis (TGA) experiment originates from desorption of water, dihydroxylation and the combustion reaction of carbon contents. The TGA analysis was conducted using the surfactant HPC as a reference run to monitor the decomposition temperature (Supporting Information File 1, Figure S3a). It should be noted that HPC is dramatically decomposed in the range 300–500 °C. Amorphous TiO_2 and the TiO_2-350 sample showed steep weight loss in the range of ambient temperature to ≈150 °C, which is attributed to desorption of water, and continuous loss in the range of 300 to 500 °C, indicating the thermal oxidation and decomposition of HPC and carbon remained in the particle. However, TiO_2-500 and TiO_2-800 showed a negligible weight loss, indicating no obvious carbon species in the particle (Supporting Information File 1, Figure S3b). In addition, we measured the zeta potential of the calcined TiO_2 samples for estimating the surface charge. Although zeta potential values of TiO_2 samples do not exactly represent quantitative analysis of surface functional groups, it is a useful method to estimate the surface charge which is highly related with the surface OH group. The results show that the zeta potential values are estimated to be approximately −40, −23.8 and −24.9 mV nm for TiO_2-350, TiO_2-500, and TiO_2-800, respectively. It means that the TiO_2 sample calcined at low temperature (350 °C) should have a relatively large amount of surface OH groups. Once the calcination temperature is higher than a certain point (e.g., 500 °C), the zeta potential values of the TiO_2 samples (TiO_2-500 and TiO_2-800) are almost similar, indicating the presence of a similar number of surface OH groups.

The photocatalytic activity of the prepared TiO_2 samples was evaluated by monitoring the degradation of rhodamine B (RhB) under UV–vis light irradiation. Figure 6a shows the typical absorption spectra change for an aqueous RhB solution after UV–vis light irradiation for constant time intervals using TiO_2 particles (TiO_2-500) calcined at 500 °C. The strong absorption peak at 553 nm continuously decreased and finally disappeared after 60 minutes. This indicated that our TiO_2 particles photochemically degraded the RhB molecule completely under UV–vis light irradiation conditions. The photocatalytic performance of the TiO_2 sample towards RhB degradation, determined by monitoring the peak intensity change at 553 nm vs time, was summarized in Figure 6b. Before UV-light irradiation, the reaction mixture containing the catalyst and RhB was stirred for 30 min to ensure saturation of the RhB adsorption on the surface of the TiO_2 particles. All of the TiO_2 catalysts showed a similar adsorption capacity in the range of ≈9% of C/C_0. In the blank experiment (i.e., no catalyst), the C/C_0 of

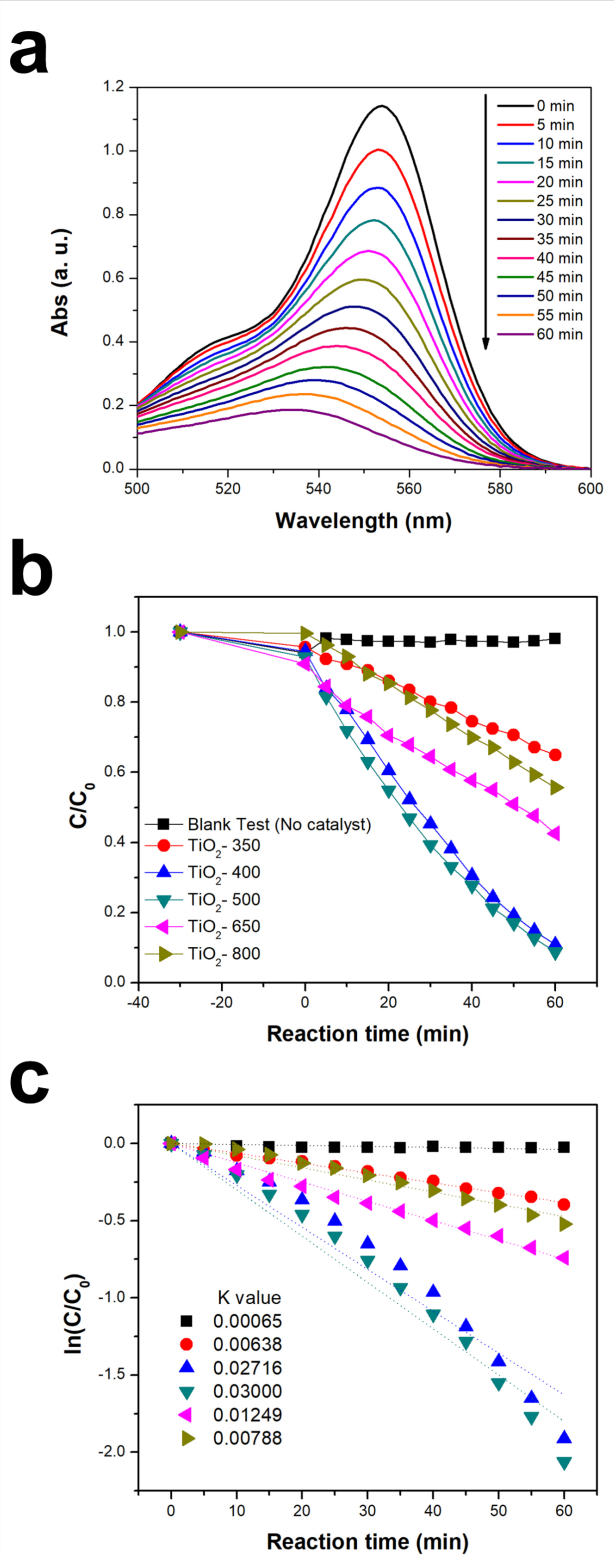

Figure 6: (a) UV–vis absorption spectra indicating degradation of rhodamine B (RhB) using the TiO_2-500 sample, (b) photocatalytic degradation of RhB under UV–vis light irradiation and (c) semilogarithmic plot versus time for the different TiO_2 samples: Blank Test (no catalyst) (■), TiO_2-350 (●), TiO_2-400 (▲), TiO_2-500(▼), TiO_2-650 (◀) and TiO_2-800 (▶).

RhB was decreased by only ≈2% after UV–vis irradiation for 60 min, while the degradation of RhB significantly improved when the TiO_2 catalysts were used. The TiO_2 sample calcined at 350 °C (TiO_2-350) exhibited the lowest catalytic activity among all of the catalysts employed in this study. When the TiO_2 sample was calcined at 400 °C (TiO_2-400), it showed a dramatically enhanced catalytic activity. In particular, the TiO_2 sample calcined at 500 °C (TiO_2-500) showed the best performance among the TiO_2 samples tested in this study. The relative photocatalytic activity of the TiO_2 samples for RhB degradation were as follows: TiO_2-500 ≥ TiO_2-400 > TiO_2-650 > TiO_2-800 ≥ TiO_2-350.

In order to estimate the first-order reaction rate constant and compare reaction kinetics, Figure 6c displays the data in semilogarithmic form. The blank test (i.e., no catalyst) result showed a negligible rate constant (0.00065 min^{-1}). The TiO_2-350 sample showed the lowest k value among all of the TiO_2 samples. As the calcination temperature was increased up to 500 °C, the k value continuously increased. The TiO_2-500 sample had the highest k value (0.03 min^{-1}), which indicated the highest photocatalytic activity. As the calcination temperature was further increased, the k values were reduced, which indicated a decrease of photocatalytic efficiency.

In order to further ensure the relationship between photocatalysis performance and calcination temperature, we carried out calcination at different temperatures using other TiO_2 particles which were prepared in pure ethanol conditions as presented in Figure 1a. Similar to the results presented in Figure 4, when a sample was calcined at different temperatures, the resulting TiO_2 particles showed different crystalline phases and degrees of crystallinity. Especially, when the TiO_2 sample prepared in pure ethanol solvent was calcined at 500 °C, it showed sharp anatase peaks with a weak (110) diffraction peak of rutile phase (Supporting Information File 1, Figure S4), indicating that the sample has a mixed phase of well-crystallized anatase with minor rutile. In addition, we also tested the photocatalytic activity of the TiO_2 particles which were prepared in pure ethanol solvent conditions followed by calcination at different temperatures. As shown in Supporting Information File 1, Figure S5, The TiO_2 sample calcined at 500 °C showed the highest photocatalytic activity compared to other TiO_2 samples calcined at either 350 or 800 °C.

We also investigated the effect of other synthesis parameters, such as change in the HPC concentration, on the photocatalytic performances of TiO_2 samples. We calcined the TiO_2 samples prepared using different HPC concentrations with a fixed calcination temperature (500 °C). When the as-synthesized TiO_2 samples prepared using different HPC conditions were calcined

at 500 °C, all samples showed the mixed crystalline phase of well-developed anatase with minor rutile (Supporting Information File 1, Figure S6a). Thus, it should be noted that the crystalline properties of all TiO_2 samples calcined at same temperature (500 °C) are similar even though different amounts of surfactant are used during the synthesis steps. However, the use of different HPC concentrations can eventually affect the pore-forming properties (such as pore size and surface area) of the final TiO_2 particles. When a relatively large amount of HPC was used during the synthesis, the final TiO_2 sample showed a large surface area. The samples TiO_2(HPC-1666.67)-500 and TiO_2(HPC-416.67)-500 showed the most well-developed mesoporous structure with a high surface area compared to the other TiO_2 samples including TiO_2(HPC-166.67)-500, TiO_2(HPC-41.67)-500 and TiO_2(HPC-0)-500 (Supporting Information File 1, Figure S6b). The calculated BET surface area of TiO_2 samples prepared using 1666.67, 416.67, 166.67, 41.67 and 0 mg/L of HPC were ≈43, 62, 12, 20 and 0.7 m^2/g, respectively.

Supporting Information File 1, Figure S7 compares the photocatalytic performance of TiO_2 samples prepared using different concentrations of HPC followed by calcination at a fixed temperature of 500 °C. The samples TiO_2(HPC-1666.67)-500 and TiO_2(HPC-416.67)-500 showed relatively fast RhB degradation kinetics compared to the other samples. Considering that all of the TiO_2 samples have similar crystalline properties (i.e., all samples have a well-developed anatase crystalline structure with minor rutile phase), the performance difference likely originates from differences in the surface area. It is well known that the photocatalytic activity is highly influenced by several factors, such as crystalline properties, surface area, dispersity, etc. Since we calcined all TiO_2 samples at the same temperature, it can be regarded that the crystalline properties and surface properties are similar. However, different concentrations of surfactant used during the synthesis affect the surface area of the final TiO_2 samples, resulting in different photocatalytic activity. Based on our observations, we can conclude that our TiO_2 particles, having high anatase crystallinity with mixed phase as well as a large surface area, should have beneficial effects including light absorption, charge separation and facile surface reaction, all resulting in the enhanced photocatalytic efficiency towards RhB degradation.

As pointed out in the Introduction section and in our previous study, many factors play an important role in determining the photocatalytic activity, such as high crystallinity with the right crystalline phase and large surface area [13,15]. In this study, as the calcination temperature was increased up to 400 °C, amorphous TiO_2 was converted to a metastable anatase phase. When the calcination temperature was increased even higher (e.g., 500 °C), the anatase phase grew and transformed into crystalline rutile. As the calcination temperature was increased up to 800 °C, the anatase phase continuously transformed to rutile and only the rutile phase could be observed. Although the high calcination temperature leads to an increase of crystallinity with the controllable crystalline phase, it resulted in a significantly small surface area. In this study, when the TiO_2 sample was calcined at 500 °C (TiO_2-500), it eventually showed high anatase crystallinity with the mixed crystalline phase of anatase and rutile and it had a significantly higher surface area of ≈61 m^2/g. As previously mentioned, the outstanding catalytic performance of commercial P25 TiO_2 is mainly attributed to the mixed phase composition of anatase and rutile, which might have a beneficial effect on light absorption and charge separation [20]. It should be noted that the increased activity of P25 TiO_2 is due to the electron sink of rutile preventing electron–hole recombination in the anatase phase. It allows an anatase-originating hole to move to the surface, resulting in a high surface reaction under UV light [34]. Another hypothesis regarding the exceptional activity of anatase and rutile P25 is that the presence of rutile crystallites generates a favorable structure in which rapid electron transfer from rutile to lower energy lattice trapping centers of anatase phase occurs under visible-light irradiation. This leads to a more stable charge separation and allows holes to reach the surface for redox reactions. In addition, the small band gap of the rutile phase extends the useful range of light energy into the visible light spectrum [20]. Although our TiO_2-500 catalyst does not have the same dimensions and particle shape, it has a mixed phase of well-crystallized anatase with rutile, which is like highly active P25 TiO_2. Even though the exact functions of rutile phase in mixed phase materials is still controversial in photocatalysis, our TiO_2-500 catalyst should have similar beneficial effects on light absorption and charge separation by high anatase crystallinity with mixed phase composition as well as an additional large surface area, which would result in the enhanced photocatalytic efficiency towards RhB degradation.

Conclusion

We demonstrated the general synthesis of uniform TiO_2 colloidal particles with controllable properties and enhanced photocatalytic activity towards RhB degradation. The particle synthesis was conducted in mixed solvent conditions by sol–gel chemistry through a one-pot process followed by calcination. This study allowed for the systematic investigation of the influences of synthetic parameters such as a solvent composition, surfactant concentration, and concentration of the titanium butoxide. Under the optimum ratio of mixed solvent conditions (ethanol/acetonitrile 3:1), uniform and monodisperse colloidal TiO_2 particles were obtained. As the concentration of surfactant was decreased and the concentration of the TiO_2 precursor was increased, the size of the TiO_2 particles increased. Tuning

the calcination temperature can control the crystallinity and crystalline phase of the colloidal TiO_2 particles. As the calcination temperature was increased and the anatase crystalline phase transformed to its rutile counterpart, the surface area correspondingly decreased. This study determined the optimum crystallinity and surface area that yields the highest photocatalytic performance towards RhB degradation under UV–vis irradiation. Our systematic investigation may provide a good example for elucidating a rational design for more efficient colloidal TiO_2-based photocatalysts.

Experimental

Materials and Chemicals: Ethyl alcohol (C_2H_5OH, 99.9%, anhydrous), acetonitrile (ACN, CH_3CN 99.9%, special guaranteed grade) and ammonium hydroxide (NH_4OH, 28%) were obtained from Daejung Chemical Company. Hydroxypropylcellulose (HPC, MW ≈80,000) and titanium(IV) butoxide (TBOT, 97%, reagent grade) were obtained from Aldrich. Rhodamine B (RhB, 95%, HPLC grade) was purchased from Sigma-Aldrich. All chemicals were used as received without further treatment.

Synthesis: Uniform spherical TiO_2 particles were prepared via a sol–gel reaction of titanium alkoxide in a mixed solvent solution in the presence of a surfactant and an aqueous ammonia solution. The desired amount of hydroxypropylcellulose (HPC) was dissolved in a solution of ethanol and acetonitrile with different volume ratios under vigorous stirring. After completely dissolving the HPC, aqueous ammonia (0.8 mL) was added to the solution. After stirring for 10 min, a solution of tetrabutyl titanate (TBOT) with the desired amount in a mixture of ethanol and acetonitrile was quickly injected into the above solution. The total volume of the reaction mixture was ≈120 mL. The mixture was stirred for 2 h under ambient conditions and the white precipitate was isolated by centrifugation. The white precipitate was washed with ethanol and with DI water a couple of times and dried under vacuum to obtain amorphous spherical TiO_2 particles. The dried TiO_2 particles were charged into an alumina boat in a tubular furnace and calcined at the desired temperature for 3 h under air conditions. After calcination under air, the amorphous TiO_2 particles were crystallized to either the anatase or rutile phase. Before the photocatalytic reaction experiment, the calcined sample (30 mg) was treated with an aqueous NaOH solution (10 mL, 2 M) to improve dispersity in aqueous solution.

Characterization: The particle morphology and dispersity were observed using transmission electron microscopy (TEM, JEM-2100, JEOL). The crystalline phases of the samples were determined by X-ray diffraction (XRD) analysis using a Rigaku D/mas-2200 diffractometer with Cu Kα radiation (λ = 1.5406 Å). The pore property was characterized using the nitrogen adsorption/desorption technique at 77 K using a nitrogen sorption instrument (ASAP 2000, Micromertics).

Catalytic activity test: The photocatalytic activity of the prepared samples was evaluated by following the photocatalytic degradation of rhodamine B. Before the photocatalysis test was initiated, the well-dispersed catalyst in the solution was first irradiated under UV light for 30 min to remove any residual organic contaminates on the surface of the catalyst. The catalyst (30 mg of TiO_2) was dispersed in an aqueous RhB solution (50 mL, 10^{-5} M) in a 100 mL reactor cell and the solution was stirred in dark conditions for 30 min to ensure the adsorption of RhB onto the surface of the catalyst. A 70 W commercial LED lamp was used as the light source during the photocatalysis experiments. The concentration of RhB was monitored by UV–vis spectrophotometry (Thermo Fisher Scientific, Genesys 10S) during the reaction.

Supporting Information

Supporting Information File 1

Additional experimental results.
[https://www.beilstein-journals.org/bjnano/content/supplementary/2190-4286-9-163-S1.pdf]

Acknowledgements

This research was supported by the Basic Science Research Program through the National Research Foundation of Korea (NRF) funded by the Ministry of Science, ICT & Future Planning (NRF-2017R1A4A1014806). This work was supported by Korea Environment Industry & Technology Institute (KEITI) through "The Chemical Accident Prevention Technology Development Project", funded by the Korea Ministry of Environment (MOE)(#2017001960004).

References

1. Lu, Z.; He, L.; Yin, Y. *Chem. Commun.* **2010,** *46,* 6174–6176. doi:10.1039/c0cc01734e
2. Lu, Z.; Ye, M.; Li, N.; Zhong, W.; Yin, Y. *Angew. Chem., Int. Ed.* **2010,** *49,* 1862–1866. doi:10.1002/anie.200906648
3. Moon, H. G.; Shim, Y.-S.; Jang, H. W.; Kim, J.-S.; Choi, K. J.; Kang, C.-Y.; Choi, J.-W.; Park, H.-H.; Yoon, S.-J. *Sens. Actuators, B* **2010,** *149,* 116–121. doi:10.1016/j.snb.2010.06.014
4. Chen, J. S.; Archer, L. A.; Wen Lou, X. *J. Mater. Chem.* **2011,** *21,* 9912–9924. doi:10.1039/c0jm04163g
5. Chen, J. S.; Luan, D.; Li, C. M.; Boey, F. Y. C.; Qiao, S.; Lou, X. W. *Chem. Commun.* **2010,** *46,* 8252–8254. doi:10.1039/c0cc02973d
6. Lee, I.; Joo, J. B.; Yin, Y.; Zaera, F. *Angew. Chem., Int. Ed.* **2011,** *50,* 10208–10211. doi:10.1002/anie.201007660
7. Joo, J. B.; Zhang, Q.; Dahl, M.; Lee, I.; Goebl, J.; Zaera, F.; Yin, Y. *Energy Environ. Sci.* **2012,** *5,* 6321–6327. doi:10.1039/C1EE02533C

8. Joo, J. B.; Zhang, Q.; Lee, I.; Dahl, M.; Zaera, F.; Yin, Y. *Adv. Funct. Mater.* **2012,** *22,* 166–174. doi:10.1002/adfm.201101927
9. Joo, J. B.; Lee, I.; Dahl, M.; Moon, G. D.; Zaera, F.; Yin, Y. *Adv. Funct. Mater.* **2013,** *23,* 4246–4254. doi:10.1002/adfm.201300255
10. Chen, D.; Cao, L.; Huang, F.; Imperia, P.; Cheng, Y.-B.; Caruso, R. A. *J. Am. Chem. Soc.* **2010,** *132,* 4438–4444. doi:10.1021/ja100040p
11. Wang, H.; Liu, H.; Wang, S.; Li, L.; Liu, X. *Appl. Catal., B: Environ.* **2018,** *224,* 341–349. doi:10.1016/j.apcatb.2017.10.039
12. Fujishima, A.; Honda, K. *Nature* **1972,** *238,* 37–38. doi:10.1038/238037a0
13. Joo, J. B.; Zhang, Q.; Dahl, M.; Zaera, F.; Yin, Y. *J. Mater. Res.* **2013,** *28,* 362–368. doi:10.1557/jmr.2012.280
14. Joo, J. B.; Liu, H.; Lee, Y. J.; Dahl, M.; Yu, H.; Zaera, F.; Yin, Y. *Catal. Today* **2016,** *264,* 261–269. doi:10.1016/j.cattod.2015.09.008
15. Joo, J. B.; Dahl, M.; Li, N.; Zaera, F.; Yin, Y. *Energy Environ. Sci.* **2013,** *6,* 2082–2092. doi:10.1039/c3ee41155a
16. Banerjee, A. N.; Hamnabard, N.; Joo, S. W. *Ceram. Int.* **2016,** *42,* 12010–12026. doi:10.1016/j.ceramint.2016.04.128
17. Wang, X.; Bai, L.; Liu, H.; Yu, X.; Yin, Y.; Gao, C. *Adv. Funct. Mater.* **2018,** *28,* 1704208. doi:10.1002/adfm.201704208
18. Yun, H. J.; Lee, H.; Joo, J. B.; Kim, N. D.; Kang, M. Y.; Yi, J. *Appl. Catal., B: Environ.* **2010,** *94,* 241–247. doi:10.1016/j.apcatb.2009.11.014
19. Yun, H. J.; Lee, H.; Joo, J. B.; Kim, W.; Yi, J. *J. Phys. Chem. C* **2009,** *113,* 3050–3055. doi:10.1021/jp808604t
20. Hurum, D. C.; Agrios, A. G.; Gray, K. A.; Rajh, T.; Thurnauer, M. C. *J. Phys. Chem. B* **2003,** *107,* 4545–4549. doi:10.1021/jp0273934
21. Liu, H.; Joo, J. B.; Dahl, M.; Fu, L.; Zeng, Z.; Yin, Y. *Energy Environ. Sci.* **2015,** *8,* 286–296. doi:10.1039/C4EE02618G
22. Fujishima, A.; Zhang, X.; Tryk, D. A. *Surf. Sci. Rep.* **2008,** *63,* 515–582. doi:10.1016/j.surfrep.2008.10.001
23. Wu, B.; Guo, C.; Zheng, N.; Xie, Z.; Stucky, G. D. *J. Am. Chem. Soc.* **2008,** *130,* 17563–17567. doi:10.1021/ja8069715
24. Trentler, T. J.; Denler, T. E.; Bertone, J. F.; Agrawal, A.; Colvin, V. L. *J. Am. Chem. Soc.* **1999,** *121,* 1613–1614. doi:10.1021/ja983361b
25. Zhang, Q.; Joo, J.-B.; Lu, Z.; Dahl, M.; Oliveira, D. Q. L.; Ye, M.; Yin, Y. *Nano Res.* **2011,** *4,* 103–114. doi:10.1007/s12274-010-0058-9
26. Dahl, M.; Dang, S.; Bong Joo, J.; Zhang, Q.; Yin, Y. *CrystEngComm* **2012,** *14,* 7680–7685. doi:10.1039/c2ce25799h
27. Liu, H.; Ma, H.; Joo, J.; Yin, Y. *Sci. China Mater.* **2016,** *59,* 1017–1026. doi:10.1007/s40843-016-5127-7
28. Guo, W.; Liu, X.; Huo, P.; Gao, X.; Wu, D.; Lu, Z.; Yan, Y. *Appl. Surf. Sci.* **2012,** *258,* 6891–6896. doi:10.1016/j.apsusc.2012.03.126
29. Hu, Y.; Ge, J.; Sun, Y.; Zhang, T.; Yin, Y. *Nano Lett.* **2007,** *7,* 1832–1836. doi:10.1021/nl0708157
30. Stöber, W.; Fink, A.; Bohn, E. *J. Colloid Interface Sci.* **1968,** *26,* 62–69. doi:10.1016/0021-9797(68)90272-5
31. Joo, J. B.; Vu, A.; Zhang, Q.; Dahl, M.; Gu, M.; Zaera, F.; Yin, Y. *ChemSusChem* **2013,** *6,* 2001–2008. doi:10.1002/cssc.201300416
32. Wang, P.; Chen, D.; Tang, F.-Q. *Langmuir* **2006,** *22,* 4832–4835. doi:10.1021/la060112p
33. Zheng, R.; Meng, X.; Tang, F. *J. Solid State Chem.* **2009,** *182,* 1235–1240. doi:10.1016/j.jssc.2009.01.032
34. Bickley, R. I.; Gonzalez-Carreno, T.; Lees, J. S.; Palmisano, L.; Tilley, R. J. D. *J. Solid State Chem.* **1991,** *92,* 178–190. doi:10.1016/0022-4596(91)90255-G

License and Terms

This is an Open Access article under the terms of the Creative Commons Attribution License (http://creativecommons.org/licenses/by/4.0), which permits unrestricted use, distribution, and reproduction in any medium, provided the original work is properly cited.

The license is subject to the *Beilstein Journal of Nanotechnology* terms and conditions: (https://www.beilstein-journals.org/bjnano)

The definitive version of this article is the electronic one which can be found at:
doi:10.3762/bjnano.9.163

BEILSTEIN JOURNAL OF NANOTECHNOLOGY

Nanocellulose: Recent advances and its prospects in environmental remediation

Katrina Pui Yee Shak*, Yean Ling Pang* and Shee Keat Mah

Review

Open Access

Address:
Department of Chemical Engineering, Lee Kong Chian Faculty of Engineering and Science, Universiti Tunku Abdul Rahman, Jalan Sungai Long, Bandar Sungai Long, Cheras 43000 Kajang, Selangor Darul Ehsan, Malaysia

Email:
Katrina Pui Yee Shak* - shakpy@utar.edu.my;
Yean Ling Pang* - pangyl@utar.edu.my

* Corresponding author

Keywords:
adsorbent; environmental remediation; membrane; nanocellulose; nanomaterials; photocatalyst

Beilstein J. Nanotechnol. **2018,** *9,* 2479–2498.
doi:10.3762/bjnano.9.232

Received: 07 April 2018
Accepted: 27 August 2018
Published: 19 September 2018

This article is part of the thematic issue "Energy conversion, storage and environmental remediation using nanomaterials".

Guest Editor: W.-J. Ong

© 2018 Shak et al.; licensee Beilstein-Institut.
License and terms: see end of document.

Abstract

Among many other sustainable functional nanomaterials, nanocellulose is drawing increasing interest for use in environmental remediation technologies due to its numerous unique properties and functionalities. Nanocellulose is usually derived from the disintegration of naturally occurring polymers or produced by the action of bacteria. In this review, some invigorating perspectives on the challenges, future direction, and updates on the most relevant uses of nanocellulose in environmental remediation are discussed. The reported applications and properties of nanocellulose as an adsorbent, photocatalyst, flocculant, and membrane are reviewed in particular. However, additional effort will be required to implement and commercialize nanocellulose as a viable nanomaterial for remediation technologies. In this regard, the main challenges and limitations in working with nanocellulose-based materials are identified in an effort to improve the development and efficient use of nanocellulose in environmental remediation.

Review

Introduction

The rampant emergence of advanced, new nanomaterials is redefining many industries and blurring traditional research boundaries. In the drive towards sustainable development, the growing application of renewable, biodegradable, green materials to substitute non-renewable resources have roused substantial interest on a global scale. In addition, the uprising environmental concerns warrant the application of bio-renewable polymers in the production of nanomaterials.

In recent years, nanomaterials have displayed potential in effective detection and removal of greenhouse gases, chemical contaminants, organic pollutants, and biological agents. These mate-

rials come in various morphologies and have various functions (e.g., adsorbents, catalysts, or membranes). The high reactivity and high surface area of nanomaterials are some of the notable features which provide an advantage in environmental remediation over other conventional alternatives [1]. Promising materials such as graphitic carbon nitride [2,3], carbon nanodots [4], and two-dimensional carbon-based nanocomposites [5-7] are a few trending nanomaterials that have already found extensive applications in both environmental remediation and energy generation. In the past, carbon nanotubes (CNTs) have received a great deal of attention as materials for environmental remediation due to their impressive mechanical properties and superior adsorption capability. However, the need for non-renewable sources such as fossil fuel to produce CNTs remains a challenge. As of late, research progression in environmental science continues to push for materials which are renewable, biocompatible, and less toxic as a replacement for CNTs.

Given the abundance of plant resources, plant extracts are the most studied category to date for the synthesis of green nanomaterials [8]. Cellulose, one of the most abundant natural polymers, has the potential to overcome challenges pertaining to material biodegradability, renewability, cost, and energy. Furthermore, cellulose found in most lignocellulosic biomass, derived from agricultural waste, energy crops and forestry residues, provides a better option over food crops as a renewable resource for the production of new materials due to its availability in large amounts and low cost [9]. Moreover, cellulose is known as a nontoxic material [10-12].

In the past few decades, nanocellulose has demonstrated good performance in numerous applications, including paper making [13], water [14] and wastewater treatment [15], biomedical engineering [16], and energy production [17]. Different types of nanocellulose were first mentioned in articles by Ranby [18] and Turbak et al. [19], not only as a concept for scientific theoretical discussion, but also to report actual new cellulose products known as cellulose nanocrystal (CNC) and microfibrillated cellulose (MFC) or cellulose microfibril (CMF), respectively. Decades later, nanocellulose of various nanoparticle-size distribution and structure is still being produced by numerous active organizations until today.

As a case in point, the potential applications of nanocellulose are gaining a significant level of attention and have been extensively reviewed. Recent studies have significantly contributed to the understanding of the many properties, applications, and functionalization of nanocellulose. To date, most reviews are focused on only a specific type of nanocellulose-based material (either aerogel sorbents or adsorbents only) [11,20,21] or a specific type of treatment under environmental remediation (e.g., water treatment only) [22,23]. This review aims to provide an overview of the recent development and prospects of various nanocellulose-based materials used in various applications under the category of environmental remediation, including past achievements, current advances, and potential directions. The recent developments of nanocellulose used as an adsorbent, photocatalyst, flocculant or membrane for various applications in environmental remediation are detailed in this review.

Categorization of nanocellulose

Cellulose nanomaterials (nanocellulose) can be categorized into two major groups based on its size and structure: nano-objects and nanostructures [24]. The two major groups can be branched down into specific subgroups: cellulose microcrystal (CMC) and cellulose microfiber under nano-object cellulose, and cellulose nanocrystal (CNC) along with cellulose nanofiber (CNF) under nanostructured cellulose. The main difference between nano-object cellulose (10–100 μm) and nanostructured cellulose (1–50 nm) is the size of the cellulose nanomaterial. Figure 1 illustrates the difference in length of CNF and CNC alongside with a few examples of microscopic images of nanocellulose derived from plants [25-28].

However, the Technical Association of the Pulp and Paper Industry (TAPPI) and multiple concerned bodies have recommended that nanocellulose be categorized into two main groups: CNC and CNF [20]. Overall, there are no fixed definitions for each group, since many nanocellulose sources coexist in the extensive and overlapping material space [29].

Cellulose nanofiber (CNF)

Various terms have been used interchangeably with CNF, such as nanofibrillated cellulose (NFC), nanofibrillar cellulose, nanofibrous cellulose, and bacterial nanocellulose (BC) [24,29,30]. CNFs can be distinguished through their structure which is comprised of stretched masses of elementary nanofibrils with alternating crystalline and amorphous domains [24] (Figure 2a).

Due to the complex structure of cellulose fibre, the plant cell wall must be subjected to strong mechanical disintegration before turning the fibres into CNF [24]. The diameter of the fibres is commonly within the range of 10–100 nm, depending on the disintegration power [24]. In the context of CNF extraction from feedstocks, numerous mechanical techniques have been applied as discussed later. To our knowledge, BC is the only cellulose synthesized using the bottom-up approach via enzymatic synthesis. It is one of the purest forms of cellulose produced by non-photosynthetic organisms through enzymatic polymerization of organic substrates such as sugar and glycerol [11,31]. The main difference between BC and other

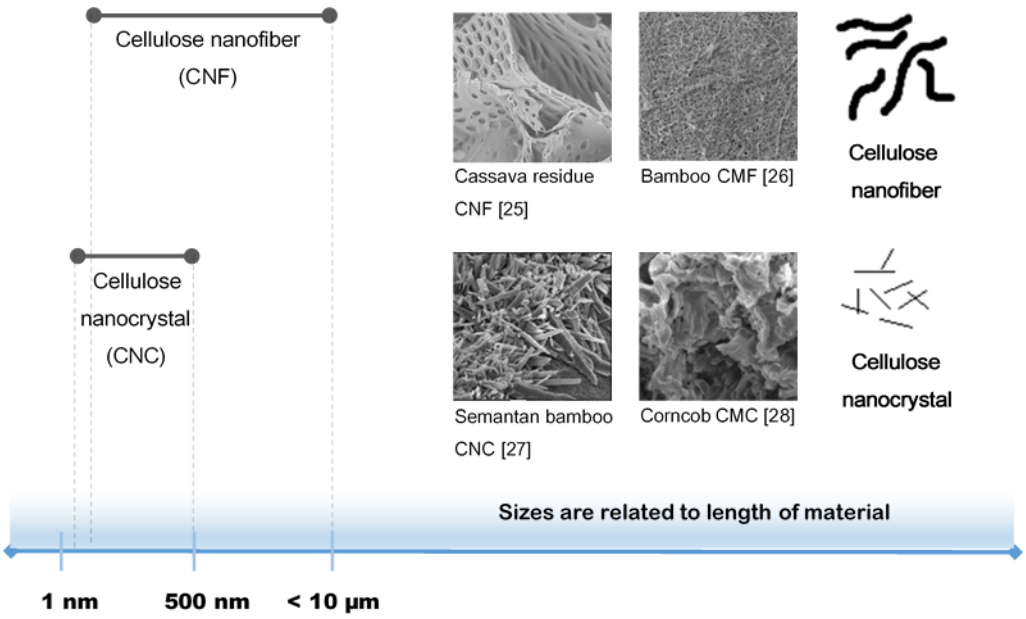

Figure 1: Size chart of nanocellulose based on material length (with microscopic images of various nanocellulose sources). Reprinted in part from Huang et al. [25], Nguyen et al. [26], Razalli et al. [27], and Kunusa et al. [28].

plant-derived CNFs is the absence of certain functional groups (except alcohol) and polymers (lignin, hemicellulose, and pectin) in BC [32]. Therefore, BC is known for its high-purity in CNF form as well as high water-retaining capacity and crystallinity (80–90%) among the various types of CNFs [11].

Cellulose nanocrystal (CNC)

CNC goes by a few other terms: nanocrystalline cellulose (NCC) and cellulose nanowhisker (CNW). In contrast to CNF, CNC is less flexible due to its higher crystallinity (Figure 2b). This is because CNCs have an elongated rod-like shape made up of crystalline regions isolated from CNFs [24]. Its assembly occurs through a series of alterations, beginning with the excision of amorphous regions in CNFs to isolate the crystalline regions, which is categorized today as CNC [24]. Conventionally, this process is achieved using concentrated acid via acid digestion prior to additional treatment methods [33]. Chemical treatment methods are predominantly used as the main treatment method for CNC extraction. Overall, multiple post-treatments and purification steps must be taken to extract and obtain CNC.

Sources of nanocellulose

Cellulose, generally speaking, has to be extracted from a source before nanocellulose can be produced. To date, cellulose can

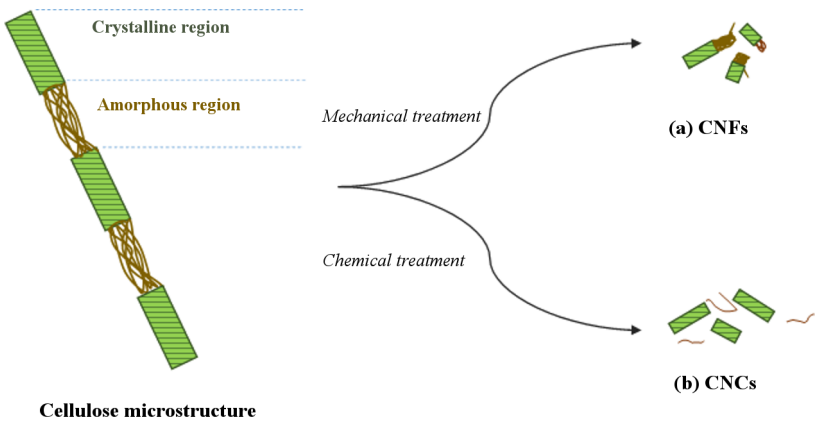

Figure 2: The structures of (a) cellulose nanofibers (CNFs) and (b) cellulose nanocrystals (CNCs) produced from cellulose.

be obtained from a broad range of sources including algae, bacteria, plants, and tunicates. The source of the cellulose determines not only its size and properties, but also the energy consumption of the extraction process to produce nanocellulose [24]. Although it was reported that the source of cellulose only plays a minor role on the final properties of CNF [34], this is probably process-specific and true only under certain conditions [35]. Conversely, CNC properties are source-dependent, thus suitable cellulosic raw material and appropriate extraction techniques must be established based on the required final CNC properties and applications [33]. Furthermore, the environmental impact associated with the sourcing, extraction, processing, and use of raw materials used to fabricate products for environmental applications should be taken into consideration [36].

Algae

Much progress towards environmental sustainability has been made by utilizing the upcoming secret weapon of green energy: algae. Recent research on artificial photosynthesis such as CO_2 fixation and water splitting has boosted the appeal of algae [37]. Significant attention has been given to the use of algae to fabricate adsorbents and membranes from its extracted nanocellulose for environmental remediation. The green alga, known by its scientific name *Cladophora*, is also known for its use for nanocellulose production. *Cladophora* green algae is also known as the *Shiogusa* seaweed in Japan. The use of these green filamentous algae for nanocellulose production is appealing as it can help resolve issues concerning water pollution in coastal areas. Nicolai and Preston's findings offer compelling insights into the differences in cell-wall characteristics of various algae species, concluding that most *Cladophorales* algae are highly crystalline [38]. According to Mihranyan [39], the highly crystalline characteristic of *Cladophora* cellulose suggests higher inertness of its cellulose which reduces its susceptibility to chemical treatments compared to most native cellulose derived from conventional land plants. The filters fabricated from *Cladophora* algae cellulose have been tested and proven for trapping swine influenza virus particles with retention efficiency that matches industrial filters [40]. In addition, adsorbent beads have been fabricated using *Cladophora* cellulose for fast adsorption of palladium (II) ions of up to 80% maximum capacity in 2 h [41]. The initiation of this study could develop an alternative for electronic waste management by recovering and recycling palladium through an efficient and low-cost technology [42]. Algae as a supply for nanocellulose production could increase the production of cellulose significantly in an inexpensive manner and reduce greenhouse gases by absorbing carbon dioxide compared with bacteria [43].

Bacteria

Building on the multifunctional and environmental benefits of nanocellulose materials, many researchers have started to investigate the capacity for nanocellulose production through microbial hosts. Similar to algae-based cellulose, BC is of high purity as it is free from other polymers and functional groups except alcohol [32,44]. According to Gatenholm and Klemm [45], a typical BC production process can take up to two weeks to produce cellulose. Furthermore, nanocellulose produced from BC possesses higher crystallinity than plant-derived nanocellulose [46]. Over the decades, the types of sources used for cellulose production has varied widely. So far, cellulose produced by one of the few common bacterial species, such as *Acetobacter xylinum* (presently *Gluconacetobacter xylinus* or *Komagataeibacter medellinensis*) and *Gluconacetobacter medellinensis,* were investigated for their potential as adsorbent, catalyst, and membrane. BC-based adsorbent, catalyst, and aerogel membrane were applied for the removal of copper and lead [47], dye removal [44], and membrane distillation [48]. Ultimately, the current goal in BC production is linked to resolving the challenging aspect of its fermentation process which requires new cost-effective culture mediums to facilitate high BC production within short periods of time [49].

Plants

Plant cellulose fibres are one of the most extensively studied and used main sources for nanocellulose fabrication. Usually, it is chosen over BC and tunicate-based cellulose when thinner nanofibers are required for its applications [50]. According to García et al. [33], plant fibres used as cellulose sources can be classified into six groups: bast fibres, core fibres, grass and reed fibres, leaf fibres, seed fibres, and other fibres. The most common type of plant fibre used for cellulose fabrication is wood pulps (categorized under other fibres) due to its relatively high cellulose purity, durable and ductile networks, and good physical properties compared with other plant-based sources [51]. In the past decade, wood pulp nanocellulose has been used to fabricate catalysts for the reduction of 4-nitrophenol [52] and microfiltration membranes for bacteria, virus, and heavy metal ion removal [53]. In addition, bleached birch fibres from *Betula verrucosa* and *B. pendula* were also investigated in a study led by Suopajärvi et al. [54] to fabricate dicarboxylic acid nanocellulose flocculant and examine its effectiveness in the treatment of municipal wastewater (removal of turbidity and chemical oxygen demand (COD)). In another study, cotton microfibers were subjected to acid treatment, washing, and filtration to produce nanocellulose adsorbents for the removal of cadmium and nickel ion from water [55]. In view of these recent developments, there is much that plant-based nanocellulose can offer to green chemistry and biomaterial sciences for environmental remediation.

Tunicates

Nanocellulose can also be obtained from tunicates (sea or marine invertebrate animals). Many studies have identified the use of sea squirts in particular as a contemporary alternative for nanocellulose fabrication. In general, cellulose is formed on the outer tissue of the tunicates (*tunic*) and is comprised of highly pure and crystalline cellulose of CI_{β} allomorph type [24]. A number of sea squirts species, such as *Halocynthia roretzi* [56], *Halocynthia papillosa* [57], and *Metandroxarpa uedai* [58], have been used by researchers to produce CMF. Several attempts have been made to employ tunicate nanocellulose for environmental remediation. For example, Cheng et al. [59] has synthesized a highly efficient filter membrane for oil/water separation by combining super hydrophilic tunicate cellulose nanocrystal and cholesteric liquid crystal structure. The tunicate cellulose was derived from *Halocynthia roretzi drasche*, also known as the sea pineapple. In addition, nanocomposites fabricated from another species known as the stalked sea squirt (*Styela Clava*) has also demonstrated its usefulness as a catalyst for water remediation [60]. In a separate investigation led by Yu et al. [61], stalked sea squirt nanocellulose were also used as an environmentally friendly and inexpensive flocculant to flocculate and harvest microalgae for biodiesel production.

Preparation techniques of nanocellulose

Prior to nanocellulose production, most cellulose is isolated from untreated cellulose pulp which contains hemicelluloses and lignin. Further processing on the purified cellulose pulp is required to produce CNF/CNC. In general, most CNCs and CNFs are produced through breaking down the cellulose fibres into nanosize fragments (top-down process), except for BC and electrospun cellulose nanofiber (ECNF) which utilize bacteria and an electrospinning technique (bottom-up process), respectively [62]. Typically, the production techniques employ several processes in sequence to produce various types of CNF/CNC which differ in terms of morphology, crystallinity, and surface chemistry [32]. These processes involve mechanical disintegration as well as biological and chemical pretreatments (Figure 3). The relevant techniques used to produce nanocellulose from purified cellulose are discussed briefly in this section.

Mechanical disintegration

In general, the majority of literature focuses on mechanical treatment as the principal treatment to produce CNFs [20] while it is also used as post-treatment and purification steps for CNC production [33]. Mechanical disintegration is commonly used to break cellulose pulp into smaller particles. However, efficient mechanical disintegration of cellulosic fibre normally requires elementary fibril delamination of cellulosic fibre instead of merely fibre shredding [32]. The occurrence of fibre shredding during mechanical disintegration of dry cellulose pulp tends to produce nanocellulose with poor mechanical properties. For improved delamination of nanofibrils, an aqueous medium is employed during mechanical disintegration to loosen interfibrillar hydrogen bonding and avoid reverse coalescence or fibril aggregation [32]. Several examples of commonly used techniques for

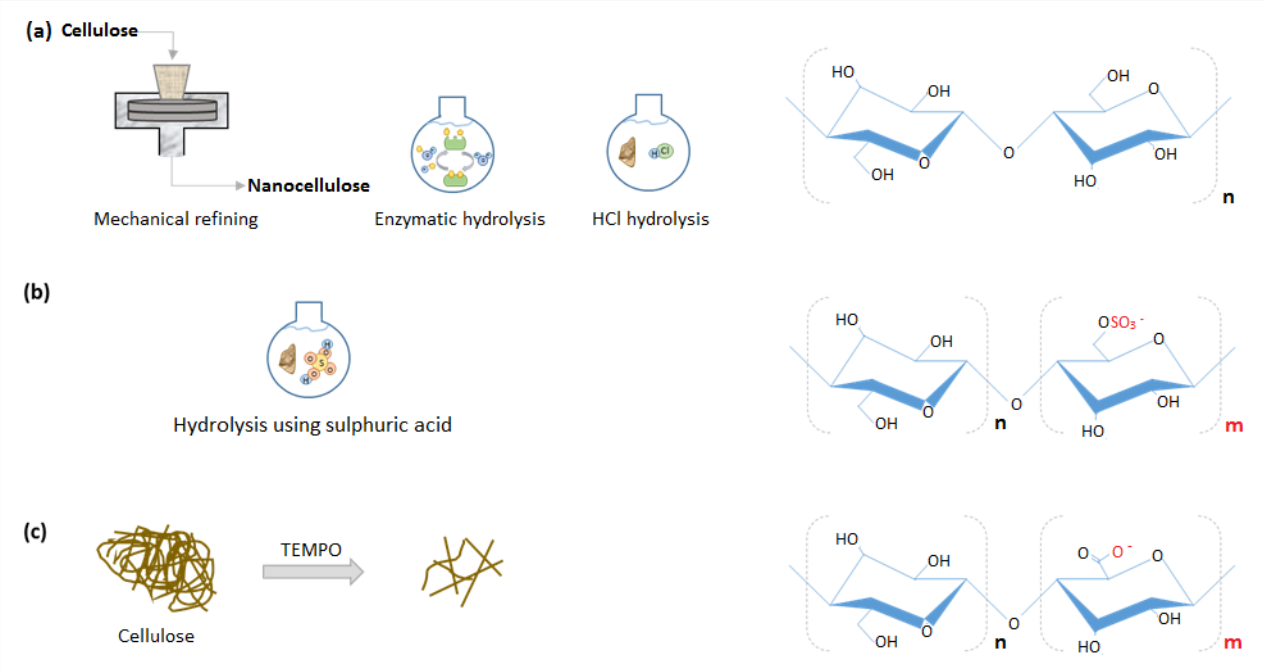

Figure 3: Resultant chemical structures of nanocellulose prepared via (a) mechanical refining, enzymatic hydrolysis, hydrolysis using hydrochloric acid, (b) hydrolysis using sulphuric acid, and (c) TEMPO-oxidation.

efficient delamination of cellulosic fibre include homogenization [63], grinding [64,65], and refining [66]. Unlike finely structured or short rod-like nanocelluloses produced via chemical pretreatment, mechanically disintegrated nanocellulose is clustered (agglomerated) with larger dimensions [66].

According to Park et al. [67], the chemical composition in wood-based CNF has an effect on the defibrillation efficiency in wet disk-milling, which improved defibrillation in the absence of lignin and hemicellulose in cellulose. The transition from micro- to nanoscale during mechanical disintegration of fibres is usually evident in a reduction of viscosity, thermal stability, and crystallinity. In most cases, the principal mechanical treatments used are either aqueous counter collision, ball milling, blending, cryocrushing, electrospinning, extrusion, grinding, homogenization, refining, steam explosion, ultrasonication, or a combination thereof.

Chemical reaction

Effective and energy-efficient nanocellulose preparation techniques are being pursued to sustain and meet the high volumetric output of large-scale production. As a result, the chemical approach has emerged as a strong contender. According to Fan et al. [68], the usage of chemical agents is a significant contributor to the defibrillation process in the nanocellulose production.

Chemical treatments are used to isolate cellulose fibres to generate nanocellulose. Existing chemical pretreatment techniques include acid hydrolysis [69], carboxylation [70], carboxymethylation [71], quaternization [72], sulphonation [73], ionic liquid [74], and solvent-assisted pretreatments [75].

Acid hydrolysis is a common technique used to extract CNC from cellulose. Unlike mechanical disintegration, this technique destroys the amorphous region (non-crystalline region) in microfibrils, leaving the crystalline regions intact. Liu et al. [76] have demonstrated that CNC obtained through sulphuric acid hydrolysis (with $–SO_3^-$ functional group) (Figure 3b) showed superior Ag(I) adsorption capacity over CNC obtained via mechanical grinding. Similar to CNC extraction from cellulose, acid hydrolysis is commonly used to fabricate bacteria nanocrystals from BC microfibrils [77].

To aid in the delamination of nanofibrils in the subsequent step of mechanical disintegration, researchers have devised several chemical pretreatment techniques as supplemental steps to prepare nanocellulose. These techniques involve carboxylation, carboxymethylation, sulphonation, and quaternization to introduce surface charges onto the cellulose. Surface charge modification by carboxylation, carboxymethylation, and sulphonation introduces anionic functionality to aid the defibrillation of cellulose fibres based on the principle of electrostatic repulsion between similar charges [32]. Wågberg et al. [78] revealed that carboxymethylation of CNFs produced thin nanofibrils (3–15 nm) with minimal aggregation and improved uniform width distribution when compared to CNFs with no chemical pretreatment. Other methods like carboxylation via 2,2,6,6-tetramethylpiperidin-1-oxyl (TEMPO)-mediated oxidation (Figure 3c) have been shown to improve the delamination of nanofibrils [32] and produce well-defined individual CNFs when coupled with mechanical treatment. Recently, oxidative sulphonation of cellulose using periodate and bisulphate has been considered a potential green technique to promote nanofibrillation of cellulose compared with TEMPO-mediated oxidation. Sulphonation of cellulose provides lower anionic charges, broader functionalities, and consumes less harmful and expensive chemicals in its recyclable process which does not generate halogenated waste [79]. In contrast, quaternization has been used to provide cationic functionality to nanocellulose, which could be particularly useful for particle aggregation of negatively charged pollutants to coagulate and flocculate kaolin colloids as reported by Liimatainen et al. [79].

On the other hand, the utilization of green solvents (ionic liquids) as both solvent and catalyst for cellulose hydrolysis has become a popular alternative method for nanocellulose extraction. The extraction of nanocellulose using ionic liquids, such as 1-butyl-2-methyllimidazolium hydrogen sulphate ($BmimHSO_4$), has been considered as a green approach for its economical process (due to high recovery of ionic liquid for reuse) and zero hazardous waste products [80].

Biological reaction

To combat challenges pertaining to high energy cost (linked to mechanical disintegration) and environmental concerns (linked to chemical pretreatment), enzymatic hydrolysis is introduced as an additional pretreatment step to reduce chemical waste and energy consumption. Enzymatic hydrolysis is commonly applied before mechanical disintegration of cellulose (refining or blending) in nanocellulose production. The addition of mono-component endoglucanase enzymes has proven to promote cell wall delamination during mechanical disintegration of cellulose in a homogenizer [81]. Furthermore, nanofibers produced via enzymatic treatment using endoglucanase were proven to yield better structure in terms of average molar mass and larger aspect ratio than nanofibers produced from acid hydrolysis (chemical treatment) [82].

Several other enzymes have been used for the preparation of nanocellulose: (1) cellulases [83], (2) pectinases [84], (3) xylanases [85], and (4) ligninases. Beltramino and

co-workers [83] demonstrated that the application of cellulase as an enzyme substrate in the presence of acetate buffer was able to generate CNC with greater crystal dimensions and reduced sulphur content from cotton linter. Conversely, chemically treated banana fibres showed larger crystallinity (300%) in nanofibers than nanofibers treated with xylanase (200%) [85] since the enzyme showed difficulty in solubilizing the hemicelluloses and could not penetrate the cellulose chains to undergo efficient cellulose hydrolysis. Hemicellulose is a common component found in cellulose sources which hampers the separation of cellulose nanofibrils. Recently, Hu et al. [86] combined the use of endogluconase, lytic polysaccharide monoxygenase (LPMO), and xylanase as enzymes before ultrasound treatment for the nanofibrillation of cellulose derived from Kraft pulp. "Accessory enzymes" such as LPMO and xylanase were used to boost the hydrolytic performance of cellulose cocktails while endoglucanase facilitated the refining and fibrillation of cellulose. Overall, the potential of increasing substrate accessibility was made possible by the synergistic effect of the enzymes. On the other hand, Nechyporchuk et al. [32] reported that the rheological behaviour of CNF suspensions produced with enzymatic pretreatment showed superior flocculation ability compared with CNF produced from chemical pretreatment.

Nanocellulose-based materials for environmental remediation

The global demand on utilizing sustainable and ecologically friendly products from natural resources such as cellulose has paved the way for intensive research on the potential application of micro- and nanometre-sized cellulose materials. Cellulose has been mainly used as reinforcement for plastic and paper industries while at the same time its application in the environmental field has recently aroused much attention. Nanometre-sized cellulose materials or nanocellulose has acquired an advantage over conventional cellulose fibres due to its higher surface area, aspect ratio, and Young's modulus [87]. The versatility of cellulose-based materials has opened up doors for its use in a wide range of applications. In this section, an overview on the recent advanced applications of cellulose-based composites as adsorbents, photocatalysts, flocculants, and membranes in the field of environmental remediation will be reviewed.

Nanocellulose-based adsorbents

Wastewater purification using cellulose-based adsorbents materials has been developed as an alternative to the energy intensive and expensive technology based on commercial, activated carbon-based adsorption (Table 1).

Unmodified cellulose usually does not exhibit good adsorption performance, therefore it needs to be specifically tailored to provide selective and enhanced interactions for a positive outcome. The essential and fundamental characteristics of cellulose include its hydrophilicity, functionalization ability, and ease of tunability of various properties like surface area, aspect ratio, quantum size effects as well as chemical accessibility [105]. Nanocellulose has been recognized as an excellent natural biomaterial adsorbent for wastewater treatment due to its adsorption affinity towards organic pollutants. Unlike micrometre-sized cellulose, the nanometre-sized counterparts are relatively smaller in dimensional size but also possess a larger surface area with improved porosity, which limits internal diffusion and quantum size effects [106]. The improvement in adsorption removal efficiency of nanocellulose could be due to the increased surface area, crystalline nature, and number of available functional moieties. Taleb et al. [98] reported that the introduction of amino-terminal functionalities on MFC and nanocellulose surfaces can improve their function as magnetite-based adsorbents for arsenic removal. It is proven that amino groups accessible for iron coordination result in a larger number of adsorption sites on the nanocellulose surface as compared to MFC.

In addition, nanocellulose has also been proposed as an adsorbent of residual antibiotics which are commonly found in industrial discharge, aquaculture, and effluent with medicinal residues. By converting cellulose to nanocellulose, the surface area increases exponentially along with its crystalline nature and the number of surface hydroxy groups (–OH) [101]. The abundant surface –OH groups act as hydrophilic sites to accelerate nucleation and growth of inorganic particles, consequently controlling the morphology, particle size, and crystallinity [107]. Such readily available surface –OH groups offer an ideal platform for the fabrication of hybrid nanocomposites with hierarchical structure. Besides, these –OH groups can be tailored for selective and improved interactions through a variety of chemical modifications [88]. The hydrophilicity of nanocellulose can be improved by inserting hydrophilic groups, such as carboxylic acids, alcohols, and amides, into its polymer chains. Reactive –OH groups are proven to enhance the adsorption behaviour of modified nanocellulose, especially towards organic contaminants. However, the hydrophilic nature of nanocellulose might cause it to aggregate during the drying process due to the greater number of –OH groups on the surface [93]. Therefore, an overabundance of –OH groups can produce an opposing effect, which is not ideal for wastewater treatment.

Among the hydrophilic functional groups, the functionalization of nanocellulose with carboxy groups through carboxylation can improve its adsorption performance for the removal of toxic metal ions from wastewater. A carboxy group has two lone

Table 1: Cellulose-based biopolymer adsorbents for various types of organic pollutants.

Biopolymer adsorbent	Model pollutants	Adsorption capacity (mg/g)	Duration (min)	Ref.
calcium hydroxyapatite microfibrillated cellulose	Cr(VI)	114.79	5	[88]
magnetic Fe_3O_4@SiO_2@cellulose composite	Cr(VI)	171.5	30	[89]
aminopropyltriethoxysilane-modified microfibrillated cellulose	Ni(II) Cu(II) Cd(II)	159.88 200.17 471.58	300	[90]
cotton fibre functionalized with triethylenetetramine and carboxymethyl chitosan	Pb(II) Cu(II)	144.93 95.24	120	[91]
poly(itaconic acid)–poly(methacrylic acid)-grafted-nanocellulose/nanobentonite composite	Co(II)	350.8	120	[92]
	U(VI)	121.02	120	[93]
MnO_2-loaded biocomposite based on microcrystalline cellulose	Pb(II)	247.5	180	[94]
sulphonated cellulose	Fe(III) Pb(II) Cu(II)	98.7 83 47.5	30	[95]
sulphonated nanofibrillar cellulose	Pb(II)	248.6	1200	[96]
cationic cellulose nanofibers functionalized with glycidyltrimethylammonium chloride	PO_4^{3-} SO_4^{2-} F^- NO_3^-	55 50 10.6 44		[97]
nanocellulose-amino linked by maleic acid supported on magnetite	arsenic	85.3	90	[98]
Fe_3O_4@cellulose core–shell magnetic biopolymer	congo red	131	11	[99]
amino-functionalized nanocrystalline cellulose	acid red GR congo red 4BS reactive light yellow K-4G	134.7 199.5 183.0	300	[100]
carboxylate-functionalized adsorbent based on cellulose nanocrystals	crystal violet methylene blue malachite green basic fuchsin	243.90	240	[101]
functionalization of cellulose with hyperbranched polyethylenimine	congo red cationic basic yellow 28	2100 1860	60	[102]
cellulose nanocrystal–alginate hydrogel beads	methylene blue	255.5	210	[103]
cellulose aerogel based on cationic cellulose nanofibrils	blue dye CR19 red dye 180 orange dye 142	230 160 560	80	[104]

pairs of electrons on the oxygen, and hence it is required to form a chelate with a divalent metal. In this regard, Qiao et al. [101] synthesized a carboxylate-functionalized adsorbent by grafting maleic anhydride on primary –OH of CNC. This modified nanocellulose adsorbent was used for the removal of cationic dyes from aqueous solution by forming a bidentate arrangement between the dye and the adsorbent's carboxy groups. Meanwhile, Anirudhan et al. [92,93] modified a nanocellulose/nanobentonite composite adsorbent with multiple carboxy functional groups for the adsorption of uranium(VI) and cobalt(II). The co-polymerization of itaconic acid and methacrylic acid was able to introduce three carboxy functionalities which increased reactivity and hydrophilicity for effective removal of the metal ions from the aqueous solution. The adsorption capacity of the resultant adsorbent increased with increasing surface carboxylic group concentration of the adsorbent. A large amount of strongly ionisable COO^- groups could be generated through functionalization with poly(acrylic acid) [105]. Besides, carboxylated nanocellulose displayed high uptake adsorption capacity for several cationic dyes such as methylene blue, basic fuchsin, crystal violet and malachite green [101]. Carboxylated CNC, with a high COOH content of 2.1 mmol/g, showed a significant uptake of about 769 mg/g for methylene blue as compared to CNC with surface sulphate groups.

Alternatively, amine modification aids the chelating action on the desired pollutant anions, thereby enhancing the adsorption capacity of the nanocellulose adsorbent materials. Metal ions can adsorb onto the adsorbent via electrostatic interaction and ion exchange since amino groups are easily protonated under acidic conditions [89]. The amino group possesses a lone pair of electrons which is attributed to the nitrogen atoms and may form a covalent bond with metal ions. The adsorption of metals ions is coordinated by amino and hydroxy groups found in the functionalized cellulose. Amine functional groups usually

induce a high adsorption rate at low pH while a decrease in the adsorption uptake capacity is observed in medium with pH above 8. The aminopropyltriethoxysilane modified MFC's affinity for different metal ions follows the order of Cd(II) > Cu(II) > Ni(II) [90]. The modified nanocellulose materials were able to adsorb metal ions due to the presence of amino ($–NH_2$) on aminosilane and/or –OH groups on cellulose fibre. Besides, cationic functionality such as amine-functionalized nanocellulose is usually effective for the removal of anionic dyes. Zhu et al. [102] found that functionalization of cellulose with cationic hyperbranched polyethylenimine presented high adsorption capacity for congo red (2100 mg/g) and basic yellow (1860 mg/g).

Sulphonated cellulose possesses a high amount of sulphur binding sites, high anionic charge, and larger surface area, thereby displaying a high affinity towards multiple metal ions and an increase in adsorption [95]. Dong et al. [95] discovered that the order of removal and regeneration efficiencies of sulphonated cellulose for three metal ions were in the order of Fe(III) > Pb(II) > Cu(II) and Cu(II) > Pb(II) > Fe(III), respectively, and hence consistent with its affinity to the adsorbent. It has been reported that the sulphonic group has a larger degree of ionization than other functional groups such as hydroxy and carboxy groups, and thus the electrostatic affinity of the sulphonic group to metal ions is stronger [96,108].

In addition, Sehaqui et al. [97] found that the adsorption capacity of cationic CNFs toward anions increased with the surface charge content of cellulose. They concluded that cationic CNFs with an ammonium content of 1.2 mmol/g can be considered as an efficient adsorbent for negatively charged ions such as nitrate (NO_3^-), phosphate (PO_4^{3-}), fluoride (F^-), and sulphate (SO_4^{2-}). Cationic CNFs exhibited higher selectivity towards multivalent ions (PO_4^{3-} and SO_4^{2-}) than monovalent ions (F^- and NO_3^-).

On the other hand, the development of nanocellulose composites as adsorbents with numerous supportive properties, magnetic nanocellulose for example, is desired due to their good performance in the removal of organic pollutants. Hokkanen et al. [88] reported that calcium hydroxyapatite-microfibrillated cellulose adsorbent was effective for the removal of chromium (Cr(VI)) from aqueous solution. They found that calcium hydroxyapatite nanostructures can interact with cellulose structures effectively, resulting in the enhancement of nanocomposites properties due to their strong hydrogen bond, divalent character, and relatively small ionic radius. Anirudhan et al. [92] chemically modified a composite polymer to produce a poly(itaconic acid)–poly(methacrylic acid)-grafted-nanocellulose/nanobentonite composite as an efficient adsorbent for the removal of cobalt (Co(II)) from aqueous solution. This could increase the availability of the multi-carboxy functional moiety, which is covalently bonded to the inorganic matrix, to effectively bind metal ions.

Conventional cellulose-based adsorbents are difficult to recover from treated wastewater. The recovery step usually requires filtration or high-speed centrifugation. In contrast, magnetic cellulose nanocomposites can easily overcome the recovery issue by application of an external magnetic field. As a result, magnetic nanomaterials have drawn increasing attention. Nanocellulose incorporated with other magnetic nanomaterials is presented as an excellent composite adsorbent with magnetic properties. For example, a core–shell cellulose magnetite (Fe_3O_4) polymeric ionic liquid magnetic biosorbent has been developed and employed for congo red adsorption [99]. The benzyl groups within the cellulose structures are responsible for the magnetic nature of the polymeric ionic liquid which was created via reaction with epichlorohydrin and 1-methylimidazole. In addition, the functionalization could increase its aromatic character, anion exchange capability, and hydrophilic nature of cellulose. Cellulose could also act as a stabilizer for the Fe_3O_4 nanoparticles to prevent crystal growth and aggregation of particles.

In general, magnetic iron oxide is anchored in the polymer matrix to induce magnetic properties in nanocomposites such as Fe_3O_4@SiO_2@cellulose nanocomposite and amino-functionalized magnetic cellulose nanocomposite grafted with glycidyl methacrylate followed by reaction with ethylenediamine [89]. Furthermore, a 7 wt % NaOH/12 wt % urea aqueous solvent was found useful for regenerating Cr(VI) from the amino-functionalized magnetic cellulose nanocomposite. In short, the development of new biomaterials by combining two or more natural materials (or through functionalization of nanocellulose) have become increasingly interesting techniques to construct materials with combined properties which could not be achieved by the individual material alone.

The prospects for nanocellulose-based adsorbents in wastewater treatment have never looked better. But given the mixed results from studies (Table 1), and the practical challenges for implementation (treatment duration, upscaling, and material toxicology) for some cases, further optimization and improvement must be made. Furthermore, the fabrication of nanocellulose-based adsorbents is mostly established based on CNF, and limited when it comes to CNC.

Nanocellulose-based photocatalysts

Recently, numerous inorganic-organic hybrid-based nanostructured composites have emerged as new types of photocatalysts

with remarkable optical, electrical, mechanical, and thermal properties. The gravitation from petrochemical-based feedstock to environmentally friendly biomaterials such as cellulose-based materials is making headway for a cleaner and more sustainable environment [109]. Cellulose-derived materials have been identified as an almost limitless source of chemical raw material as it is the most abundant renewable organic resource on earth. Cellulose has shown attractive potential as an environmental friendly and biocompatible support due to its exceptional properties of chirality, hydrophilicity, and broad chemical variability [110]. Besides, cellulose is usually considered as a good host material for nanoparticles because cellulose can improve the stability and control the growth of nanoparticles while retaining its special morphology [111].

Although cellulose alone exhibits limited photocatalytic activity under UV or visible light irradiation, many semiconductor materials have been added to enhance the photocatalytic activity. Several research groups have demonstrated photocatalytic wastewater treatment using cellulose-based metal oxide nanostructures in the form of thin film, membrane, fibre and hybrid materials under UV and visible light irradiation. Nanocellulose–metal oxide (TiO_2, ZnO, graphene oxide, and Fe_2O_3) composites have been used as photocatalysts to improve

Table 2: Application of nanostructured cellulose-based hybrid photocatalysts in photocatalytic degradation of various types of organic pollutants.

Type of catalyst	Model pollutants	Light source	Photocatalytic degradation efficiency (%) and reaction time (min)	Ref.
graphene oxide and TiO_2 nanoparticle incorporated alginate/carboxymethyl cellulose nanocomposite	30 mL of 30 mg/L congo red	solar light with average intensity of ≈900 W/m^2	98%, 240 min	[112]
nanoscale zinc oxide incorporated graphene oxide/nanocellulose composite	25 mL 2–4 mg/L ciprofloxacin	solar light 100 mW/cm^2	98%, 40 min	[113]
ZnO/cellulose nanocomposite	50 mL 3.25 g/L methylene blue	UV lamp with unknown wavelength and intensity	79%, 300 min	[114]
hydroxypropyl cellulose/molybdenum disulphide nanocomposite hydrogels	250 mL methylene blue	sunlight	90%, 180 min	[115]
TiO_2–hydroxypropyl methyl cellulose nanocomposite	100 mL 10 ppm 4-nitrophenol	250 W halogen lamp (main range 400–800 nm)	85%, 180 min	[116]
graphene oxide/TiO_2/bacterial cellulose nanocomposite	100 mL 10 mg/L methyl orange	UV lamp (365 nm, 175 W)	100%, 120 min	[117]
alginate/carboxymethyl cellulose/TiO_2 nanocomposite hydrogel	30 mL 30 mg/L congo red	sunlight	91.5%, 240 min	[118]
nanocrystalline TiO_2 on cellulose fabric	99.995% CO_2 at flow rate 300 mL/min for 1 h	four UVA lamps (8 W each lamp) λ = 365 nm	194.0 ppm/g and 50.8 ppm/g for CO and CH_4, 360 min	[119]
CdS nanoparticle/bacterial cellulose nanofibers	200 mL 20 ppm methyl orange	300 W Xe lamp with a cut-off of λ < 420 nm	82%, 90 min	[109]
cellulose fibre supported zinc phthalocyanine	10 mL of 50 μM basic green 1	100 W lamp visible light, λ > 400 nm	98%, 90 min	[110]
immobilized Cu_2O nanoparticles in cellulose/graphene oxide composite film	10 mg/L methyl orange	sunlight (cloudy, 20 °C)	72%, 300 min	[120]
N-doped TiO_2 nanorods in regenerated cellulose thin films	150 mL 40 mg/L methylene blue	UV lamp at λ = 312 nm, 30 W	96%, 360 min	[121]
electrospun cellulose acetate membrane supported Ag@AgCl	methyl orange	500 W Xe arc lamp equipped with a UV cut-off filter (λ > 420 nm)	73% , 160 min	[122]
immobilized TiO_2 nanoparticles and laccase on bacterial cellulose membrane	3 mL 15 mg/L reactive red X-3B	UV irradiation with unknown wavelength and intensity	95%, 180 min	[123]
graphene oxide/TiO_2 based ultrafiltration cellulose membranes	3.40×10^{-5} mol/L diphenhydramine at flow rate of ≈0.25 mL/min	UV irradiation 350 nm and 33 mW/cm^2	65%, 240 min	[124]

the degradation rate of organic pollutants as compared to individual materials. Table 2 summarizes the application of cellulose-based photocatalyst nanostructured materials for photocatalytic degradation of various organic pollutants.

Cellulose derivatives can easily adsorb on metal oxide surface layers and provide additional –OH groups on the surface of metal alkoxides [116]. As a result, the surface area of this hybrid structure is expected to increase and expand its wavelength response up to the visible range. Bacterial cellulose shows the ability to act as a metal oxide nanoparticle support due to its high surface-area-to-volume ratio with a fibre diameter in the range of 40–70 nm, high mechanical strength and super-hydrophilicity properties [123]. Its ultrafine three-dimensional network provides bacterial cellulose with a high specific surface area, owing to the well-separated nano- and microfibrils. Besides, the presence of –OH binding sites and a fibrous network can facilitate the adsorption of metal oxide to its surface. Thus, Li et al. [123] proposed the immobilization of TiO_2 nanoparticles on a fine fibrous network of bacterial cellulose via hydrogen bonds and electrostatic adsorption effect for the photocatalytic degradation of reactive X-3B. TiO_2 nanoparticles and cellulose chains are compatible due to covalent bonds, which can improve the rigidity of the polymer chain and increase the energy required to break down the polymer chain [121]. Similar enhancement results were also obtained with cadmium sulphide (CdS) nanocrystals deposited on NCC which was derived from microbial cellulose to act as a highly efficient photocatalyst [109]. The composite catalyst demonstrated a high photocatalytic degradation efficiency of about 82% after 90 min of irradiation and exhibited high recyclability of up to five catalytic cycles.

In addition, the potential of fibrillated cellulose as a support/carrier for catalyst nanoparticles has attracted a lot of attention in recent years. For example, a study led by An et al. [125] discusses the application of CNFs as a support for titanium dioxide nanoparticles to prepare nano-fibrillated cellulose–TiO_2 nanoparticle nanocomposites for photocatalytic hydrogen generation. The as-prepared nanocomposites generated 2–5 more hydrogen molecules in comparison with the control TiO_2 nanoparticles. However, they found that the nanocomposites tend to photodegrade during photocatalytic reaction, and hence some of the nanocomposite particles will be lost during the recycling process. In another study, Taranto et al. [126] found that cellulose was sensitive to UV irradiation and prone to degradation during photocatalysis. The cellulose might compete with organic pollutants such as methanol for photocatalytically generated active species/sites, leading to a decrease in methanol reaction rate. Besides, Puls et al. [127] clarified that TiO_2 could cause pitting on the surface of cellulose acetate/cellulose pulp fibres under UV illumination. Therefore, cellulose nanomaterials need to be coated and covered perfectly by inert UV-absorbing materials in order to protect cellulosic fibres from UV bleaching [128].

An et al. [129] claimed that the prepared nano-fibrillated cellulose/magnetite/titanium dioxide nanocomposites had a higher photocatalytic hydrogen generation rate as compared to the nano-fibrillated cellulose/titanium dioxide sample. The incorporation of magnetite was able to inhibit the photodegradation of the cellulose structure during UV irradiation and this hybrid structure demonstrated high catalyst recyclability using an external magnetic field. Nanoparticles generally tend to aggregate, leading to difficulties in recycling and reuse. However, a rigid cellulose matrix has been recruited for its three-dimensional porous structure to act as a catalyst support and prevent the aggregation and growth of nanoparticles [120]. The application of a nanocellulose-based thin film and membrane showed great potential in wastewater treatment due to its ease of recollection and recycling purpose, resulting in no photocatalyst residue in the reaction system.

Moreover, metal oxide nanoparticles of smaller particle size and larger surface area can be expediently immobilized in the cellulose film to obtain a metal oxide nanoparticles/cellulose nanocomposite. Photogenerated electrons and holes inside the metal oxide nanoparticles are able to migrate to the particle surface, while metal oxide nanoparticles within the nanocomposite film are also inclined to accelerate the interfacial charge carrier transfer and separation [130]. Mohamed et al. [121] reported that the optical properties of a transparent nanocellulose/TiO_2 hybrid thin film were imperative for the UV or visible light irradiation. This led to the enhancement of the electron distribution and transfer to the surface of metal oxide. Consequently, the recombination rate of the photogenerated carriers decreased during the photochemical reaction.

It was reported that electrospun cellulose acetate nanofibrous membranes with large specific surface area, high porosity, and high permeability could be an effective support for photocatalysts [122]. This could create a synergistic effect that enhanced the catalytic performance of the individual materials. Besides, Pastrana-Martínez et al. [124] observed that three photocatalysts, i.e., commercial TiO_2 P25, lab-made TiO_2, and graphene oxide doped TiO_2 (GO-TiO_2), which were assembled on flat sheet cellulose membranes, exhibited multifunctionality of water filtration and photodegradation of diphenhydramine and methyl orange. This study demonstrated the advantage of using a cellulose-derived film to support the TiO_2 nanoparticle–cellulose film as a good support to avoid TiO_2 loss during photocatalytic treatment of wastewater.

Nanocellulose-based flocculant

Common chemical conditioning is usually performed by using inorganic, multivalent cationic coagulants such as aluminium, iron salts or synthetic polyelectrolytes such as synthetic polyacrylamides. These synthetic polyelectrolyte materials pose environmental problems due to their derivatives, monomers or intermediate products that are hazardous, not readily biodegradable, and hold potential toxicity, which can cause secondary pollution to the environment [131]. Consequently, there is a need to look for suitable flocculants which are sustainable and natural bio-based alternatives for wastewater purification. These flocculants are expected to be degradable and prevent secondary pollution to the natural environment.

Biopolymer-based flocculants such as chitosan, tannins, cellulose and alginate are attracting wide interest from many researchers. Bio-based flocculants are not only known for being biodegradable but also have a high specific surface area and have dimensions in the nanoscale regime [132]. Commonly, there are two categories of natural polymer based flocculants [133]. One of these categories involves the grafting of natural polymers to fabricate semi-natural flocculants such as polyacrylamide-grafted hydroxypropyl methyl cellulose [134]. The other type is derived by directly modifying natural polymers to construct improved natural flocculants such as dicarboxylic acid nanocellulose [54].

Reports on the usage of nanocellulose as water chemicals are still rare since researchers mainly focused on adsorption of metals from diluted aqueous solution or photocatalysis as discussed in previous sections. Agglomeration remains an issue in the application of CNCs as flocculants. This is due to the hydrogen bond networks arising from the –OH groups on the CNCs' surface [135]. However, the properties of CNC flocculants can vary with changes in the surface –OH group, and hence the right amount of –OH surface groups must be established to produce an effective flocculant. Anionic surface groups such as hydroxy groups are commonly found in nanocellulose after pulp processing and due to the presence of compounds from the plant cell wall [79]. Consequently, the interaction and compatibility among anionic nanocellulose and several inorganic minerals are commonly negatively charged and weak. It has been reported that an anionic flocculation agent possesses poor solubility in acidic solution and hence, limits its practical application as a flocculant in these conditions [136].

Therefore, chemical pretreatments such as carboxymethylation [79], periodate-chlorite oxidation [79,131], aminoguanidine-reacted wood celluloses [131], 2,2,6,6-tetramethylpiperidin-1-oxyl-mediated (or TEMPO-mediated) [137], and citric/hydrochloric acid hydrolysis [135] are used to increase the anionic charge density or provide cationic charges to the nanocellulose, which has diversified the application of nanocellulose. For example, the modification of nanocellulose to produce such cationic counterparts are especially useful for the removal of anionic particles through molecular interaction of opposing charges which promotes particle aggregation in wastewater treatment.

Currently, functionalization of nanocellulose to generate effective flocculants is carried out by introducing anionic, cationic, or hydrophobic functional groups to the nanocellulose surfaces through a charge neutralization mechanism. The –OH groups on the cellulose surface enables facile functionalization of nanocellulose to introduce the desired functionality and produce highly effective flocculants [138]. The interaction of cellulose with various compounds could be enhanced after introducing new functional groups in order to increase the surface polarity and hydrophilicity [87]. Reported applications of cellulose-based flocculants in wastewater treatment are summarized in Table 3.

Suopajärvi and co-workers had investigated various functionalized nanocellulose materials such as anionic and cationic dialdehyde as water chemicals in flocculation of real wastewater [54,87,131]. The results are promising and proved that functionalized nanocellulose could be employed as potential wastewater treatment agents. The modification on the surface groups on nanocellulose can be done by introducing anionic groups such (such as carboxy) to improve its effectiveness as an adsorbent by loosening the network form through surface hydrogen bonding [139]. Periodate oxidation has been applied for such modification to introduce aldehyde groups through oxidation of surface –OH groups and alteration of the carbon network of the glucopyranose ring [140]. These aldehyde groups of 2,3-dialdehyde cellulose can easily be converted further into various functional groups such as carboxylic acids, sulphonates or imines [87]. Liimatainen et al. [141,142] investigated the usage of anionic dialdehyde cellulose and cationic dialdehyde cellulose, derived via aqueous periodate oxidation. The study showed that anionic cellulose nanoparticles resulted in better flocculation performance of kaolin than that of cationic dialdehyde cellulose derivatives.

Another effective method to chemically modify nanocellulose to produce high charge material is by using TEMPO-mediated oxidation under aqueous and mild conditions. This method is suitable for the conversion of surface hydroxymethyl groups to their respective carboxylic forms [137]. The negatively charged groups on the surface of nanocellulose could prevent aggregation of nanocellulose via electrostatic repulsion. Chen et al. [143] reported that this electrosterically stabilized NCC can be produced by a three-step reaction: periodate, chlorite, and

Table 3: Application of cellulose-based flocculants in wastewater treatment.

Flocculant	Model pollutant	Analytical test	Optimum result (%)	Ref.
anionic sodium carboxymethylcellulose	natural surface water	turbidity	93	[70]
anionic dicarboxylic acid nanocellulose	municipal wastewater	turbidity COD	80 60	[58]
crystalline nanocellulose grafted with cationic pyridinium functional groups	freshwater microalgae	microalgae biomass	95	[71]
nanofibrillated into cationic nanocelluloses	activated sludge	turbidity COD	90 60	[53]
cationic dialdehyde cellulosic nanofibrils	kaolin wastewater	colloid aggregation	95	[60]
anionic sulphonated nanocelluloses	municipal wastewater	turbidity COD	80 60	[87]
hydroxypropyl methyl cellulose grafted with polyacrylamide	mine wastewater	turbidity	94	[57]
cationic pyridinium cellulose nanocrystals	microalgal biomass	flocculation efficiency	100	[63]
cationic cellulose nanofibrils	municipal activated sludge	turbidity COD	90 20–70	[53]
anionic carboxylated cellulose nanocrystals	kaolin suspension	turbidity	80.9	[59]
rod-shaped cellulose nanocrystals	flocculation and phase separation of bacteria	aggregation percentage	100	[69]
poly(*N*,*N*-dimethylacrylamide) and polyacrylamide grafted cellulose nanocrystals	kaolin suspension	turbidity	69–91	[72]

TEMPO oxidation. They claimed that periodate oxidation resulted in cellulose degradation. However, the cellulose degradation could be minimized by using less periodate oxidation and more TEMPO-mediated oxidation.

Many studies have focused on the modification of the physical and chemical structure to improve nanocellulose properties. For instance, Sun et al. [144] reported the effectiveness of applying CNCs to flocculate Gram negative bacteria (*Pseudomonas aeruginosa* PAO1). The study found that the flocculation efficiency based on the depletion of bacteria depended on the shape of the cellulose colloidal particles. In this case, rod-shaped particles (commonly found in CNC) could deplete larger colloids than spherical particles [145]. Besides, the introduction of cationic pyridinium and imidazole functional groups through grafting provided an advantage to CNCs over common polymer flocculants in terms of flocculation efficiency (flocculation of negatively charged microalgal cells) [138,139]. In short, researchers have been working to investigate various modifications of nanocellulose in order to broaden its industrial applications.

Nanocellulose-based membranes

In this section, the role of nanocellulose as a fabrication material in the field of membrane technology for environmental remediation will be discussed. Cellulose nanofibers and nanocrystals have been studied as membrane construction materials for wastewater treatment [146], gas separation [147], removal of dyes [148], removal of heavy metals through ion exchange [149], ultrafiltration [14,150], and adsorption [151]. The key information related to nanocellulose used in membrane technology for application in environmental remediation is summarized in Table 4.

Metalized nanocellulose composites (MNCs) used to construct the support of a forward osmosis membrane for wastewater treatment has been reported by Cruz-Tato et al. [146]. The nanocellulose was modified to incorporate amino silane functionalities before deposition of silver and platinum nanoparticles (Figure 4).

The fabricated MNC forward osmosis membrane performed better in terms of water flux when compared with a commercial HTI-CTA membrane. The total organic carbon rejection of the fabricated MNC membrane (94.6%) was found to be slightly lower than HTI-CTA (96.6%). On the other hand, Chitpong and Husson have prepared a high productivity, high capacity cation-exchange membrane for the removal of trace cadmium from water [149]. The performance of an ion exchange membrane in terms of cadmium binding capacity was found to be greatly influenced by the selection of grafting solvent. In other studies, Ansaloni and co-workers have taken the advantage of a unique feature of nanocellulose under humid conditions for carbon dioxide gas separation [147]. The gas separation membrane that

Table 4: Application of nanocellulose material in membrane technology for environmental remediation.

Membrane application	Cellulose type	Membrane fabrication feature	Membrane type	Operating condition	Membrane performance	Ref.
wastewater treatment (to remove urea)	nanocellulose	metalized nanocellulose composites–thin film composite membrane (MNC-TFC)	forward osmosis membrane	crossflow forward osmosis	water flux (LMH/bar): 1. urea: 7.4; wastewater: 11.8 2. urea: 5.4; wastewater: 11.5 (both membranes performed better than a commercial HTI-CTA membrane)	[146]
removal of heavy metals (ion exchange of Cd(II) ions)	cellulose nanofibers	regenerated cellulose nanofiber membrane with poly(glycidyl methacrylate) (PGMA) coating and poly(acrylic acid) (PAA) grafting using ethanol or/and water as grafting solvent	ion exchange membrane	dead-end filtration	maximum Cd binding capacity, Q_{max} (mg/g): 1. 40.0 2. 39.8 3. 162.5 4. 138.7	[149]
carbon dioxide capture	cellulose nanofibers	casting of pure microfibrillated cellulose membrane (MFC) and MFC–polyvinylamin (Lup) 50/50 wt/wt nanocompositemembrane	gas permeation membrane	gas permeation with constant humidity control; temperature, 35 °C; low pressure condition, 1 bar	selectivity: 1. CO_2/N_2 500; CO_2/CH_4 350 2. CO_2/N_2 35; CO_2/CH_4 20	[147]
removal of metal ions (removal of Ag^+, Cu^{2+} and Fe^{2+}/Fe^{3+} ions)	cellulose nanofibers; cellulose nanocrystals (cellulose sludge based (SL) and bioethanol based (BE)); phosphoryl group modified cellulose nanocrystal (PCNC), cellulose sludge based (SL)	support layer fabricated by vacuum filtration of cellulose nanofibers (CNF) and active layer fabricated by dip coating of cellulose nanocrystals (CNC) support layer fabricated by vacuum filtration of cellulose sludge (S-G) and active layer fabricated by further vacuum filtration of cellulose nanocrystals (CNC)	ultrafiltration membrane	crossflow filtration	removal (%): 1. 77% Ag^+, 94% Cu^{2+} and 95% Fe^{2+}/Fe^3 2. 91% Ag^+, 99% Cu^{2+} and 100% Fe^{2+}/Fe^3 3. 94% Ag^+, 99% Cu^{2+} and 100% Fe^{2+}/Fe^3 4. 100% Ag^+, 13% Cu^{2+} and 14% Fe^{2+}/Fe^3 5. 100% Ag^+, 36% Cu^{2+} and 33% Fe^{2+}/Fe^3 6. 100% Ag^+, 86% Cu^{2+} and 74% Fe^{2+}/Fe^3	[14,150]
adsorption of metal ions	cellulose nanofibers; cellulose nanocrystals (cellulose sludge based (SL) and bioethanol based (BE)); TEMPO functionalized nanocrystals (bioethanol based (BE))	support layer fabricated by vacuum filtration of cellulose sludge (S) or cellulose sludge with nanocellulose nanocrystal (SL) and active layer fabricated by further vacuum filtration of cellulose nanocrystals (CNC); in situ TEMPO functionalization on active layer	ultrafiltration membrane	crossflow filtration	adsorption capacity (mg/g): 1. 0.81 Ag^+, 250 Cu^{2+} and 384 Fe^{2+}/Fe^3 2. 0.83 Ag^+, 254 Cu^{2+} and 396 Fe^{2+}/Fe^3 3. 0.86 Ag^+, 339 Cu^{2+} and 416 Fe^{2+}/Fe^3 4. 0.87 Ag^+, 374 Cu^{2+} and 456 Fe^{2+}/Fe^3	[151]
removal of dyes	cellulose nanocrystals	casting of cellulose nanocrystals and chitosan solution	ultrafiltration membrane	dead-end filtration	removal (%): 1. 69–98% 2. 71–98%	[148]

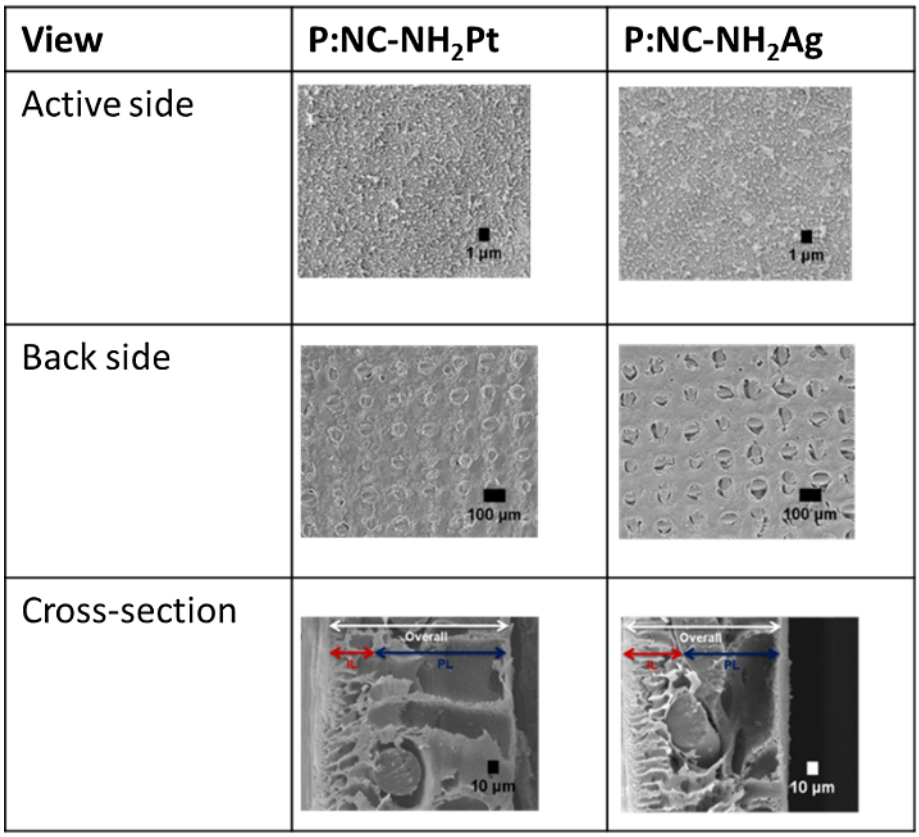

Figure 4: The morphology of MNC forward osmosis membranes with amino silane functionality as well as Pt and Ag nanoparticles. The ridge-and-valley morphology is commonly attributed to polyamide membranes. Reprinted (adapted) with permission from [146], copyright 2017 American Chemical Society.

was fabricated using pure MFC was found to be promising in terms of carbon dioxide selectivity (CO_2/N_2: 500; CO_2/CH_4: 350), especially when the controlled relative humidity is greater than 80%. The addition of polyvinylamin to pure MFC in the membrane construction improved the gas permeability consistency at a cost of selectivity (CO_2/N_2: 35; CO_2/CH_4: 20). According to Karim et al. [14], cellulose nanofibers can be used to fabricate a membrane through vacuum filtration with and without active layers of the membrane dip. The active layer membrane was prepared by coating both sides of the membrane surface with cellulose nanocrystals to form an ultrafiltration membrane for the removal of metal ions (Ag^+, Cu^{2+} and Fe^{2+}/Fe^{3+}). In this case, acetone treatment was effective in controlling the pore structure, mechanical properties, and permeability of the nanocellulose membrane. High metal ion rejection and flux were achieved using the membrane that underwent acetone treatment. A subsequent study led by Karim et al. demonstrated the fabrication of membranes using vacuum filtration of cellulose sludge followed by cellulose nanocrystals [150]. The change in the membrane fabrication method resulted in improved removal of Ag^+ with the with the consequence of reduced rejection performance of Fe^{2+}/Fe^{3+}. In situ TEMPO functionalization of the active layer of the nanocellulose membrane for the adsorption of metals ion was also reported by Karim et al. [151] as an innovative route to increase the membrane functionality without altering the bulk network structure. The metal ion adsorption ability, wettability, and negative surface zeta potential of the membrane was further enhanced after in situ TEMPO functionalization. In addition, the removal of positively charged dyes was reported using cellulose nanocrystals and chitosan through cross-linked and non-cross-linked treatment [148]. The mechanical stability, dimensional stability, and removal performance of the membrane has been further enhanced after the crosslinking process treatment.

As a construction material in the field of membrane technology for environmental remediation, nanocellulose is still at the development stage. To date, very limited literature is available and hence further study in this area is needed. This promising material could be used to replace or reduce the amount of non-renewable polymeric materials for membrane fabrication in the near future.

Challenges and limitations

Although nanocellulose appears as a promising material for environmental remediation, there are still many challenges and drawbacks affecting the application of this nanomaterial. To promote the commercialization and marketability of nanocellulose for environmental remediation, the application must be easily scalable, low cost, and produce valuable end-products [20]. So far, most investigations on nanocellulose production are only on a laboratory scale. The challenges lies in the scalability, environmental impact, and cost that come with the selection of treatment routes to produce nanocellulose. Several commonly used techniques related to mechanical disintegration are suitable for upscaling. However, these techniques are inclined toward high energy consumption. Although other mechanical techniques are being studied to overcome this issue, most are still in its infancy and considered not suitable for upscaling. As an alternative, biological and chemical pretreatment techniques were developed to tackle this issue. On the contrary, chemical pretreatment does not necessarily reduce the energy demand for nanocellulose production according to a life cycle study done by Arvidsson et al. [152]. The study showed that the carboxymethylation process (chemical pretreatment) exhibited a higher cumulative energy demand than the no pretreatment route (homogenization only) due to the high input of chemicals such as ethanol, isopropanol, and methanol for CNF production [152]. In this case, chemical pretreatment of nanocellulose could actually result in a higher environmental impact due to the presence of solvent waste and acidic waste although lower electricity usage is required [20]. Another challenge would be the questionable large-scale production of BC and ECNF, which is difficult due to the nature of their production (low yield). This is because BC and ECNF production depends on the build-up of nanofibers from low molecular weight sugars by bacteria and dissolved cellulose by electrospinning, respectively [32]. The production strategies of nanocellulose still require continuous examination to construct environmentally responsible and economically feasible nanocellulose.

Furthermore, the economic and regulatory hindrances due to the unclear toxicology of various modified nanocellulose materials for environmental remediation may be the greatest obstacle for its application and marketability. The environmental and biological toxicity of cellulose nanomaterial is of utmost importance when one considers its use in environmental remediation. Eco-toxicology studies on nanocellulose-based composites are still limited and are at a primary stage [153]. In general, the danger of nanoparticles increases with decreasing particle size when inhaled as the small size eases uptake into cells, blood, and lymph circulation to reach potentially sensitive target areas [154]. Although most nanocellulose-based materials are non- (or only slightly) toxic, there have been reports of negative effects on living cell viability and proliferation [155], especially at high concentrations. In addition, it was recently reported that CNC could induce cytotoxic and inflammatory effects on human lung cells, particularly upon inhalation exposure to CNC powders [156]. Furthermore, Yanamala et al. [157] discovered an inflammatory response in the lungs of mice after being exposed to wood-based CNC.

Conclusion

The discovery of cellulose nanomaterial is perceived as a milestone in the field of materials science and engineering. This is proven by the global attention which cellulose nanomaterials have received in various applications, including bio-based food packaging, optoelectronics, and tissue regeneration, to name a few. The large surface area, environmentally friendly nature (low toxicity and renewable), and functionality (easily functionalized) of nanocellulose makes it a potential candidate for environmental applications such as wastewater and water treatment as well as carbon sequestration as demonstrated in this review article. Taking the time to understand the challenges linked to its preparation and its significance as catalyst, membrane, and treatment agents may help in its development for environmental remediation. Nanocellulose-based nanocomposites have demonstrated many advantages suited for environmental remediation in terms of heavy metal removal, dye removal, carbon sequestration, and antimicrobial activity. The main challenges lies with the energy consumption and yield during the preparation stage as well as the toxicity of its end product. Synergistic effects were observed in integrated treatment methods for the preparation of nanocellulose. On the other hand, modification of nanocellulose improved its functionality for the removal of a wide range of target pollutants. Despite its advantages, further investigation should aim to implement improved treatment schemes to effectively extract nanocellulose and its functionality as agents for environmental remediation in terms of economic viability and its performance in the treatment of actual wastewater.

References

1. Khin, M. M.; Nair, A. S.; Babu, V. J.; Murugan, R.; Ramakrishna, S. *Energy Environ. Sci.* **2012,** *5,* 8075–8109. doi:10.1039/c2ee21818f
2. Ong, W.-J.; Tan, L.-L.; Ng, Y. H.; Yong, S.-T.; Chai, S.-P. *Chem. Rev.* **2016,** *116,* 7159–7329. doi:10.1021/acs.chemrev.6b00075
3. Zeng, D.; Ong, W.-J.; Chen, Y.; Tee, S. Y.; Chua, C. S.; Peng, D.-L.; Han, M.-Y. *Part. Part. Syst. Charact.* **2018,** *35,* 1870003. doi:10.1002/ppsc.201870003
4. Cringoli, M. C.; Kralj, S.; Kurbasic, M.; Urban, M.; Marchesan, S. *Beilstein J. Nanotechnol.* **2017,** *8,* 1553–1562. doi:10.3762/bjnano.8.157
5. Kumar, S.; Kumar, A.; Bahuguna, A.; Sharma, V.; Krishnan, V. *Beilstein J. Nanotechnol.* **2017,** *8,* 1571–1600. doi:10.3762/bjnano.8.159

6. Chen, P.; Li, N.; Chen, X.; Ong, W.-J.; Zhao, X. *2D Mater.* **2017,** *5,* 014002. doi:10.1088/2053-1583/aa8d37
7. Ma, T.; Fan, Q.; Tao, H.; Han, Z.; Jia, M.; Gao, Y.; Ma, W.; Sun, Z. *Nanotechnology* **2017,** *28,* 472001. doi:10.1088/1361-6528/aa8f6f
8. Lu, L.; Ozcan, S. *Nano Today* **2015,** *10,* 417–420. doi:10.1016/j.nantod.2015.04.010
9. Loow, Y.-L.; New, E. K.; Yang, G. H.; Ang, L. Y.; Foo, L. Y. W.; Wu, T. Y. *Cellulose* **2017,** *24,* 3591–3618. doi:10.1007/s10570-017-1358-y
10. Bhatnagar, A.; Sillanpää, M.; Witek-Krowiak, A. *Chem. Eng. J.* **2015,** *270,* 244–271. doi:10.1016/j.cej.2015.01.135
11. Mahfoudhi, N.; Boufi, S. *Cellulose* **2017,** *24,* 1171–1197. doi:10.1007/s10570-017-1194-0
12. Vartiainen, J.; Pöhler, T.; Sirola, K.; Pylkkänen, L.; Alenius, H.; Hokkinen, J.; Tapper, U.; Lahtinen, P.; Kapanen, A.; Putkisto, K.; Hiekkataipale, P.; Eronen, P.; Ruokolainen, J.; Laukkanen, A. *Cellulose* **2011,** *18,* 775–786. doi:10.1007/s10570-011-9501-7
13. Park, N.-M.; Koo, J. B.; Oh, J.-Y.; Kim, H. J.; Park, C. W.; Ahn, S.-D.; Jung, S. W. *Mater. Lett.* **2017,** *196,* 12–15. doi:10.1016/j.matlet.2017.03.003
14. Karim, Z.; Claudpierre, S.; Grahn, M.; Oksman, K.; Mathew, A. P. *J. Membr. Sci.* **2016,** *514,* 418–428. doi:10.1016/j.memsci.2016.05.018
15. Putro, J. N.; Kurniawan, A.; Ismadji, S.; Ju, Y.-H. *Environ. Nanotechnol. Monit. Manage.* **2017,** *8,* 134–149. doi:10.1016/j.enmm.2017.07.002
16. Liu, J.; Willför, S.; Mihranyan, A. *Carbohydr. Polym.* **2017,** *172,* 11–19. doi:10.1016/j.carbpol.2017.05.002
17. Du, X.; Zhang, Z.; Liu, W.; Deng, Y. *Nano Energy* **2017,** *35,* 299–320. doi:10.1016/j.nanoen.2017.04.001
18. Rånby, B. G. *Acta Chem. Scand.* **1949,** *3,* 649–650. doi:10.3891/acta.chem.scand.03-0649
19. Turbak, A. F.; Snyder, F. W.; Sandberg, K. R. Microfibrillated cellulose: A new cellulose product: properties, uses, and commercial potential. In *Journal of Applied Polymer Science: Applied Polymer Symposium,* Ninth International Cellulose Conference, Syracuse, NY, May 24, 1982; Wiley: NY, 1983.
20. Carpenter, A. W.; de Lannoy, C.-F.; Wiesner, M. R. *Environ. Sci. Technol.* **2015,** *49,* 5277–5287. doi:10.1021/es506351r
21. Voisin, H.; Bergström, L.; Liu, P.; Mathew, A. *Nanomaterials* **2017,** *7,* 1–18. doi:10.3390/nano7030057
22. Liu, H.; Geng, B.; Chen, Y.; Wang, H. *ACS Sustainable Chem. Eng.* **2016,** *5,* 49–66. doi:10.1021/acssuschemeng.6b02301
23. Maleki, H. *Chem. Eng. J.* **2016,** *300,* 98–118. doi:10.1016/j.cej.2016.04.098
24. Kargarzadeh, H.; Ioelovich, M.; Ahmad, I.; Thomas, S.; Dufresne, A. Methods for Extraction of Nanocellulose from Various Sources. In *Handbook of Nanocellulose and Cellulose Nanocomposites;* Kargarzedeh, H.; Ahmad, I.; Thomas, S.; Dufresne, A., Eds.; Wiley-VCH: Weinheim, Germany, 2017; pp 1–49. doi:10.1002/9783527689972.ch1
25. Huang, L.; Zhang, X.; Xu, M.; Chen, J.; Shi, Y.; Huang, C.; Wang, S.; An, S.; Li, C. *AIP Adv.* **2018,** *8,* 025116. doi:10.1063/1.5023278
26. Nguyen, H. D.; Mai, T. T. T.; Nguyen, N. B.; Dang, T. D.; Le, M. L. P.; Dang, T. T.; Tran, V. M. *Adv. Nat. Sci.: Nanosci. Nanotechnol.* **2013,** *4,* 015016. doi:10.1088/2043-6262/4/1/015016
27. Razalli, R. L.; Abdi, M. M.; Tahir, P. M.; Moradbak, A.; Sulaiman, Y.; Heng, L. Y. *RSC Adv.* **2017,** *7,* 25191–25198. doi:10.1039/C7RA03379F
28. Kunusa, W. R.; Isa, I.; Laliyo, L. A. R.; Iyabu, H. *J. Phys.: Conf. Ser.* **2018,** *1028,* 012199. doi:10.1088/1742-6596/1028/1/012199
29. Kaushik, M.; Moores, A. *Green Chem.* **2016,** *18,* 622–637. doi:10.1039/C5GC02500A
30. Yuwawech, K.; Wootthikanokkhan, J.; Tanpichai, S. *J. Nanomater.* **2015,** *2015,* No. 908689. doi:10.1155/2015/908689
31. Gama, M.; Gatenholm, P.; Klemm, D. *Bacterial Nanocellulose: A Sophisticated Multifunctional Material;* CRC Press: Boca Raton, Florida, 2017.
32. Nechyporchuk, O.; Belgacem, M. N.; Bras, J. *Ind. Crops Prod.* **2016,** *93,* 2–25. doi:10.1016/j.indcrop.2016.02.016
33. García, A.; Gandini, A.; Labidi, J.; Belgacem, N.; Bras, J. *Ind. Crops Prod.* **2016,** *93,* 26–38. doi:10.1016/j.indcrop.2016.06.004
34. Missoum, K.; Belgacem, M. N.; Bras, J. *Materials* **2013,** *6,* 1745–1766. doi:10.3390/ma6051745
35. Smyth, M.; Fournier, C.; Driemeier, C.; Picart, C.; Foster, E. J.; Bras, J. *Biomacromolecules* **2017,** *18,* 2034–2044. doi:10.1021/acs.biomac.7b00209
36. Rosa, M. F.; Medeiros, E. S.; Malmonge, J. A.; Gregorski, K. S.; Wood, D. F.; Mattoso, L. H. C.; Glenn, G.; Orts, W. J.; Imam, S. H. *Carbohydr. Polym.* **2010,** *81,* 83–92. doi:10.1016/j.carbpol.2010.01.059
37. Huang, X.; Wang, J.; Li, T.; Wang, J.; Xu, M.; Yu, W.; El Abed, A.; Zhang, X. *Beilstein J. Nanotechnol.* **2018,** *9,* 30–41. doi:10.3762/bjnano.9.5
38. Nicolai, E.; Preston, R. D. *Proc. R. Soc. London, Ser. B* **1952,** *140,* 244–274. doi:10.1098/rspb.1952.0061
39. Mihranyan, A. *J. Appl. Polym. Sci.* **2011,** *119,* 2449–2460. doi:10.1002/app.32959
40. Metreveli, G.; Wågberg, L.; Emmoth, E.; Belák, S.; Strømme, M.; Mihranyan, A. *Adv. Healthcare Mater.* **2014,** *3,* 1546–1550. doi:10.1002/adhm.201300641
41. Ruan, C.; Strømme, M.; Jonas, L. *Cellulose* **2016,** *23,* 2627–2638. doi:10.1007/s10570-016-0976-0
42. El-Safty, S. A.; Shenashen, M. A.; Sakai, M.; Elshehy, E.; Halada, K. *J. Visualized Exp.* **2015,** e53044. doi:10.3791/53044
43. Is algae the next super material? Bacteria used to create substance that could make everything from armour to phone screens. http://www.dailymail.co.uk/sciencetech/article-2307582/Is-algae-super-material-Bacteria-used-create-substance-make-armour-phone-screens.html (accessed Sept 12, 2016).
44. Uzyol, H. K.; Saçan, M. T. *Environ. Sci. Pollut. Res.* **2017,** *24,* 11154–11162. doi:10.1007/s11356-016-7049-7
45. Gatenholm, P.; Klemm, D. *MRS Bull.* **2010,** *35,* 208–213. doi:10.1557/mrs2010.653
46. Jonas, R.; Farah, L. *Polym. Degrad. Stab.* **1998,** *59,* 101–106. doi:10.1016/S0141-3910(97)00197-3
47. Chen, S.; Zou, Y.; Yan, Z.; Shen, W.; Shi, S.; Zhang, X.; Wang, H. *J. Hazard. Mater.* **2009,** *161,* 1355–1359. doi:10.1016/j.jhazmat.2008.04.098
48. Leitch, M. E.; Li, C.; Ikkala, O.; Mauter, M. S.; Lowry, G. V. *Environ. Sci. Technol. Lett.* **2016,** *3,* 85–91. doi:10.1021/acs.estlett.6b00030
49. Jozala, A. F.; de Lencastre-Novaes, L. C.; Lopes, A. M.; de Carvalho Santos-Ebinuma, V.; Mazzola, P. G.; Pessoa, A., Jr.; Grotto, D.; Gerenutti, M.; Chaud, M. V. *Appl. Microbiol. Biotechnol.* **2016,** *100,* 2063–2072. doi:10.1007/s00253-015-7243-4
50. Chirayil, C. J.; Mathew, L.; Thomas, S. *Rev. Adv. Mater. Sci.* **2014,** *37,* 20–28.

51. Menon, M. P.; Selvakumar, R.; Kumar, P. S.; Ramakrishna, S. *RSC Adv.* **2017,** *7,* 42750–42773. doi:10.1039/C7RA06713E
52. Lin, X. B.; Wu, M.; Wu, D. Y.; Kuga, S.; Endo, T.; Huang, Y. *Green Chem.* **2011,** *13,* 283–287. doi:10.1039/C0GC00513D
53. Wang, R.; Guan, S.; Sato, A.; Wang, X.; Wang, Z.; Yang, R.; Hsiao, B. S.; Chu, B. *J. Membr. Sci.* **2013,** *446,* 376–382. doi:10.1016/j.memsci.2013.06.020
54. Suopajärvi, T.; Liimatainen, H.; Hormi, O.; Niinimäki, J. *Chem. Eng. J.* **2013,** *231,* 59–67. doi:10.1016/j.cej.2013.07.010
55. Taleb, K. A.; Rusmirović, J. D.; Rančić, M. P.; Nikolić, J. B.; Drmanić, S. Ž.; Veličković, Z. S.; Marinković, A. D. *J. Serb. Chem. Soc.* **2016,** *81,* S316–S323. doi:10.2298/JSC160529063T
56. Elazzouzi-Hafraoui, S.; Nishiyama, Y.; Putaux, J.-L.; Heux, L.; Dubreuil, F.; Rochas, C. *Biomacromolecules* **2008,** *9,* 57–65. doi:10.1021/bm700769p
57. Iwamoto, S.; Isogai, A.; Iwata, T. *Biomacromolecules* **2011,** *12,* 831–836. doi:10.1021/bm101510r
58. Kimura, S.; Itoh, T. *Protoplasma* **1996,** *194,* 151–163. doi:10.1007/BF01882023
59. Cheng, Q.; Ye, D.; Chang, C.; Zhang, L. *J. Membr. Sci.* **2017,** *525,* 1–8. doi:10.1016/j.memsci.2016.11.084
60. Wei, H.; Rodriguez, K.; Renneckar, S.; Vikesland, P. J. *Environ. Sci.: Nano* **2014,** *1,* 302–316. doi:10.1039/C4EN00059E
61. Yu, S. I.; Min, S. K.; Shin, H. S. *Sci. Rep.* **2016,** *6,* No. 35684. doi:10.1038/srep35684
62. Rajinipriya, M.; Nagalakshmaiah, M.; Robert, M.; Elkoun, S. *ACS Sustainable Chem. Eng.* **2018,** *6,* 2807–2828. doi:10.1021/acssuschemeng.7b03437
63. Abdul Khalil, H. P. S.; Davoudpour, Y.; Islam, M. N.; Mustapha, A.; Sudesh, K.; Dungani, R.; Jawaid, M. *Carbohydr. Polym.* **2014,** *99,* 649–665. doi:10.1016/j.carbpol.2013.08.069
64. Nair, S. S.; Zhu, J. Y.; Deng, Y.; Ragauskas, A. J. *J. Nanopart. Res.* **2014,** *16,* 2349. doi:10.1007/s11051-014-2349-7
65. He, M.; Yang, G.; Chen, J.; Ji, X.; Wang, Q. *J. Wood Chem. Technol.* **2018,** *38,* 149–158. doi:10.1080/02773813.2017.1411368
66. Sacui, I. A.; Nieuwendaal, R. C.; Burnett, D. J.; Stranick, S. J.; Jorfi, M.; Weder, C.; Foster, E. J.; Olsson, R. T.; Gilman, J. W. *ACS Appl. Mater. Interfaces* **2014,** *6,* 6127–6138. doi:10.1021/am500359f
67. Park, C.-W.; Han, S.-Y.; Namgung, H.-W.; Seo, P.-n.; Lee, S.-Y.; Lee, S.-H. *BioResources* **2017,** *12,* 5031–5044. doi:10.15376/biores.12.3.5031-5044
68. Fan, M.; Dai, D.; Yang, A. *Int. J. Polym. Mater.* **2011,** *60,* 1026–1040. doi:10.1080/00914037.2010.551347
69. Vanderfleet, O. M.; Osorio, D. A.; Cranston, E. D. *Philos. Trans. R. Soc., A* **2018,** *376,* 20170041. doi:10.1098/rsta.2017.0041
70. Sharma, P. R.; Cattopadhyay, A.; Sharma, S. K.; Geng, L.; Amiralian, N.; Martin, D.; Hsiao, B. S. *ACS Sustainable Chem. Eng.* **2018,** *6,* 3279–3290. doi:10.1021/acssuschemeng.7b03473
71. Onyianta, A. J.; Dorris, M.; Williams, R. L. *Cellulose* **2018,** *25,* 1047–1064. doi:10.1007/s10570-017-1631-0
72. dos Santos, D. M.; Leite, I. S.; de Lacerda Bukzem, A.; de Oliveira Santos, R. P.; Frollini, E.; Inada, N. M.; Campana-Filho, S. P. *Carbohydr. Polym.* **2018,** *186,* 110–121. doi:10.1016/j.carbpol.2018.01.045
73. Rocha, I.; Ferraz, N.; Mihranyan, A.; Strømme, M.; Lindh, J. *Cellulose* **2018,** *25,* 1899–1910. doi:10.1007/s10570-018-1661-2
74. Ninomiya, K.; Abe, M.; Tsukegi, T.; Kuroda, K.; Tsuge, Y.; Ogino, C.; Taki, K.; Taima, T.; Saito, J.; Kimizu, M.; Uzawa, K.; Takahashi, K. *Carbohydr. Polym.* **2018,** *182,* 8–14. doi:10.1016/j.carbpol.2017.11.003
75. Laitinen, O.; Suopajärvi, T.; Österberg, M.; Liimatainen, H. *ACS Appl. Mater. Interfaces* **2017,** *9,* 25029–25037. doi:10.1021/acsami.7b06304
76. Liu, P.; Sehaqui, H.; Tingaut, P.; Wichser, A.; Oksman, K.; Mathew, A. P. *Cellulose* **2014,** *21,* 449–461. doi:10.1007/s10570-013-0139-5
77. Börjesson, M.; Westman, G. Crystalline Nanocellulose – Preparation, Modification, and Properties. In *Cellulose – Fundamental Aspects and Current Trends;* Poletto, M., Ed.; IntechOpen, 2015. doi:10.5772/61899
78. Wågberg, L.; Decher, G.; Norgren, M.; Lindström, T.; Ankerfors, M.; Axnäs, K. *Langmuir* **2008,** *24,* 784–795. doi:10.1021/la702481v
79. Liimatainen, H.; Suopajärvi, T.; Sirviö, J.; Hormi, O.; Niinimäki, J. *Carbohydr. Polym.* **2014,** *103,* 187–192. doi:10.1016/j.carbpol.2013.12.042
80. Tan, X. Y.; Abd Hamid, S. B.; Lai, C. W. *Biomass Bioenergy* **2015,** *81,* 584–591. doi:10.1016/j.biombioe.2015.08.016
81. Pääkkö, M.; Ankerfors, M.; Kosonen, H.; Nykänen, A.; Ahola, S.; Österberg, M.; Ruokolainen, J.; Laine, J.; Larsson, P. T.; Ikkala, O.; Lindström, T. *Biomacromolecules* **2007,** *8,* 1934–1941. doi:10.1021/bm061215p
82. Henriksson, M.; Henriksson, G.; Berglund, L.; Lindström, T. *Eur. Polym. J.* **2007,** *43,* 3434–3441. doi:10.1016/j.eurpolymj.2007.05.038
83. Beltramino, F.; Roncero, M. B.; Vidal, T.; Torres, A. L.; Valls, C. *Bioresour. Technol.* **2015,** *192,* 574–581. doi:10.1016/j.biortech.2015.06.007
84. Hideno, A.; Abe, K.; Yano, H. *J. Food Sci.* **2014,** *79,* N1218–N1224. doi:10.1111/1750-3841.12471
85. Tibolla, H.; Pelissari, F. M.; Menegalli, F. C. *LWT-Food Sci. Technol.* **2014,** *59,* 1311–1318. doi:10.1016/j.lwt.2014.04.011
86. Hu, J.; Tian, D.; Renneckar, S.; Saddler, J. N. *Sci. Rep.* **2018,** *8,* 3195. doi:10.1038/s41598-018-21016-6
87. Suopajärvi, T.; Koivuranta, E.; Liimatainen, H.; Niinimäki, J. *J. Environ. Chem. Eng.* **2014,** *2,* 2005–2012. doi:10.1016/j.jece.2014.08.023
88. Hokkanen, S.; Bhatnagar, A.; Repo, E.; Lou, S.; Sillanpää, M. *Chem. Eng. J.* **2016,** *283,* 445–452. doi:10.1016/j.cej.2015.07.035
89. Sun, X.; Yang, L.; Li, Q.; Zhao, J.; Li, X.; Wang, X.; Liu, H. *Chem. Eng. J.* **2014,** *241,* 175–183. doi:10.1016/j.cej.2013.12.051
90. Hokkanen, S.; Repo, E.; Suopajärvi, T.; Liimatainen, H.; Niinimaa, J.; Sillanpää, M. *Cellulose* **2014,** *21,* 1471–1487. doi:10.1007/s10570-014-0240-4
91. Niu, Y.; Li, K.; Ying, D.; Wang, Y.; Jia, J. *Bioresour. Technol.* **2017,** *229,* 63–68. doi:10.1016/j.biortech.2017.01.007
92. Anirudhan, T. S.; Deepa, J. R.; Christa, J. *J. Colloid Interface Sci.* **2016,** *467,* 307–320. doi:10.1016/j.jcis.2016.01.023
93. Anirudhan, T. S.; Deepa, J. R.; Binusreejayan. *Chem. Eng. J.* **2015,** *273,* 390–400. doi:10.1016/j.cej.2015.03.007
94. Jiao, C.; Tao, J.; Xiong, J.; Wang, X.; Zhang, D.; Lin, H.; Chen, Y. *Cellulose* **2017,** *24,* 2591–2604. doi:10.1007/s10570-017-1271-4
95. Dong, C.; Zhang, F.; Pang, Z.; Yang, G. *Carbohydr. Polym.* **2016,** *151,* 230–236. doi:10.1016/j.carbpol.2016.05.066
96. Suopajärvi, T.; Liimatainen, H.; Karjalainen, M.; Upola, H.; Niinimäki, J. *J. Water Process Eng.* **2015,** *5,* 136–142. doi:10.1016/j.jwpe.2014.06.003

97. Sehaqui, H.; Mautner, A.; Perez De Larraya, U.; Pfenninger, N.; Tingaut, P.; Zimmermann, T. *Carbohydr. Polym.* **2016,** *135,* 334–340. doi:10.1016/j.carbpol.2015.08.091
98. Taleb, K.; Markovski, J.; Veličković, Z.; Rusmirović, J.; Rančić, M.; Pavlović, V.; Marinković, A. *Arabian J. Chem.* **2016,** in press. doi:10.1016/j.arabjc.2016.08.006
99. Beyki, M. H.; Bayat, M.; Shemirani, F. *Bioresour. Technol.* **2016,** *218,* 326–334. doi:10.1016/j.biortech.2016.06.069
100. Jin, L.; Li, W.; Xu, Q.; Sun, Q. *Cellulose* **2015,** *22,* 2443–2456. doi:10.1007/s10570-015-0649-4
101. Qiao, H.; Zhou, Y.; Yu, F.; Wang, E.; Min, Y.; Huang, Q.; Pang, L.; Ma, T. *Chemosphere* **2015,** *141,* 297–303. doi:10.1016/j.chemosphere.2015.07.078
102. Zhu, W.; Liu, L.; Liao, Q.; Chen, X.; Qian, Z.; Shen, J.; Liang, J.; Yao, J. *Cellulose* **2016,** *23,* 3785–3797. doi:10.1007/s10570-016-1045-4
103. Mohammed, N.; Grishkewich, N.; Waeijen, H. A.; Berry, R. M.; Tam, K. C. *Carbohydr. Polym.* **2016,** *136,* 1194–1202. doi:10.1016/j.carbpol.2015.09.099
104. Maatar, W.; Boufi, S. *Cellulose* **2017,** *24,* 1001–1015. doi:10.1007/s10570-016-1162-0
105. Anirudhan, T. S.; Rejeena, S. R. *J. Colloid Interface Sci.* **2012,** *381,* 125–136. doi:10.1016/j.jcis.2012.05.024
106. Olivera, S.; Muralidhara, H. B.; Venkatesh, K.; Guna, V. K.; Gopalakrishna, K.; Kumar K, Y. *Carbohydr. Polym.* **2016,** *153,* 600–618. doi:10.1016/j.carbpol.2016.08.017
107. Li, Y.; Cao, L.; Li, L.; Yang, C. *J. Hazard. Mater.* **2015,** *289,* 140–148. doi:10.1016/j.jhazmat.2015.02.051
108. Dong, C.; Zhang, H.; Pang, Z.; Liu, Y.; Zhang, F. *Bioresour. Technol.* **2013,** *146,* 512–518. doi:10.1016/j.biortech.2013.07.108
109. Yang, J.; Yu, J.; Fan, J.; Sun, D.; Tang, W.; Yang, X. *J. Hazard. Mater.* **2011,** *189,* 377–383. doi:10.1016/j.jhazmat.2011.02.048
110. Gao, M.; Li, N.; Lu, W.; Chen, W. *Appl. Catal., B* **2014,** *147,* 805–812. doi:10.1016/j.apcatb.2013.10.015
111. Zeng, J.; Liu, S.; Cai, J.; Zhang, L. *J. Phys. Chem. C* **2010,** *114,* 7806–7811. doi:10.1021/jp1005617
112. Thomas, M.; Natarajan, T. S.; Sheikh, M. U. D.; Bano, M.; Khan, F. *J. Photochem. Photobiol., A* **2017,** *346,* 113–125. doi:10.1016/j.jphotochem.2017.05.037
113. Anirudhan, T. S.; Deepa, J. R. *J. Colloid Interface Sci.* **2017,** *490,* 343–356. doi:10.1016/j.jcis.2016.11.042
114. Lefatshe, K.; Muiva, C. M.; Kebaabetswe, L. P. *Carbohydr. Polym.* **2017,** *164,* 301–308. doi:10.1016/j.carbpol.2017.02.020
115. Chen, P.; Liu, X.; Jin, R.; Nie, W.; Zhou, Y. *Carbohydr. Polym.* **2017,** *167,* 36–43. doi:10.1016/j.carbpol.2017.02.094
116. Nsib, M. F.; Hajji, F.; Mayoufi, A.; Moussa, N.; Rayes, A.; Houas, A. *C. R. Chim.* **2014,** *17,* 839–848. doi:10.1016/j.crci.2014.01.010
117. Liu, L.-P.; Yang, X.-N.; Ye, L.; Xue, D.-D.; Liu, M.; Jia, S.-R.; Hou, Y.; Chu, L.-Q.; Zhong, C. *Carbohydr. Polym.* **2017,** *174,* 1078–1086. doi:10.1016/j.carbpol.2017.07.042
118. Thomas, M.; Naikoo, G. A.; Sheikh, M. U. D.; Bano, M.; Khan, F. *J. Photochem. Photobiol., A* **2016,** *327,* 33–43. doi:10.1016/j.jphotochem.2016.05.005
119. Dong, P.; Cheng, X.; Huang, Z.; Chen, Y.; Zhang, Y.; Nie, X.; Zhang, X. *Mater. Res. Bull.* **2018,** *97,* 89–95. doi:10.1016/j.materresbull.2017.08.036
120. Tu, K.; Wang, Q.; Lu, A.; Zhang, L. *J. Phys. Chem. C* **2014,** *118,* 7202–7210. doi:10.1021/jp412802h
121. Mohamed, M. A.; Salleh, W. N. W.; Jaafar, J.; Ismail, A. F.; Abd Mutalib, M.; Jamil, S. M. *Carbohydr. Polym.* **2015,** *133,* 429–437. doi:10.1016/j.carbpol.2015.07.057
122. Zhou, Z.; Peng, X.; Zhong, L.; Wu, L.; Cao, X.; Sun, R. C. *Carbohydr. Polym.* **2016,** *136,* 322–328. doi:10.1016/j.carbpol.2015.09.009
123. Li, G.; Nandgaonkar, A. G.; Wang, Q.; Zhang, J.; Krause, W. E.; Wei, Q.; Lucia, L. A. *J. Membr. Sci.* **2017,** *525,* 89–98. doi:10.1016/j.memsci.2016.10.033
124. Pastrana-Martínez, L. M.; Morales-Torres, S.; Figueiredo, J. L.; Faria, J. L.; Silva, A. M. T. *Water Res.* **2015,** *77,* 179–190. doi:10.1016/j.watres.2015.03.014
125. An, X.; Wen, Y.; Almujil, A.; Cheng, D.; Li, J.; Jia, X.; Zou, J.; Ni, Y. *RSC Adv.* **2016,** *6,* 89457–89466. doi:10.1039/C6RA21042B
126. Taranto, J.; Frochot, D.; Pichat, P. *Sep. Purif. Technol.* **2009,** *67,* 187–193. doi:10.1016/j.seppur.2009.03.017
127. Puls, J.; Wilson, S. A.; Hölter, D. *J. Polym. Environ.* **2011,** *19,* 152–165. doi:10.1007/s10924-010-0258-0
128. Cheng, F.; Lorch, M.; Sajedin, S. M.; Kelly, S. M.; Kornherr, A. *ChemSusChem* **2013,** *6,* 1392–1399. doi:10.1002/cssc.201300305
129. An, X.; Cheng, D.; Dai, L.; Wang, B.; Ocampo, H. J.; Nasrallah, J.; Jia, X.; Zou, J.; Long, Y.; Ni, Y. *Appl. Catal., B* **2017,** *206,* 53–64. doi:10.1016/j.apcatb.2017.01.021
130. Ke, D.; Liu, S.; Dai, K.; Zhou, J.; Zhang, L.; Peng, T. *J. Phys. Chem. C* **2009,** *113,* 16021–16026. doi:10.1021/jp903378q
131. Suopajärvi, T.; Sirviö, J. A.; Liimatainen, H. *J. Environ. Chem. Eng.* **2017,** *5,* 86–92. doi:10.1016/j.jece.2016.11.021
132. Van Haver, L.; Nayar, S. *Algal Res.* **2017,** *24,* 167–180. doi:10.1016/j.algal.2017.03.022
133. Zhu, H.; Zhang, Y.; Yang, X.; Liu, H.; Shao, L.; Zhang, X.; Yao, J. *J. Hazard. Mater.* **2015,** *296,* 1–8. doi:10.1016/j.jhazmat.2015.04.029
134. Das, R.; Ghorai, S.; Pal, S. *Chem. Eng. J.* **2013,** *229,* 144–152. doi:10.1016/j.cej.2013.05.104
135. Yu, H. Y.; Zhang, D. Z.; Lu, F. F.; Yao, J. *ACS Sustainable Chem. Eng.* **2016,** *4,* 2632–2643. doi:10.1021/acssuschemeng.6b00126
136. Kono, H. *Resour.-Effic. Technol.* **2017,** *3,* 55–63. doi:10.1016/j.reffit.2016.11.015
137. Habibi, Y.; Lucia, L. A.; Rojas, O. J. *Chem. Rev.* **2010,** *110,* 3479–3500. doi:10.1021/cr900339w
138. Eyley, S.; Vandamme, D.; Lama, S.; Van Den Mooter, G.; Muylaert, K.; Thielemans, W. *Nanoscale* **2015,** *7,* 14413–14421. doi:10.1039/C5NR03853G
139. Vandamme, D.; Eyley, S.; Van den Mooter, G.; Muylaert, K.; Thielemans, W. *Bioresour. Technol.* **2015,** *194,* 270–275. doi:10.1016/j.biortech.2015.07.039
140. Hartmann, R.; Sirviö, J. A.; Sliz, R.; Laitinen, O.; Liimatainen, H.; Ämmälä, A.; Fabritius, T.; Illikainen, M. *Colloids Surf., A* **2016,** *489,* 207–215. doi:10.1016/j.colsurfa.2015.10.022
141. Liimatainen, H.; Sirviö, J.; Sundman, O.; Hormi, O.; Niinimäki, J. *Water Res.* **2012,** *46,* 2159–2166. doi:10.1016/j.watres.2012.01.035
142. Liimatainen, H.; Sirviö, J.; Sundman, O.; Visanko, M.; Hormi, O.; Niinimäki, J. *Bioresour. Technol.* **2011,** *102,* 9626–9632. doi:10.1016/j.biortech.2011.07.099
143. Chen, D.; van de Ven, T. G. M. *Colloids Surf., A* **2016,** *504,* 11–17. doi:10.1016/j.colsurfa.2016.05.023
144. Sun, X.; Danumah, C.; Liu, Y.; Boluk, Y. *Chem. Eng. J.* **2012,** *198–199,* 476–481. doi:10.1016/j.cej.2012.05.114

145. Grishkewich, N.; Mohammed, N.; Tang, J.; Tam, K. C. *Curr. Opin. Colloid Interface Sci.* **2017,** *29,* 32–45. doi:10.1016/j.cocis.2017.01.005
146. Cruz-Tato, P.; Ortiz-Quiles, E. O.; Vega-Figueroa, K.; Santiago-Martoral, L.; Flynn, M.; Díaz-Vázquez, L. M.; Nicolau, E. *Environ. Sci. Technol.* **2017,** *51,* 4585–4595. doi:10.1021/acs.est.6b05955
147. Ansaloni, L.; Salas-Gay, J.; Ligi, S.; Baschetti, M. G. *J. Membr. Sci.* **2017,** *522,* 216–225. doi:10.1016/j.memsci.2016.09.024
148. Karim, Z.; Mathew, A. P.; Grahn, M.; Mouzon, J.; Oksman, K. *Carbohydr. Polym.* **2014,** *112,* 668–676. doi:10.1016/j.carbpol.2014.06.048
149. Chitpong, N.; Husson, S. M. *J. Membr. Sci.* **2017,** *523,* 418–429. doi:10.1016/j.memsci.2016.10.020
150. Karim, Z.; Mathew, A. P.; Kokol, V.; Wei, J.; Grahn, M. *RSC Adv.* **2016,** *6,* 20644–20653. doi:10.1039/C5RA27059F
151. Karim, Z.; Hakalahti, M.; Tammelin, T.; Mathew, A. P. *RSC Adv.* **2017,** *7,* 5232–5241. doi:10.1039/C6RA25707K
152. Arvidsson, R.; Nguyen, D.; Svanström, M. *Environ. Sci. Technol.* **2015,** *49,* 6881–6890. doi:10.1021/acs.est.5b00888
153. Lin, N.; Dufresne, A. *Eur. Polym. J.* **2014,** *59,* 302–325. doi:10.1016/j.eurpolymj.2014.07.025
154. Oberdörster, G.; Oberdörster, E.; Oberdörster, J. *Environ. Health Perspect.* **2005,** *113,* 823–839. doi:10.1289/ehp.7339
155. Alexandrescu, L.; Syverud, K.; Gatti, A.; Chinga-Carrasco, G. *Cellulose* **2013,** *20,* 1765–1775. doi:10.1007/s10570-013-9948-9
156. Clift, M. J. D.; Foster, E. J.; Vanhecke, D.; Studer, D.; Wick, P.; Gehr, P.; Rothen-Rutishauser, B.; Weder, C. *Biomacromolecules* **2011,** *12,* 3666–3673. doi:10.1021/bm200865j
157. Yanamala, N.; Farcas, M. T.; Hatfield, M. K.; Kisin, E. R.; Kagan, V. E.; Geraci, C. L.; Shvedova, A. A. *ACS Sustainable Chem. Eng.* **2014,** *2,* 1691–1698. doi:10.1021/sc500153k

License and Terms

This is an Open Access article under the terms of the Creative Commons Attribution License (http://creativecommons.org/licenses/by/4.0). Please note that the reuse, redistribution and reproduction in particular requires that the authors and source are credited.

The license is subject to the *Beilstein Journal of Nanotechnology* terms and conditions: (https://www.beilstein-journals.org/bjnano)

The definitive version of this article is the electronic one which can be found at:
doi:10.3762/bjnano.9.232